

61st ICFA Advanced Beam Dynamics Workshop
on High-Intensity and High-Brightness Hadron Beams

HB2018

2018, June 18~22

Institute for Basic Science (IBS), Daejeon, KOREA



Working Groups

- Beam Dynamics in Rings
- Beam Dynamics in Linacs
- Accelerator Systems
- Commissioning and Operations
- Diagnostics, Instrumentation and Beam Interactions

Register



hb2018.ibs.re.kr

Deadlines

- Abstract submission : 2018 February 16
- Early registration : 2018 April 13
- Paper submission : 2018 June 13



61st IFA Advanced Beam Dynamics Workshop on
High-Energy and High-Brightness Electron Beams

HB2018 Workshop

June 11-21, 2018

IBS Science Center Center, Gyeongju, Korea

sponsored by

supported by



QUANTA

TECHNOLOGIES

PROGRAMS



Welcome to the HB2018

Welcome to the 61st ICFA Advanced Beam Dynamics Workshop on High-Intensity and High-Brightness Hadron Beams.

It is a great pleasure to have the HB2018 workshop first time in Korea. It is a very nice time to host the HB2018 workshop at the Institute for Basic Science, as the construction of the RAON heavy ion accelerator facility is currently underway.

The construction of the Spallation Neutron Source that started in the year of 1998 presented urgent needs to further the understanding of space-charge mechanisms and the beam loss. And the HB workshop series was conceived in the ICFA (International Committee for Future Accelerators) ABDW (Advanced Beam Dynamics Workshops). The 1st HB workshop was held in the year of 2002 at the Fermilab in the United States. And since then the HB workshop has become the main international event for the high-intensity hadron beam accelerator community.

At the time of the 1st HB workshop, the highest power accelerator had about 0.1 MW beam power. Since then, brilliant progresses have been made. Now the Spallation Neutron Source reached its design power of 1.4 MW and is striving for power-upgrade. The J-PARC reached 0.5 MW and is ramping up the beam power. The beam power of the European Spallation Source is 5 MW which is under construction and the beam power of the IFMIF is 10 MW.

The HB starts with the Monday morning plenary session, followed by two parallel sessions. Also there is one plenary session in Wednesday morning and the poster session in Wednesday afternoon. The HB consists of five working groups: Beam Dynamics in Rings (WG-A), Beam Dynamics in Linacs (WG-B), Accelerator Systems (WG-C), Commissioning and Operations (WG-D) and Beam Instruments and Interactions (WG-E).

The program of the HB is set by the International Organizing Committee (IOC), which selects the plenary speaker and working group conveners. The invited oral programs are formulated by each working groups and approved by the IOC. These committees have done an excellent work in setting up the scientific program.

Daejeon is known as the science city of Korea and is a home to majority of thenational laboratories and several prestigious universities. Daejeon has a population of 1.5-million people and has a rich culture. We hope that you all enjoy the HB2018 workshop and your stay in Daejeon.

Dong-O Jeon
HB2018 Chairman

International Organizing Committee (IOC)

Alex Chao	SLAC	USA
Jia-er Chen	Peking University	China
Yong Ho Chin	KEK	Japan
Sarah Cousineau	ORNL	USA
Mohammad Eshraqi	ESS	Sweden
Shinian Fu	IHEP	China
Simone Gilardoni	CERN	Switzerland
Ingo Hofmann	GSI	Germany
Hideaki Hotchi	JAEA	Japan
Sergey Ivanov	IHEP	Russia
Ji-Ho Jang	IBS	Korea
Dong-O Jeon	IBS	Korea
In Soo Ko	POSTECH	Korea
Srinivas Krishnagopal	Bhabha	India
Jean-Michel Lagniel	GANIL	France
Valeri Lebedev	FNAL	USA
Yoshi Mori	Kyoto University	Japan
Jose Manuel Perez	CIEMAT	Spain
Andrea Pisent	INFN	Italy
Christopher Prior	RAL	UK
Ji Qiang	LBL	USA
Thomas Roser	BNL	USA
Lawrence Rybarcyk	LANL	USA
Todd Satogata	Jefferson lab	USA
Mike Seidel	PSI	Switzerland
Jingyu Tang	IHEP	China
Jiuqing Wang	IHEP	China
Jie Wei	FRIB	USA
Bill Weng	BNL	USA
Yoshishige Yamazaki	FRIB	USA
Hongwei Zhao	IMP	China

Editorial Team

Jan Chrin	PSI	Switzerland
Dong Eon Kim	PAL	Korea
Ghyung Hwa Kim	PAL	Korea
Christine Petit-Jean-Genaz	CERN	Switzerland
Volker RW Schaa	GSI	Germany

Local Organizing Committee (LOC)

Dong-O Jeon (Chair)	IBS
Ji-Ho Jang	IBS
In Seok Hong	IBS
Hyunchang Jin	IBS
Beom Soo Joo	IBS
Jeehyun Cho	IBS
Dong-Eon Kim	PAL
Eun Hee Lee	PAL
Byoung-Seob Lee	KBSI
Mi-Sook Won	KBSI
Moses Chung	UNIST
En-San Kim	Korea Univ
Seong Hee Park	Korea Univ

Working Groups & Conveners

WG-A: Beam dynamics in Rings

Yong Ho Chin (KEK)
Giuliano Franchetti (GSI)
Valeri Lebedev (FNAL)

WG-B: Beam dynamics in Linacs

Peter Ostroumov (FRIB)
P.A.P. Nghiem (CEA-Saclay)
Hongwei Zhao (IMP)

WG-C: Accelerator Systems

Fernanda Garcia (FNAL)
Nicolas Pichoff (CEA)
Moses Chung (UNIST)

WG-D: Commissioning and Operations

Hideaki Hotchi (JAEA)
Yannis Papaphilippou (CERN)
Deepak Raparia (BNL)

WG-E: Instrumentation and Beam Interactions

Peter Forck (GSI)
Michiko Minty (BNL)
Hee Seock Lee (PAL)

Contents

Preface	i
Poster	i
Group Photo	ii
Foreword	iii
Committees	iv
Contents	vi
Papers	1
MOA1PL01 – Challenges in Understanding Space Charge Dynamics	1
MOA1PL02 – Beam Dynamics Challenges for the LHC and Injector Upgrades	8
MOA1PL03 – Linac4 Commissioning Status and Challenges to Nominal Operation	14
MOP1WA01 – J-PARC RCS: Effects of Emittance Exchange on Injection Painting	20
MOP2WA01 – Beam Physics Limitations for Damping of Instabilities in Circular Accelerators	26
MOP2WA03 – Experiments and Theory on Beam Stabilization with Second-Order Chromaticity	32
MOP2WA04 – Recent Results from the Wideband Feedback System Tests at the SPS and Future Plans	38
MOP2WA05 – Simulation and Measurement of the TMCI Threshold in the LHC	43
MOP1WB02 – Understanding the Source and Impact of Errant Beam Loss in the Spallation Neutron Source (SNS) Super Conducting Linac (SCL)	48
MOP1WB03 – Experimental Study of Beam Dynamics in the PIP-II MEBT Prototype	54
MOP2WB01 – 60 mA Beam Study in J-PARC Linac	60
MOP2WB02 – Simulation and Measurement Campaigns for Characterization and Performance Improvement of the CERN Heavy Ion Linac3	64
MOP2WB03 – Emittance Growth and Beam Losses in LANSCE Linear Accelerator	70
TUA1WC01 – Installation and Commissioning of the Upgraded SARAF 4-rods RFQ	75
TUA2WC01 – Discussion on SARAF-LINAC Cryomodules	80
TUA2WC02 – Status of R&D on New Superconducting Injector Linac for Nuclotron-NICA	83
TUA2WC03 – Studies on Superconducting Deuteron Driver Linac for BISOL	88
TUP1WE02 – Hollow Electron-Lens Assisted Collimation and Plans for the LHC	92
TUP1WE03 – Beam Instruments for High Power Spallation Neutron Source and Facility for ADS	99
TUP2WE01 – Injection Foil Temperature Measurements at the SNS Accelerator	104
TUP2WE02 – The Beam Conditions on the Target and its Operational Impacts on Beam Intercepting Devices at European Spallation Source	110
TUP2WE03 – Radiation Damage Calculation in PHITS and Benchmarking Experiment for Cryogenic-Sample High- Energy Proton Irradiation	116
TUP2WE04 – Design of the Target Dump Injection Segmented (TDIS) in the Framework of the High Luminosity Large Hadron Collider (HL-LHC) Project	122
TUA1WD01 – ESS Commissioning Plans	127
TUA1WD03 – Commissioning Status and Plans of CSNS/RCS	133
TUA1WD04 – High Intensity Proton Stacking at Fermilab: 700 kW Running	136
TUA2WD01 – FAIR Commissioning - Concepts and Strategies in View of High-Intensity Operation	141
TUA2WD02 – High-Power Beam Operation at J-PARC	147
TUA2WD03 – Automated Operation of EBIS Injector at BNL	153
TUP1WA02 – Fixed Field Accelerators and Space Charge Modeling	158
TUP1WA03 – Beam Instabilities After Injection to the LHC	163
TUP2WA01 – Optical Stochastic Cooling Experiment at the Fermilab IOTA Ring	168
TUP2WA02 – Momentum Slip-Stacking Simulations for CERN SPS Ion Beams with Collective Effects	174
TUP2WA03 – Studies of Capture and Flat-Bottom Losses in the SPS	180
TUP2WA04 – Dynamic Vacuum Simulation for the BRing	186
TUP2WA05 – Effect of the Extraction Kickers on the Beam Stability in the CERN SPS	189
WEA1PL01 – What is Missing for the Design and Operation of High-Power Linacs?	195
WEA2WB02 – Recent Studies of Beam Physics for Ion Linacs	200
WEP1WB01 – Beam Dynamics of the ESS Linac	206
WEP1WB02 – Beam Dynamics Simulation and Measurements for the IFMIF/EVEDA Project	210
WEP1WB03 – First Heavy Ion Beam Acceleration with a Superconducting Multi Gap CH-cavity	215
WEP1WB04 – Design of Linac-100 and Linac-30 for New Rare Isotope Facility Project DERICA at JINR	220

WEA1WA01 – Sum Resonances with Space Charge	226
WEA1WA02 – Approaching the High-Intensity Frontier Using the Multi-Turn Extraction at the CERN Proton Synchrotron	231
WEA2WA01 – High Intensity Effects of Fixed Target Beams in the CERN Injector Complex	237
WEA2WA02 – Microbunched Electron Cooling (MBEC) for Future Electron-ion Colliders	243
WEA2WA04 – Space-Charge Compensation Using Electron Columns at IOTA	247
WEP1WA03 – IBS Near Transition Crossing in NICA Collider	252
WEP2PO001 – Upgraded Transverse Feedback for the CERN PS Booster	256
WEP2PO002 – Scaling Laws for the Time Dependence of Luminosity in Hadron Circular Accelerators based on Simple Models of Dynamic Aperture Evolution	260
WEP2PO003 – Beam Loading and Longitudinal Stability Evaluation for the FCC-ee Rings	266
WEP2PO006 – Overview of the CERN PSB-to-PS Transfer Line Optics Matching Studies in View of the LHC Injectors Upgrade Project	272
WEP2PO007 – Multi-Particle Simulations of the Future CERN PSB Injection Process with Updated Linac4 Beam Performance	278
WEP2PO008 – SPS Long Term Stability Studies in the Presence of Crab Cavities and High Order Multipoles	284
WEP2PO010 – Fermilab - The Proton Improvement Plan (PIP)	287
WEP2PO011 – Studies of Transverse Instabilities in the CERN SPS	291
WEP2PO015 – Progress and Plan of the Fast Protection System in the RAON Accelerator	296
WEP2PO016 – Temperature Measurement of Cryomodules	299
WEP2PO017 – Study on the Leakage Fields of the Septum and Lambertson Magnets during the Beam Commissioning	303
WEP2PO018 – Magnetic Field Tracking at CSNS/RCS	306
WEP2PO022 – Study on the Phase Space Painting Injection during the Beam Commissioning for CSNS	309
WEP2PO023 – Timing Adjustment of Eight Kickers and a Method to Calibrate the Kicker Current Curves During the Beam Commissioning for CSNS	312
WEP2PO024 – Resonance Stop-bands Compensation at Booster Ring of HIAF	315
WEP2PO027 – Simulation of the Axial Injection Beam Line of the Reconstructed U200 Cyclotron of FLNR JINR	319
WEP2PO028 – Conceptual Design of FLNR JINR Radiation Facility Based on DC130 Cyclotron	324
WEP2PO030 – A 4D Emittance Measurement Device for the 870 keV HIPA Injection Line	329
WEP2PO032 – A Secondary Emission Monitor in the SINQ Beam Line for Improved Target Protection	334
WEP2PO033 – A Test of Stripper Foil Lifetime in PSI's 72 MeV Proton Beam	338
THA1WD01 – Experience and Perspective of FFAG Accelerator	342
THA1WD03 – Status and Beam Power Ramp-Up Plans of the Slow Extraction Operation at J-Parc Main Ring	347
THA1WD04 – High-Brightness Challenges for the Operation of the CERN Injector Complex	352
THA2WD01 – Operation Challenges and Performance of the LHC During Run II	357
THA2WD03 – Real-Time Measurement of Fluctuations of Building Floor and Installed Devices of Large Scientific Equipment	362
THP1WB01 – Commissioning Status of Linear IFMIF Prototype Accelerator (LIPAc)	366
THP2WB01 – Revisiting the Longitudinal 90 Degree Limit for Superconducting Linear Accelerators	369
THP2WB02 – High-Intensity Beam Dynamics Simulation of the IFMIF-like Accelerators	373
THP2WB03 – Influence of the Cavity Field Flatness and Effect of the Phase Reference Line Errors on the Beam Dynamics of the ESS Linac	377
THP2WB04 – Longitudinal Dynamics of Low Energy Superconducting Linac	383
THP2WB05 – Halo Formation of the High Intensity Beams in a Periodic Solenoidal Fields	387
THA1WE02 – Requirements and Results for Quadrupole Mode Measurements	393
THA1WE03 – BPM Technologies for Quadrupolar Moment Measurements	399
THA1WE04 – ESS nBLM: Beam Loss Monitors based on Fast Neutron Detection	404
THA2WE02 – Application of Machine Learning for the IPM-Based Profile Reconstruction	410
THP1WC01 – MEBT Laser Notcher (Chopper) for Booster Loss Reduction	416
THP1WC02 – Status of Proof-of-Principle Demonstration of 400 MeV H-Stripping to Proton by Using Only Lasers at J-PARC	422
THP1WC03 – Design of 162-MHz CW Bunch-by-Bunch Chopper and Prototype Testing Results	428
THP2WC01 – The FNAL Booster Second Harmonic RF Cavity	434
THP2WC02 – LLRF Studies for HL-LHC Crab Cavities	440
THP2WC03 – The Choosing of Magnetic Structure of Isochronous Cyclotron DC-130 for Applied Research	446

Appendices	451
List of Authors	451
Institutes List	457
Participants List	465

CHALLENGES IN UNDERSTANDING SPACE CHARGE EFFECTS

H. Bartosik*, CERN, Geneva, Switzerland

Abstract

Space charge effects in high intensity and high brightness synchrotrons can lead to undesired beam emittance growth, beam halo formation and particle loss. A series of dedicated machine experiments has been performed over the past decade in order to study these effects in the particular regime of long-term beam storage (10^5 - 10^6 turns) as required for certain applications. This paper gives an overview of the present understanding of the underlying beam dynamics mechanisms. In particular it focuses on the space charge induced periodic resonance crossing, which has been identified as the main mechanism causing beam degradation in this regime. The challenges in further progressing with the understanding, the modelling and the mitigation of these space charge effects and the resulting beam degradation are discussed. Furthermore, an outlook for possible future directions of studies is presented.

INTRODUCTION

Space charge effects in high intensity and high brightness synchrotrons can lead to undesired beam emittance growth, beam halo formation and particle loss. Some accelerator projects require long-term storage (up to several seconds) of high brightness bunches at injection energy in order to allow accumulating several injections from an upstream machine. This is the case for the Proton Synchrotron (PS) and the Super Proton Synchrotron (SPS) at CERN, which are part of the injector chain for the Large Hadron Collider (LHC). In preparation for the High Luminosity era of the LHC (HL-LHC), the injector chain at CERN is in the course of being upgraded in the framework of the LHC Injectors Upgrade (LIU) [1]. In simplified terms, the aim of this project is to enable the injectors to deliver twice higher intensity at equal emittance, i.e. twice as high brightness, as compared to today's performance. Table 1 shows an overview of the required storage times, the space charge tune shifts and the loss and emittance growth budgets for the various machines of the proton injector chain at CERN. For the heavy ion injector chain, space charge is critical in the Low Energy Ion Ring (LEIR). In the SPS, a space charge tune shift of up to $\Delta Q_y = -0.3$ is achieved and storage times of up to 40 s are required. In this case the beam quality is subject to strong degradation, which has been taken into account for the projection of the LIU-ion target parameters [2].

At the Facility for Antiproton and Ion Research project (FAIR) at GSI, the future SIS100 is required to store high brightness beams with a maximum space charge tune shift of about $\Delta Q_y \approx -0.3$ for about 1 s to accumulate several injections from SIS18 with losses on the percent level [3]. In this case, the tight constraint on beam losses is (at least

Table 1: Target Parameters for LIU Project at CERN

Machine	ΔQ_y	Storage time	Budget for losses / Emittance growth
PSB	-0.5	-	5% / 5%
PS	-0.31	1.2 s	5% / 5%
SPS	-0.21	10.8 s	10% / 10%

partially) imposed by dynamic vacuum issues stemming from the large ionization cross section of U^{+28} ions with the residual gas.

Keeping the beam degradation within tight tolerances for long storage times can be quite challenging in presence of large space charge tune spread. A detailed understanding of the underlying beam dynamics mechanisms is required. A series of dedicated machine experiments has been performed over the past decade in collaboration between CERN and GSI in order to study the space charge dynamics in this regime. The aim of this paper is to give an overview of the present understanding, discuss the challenges faced and provide an outlook for future directions of study.

OVERVIEW OF STUDIES AND PRESENT UNDERSTANDING

One-dimensional Resonances

The first systematic experimental study of long-term space charge effects in presence of non-linear resonances was performed at the CERN PS in 2002-2003, as reported in [4] and [5]. In this experiment, the fourth order horizontal resonance $4Q_x = 25$ was deliberately excited by a single octupole. A bunched proton beam with a horizontal (vertical) incoherent direct space charge tune shift of -0.075 (-0.12) was stored at injection energy for about 1 s for different working points. Depending on how the space charge tune spread overlaps the resonance, two regimes of beam degradation could be clearly identified. For bare machine working points only slightly above the resonance, beam loss dominates. At the same time a reduction of both the horizontal emittance as well as the bunch length are observed. For higher machine tunes, losses are reduced but a large halo is formed in the horizontal plane leading to an enlarged emittance.

The beam degradation observed in the PS experiment was explained by trapping and scattering of particle trajectories during the periodic resonance crossing induced by space charge in a bunched beam, as anticipated by a simplified simulation model in 2002 [6]. This picture was refined in the following years [7-9], describing the main features of the phenomenon as follows:

- Space charge couples transverse and longitudinal planes: due to the change of line charge density along

* hannes.bartosik@cern.ch

the bunch, the instantaneous transverse Coulomb force depends on the particle location in the longitudinal plane. Therefore, the longitudinal motion induces, via space charge, a variation of transverse tunes.

- The presence of a relatively small tune shift compared to the machine tunes ($\Delta Q_x/Q_{x0}$ of a few percent), does not destroy the validity of standard transverse non-linear dynamics, but rather induces a slow modulation of transverse tunes according to twice the synchrotron frequency.
- The transverse-longitudinal space charge coupling determines, via the depression of tunes, the transverse position of the fixed-points generated by the 1D resonance.
- The strength of the resonance determines the tune of particles around the fixed-points and also the resonance island size. The island size is also determined by the detuning created by space charge: a stronger gradient in the amplitude dependent detuning leads to smaller islands,
- The synchrotron tune determines the speed of the resonance crossing. A figure of merit on the speed of the resonance crossing is given by the adiabaticity parameter T , which is obtained as the ratio between the speed of migration of the fixed-points to the maximum speed of rotation of the particle in the island. If this ratio is small ($T \ll 1$) the motion is adiabatic and the particles remain locked to the island. As a consequence, the particle gains large amplitudes (trapping). If instead $T > 1$, a single resonance crossing results in a “kick” to the particle invariant (scattering).
- Particles that periodically cross the resonance will slowly diffuse to large amplitudes to form a halo. Its density and extension depend on the number of particles that cross the resonance, and on the outer position of the islands. If the outer position of islands intercepts the beam pipe or reaches the dynamic aperture, beam loss occurs according to a rate which is function of the distance from the resonance. When the accelerator is tuned close to a resonance (and above it), only particles with large synchrotron amplitude may cross the resonance and therefore become trapped or scattered into a halo and eventually be lost. This leads to a correlation between beam loss and longitudinal beam size such that only particles with large synchrotron amplitude will be lost resulting in a reduction of the bunch length.
- The space charge induced tune modulation due to longitudinal particle motion has twice the synchrotron frequency. The tune modulation introduced by chromaticity, instead, has the same frequency as the synchrotron motion. When maximum space charge detuning and maximum chromaticity detuning are comparable, the resulting slow modulation of the transverse tunes is

the composition of these two effects with different frequencies. Consequently, the position of the fixed points is different in the two synchrotron half-periods. The overall effect is that islands are pushed further out (during half of the synchrotron period) and the halo size is increased.

This mechanism was confirmed in a systematic measurement campaign performed at the GSI SIS18 in 2007, where the horizontal third order resonance $3Q_x = 13$ was studied for both coasting and bunched beams with different beam intensities and space charge tune spreads [10]. The strong emittance growth was only observed for the high intensity bunched beam but not for the coasting beam with the same space charge tune shift, since for the coasting beam there is no periodic resonance crossing.

Two-dimensional Sum Resonances

While all the studies reported above concentrated on one-dimensional non-linear resonances, an experiment in 2012 at the CERN PS was dedicated to studying the beam behaviour close to the third order coupled sum resonance $Q_x + 2Q_y = 19$ deliberately excited by a sextupole magnet [11]. The beam was stored for about 1 s. Also in this experiment the loss dominated and the emittance growth dominated regimes were observed depending on the working point. However, the halo formation measured with wire scanners was observed to be very asymmetric between the horizontal and vertical planes. In particular, the beam developed much larger tails in the vertical plane. This observation could not be explained by a naive extension of the one-dimensional model developed earlier, since the particle trajectory on the coupled resonance follows resonant tori in phase space rather than fixed points. These resonant tori, in this context referred to as “fixed lines” [12–14], have a peculiar shape in the 4 dimensional phase space of horizontal and vertical coordinates. In the case of the $Q_x + 2Q_y$ resonance, the projection of the single particle trajectory in the physical $x - y$ space has a larger excursion in the vertical plane and, depending on the phase advance from the driving sextupole to the observation point, follows either a figure-of-eight or a C-shape. This explains the larger vertical halo observed in this experiment at the PS.

It should be mentioned that there is an experimental campaign ongoing at the CERN SPS to study the fixed lines on the $Q_x + 2Q_y$ resonance in the “zero” space charge limit [15]. Furthermore, a general theory of space charge dynamics in the presence of non-linear coupled sum resonance of arbitrary order is being developed [16].

(REMAINING) CHALLENGES

Macroparticle Simulations

Space charge in a synchrotron is usually modelled by alternating space charge interaction (“space charge kicks”) with particle tracking in the magnetic guide field. As the space charge forces depend on the transverse beam sizes,

the rule of thumb is that about 10 space charge kicks per beam size variation period (sometimes referred to as betatron wavelength) are needed.

The brute force way of calculating the space charge forces is based on the Particle-In-Cell (PIC) algorithm [17]. In this approach the real number of particles is represented by macroparticles (usually about 10^6), where the total beam intensity is equally distributed to the charge of each macroparticle. The charge distribution is binned onto a spatial grid and the Poisson equation is solved numerically on the grid points to obtain the space charge kicks through the electric field. This method is self-consistent, i.e. the evolution of the particle distribution as a function of time is fully taken into account. However, a large number of macroparticles is needed to reduce emittance growth due to numerical noise in the particle distribution [18]. This approach is therefore very demanding in terms of computational power, necessitating the implementation of parallel computing. In addition, there is some artificial emittance growth induced by the grid (“grid heating”) [19] and special care needs to be taken to make the calculation symplectic [20], which comes at additional computational cost.

To avoid the issue with noise, simulations with a so-called “frozen” space charge potential are commonly used for long-term simulations. In this approach, the space charge kicks are computed analytically for a chosen (fixed) particle distribution. A closed analytic expression for the electric field generated by a bi-dimensional Gaussian transverse distribution was derived by Bassetti and Erskine [21]. For each particle in the simulation, this formula is evaluated at the position of the particle using the actual horizontal and vertical beam sizes at the location of the space charge interaction and taking the local longitudinal line density into account. Simulations with this approach require only a few thousand particles to study the emittance growth and losses statistically. The drawback of this approach is that coherent collective effects cannot be taken into account. Furthermore the evolution of the particle distribution is not treated self-consistently.

The latter is partially overcome by adapting the beam parameters such as intensity and transverse emittances periodically and recomputing the frozen potential, as implemented in MAD-X [22] and in PyOrbit [23]. PyOrbit allows furthermore to partially account for the generation of halo by representing the beam by two transverse Gaussian distributions with different weights and different transverse emittances.

Some years ago a code-to-code benchmarking suite has been put in place in order to check the space charge induced particle trapping phenomenon [24]. In addition to MICROMAP [25] and SIMPSONS [26], this benchmarking case has been successfully passed by MAD-X [22], PTC-ORBIT [27] and lately also SYNERGIA [28, 29]. It should be highlighted that SYNERGIA is a PIC code and all the features observed in the frozen space charge codes could be reproduced. Even the long term emittance evolution test case was in very good agreement, once a sufficient number of macroparticles was used [30]. Work is presently ongoing

to check the frozen space charge module of PyOrbit against this benchmarking case.

A more general overview of space charge code benchmarking can be found in [31, 32].

Quantitative Agreement Between Measurements and Simulations

Achieving quantitative agreement between machine experiments and space charge simulation codes is challenging. In fact, reproducing the evolution of the particle distribution during long-term storage requires several ingredients:

- **Accurate measurement of beam parameters** The measurement of the transverse beam profiles in synchrotrons is particularly challenging, because a high signal to noise ratio is required in order to resolve the beam halo.
- **Good knowledge of machine linear and non-linear errors** The long-term evolution of the particle distribution in the presence of space charge is very sensitive to machine errors and non-linearities. Having a good model of the machine is crucial. In general, the information on magnet errors for machines, which have been in operation for more than two decades, is sparse. In this case an effective non-linear model of the machine can be established from beam-based measurements, as done for example at the SPS [33].
- **Accurate aperture model including misalignments** Reproducing losses relies critically on a good model of the machine aperture, including element misalignments and the closed orbit. This information is unfortunately not always readily available, especially concerning the alignment data.
- **Properly identifying and accounting for interfering effects** To achieve quantitative agreement with simulations it is crucial to identify any effects that contribute to emittance growth and or losses in the machine under study. If these effects cannot be suppressed in the machine, they need to be quantified and eventually taken into account in the simulations. In some cases the interplay between space charge and other effects requires a study on its own. This might become more and more relevant in the future, when the accelerator performances will be pushed further. This aspect will be addressed in more detail later in this paper.

An example where a good quantitative agreement between measurements and simulations could be achieved is the PSB. As reported in [34], a benchmark experiment was performed for a working point slightly above the $2Q_y = 9$ half integer resonance. The beam loss evolution over about 200 ms was studied on a constant energy plateau when switching off the half integer correctors. To reproduce the observed losses in PIC simulations, a very accurate machine model of the

linear errors had to be developed using beam-based measurements. In the end, even the evolution of the longitudinal bunch profile measured in the experiment was in very good agreement with the simulations.

A similar level of agreement has not yet been reached for the PS. Studies performed in 2013 have shown that high brightness beams suffer from losses for machine working points above $Q_y = 6.25$, while practically no losses are observed for beams with low brightness [35]. Further studies have shown that the non-linear space charge potential of the Gaussian particle distribution drives the 8th order resonance $8Q_y = 50$, because 50 is the strongest harmonic of the PS lattice functions [36, 37]. More recent campaigns concentrated on tune scans in different experimental conditions. However, simulations using a frozen adaptive model in PyOrbit for the ideal PS lattice do not explain the observed losses quantitatively (about a factor 3 higher losses in the measurements for high brightness beams) as shown

in Fig. 1 [38]. The space charge tune shift of the beam used in this study was about $\Delta Q_y = -0.25$. As the discrepancy between measurements and simulations is relatively large, detailed investigations on this subject are ongoing. In particular, the interplay with some residual, but yet to be quantified, magnetic resonance excitation at $Q_y = 6.25$ (e.g. octupole components) is being studied. A direct measurement of such residual resonance excitation is however difficult. Furthermore, the aperture model of the machine is being refined (e.g. comparison of model aperture with direct measurement of the effective physical aperture). Finally the importance of other effects like indirect space charge, as recently proposed in [39], and coherent space charge effects is being investigated. It should be mentioned that, since the beam loss at these working points is observed only for high brightness beams, the studies need to be performed with a relatively large tune spread. It could therefore be that multiple resonances are contributing to the beam degradation, which is an additional complication for these studies. In fact, driving term calculations have shown that there are also 8th order coupled sum resonances excited by space charge [40], in addition to third order (skew) resonances in the tune space investigated (as indicated in the top of the graphs in Fig. 1).

Mitigation of Beam Degradation

In view of pushing the accelerator performance further, an important aspect to be addressed is the mitigation of the space charge induced beam degradation. On the one hand, individual non-linear resonances excited by magnetic errors can be compensated in case appropriate corrector magnets are available in the machine (at the expense of possibly further exciting other resonances or reducing the dynamic aperture). Typically two independent correctors with adequate phase advance are needed in order to control the resonance driving term in the complex plane. This has been tested in the PS for third order normal and skew resonances, see for example [38, 40, 41]. Experimental studies in the SIS18 on this subject are summarized in [42]. It seems that after the compensation, some minor residual resonance excitation left. It is not yet clear if this is related to the space charge detuning or to non-ideal resonance compensation settings, or due to another reason.

The other approach could be to try compensating the space charge detuning in the first place. A study in this direction was performed recently based on using electron lenses [43].

FUTURE DIRECTIONS

As described above, the main mechanism for beam degradation of high brightness bunches in the long-term storage regime has been attributed to periodic resonance crossing. Future study efforts could focus on identifying and better understanding the interplay with other collective effects or beam dynamics mechanisms such as:

- Tune modulation induced by power converter ripple
- Intra Beam Scattering (especially for ions)

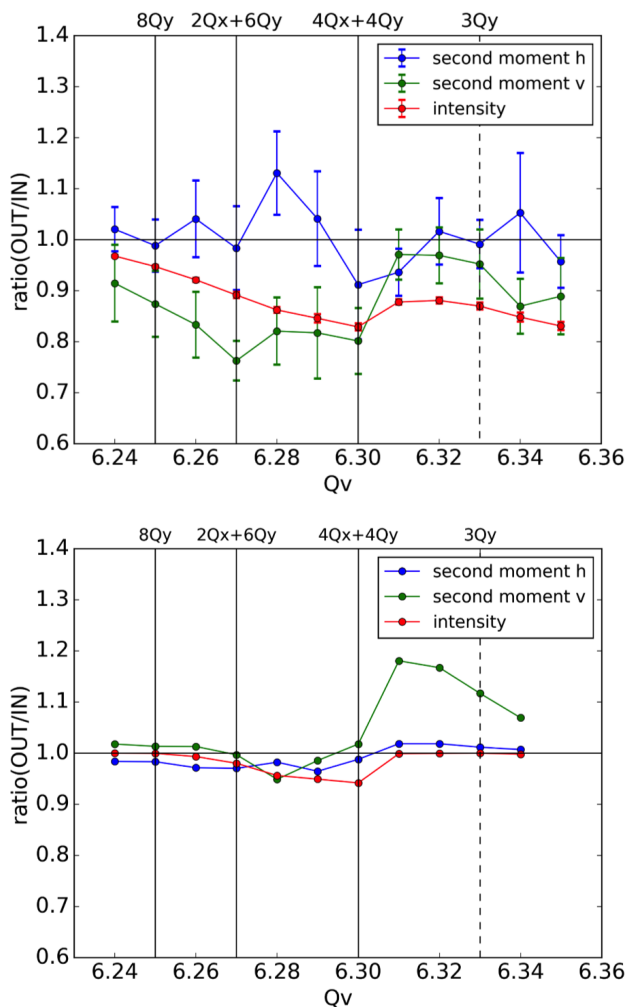


Figure 1: Relative emittance growth and losses as a function of the vertical machine tune in measurements (top) and in simulations (bottom) [38]. The horizontal tune was set to 6.2 in all cases.

- Electron-cloud
- Indirect space charge and impedance

which are encountered in some operational conditions in the CERN injectors. A good example is the SPS, as discussed in more detail below.

Reaching the LIU target beam parameters requires injecting 25 ns beams with unprecedented intensity (about twice compared to today’s nominal) and beam brightness. In the past, coherent and incoherent electron cloud effects were encountered in the SPS already with the nominal intensity. Over the years this effect was slowly reduced by beam induced scrubbing. In recent machine studies with high intensity beams (not yet LIU intensity) a strong incoherent emittance growth was observed when storing the beam for about 20 s at injection energy. However, a clear improvement of the beam quality could already be observed after running the machine in this scrubbing configuration for two days [44]. Nevertheless, some residual electron-cloud might always be present in future operation and the interplay with space charge effects could become important.

Other recent studies at the SPS indicate that the tune modulation induced by power converter ripple can play an important role in the beam degradation during the long storage in presence of space charge [45]. Figure 2 (top graph) shows the relative emittance growth and transmission for different working points in the SPS close to excited resonances ($Q_x = 20.33$ deliberately excited using a single sextupole and at $Q_x = 20.40$ most likely driven by space charge itself). Simulations using a frozen potential are far from the experimental observations (middle graph) unless the measured tune ripple induced by the power converters for the main quadrupoles of the SPS is taken into account (bottom graph). Detailed studies on this subject are ongoing.

It should be pointed out that the tune ripple might also play a role for the strong emittance growth and losses observed for the Pb⁸²⁺ ion beam on the SPS injection plateau. This beam has to be stored for more than 40 s for accumulation of several batches from the PS to reach the LIU ion target parameters [2] and the space charge tune shift at injection reaches up to $\Delta Q_y = -0.3$. On the other hand, Intra Beam Scattering is also contributing to emittance growth [46] and the interplay between space charge and Intra Beam Scattering needs to be studied.

ACKNOWLEDGEMENTS

The author would like to acknowledge the contributions of Y. Alexahin, F. Asvesta, E. Benedetto, O. Boine-Frankenheim, S. Cousineau, V. Forte, G. Franchetti, S. Gilardoni, I. Hofmann, J. Holmes, A. Huschauer, S. Kostoglou, S. Machida, E. Metral, Y. Papaphilippou, J. Qiang, A. Saa Hernandez, F. Schmidt, A. Shishlo, E. Stern, R. Wasef, and all other colleagues of the CERN space charge collaboration.

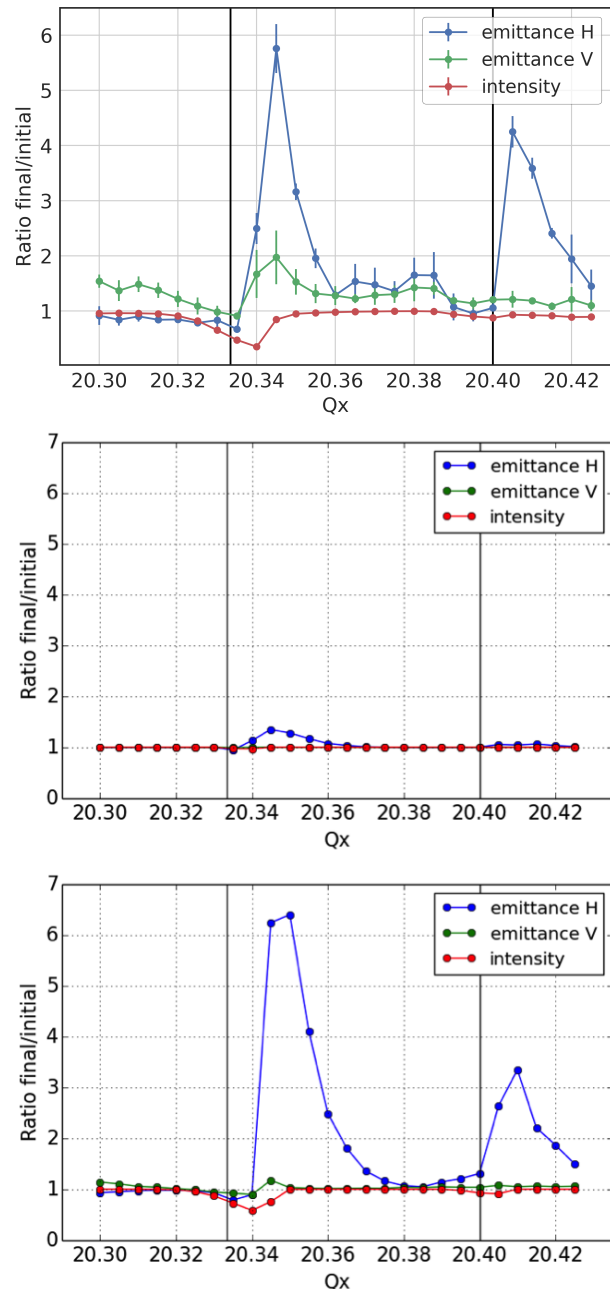


Figure 2: Relative emittance growth and losses as a function of the measured horizontal machine tune in measurements (top), in simulations (middle) and in simulations including the tune ripple induced by power converters in the SPS (bottom).

REFERENCES

- [1] J. Coupard *et al.*, “LIU Technical Design Report - Volume I: Protons”, CERN, Geneva, Switzerland, Rep. CERN-ACC-2014-0337, Dec. 2014.
- [2] J. Coupard *et al.*, “LIU Technical Design Report - Volume II: Ions”, CERN, Geneva, Switzerland, Rep. CERN-ACC-2016-0041, April 2016.

- [3] “Facility for Antiproton and Ion Research”, <https://fair-center.eu>
- [4] E. Métral *et al.*, “Observation of octupole driven resonance phenomena with space charge at the CERN Proton Synchrotron”, *Nuclear Instruments and Methods in Physics Research A*, vol. 561, pp. 257-265, 2006, doi:10.1016/j.nima.2006.01.029
- [5] G. Franchetti, *et al.*, “Space charge and octupole driven resonance trapping observed at the CERN Proton Synchrotron”, *Phys. Rev. ST Accel. Beams*, vol. 6, p. 124201, Dec. 2003, doi:10.1103/PhysRevSTAB.6.124201
- [6] G. Franchetti and I. Hofmann, “Modeling of Space Charge Induced Resonance Loss”, in *Proc. of High Intensity and High Brightness Hadron Beams 2002*, AIP Conf. Proc. No. 642, AIP, New York, 2002, p. 260, doi:10.1063/1.1522641
- [7] G. Franchetti and I. Hofmann, “Particle Trapping by Nonlinear Resonances and Space Charge”, in *Proc. of High Intensity Beam Dynamics - COULOMB’05*, Senigallia (AN), Italy, 2005.
- [8] G. Franchetti and I. Hofmann, “Resonance Trapping due to Space Charge and Synchrotron Motion, in Theory, Simulations and Experiments”, in *Proc. of High Intensity and High Brightness Hadron Beams 2006*, Tsukuba, Japan, 2006.
- [9] G. Franchetti and I. Hofmann, *Nucl. Instrum. Methods Phys. Res., Sect. A*, vol. 561, p. 195, 2006.
- [10] G. Franchetti *et al.*, “Experiment on space charge driven nonlinear resonance crossing in an ion synchrotron”, *Phys. Rev. ST Accel. Beams*, vol. 13, p. 114203, 2010, doi:10.1103/PhysRevSTAB.13.114203
- [11] G. Franchetti *et al.*, “Space charge effects on the third order coupled resonance”, *Phys. Rev. Accel. Beams*, vol. 20, p. 081006, 2017, doi:10.1103/PhysRevAccelBeams.20.081006
- [12] F. Schmidt, “Untersuchungen zur dynamischen Akzeptanz von Protonenbeschleunigern und ihre Begrenzung durch chaotische Bewegung”, PhD thesis, DESY HERA 88-02, 1988.
- [13] G. Franchetti and F. Schmidt, “Extending the Nonlinear-Beam-Dynamics Concept of 1D Fixed Points to 2D Fixed Lines”, *Phys. Rev. Lett.*, vol. 114, p. 234801, June 2015, doi:10.1103/PhysRevLett.114.234801
- [14] G. Franchetti and F. Schmidt, “Fix-lines and stability domain in the vicinity of the coupled third order resonance”, April 2015, <http://arxiv.org/abs/1504.04389>
- [15] H. Bartosik, G. Franchetti, F. Schmidt, M. Titze, private communication.
- [16] G. Franchetti, “Sum Resonances with Space Charge”, presented at HB2018, Daejeon, Korea, June 2018, paper WEA1WA01, this conference.
- [17] R.W Hockney and J.W Eastwood, “Computer Simulation Using Particles”, ISBN9780852743928.
- [18] F. Kesting and G. Franchetti, “Propagation of numerical noise in particle-in-cell tracking”, *Phys. Rev. ST Accel. Beams*, vol. 18, p. 114201, Nov. 2015, doi:10.1103/PhysRevSTAB.18.114201
- [19] A. Bruce Langdon, “Effects of the spatial grid in simulation plasmas”, *Journal of Computational Physics*, vol. 6, Issue 2, October 1970, pp. 247-267, doi:10.1016/0021-9991(70)90024-0
- [20] J. Qiang, “Symplectic multiparticle tracking model for self-consistent space-charge simulation”, *Phys. Rev. Accel. Beams*, vol. 20, p. 014203, 2018, doi:10.1103/PhysRevAccelBeams.21.054201
- [21] M. Bassetti and G.A. Erskine, “Closed Expression for the Electric Field of a two-dimensional Gaussian Charge”, CERN-ISR-TH/80-06, Geneva, March 1980.
- [22] Y. Alexahin *et al.*, “Adaptive Space Charge Calculations in MADX-SC”, in *Proc. NA-PAC’16*, Chicago, IL, USA, Oct. 2016, paper THPOA15, doi:10.18429/JACoW-NAPAC2016-THPOA15
- [23] Andrei Shishlo *et al.*, “The Particle Accelerator Simulation Code PyORBIT”, *Procedia Computer Science*, vol. 51, pp. 1272-1281, 2015.
- [24] G. Franchetti, “The GSI Bench-Marking Suite”, http://web-docs.gsi.de/~giuliano/research_activity/trapping_benchmarking/main.html
- [25] G. Franchetti *et al.*, “MICROMAP Library”, http://web-docs.gsi.de/~giuliano/micromap_manual/micromap_reference_manual.html
- [26] S. Machida, “The Simpsons program 6-D phase space tracking with acceleration”, *AIP Conference Proceedings*, vol. 297, p. 459, 1993, doi:10.1063/1.45344
- [27] J. Galambos *et al.*, “Orbit - A ring injection code with space charge”, *ibid*, p. 3143.
- [28] E. Stern *et al.*, “SYNERGIA”, <https://cdcvs.fnal.gov/redmine/projects/synergia2/wiki>
- [29] J. Amundson *et al.*, “High Performance Computing Modeling Advances Accelerator Science for High Energy Physics”, *IEEE Comput.Sci.Eng.*, vol. 16, no. 6, pp. 32-41, 2014.
- [30] E. Stern, “Studies on space charge compensation”, 2nd CERN Space Charge Collaboration Meeting, March 2018, <https://indico.cern.ch/event/688897>
- [31] S. Machida, “Benchmarking and Application of Space Charge Codes for Rings”, in *Proc. IPAC’15*, Richmond, VA, USA, 2015, pp. 2402-2407.
- [32] F. Schmidt *et al.*, “Code Bench-marking for Long-term Tracking and Adaptive Algorithms, in *Proc. HB’16*, Malmö, Sweden, 2016, paper WEAM1X01, pp. 357-361, ISBN978-3-95450-178-6
- [33] H. Bartosik *et al.*, “Improved Methods for the Measurement and Simulation of the CERN SPS Non-linear Optics”, in *Proc. IPAC’16*, Busan, Korea, 2016, paper THPMR036, pp. 3464-3467.
- [34] V. Forte *et al.*, “CERN Proton Synchrotron booster space charge simulations with a realistic model for alignment and field errors”, *Phys. Rev. Accel. Beams*, vol. 19, p. 124202, 2016, doi:10.1103/PhysRevAccelBeams.19.124202
- [35] R. Wasef, “PS Experiments and Simulations”, 1st CERN Space Charge Collaboration Meeting, CERN, Geneva, May 2014, <https://indico.cern.ch/event/292362>
- [36] S. Machida, “Space charge simulation for 4th order resonance”, CERN Space Charge Collaboration Meeting, CERN, Geneva, May 2014, <https://indico.cern.ch/event/292362>

- [37] R. Wasef, “Space charge in the PS”, Machine Studies Working Group meeting, CERN, Geneva, July 2015, <https://indico.cern.ch/event/433250/>
- [38] F. Asvesta *et al.*, “PS: Studies on $Q_y=6.25$ and other resonances”, 2nd CERN Space Charge Collaboration Meeting, CERN, Geneva, March 2018, <https://indico.cern.ch/event/688897>
- [39] S. Machida, “About indirect space charge driven resonances”, 2nd CERN Space Charge Collaboration Meeting, CERN, Geneva, March 2018, <https://indico.cern.ch/event/688897>
- [40] F. Asvesta *et al.*, “Resonance Identification Studies at the CERN PS”, in *Proc. IPAC'18*, Vancouver, BC, Canada, 2018, paper THPAK056.
- [41] A. Huschauer *et al.*, “Identification and compensation of resonances in the CERN Proton Synchrotron”, presentation at Space Charge 13 workshop, CERN, Geneva, April 2013, <https://indico.cern.ch/event/221441/>
- [42] G. Franchetti, “Resonance Compensation for High Intensity Bunched Beam”, in *Proc. IPAC'15*, Richmond, VA, USA, 2015, paper MOPWA028, pp. 159-161.
- [43] O. Boine-Frankenheim and W. Stem, “Space charge compensation for intense ions beams in booster synchrotrons”, arXiv:1705.01057
- [44] G. Rumolo, “Beam Dynamics Challenges for the LHC and Injector Upgrades”, presented at HB2018, Daejeon, Korea, June 2018, paper MOA1PL02, this conference.
- [45] H. Bartosik *et al.*, “SPS: Power converter ripple and space charge driven resonance”, 2nd CERN Space Charge Collaboration Meeting, CERN, Geneva, March 2018, <https://indico.cern.ch/event/688897>
- [46] A. Saa Hernandez *et al.*, “Characterization of Losses and Emittance Growth for Ion Beams on the SPS Injection Plateau”, in *Proc. IPAC'18*, Vancouver, BC, Canada, 2018.

Content from this work may be used under the terms of the CC BY 3.0 licence (© 2018). Any distribution of this work must maintain attribution to the author(s), title of the work, publisher, and DOI.

BEAM DYNAMICS CHALLENGES FOR THE LHC AND INJECTOR UPGRADES

G. Rumolo*, CERN, CH-1211 Geneva 23, Switzerland

Abstract

The High Luminosity upgrade of the Large Hadron Collider (HL-LHC) will rely on significantly higher bunch current and brightness to meet the future yearly integrated luminosity target. The implications are twofold. On one side, all the accelerators of the LHC injection chain will have to be upgraded to produce the desired beam parameters. For this purpose, the LHC Injectors Upgrade (LIU) program has been established to implement all the needed modifications for meeting the required beam specifications. These upgrades will lead to the lifting of the main intensity and brightness limitations in the injectors, linked to beam instabilities driven by impedance or electron cloud (e-cloud), and space charge. On the other side, the LHC will have to be able to swallow the new beam parameters. This will mainly require control of impedance driven instabilities and beam-beam effects, and e-cloud mitigation. In this paper, we will focus on proton beams by describing the identified performance limitations of the LHC and its injectors, as well as the actions envisioned to overcome them.

INTRODUCTION

The LHC Injectors Upgrade (LIU) project [1, 2] aims at increasing the intensity and brightness of the beams in the injectors in order to match the beam requirements set out by the High Luminosity LHC (HL-LHC) project [3], while ensuring high availability and reliable operation of the injector complex well into the HL-LHC era (up to about 2037) in synergy with the Consolidation (CONS) project [4]. For the upgrade of the LHC injector proton chain, LIU includes the following principal items:

- The replacement of Linac2, which accelerates protons to 50 MeV, with Linac4, providing 160 MeV H^- ions;
- Proton Synchrotron Booster (PSB): New 160 MeV H^- charge exchange injection, acceleration to 2 GeV from current 1.4 GeV with new power supply and RF system;
- Proton Synchrotron (PS): New 2 GeV injection, broadband longitudinal feedback;
- Super Proton Synchrotron (SPS): Upgrade of the 200 MHz RF system, impedance reduction and e-cloud mitigation, new beam dump and protection devices.

All these upgrades will lead to the production of beams with the challenging HL-LHC parameters and, if not already installed, they will for the most part be implemented during the Long Shutdown 2 (LS2) in 2019-20.

To extend its discovery potential, the LHC will undergo a major upgrade during Long Shutdown 3 (LS3) in 2024-25 under the HL-LHC project. The goal will be to increase the rate of collisions by a factor of 5-7.5 beyond the original

* Giovanni.Rumolo@cern.ch

LHC design value, leading to a target integrated luminosity of 3000-4000 fb^{-1} over the full HL-LHC run (2026-2037). The new configuration will rely on the replacement of the final focusing quadrupoles at the high luminosity Interaction Points (IPs), which host ATLAS and CMS, with new and more powerful magnets based on the Nb_3Sn technology, as well as a number of key innovations that push accelerator technology beyond its present limits while enabling, or even broadening, the future desired performance reach. Among these are the cutting-edge 11 T superconducting Nb_3Sn -based dipoles, the new superconducting link technology with MgB_2 , compact superconducting cavities for transverse beam tilting along the longitudinal axis to compensate for the crossing angle at collision (crab cavities), the upgrade of the cryogenic system and general infrastructure, new technology and material for collimators, the optional use of hollow electron lenses for beam halo cleaning.

The beam dynamics aspects of the LIU and HL-LHC projects are challenging, because during the HL-LHC era:

- The LHC injectors will have to be able to routinely produce, stably control and safely handle beams with unprecedented intensity and brightness;
- The LHC will have to be able to run with the future beams, preserve their stability and make them available for collisions all along the calculated optimum fill length with the desired levelling scheme, ensuring as little as possible beam quality degradation.

Addressing the beam intensity limitations of the LHC and its injectors and illustrating the envisaged strategies to cope with them will be the subject of the next sections.

BEAM PERFORMANCE LIMITATIONS IN THE LHC INJECTORS AND GOALS

In this section we will first present a general overview on the present LHC beam performance of the injectors and the beam requirements for the LIU project. We will only focus on the so called 'standard LHC beam', which is baseline for the projects and produced as follows:

- Two subsequent injections of 4+2 bunches from the four PSB rings into the PS at $E_{kin}=1.4$ GeV;
- In the PS, triple splitting of the injected bunches at 2.5 GeV, then acceleration to 25 GeV and two consecutive double splittings of all 18 bunches at 25 GeV;
- Four subsequent injections of trains of 72 bunches spaced by 25 ns into the SPS (train spacing 200 ns) at 25 GeV and acceleration to 450 GeV.

Then, we will describe the actions that the LIU project has (planned to) put in place to overcome the intensity/brightness limitations in the various accelerators of the injector chain.

Present Performance of the LHC Injector Chain

An upper limit for the brightness of standard LHC beam is determined at the PSB injection, because of the efficiency of the multi-turn injection process as well as the effects of space charge during injection. The normalised transverse emittance has been measured as a function of intensity at the PSB extraction after optimization of the injection settings and for a longitudinal emittance of 1.2 eVs at extraction [5]. The relation is found to be linear and the resulting line defines the “PSB brightness” line. The longitudinal emittance at extraction can be made in principle as high as 2.8 eVs via longitudinal emittance blow up along the PSB cycle [6] compatibly with other constraints coming from the transfer to the PS and further longitudinal beam manipulation in the PS ring. Although this is believed to be beneficial in terms of space charge in the PS since it would allow the transfer of longer bunches with larger momentum spreads, the experimental proof is to date still missing – probably due to other issues related to the transfer of bunches with large momentum spread. The PSB does not have an intensity limitation for the LHC beams, as it already nowadays successfully accelerates to 1.4 GeV beams up to 6 times more intense than the current LHC beams, which are used for fixed target experiments at the ISOLDE facility.

Combining the experience accumulated with operational beams with the outcomes of several dedicated space charge Machine Development (MD) studies conducted throughout 2012 – 2017, it can be assumed that the maximum values of space charge vertical tune spread, ΔQ_y , compatible with the beam loss and emittance blow up budgets reported below, are 0.31 and 0.21 at the PS and SPS injection, respectively. Besides, prior to the LIU upgrade program, due to longitudinal dipolar coupled bunch instabilities on the ramp and at top energy, the PS was not able to produce 25 ns beams with more than 1.8×10^{11} p/b within the longitudinal emittance of 0.35 eVs, which is currently the optimised value to limit capture losses and keep the beam longitudinally stable in the SPS. Finally, due to RF power constraints on the main SPS RF system (200 MHz) and longitudinal coupled bunch instabilities along the cycle, beams with more than 1.3×10^{11} p/b could not be extracted from the SPS with the desired bunch length of 1.6 ns for a basically lossless injection into LHC. E-cloud has been also affecting 25 ns beams in the SPS, but currently the SPS has undergone sufficient beam induced scrubbing to produce beams with 1.3×10^{11} p/b transversely stable and without the characteristic pattern imprinted by e-cloud on the bunch intensities and emittances along the trains. Finally, the onset of the vertical Transverse Mode Coupling Instability (TMCI) limited in the past the bunch intensity to 1.6×10^{11} p/b [7], but this limitation was lifted in 2012 by commissioning a new optics with γ_t lower by 4 units, which increases the TMCI threshold by a factor 2.5 [8].

After including some predefined budgets for emittance blow up and beam loss (5% in the PSB and PS for both, and 10% in the SPS) we can represent in the plane emittance vs. intensity per bunch at the SPS extraction the curves corre-

sponding to PSB brightness, PS and SPS space charge limits, and intensity limitations of the PS and SPS. The regions of inaccessible parameter ranges are shaded. The outcome of this exercise is displayed in Fig. 1, from which we deduce that presently the best standard LHC beam produced by the injectors has 1.3×10^{11} p/b within about $2.7 \mu\text{m}$ transverse emittance. All the points measured at LHC injection over the years 2015 – 2018 fully confirm this analysis.

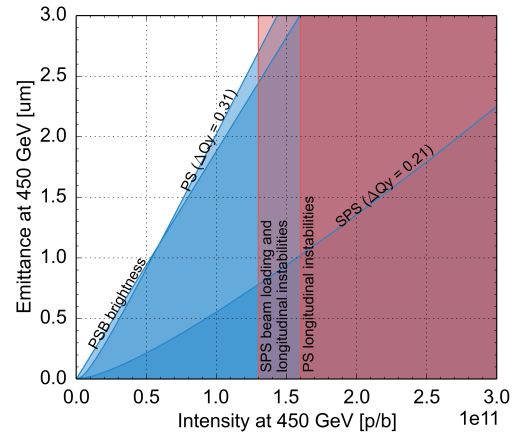


Figure 1: Limitation diagram for the standard LHC beam in the present injectors' chain.

Other methods of LHC beam production exist, which can lead to brighter bunches at the expense of the length of the trains transferred from the PS to the SPS at each cycle. For example, by transferring trains of 48 bunches instead of 72, obtained through a different sequence of batch compression and bunch merging/splitting actions at 2.5 GeV in the PS, the beam brightness can be almost doubled with respect to the scheme discussed above. The beam obtained in this way has been preferred for physics production in the LHC for most of the current run and has been routinely employed since the beginning of 2018. More details about alternative LHC beam production schemes can be found in [9–11].

HL-LHC Beam Requirements

The HL-LHC upgrade aims at accumulating an integrated luminosity of $250 \text{ fb}^{-1}/\text{year}$ at the high luminosity IPs. Assuming 50% HL-LHC performance efficiency, this goal can be achieved assuming a standard LHC beam with bunch intensity of 2.3×10^{11} p/b and a transverse emittance of $2.1 \mu\text{m}$ injected from the SPS. In order not to exceed a pile up of 140 events/crossing, the luminosity is levelled at $5 \times 10^{34} \text{ cm}^{-2}\text{s}^{-1}$ by gradually lowering the beta functions at the IPs (β^*) down to 15 cm while partially compensating for the crossing angle with the crab cavities. An ultimate goal of $320 \text{ fb}^{-1}/\text{year}$ is also set assuming levelling at $7.5 \times 10^{34} \text{ cm}^{-2}\text{s}^{-1}$, allowing for a pile up of 200 events/crossing. Table 1 shows achieved and HL-LHC specified beam parameters at the SPS exit.

It is clear that both intensity and brightness of the LHC beams will need to be roughly doubled in the HL-LHC era. Looking back at Fig. 1, HL-LHC is basically targeting a point right in the middle of the currently inaccessible region.

Table 1: Current and HL-LHC Beam Parameters Out of SPS

	N_b (10^{11} p/b)	$\epsilon_{x,y}$ (μm)
Achieved	1.3	2.7
HL-LHC target	2.3	2.1

LIU CHALLENGES TO REACH THE HL-LHC BEAM PARAMETERS

Figure 1 directly suggests the path to reach the challenging beam parameters specified in the second row of Table 1. We will discuss first how to achieve the desired brightness and we will focus later on the intensity reach.

Achieving the future brightness relies on two main pillars:

- Reduction of the slope of the PSB brightness line by at least a factor two;
- Mitigation of the space charge effect in the PS.

The space charge in the SPS does not seem to limit the performance even for the future beams, as its limitation curve clearly lies below the HL-LHC target point. The two goals listed above will be realised within the LIU project by means of the following actions. Firstly, the PSB brightness line with half slope will be made possible by using Linac4 with H^- charge exchange injection into the PSB at 160 MeV. It has been simulated that if Linac4 provides 40 mA within $0.4 \mu\text{m}$, the future LHC beams can be injected in about 20 turns and the desired transverse emittance is compatible with the blow up due to space charge at the new injection energy (as was expected from a naive $\beta^2\gamma$ scaling) [12]. If the current from Linac4 is lower (compatibly with the goal set for the future fixed target beams), the number of injected turns will have to be correspondingly increased. Secondly, the injection energy into the PS will be raised to 2 GeV, which alone guarantees a 63% intensity increase for a fixed transverse emittance while keeping the space charge tune spread the same as nowadays. Besides, the longitudinal beam parameters at the PSB-PS transfer will have to be optimised to further reduce the tune spread at PS injection and ensure that the PS space charge curve in the limitation diagram ends up in the shadow of the PSB brightness line. The longitudinal emittance will be blown up along the PSB cycle to provide longer bunches at the PS injection, while the larger momentum spread will also further reduce the space charge tune spread due to the increase of the average beam horizontal size through dispersion. The longitudinal emittance blow up can be reproducibly applied in the PSB via either phase modulation of a higher harmonic or injection of band limited phase noise on the main harmonic, as has been demonstrated in MDs in 2017 [6] and 2018.

The achievement of the future intensity relies on:

- Longitudinal stabilisation of the beam along the PS accelerating ramp and at top energy;
- Increase of the available power of the 200 MHz RF system in the SPS in combination with a program of longitudinal impedance reduction;
- E-cloud mitigation in the SPS.

The main longitudinal limitation for LHC-type beams in the PS are dipolar coupled-bunch instabilities. A dedicated broad-band feedback system using a Finemet cavity as a longitudinal kicker has been installed and commissioned in the PS. Extensive tests with beam have been performed since 2016 to explore the intensity reach with this system. The maximum intensity with nominal longitudinal emittance at PS extraction has been measured to be above 2.0×10^{11} p/b [13]. Due to quadrupolar instabilities and incoherent longitudinal emittance growth, it is not yet clear whether a higher harmonic system will be required eventually to keep the beam longitudinally stable with the desired longitudinal emittance at the design intensity for HL-LHC reported in table 1.

The LIU baseline for the SPS includes an upgrade of the low-level RF and a major upgrade of the 200 MHz RF system [14]. The low-level RF upgrade will allow pulsing the RF amplifiers with the revolution frequency (the LHC beam occupies less than half of the SPS circumference) leading to an increase of the available RF power from the existing power plant up to about 1.05 MW per cavity. The main upgrade consists of the re-arrangement of the four existing cavities and two spare sections into two 4-section cavities and four 3-section cavities, and the construction of two additional power plants providing 1.6 MW each. This will entail a reduction of the beam loading per cavity, an overall increase of the available RF voltage and a reduction of the peak beam coupling impedance at the fundamental frequency. With all this massive upgrade in place, the SPS will be able to provide LHC beams with up to about 2×10^{11} p/b, still limited by coupled bunch longitudinal instabilities on the ramp and at top energy [15]. To achieve 2.3×10^{11} p/b it is necessary to reduce the SPS longitudinal impedance. LIU has foreseen shielding of the vacuum flanges between the focusing quadrupoles and the adjacent straight sections as well as installation of High Order Mode (HOM) couplers to improve the damping of the HOMs of the 200 MHz cavities. Numerical simulations have shown that these two measures will allow matching the HL-LHC beam requirement [16]. Finally, the e-cloud in the SPS is a potential limiting factor for operation with higher intensity. Accelerating the present LHC beam without significant degradation from the e-cloud has required an integrated time of several days of dedicated scrubbing distributed over several years. Scrubbing is preserved from year to year in the SPS regions not exposed to air during the stop, while it is partially lost, but usually quickly recovered, where there has been air exposure. Studies of e-cloud build up in the different SPS chambers have revealed that the Secondary Electron Yield (SEY) thresholds will not change significantly when going to the HL-LHC intensity for most cases [17]. Although instability simulations showed that the beam becomes more sensitive to the e-cloud in the dipoles when increasing the beam intensity, it is believed that scrubbing will work also up to the HL-LHC bunch intensity. Recent experience with beams with 2×10^{11} p/b already injected into the SPS has indeed revealed that scrubbing can be efficiently carried out over few days and results in a clear reduction of the e-cloud induced emittance growth

(see Fig. 2). Coating with amorphous carbon (a-C) [18] will be applied to the chambers of the focusing quadrupoles (QF) and adjacent drift chambers during LS2 in synergy with the impedance reduction campaign, which will also gain an extra margin on the instability threshold.

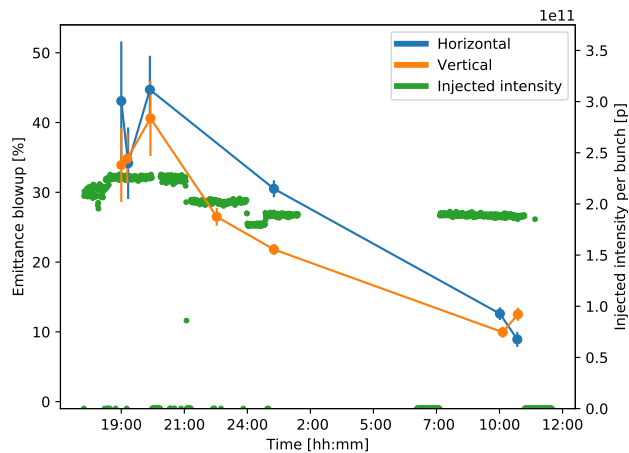


Figure 2: Evolution of emittance growth in SPS during high intensity run. Courtesy of H. Bartosik and M. Carlà.

Putting together all the points discussed in this section, we can draw the new brightness and intensity curves representing the projected limitations after the implementation of the LIU upgrades or actions, obtaining the limitation diagram in Fig. 3. The HL-LHC required point from Table 1 is also shown in yellow, demonstrating that the LIU upgrades are indeed compliant with the achievement of this final goal.

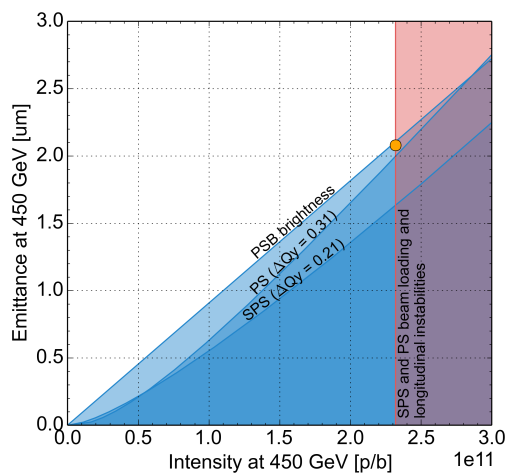


Figure 3: Limitation diagram for the standard LHC beam in the injectors' chain after the LIU upgrades.

HL-LHC CHALLENGES

The HL-LHC layout is based on the nominal LHC ring configuration, in which about 1.2 km of beam line will be changed. The nominal configuration is designed for a realistic, cost-efficient and achromatic implementation of the low β^* collision optics, based on the deployment of the

Achromatic Telescopic Squeeze (ATS) scheme [19]. The installation of triplet quadrupoles of larger aperture is needed to safely accommodate the beams, which reach large dimensions (peak beta functions >20 km), and the shielding to limit the energy deposition and radiation in the SC coils and cold mass [3]. Single particle stability in HL-LHC is challenged by the large beta functions in the triplets and in the adjacent arcs, which enhance the effect of linear and non-linear errors in those regions leading to potentially low Dynamic Aperture (DA) in absence of correction. Even to allow for basic optics measurements pre-computed corrections based on accurate magnetic measurements will have to be used. Besides, the β^* levelling during many hours of operation at constant luminosity will require the commissioning of a large number of optical configurations. This further challenges the efficiency of the optics measurement and correction tools, needed to fulfil the tight tolerances coming from DA or coherent stability constraints [20].

In terms of effects related to the collective beam dynamics, running HL-LHC with double intensity and brightness will pose notable challenges, such as beam stability, beam induced heat loads in the cold regions and beam-beam [21]. (1) Transverse instabilities have been observed in the LHC with different types of beams and during different machine processes, and have required operation with quite extreme settings, e.g. with $Q' = +15$, octupole strength close to the maximum, as well as with maximum gain and maximum bandwidth of the transverse feedback (50 turns and 20 MHz, respectively) at high energy. The instabilities observed at injection energy (450 GeV), which are also cured by high chromaticity and octupole strength, are ascribed to e-cloud. Due to some features (such as symmetry between the transverse planes, heat load measurements on single magnets, simulated electron distributions with different magnetic fields), the e-cloud forming in the quadrupoles is likely to be the main culprit. Combined e-cloud build up and instability simulations show that the electron density in quadrupoles decreases for higher bunch currents and therefore these instabilities should become less critical for HL-LHC intensities. The underlying assumption is of course that all beam chambers will scrub for the higher HL-LHC beam intensities at least as much as they have for the present intensity. To gain margin in the octupole strength needed for suppressing instabilities driven at least partly by impedance, impedance reduction will be applied to the main existing contributors (i.e. the collimators) and to new elements in high beta regions (e.g. crab cavities). In particular, all secondary beta-tron collimators will be replaced with new ones based on a low-impedance design. The present baseline foresees using Mo-Graphite jaws coated with a $5\mu\text{m}$ Mo layer. This material exhibits comparable robustness as the present carbon-based secondary collimators, but has an electrical resistivity 5 (uncoated) to 100 times (coated) lower [22]. Through an iterative process between the RF and the impedance teams, the HL-LHC crab cavities have been already designed with attention to minimise the impact of HOMs on beam stability. (2) Within HL-LHC, the SEY in the insertion regions will

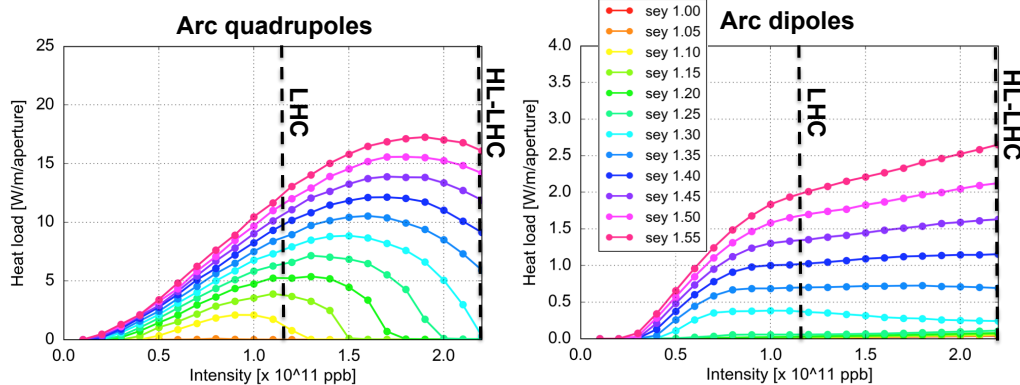


Figure 4: E-cloud generated heat load as a function of bunch intensity in LHC arc dipoles (left) and quadrupoles (right) for different SEYs, as labeled. Courtesy of G. Iadarola and G. Skripka.

be actively reduced by surface treatments (a-C coating [18] or laser treatment [23]), with an expected reduction of the heat load due to e-cloud in these regions. However, no intervention is foreseen on the beam screen of the arcs, which cover more than two thirds of the whole machine. When operating with 25 ns beams, the measured heat loads in the arcs have been consistently much larger than those expected from impedance and synchrotron radiation and they exhibited a still unexplained spread between arcs, being very close to the nominal cryogenics limits in the “hottest” arcs [24]. In future operation, we will be faced with two main issues. First, when moving to HL-LHC intensities and 7 TeV, the contribution of impedance and synchrotron radiation will become three-fold, which roughly halves the available margin of the cryogenic system for additional heat loads. Second, the scaling with intensity of the observed additional heat loads is quite uncertain. Making the educated assumption that e-cloud is the most plausible source of these heat loads (since it is compatible with a number of observations), we can however predict the heat load in the new parameter regime, as displayed in Fig. 4. For SEYs in the 1.2-1.4 range, as inferred from the present excess heat load in the various sectors, e-cloud build up simulations foresee a relatively mild change of e-cloud generated heat load when increasing the bunch intensity to HL-LHC values. This scaling needs to be validated experimentally after LS2 (when LIU will make higher intensity beams available from the injectors [25]). When summing up all the heat load contributions from the e-cloud in the different regions and those from impedance and synchrotron radiation, one finds out that, while the heat load in low-load sectors would be below 8 kW/arc and thus compatible with HL-LHC, the heat load in high-load sectors exceeds the maximum value by at least 20%. If this is confirmed, a back-up filling scheme featuring several 125 ns gaps within the bunch trains will be used for keeping the heat load in the high-load sectors within the capacity of the cryogenic plant. This will be at the expense of a 10-30% lower number of bunches in LHC.

(3) The beam-beam interaction introduces additional strong nonlinearities in the particle motion and leads to resonance

excitation as well as a large tune spread, potentially resulting in a significant restriction of the DA and thus beam degradation. Operational experience and machine studies have proven that the present LHC has surpassed the head-on beam-beam tune shift limit, which was assumed based on experience from past colliders [26, 27]. However, the HL-LHC represents yet another jump into an unexplored parameter range, furthermore with a baseline configuration of luminosity β^* levelling and crossing angle compensation with crab cavities. The beam-beam studies for HL-LHC are performed by tracking the particles over a few million turns under the weak-strong approximation for the beam-beam interaction and for HL-LHC baseline parameters. The DA is calculated and compared with the target value of 6σ over $1e6$ turns. Simulations seem to confirm so far that the target DA is comfortably achieved during the whole levelling process and including the chromaticity and octupole settings necessary for beam stability. This gives room to crossing angle adjustments during the levelling process to reduce the pile-up density and the radiation on the inner triplets [28]. A global exploration of the impact on DA of all the related parameters, including possible compensation of the long-range beam-beam effects with wires or electron lenses, is underway to refine operational scenarios and optimise the projected HL-LHC performance.

ACKNOWLEDGEMENTS

This paper summarises the enormous and excellent work carried out by the LIU and HL-LHC beam dynamics teams. Special thanks to H. Bartosik, G. Iadarola and R. Tomás. Then, I would also like to thank S. Albright, R. Alemany, S. Antipov, F. Antoniou, G. Arduini, M. Beck, E. Benedetto, N. Biancacci, R. Bruce, O. Brüning, X. Buffat, M. Carlà, H. Damerou, G.P. Di Giovanni, R. Di Maria, S. Fartoukh, V. Forte, M. Fraser, B. Goddard, K. Hanke, A. Huschauer, V. Kain, A. Lasheen, K. Li, M. Meddahi, L. Mether, E. Métral, B. Mikulec, Y. Papaphilippou, T. Pieloni, D. Quartullo, S. Redaelli, J. Repond, A. Romano, L. Rossi, B. Salvant, M. Schenk, R. Scrivens, E. Shaposhnikova, G. Skripka, F. Velotti, C. Zannini.

REFERENCES

- [1] J. Coupard *et al.*, “LIU Technical Design Report - Volume I: Protons”, CERN, Geneva, Switzerland, Rep. CERN-ACC-2014-0337, Dec. 2014.
- [2] J. Coupard *et al.*, “LIU Technical Design Report - Volume II: Ions”, CERN, Geneva, Switzerland, Rep. CERN-ACC-2016-0041, Apr. 2016.
- [3] G. Apollinari, I. Béjar Alonso, O. Brüning, P. Fessia, M. Lamont, L. Rossi, and L. Taviani, “High-Luminosity Large Hadron Collider (HL-LHC): Technical Design Report V.0.1”, CERN, Geneva, Switzerland, CERN Yellow Reports: Monographs, Rep. CERN-2017-007-M, April 2017, doi:10.23731/CYRM-2017-004
- [4] M. Benedikt *et al.*, “Summary of Session 7: Accelerators and non LHC Experiment Areas Consolidation up to LS3”, in *Proc. Chamonix 2014 Workshop*, Chamonix, France, Sep. 2014, CERN-ATS-2015-002, pp. 31-32.
- [5] G. Rumolo *et al.*, “Expected Performance in the Injectors at 25 ns Without and With Linac4”, in *Proc. Review of LHC and Injector Upgrade Plans (RLIUP) Workshop*, Archamps, France, Oct. 2013, CERN-2014-006, pp. 17-24.
- [6] S. Albright, E. Shaposhnikova and D. Quartullo, “Longitudinal emittance blow up and production of future LHC beams”, in *Proc. Injector MD days 2017*, Geneva, Switzerland, March 2017, CERN-Proceedings-2017-002.23, pp. 23-26.
- [7] G. Arduini *et al.*, “Fast vertical single-bunch instability at injection in the CERN SPS - an update”, in *Proc. PAC’07*, Albuquerque, New Mexico, US, Jun. 2007, paper FRPMN065, pp. 4162-4164.
- [8] H. Bartosik, “Beam dynamics and optics studies for the LHC injectors upgrade”, Ph.D. thesis, CERN, Geneva, Switzerland, CERN-THESIS-2013-257, Nov. 2013.
- [9] R. Garoby, *IEEE Transactions on Nuclear Science*, vol. 32, no. 5, pp. 2332 - 2334, Oct. 1985, doi:10.1109/TNS.1985.4333903
- [10] H. Damerou *et al.*, “LIU: Exploring alternative ideas”, in *Proc. Review of LHC and Injector Upgrade Plans (RLIUP) Workshop*, Archamps, France, Oct. 2013, CERN-2014-006, pp. 127-138.
- [11] H. Bartosik and G. Rumolo, “Beams in the injectors”, in *Proc. 5th Evian Workshop on LHC beam operation*, Evian-les-Bains, France, June 2014, CERN-ACC-2014-0319, pp. 93-98.
- [12] E. Benedetto *et al.*, “Space charge effects and mitigation in the CERN PS-Booster, in view of the upgrade”, in *Proc. HB’16*, Malmö, Sweden, Jul. 2016, paper THPM9X01, pp. 517-522.
- [13] H. Damerou and L. Ventura, “Longitudinal coupled-bunch instability studies in the PS”, in *Proc. Injector MD days 2017*, Geneva, Switzerland, March 2017, CERN-Proceedings-2017-002.59, pp. 59-62.
- [14] E. Shaposhnikova, E. Chapala and E. Montesinos, “Upgrade of the 200 MHz RF System in the CERN SPS”, CERN, Geneva, Switzerland, Rep. CERN-ATS-2011-042, Aug. 2011.
- [15] M. Meddahi *et al.*, “LHC Injectors Upgrade (LIU) project at CERN”, in *Proc. IPAC’15*, Richmond, VA, USA, May 2015, paper THPF093, pp. 3915-3918.
- [16] E. Shaposhnikova *et al.*, “Identification and reduction of the SPS impedance”, in *Proc. HB’16*, Malmö, Sweden, July 2016, paper TUAM3X01, pp. 260-265.
- [17] G. Iadarola and G. Rumolo, “Electron cloud in the CERN accelerators (PS, SPS, LHC)”, in *Proc. E-CLOUD’12*, Elba Island, Italy, June 2012, CERN-2013-002, pp. 19-26.
- [18] C. Yin Vallgren *et al.*, “Amorphous carbon coatings for the mitigation of electron cloud in the CERN Super Proton Synchrotron”, vol. 14, p. 071001, Jul. 2011, doi:10.1103/PhysRevSTAB.14.071001
- [19] S. Fartoukh, “Achromatic telescopic squeezing scheme and application to the LHC and its luminosity upgrade”, *Phys. Rev. ST Accel. Beams*, vol. 16, p. 111002, Nov. 2013, doi:10.1103/PhysRevSTAB.16.111002.
- [20] F. Carlier *et al.*, “Optics Measurement and Correction Challenges for the HL-LHC”, CERN, Geneva, Switzerland, Rep. CERN-ACC-2017-0088, Nov. 2017.
- [21] G. Arduini *et al.*, *JINST* vol. 11, p. C12081, Dec. 2016, doi:10.1088/1748-0221/11/12/C12081.
- [22] E. Quaranta *et al.*, “Towards optimum material choices for the HL-LHC collimator upgrade”, CERN, Geneva, Switzerland, Rep. CERN-ACC-2016-0062, May 2016.
- [23] R. Valizadeh *et al.*, “Low secondary electron yield of laser treated surfaces of copper, aluminum and stainless steel”, in *Proc. IPAC’16*, Busan, Korea, Jun. 2016, paper TUOCB02, pp 1089-1092.
- [24] G. Iadarola, G. Rumolo, P. Dijkstal, and L. Mether “Analysis of the beam induced heat loads on the LHC arc beam screens during Run 2”, CERN, Geneva, Switzerland, Rep. CERN-ACC-Note-2017-0066, Dec. 2017.
- [25] G. Rumolo *et al.*, “Update on the HiLumi/LIU parameters and performance ramp up after LS2”, presented at HiLumi Collaboration meeting, Madrid, Spain, Nov. 2017, unpublished.
- [26] W. Herr *et al.*, “Observations of beam-beam effects in the LHC in 2011”, in *Proc. Chamonix Workshop 2012 on LHC Performance*, Chamonix, France, Jan. 2012, CERN-2012-006, pp. 99-104.
- [27] T. Pieloni *et al.*, “Colliding high brightness beams in the LHC”, in *Proc. HB’12*, Beijing, China, Sep. 2012, paper MOP250, pp. 180-182.
- [28] Y. Papaphilippou *et al.*, “Long Range Beam-Beam effects for HL-LHC”, presented at LHC Performance Workshop (Chamonix 2018), Chamonix, France, Jan. 2018, unpublished.

LINAC4 COMMISSIONING STATUS AND CHALLENGES TO NOMINAL OPERATION

G.Bellodi* for the Linac4 team, CERN, Geneva, Switzerland

Abstract

Linac4 will be connected to the Proton Synchrotron Booster (PSB) during the next long LHC shutdown in 2019 and it will operationally replace Linac2 as provider of protons to the CERN complex as of 2021. Commissioning to the final beam energy of 160 MeV was achieved by the end of 2016. Linac4 is presently undergoing a reliability and beam quality test run to meet the beam specifications and relative tolerances requested by the PSB. In this paper we will detail the main challenges left before achieving nominal operation and we will report on the commissioning steps still needed for final validation of machine readiness before start of operation.

INTRODUCTION

Linac4 is a 160 MeV H-linear accelerator that will replace Linac2 as injector of the CERN PS Booster (PSB) and provider of protons to the whole CERN complex as of 2021. The pre-injector part is composed of a RF volume source producing a 45 keV beam at 2 Hz maximum repetition rate, followed by a Low Energy Beam Transport section (LEBT), a Radio Frequency Quadrupole (RFQ) accelerating the beam to 3MeV, and finally a Medium Energy Beam Transport Line (MEBT), matching the beam to the linac. The MEBT is composed of 11 quadrupoles, 3 bunchers and a chopper, formed by two sets of deflecting plates, which are used to selectively remove micro-bunches in the 352 MHz sequence, in order to optimise injection into the 1 MHz CERN PSB RF bucket. The nominal scheme currently envisaged is to chop 133 bunches out of 352, with a consequent current reduction by 40%. After the MEBT, the linac consists of three distinct sections: a conventional Drift Tube Linac (DTL) accelerates the beam to 50 MeV. It is divided in 3 tanks and is equipped with 111 Permanent Magnet Quadrupoles (PMQs). This is followed by a Cell-Coupled Drift Tube Linac (CCDTL), made up of 21 tanks of 3 cells each, accelerating the beam to 100 MeV. The CCDTL was constructed by the Russian Scientific Research Institute for Technical Physics (VNIITF) and the Budker Institute of Nuclear Physics. Focusing is provided by Electro-Magnetic Quadrupoles (EMQs) placed outside each module, and PMQs between coupled tanks. Final acceleration to 160 MeV is done through a PI-Mode Structure (PIMS), composed of 12 tanks of 7 cells each, interspersed with 12 EMQs for beam focusing. The PIMS were constructed within a CERN-NCBJ-FZ Julich collaboration and assembled and tuned at CERN. Both CCDTL and PIMS represent the first such cavities to work in an operational machine. A 70 m long transfer line, including 17 EMQs, 5

dipoles (3 horizontal and 2 vertical) and a PIMS-like debuncher cavity connects Linac4 to the present injection line into the PSB, which will be only slightly modified for the remaining 110 m to the PSB entrance. A sketch of Linac4 is shown in Fig. 1.

COMMISSIONING

The commissioning of Linac4 was organised in six different phases over 3 years, alternating hardware installation and beam validation periods at increasing energy values. The commissioning was prepared and accompanied by extensive beam simulations, which turned out to be crucial to successfully optimise beam transmission and quality. A key decision was to start simulations with a particle distribution obtained by measuring the beam in the LEBT under different solenoid focusing and back-tracing the measurements to the start of the line.

In the first commissioning stage a dedicated 3 MeV test stand was used for a systematic beam measurement campaign that lasted 6 months. The following stages at higher energies (12 MeV, 50 MeV, 100 MeV and 160 MeV) lasted on average 3 weeks each. Two diagnostics test benches were used during commissioning. The low energy one (used at 3 and 12 MeV), allowed direct measurements of transverse emittance and energy spread via a slit-and-grid system and a spectrometer arm respectively. The high energy bench (used at 50 and 100 MeV) contained 3 profile harps and wire-scanners at 60 deg phase advance from each other for emittance reconstruction; a Bunch Shape Monitor (BSM) and lasing station for beam stripping and two Beam Position Monitors for Time-Of-Flight (TOF) and trajectory measurements.

Table 1: Energy and Beam Intensity Milestones

Energy [MeV]	Date (beam energy)	Record peak current	Date (record current)	2017 operational current
0.045	2013	50 mA	11/2015	40 mA
3	03/2013	30 mA	10/2015	26 mA
12	08/2014	24 mA	11/2016	20 mA
50	11/2015	24 mA	11/2016	20 mA
105	06/2016	24 mA	06/2016	20 mA
160	10/2016	24 mA	10/2016	20 mA

A very important result of the low energy commissioning was the agreement between direct measurements of the beam transverse emittance via the slit-and-grid method and indirect measurements based on emittance reconstruction from profiles, using either a “forward-method” technique or a tomographic reconstruction method [1].

* Giulia.Bellodi@cern.ch

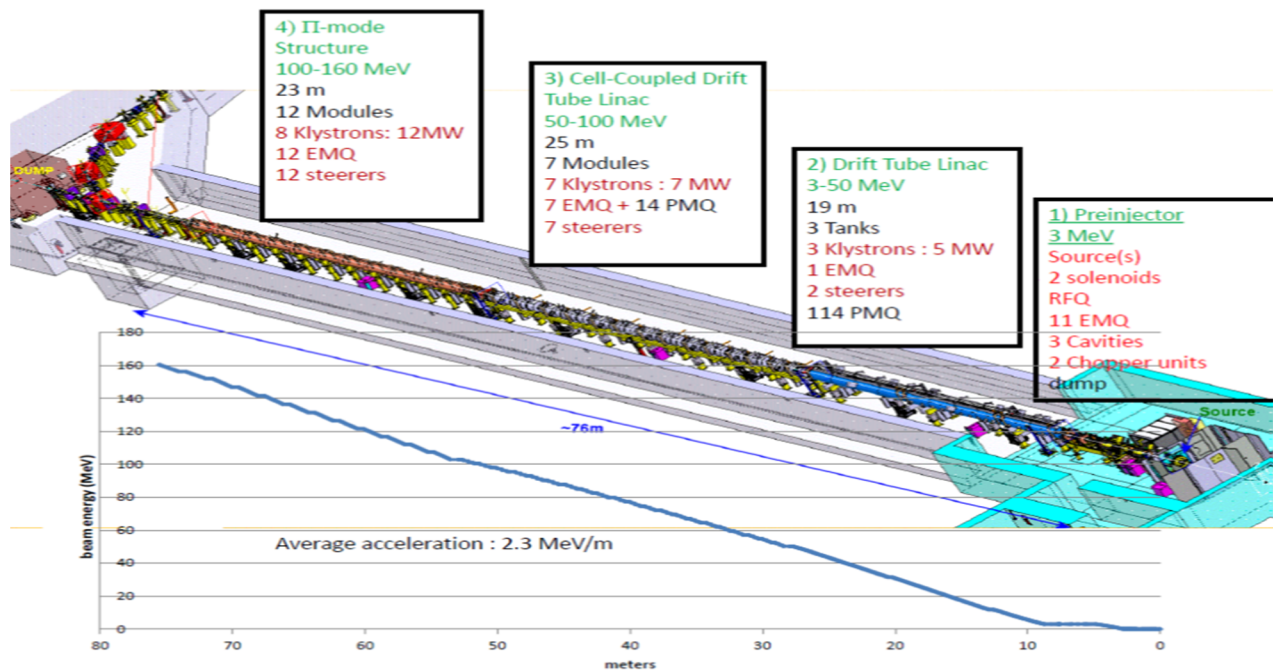


Figure 1: Sketch of Linac4.

We refer to past publications for a more complete description of commissioning measurements [2]; timelines and main milestones of the different commissioning stages are summarised in Table 1. Note that record peak currents were not always taken during the measurement campaign at the corresponding energy. Beam commissioning to the final energy of 160 MeV was successfully completed by the end of 2016.

HALF SECTOR TEST

After achieving this milestone, the 160 MeV beam was used for a few months at the end of 2016 to feed a test setup of the PSB injection chicane, the Half Sector Test (HST). The purpose of this test was to gain information about the $H^- \rightarrow$ proton stripping system, to help reduce risks and facilitate the commissioning during the Long-Shutdown-2 (LS2, 2019-2020), when many modifications are foreseen in the framework of the LHC Injectors Upgrade (LIU) programme, and to ensure that the new equipment works according to specifications. The Linac4 connection requires a complete renewal of the PSB injection scheme, due to the energy increase from 50 to 160 MeV and the injection of H^- ions instead of protons as currently done from Linac2. Protons are presently injected via a multi-turn injection process using kickers and an injection septum. After connection, the H^- ions from Linac4 will be injected through a stripping foil located in the centre of the injection bump. Fast kicker magnets will be used for phase-space painting. The new injection scheme will benefit from reduced space charge effects and injection losses (from the current 50% to $\sim 2\%$ due to unstripped or partially stripped particles). The high complexity of integration in a limited space availability, however, justified the proposal for a test installa-

tion in the Linac4 transfer line, consisting of a half injection chicane of one PSB ring (see Fig. 2). The installation was composed of:

- a stripping foil system with a loader containing 6 foils and a screen with radiation-hard camera
- half of the injection chicane
- a monitor measuring partially and unstripped particles (H^0/H^-) and the H^0/H^- dump
- beam-loss monitors in vicinity of the dump
- beam current transformers upstream and downstream of the HST for stripping efficiency measurements
- a screen for beam profile and position measurements.

A separate stripping foil test stand was installed at the beginning of the Linac4 transfer line in order to:

- test foil changing mechanisms and interlock functions
- gain experience on foil handling
- test different foil materials and thicknesses
- gain information on foil lifetime.

The HST received first beam at the end of October 2016 and stopped operation in April 2017. Stripping efficiency was confirmed to be $>99\%$ for $200 \mu\text{g}/\text{cm}^2$ thick carbon foils, fulfilling the design specifications.

A few foil breakages were observed, possibly due to interference with the Beam Television (BTV) screen, used for beam observation (see a sample measurement in Fig. 3). All the main functionalities were checked and validated. Input was gained on possible design changes to improve measurement precision and stability and for noise reduction. The operational experience gained with equipment handling, controls and interlocks, was crucial for future commissioning phases.

Content from this work may be used under the terms of the CC BY 3.0 licence (© 2018). Any distribution of this work must maintain attribution to the author(s), title of the work, publisher, and DOI.

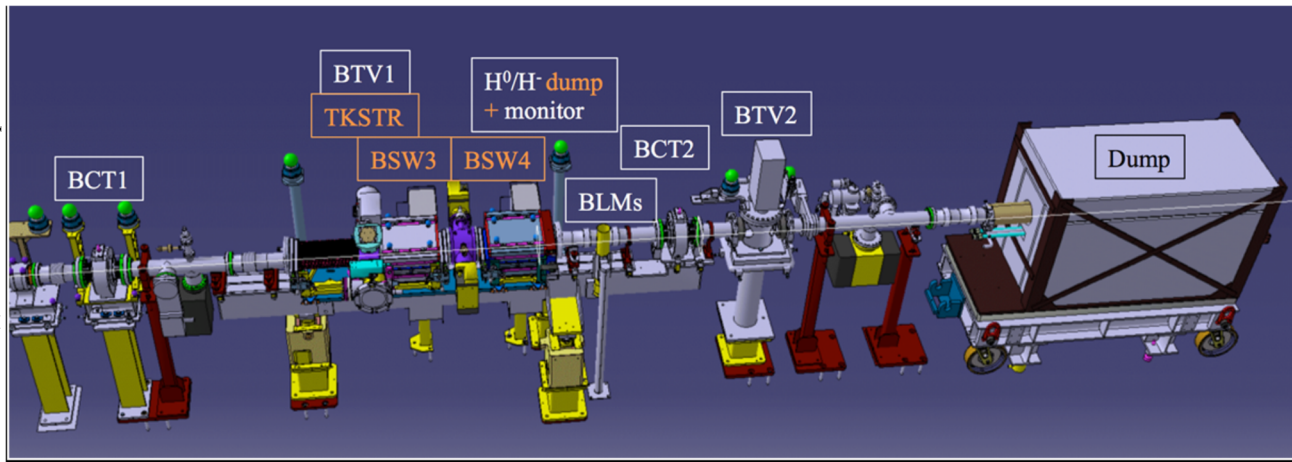


Figure 2: Sketch of the half-sector test installation.

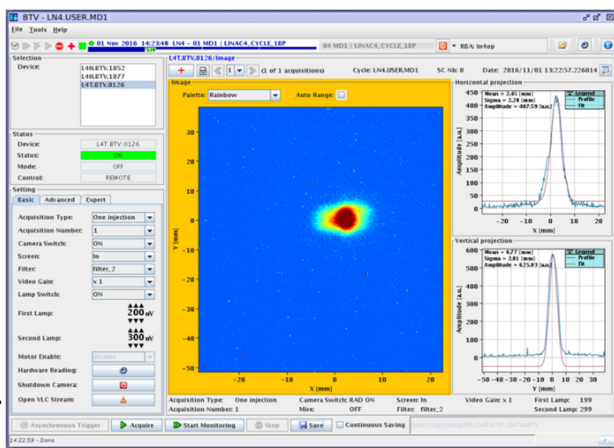


Figure 3: Transverse profile of the beam at 160 MeV measured on the Beam Television (BTv) screen.

RELIABILITY RUN

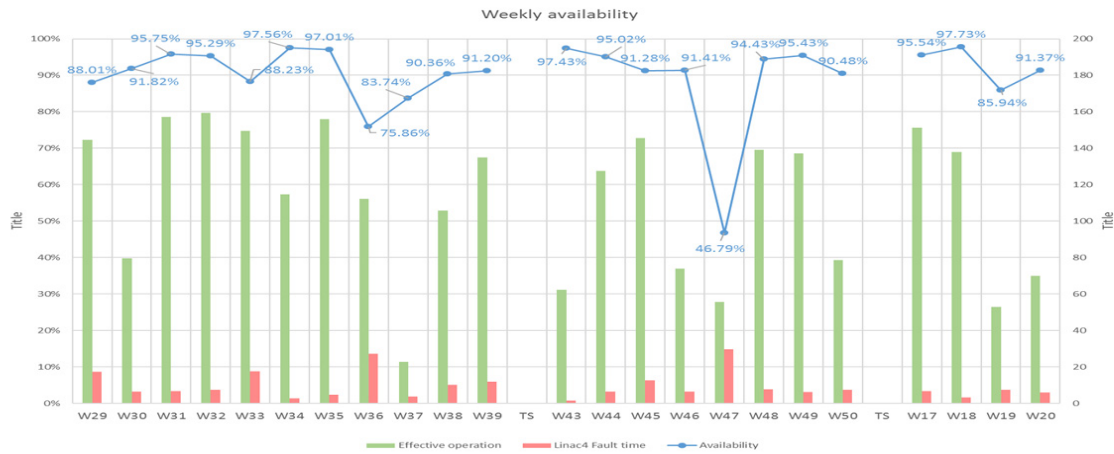
Once connected to the PSB, Linac4 will be the sole provider of protons to the whole CERN accelerator complex. This sets very high requirements in terms of machine availability, which will ultimately need to match the current performance of Linac2, running today, after 40 years, with an average availability of more than 98%. After successful completion of machine commissioning, a Reliability Run was therefore planned, intended also as a transitional period towards operation. The main aim of the run was essentially consolidation of routine operation and identification of potential recurring problems, thus providing a unique opportunity for early identification of weak points and for improving procedures. The Reliability Run took place from June to the end of December 2017, and it was divided in two phases to allow for scheduled Technical Stops for maintenance and technical interventions. The first phase lasted until the end of September, and it was composed of short periods of operation followed by repairs and optimization. The second phase took place from the end of October to the end of the year, with longer periods of operation followed by technical interventions, to approach more re-

alistic operating conditions. In total, 19 weeks were dedicated to the Reliability Run. The Accelerator Fault Tracking system [3], initially developed for the LHC, was also adopted for Linac4 fault tracking, with some ad hoc adjustments, needed to account for the fact that Linac4 is not yet an operational machine (hence call-out support is not available on a round-the-clock basis). Machine availability and beam-on time was thus calculated manually from logbook entries during working hours only, subtracting scheduled interventions and machine studies.

The analysis of the weekly availability is shown in Fig. 4. The average machine availability over the 19 weeks of the run exceeded 90%. There were 2 specific weeks where long faults were recorded: 1) week 36, with a controls timing issue and a RF cavity cooling problem, and 2) week 47, with the failure of a power converter anode module needing replacement. Apart from these two occurrences, most of the down-time was due to short and recurrent faults, mainly affecting the RF systems, power converters, the pre-chopper and the source. A full fault distribution covering the entire run period is shown in Fig. 5. Some of the problems identified were addressed and fixed immediately during the ensuing End-of-the-Year-Technical-Stop, while others will be corrected during the Extended Technical Stop foreseen in summer 2018.

BEAM QUALITY RUN

The last Linac4 operational period took place between February and May 2018. Substantial RF interventions had taken place during the previous End-of-Year-Technical-Stop (LLRF upgrades, maintenance of high-power RF systems, upgrades of the RF restart procedures etc). The focus of this run was therefore placed on recommissioning all the changes implemented and on the validation of a series of beam quality requirements that had been agreed amongst different groups as necessary for future Linac4 operation with the PSB.



Availability	Fault Count	Operation	Suspended OP	Effective Operation	Fault Mean Time to Repair
91.5%	449	23 weeks	~ 8 weeks	~15 weeks	~29 min

Figure 4: Linac4 weekly availability during the 2017/2018 reliability run.

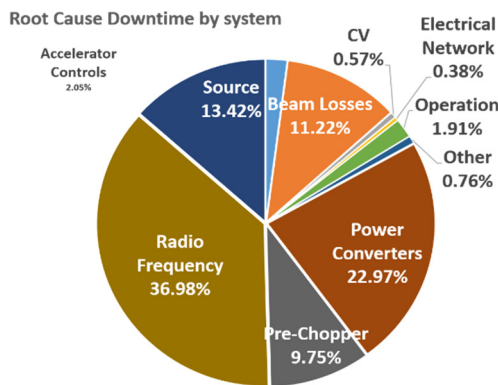


Figure 5: Linac4 fault distribution by system.

The following list of measurements can be earmarked as main achievements of the run:

- i) Beam intensity flatness along the pulse and shot-to-shot stability were both confirmed to be within $\pm 2\%$ (excluding the initial current rise time due to space charge compensation build-up at low energy), which is comparable or slightly better than the current performance from Linac2.
- ii) Similarly, the horizontal and vertical position variations along the pulse were measured to be contained within ± 1 mm (requested margin at the entrance of PSB not to exceed a transverse emittance of $1.7 \mu\text{m}$ for LHC beams, see Table 3).
- iii) The chopper performance was tested in depth, by operating with different (and sometimes extreme) chopping patterns on two parallel users in the machine supercycle. In the first case a LHC-type test beam was used, with a pulse length of $160 \mu\text{s}$ and a chopping factor of 60% at 352 MHz (equivalent to a ~ 625 ns long bunch train being accelerated

and ~ 375 ns long bunch train being chopped off and deflected onto the 3 MeV dump). In the second case a substantially different chopping pattern was implemented ($3.6 \mu\text{s}$ beam transmitted, $2.4 \mu\text{s}$ chopped off), with a longer pulse length. This validated the pulse-to-pulse use of the chopper and was a test exercise to mimic production of different beams in parallel for the LHC and fixed target physics experiments. The remnant current transmitted when the chopper is activated was measured to be ~ 0.15 mA, which is at the limit of resolution of the measuring devices and amounts to $\sim 1\%$ of the total transmitted beam intensity. Rise and fall times of the chopper signals were confirmed to be within a few ns, in agreement with the technical specifications of the pulse amplifier and PSB requests to minimize losses and reduce activation of the vertical injection septum.

Dedicated time was also set aside to progress with the commissioning of several beam diagnostics devices, particularly the laser emittance monitor [4] and the Bunch Shape Monitor (BSM) [5]. The laser emittance monitor uses a pulsed laser beam delivered to the tunnel by optical fibres to detach electrons from the H^- ions, which are then deflected into an electron multiplier. The resulting neutral H^0 atoms are separated from the main beam and recorded downstream by diamond-strip detectors. By scanning the laser through the H^- beam, transverse profiles can be obtained from the signals on the electron multiplier. The H^0 profiles on the diamond detector allow to determine the beam divergence, which in combination with the laser position, allows the H^- transverse emittance to be reconstructed (see Fig. 6).

Content from this work may be used under the terms of the CC BY 3.0 licence (© 2018). Any distribution of this work must maintain attribution to the author(s), title of the work, publisher, and DOI.

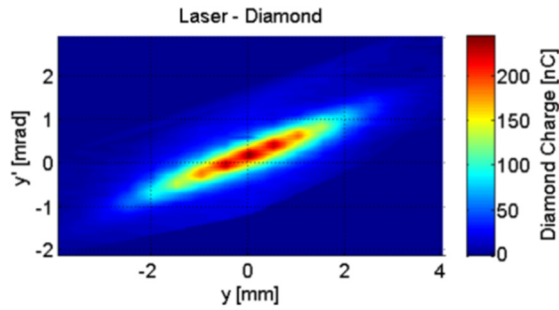


Figure 6: Beam phase space reconstruction at 160 MeV in the Linac4 transfer line using the laser emittance monitor.

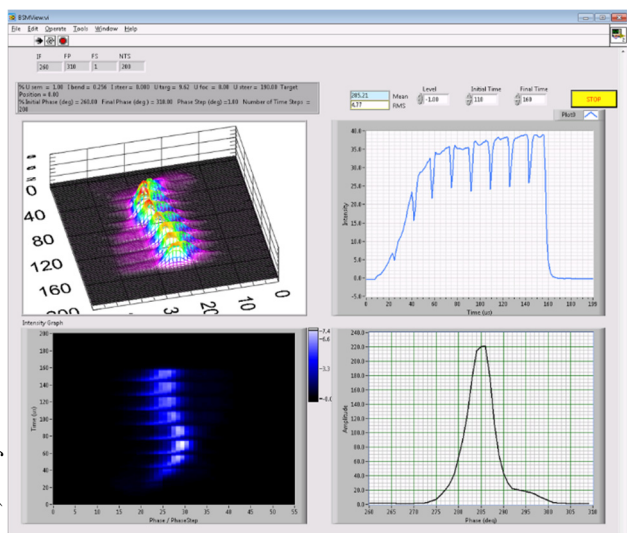


Figure 7: Screenshot from a BSM measurement at Linac4 showing clockwise: 1) beam intensity along the pulse length (top right); 2) longitudinal beam phase profile (bottom right); evolution of the phase profile along the pulse length (mountain and cascade plots on the left).

The BSM was developed and fabricated at INR in Russia, to make longitudinal beam profile measurements with a phase resolution of 1° (over a full range of 180° at 352 MHz). Two such devices are installed at Linac4: the first one after the PIMS in the straight line to the dump, and the second one after the debunching cavity in the transfer line to the PSB. Hardware and beam commissioning were successfully completed in varied measurement conditions (changing chopping pattern, pulse length etc- see Fig. 7).

OUTLOOK AND FUTURE PLANNING

Table 2 shows a comparison of the nominal Linac4 beam parameters with the results achieved during the 2017 reliability run. The beam current amounts to 60% of the target value. This intensity limitation occurs in the low-energy pre-injector section and is due to the fact that the beam extracted from the currently installed cesiated RF volume source has an emittance exceeding the transverse acceptance

Table 2: Linac4 Design Targets vs Today’s Achievements

	Linac4 design targets	Linac4 achieved
Peak current in the linac	40 mA	24 mA
Routine current in the linac	40 mA	20 mA
Transverse emittance at 160 MeV	0.4 π mm mrad	0.3 π mm mrad
Energy at PSB injection	160 MeV	160 MeV
Pulse length / rep rate	400 μs/ 1 Hz	Up to 600 μs/ 1 Hz

of the RFQ. Target performance for Linac4 after connection to the PSB is to inject via charge-stripping up to 1×10^{13} protons per ring at 160 MeV. The current performance is still sufficient to guarantee the production of LHC-type and fixed-target-physics-type beams (see Table 3), by compensating the lower intensity with a higher number of injected turns [6].

Table 3: Beam Specifications at the PSB

Beam	Intensity (protons/ring)	Emittance at PSB – [mm mrad]	N° turns at 20 mA beam current
LHC-type	3.4×10^{12}	1.7	45
Fixed target physics	$1-1.2 \times 10^{13}$	10	110-150

A R&D programme has however been launched in parallel on a separate dedicated ion source test stand to study alternative source extraction geometries and plasma generators in order to maximise the current in the RFQ acceptance. This will open the way to upgrades and will allow to exploit the full potential of the linac.

Linac4 has now entered a phase of Extended Technical Stop (ETS) for 3 months until September 2018 to allow the RF team to complete a series of scheduled upgrade and maintenance activities. This will be followed by a re-commissioning run until the end of the year with the aim of validating all changes implemented.

Linac4 will be connected to the PSB during the first semester of 2019, and further commissioning periods are being planned in the following to complete validating the whole installation and its beam performance before the start of official operation in 2021.

REFERENCES

- [1] V.A.Dimov *et al*, “Emittance reconstruction techniques in presence of space charge applied during the Linac4 beam commissioning”, in *Proc. HB’16*, Malmö, Sweden, Jul. 2016, paper WEPM1Y01, pp. 433-438.
- [2] A.M. Lombardi, “The Linac4 project”, in *Proc. HB’16*, Malmö, Sweden, Jul. 2016, paper MOAM2P20, pp. 1-5.

- [3] C. Roderick *et al.*, “Accelerator Fault Tracking at CERN”, in *Proc. ICALEPCS’17*, Barcelona, Spain, Oct. 2017, paper TU-PHA013, pp. 397-400.
- [4] T.Hofmann *et al.*, “Results from the laserwire emittance scanner and profile monitor at CERN’s Linac4”, in *Proc. 28th Linear Accelerator Conf. (LINAC’16)*, East Lansing, MI, USA, Sep. 2016, pp. 715-719.
- [5] A. V. Feshenko, “Methods and instrumentation for bunch shape measurements”, in *Proc. 2001 Particle Accelerator Conf. (PAC’01)*, Chicago, IL, USA, Jun. 2001, pp. 517-521.
- [6] V. Forte *et al.*, “Multi-Particle Simulations of the Future CERN PSB Injection Process With Updated Linac4 Beam Performance”, presented at HB’18, Daejeon, Korea, Jun. 2018, paper WEP2PO007, this conference.

J-PARC RCS: EFFECTS OF EMITTANCE EXCHANGE ON INJECTION PAINTING

H. Hotchi[#] and the J-PARC RCS beam commissioning group,
 J-PARC Center, Japan Atomic Energy Agency, Tokai, Naka, Ibaraki, 319-1195 Japan

Abstract

The J-PARC 3 GeV rapid cycling synchrotron (RCS) is a high-power pulsed proton driver aiming for a 1 MW output beam power. This paper presents our recent efforts for beam dynamics issues that we faced during the RCS beam power ramp-up, especially about the optimization of the injection painting method in a situation involving the emittance exchange caused by the Montague resonance.

INTRODUCTION

The J-PARC 3 GeV rapid cycling synchrotron (RCS) is the world's highest class of a high-power pulsed proton driver aiming for a 1 MW beam power [1, 2]. A 400 MeV H^- beam from the injector linac is multi-turn charge-exchange injected into the RCS through a carbon foil over a period of 0.5 ms. The RCS accelerates the injected protons up to 3 GeV with a repetition rate of 25 Hz. Most of the RCS beam pulses are delivered to the materials and life science experimental facility (MLF), while only four pulses every several second are injected to the main ring synchrotron (MR) by switching the beam destination pulse by pulse.

The requirements for the beam operations to the MLF and the MR are different. Thus, different parameter optimizations are required for the two operation modes. Due to the higher operational duty, the machine activations of the RCS are mainly determined by the beam operation to the MLF. Therefore, a sufficient beam loss mitigation is required for this operation mode. In addition, for the MLF, a wide-emittance beam with low charge density is required to mitigate a shockwave on the neutron target, which is essential to obtain a sufficient lifetime of the neutron target. On the other hand, for the MR, a narrow-emittance beam with low beam halo is required contrary to the MLF case, which is essential to mitigate beam loss at the MR. In order to meet the different requirements for the beam operations to the MLF and the MR, we can utilize transverse injection painting [3], that is, applying large painting for the MLF and small painting for the MR.

Figure 1 shows the tune diagram around the operational point, in which the red lines represent the structure resonances up to 4th order derived from the three-fold symmetric lattice of the RCS, and the green circle shows the operational betatron tune that we had used until very recently. This operational point allows space-charge tune shifts to avoid serious structure resonances such as $\nu_{x,y} = 6$, $4\nu_{x,y} = 27$ and $2\nu_x + 2\nu_y = 27$, but, in exchange, it is very close to the Montague resonance $2\nu_x - 2\nu_y = 0$ [4]. As well known, the $2\nu_x - 2\nu_y = 0$ resonance, which is mainly excited by space-charge nonlinear fields such as octupole,

causes emittance exchange. The emittance exchange has a major influence on the formation of the beam distribution during injection painting. This is the major issue in optimizing the injection painting for the MLF and the MR.

In this paper, the influence of the emittance exchange on injection painting and the optimization of the painting method in such a situation involving the emittance exchange are discussed for a high-intensity beam of 8.33×10^{13} ppp (1 MW-equivalent intensity). The present status of the RCS beam operation, optimized through the above discussion, and the future prospect are also mentioned in the latter part.

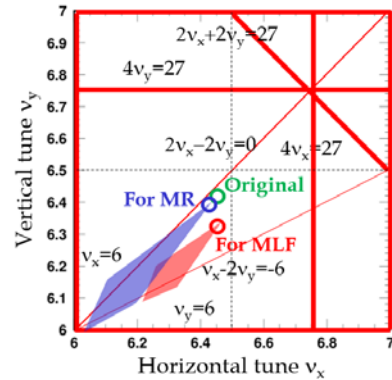


Figure 1: Tune diagram around the operational point.

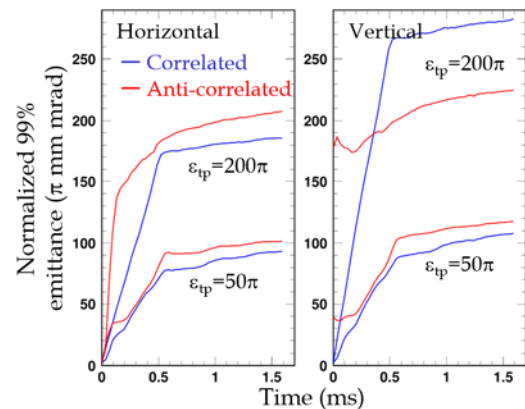


Figure 2: Time dependences of the beam emittances calculated for the first 1.5 ms.

EMITTANCE GROWTH DURING INJECTION PAINTING

In the RCS, both correlated painting and anti-correlated painting are available, and the painting emittance (ϵ_{ip}) is adjustable from 0 to 200π mm mrad for both the horizontal and the vertical planes [3], where ϵ_{ip} is defined as the un-

[#]hotchi.hideaki@jaea.go.jp

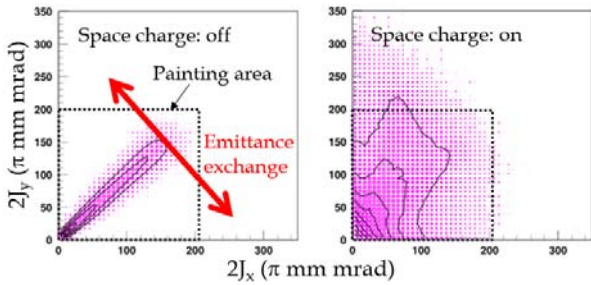


Figure 3: 2d plots of the betatron actions (J_x, J_y) at the end of injection calculated with the correlated painting of $\varepsilon_{ip}=200\pi$ mm mrad.

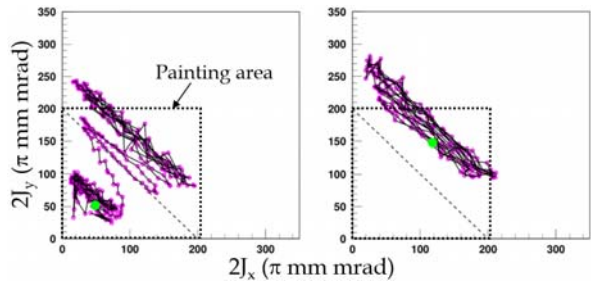


Figure 4: Single-particle motions during the correlated painting of $\varepsilon_{ip}=200\pi$ mm mrad.

normalized value of the entire painting area.

Figure 2 shows time dependences of the beam emittances for the first 1.5 ms calculated with $\varepsilon_{ip} = 200\pi$ mm mrad and $\varepsilon_{ip} = 50\pi$ mm mrad for correlated painting and anti-correlated painting. As shown in the figure, the correlated painting and the anti-correlated painting give the opposite result for the large painting and the small painting. In case of the large painting, the anti-correlated painting provides less emittance growth. But, in case of the small painting, the correlated painting rather than the anti-correlated painting gives narrower beam emittance. The opposite phenomena observed in the large painting and the small painting can be comprehended by considering the emittance exchange caused by the $2\nu_x - 2\nu_y = 0$ resonance, as is discussed below.

PARTICLE MOTIONS DURING LARGE PAINTING

First, we discussed the particle motions during injection painting with a large painting emittance of $\varepsilon_{ip} = 200\pi$ mm mrad, which is required for the beam operation to the MLF.

Figure 3 shows a 2d plot of the betatron actions (J_x, J_y) at the end of injection calculated with the correlated painting of $\varepsilon_{ip} = 200\pi$ mm mrad. As is shown in the left panel obtained with no space charge, in correlated painting, the injection beam is painted along the line of $J_x - J_y = 0$, namely, from the middle to the outside on both the horizontal and the vertical planes. This situation with no space charge significantly changes when the space charge is turned on, as shown in the right panel; one can see a significant diffusion of beam particles swerving from the

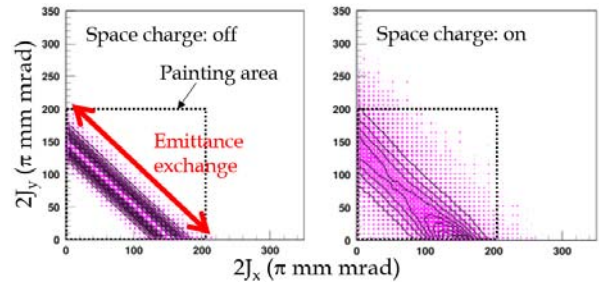


Figure 5: 2d plots of the betatron actions (J_x, J_y) at the end of injection calculated with the anti-correlated painting of $\varepsilon_{ip}=200\pi$ mm mrad.

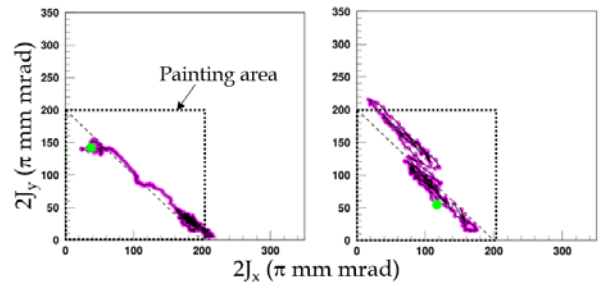


Figure 6: Single-particle motions during the anti-correlated painting of $\varepsilon_{ip}=200\pi$ mm mrad.

path of beam painting. This large emittance dilution over the painting area is mainly caused by the emittance exchange. As illustrated in the left plot in Fig. 3, the directions of the beam painting and the emittance exchange are perpendicular to each other in case of correlated painting. This geometrical situation more directly leads the emittance exchange to significant emittance growths. Figure 4 shows a single-particle motion of one macro-particle leading to large emittance growths. It clearly shows that the emittance growth formed in the correlated painting is originated from the emittance exchange which occurs perpendicularly to the path of beam painting.

Figure 5 shows the case of the anti-correlated painting with $\varepsilon_{ip} = 200\pi$ mm mrad. As is shown in the left panel obtained with no space charge, in anti-correlated painting, the injection beam is painted along the line of $J_x + J_y = \text{const.}$, namely, from the middle to the outside on the horizontal plane, while, from the outside to the middle on the vertical plane. As illustrated in the left plot in Fig. 5, the direction of the anti-correlated painting is the same as that of the emittance exchange. Figure 6, displaying a single-particle motion of one macro-particle during the anti-correlated painting, clearly shows such a situation. This geometrical situation prevents the emittance exchange from causing large emittance growths. In the right panel in Fig. 5, one can confirm that most of the beam particles stay in the painting area even if the emittance exchange occurs, thanks to the same directions of the beam painting and the emittance exchange.

Thus, the emittance exchange has a different effect on the formation of the beam distribution depending on the

Content from this work may be used under the terms of the CC BY 3.0 licence (© 2018). Any distribution of this work must maintain attribution to the author(s), title of the work, publisher, and DOI.

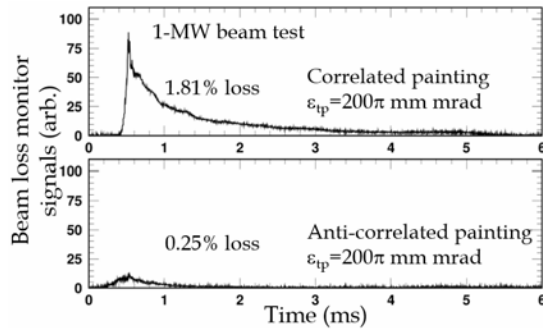


Figure 7: Beam loss monitor signals measured at the RCS collimator section.

geometrical relation between the beam painting and the emittance exchange in the (J_x, J_y) space. The above analysis concludes that the anti-correlated painting more favours the suppression of emittance growths caused by the emittance exchange. Figure 7 is the result of the 1 MW beam test [5], showing the beam loss monitor signals at the RCS collimator section. As shown in the figure, a significant beam loss was observed for the correlated painting with $\epsilon_{ip} = 200\pi$ mm mrad. But, by introducing the anti-correlated painting with the same painting emittance, the beam loss was successfully reduced to the order of a couple of 10^{-3} as expected. This empirical situation was well reproduced by the numerical simulations, as shown in Fig. 8. Through the measurements and the numerical simulations, we confirmed the advantage of anti-correlated painting. But, we have to note that the conclusion here is just for the case of large painting.

PARTICLE MOTIONS DURING SMALL PAINTING

Next, we investigated the case of small painting, which is required for the beam operation to the MR.

Figure 9 shows the beam emittance 1-ms after the end of injection, calculated as a function of the painting emittance for correlated painting and anti-correlated painting. This dependence is ascribed to the balance between the painting emittance and its resultant space charge mitigation; they are well balanced at $\epsilon_{ip} = 50\pi$ mm mrad, providing the minimum beam emittance there. In addition, in this figure, one can find the correlated painting rather than the anti-correlated painting achieves the narrower beam emittance at $\epsilon_{ip} = 50\pi$ mm mrad. This situation for correlated painting and anti-correlated painting is completely opposite to the case of large painting. This characteristic phenomenon observed in the small painting is also understandable by considering the effect of the emittance exchange, as is discussed below.

In anti-correlated painting, the direction of the beam painting is the same as the direction of the emittance exchange. This geometrical situation well suppresses emittance growths directly caused by the emittance exchange, but it has a potential of causing a significant modulation of the charge density. Figure 10 shows a 2d

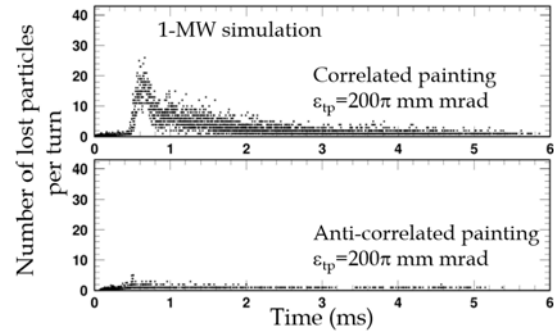


Figure 8: Numerical simulation results corresponding to the results of the 1 MW beam test in Fig. 7.

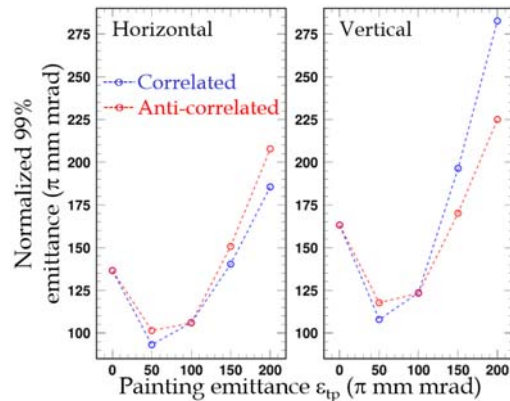


Figure 9: Beam emittances 1-ms after the end of injection calculated as a function of ϵ_{ip} .

plot of the betatron actions (J_x, J_y) during the anti-correlated painting with $\epsilon_{ip} = 50\pi$ mm mrad. In this figure, one can find the formation of a high-density isle at the late stage of injection. This concentration of beam particles is ascribed to the synchronism between the beam painting and the move of the beam distribution caused by the emittance exchange, as shown in Fig. 11. But, such a significant charge density modulation is not found in the large painting, as shown in Fig. 5. The synchronism between the two motions is lost in going to larger painting, so a uniform distribution is relatively maintained in the large painting. That is, it can be said that the charge density modulation is a characteristic phenomenon enhanced in the anti-correlated painting with a small painting emittance.

Figure 12 shows the case of the correlated painting with $\epsilon_{ip} = 50\pi$ mm mrad. In correlated painting, the emittance exchange occurs in the orthogonal direction to the path of beam painting. This geometrical situation enhances emittance growths simply caused by the emittance exchange itself, but, in exchange, it has the advantage of avoiding a modulation of the charge density, as shown in the figure.

These characteristic behaviours of beam particles during the small painting were experimentally confirmed as shown in Fig. 13; a high-density peak structure was found for the anti-correlated painting with $\epsilon_{ip} = 50\pi$ mm mrad, while a more uniform beam distribution was observed for

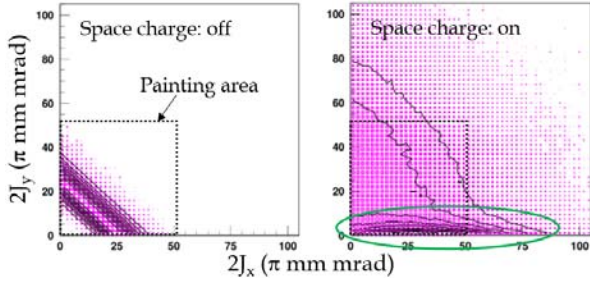


Figure 10: 2d plots of the betatron actions (J_x, J_y) at the end of injection calculated with the anti-correlated painting of $\epsilon_{ip}=50\pi$ mm mrad.

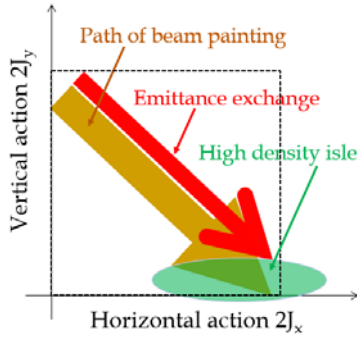


Figure 11: Schematic diagram of the geometrical relationship in the (J_x, J_y) space between the emittance exchange and the anti-correlated painting with a small painting emittance.

the correlated painting with $\epsilon_{ip} = 50\pi$ mm mrad, as predicted.

The high-density isle formed in the anti-correlated painting with $\epsilon_{ip} = 50\pi$ mm mrad causes a large space-charge detuning as shown in Fig. 14, leading to significant additional emittance growths afterward. The emittance growth caused via the formation of the high-density isle is more critical than that caused by the emittance exchange itself in the correlated painting. This is the main reason why the anti-correlated painting leads to larger emittance growths in case of $\epsilon_{ip} = 50\pi$ mm mrad.

RESULT OF DISCUSSION

The emittance exchange makes two major effects during injection painting. One (i) is the emittance growth simply caused by the direct effect of the emittance exchange, which is more enhanced in correlated painting. Another (ii) is from the secondary effect of the emittance exchange, namely, the emittance growth caused through a modulation of the charge density, which is more enhanced in anti-correlated painting. In large painting such as $\epsilon_{ip}=200\pi$ mm mrad, the former effect (i) is more significant, so anti-correlated painting, suppressing the effect (i), leads to less beam loss. On the other hand, in small painting such as $\epsilon_{ip} = 50\pi$ mm mrad, the latter effect (ii) is more critical, so correlated painting avoiding the effect (ii), leads to less emittance growth.

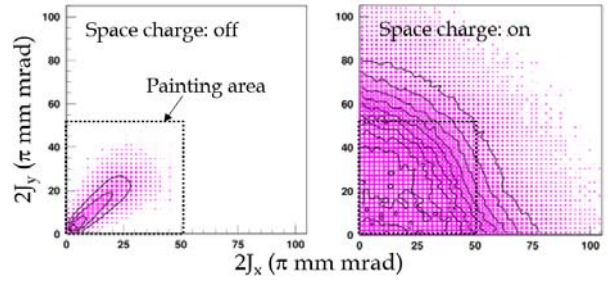


Figure 12: 2d plots of the betatron actions (J_x, J_y) at the end of injection calculated with the correlated painting of $\epsilon_{ip}=50\pi$ mm mrad.

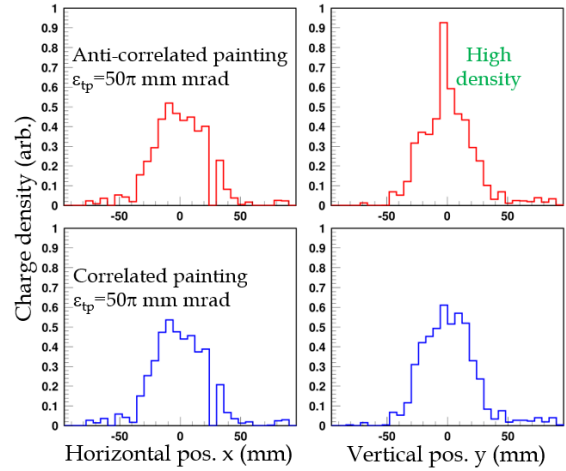


Figure 13: Beam profiles measured at the end of injection.

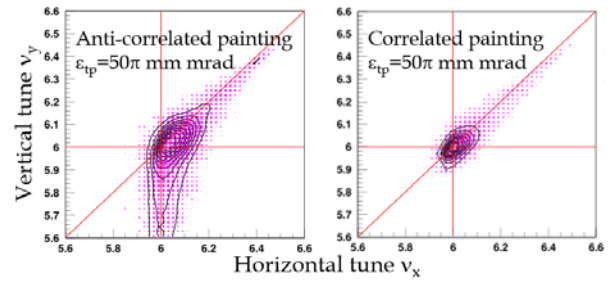


Figure 14: Space-charge tune shifts calculated at the end of injection.

PRESENT STATUS AND FUTURE PROSPECT OF RCS BEAM OPERATION

Based on the above result, we optimized the operational parameters including injection painting for the MLF and the MR, which are now applied for the routine user operations.

For the MLF, the betatron tune is now set to (6.45, 6.32) as shown in Fig. 1 (red circle), where the large painting with $\epsilon_{ip} = 200\pi$ mm mrad is applied. This operational point is relatively far from the $2\nu_x - 2\nu_y = 0$ resonance, so the effect of the emittance exchange is not critical. Therefore, the correlated painting as well as the anti-correlated

Content from this work may be used under the terms of the CC BY 3.0 licence (© 2018). Any distribution of this work must maintain attribution to the author(s), title of the work, publisher, and DOI.

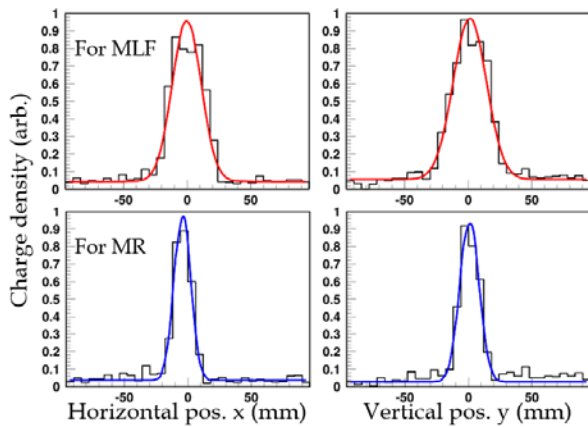


Figure 15: Beam profiles measured at extraction.

painting are now feasible for the MLF.

For the MR, the operational point is set to (6.42, 6.40) as shown in Fig. 1 (blue circle), where the small painting with $\varepsilon_{ip} = 50\pi$ mm mrad is applied. This small painting causes a large space-charge detuning, so a part of beam particles possibly reaches the integers of $v_{x,y} = 6$ as illustrated by a blue necktie in Fig. 1. The integers involve all-order systematic resonances and strongly affect the beam. This operational point provides a larger separation from $v_{x,y} = 6$, but it is very close to $2v_x - 2v_y = 0$; the beam suffers heavy effects of the emittance exchange in exchange for less effects of $v_{x,y} = 6$. Therefore, we are now applying the correlated painting for the MR. As discussed in the last section, the correlated painting more favours the suppression of emittance growths originating from the emittance exchange in case of small painting such as $\varepsilon_{ip} = 50\pi$ mm mrad.

To realize the optimal beam operations for the MLF and the MR compatibly, we have recently introduced a pulse-by-pulse switching of the operational parameters according as the beam destination [6]; the pulse-by-pulse switching of the betatron tune is conducted with 6 sets of pulsed trim quadrupole magnets, while the pulse-by-pulse switching of the injection painting is performed with 6 sets of pulsed injection bump magnets. By optimizing the operational parameters for each beam destination, and, in addition, by realizing their pulse-by-pulse switching, we successfully met the requirements for the MLF and the MR; a wide-emittance beam for the MLF and a narrow-emittance beam for the MR were achieved as requested while keeping beam loss within acceptable levels, as shown in Fig. 15.

Thus, the accelerator itself is now ready to try a continuous 1 MW beam operation for the MLF. But, unfortunately, we had troubles in the liquid mercury targets used for neutron production at the MLF; a water leak from the target vessel happened two times one after another at the 500 kW beam power in 2015 - 2016. Therefore, since then, the routine beam power had been limited to 150~200 kW. But, in the last summer maintenance period in 2017, a new robust target was installed, so we are now back to the beam power ramp-up phase again. While the present beam

power for the MLF users is 500 kW, it will be increased step by step to 1 MW from now on carefully monitoring the condition of the target.

The RCS is now delivering the beam to the MR at a beam intensity of $\sim 6.5 \times 10^{13}$ ppp corresponding to 78% of the RCS design intensity. With this beam, the MR has recently achieved a new record of a 500 kW beam power for the neutrino experiment via the recent efforts for beam loss reduction including the improvement of the RCS beam quality [6, 7]. The design beam power of the MR is 750 kW. To achieve the design value and more, the MR operation cycle time will be reduced from 2.48 s to 1.3 s in the near future. Hardware upgrades to get such a rapid operation cycle, such as the upgrade of the main magnet power supplies, is in progress now.

SUMMARY

The effects of the emittance exchange on injection painting were investigated for a 1 MW-equivalent beam intensity. In this work, we found the emittance exchange makes two major effects during injection painting;

- (i) Emittance growth directly caused by the emittance exchange itself.
- (ii) Emittance growth caused by the secondary effect of the emittance exchange, namely, via a modulation of the charge density.

They each are enhanced or mitigated depending on the choice of correlated painting and anti-correlated painting, and their painting emittance. In a situation with the emittance exchange, investigating the particle motions while considering the geometrical relation in the (J_x, J_y) space between the beam painting and the emittance exchange is a key to optimizing the injection painting as well as to understanding the behavior of the beam. Based on the analysis result, the operational parameters including injection painting for the MLF and the MR were recently re-optimized, which are now successfully applied for the routine user operations.

REFERENCES

- [1] High-intensity Proton Accelerator Project Team, "Accelerator Technical design report for high-intensity proton accelerator facility project, J-PARC", Rep. JAERI-Tech-2003-044, JAERI, Tokai, Japan, Mar. 2003.
- [2] H. Hotchi *et al.*, "Beam commissioning of the 3 GeV rapid cycling synchrotron of the Japan Proton Accelerator Research Complex", *Phys. Rev. ST Accel. Beams*, vol. 12, p. 040402, Apr. 2009, doi:10.1103/PhysRevSTAB.12.040402
- [3] H. Hotchi *et al.*, "Beam loss reduction by injection painting in the 3 GeV rapid cycling synchrotron of the Japan Proton Accelerator Research Complex", *Phys. Rev. ST Accel. Beams*, vol. 15, p. 040402, Apr. 2012, doi:10.1103/PhysRevSTAB.15.040402
- [4] B.W. Montague, "Fourth-order coupling resonance excited by space-charge forces in a synchrotron", CERN, Geneva, Switzerland, Rep. CERN-68-38, Oct. 1968.

- [5] H. Hotchi *et al.*, “Achievement of a low-loss 1 MW beam operation in the 3 GeV rapid cycling synchrotron of the Japan Proton Accelerator Research Complex”, *Phys. Rev. Accel. Beams*, vol. 20, p. 060402, Jun. 2017, doi:10.1103/PhysRevAccelBeams.20.060402
- [6] H. Hotchi *et al.*, “Pulse-by-pulse switching of operational parameters in J-PARC 3 GeV RCS”, in *Proc. IPAC'18*, Vancouver, Canada, Apr. 2018, paper TUPAL018.
- [7] S. Igarashi *et al.*, “High-power beam operation at J-PARC”, presented at HB2018, Daejeon, Korea, Jun. 2018, paper TUA2WD02, this conference.

BEAM PHYSICS LIMITATIONS FOR DAMPING OF INSTABILITIES IN CIRCULAR ACCELERATORS*

V. A. Lebedev[†], Fermilab, PO BOX 500, Batavia, IL 60510, USA

Abstract

The paper considers a beam interaction with a feedback system and major limitations on the beam damping rate. In particular, it discusses limitations on the system gain and damping rate, feedback system noise and its effect on the beam emittance growth, x - y coupling effect on damping, and suppression of high order modes.

CAUSALITY IN DAMPERS

Causality binds amplitude and phase for an amplifier or electric circuit. This relationship is described by Kramers-Kronig relations. However, there are no requirements of causality in beam-based feedbacks because a reduction of delay in a signal propagation from pickup to kicker may result in that the electric signal arrives to the kicker earlier than a particle bunch which produced this signal in the pickup, thus breaking causality. That allows one to adjust the complex gain of the feedback to basically anything what may require. It can be also used for a frequency response correction of a power amplifier. At high frequencies it is done by analogue circuits. At lower frequencies digital filters represent more effective means.

To break the causality one needs to split the signal into few paths with different delays and frequency responses. Figure 1 presents an example of filter which, with use of 3 branches, makes $1/\sqrt{\omega}$ gain dependence over 4 orders of magnitude with reasonably good phase response. The filter can be described by the following expression:

$$G(\omega) = \sum_{k=1}^3 \frac{A_k e^{i\omega\tau_{1k}}}{(1+i\omega\tau_{2k})(1+i\omega\tau_{3k})} . \quad (1)$$

Such or similar filter may be used for damping rate reduction with frequency as described below.

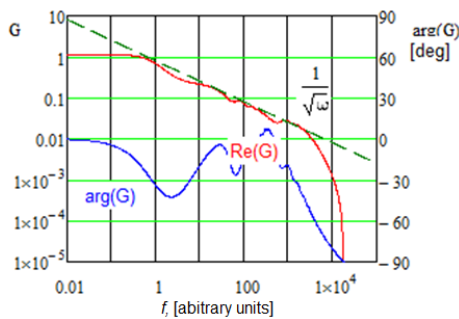


Figure 1: Amplitude and phase characteristics of $1/\sqrt{\omega}$ filter. Parameters of Eq. (1) are: $\tau_1=[0.1, 0.01, 0]$, $\tau_2=[1, 0.02, 4 \cdot 10^{-4}]$, $\tau_3=[0.02, 0.004, 8 \cdot 10^{-6}]$, $A=[1, 0.11, 0.03]$.

* Work supported by Fermi Research Alliance, LLC under Contract No. DE-AC02-07CH11359 with the United States Department of Energy.

[†] val@fnal.gov

A practical implementation of complex gain correction was carried out at Fermilab for gain correction of stochastic cooling systems during Tevatron Run II (see Section 7.2.3 in Ref [1]).

EMITTANCE GROWTH SUPPRESSION

An increase of beam energy of a hadron collider results in an increase of its size and a reduction of revolution frequency. It leads to a decrease of frequencies of lowest betatron sidebands. Considering that the spectral density of noise, which excites betatron motion, increases fast with frequency decrease one obtains that this increase may become dangerous when betatron frequency sidebands approach few kilohertz range. This effect was first observed at Tevatron where it prevented an operation at low value of fractional part of betatron tune [2]. Later experiments verified an existence of the problem (see Section 6.3.3. in Ref [1]). This effect was strongly manifested at the beginning of LHC commissioning where “transverse noise” resulted in fast emittance growth intermittent with emittance jumps called “hump” effect [3].

Major sources of emittance growth are fluctuations of bending field and quad displacements due to ground motion. The bending field fluctuations are excited by fluctuations of current in dipoles and may be also excited by mechanical oscillations of liners inside SC dipoles. Note that in the LHC the magnetic field of dipoles is “frozen” into the liners and their size oscillations, excited by acoustic noises, result in oscillations of magnetic field. Typical requirement to the bending field stability of $\Delta B/B \leq 10^{-9}$ is quite tight. Consequently, size fluctuations of sub-angstrom level may be dangerous.

The transverse emittance growth driven by transverse kicks is determined by their spectral density at the betatron sidebands [4]:

$$\left(\frac{d\varepsilon}{dt}\right)_0 = \frac{\omega_0^2}{4\pi} \sum_k \beta_k \sum_{n=-\infty}^{\infty} S_{\theta_k}((\nu-n)\omega_0) . \quad (2)$$

Here ω_0 is the circular revolution frequency, ν is betatron tune, and $S_{\theta_k}(\omega)$ is the spectral density of the angular kicks at the k -th location with beta-function of β_k . The spectral density is normalized as:

$$\overline{\Delta\theta^2} = \int_{-\infty}^{\infty} S(\omega) d\omega , \quad (3)$$

where $\sqrt{\overline{\Delta\theta^2}}$ is the rms value of the kicks. For the white noise, Eq. (2) is simplified to the well-known result: $(d\varepsilon/dt)_0 = (f_0/2) \sum_k \beta_k \overline{\Delta\theta_k^2}$, where $f_0 = \omega_0/2\pi$. Note that

the emittance growth happens only if there is a spread in particle betatron tunes. In its absence a bunch would be moving as whole without emittance growth. In the case of hadron collider of LHC size or more Eq. (2) puts severe limitations on acceptable value of noise spectral density.

A solution for the problem was first suggested in Refs. [4,5]. The idea is based on damping of betatron oscillations before betatron motion from a kick may decohere. It was shown that damping of betatron oscillations with damping rate (in amplitude) of $\lambda=f_0g/2$ is suppressed as:

$$\frac{d\varepsilon}{dt} \approx \frac{16\pi^2\overline{\Delta\nu^2}}{g^2+16\pi^2\overline{\Delta\nu^2}} \left[\left(\frac{d\varepsilon}{dt} \right)_0 + \frac{f_0g^2}{2\beta_p} \sigma_{bpm}^2 \right], \quad (4)$$

where the second addend accounts for the emittance growth excited by the feedback system (transverse damper) itself, σ_{bpm} describes the damper noise referenced to the rms accuracy of beam position measurements in the pickup, β_p is the beta-function in the pickup, g is the dimensionless gain of the damper, and $\sqrt{\overline{\Delta\nu^2}}$ is the rms spread of betatron tunes. For head-on collisions of round beams $\sqrt{\overline{\Delta\nu^2}} \approx 0.2\xi$, where ξ is the total linear tune shift due to beam-beam interactions. As can be seen from Eq. (4), if the gain is much larger than the tune spread, the gain increase does not increase the emittance growth related to the damper noise; while contribution due to external noise is suppressed as $1/g^2$. It yields that the gain should be sufficiently large so that the contribution of damper noise would dominate the emittance growth.

Note also that the betatron motion chromaticity is another source of beam decoherence. Therefore, it is desirable to have the gain larger than the synchrotron tune.

As it was already mentioned that the emittance growth due to LHC ‘‘hump’’ presented a serious challenge at the beginning of LHC commissioning. The problem was resolved by large gain increase in the LHC transverse dampers and a redistribution of gains inside their electronics which reduced the pickup noise [6]. Power supplies responsible for creation of the ‘‘hump’’ were found in about half year. For the LHC the rms pickup resolution is estimated to be in the range of 0.2 – 0.5 μm .

Spectral density of external noise decreases fast with frequency. Consequently, only external noise at the lowest betatron sidebands contributes to the emittance growth. Typically, the instability rate of multi-bunch instabilities also decreases with frequency. That enables a reduction of feedback gain with frequency increase. Let us consider how this reduction affects the emittance growth driven by the damper. The pickup signal from a collider bunch is quite large ($\gg 1$ V). Therefore, noise of a digital damper is typically determined by resolution of ADCs digitizing pickup signal, and, to good accuracy, the pickup noise can be considered as the white noise. For a ring with n_b uniformly distributed bunches ($n_b \gg 1$) we can consider that all noises are in the frequency band $[-f_0n_b/2, f_0n_b/2]$. The corresponding spectral density is $\sigma_{bpm}^2/(2\pi f_0n_b)$. Taking this into account we can rewrite Eq. (4) as follows:

$$\frac{d\varepsilon}{dt} \approx \sum_{n=-n_b/2}^{n_b} \frac{16\pi^2\overline{\Delta\nu^2}}{g_n^2+16\pi^2\overline{\Delta\nu^2}} \left[\left(\frac{d\varepsilon}{dt} \right)_n + \frac{f_0g_n^2}{2\beta_p} \frac{\sigma_{bpm}^2}{n_b} \right], \quad (5)$$

where g_n is the damping rate at the n -th betatron sideband, $(d\varepsilon/dt)_n = (\omega_0^2/4\pi) \sum_k \beta_k S_{\theta_k} ((\nu-n)\omega_0)$ is the contri-

bution to the emittance growth from the external noise at n -th betatron sideband, and we accounted that the external noise for higher harmonics is negligible (or it can be referenced to the main band). As one can see for $g_n^2 \gg 16\pi^2\overline{\Delta\nu^2}$ the contribution of damper noise to the emittance growth does not depend on gain distribution over frequency. However, if the gain at high frequencies can be reduced to be smaller than $\sqrt{16\pi^2\overline{\Delta\nu^2}}$; then accounting that the external noise is negligible at high frequencies one obtains that the effect of damper noise can be reduced resulting in a smaller emittance growth.

DIGITAL FILTERS

Modern dampers, including LHC dampers, are digital. That creates a possibility to use large number of previous turns in computation of each kick. That potentially could reduce the damper sensitivity to pickup noise. Let us consider a general damper where each turn correction is determined by weighted sum of previous beam positions:

$$\delta\theta_n = \frac{g_1}{\sqrt{\beta_p\beta_k}} \sum_{k=0}^{K-1} A_k (x_{n-k} + \delta x_{n-k}). \quad (6)$$

Here β_p and β_k are the beta-functions in the pickup and kicker, respectively, x_n and δx_n are the beam positions and their errors at turn n , and g_1 is the relative damper gain. A requirement to suppress sensitivity to the beam orbit offset in the pickup results in that $\sum_{k=0}^{K-1} A_k = 0$. We also assume that the gain g_1 is sufficiently small so that a perturbation theory could be used.

An introduction of complex variable,

$$z = \frac{x}{\sqrt{\beta}} - i \left(\sqrt{\beta}\theta + \alpha \frac{x}{\sqrt{\beta}} \right), \quad (7)$$

reduces the betatron motion to a rotation in the complex plane with betatron frequency ($z = e^{i\mu} z_0$). Substituting Eq. (7) into Eq. (6) and dropping non-resonant terms one obtains the damping rate:

$$g_d = -\frac{i}{2} g_1 e^{-i\mu_{pk}} \sum_{k=0}^{K-1} A_k e^{-i\mu_0 k}, \quad (8)$$

where $\mu_0/2\pi$ is the betatron tune, and μ_{pk} is the betatron phase advance between pickup and kicker [6].

Now we consider the emittance growth excited by noise of the BPM measurements. The same as above we assume that g is sufficiently small. Then, omitting (temporarily) the damping term (x_{n-k}) in Eq. (6) one obtains:

$$z_{n+1} = e^{i\mu_0} \left(z_n - i e^{-i\mu_{pk}} \frac{g_1}{\sqrt{\beta_p}} \sum_{k=0}^{K-1} A_k \delta x_{x-k} \right). \quad (9)$$

Each error, δx_n , makes K contributions to the sum thus multiplying the effect of this error. Let only a single measurement be erroneous. Then after K turns we obtain:

$$\begin{aligned} z_K &= e^{i\mu_0 K} z_0 - i e^{-i\mu_{pk}} \frac{g_1}{\sqrt{\beta_p}} \delta x_0 \sum_{k=0}^{K-1} A_k e^{i\mu_0(K-k)} \\ &= e^{i\mu_0 K} z_0 + \frac{2g_d}{\sqrt{\beta_p}} e^{i\mu_0 K} \delta x_0, \end{aligned} \quad (10)$$

where z_0 is the initial complex amplitude of the particle in the pickup, δx_0 is an error of position measurement, and at the end of transformations we used Eq. (8). Averaging over initial phase of the oscillations and kick amplitudes we obtain an increase of the emittance due to a single kick:

$$\delta\mathcal{E} = \frac{1}{2} (|z + \delta z|^2 - |z|^2) = \frac{1}{2} |\delta z|^2 = 2 |g_d|^2 \frac{\overline{\delta x^2}}{\beta_p}, \quad (11)$$

where $\overline{\delta x^2}$ is the squared rms error of single measurement. Taking into account that different kicks are statistically independent one obtains the emittance growth rate without its suppression by the damper:

$$\frac{d\mathcal{E}}{dt} = 2f_0 |g_d|^2 \frac{\overline{\delta x_{bpm}^2}}{\beta_p}. \quad (12)$$

Comparing this equation with Eq. (4) ($g_d \rightarrow g/2$) one can conclude that the digital filter does not help to reduce an effect of BPM noise on $d\mathcal{E}/dt$; but a usage of large number of turns in the damper increases the damper sensitivity to the betatron tune and, as it will be shown in the following section, reduces the maximum achievable gain.

LIMITATIONS ON THE GAIN

An increase of collider size results in increased sensitivity to external noise and, consequently, requires a higher damping rate. Here we consider limitations on the damping rate for a digital transverse damper. In the general case the turn-by-turn transformation referenced to the pickup location is:

$$\mathbf{x}_{n+1} = \mathbf{M}_{kp} \left(\mathbf{M}_{pk} \mathbf{x}_n + \mathbf{G} \sum_{k=0}^{K-1} A_k \mathbf{x}_{n-k} \right), \quad (13)$$

where $\mathbf{x}_n = (x, \theta_x)^T$ is the vector describing a location of the bunch center of gravity in the 2D phase space, \mathbf{M}_{kp} and \mathbf{M}_{pk} are the transfer matrices from kicker-to-pickup and pickup-to-kicker,

$$\mathbf{G} = \begin{bmatrix} 0 & 0 \\ 0 & g_1 \end{bmatrix} \quad (14)$$

and coefficients A_k are defined by Eq. (6). We look for a solution in the form $\mathbf{x}_{n+1} = \Lambda \mathbf{x}_n$ which results in an equation for the eigen-value Λ :

$$\left| \mathbf{M} - \Lambda \mathbf{I} + \mathbf{M}_{kp} \mathbf{G} \sum_{k=0}^{K-1} \frac{A_k}{\Lambda^k} \right| = 0, \quad (15)$$

where \mathbf{I} is the identity matrix, and we accounted that the ring transfer matrix is $\mathbf{M} = \mathbf{M}_{kp} \mathbf{M}_{pk}$. As one can see the number of roots of Eq. (15) is equal to $2K$. Consequently, for the filter order $K \leq 2$ this equation can be solved analytically, and a numerical solution is required otherwise. The damping rate is defined by following equation:

$$\lambda = f_0 \ln \left(\max(|\Lambda_n|) \right), \quad (16)$$

where $\max()$ chooses the largest modulo of the eigen-values of $|\Lambda_n|$. For small g_1 the perturbation theory solution yields the result presented in Eq. (8).

To demonstrate behaviour of damping for large gains we consider 3 cases: (1) one-turn system ($A_0 = 1$), (2) two-turn system with notch filter ($A_0 = -A_1 = 1$), and the LHC damper.

The solution for the one-turn system is straightforward. It has two roots:

$$\Lambda = c + \frac{g_1 s_{kp}}{2} \pm i \sqrt{1 - g_1 s_{pk} - \left(c + \frac{g_1 s_{kp}}{2} \right)^2}, \quad (17)$$

where μ_{kp} is the kicker-to-pickup phase advance, and $c = \cos(\mu_0)$, $s = \sin(\mu_0)$, $c_{kp} = \cos(\mu_{kp})$, $s_{pk} = \sin(\mu_{pk})$, $\mu_0 = 2\pi[\nu]$, and $[\nu]$ is the fractional part of betatron tune. Figure 2 shows a dependence of eigen-values modulo on the gain for $[\nu] = 0.42$ and $\nu_{pk} = 0.25$. As one can see an increase of gain results in modulo splitting for gain above:

$$g_m = \begin{cases} -\sin(\mu) / \sin^2(\mu_{kp} / 2), & \pi \leq \mu \leq 2\pi, \\ \sin(\mu) / \cos^2(\mu_{kp} / 2), & 0 \leq \mu \leq \pi, \end{cases} \quad (18)$$

where the maximum damping is achieved. Figure 3 presents a dependence of maximum of eigen-values modulo on the betatron tune for the optimal gain, g_m . As one can see damping is greatly decreased near half integer tunes. One turn damping is possible at tunes equal to 0.25 and 0.75. Note also that a properly designed system of two pickups and two kickers has not a dependence of g_m on the betatron tune and can damp oscillations in 1 turn.

The solution for the two-turn system has four roots. One of them is equal to zero and can be omitted. The three other are solutions of cubic equation. Its solution is straightforward and therefore is not presented here. Figure 4 shows a dependence of eigen-values modulo on the gain for the optimal pickup-to-kicker phase advance $\nu_{pk} = (1 - \nu)$

/2. Behaviour is similar to the case of one turn system but now there are 3 non-trivial eigen-values. Figure 5 presents a dependence of maximum of eigen-values modulo on the betatron tune for the optimal gain. As one can see the damping disappears near integer resonances and, compared to the one-turn system, the maximum damping rate is significantly degraded.

An increase in number of turns decreases the maximum damping rate approximately as $1/K$, where K is the number of turns used in computation of corrections. Figure 6 presents the damping rate, defined by Eq. (16), for the LHC horizontal damper [6] where damper corrections are computed from the beam positions at 7 previous turns. That significantly reduces the maximum achievable damping rate and introduces strong dependence of damping rate on the machine tune as shown in Figure 7.

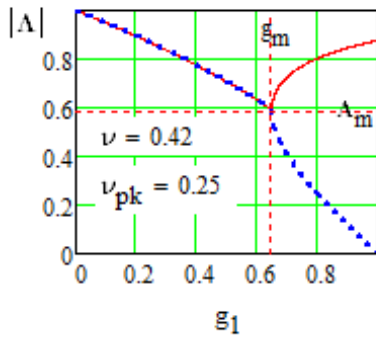


Figure 2: Dependence of eigen-values on the gain for one-turn system; $[\nu] = 0.42, \nu_{pk} = 0.25$.

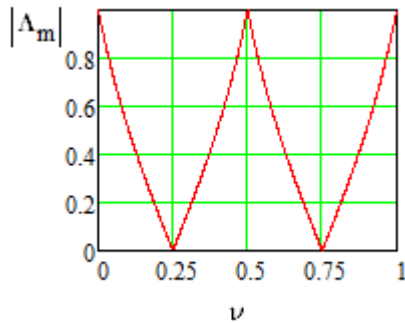


Figure 3: Dependence of maximum of eigen-values at the optimal gain on the betatron tune for the one-turn system.

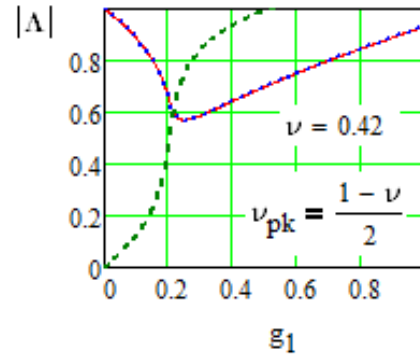


Figure 4: Dependence of eigen-values on the gain for two-turn system; $[\nu]=0.42, \nu_{pk}=0.25$.

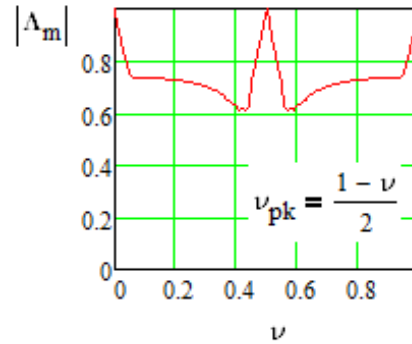


Figure 5: Dependence of maximum of eigen-values at the optimal gain on the betatron tune for two-turn system. The maximum damping gate: $\lambda / f_0 \approx -\ln(0.61) \approx 0.49$.

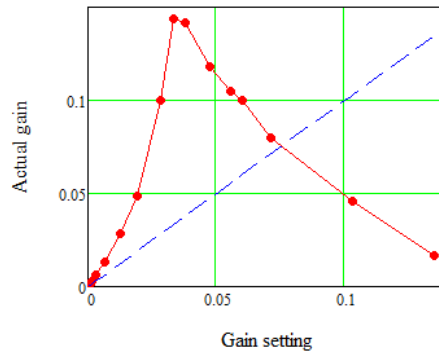


Figure 6: Dependence of damping rate on the gain setting for the LHC horizontal damper for beam 1.

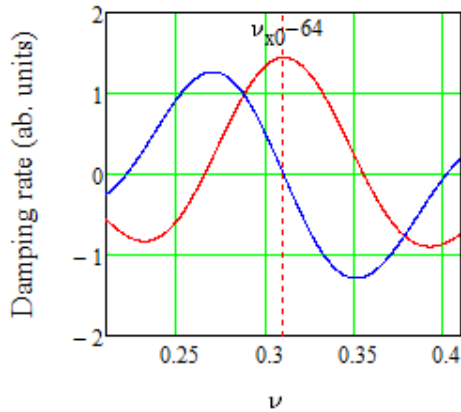


Figure 7: Dependence of real (red) and imaginary (blue) parts of damping rate on the machine tune for the LHC beam 1 horizontal damper.

ANALOG PRE-PROCESSING AND POST-PROCESSING

Analog pre-processing and post-processing in digital dampers may significantly affect an excitation of intra-bunch high order modes (HOMs) and, consequently, may limit the damping rate.

Typical signals from a strip-line pickup are shown in Figure 8. The signal consists of from the forward signal proportional to the bunch dipole moment (red line) and its reflection from the downstream end of the pickup (blue line). The total signal is shown by black curve. The way how this signal is modified before digitization and how digitization is done determines sensitivity of the damper to HOMs. Note also that a non-zero chromaticity changes the transverse offset along the bunch in the course of synchrotron motion making the signal of zero mode resembling signals of HOMs.

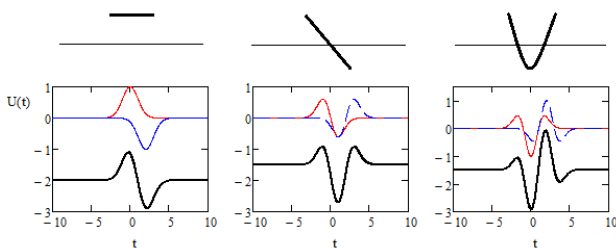


Figure 8: Typical pickup signals for the dipole (left) and higher head-tail modes. Top plots show changes of bunch transverse offset along the bunch.

The following analogue pre-processing methods applied before digitization are usually used:

- An integration which delivers the bunch center of gravity
- Mixing pickup signal with RF with subsequent low pass filtering making bell-shape form of a signal

- In the case of very short bunches an excitation of oscillator with subsequent digitization at slower sampling rate.

If the bunch length is much smaller than the bunch-to-bunch distance then, if special care is applied, this pre-processing may deliver the bunch center of gravity which is weakly sensitive to HOMs. To reduce sensitivity to the signal base line (voltage outside of signal waveform) the digitization before and at the bunch is used. It becomes close to impossible to avoid excessive sensitivity to HOMs if bunch length is comparable to the bunch-to-bunch distance which is typical for proton synchrotrons.

Normally, kicker power amplifiers do not amplify low frequencies. It makes an amplifier signal bipolar and, consequently, it makes kicks being bipolar. If bunch length is comparable to the bunch-to-bunch distance, then making uniform kick along the bunch becomes very challenging. Consequently, that makes it impossible to make uniform kick along the bunch and to avoid an excitation of HOMs.

Depending how signal of a HOM is pre-processed before the digitization and how kicker signal excites the same HOM (post-processing) the damper can amplify or damp this HOM. Note that these problems need to be addressed even if many digitization points are used in the pickup measurements and formation of kicker voltage.

EFFECTS OF X-Y COUPLING

Usually effects of x - y coupling do not play significant role in damping of instabilities. However, in the course of Tevatron Run II, it was observed that switching on a one-plane damper could introduce instability in another plane. The reason of such behaviour was strong x - y coupling which could not be completely compensated because of large uncontrolled skew-quad components in superconducting dipoles. Running dampers for both planes made the beam stable. In this section we consider how such problem can be analysed.

The analysis can be done similar to a single dimensional case described by Eq. (13) where 2D matrices have to be replaced by 4-D matrices; and the matrix \mathbf{G} has to be replaced by 4D matrix

$$\mathbf{G}_x = \begin{bmatrix} \mathbf{G} & \mathbf{0} \\ \mathbf{0} & \mathbf{0} \end{bmatrix} \quad \text{or} \quad \mathbf{G}_y = \begin{bmatrix} \mathbf{0} & \mathbf{0} \\ \mathbf{0} & \mathbf{G} \end{bmatrix} \quad (19)$$

for the horizontal and vertical dampers, respectively.

In majority of applications a perturbation theory solution is sufficient. In this case we can use a perturbation theory developed in Ref. [7]. It yields that if the perturbation changes the transfer matrix from \mathbf{M} to $\mathbf{M} + \Delta\mathbf{M}$ then the betatron tune shifts due to the perturbation are:

$$\Delta\nu_n = -\frac{1}{4\pi} \mathbf{v}_n^+ \mathbf{S} \Delta\mathbf{M} \mathbf{v}_n, \quad n=1,2. \quad (20)$$

Here \mathbf{S} is the unit symplectic matrix, and \mathbf{v}_n are the eigen-vectors of unperturbed motion. Two other eigen-vectors

(values) are complex conjugated to the first couple. That makes altogether 4 linearly independent eigen-vectors. Leaving only the first order terms in Eq. (13) one obtains:

$$\Delta \mathbf{M}_n^{x,y} = \mathbf{M}_{kp} \mathbf{G}_{x,y} \sum_{k=0}^{K-1} A_k \Lambda_n^{-k} \quad (21)$$

That results in for the horizontal damper:

$$\Delta v_n = -\frac{1}{4\pi} \left(\sum_{k=0}^{K-1} A_k \Lambda_n^{-k} \right) \mathbf{v}_n + \mathbf{S} \mathbf{M}_{kp} \mathbf{G}_x \mathbf{v}_n. \quad (22)$$

where Λ_n are corresponding eigen-values of unperturbed motion. For the vertical damper \mathbf{G}_x needs to be replaced by \mathbf{G}_y . Note that a knowledge of 4D optics is required to use Eq. (22).

DAMPER DIAGNOSTICS

The spectrum of pickup measurements has information about the betatron frequency and the phasing of the damper. Figure 9 shows the spectrum simulated for the LHC damper. Measurements resulted in similar behavior. One can see that the spectral density is suppressed at the betatron frequency. The LHC damper has two independent pickups. Therefore, the spectrum suppression at the betatron tune is about half. It would be close to 100% if only one pickup is used. The width of the gap determines the damping rate. Its asymmetry characterizes the damper phasing.

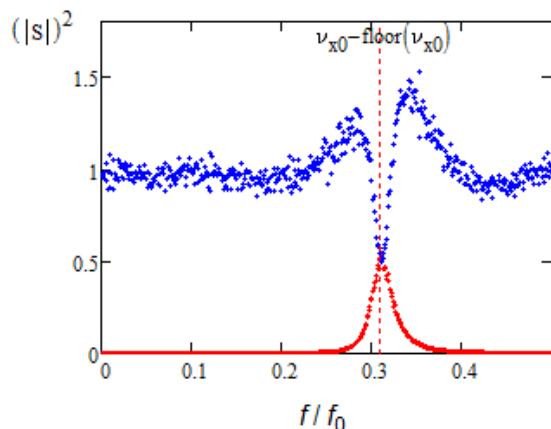


Figure 9: Spectral density of noise (blue) for two-BPM LHC damper; red dots – actual beam motion.

CONCLUSION

Next generation hadron colliders will have size significantly exceeding the LHC size. That will make them more susceptible to the external noise and will require dampers with damping time of few turns. Their maximum damping rate is limited by number of previous turns used for computation of each correction. It was shown that using large number of turns does not deliver any increase in damping efficiency but reduces the maximum achievable damping rate and makes damper more sensitive to the betatron tunes. Therefore, a usage of large number of turns is undesirable. It was also found that a reduction of system gain with frequency can be useful to reduce an effect of damper noise and, consequently, its heating power. Special care has to be applied to minimize an excitation of intrabunch HOMs which also can limit the damping rate.

REFERENCES

- [1] V. Lebedev and V. Shiltsev, Eds, *Accelerator Physics at the Tevatron Collider*. New York, NY, USA: Springer-Verlag, 2014.
- [2] P. Zhang, “A Study of Tunes Near Integer Values in Hadron Colliders”, Fermilab, Batavia, IL, USA, Rep. FERMILAB-FN-577, Dec. 1991.
- [3] G. Arduini *et al.*, “Hump: how did it impact the luminosity performance?”, in *Proc. 2010 Evian II Workshop on LHC Beam Operation*, Evian, France, 7-9 Dec. 2010.
- [4] V. Lebedev *et al.*, “Emittance growth due to noise and its suppression with feedback system in large hadron colliders”, *Particle Accelerators*, 1994, vol. 44, pp. 147-164.
- [5] V. Lebedev, “Computer simulation of the emittance growth due to noise in large hadron colliders”, *Particle Accelerators*, 1994, vol. 44, pp. 165-199.
- [6] W. Höfle *et al.*, “Suppression of Emittance growth by excited magnet noise with the transverse damper in LHC in simulation and experiment”, in *Proc. IPAC’11*, San Sebastian, Spain, Sep. 2011, paper MOP013, pp. 508-511.
- [7] A. Burov and V. Lebedev, “Coupling and its effect on beam dynamics”, in *Proc. 42nd ICFA Advanced Beam Dynamics Workshop on High-Intensity and High-Brightness Hadron Beams (HB’08)*, Nashville, TN, USA, Aug. 2008, paper WGA14, pp. 85-88.

EXPERIMENTS AND THEORY ON BEAM STABILIZATION WITH SECOND-ORDER CHROMATICITY

M. Schenk^{*1}, X. Buffat, L. R. Carver, K. Li, E. Métral

European Organization for Nuclear Research (CERN), CH-1211 Geneva, Switzerland

¹also at École Polytechnique Fédérale de Lausanne (EPFL), CH-1015 Lausanne, Switzerland

A. Maillard, École Normale Supérieure (ENS), F-75230 Paris, France

Abstract

This study reports on an alternative method to generate transverse Landau damping to suppress coherent instabilities in circular accelerators. The incoherent betatron tune spread can be produced through detuning with longitudinal rather than transverse action. This approach is motivated by the high-brightness, low transverse emittance beams in future colliders where detuning with transverse amplitude will be less effective. Detuning with longitudinal action can be introduced with a radio frequency (rf) quadrupole, or similarly, using second-order chromaticity. The latter was enhanced in the Large Hadron Collider (LHC) at CERN and experimental results on single-bunch stabilization are briefly recapped. The observations are interpreted analytically by extending the Vlasov formalism to include nonlinear chromaticity. Finally, the newly developed theory is benchmarked against circulant matrix and particle tracking models.

INTRODUCTION

Due to the strongly reduced transverse emittances of the beams in the Future Circular hadron Collider (FCC-hh), generating a betatron tune spread with magnetic octupoles for Landau damping of transverse dipole modes is ineffective, in particular at high energy [1, 2]. Betatron detuning with longitudinal amplitude introduced by means of an rf quadrupole is hence under study as a potential alternative [3]. Numerical studies performed with the *PyHEADTAIL* tracking code demonstrate that such an rf device can indeed provide beam stabilization [4, 5].

It was shown in Ref. [6] that second-order chromaticity (Q'') mimics the effect of an rf quadrupole at first order. Measurements were performed in the LHC where Q'' was enhanced and single bunches were stabilized at 6.5 TeV through detuning with longitudinal amplitude [7, 8]. *PyHEADTAIL* showed a very good agreement with the data, confirming the correct modelling of Landau damping from an rf quadrupole or nonlinear chromaticity in the code [6]. Both simulations and experiments indicate that Q'' introduces two beam dynamics effects: (i) it changes the effective impedance and hence the transverse dipole modes and their associated coherent frequencies, and (ii) it generates a betatron tune spread depending on the longitudinal amplitude and therefore Landau damping.

The objective of this study is to present the progress made on the development of the Vlasov theory for nonlinear chromaticity and to confirm analytically the two effects that were observed in the LHC. First, the main results and conclusions from the experiments are recapped before briefly explaining how the Vlasov formalism was extended to include nonlinear chromaticity. Finally, results from numerical studies with *PyHEADTAIL* and the circulant matrix solver *BimBim* are discussed to demonstrate the validity of the developed theory [9, 10]. Only the main results for airbag and Gaussian beams are presented here, with specific approximations on the impedance model. A complete study including detailed derivations and providing considerably more information on the benchmarks is currently in preparation and will be submitted to a peer-reviewed journal in the near future.

LHC EXPERIMENTS

LHC Single-Bunch Stability

At 6.5 TeV, with design bunch parameters, first-order chromaticity $Q'_{x,y}$ between 11 and 14 units, and the transverse feedback system active with a damping time of approximately 100 turns, the main transverse single-bunch instability in the LHC is a horizontal head-tail mode with azimuthal and radial numbers $l = 0$ and $m = 2$ respectively [11, 12]. During routine operation this instability is mitigated by means of the Landau octupoles [13]. The minimum current required for stabilization was measured to be $I_{\text{oct}}^{\text{meas}} = 96_{-10}^{+29}$ A. Using a detailed LHC impedance model [14], *PyHEADTAIL* predicts the correct instability threshold ($I_{\text{oct}}^{\text{sim}} = 107.5 \pm 2.5$ A) and the right azimuthal and radial numbers of the head-tail mode, confirming the high reliability of the numerical model.

Second-Order Chromaticity Study

The LHC main sextupoles are grouped into focusing and defocusing families and each of them is split further into two subfamilies interleaved by a phase advance of about π . The four groups can be powered individually for each of the eight machine sectors which makes it possible to control the second-order chromaticity independently in the two transverse planes and without affecting $Q'_{x,y}$. For each of the two beams, two orthogonal (nonlinear) knobs QPPX and QPPY were defined to enhance respectively Q''_x and Q''_y .

The experiment was performed with two bunches in each of the two beams at 6.5 TeV. The Landau octupoles were initially powered with $I_{\text{oct}} = 320$ A to ensure beam stability. The settings for QPPX and QPPY were determined using MAD-X to introduce $Q''_{x,y} \approx -4 \times 10^4$ in both beams once

* michael.schenk@cern.ch

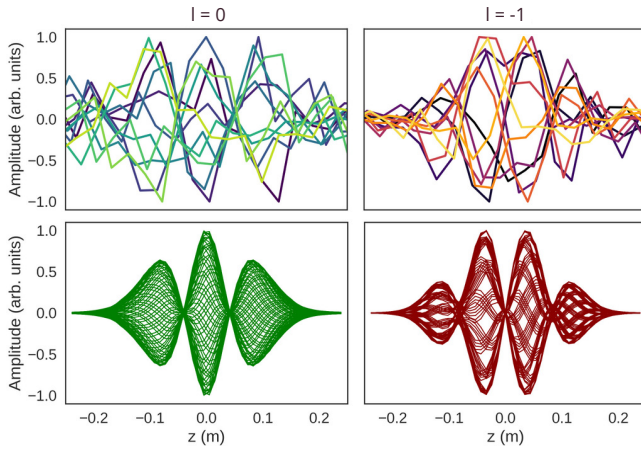


Figure 1: Comparison of the two horizontal head-tail modes observed in the LHC (top) and in *PyHEADTAIL* simulations (bottom) without (left) and with (right) Q''_x .

the current in the Landau octupoles would be reduced to zero [15]. The reason for using negative Q'' is that it provides a higher stabilizing efficiency for the head-tail mode observed in the LHC which is characterized by a negative real coherent tune shift [6, 16]. This is due to the strong asymmetry of the tune spreads and hence of the stability boundary diagrams introduced by Q'' (see theory below). As soon as the targeted sextupole settings were reached, the current in the Landau octupoles was decreased in steps of 40 A. At $I_{\text{oct}} = 40$ A all four bunches were still stable. At this stage $Q''_{x,y}$ measurements were performed that showed a good agreement with MAD-X predictions hence demonstrating that Q'' is well-controlled in the machine [6]. Once the Landau octupole current was reduced to 0 A, a horizontal instability occurred in one of the four bunches while the other three remained stable. The reason why only one bunch went unstable was its significantly higher intensity compared to the second bunch in the same beam [8]. The observed instability was now no longer a head-tail mode $(l, m) = (0, 2)$, but instead had mode numbers $(l, m) = (-1, 3)$. Figure 1 (top) displays the measured head-tail patterns without (left) and with (right) Q'' , acquired by the Head-Tail Monitor [17]. The fact that the bunches were stable at significantly reduced, or even zero octupole current indicated a strong Landau damping effect from Q'' , later confirmed by tracking simulations.

PyHEADTAIL was used to interpret the experimental observations made. 4×10^5 macroparticles were tracked over 1.8×10^6 turns, again using the detailed LHC impedance model. Figure 2 summarizes the main results. The color code shows the relative emittance growth over the simulation period in %, where ‘blue’ is stable and ‘white’ unstable. The dots represent the azimuthal mode number of the instability predicted for each setting of the Q'' knobs. Labels (a) and (b) correspond to the two experimental working points, respectively with and without Q'' . The plot shows that large regions of stability are created in the QPPX vs. QPPY plane thanks to Landau damping from Q'' . The two main stable areas are, however, separated by an unstable band indicating

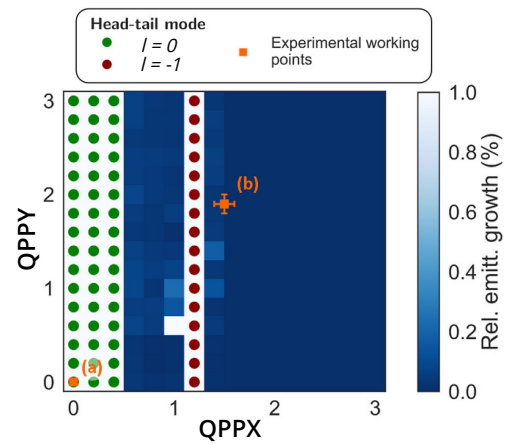


Figure 2: *PyHEADTAIL* study showing the predicted horizontal head-tail instabilities and the emittance growth in the QPPX vs. QPPY plane. Labels (a) and (b) denote the two experimental working points.

a head-tail mode $l = -1$ (red dots). This is a consequence of Q'' changing the effective impedance and hence the head-tail modes as discussed analytically in the following section. The first unstable band observed at low values of Q'' is the mode $l = 0$ (green dots), consistent with experimental observations made in absence of Q'' . The stable region between the two unstable bands arises from sufficient Landau damping of both modes. The further increase of Q'' , however, leads to a change of the effective impedance, causing a loss of Landau damping for the $l = -1$ mode. For even larger amounts of Q'' , all the instabilities are suppressed. Additionally, working point (b) lies close to the second unstable band. This is consistent with experimental data which clearly show that the observed horizontal instability is indeed of mode -1 . Overall, the experimental results, and in particular the Head-Tail Monitor signals, are in excellent agreement with the simulations, displayed in Fig. 1 (bottom).

In the following section, the existing Vlasov theory will be extended to include the effects of nonlinear chromaticity, making it possible to confirm the interpretation of the experimental observations analytically.

VLASOV THEORY

Vlasov’s equation in transverse (q, θ) and longitudinal (r, ϕ) polar coordinates reads [18]

$$\left[\partial_s + \frac{1}{c} \omega_\beta(\delta) \partial_\theta + \frac{\omega_s}{c} \partial_\phi + \frac{F_y}{E} \partial_{p_y} \right] \Psi = 0, \quad (1)$$

where Ψ is the particle distribution in 4D phase space (including the longitudinal and *one* transverse plane), s the longitudinal position of the bunch along the accelerator, c the speed of light, E the total energy of the beam particles, F_y the transverse force representing here the effect of transverse dipolar wakefields, $p_y(q, \theta)$ the transverse momentum, δ the relative longitudinal momentum error, and ω_s the synchrotron frequency. Nonlinear chromaticity terms up to

order m are included in the equation through a dependency of the betatron frequency on δ

$$\omega_\beta(\delta) = \omega_{\beta,0} + \Delta\omega_\beta(\delta) = \omega_{\beta,0} \sum_{k=0}^m \frac{\xi^{(k)}}{k!} \delta^k, \quad (2)$$

with $\omega_{\beta,0}$ the unperturbed betatron frequency, and

$$\xi^{(n)} = \frac{1}{\omega_{\beta,0}} \left. \frac{\partial^n \omega_\beta}{\partial \delta^n} \right|_{\delta=0} \quad (3)$$

the nonlinear chromaticity of order n .

To simplify the Vlasov equation and to find the solutions Ψ of the collective transverse dipole modes, one proceeds in a similar way as explained in Ref. [18], Eqs. (6.166) to (6.179), while allowing for an arbitrary dependence of the betatron frequency on the longitudinal momentum deviation. First, Ψ is described as a sum of a stationary solution and a perturbation term $\Psi = \Psi_0 + \Psi_1$, where $\Psi_0 = g_0(r)f_0(q)$ and $\Psi_1 = -Dg_1(r, \phi) f_0'(q) e^{i\theta} e^{-i\Omega s/c}$. g_0 and g_1 are the stationary and perturbed longitudinal distributions respectively, and f_0 is the transverse stationary distribution. D is the dipolar moment of the perturbed distribution and Ω the complex coherent frequency associated with the mode. Using this approach, the Vlasov equation can be reduced such that it involves only longitudinal coordinates. The wakefield term is expressed in frequency domain using the transverse dipolar impedance $Z_1^\perp(\omega)$ and one can obtain an equation similar to (6.174) in Ref. [18]. From this point onwards, one deviates from the path described in Ref. [18] and instead rewrites the Vlasov equation in terms of the functions

$$G_1(r, \phi) \doteq g_1(r, \phi) e^{\frac{i}{\omega_s} \int_0^\phi \Delta\omega_\beta(\delta(r, u)) du}. \quad (4)$$

They can be further decomposed into the azimuthal eigenmodes $G_1^l(r, \phi)$ (with eigenvalues $\Omega^{(l)}$) of the *free* ($Z_1^\perp \equiv 0$) Vlasov equation

$$G_1^l(r, \phi) = R_l(r) e^{i\left(l + \frac{\langle \Delta\omega_\beta \rangle_\phi}{\omega_s}\right)\phi}, \quad (5)$$

$$\Omega^{(l)} = \omega_{\beta,0} + l\omega_s + \langle \Delta\omega_\beta \rangle_\phi,$$

where $l \in \mathbb{Z}$ is the azimuthal mode number, and $\langle \Delta\omega_\beta \rangle_\phi(r)$ denotes the betatron frequency change $\Delta\omega_\beta(\delta(r, \phi))$ averaged over the longitudinal phase ϕ in the interval $[0, 2\pi)$. This quantity is, in general, dependent on the longitudinal amplitude r of the particles and thus describes the betatron frequency spread introduced through detuning with longitudinal amplitude. This term will eventually lead to Landau damping as demonstrated below when computing the dispersion relation. One can already see at this stage that $\langle \Delta\omega_\beta \rangle_\phi(r) \equiv 0$ for odd orders of chromaticity $\xi^{(2n+1)}$, $n \in \mathbb{N}_0$, i.e. the average frequency spread vanishes. This result is independent of the longitudinal particle distribution. Odd orders of chromaticity do not introduce Landau damping. On the other hand, even orders of chromaticity $\xi^{(2n)}$, $n \in \mathbb{N}$ introduce a betatron frequency spread with longitudinal amplitude that does not average out over time. In

any case, though, both odd and even orders of chromaticity introduce a change of the effective impedance and modify the coherent frequencies of the modes which will also be demonstrated and discussed in the following section.

Having rewritten the Vlasov equation in terms of the azimuthal eigenmodes $G_1^l(r, \phi)$, one can multiply the result by $e^{-il\phi}$ and perform the integration over ϕ from 0 to 2π . Finally, one can integrate over r from 0 to ∞ to obtain Vlasov's equation in its 'final' form

$$\sigma_{lp} = -i \frac{q^2 \omega_s \omega_0^2}{4\pi \omega_{\beta,0} E \eta} \sum_{l', p'=-\infty}^{\infty} \sigma_{l'p'} Z_1^\perp(\omega')$$

$$\times \int_0^\infty \frac{r g_0(r) \overline{H_1^{p'}(r)} H_1^p(r)}{\Omega^{(l)} - \omega_{\beta,0} - l\omega_s - \langle \Delta\omega_\beta \rangle_\phi(r)} dr, \quad (6)$$

where q is the electric charge of the particles, ω_0 the angular revolution frequency, and η the slip factor. Furthermore,

$$\sigma_{lp} \doteq \int_0^\infty r R_l(r) H_l^p(r) dr,$$

$$H_l^p(r) \doteq \frac{1}{2\pi} \int_0^{2\pi} e^{il\phi} e^{-\frac{i\omega'}{c} r \cos\phi} e^{-\frac{i}{\omega_s} B(r, \phi)} d\phi, \quad (7)$$

$$B(r, \phi) \doteq \int_0^\phi [\Delta\omega_\beta(\delta(r, u)) - \langle \Delta\omega_\beta \rangle_\phi(r)] du,$$

with $l, p \in \mathbb{Z}$, and $\omega' \approx p'\omega_0 + \omega_{\beta,0} + l\omega_s$. In the weak-wake approximation, the summation over l' can be neglected and one can instead consider Eq. (6) as a set of independent equations in l . $H_l^p(r)$ can be perceived as a generalized Bessel function. It can be shown that in the event of a purely linear chromaticity, $H_l^p(r)$ reduces to the Bessel function of the first kind and Eq. (6) becomes identical to Eq. (6.179) in Ref. [18]. The phase terms $e^{-iB(r, \phi)/\omega_s}$ describe the alteration of the interaction of the beam with the impedance caused by arbitrary orders of chromaticity. The result is that the overlap sum over index p' in Eq. (6) between the $H_1^{p'}(r)$ functions and the impedance $Z_1^\perp(\omega')$ changes. This causes a change of the coherent frequencies $\Omega^{(l)}$, both for the real and imaginary components, of all the modes, an effect that is not related to Landau damping. Instead, Landau damping can be seen from the dispersion integral in the bottom line of Eq. (6). The incoherent detuning term $\langle \Delta\omega_\beta \rangle_\phi(r)$ in the denominator leads to an increase of the stable area in the complex frequency space as demonstrated in the following section. Equation (6) hence decouples the two beam dynamics effects introduced by nonlinear chromaticity and observed consistently in LHC experiments and in *PyHEADTAIL* simulations.

SOLUTIONS AND BENCHMARKS

This section discusses specific solutions to the previously derived Vlasov equation and summarizes the benchmarks performed to validate the formalism by means of the circulant matrix solver *BimBim* and the *PyHEADTAIL* tracking

code. While the theory and the circulant matrix solver directly output the coherent frequencies for each azimuthal mode, the tracking results have to undergo additional post-processing. The real and imaginary parts of the coherent frequencies are obtained respectively from a SUSSIX frequency analysis and from exponential fits to the bunch centroid signals [19].

Equation (6) is first evaluated for a longitudinal airbag model where all the particles have the same longitudinal amplitude and hence there is no net frequency spread from any order of chromaticity. In that case, there is no Landau damping (the dispersion integral disappears from Eq. (6)) and one can thus study separately the change of the effective impedance. Thereafter, a longitudinal Gaussian bunch is analyzed where the two beam dynamics effects introduced by nonlinear chromaticity are both present. Here, even orders of chromaticity introduce a frequency spread and Landau damping. Stability boundary diagrams are computed and detailed comparisons with *PyHEADTAIL* tracking simulations are made.

Airbag Model

To benchmark the developed theory against numerical models, a scan in second-order chromaticity is performed at fixed first-order chromaticity $\xi^{(1)} = 0.25$ for a longitudinal airbag distribution. The machine parameters used for the test are loosely based on the CERN Super Proton Synchrotron (SPS) at injection energy ($\gamma = 27.7$, $\omega_s/\omega_0 = Q_s = 0.017$, $\beta_z = 115$ m), where γ , Q_s , and β_z are the relativistic Lorentz factor, the (linear) synchrotron tune, and the longitudinal Courant-Snyder beta function respectively. The bunch intensity is at 10^9 p and the particles are set to have a longitudinal action of $J_z = 3 \times 10^{-4}$ m. A simple broad-band resonator impedance is used ($R_s = 10^7$ Ω /m, $f_r = 0.8$ GHz, $Q = 1$), with R_s , f_r , Q respectively the resonator shunt impedance, its frequency, and its Q-value. Equation (6) is evaluated numerically and the results are plotted in Fig. 3 (solid lines) for azimuthal modes up to order $|l| = 5$. The theoretical predictions are in excellent agreement with the tracking (green crosses) and circulant matrix (red dots) models confirming the validity of the developed formalism. Also, the results demonstrate that second-order chromaticity modifies the effective impedance which leads to a change of the most unstable mode as a function of $\xi^{(2)}$. This effect was experimentally observed in the LHC. The real coherent frequency shifts are dominated by the constant (i.e. independent of r) and real-valued term $\langle \Delta\omega_\beta \rangle_\phi$ which is identical for all the azimuthal modes of an airbag beam.

Gaussian Beam

To study the effect of Landau damping from nonlinear chromaticity, a Gaussian beam is used for the comparison between the theory and the *PyHEADTAIL* model. For Gaussian beams, there is a longitudinal amplitude spread among the particles. In combination with even orders of chromaticity, this translates into a betatron frequency spread and an

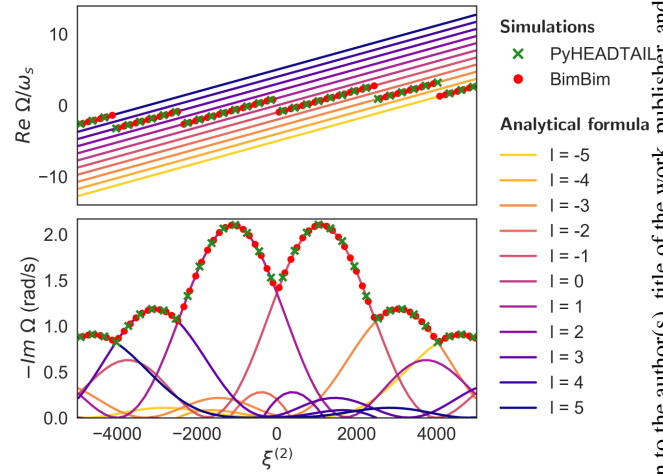


Figure 3: Real (top) and imaginary (bottom) coherent frequencies as a function of $\xi^{(2)}$ at fixed $\xi^{(1)} = 0.25$ for an airbag model using *BimBim* (red dots), *PyHEADTAIL* (green crosses), and analytical calculations (solid lines).

increase of the stability boundary diagram in the complex frequency space. In general, however, the eigenvalue problem in Eq. (6) is difficult to solve. To write down an analytical solution where the dispersion relation and Landau damping become more apparent, constraints are imposed on the shape of the impedance. A highly narrow-band resonator impedance is considered, for instance, such that effectively $Z_1^\perp(\omega') = Z_{p_0} \neq 0$ for $p' = p_0$, and $Z_1^\perp(\omega') = 0$ everywhere else. For this type of impedance, Eq. (6) simplifies greatly. To compute the stability boundary diagram, one considers the coherent frequency shift $\Delta\Omega_{\text{lin}}^{(l)}$ in absence of Landau damping (*linear lattice*), determined by ignoring the frequency spread in Eq. (6). This yields

$$\begin{aligned} (\Delta\Omega_{\text{lin}}^{(l)})^{-1} &= \frac{1}{\mathcal{N}} \int_0^\infty \frac{r g_0(r) |H_l^{p_0}(r)|^2}{\Omega^{(l)} - \omega_\beta(r) - l \omega_s} dr, \\ \mathcal{N} &= \int_0^\infty r g_0(r) |H_l^{p_0}(r)|^2 dr, \end{aligned} \quad (8)$$

where $\omega_\beta(r) = \omega_{\beta,0} + \langle \Delta\omega_\beta \rangle_\phi(r)$. The dispersion relation is evaluated by adding a small complex part $i\epsilon$ to the denominator of the integral (Landau bypass rule). By making additional assumptions on the beam spectrum and impedance, one can also show that Eq. (8) is equivalent to the results found by Scott Berg and Ruggiero in Ref. [16].

To benchmark Eq. (8) against *PyHEADTAIL*, the assumption on the strongly-peaked impedance needs to be fulfilled. This can be achieved by choosing a high quality factor resonator and tuning its frequency to match the spectral maximum of the azimuthal mode zero while remaining small for all the other modes. At the end of the tuning procedure, the values for the resonator were $R_s = 5 \times 10^{12}$ Ω /m, $f_r = 0.7993$ GHz, and $Q = 5 \times 10^4$. Due to the high quality factor, multi-turn wakefield effects had to be enabled in *PyHEADTAIL*. A bunch length of $\sigma_z = 0.21$ m was used for

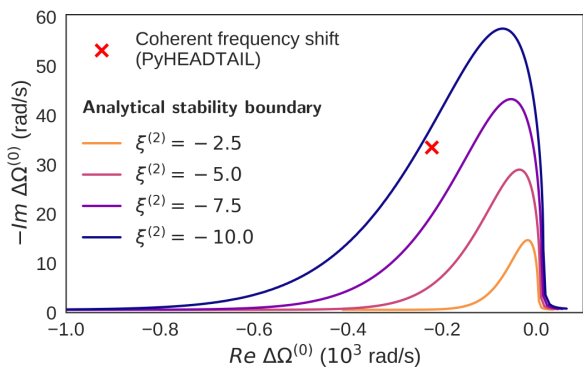


Figure 4: Stability boundary diagrams for different values of $\xi^{(2)}$ obtained by numerically solving the dispersion relation in Eq. (8). The coherent frequency shift of the mode under consideration is obtained from *PyHEADTAIL* (red cross).

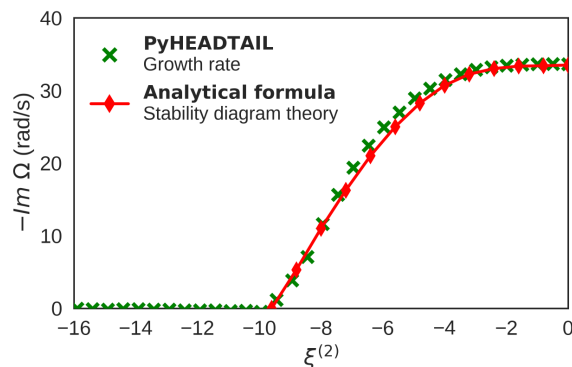


Figure 5: Stabilization of the head-tail mode zero as a function of $\xi^{(2)} < 0$ for a Gaussian beam. *PyHEADTAIL* simulations (green crosses) are shown together with predictions obtained from stability diagram theory (red diamonds).

the Gaussian distribution. All the other machine parameters were kept the same as above.

To evaluate beam stability analytically, the dispersion relation in Eq. (8) is solved numerically for different $\xi^{(2)}$. Solutions of the stability boundary diagrams are shown in Fig. 4 (solid lines) for four specific values of $\xi^{(2)}$. Due to the negative real part of the coherent frequency shift of the mode under consideration (red cross), negative values of $\xi^{(2)}$ are used as they provide stability more efficiently given the asymmetry of the frequency spread and of the stability diagrams. The plots illustrate the growth of the area of stability with increasing $|\xi^{(2)}|$. For $\xi^{(2)} \leq -10$, the area is large enough as to include the unstable mode from which point onwards it is fully Landau damped. It has been verified that by removing the frequency spread from the formula, the modes *cannot* be stabilized at least up to $|\xi^{(2)}| = 1000$. Furthermore, theoretical calculations show that within a few tens of units of $|\xi^{(2)}|$, there is no strong dependence of the coherent frequency on $\xi^{(2)}$, i.e. the change of effective impedance is insignificant here.

Figure 5 displays the dependence of the imaginary coherent frequency shift (instability growth rate) on the second-order chromaticity as obtained analytically (red diamonds) and from *PyHEADTAIL* simulations (green crosses). The analytical solutions were calculated using stability diagram theory: different values for $i\varepsilon$ were plugged in the denominator of Eq. (8) to compute the ‘distortion’ of the complex frequency space and therefore deduce the growth rates of the instability as a function of $\xi^{(2)}$. The *PyHEADTAIL* results were determined using exponential fits to the bunch centroid signals. The theory and the tracking model demonstrate an excellent agreement, not only on the stability threshold, but also on the evolution of the growth rate for intermediate $\xi^{(2)}$. It has also been verified that there is no other mode that becomes unstable, at least up to $|\xi^{(2)}| = 1000$.

CONCLUSIONS

The existing Vlasov theory on transverse dipole modes has been extended to include the effects of nonlinear chromaticity up to arbitrary order. This new formalism made it possible to confirm the hypothesis that nonlinear chromaticity has two effects on the beam dynamics of transverse coherent modes, observed in experiments with second-order chromaticity in the LHC: (i) it introduces Landau damping thanks to the incoherent betatron frequency spread with longitudinal amplitude, e.g. providing stability for single bunches in the LHC, and (ii) it alters the effective impedance, observed as a change of the most unstable mode in the LHC.

The theory has been successfully benchmarked up to second-order chromaticity for an airbag model and a Gaussian beam using a tracking model and a circulant matrix solver. All the benchmarks revealed an excellent agreement with the theory. For the Gaussian beam it has been shown that, given the assumption of a strongly-peaked impedance, analytical predictions from stability diagram theory are in perfect agreement with tracking simulations. This proves that detuning with longitudinal amplitude indeed provides Landau damping. The frequency spread can be introduced for example with even orders of chromaticity, or, similarly, with an rf quadrupole. This is in accordance with experiments and simulations that were carried out on the rf quadrupole and on second-order chromaticity in the LHC, confirming the interpretation of these results.

ACKNOWLEDGMENTS

The authors thank R. De Maria and G. Rumolo for important contributions to these studies and the LHC OP teams for their support during the experiments.

REFERENCES

- [1] L. Landau, “On the vibration of the electronic plasma”, *J. Phys. USSR*, vol. 10, pp. 25–34, 1946.
- [2] M. Benedikt and F. Zimmermann, “Future Circular Colliders”, CERN, Geneva, Switzerland, Rep. CERN-ACC-2015-0164, Jul. 2015.
- [3] A. Grudiev, “Radio frequency quadrupole for Landau damping in accelerators”, *Phys. Rev. ST Accel. Beams*, vol. 17, p. 011001, Jan. 2014.

- [4] M. Schenk, A. Grudiev, K. Li, K. Papke, “Analysis of transverse beam stabilization with radio frequency quadrupoles”, *Phys. Rev. Accel. Beams*, vol. 20, p. 104402, Oct. 2017.
- [5] E. Métral *et al.*, “Beam instabilities in hadron synchrotrons”, *IEEE Transactions on Nuclear Science*, vol. 63, no. 2, pp. 1001–1050, Apr. 2016.
- [6] M. Schenk *et al.*, “Practical stabilisation of transverse collective instabilities with second order chromaticity in the LHC”, in *Proc. 8th Int. Particle Accelerator Conf. (IPAC’17)*, Copenhagen, Denmark, May 2017, paper THPVA026, pp. 4477–4480.
- [7] O. Brüning *et al.*, “LHC Design Report”, CERN Yellow Reports: Monographs, CERN, Geneva, Switzerland, CERN-2004-003-V-1, Jun. 2004.
- [8] L. R. Carver *et al.*, “MD1831: Single bunch instabilities with Q'' and non-linear corrections”, CERN, Geneva, Switzerland, CERN-ACC-NOTE-2017-0012, Feb. 2017.
- [9] V. V. Danilov and E. A. Perevedentsev, “Feedback system for elimination of the transverse mode coupling instability”, *NIM A*, vol. 391, no. 1, pp. 77–92, 1997.
- [10] X. Buffat, “Transverse beams stability studies at the Large Hadron Collider”, Ph.D. thesis, LPAP, École Polytechnique Fédérale de Lausanne (EPFL), Lausanne, Switzerland, 2015.
- [11] L. R. Carver *et al.*, “Current Status of Instability Threshold Measurements in the LHC at 6.5 TeV”, in *Proc. 7th Int. Particle Accelerator Conf. (IPAC’16)*, Busan, Korea, May 2016, paper TUPMW011, pp. 1434–1437.
- [12] L. R. Carver *et al.*, “MD1228: Validation of Single Bunch Stability Threshold & MD1751: Instability Studies with a Single Beam”, CERN, Geneva, Switzerland, Rep. CERN-ACC-NOTE-2017-0013, Feb. 2017.
- [13] J. Gareyte, J.-P. Koutchouk, F. Ruggiero, “Landau damping, dynamic aperture and octupoles in LHC”, CERN, Geneva, Switzerland, Rep. CERN-LHC-Project-Report-91, Feb. 1997.
- [14] N. Mounet, “The LHC Transverse Coupled-Bunch Instability”, Ph.D. thesis, LPAP, École Polytechnique Fédérale de Lausanne (EPFL), Lausanne, Switzerland, 2012.
- [15] Methodical Accelerator Design, mad.web.cern.ch.
- [16] J. S. Berg and F. Ruggiero, “Stability diagrams for Landau damping”, in *Proc. 17th Particle Accelerator Conf. (PAC’97)*, vol. 2, Vancouver, B.C., Canada, May 1997, pp. 1712–1714.
- [17] T. Levens *et al.*, “Instability diagnostics”, in *Proc. 2015 Evian Workshop on LHC beam operation*, Evian, France, Dec. 2015, CERN-ACC-2015-376, pp. 137–141.
- [18] A. W. Chao, *Physics of collective beam instabilities in high energy accelerators*, Wiley Series in Beam Physics and Accelerator Technology, Wiley, 1993.
- [19] R. Bartolini and F. Schmidt, “A Computer Code for Frequency Analysis of Non-Linear Betatron Motion”, CERN, Geneva, Switzerland, Rep. SL-Note-98-017-AP, Feb. 1998.

RECENT RESULTS FROM THE WIDEBAND FEEDBACK SYSTEM TESTS AT THE SPS AND FUTURE PLANS

Kevin Shing Bruce Li^{*}, H. Bartosik, M. Beck, E. R. Bjørsvik, W. Höfle,
G. Kotzian, T. E. Levens, M. Schenk¹, CERN, Geneva, Switzerland
J. E. Dusatko, J. D. Fox, C. H. Rivetta, SLAC, Menlo Park, CA, USA
O. Turgut, Stanford University, Stanford, CA, USA
¹also at EPFL, Lausanne, Switzerland

Abstract

A high bandwidth transverse feedback demonstrator system has been devised within the LARP framework in collaboration with SLAC for the LHC Injectors Upgrade (LIU) Project. The initial system targeted the Super Proton Synchrotron (SPS) at CERN to combat TMCI and electron cloud instabilities induced for bunches with bunch lengths at the 100 MHz scale. It features a very fast digital signal processing system running at up to 4 GS/s and high bandwidth kickers with a frequency reach of ultimately beyond 1 GHz. In recent years, the system has gradually been extended and now includes two stripline kickers for a total power of 1 kW delivering correction signals at frequencies of currently more than 700 MHz. This talk will cover recent studies using this demonstrator system to overcome TMCI limitations in the SPS. We will conclude with future plans and also briefly mention potential applications and requirements for larger machines such as the LHC or the HL-LHC.

INTRODUCTION

The CERN Super Proton Synchrotron (SPS) will have to deliver high intensity beams up to 2.3×10^{11} ppb – twice the value of today – after the LHC Injectors Upgrade (LIU) in preparation for HL-LHC. Up to 288 bunches will have to be accelerated from 26 GeV to 450 GeV before extraction to the LHC. Transverse Mode Coupling Instability (TMCI) and electron cloud instabilities have been a concern in the past. One of the strategies for the mitigation of these types of instabilities was to use novel wideband feedback systems to combat the high frequency coherent motion.

A demonstrator system has been developed in a multi-laboratory effort under the LARP framework within LIU. The system features a very fast 4 GS/s digital signal processing unit which is fully reconfigurable and able to deal with up to 64 bunches independently [1]. A set of two stripline kickers with a frequency reach of 700 MHz are powered by four wideband power amplifiers for a total power of 1 kW. The system has been operated during the last two years to demonstrate control of intra-bunch motion as well as independent control of individual bunches in a train [2]. Recently, a slotline kicker has been added but has not yet been put into operation [3, 4]. Figure 1 shows the installations with their locations in the SPS ring all around BA3.

^{*} kevin.shing.bruce.li@cern.ch

Today, the TMCI threshold is usually kept high by means of the Q20 optics which features a high synchrotron tune. However, the Q20 optics has high RF power requirements. During the last year, a new optics (Q22 optics) was tested in the SPS with relaxed RF power requirements during certain parts of the cycle [5]. On the other hand, the TMCI threshold for the Q22 optics is expected around 2.6×10^{11} ppb for nominal longitudinal parameters ($\epsilon_z \approx 0.35$ eVs) which on the other hand is the required intensity for nominal beams at injection after LIU [6]. For this reason, during 2017, the wideband feedback demonstrator system was used to show that it is possible to overcome the fast TMCI by means of a transverse feedback system.

Section 2 discusses TMCI in the SPS. Section 3 shows measurements of the TMCI thresholds for the Q22 optics in the SPS. Section 4 shows results using the wideband feedback system to mitigate the observed TMCI in the SPS. Finally, Section 5 shows possible needs and requirements for similar feedback systems for LHC or HL-LHC.

TMCI IN THE SPS

In the SPS, the comparatively large bunch length leads to coupling of synchrotron sidebands at both low as well as higher orders. There is a regime of weak coupling between modes 0 and -1 where the TMCI growth rates are relatively low. These modes tend to decouple again at higher intensities. Then, there is the regime of strong coupling between modes -2 and -3 which generates a very fast and violent TMCI and leads to immediate loss of intensity down to just below the value of the threshold intensity. This fast TMCI establishes a hard limit on the maximum attainable intensity in the SPS. Figure 2 illustrates these different regimes of weak and strong coupling. The results were obtained from simulations using a slightly simplified representation of the SPS impedance model (a 1.3 GHz broadband resonator model). The figure also shows the corresponding signals observed in a wideband pickup revealing the different characteristics of the two regimes and also compares both simulated and measured signals which indeed show very good agreement [7].

The TMCI threshold of the SPS in its original design has been around 1.4×10^{11} ppb with an integer tune of 26 (Q26 optics). This would have been a serious limitation for the requirements of LIU. Today, this threshold is dealt with by means of a new optics (Q20 optics) which features a higher synchrotron tune [7] and therefore increases the threshold

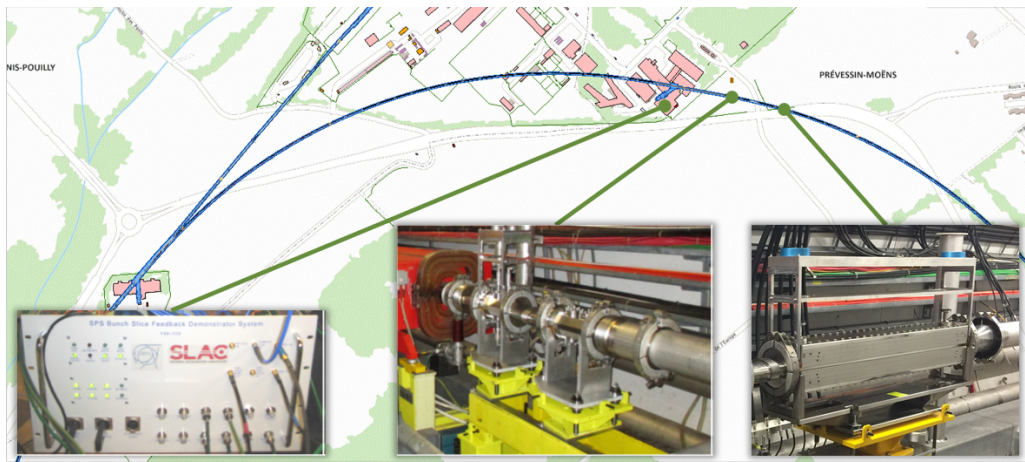


Figure 1: Installation of the wideband feedback system in the SPS. The fast digital signal processing unit is located on the surface in a Faraday cage. Two stripline kickers are installed in the SPS tunnel together with a set of power amplifiers. Recently, a slotline kicker has been installed slightly further downstream.

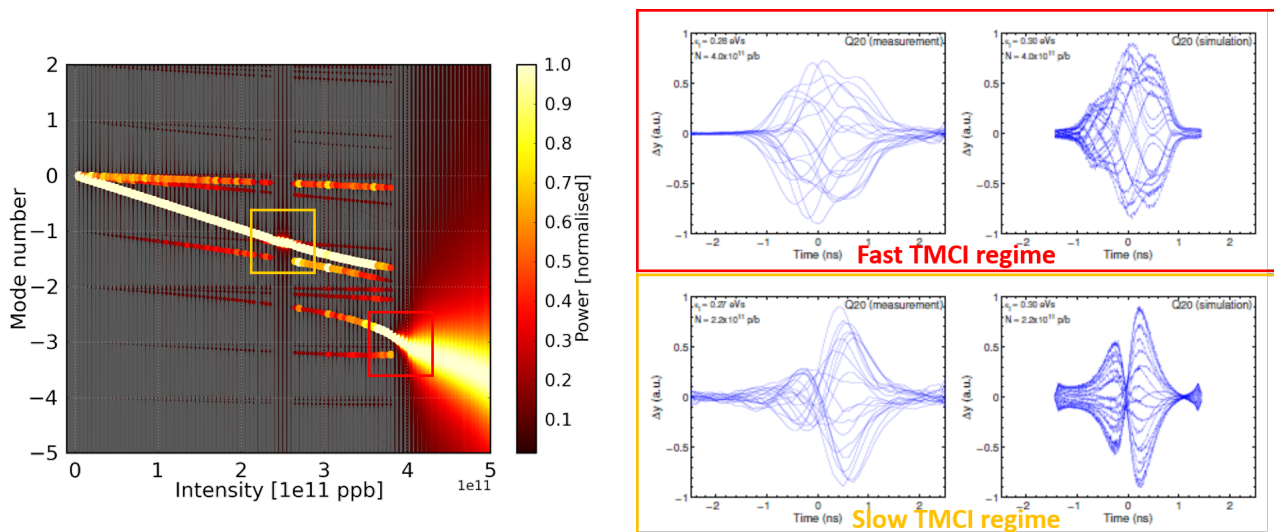


Figure 2: The tune shifts of the azimuthal modes with intensity are shown on the power spectrum plot on the left hand side. The two regimes of weak (yellow box) and of strong (red box) coupling are clearly visible. The right hand side shows the corresponding signals in a wideband pickup from measurements (left) and from simulations (right) [7].

well beyond the operational intensities. As already mentioned above, the Q20 optics is very demanding in terms of required RF power and voltage. The intermediate Q22 optics can give some margin on the RF power during certain parts of the cycle. This comes at the price of a lower synchrotron tune, however [8]. As a consequence, the TMCI threshold decreases down to around 2.6×10^{11} ppb. In this configuration the Q22 optics is hardly suited for LIU. On the other hand, it provides the ideal testing platform for the wideband feedback system to demonstrate its capability to mitigate TMCI, in particular also, in the regime of strong coupling. If successful, the Q22 optics can become a viable option for LIU.

MEASUREMENTS OF THE TMCI THRESHOLD FOR Q22 OPTICS

In 2017 the new Q22 optics was prepared in the SPS and a high intensity beam was set up. The beam was used to explore the TMCI threshold for this optics configuration. As already mentioned, from simulations done in the past using the SPS impedance model, the threshold was predicted to be around 2.6×10^{11} ppb.

During the measurements, single bunches were injected into the SPS at different intensities. The bunch intensity was measured just before extraction in the pre-injector of the SPS, the Proton Synchrotron (PS), and a couple of hundreds of milliseconds after injection into the SPS. Figure 3 shows this intensity scan where the PS extracted intensity is plot-

Content from this work may be used under the terms of the CC BY 3.0 licence (© 2018). Any distribution of this work must maintain attribution to the author(s), title of the work, publisher, and DOI.

ted against the measured intensity in the SPS. It is clearly visible how an intensity of roughly 2.4×10^{11} ppb cannot be exceeded despite injecting higher intensities from the PS.

Once injecting intensities above this threshold value into the SPS one can observe a strong coherent activity associated with high losses. Looking at the headtail monitor one can see clear signatures of TMCI exhibiting a strong coherent oscillation along the bunch which is pronounced towards the tail of the bunch as shown in Figure 4. The top plot shows the turn-by-turn vertical delta signal along the bunch. On the bottom, the corresponding sum signal is shown. Later turns are colored in light colors and one can clearly observe the fast losses leading to a decrease of the sum signal.

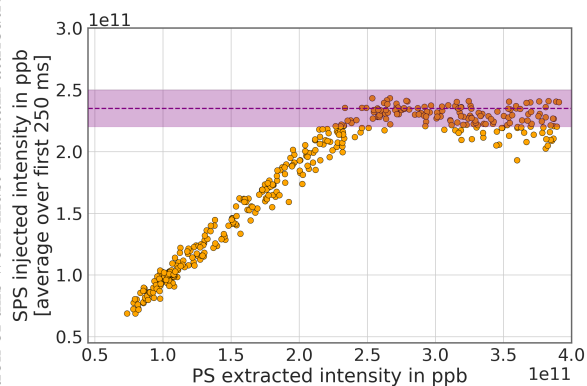


Figure 3: The intensity scan done to evaluate the TMCI threshold in the SPS. The plot shows the extracted intensity from the PS on the horizontal and the measured intensity in the SPS on the vertical axis. It is clearly visible how the maximum measured intensity after injection is limited to around 2.4×10^{11} ppb.

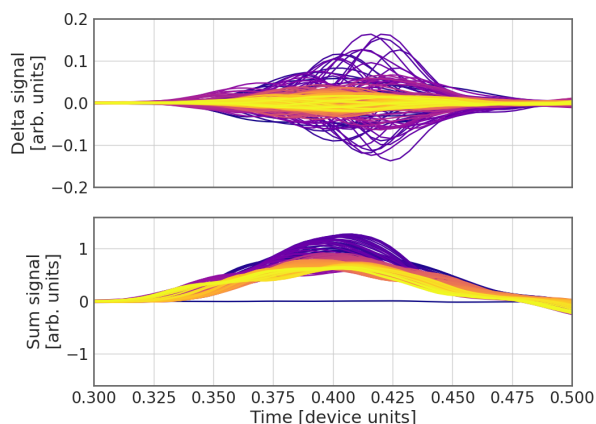


Figure 4: A typical signature of a fast TMCI instability as observed via an oscilloscope. Left is the head of the bunch, right is towards the tail of the bunch. The top figure shows the vertical delta signal, the bottom plot shows the sum signal. Early turns are in dark, later turns are in light colors.

MITIGATION OF TMCI USING THE WIDEBAND FEEDBACK SYSTEM

Having measured the TMCI threshold as a hard limit on the reachable intensity in the SPS for Q22 optics the question arises whether the wideband feedback system could be used to mitigate the instability and push the reachable intensity beyond the LIU limits. At the same time, this would serve as demonstration that such a system is indeed capable of mitigating also violent instabilities which exhibit a strong intra-bunch motion posing hard limits for many machines. Whereas in the past, the system had been used in the slow TMCI regime showing control of intra-bunch motion, it had never been used in the fast TMCI regime to actually extend the intensity reach beyond the TMCI threshold.

During these tests of the wideband feedback system, the TMCI threshold was artificially lowered using a decreased RF voltage due to temporary operational limitations, rendering a TMCI threshold around 1.6×10^{11} ppb. The TMCI mechanism itself does not change due to this, however. Figure 5 shows the intensities measured along the cycle, once in absence of any transverse feedback, then using only the SPS transverse damper, which has a frequency reach of up to 20 MHz, and finally, using the SPS transverse damper in combination with the wideband feedback system. It is clear, that only with the wideband feedback system active, the TMCI threshold could be exceeded.

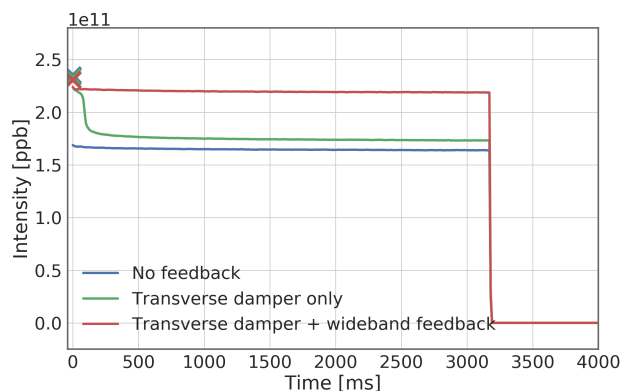


Figure 5: The DC BCT signals showing the intensity evolution on the flat bottom in the SPS for different combinations of active feedback systems. The crosses indicate the intensity measured at the extraction of the PS. The full extracted intensity can be maintained only with the combined operation of both the transverse damper and the wideband feedback system (red curve).

The crosses on the plot indicate the injected intensities as received from the PS. Without any feedback, looking at the DC beam current transformer (BCT) signal, already at the first sampling point after 5 ms, the bunch has lost all of its intensity down to below the TMCI threshold. In fact, these losses are so fast, that without knowledge of the intensity coming from the transfer line, they would go unnoticed from the pure BCT signal. The losses can be slowed down when

using the transverse damper. However, the transverse damper alone does not have the necessary bandwidth to deal with the very fast intra-bunch motion excited during the TMCI and for this reason it can ultimately not stop the instability and the associated losses which reduce the bunch intensity below the threshold. Finally, the wideband feedback system was added to the active transverse damper and in this configuration, the instability could be kept under control and the bunch intensity constant beyond the TMCI threshold.

It is noteworthy that the wideband feedback system alone was also not able to stabilize the beam. The strong dipole components during the injection transient in combination with the fast TMCI tend to quickly drive the wideband system into saturation, rendering it ineffective. Despite the bandwidth limitations, the transverse damper has a lot more power to deal with the coherent dipole motion. Hence, the transverse damper is required to first remove the strong dipole component of the beam motion, after which the wideband feedback can be used effectively, to take care of the remaining high frequency components in the beam motion.

OTHER POTENTIAL APPLICATIONS FOR WIDEBAND FEEDBACK SYSTEMS

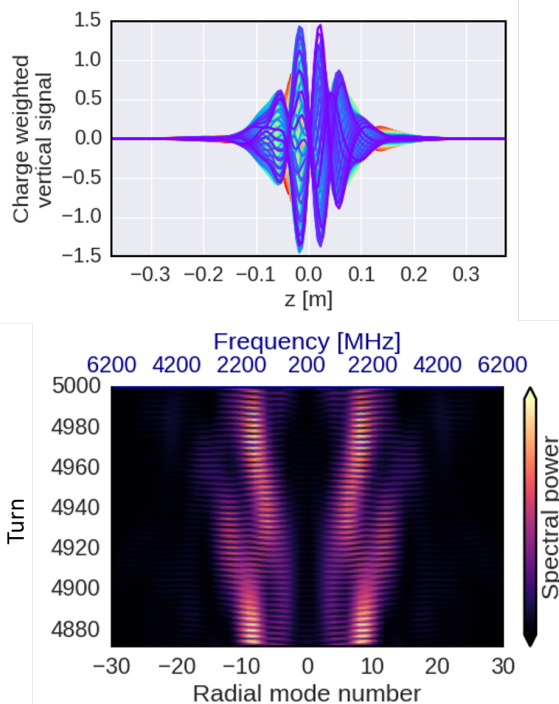


Figure 6: Signature of an electron cloud instability as simulated in the LHC at top energy. Fast intra-bunch oscillations are visible. A frequency analysis reveals frequencies up to 4 GHz. A gigahertz feedback system is likely required to reliably mitigate these types of instabilities.

With the successful demonstration of control of intra-bunch motion for nanosecond scale bunches as well as the

mitigation of TMCI, the wideband feedback system technology has gained a level of maturity where other fields of application can be considered. One potential application is the use for instability mitigation in the LHC or the HL-LHC.

Impedance-driven instabilities in the LHC, to date, are dealt with by means of the LHC transverse damper for coupled-bunch instabilities and Landau octupoles to keep under control single-bunch instabilities [9]. The dominating sources of instabilities in the LHC are due to electron clouds which are generated in the LHC straight sections, dipole, quadrupole as well as higher multipole magnets [10]. Especially at flat top, simulations show that these instabilities contain very high frequency components (see fig. 6) as discussed in [11]. Most of the time, these instabilities can be kept under control by operating the LHC at very high chromaticities and strong Landau octupoles. This, however, limits the dynamic aperture and significantly reduces the operational parameter space.

A wideband feedback system could be used to handle these instabilities without introducing any non-linearities or generating large tune spreads, thus, keeping the dynamic aperture large and improving the beam lifetime.

CONCLUSIONS

In the present paper we have shown measurements of the TMCI threshold for the Q22 optics in the SPS. The maximum attainable intensity is limited by the strong coupling of modes -2 and -3 and, for nominal beam parameters, is at 2.6×10^{11} ppb. We have used a wideband feedback system in an attempt to overcome this intensity limit.

It turned out that the successful configuration to mitigate the TMCI is using the combined capabilities of both the standard transverse damper which has limited bandwidth, but high power output, together with the high bandwidth feedback system within its power limitations. The transverse damper is designed for fast damping of injection oscillations and mitigation of coupled-bunch instabilities which for LHC beams reach up to 20 MHz. As such it is well suited to efficiently remove any coherent dipole oscillations of the bunch centroid motion. The remaining high frequency signals are then within the dynamic range of the wideband feedback system and can successfully be processed and removed in order to stabilize the bunch against the TMCI. This has now been experimentally demonstrated in the SPS and the results have been presented.

In the near future the plan is to commission the newly installed nearline kicker which will have a yet extended bandwidth for increased power at 1 GHz and beyond. Initial tests will focus on measuring the response of the slotline structure. The current plan is then to move one of the existing sets of power amplifiers, currently used for the stripline kickers, to the slotline kicker to test the device with power and its performance to actively mitigate coherent intra-bunch motion.

Further use cases in the LHC or the HL-LHC were shown as well, where instability signatures at flat top triggered by

electron clouds, feature coherent frequencies in the GHz range. To date, these types of instabilities can only be dealt with by means of high chromaticity and strongly powered Landau octupoles which can have a negative impact on the beam lifetime. A wideband feedback system could be used to mitigate these instabilities without at the same time compromising on the available operational parameter space or beam lifetime. Research and development is required, in particular, for kicker structures [12] and to extend the fast digital signal processing to higher sampling rates [13], including the evaluation of modern state of the art platforms such as uTCA and a fixed frequency sampling clock.

REFERENCES

- [1] J. Dusatko *et al.*, “The SPS wideband feedback processor: a flexible FPGA-based digital signal processing demonstrator platform for intra-bunch beam stability studies”, in *Proc. 6th Int. Beam Instrumentation Conf. (IBIC’17)*, Grand Rapids, MI, USA, Aug. 2017, pp. 309–313, doi:10.18429/JACoW-IBIC16-WE1AB1
- [2] K. Li *et al.*, “Concept and simulations of unconventional damping devices: wideband damper and RFQ”, presented at the Int. Workshop on Impedances and Beam Instabilities in Particle Accelerators, Benevento, Italy, Sep. 2017.
- [3] J. Cesaratto *et al.*, “SPS Wideband Feedback Kicker: Design Report”, CERN, Geneva, Switzerland, Rep. ACC-NOTE-2013-0047, Dec. 2013; also available as SLAC, Stanford, CA, USA, Rep. SLAC-R-1037.
- [4] M. Wendt, S. J. Calvo, W. Hoffe, O. R. Jones, E. Montesinos, and I. A. Romero, “A broadband transverse kicker prototype for intra-bunch feedback in the CERN SPS”, in *Proc. 8th Int. Particle Accelerator Conf. (IPAC’17)*, Copenhagen, Denmark, May 2017, pp. 1812–1815, doi:10.18429/JACoW-IPAC2017-TUPIK053
- [5] M. Carlá, H. Bartosik, M. Beck, K. Li, and M. Schenk, “Studies of a new optics with intermediate transition energy as alternative for high intensity LHC beams in the CERN SPS”, in *Proc. 9th Int. Particle Accelerator Conf. (IPAC’18)*, Vancouver, BC, Canada, Apr.-May 2017, doi:10.18429/JACoW-IPAC2018-WEPAF-073
- [6] H. Bartosik *et al.*, “Other Means to Increase the SPS 25 ns Performance - Transverse Plane”, in *Proc. LHC Performance Workshop (Chamonix 2014)*, Chamonix, France, 22-25 Sep. 2014, pp. 180–184, doi:10.5170/CERN-2015-002
- [7] H. Bartosik, “Beam dynamics and optics studies for the LHC injectors upgrade”, Ph.D. thesis, Vienna University of Technology, Austria, Oct. 2013; also available as CERN, Geneva, Switzerland, Rep. CERN-THESIS-2013-257.
- [8] T. Argyropoulos, E. Shaposhnikova, and J. Varela, “Other Means to Increase the SPS 25 ns Performance - Longitudinal Plane”, in *Proc. LHC Performance Workshop (Chamonix 2014)*, Chamonix, France, 22-25 Sep. 2014, pp. 185–191, doi:10.5170/CERN-2015-002
- [9] E. Métral *et al.*, “Summary of the half-day internal review of LHC performance limitations (linked to transverse collective effects) during run II”, CERN, Geneva, Switzerland, Rep. CERN-ACC-NOTE-2017-0005, 2017.
- [10] A. Romano, O. Boine-Frankenheim, X. Buffat, G. Iadarola, and G. Rumolo, “Electron cloud buildup driving spontaneous vertical instabilities of stored beams in the Large Hadron Collider”, *Phys. Rev. Accel. Beams*, vol. 21, p. 061002, 2018, doi:10.1103/PhysRevAccelBeams.21.061002
- [11] K. Li *et al.*, “Feedback needs and potential applications of the technology in other accelerators (e.g. HL-LHC)”, presented at the LIU-SPS Wideband Feedback Review, CERN, Geneva, Switzerland, 20. Sep. 2016.
- [12] W. Höfle *et al.*, “From SPS Wideband Feedback R&D to a Kicker Design with Reach to 4 GHz”, presented at the 7th HL-LHC Collaboration Meeting, CIEMAT, Madrid, Spain, 13-16 Nov. 2017.
- [13] J. Dusatko and J. D. Fox, “Ultra-wideband transverse intra-bunch feedback: beginning development of a next generation 8GSa/s system”, in *Proc. 9th Int. Particle Accelerator Conf. (IPAC’18)*, Vancouver, BC, Canada, Apr.-May 2017, doi:10.18429/JACoW-IPAC2018-WEPAF-073

SIMULATION AND MEASUREMENT OF THE TMCI THRESHOLD IN THE LHC

D. Amorim^{*1}, S. Antipov, N. Biancacci, X. Buffat, L. Carver, E. Métral, CERN, Geneva, Switzerland
¹also at Université Grenoble-Alpes, Grenoble, France

Abstract

The Transverse Mode Coupling Instability (TMCI) occurs in individual bunches when two transverse oscillation modes couple at high bunch intensity. Simulations predict an instability threshold in the LHC at a single bunch intensity of $3 \cdot 10^{11}$ protons. The TMCI threshold can be inferred by measuring the tune shift as a function of intensity. This measurement was performed in the LHC for different machine impedances and bunch intensities. The impedance was changed by varying the primary and secondary collimators gaps to increase their contribution to the resistive wall impedance. The experiment also allowed to assess the validity of the LHC impedance model in the single bunch regime, at low chromaticities.

INTRODUCTION

The transverse mode coupling instability (TMCI), also named strong head-tail instability, can affect high intensity single bunches in circular accelerators. The instability mechanism can be described with a two particle model [1, p. 180], assuming a broad-band impedance (i.e short-range wake-field). During the first half of the synchrotron period, the electromagnetic field induced by the particle at the head of the bunch perturbs the particle at the tail of the bunch. The same happens during the second half of the synchrotron period but the two particles have swapped their positions. Below a certain bunch intensity, the disturbance is not strong enough and the perturbations do not accumulate. However above a certain intensity threshold the perturbations accumulate and the particles motion grows exponentially. This description can be reproduced and visualized with the tracking code PyHEADTAIL [2], an example is made available in the PyHEADTAIL examples repository [3, 4].

The TMCI can clearly be observed in electron machines [1, p. 184] because of the short length of the bunches [5]. In proton machines, such an instability was observed in the CERN SPS but with higher order azimuthal oscillation modes [6, 7]. However in the LHC, because of the relatively short length of the bunches (1.08 ns in 2017 and 2018), a coupling between mode 0, i.e the mode where the bunch head and tail oscillate in phase, and -1 i.e where the bunch head and tail oscillate in counter-phase, may occur. As the High Luminosity LHC project plans to increase the bunch intensity by a factor of two compared to the nominal LHC value [8, 9], the transverse mode coupling instability could become a limitation to the machine operation. The study can also be used to assess the validity of the accelerator impedance model and thus help to understand discrepancies between predicted stability

limits and instability observations [10]. The problem was first studied by performing stability simulations with the LHC impedance model and the Vlasov solver DELPHI [11]. In a second step, the tune-shift as a function of intensity was measured in the LHC for different collimator settings, allowing to modify the machine impedance. This measurement allows to infer the TMCI intensity threshold and notably for the HL-LHC case.

SIMULATION OF THE TMCI INTENSITY THRESHOLD

To understand and predict beam instabilities, an impedance model of the LHC has been developed [12] and is extensively used. It has also been extended to the HL-LHC case [13]. It models many contributors to the beam coupling impedance, among which the main ones are the beam screens, the vacuum chambers and the collimation system. At the top energy of 6.5 TeV, the collimation system is the main contributor to the overall machine impedance. This results from the scaling of the resistive wall impedance in $1/b^3$ in the frequency range of interest and in the presence of a transverse damper, where b is the collimator gap [1, p. 38]. The collimator gap itself scales with the transverse beam size as:

$$b = n\sigma_t = n\sqrt{\frac{\epsilon_n}{\beta\gamma} (\beta_x \cos(\theta)^2 + \beta_y \sin(\theta)^2)} \quad (1)$$

where σ_t is the RMS transverse beam size, n the collimator position setting, ϵ_n the beam normalized emittance, β the ratio of the beam velocity to the speed of light c , γ the Lorentz factor, β_x and β_y the Twiss functions at the collimator position, θ the azimuthal angle of the collimator. These scaling laws highlight that in the LHC the impedance is higher at top energy because of the tighter gaps in the collimators. In turns the stability margins are tighter at top energy than at injection energy [10].

The fact that the collimators can mechanically adjust their aperture to follow the beam size makes it possible to modify the machine impedance by moving in or out the collimators. This will allow to change the TMCI threshold and possibly reach it with nominal LHC beams. To quantify this effect as well as the influence of other beam parameters such as chromaticity, stability simulations were performed with the Vlasov solver DELPHI [14]. The treatment of Vlasov's equation leads to an eigensystem which is solved by the code which then outputs complex eigenvalues and eigenvectors. The eigenvalues give informations on the azimuthal and radial modes frequency shifts and growth rates. The eigenvectors allow to reconstruct the longitudinal bunch profile for

* david.amorim@cern.ch

Content from this work may be used under the terms of the CC BY 3.0 licence (© 2018). Any distribution of this work must maintain attribution to the author(s), title of the work, publisher, and DOI.

each oscillation mode. DELPHI simulations were performed for different machine chromaticities and collimators settings. To find the TMCI intensity threshold, the single bunch intensity was scanned between 0 p.p.b. to 5×10^{11} p.p.b. (protons per bunch). The beam parameters are summarized in Table 1.

Table 1: Stability Simulations Parameters

Parameter	Value
Number of bunches	1
Bunch intensity / 10^{11} p.p.b	0 to 5
Full bunch length / ns	1.08
Unnormalized chromaticity	0 to 5
Damping rate	no damper, 100 turns, 50 turns

In Figs. 1, 2 and 3, the top plot shows the real tune-shift of the different oscillation modes as a function of bunch intensity and the bottom plot shows the growth rate associated to these modes, both obtained with DELPHI. Figure 1 shows the case with the nominal collimator settings at zero chromaticity. The plot clearly shows the mode coupling occurring for a single bunch intensity of 3×10^{11} p.p.b.: the mode 0 and -1 have their growth rates suddenly increasing for this intensity value and beyond. While the LHC injector chain can create LHC type bunches with an intensity up to 3×10^{11} p.p.b., it is at the moment impossible to reach in the LHC a single bunch intensity higher than 2.2×10^{11} p.p.b.. But as exposed previously, the machine impedance can be modified by changing the collimators gaps. Simulations with tighter collimators settings were thus performed: Fig. 2 shows the results for a configuration in which the primary (TCP) collimators are brought in closer to the beam by $0.5\sigma_T$ and the secondary collimators (TCSG) by $1\sigma_T$. In this case the TMCI threshold appears at 2×10^{11} p.p.b., an intensity reachable in the LHC.

These two cases assume that the machine chromaticity is equal to zero units. Operational experience shows that the unnormalized chromaticity can be controlled within ~ 2 units [15] so to ensure beam stability, the LHC is operated with a positive chromaticity. To measure the tune-shift as a function of intensity while ensuring beam stability, a slightly positive chromaticity should be used. Simulations were made with DELPHI taking into account this effect. Figure 3 shows the results for the same collimator configuration as in Fig. 2, but with a unnormalized chromaticity of 5 units. For intensities below 2×10^{11} p.p.b., the real part of the eigenvalues are not too affected by the chromaticity effects. The imaginary part however shows that the mode -1 has a small growth rate for all intensity values: as the chromaticity is now non zero, this mode is affected by a classic head-tail instability [1, p. 197].

In conclusion, stability simulations with the LHC impedance model indicate that:

- In the nominal configuration, the TMCI intensity threshold is at a single bunch intensity of 3×10^{11} p.p.b., currently impossible to reach in the LHC;
- Closing further the machine collimators gaps can reduce the threshold to 2×10^{11} p.p.b.;
- Because of the operational uncertainties, a slightly positive chromaticity should be used to ensure beam stability;
- This positive chromaticity affects the modes shifts, but the tune-shift as a function of intensity remains similar to the cases with zero chromaticity, it can thus be measured to infer the TMCI threshold.

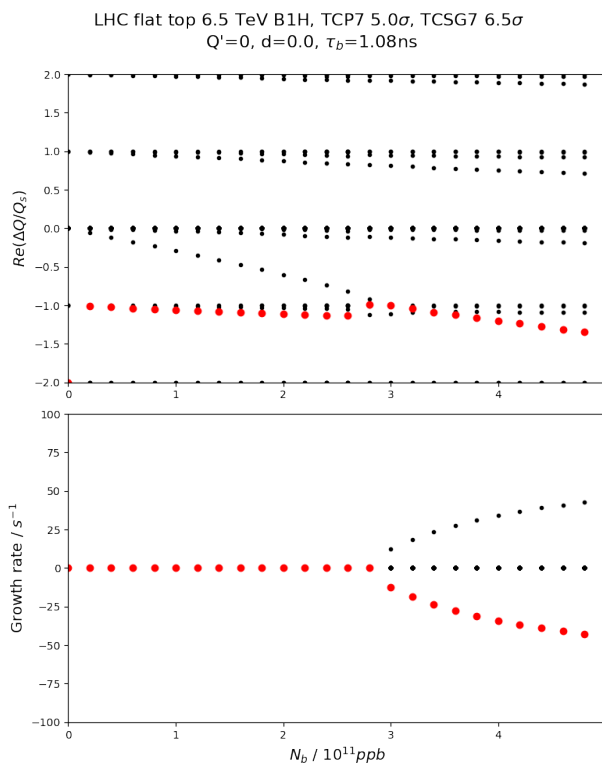


Figure 1: Complex Tune Shift as a Function of Intensity. The nominal LHC collimators configuration is showed, for a chromaticity of zero units.

MEASUREMENT OF THE TUNE-SHIFT VERSUS INTENSITY

In the framework of the LHC Machine Development program, an 8 h time slot was approved to measure the tune shift as a function of bunch intensity for different collimators settings. The measurement took place on the night of the 15th to 16th September 2017. Because of the setup and energy ramping time taken by the machine, two sets of measurement at top energy could be performed. The first set used 3 bunches of different intensities, the second set two. These numbers were constrained by machine protection requirements: the total intensity in each beam could not exceed 3×10^{11} p.p.b. if some collimators were to be moved in or out. Doing so

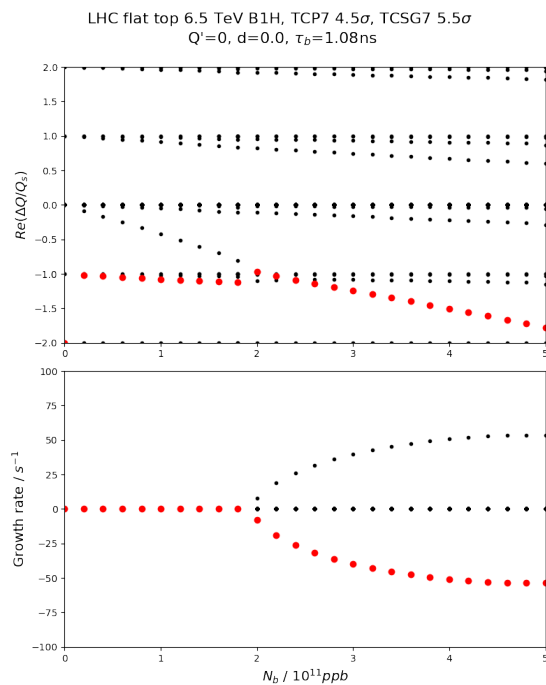


Figure 2: Complex Tune Shift as a Function of Intensity. Results for tighter collimators settings are showed, for a chromaticity of zero units.

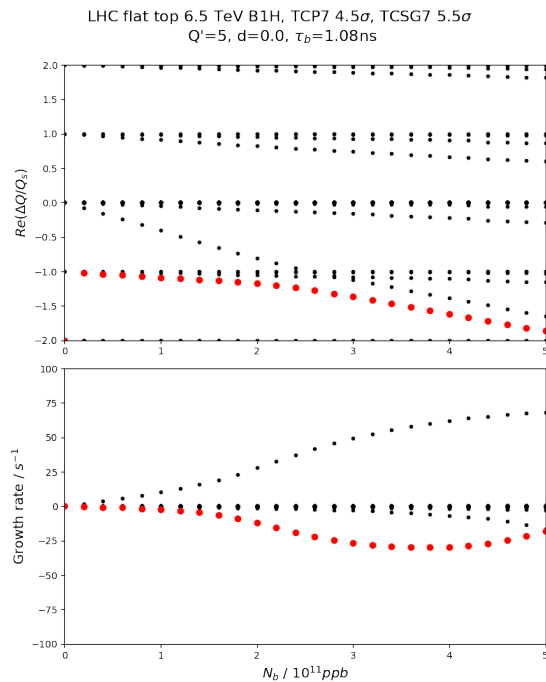


Figure 3: Complex Tune Shift as a Function of Intensity. Results for tighter collimators settings are showed. The unnormalized chromaticity is now 5 units.

with a higher beam intensity would have led to a beam dump from the interlock system. The beam parameters for the two measurements are given in Tables 2 and 3.

Table 2: Beam Parameters During the First Measurement

Parameter	Value
Number of bunches	3
Bunch intensities / 10^{11} p.p.b	0.6, 1.0 and 1.3
Full bunch length / ns	1.1
Normalized emittance / μm	3
Unnormalized chromaticity	5

Table 3: Beam Parameters During the Second Measurement

Parameter	Value
Number of bunches	2
Bunch intensities / 10^{11} p.p.b	0.9 and 1.9
Full bunch length / ns	1.1
Normalized emittance / μm	3
Unnormalized chromaticity	5

During the first measurement, selected collimators were moved closer to the beam in several steps in order to increase the machine impedance and so the tune-shift. The primary (TCP) and secondary (TCSG) collimators were the ones moved, the steps taken are reported in Tables 4 and 5 respectively for the first and second measurement. The gap settings are given in number of transverse beam size at the collimators position σ_t : the gap in mm can then be computed using Eq. 1. During the second measurement, which included a higher intensity bunch (see Table 5), the collimators were first moved out from the beam. This was done to reproduce an equivalent HL-LHC impedance [13] and so to assess the impact of the planned impedance reduction on the tune-shift [16].

Table 4: Primary and Secondary Collimators Gaps Settings During the First Measurement

Step	TCP gap / σ_t	TCSG gap / σ_t
1	5	6.5
2	5	6
3	4.5	6

At every step in the collimators position, the bunches were coherently excited multiple times with the LHC transverse damper (ADT) operated in AC-dipole mode [17]. The bunch-by-bunch and turn-by-turn position at the ADT pick-up was recorded with the ADTObsBox [18]. The data were then post-processed with PySUSSIX [19], a Python wrapper of SUSSIX [20]. The intensity of each bunch being recorded over time with the Fast Beam Current Transformer (FBCT), it is then possible to compute the tune-shift versus intensity slope, after having removed the baseline tune from the one computed for each bunch.

The measurements results are given in Table 6. Both beam and planes are reported for the different steps in the collimators gaps. Each table entry shows two values: the

Content from this work may be used under the terms of the CC BY 3.0 licence (© 2018). Any distribution of this work must maintain attribution to the author(s), title of the work, publisher, and DOI.

Table 5: Primary and Secondary Collimators Gaps Settings During the Second Measurement

Step	TCP gap / σ_t	TCSG gap / σ_t
1	5	14
2	5	6.

top one reports the simulated values obtained from DELPHI simulations with the LHC impedance model, the bottom one the measurement result. The reduction of the tune-shift versus intensity for larger collimators gaps (first row of Table 6) is clear, highlighting the potentially large gain in impedance from coating the collimators [16]. Measurements with nominal or tighter than nominal collimators settings (second, third and fourth rows of Table 6) show that the measured values are consistently higher than the simulated ones. The more critical situation in terms of stability margins in 2017 [10] could thus be partly explain by a higher impedance than used in the simulations.

Table 6: Measured Tune-shifts for the Two Beams and Planes. The values are given in $(10^{11} \text{ p.p.b} * Q_s)^{-1}$ where Q_s is the synchrotron tune ($Q_s = 2 \cdot 10^{-3}$ in the LHC). For the measured value, the number inside the parenthesis is the uncertainty of the measurement. The first column indicates the TCP/TCSG collimators gaps for the measurement.

Gaps	B1H	B1V	B2H	B2V
5/14	-0.17 -0.20(4)	-0.12 -0.17(5)	-0.18 -0.25(4)	-0.12 -0.13(3)
5/6.5	-0.30 -0.34(3)	-0.23 -0.38(4)	-0.32 -0.37(3)	-0.24 -0.27(2)
5/6	-0.34 -0.41(5)	-0.27 -0.38(5)	-0.36 -0.39(3)	-0.27 -0.30(2)
4.5/6	-	-	-0.38 -0.45(4)	-0.29 -0.30(3)

As for the TMCI threshold, the measurement of the tune-shift implies that it would be lower than simulated. Figure 4 shows for the horizontal plane of Beam 1 the simulated and the measured tune-shifts as a function of intensity. From simulations with an unnormalized chromaticity of +5 units, the TMCI threshold for the nominal LHC case lies at 3.2×10^{11} p.p.b.. For the simulated HL-LHC case it lies at 6×10^{11} p.p.b.. Measurement results plotted alongside show that the TMCI intensity threshold in the nominal LHC case might be closer to 3×10^{11} p.p.b.. The HL-LHC case however shows a clear improvement and the inferred TMCI threshold is above 5×10^{11} p.p.b.. The foreseen impedance reduction for HL-LHC would therefore increase the TMCI threshold and help maintain a factor 2 safety margin in terms of single bunch intensity.

An attempt to observe a mode coupling instability was made at the end of the first measurement by reducing the collimators gaps even further. The LHC head-tail monitor [21] is used to record the intra-bunch motion if an instability is detected. In the case of a mode coupling instability, a

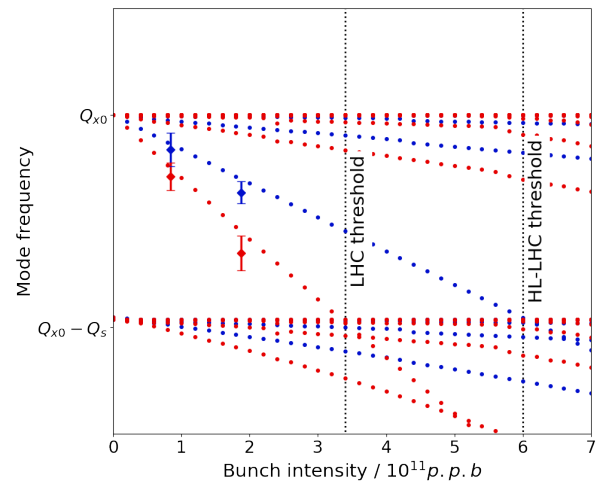


Figure 4: Measured (diamonds) and simulated (dots) tune-shifts as a function of intensity for the nominal LHC collimators settings (in red) and for the equivalent HL-LHC impedance collimators settings (in blue). The plane showed is B1H, for an unnormalized chromaticity of +5, without damper.

traveling wave pattern would be seen along the bunch, as showed in Fig. 5. However because of the slightly positive chromaticity and the lower bunch intensities in the first measurement, a classic head-tail instability was observed. This measurement with a higher intensity bunch during the second ramp could not be attempted because of a beam dump triggered by a superconducting magnet quench before the end of the measurement session.

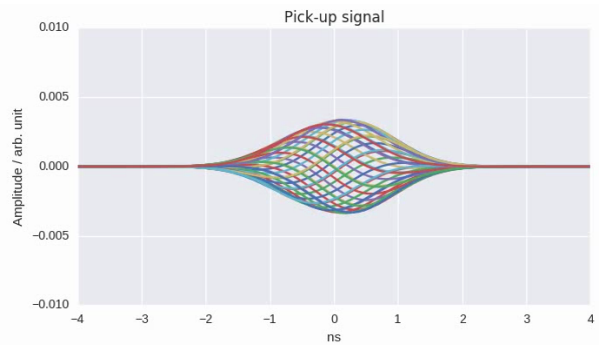


Figure 5: Intrabunch motion in the mode coupling regime, with a positive chromaticity and above transition. The signal is reconstructed from the eigenvectors output of DELPHI. The horizontal axis is the bunch length.

CONCLUSION

The Transverse Mode Coupling Instability threshold was simulated using the LHC impedance model and the Vlasov solver DELPHI. Different cases of machine impedance were assessed by varying the collimators gaps. They showed that for tight enough settings, the mode coupling instability is within the intensity reach of the LHC.

Measurements of the tune-shift versus intensity were performed at the LHC top energy for these different collimators settings. The resulting values appear to be 10% to 20% higher than the simulations for the nominal and tight collimators settings. This could partly explain the discrepancies observed between instabilities observations and predictions during the year 2017. A measurement with larger collimators gaps was also carried out to mimic the HL-LHC impedance. A clear tune-shift reduction could be observed, highlighting the positive impact of the planned upgrade of the LHC collimation system.

ACKNOWLEDGEMENTS

The author would like to thank D.Valuch, A.Mereghetti, T.Levens as well as the LHC and Injectors operations teams for their invaluable help to perform the Machine Development session. The present study has been conducted in the context of the High Luminosity LHC project, which is partly funded by the European Commission within the Framework Programme 7 Capacities Specific Programme, Grant Agreement 284404.

REFERENCES

- [1] A. W. Chao, “Physics of Collective Beam Instabilities in High Energy Accelerators”, New York, NY, USA: Wiley, 1993.
- [2] PyHEADTAIL, <https://github.com/PyCOMPLETE/PyHEADTAIL>
- [3] PyHEADTAIL examples repository, <https://github.com/PyCOMPLETE/PyHEADTAIL-playground>
- [4] PyHEADTAIL Transverse Mode Coupling Instability in the LHC notebook, https://nbviewer.jupyter.org/github/PyCOMPLETE/PyHEADTAIL-playground/blob/master/Transverse_Mode_Coupling_Instability/TMCI_2particle_model.ipynb
- [5] J. Gareyte, “Transverse Mode Coupling Instabilities”, CERN, Geneva, Switzerland, Rep. CERN-SL-2000-075-AP, Oct. 2000.
- [6] B. Salvant, “Impedance Model of the CERN SPS and Aspects of LHC Single-Bunch Stability”, Ph.D. thesis, École Polytechnique Fédérale de Lausanne, Lausanne, Switzerland, 2010.
- [7] H. Bartosik *et al.*, “TMCI Thresholds for LHC Single Bunches in the CERN SPS and Comparison with Simulations”, in *Proc. IPAC’14*, Dresden, Germany, June 2014, doi: 10.18429/JACoW-IPAC2014-TUPME026
- [8] G. Apollinari *et al.* (Ed.), “High-Luminosity Large Hadron Collider (HL-LHC) technical design report v0.1”, CERN, Geneva, Switzerland, Rep. CERN-2017-007-M, 2017.
- [9] E. Métral *et al.*, “Update of the HL-LHC operational scenarios for proton operation”, CERN, Geneva, Switzerland, Rep. CERN-ACC-NOTE-2018-0002, Jan. 2018.
- [10] X. Buffat *et al.*, “Our Understanding of Transverse Instabilities and Mitigation Tools/Strategy”, 8th LHC Operations Evian Workshop, Évian-les-Bains, France, Dec. 2017.
- [11] N. Mounet, “DELPHI: an Analytic Vlasov Solver for Impedance-Driven Modes”, CERN, Geneva, Switzerland, Rep. CERN-ACC-SLIDES-2014-0066, May 2014.
- [12] N. Mounet, “The LHC Transverse Coupled-bunch Instability”, Ph.D. thesis, École Polytechnique Fédérale de Lausanne, Lausanne, Switzerland, 2012.
- [13] B. Salvant *et al.*, “HL-LHC impedance model”, CERN, Geneva, Switzerland, report to be published.
- [14] DELPHI, https://gitlab.com/IRIS_mirror/DELPHI_mirror
- [15] J. Wenninger, “LHC Parameter reproducibility”, in *Proc. 7th Evian Workshop on LHC beam operation*, Évian-les-Bains, France, Dec. 2016, pp. 45-52.
- [16] S. Antipov *et al.*, “Machine impedance and HOM power update”, 7th HL-LHC Collaboration Meeting, Madrid, Spain, Nov. 2017.
- [17] D. Valuch, “Excitation by ADT and Active Bunch by Bunch Tune Measurements”, presentation at the 129th SPS and LHC Machine Protection Panel Meeting, 10th June 2016, CERN, Geneva, Switzerland.
- [18] M. Soderen and D. Valuch, “ADT ObsBox Data Acquisition”, presentation at the LHC Beam Operation Committee, 13th June 2017, CERN, Geneva, Switzerland.
- [19] PySUSSIX code repository, <https://github.com/PyCOMPLETE/PySUSSIX>
- [20] R. Bartolini and F. Schmidt, “A Computer Code for Frequency Analysis of Non-Linear Betatron Motion”, CERN, Geneva, Switzerland, Rep. SL-Note-98-017-AP, June 1998.
- [21] T. Levens *et al.*, “Recent Developments for Instability Monitoring at the LHC”, in *Proc. IBIC’16*, Barcelona, Spain, Sep. 2016, doi: 10.18429/JACoW-IBIC2016-THAL02

UNDERSTANDING THE SOURCE AND IMPACT OF ERRANT BEAM LOSS IN THE SPALLATION NEUTRON SOURCE SUPERCONDUCTING LINAC*

C. C. Peters[†], A. Aleksandrov, W. Blokland, D. Curry, B. Han, G. Johns, A. Justice, S. Kim, M. Plum, A. Shishlo, T. Southern, M. Stockli, J. Tang, R. Welton, Spallation Neutron Source, Oak Ridge National Laboratory, Oak Ridge, TN, 37831, USA

Abstract

The Spallation Neutron Source (SNS) Linear Accelerator (Linac) delivers a high power proton beam (>1 MW) for neutron production with high neutron availability (>90%). For beam acceleration, the linac has both normal and superconducting RF sections, with the Superconducting Linac (SCL) portion providing the majority of beam acceleration (81 of 96 RF cavities are superconducting). Operationally, the goal is to achieve the highest possible beam energy by maximizing SCL cavity RF gradients, but not at the expense of cavity reliability [1, 2]. One mechanism that has negatively impacted both SCL cavity peak RF gradients and reliability is beam lost into the SCL due to malfunctions of upstream components. Understanding the sources and impact of errant beam on SCL cavity performance will be discussed.

INTRODUCTION

The Spallation Neutron Source (SNS) is an accelerator driven pulsed neutron source used for scientific research and industrial development.

The facility utilizes a linear accelerator (linac), a storage ring, and a mercury target to produce short high intensity bursts of neutrons. The 6% duty factor linac produces a 1 millisecond long H- beam pulse at a 60 Hz beam repetition rate. Within each 1 millisecond beam pulse the beam is chopped into 750 nanosecond beam slices. Using charge-exchange injection the ring accumulates the beam by painting the slices in both horizontal and vertical phase space. After the 1 millisecond accumulation the protons are extracted using fast kicker magnets to a mercury target for neutron production [3].

SNS low power neutron production began in 2006, and since that time the beam power has been increased slowly up to 1.4 MW. The ramp up to the design power of 1.4 MW has been slowed mostly by mercury target reliability issues. Since 2016 a strict beam power ramp up plan has been followed, which has been productive for both the accelerator and target. Currently the neutron

production beam power is at 1.3 MW, and in September 2018 the scheduled neutron production beam power will be 1.4 MW.

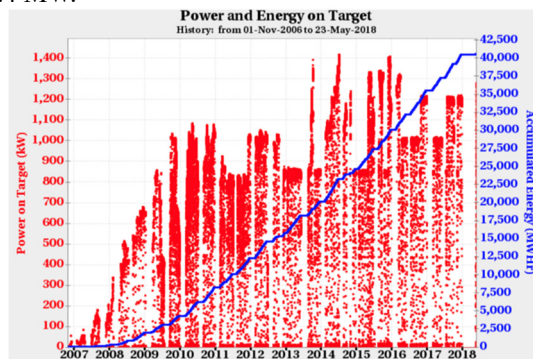


Figure 1: Beam power ramp up history.

The linac is currently the highest power pulsed proton linac in the world. The linac is capable of delivering >1.4 MW of beam power at beam availabilities >90%. Recently peak beam currents of >50 mA have been delivered to the target with nominal beam losses. This opens up the possibility of reaching average beam currents of >40 mA. The linac duty factor is 6% so this would make the linac capable of producing >2.8 MW of beam power with necessary High-Power RF (HPRF) upgrades.



Figure 2: Linac peak beam currents are able to support beam powers exceeding 2.8 MW.

ERRANT BEAM HISTORY

In 2009 beam powers quickly reached 1 MW, and soon after the SCL began experiencing reliability issues.

Content from this work may be used under the terms of the CC BY 3.0 licence (© 2018). Any distribution of this work must maintain attribution to the author(s), title of the work, publisher, and DOI.

* This manuscript has been authored by UT-Battelle, LLC under Contract No. DE-AC05-00OR22725 with the U.S. Department of Energy. The United States Government retains and the publisher, by accepting the article for publication, acknowledges that the United States Government retains a non-exclusive, paid-up, irrevocable, worldwide license to publish or reproduce the published form of this manuscript, or allow others to do so, for United States Government purposes. The Department of Energy will provide public access to these results of federally sponsored research in accordance with the DOE Public Access Plan (<http://energy.gov/downloads/doe-public-access-plan>).

[†] peterscc@ornl.gov

Machine Protection System (MPS) Issues

In 2009 SCL cavity reliability began to abruptly decrease. In order to maintain as high reliability as possible SCL cavity gradients were decreased. This in turn reduced the linac output beam energy. SCL experts investigated the issue and were able to correlate beam loss events with SCL cavity downtime events.

Investigation into the beam loss events narrowed down the issue to the Machine Protection System (MPS) [4]. The goal turn-off time for the MPS is 20 microseconds [5], and testing showed that in some cases the MPS turn off time was >1 millisecond. In Figure 3 below is an example of a turn time of 200 microseconds, which is an order of magnitude longer than design.

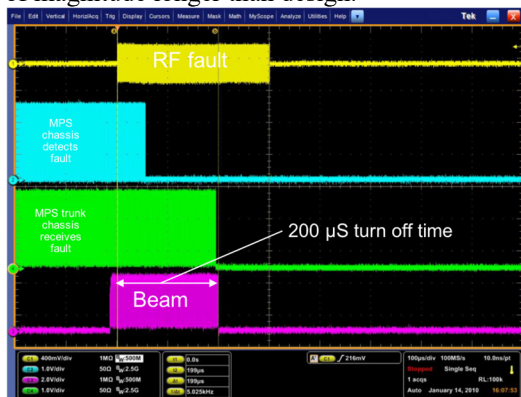


Figure 3: Scope snapshot showing delays of 200 microseconds during the MPS issues found in 2009.

The issue was found to be delays from poorly chosen MPS chassis input capacitors, and MPS sublink output drive circuits [6]. The capacitors were removed and the drive circuits were upgraded. This reduced the beam turn off time to the design requirement of 20 microseconds.

Though the MPS issues were resolved SCL degradation has continued, though at a reduced rate compared with the abrupt degradation from the MPS issues.

SLOW DEGRADATION OF SCL CAVITY RF GRADIENTS

Operationally at SNS the highest priority is neutron availability. If an SCL cavity begins to trip off repeatedly then the RF gradient will be reduced until reliability improves [7].

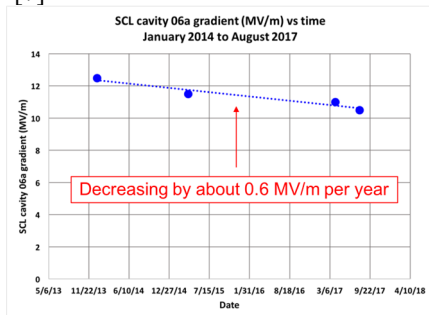


Figure 4: The plot above shows the need to decrease SCL cavity 06a gradient over time. The reduction is about 0.6 MV/m per year.

To compensate for the reduced energy the remaining SCL cavity phases will be adjusted to maintain the same linac output beam energy. The last SCL cavity is always left non-accelerating to leave energy reserve to be used in case issues listed above develop. Figure 4 shows an example of the decreasing SCL cavity 06a gradient over time due to slow degradation from errant beam.

ERRANT BEAM TASK FORCE ESTABLISHED

In 2012 it was realized that SCL cavities were still being damaged by errant beam, and additional analysis needed to be done to limit SCL cavity degradation.

The task force came up with the following plan to try to limit the impact from errant beam.

- Verify proper MPS operation.
- Gather errant beam statistics.
- Reduce errant beam frequency and the amount lost per event.

MPS Operation Verified

The first check done was to measure the amount of beam being lost during an errant beam event. This would verify the MPS was working properly by showing the beam turn off time, and also gather statistics on the frequency of errant beam events. The system used Beam Current Monitors (BCMs) upstream and downstream of the SCL. The system ran at 60 Hz (the maximum beam repetition rate), and saved the BCM waveforms to a web-server for viewing after each event. The system was just a diagnostic with no connection to the MPS.

First and foremost the BCMs in the MEBT, CCL, and HEBT showed that the beam turn off times ranged from 15-20 microseconds. This verified that the MPS was working properly. Figure 5 shows a typical snapshot of BCM waveforms during an errant beam event. The BCM in the High Energy Beam Transport (HEBT) downstream of the SCL shows about 16 microseconds less beam compared with the BCMs in the MEBT and CCL.

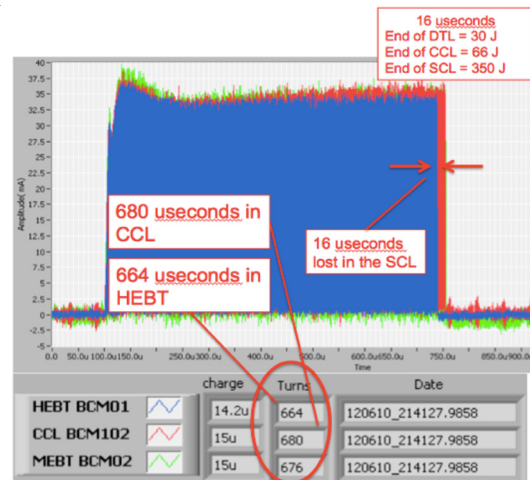


Figure 5: The above figure shows the BCM system used to verify that the MPS was turning off the beam at the design time of 20 microseconds.

Content from this work may be used under the terms of the CC BY 3.0 licence (© 2018). Any distribution of this work must maintain attribution to the author(s), title of the work, publisher, and DOI.

Not all of the errant beam pulses looked similar to Figure 5, but most did. Some of the errant beam pulses showed that it was introduced in the MEBT from malfunctions in the ion source. Most of the errant beam events came downstream of the MEBT and upstream of the SCL from malfunctions in the warm linac.

Low-Level Radio Frequency (LLRF) Adaptive Feed Forward (AFF) Background

High beam currents at the SNS make it necessary to use a LLRF feed-forward based approach in order to maintain the appropriate cavity field and phase under heavily beam-loaded conditions [8]. At the SNS a system of Adaptive Feed Forward (AFF) was developed for this compensation.

The system works by the following method. A beam pulse is triggered. The system creates error waveforms as it measures the field and phase errors during the beam pulse. The LLRF “learns” from those errors and adjusts LLRF gains for the next beam pulse (the system is currently only capable of running at a 20 Hz repetition rate). The system works extremely well as long as pulse to pulse beam current shapes are reproducible.

The AFF system does not “learn” if an MPS fault is detected during the beam pulse.

Ion Source Ignition Instability and LEPT Arcing

The ion source can trigger errant beam in multiple ways. One way is an abrupt change in beam current output.

An abrupt change in beam current can have a two-fold effect on SCL cavity reliability. As stated above the AFF system expects a certain beam current shape from pulse to pulse. If the beam current shape changes unexpectedly the AFF will be unaware and the LLRF gain settings will be incorrect for the odd beam pulse. Figure 6 shows an example of an ion source pulse during a high voltage arc. The reduced beam current means the LLRF system will overdrive causing an elevated cavity field creating a higher probability for an arc. The elevated field and likely incorrect phase will also cause incorrect beam acceleration and result in beam losses. So, the effect is two-fold: overdriving to high fields, and beam loss due to incorrect field and phase.

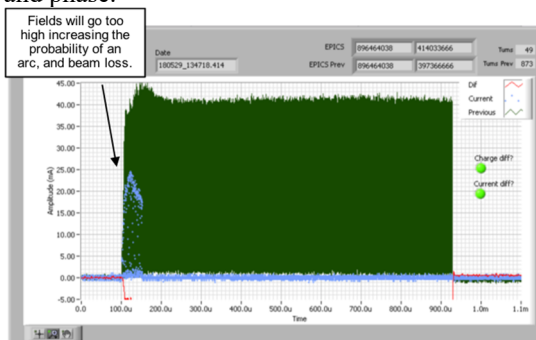


Figure 6: Example of an ion source high voltage arc. The green pulse is a nominal pulse and the blue is the beam current during an ion source malfunction.

Ion Source Beam Halo

Another source of errant beam from the ion source is beam halo.

Ion source equipment is not monitored by the MPS. If equipment malfunctions within the ion source or LEPT the indications of a problem come from secondary equipment.

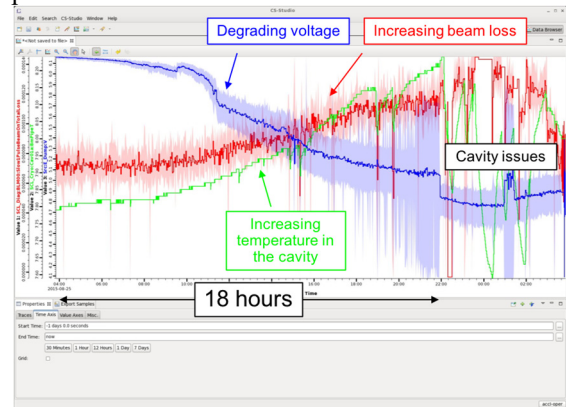


Figure 7: The plot above shows the degrading ion source voltage (blue), increasing beam loss (red), and the increasing beam pipe temperature (green) in an SCL cavity. After ~18 hours of increasing beam loss SCL cavity issues developed requiring reduced gradient.

Figure 7 above shows an example of a decaying high voltage in the ion source. As the voltage decays beam losses begin to increase in the SCL. Beam pipe temperature within a cavity correlates with the beam loss, and after about 18 hours of the increasing beam loss the SCL cavity begins to fault off. The cavity gradient must be reduced in order to maintain high reliability. After a few hours operators retune the ion source to reduce the beam halo, but even after the tuning the cavity gradient must remain reduced. The cryomodule must be warmed up to restore the previous gradient setting.

Errant beam from the ion source has been significantly reduced due to significant analysis and development work performed by ion source experts at the SNS [9].

Warm Linac Arcing/Multipacting

The dominant source of errant beam was found to be the warm linac. When a warm linac cavity faults from arcing or multipacting the field decay is on the order of a few microseconds so the beam loss is fast and significant.

Most of the arcing and multipacting seen in the warm linac cavities occurred during the fill time of the RF cavities. The point where the RF wave is transitioning from a traveling wave to a standing wave. In order to affect the fault rates two methods were employed.

The first method was to use a linear fill of the forward power to minimize the reflected RF power during the fill time of the cavity. The normal filling method used is to start with nominal forward power and maintain the forward power fixed during the fill, but early in the pulse the reflected power is elevated. Though these faults would normally occur before the beam pulse the reduction in the

fault rates translated to fewer faults later in the RF pulse when beam is present. Figure 8 shows an example of the difference in RF waveform shape with the natural RF cavity fill versus the linear forward power fill.

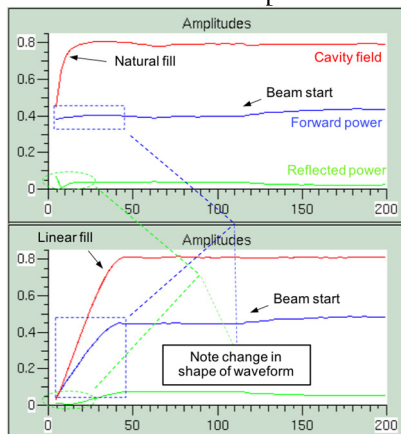


Figure 8: Top shows the natural cavity fill. The bottom shows the adjustment to the linear forward power fill.

The second method used was to slowly change the resonant frequency of the cavities while monitoring the vacuum and reflected power RF waveforms. Minimum fault rates for the Drift Tube Linac (DTL) cavities occurred with minimal reflected power during the fill time of the cavity. When running the cavities at frequencies slightly below 402.5 MHz the vacuum near the ceramic RF window decreased though the reflected power near the end of the beam pulse actually increased. Figure 9 shows the significant decrease in fault rate for DTL5 when lowering the resonant frequency by 2.5 kHz.

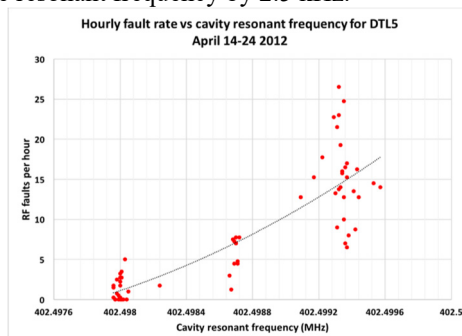


Figure 9: Reduction in fault rate by lowering the DTL5 cavity resonant frequency.

Warm Linac Vacuum

Throughout the warm linac vacuum capture pumps were used as the dominant pumping system. Ion pumps were used on the cavities and Non-Evaporable Getter (NEG) pumps on the ceramic RF windows.

The NEG pumps had to be routinely regenerated, and if not regenerated routinely the systems would burst and cause the protection system to interlock the LLRF, and cause errant beam.

The entire vacuum system was upgraded for both the DTL and Coupled Cavity Linac (CCL) to replace all capture pumps with turbopumps. The upgrade has not

only reduced errant beam faults, but it's also decreased overall downtime by 2%.

Warm Linac Operating Practices

One specific area of additional concern in the CCL has been damage to secondary equipment from field emitted electrons. Two BCMs in the CCL have failed due to cracked ceramics. A vacuum valve downstream of CCL cavity 4 has repeatedly been damaged.

One correlation is increases in vacuum pressures when the CCL RF is on without quadrupole magnet power supplies energized. Figure 10 shows multiple points in time where a specific magnet power supply was off and on with RF on for CCL cavity 1.

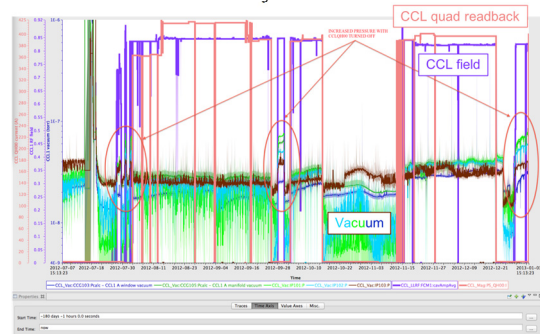


Figure 10: The plot above shows elevated vacuum pressures when quads powered off with RF on.

The likely issue is heating up of an upstream vacuum valve from the field emitted electrons. It appears with quads on the electrons are disbursed instead of striking a localized spot somewhere on secondary equipment. Administrative rules were established to always have quadrupole magnet power supplies on when RF is on in the CCL. This is not an issue with the DTL because the quadrupole magnets are permanent magnet installations.

The previous method to condition the RF window was to increase the RF power to the beam loaded level (about a 10% increase over the nominal cavity field level). Increasing the field in the structure to that level significantly increased field emission levels. The field emitted electrons were striking a vacuum valve downstream of the cavity, and causing contamination.



Figure 11: The picture above shows a damaged o-ring seal on a vacuum valve after being damaged by stray field emitted electrons.

Content from this work may be used under the terms of the CC BY 3.0 licence (© 2018). Any distribution of this work must maintain attribution to the author(s), title of the work, publisher, and DOI.

Errant Beam Frequency Reduced

The largest reduction in errant beam frequency came in 2012, and has been slowly decreasing since. The fault frequency cannot be reduced to zero, and at any point the fault rate can increase abruptly. Figure 12 shows the reduction in fault frequency.

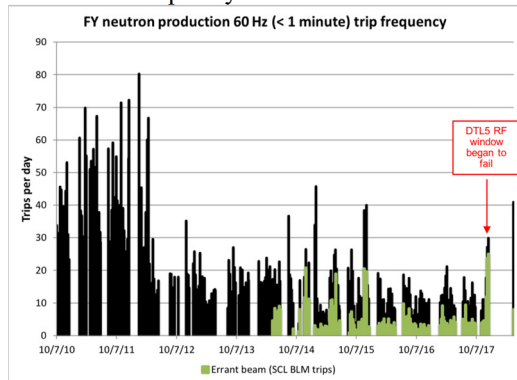


Figure 12: The plot above shows the reduction in short fault frequency dominated by errant beam faults.

In 2017, for example, the DTL cavity 5 RF window began to slowly fail. Since the failure was slow the decision was made to continue running until the end of the scheduled run period before changing the failing window.

Reducing Beam Loss During Each Errant Beam Event

The last step to try to minimize the effect of errant beam on the SCL was to reduce the turn off time of the MPS. Instead of trying to figure out a way to modify the MPS beam turn off mechanism the decision was made to have a separate system connect directly to the LEBT chopper without going through the MPS.

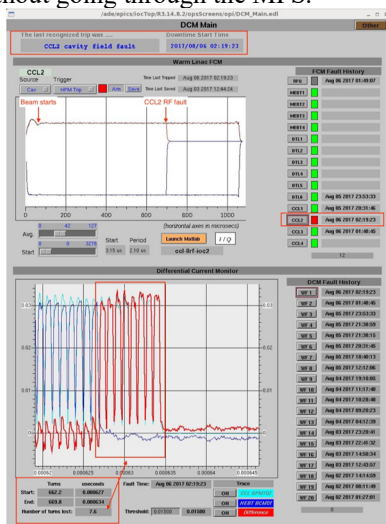


Figure 13: The snapshot above is an example fault detection by the SCL DCM system.

The system implemented was based on the system used during the MPS checkout to use a differential charge measurement between BCMS upstream and downstream of the SCL. The system uses a Beam Position Monitor

(BPM) in the CCL and a BCM in the HEBT and compares the charge difference based on a settable level. The system runs at 60 Hz and is able to detect a charge difference within 1 microsecond. The fault signal then goes directly to the LEBT chopper and is able to turn off the beam within about 8 microseconds [10]. Figure 13 shows an example of the system interlocking due to a CCL cavity 2 fault.

The system also sends the fault information to the MPS. The LEBT chopper chops the beam for approximately 30 microseconds, which gives the MPS time to turn off the ion source and RFQ timing gates.

FUTURE UPGRADES

Even with the factor of two reduction in turn off time SCL cavity downtime can still happen with an errant beam event. There are plans to install a pulse to pulse system to monitor beam pulses in the MEBT to reduce damage from ion source malfunctions. It is not logical to expect to reduce the turn off time much more than is currently being done. One possibility is to use a machine learning algorithm to predict errant beam. Recent analysis suggests that using the SCL DCM waveforms it is possible to predict errant beam pulses with up to a 94% success rate [11]. Far from the likely >99% certainty needed to be used as a production system.

CONCLUSION

The frequency of errant beam events as well as the amount of beam lost per errant beam event have been significantly reduced. Even with the reductions SCL cavity degradation continues at a slow rate. Figure 14 shows that plasma processing is increasing the output energy of the linac, and with continued diligence with errant beam reduction there will be no loss of the gains from plasma processing.

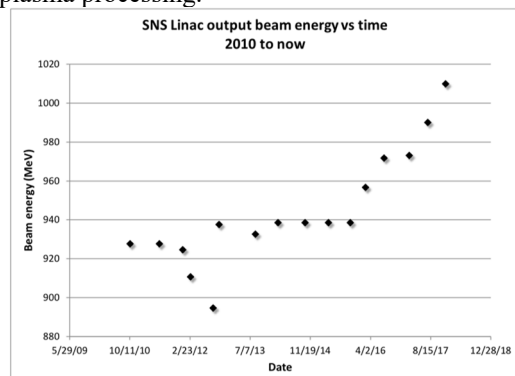


Figure 14: The plot above shows the linac beam output energy versus time. Since 2016 plasma processing has significantly increased the beam energy.

ACKNOWLEDGMENTS

Authors would like to thank Control Room Shift Supervisors and Accelerator Specialists for taking data that were used for errant beam analysis.

REFERENCES

- [1] S. Kim *et al.*, “The status of the Superconducting Linac and SRF Activities at the SNS,” in *Proc. 16th International Conference on RF Superconductivity (SRF’13)*, Sep. 2013, Paris, France, 2013, paper MOP007, pp. 83-88.
- [2] M. Plum, “High Power Operation of SNS SC Linac”, in *Proc. Linear Accelerator Conference (LINAC’16)*, East Lansing, MI, USA, 2016, p. 348.
- [3] S. Henderson *et al.*, “The Spallation Neutron Source accelerator system design”, *Nucl. Inst. Meth.*, vol. A763, pp. 610-673, 2014.
- [4] C. Peters *et al.*, “Superconducting Radio Frequency Cavity Degradation due to Errant Beam”, in *Proc. IPAC’15*, Richmond, VA, USA, 2015, p. 805.
- [5] C. Sibley III *et al.*, “The SNS Machine Protection System: Early Commissioning Results and Future Plans”, in *Proc. PAC’05*, Knoxville, TN, May 2005, p. 1727-1729.
- [6] D. Curry *et al.*, “MPS Delay Measurements,” unpublished.
- [7] C. Peters *et al.*, “Minimizing Errant Beam at the Spallation Neutron Source”, in *Proc. IBIC’17*, Grand Rapids, MI, USA, 2017, p. 491.
- [8] Kay-Uwe Kasemir *et al.*, “Adaptive Feed Forward Beam-Loading Compensation Experience at the Spallation Neutron Source Linac,” in *Proc. PAC’05*, Knoxville, TN, May 2005, p. 1467-1469.
- [9] Martin P. Stockli, Robert F. Welton, and Baoxi Han, “Record productions establish RF-driven sources as the standard for generating high-duty-factor, high-current H- beams for accelerators (Winner of the ICIS 2017 Brightness Award),” *Rev. Sci. Instrum.*, vol. 89, p. 052202, 2018.
- [10] W. Bloklund, “A New Differential and Errant Beam Current Monitor for the SNS Accelerator,” in *Proc. IBIC’13*, Oxford, UK, Sep. 2013, paper THAL2, pp. 921-24.
- [11] M. Rescic *et al.*, “Follow-up analysis of K-nearest neighbors for SNS pulses,” unpublished.

Content from this work may be used under the terms of the CC BY 3.0 licence (© 2018). Any distribution of this work must maintain attribution to the author(s), title of the work, publisher, and DOI.

EXPERIMENTAL STUDY OF BEAM DYNAMICS IN THE PIP-II MEBT PROTOTYPE*

A. Shemyakin[†], J.-P. Carneiro, B. Hanna, V. Lebedev, L. Prost, A. Saini, V. Scarpine
 Fermilab, Batavia, IL 60510, USA

V.L.S. Sista, Bhabha Atomic Research Centre (BARC), Mumbai, India

C. Richard, Michigan State University, East Lansing, MI, USA

Abstract

The Proton Improvement Plan, Stage Two (PIP-II) [1] is a program of upgrades proposed for the Fermilab injection complex, which central part is an 800 MeV, 2 mA CW SRF linac. A prototype of the PIP-II linac front end called PIP-II Injector Test (PIP2IT) is being built at Fermilab. As of now, a 15 mA DC, 30-keV H⁻ ion source, a 2 m-long Low Energy Beam Transport (LEBT), a 2.1 MeV CW RFQ, followed by a 10 m Medium Energy Beam Transport (MEBT) have been assembled and commissioned. The MEBT bunch-by-bunch chopping system and the requirement of a low uncontrolled beam loss put stringent limitations on the beam envelope and its variation. Measurements of transverse and longitudinal beam dynamics in the MEBT were performed in the range of 1-10 mA of the RFQ beam current. Almost all measurements are made with 10 μs beam pulses in order to avoid damage to the beam line. This report presents measurements of the transverse optics with differential trajectories, reconstruction of the beam envelope with scrapers and an Allison emittance scanner, as well as bunch length measurements with a Fast Faraday Cup.

The combination of the ion source and LEBT can deliver up to 10 mA at 30 keV to the RFQ with pulse lengths ranging from 1 μs to 16 ms at up to 60 Hz, or a completely DC beam. An atypical LEBT transport scheme [3] minimizes changes of the beam properties throughout a pulse due to neutralization, which allows to tune the beam line at a short pulse length (typically 10 μs). Following the RFQ is a long MEBT, which provides transverse and longitudinal focusing to match the 2.1 MeV beam into the Half-Wave Resonator (HWR) cryomodule. As the latter is not yet installed, the beam line currently ends with a high-power dump capable of dissipating 10-20 kW, depending on the beam size.

PIP2IT MEBT

The present MEBT configuration is shown in Fig. 2. The MEBT transverse focusing is provided by quadrupoles [4], referred as either F or D type according to their yoke length, 100 or 50 mm, which can be powered to focus either in horizontal (+) or vertical (-) directions. The quadrupoles are grouped into two doublets followed by seven triplets, where the magnets are arranged as F⁻-F⁺ and D⁻-F⁺-D⁻, respectively. The spaces between the focusing groups are addressed as “sections” (650-mm long flange-to-flange for sections #1 through #7, and 480 mm for section #0). Each group includes a Beam Position Monitor (BPM), whose capacitive pickup is bolted to the poles of one of the quadrupoles and is followed by an assembly with two (X/Y) dipole correctors. The distance between centers of the triplets is 1175 mm.

PIP2IT WARM FRONT END

The PIP2IT warm front end (Fig. 1) has been installed in its nearly final configuration [2].

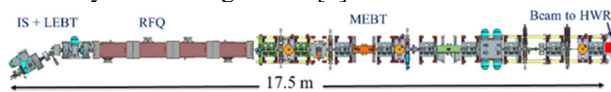


Figure 1: PIP2IT warm front end (top view).

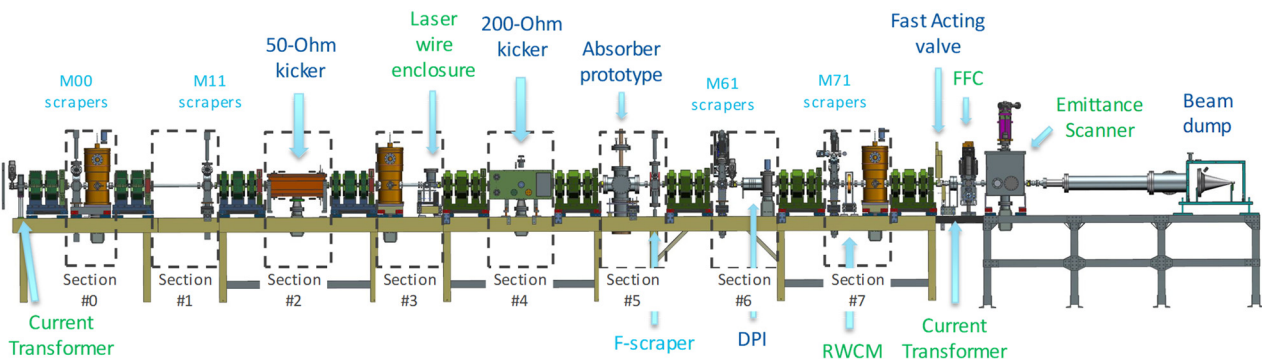


Figure 2: Medium Energy Beam Transport line (side view).

* This manuscript has been authored by Fermi Research Alliance, LLC under Contract No. DE-AC02-07CH11359 with the U.S. Department of Energy, Office of Science, Office of High Energy Physics
[†]shemyakin@fnal.gov

The prototype kickers [5] are installed in sections 2 and 4, and the Differential Pumping Insert (DPI) is in section 6. The 200 mm (L) × 10 mm (ID) beam pipe of the DPI as well as the 13-mm high gaps in the protection electrodes,

placed on both sides of each kicker, are the aperture limitations in the MEBT. Otherwise, the typical vacuum pipe ID is 30 mm.

Longitudinal focusing is provided by 3 bunching cavities in sections 0, 3, and 7, which, if phased for acceleration, can increase the beam energy by up to 100 keV each. Movable scrapers [6] installed with the main goal to protect the cryomodules against an errant beam or halo were also used to measure the beam size. Shown in Fig. 2 are 4 sets of 4 scrapers (each set consists of a bottom, top, right and left scraper) plus a temporary set of two scrapers (a.k.a. F-scraper, top and right).

Current transformers are located at the beginning and end of the MEBT. An emittance scanner and Fast Faraday Cup (FFC) (moved to various locations) were used to characterize the beam emittance. A Resistive Wall Current Monitor (RWCM) completes the set of diagnostics available.

TRANSVERSE OPTICS

Reconstruction of the beam transverse optics in the MEBT was performed in two steps [7]. First, the beam dipole motion was characterized using differential trajectories analyses, and the calibration of magnetic elements was adjusted in the optics model to fit the measurements. Then, the measurements of the transverse beam size along the MEBT were used to reconstruct the Twiss functions of the beam coming out of the RFQ and simulate the beam envelope in the line. This knowledge allows to adjust the beam position and size in a predictable manner.

Differential Trajectory Analysis

A Java program developed for the differential trajectory measurements at the PIP2IT, records the BPM positions with the nominal settings and then when one of the dipole correctors is changed. The difference in the BPM readings is then compared to the optical model in OptiM [8]. The procedure is repeated for all available correctors, and for each case, the calibrations of the correctors and quadrupoles are adjusted in OptiM, with respect to initial values based on magnetic measurements, to match the data points. After several series of measurements and adjustments, the procedure converges and the model fits well the differential trajectories results in all cases, like the ones shown in Fig. 3.

Typically, the quadrupole calibrations obtained from beam measurements are consistently lower by 5-10% than those found from the magnetic measurements. Note that all magnets were measured at BARC (where they were manufactured) and several were re-measured at Fermilab, where the results from BARC were reproduced well, with difference in calibrations $< 1\%$. The accuracy of the beam measurements, determined by the beam jitter (see below) and drifts, is estimated to be $\sim 4\%$ and cannot explain the deviation. While the discrepancy has not been resolved, in the following analysis we use the calibrations from the beam measurements.

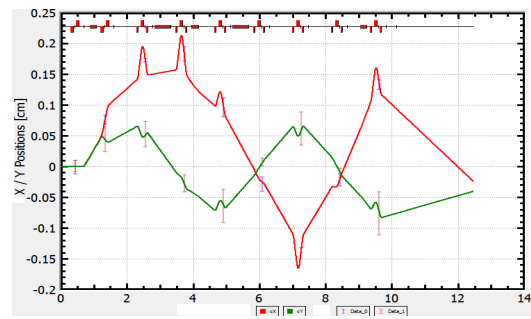


Figure 3: Response of trajectories to changing the current in the first dipole correctors by 0.4 A: horizontal x (red) and vertical y (green). The measured data points are averages of 50 pulses, and the error bars are the rms scatter. The solid lines are the corresponding simulations.

Beam Size Measurements

Transverse beam sizes along the MEBT are measured primarily with scraper scans fitted to an integrated Gaussian distribution (see more details in [9]). In addition, the Allison scanner, installed at the end of the beamline, provides the vertical phase space portrait hence the vertical beam size.

To describe the beam envelope along the MEBT, the initial transverse Twiss parameters at the exit of the RFQ were defined through an iterative process using TRACEWIN [10] simulations to fit to the measured rms beam sizes at the first three scrapers. Fig. 4 shows the reconstructed transverse rms envelope, which agrees with all measured sizes within their typical reproducibility of $\sim 10\%$.

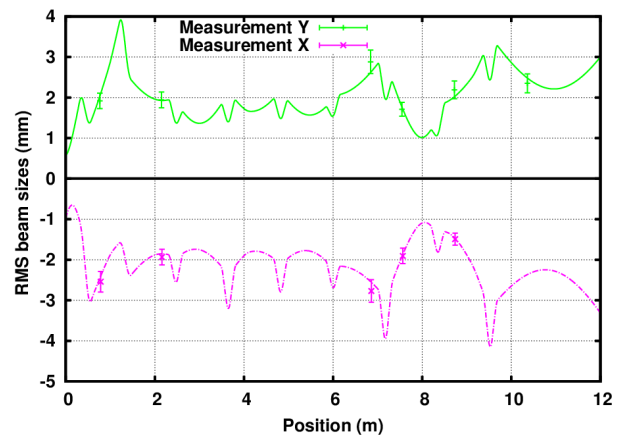


Figure 4: Rms beam envelope along the MEBT simulated with TRACEWIN. Horizontal envelope is shown negated for the presentation purpose. Error bars are $\pm 10\%$ of the measured sizes. Normalized rms transverse and longitudinal emittances were assumed to be $0.2 \mu\text{m}$ and $0.28 \mu\text{m}$, respectively. Beam current is 5 mA.

Beam Tuning

The accuracy of the optics model helped with beam tuning. The beam envelope presented in Fig. 4 is optimized for the MEBT line operating with two kickers and the DPI. Consequently, the vertical beam size is lower than the horizontal in the kickers, and both sizes are small

Content from this work may be used under the terms of the CC BY 3.0 licence (© 2018). Any distribution of this work must maintain attribution to the author(s), title of the work, publisher, and DOI.

when passing through the 10-mm aperture of the DPI. In high-power runs, the beam size in the dump was increased by over-focusing the beam with the last triplet.

Also, the model easily predicts how to combine setting changes to several correctors to move the beam in specific locations without disturbing the trajectory elsewhere.

Beam Jitter

The beam in the MEBT experiences a significant pulse-to-pulse jitter that affects the accuracy of the measurements, the effective emittance, and aperture limitations. The amplitude varies dramatically along the beam line, reaching up to 0.2 mm rms. In an attempt to localize the source of that jitter, the BPM readings of 10 μ s x 20 Hz pulses were recorded over 35 minutes from all BPMs. The resulting matrix was analysed with Singular Value Decomposition similar to Ref. [11]. The analysis showed that the noise is dominated by a single spatial component, which eigenvalue exceeded the next closest one by a factor of ~ 10 (Fig. 5). Components beyond the second one are already at the noise floor. The FFT analysis of the noise temporal structure showed that the noise is dominated by low frequencies,

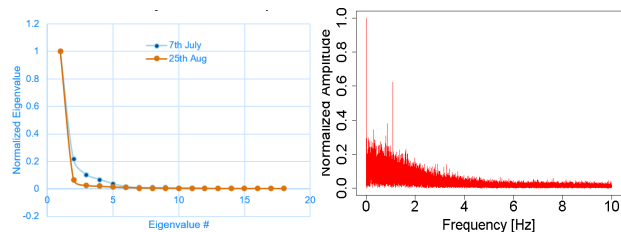


Figure 5: Characteristics of the BPMs noise. Left – eigenvalues. The data set marked “7th July” represents 10 Hz x 10 min set. Right – FFT of the signal in one of the BPMs.

Comparing the first two spatial eigenvectors (Fig. 6) to the MEBT betatron modes clearly indicates that the beam jitter originates upstream of the MEBT.

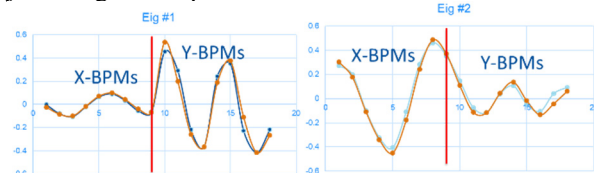


Figure 6: Comparison of the first two eigenvectors (orange) with betatron modes (blue).

After subtracting the contribution of the first two modes from the original data, the remaining noise is at the level of several μ m, probably defined by the electronics.

To further localize the noise source, we varied the last two (out of 3) LEBT solenoids and found two combinations of their currents (in addition to the nominal settings) for which the RFQ transmission was good ($>95\%$). The solenoids rotate the beam as well as the plane of the jitter proportionally to the sum of Amp-turns in them, while the motion in the RFQ and MEBT is uncoupled. The BPM signals were recorded for both cases, and the same SVD analysis was performed. The plane of oscillation of the

first spatial eigenvector was found changing in agreement with angles expected from the rotation by the solenoids, indicating that the source of the jitter is upstream of the second solenoid. Unfortunately, as of now, the jitter has not been eliminated. The present speculation is that it comes from within the ion source where faint indications of the presence of the same 1.09 Hz line as in Fig. 5 were observed.

Road to Beam Tails Analysis

So far, the beam properties were characterized in terms of either the centroid motion or rms sizes. To analyse the beam transverse tails, we initially intended to use the scraping system. It was not successful. On one hand, the noise of the current measuring devices is too large to resolve variations below 1% when a scraper is moved into the beam. On the other hand, the signals from the scrapers themselves drop to nearly zero if their plates are at the ground potential because of secondary electron emission. Since the scraper currents are to be included into the Machine Protection System (MPS), the plates are biased by +100 V. In this case the scraper current starts already rising when the scraper plate is far from the beam. When the plate is deep inside the beam, the scraper reading is typically 10-20% higher than the intercepted beam current and fluctuates significantly. We interpret this as an indication of the presence of a significant amount of secondary electrons in the vacuum pipe, e.g. originated by lost or reflected ions from the pipe’s walls. While such behaviour is tolerable for the purpose of the MPS, it does not allow measuring the tails of the particles distribution. We hope that the implementation of a negatively biased wire scanner will provide much more consistent readings.

Another available tool is the MEBT Allison scanner. A dedicated Python application is being written to better analyze the tails. First, attention is paid to the background analysis. In the present LabView program, inherited from SNS, the background is rejected at the level equal to 1% of the maximum signal, distorting the output for low beam currents or large footprints. Instead, the new code analyses the level of the background noise far from the beam and reject the background at the level of several times the rms noise (Fig. 7). The typical ratio of the maximum signal to the cut-off is 0.5%.

Then, efforts are being made to define more consistently the beam core. The rms definition of the Twiss parameters depends on the level of the noise cut since the tails are generally phase-dependent. In addition, the Twiss parameters change if tails are cut by a scraper, making the analysis of the scraping efficiency difficult in terms of maximum action. We are implementing a procedure that calculates the Twiss parameters for only 50% of the total phase portrait integral, composed by the pixels with highest intensities. One of the consequences of using such “central” definition is that in the core the pixels corresponding to the same action have the same intensity, i.e. the core distribution is independent on the phase (Fig. 7). Note that this “central” definition is likely more consistent with the envelopes derived from scraper

measurements since fitting to a Gaussian distribution essentially ignores the behaviour of the tails.

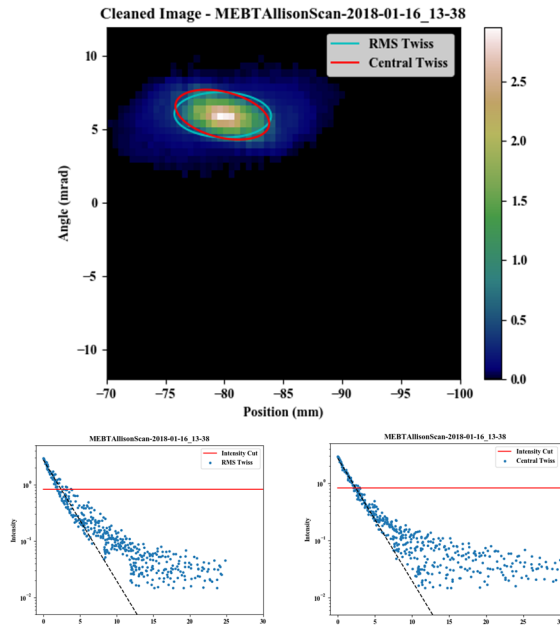


Figure 7: Illustration of the different Twiss parameters calculation. Top- the image cleaned with the Python code. Bottom- pixel intensity (in mV) vs the action (in μm) for the rms (left) and “central” definitions. In the core, the scatter of intensities is significantly lower in the right plot.

LONGITUDINAL MOTION

Longitudinal focusing at PIP2IT is provided by three bunching cavities. Normally the cavities’ phases are set to -90° with respect to the beam, i.e. the bunches are longitudinally focused without changing the average energy of the ions.

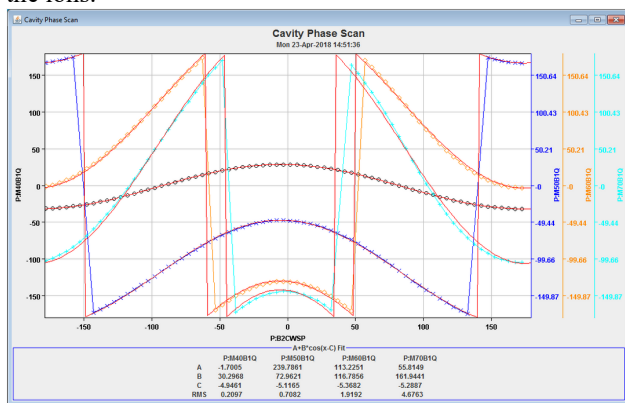


Figure 8: Screenshot of the cavity phasing program showing the dependence of 4 BPM phases on the reference phase of bunching cavity #2. Cavity voltage is 60 kV. In this specific case, the cavity phase offset needs to be adjusted by 5° .

The phasing is made by rotating the cavity reference phase by 360° , recording the resulting changes in phases of the downstream BPMs and fitting them to sinusoids (Fig. 8). The found phase offset is then corrected via the LLRF settings so that the zero degrees of the reference

phase corresponds to maximum acceleration. Typical scatter in these measurements is $\sim 0.5^\circ$.

Note that the cavities’ voltages can also be deduced from phasing measurements (as in Fig. 8) since the amplitude of BPM phase variations is proportional to the cavity voltage. These measurements provide amplitudes that are $\sim 10\%$ higher than previously established calibrations. The reason of this discrepancy is under investigation.

The longitudinal charge distribution of the bunches is measured with a Fast Faraday Cup, which can be moved vertically in and out of the beam path. Its 0.8-mm entrance hole in the ground electrode cuts a beamlet, which current is measured by a collector. The 1.7 mm gap between the ground electrode and collector results in widening of the measured signal in comparison with the actual bunch length. According to estimations in [12], a point charge flying at 20 mm/ns (equivalent to 2.1 MeV) would generate a pulse with an rms width of 25 ps. For all bunch length measurements at PIP2IT, this correction is negligible. All FFC measurements are made with $10 \mu\text{s} \times 1 \text{ Hz}$ pulsing.

The bunch length measurements were carried out in two locations, first in section 6 and then at the end of the beam line as shown in Fig. 2. The measured distributions are characterized by the rms bunch length and integral, which are obtained from fitting the signals to a Gaussian distribution. A typical FFC signal and corresponding Gaussian fit are shown in Fig. 9.

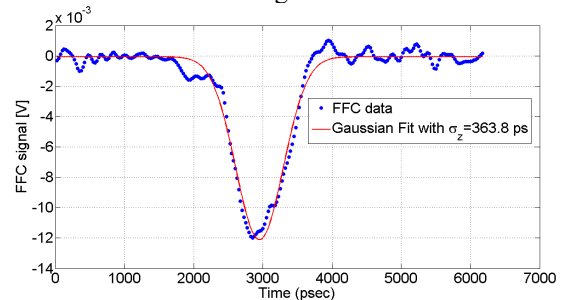


Figure 9: One period of the FFC signal (blue) and its Gaussian fit (red). The FFC is at the end of the beam line. Beam current is 9.3 mA.

Location of the FFC in section 6 is optimum for reconstructing the bunch longitudinal emittance since the dependence of the bunch length on the voltage of bunching cavity #2 upstream exhibits a minimum (Fig. 10).

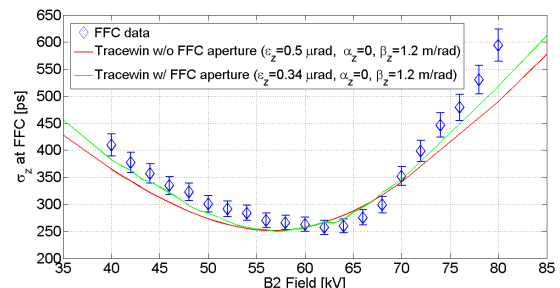


Figure 10: Rms bunch length vs voltage of bunching cavity #2 (blue) and two fitting curves (see text).

The initial interpretation of the data yielded a large longitudinal emittance, $0.5 \mu\text{m}$ rms normalized (red curve in

Content from this work may be used under the terms of the CC BY 3.0 licence (© 2018). Any distribution of this work must maintain attribution to the author(s), title of the work, publisher, and DOI.

Fig. 10), in a strong disagreement with simulations. The contradiction was traced to the implicit assumption that the bunch length measured at the beam center is representative of the entire beam, which is valid for a fully uncoupled particle distribution. Detailed measurements of the bunch length in various positions across the beam clearly showed that this assumption is incorrect: the bunch length is consistently lower toward the beam edges (Fig. 11).

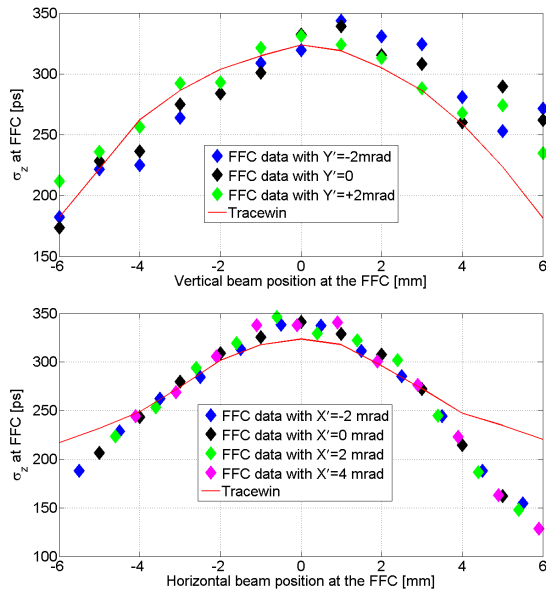


Figure 11. Rms bunch length vs vertical (top) and horizontal (bottom) position across the beam. Different colors of data points correspond to different angles between the beam and the FFC axis. The red solid curves are simulations with TraceWin assuming an uncoupled 6D distribution at the exit of the RFQ. Beam current is 5 mA. The beam transverse rms size is 2.6 mm in X and 2.0 mm in Y.

For a more adequate comparison with measurements, the bunch length of a beamlet cut by same 0.8 mm aperture was simulated by TraceWin. In this case, the simulation exhibits the behaviour observed experimentally (solid curves in Fig. 11), and the best fit for the bunch longitudinal emittance, $0.34 \mu\text{m}$, is close to the one expected from RFQ simulations (green curve in Fig. 10). These simulations use as an input file a fully uncoupled 6D Gaussian distribution, primarily because the procedure of adjusting the initial Twiss functions is clear in this case. The significant difference between the rms bunch length of the entire beam and the central beamlet appears only with significant space charge and only after propagation through a large part of the MEBT. At the same time, the beam longitudinal emittance stayed essentially constant along the MEBT.

Note that analyses of the distribution coming out of the RFQ in simulations with TOUTATIS [10] showed a difference between the “central” and overall bunch length comparable to numbers in Fig. 11. Ignoring this effect in the present MEBT simulations may be affecting the accuracy of comparison with measurements.

SUMMARY

The transverse optics of the PIP2IT MEBT was reconstructed by first adjusting calibrations of the magnets based on analyzing the beam dipole motion and then defining the initial Twiss parameters through fitting the beam sizes measured along the beam line. Good understanding of the optics helps with tuning the beam, e.g. allowing to predict the beam envelope within 10% or look for the source of the beam position jitter.

The longitudinal optics is defined with less certainty, though its study follows the same combination of analyzing the dipole motion by BPM phases and the rms bunch length by the FFC. One of the results of the latter measurements is that there is significant coupling between the transverse and longitudinal beam distributions.

ACKNOWLEDGMENT

The authors are thankful to the many people who built the PIP2IT MEBT and helped with the measurements, including R. Andrews, C. Baffes, B. Chase, A. Chen, E. Cullerton, N. Eddy, J. Einstein-Curtis, B. Fellenz, B. Hartsell, M. Kucera, D. Lambert, R. Neswold, D. Peterson, A. Saewert. FFC RF design by D. Sun was crucial for the bunch measurements. Scanning programs were written by W. Marsh. Support and encouragement from P. Derwent is highly appreciated.

REFERENCES

- [1] PIP-II Conceptual Design Report, 2017, <http://pip2-docdb.fnal.gov/cgi-bin/ShowDocument?docid=113>
- [2] L.R. Prost, R. Andrews, C.M. Baffes, J.-P. Carneiro, B.E. Chase, A.Z. Chen, E. Cullerton, P. Derwent, J.P. Edelen, J. Einstein-Curtis, D. Frolov, B.M. Hanna, D.W. Peterson, G.W. Saewert, A. Saini, V.E. Scarpine, A.V. Shemyakin, V.L. Sista, J. Steimel, D. Sun, A. Warner, C.J. Richard, V.L. Sista, “PIP-II Injector Test Warm Front End: Commissioning Update”, presented at IPAC’18, Vancouver, Canada May 2018, paper THYGBF2, unpublished
- [3] L. Prost, J.-P. Carneiro and A. Shemyakin, *Phys. Rev. Accel. Beams*, vol. 21, p. 020101, 2018.
- [4] All MEBT magnets were designed and built by the Bhabha Atomic Research Center in Mumbai, India.
- [5] A. Shemyakin, C. Baffes, J.-P. Carneiro, B. Chase, A. Chen, J. Einstein-Curtis, D. Frolov, B. Han-na, V. Lebedev, L. Prost, A. Saini, G. Saewert, D. Sun, D. Sharma, C. Richard, “Design of 162-MHz CW bunch-by-bunch chopper and prototype testing results”, presented at HB’18, Daejeon, Korea June 17- 22, 2018, paper THP1WC03, this conference.
- [6] A. Saini and A. Shemyakin, “Optical design of the PI-Test MEBT beam scraping system”, in *Proc. LINAC’16*, East Lansing, MI, USA, Sep. 2016, paper THPRC026, pp. 827-829.
- [7] A. Saini *et al.*, “Beam Optics Measurements in Medium Energy Beam Transport at PIP-II Injector Test facility”, in *Proc. IPAC’18*, Vancouver, Canada, Apr.-May 2018, paper TUPAF077.
- [8] OptiM, <http://home.fnal.gov/~ostiguy/OptiM/>

- [9] A. Shemyakin *et al.*, “Characterization of the beam from the RFQ of the PIP-II Injector Test”, in *Proc. IPAC'17*, Copenhagen, Denmark, May 2017, paper TUPVA139, pp. 2425-2428.
- [10] TraceWin and TOUTATIS codes,
<http://irfu.cea.fr/Sacm/logiciels/>
- [11] J. Irwin, C.X. Wang, Y.T. Yan, K.L.F. Bane, Y. Cai, F.-J. Decker, M.G. Minty, G.V. Stupakov, F. Zimmermann, “Model-independent analysis with BPM correlation matrices”, in *Proc. EPAC'98*, Stockholm, Sweden, Jun. 1998, paper WEP21G, pp. 1644-1646.
- [12] A. Shemyakin, “Estimation of dilution of a Fast Faraday Cup response due to the finite particles speed”, arXiv:1612.09539, 2016.

60 mA BEAM STUDY IN J-PARC LINAC

Y. Liu, M. Otani, T. Miyao, T. Shibata, KEK/J-PARC, Ibaraki-ken, Japan
 A. Miura, JAEA/J PARC, Ibaraki-ken, Japan

Abstract

Upgrade of Linac peak current from 50mA to 60mA is one of the keys to the next power upgrade in J-PARC. Beam studies with 60 mA were carried out in July and December 2017, for the challenging issues such as investigation of beam property from the ion source, halo behavior throughout the LEBT, RFQ and MEBT1, emittance/Twiss measurement at MEBT1, beam emittance control, etc. Expected/unexpected problems, intermediate results and preparation for the next trials were introduced in this paper.

INTRODUCTION

The Japan Proton Accelerator Research Complex (J-PARC) is a high-intensity proton accelerator facility, which consists of a Linac, a 3 GeV synchrotron (rapid cycling synchrotron, RCS), and a main ring synchrotron (MR).

The J-PARC Linac [1] consists of a 3 MeV RFQ, 50 MeV DTL (Drift Tube Linac), 181/190 MeV SDTL (Separate-type DTL) and 400 MeV ACS (Annular-ring Coupled Structure), as shown in Fig. 1.

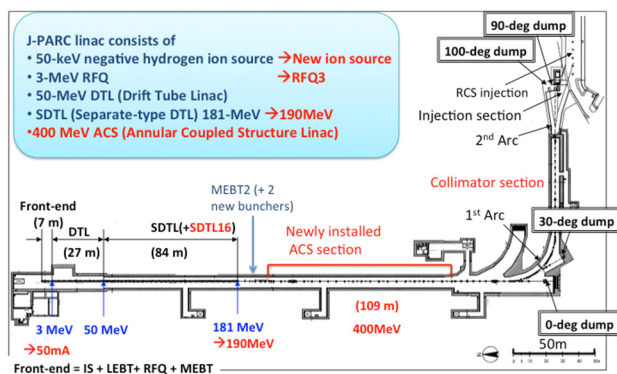


Figure 1: Layout of J-PARC Linac, before and after 2014.

From Oct. 2014, J-PARC Linac started operation at 30mA/400MeV. Maximum peak current of 50 mA became available for beam study, and 1 MW equivalent beam at RCS was demonstrated in Dec. 2014.

From Jan. 2016, J-PARC Linac started 40 mA operation, and ramp-up of the power in neutron target was scheduled toward the target limit.

Next steps will be equivalent 1.2/1.5 MW beam from RCS, which require Linac either/both of peak current upgrade from 50 to 60 mA, or/and extension of beam pulse from 500 to 600 μ s.

First trial of 60 mA was conducted on Jul. 5 2017, and 68 mA of H⁻ beam from RF ion source and 62 mA at

MEBT1 were achieved. Beam transverse property was studied with quadrupole-scan scheme.

Second trial of 60mA was on Dec. 25 - 26 2017. 60 mA beam passed (no acceleration in DTL) through DTL with roughly 100% transmission. 400 MeV 56 mA beam was obtained at the Linac exit.

Third trial is scheduled on Jul. 3 2018. And it is decided peak current of 50mA with be in operation from Oct. 2018.

PREPARATION FOR 60MA STUDY

At J-PARC ion source test-stand > 60 mA stable H⁻ beam were achieved and studied [2]. A typical distribution for 66 mA is shown in Fig. 2, in which it is found that for present ~60 mA beam in J-PARC about 5% of beam could be identified as “halo”. And for the 95% “core” of the beam rms emittance is about 30% higher than that of present 40mA beam in operation. This situation is so different from nominal 40 mA beam that we will confront a “new beam” for the 60 mA trial study.

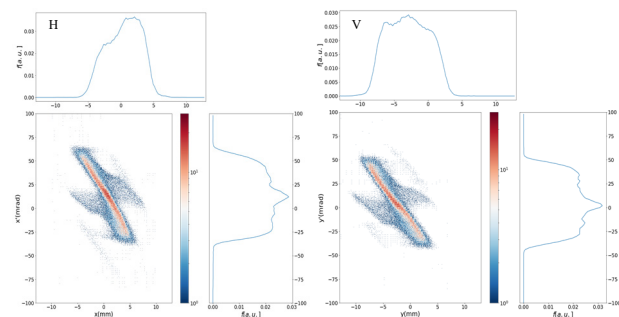


Figure 2: A typical distribution for 66 mA from ion source.

One of the most crucial problem expected is the DTL1 aperture. In the Tōhoku earthquake in 2011, DTL1 suffered deformation and the aperture were significantly reduced. For instance, if the emittance in MEBT1 of 60 mA beam is 30% higher than nominal level, the feasibility of DTL transmission will need a critical decision.

RFQ simulation with the realistic distribution as shown in Fig. 2 was conducted, and the results were shown in Table 1. It is found that instead of emittance growth at the RFQ exit, the halo is scraped in the RFQ at the cost of transmission decrease for ~60 mA beam.

Another countermeasure is the increase of DTL quapoles (DTQ) strength, offering stronger focusing to control the transverse envelop in the DTL. By the way, in this case DTQ might need to be run in pulse mode to reduce the heat load.

Content from this work may be used under the terms of the CC BY 3.0 licence (© 2018). Any distribution of this work must maintain attribution to the author(s), title of the work, publisher, and DOI.

Table 1: RFQ Simulation Results Inputting of Measure Distribution at 66mA as Shown in Fig. 2.

I(mA)	η	Norm. rms (mm*mrad)			Trace3d definition (mm*mrad/deg*keV)			Envelope (mm)		
		ϵ_x	ϵ_y	ϵ_z	ϵ_x	ϵ_y	ϵ_z	rx	ry	
(For ref.)	30	0.95	0.26	0.26	0.32	20.68	20.92	583.35	2.16	1.23
(For ref.)	40	0.94	0.24	0.24	0.33	19.07	19.04	600.90	2.15	1.21
(For ref.)	50	0.93	0.22	0.23	0.34	17.81	18.02	624.95	2.12	1.20
	60	0.91	0.22	0.22	0.34	17.41	17.41	624.50	2.14	1.19
	70	0.90	0.22	0.21	0.34	17.25	17.08	630.30	2.15	1.20

Five sets of lattices were prepared for the study, as shown in Fig. 3.

- A. 40mA lattice for operation (as reference)
- B. 50mA lattice for beam study (as reference)
- C. 40mA lattice scaled for 65 mA, to keep the same envelop and same phase advance. About 5% increase of DTQ strength.
- D. 40mA lattice scaled for 65 mA according to large emittance, with About 5% increase of DTQ strength.
- E. Equipartitioning setting for 65 mA.

C and D need DTQ to run in pulse mode.

When DTQs run in pulse mode, noises will be generated in the nearby slow current transformer (SCT) used for particle counters for the personal protection system (PPS). It is necessary to correct sufficiently to keep the accelerator operating normally.

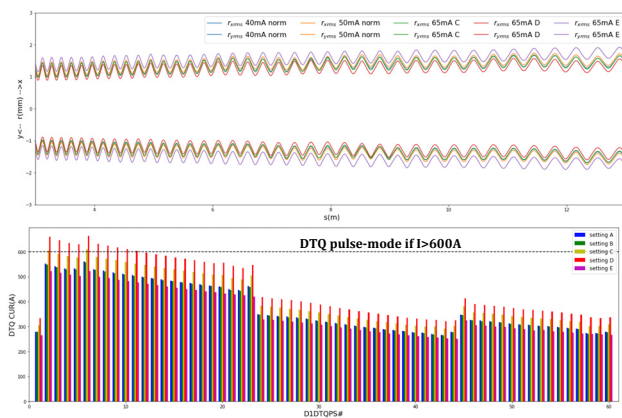


Figure 3: DTL lattice preparation, beam envelope (5*rms) and operational DTQ current.

INTERMEDIATE RESULTS

The first ~60 mA beam was obtained manually from 38 mA to 61 mA at MEBT1 entry. After fine scanning, 62 mA was achieved at MEBT1 as a J-PARC milestone in Jul. 5 2017.

Then the Q scan measurements, as sketched in Fig. 4, for both horizontal and vertical planes were conducted to obtain the emittance and Twiss parameters. For measurements like Q scan beam is stopped at the scraper to protect the downstream parts.

The Q scan results, as shown in Fig. 5 were to be used for evaluation feasibility of the DTL transmission and selection of lattice. Multi-particle simulation with

IMPACT code [3] was applied to fit the Q scan results to find MEBT1 emittance initial Twiss parameters as shown in Fig. 6.

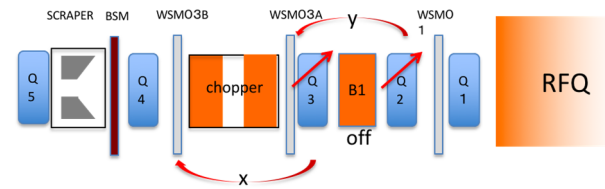


Figure 4: MEBT1 Q scan scheme for transverse measurement.

The Q scan results were consistent with simulation and close to measurements of 50 mA beam. So that both studies could continue with downstream of MEBT1.

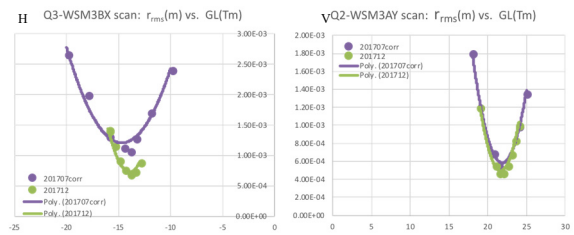


Figure 5: MEBT1 Q scan measurement results.

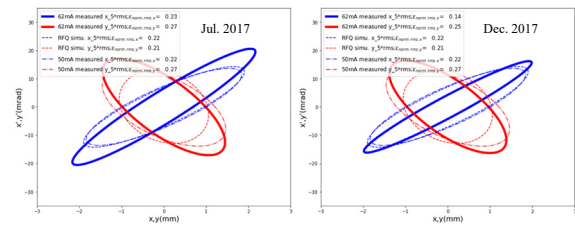


Figure 6: MEBT1 Q scan measurement analysis.

Many lessons were learnt in the first trial study. For safety reason, chopped beam with thinning was used in study, which brought difficulties to the beam monitoring. Moreover, beam chopping rate is dependent on orbit of chopper and scraper, which made much confusions. So it was concluded that unchopped beam will be used for MEBT1 orbit correction in the next study.

The candidate lattice D, with stronger transverse focusing to control envelope in DTL was chosen. And the DTQ pulse operation was successfully applied online for the first time in the study in Jul. 2018. Noises generate by DTQ pulse operation were compensated successfully, for which a few hours of beam time should be scheduled.

Based on the Twiss measurement at MEBT1 and many experiences in the first trial, 3 MeV 60 mA beam was obtained at DTL end, in second trial experiment in Dec. 2017, and 56 mA for the full-accelerated beam, as shown in Fig. 7.

The main beam loss happened in RFQ and MEBT1 scraper. Further analyses are shown in the next section.

Content from this work may be used under the terms of the CC BY 3.0 licence (© 2018). Any distribution of this work must maintain attribution to the author(s), title of the work, publisher, and DOI.

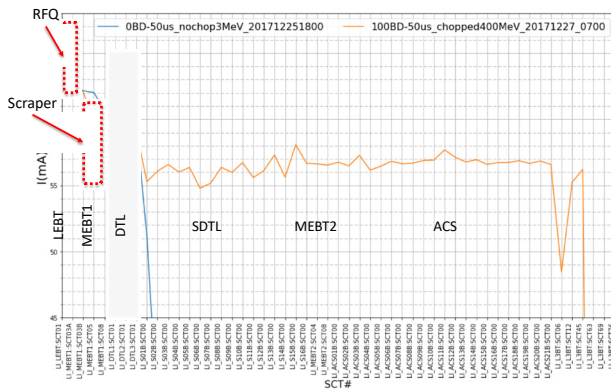


Figure 7: Transmission measured 60 mA trial in December 2018.

STRATEGY FOR NEXT TRIALS

Transmission problem is the homework left by the second trial study, which must be fully understood and solved.

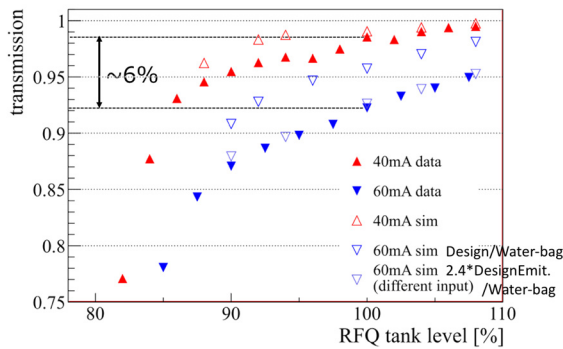


Figure 8: RFQ transmission measurement and simulation.

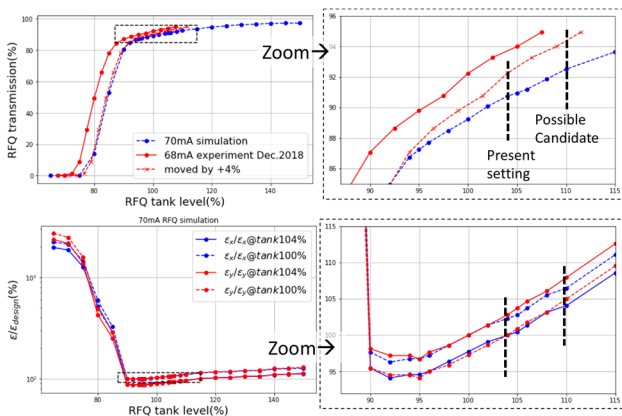


Figure 9: A more realistic RFQ simulation compared with measured transmission.

Measurements and simulation with design input emittance and Twiss with water-bag model for 40 and 60 mA were shown in Fig. 8. Measurements and simulation are quite consistent for 40 mA, but not for 60 mA. For “100%” tank level used in nominal operation, measured transmission for both current differed by 6%. It is implied that for 40 mA the real distribution from ion

source is effectively the same as water-bag model assumed in design. Different behavior of 60 mA is attributed to halo, as shown in Fig. 2. Results from a more realistic simulation inputting this typical distribution is shown in Fig. 9.

Many features could be found in Fig. 9. Transmission curves have 4% gap between measurement and simulation, which could be identified as tank level calibration error. Actually the nominal “100%” tank level is 104% of design. RFQ tank level could be used as a knob for transmission according to the of the present situation of ~60 mA beam, although it is not a normal way. For example, 2% could be gained at the cost of 5% of transverse emittance growth according to 6% increase from present tank level. Of course, it is also clear that ion source should eventually reduce the halo to negligible level.

The other main source of beam loss is near the scrapper, as shown in Fig. 10.

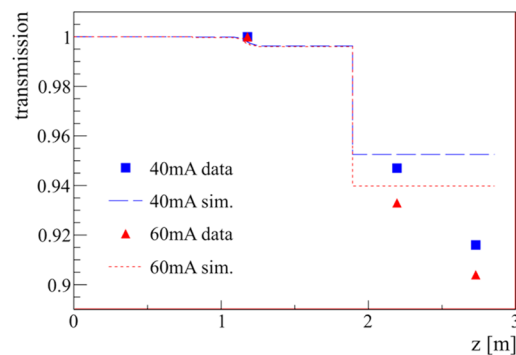


Figure 10: RFQ transmission measurement and simulation.

It is found that simulation and measurement have similar results for both currents. However, for 40 mA operation, chop-extinction has been put to a high priority and ion source output has enough margin, so that this drop is accepted.

The MEBT1 lattice is re-optimized adding condition of horizontal envelop at scrapper, besides envelope at chop and bunchers. A trial optimized scheme is shown in Fig. 11.

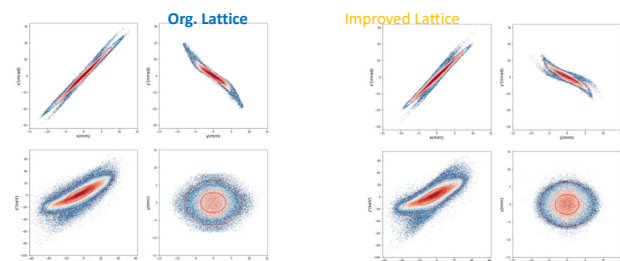


Figure 11: A trial optimization for horizontal envelop at scrapper.

Base on these optimization, scrapper position could be optimized, as shown in Fig. 12.

It could be expected that the scraper position change from present 6.4 mm to 7.5 mm, the transmission will increase by about 2%. MEBT1 lattice optimization might also contribute a few percent to the transmission.

The total transmission will be improved by > 4%, i.e. from present 83% to 87%, with above practical countermeasures. It is proposed for the third trial study ion source will output 72 mA aiming at 62 mA in the Linac.

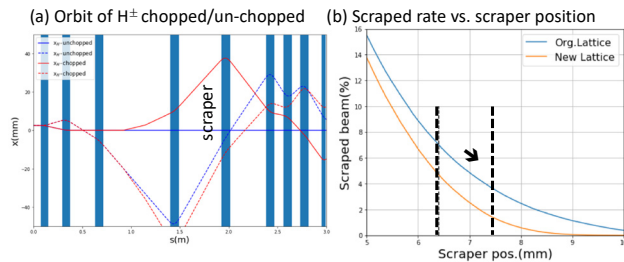


Figure 12: A trial optimization for horizontal envelop at scraper.

CONCLUSION AND OUTLOOK

J-PARC started to prepare for equivalent 1.2/1.5 MW beam from RCS. As a key of next power upgrade, 60 mA studies were conducted and two milestones were

achieved. First 62 mA beam at MEBT1 and transverse measurement were obtained on Jul. 5 2017. First 56 mA beam at J-PARC Linac exit were obtained on Dec. 25~26 2017.

Third trial study of 60mA is planned on Jul. 3 2018.

Key points are transmission in RFQ and MEBT1 scraper. RFQ transmission is about 6% lower than that of nominal 40 mA because of halo from ion source. MEBT1 scraper transmission drop happened both for 40 mA and 60 mA.

Ion source should be eventually improved to minimize halo. However, for the present situation practical countermeasures, such as RFQ tank level, MEBT1 lattice re-optimization and scraper gap adjustment, are proposed to achieve ~60 mA now. All together > 4% increase of transmission is expected, and ion source will provide 72 mA aiming at ~62 mA in Linac.

REFERENCES

- [1] H. Oguri, "Power upgrade of J-PARC linac", in *Proc. 4th Int. Particle Accelerator Conf. (IPAC'13)*, Shanghai, China, May 2013, paper WEYB101, p. 2047.
- [2] A. Ueno *et al.*, *New J. Phys.*, vol. 19, p. 015004, 2017.
- [3] J. Qiang, R. Ryne, S. Habib, and V. Decyk, *J. Comput. Phys.*, vol. 163, p. 434, 2000.

SIMULATION AND MEASUREMENT CAMPAIGNS FOR CHARACTERIZATION AND PERFORMANCE IMPROVEMENT OF THE CERN HEAVY ION LINAC3

G. Bellodi*, S. Benedetti, D. Kuchler, F. Wenander, CERN, Geneva, Switzerland
V. Toivanen, Grand Accélérateur National d'Ions Lourds (GANIL), Caen, France

Abstract

In the framework of the LHC Injector Upgrade programme (LIU), several activities have been carried out to improve the GTS-LHC ion source and Linac3 performance (Linac3 providing the charged heavy ion beams for CERN experiments). A restudy of the beam dynamics and transport through the linac was initiated, through a campaign of systematic machine measurements and parallel beam simulations, generalising techniques developed for beam characterization during Linac4 commissioning. The work here presented will review the most relevant findings and lessons learnt in the process.

INTRODUCTION

The Linac3 linear accelerator is the first element of the CERN heavy ion injector chain, providing highly charged heavy ion beams for the CERN experimental program.

The ion beams are produced with the 14.5 GHz room temperature Electron Cyclotron Resonance (ECR) ion source GTS-LHC, which is based on the Grenoble Test Source (GTS) developed at CEA (France). Lead is the predominant ion beam delivered by the source, though production of argon and xenon beams for fixed target experiments has also been performed.

The GTS-LHC source was installed in 2005, replacing the original ECR4 ion source with the goal to increase the beam current delivered by Linac3. However, the projected gain was not reached due to a lower than expected transmission through the linac.

Linac3 itself has been operational since 1993, accelerating heavy ions from 2.5 keV/u to 4.2 MeV/u for injection and accumulation into the Low Energy Ion Ring (LEIR). Charge state selection is first carried out on the beam extracted from the source via a 135° spectrometer bend. Acceleration is then done in two stages: first a 101.28 MHz Radio-Frequency Quadrupole (RFQ) increases the beam energy to 250 keV/u; then a system of 3 Interdigital-H tanks (the first one at 101.28 MHz, the other two at 202.56 MHz) takes the beam to 4.2 MeV/u. The beam is then stripped in passing through an amorphous carbon foil, and a new charge state is selected for injection in LEIR. Here the beam is accumulated and cooled before being transferred to the Proton Synchrotron (PS), the Super Proton Synchrotron (SPS), and ultimately the Large Hadron Collider (LHC).

Typical currents delivered for Pb⁵⁴⁺ ion beams at the end of Linac3 before 2015 were approximately 20-25 μAe, with a stripping efficiency from Pb²⁹⁺ to Pb⁵⁴⁺ of 15% and

a cumulative acceleration efficiency through RFQ and IH of 55-60%. This corresponds to a Pb²⁹⁺ current at the source of ~150 μA.

An in-depth restudy of the Linac3 beam extraction and transport was initiated a few years ago in the context of the LHC Injector Upgrade (LIU) programme, with the aim of improving the performance of the accelerator chain for future high luminosity operation of the LHC. The target parameter of 8x10⁸ Pb⁵⁴⁺ ions/bunch extracted intensity from LEIR was comfortably exceeded in 2016 operation thanks to the combined improved performance of both Linac3 and LEIR (+40%) and mitigation of the main intensity limitations.

The Linac3 performance upgrade campaign was articulated around a comprehensive restudy of the beam formation from the GTS-LHC ion source and of its transport through the Low Energy Beam Transport (ITL) section, RFQ and IH linac. Previous simulation studies had been carried out either with TRACE2D envelope tracking or with multi-particle tracking with PATH using ideal input beam distributions. Focus was only recently placed on a more rigorous modelling of the beam extraction from the source, with the aim of providing more realistic input beam conditions for tracking studies. A systematic campaign of machine measurements was also launched to provide input and cross-check for the simulation results. In this paper we review the current understanding of beam dynamics in Linac3 and the limitations still affecting the present modelling.

SOURCE EXTRACTION SIMULATIONS

The GTS-LHC ion beam extraction has been simulated with the ion optical code IBSimu [1], with 3D magnetic field maps and electrode geometry. The afterglow discharge is modelled by assuming an increased plasma potential of 200V and low 10eV temperature cold electron population. The initial ion species distribution was defined based on the measured Charge State Distributions (CSD). The simulation assumes full space charge in the extraction region, due to the presence of strong electric fields preventing the accumulation of low-energy electrons and consequent compensation mechanisms.

Extraction simulations were carried out for all operational beams: lead, argon and xenon [2]. In the case of Pb beams the strong charge-over-mass dependent focusing effect causes the formation of a beam waist inside the grounded electrode and envelope separation of the different ion species. For Ar and Xe this effect is mitigated and the transverse distributions are more uniform (see Fig. 1). In all cases, due to the lack of additional focusing elements

* Giulia.Bellodi@cern.ch

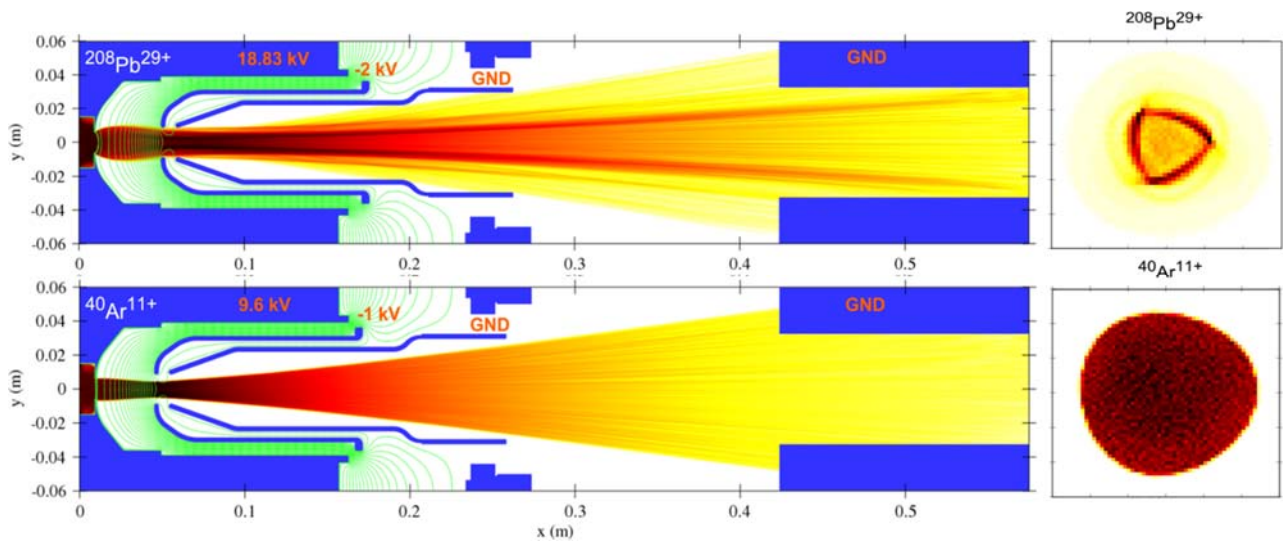


Figure 1: Beam extraction simulations with IBSimu: trajectory densities (left) and transverse beam profile distributions (right), taken at the axial location $x=0.423$ m.

in the extraction region, the beams are highly divergent, causing significant beam collimation on the walls of the extraction pumping chamber and downstream solenoid beam pipe. This was confirmed by a visual inspection of the GTS-LHC extraction system, showing clear beam-induced markings at the location predicted by the simulations (see Fig. 2).

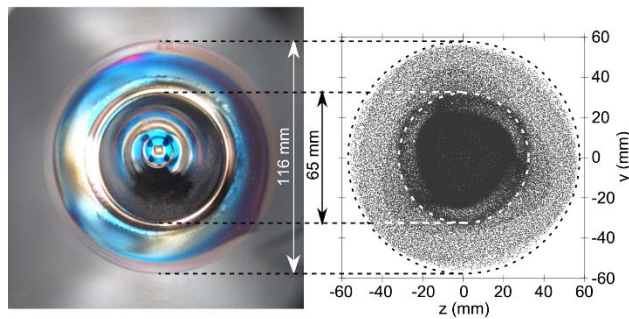


Figure 2: Observed beam induced markings from beam scraping (left) compared to the transverse distribution at the same location obtained with IBSimu (right).

A redesign of the beam extraction region was prompted by these studies, with the aim of reducing the losses due to beam scraping and improve transmission from the source. Two main modifications were put in place: 1) the aperture restriction was mitigated by increasing the beam pipe diameter at extraction and through the first solenoid from 65 to 100 mm; 2) a bipolar Einzel lens was installed to provide additional beam focusing and matching. The first action alone yielded a gain of +20% in the transmitted beam current from the source to the exit of the spectrometer bend. The second modification, on the other hand, did not prove to be beneficial in the end, and the lens was subsequently removed.

The IBSimu extraction results were used to define the initial beam distribution for input to beam dynamics studies in Linac3 with the 3D multiparticle tracking code PATH [3]. Machine operational settings and beam aperture model were used in the simulations to allow direct comparison with beam measurements. All the measurements and simulations reported in the following refer to the 2017 operation with xenon beams at Linac3.

EMITTANCE MEASUREMENTS

A layout of Linac3 is presented in Fig. 3. No beam diagnostics is available between the source and the spectrometer magnets. The first instruments are located after the slit (a Faraday cup) and quadrupole triplet (profile harp) downstream of the bend, before entering the RFQ. As will be shown later, this is at present one of the main limitations to any further progress in the understanding of the beam dynamics at Linac3.

The available diagnostics consists in several Beam Current Transformers (BCT) and Faraday cups for beam intensity measurements and harps (SEM grids) for transverse profile measurements. These are placed at several locations along the machine: 1) at the end of the ITL (LEBT) line, before entering the RFQ, 2) at the RFQ output, in the MEBT; 3) at the exit of the IH tanks, after the stripper foil and 4) finally in the ITF filter line selecting the charge state for injection in LEIR.

A pepper-pot device is installed after the spectrometer bend just downstream of the slit selecting the nominal charge state. After long and unsuccessful commissioning efforts, however, it was concluded that the beam characteristics at the installation location are not adapted to detection with this device. If measurements in the horizontal plane were indeed possible, the large beam divergence causes a superposition of beamlets in the vertical plane and

Content from this work may be used under the terms of the CC BY 3.0 licence (© 2018). Any distribution of this work must maintain attribution to the author(s), title of the work, publisher, and DOI.

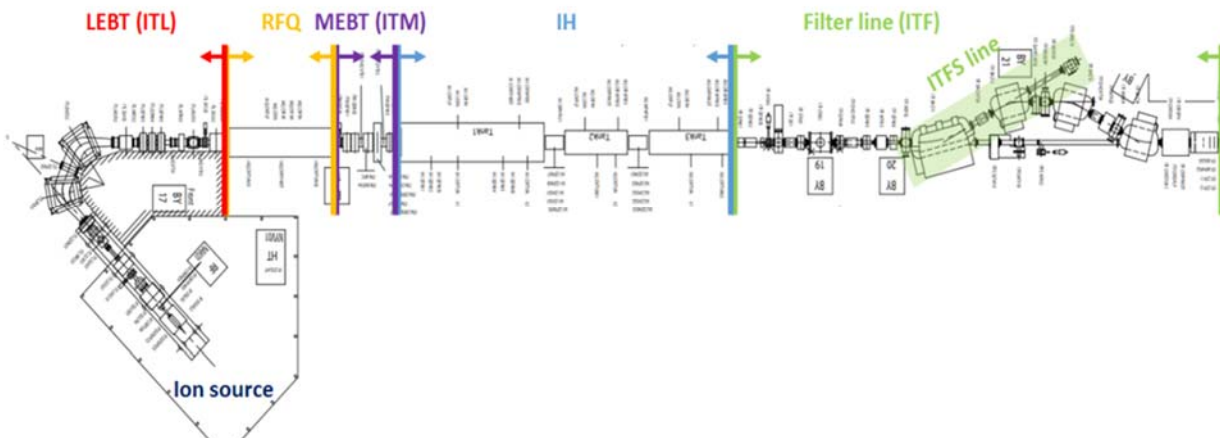


Figure 3: Linac3 layout.

makes virtually impossible the correct association between beamlets and pepper pot mask holes where they originate, which is at the basis of the data analysis process.

Beam transverse emittance has been measured indirectly from profile measurements via a quadrupole scan technique, using two independent methods originally developed during Linac4 commissioning [4]. The “forward method” technique builds up on the classical analytic calculations using transfer matrices: it consists in iteratively varying the Twiss parameters of the beam at the reconstruction point, tracking it to the measurement location taking into account space charge effects and comparing the measured and simulated RMS beam sizes. The method is relatively simple, since it deals with RMS beam sizes calculated from the measured profiles. This implies however a loss of information on the beam distribution, as only a

projection of the phase space is measured. A more sophisticated method is the phase space tomography, which is based on linear mapping of the measured beam profiles onto the initial phase space to estimate the particle density distribution. The projections of the reconstructed phase space are then compared to measured data and the initial distribution is modified iteratively until agreement is reached with the measured profiles.

The results of several emittance measurements taken during the year at different machine locations are listed in Table 1: values show a good reproducibility over time and agreement between analytical and tomographic technique of reconstruction, within a 15% range. The only exception is given by the vertical emittance measurements in the MEBT section. Here the insufficient resolution of the profile harp had a great impact on the quality of the measurements and yielded overestimated emittance values. At the

Table 1: Reconstructed Normalized RMS Emittance Values for Xenon Beams in the ITL, ITM and ITF Lines

		ϵ_x π mm mrad	ϵ_y π mm mrad	α_x	α_y	β_x m/rad	β_y m/rad	
ITL	<i>Analytical reconstruction</i>	0.13	0.15	-3.90	-1.59	1.32	0.57	
		0.14	0.18	-3.49	-2.50	1.15	0.72	
		0.13	0.18	-3.37	-2.77	1.08	0.83	
		0.11	0.18	-3.39	-2.67	0.96	1.11	
	<i>Tomographic reconstruction</i>	0.11	0.14	-4.68	-1.73	1.65	0.97	
		0.11	0.15	-3.98	-2.57	1.37	0.88	
0.12		0.16	-4.02	-2.54	1.41	0.89		
ITM	<i>Analytical reconstruction</i>	0.08	0.21	0.05	3.63	0.06	0.79	
		0.07	0.20	0.18	4.87	0.10	1.07	
	<i>Tomographic reconstruction</i>	0.08	0.29	0.07	2.38	0.06	0.63	
		0.08	0.36	0.25	3.04	0.09	0.80	
	ITF	<i>Analytical reconstruction</i>	0.13	0.16	-2.76	-1.75	6.17	1.56
			0.12	0.13	-1.82	-1.25	4.87	1.07
<i>Tomographic reconstruction</i>		0.14	0.17	-2.38	-1.81	5.17	1.58	
		0.12	0.15	-2.09	-1.60	5.04	1.30	

RFQ exit the beam should be approximately anti-symmetric, hence transverse emittance values should be similar in both planes.

SIMULATIONS

These emittance values and other beam measurements taken at Linac3 were used both as input and feedback for simulation studies, in an effort to validate our modelling of the machine. In particular, the particle distribution reconstructed tomographically from beam profiles in the LEBT was compared to the result of tracking the input beam obtained by IBSimu at source extraction all through the spectrometer line (consisting of one focusing solenoid, a quadrupole and two bending magnets). As shown in Fig. 4, agreement is fairly good in the horizontal plane, but not in the vertical one. Transmission values are also more pessimistic in the IBSimu-simulated case than in reality.

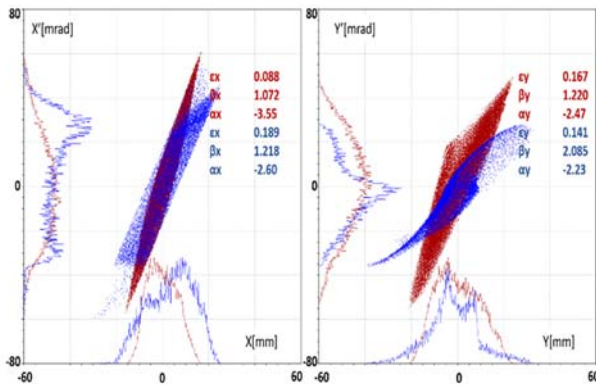


Figure 4: Comparison between beam phase space tomographic reconstruction from measurements (red dots) and simulation results (blue dots) in the ITL line [5].

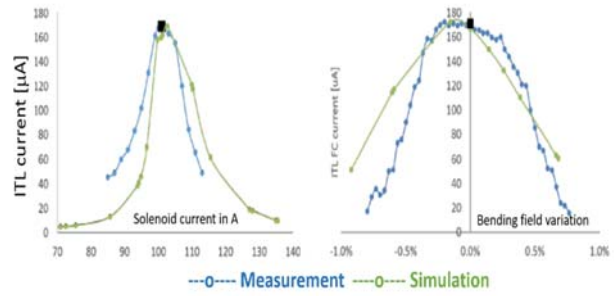


Figure 5: Comparison between measurements and simulation results for the transmitted current in the ITL Faraday cup when scanning: the solenoid current downstream of source extraction (left) and the spectrometer magnet current (right). The black marker indicates the operational point [5].

The absence of diagnostics in the spectrometer line and the difficulty in making diagnostics that distinguish between the many species in this zone makes it impossible to validate the assumptions taken in the simulation of the beam extraction from the source. A scan of beam intensity as a function of magnetic strength values for either the solenoid or the dipoles (Fig. 5) could only give agreement between measurements and simulations after some parameter rescaling, thus pointing at the fact that some of the values assumed in our modelling are not correctly known.

Simulated transmission values through the RFQ are also considerably more pessimistic than in reality. For all these reasons and difficulties it was decided to use as input for tracking studies the beam distribution reconstructed tomographically after the spectrometer bend, and focus on the beam dynamics downstream of this location. The beam was transported through the RFQ and IH cavities, and the

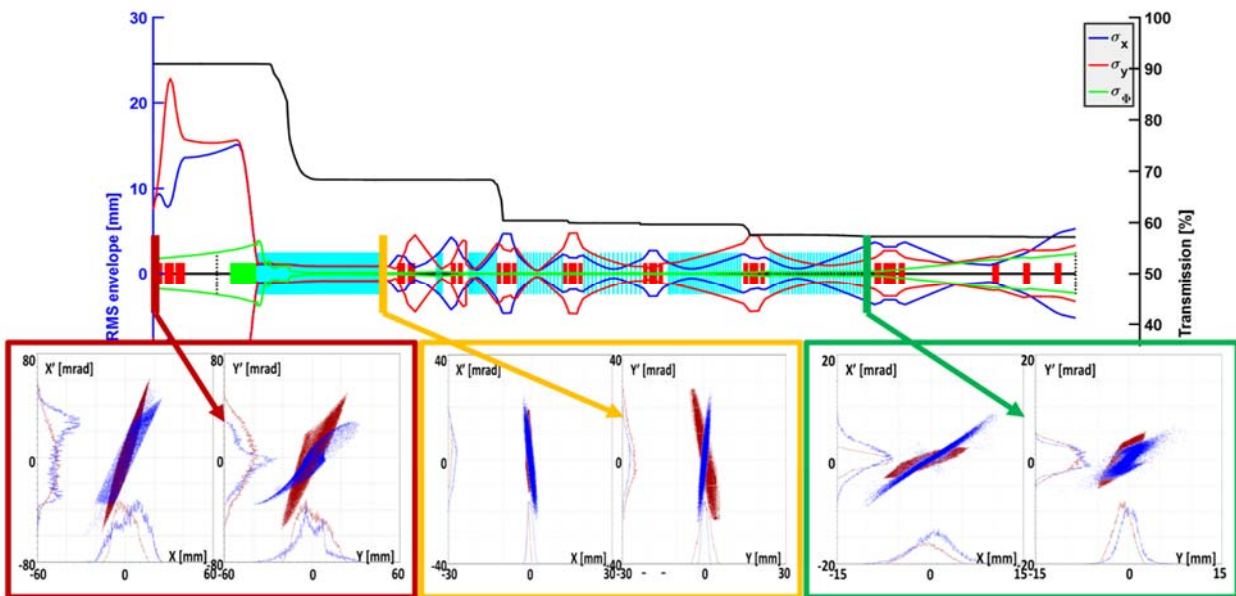


Figure 6: Summary of beam dynamics simulations: RMS envelopes, transmission and simulated vs measured beam distributions at selected locations along Linac3 [5].

Content from this work may be used under the terms of the CC BY 3.0 licence (© 2018). Any distribution of this work must maintain attribution to the author(s), title of the work, publisher, and DOI.

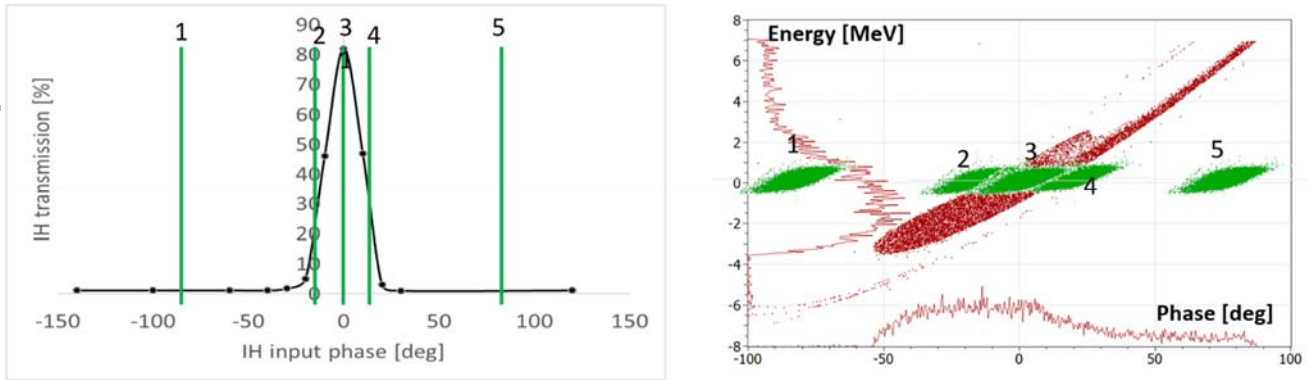


Figure 7: Measured transmission through the IH as a function of the input RF phase (left). Simulated IH longitudinal acceptance (red) in comparison with the longitudinal IH input beam for several input RF phases (in green)[6].

simulation results were again validated through comparison with measurements. As shown in Fig. 6, the operational beam current transmission through the RFQ was confirmed in simulations to be around 70%. The beam distribution at the exit of the RFQ (yellow box in the figure) was found to be in very good agreement in the horizontal plane with the corresponding tomographic reconstruction. The mismatch in the vertical plane is most likely due to an insufficient resolution of the profile harp, affecting the precision of the beam measurements, possibly combined with an uncertainty in the calibration curves of the quadrupoles scanned due to magnetic cross-talk. The short distance between the diagnostics device and the quadrupoles also causes larger fluctuations in the results.

The description of the IH cavities and the KONUS beam dynamics simulation results were also validated by beam profiles and transmission measurements. The reconstructed phase space at the IH output is quite similar to the simulated one (see Fig. 6 in the green box). The dependence of beam transmission on several machine parameters (tank amplitude and phase setpoints, IH quadrupole gradients etc) was measured through variable scans and well reproduced in simulations. The overall ~80% transmission through the IH was also confirmed by beam tracking.

Comparing this value with transport efficiency at lower energy showed that the RFQ remains the main bottleneck for beam transmission. This prompted research into a possible re-design of the cavity, with the aim of increasing its transverse acceptance while maintaining cavity length and field and constant or lower output longitudinal emittance. The latter constraint comes from the necessity to fit the beam in the small longitudinal acceptance of the IH, thus avoiding to just shift the bottleneck problem downstream. This acceptance was measured by detecting the change in transmission through the IH while scanning its input RF phase. A sharp drop is measured as soon as the input RF phase deviates from the nominal value (Fig. 7 left). This is confirmed by beam simulations, as the IH input beam phase space in the longitudinal plane is tightly contained in the IH acceptance (Fig. 7 to the right). A redesign solution was eventually found on paper: a new rods design fitting in the same footprint that could increase the transmission through the RFQ by 20% [6].

SUMMARY AND LESSONS LEARNT

A thorough restudy of the beam dynamics and transport through Linac3 was carried out, through a campaign of systematic machine measurements and parallel beam simulations.

For the first time beam production from the source was the object of detailed studies with the help of the IBSimu ion optical code. The absence of diagnostics immediately downstream of beam extraction severely affected the capacity of achieving a realistic initial beam distribution. Some input assumptions of the simulations would still need further tuning and optimisation before reaching full validation. An important result of these studies was however to confirm the performance limitation induced by beam scraping at extraction from the source. Reduction of these losses by an increase of the beampipe aperture diameter could gain a 20% improvement in transmitted beam intensity.

Emittance measurement techniques, which were initially developed for beam characterization during Linac4 commissioning, were successfully applied to Linac3. They also allowed the reconstruction of the beam phase space from profile measurements, and the distributions found could be used as input for tracking studies and cross-check of simulations. End-to-end beam tracking from the LEBT to the output of the IH gave results consistent with the observed beam transmission and profiles, thus providing a full validation of the models and machine description used. This allowed the possibility to conduct further studies and improve the understanding of beam dynamics in Linac3. A first conclusion reached was the identification of the RFQ as main bottleneck for beam transmission, due to its limited transverse acceptance compared to the emittance of the beam extracted from the GTS-LHC ion source. A dedicated study showed a possible mitigation could be put in place by a redesign of the RFQ geometry, with a 20% scope of increased beam transmission downstream through the IH.

REFERENCES

- [1] T. Kalvas, O. Tarvainen, T. Ropponen, O. Steczkiewicz, J. Arje, H. Clark, *Rev. Sci. Instrum.*, vol 81, no. 02B703, 2010.
- [2] V. Toivanen *et al.*, “Simulation of the CERN GTS-LHC ECR ion source extraction system with lead and argon ion beams”, CERN, Geneva, Switzerland, Rep. CERN-ACC-2014-0205, 2014.
- [3] A. Perrin and J. F. Amand, “Travel v4.06 user manual”, CERN, Geneva, Switzerland, 2003.
- [4] V.A.Dimov *et al.*, “Emittance reconstruction techniques in presence of space charge applied during the Lina4 beam commissioning”, in *Proc. HB'16*, Malmö, Sweden, Jul. 2016, paper WEPM1Y01, pp.433-438.
- [5] S. Benedetti *et al.*, “The 2017 Xe run at CERN Linac3: measurements and beam dynamics simulations”, CERN, Geneva, Switzerland, Rep. CERN-ACC-NOTE-2018-0043, to be published.
- [6] S. Benedetti *et al.*, “Redesign of CERN LINAC3 RFQ for Lead 29+”, CERN, Geneva, Switzerland, Rep. CERN-ACC-NOTE-2018-0044, to be published.

Content from this work may be used under the terms of the CC BY 3.0 licence (© 2018). Any distribution of this work must maintain attribution to the author(s), title of the work, publisher, and DOI.

EMITTANCE GROWTH AND BEAM LOSSES IN LANSCE LINEAR ACCELERATOR*

Y. K. Batygin[#], R. W. Garnett, L. J. Rybarczyk, LANL, Los Alamos, NM 87545, USA

Abstract

The LANSCE Accelerator facility currently utilizes four 800-MeV H⁻ beams and one 100-MeV proton beam. Multi-beam operation requires careful control of the accelerator tune to minimize beam losses. The most powerful 80-kW H⁻ beam is accumulated in the Proton Storage Ring and is extracted to the Lujan Neutron Scattering Center facility for production of moderated neutrons with meV- keV energy. Another H⁻ beam is delivered to the Weapon Neutron Research facility to create un-moderated neutrons in the keV - MeV energy range. The third H⁻ beam is shared between the Proton Radiography Facility and the Ultra-Cold Neutron facility. The 23-kW proton beam is used for isotope production in the fields of medicine, nuclear physics, national security, environmental science and industry. Minimization of beam losses in the linac is achieved by careful tuning of the beam in each section of the accelerator facility, imposing limitations on amplitudes and phases of RF systems, control of H⁻ beam stripping, and optimization of ion source operation. This paper summarizes experimental results obtained during accelerator tuning and identifies various sources of emittance growth and beam losses.

LANSCE ACCELERATOR FACILITY

The LANSCE Accelerator facility has been in operation for more than 40 years. Currently it delivers 800-MeV H⁻ beams to four experimental areas and one 100-MeV proton beam (see Fig. 1 and Table 1). The accelerator facility is equipped with two independent injectors for H⁺ and H⁻ beams, merging at the entrance of a 201.25-MHz Drift Tube Linac (DTL). The DTL accelerates the two beams to 100 MeV. After the DTL, the Transition Region (TR) beamline directs the 100-MeV proton beam to the Isotope Production Facility (IPF), while the H⁻ beam is accelerated up to the final energy of 800 MeV in an 805-MHz Coupled-Cavity Linac (CCL). The H⁻ beams, created by different time structures of a low-energy chopper, are distributed in the Switch Yard (SY) to four experimental areas. Minimization of beam losses is one of the main criteria of successful operation of the accelerator facility.

BEAM LOSS IN ACCELERATOR

Beam losses in the LANSCE accelerator are mostly determined by the two most powerful beams: the 80-kW H⁻ beam injected into Proton Storage Ring, and the 23-kW H⁺ beam, which is used at the Isotope Production Facility. The main sources of beam losses in the linac are mismatch of the beam with the accelerator structure,

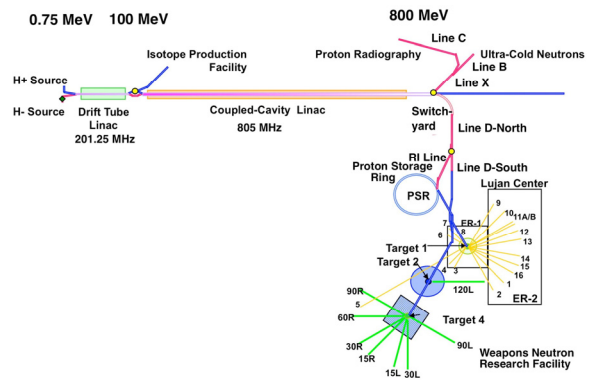




Figure 2: Beam loss along linear accelerator.

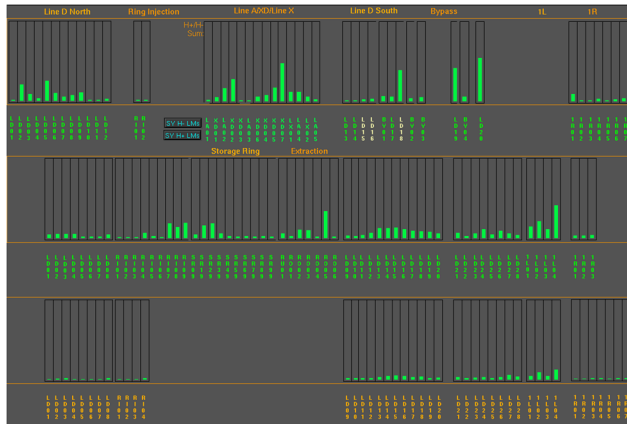


Figure 3: Beam losses in high-energy beam transport.

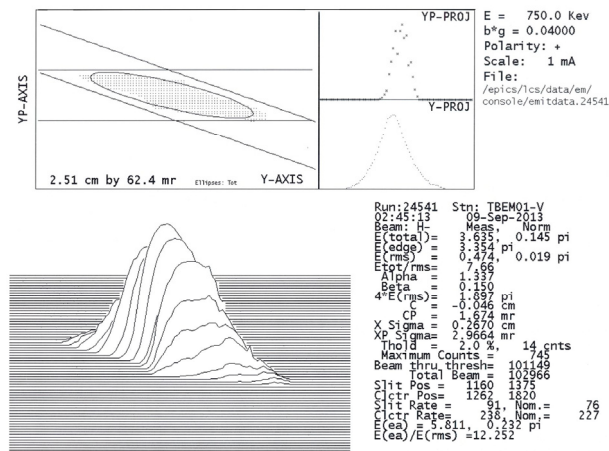


Figure 4: Emittance measurement of H⁻ beam at the beginning of Low Energy Beam Transport.

The third type of beam loss monitor are Hardware Transmission Monitors (HWTM). The HWTM system measures the beam current losses between current monitors and can limit beam current to a value at one current monitor.

Distribution of beam losses along the accelerator facility are presented in Figs. 2, 3. Typical averaged beam losses along the linear accelerator are 2×10^{-3} which corresponds to loss rate of $3 \times 10^{-6} \text{ m}^{-1}$, or 0.2 W/m. In the high-energy beamlines (HEBT), the total beam losses are 4×10^{-3} which corresponds to a loss rate of $2 \times 10^{-5} \text{ m}^{-1}$, or 1.6 W/m. Higher beam losses in the HEBT are explained by smaller transverse acceptance and the dispersive nature of the beamlines, which generates additional losses due to

longitudinal (energy) tails in the beam. Typical average losses in Proton Storage Ring (PSR) are at the level of 0.3%.

BEAM EMITTANCE MEASUREMENTS

Beam emittance is measured using the slit-collector method for beams with energies not exceeding 100 MeV. There are seven beam emittance measurement stations in the low-energy beam transports, and three stations after the DTL. A threshold of 2% out of the peak value of the beam distribution is added to remove experimental noise (see Fig. 4). After measurement, both rms emittance and total emittance of the beam are calculated. For energies higher than 100 MeV, beam emittance is measured using a combination of wire scanners, while emittance is recalculated using a matrix method. Evolution of transverse beam emittance along accelerator is presented in Tables 2, 3.

Determination of longitudinal beam emittance is performed through measurement of the longitudinal beam size after Tank 3 in the DTL at a beam energy of 70 MeV [1], and measurement of momentum spread of the 800-MeV beam in a high-dispersive point of Line D. The typical value of the phase length of the bunch at 70 MeV is 7° , which corresponds to a half-bunch length of 5 mm. The typical value of the beam size at a high-dispersive point of the high-energy beam transport is 5.8 mm and is mostly determined by the beam momentum spread of $\Delta p / p \approx 10^{-3}$.

Due to adiabatic damping of phase oscillations in a linear accelerator, the momentum spread is changing as

$$\frac{\Delta p}{p} \sim \frac{1}{\beta^{5/4} \gamma^{1/4}} \quad (1)$$

A combination of the beam size and momentum spread gives an estimate of the longitudinal normalized beam emittance at 70 MeV as $4\epsilon_{rms_long} \approx 0.7 \pi\text{-cm-mrad}$.

ION SOURCES

Proton Ion Source

Optimal operation of the accelerator facility critically depends on the emittance and brightness of the beam extracted from the ion sources and beam formation in the low-energy beam transport (LEBT). The proton ion source is a duoplasmatron source with a Pierce extraction geometry. Presently the source delivers a proton beam with a current of 5-7 mA at 100 Hz x 625 μsec pulse length. An intrinsic limitation in particle-source beam-emittance comes from the finite value of the plasma temperature in the ion source. The normalized emittance of the beam, extracted from a particle source with aperture radius R and plasma ion-temperature T , is estimated as:

$$\epsilon = 2R \sqrt{\frac{kT}{mc^2}} \quad (2)$$

Besides the emittance determined by Eq. (2), additional sources contributing to beam emittance are irregularities in the plasma meniscus extraction surface, aberrations due to ion-source extraction optics, non-linearity of the electric field created by the beam space charge, beam fluctuations due to ion-source instability or power regulation. A typical value of the normalized rms proton beam emittance is $\varepsilon_{rms} = 0.002 - 0.003 \pi \text{ cm-mrad}$.

H- Ion Source

The H⁻ beam injector includes a cesiated, multicusp-field, surface-production ion source. Negative ions are created as a result of charge exchange at a molybdenum surface converter, in the presence of a thin layer of cesium. The generated H⁻ particles are then accelerated towards the extraction aperture. Correspondingly, the normalized beam emittance of this type of source is estimated as the phase space area comprised by a converter with radius R_{conv} , extractor aperture with radius R_{ext} , and distance L_{conv} between them (admittance of source) [2]

$$\varepsilon = \frac{4}{\pi} \sqrt{\frac{2eU_{conv}}{mc^2}} \frac{R_{conv}R_{ext}}{L_{conv}}, \quad (3)$$

where U_{conv} is the voltage between the converter and the source body. In the LANSCE H⁻ ion source, $R_{conv} = 1.9 \text{ cm}$, $R_{ext} = 0.5 \text{ cm}$, $L_{conv} = 12.62 \text{ cm}$, $U_{conv} = 300 \text{ V}$, which yields a normalized beam emittance of $\varepsilon = 0.076 \pi \text{ cm mrad}$. This quantity is close to the experimentally observed value of four-rms normalized beam emittance $4\varepsilon_{rms} = 0.072 \pi \text{ cm-mrad}$.

LOW ENERGY BEAM TRANSPORTS

Both beams are transported in 750-keV beamlines and merged before injection into the Drift Tube Linac. Each beamline is 11 m long containing 18 quadrupoles. After merging, both H⁺ and H⁻ beams are transported in a common 2.5-m-long beamline containing 4 quads for matching into the DTL. Both beams experience emittance growth in the LEBT due to RF bunching. The relative increase of proton beam emittance is around 1.9, and that of the H⁻ ion beam is 1.2. Space charge induced emittance growth in the transport beamlines is insignificant. Additionally, the 36-ns H⁻ WNR beam experiences 30% emittance growth due to chopping.

The proton beam dynamics is sensitive to beam alignment in the LEBT. Matching of the proton beam with the transport lattice requires beam waists at the entrance of the RF cavities and in the middle of the beam deflector. Typical relative beam emittance growth in the beamline was observed to be approximately a factor of 3. A beam based steering procedure was implemented to minimize emittance growth in the LEBT [3]. It included the determination of beam offset and beam angle upon entering a group of quadrupoles, which requires a subsequent

correction of the beam centroid trajectory to minimize beam offset. Application of this procedure resulted in a reduction of up to a factor of 2 in emittance growth.

Dynamics of the H⁻ beam in the LEBT is significantly affected by space charge neutralization. Typical spectra of residual gas in the 750-keV H⁻ transport channel indicate that the main components are H₂ (48%), H₂O (38%) and N₂ (9%), while the residual gas pressure is 10^{-6} Torr. Measurements show that space charge neutralization of the H⁻ beam along the LEBT varies between 50%-100%. Knowledge of the effective beam current under space charge neutralization allows precise beam tuning in the structure. Neutralization of H⁺ beam does not exceed 20%. Typical beam losses in each beamline are within 0.5 mA peak current.

DRIFT TUBE LINAC

The Drift Tube Linac consists of 4 tanks with output energies of 5 MeV, 41 MeV, 73 MeV, and 100 MeV, respectively. Originally designed for operation with a synchronous phase of -26° , the linac was historically retuned for -32° , -23° , -22° , -32° tank synchronous phases with field amplitudes of 98%, 96%, 94%, and 98% of nominal values to minimize beam spill. Both H⁻ and proton beams are captured with efficiencies of 75%-80% into the Drift Tube Linac, so initially 20%-25% of the beam is lost in the beginning of Tank 1. Subsequent beam losses of 0.1%-1% in the DTL result due to additional uncaptured particles and by expansion of the phase-space volume occupied by the beam (emittance growth). Figure 5 and Tables 2, 3 illustrate the increase of beam emittance of H⁻ and H⁺ beams in the DTL. Rapid emittance growth of the total beam is observed while the beam core is changing at a smaller rate. The H⁻ beam emittance is observed to increase by a factor of 1.8-2.3, while the H⁺ beam emittance increases a factor of 5-6. These values agree with earlier simulation results [4]. While beam distributions and beam currents are significantly different at the entrance of DTL for the two beam species, the distributions of all beams at the end of DTL tend to be the same. It reflects the fact that during acceleration the beam tends to occupy the full available phase space acceptance.

The dominant cause of beam emittance growth at low energy is transverse-longitudinal coupling in the RF cavity fields. Estimated beam emittance growth due to this process is [5]

$$\frac{\varepsilon}{\varepsilon_o} = 1 + \frac{\Phi}{\tan \varphi_s} \left(\frac{\Omega^2}{4\Omega_{rs}^2 - \Omega^2} \right), \quad (4)$$

where Φ is the phase length of the bunch, φ_s is the synchronous phase, Ω is the longitudinal oscillation frequency, and Ω_{rs} is the transverse oscillation frequency in presence of RF field. In the 201.25-MHz DTL $\Phi \sim 1.57 \text{ rad}$, $\varphi_s \sim 30^\circ$, $\Omega/\Omega_{rs} \sim 0.75$. The expected emittance growth from Eq. (4) is $\varepsilon/\varepsilon_o = 1.62$.

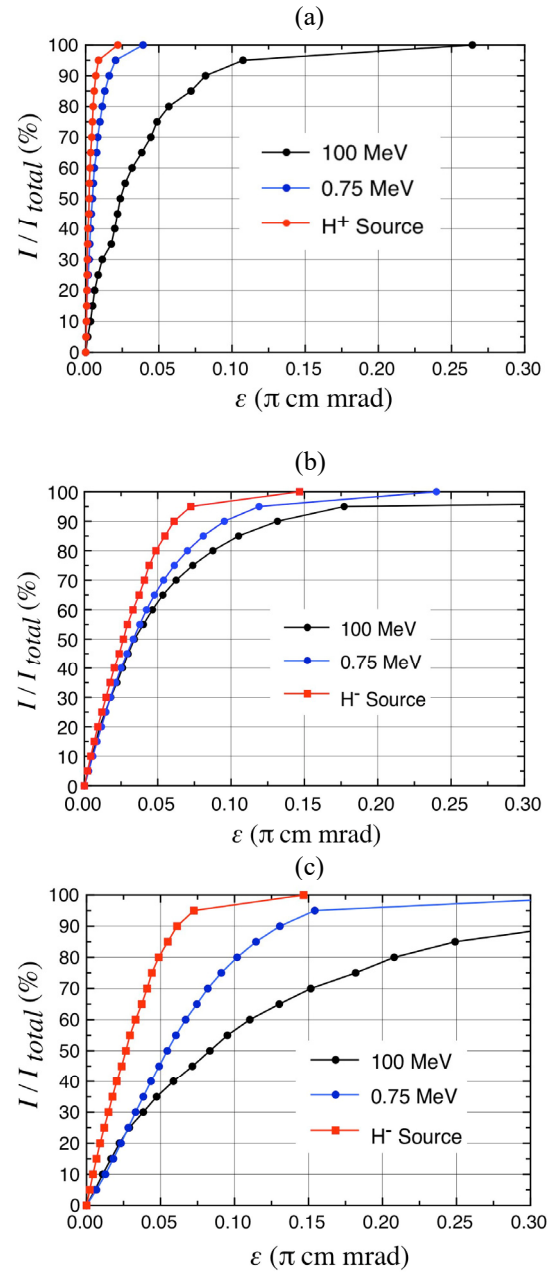


Figure 5: The distribution of the current in the phase space of the different beams in sources, LEBT (0.75 MeV) and after DTL (100 MeV): (a) H⁺ beam, (b) H⁻ Lujan/pRad/UCN beam, (c) H⁻ WNR beam.

An important parameter, which characterizes the beam distribution is the ratio of total emittance to rms emittance. From Table 2 it follows, that for ion sources, this ratio is close to $\epsilon_{total} / \epsilon_{rms} \approx 6$, while at the end of the DTL this ratio is around $\epsilon_{total} / \epsilon_{rms} \approx 7...9$. It indicates that the beam distribution after the DTL becomes more diffusive with longer tails.

Table 2. Normalized Beam Emittance in LEBT and DTL (π cm mrad)

	H ⁻ (Lujan / pRad / UCN)			H ⁻ (WNR)			H ⁺ (IPF)		
	ϵ_{rms}	ϵ_{total}	$\frac{\epsilon_{total}}{\epsilon_{rms}}$	ϵ_{rms}	ϵ_{total}	$\frac{\epsilon_{total}}{\epsilon_{rms}}$	ϵ_{rms}	ϵ_{total}	$\frac{\epsilon_{total}}{\epsilon_{rms}}$
Ion Source	0.018	0.11	6.10	0.018	0.11	6.10	0.002	0.01	6.02
0.75 MeV	0.022	0.14	6.42	0.034	0.219	6.47	0.004	0.027	7.18
100 MeV	0.041	0.34	8.34	0.058	0.415	7.19	0.02	0.17	8.76

Table 3: Beam Emittance Growth in DTL

H ⁻ (Lujan / pRad / UCN)		H ⁻ (WNR)		H ⁺ (IPF)	
ϵ_{rms} (100)	ϵ_{tot} (100)	ϵ_{rms} (100)	ϵ_{tot} (100)	ϵ_{rms} (100)	ϵ_{tot} (100)
ϵ_{rms} (0.75)	ϵ_{tot} (0.75)	ϵ_{rms} (0.75)	ϵ_{tot} (0.75)	ϵ_{rms} (0.75)	ϵ_{tot} (0.75)
1.86	2.42	1.7	1.89	5.0	6.3

Table 4: Normalized rms Beam Emittance in CCL (π cm mrad)

Energy	100 MeV	800 MeV
H ⁻ (Lujan / pRad / UCN)	0.04	0.065
H ⁻ (WNR)	0.058	0.124

ISOTOPE PRODUCTION FACILITY

After the DTL, the 100-MeV protons enter the transition region (TR) and continue propagation to the IPF beamline. Operation of the TR and IPF beamlines include beam position monitors (BPMs) to measure and control the beam centroid, correction of beam position at the target and control of beam losses using the Activation Protection devices. Typical beam losses in the IPF beamline are characterized by summed AP device readings of 15% - 20%, which is equivalent to 1- μ A beam losses, or relative beam losses of 4×10^{-3} .

During the 2015-2016 accelerator run cycle, a series of beam development experiments were undertaken to reduce beam losses. Analysis of beam dynamics, using 100-MeV beam emittance scans, indicated that beam envelopes had excessive variation, which was corrected by quadrupole setup. Additional improvement of beam quality was achieved by beam steering in the IPF beamline. A combination of the steering and bending magnets were adjusted to center the beam through the sequence of quadrupoles. As a result of improved beam matching and steering, the beam losses were reduced and reached 5×10^{-4} .

COUPLED CAVITY LINAC

In the Coupled Cavity Linac (CCL), the H⁻ beam experiences additional emittance growth, and normalized rms beam emittance at the end of linac is 1.5-2 larger than that at the beginning of the CCL (see Table 4). A dominant factor of beam emittance growth in this high energy part of the linac is diffusion of the beam distribution due to misalignments of the accelerator lattice.

Figure 6 displays a typical distribution of beam spill in the CCL as a function of increasing beam energy. This

Content from this work may be used under the terms of the CC BY 3.0 licence (© 2018). Any distribution of this work must maintain attribution to the author(s), title of the work, publisher, and DOI.

dependence is opposite to that previously observed; previously decreasing beam spill as a function of beam energy was observed for the proton beam. A dedicated study [6] showed that H⁻ beam stripping on residual gas and intra-beam stripping play a significant role in beam losses at high energy. Another study [7] indicated a strong dependence of H⁻ beam losses on the stability of RF amplitude and phase in the DTL linac. Maximum beam spill excited by DTL RF systems is estimated as:

$$\text{Max Beam Spill} \sim 10^{n \cdot \text{err}}, \quad (5)$$

where $n \sim 3 - 4$, and err is equal to the relative error in RF amplitude in percent, and/or RF error of RF phase in degrees. This study was extended for beam losses generated by RF instabilities in the 805-MHz CCL [8]. Results of the study imply new limits on stability of RF parameters provided by the Low-Level RF control systems, which require $\pm 0.1\%$ in RF amplitude and $\pm 0.1^\circ$ in RF phase to keep losses at a level that allows hands-on maintenance of the accelerator.

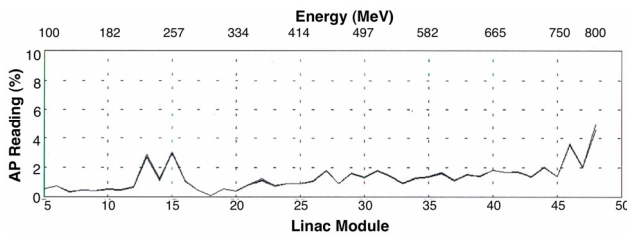


Figure 6: H⁻ beam spill in Coupled Cavity Linac.

SUMMARY

The LANSCE is a unique accelerator facility that simultaneously delivers beams to five experimental areas. Multi-beam operation requires compromises in beam tuning to meet beam requirements at the different target areas while minimizing beam losses throughout the accelerator, proton storage ring, and beam transport lines. Beam losses and emittance growth are controlled through careful beam matching along the accelerator, ion-source and LEBT adjustments, beam-based alignment, and improved RF phase and amplitude control.

REFERENCES

- [1] I.N. Draganic *et al.*, in *Proc. North American Particle Accelerator Conf. (NAPAC'16)*, Chicago, IL, USA, Oct. 2016, p. 25, doi:10.18429/JACoW-NAPAC2016-MOA3C003
- [2] B. A. Prichard, Jr. and R. R. Stevens, Jr., Los Alamos Nat. Lab., NM, USA, Tech. Rep. LA-UR-02-547, 2002.
- [3] Y. K. Batygin, in *Proc. 8th Int. Particle Accelerator Conf. (IPAC'17)*, Copenhagen, Denmark, May 2017, doi:10.18429/JACoW-IPAC2017-TUPVA144
- [4] R. W. Garnett, E. R. Gray, L. J. Rybarczyk, and T.P. Wangler, in *Proc. 5th European Particle Accelerator Conf. (EPAC'96)*, 1996, p. 3185.
- [5] I. M. Kapchinsky, *"Theory of Resonance Linear Accelerators"*, New York NY, USA: Harwood, 1985.
- [6] L. J. Rybarczyk, C.Kesley IV, R.McCrady, and X.Pang, in *Proc. IPAC'12*, New Orleans, LA, USA, May 2012, paper MOPLR072, p. 3892.
- [7] L. J. Rybarczyk *et al.*, in *Proc. LINAC'16*, East Lansing, MI, USA, 2016, doi:10.18429/JACoW-LINAC16-MOPLR072
- [8] Y. K. Batygin, "Effect of 805-MHz Linac RF Stability on Beam Losses in LANSCE High-Energy Beamlines", in *Proc. 9th Int. Particle Accelerator Conf. (IPAC'18)*, Vancouver, BC, Canada, Apr.-May 2018, paper TUPAL034.

INSTALLATION AND COMMISSIONING OF THE UPGRADED SARAF 4-RODS RFQ

L. Weissman[†], A. Perry, D. Berkovits, B. Kaizer, Y. Luner, J. Rodnizki, I. Silverman, A. Shor and D. Nusbaum, 1. Soreq Nuclear Research Center, Yavne 81800, Israel
A. Bechtold, P. Niewieczerzal Neue Technologien GmbH, Gelnhausen 63571, Germany

Abstract

Acceleration of a 1mA Continuous Wave (CW) deuteron ($A/Q=2$) beam at SARAF has been demonstrated for the first time. A 5.3mA pulsed deuteron beam with RFQ CW voltages has been accelerated as well. These achievements cap a series of major modifications to the Radio Frequency Quadrupole (RFQ) 4-rods structure which included the incorporation of a new end flange, introduction of an additional RF power coupler and, most recently, installation of a new set of rod electrodes. The new rod modulation has been designed to enable deuteron beam acceleration at a lower inter-electrode voltage, to a slightly reduced final energy of 1.27 MeV/u and with stringent constraints on the extent of beam tails in the longitudinal phase space. This report will focus primarily on the installation and testing of the new rods. The successful conditioning campaign to 200kW CW will be described. Beam commissioning with proton and deuteron beams will also be detailed. Results of beam measurements will be presented, including the characterization of the output beam in the transverse and longitudinal phase space. Finally, future possible improvements are discussed.

INTRODUCTION

The SARAF 176 MHz, 3.8 m long 4-rod RFQ is a critical component of the SARAF Phase I linac [1] which will also serve as an injector for the Phase II superconducting (SC) linac [2]. The original RFQ was designed by the University of Frankfurt [3], built by Neue Technologien (NTG) GmbH and RI-ACCEL GmbH, and has been able to generate up to 4 mA 1.5 MeV CW proton beams at RF power of about 60 kW. However, attempts to bring the RFQ to the level needed for CW deuteron operation (240-250 kW) were not successful [4,5].

Numerous improvements were introduced into the RFQ design since the earlier commissioning efforts [6-8]. Those measures have led to a considerable improvement of the RFQ performance, but the more recent RFQ commissioning campaigns still failed to bring the RFQ to CW operation at 250 kW [9-10].

At this stage it became evident that the RF coupler was the limiting factor. In 2016 the original RF coupler was replaced by two new couplers of superior design [11] in order to reduce the RF power density per coupler. The RF coaxial line was split and the RF coaxial sections were adjusted to match phases. Proper RF coupling was achieved successfully by a tedious, iterative procedure. In the following

[†] email address: weissman@soreq.gov.il.

commissioning campaign, it was demonstrated that the new coupler configuration did not affect the RFQ beam transport. The upgrade of the RF system enabled us to improve the RFQ performance and its availability for beam operation. Record results of the high power operation were achieved (April 2016). For example, the RFQ was kept at 240 kW CW for a period of more than two hours without a trip. Nevertheless, reliable CW operation at the 250 kW level was still non-achievable.

A proposal for a redesign of the SARAF RFQ rods with the purpose of reducing the integrated RFQ load required for deuteron operation at a comfortable operation level, 190 kW, was under consideration for several years [12]. The idea was to scale the rod modulation to allow for lowering of the required RFQ voltage from 65 kV to 56 kV. The new design involves a detailed redesign of the RFQ electrode modulation to maintain the desired beam characteristics for efficient matching to SARAF Phase II linac. Lowering of the applied RFQ voltage has the unavoidable consequence of a lowering of the inter-rod separation and a lowering of the outgoing beam energy from 1.5 MeV/u to 1.27 MeV/u. The most updated report on the RFQ redesign is given in [13]. The extensive beam dynamics simulations of the redesign RFQ were performed using the GPT beam dynamics code [14] with external routines for RFQ accelerating element [15]. The simulations showed that the optimized rod modulation should yield 5 mA proton and deuterons at 1.27 MeV/u with 93 % beam transmission with very few longitudinally lost particles and good beam optics and acceptance to the planned Phase II medium energy beam transport (MEBT) [2]. The transverse normalized rms emittance for a 5 mA deuteron beam should be of the order $0.2 \pi \cdot \text{mm} \cdot \text{mrad}$ and the corresponding longitudinal emittance of $0.85 \pi \cdot \text{keV/u} \cdot \text{ns}$. Extensive CST calculations [16] of the upgraded RFQ were performed to guarantee proper RF resonance frequency and capacitance of the individual cells and the overall structure.

As result of this work the precise information for the new rod production was delivered to the manufacturer (NTG).

MANUFACTURE AND INSTALLATION OF THE NEW RODS

After production the electrodes have been measured by means of the WENZEL 3d portal measuring gauge with measuring precision of $2.7 \mu\text{m/m}$. The measurement showed that the fabrication precision was well within the specs (better than $\pm 30 \mu\text{m}$ between adjacent cells) with the surface roughness within the range of $0.4\text{-}0.8 \mu\text{m}$

Content from this work may be used under the terms of the CC BY 3.0 licence (© 2018). Any distribution of this work must maintain attribution to the author(s), title of the work, publisher, and DOI.

Short stainless steel cooling pipes were brazed to the electrodes before the precise machining. After the electrode production the length of the cooling pipes was increased by welding of stainless steel pipes.

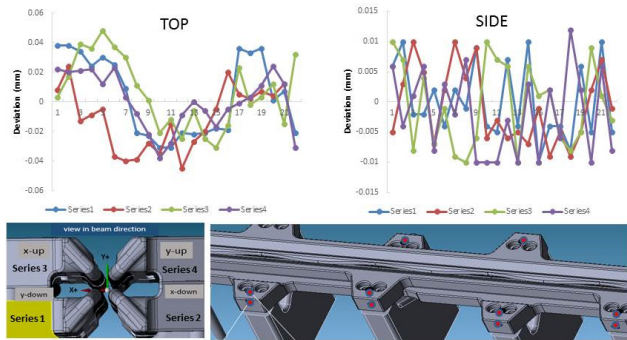


Figure 1: Deviations between the measured and calculated positions of the top and side surfaces of the installed new rods. The red spots indicate the measured positions.

Installation of electrodes has been accomplished by means of two sessions with a laser tracking system. The RFQ tank was opened and the old rods and tuning plates were disassembled and stored prior the first laser tracker campaign. The first campaign (May 2017) focused on measurements of the stems heights. As a first step we established the coordinate system by means of the two end flanges of the RFQ tank. The centres of the outer diameter of the flanges were measured and the connecting line between those points was defined as the beam axis. There were 5 measuring fiducials glued to the surface to find the coordinate system back again on the next working day or after moving the system. On the basis of the stem measurements and the metrology of the electrodes a set of precise shims spacers was manufactured to compensate for errors on stems and electrodes.

The new electrodes were installed in their positions with the adapted shims during the second installation campaign (June 2017). The top and side positions of all electrode supports were measured. The measuring positions are indicated as red spots in Fig. 1. As seen in Fig. 1 the deviations of the measured and calculated positions are within ± 40 and ± 10 microns for the top and side surfaces respectively.

The tuning plates had to be installed after the installation of the electrodes to adjust the resonance frequency and the field homogeneity. The exact height of the plates was determined by dummy plates made of aluminium. Fifteen dummy tuning plates were placed in between the stems into initial calculated positions. The RFQ couplers were adjusted manually to obtain good RF coupling. The resonance frequency and the field distribution were brought to the optimum via iterative procedure (Fig. 2). The field distribution was measured by means of the perturbation method.

After determination the optimum tuning plates positions the dummy tuning blocks were replaced by the newest generation high power tuning plates (made by copper covered

by a silver plate). The high power plates have been installed after shortening the water tubes to match their individual mounting situation. The fine tuning of the plates positions was performed via additional field measurements. In the final state the resonance frequency was 175.943 MHz in air or 175.986 MHz in vacuum. This frequency corresponded to the positions of the RFQ plungers in the middle of their tuning range. The final field non homogeneity was around 1.8 % (standard deviation). For comparison the corresponding number for the old structure was 2.7 %, which only could be achieved by a deliberate misalignment of the rods toward the high energy end [5]. A typical RF coupler coupling value was better than -40 dB, although better values down to -60 dB were observed during the tuning.

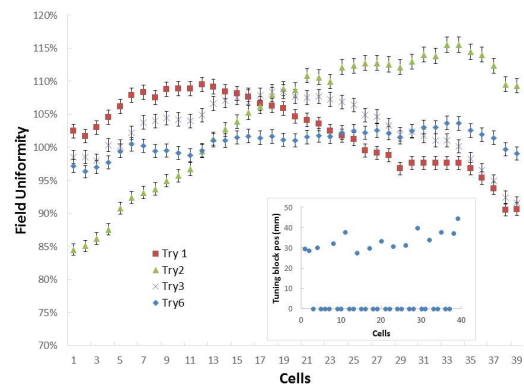


Figure 2: Iterative procedure for tuning the field homogeneity. The final position of the tuning plates is indicated in the inset.

HIGH POWER CONDITIONING

The first tests with proton beams (July 2017) demonstrated that the new RFQ structure is performing well within the designed parameters. According to the primary measurements with protons the power required for deuteron operation is in the range of 180-190 kW. However, conditioning at a higher power (>200 kW) is required to achieve stable operation at 180 kW.

It took five operational days (36 net hours) to reach 180 kW RF power (Fig. 3, left). In the first day only low duty cycle (<1 %) was used to bring the pulsed forward power to the 200 kW level. During the consecutive four days the pseudo CW duty cycle (>99 %) was used and the RF power was gradually increased. Relatively fast progress can be explained by all the recent modifications [6-8,11]. In addition a digital reflection protection box was used for the first time instead of a similar analogue device. The reflected power pulse measured by the directional coupler was analysed and introduced in a FPGA processor. In case of high reflected power the FPGA processor switched off for a predetermined period (usually ~ 60 msec) the input signal to the RF amplifier allowing for a discharge event to decay. Utilization of the protection box is the main reason for performing conditioning in the pulsed pseudo CW mode rather than real CW operation.

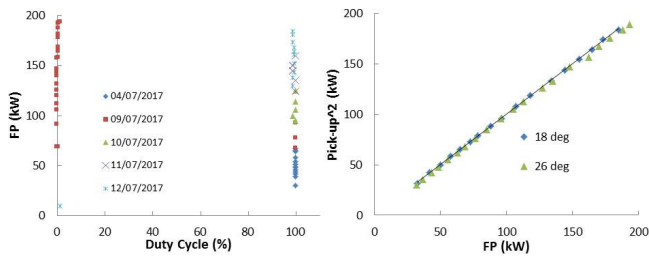


Figure 3: Left. The progress of the first stage of the high power conditioning. Right. Dependence of the normalized square of the pick-up amplitude versus the forward power taken for two temperatures of the cooling water.

As an example, the log of a 6 hour long operation at 180 kW is shown in Fig. 4. The forward power trace (orange) is almost constant during that time. The strip pattern of the orange trace is due to sampling of the pseudo CW signal. The power signal drops to 10% of its maximum value when it samples low RF power (1% of the time). However, one can also observe a few events when the forward power drops to zero (Fig. 4). These are high reflection power events which would cause a trip without the reflection box intervention. There were about 15 events of such type during the 6 hours operation presented in Fig. 4.

The following 30 net hours of conditioning were onset by two vacuum events when Viton o-rings in the vacuum barriers of the cooling tubes of the 39th and 19th stems were damaged. During further operation at the high power (>180 kW) it appeared that the tuning range of the RFQ plungers became marginal. It was decided then to open the RFQ chamber for minor modification of the resonance frequency. Only two tuning plates were slightly shifted down by less than 1 mm in order to shift the resonance frequency by approximately 60 kHz (plates # 2 and 39 in Fig. 2 inset) Consequent measurements showed that the field homogeneity practically did not change as result of this action.

The final stage of the high power conditioning (August 2017) comprised four days (33 net hours). At the end of this period we were able to keep RFQ: at 195 kW CW for many hours without a single trip and at 205-210 kW CW at the trip rate of one per hour. Note that the electric field at a power of level of 200kW in the new RFQ structure (1.58 Kilpatrick) corresponds to the electric field at a power level of 260kW in the old structure. The dependence of the electrical field (measured using a pick-up antenna) on the forward power is shown in Fig. 3, right. A deviation from linearity may be an indication of ‘dark currents’ in the RFQ. However, the measurements demonstrate that there is no measurable loss of RF power up to the highest used power values.

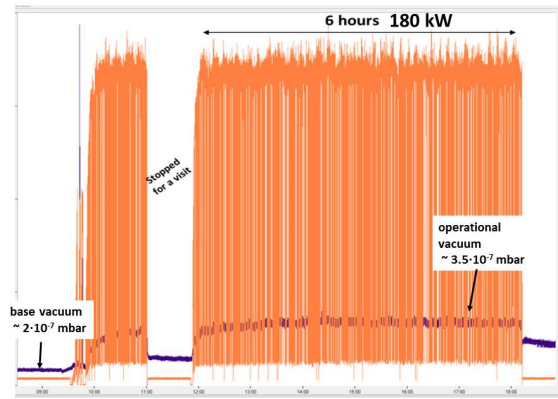


Figure 4: The log (forward power in orange, RFQ vacuum pressure in blue) at the end of the first part of the conditioning campaign; 6 hours of operation at 180 kW without a trip.

BEAM COMMISSIONING

The next stage of the RFQ commissioning (September 2017) included detailed beam characterization using the SARAF diagnostic (D) plate. The D-plate is situated after the SARAF cryomoule which considerably hindered of measurement of some beam properties at the RFQ exit.

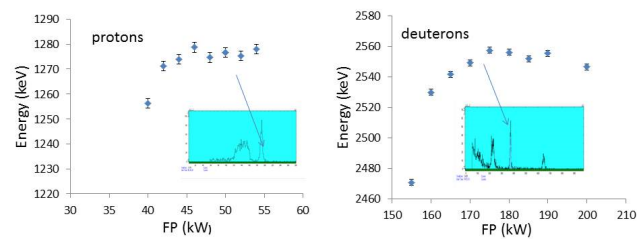


Figure 5: RBS measurement of beam energy as a function of the RF power for protons (a) and deuterons (b) are presented. The RBS spectra are shown in the inserts.

Accurate measurements of the beam energy were done using the Rutherford backscattering (RBS) of beam from a thin gold foil [17]. The Si detector used for particle detection was calibrated in situ by ¹⁴⁸Gd and ²²⁸Th alpha sources. The results of energy measurements for proton and deuteron beams as a function of RF power are displayed in Fig. 5. The obtained beam energy is about 1.275 keV and 2.555 keV for protons and deuterons correspondingly which is very close to the designed values.

Transverse emittance measurements were performed using vertical and horizontal slit-wire sets at the D-plate. The measurements were done with beam pulses of 0.5 ms of protons and deuterons and for various intensities up to 5.5 mA. The measured values of the normalized rms emittances are within the specifications for both protons and deuterons (~0.2 π·mm·mrad).

The RFQ transmission was measured by comparing the current readings at the LEBT and the D-plate Faraday cups. The dependence of the transmission values on the input beam current is compared for the old and new rod structures in Fig. 6. The present and the previous (December

Content from this work may be used under the terms of the CC BY 3.0 licence (© 2018). Any distribution of this work must maintain attribution to the author(s), title of the work, publisher, and DOI.

2015) measurements were performed in the same manner - only the ion source magnetron RF power was changed to vary the LEBT current and all the LEBT optical parameters were kept the same, except fine tuning of the last LEBT solenoid. It is seen in Fig. 6 that the RFQ transmission has improved slightly for the proton beam, although the general trend of the transmission decrease with increase of the current persisted. There is also a modest increase of the transmission for deuterons for the new rod structure. Moderate improvement in RFQ transmission took place in spite of the fact that the physical aperture area between the new rods was reduced effectively by 30 % [13]. The improvement is due, in part, to a smother gentle bunching section and, in part, to a constant aperture in the accelerator region [13], as well as, due to better field homogeneity achieved with the new rod structure.

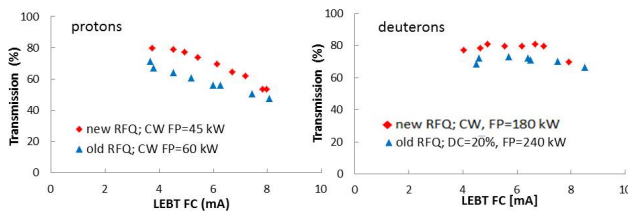


Figure 6: The RFQ transmission as a function of the input current for protons (left) and deuterons (right). Measurements for the new and old rod structures are compared.

Improvements are also seen in behaviour of the beam distribution as a function of the RF power. The horizontal beam profiles measured in the MEBT at various RF powers are compared for the new and the old structures in Fig. 7. The forward power was varied in 40-55 kW and 55-70 kW range for the new and old structure respectively. As it seen from the comparison that the new structure does not exhibit strong power dependent steering, that was observed with the previous rods [18].

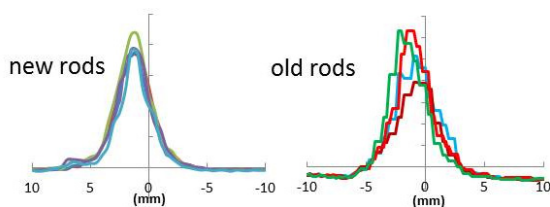


Figure 7: The effect of RF power on the MEBT beam profiles for new (left) and old (right) structure.

Significant efforts were devoted to the measurement of the longitudinal emittance. The emittance is measured for protons by monitoring the RBS energy distribution of the beam while varying longitudinal focusing by a superconducting cavity (gradient variation method [19]). The main difficulties of this measurement are associated with the fact that the longitudinal emittance value is affected by beam transport via the cryomodule. One has to rely on beam dynamics simulations in order to choose the appropriate tune with a moderate effect on the emittance in the whole tuning

range. Three half wave resonator (HWR) cavities were used in the tune which was applied in the measurement: HWR1 in the bunching mode, HWR2 in accelerating mode and HWR4 also in the bunching mode. The HWR4 bunching voltage was varied in steps from 0 to 300 kV. The energy distribution was measured by the RBS monitor with typical energy resolution better than 15 keV. The results of energy width distribution measurements as a function of the focusing HWR4 voltage are presented in Fig. 8, left together with examples of the obtained RBS peak. As results of the measurements the longitudinal phase space rms ellipse at the RFQ exit was obtained (Fig. 8, right). This was done by propagating the results obtained at the D-plate back to the position of HWR4 resonator for each HWR4 bunching voltage and deducing the minimum size rms ellipse. The result for longitudinal emittance was measured for the position of the HWR4 resonator. The simulations show in the transport from the RFQ exit to that point an emittance grows of approximately 20 %. The result at the RFQ exit corresponds to $\sim 1.1 \pi \cdot \text{keV} \cdot \text{u} \cdot \text{nsec}$.

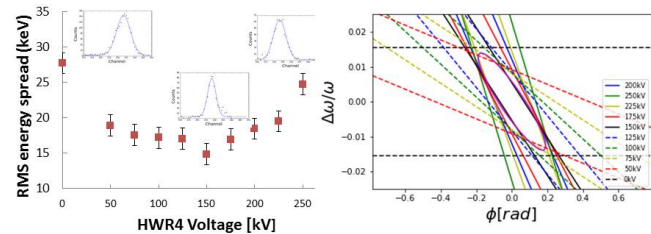


Figure 8: Left. The results for measurement of energy distributions are presented. Some examples of spectra are shown in the insets. Right. The phase space ellipse obtained from the RBS measurements.

Demonstration of CW deuteron operation is the important milestone of SARAF Phase I which was overdue for a decade. The test, performed in October 2017, started with acceleration of a low duty cycle beam while RFQ was working in CW mode at 190 kW. The cryogenic cavities were detuned. The beam duty cycle was set by the slow chopper, beam was stopped at the beam dump after the D-plate. The pulse intensity was kept at 1.15 mA. The duty cycle was gradually increased to 99.5 % while monitoring vacuum in the cavities and cryogenics. After reaching the pseudo CW level RFQ was operational for half an hour smoothly until a RFQ trip. Operation of deuteron beam in CW mode is feasible now with the upgraded RFQ structure.

SUMMARY

A new 4-rod structure has been designed and implemented at SARAF, with the goal of reducing the RF power required for CW deuteron operation while compromising the RFQ exit energy to 1.27 MeV/u. The new 4-rod structure was manufactured by NTG, and successfully installed in place of the old rod electrodes. Superior field homogeneity was achieved during the installation. The upgraded RFQ was successfully conditioned to the RF power of

200 kW required for CW deuteron operation, with a sufficient power margin. The first operation of ~1 mA CW deuteron beam was demonstrated and up to 5.6 mA deuteron pulses were extracted while the RFQ was operated in pseudo CW mode. The extensive commissioning tests with proton and deuteron beams were performed. The main designed and measured RFQ parameters are compared in Table I. As seen from the table the main RFQ parameters such as the working RF power, exit energy, and emittances (transverse and longitudinal) are close to the design specifications. The relatively low value of the RFQ transmission is a long standing issue, which is, at least partially, the result of beam neutralization loss in the LEBT/RFQ interface region [20]. Nevertheless, the new rod structure exhibits a slight improvement in transmission in spite of its lower effective aperture. We also do not observe the strong power dependent steering effects which took place in the previous structure. A more detailed report on this work is available [21].

Table 1: The Comparison of the Designed and Measured RFQ Specifications. The beam current at the RFQ exit. “zero” current values correspond to the measurements involving the RBS monitor.

Parameter		Beam (mA)	Designed value	Measured value	
Energy (keV/u)		5/0	1.270	1.275(5)	
Working power (kW)	p	5/0	46.5	45-50	
	d	5/0	186	180-190	
Transmission (%)	p	5	88	60	
	d	5	93	70	
emittance rms norm.	Transversal (π -mm-mrad)	p	5	0.2	≤ 0.2
		d	5	0.2	≤ 0.2
	Longitudinal (π -keV/u-nsec)	p	0	1.35	1.1
		d		1.35	N/A

A number of issues still need to be resolved in the near future include: further improvement reliability of the vacuum sealing, improvement of stability of the RF amplifier at the high power and solving some issues with the control system. The low RFQ transmission, especially in the case of high proton current, calls for further studies of all complex phenomena taken place at the RFQ entrance. With further RFQ operation some fresh copper evaporation was observed on the insulated ceramic of one coupler. This issue will be further studied. More work and improvements will be done in the next future to make the SARAF RFQ a reliable injector of the SARAF Phase II superconducting linac.

REFERENCES

- [1] A. Nagler *et al.*, "Status of the SARAF Project", in *Proc. 24th Linear Accelerator Conf. (LINAC'08)*, Victoria, Canada, Sep.-Oct. 2008, paper MO203.
- [2] N. Pichoff *et al.*, "Status of the Phase II SARAF Project", in *Proc. 8th Int. Particle Accelerator Conf. (IPAC'17)*, Copenhagen, Denmark, May 2017, paper TUPVA052.
- [3] P. Fischer *et al.*, "Tuning a CW 4-Rod RFQ", in *Proc. 23rd Linear Accelerator Conf. (LINAC'06)*, Knoxville, TN, USA, Aug. 2006, paper THP064, p. 728.
- [4] I. Mardor *et al.*, "The Status of the SARAF CW 40 MeV Proton/Deuteron Accelerator", in *Proc. 23rd Particle Accelerator Conf. (PAC'09)*, Vancouver, Canada, May 2009, paper FR5REP087.
- [5] L. Weissman *et al.*, "The status of SARAF linac project", in *Proc. 25th Linear Accelerator Conf. (LINAC'10)*, Tsukuba, Japan, Sep. 2010, paper WE102.
- [6] J. Rodnizki, Tz. Horowitz, in *Proc. 25th Linear Accelerator Conf. (LINAC'10)*, Tsukuba, Japan, Sep. 2010, paper TUP045.
- [7] J. Rodnizki *et al.*, "SARAF RFQ, RF and thermal improvements", SNRC report #4716, 2014, available per request.
- [8] L. Weissman *et al.*, "The SARAF Phase I linac in 2012", *JINST*, vol. 9, p. T05004, 2014.
- [9] L. Weissman *et al.*, "SARAF Phase I linac operation in 2013–2014", *JINST*, vol. 10, p. T10004, 2015.
- [10] L. Weissman *et al.*, "SARAF RFQ; conditioning campaign May-June 2014", SNRC report #4515, 2014, available per request.
- [11] J. Rodnizki *et al.*, "SARAF 4-rod RFQ RF power Line splitting design and test", in *Proc. 28th Linear Accelerator Conf. (LINAC'16)*, East Lansing, MI, USA, Sep. 2016, doi:10.18429/JACoW-LINAC16-TH1A04
- [12] A. Shor and J. Rodnizki, "Redesign of SARAF 4-rods RFQ for CW deuteron acceleration", SNRC report #4517, 2014, available per request.
- [13] A. Shor and A. Perry, "Detailed redesign of SARAF 4-rods RFQ for CW deuteron acceleration", SNRC report #4815, 2017, available per request.
- [14] General Particle Tracer (GPT) code, www.pulsar.n1
- [15] B. Bazak, M. Sc. Thesis, Hebrew University of Jerusalem.
- [16] CST Microwave Studio, www.cst.com
- [17] L. Weissman *et al.*, "First experience at SARAF with protons beam using Rutherford scattering monitor", in *Proc. 9th European Workshop on Beam Diagnostics and Instrumentation for Particle Accelerators (DIPAC'09)*, Basel, Switzerland, May 2009, paper TUPB102.
- [18] L. Weissman *et al.*, "SARAF Phase I linac operation in 2011", SNRC report #4341, 2012, available per request.
- [19] P. Strehl, *Beam Instrumentation and Diagnostics*. Berlin: Springer, 2006.
- [20] L. Weissman, A. Perry, L. Baron and J. Rodnizki, "Beam optics effects at the entrance of SARAF RFQ", ICIS2017, Geneva 2017, in print.
- [21] L. Weissman *et al.*, "Installation and Commissioning of the Upgraded SARAF 4-rods RFQ", *JINST*, vol. 13, p. T05004, 2018.

DISCUSSION ON SARAF-LINAC CRYOMODULES

N. Pichoff, D. Chirpaz-Cerbat, R. Cubizolles, J. Dumas, R. Duperrier, G. Ferrand, B. Gastineau, F. Leseigneur, C. Madec, T. Plaisant, J. Plouin, CEA/IRFU, Gif-sur-Yvette, France

Abstract

CEA is in charge of the design, construction, installation and commissioning at SNRC of the Linac of the SARAF project. The linac is composed of an MEBT and a Superconducting linac (SCL) integrating 4 cryomodules. Nowadays, the HWR cavities and superconducting magnets prototypes are being built. The Critical Design Review of the cryomodules has just been passed in March 2018. This paper present the status of the SARAF-LINAC cryomodules.

INTRODUCTION

CEA (Commissariat à l’Energie Atomique, France) is in charge of the design, construction, installation and commissioning at SNRC (Soreq Nuclear Research Center, Irsrael) of four cryomodules for the SARAF (Soreq Applied Research Accelerator Facility) project [1]. The HWR cavities and superconducting magnets prototypes are being built. The Critical Design Review of the cryomodules has just been passed in March 2018.

This paper is presented in a workshop (HB2018) whose most of the participants are not cryomodule experts. For this reason, in order to enlarge the discussions among all participants, it is not addressing technically advanced concepts but the cryomodules through their requirements and functions and not through their solutions. Of course, these discussions can also address advanced solutions which will be described during the presentation.

SARAF-LINAC TLR

SNRC defined following Top-Level Requirements for the SARAF-LINAC:

- Input beam: Proton or Deuteron; 176 MHz; 40 μ A-5 mA; cw to pulse (0.1-1 ms @ 0.1-400 Hz); 0.2 π .mm.mrad rms norm. emittance; 1.3 MeV/u;
- Output beam: 40 MeV for deuterons or 35 MeV for protons; Emittance growth < 25%.
- Operation: beam losses lower than 150 nA/m below 5 MeV, 40 nA/m below 10 MeV, 5 nA/m below 20 MeV and 1 nA/m above; 6000 h/y 90% availability.

These TLR drives the SARAF-LINAC solution (Figure 1).

CRYOMODULE MAIN FUNCTIONS

The main functions of the cryomodules (and the linac) is to accelerate the beam to the final energy (satisfied by HWR cavities). Other functions with respect to the beam is to keep it focused and on path to allow its acceleration and maintain its emittance low (satisfied by Solenoid Packages). Finally, other functions with respect to these critical components are necessary to maintain them in operating conditions (satisfied by Cryostats):

- cool down (4 K) /warm up (300 K) cavities and magnets with controlled pressure and temperature conditions, limit thermal loss
- align cavities, BPMs and magnets,
- reduce magnetic field at cavities,
- distribute electrical power and signals,

Finally a cryomodule has to be controlled from the Main Control System relying on the EPICS technology. The interface layer is satisfied by a Local Control System.

Acceleration Function

Initial beam dynamics studies led to the choice of 2 families of HWR superconducting cavities (Figure 2). 13 low-beta (0.092) are used at “low” energy in 2 cryomodules and 14 high-beta (0.182) are used at “high” energy in 2 cryomodules.

The other requirements on these cavities are mainly based on their accelerating field (respectively 7 MV/m and 8.1 MV/m, by limiting the peak magnetic field to 70 mT) and their cryogenics power consumption (based on a 40 nOhm surface resistance). RI Company is in charge of the manufacturing of these cavities. In operation, the volume enclosed in the cavity should be as clean as possible to keep the field performances.

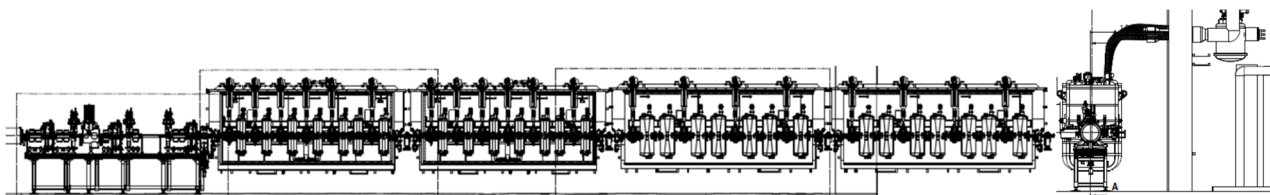


Figure 1: SARAF-LINAC layout, side view (left) and beam view (right).

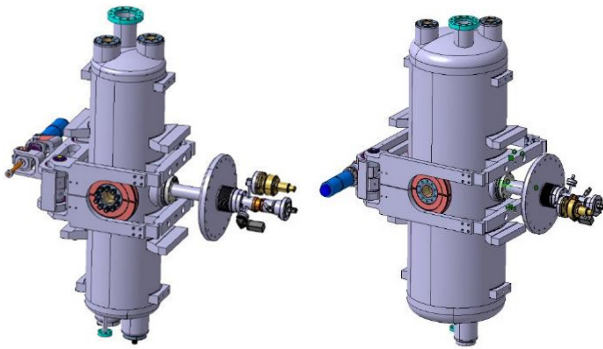


Figure 2: HWR cavities (left-LB; Right-HB).

The phase (and amplitude) cavity field law is set to maintain the beam bunched and accelerated within acceptable beam losses, even in case of errors on components (iterative process). The unhooked particles are the main sources of beam losses (Figure 3).

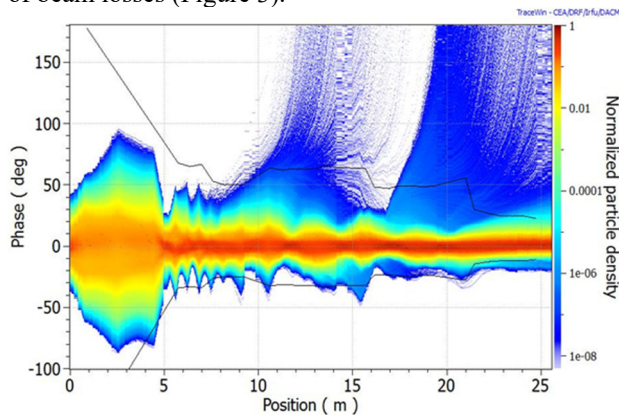


Figure 3: Longitudinal beam profile (log, with errors).

Transport Functions

During the acceleration, the beam is naturally growing (emittance, cavity defocusing, space-charge) and deviating (dipolar field, electromagnetic component misalignments). The superconducting coils in the Solenoid Packages (Figure 4) combine the function of focusing and steering the beam as BPM placed upstream are here to measure the position, charge and phase of the beam.

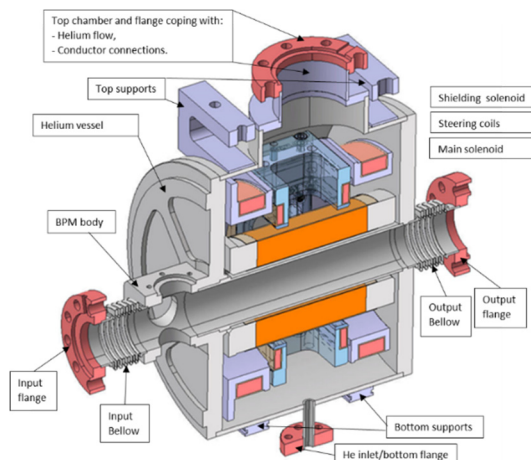


Figure 4: Solenoid Package.

Initial beam dynamics studies led to the choice of 1 family of solenoid package. 12 in the 2 low-beta cryomodules and 8 in the 2 high-beta cryomodules. The design focusing force is 3.5 T².m and the design steering force is 8 T.mm. Active shielding (compensation coils) are used to limit the fringe magnetic field below 20 mT on neighbouring cavities. Elytt Company is in charge of the manufacturing of these solenoid packages.

The field law is set to limit emittance growth and to maintain the beam on accelerator axis even in case of errors on components (iterative process). The particle lost in the linac are not lost transversally but are firstly unhooked in the cavities (Figure 5).

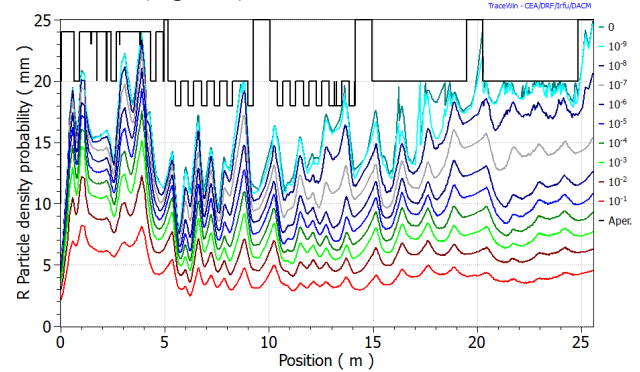


Figure 5: Transverse beam contour plot (log, with errors).

Operation Functions

The cryostat (Figure 6) is in charge of keeping the SC cavities and solenoid package in operation conditions:

- At cryogenic temperature (4.45 K),
- On linac axis (± 1 mm),
- With beam pipe under vacuum,
- $< 2 \mu\text{T}$ on cavity surfaces during NC/SC transition,
- Feed by power (DC current or RF),
- Connected to control system (BPM, LLRF, operation sensors...),
- With easy access for some “fast” maintenance procedures.

Cryogenics The cryogenics distribution (4.45 K LHe and 60 K GHe) is done with valve boxes and circuitry in the cryomodule. The cryogenics consumption is reduced by using an intermediate thermal shield (cooled by 60 K) and putting all the components in a cryostat under vacuum ($< 10^{-4}$ mbar) to limit warming by convection.

Alignment Because of required cleanness of cavities, all the major components are assembled in clean room. They are then attached on a frame then on the cryomodule top plate. They are then aligned to positions taking in account the calculated displacement from future cryomodule pumping and cool down. The position of each element can be controlled through optical system when the cryomodule will be pumped and cooled.

Content from this work may be used under the terms of the CC BY 3.0 licence (© 2018). Any distribution of this work must maintain attribution to the author(s), title of the work, publisher, and DOI.

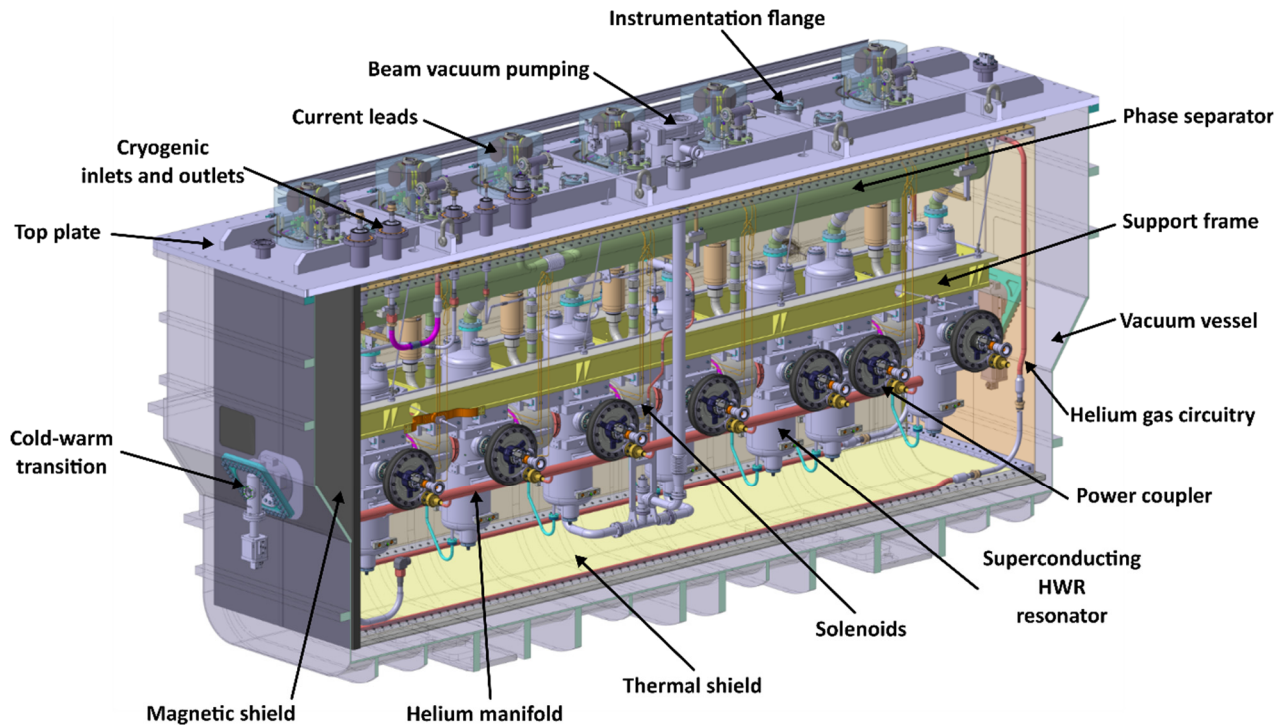


Figure 6: SARAF Cryomodule 2 overview.

Beam vacuum The beam pipe should be under vacuum for many reasons: reduce interaction with beam, limit possible pollution of cavities, limit warming of components by convection. The pumping is made through beam port (pumping in warm section at both ends of cryomodules) and through one HPR port of the 2 central cavities. The warm section pumping is more efficient (better conductance) but the pumping through central cavities is made necessary to keep the vacuum when end valves are closed.

Magnetic hygiene The impact of the trapped magnetic field on cavity surface resistance is estimated to about $2n\Omega/\mu T$ during NC/SC transition. This means that a special care should be made to material used in the cryostat (depending on their distance with respect to the cavities), but also the earth magnetic field ($\sim 50\mu T$) should be screened by a dedicated magnetic shield in the cryomodule.

Power feeding Each solenoid package is feed by 3 power supplies (100 A for the focusing solenoids and 2×20 A for the steering coils). The current goes to SC coils through cryostat top-plate feedthroughs and current leads half plunged in LHe. The SC cavities are feed by RF amplifier (10 kW max. for LB and 20 kW max. for HB cavities). The RF power goes to cavities through RF coupler attached to the cryostat side.

Instruments In order to control the operation condition, many sensors (temperature, magnetic field, voltage, RF...) are connected to the control-system through cryomodule top-plate.

Trap doors In order to allow some access to potentially weak components (tuner motors, spare sensors...), the cryostat contains side trap doors which can be opened when the cryomodule is warm and at atmospheric pressure.

CONCLUSION

A special care has been performed for defining functional requirements for the cryomodules. This facilitates the selection and justification of the solutions and to prepare inspection and testing occurring during the integration and commissioning phases.

REFERENCES

- [1] N. Pichoff *et al.*, "The SARAF-LINAC project 2018 status", in *Proc. IPAC'18*, Vancouver, British Columbia, Canada, 2018, paper TUPAK015.

STATUS OF R&D ON NEW SUPERCONDUCTING INJECTOR LINAC FOR NUCLOTRON-NICA

A.V. Butenko, N.E. Emelianov, A.O. Sidorin¹, E.M. Syresin, G.V. Trubnikov,
Joint Institute for Nuclear Research, Dubna, Moscow Region, Russia,

M.A. Gusarova², T.V. Kulevoy³, M.V. Lalayan², T.A. Lozeeva, S.V. Matsievskiy,
R.E. Nemchenko, S.M. Polozov, A.V. Samoshin, V.L. Shatokhin², N.P. Sobenin, D.V. Surkov,
K.V. Taletskiy, V.L. Zvyagintsev⁴, National Research Nuclear University – Moscow Engineering
Physics Institute, Moscow, Russia,

M.A. Batouritski, V.A. Karpovich, S.A. Maksimenko, V.N. Rodionova,
Institute for Nuclear Problems, Belarusian State University, Minsk

A.A. Bakinowskaya, V.S. Petrakovskiy, I.L. Pobol, A.I. Pokrovskiy, D.A. Shparla, A. Shvedau,
S.V. Yurevich, V.G. Zaleski, Physical-Technical Institute,
National Academy of Sciences of Belarus, Minsk,

S.E. Demyanov, Scientific-Practical Materials Research Centre of the National Academy of
Sciences of Belarus, Minsk

¹also at Saint-Petersburg State University, Saint-Petersburg, Russia

² also at Joint Institute for Nuclear Research, Dubna, Moscow Region, Russia

³also at Inst. of Theoretical and Experimental Phy. of NRC “Kurchatov Institute”, Moscow, Russia,

⁴also at TRIUMF, Vancouver, Canada

Abstract

The progress in R&D of QWR and HWR superconducting cavities will be discussed. These cavities are designed for the new injection linac of Nuclotron-NICA facility at JINR. The goal of new linac is to accelerate protons up to 25 MeV (and up to 50 MeV at the second stage) and light ions to ~ 7.5 MeV/u for Nuclotron-NICA injection. Current results of beam dynamics simulations, SC cavities design and SRF technology development will be presented in this paper.

INTRODUCTION

Nuclotron-based Ion Collider Facility (NICA) is new accelerator complex under construction at JINR [1-5]. It was proposed for ion collision and high-density matter study. NICA facility will include the operating ion synchrotron Nuclotron and new booster and two collider rings being under construction. The injection system of Nuclotron-NICA was upgraded in 2011-2016. The pulse DC forinjector of Alvarez-type DTL linac LU-20 was replaced by the new RFQ developed and commissioned by joint team of JINR, ITEP and MEPHI [6] and is under operation since December, 2015. New RFQ linac can accelerate ions with charge-to mass ratio $Z/A > 0.3$. The first technical session of Nuclotron with new injector was ended on May-June, 2016, [7] and regular experimental sessions were done in 2016-2018. The LU-20 with new RFQ for-injector was used for p, p \uparrow , d, d \uparrow , He, C and Li ions acceleration till now. The other heavy ion linac for particles with $Z/A = 1/8 - 1/6$ was developed by joint team of JINR, Frankfurt University and BEVATECH and commissioned in 2016.

It must be noted that LU-20 operation causes many technical issues because of its age: it was commissioned in 1972. The possibility of LU-20 replacement by the new linac of 30 MeV energy for protons [8-12] and ≥ 7.5 MeV/nucleon for deuterium beam is discussed now. Project should also include an option of the linac upgrade for the proton beam energy upgrade up to 50 MeV by means of a number of cavities in additional section. It is proposed that new linac will include a number of superconducting (SC) cavities.

The key problem of SC cavities and SC linac construction for Nuclotron-NICA is the absence of SRF technology in Russia today. The development of the SRF technologies is the key task of new Russian - Belarusian collaboration started on March 2015. Now the JINR, NRNU MEPHI, ITEP of NRC “Kurchatov Institute”, INP BSU, PTI NASB, BSUIR and SPMRC NASB are participating in new collaboration.

Two possible schemes for new linac were discussed. First it was proposed to use a number of superconducting cavities for medium and high energy ranges of the linac starting 2.5 or 5 MeV/u. The second way is to start SRF part of the linac from 10-15 MeV.

LINAC GENERAL LAYOUT AND BEAM DYNAMICS

In the first case linac will consist of several superconducting independently phased cavities and focusing solenoids. Starting 2014 three SC linac designs were proposed, simulated and discussed [8-12]. The normal conducting 2.5 MeV RFQ and five [8] or four [9] SC cavities groups respectively were in the first and the second linac designs. Main results of the beam dynamics

Content from this work may be used under the terms of the CC BY 3.0 licence (© 2018). Any distribution of this work must maintain attribution to the author(s), title of the work, publisher, and DOI.

simulations were presented in [8-12] in detail. The basic parameters of the linac are the following: the injection energy for SC part of linac is increased to 5 MeV (as LU-20 gives at present, but normal conducting cavities for 5-13 MeV energy band are also discussed). The normal conducting part will consist of 2.5 MeV/nucleon RFQ linac followed by QWR cavities for the acceleration of beams with charge-to-mass ratio $Z/A > 1/2$. Main parameters of the linac are presented in Figure 1.

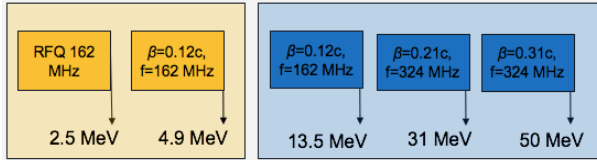


Figure 1: General layout of new injector linac. The section from 5 to 13 MeV can be chosen normal conducting or superconducting.

The second way was proposed later to decrease the time of linac R&D and construction. It was proposed to use RFQ section and a number of IH-DTL normal conducting sections for energies up to 5 MeV/u. These sections will be developed and constructed by BEVATEC Ltd. The section for energies from 5 to 13 MeV will consist of a number of identical normal conducting cavities being under development by ITEP now. SC cavities will be used starting only at 13 MeV and early developed QWRs are not necessary in this layout. Only HWRs are used and today all Russian-Belorussian SRF activities are directed to their development and manufacturing.

The beam dynamics simulation for superconducting part of the first linac layout was done using BEAMDULAC-SCL code designed at MEFPhI [13-15]. For the chosen types of accelerating cavities (QWR for low energies and HWR for higher energies) the third version of SC linac design was developed and now the accelerator is divided into three groups of cavities with geometric velocities $\beta_G = 0.12, 0.21$ and 0.314 . It was also proposed that linac normal conducting part for the energy band of 2.5-5 MeV will consist of QWRs with the parameters equal to SC QWRs of 1st group (so-called 0th group).

The accelerating RF field was limited by 6.0 MV/m for superconducting QWR and HWR cavities. It is caused by the electrical field overvoltage limited by the factor ~ 6 due to the simplest QWR design chosen to gain the first manufacturing experience. Contrary to it the peak solenoid field was increased to 2.0-2.5 T and a beam envelope limitation was also increased from 3 to 5-6 mm [9]. The number of cavities in the 1st and the 2nd groups should be increased due to lower accelerating gradient E_{acc} (≤ 6 MV/m instead of 7.5 MV/m for the 2nd linac version). The beam dynamics of deuterium ions was studied also [9].

Parameters of the 0th, the 1st and the 2nd groups of cavities are shown in Table 1. The slipping factor will be not higher than 24% for proton and deuterium beams here (see Figure 2). The number of QWR cavities in the 1st

group should be increased from five to eight both to decrease the accelerating field and to have deuterium ion beam of 7.5-8.0 MeV/nucleon after the 1st group (see below). The total length of the linac increases by 1.9 m.

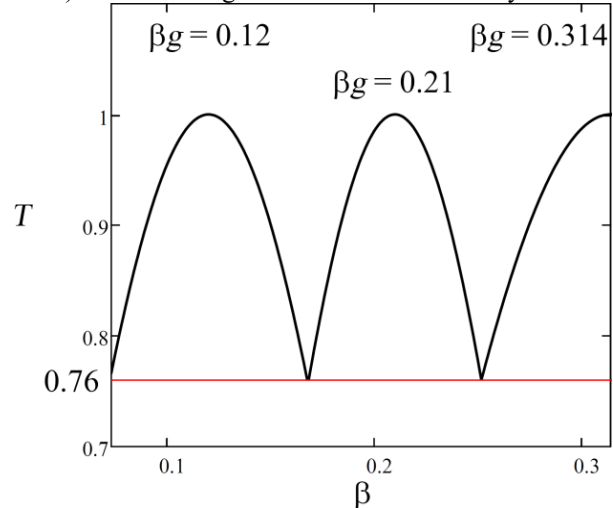


Figure 2: The slipping factor T for proton and deuterium beams, identical QWR's with $\beta_g=0.12$ are used for the 0th and the 1st groups.

Table 1: Current Parameters of the SC Linac for Proton and Deuterium Beams Acceleration.

Cavity group	0 *		1		2	
	Proton beam			Deuterium beam		
β_g	0.12	0.21	0.12	0.21	0.12	0.21
F , MHz	162	324	162	324	162	324
T , %	24.0	24.0	24.0	24.0	24.0	24.0
N_{gap}	2	2x2**	2	2x2**	2	2x2**
L_{res} , m	0.222	0.39	0.222	0.39	0.222	0.39
L_{sol} , m	0.2	0.2	0.2	0.2	0.2	0.2
L_{gap} , m	0.1	0.1	0.1	0.1	0.1	0.1
L_{per} , m	0.622	0.79	0.622	0.79	0.622	0.79
N_{per}	3	8	3	8	3	8
L , m	1.87	4.98	6.32	1.87	4.98	6.32
E_{acc} , MV/m	4.50	5.86	6.4	4.50	5.86	6.4
U_{res} , MV	1.0	1.3	1.25	1.0	1.3	1.25
Φ , deg	-20	-20	-20	-20	-20	-90
B_{sol} , T	1.35	1.3	1.9	1.8	2.0	1.0
W_{in} , MeV	2.5	4.9	13.47	2.5	3.65	8.3
β_{in}	0.073	0.102	0.168	0.073	0.088	0.133
W_{out} , MeV	4.9	13.47	31.0	3.65	8.3	8.3
β_{out}	0.102	0.168	0.251	0.088	0.133	0.133
K_T , %	100	100	100	100	100	100

* cavities in 0th group are normal conducting.

** two 2-gap HWR per one period

The deuterium beam dynamics was simulated later for this version of linac layout. The amplitude of RF field of 5.86 MV/m is quite enough to accelerate deuterons up to

energy 8.3 MeV (see Table 1), it corresponds to the project aim and the 2nd and the 3rd groups of cavities can be used in transit regime for the deuterium beam. Note that the solenoid field in the 1st group of cavities should be increased up to 2 T for the deuterium beam.

SC QWR DESIGN

The operating frequency of the linac was chosen first equal to 162 MHz for QWRs with further increase to 324 MHz for HWR cavities. Results of the 162 MHz SC QWR cavities design were early presented on IPAC'2017 [16]. The simplest design (Figure 3) of QWR with cylindrical central conductor was chosen to work out fabrication and testing routines.

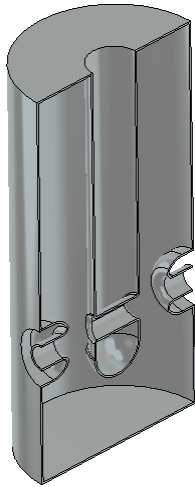


Figure 3: General view of 162 MHz QWR for $\beta_g = 0.12$.

Simplest design of this prototype satisfies the initial data. In addition, it helps to decrease the fabrication time and necessary funding for SRF technology development. But the ratio of peak to accelerating field for this design is high $E_p/E_{acc} \sim 6$ and we should limit the RF field to only $E_{acc}=6$ MV/m (the limit surface field should not exceed 35 MV/m).

Then the helium vessel was designed at PTI NASB. The vessel design (shown on Figure 4) includes QWR inside, frequency tuning plunger mounted on the cavity bottom, two beam ports with flanges, the RF power coupler, field measurement pickup, helium and vacuum ports, etc.

It was proposed to shift the operating frequency of QWR cavities to 162.5 MHz as it is mostly used in many international laboratories. It can be easily done by means of the sorter central conductor and the cavity shell.

SC HWR DESIGN

The operating frequency was initially chosen to 324 MHz for HWRs [9, 17] but today it is proposed to shift it to 325 MHz as it is mostly used. Two types of HWR were simulated and studied (see Figure 5): simplest design with the cylindrical central conductor and improved design with the conical one. The second design is more difficult for manufacturing but give much lower values of the magnetic and the electric overvoltage [18].

Components of the central conductor are planning to manufacture at PTI NANB by means of the polymer hydroforming technology and it give us some optimism for its quality.



Figure 4: General view of 162 MHz QWR design model for $\beta_g = 0.12$, the RF frequency tuner is placed bottom of the cavity, the RF load loop and the measurement loop are not visible.

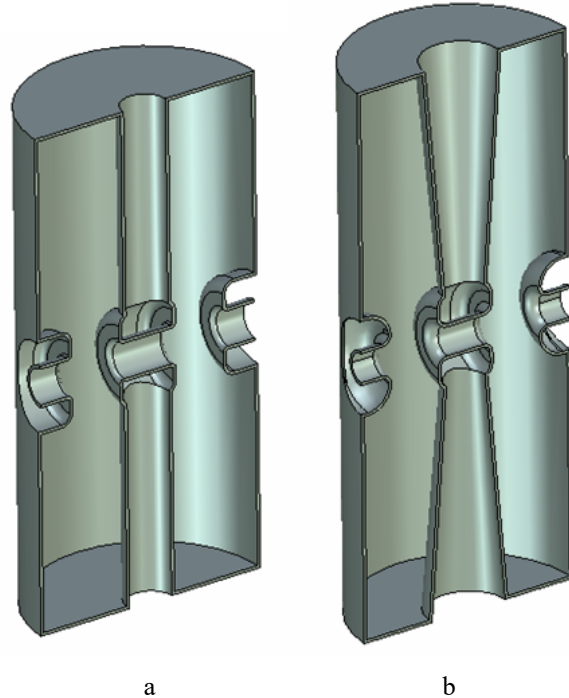


Figure 5: Two types of HWR's with $\beta_g=0.21$: with the cylindrical central conductor (a) and with the conical one (b).

Geometric and electrodynamic parameters for both types of the cavities are presented in Table 2. It can be

Content from this work may be used under the terms of the CC BY 3.0 licence (© 2018). Any distribution of this work must maintain attribution to the author(s), title of the work, publisher, and DOI.

seen that the simplest cavity design having the cylindrical central conductor breaks the surface field limitation. For accelerating field of 7.7 MV/m the magnetic field on the surface exceeds 50 mT mentioned above as MFQS origin and reaches 80 mT. For a conical central conductor design, due to drift tube rounding and increasing the central conductor radii in the cavity cover, it is possible to reduce the peak electric field to $E_p/E_a = 3.3$. Peak magnetic field to accelerating gradient ratio B_p/E_a in this case is 5.6 mT/(MV/m). Data presented in Table 2 show that both QWR designs satisfy the requirement for the accelerating gradient. By the second design with the conical central conductor cavity has much better parameters to prevent the multipactor discharge. This discharge is observed for coaxial cavities for low RF field levels and leads to the tuning and commissioning time increase.

Table 2: RF Parameters of 325 MHz HWR for $\beta_g = 0.21$

Parameter	Value	
	(a)	(b)
HWR type		
Operating frequency, f , MHz	324	
Geometrical velocity, β_g	0.21	
Cavity height, mm	431	448
Cavity radius, mm	97	97
Ratio of the peak electric surface field to the accelerating field, E_p/E_{acc}	3.9	3.3
Ratio of the peak surface magnetic field to the accelerating field, B_p/E_{acc} , mT/(MV/m)	7.3	5.6
Effective shunt impedance, r/Q_0 , Ohm	252	303
Geometric factor, $G=R_s/Q$, Ohm	57	58

TEST CRYOSTAT DESIGN

It is proposed to use one cryostat to test either QWR's and HWR's. The liquid nitrogen free cryostat type was chosen. This cryostat has two liquid helium jackets. One detachable titanium jacket will be used for preliminary cryogenic tests only and the second jacket will be welded to the cavity for final tests. Beam ports should be closed by vacuum covers for these tests. Two different carrying insert covers used individually with two jackets. The general view and main dimensions of the designed cryostat is shown in Figure 6. Now the cryostat is ready for development and drawings preparation for the future manufacturing.

RF COUPLER FOR QWR/HWR

Each SC cavity will be equipped by the RF coupler and the RF measurement pickup. Coaxial power coupler type was chosen both for QWRs and HWRs [19] (see Figure 7). Coupler coaxial line has two identical ceramic vacuum windows. Two different feeding line shapes were considered: straight one (as shown on Fig.7) with feeding port located on the cryostat side and the second one with

90 degree elbow. The latter allows simpler cryostat design with RF power feedthrough via top cover.

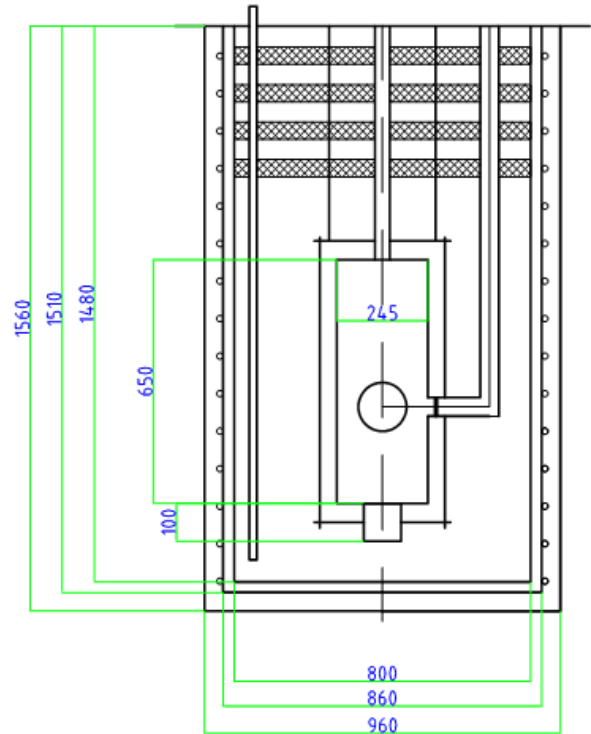


Figure 6: The general view and main dimensions of the cryostat for cryotests of QWR's and HWR's.

Outer and inner conductors of the coupler will be made of stainless steel. Optional thin layer of plated copper is considered for better electrical and thermal conductivity. This design was chosen because of low overall cost and cavity production capabilities despite the phase slipping occurred. It was decided to develop one power coupler suitable for all cavities. It requires cavity external Q-factor value to be varied for different cavities in the sections. Power coupler antenna is cylindrical and it couples to electric field in the cavity. The required external Q-factor tuning range calculated to be covered by the antenna with total tip penetration is varied within ± 10 mm.

Half-wave cavity power coupler located on the beamports plane has the same design as coupler for QWR described above (Figure 8). Coaxial line inner and outer conductors diameters are 20.44 mm and 47.5 mm. Necessary external Q-factor adjustment for coupling factor Q_0/Q_{ext} fall in desired range $\chi=(1.5 \dots 3) \cdot 10^3$. That requires antenna tip is retracted to 21...25 mm off the cavity wall (see Figure 9). Relatively small travelling is provided by bellows on feeding line outer conductor. The actuating mechanics able to operate in cryostat is under development.

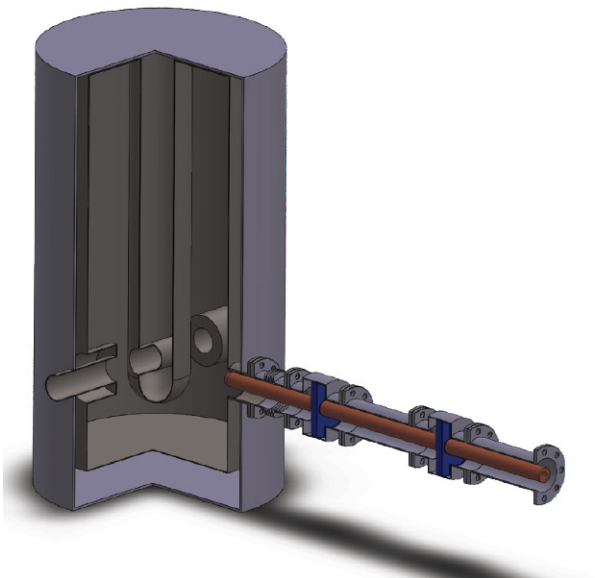


Figure 7: Assembly of the QWR with the coupler.

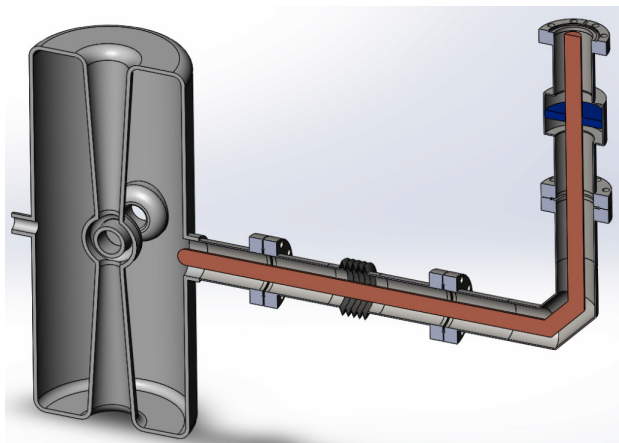


Figure 8: HWR with the coupler and field measurement pickup.

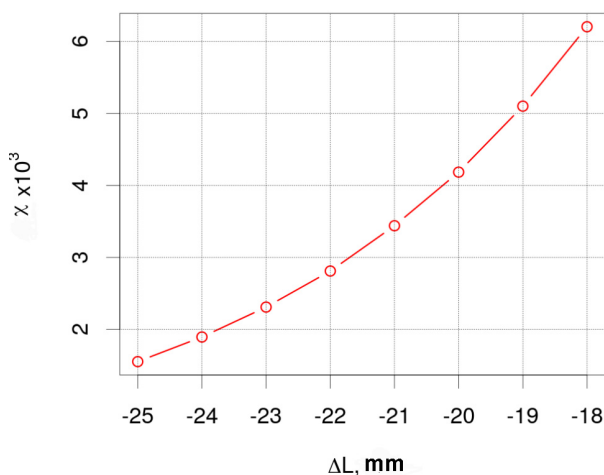


Figure 9: Coupling factor vs. antenna tip retraction length.

CONCLUSION

Current results of new SC proton linac development for JINR NICA project were discussed. Beam dynamics

simulation and cavities results were briefly presented. The design of QWR and HWR for new linac was discussed. Current activities in the test cryostat design and the RF couplers are also described.

ACKNOWLEDGEMENTS

Authors would like to thank Dr. W. Barth, Dr. S. Yaramyshev (GSI/HIM/MEPH), Dr. M. Miski-Oglu and Dr. V. German (GSI/HIM) for fruitful discussions and support.

REFERENCES

- [1] G. Trubnikov, N. Agapov, V. Alexandrov *et al.*, in *Proc. IPAC'10*, p. 693, 2010.
- [2] O. Kozlov, H. Khodzhibagiyan, S. Kostromin *et al.*, in *Proc. IPAC'11*, p. 1108, 2011.
- [3] A.V. Butenko, E.E. Donets, E.D. Donets *et al.*, in *Proc. IPAC'13*, p. 3915, 2013.
- [4] A.V. Butenko, E.E. Donets, E.D. Donets *et al.*, in *Proc. IPAC'14*, p. 2103, 2014.
- [5] A.V. Butenko, A.M. Bazanov, D.E. Donets *et al.*, in *Proc. IPAC'17*, pp. 2366-2368, 2017.
- [6] V.A. Andreev, A.I. Balabin, A.V. Butenko *et al.*, *Problems of Atomic Science and Technology. Series: Nuclear Physics Investigations*, vol. 6, no. 88, pp. 8-12, 2013.
- [7] A.V. Butenko *et al.*, in *Proc. RuPAC'16*, pp. 153-155, 2016.
- [8] G.V. Trubnikov, T.V. Kulevoy, S.M. Polozov *et al.*, *PEPAN Letters*, vol. 13, no. 7, pp. 943-946, 2016.
- [9] G.V. Trubnikov, T.V. Kulevoy, S.M. Polozov *et al.*, in *Proc. IPAC'16*, pp. 941-943, 2016.
- [10] M. Gusarova, T. Kulevoy, M.V. Lalayan *et al.*, in *Proc. RuPAC'16*, pp. 273-275, 2016.
- [11] G.V. Trubnikov, A.V. Butenko, N. Emelianov, *et al.*, in *Proc. IPAC'17*, pp. 3282-3285, 2017.
- [12] G.V. Trubnikov, T.V. Kulevoy, S.M. Polozov *et al.*, in *Proc. RuPAC'16*, pp. 626-628, 2016.
- [13] A.V. Samoshin, *Problems of atomic science and technology*, vol. 4, no. 80, pp. 78-82, 2012.
- [14] E. S. Masunov, A. V. Samoshin, *Technical Physics*, vol. 55, Issue 7, pp. 1028-1035, 2010.
- [15] E. S. Masunov, A. V. Samoshin, *Atomic Energy*, vol. 108, Issue 2, pp. 141-153, 2010.
- [16] D.V. Surkov, M.A. Gusarova, M.V. Lalayan *et al.*, in *Proc. IPAC'17*, pp. 1058-1060, 2017.
- [17] M.A. Gusarova, M.V. Lalayan, N.P. Sobenin *et al.*, in *Proc. IPAC'17*, pp. 1061-1063, 2017.
- [18] M. Gusarova, A.A. Gorchakov, M.V. Lalayan *et al.*, in *Proc. SRF'17*, pp. 125-127, 2017.
- [19] M.V. Lalayan, T.A. Bakhareva, M. Gusarova, S. V. Matsievskiy, in *Proc. SRF'17*, pp. 61-63, 2017.

STUDIES ON SUPERCONDUCTING DEUTERON DRIVER LINAC FOR BISOL *

F. Zhu[†], M. Chen, A.Q. Cheng, S.W. Quan, F. Wang, H.P. Li, J.K. Hao

State Key Laboratory of Nuclear Physics and Technology, Peking University, Beijing, China

Abstract

Beijing isotope separation on line type rare ion beam facility (BISOL) for both basic science and applications is a project proposed by China Institute of Atomic Energy and Peking University. Deuteron driver accelerator of BISOL would adopt superconducting half wave resonators (HWRs) with low beta and high current. The HWR cavity performance and the beam dynamic simulation of the superconducting deuteron driver accelerator will be presented in this paper.

INTRODUCTION

In China, a new large-scale nuclear-science research facility, namely the "Beijing Isotope-Separation-On-Line neutron rich beam facility (BISOL)", has been proposed and reviewed by the governmental committees. In Dec. 2016, the government has officially announced the results for the 13th 5-year plan. BISOL was successfully classed into the list of the preparation facilities. This facility aims at both basic science and application goals, and is based on a double-driver concept [1]. Figure 1 shows the schematic view of the BISOL facility. The intense deuteron driver accelerator (IDD) can be used to produce radioactive ion beam for basic research. It can also produce intense neutron beams for the material research associated with the nuclear energy system.

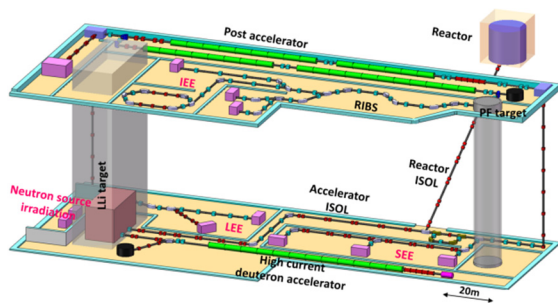


Figure 1: Schematic view of BISOL facility.

Figure 2 shows the layout of the deuteron accelerator. IDD consists of ECR ion source, low energy beam transport (LEBT), a radio frequency quadrupole (RFQ), a medium energy beam transport (MEBT), a superconducting rf (SRF) linac with four cryomodules, a high energy

beam transport (HEBT) and a liquid Lithium target system (LLT). The deuteron driver linac of BISOL aims to accelerate the beam up to 40 MeV with maximum beam current of 10 mA in phase I. In the future, the facility will be upgraded to accelerate CW deuteron beams with current of 50 mA. Table 1 gives the main design specifications of the deuteron accelerator. The beam dynamic simulation of the IDD for the first stage and the progress of the linac preparation will be presented in this paper.

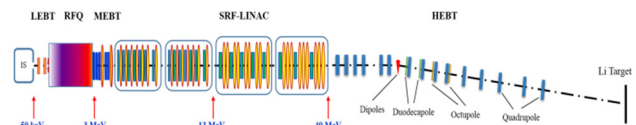


Figure 2: Layout of the deuteron accelerator.

Table 1: Design Parameters of the Deuteron Accelerator

Particles	Deuteron	
Energy	40	MeV
Current (Phase I)	10	mA
Beam power	400	kW
RF frequency	162.5	MHz
Duty factor	100	%
Beam loss	<1	W/m
Neutron flux	5×10^{14}	n/cm ² /s

BEAM DYNAMIC SIMULATION OF THE SRF DEUTERON LINAC

The deuteron beam is accelerated from 3 MeV to 40 MeV by the SRF linac after the RFQ and MEBT. Because its good mechanical properties and high performance, symmetric structure and thus has no dipole steering, HWR structure is adopted for the SRF linac. The SRF linac consists of two different families of half wave resonator (HWR) cavities with geometry beta β_g are 0.09 and 0.16, respectively. Table 2 shows the design parameters of the two families of HWR cavities.

Table 2: Properties of the Deuteron Accelerator

Properties	Low-beta	High-beta
Frequency (MHz)	162.5	162.5
β_g	0.09	0.16
Beam aperture (mm)	40	40

* Work supported by the National Basic Research Program of China (Grant No. 2014CB845504).

[†] Corresponding author: zhufeng7726@pku.edu.cn

Coupler port diameter (mm)	80	80
$L_{cav}=\beta\lambda$ (mm)	166	295
E_{pk}/E_{acc}	5.3	4.7
B_{pk}/E_{acc} (mT/(MV/m))	6.4	6.8
R/Q (Ω)	255	264
G (Ω)	39	58
Thickness (mm)	3.0	3.0
Operating gradient (MV/m)	6.0	6.5

The beginning two cryomodules are the same, each consists of seven periods of one solenoid and one low-beta HWR cavity. The third cryomodule consists of five solenoids and nine high-beta HWR cavities. And the last cryomodule contains three periods of one solenoid and three high-beta HWR cavities. The total length of SRF linac is 22.46 m and the length of three kinds of cryomodules are 4.99 m, 6.10 m and 5.60 m, respectively. The drift space between consecutive cryomodules has great influences on beam matching and it should be designed as short as possible. After considering space to install end covers of the cryostats, vacuum valves and beam instrumentation, the distance is set to be 26 cm.

Figure 3 presents the beam envelope at 3σ size in transverse and longitudinal plane through the SRF linac after optimization. The transverse rms beam size in SRF linac is approximately 2 mm and the beam pipe radius is 10 times the rms beam size. Particle phase space distribution at the exit of the SRF linac is shown in Figure 4. The normalized rms transverse emittances of the output beam are $\epsilon_x=0.23$ mm·mrad, $\epsilon_y=0.22$ mm·mrad, and the longitudinal emittance is $\epsilon_z=0.26$ mm·mrad. The emittance growths through the SRF-linac are 5% and 2% in the transverse and longitudinal planes.

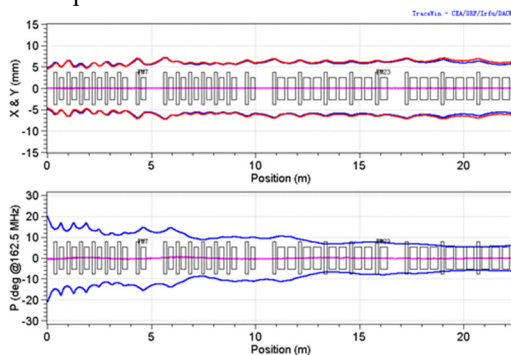


Figure 3: Envelope of deuteron beam along the SRF linac. Top: transverse envelope, x in blue and y in red. Bottom: longitudinal envelope.

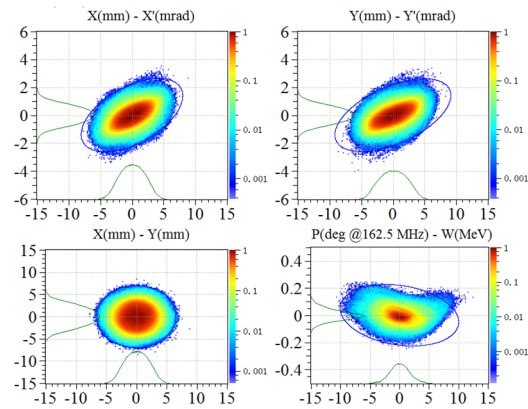


Figure 4: Particle phase space distribution at the exit of the SRF linac.

Multi-particles simulations from extraction of ion source to the end of SRF linac have been thoroughly carried out based on TraceWin code [2]. 10^7 macro-particles are used in the tracking and the normalized beam density is presented in Figure 5. In the transverse dimension, there is a comfortable margin between the beam external border and the pipe wall. The beam external border is relatively large in the drift space between consecutive cryomodules in the SRF linac. Almost all of the losses occur in the RFQ and MEBT and fulfill the requirement of beam loss. Figure 6 gives the normalized rms emittance along the BISOL deuteron linac. The emittance growth can be controlled well.

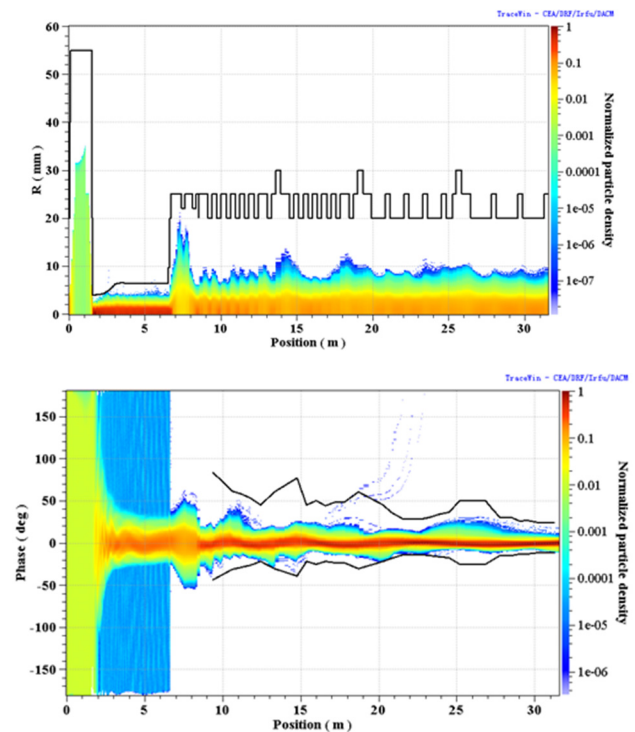


Figure 5: Beam density in transverse (top) and longitudinal (bottom) from start to end.

Content from this work may be used under the terms of the CC BY 3.0 licence (© 2018). Any distribution of this work must maintain attribution to the author(s), title of the work, publisher, and DOI.

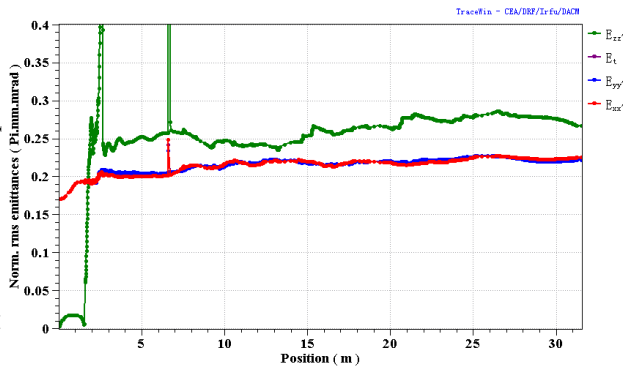


Figure 6: Normalized rms emittance along the BISOL deuteron driver linac.

The residual errors are inevitable because of the installation, manufacture and other reasons. The error study was also performed to prove the available and stability of the dynamics design.

HWR CAVITY PERFORMANCE

The HWR cavities were designed to accelerate 50 mA CW deuteron beams. We have finished the design, fabrication, surface treatment and vertical test of the $\beta_g=0.09$ HWR cavity [3].

The $\beta_g=0.09$ 162.5MHz HWR cavity has large aperture of 40 mm for high current beam acceleration. It is taper type and has ring-shaped centre conductor to have low surface fields, high shunt impedance and better mechanical properties [4]. The cavity parameters are listed in Table 2. The cavity short plates have asymmetric flat structure to suppress multipacting (MP) occurred at the short plates. Figure 7 shows the pieces during fabrication.



Figure 7: Fabrication of $\beta_g=0.09$ HWR cavity.

After fabrication, the HWR cavity was polished 150 μm by standard buffered chemical polishing (BCP) treatment, then 800°C high temperature treated, followed by a slight

BCP. At last, 100 bar high pressure rinsing (HPR) was performed to the cavity. A special nozzle with stem diameter of 20 mm and 13 holes was used to clean the HWR cavity efficiently through 8 ports.



Figure 8: Adjustable Q_e coupler structure for HWR cavity vertical test.

Figure 8 shows the external quality factor Q_e adjustable structure which can make the vertical movement into horizontal movement during Q_e adjustment. The antenna moving range is ± 20 mm and the corresponding Q_e adjustment range is about four orders of magnitude. At the first test, the RF power was coupled into the cavity through the beampipe and the antenna was inserted deep into the cavity for the proper Q_e . The cavity gradient only reached 10.7 MV/m at 4.2 K limited by strong field emission. Then we did another HPR and coupled power to the cavity through the large coupler port and tried the second vertical test of the HWR cavity. Figure 9 gives the vertical test results of the cavity at 4.2K and 2 K. The maximum gradient of the cavity reached 14.5 MV/m at 4.2K and 17 MV/m at 2 K, which is much higher than the operating gradient.

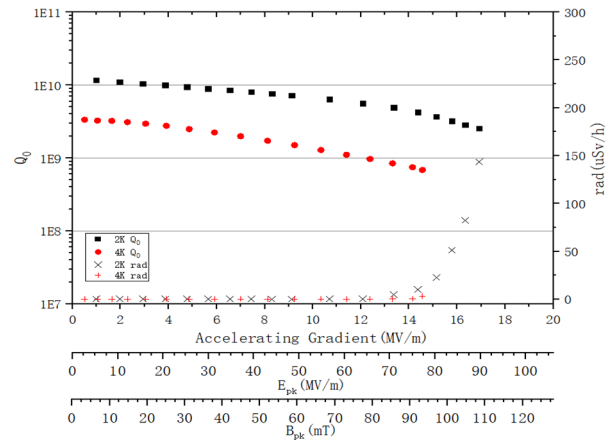


Figure 9: Q v.s. E_{acc} of the $\beta_g=0.09$ HWR cavity at 4.2 K and 2 K.

MP conditioning was done to the cavity before the Q v.s. E_{acc} measurement. Simulation result shows that there might be MP between the middle part of inner conductor and the outer conductor at very low gradient of about 0.02-

0.15 MV/m. Figure 10 shows the MP conditioning signal at frequency sweeping modes at 4.2 K. It normally takes half a day to eliminate MP.

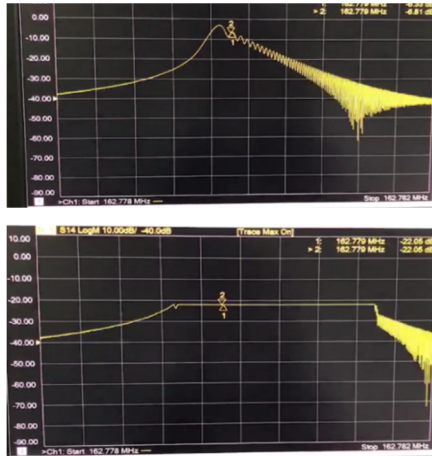


Figure 10: MP conditioning at frequency sweeping modes at 4.2K. Top: No MP. Bottom: MP was on.

During the vertical test, we also measured the mechanical parameters of the cavity. Figure 11 gives the frequency shift as the pressure or the gradient. We can get the Lorentz force detuning coefficient $K_L = -1.56 \text{ Hz}/(\text{MV}/\text{m})^2$ and $df/dP = -7.43 \text{ Hz}/\text{mbar}$.

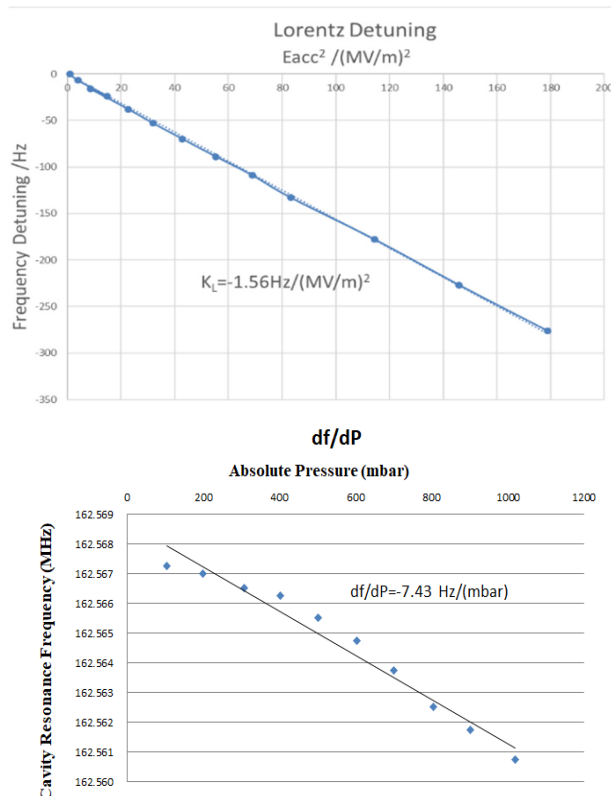


Figure 11: Lorentz force detuning measurement (top) and df/dP measurement (bottom).

CONCLUSION

Primary beam dynamic simulation of BISOL high current deuteron accelerator has been carried out. The simulation results predict that the proposed design can accelerate safely a 10 mA deuteron CW beam at 40 MeV. And the emittance growth and halo formation are under control. Error study was also performed to prove the available and stability of the dynamics design. We have designed, fabricated and vertical tested a $\beta_g = 0.09$ 162.5MHz taper type HWR cavity. The cavity was designed to accelerate deuteron beams with CW current of 50 mA. The vertical test showed it had high gradient and good mechanical properties. The maximum gradient reached 17 MV/m and Q value at low gradient is about 1×10^{10} .

ACKNOWLEDGEMENTS

The authors wish to thank members of the PKU BISOL collaboration who have contributed to beam dynamic study of BISOL deuteron accelerator and also thank my colleagues who have contributed to vertical tests of the HWR cavity.

REFERENCES

- [1] Yanlin Ye, Proposed BISOL Facility – a Conceptual Design, *EPJ Web of Conferences*, vol. 178, p. 01005, 2018.
- [2] TraceWin, <http://irfu.cea.fr/dacm/logiciels/>
- [3] F. Zhu, *et al.*, “Study on a low beta high current taper type superconducting half wave resonator for BISOL”, in *Proc. SRF’17*, Lanzhou, China, Jul. 2017, paper TUPB056.
- [4] P. L. Fan, F. Zhu, *et al.*, “Mechanical Analysis of a $\beta=0.09$ 162.5 MHz Taper HWR cavity”, *High Power Laser and Particle Beams*, vol.28, no.4, pp. 170-174, 2016.

HOLLOW ELECTRON-LENS ASSISTED COLLIMATION AND PLANS FOR THE LHC

D. Mirarchi*¹, H. Garcia Morales², A. Mereghetti, S. Redaelli, J. Wagner³
CERN, Geneva, Switzerland

W. Fischer, X. Gu, BNL, Upton, USA

G. Stancari, Fermilab, IL, Batavia, USA

¹also at The University of Manchester, Manchester, UK

²also at Royal Holloway, Egham, UK

³also at Johann Wolfgang Goethe-Universitat, Frankfurt, Germany

Abstract

The hollow electron lens (e-lens) is a very powerful and advanced tool for active control of diffusion speed of halo particles in hadron colliders. Thus, it can be used for a controlled depletion of beam tails and enhanced beam halo collimation. This is of particular interest in view of the upgrade of the Large Hadron Collider (LHC) at CERN, in the framework of the High-Luminosity LHC project (HL-LHC). The estimated stored energy in the tails of the HL-LHC beams is about 30 MJ, posing serious constraints on its control and safe disposal. In particular, orbit jitter can cause significant loss spikes on primary collimators, which can lead to accidental beam bump and magnet quench. Successful tests of e-lens assisted collimation have been carried out at the Tevatron collider at Fermilab and a review of the main outcomes is shown. Preliminary results of recent experiments performed at the Relativistic Heavy Ion Collider (RHIC) at Brookhaven, put in place to explore different operational scenarios studies for the HL-LHC, are also discussed. Status and plans for the deployment of hollow electron lenses at the HL-LHC are presented.

INTRODUCTION

The present LHC collimation system [1] has achieved excellent performance with cleaning inefficiency of about 1×10^{-4} and ensured safe operation without quenches from circulating beam losses with stored beam energies up to 270 MJ at 6.5 TeV [2–4]. Although this performance is very satisfactory, further improvements are deemed necessary for the High-Luminosity upgrade (HL-LHC) of the LHC [5–8] that aims at achieving stored energies of about 700 MJ. In this framework, the installation of hollow electron-lens (HEL) is considered as a possible option to improve various aspects of beam collimation. In particular, one of the main concerns come from the estimated stored energy in the beam tails. Various measurements have been carried out at the LHC, which show overpopulated tails with respect to usual gaussian assumption [9]. The scaling to HL-LHC beams lead to an estimation of about 30 MJ of stored energy in the beam tails. This large amount of energy can cause unforeseen beam dump in case of orbit jitter and fast failure scenarios related to crab cavities, due to the high losses that would

take place on primary collimators. Moreover, the deposited energy during these events can lead to magnet quench on beam loss peak around the machine, together with permanent damages to collimators. Thus, a controlled and safe disposal of overpopulated beam tails has been recommended by two international reviews carried out in recent years [10, 11].

LHC COLLIMATION SYSTEM AND ITS UPGRADE FOR HL-LHC

An illustrative picture of the working principle of the present collimation system is given in Fig. 1. The present LHC system [1, 2] is composed by 44 movable ring collimators per beam, placed in a precise multi-stage hierarchy that must be maintained in any machine configuration to ensure optimal cleaning performance. Two LHC insertions (IR) are dedicated to collimation: IR3 for momentum cleaning, i.e. removal of particles with a large energy offset (cut from $\delta p/p \sim 0.2\%$ for zero betatron amplitude); and IR7 for betatron cleaning, i.e. continuous controlled disposal of transverse halo particles. Each collimator insertion features a three-stage cleaning based on primary collimators (TCP), secondary collimator (TCSG) and absorber (TCLA). In this scheme, the energy carried by the beam halo intercepted by TCPs is distributed over several collimators (e.g. 19 collimators are present in the betatron cleaning insertion). Dedicated collimators for protection of sensitive equipment (such as TCTP for the inner triplets), absorption of physics debris (TCL) and beam dump protection (TCSP) are present at specific locations of the machine. A detailed description of these functionalities goes beyond the scope of this paper and can be found in [1].

The main upgrades of the present collimation system in the present HL-LHC baseline [6] are the replacement of one 8.3 T dipole in the IR7 Dispersion Suppressor with two 11 T dipoles and a collimator in-between, together with the replacement of present collimator jaws with low impedance material. Their aim is to improve the cleaning performance of the system, while reducing its contribution to the resistive wall impedance budget of the machine.

However, these upgrades go in the direction of improving the passive nature of the system and do not allow for an active control on overpopulated beam tails and their safe disposal. Several experimental tests are on-going in the LHC to study

* daniele.mirarchi@cern.ch

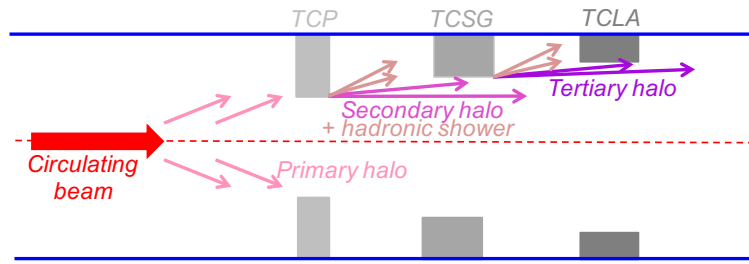


Figure 1: Working principle of the present collimation system.

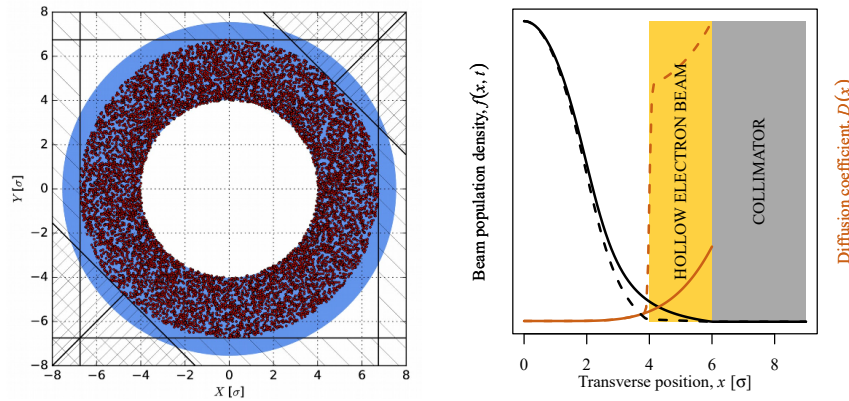


Figure 2: Concept of HEL assisted collimation: (left) the halo particles are shown by red dots, the geometrical cut performed by the horizontal–vertical–skew TCPs is represented by surrounding boxes and the hollow electron beam is depicted by the light blue ring overlapping with the halo particles and extending beyond the TCPs aperture; (right) qualitative illustration of diffusion coefficient and beam halo population with and without HEL shown by dashed and solid lines, respectively.

the possibility to perform such active control with present hardware [12–14]. Nevertheless, the installation of HEL represent one of the most promising option.

HEL Assisted Collimation

The concept of HEL assisted collimation consists of introducing an additional hierarchy layer represented by the hollow electron beam surrounding the proton beam for few meters, with the inner radius at a smaller aperture than TCPs [15]. An illustrative picture is reported in Fig. 2 (left), where beam halo particles are shown by red dots, the geometrical cut performed by the TCPs is represented by surrounding boxes and the hollow electron beam is depicted by the light blue ring overlapping with the halo particles and extending beyond the TCPs aperture. This allows to control the diffusion speed of halo particles with betatronic amplitude larger than the inner electron beam radius, depleting such halo between the beam core and TCPs. A qualitative illustration is reported in Fig. 2 (right).

In principle, the main benefit would be a loss spike free operation in the case of orbit jitter. Moreover, the control of halo population will help also in case of crab cavities fast failures. In particular, the worst accidental scenario is a phase slip that will induce a significant bunch rotation in the longitudinal plane [16]. Thus, a depleted halo population would reduce losses at TCPs also in this failure scenario. Additional benefits from a controlled diffusion speed would be a possible increase of impact parameters on TCPs with relative improvement of cleaning performance. If the

impedance budget of the machine allows, collimator jaws could be closed at smaller transverse amplitude thanks to the depleted halo, allowing a β^* and crossing angle reduction at the high-luminosity experiments [17].

Nevertheless, possible drawbacks due to a depopulated halo can be the loss of Landau damping, which could be mitigated thanks to a tunable inner radius of the electron beam. Detection of unusual loss rates is one of the most important observables for machine protection purposes. Thus, a depleted halo could jeopardize the performance of the present machine protection strategy. A solution could be the presence of witness bunch trains on which the HEL does not act. Perturbation to the circulating beam could come from residual field and imperfections of the magnets used to guide the electron beam and from the hollow electron beam itself. To minimize these effects, the preferred operation mode is DC on selected bunch trains, together with an “S” shape design to self-compensate edge effects. Perturbations from the electron beam itself are minimized ensuring its symmetric shape. Possible concerns are also the complexity of the device that includes many superconducting magnets. However, the operational experience at Tevatron and RHIC give us the required confidence on the high availability and low failure rate of the entire apparatus.

FERMILAB EXPERIENCE

Two e-lenses were installed in the Tevatron collider, which were used in operations for long range beam-beam compensation and abort gap cleaning [18–20]. Studies were also

Content from this work may be used under the terms of the CC BY 3.0 licence (© 2018). Any distribution of this work must maintain attribution to the author(s), title of the work, publisher, and DOI.

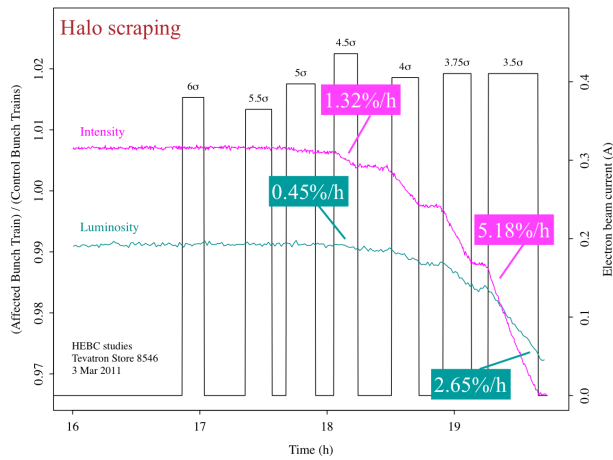


Figure 3: Normalized intensity and luminosity of the affected e-lens train with respect to the witness ones [21].

performed to demonstrate halo scraping with hollow electron beams [21, 22], which is of main interest in the context of this paper.

Several studies were performed to characterize the hollow electron beam as a function of magnetic field in the main solenoid and cathode-anode voltage [23]. This is crucial in order to provide the electron beam current required to enhance the halo diffusion speed, while ensuring its symmetry.

Another important milestone has been the demonstration of halo scraping without affecting the beam core. This evidence was obtained by injecting three trains of 12 antiproton bunches in the machine, with the HEL acting on only one of them. The bunch by bunch intensity and luminosity were monitored while changing the inner radius and current of the electron beam. Normalizing the intensity of the affected train with respect to the witness ones, it is possible to extrapolate if the loss rate is enhanced. On the other hand, the same normalization applied to the luminosity give us information regarding effects on the core. A decrease on normalized intensity at constant normalized luminosity, demonstrates that the loss rate of the affected train is enhanced acting on the diffusion speed of halo particles without any effect on the beam core. This is clearly visible in Fig. 3 [21].

As introduced previously, one of the main benefits of the installation in HL-LHC would be a loss spike free operation in the case of orbit jitter thanks to depleted beam halo. The reduced tail population thanks to HEL has been successfully proven by means of collimator scans, reported in Fig. 4 [24]. In particular, loss spikes coming from the affected train were observed about 300 μm after touching the tail of the witness train.

BROOKHAVEN EXPERIENCE

Two e-lenses are installed in the Yellow and Blue ring of the RHIC collider, which were used in p-p operations for head-on beam-beam compensation [25–32], where none of the 112 stores was aborted due to e-lens equipment failure. A gaussian beam overlapping to the proton beam is

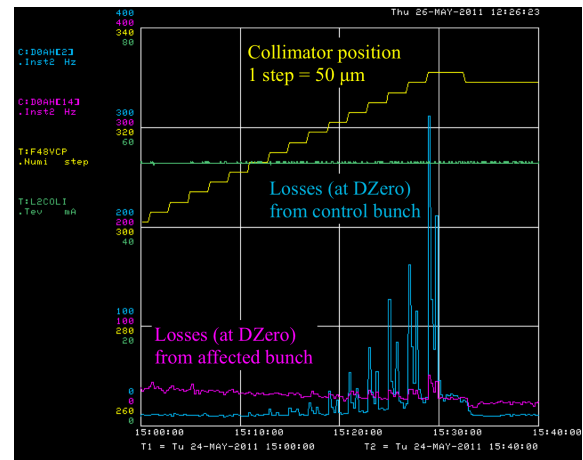


Figure 4: Loss spikes from affected and witness train during collimator scraping [15].

required for these purposes. Presently, and until the completion of the sPHENIX detector upgrade, only heavy ions are used in operation, which do not require head-on beam-beam compensation. Thus, it was agreed to change the electron gun of the e-lens in the Yellow ring in order to provide an hollow electron beam. Being the only active e-lens in the world, this provides a unique opportunity to explore different operational scenarios studies for the HL-LHC.

Different tests have been performed and are still on-going. One of the main achievements was the successful demonstration that back-scattered electrons can be used to centre the electron beam around the circulating one. The electron beam is kept stable while the circulating beam is moved by means of a local 4-correctors bump. When the main beam intercepts the electrons some of them are back-scattered and detected [33]. Due to the fact that back scattered electrons are guided by the solenoidal fields in the e-lens, they are deflected upward making impossible measurements on the bottom part of the electron beam. To overcome this limitation, different scans in the horizontal plane are performed for different vertical position. The main beam is then centered in the position that minimizes the rate of back-scattered electrons for different vertical positions. In principle, this operation should be repeated also for different angles of the main beam. However, this procedure was skipped for these first tests due to the significant time needed and good confidence obtained by varying the beam angle for fixed transverse positions.

Similar measurements as done at Tevatron were repeated with 100 Z GeV Ru and 13.6 Z GeV Au beams. In particular, two trains of 28 Ru bunches were injected in the two RHIC rings, with the e-lens acting only on one train in the Yellow ring. First the electron beam inner radius (r) was changed with a fixed electron beam current (I), while monitoring bunch-by-bunch losses and integrated loss rate in the two beams. As second test, r was fixed and I was changed. Measured bunch-by-bunch losses were integrated for each train and losses from the affected train were normalized with respect to the witness one. Normalized bunch-by-bunch

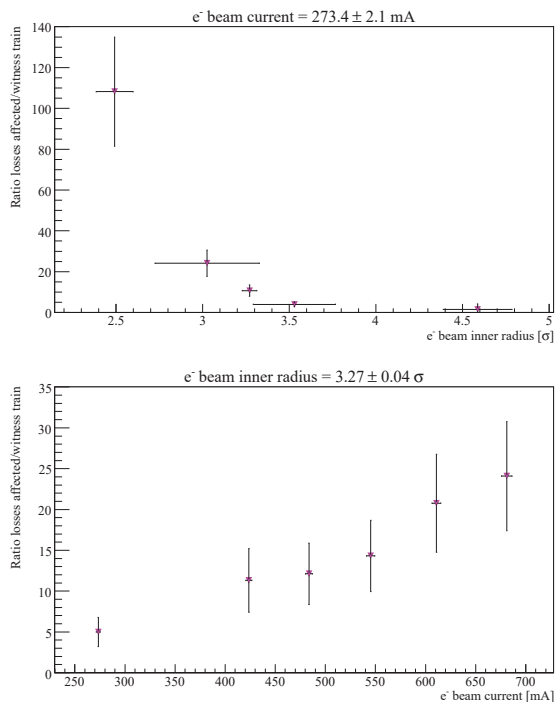


Figure 5: (top) Normalized bunch by bunch losses varying inner electron beam radius and (bottom) electron beam current.

losses during the two measurements are shown in Fig 5. As clearly visible a $1/r$ trend is observed in the losses while changing r , while a linear trend as a function of I is observed when varying I .

Similar tests were performed with 13.6 Z Au beams, in which scans of octupoles and chroma were also performed with fixed radius and current of the electron beam. Moreover, bunch by bunch luminosity were also available allowing to study effects on the circulating beam core. Encouraging results were observed on-line, the detailed off-line analysis is on-going.

LHC PLANS

Two international reviews [10, 11] were carried out to assess the need, cost and readiness for the installation of the HEL in the LHC tunnel, in particular for operations in the HL-LHC era. Although they are not yet part of the HL-LHC baseline, their installation was recommended and final integration studies are on-going.

HEL Design

The candidate locations for the HELs installation in the LHC tunnel are at both sides of the interaction region IR4. This location provides the required distance between the two beams and the longitudinal space. The main requirements are: compact design, reasonable magnetic fields in the solenoids, smooth and high magnetic fields in the transition regions, technically feasible dimensions and current density of the cathode, adjustable inner radius of the electron beam to be adapted to the beam size for different energies. The

present design [34] that fulfill all these requirements is shown in Fig. 6 and functional specifications are reported in Table 1. The main components are the main solenoid that ensures 3 m of overlap between the circulating and electron beams, two bending solenoids for the injection and extraction of the electron beam, electron gun solenoid to adjust the inner radius of the electron beam. Several corrector coils are also present. All the magnets involved are superconducting and the “S” shape of the entire assembly allow to self-compensate edge effects. Thermal and structural verification were performed by means of numerical simulations for all the components, from the electron gun to the collector [35].

Table 1: Design Parameters for the HL-LHC HEL [36]

Parameter	Value or range
Magnetic field main solenoid [T]	5
Magnetic field cathode [T]	0.2 - 2
Inner radius electron beam [mm]	0.9 - 5.67
Outer radius electron beam [mm]	1.8 - 11.34
Inner diameter cathode [mm]	8.05
Outer diameter cathode [mm]	16.10
Nominal current cathode [A]	5

Cryogenics

As described above, all the magnets in the HEL are superconducting. Thus, a solid connection to the cryogenic system is required. Upgrades of the cryogenic system in IR4 are foreseen in the framework of HL-LHC, aiming at providing cooling capacity and distribution to match the needs with efficient solutions without making it the weakest sector, allowing to connect future users such as the HEL. The present concept could be integrated to the cryogenic system of the LHC without any showstopper [37].

Beam Instrumentation

Beam instrumentation concepts are based on experience in FNAL and BNL. The main requirements to allow reliable HEL operations are: alignment of proton and electron beams with resolution $< 60 \mu\text{m}$, profile and current measurements of the electron beam, beam loss monitoring for solenoid quench protection. The preliminary baseline detectors are: beam position monitors for general alignment of proton and electron beams, gas jet curtain combined with luminescence detection for characterization of the electron beam and relative alignment with respect to circulating beam, standard LHC ionization chamber for beam loss monitoring [38]. Possible options could be also back-scattered electron detector and YAG Screen in the case of problems with gas jet curtain combined with luminescence.

Operational Aspects

Several operational aspects were taken into account [39]. A round pipe of 60 mm radius is foreseen, in order to avoid issues in terms of available aperture for the circulating beam.

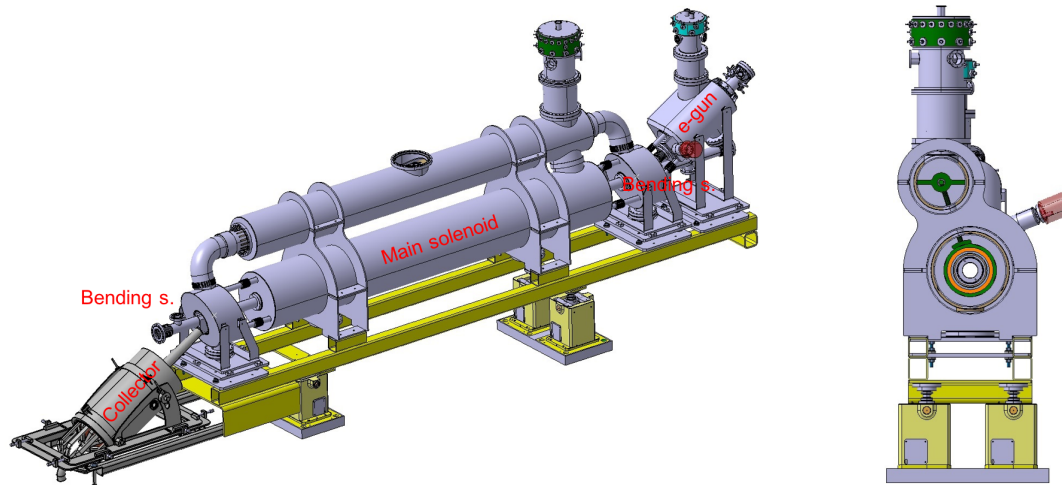


Figure 6: (left) Side and (right) front view of the present HL-LHC hollow electron lens design.

Effect of linear coupling from solenoidal fields show a negligible effect. In case of quench, missing dipole kick could cause losses and a proper interlock strategy is needed. Impedance calculations on pipe were performed using CST Particle Studio [40], which show good performance and negligible impact to total machine impedance budget. The “S” shape of e-lens is conceived so that the effect on the proton beam core from the two electron beam crossings cancels out. However, dipolar kicks from bending solenoids add up. Thus, a dedicated orbit corrector connected in series with the bending solenoids is foreseen. Moreover, also imperfections on the bends or electron beam profile can induce a non-zero kick at the center of the beam. All these effects, except dipolar kick from bending solenoids, are negligible in DC operations but can become significant for pulsed modes. Thus, several simulation and experimental studies were carried out in 2016 and 2017 [41, 42] in order to find possible pulsing operation mode that would enhance the HEL effect without jeopardizing machine performance and its protection.

CONCLUSIONS

A wide overview of HEL assisted collimation tests done in different laboratories has been reported, together with plans for the LHC and its upgrade HL-LHC. Their installation in the LHC tunnel can lead to several benefits for operations in the HL-LHC era, in particular for an active control of the about 30 MJ of expected stored energy in the beam tails. Possible drawbacks have been studied and appropriate solutions have been found. Experimental and operational experiences at Tevatron and RHIC show results in agreement with expectations, with an extremely high hardware reliability despite their complexity. Although HEL are not yet part of the HL-LHC baseline, their integration has been recommended by two international reviews. All the relevant aspects for HEL installation have been studied and its design is considered mature for a possible installation. Final and

detailed tracking simulation studies are on-going to define optimal operational scenario.

ACKNOWLEDGEMENTS

This manuscript has been authored by Fermi Research Alliance, LLC under Contract No. DE-AC02-07CH11359 with the U.S. Department of Energy (DOE), Office of Science, Office of High Energy Physics. This work was partially supported by the U.S. DOE LHC Accelerator Research Program (LARP), by the European FP7 HiLumi LHC Design Study, Grant Agreement 284404, and by the High Luminosity LHC (HL-LHC) Project.

REFERENCES

- [1] R. Assmann *et al.*, “The final collimation system for the LHC”, in *Proc 10th European Particle Accelerator Conference (EPAC’08)*, Edinburgh, UK, 26–30 Jun 2006, pp. 986.
- [2] G. Valentino *et al.*, “Performance of the Collimation System during 2015”, in *Proc. 6th Evian Workshop on LHC beam operation*, Evian Les Bains, France, 15–17 Dec 2015, pp. 149–154.
- [3] D. Mirarchi *et al.*, “Collimation: experience and performance”, in *Proc. 7th Evian Workshop on LHC beam operation*, Evian Les Bains, France, 13–15 Dec 2016, pp. 105–112.
- [4] A. Mereghetti *et al.*, “Beam Losses, lifetime and collimators hierarchy”, 8th Evian Workshop on LHC beam operation, Evian Les Bains, France, 12–14 Dec 2017.
- [5] G. Apollinari *et al.*, “High Luminosity Large Hadron Collider HL-LHC”, High-Luminosity Large Hadron Collider (HL-LHC).
- [6] B. Alonso *et al.*, “HiLumi LHC Technical Design Report”, CERN-ACC-2015-0140.
- [7] The HiLumi LHC Collaboration, “HL-LHC Preliminary Design Report: FP7 HiLumi LHC Deliverable D1.5”, CERN-ACC-2014-0300.

- [8] G. Arduini *et al.*, “High Luminosity LHC: challenges and plans”, *JINST*, vol. 11, pp. C12081 (2016), doi:10.1088/1748-0221/11/12/C12081
- [9] G. Valentino *et al.*, “What did we learn about HALO population during MDs and regular operation?”, Review of the needs for a hollow e-lens for the HL-LHC, CERN, 6–7 Oct 2016.
- [10] Review of the needs for a hollow e-lens for the HL-LHC, <https://indico.cern.ch/event/567839/>
- [11] International Review on the e-lens concept readiness for integration into the HL-LHC baseline, <https://indico.cern.ch/event/648237/>
- [12] H. Garcia Morales *et al.*, “MD 1691: Active halo control using tune ripple at injection”, CERN-ACC-NOTE-2017-0031.
- [13] H. Garcia Morales *et al.*, “MD 2485: Active halo control using narrowband and colored noise excitations”, CERN-ACC-NOTE-2018-0020.
- [14] J. Wagner *et al.*, “Active halo control through narrow-band excitation with the ADT at injection”, CERN-ACC-NOTE-2016-0062.
- [15] G. Stancari, “New methods of particle collimation in colliders”, arXiv:1110.0144[physics.acc-ph].
- [16] D. Wollmann *et al.*, “Potential failure scenarios that can lead to very fast orbit changes and machine protection requirements for HL-LHC operation”, Review of the needs for a hollow e-lens for the HL-LHC, CERN, 6–7 Oct 2016.
- [17] G. Arduini *et al.*, “Potential performance reach for the HL-LHC in case of a depleted beam halo”, Review of the needs for a hollow e-lens for the HL-LHC, CERN, 6–7 Oct 2016.
- [18] V. Shiltsev *et al.*, “Experimental demonstration of colliding-beam-lifetime improvement by electron lenses”, *Phys. Rev. Lett.*, vol. 99, pp. 244801 (2007), doi:10.1103/PhysRevLett.99.244801
- [19] X.L. Zhang *et al.*, “Generation and diagnostics of uncaptured beam in the Fermilab Tevatron and its control by electron lenses”, *Phys. Rev. ST Accel. Beams*, vol. 11, pp. 051002 (2008), doi:10.1103/PhysRevSTAB.11.051002
- [20] G. Stancari *et al.*, “Beam-beam compensation studies in the Tevatron with electron lenses”, in *Proc. ICFA Mini-Workshop on Beam-Beam Effects in Hadron Colliders*, CERN, Geneva, Switzerland, 18–22 Mar 2013, pp. 121–125.
- [21] G. Stancari *et al.*, “Collimation with hollow electron beams”, *Phys. Rev. Lett.*, vol. 107, pp. 084802 (2011), doi:10.1103/PhysRevLett.107.084802
- [22] G. Stancari *et al.*, “Measurements of transverse beam diffusion rates in the Fermilab Tevatron collider”, in *Proc. 11th International Particle Accelerator Conference (IPAC’11)*, San Sebastian, Spain, 4–9 September 2011, pp. 1882, paper TUPZ033.
- [23] G. Stancari *et al.*, “Characterization of the CERN hollow electron gun at the Fermilab electron-lens test stand”, 84th Collimation Upgrade Specification Meeting, <https://indico.cern.ch/event/623634/>
- [24] G. Stancari *et al.*, “Measured effects of depleted halo population with hollow e-lens and relevance for HL-LHC”, Review of the needs for a hollow e-lens for the HL-LHC, CERN, 6–7 Oct 2016.
- [25] X. Gu *et al.*, “The effects of realistic pancake solenoids on particle transport”, *Nucl. Instrum. Methods A*, vol. 637, pp. 190 (2011), doi:10.1016/j.nima.2011.01.123
- [26] Y. Luo *et al.*, “Six-dimensional weak-strong simulation of head-on beam-beam compensation in the Relativistic Heavy Ion Collider”, *Phys. Rev. ST Accel. Beams*, vol. 15, pp. 051004 (2012), doi:10.1103/PhysRevSTAB.15.051004
- [27] X. Gu *et al.*, “The electron lens test bench for the relativistic heavy ion collider at Brookhaven National Laboratory”, *Nucl. Instrum. Methods A*, vol. 743, pp. 56 (2014).
- [28] W. Fischer *et al.*, “Operational head-on beam-beam compensation with electron lenses in the Relativistic Heavy Ion Collider”, *Phys. Rev. Lett.*, vol. 115, pp. 264801 (2015), doi:10.1103/PhysRevLett.115.264801
- [29] Y. Luo *et al.*, “Analysis and modeling of proton beam loss and emittance growth in the Relativistic Heavy Ion Collider”, *Phys. Rev. Accel. Beams*, vol. 19, pp. 021001 (2016), doi:10.1103/PhysRevAccelBeams.19.021001
- [30] P. Thieberger *et al.*, “High energy Coulomb-scattered electrons for relativistic particle beam diagnostics”, *Phys. Rev. Accel. Beams*, vol. 19, pp. 041002 (2016), doi:10.1103/PhysRevAccelBeams.19.041002
- [31] X. Gu *et al.*, “Electron lenses for head-on beam-beam compensation in RHIC”, *Phys. Rev. Accel. Beams*, vol. 20, pp. 023501 (2017), doi:10.1103/PhysRevAccelBeams.20.023501
- [32] W. Fischer *et al.*, “Compensation of head-on beam-beam induced resonance driving terms and tune spread in the Relativistic Heavy Ion Collider”, *Phys. Rev. Accel. Beams*, vol. 20, pp. 091001 (2017), doi:10.1103/PhysRevAccelBeams.20.091001
- [33] P. Thieberger *et al.*, “High energy Coulomb-scattered electrons for relativistic particle beam diagnostics”, *Phys. Rev. Accel. Beams*, vol. 19, pp. 041002 (2016), doi:10.1103/PhysRevAccelBeams.19.041002
- [34] D. Perini *et al.*, “Summary of reference design and CERN reference baseline overview”, International Review on the e-lens concept readiness for integration into the HL-LHC baseline, CERN, 19–20 Oct 2017.
- [35] G. Gobbi *et al.*, “Injector and dump design details and developments”, International Review on the e-lens concept readiness for integration into the HL-LHC baseline, CERN, 19–20 Oct 2017.
- [36] S. Redaelli *et al.*, “Functional specifications and parameter requirements”, International Review on the e-lens concept readiness for integration into the HL-LHC baseline, CERN, 19–20 Oct 2017.
- [37] S. Claudet *et al.*, “Existing technical infrastructure boundaries (cryogenics)”, International Review on the e-lens concept readiness for integration into the HL-LHC baseline, CERN, 19–20 Oct 2017.
- [38] R. Jones *et al.*, “Proposed beam instrumentation for the hollow electron lens”, International Review on the e-lens concept readiness for integration into the HL-LHC baseline, CERN, 19–20 Oct 2017.
- [39] R. Bruce *et al.*, “Operational aspects and machine protection considerations”, International Review on the e-lens concept readiness for integration into the HL-LHC baseline, CERN, 19–20 Oct 2017.

- [40] <https://www.cst.com>
- [41] M. Fitterer *et al.*, “Effects of resonant and random excitations on the proton beam in the Large Hadron Collider, with applications to the design of pulsed hollow electron lenses for active halo control”, arXiv:1804.07418[physics.acc-ph]
- [42] J. Wagner *et al.*, “Hollow Electron Lens for HL-LHC: Effect on tails”, Joint LARP CM28/HiLumi Meeting, Embassy Suites, Napa, CA, <https://conferences.lbl.gov/event/76/other-viewfr=no&view=ATAPCrystalClear&showSession=all&showDate=all>

BEAM INSTRUMENTS FOR HIGH POWER SPALLATION NEUTRON SOURCE AND FACILITY FOR ADS

Shin-ichiro Meigo*, J-PARC Center, Japan Atomic Energy Agency (JAEA), Ibaraki 319-1195, Japan

Abstract

As increase of beam power, beam instruments play an essential role in the Hadron accelerator facility. In J-PARC, the pitting erosion on the mercury target vessel for the spallation neutron source is one of a pivotal issue to operate with the high power of the beam operation. Since the erosion is proportional to the 4th power of the beam current density, the minimization of the peak current density is required. To achieve low current density, the beam-flattening system by nonlinear beam optics using octupole magnets in J-PARC. By the present system, the peak density was successfully reduced by 30% compared to the conventional linear optics. Also in J-PARC, transmutation experimental facility is planned for the realization of the accelerator-driven system (ADS), which will employ powerful accelerator with the beam power of 30 MW. To achieve similar damage on the target as the ADS, the target will be received high current density. For the continuous observation of the beam status on the target, a robust beam profile monitor is required. Beam profile monitors have been developed with irradiation of the heavy-ion of Ar to give the damage efficiently.

INTRODUCTION

In the Japan Proton Accelerator Research Complex (J-PARC) [1], a MW-class pulsed neutron source, the Japan Spallation Neutron Source (JSNS) [2], and the Muon Science facility (MUSE) [3] will be installed in the Materials and Life Science Experimental Facility (MLF) shown in Fig. 1. Since 2008, this source has produced a high-power proton beam of 300 kW. In 2015, J-PARC successfully ramped up beam power to 500 kW and delivered the 1-MW beam to the targets. To produce a neutron source, a 3 GeV proton beam collides with a mercury target, and to produce a muon source, the 3 GeV proton beam collides with a 2-cm-thick carbon graphite target. To efficiently use the proton beam for particle production, both targets are aligned in a cascade scheme, with the graphite target placed 33 m upstream of the neutron target. For both sources, the 3 GeV proton beam is delivered from a rapid cycling synchrotron (RCS) to the targets by the 3NBT (3 GeV RCS to Neutron facility Beam Transport) [4–6]. Before injection into the RCS, the proton beam is accelerated up to 0.4 GeV by a LINAC. The beam is accumulated in two short bunches and accelerated up to 3 GeV in the RCS. The extracted 3 GeV proton beam, with a 150 ns bunch width and a spacing of 600 ns, is transferred to the muon production target and the spallation neutron source.

As the increase of beam power, beam profile monitoring plays an important role to avoid the damage to the target

Therefore it is imperative to watch continuously the status of the beam at the target at the JSNS especially for the peak current density. At the MLF, a reliable beam profile monitor has been developed with Multi-Wire Profile Monitor (MWPM). In order to watch the two-dimensional profile on the target, a beam profile monitor system has been developed base on the imaging of radiation of the target vessel after beam irradiation. For observation beam introduced to the target, MWPM was placed at the proton beam window. Furthermore, in J-PARC center, facilities for research and development for Accelerator Driven System (ADS) is planned. To satisfy the users' demand for neutron and muon, a new target facility called second target station is also planned. In those facilities, the beam will be more focused than the JSNS employs so that a robust beam profile monitor will be required [7], which will stand higher current density than the JSNS.

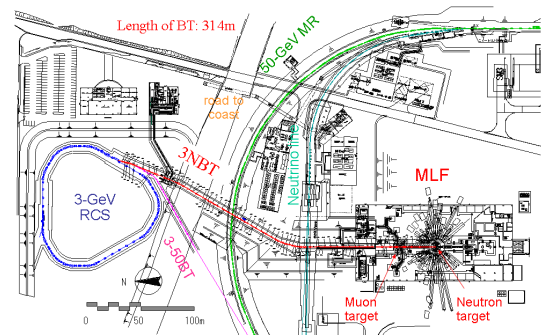


Figure 1: Plan of rapid cycling synchrotron (RCS) at the Materials and Life Science Experimental Facility (MLF) at J-PARC.

BEAM MONITOR SYSTEM AT THE BEAM TRANSPORT TO THE TARGET

Monitors Placed at Proton Beam Window

Continuously observing the characteristics of the proton beam introduced to the spallation target is very important. Due to the high activations caused by the neutron produced at the target, remote handling technique is necessary to exchange the beam monitor for the target. In order to decrease the radiation produced at the spallation neutron target, shielding above the monitor was required. To reduce the difficulties of the exchange work and decrease of the shielding, beam monitors were coupled with a Proton Beam Window (PBW) utilized as a physical separation between the vacuum region of the accelerator and the helium region around the neutron target. The PBW is better to be placed closer to the target where the distance between the target and the PBW is 1.8

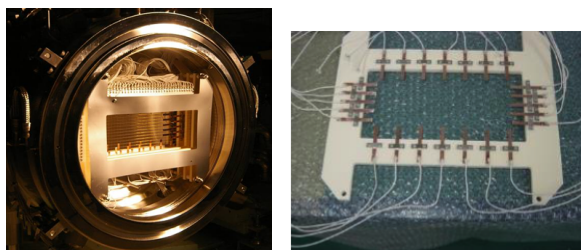
* meigo.shinichiro@jaea.go.jp

Content from this work may be used under the terms of the CC BY 3.0 license (©2018). Any distribution of this work must maintain attribution to the author(s) and the work publisher and DOI.

an, which gives reliable profile at the target. In Fig. 2, the MWPM placed at the center of a vacuum chamber of the PBW is shown. To avoid excessive heat at target vicinities, beam halo monitors are placed as well. The chamber of the PBW has inflatable vacuum seal called pillow seal. Due to the pillow seal, the monitors can be changed by the remote handling. To calibrate the sensitivity of each wire, the signal was observed by the scanning the position with narrow width beam. It was found that the difference of individual sensitivity was 6% at most.

In an actual beam operation, the heat at the target vicinities such as shielding, which mainly does not have water cooling channel, is necessary for reducing the peak density. Beam halo monitors attached at the PBW to observe the heat deposition at the target vicinities such as reflector and shielding, which is not allowed to exceed 1 W/cm^3 . A close-up view of the beam halo monitor is also shown in Fig. 2. Two types of beam halo monitors were utilized to obtain the thermal information by thermocouples and the emission of an electron by the electrode. Since the emission of electron indicates relative intensity of the beam halo, the beam halo relative strength, which can be normalized by the following thermal observation, can be obtained by several shots of the beam. To observe the absolute intensity of the halo, the thermocouple type was implemented, which consists of copper strips coupled with the thermocouple. With 5 minutes of 25 Hz beam operation, the absolute intensity of the beam halo can be determined by the differential of temperature by time. These procedures were typically performed in actual beam operation.

The temperature observed by the thermocouples gives essential information to the operator, which are included in the machine protection system (MPS). On May 27 in 2018, a quadrupole magnet had a malfunction of layer short, which lost field about 30% at a pole. Due to the magnetic center shift, the beam center at the target was offset about 20 mm at the target for both horizontal and vertical directions. In such abnormal condition, the beam halo monitors detected anomaly by the temperature of thermocouples, which immediately halted the beam and noticed operators the anomaly.



(a) Beam monitors placed at the PBW (b) Halo monitor

Figure 2: Multit-Wire Profile Monitor (MWPM) and beam halo monitors placed at the Proton Beam Window (PBW). (a) Whole view of the MWPM and halo monitors. (b) Close-up of the thermocouple type of beam halo monitors.

Since wires at the MWPM placed at the PBW are fixed type and continuously irradiated with the beam, long lifetime wire is required. The profile monitor at the PBW is essential so that a redundant system using SiC and tungsten wires was applied. In summer of 2013, some spots were observed at the surface of helium side of the PBW, which were thought to be produced by the erosion with the nitric acid produced by the radiolysis around the target. The 1st PBW has already received the integration beam power of 2 GWh to the new one. After exchange 1st PBW, because of stability of signal, only SiC wires were employed, which were deployed 2nd PBW. After 4 years operation, the 2nd PBW was changed in summer of 2017.

Lifetime of SiC Wires

As a material of sensitive wire, usually, tungsten wire is selected due to the large emission amount of the electron and having a high-temperature melting point. In the present system, silicon carbide (SiC) was chosen due to the high resistance of the radiation, which is thought to survive up to 80 DPA [8]. To obtain accurate displacement on the wire, a measurement of the displacement cross section has started for 0.4 to 3 GeV protons [9, 10].

Due to the interaction, the beam loss is caused, which is one of the issues of the high-intensity proton accelerator and the optimization of the beam loss is essential. The angular differential cross-section of Coulomb scattering is proportional to a square of an atomic number of the wire material. Since the average atomic number of the SiC is about 10, the cross-section of the SiC becomes 2% of tungsten. Therefore, a material of low atomic number has an advantage for the loss and distortion of the beam.

Until receiving 2 GWh, the wires still gave standard signals and, it was not found severe damage by inspection after irradiation. However, slight elongation of the SiC wires was observed as shown in Fig. 3. This elongation could be caused by the periodical thermal expansion of wire. By revision fixing of the wire, the elongation can be thought to be mitigated, which will be applied next generation of the monitor.

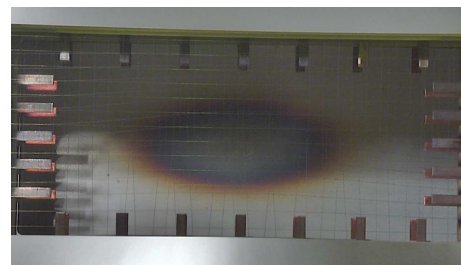


Figure 3: Elongated SiC wire utilized as the MWPM on the 1st PBW.

Beam Profile with Nonlinear Optics

To obtain the beam profile at the neutron source, the SAD code is utilized, which provide beam information by fitting

the result given by the MWPM placed at upstream of the octupole magnet. Also revised DECAF-TURTLE [11] by Paul Scherrer Institute (PSI) [12] is utilized to simulate multiple scattering at the muon target. Figure 4 shows results of beam profile for 800 kW beam with and without excitation of the octupole magnets. The beam profile is shown in Fig. 4, which was observed by the MWPM placed at the PBW. It can be found that considerable flat distribution can be obtained by the nonlinear optics. The calculation results with and without excitation are also shown in Fig. 4. The calculation shows good agreement with the experiment for the cases with and without octupole magnetic field. It is also confirmed that the calculated beam profile by using the muon target showed good agreement with the experiment for both cases with and without octupole magnetic field. By the calculation result, the peak density can be thought to be reduced by 30% compared with the linear optics.

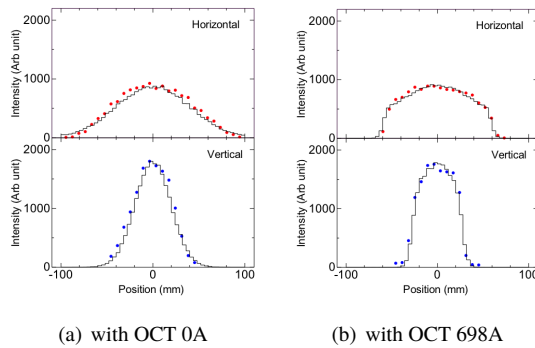


Figure 4: Beam profile obtained with calculations (line) compared with result by the MWPM (dots) supplying current of (a) 0 A and (b) 698 A to octupole magnet. Upper and bottom figure represents for horizontal and vertical directions, respectively.

DEVELOPMENT OF NEW PROFILE MONITOR

Until now the wire of the monitor survived up to 2 GWh, which was at attached the first and the second generation of the PBW, however, it is not clear that the MWPM will survive for the long duration of 1 MW beam. The lifetime of the PBW is expected as 2 years for 1 MW beam [13], which has proton fluence $2 \times 10^{21} \text{ cm}^{-2}$ and the integral beam power of 10 GWh. To observe beam profile in 2D, an online type profile monitor is desired because the present 2D beam profile by IP can be obtained after the irradiation. Therefore a new beam profile monitor based on luminescence due to the beam was started to develop.

Beam Imaging Test Using Ar Beam

In order to obtain a 2D profile on the target, luminescence monitor is planned which is painted on the vessel of the mercury target. It was reported that degradation of luminescence was observed by the profile monitor used at the SNS

in ORNL so that the intensity of light was observed by using $^{40}\text{Ar}^{+15}$ with total kinematic energy of 150 MeV, providing 10^6 times displacement on the sample than 3-GeV protons at Takasaki Advanced Radiation Research Institute (TIARA) of Quantum Beam Science Research Directorate (QST). To simplify the damage on the light emission, flat-shaped beam distribution was employed with nonlinear focus made by octupole field [14]. In the experiment, AF995R (Al_2O_3 99.5% and CrO_3 0.5%, Demarquest) with a thickness of 5 mm and DRZ-High ($\text{Gd}_2\text{O}_2\text{S:Tb}$) with a thickness of 5 mm were irradiated with Ar beam. The spectrum of the photon emitted from the sample was observed with the spectrometer (Flame-NIR: Ocean Photonics).

For the development of profile monitor system, the image of the luminescence from the AF995R and DRZ-High ($\text{Gd}_2\text{O}_2\text{S:Tb}$) was observed with the ordinary CCD camera through imaging fiber (Fujikura FISR-20) having 20,000 pixels and length of 5 m having high radiation hardening.

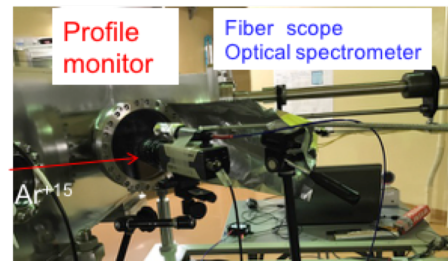


Figure 5: Experimental setup of beam profile imaging system for Ar beam irradiation.

Result of Beam Imaging

The 2D image of the beam obtained by the AF995R and DRZ-High is shown in Fig. 6, which is utilized square flat beam by nonlinear optics. Since the ordinary CCD camera was utilized being insensitive to the light in the long wavelength, the red light emitted from the AF995R was observed to be low intensity. Using 3 CCD camera being less dependence on wavelength, a clear image will be obtained. The DRZ-High has high photon emission rate in short wavelength, so that the image was clear and high intensity. However, the degradation of light yield was found to be more rapid than AF995R. By the present system, it was demonstrated that a clear image of the beam profile can be obtained.

Result of Luminescence Spectrum and Intensity

The spectrum is shown in solid line in Fig. 5 for the first shot of beam. The spectrum has a prominent peak at 694 nm with several unresolved shoulder peaks produced by the excitation state of Cr^{3+} . After the irradiation of Ar beam with 75 nA for 2.4 h to AF995R, it was found that the peak intensity decreased by 35% as shown in Fig. 7. In the first 0.2 h from the beginning, the intensity decreased rapidly. After the 0.2-h irradiation, the intensity decreased slowly and steadily, which can be fit well by one-dimensional function

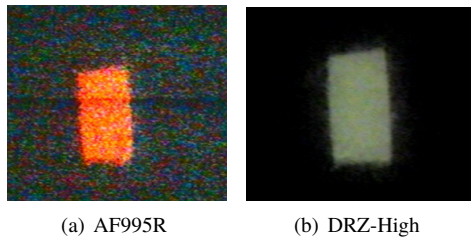


Figure 6: Beam profile obtained with fiber imaging system for (a) AF995R and (b) DRZ-High. Beam shape was ununiformed by nonlinear focus.

as shown in solid line in Fig. 8. The spectrum after the 2.4-h irradiation is also shown in Fig. 7. The intensity of the unresolved peak with wavelength region shorter than 694 nm had less decreased than one for 694 nm. It can be thought that the influence of degradation may mitigate by observing the light in short wavelength with optical filter cutting long wavelength.

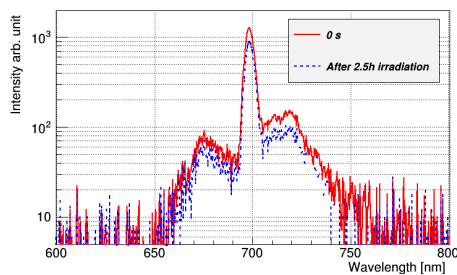


Figure 7: Spectrum of luminescence before and after irradiation of the Ar beam for 2.4 h.

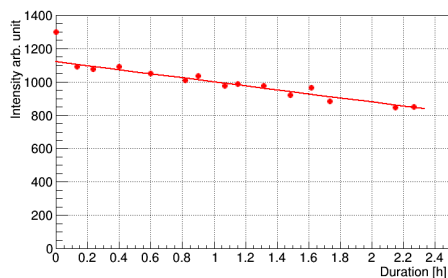
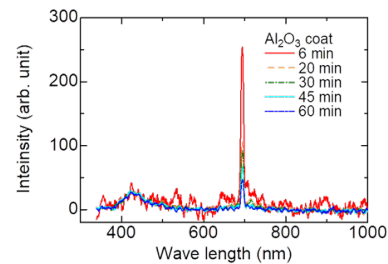


Figure 8: Trend of peak intensity for long duration irradiation of the Ar beam with 75 nA. Line shows result by linear fitting.

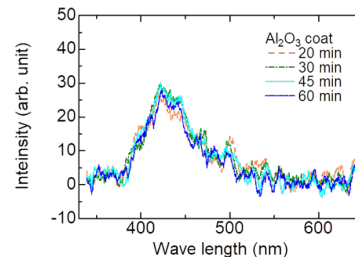
Development Luminescence Material for Profile Monitor

Many candidate materials have been examined to observe the degradation of light emission. As one of the candidate, AlO_2 paint with a low amount of Cr existing as an impurity was examined (Fig. 9).

Although the peak for Cr showed drastically decrease at 694 nm, the light in the shortwave length remained irrespectively to the beam amounts, which implies that the less degradation image can be obtained by using shortwave pass filter. It should be noted that the total intensity of the shortwave is smaller than the peak due to Cr ions. In future, the absolute photon intensity for the proton from 0.4 to 3 GeV will be examined at the beam transport system to the MLF. If the light yield is small, the intensity can be amplified by such as the image intensifier.



(a) Total wavelength



(b) Zoomed in short wavelength

Figure 9: Spectral intensity of AlO_2 paint for (a) total wavelength and (b) short wavelength for various irradiation time of the Ar beam.

CONCLUSION

For reliable beam operation at the spallation neutron source in J-PARC, beam monitor system with the MWPM and the halo monitor was developed. With the present MWPM, beam parameter such as the emittance and Twiss parameter can be obtained by several shots of the beam. To mitigate pitting erosion on the mercury target vessel, a beam transport system with nonlinear optics has been developed. By introducing nonlinear optics with octupole magnets, peak current density can be reduced by $\approx 30\%$, which decreases the damage of pitting erosion about 80%. For future facility in J-PARC aimed for the research and development of the ADS, profile monitor experiment has carried out with Ar beam. Although AlO_2 doped with Cr showed significant degradation of photoemission, AlO_2 paint showed to stand a high dose of the beam in the short wavelength.

REFERENCES

- [1] The Joint Project Team of JAERI and KEK, JAERI-Tech 99-56, 1999.
- [2] Y. Ikeda, *Nucl. Instr. Meth. A*, vol. 600, pp. 1–4, 2009, doi: 10.1016/j.nima.2008.11.019
- [3] Y. Miyake *et al.*, *Physica B*, vol. 404, pp. 957–961, 2009, doi:10.1016/j.physb.2008.11.227
- [4] S. Meigo *et al.*, *Nucl. Instrum. Meth. A*, vol. 562, pp. 569–572, 2006, doi:10.1016/j.nima.2006.02.011
- [5] S. Sakamoto *et al.*, *Nucl. Instrum. Meth. A*, vol. 562, pp. 638–641, 2006, doi:10.1016/j.nima.2008.11.068
- [6] S. Meigo *et al.*, *Nucl. Instr. Meth. A*, vol. 600, pp. 41–49, 2009, doi:10.1016/j.nima.2008.11.068
- [7] S. Meigo, *J. Nucl. Mater.*, vol. 450, pp. 8–15, 2014, doi: 10.1016/j.jnucmat.2013.11.020
- [8] G. E. Youngblood *et al.*, *J. Nucl. Mater.*, vol. 258–263, pp. 1551–1556, 1998, doi:10.1016/S0022-3115(98)00217-7
- [9] S. Meigo *et al.*, “Measurement of Displacement Cross-Section for Structural Materials in High-Power Proton Accelerator Facility”, presented at IPAC’18, Vancouver, Canada, Apr.-May 2018, paper MOPML045.
- [10] Y. Iwamoto *et al.*, “Radiation Damage Calculation in PHITS and Benchmarking Experiment for Cryogenic-sample High-energy Proton Irradiation”, presented at HB2018, Daejeon, Korea, Jun 2018, paper TUP2WE03.
- [11] K. L. Brown, Ch. Iselin and D. C. Carey: “Decay Turtle”, CERN 74-2, 1974.
- [12] PSI Graphic Turtle Framework by U. Rohrer based on a CERN-SLAC-FERMILAB version.
- [13] S. Meigo *et al.*, *J. Nucl. Mater.*, vol. 450, pp. 141–146, 2014, doi:10.1016/j.jnucmat.2014.02.011
- [14] Y. Yuri *et al.*, *Phys Rev ST Accel. Beams*, vol. 10, 10401, 2007, doi:10.1103/PhysRevSTAB.10.104001

INJECTION FOIL TEMPERATURE MEASUREMENTS AT THE SNS ACCELERATOR*

W. Blokland, N. Evans, C. Luck, A. Rakhman, Oak Ridge National Laboratory, Oak Ridge, USA.

Abstract

The SNS uses charge exchange injection to minimize losses during the accumulation of the accelerated beam in the ring. A stripper foil implements this by removing the electrons from the high intensity H⁻ beam coming from the linac. At a beam power of 1.2 MW, the foil lasts for many weeks, sometimes months. However, given the upgrade to 2.8 MW, it is important to know the current temperature of stripper foil in order to estimate its lifetime for the new beam power and beam size. In this paper, we discuss several methods to measure the temperature of stripper foil exposed to current operating conditions of the SNS accelerator. Given the high radiation in the vicinity of the foil, the uncertainty in the foil's emissivity, and available resources, we chose a two-wavelength pyrometer that is located 40 m from the foil. The pyrometer is composed of two mirrors, a refracting telescope, and two photodiodes. We present the calibration data and the temporally resolved measurements made with this pyrometer.

INTRODUCTION

The Spallation Neutron Source (SNS) uses a nanocrystalline diamond foil, see Fig. 1, to implement a charge-exchange scheme to efficiently accumulate bunches from the linac into the ring to deliver a short and intense pulse to the target [1]. The lifetime of the foil is limited by temperature induced sublimation and by radiation damage [2]. Currently, the foils have lifetimes of several months, over 2500 MWhr of beam at 1.2 MW, before they need to be exchanged. Foils can be exchanged quickly with the foil exchanger, which has up to 12 foils installed. More beam power, such as planned for the Second Target Station, can lead to higher temperatures and these higher temperatures can reduce the lifetime of the foil, potentially complicating operations.



Figure 1: Unused foil, left, and used, right.

In the early days of SNS operations, when the foil lifetime was not yet known, attempts were made to measure temperatures in the tunnel with cameras. An unshielded infrared camera died immediately, even at the much lower beam powers at the time. A second attempt with a shielded visible light camera with two bandpass filters, a two-color pyrometer, was also not successful due to the radiation. However, we found by experience, that the foil lifetimes were high enough that we did not have to worry, and interest in measuring the foil temperature waned. However, with the eye on the future power upgrades, up to 2.8 MW, the interest in measuring the foil temperature and understanding the foil lifetime has been renewed.

OPTICAL PATH

Only two mirrors were needed to get light from the foil from the high radiation area to the Ring Service Building by using an existing and unoccupied cable chase. The disadvantage is the long path length, about 40 meters. This optical path was in use to look at the foil with a regular visible light digital camera mounted on a telescope, see Fig. 2. Figure 2 also shows, on the right, a picture made with a regular camera of the foil with the beam spot clearly visible.

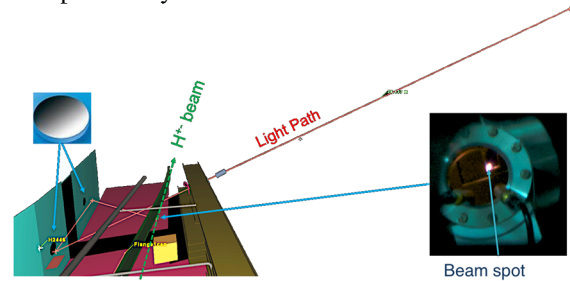


Figure 2: Optical light path to foil.

TWO-WAVE PYROMETER

A two-wave or two-color pyrometer removes the dependency of the temperature measurement on the emissivity by taking the ratio of the received light intensity from two different wavelengths. The pyrometer equation can be derived by dividing Planck's equation (1) for each wavelength's intensity and using Wien's approximation and assuming that the emissivity is the same for both wavelengths (2):

$$I(\lambda, \epsilon, T) = \frac{2hc^2}{\lambda^5} \frac{\epsilon(\lambda)}{e^{\frac{hc}{\lambda kT}} - 1} \quad (1)$$

$$Ratio_{1/2} = \frac{s_1 I(\lambda_1, \epsilon(\lambda_1), T)}{s_2 I(\lambda_2, \epsilon(\lambda_2), T)} = \frac{s_1}{s_2} \left(\frac{\lambda_1}{\lambda_2}\right)^{-5} e^{\frac{2hc^2}{T} \left(\frac{1}{\lambda_2} - \frac{1}{\lambda_1}\right)} \quad (2)$$

The transmission coefficients, s_i , need to be determined through calibration for each wavelength. Ratio

*This manuscript has been authored by UT-Battelle, LLC, under Contract No. DE-AC05-00OR22725 with the U.S. Department of Energy. The United States Government retains, and the publisher, by accepting the article for publication, acknowledges that the United States Government retains a non-exclusive, paid-up, irrevocable, world-wide license to publish or reproduce the published form of this manuscript, or allow others to do so, for United States Government purposes. The Department of Energy will provide public access to these results of federally sponsored research in accordance with the DOE Public Access Plan (<http://energy.gov/downloads/doe-public-access-plan>).

curves for different wavelength combinations are shown in Fig. 3. A combination of filters that gives a steeper curve, but still with enough radiance for the expected temperature, is often preferred to maximize the resolution.

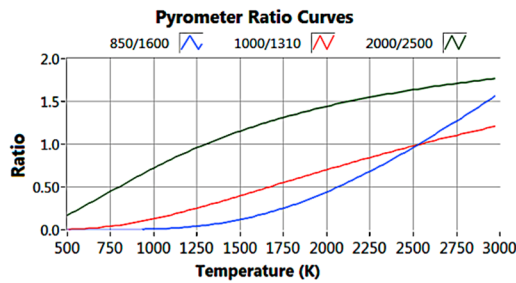


Figure 3: Different ratio curves for different filter combinations.

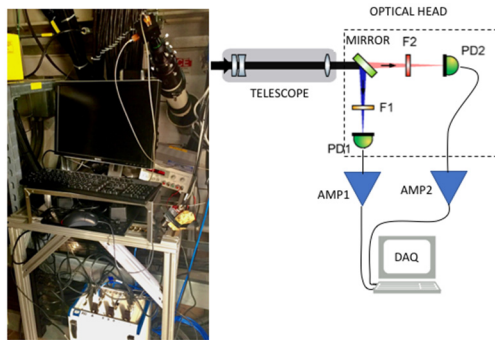


Figure 4: Pyrometer setup.

The implementation of our pyrometer is shown in Fig. 4. We manufactured an optical head with a dichroic mirror to reflect the shorter wavelengths to one photodiode and pass the longer wavelengths to a second photodiode. In front of each photodiode is an appropriate bandpass filter. The signals from the Hamamatsu G10899 InGaAs PIN photodiodes are amplified by the Femto DLPCA-200 current amplifiers and digitized by National Instruments PXI digitizers.

CALIBRATION

Optical Transmission and Reflections

To determine the transmission coefficients, S_i , we measured the spectral response of different optical elements, such as the vacuum window, glass window, telescope, dichroic mirrors, and bandpass filters. The photodiode has a detection range of approximately 0.4 to 1.7 μm . To measure over that range, we had to use two available optical spectrum analyzers, the Thorlabs CCS200, with a spectral range of 0.2 to 1.0 μm , and the Anritsu MS9740A, with a spectral range of 0.6-1.7 μm .

We found that several bandpass filters leak light outside their pass band. While a properly selected dichroic mirror can help reduce the leakage, one is better off with a bandpass filter that only lets through light in the pass band for the entire band of the photo detector. Figure 5 shows several of the measured bandpass filters. It shows that the 1050 nm filter leaks a lot of light above 1300 nm. If used

with the right dichroic mirror, this bandpass filter could still be used. The long pass mirrors can also leak light outside their specifications, so combinations should be carefully selected. We selected bandpass filters with minimal leakage.

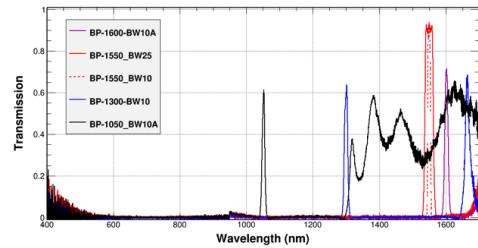


Figure 5: Bandpass measurements.

While it was relatively easy to measure the transmission of the mirrors, windows, and bandpass filters with the optical spectrum analyzers, it was very difficult to measure the telescope transmission given the fiber-coupling requirement. Also, because of the large difference in transmission for the visible light and the near infrared light, we are not sure how accurate the offset on this measured curve is, thus enabling a potentially large error in a S_i for the near infrared range.

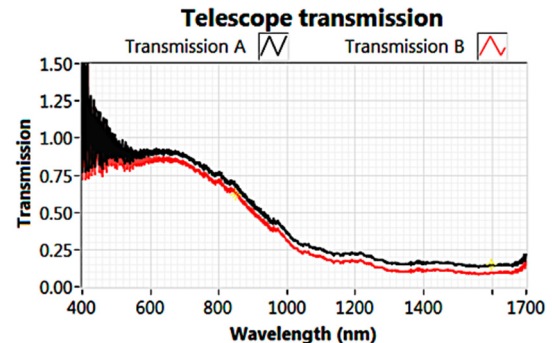


Figure 6: Telescope transmission measurement.

For example, see Fig. 6, looking at just moving the curve, transmission A, down by 0.05 to get transmission B, changes the 800 nm transmission from 0.67 to 0.62, but the 1600 nm transmission changes from about 0.15 to 0.1 leading to an almost 50% change. This can lead to a temperature error of about 125 K, if the temperature is 1500 K. We hope to redo this measurement once the new free space optical spectrometer has been delivered.

Blackbody Source

Beginning of April of this year, we had the availability of a blackbody source, the LumaSense M305. We used this source to calibrate two optical heads, one with 850 and 1600 nm bandpass filters and a 1000 nm longpass dichroic mirror, and one with a 1000 and 1310 nm bandpass as well as an 1180 nm longpass dichroic mirror.

The setup is shown in Fig 7. We used the same mirrors as installed in the tunnel to fold the optical path in the lab for an approximate 20 meters path length. We measured the response up to 1273 K, the maximum of the black-

Content from this work may be used under the terms of the CC BY 3.0 licence (© 2018). Any distribution of this work must maintain attribution to the author(s), title of the work, publisher, and DOI.

body source. The measured ratios for the 1000/1310 head are shown in Table 1. We calibrated by applying a single multiplier, 0.89, to the ratios to match the blackbody temperature with the calculated temperature. We can now use this same multiplier in the field with the foil to derive the foil peak temperature, instead of using the optical transmission measurements. We also calibrated the 850/1600 optical head with the blackbody source and also got well within 1% and with steps close to 100 K. However, there was a significant difference, 1.8 times, with the optical transmission calculated multiplier. Given the uncertainty in the telescope calibration, we will use the blackbody source derived multiplier for the foil temperature measurements.



Figure 7: Using the blackbody source for calibration.

Table 1: Optical Head 1000/1310 Calibration

BB T (K)	Measured Ratio	New Ratio (x0.89)	Calculated T (K)	Error %
1073.2	0.181	0.162	1073.1	-0.02
1173.2	0.238	0.213	1175.1	0.21
1273.2	0.298	0.267	1273.1	0.09

BEAM SPOT

The telescope is mounted on a motorized mount and our initial plan was to put a pinhole in front of the photodiodes and scan the telescope across the foil to build up an image. However, the pinhole had to be as big as the projected beam spot to get enough signal-to-noise. To be able to estimate the peak temperature from the whole beam spot, we assumed that the gaussian beam from the linac produces the same gaussian temperature distribution. We also assumed that the emissivity is constant over the beam spot and that we projected the complete beam spot on each photodiode. The new radiation curve then becomes a summation of many blackbody radiators, see (3).

$$BBS(T) = \sum_{\substack{-l < x < l \\ -k < y < k}} BB(T(x, y)) \quad (3)$$

The change in the radiation spectrum is shown in Fig 8. The curve named BB is the standard blackbody radiation curve and the BBS (BlackBody Sum) curve is the sum of a gaussian temperature distribution. The BBA (BlackBody Accelerator physics) curve represents the calculated beam spot [3], shown on the right side of the figure. The BBA includes the hits from protons circulating in the ring. The difference between the BBS and BBA curves is very small and leads to small differences in the calculated temperatures of about 5 to 10 K.

We verified that the projected beam spot is much smaller than the photodiode sensitive area by using a camera image to calculate the projected spot size from the pixel size and pixels occupied by the image. The visible light part of the projected spot is around 200 μm, much smaller than the 3 mm photodiode area. The telescope aim is adjusted until both photodiodes reach their maximum signal for the conditions.

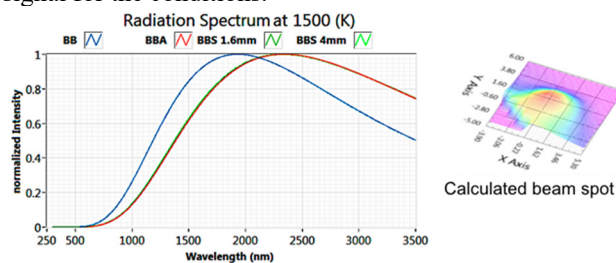


Figure 8: Radiation Spectra.

MEASUREMENTS

Signals

A typical signal measured from the photodiodes is shown in Fig 9. Every 16.6 ms, an approximately 1 ms long pulse hits the foil. We see a steep rise in the signals followed by a much longer decay. The signals are filtered with a median and/or a Savitzky-Golay filter to reduce the noise.

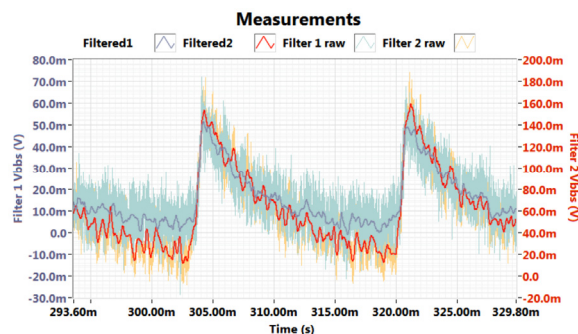


Figure 9: Raw and filtered photodiode signals.

The filtering still leaves too much noise to take the ratio of the signals. To further reduce the noise, we apply a rather stiff spline fit to smoothly follow the steep rise and the decay. To allow for the spline to quickly change direc-

tion from the cooling curve to the heating slope and vice versa, the spline is relaxed around those turning points, see Fig 10.

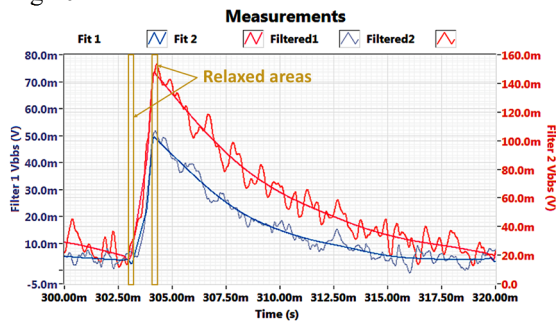


Figure 10: The filtered and fitted photodiode signals.

Studies

To test the prototype pyrometer, we set the linac up to deliver exactly 20 beam pulses, each 1ms long. This allows us to see the baseline, the heating up of the foil, and the full cool down curve after the last pulse, see Fig 11. The first pulse is barely or not visible as the temperature still has to build up with the following pulses.

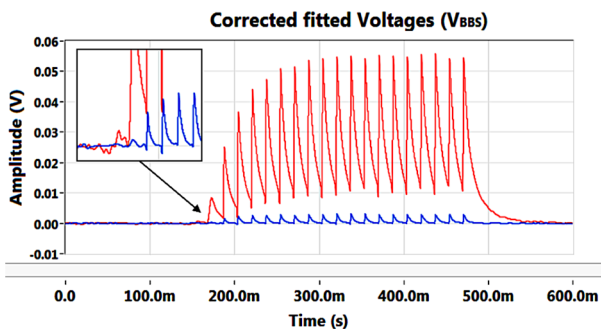


Figure 11: The signals for 20 pulses.

Data from 1.3 MW equivalent pulses are shown in Fig. 12 for the 850/1600 optical head and in Fig. 13 for the 1000/1310 optical head. Both measurements show a temperature between 1450 and 1500 K. The same foil was running at about 1600 K earlier in the run.

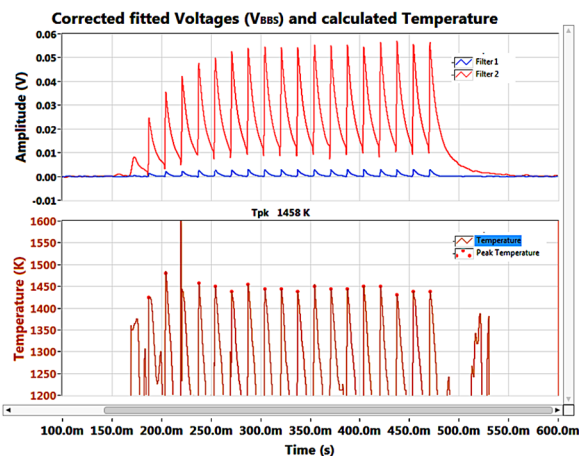


Figure 12: Calculated temperature curves using the 850/1600 optical head.

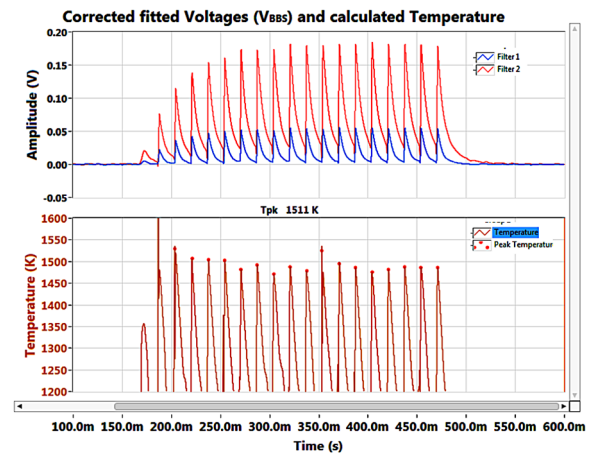


Figure 13: Calculated temperature curves using the 1000/1310 optical head.

Control Room Screen

The data from the pyrometer is available over EPICS in the control room so we can observe the temperature over time and archive the data. The Control Room screen is shown in Fig. 14. At this point the foil is being conditioned and its peak temperature is 1700 K.

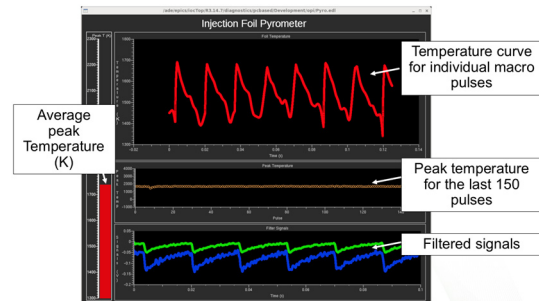


Figure 14: EDM screen during conditioning.

Foil Conditioning

We condition a foil before using it in a production run to extend its life. Foil conditioning consists of running beam at lower power and over approximately half a day, slowly increasing the beam power up to full production levels. From experience we know that if a foil is not conditioned, it does not last long. The Raman spectra of the conditioned foils show strong peaks from graphitic carbon which has a higher emissivity of around 0.8 instead of about 0.4 for diamond, see [4].

The overall conditioning process is shown in Fig 15. The temperature of the new foil, the red trace, starts out at above 2000 K. We see the vacuum pressure, the green trace, go up as the foil is conditioning. But the temperature goes down quickly, as well as the vacuum pressure. The beam power, the blue trace, is then increased, and we see that the temperature increases again and the vacuum pressure going up. However, soon after each beam power increase, the temperature eventually decreases, and the vacuum pressure goes down. The foil temperature stabilizes to around 1700 K during the conditioning process.

Content from this work may be used under the terms of the CC BY 3.0 licence (© 2018). Any distribution of this work must maintain attribution to the author(s), title of the work, publisher, and DOI.

Over time, the foil will go down even further to 1600 K or less.

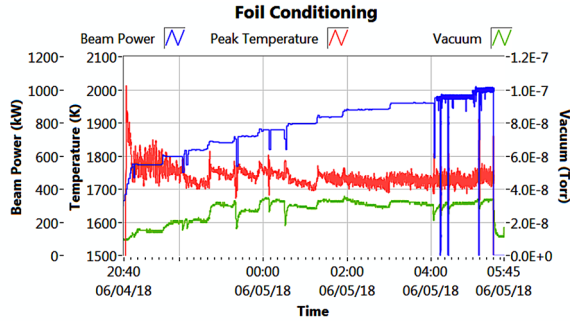


Figure 15: Foil conditioning.

Foil Sublimation

The foil sublimation due to high temperatures is a main factor of the foil lifetime. We defined the lifetime of the foil to end once 30% of the foil has sublimated. Radiation damage is another factor but not considered in this paper. An equation for foil sublimation can be found in [2]:

$$\frac{dh(t)}{dt} \cdot \frac{1}{\rho} = -4.06 \cdot 10^8 \cdot \frac{e^{-\left(\frac{83500}{T}\right)}}{\sqrt{T}} \quad (4)$$

The density of the foil, ρ , is approximately 3.5 g/cm³ for diamond and about 2.2 g/cm³ for graphite. We used this equation and the density for graphite to calculate the foil sublimation as a function of the temperature. At the lower temperatures of the foil, 1500 K, there is no limitation to the foil lifetime due to sublimation as this is integrated to be around 5.4 · 10⁻¹⁴ m per day, see Fig. 16. At a temperature of around 2100 K, the foil loss would be about 8.5 · 10⁻⁸ m per day which would give a lifetime estimated of only a few days with the pulsed SNS beam.

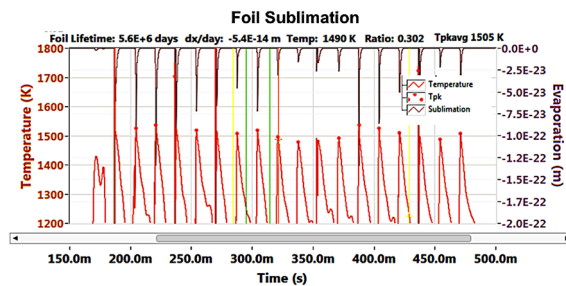


Figure 16: Sublimation of the foil along the temperature per pulse.

Radiative Cooling

We have started looking at the cooling curve of the foil, assuming there is only radiative cooling and assuming the foil temperature is much higher than the environment temperature, the expected temperature is:

$$T = T_{pk} \sqrt[3]{\frac{1 + 3kT_{pk}^3 \cdot t}{3Nk_B}} \quad \text{with } k = \frac{2\varepsilon\sigma A}{3Nk_B}$$

with $\sigma = 2\pi^5 k^4 / 15h^3 c^2 = 5.76 \cdot 10^{-8} \text{ W/m}^2 \text{ K}^4$

This means that we need to know the foil's thickness and emissivity. We know that the foil has a different thickness and/or density after conditioning, but we don't know this number given that the foil turns graphite-like and the possible sublimation or outgassing during foil conditioning process. While we have developed code to fit the measured cool down curve, again assuming that our signal is derived from the 2-D sum of gaussians, the wide range in parameters means that a wide range, > 150 K, in temperature is possible. We hope to look closer at this technique in the near future. An example of the analysis is shown in Fig 17. The graph on the left shows the cooldown curve of the last pulse with fit, while on the right side the pulse train is shown. With best estimates for emissivity, 0.83 and assuming 1 μm thickness of graphite, a reasonable temperature can be calculated, 1628 K, as shown in Fig. 17.

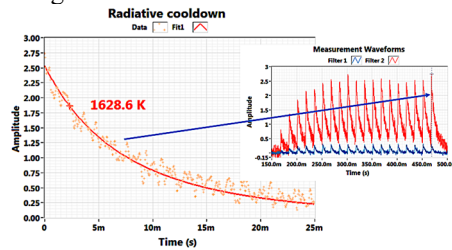


Figure 17: Estimation of the foil peak temperature based on the cooldown curve.

DISCUSSION AND FUTURE

We have installed a new prototype foil temperature measurement system and can now start correlating the foil temperature with actual foil lifetime, accelerator setup, and variations in beam parameters. Already, we have been able to use it to observe the foil conditioning process. The temperature is estimated around 1500-1600 K at 1.3 MW beam power. We are still looking at the errors due to the assumptions, but estimate that the errors due to signal noise, signal processing, and fitting are less than ± 100 K. Further improvements in the code can be made to reduce these errors.

Further increases in signal-to-noise can be made by a combination of widening the bandpass filters, using more sensitive, possibly cooled detectors, and optics in the tunnel to increase light collection. Much better light collection will also allow the use of cameras with bandpass filters in front to create a 2-D temperature picture of the beam spot, eliminating the need for assuming a gaussian distribution.

Developments in the foil testing in the lab will help with further establishing the foil's emissivity and the foil sublimation process. The foil lab's measurements, coupled with the field temperature measurements, will provide estimates for foil lifetimes at higher temperatures, and should help us improve the analysis of the cooldown curve, increasing our confidence in the measured temperature.

We also plan to compare the infrared camera measurements with the pyrometer measurements in the foil lab.

REFERENCES

- [1] J. Wei, *et al.*, “Low-Loss Design for the High- Intensity Accumulator Ring of the Spallation Neutron Source,” *Phy. Rev. Lett. ST Accel. Beams*, vol. 3, p. 080101, Aug. 2000, doi:10.1103/PhysRevSTAB.3.080101
- [2] Lebedev S.G. *et al.*, “Calculation of the lifetimes of thin stripper targets under bombardment of intense pulsed ions,” *Phy. Rev. Lett. ST Accel. Beams*, vol. 11, p. 020401, Feb. 2008, doi:10.1103/PhysRevSTAB.11.020401
- [3] Plum M., *et al.*, “SNS stripper foil development program,” *Nucl. Instr. Meth*, vol. 590, Iss. 1–3, pp. 43-46, 2008, doi:10.1016/j.nima.2008.02.065
- [4] Barrowclough E.P., “Analysis of Primary Stripper Foils at the Spallation Neutron Source by an Electron Beam Foil Test Stand,” Ph.D. thesis, Chem. Dept., University of Tennessee, Knoxville, USA.

THE BEAM CONDITIONS ON THE TARGET AND ITS OPERATIONAL IMPACTS ON BEAM INTERCEPTING DEVICES AT EUROPEAN SPALLATION SOURCE

Y. Lee*, R. Miyamoto, T. Shea, European Spallation Source ERIC, SE-225 92 Lund, Sweden
H. D. Thomsen, ISA - Centre for Storage Ring Facilities, DK-8000 Aarhus, Denmark

Abstract

A large flux of spallation neutrons will be produced at the European Spallation Source (ESS) by impinging high power proton beam on the tungsten target. Until the 5 MW proton beam is stopped by the spallation target, it travels through a number of beam intercepting devices (BIDs), which include the proton beam window, a multi-wire beam profile monitor, an aperture monitor, the beam entrance window, spallation material and the target shroud. The beam-induced thermo-mechanical loads and the damage dose rate in the BIDs are largely determined by the beam energy and the beam current density. At ESS, the proton beam energy will be commissioned step-wisely, from 571 MeV towards 2 GeV. The beam current density on the BIDs in the target station is uniformly painted by raster beam optics. The ESS Linac and its beam optics will create rectangular beam profiles on the target with varying beam intensities. In this paper, we study the impact of different plausible beam intensities and beam energies on the thermo-mechanical loads and radiation damage rates in the BIDs at the ESS target station.

INTRODUCTION

Upon full commissioning of the European Spallation Source (ESS) in the next decade, the spallation target will receive 5 MW beam from the linac [1, 2]. For a reliable operation of the facility, it is crucial to keep structural integrity of the beam intercepting devices (BIDs) under the dynamic load induced by the beam pulses with 4% duty cycle and occasional beam trips. From a maintenance viewpoint, it is important to achieve a longest possible lifetime of these devices under radiation damage. The BIDs under heavy proton beam load are the spallation target, the proton beam window (PBW), and the multi-wire profile monitor (MWPM).

The dynamic beam load on the BIDs can be reduced by creating a uniform beam spot with a reduced beam current density. This slows down the radiation damage rate and lowers the cyclic thermo-mechanical load, prolonging the lifetimes of the BIDs. In order to create a uniform beam footprint on the BIDs, the ESS applies a raster system that sweeps the beam in a transverse pattern. The dimension of the raster area and the size of the beam determine the radiation damage and beam induced thermo-mechanical loads on the BIDs. A focused raster area and beam intensity cause a higher damage and heat deposition intensity in the BIDs. On the contrary, widely spanned raster beam causes a high

level of beam loss from the PBW to the target, as the PBW induces a beam divergence via multiple scattering.

Besides the beam intensity, the radiation damage rate and heat deposition also depend on the beam energy. The ESS beam energy will be ramped up step-wisely from 571 MeV towards 2 GeV upon commissioning, with installation of additional cryomodules during long shut down periods. It is important to know the correlation between the beam conditions and the material behaviour of the BIDs, in assessing the system reliability and the service lifetime.

In this paper, we study the impact of different plausible beam intensities and beam energies on the thermo-mechanical loads and radiation damage rates in the BIDs at ESS.

BEAM INTERCEPTING DEVICES AT TARGET STATION

Once the proton beam enters the target station, it passes through PBW, MWPM, and beam entrance window (BEW) in a sequence until the beam is finally stopped by the tungsten spallation volume. Each of these beam intercepting devices are introduced in the following.

Proton Beam Window

The PBW is located at 3.5 meter upstream beam direction of the target. It interfaces to accelerator vacuum and serves as the gate for the incoming proton beam to target. The PBW consists of two convex plates made of Al6061-T651, which are 1 mm (upstream window) and 1.25 mm (downstream window) thin respectively. The precipitation hardened aluminium alloy is chosen, due to its low scattering cross-sections to incoming proton beam, good radiation resistance and good mechanical strength. The deposited beam power in the PBW is removed by the water flow running between the two plates.

Multiwire Beam Profile Monitor

The Multiwire Beam Profile Monitor (MWPM) is located 1.7 meter upstream of the target. It consists of five layers of horizontal, vertical, and diagonal wires. Each wire for the beam interception is made of SiC and has a diameter of 100 μm . It measures the position, profile, and peak density of the high intensity proton beam traveling to the spallation target.

Beam Entrance Window

The tungsten spallation volume is contained in the gas-tight target vessel. The BEW is a part of the target vessel

* yongjoong.lee@ess.se

which faces the impinging proton beam. It is made of solution annealed 316L type stainless steel material, due to its proven lifetime under high power proton irradiation environments. The BEW is cooled by gaseous helium jet flow.

Tungsten Bricks

The spallation volume of the target consists of 6696 tungsten bricks. Each brick is 10 mm in width, 30 mm in depth and 80 mm in height. The spacing between two adjacent bricks is 2 mm. Figure 1 shows the layout of tungsten bricks placed on the cassette. Maximum 16 tungsten bricks span

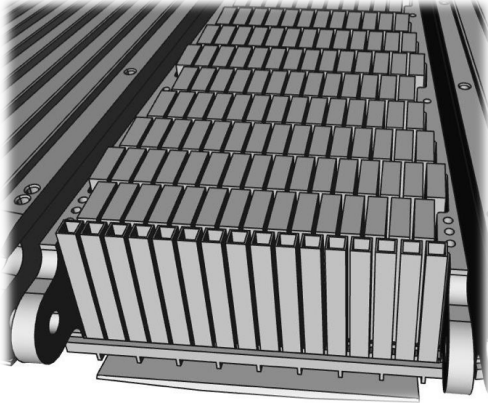


Figure 1: Layout of tungsten bricks in the cassette.

190 mm horizontally in each target segment. Each brick is held by top and bottom cassette plates, which shadow 10 mm of 80 mm height of the tungsten bricks. Therefore, the view area of the tungsten spallation volume seen by the proton beam is defined by $-95 \text{ mm} \leq x \leq +95 \text{ mm}$ and $-35 \text{ mm} \leq y \leq +35 \text{ mm}$.

BEAM RASTER PARAMETER

Target Area Definition

Ideally, should all the incoming protons land on the tungsten spallation volume, while not hitting the structural parts made of stainless steel. The beam footprint on the target may deviate from the centre point of the segment by maximum $\pm 14.7 \text{ mm}$ horizontally and by maximum $\pm 3.0 \text{ mm}$ vertically [3]. The front face of the tungsten is 1250 mm in distance from the rotation axis of the target wheel. The target wheel rotates with a frequency of 14/36 Hz, and the front face of the tungsten drifts by 9 mm during the pulse length of 2.86 ms. The requirement on the positioning accuracy of beam footprint on target is set to be less than $\pm 5 \text{ mm}$. The horizontal runout of the target wheel is maximum $\pm 2.4 \text{ mm}$. The tolerance on the horizontal displacement of the wheel position is limited by $\pm 2.0 \text{ mm}$. The phase error from the target rotation speed contributes to maximum $\pm 2.0 \text{ mm}$ horizontal deviation of the beam footprint from its centre position. The vertical deviation is mainly contributed by the positioning accuracy of beam footprint on target, which is set to be less than $\pm 3 \text{ mm}$.

Taking the maximum beam deviations from the centre point of each segment into account, the effective view area of tungsten by the proton beam is reduced from the ideal view area of $190 \times 70 \text{ mm}^2$ to $160 \times 64 \text{ mm}^2$.

Nominal Raster Parameter

The raster magnet system generates a Lissajous-like pattern using triangular wave forms to create a two dimensional mesh of interweaved sweep trajectories. During the beam pulse starting at the time $t = t_0$, the trajectory of the beam centroid in the plane perpendicular to the beam direction at the BEW is described by

$$x_i(\tilde{t}) = \Delta_i \left[4 \left\lfloor \text{mod} \left(\frac{n_i \tilde{t}}{\tau} - \phi_i, 1 \right) - \frac{1}{2} \right\rfloor - 1 \right], \quad (1)$$

for $i = x, y$ and $\tilde{t} \equiv t - t_0$. Here, τ represents the beam pulse length, and Δ_x and Δ_y respectively represent the raster amplitudes in the horizontal and vertical directions. The parameters n_x and n_y represent the number of sweeps during the beam pulse respectively in the horizontal and vertical directions. These are correlated to the raster frequency f_x and f_y via $n_i = f_i \cdot \tau$. The ϕ_i s are free parameters representing phase shifts. Table 1 summarises the nominal beam raster parameters at the BEW.

Table 1: Nominal Beam Raster Parameters on the BEW

Parameter	Symbol	Value	Unit
Pulse length	τ	2.86	[ms]
Maximum displacements	Δ_x	60.0	[mm]
	Δ_y	20.0	[mm]
Sweep frequency	f_x	39.55	[kHz]
	f_y	29.05	[kHz]

BEAM FRACTION ON TARGET FOR DIFFERENT BEAM ENERGIES

Proton Scattering at PBW

The protons are lost on its way to the target. The main cause of loss is the multiple scattering at the PBW. The extent of proton scattering depends on the beam energy. Three beam energies are considered, the 571 MeV, 1300 MeV and 2 GeV. When the linac unit up to the medium beta cryomodules is fully functional, a 571 MeV beam will be delivered to the target. The 1.3 GeV beam will be delivered when about a half of the high beta cryomodules are commissioned. With a full commissioning of the linac, a 2 GeV beam will be delivered to the target.

In order to calculate the additional beam divergence due to the presence of the PBW, Monte-Carlo simulations are made using FLUKA [4, 5]. The beam source distribution at 6 meters upstream of the target is calculated by TraceWin [6], which is then read by FLUKA for particle transport simulations. Figure 2 shows the angular distribution of the proton

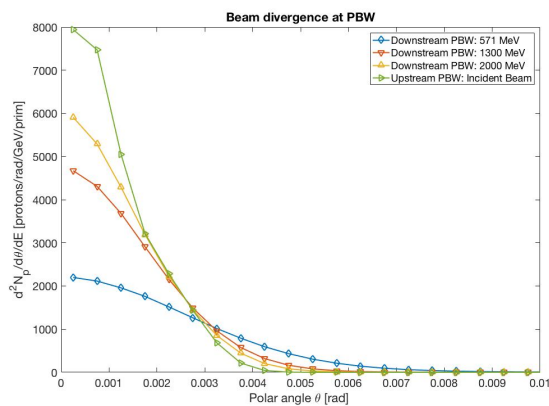


Figure 2: The polar angle distribution of proton momentum upstream and downstream of the PBW.

momentum upstream and downstream of the PBW. For reference, a polar angle divergence of 1.0 mrad implies a 3.5 mm transverse offset on the target. The simulation shows that about 1 % of the protons are lost at the PBW, depositing about 2 MeV per proton in there.

By tracing the free particle trajectories which are scattered by the PBW, the fraction of beam that land on the target area $160 \times 64 \text{ mm}^2$ on the tungsten bricks are calculated, for different beam energies. The energy dependence of beam loss on the target is summarised in Table 2. In order to show the beam loss due to scattering at the PBW, MWPM and BEW, a reference case is also shown, which assumes no beam interception in the upstream beamline of the target.

Table 2: The Fraction of Beam that Land on the Target Area

Beam energy	Fraction on target	Reference fraction	Statistical Error
0.571 GeV	0.885	0.961	$\pm 0.01\%$
1.300 GeV	0.928	0.961	$\pm 0.01\%$
2.000 GeV	0.965	0.988	$\pm 0.01\%$

Compared to the reference fraction, which is determined by linac optics and raster parameters, the presence of BIDs causes additional beam losses of 2% for a 2 GeV beam, 3% for a 1.3 GeV beam and 7% for a 571 MeV beam. The deviations from the reference beam loss could be reduced if the collimation effect of the proton channel surrounded by the monolith shielding structure is taken into account. Further analysis will be made to fine-tune the raster parameters further, for different proton beam energies.

Beam Loss and Thermal Stress in Target Vessel

If the beam on target suffers from maximum allowed offset, the maximum heat deposition at the target boundary per pulse is calculated to be less than $10 \text{ MJ}\cdot\text{m}^{-3}$ in stainless steel. If the edge of the raster boundary misses tungsten bricks and hits the target vessel structure instead, the maximum temperature increase in the steel structure is calculated to be

less than 3°C per pulse. This temperature increase per pulse makes the 316L stainless steel to expand by $4.8 \mu\text{m}\cdot\text{m}^{-1}$, resulting in less than 10 MPa additional thermal stress, which is about 5% of the yield stress. From this, we conclude that protons landing off the target area do not risk the structural integrity of the target wheel.

EFFECTS OF BEAM SIZE

Raster Failure and Heat in PBW and BEW

In case beam raster fails completely, a single beam deposits a concentrated heat load in the PBW and BEW. During a single full power pulse, the maximum temperature increases by ΔT_{max} in the PBW and BEW are expressed by

$$\Delta T_{\text{max}} = \frac{\tau}{\rho C_p} \frac{i_{\text{total}}}{2\pi\sigma_x\sigma_y} \left. \frac{dE}{dz} \right|_{\text{max}} \quad (2)$$

Here, τ is the pulse length, ρ is the mass density, C_p is the specific heat, i_{total} is the beam current, the $dE/dz|_{\text{max}}$ is the maximum energy deposition per single incident proton per unit length, and σ_x and σ_y are the beam RMS sizes.

A requirement on the beam size is that the structural functionality of the PBW and BEW shall not change with a failure of beam raster for single pulse. The aluminium alloy Al6061-T651 of which the PBW is made overages if the temperature on it temporarily reaches above 250°C [7]. Therefore, the temperature in the PBW shall not increase above $T_{\text{max:PBW}} = 250^\circ\text{C}$ during single pulse. On the other hand, a prolonged exposure to temperatures in the range of 550°C to 850°C in austenitic steel may cause chromium-rich carbides to precipitate at the grain boundaries. This limits the maximum temperature in the BEW to be below $T_{\text{max:BEW}} = 550^\circ\text{C}$.

The maximum operational temperatures in the PBW and BEW are 60°C and 160°C respectively. The threshold beam sizes to raise the maximum temperatures above $T_{\text{max:PBW}}$ and $T_{\text{max:BEW}}$ are calculated to be $\sigma_x \cdot \sigma_y = 33.5 \text{ mm}^2$ on BEW and $\sigma_x \cdot \sigma_y = 32.6 \text{ mm}^2$ on PBW. The nominal beam cross sections are $\sigma_x \cdot \sigma_y = 68.2 \text{ mm}^2$ on BEW and $\sigma_x \cdot \sigma_y = 42.5 \text{ mm}^2$ on PBW, satisfying the requirements with a safety margin of 30%.

Dynamic Stress Wave in Tungsten Bricks

The raster sweep during beam pulse induces dynamic stress wave in the tungsten bricks inside the target. For the nominal beam size and raster parameters, each sweep of beam raster on a tungsten brick induces an effective pulsed beam load with a few microseconds' pulse length.

Coupled thermal and transient structural simulations are made for a tungsten brick for 30 beam raster sweeps, using ANSYS Workbench [8]. Two different beam sizes are considered, the nominal one with $\sigma_x \times \sigma_y = 13.5 \times 5.05 \text{ mm}^2$, and the one with $\sigma_x \times \sigma_y = 10.8 \times 4.04 \text{ mm}^2$ having 40% higher beam intensity. Figure 3 shows the dynamic transient and quasi-static von Mises stress responses of a tungsten brick located at the centre of a target wheel segment.

Content from this work may be used under the terms of the CC BY 3.0 licence (© 2018). Any distribution of this work must maintain attribution to the author(s), title of the work, publisher, and DOI.

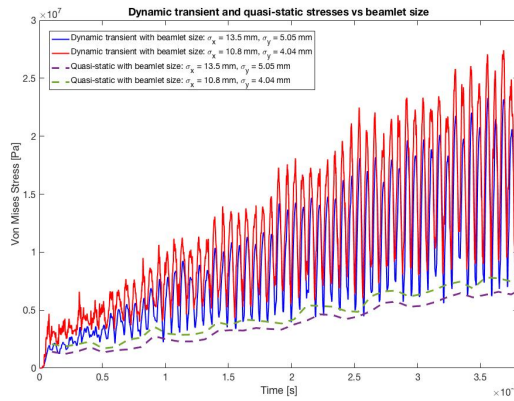


Figure 3: The dynamic transient and quasi-static von Mises stress responses of a tungsten brick located at the centre of a target wheel segment.

With a smaller beam size, the stress amplitude gets higher. This should be due to higher beam intensity combined with shorter beam exposure time per raster sweep. The amplitudes of dynamic transient stresses amplify with time, without showing a sign of saturation. The peak transient stress during the simulated time interval is almost 4 times higher than that of quasi-static stress. The reason for this could be attributed to proximity of the multiples of horizontal raster frequency $f_{\text{raster}} = 39.55$ kHz to the resonance frequency of the tungsten brick. The calculated resonance modes are at the frequencies of 41.2 kHz ($1.04f_{\text{raster}}$) and 78.4 kHz ($1.98f_{\text{raster}}$). The coherence between the resonance frequency and the beam raster sweep rate will be further analysed. The raster parameters will be fine tuned to avoid the raster sweep rate lies within a band-width of a resonance mode of tungsten bricks.

HEAT LOADS AND BEAM ENERGIES

The heat deposition in the BIDs differ for different beam energies. Table 3 summarises the calculated maximum beam energy per single proton deposited in the beam intercepting materials. For the same beam current, the beam energy de-

Table 3: Calculated Beam Stopping Power per Single Proton in the Beam Intercepting Materials

Beam Energy [GeV]	PBW	BEW [MeV·proton ⁻¹]	Tungsten (Max.) [MeV·proton ⁻¹]
0.571	1.41	3.98	8.12
1.300	1.24	4.38	10.8
2.000	1.22	5.01	14.5

posited in the BEW and tungsten bricks increase with beam energy. This is due to larger contribution of back scattered neutrons from the dense spallation volume at higher beam energies. However, the heat deposited in the PBW is the highest at 571 MeV, which is about 16% higher than that of the 2 GeV beam. At the early stage of the linac commission-

ing with a lower energy beam, an attention should be paid to this higher heat load and associated higher thermal stress in the PBW.

RADIATION DAMAGE

Proton Beam Window

The proton dose limited lifetime of the PBW is determined by the helium production in the aluminium alloy [9]. The helium production rate depends on proton energy and beam current density. At ESS, the total helium production in the aluminium alloy is limited by 2400 He-appm. FLUKA simulations are performed to calculate the helium production rate in the PBW. In steady operation, full current beam will be delivered to the target for 5400 hours per year. With the maximum time averaged beam current of 2.5 mA, the calculated accumulated helium production in the PBW per year are respectively 2240 appm at 571 MeV, 3160 appm at 1.3 GeV and 3620 appm at 2.0 GeV. Applying the maximum 2400 He-appm criterion in the PBW, the lifetimes of the PBW are respectively 5780 hours (8.25 GWh of accumulated beam energy) at 571 MeV, 4110 hours (13.3 GWh of accumulated beam energy) at 1.3 GeV, and 3580 hours (17.9 GWh of accumulated beam energy) at 2.0 GeV.

Beam Entrance Window

The maximum displacement damage on the BEW made of stainless steel 316L is 0.4 dpa at 2 GeV, 0.35 dpa at 1.3 GeV and 0.25 dpa at 571 MeV for the 5400 hours of annual operation at full current. During the 5 year lifetime of the target wheel, the BEW will receive less than 2.5 dpa of the damage dose, which is more than three times less than the maximum displacement damage dose recorded in the SNS target window [10]. Indeed, the maximum displacement dose in the ESS target wheel is located at the horizontal vessel plates mainly due to a high intensity fast neutron flux [11]. The lifetime of the target wheel is limited by the maximum displacement dose of 7.5 dpa in the target wheel during 5 years of full power operation. With a lower beam energy than 2.0 GeV, the target lifetimes are extrapolated to be 6 years at 1.3 GeV and 8 years at 571 MeV.

Spallation Material

As the spallation material does not carry any structural function, there is no dose limited lifetime defined for the tungsten. The calculated maximum displacement damage in the tungsten bricks are 1.0 dpa/year at 571 MeV, 3.0 dpa/year at 1.3 GeV and 2.6 dpa/year at 2.0 GeV. Tungsten is known to show completely brittle behaviour at the operational temperature of 500 °C already at above 0.1 dpa [12]. With the proton and neutron induced radiation damage, the thermal conductivity will also degrade with time [13]. The radiation damage in tungsten also makes the material stiffer. Pure tungsten irradiated by heavy ion up to the maximum damage level of 0.05 dpa showed an increased material stiffness by 12% [14].

Content from this work may be used under the terms of the CC BY 3.0 licence (© 2018). Any distribution of this work must maintain attribution to the author(s), title of the work, publisher, and DOI.

The effect of radiation induced changes of thermal conductivity and stiffness on the operational temperature and related static stress level in the tungsten brick has been studied with FLUKA and ANSYS simulations. The temperature dependent thermal conductivity of irradiated tungsten is taken from Ref. [13] for 3.8 dpa, and 20% higher Young's modulus has been assumed for the irradiated tungsten based on Ref. [14]. The results of analyses, based on a quarter of single wheel segment model shown in Fig. 4, are summarised in Table 4. Specifically, a transient simulation for 10 beam pulses are made, where the initial condition is provided by a calculated steady state configuration.

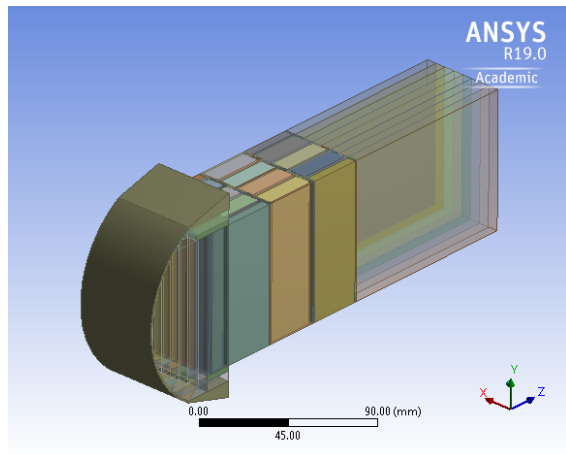


Figure 4: The geometry model used for the flow simulations, which represent a quarter of single target wheel segment.

Table 4: Radiation Damage Effect on Operation Temperature and Maximum von Mises Stress in a Tungsten Brick

Parameter	Time	Unirr.	Irrad.
maximum temperature	Pre-pulse	321 °C	337 °C
	Post-pulse	395 °C	411 °C
maximum stress	Pre-pulse	27 MPa	50 MPa
	Post-pulse	83 MPa	117 MPa

Also the effect of different raster sweep areas is analysed. For an un-irradiated tungsten brick, the reduced maximum raster amplitudes $\Delta_x = 54.3$ mm and $\Delta_y = 18.7$ mm result in higher temperatures and thermal stresses. The calculated pre and post-pulse temperatures are 341 °C and 427 °C respectively, showing a marginal increase of temperature compared to the nominal beam case. The corresponding von Mises stresses are 31 MPa and 117 MPa respectively, which are considerably larger than the nominal beam case. This shows that the beam raster area need to be monitored with an order of milli-meter scale precision to avoid a higher than design stress in tungsten bricks.

Multiwire Beam Profile Monitor

At 5 MW proton beam power with nominal raster parameters, the displacement damage in the MWPM made of SiC is

5 dpa per year. A highest damage level in SiC wires for beam profile monitoring is known to be deposited at Target Station 2 of ISIS, which is estimated to be 3 dpa and it continues operating without failure. Based on this, the proton damage lifetime of the MWPM is estimated to be 1 year at 5 MW operation of proton beam at ESS.

NEUTRON YIELDS FOR DIFFERENT BEAM ENERGIES

In order to assess the neutron yield from the target, a toy FLUKA model consisting of a tungsten slab with dimension 180×80×400 mm³ subject to a pencil beam is studied. Figure 5 shows the energy dependent spallation neutron flux from the top and bottom surfaces of the tungsten slab per MW beam power.

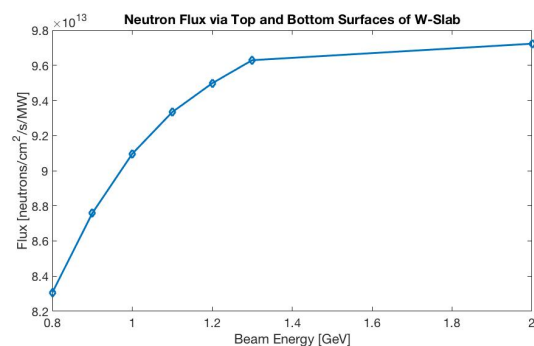


Figure 5: The energy dependent spallation neutron flux from the top and bottom surfaces of the tungsten slab per MW beam power.

The flux of spallation neutron per unit power increases with the beam energy, until it saturates at above 1.3 GeV. This loss of spallation neutron flux at lower beam energies can be compensated to a certain extent by optimising moderators and reflectors [15].

CONCLUSIONS

The correlation between the beam parameters on the target and its implications on the operational conditions of the beam intercepting devices are studied. The thermo-mechanical loads on the BIDs could differ considerably with a minor change of beam parameters, which shows the importance of beam diagnostics with precision. The beam parameters will be further fine-tuned from its baseline values, to gain higher reliability of the BIDs than is predicted under nominal beam parameters.

REFERENCES

- [1] S. Peggs *et al.*, “ESS Technical Design Report”, ISBN 978-91-980173-2-8 in ESS-doc-274, April 2013.
- [2] R. Garoby *et al.*, “The European Spallation Source design”, *Phys. Scr.* vol. 93, pp. 014001, 2018, doi:10.1088/1402-4896/aa9bff

- [3] K. Sjögreen, “WP2 Target wheel, drive and shaft description of operational limits”, Technical Report ESS-0084036, European Spallation Source ERIC, 2018.
- [4] A. Ferrari, P. R. Sala, A. Fassò, and J. Ranft, “FLUKA: a multi-particle transport code”, CERN-2005-10, INFN/TC_05/11, SLAC-R-773, 2005.
- [5] T. T. Böhlen, F. Cerutti, M. P. W. Chin, A. Fassò, A. Ferrari, P. G. Ortega, A. Mairani, P. R. Sala, G. Smirnov, and V. Vlachoudis, “The FLUKA Code: Developments and Challenges for High Energy and Medical Applications”, *Nuclear Data Sheets*, vol. 120, pp. 211–214, 2014, doi:10.1016/j.nds.2014.07.049
- [6] R. Duperrier, N. Pichoff, and D. Uriot, “Saclay Codes Review for High Intensities Linacs Computations”, in *Proc. ICCS'02*, pp. 411-418, 2002.
- [7] “RCC-MRx: Design and Construction Rules for Mechanical Components of Nuclear Installations”, ISBN 2-913638-40-6, AFCEN, 2012 Edition, 2012.
- [8] ANSYS[®] Academic Research Workbench, Release 19.0, ANSYS, Inc.
- [9] Y. Dai and D. Hamaguchi, “Mechanical Properties and Microstructure of AlMg₃ Irradiated in SINQ Target-3”, *Journal of Nuclear Materials*, vol. 343, pp. 184–190, 2005, doi:10.1016/j.jnucmat.2004.11.021
- [10] B. J. Vevera, D. A. McClintock, J. W. Hyres, and B. W. Riemer, “Characterization of Irradiated AISI 316L Stainless Steel Disks Removed from the Spallation Neutron Source”, *Journal of Nuclear Materials*, vol. 450, pp. 147–162, 2014, doi:10.1016/j.jnucmat.2014.02.035
- [11] F. Sordo *et al.*, “Radiation Damage Analysis for the ESS Target”, Technical Report ESS-0037287, ESS-Bilbao, 2017.
- [12] H. Ullmaier and F. Carsughi, “Radiation Damage Problems in High Power Spallation Neutron Sources”, *Nuclear Instruments and Methods in Physics Research B*, vol. 101, pp. 406–421, 1995, doi:10.1016/0168-583X(95)00590-0
- [13] J. Habainy, Y. Dai, Y. Lee, and S. Iyengar, “Thermal Diffusivity of Tungsten Irradiated with Protons up to 5.8 dpa”, *Journal of Nuclear Materials*, submitted.
- [14] J. Habainy, Y. Lee, K. B. Surreddi, A. Prosvetov, P. Simon, S. Iyengar, Y. Dai, and M. Tomut, “A study of heavy ion beam induced damage in tungsten for high power target applications”, in preparation.
- [15] Luca Zanini, “The brightness per unit power of the ESS moderators at 570 MeV, 1.3 GeV and 2 GeV”, Technical Report ESS-0090138, European Spallation Source ERIC, Jan. 2017

RADIATION DAMAGE CALCULATION IN PHITS AND BENCHMARKING EXPERIMENT FOR CRYOGENIC-SAMPLE HIGH-ENERGY PROTON IRRADIATION

Y. Iwamoto*, H. Matsuda, S. Meigo, D. Satoh,
Japan Atomic Energy Agency, Tokai, Ibaraki 319-1195, Japan
T. Nakamoto, M. Yoshida, KEK, Tsukuba, Ibaraki 305-0801, Japan
Y. Ishi, Y. Kuriyama, T. Uesugi, H. Yashima, T. Yoshiie,
KURNS, Kyoto University, Kumatori, Osaka 590-0494, Japan
T. Shima, RCNP, Osaka University, Ibaraki, Osaka 567-0047, Japan
R. M. Ronningen, FRIB, Michigan State University, East Lansing, MI 48824, USA
K. Niita,

Research Organization for Information Science and Technology, Tokai, Ibaraki 319-1106, Japan

Abstract

The radiation damage calculation model in the Particle and Heavy Ion Transport code System (PHITS) has been developed to calculate the displacement per atom (DPA) value due to the target Primary Knock-on Atom (PKA) created by the projectile and the secondary particles which include all particles created from the sequential nuclear reactions. For the DPA value in the high-energy ($E > 100$ MeV) proton incident reactions, a target PKA created by the secondary particles was more dominant than a target PKA created by the projectile. To validate prediction of displacement cross sections in copper and aluminum irradiated by >100 MeV protons, we developed a proton irradiation device with a Gifford-McMahon (GM) cryocooler to cryogenically cool wire samples. By using this device, the defect-induced electrical resistivity changes related to the displacement cross section of copper were measured under irradiation with 125, 200 MeV and 3 GeV protons and that of aluminum under 200 MeV protons at cryogenic temperature. A comparison of the experimental displacement cross sections with the calculated results indicates that the athermal recombination-corrected displacement cross section (arc-dpa) provides better quantitative descriptions than the conventional displacement cross section (NRT-dpa) used widely for radiation damage estimation.

INTRODUCTION

As the power of proton and heavy-ion accelerators increases, the prediction of the structural damage to materials under irradiation is essential. Radiation damage of materials is usually measured as a function of the average number of displaced atoms per all atoms in a material. DPA is related to the number of Frenkel pairs, where a Frenkel pair is defined as a vacancy and a self-interstitial atom in the irradiated material. For example, ten DPA means each atom in the material has been displaced from its lattice site of the material an average of ten times. DPA serves as a quantitative measure of damage: $DPA = \sigma_d \phi$. σ_d is the displacement cross

section; and ϕ is the irradiation fluence. The level of the radiation damage in DPA units is used, for example, to estimate radiation damage of those materials experiencing significant irradiation by primary and "secondary particles" which include all particles created from the sequential nuclear reactions at high-energy ($E > 100$ MeV), high intensity facilities such as the Facility for Rare Isotope Beams (FRIB) [1], the Japan Proton Accelerator Research Complex (J-PARC) [2], European Spallation Source (ESS) [3], and others. The DPA value is a useful measure in correlating results determined by different particles and fluxes in an irradiation environment. It is however difficult to measure the DPA value in high energy reactions and the relationships between DPA and material property changes are at present unclear.

SRIM [4] is one of the major codes used to estimate radiation damage in the low-energy reaction region. SRIM treats the transport of the projectile with its Coulomb scattering and makes an approximation of cascade damage. As SRIM does not treat nuclear reactions, the calculated damage is that produced by the primary knock-on atom, PKA, because damage created by the "secondary particles" produced in nuclear reactions is not considered. On the other hands, the nuclear reaction models in advanced Monte Carlo particle transport code systems such as PHITS [5], MARS15 [6], FLUKA [7] and MCNPX [8] have been developed for the calculation of the transport of particles, nuclear reactions between particles and materials, energy distribution of PKAs, and DPA values [9, 10].

For validation of calculated DPA values, one possibility is to measure displacement cross-sections in relation to changes in electrical resistivity at cryogenic temperature. The number of surviving defects is related experimentally to defect-induced changes in the electrical resistivity of metals at around 4 K, where the recombination of Frenkel pairs by thermal motion is well suppressed. The increase in electrical resistivity due to incident high-energy protons can be used to determine the experimental displacement cross section. Recently, we developed a proton irradiation device with a Gifford-McMahon (GM) cryocooler to cryogenically cool wire samples. By using this device, we measured

* iwamoto.yosuke@jaea.go.jp

the defect-induced electrical resistivity changes related to the displacement cross section of copper were measured under irradiation with 125 MeV [11], 200 MeV [12] and 3 GeV [13, 14] protons and that of aluminum under irradiation with 200 MeV [12] protons at cryogenic temperature.

RADIATION DAMAGE MODEL IN PHITS

High-energy ions traveling through a target lose their energy in three ways: nuclear reactions, electron excitations, and Coulomb scattering. The lower the projectile energy, the higher is the energy transfer to the target atom via Coulomb scattering. The target atom directly hit by the projectile usually has much lower energy than the projectile itself and, therefore, has a larger cross-section for Coulomb scattering with other target atoms. Thus, the target PKA creates localized cascade damage where many target atoms are displaced from their original lattice site, leaving the same number of interstitials and vacancies. These point defects and their clusters affect the macroscopic material properties, such as hardness [15].

The conditions of various irradiations will be described by using the damage energy to characterize the displacement cascade. This is defined as the initial energy of target PKA, corrected for the energy lost to electronic excitations by all of the particles composing the cascade. There are mainly two ways to produce the target PKA. One is the Coulomb scattering due to PKA's directly created by the projectile, and the other is that due to PKA's created by the secondary particles. For the secondary particle production, the conservation of energy and momentum is sustained in each event using nuclear reactions for high energy particles.

To estimate the displacement cross sections, the "NRT" formalism of Norgett, Robinson, and Torrens [16] is employed as a standard to determine the fraction of the energy of the target PKA to produce damage, e.g., further nuclear displacements. The displacement cross sections can be evaluated using the following expression:

$$\sigma_{NRT} = \int_{t_d}^{t_{max}} d\sigma_{sc}/dt \cdot N_{NRT} dt \quad (1)$$

where $d\sigma_{sc}/dt$ is a universal one-parameter differential scattering cross section equation using the screening functions $f(t^{1/2})$ in reduced notation is expressed as:

$$d\sigma_{sc}/dt = \pi a_{TF}^2/2 \cdot f(t^{1/2})/t^{3/2} \quad (2)$$

where a_{TF} is the screening distance and t is a dimensionless collision parameter defined by

$$t \equiv \epsilon^2 T/T_{max} = \epsilon^2 \sin^2(\theta/2) \quad (3)$$

where θ is the center-of-mass (CM) scattering angle. One-parameter "t" in a function is convenient to integrate Eq. (1) in the PHITS calculation. T is the transferred energy to the target, and T_{max} is the maximum transferred energy as

$$T_{max} = 4M_1M_2/(M_1 + M_2)^2 \cdot E_p \quad (4)$$

where E_p is the projectile or secondary energy. ϵ is the dimensionless energy as

$$\epsilon = a_{TF}E/(Z_1Z_2e^2) \quad (5)$$

$f(t^{1/2})$ in Eq. (2) can be generalized to provide a one parameter universal differential scattering cross section equation for interatomic potentials such as screened and unscreened Coulomb potentials. The general form is

$$f(t^{1/2}) = \lambda t^{1/2-m} [1 + (2\lambda t^{1-m})^q]^{-1/q} \quad (6)$$

where λ , m , and q are fitting variables, with $\lambda=1.309$, $m=1/3$ and $q=2/3$ [9] for the Thomas-Fermi version of $f(t^{1/2})$.

N_{NRT} in Eq. (1) is the number of defects produced in irradiated material as shown in the following equation:

$$N_{NRT} = (0.8 \cdot T_d)/(2 \cdot E_d) \quad (7)$$

The displacement threshold energy E_d is typically in the range between 10 and 90 eV for most metals [9]. The damage energy, T_d , is the energy transferred to the lattice atoms and is reduced by the losses from electronic stopping in the atom displacement cascade and is given:

$$T_d = T/(1 + k_{cascade} \cdot g(\epsilon)) \quad (8)$$

where T is the transferred energy to target atom given by Eq. (3) as

$$T = T_{max} \cdot t/\epsilon_p^2 \quad (9)$$

where ϵ_p is the dimensionless projectile energy given by Eq. (4) and the projectile energy E_p . The parameters $k_{cascade}$, and $g(\epsilon)$ are as follows:

$$k_{cascade} = 0.1337Z_2^{1/6}(Z_2/A_2)^{1/2} \quad (10)$$

$$g(\epsilon) = \epsilon + 0.40244 \cdot \epsilon^{3/4} + 3.4008 \cdot \epsilon^{1/6} \quad (11)$$

The dimensionless transferred energy, ϵ , is given by Eqs. (5) and (7).

In Eq. (1), t_{max} , which is dimensionless, is equal to ϵ^2 from Eq. (3) when $\theta = \pi$. t_d is the displacement threshold energy, also dimensionless, given by Eq. (5).

DPA Distributions in Thick Targets

Based on the above formalism, we calculated DPA distributions in thick copper and tungsten targets when irradiated by 20, 200 and 800 MeV/u (MeV per atomic mass unit) proton, ^3He and ^{48}Ca ions using the PHITS and SRIM codes [4].

Figure 1 shows the depth dependence of the DPA per beam fluence for 5 cm radius and 0.1 cm thick copper and tungsten targets irradiated by 20 MeV/u beams. The DPA value in a material is related to the energy deposition. The ion ranges of proton, ^3He and ^{48}Ca are less than the mean free path for nuclear collisions with nuclear reactions, and therefore most of the ions stop without undergoing collisions. The energy dependence of the DPA value thus exhibits a so-called Bragg peak. Because the production rate of the

Content from this work may be used under the terms of the CC BY 3.0 licence (© 2018). Any distribution of this work must maintain attribution to the author(s), title of the work, publisher, and DOI.

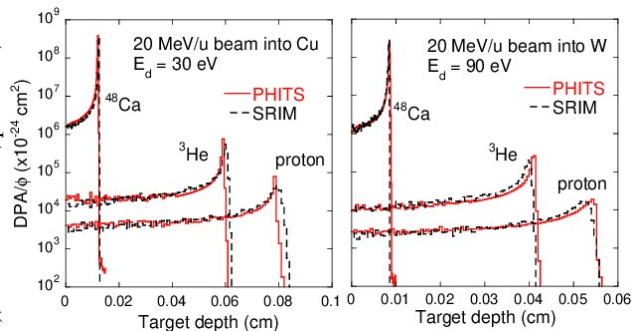


Figure 1: Depth dependence of DPA values per beam fluence for a 5 cm radius and 0.1 cm thick copper and 0.06 cm thick tungsten target irradiated by 20 MeV/u proton, ³He and ⁴⁸Ca beams.

“secondary particles” is small, SRIM results are in good agreement with PHITS results.

In the cases of the 200 MeV/u proton and ³He beams, nuclear collisions occur before the stopping range is reached, and displacement cross section contributions produced by PKA created by the “secondary particles” increase the overall DPA value at target depths smaller than the range, as shown by the PHITS results in Fig. 2. SRIM results however keep the shape of Bragg peak due to the lack of the nuclear reaction model.

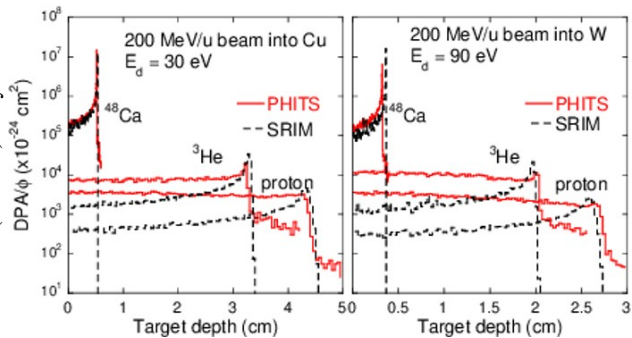


Figure 2: Depth dependence of DPA values per beam fluence for a 5 cm radius and 5 cm thick copper and 3 cm thick tungsten target irradiated by 200 MeV/u proton, ³He and ⁴⁸Ca beams.

In the case of the 800 MeV/u proton and ³He beams as shown in Fig. 3, the amount of production of the “secondary particle” is larger than that for the 200 MeV/u proton and ³He beams, and the DPA values as a function of target depth shows the characteristics of well-developed hadronic cascade. Because many secondary protons are produced by nuclear reactions, a Bragg peak of the projectile is not appeared in Fig. 3. DPA values for the 800 MeV/u ⁴⁸Ca ion beam also exhibits an increase for target depths smaller than the ion beam range.

We can conclude that damage calculations using only PKA’s directly created by the projectile, such as within SRIM, leads to severe underestimation when the projectile energy is high enough to create nuclear reactions. For

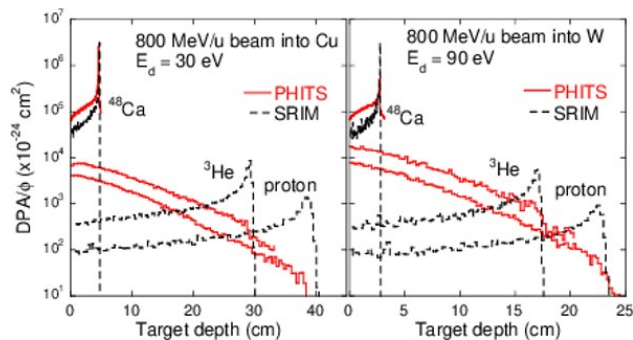


Figure 3: Depth dependence of DPA values per beam fluence for a 5 cm radius and 45 cm thick copper and 25 cm thick tungsten target irradiated by 800 MeV/u proton, ³He and ⁴⁸Ca beams.

proton and ³He beams, the DPA values near surface of the target increase with the incident energy ($E > 200$ MeV/u) of ions [9].

BENCHMARKING EXPERIMENTS OF DISPLACEMENT CROSS SECTIONS

For validation of the displacement cross section calculations, we have obtained experimental displacement cross sections of copper in the case of 125, 200 MeV and 3 GeV proton irradiation using the Fixed-Field Alternating Gradient (FFAG) [17] accelerator facility at Institute for Integrated Radiation and Nuclear Science (KURNS) [11], the cyclotron facility at Research Center for Nuclear Physics (RCNP), Osaka University [12] and J-PARC [13, 14]. The experimental displacement cross section of aluminum was also obtained at RCNP. In this section, we introduce measurements of displacement cross sections of copper and aluminum under 200 MeV protons at RCNP.

Figure 4 shows a schematic of the cryogenic irradiation chamber with the GM cryocooler (RDK-408D2, Sumitomo Heavy Industries, Ltd.) with a cooling capacity of 1 W at 4 K and the twin sample assembly connected to the 2nd stage of the cold head. The GM cryocooler cooled the sample by means of a conduction coolant via the aluminum plate and the oxygen-free high thermal conductivity copper (OFHC) block. The 1-mm-thick aluminum plates of the thermal radiation shield connected to the 40 K stage of the refrigerator covered the entire sample assembly to intercept any thermal radiation from the ambient irradiation chamber.

A pre-calibrated electrical resistance thermometer (Cernox thermometer, Lake Shore Cryotronics, Inc.) was attached in the OFHC block and the aluminum nitride (AlN) plate to confirm the cooling performance of the GM cryocooler. To simultaneously measure the changes in electrical resistivity of two samples under 200 MeV proton irradiation, two aluminum plates with the aluminum and copper wire samples were connected to the OFHC block by using bolts, as shown in Fig. 4.

Table 1 lists the characteristics of the wire samples. Each aluminum and copper wire with a 0.25-mm diameter, pur-

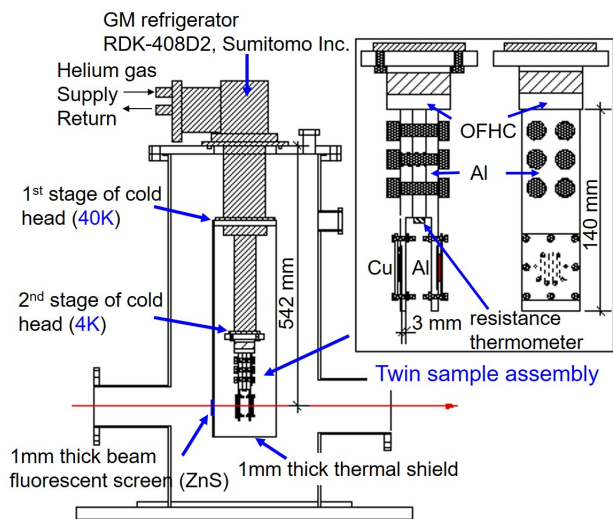


Figure 4: Schematic of cryogenic irradiation chamber and twin sample assembly with side view and view from beam upstream.

chased from the Nilaco Corporation, was set on the AlN plate in a serpentine-shaped line. The AlN plate was used because of its excellent electrical insulation and high thermal conductivity. Before irradiation, the aluminum wire and the copper wire were annealed in vacuum for 1 h at 550 °C (823 K) and 1100 °C (1273 K), respectively. The wire and the CX1050-SD Cernox resistance thermometer were carefully sandwiched between the 1-mm-thick AlN plate and the 1.5-mm-thick AlN plate.

Table 1: Characteristics of Wire Samples in the RCNP Experiment

Material	Aluminum	Copper
Diameter	0.25 mm	0.25 mm
Length	123 mm	134 mm
Electrical resistivity at room temperature	$2.19 \times 10^{-8} \Omega\text{m}$	$1.47 \times 10^{-8} \Omega\text{m}$
Electrical resistivity at 3 K	$4.43 \times 10^{-11} \Omega\text{m}$	$2.02 \times 10^{-11} \Omega\text{m}$

The electrical resistance of the wire was measured using an apparatus combining a current source (model 6221, Keithley Instruments, Inc.) and a nano-voltmeter (model 2182A, Keithley Instrument, Inc.). This apparatus is based on the current-reversal method (four-point technique) in the delta mode, which works by sourcing pulses with opposite polarity and taking one measurement during each pulse. A current of ± 100 mA was fed into the copper wire with the polarity changing at a frequency of (10 Hz). The precision of this resistance measurement at 3 K was $\pm 0.001 \mu\Omega$ corresponding to an electrical resistivity of $\pm 0.67 \text{ f}\Omega\text{m}$ for aluminum and $\pm 0.60 \text{ f}\Omega\text{m}$ for copper, where the electrical resistivity of the

sample ρ is expressed as follows:

$$\rho = RA/L \quad (12)$$

where R is the measured electrical resistance, L is the length between two potential points, and A is the area of the sample. The temperature of the Cernox resistance thermometer was measured using a temperature controller (model 335, Lake Shore Cryotronics, Inc.). According to the manual of the temperature controller, the accuracy of temperature measurement using the Cernox thermometer is 7.1 mK at 4.2 K.

The number of protons during irradiation was measured at the beam relative monitor in situ by counting the number of events produced by neutron-proton scattering at the 2.2 mg/cm² thick polyethylene in front of the cryogenic irradiation chamber [12]. Because the 200 MeV proton beam lost energy in the sample holder to materials such as AlN and aluminum plates in the beam line, the proton energies incident on the samples were estimated to be 185.3 ± 0.9 MeV for the aluminum wire and 195.5 ± 0.5 MeV for the copper wire, as determined using the PHITS code

The temperature increase due to beam heating was 1.2 K, 1.5 K, and 2.0 K in the cases of the 1.35 nA, 2.0 nA, and 3.0 nA currents, respectively, and the temperature was maintained below 5 K during beam irradiation. The electrical resistances of the aluminum and copper samples increased during beam irradiation owing to the production of defects in the wires. The total beam fluence on the sample was 3.89×10^{18} protons/m². The total increase in resistance was 0.76 $\mu\Omega$ for aluminum wire and 2.34 $\mu\Omega$ for copper wire. The damage rates of the aluminum and copper wires did not change considerably under proton irradiation with currents between 1.35 and 3.0 nA.

The displacement cross section can be related easily to the measured increase in resistivity and the calculated damage energy in the metal. The experimental displacement cross-section σ_{exp} was obtained using the measured damage rate, which is the ratio of the change in resistivity of metal $\Delta\rho_{metal}$ at around 5 K to the beam average fluence $\bar{\phi}$ [12]:

$$\sigma_{exp} = \Delta\rho_{metal}/(\rho_{FP} \cdot \bar{\phi}) \quad (13)$$

where ρ_{FP} is the change in resistivity per Frenkel-pair density for a particular metal (experimental data on ρ_{FP} were summarized and discussed in [18, 19]). In this work, ρ_{FP} was set to $3.9 \pm 0.6 \mu\Omega\text{m}$ for aluminum [20] and $2.2 \pm 0.5 \mu\Omega\text{m}$ for copper [21], and the same values were used for estimating the displacement cross section of the 125-MeV-proton-irradiation experiments [11], the 1.1- and 1.94-GeV-proton-irradiation experiments [22], the 3-GeV-proton-irradiation experiments [13, 14] and the Jung data [23] for the sake of comparison with our experimental data.

Figure 5 shows the experimental displacement cross-section data of aluminum and copper obtained in FFAG data [11], RCNP data [12], J-PARC data [13, 14], BNL data [22] and Jung data [23]. It is assumed that the increase in resistivity is the sum of resistivity-per-Frenkel-pair values.

The displacement cross-sections with energies are almost constant with energies above 100 MeV.

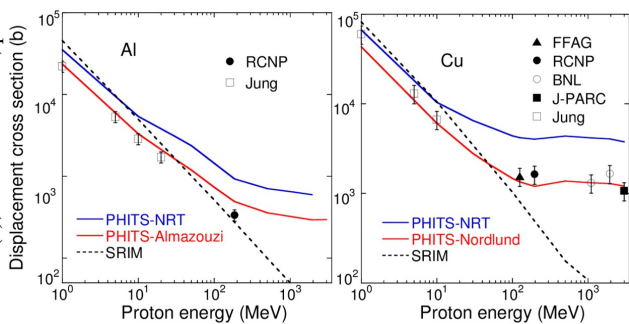


Figure 5: Displacement cross-sections for proton irradiation of aluminum (left) and copper (right): FFAG data [11] (black triangle), RCNP data [12] (black circles), BNL data [22] (open circles), J-PARC data [13, 14] (black square), Jung data [23] (open squares), NRT-dpa cross-section (blue line), the arc-dpa cross section (red line) and SRIM results (dashed line). The displacement energy is 27 eV for aluminum and 30 eV for copper.

Moreover, Fig. 5 shows results calculated by SRIM code, PHITS code with the NRT-dpa in Eq. (1) and the athermal-recombination-corrected displacement damage (arc-dpa) cross sections, which includes the results of the Molecular Dynamics simulation method (MD) for more accurate estimation of the actual damage production [24]. Because SRIM cannot calculate nuclear reactions, SRIM results are much smaller than others in high-energy region. The arc-dpa cross section was calculated using the efficiency function ζ [24].

$$\sigma_{arc-dpa} = \int_{t_d}^{t_{max}} d\sigma_{sc}/dt \cdot N_{NRT} \cdot \zeta dt \quad (14)$$

$$\zeta = \frac{1 - c_{arc-dpa}}{(2E_d/0.8)^{b_{arc-dpa}}} T_d^{b_{arc-dpa}} + c_{arc-dpa} \quad (15)$$

The arc-dpa displacement parameter is based on two tabulated parameters: $b_{arc-dpa}$, and $c_{arc-dpa}$. To obtain these parameters, the results of MD modelling were taken for aluminum from Almazouzi et al. [25] and copper from Nordlund et al. [24]. These parameters are listed in [12]. In terms of the cross sections of aluminum and copper in the experimental data and those determined using arc-dpa, PHITS with the efficiency function shows better agreement with the experimental data than with the NRT-dpa cross section, which has been widely used for radiation damage estimation. Further studies on measuring other metals under the low radiation damage are in progress, which will allow us to study the basic physics of point defects in the high-energy ion irradiation region.

CONCLUSION

The radiation damage calculation model in the PHITS cde has been developed to calculate the DPA value due to

the target PKA created by the projectile and the secondary particles which include all particles created from the sequential nuclear reactions. For the DPA value in the high-energy ($E > 100$ MeV) proton incident reactions, a target PKA created by the secondary particles was more dominant than a target PKA created by the projectile.

To validate predictions of displacement cross sections in copper and aluminum irradiated by >100 MeV protons, we developed a proton irradiation device with a GM cryocooler to cryogenically cool wire samples. By using this device, the defect-induced electrical resistivity changes related to the displacement cross section of copper were measured under irradiation with 125, 200 MeV and 3 GeV protons and that of aluminum under 200 MeV protons at cryogenic temperature. It is concluded that the experimental displacement cross sections agree better with calculated arc-dpa cross sections than with calculated NRT-dpa cross sections.

ACKNOWLEDGEMENTS

The authors wish to express their gratitude to Prof. Dr. M. Fukuda and the staff at RCNP for their generous support for beam operation. They also wish to thank to Prof. Dr. T. Ogitsu at KEK and the staff at KURNS, KEK and Japan Atomic Energy Agency (JAEA) for their generous support for device development. Y. Iwamoto wishes to express his gratitude to Prof. Dr. G. Bollen for his generous support to simulation study at MSU.

This work was supported by JSPS KAKENHI Grant Number JP16H04638. The calculation work was supported in part by the US National Science Foundation under grant PHY06-06007. The present study includes the results of “Measurement of displacement cross-section at J-PARC for structural material utilized at ADS” entrusted to JAEA by the Ministry of Education, Culture, Sports, Science and Technology of Japan (MEXT).

REFERENCES

- [1] Facility for Rare Isotope Beams (FRIB), <http://www.frib.msu.edu/>
- [2] Japan Proton Accelerator Research Complex (J-PARC), <http://j-parc.jp/index-e.htm>
- [3] European Spallation Source (ESS), <http://ess-scandinavia.eu/>
- [4] J. F. Ziegler, J. P. Biersack and U. Littmark, *The Stopping and Range of Ions in Solids*. New York, USA: Pergamon Press, 1985.
- [5] T. Sato et al., “Features of particle and heavy ion transport code system (PHITS) version 3.02”, *J. Nucl. Sci. Technol.*, vol. 55, pp. 684–695, 2018, doi:10.1080/00223131.2017.1419890
- [6] N.V. Mokhov et al., “The MARS code system user’s guide”, Fermilab, Batavia, USA, Rep. Fermilab-FN-628, 1995.
- [7] T. T. Bohlen et al., “The FLUKA code: Developments and Challenges for High Energy and Medical Applications”, *Nuclear Data Sheets*, vol. 120, pp. 211–214, 2014, doi:10.1016/j.nds.2014.07.049

- [8] L.S. Water *et al.*, “MCNPX user’s manual version 2.4.0”, Los Alamos National Laboratory, Los Alamos, New Mexico, USA, Rep. LA-CP-02-408, 2002.
- [9] Y. Iwamoto *et al.*, “Improvement of radiation damage calculation in PHITS and tests for copper and tungsten irradiated with protons and heavy-ions over a wide energy range”, *Nucl. Instr. Meth. B*, vol. 274, pp. 57–64, 2012, doi:10.1016/j.nimb.2011.11.038
- [10] Y. Iwamoto *et al.*, “Calculation of displacement cross-sections for structural materials in accelerators using PHITS event generator and its applications to radiation damage”, *J. Nucl. Sci. Technol.*, vol. 51, pp. 98–107, 2014, doi:10.1080/00223131.2013.851042
- [11] Y. Iwamoto *et al.*, “Measurement of the displacement cross-section of copper irradiated with 125 MeV protons at 12 K”, *J. Nucl. Mater.*, vol. 458, pp. 369–375, 2015, doi:10.1016/j.jnucmat.2014.12.125
- [12] Y. Iwamoto *et al.*, “Measurement of displacement cross sections of aluminum and copper at 5 K by using 200 MeV protons”, *J. Nucl. Mater.*, vol. 508, pp. 195–202, 2018, doi:10.1016/j.jnucmat.2018.05.038
- [13] S. Meigo *et al.*, “Measurement of displacement cross-section for structural materials in high-power proton accelerator facility”, presented at the 9th Int. Particle Accelerator Conf. (IPAC’18), Vancouver, Canada, Apr. 2018, paper MOPML045.
- [14] S. Meigo *et al.*, “Beam instruments for high power spallation neutron source and facility for ADS in J-PARC”, presented at the 61st ICFA Advanced Beam Dynamics Workshop on High-Intensity and High-Brightness Hadron Beams (HB2018), Daejeon, Korea, June 2018, paper TUP1WE03, this conference.
- [15] G. S. Was, *Fundamentals of Radiation Materials Science, Materials and Alloys*. New York, USA: Springer Press, 2017.
- [16] M. J. Norgett *et al.*, “A proposed method of calculating displacement dose rates”, *Nucl. Engineering and Design*, vol. 33, pp. 50–54, 1975, doi:10.1016/0029-5493(75)90035-7
- [17] S. L. Sheehy *et al.*, “Characterization techniques for fixed-field alternating gradient accelerators and beam studies using the KURRI 150 MeV proton FFAG”, *Prog. Theor. Exp. Phys.*, 073G01(31 pages), 2016, doi:10.1093/ptep/ptw086
- [18] A. Yu. Konobeyev *et al.*, “Evaluation of effective threshold displacement energies and other data required for the calculation of advanced atomic displacement cross-sections”, *Nucl. Energy and Technology*, vol. 3, pp. 169–175, 2017, doi:10.1016/j.nucet.2017.08.007
- [19] C. H. M. Broeders and A. Yu. Konobeyev, “Defect production efficiency in metals under neutron irradiation”, *J. Nucl. Mater.*, vol. 328, pp. 197–214, 2004, doi:10.1016/j.jnucmat.2004.05.002
- [20] P. Ehrhart and W. Schilling, “Investigation of interstitials in electron-irradiated aluminum by diffuse-X-Ray scattering experiments”, *Phys. Rev. B*, vol. 8, pp. 2604–2621, 1973, doi:10.1103/PhysRevB.8.2604
- [21] H. G. Haubold and D. Martinsen, “Structure determination of self-interstitials and investigation of vacancy clustering in copper by diffuse X-ray scattering”, *J. Nucl. Mater.*, vol. 69–70, pp. 644–649, 1978, doi:10.1016/0022-3115(78)90302-1
- [22] G. A. Greene, “Direct measurements of displacement cross sections in copper and tungsten under irradiation by 1.1-GeV and 1.94-GeV protons at 4.7 K”, in *Proc. 6th International Meeting on Nuclear Applications of Accelerator Technology (AccApp’03)*, San Diego, CA, USA, June 2004, pp. 881–892.
- [23] P. Jung, “Atomic displacement functions of cubic metals”, *J. Nucl. Mater.*, vol. 117, pp. 70–77, 1983, doi:10.1016/0022-3115(83)90011-9
- [24] K. Nordlund *et al.*, “Improving atomic displacement and replacement calculations with physically realistic damage models”, *Nature Communications*, vol. 9, pp. 1084, 2018, doi:10.1038/s41467-018-03415-5
- [25] A. Almazouzi *et al.*, “Defect production and damage evolution in Al: a molecular dynamics and Monte Carlo computer simulation”, *Nucl. Instr. Meth. B*, vol. 153, pp. 105–115, 1999, doi:10.1016/S0168-583X(98)00989-6

DESIGN OF THE TARGET DUMP INJECTION SEGMENTED (TDIS) IN THE FRAMEWORK OF THE HIGH LUMINOSITY LARGE HADRON COLLIDER (HL-LHC) PROJECT

L. Teofili^{*,1,2}, M. Migliorati^{1,2}, Sapienza University of Rome, Rome, Italy
D. Carbajo, I. Lamas, A. Perillo, CERN, Geneva, Switzerland
¹also at CERN, Geneva, Switzerland; ²also at INFN, Rome, Italy

Abstract

The High Luminosity Large Hadron Collider (HL-LHC) Project at CERN calls for increasing beam brightness and intensity. In this scenario, most equipment has to be redesigned and rebuilt. In particular, beam intercepting devices (such as dumps, collimators, absorbers and scrapers) have to withstand impact or scraping of the new intense HL-LHC beams without failure. Furthermore, minimizing the electromagnetic beam-device interactions is also a key design driver since they can lead to beam instabilities and excessive thermo-mechanical loading of devices. In this context, the present study assesses the conceptual design quality of the new LHC injection protection absorber, the Target Dump Injection Segmented (TDIS), from an electromagnetic and thermo-mechanical perspective. This contribution analyzes the thermo-mechanical response of the device considering two cases: an accidental beam impact scenario and another accidental scenario with complete failure of the RF-contacts. In addition, this paper presents the preliminary results from the simulation of the energy deposited by the two counter-rotating beams circulating in the device.

INTRODUCTION

The CERN accelerator complex has been undergoing upgrades to improve its performance. In the framework of the LIU (LHC Injection Upgrade) [1] and HL-LHC (High Luminosity LHC) [2] projects, an increase of the beam brightness and intensity is foreseen [1]. Several systems have to be redesigned and rebuilt to survive the new demanding situation. This is particularly true for the beam intercepting devices (BIDs), such as dumps, collimators, absorbers and scrapers [3], since they have to deal with two main beam intensity related phenomena:

- Nuclei-Matter Interactions (NMI). BIDs are usually responsible for absorbing a large part of the beam energy (beam dumping) or for the beam scraping, i.e. the removal of the unstable peripheral beam particles (beam halos). Thus, they are directly exposed to beam impacts and particle irradiation. It is well known that the incidence of the proton beam on the device material results in an energy deposition in the material itself and that this effect increases linearly with the beam intensity.
- Electromagnetic Beam-Device Interactions. BIDs usually operate in close proximity to the particle beam. In

this context, if the device impedance (the electromagnetic beam-device coupling index) is not minimized, they will experience strong electromagnetic interaction with the beam circulating in the accelerator. This interaction causes an energy deposition in the equipment (RF-Heating), proportional to the square of the beam intensity and to the device impedance [4].

The induced energy deposition on the BIDs may lead to an uneven temperature distribution, the resulting thermal gradients can generate high mechanical stresses, potentially causing material failure or other undesired effects [5–7].

The higher HL-LHC beams intensity will increase the energy deposited in equipment by NMI and RF-Heating. Thus, these phenomena needs to be carefully accounted for during the design of the new BIDs. Their thermo-mechanical effects must be investigated through a series of simulations. Thus, the present work reports the results of the studies performed to assess the electro-thermo-mechanical behaviour of the new LHC injection protection absorber, the Target Dump Injection Segmented (TDIS) [8], see Fig. 1.

The first section of this contribution describes the scope of the device, its functionality, its location in the CERN accelerator complex and its geometry. Subsequently, the results of the electromagnetic and thermo-mechanical simulations are shown. Two worst case scenarios are discussed. Case one: beam impacting on the device. Case two: complete failure of the RF-contacts, i.e. maximum RF-heating load. Finally, the paper presents the preliminary strategy for simulating the power dissipated by the two counter-rotating beams circulating in the device.

THE TDIS

The TDIS is a dump/absorber aimed at protecting downstream LHC equipment during the injection phase. Since the LHC stores two counter rotating beams, two of these devices will be installed in the machine. They will be located in the LHC ring, immediately downstream of the connection between the transfer line from Super Proton Synchrotron (SPS)-to-LHC [8], in order to absorb the injected beam in case of an injection kicker malfunctions [9]. Furthermore, the device will be used as a dump for the proton beam during commissioning operations [9].

The TDIS has been developed as an improved version of the current absorber, Target Dump Injection (TDI) [8]. In 2015 and in the LHC first operational run (2009-2013), the TDI experienced severe issues, as structural damage and

* lorenzo.teofili@uniroma1.it

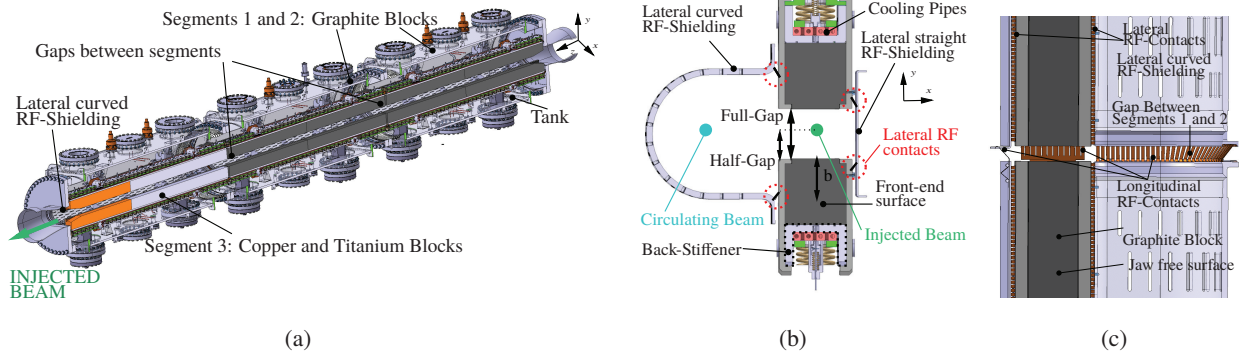


Figure 1: (a) Complete TDIS design Geometry. (b) Section view in x - y plane. The main components are labeled. (c) Section view in x - z plane. The main components are labeled.

jaws deformations [10]. These issues are believed to be due to unexpected, excessive RF-Heating [6]. To avoid such problems, in the TDIS a new system of RF-contacts and RF-shielding (see Fig. 1b and 1c) will be implemented. It will allow an impedance reduction with respect to the TDI, a crucial requirement to decrease the RF-heating load of the high intensity/brightness HL-LHC beams [11].

The geometry of the TDIS is presented in Fig. 1 and described in detail in [8]. The core of the TDIS are two vertically movable jaws (upper and lower jaw), divided into three segments, each of them composed of absorbing blocks of different materials. The three segments of a jaw are separated by gaps of 15 mm (see Fig. 1a and 1c). This arrangement limits jaw bending and deformation allowing unconstrained thermal expansion at the gaps. This makes the TDIS design mechanically more robust if compared with the TDI.

In the TDIS there are two counter rotating beams circulating at all time: the injected beam that is passing between the jaws and the circulating one traversing the device in the RF-screen, Fig. 1b. During the injection phase the jaws have a half-gap of 4 mm with respect to the injected beam reference orbit (golden orbit), refer to Fig. 1b. If the orbit of the actual injected beam differs more than the allowed tolerance, it will impact against the jaws so it is dumped. After the injection phase the jaws are completely open (half gap 55 mm) [9].

THE ACCIDENTAL BEAM IMPACT SCENARIO

The TDIS will cope with different failure scenarios of the SPS-to-LHC injection magnet [9] that can arise during the injection phase until the LHC ring is completely filled. In such failure cases, the proton beam is misdirected resulting in an impact against the absorbing blocks of the TDIS jaws [12]. Two main types of accidents could occur during the lifespan of the device. They are defined by the impact parameter b , the distance between the beam impact position and the jaw free surface, (Fig. 1b).

- Grazing (small impact parameter, $0\sigma_y \leq b \leq 1\sigma_y$, where σ_y is the transverse root mean square beam dimension on the y axis): the proton beam impacts the graphite block at a small depth (compared to the beam core dimension) with respect to the jaw free surface. Most of the energy is deposited on the material surface.
- Central impact (large impact parameter, $b \gg \sigma_y$): the proton beam impacts the front end of the graphite block. Most of the energy is deposited in the material bulk.

Furthermore, in both cases only one jaw, either the upper or lower one is expected to receive the beam impact. Thus, the thermo-mechanical response of only one jaw has been investigated. The jaw model is shown in Fig. 1b. The beam-matter interaction was simulated using the FLUKA Monte Carlo code [13, 14]. Subsequently, the 3D dissipated energy density map, obtained from FLUKA, was imported as a thermal load into the software ANSYS[®] [15], to analyze the thermo-mechanical behavior of the device.

Both in the grazing impact scenario and in the central impact one the first jaw segment experienced the highest temperatures and stresses. The thermal analysis revealed that a grazing impact may lead to a rise of the absorbing blocks temperature up to 1392°C in the first impacted graphite block (see Fig. 2) whilst the other jaw components experience a negligible increase in temperature. This is due to the fact that most of the energy is deposited in the graphite block, on its jaw free surface, far from other components. A temperature of 1392°C is not critical for the graphite, as it can tolerate up to 2800°C [16]. Mechanical studies have shown that the maximum mechanical stresses induced by the thermal gradients are also localized in the first graphite block. Since graphite is a brittle material, the Christensen criterion [17] was used to assess its mechanical resistance. The local Christensen coefficient is shown for the graphite block in Fig. 3. The fact that this coefficient remains locally below 1 guarantees the mechanical robustness of the block, provided that the principal stresses are lower than the compressive and tensile limits of the material.

Regarding the central impact scenario, the thermal analysis has shown that the most dangerous thermal gradient

Content from this work may be used under the terms of the CC BY 3.0 licence (© 2018). Any distribution of this work must maintain attribution to the author(s), title of the work, publisher, and DOI.

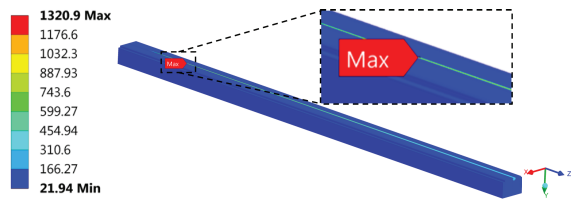


Figure 2: Surface temperature [°C] of the graphite block due to grazing impact. The high temperature is extremely localized on a longitudinal line in the jaw free surface.

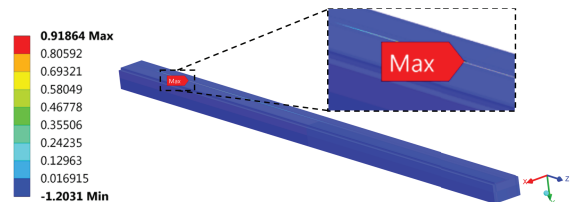


Figure 3: Christensen coefficient [adimensional unit] on the graphite block due to grazing impact. A value superior or equal to 1 implies material failure. However, 0.91 is acceptable because of the conservative assumption of considering the static yield stress at room temperature as maximum tensile limits. Indeed, the static yield stress for the graphite increases with temperature in this temperature range [18]. Like the high temperature, the stresses are also extremely localized on a longitudinal line in the free jaw surface.

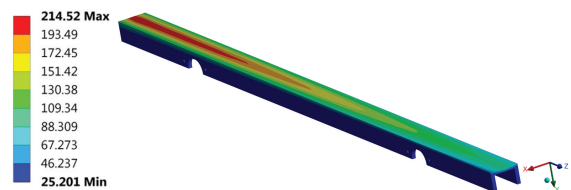


Figure 4: Surface temperature [°C] of the back stiffener due to the particle shower after the central impact.

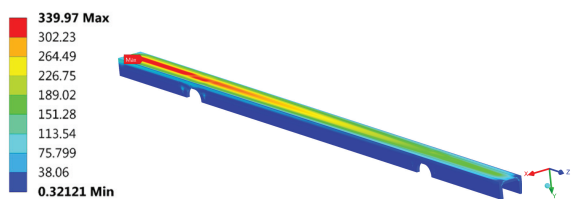


Figure 5: Surface Stresses [MPa] of the back stiffener due to the thermal gradient.

develops in the molybdenum alloy (TZM) back-stiffener, which reaches a peak temperature of 215°C (see Fig. 1b and 4), and in the oxygen-free copper cooling pipes (see Fig. 1b), which reaches a peak temperature of 92°C. Mechanical analyses have revealed significant stresses in these two key components. They have shown that the pipes are likely to undergo some minor plastic deformation as a consequence of the thermal gradients caused by the particle shower energy deposition. However, this is not expected to be detrimental for the device function, given the high ductility of the

material. For the back-stiffener, the Finite Element Analysis (FEA) shows that, in the event of a central impact, it will be subjected to mechanical stresses of 340 MPa. This stress value is below the elastic limit of the material for that temperature which is 455 MPa [18] (resulting in a safety margin of 1.33). It must be noted that this is a conservative approach. Indeed, the energy deposition due to the beam impact is very localized in space and takes place in an extremely short time scale (strain rate 1.610^2 [s⁻¹]). Thus, a dynamic behavior for the TZM must be considered, i.e. elastic waves are generated in the material because of the sudden sharp temperature increase and the induced localized material expansion immediately after the beam impact [5]. In this case, the maximum stress obtained by the simulation must be compared with the dynamic yield strength for TZM, which is significantly larger than the static one [19].

COMPLETE RF-CONTACT FAILURE SCENARIO

To minimize the TDIS impedance, and so the RF-heating, four main elements are present in the device design: the lateral curved RF-shielding, the lateral straight RF-shielding, the longitudinal RF-contacts and the lateral RF-contacts (see Fig.1). The RF-contacts keep the electrical connection of all the device components, allowing the image currents (a flow of electrons induced by the beam electromagnetic field in the device walls) to flow easily. The shielding modifies the geometry seen by the beam in order to avoid the excitation of electromagnetic high order resonant modes (HOM) in the device structure. The overall effect of these components is a low impedance for the TDIS as shown in detail in the work of Teofili et al. [20]. In the same work the thermo-mechanical effects of the RF-heating and of the secondary beam halos are also discussed in the case of complete failure of the longitudinal RF-finger in the device. Thus, since in this paper the whole TDIS project is discussed, for the sake of completeness, the main results are summarized. In case of complete failure of the longitudinal RF-contacts, for a jaws half-gap of 4 mm, electromagnetic simulations performed by CST studio suite® [21] have shown that High Order Modes (HOMs) can develop in the structure at frequencies of 0.75 GHz and higher. Since the HL-LHC beams spectrum has a frequency content up to 1.5 GHz, the HOMs between 0.75 and 1.50 GHz are excited. Considering only the injected beam as a source of HOMs excitation, the power dissipated is 1003 W, (the two beam case scenario is considered in the next section). Moreover, the RF-heating due to resistive wall impedance has to be considered, a further 798 W. Finally, 580 W, due to the interaction between the secondary beam halos and the jaws, needs to be added. These thermal loads occur simultaneously and continuously during the injection phase, which can last up to 45 minutes. The thermo-mechanical simulations have shown a high temperature, 293°C, around the longitudinal gaps between the TDIS modules whereas the maximum stresses are on the lateral RF-shielding, at the connection with the tank. However, the

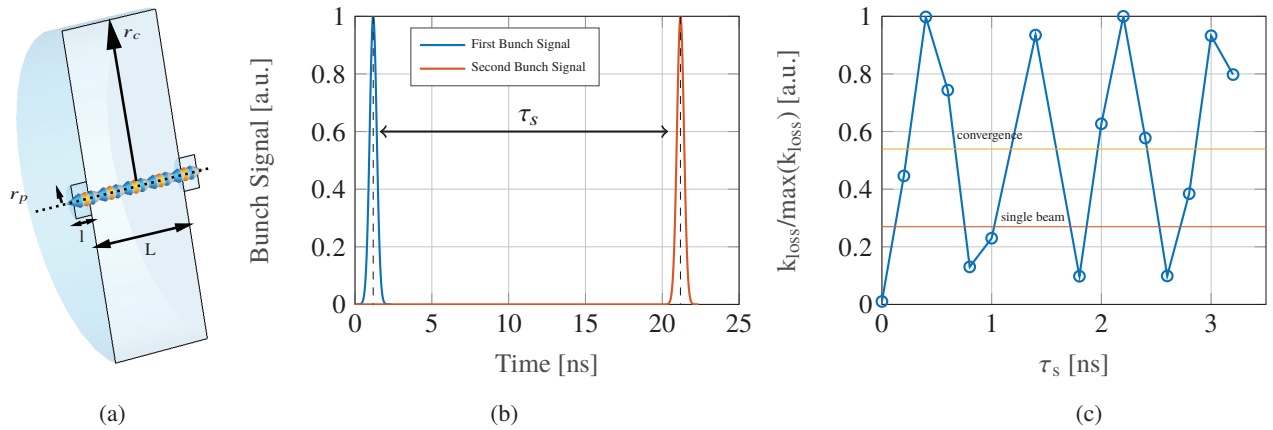


Figure 6: (a) Simulated cavity model with geometrical entities: $r_c = 100$ mm, $r_p = 10$ mm, $L = 60$ mm, $l = 10$ mm. (b) Gaussian bunch signal, the time delay τ_s is indicated. (c) Normalized energy loss factor [adimensional unit] for different time delays τ_s between bunches computed for an electrical conductivity of the wall of 10^{-3} S/m. The convergence value is reported (the constant value of the energy loss factor of the two beam for $\tau_s > 100$ ns). Furthermore, also the energy loss of a single beam ($q = 4.5 \cdot 10^{-8}$ C, $\sigma = 70$ mm) passing in the structure is plotted.

maximum von Mises stress value (85 MPa) is well below the static yield strength of the material (250 MPa for stainless steel) and the temperatures reached are not dangerous for the material.

FUTURE STRATEGY FOR RF-HEATING LOAD DUE TO DOUBLE BEAM

Another scenario to be investigated carefully is the one in which the TDIS operates in nominal conditions. In this case there is no failure in any of the device components, the injected beam is passing in its golden orbit between the jaws (the latter has a half-gap of 4 mm) and the circulating beam traverses the TDIS at the center of the curved RF-shielding. In this framework, it is crucial to consider as simultaneous source of heating the two beams. The main heat load mechanisms are still NMI and RF-heating. The contribution of NMI is expected to be unchanged with respect to the already discussed case of complete RF-contacts failure (580 W for 45 minutes) whereas, this is not the case for the RF-Heating. Indeed, the NMI contribution mainly arises from the interaction of the injected beam secondary halos with the close jaws; the circulating beam is too far from the TDIS components to deposit a significant amount of energy due to NMI. Regarding the RF-heating, both beams act as a source of excitation for HOMs in the structure; thus, they both contribute to the energy deposition. Unfortunately, while the problem of the energy deposition due to the device impedance for a single beam has been rigorously investigated [4], the same problem for a double beam has remained relatively unexplored and is still unsolved for the general case. The pioneering study of C. Zannini, G. Rumolo and G. Iadarola [22] has solved it for a simple pipe geometry. It seems to indicate an interference-like behaviour of the RF deposited energy in the considered structure dependent on the time delay between the entrance of the first and the

second beam in the device, τ_s (see Fig. 6b). Thus, the RF-heating load of two counter-rotating beams in a worst case scenario could be up to four times the heat load induced in the same device by a single beam. In order to benchmark this thesis for more complex geometries the pill-box cavity represented in Fig. 6a was simulated with the software CST particle studio. Using the Wakefield solver [23] the passage of two counter rotating beams, both positioned exactly at the center of the structure was modelled. Both beams were composed of only one gaussian bunch with a charge $q = 4.5 \cdot 10^{-8}$ C and a root mean square $\sigma_r = 70$ mm. The first beam entered the structure at time $t_1 = 0$ s, while the second one entered with an arbitrary delay τ_s (see Fig. 6b). Computing the total energy loss factor for every τ_s as a sum of the loss factors of the two beams, the results shown in Fig. 6c were obtained. In the same figure the normalized energy loss factor of a single beam traversing the structure is also represented. It is possible to notice the oscillating, interference-like, behaviour, i.e. the deposited energy of two counter rotating beams passing in the pill-box have peaks four times higher than the energy deposited in the same pill-box by a single beam. Furthermore, simulations not reported in this work displayed that for high values of τ_s , more than 100 ns with a wall conductivity $\sigma = 10^{-3}$ S/m, there is no more oscillations in the loss factor. It converges to a value that is the double of the loss factor of a single beam. This is because, with the considered value of the electrical conductivity σ , the resonant electric field induced by the first bunch is completely decayed after 100 ns. Thus, the second bunch experiences the same initial condition than the first one and generates the same energy loss. Thus, as can be easily seen, the simulation results, for the particular case proposed, validate the thesis of an interference like behaviour of the deposited energy for two counter-rotating beams. Please note that the results shown in this section are preliminary and neglect various aspects, for instance the fact that in the

real case the two counter rotating beams cannot share the exact same orbit. However, they are encouraging as they reveal the capability of the CST software to simulate this kind of phenomenon. Additionally, they can be used to have an initial estimate of the total deposited energy in a device given a delay τ_s between the beams entrance in the structure. Further investigations are currently on going at CERN with the goal of better understanding the phenomenon and of obtaining a general solution of the two counter rotating beam energy deposition problem, valid also for complex geometries.

CONCLUSION

In this work we reviewed the electromagnetic and thermo-mechanical analysis performed to assess the quality of the new Target Dump Injection Segmented. In particular, we discussed two critical scenarios: an accidental case of beam impact on the device and another accidental case of complete longitudinal RF-contacts failure. In both cases, the design was found to be robust and capable of withstanding the generated temperatures and stresses. Furthermore, another possible critical scenario was outlined. It is the one in which the device operates in nominal conditions and the two beams that are passing through it are both considered as a source of RF-heating loads. This problem was found unsolved in the literature in the general case. Hence, this study analyzed it for the simple case of a pill-box, obtaining an interference like behaviour for the deposited energy. Future work will try to extend such a results for more complex cases, investigating a possible analytic solution.

ACKNOWLEDGMENTS

The authors would like to thank S. Gould, J. Briz and J. Maestre for the helpful discussions on the topic.

REFERENCES

[1] J. Coupard *et al.*, “LHC Injectors Upgrade Projects at CERN”, in *Proc. 7th Int. Particle Accelerator Conf. (IPAC’16)*, Busan, Korea, May 2016, paper MOPOY059, pp. 992–995.

[2] G. Apollinari, A. Bejar, O. Bruning, M. Lamont, and L. Rossi, “High-Luminosity Large Hadron Collider (HL-LHC) : Preliminary Design Report”, CERN, Geneva, Switzerland, Rep. CERN-2015-005, Dec. 2015.

[3] Beam Intercepting Design Review, <https://en-sti-tcd.web.cern.ch/en-sti-tcd/html/equipment.html>

[4] M. Furman, H. Lee, and B. Zotter, “Energy loss of bunched beams in RF cavities”, Lawrence Berkeley National Laboratory, Berkeley, California, Rep. SSC-086, 1986.

[5] A. Bertarelli, “Beam Induced Damage Mechanisms and Their Calculation”, in *Joint International Accelerator School: Beam Loss and Accelerator Protection*, Newport Beach, CA, USA, 5–14 Nov. 2014, edited by R. Schmidt, CERN-2016-002 (CERN, Geneva, 2016), pp. 159–227.

[6] B. Salvant *et al.*, “Beam Induced RF Heating in LHC in 2005”, in *Proc. 7th Int. Particle Accelerator Conf. (IPAC’16)*, Busan, Korea, May 2016, paper MOPOR008, pp. 602–605.

[7] D. Lipka, “Heating of a DCCT and a FCT due to wake losses in PETRAIII, simulations and solutions”, presented at the Simulation of Power Dissipation & Heating from Wake Losses Workshop, Diamond Light Source, Oxfordshire, UK, Jan. 2013, unpublished.

[8] D. Carbajo Perez *et al.*, “Operational Feedback and Analysis of Current and Future Designs of the Injection Protection Absorbers in the Large Hadron Collider at CERN”, in *Proc. 8th Int. Particle Accelerator Conf. (IPAC’17)*, Copenhagen, Denmark, May 2017, paper WEPVA108, pp. 3517–3520.

[9] C. Bracco, A. Lechner, D. Carbajo, and A. Perillo, “TDIS - Functional Specification”, CERN, 2017, EDMS 1865250, to be released.

[10] A. Lechner *et al.*, “TDI - Past Observations and Improvements for 2016”, in *Proc. Evian Workshop on LHC Beam Operations*, Evian, France, Dec. 2015, pp. 123–129.

[11] C. Bracco, “The new injection protection dump TDI”, CERN, 2016, EDMS 1936580, to be released.

[12] A. Lechner *et al.*, “Energy Deposition Studies for Fast Losses during LHC Injection Failures”, CERN, Geneva, Switzerland, Rep. CERN-ACC-2013-0288, 2013.

[13] G. Battistoni *et al.*, “Overview of the FLUKA code”, *Annals of Nuclear Energy*, vol. 82, pp. 10-18, 2015.

[14] A. Ferrari, P.R. Sala, A. Fassò, and J. Ranft, “FLUKA: a multi-particle transport code”, Rep. CERN-2005-10, INFN/TC_05/11, SLAC-R-773.

[15] ANSYS, <https://www.ansys.com/>

[16] F.X. Nuiry *et al.*, “Low-Z material R&D application for Beam Intercepting Devices (BID) at CERN”, presented at the 13th Int. Work. on Spallation Materials Technology, Chattanooga, USA, Nov. 2016.

[17] R.M. Chistensen, “A Two Property Yield, Failure (Fracture) Criterion for Homogeneous, Isotropic Materials”, *J. Eng. Mater. Technol.*, 2004, vol. 126, pp. 45–52

[18] A. Bertarelli, A. Lafuente, F. Carra, and P. Gradassi, “TDI thermo-mechanical simulations: Boron Nitride versus Graphite”, presented at the 235th LHC machine committee, Geneva, Switzerland, Sep. 2015.

[19] G. Filacchioni, E. Casagrande, U. De Angelis, G. De Santis, and D. Ferrara, “Effects of strain rate on tensile properties of TZM and Mo–5%Re”, *Journal of Nuclear Materials*, vol. 307-311, Dec. 2002, pp. 705-709.

[20] L. Teofili *et al.*, “Analysis on the Mechanical effects induced by beam impedance heating on the HL-LHC Target Dump Injection Segmented (TDIS) absorber”, presented at the 9th Int. Particle Accelerator Conf. (IPAC’18), Vancouver, Canada, May 2018, paper THPAK092.

[21] CST Studio Suite, <https://www.cst.com/products/csts2>

[22] C. Zannini, G. Rumolo, and G. Iadarola, “Power loss calculation in separated and common beam chambers of the LHC”, CERN, Geneva, Switzerland, CERN-ACC-2014-0122, 2014.

[23] CST Studio Suite: Wakefield Solver, <https://www.cst.com/products/cstps/solvers/wakefieldsolver>

ESS COMMISSIONING PLANS

N. Milas*, R. Miyamoto, M. Eshraqi, Y. Levinsen, C. Plostinar, R. de Prisco, M. Muñoz
European Spallation Source ERIC, Lund, Sweden

Abstract

The ESS linac is currently under construction in Lund, Sweden, and once completed it will deliver an unprecedented 5 MW of average power. The ion source and LEBT commissioning starts in 2018 and will continue with the RFQ, MEBT and the first DTL tank next year and up to the end of the fourth DTL tank in 2020. This paper will summarize the commissioning plans for the normal conducting linac with focus on the ion source and LEBT and application development for both commissioning and operation.

INTRODUCTION

The European Spallation Source, currently under construction in Lund, Sweden, will be a spallation neutron source driven by a superconducting proton linac [1]. The linac accelerates a beam with a 62.5 mA peak current and 4% duty cycle (2.857 ms pulse length at 14 Hz) up to 2 GeV and thus produces an unprecedented 5 MW average beam power. The superconducting linac has a normal conducting (NC) linac as its injection, which consists of an ion source (IS), radio frequency quadrupole (RFQ), drift tube linac (DTL), as well as low and medium energy beam transports (LEBT and MEBT) and accelerates the generated proton beam from 75 keV to 90 MeV. A schematic layout of the (ESS) linac is shown in Fig. 1.

Beam commissioning of the ESS linac will be conducted in stages [2–4]. The first and upcoming stage is for the IS and LEBT, planned to start in the summer of 2018 and continue until fall. Commissioning of the NC linac up to the first DTL tank should happen at end of 2019 and up to the fourth tank in the first quarter of 2020. This paper presents the updated plan of the NC linac beam commissioning with a major focus on the IS and LEBT commissioning, high level applications development and beam parameters.

NC LINAC OVERVIEW

IS and LEBT

The IS and LEBT are in-kind contributions from INFN-LNS [5]. Table 1 lists a possible set of operational parameters of the IS. Note that the operational parameters are ultimately determined after all the sections of the linac are installed and tested. The proton current larger than the nominal 62.5 mA is to take into account possible beam losses in the LEBT and RFQ. The off-site commissioning confirmed that the IS is indeed capable of producing this level of current [6]. The pulse length longer than the nominal 2.857 ms is due to the required ~3 ms stabilization time of the IS. The

Table 1: ESS IS Possible Operational Parameters

Parameter	Value	Unit
Energy	~75	keV
Peak current (total)	~85	mA
Peak current (proton)	~70	mA
Proton fraction	~80	%
Pulse length	~6	ms
Pulse repetition rate	14	Hz
Duty cycle	~8	%

excess ~3 ms in the leading part is removed by a chopper in the LEBT, before the beam enters into the RFQ.

The LEBT is a focusing channel with two solenoids. Each solenoid also houses coils of dipole correctors (*steerers*) for both planes. Tuning of the linac requires a beam with a much lower power than the nominal 5 MW. Standardized sets of limits in the current, pulse length, and repetition rate have been defined as *beam modes* [7] and an important function of the LEBT is to produce the beam modes by adjusting the current and pulse length with its iris and chopper.

The LEBT also houses a suite of beam diagnostics devices. Most of them are either in the permanent tank, between the solenoids, or in the commissioning tank, temporary placed in the position of the RFQ (Fig. 2). The beam current monitor (BCM) and Faraday Cup (FC) are used for current measurements. The first BCM actually monitors the current extracted from the high-voltage power supply and thus indirectly provides the total current of the IS. The Doppler detector measures fractions of ion species from Doppler shifts of the light induced by the beam. In total four cameras (Non-invasive profile monitors or NPMs), one for each plane at two locations, also detect the beam induced light and measures the beam profile and centroid position. An Allison scanner type emittance measurement unit (EMU) measures the phase space distribution in either the permanent or commissioning tank. The commissioning tank also houses a temporary beam stop, which could stop the beam with a full peak current and duty cycle, at its end.

RFQ

The RFQ is an in-kind contribution from CEA-Irfu and will be delivered to ESS in the last quarter of 2018. It consists of five sections with a total length of 4.6 m and accelerates the proton beam from 75 keV up to 3.6 MeV. The RFQ design was optimized for a high transmission (> 97%). The maximum total power coupled into the RFQ is expected to be 1.6 MW [8]. The only diagnostics in the RFQ section is a BCM attached to the exit wall and right before the MEBT.

* natalia.milas@ess.se

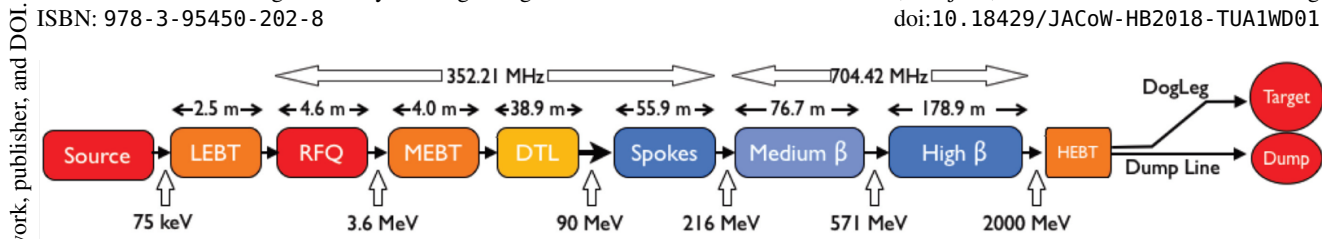


Figure 1: Schematics of the ESS linac. The red/orange section represent the warm parts of the linac while the blue are the superconducting/cold sections.

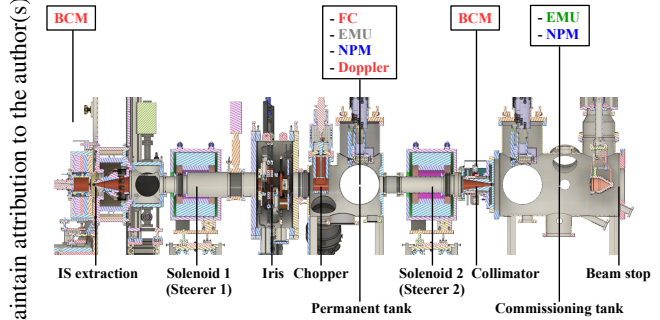


Figure 2: Schematic of the LEBT during the IS and LEBT beam commissioning. The EMU can be also housed in the permanent tank (indicated by the grey text).

As far as diagnostics goes, there are seven BPMs, two NPMs, one FC, two BCMs, two Fast BCMs (FBCMs), a set of 3 wire scanner profile monitors (WS), one EMU and a Longitudinal Beam Profile Monitor (LBM). The BPMs in the MEBT and downstream the linac can also be used as phase monitor. A schematics of the MEBT elements can be seen in Fig. 3.

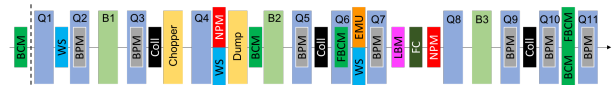


Figure 3: Schematics of the MEBT.

MEBT

The MEBT section follows the RFQ and most of its components are in-kind contributions from ESS Bilbao [9]. It is 4 m long and includes eleven quadrupoles, three buncher cavities, one fast chopper, one beam chopper dump and three vertical blades used as collimators. It also contains steerers in every quadrupole as extra windings for both planes. When the beam pulse length is adjusted with the slow chopper in the LEBT, an extra 20 μs is left in the leading part. This extra 20 μs part remains in the RFQ and is removed by the fast chopper in the MEBT. This is because the space charge neutralization effect in the LEBT has a finite build-up time, estimated up to 20 μs, and this part of the pulse is expected to have wrong beam parameters.

The transverse lattice of the MEBT is separated into two parts at the chopper dump. The initial part produces a waist in the vertical plane (plane of the fast chopper's deflection) and a parallel beam in the horizontal plane, in a section between the fast chopper and its dump. These are to guarantee a good efficiency of chopping as well as a good transport in a relatively long section with only one weak quadrupole focusing in the horizontal plane. When the beam passes through the fast chopper dump, it is diverging in both planes. The transverse lattice after the dump refocuses this expanded beam and matches to the following DTL. Three buncher cavities maintain the bunch length within the MEBT and match the longitudinal Twiss parameters at the DTL entrance. The first buncher cavity defines the mean bunch length throughout the MEBT and the other two are used to achieve the matching.

DTL

The DTL will be delivered by INFN-LNL [10]. It is a 38.8 m long system, divided in five tanks. Each tank is a standalone structure, composed of four 2 m long modules made of stainless steel with internal electro-copper deposition. Every other drift-tube is equipped with permanent magnet quadrupoles (PMQs), forming the FODO layout (transverse focusing channel). Some drift-tubes not housing a PMQ are equipped with a BPM or a single plane steerer. A BCM is present in each inter-tank section and a FC every two tanks. In the DTL the beam is further accelerated from 3.6 MeV to 90 MeV and no adjustment in the transverse focusing is possible, given the nature of its quadrupoles. A schematic of the DTL diagnostics and steerer elements can be seen in Fig. 4.

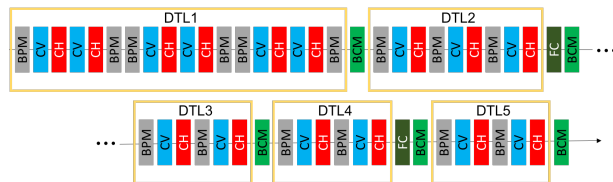


Figure 4: Layout of the DTL diagnostics and steerers. Drift-tubes with a PMQ or no additional element are omitted.

NC LINAC INSTALLATION SCHEDULE

Installation of the IS and LEBT components was finalized in May 2018 (Fig. 5). Hardware commissioning of the components has been on-hold due to lack of electrical power in the tunnel but is anticipated to commence in the summer. An exception for the yet-started hardware commissioning

is the control system, which is based on the EPICS framework and an in-kind contribution from CEA Saclay [11]. Its acceptance test was successfully performed already as a part of the off-site commissioning in September 2017. Also on ESS site, trial connections to EPICS channels from the local control room, using temporary power, were successfully conducted in April 2018, making it ready for the full re-verification as soon as the power becomes available in the tunnel. A readiness review for the IS and LEBT, focusing on the safety aspect, follows completion of the hardware commissioning, and pass on the review allows to start the beam commissioning, planned to begin end of August and run for 3 months.

The RFQ is scheduled for delivery and installation in fourth quarter of 2018, but RF conditioning and beam commissioning can only start in the second half of 2019 due to the unavailability of the RF system. The first four DTL tanks are also scheduled for delivery and installation in 2019. The beam commissioning of the RFQ, MEBT, and first DTL tank will be conducted together, while commissioning up to the fourth DTL tank will continue in 2020, after the full RF system for the NC linac is installed. Up to this point, the beam will be stopped with the FCs in the MEBT and between the DTL tanks and a temporary shield wall will be placed after the DTL tank 4 (taking the space of DTL tank 5), allowing the beam commissioning of the NC linac while installation work in the superconducting part of the linac happens in parallel.

Since the RFQ and MEBT will be installed and commissioned together, this means that the beam out of the RFQ must be characterized with diagnostics devices in the MEBT. For some hadron linacs, for instance CERN LINAC4, the IS, LEBT, and RFQ were commissioned by itself without the following sections and the output beam of each section was characterized with a common movable test bench [12]. The movable bench was also considered for the beam commissioning of the ESS NC linac [13] but is not currently in the plan due to the limitations in budget and schedule.

BEAM COMMISSIONING STRATEGY

The initial phase of every beam commissioning consists of verification of systems which require the beam presence,



Figure 5: IS and LEBT installed in the ESS linac tunnel.

such as beam diagnostics devices. Afterwards, a series of characterization and optimization activities should follow and the beam commissioning is concluded with long-term stability tests. The main activities during the commissioning for the NC linac are listed in the following subsections.

Beam Modes

As already stated, several sets of beam modes are defined to be used during the beam commissioning and general linac tuning [7] (see Table 2). The probe mode has the lowest beam power and is used mainly for the very first check of the system and hardware and the beam threading, the process to correct the trajectory and deliver the beam to the designated beam stop. The fast tuning and slow tuning modes are used to characterize the beam and achieve the desired beam parameters and thus the main types of modes during the beam commissioning. The fast tuning mode is mainly for setting the phases and amplitudes of cavity fields. The slow tuning mode could have a pulse length up to 50 μ s and this is meant to provide a good quality signal to invasive diagnostics devices, such as FCs and WS profile monitors. The slow tuning mode will be also used to set the low-level RF (LLRF) feed-backs and feed-forwards loops for the cavities. All beam modes mentioned above can be sent to any of the beam stops in the NC linac, however they are constrained by the total dose produced for the FCs at the DTL inter-tanks [14], which can restrict the amount of time that each one can be used. The other available beam modes listed in [7] can only be stopped at the tuning dump or target and thus will not be used for the NC linac tuning.

IS and LEBT Phase

Prior to the delivery to ESS in December 2017, the IS and LEBT were successfully commissioned with the beam at INFN-LNS [5, 6, 15, 16]. Given this successful off-site commissioning, the re-commissioning of the IS in Lund begins with verification of the IS beam characteristics (see Table 1), observed during the off-site commissioning, followed by fine-tuning adapting to the needs of the following sections.

Having steerers and NPMs at two locations for each plane in the LEBT allows a simple beam steering based on the measured trajectory responses. Ideally, we would like to cancel both position and angle errors at the RFQ interface and this requires the position error being canceled in the middle of the second solenoid. The location of the first set of cameras is not far from the second solenoid and thus we are not far from this ideal situation.

The RFQ transmission is very sensitive to the beam parameters at its entrance. Once we have the RFQ, good matching is achieved by simply scanning the solenoids and identifying the strengths for the best transmission. During the IS and LEBT beam commissioning, an EMU is placed in the commissioning tank, ~ 15 cm from the LEBT-RFQ interface. Due to a strong space charge and never-known space charge compensation level in this region, reconstructing the transverse phase space distribution at the interface can be difficult. On the other hand, once the RFQ is connected, this EMU

Table 2: List of Beam Modes for the NC Linac Tuning

Type	Destination	Main usage	Peak current [mA]	Pulse length [μs]	Repetition rate [Hz]
Probe	Any beam stop	Initial check Beam threading	6	≤5	≤1
Fast tuning	Any beam stop*	RF check	6-62.5	≤5	≤14
Slow tuning	Any beam stop*	Invasive measurement LLRF setting	6-62.5	≤50	≤1

* Subject to maximal dose limit for DTL FCs during NC linac commissioning.

Content from this work may be used under the terms of the CC BY 3.0 licence (© 2018). Any distribution of this work must maintain attribution to the author(s), title of the work, publisher, and DOI.

is no longer available. Therefore, our strategy during the IS and LEBT beam commissioning is to collect EMU data for a range of the two solenoids field strengths, where simulations predict good matching. This allows us to look back the data of the emittance meter for a given (or at least close) condition of the IS and LEBT, even after the RFQ installation.

The input current to the RFQ has to be adjusted so that the output becomes the linac-wide nominal value of 62.5 mA. This is because the sections after the RFQ are not designed for more than 62.5 mA. Transmission through the RFQ is not known during the IS and LEBT beam commissioning and this requires the preparation of several configurations of the IS and LEBT for different currents. Because of the iris, the IS itself does not need to fine-tune the current. However, extracting an excess amount of the beam could spoil the emittance [17], so it is still ideal to extract just the right amount of current from the IS and minimize the use of the iris for production of the nominal current. The permanent tank, after the first solenoid and iris, houses the FC, Doppler detector, and EMU. This allows to characterize the beam parameters against the IS configuration as well as the amount of N₂ gas injection (for enhancing the space charge neutralization effect) and helps to prepare candidates for the final IS setting.

Capability to produce the beam modes has to be verified during the IS and LEBT beam commissioning, before the beam is sent to the rest of the linac. For the chopper, its efficiency has to be carefully verified to prevent the chopped part of the pulse leaking into the RFQ. During the initial power ramp-up phase of linac operations, the beam power is managed with current, whereas the pulse length and repetition rate are fixed to the nominal values of 2.857 ms and 14 Hz due to users demand. This requires multiple configurations of the linac for different currents, already from the LEBT, and thus the matching process of the NC linac has to be re-done for intermediate currents as well, once we are ready to send the beam to the dump.

RFQ Phase

After the IS and LEBT, the RFQ and MEBT will be commissioned together. For the RFQ, the only parameter to adjust is the amplitude of the field to achieve the desired output energy of 3.62 MeV. The output energy is reconstructed from time-of-flight measurements, combined with

scans of the buncher cavities, with BPMs in the MEBT. After setting the amplitude of the field, the transmission should be verified. The efficiency of any RFQ is never perfect and the output beam includes particles not properly accelerated. There is one BCM at the and the end of the RFQ and the other around the middle of the MEBT, behind the chopper dump (see Fig. 3). These two BCMs are used to distinguish the transmissions of the particles with the right energy and the rest. This is based on the result of a study that, for the ESS RFQ, most of the particles with wrong energies have the IS output energy of 75 keV and they are lost before the third quadrupole. At this point, we revisit and fine-tune the setting of the IS and LEBT so the output current of the RFQ becomes the linac-wide nominal value of 62.5 mA.

MEBT and DTL Phase

After the IS and LEBT are commissioned and the RFQ transmission is verified, a full commissioning of the next sections should start. For the MEBT and DTL, the beam threading is done with steerers and the BPMs (see Fig. 3 and 4). The layouts of the steerers and BPMs in the MEBT and DTL are such that the simple 1-to-1 steering works. For the cases when some of BPMs and or steerers are not available, our high level application for the steering is also capable of a SVD based correction.

The MEBT and DTL are the first sections which require to set the amplitudes and phases of the cavities with the phase scan method. The first step in setting the RF is to find the rough region of RF phase and amplitude to set the klystron. The RF group will have a rough idea of the amplitude, based on the measured RF power and design shunt impedance. Each cavity should be scanned in the vicinity determined by the rough estimate described above, by ±10-20 degrees. The phase difference (difference in arrival time) will be measured with a pair of downstream BPMs and compared with the calculated signature field maps for each cavity. An additional output from this technique is knowledge of the input (and output) beam energy. The fitting results are typically quite sensitive to beam energy (i.e. within 100-300 keV [18]) and this can be used during the MEBT first buncher scan to calibrate the RFQ output energy.

As stated in one previous sections, the transverse lattice of the MEBT is separated in two in terms of its function. The initial part requires adjustments of the beam sizes for

achieving good transmission and chopping efficiency, and the second part has to achieve good Twiss parameters for matching at the DTL interface. The three Ws and one EMU should provide enough information to achieve these requirements together with a model. For the longitudinal plane, there is only one profile monitor (LBM). Thus, to reconstruct the Twiss parameters and emittance and achieve the longitudinal matching to the DTL section, measurements with different settings of the buncher cavities are needed. Since the quadrupoles of the DTL are made of permanent magnets there is no degree of freedom to adjust the optics and perform any kind of matching along this section.

HIGH LEVEL APPLICATIONS

Beam physics high-level applications are crucial tools for efficiently achieving desired machine performance. The applications for the ESS linac [19] are built on the OpenXAL framework [20]. This framework was initially developed at SNS and it has been transformed into a collaborative project between several laboratories. ESS is an active contributor to the project for developments of both (the core of) the framework itself and new applications.

The latest developments related to improving the ESS-specific online model (JELS) are listed below:

- machine description is now imported from the official lattice repository, which uses the TraceWin [21] format.
- the calculation for the RF fieldmap element was optimized 30% in speed by using a first order integrator.
- two new elements were created for the LEBT. Both 3D and 2D (cylindrical coordinate) fieldmap elements were introduced for a solenoid, based on the above-mentioned first order integrator for an RF fieldmap.
- a new element representing a whole DTL tank was introduced and it uses the same definition for the Transient Time Factor as TraceWin.

All new elements were benchmarked against TraceWin, as well as the full accelerator lattice, and results were in very good agreement. For more details, see [22].

A new framework for physics applications is being developed based on JavaFX and JacpFX [23] and it is planned to port all new applications once the framework is ready. For the moment a version that adds a tool bar with the same functionality as the OpenXAL Swing version. Current available functionalities in the new framework include: the logbook posting capability and a link to the User documentation Wiki is already being used. An expansion of the FXapplication framework, as it is called, is expected to be released still this year [24].

Ion Source and LEBT Phase

For the IS and LEBT beam commissioning, a high-level application, which allows to visualize beam parameters and control the IS and LEBT components, has been developed

[25]. In this application the trajectory and envelope along the LEBT and the commissioning tank are calculated and displayed for given initial conditions, together with readings from diagnostics (NPMs and EMUs). From the application it is possible to manipulate some of the magnets and power supplies from the source and LEBT and it is also possible to perform a simple matching based on diagnostics readings.

A generic multi-dimensional scanner application, whose main use cases include the LEBT solenoids scan, was also developed. For the Scanner Application a new widget has been developed to quickly select multiple channels to read or write to. The application allows to scan a sub-space of multiple parameters, defined with common mathematical operations, and stores data in a XML file as other OpenXAL applications. There is currently no analysis of the data acquired, so the users are for now expected to develop their own external tools

These two applications were already tested in the control room by connecting to the virtual machine and are ready for the next step of testing with the real control system.

Ion Source to DTL Phase

For the next commissioning step a trajectory correction application is under development. Two correction methods are included: a 1-to-1 and a SVD correction. The matrices used can be extracted from the machine model or can be measured, and the overall trajectory can be corrected to the BPM zeros or to a predefined reference trajectory. To complement this application a Trajectory Display Application was also developed.

The next step for the high level applications is a phase scan application for the MEBT buncher cavities and DTL tanks. This application is responsible for setting the phase and amplitude of a cavity by comparing the measured and simulated time-of-flights among BPMs. Another important application to be developed is the one responsible for the transverse matching, using the data(s) from the Ws and EMU to evaluate the optics in the MEBT and matching into the DTL.

CONCLUSION

Beam commissioning of the ESS linac starts soon in summer, 2018, from the IS and LEBT. This paper presented the strategy for the NC linac commissioning with a major focus on the IS and LEBT commissioning, high level applications development and beam deliverables. Some highlights from the preparation works of installation and testing for the IS and LEBT were also presented.

REFERENCES

- [1] R. Garoby *et al.*, “The European Spallation Source Design”, *Phys. Scr.*, vol. 93, p. 014001, 2018.
- [2] R. Miyamoto, M. Eshraqi, and M. Muños, “ESS Linac Plans for Commissioning and Initial Operations”, in *Proc. HB’16*, Malmö, Sweden, July 2016, pp. 342-347.

- [3] R. Miyamoto, M. Eshraqi, M. Muños, and C. Plostinar, "Beam Commissioning Planning Updates for the ESS Linac," in *Proc. IPAC'17*, Copenhagen, Denmark, May 2017, pp. 2407-2410.
- [4] C. Plostinar *et al.*, "Opportunities and Challenges in Planning the Installation, Testing and Commissioning of Large Accelerator Facilities," in *Proc. IPAC'18*, Vancouver, BC, Canada, Apr.-May 2018, paper TUPAF065.
- [5] L. Neri *et al.*, "Beam Commissioning of the High Intensity Proton Source Developed at INFN-LNS for the European Spallation Source," in *Proc. IPAC'17*, Copenhagen, Denmark, May 2017, pp. 2530-2532.
- [6] Ø. Middtun, "Off-site Commissioning Report for the ESS Proton Source and LEBT," Lund, Sweden, ESS Document No. ESS-0190279, 2018.
- [7] M. Muñoz, "Description of Modes for ESS Accelerator Operation," Lund, Sweden, ESS Document No. ESS-0038258, 2016.
- [8] J.S. Schmidt *et al.*, "Functional Integration of the RFQ in the ESS Systems," in *Proc. IPAC'18*, Vancouver, BC, Canada, Apr.-May 2018, paper TUPAF068.
- [9] I. Bustinduy, M. Magan, F. Sordo and R. Miyamoto, "Current Status on ESS Medium Energy Beam Transport," in *Proc. HB'14*, East-Lansing, MI, USA, Nov. 2014, pp. 170-174.
- [10] M. Comunian *et al.*, "Commissioning Plans for the ESS DTL," in *Proc. LINAC'16*, East-Lansing, MI, USA, Sep. 2016, pp. 264-266.
- [11] J.-F. Denis, "User Manual of the ESS ISrc and LEBT," Lund, Sweden, ESS Report No. 0123103, 2017.
- [12] A. Lombardi, "Commissioning of the Low-energy Part of LINAC4," in *Proc. LINAC'14*, Geneva, Switzerland, Aug.-Sep. 2014, pp. 6-10
- [13] B. Cheymol, "Potential Beam Diagnostics for a Movable Test Bench," Lund, Sweden, ESS Document No. ESS-0020683, 2015.
- [14] L. Tchelidze, "Radiological hazard analysis report for g area - prompt and residual radiation (normal conducting linac beam commissioning)," ESS Document No. ESS-0118232, 2018.
- [15] Ø. Middtun, L. Celona, B. Cheymol, R. Miyamoto, L. Neri, and C. Thomas, "Measurements and Simulations of the Beam Extraction from the ESS Proton Source," in Proc. 17th Int. Conf. on Ion Source, Geneva, Switzerland, Oct. 2017, unpublished.
- [16] L. Celona *et al.*, "Ion Source and Low Energy Beam Transport Line Final Commissioning Step and Transfer from INFN to ESS" in *Proc. IPAC'18*, Vancouver, BC, Canada, Apr.-May 2018, paper TUPML073.
- [17] Ø. Middtun, Y. Levinsen, R. Miyamoto, and C. Plostinar, "Benchmarking of the ESS LEBT in TraceWin and IBSimu," in *Proc. IPAC'17*, Copenhagen, Denmark, May 2017, pp. 4445-4447.
- [18] A. Aleksandrov *et al.*, "Commissioning experience for the SNS Linac," *AIP Conference Proceedings*, vol. 773, p. 73, 2005, <https://doi.org/10.1063/1.1949500>
- [19] Y. Levinsen, M. Eshraqi, E. Laface, I. List, M. Muñoz, R. Miyamoto, and R. de Prisco, "Plans for the European Spallation Source Beam Physics Control Software," in *Proc. IPAC'16*, Busan, Korea, May 2016, pp. 3086-3089.
- [20] A. P. Zhukov *et al.*, "Open XAL Status Report 2018," in *Proc. IPAC'18*, Vancouver, BC, Canada, Apr.-May 2018, paper THPAK069.
- [21] D. Uriot and N. Pichoff, "Status of TraceWin Code," in *Proc. IPAC'15*, Richmond, VA, USA, May 2015, pp. 92-94.
- [22] J. F. E. Müller and E. Laface, "Latest developments and updates of the ESS Linac Simulator," in *Proc. IPAC'18*, Vancouver, BC, Canada, Apr.-May. 2018, paper WEPAF086.
- [23] A. Moncsek and P. Symmangk, <http://jacpfx.org/>
- [24] C. Rosati and E. Laface, "New Approach in Developing OpenXAL Applications," in *Proc. IPAC'17*, Copenhagen, Denmark, May 2017, pp. 4043-4046.
- [25] N. Milas, S. K. Louisy, and C. Plostinar, "Transverse Dynamics and Software Integration of the ESS Low Energy Beam Transport," in *Proc. IPAC'18*, Vancouver, BC, Canada, Apr.-May 2018, paper TUPAF066.

COMMISSIONING STATUS OF CSNS/RCS

S. Y. Xu*, J. L. Chen, Y. W. An, X. H. Lu, M. Y. Huang, Y. Li, H. F. Ji, S. Wang
CSNS/IHEP, CAS, Dongguan, 523803, P.R. China

Abstract

The China Spallation Neutron Source (CSNS) is an accelerator-based science facility. CSNS is designed to accelerate proton beam pulses to 1.6 GeV kinetic energy, striking a solid metal target to produce spallation neutrons. CSNS has two major accelerator systems, a linear accelerator (80 MeV Linac) and a 1.6 GeV rapid cycling synchrotron (RCS). The Beam commissioning of CSNS/RCS has been commissioned recently. Beam had been accelerated to 1.6 GeV at CSNS/RCS on July 7, 2017 with the injection energy of 61 MeV, and 1.6 GeV acceleration was successfully accomplished on January 18, 2018 with the injection energy of 80 MeV. The beam power achieved 25 Kw in March, 2018. The initial machine parameter tuning and various beam studies were completed. In this paper, the commissioning experiences are introduced.

INTRODUCTION

The Chinese Spallation Neutron Source (CSNS) is an accelerator-based science facility. CSNS is designed to accelerate proton beam pulses to 1.6 GeV kinetic energy, striking a solid metal target to produce spallation neutrons. CSNS has two major accelerator systems, a linear accelerator (80 MeV Linac) and a rapid cycling synchrotron (RCS). The function of the RCS accelerator is to accumulate and accelerate protons from the energy of 80 MeV to the design energy of 1.6 GeV at a repetition rate of 25 Hz [1, 2]. The Beam commissioning of CSNS/RCS has been commissioned recently. Beam had been accelerated to 1.6 GeV at CSNS/RCS on July 7, 2017 with the injection energy of 61 MeV, and 1.6 GeV acceleration was successfully accomplished on January 18, 2018 with the injection energy of 80 MeV. The beam power achieved 25 Kw in March, 2018.

PREPARATION FOR CSNS/RCS COMMISSIONING

Systematic preparation work was accomplished before the beam commissioning of CSNS/RCS, including systematic magnet measurements and beam dynamics study.

Magnet Measurements

Systematic magnet measurements were undertaken before the beam commissioning of CSNS/RCS to study the magnetic field characteristics of magnets at CSNS/RCS.

To reduce the magnetic field tracking errors, a method of wave form compensation for RCS magnets, which is based on transfer function between magnetic field and exciting current, was investigated on the magnets of

CSNS/RCS [3]. There are one type of dipole named 160B and four types of quadrupoles, named 272Q, 253Q, 222Q and 206Q respectively at CSNS/RCS. Because of the differences of magnetic saturation and eddy current effects between these five types of magnets, there are magnetic field tracking errors between different magnets before wave form compensation, as shown in Fig. 1. The maximum magnetic field tracking error between the dipole and quadrupoles is larger than 2.5% over the ramping process. Wave form compensation was performed on all the magnets of CSNS/RCS. The magnetic field ramping functions for all the magnets were compensated to sine pattern. The maximum magnetic field tracking error between the dipole and quadrupoles was reduced from 2.5% to 0.08%, as shown in Fig. 2.

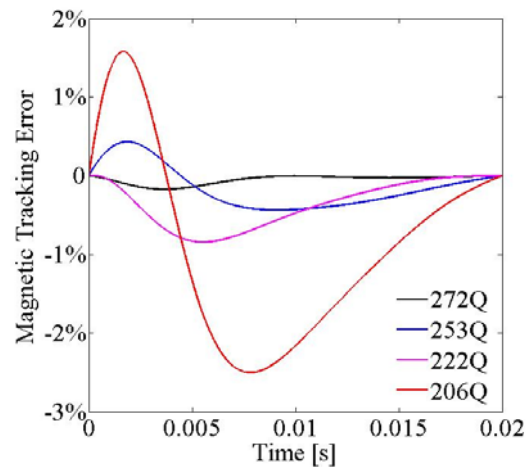


Figure 1: Magnetic field tracking errors between the dipole and four types of quadrupoles over the ramping process with no wave form compensation.

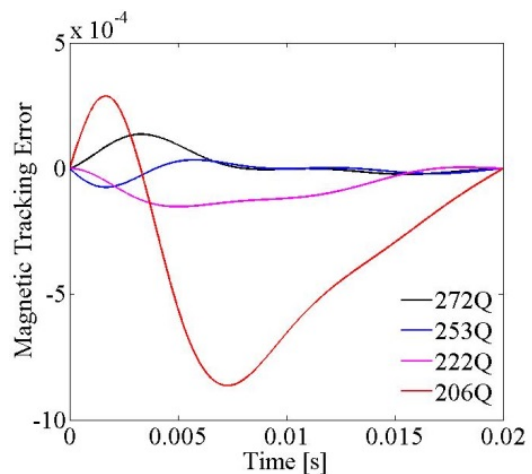


Figure 2: Magnetic field tracking errors between the dipole and four types of quadrupoles over the ramping process after wave form compensation.

* xusy@ihep.ac.cn

Content from this work may be used under the terms of the CC BY 3.0 licence (© 2018). Any distribution of this work must maintain attribution to the author(s), title of the work, publisher, and DOI.

The core-to-core distance between magnets in CSNS/RCS is rather short in some places, as shown in Fig. 3. The fringe field interference results in integral field strength reduction. The integral gradient reduction of quadrupoles due to fringe field interference with adjacent magnets was accurately measured [4, 5]. The field measurement result shows that the integral maximum gradient reduction due to adjacent magnets can get up to 2.3%.

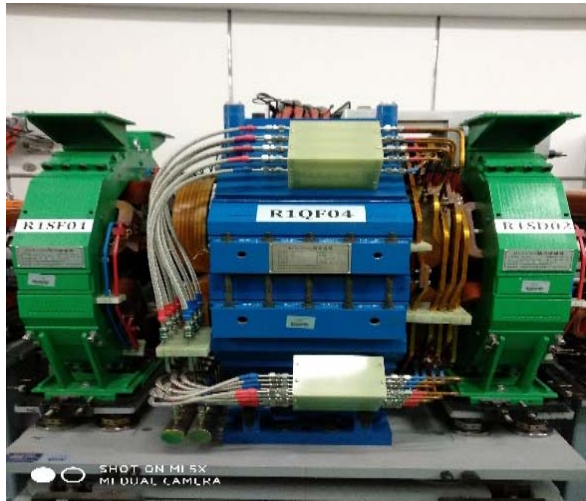


Figure 3: The layout of the Q222 and neighbor sextupole magnets.

Beam Dynamics Study

The lattice design of CSNS/RCS is based on hard edge model of quadrupoles. Because of the large aperture of quadrupoles, fringe field effect is an important issue. The systematic study of the effects of fringe field and interference of quadrupoles at CSNS/RCS was done using slicing model method before the beam commissioning. The beta-tune was matched to the design value taking into account fringe field effects and fringe field interference results for all quadrupoles.

For RCS, it is an important issue to match the dipole magnetic field ramping function with the RF frequency ramping function. The mismatch between the dipole magnetic field and RF frequency may induce serious synchrotron oscillation and large beam displacement at dispersion section. A new code was developed to study the dipole magnetic field and RF frequency tracking at CSNS/RCS.

STAGE I BEAM COMMISSIONING

Because one klystron was sent back for repair, the Linac can only accelerate the beam to 61MeV in 2017. The Beam commissioning of CSNS/RCS was started in May 2017 with the injection energy of 61MeV.

To control the beam loss during the beam commissioning, the single shot beam mode was adopted. In the first step, the beam commissioning was started in DC mode without acceleration. On May 31st, the first beam was injected into the RCS, and successfully accumulated. After the optimization of B field, RF pattern and the in-

jection, the beam transmission achieved 100% one day later. The measured tune is (4.856, 4.779), as shown in Fig. 4. The measured tune is very close to the design value (4.86, 4.78). The calculated fudge factors of quadrupoles are less than 1%, as shown in Fig. 5.

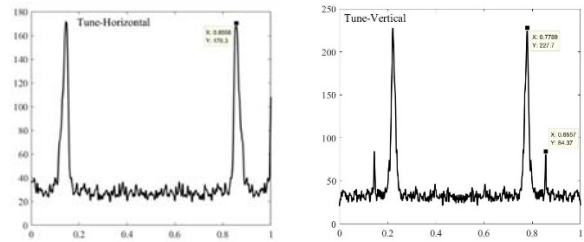


Figure 4: The measured tune of CSNS/RCS in DC mode.

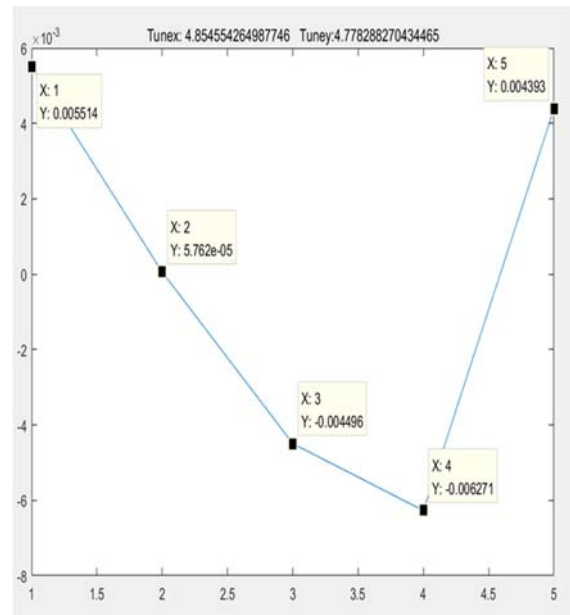


Figure 5: The measured fudge factors of quadrupoles.

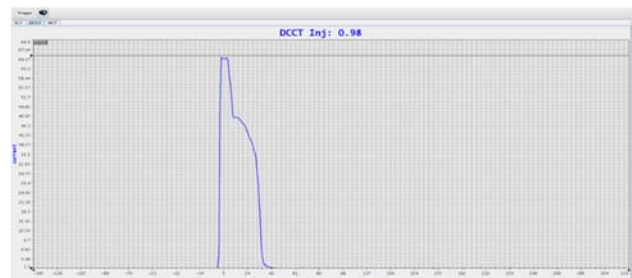


Figure 6: The beam current over one cycling period for the first beam shot in AC mode.

Beam commissioning in AC mode was started on July 7, 2017. The first beam shot was injected and accumulated successfully. However, the beam life time is only 4 ms, as shown in Fig. 6. The timing of magnet power supply and RF system were checked. The timing error of magnet power supply was about 140 μ s. The beam was accelerated to the design energy 1.6GeV successfully after timing shift of magnet power supply. Then, the match between the dipole magnetic field and RF frequency were per-

formed. The beam transmission achieved 100% on July 9, 2017.

STAGE II BEAM COMMISSIONING

The Beam commissioning of CSNS/RCS was started on January 15, 2018 with the injection energy of 80MeV. At the beginning, beam commissioning was performed in DC mode. Beam was injected into the RCS, successfully accumulated for the first beam shot. The beam transmission rate got 100% after performing the match of dipole magnetic field and injection energy on the same day.

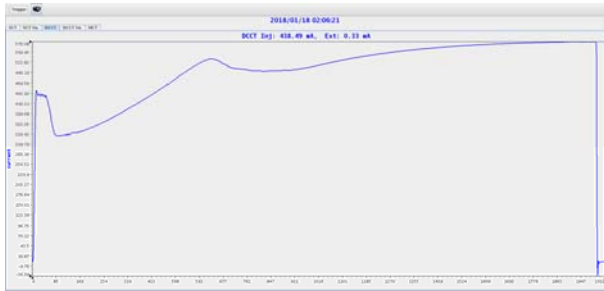


Figure 7: The beam current over one cycling period for the first beam shot in AC mode.

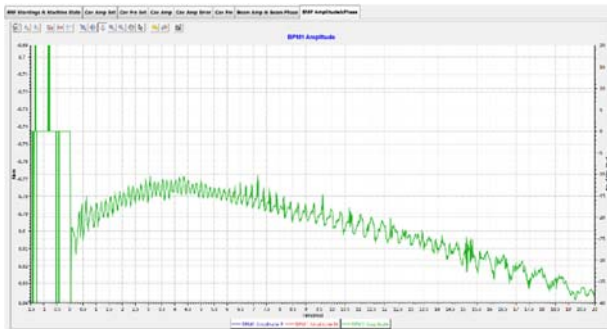


Figure 8: The beam displacement variation at dispersion section during acceleration process for the first beam shot.

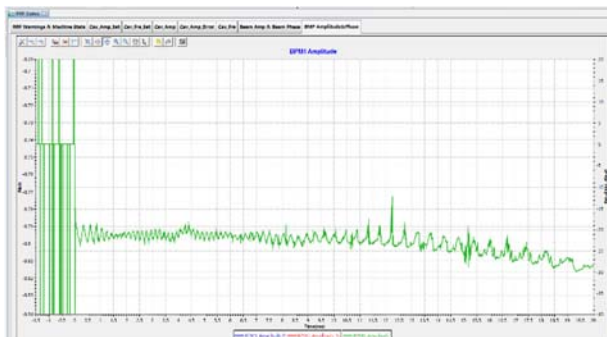


Figure 9: The beam displacement variation at dispersion section during acceleration process after the machine optimization.

The AC mode beam commissioning of CSNS/RCS with the injection energy of 80 MeV was started on January 18, 2018, and 1.6 GeV acceleration was successfully accomplished for the first beam shot. However there was serious beam loss, as shown in Fig. 7. The beam displacement at dispersion section was large and changed

greatly during the beam acceleration, as shown in Fig. 8. The timing of magnet power supply at CSNS/RCS was shifted to match the injection beam, and the match of the bottom of dipole magnetic field and injection energy was performed. The RF frequency ramping function was optimized to match the dipole magnetic field ramping function. The beam transmission rate got 100% after the machine optimization on January 18, 2018. The beam displacement variation at dispersion section during acceleration process was greatly reduced, as shown in Fig. 9. The tune was measured during acceleration process over one cycling period. The measurement results are shown in Fig. 10. The variation of horizontal tune is less than 0.02, and the variation of vertical tune is about 0.04.

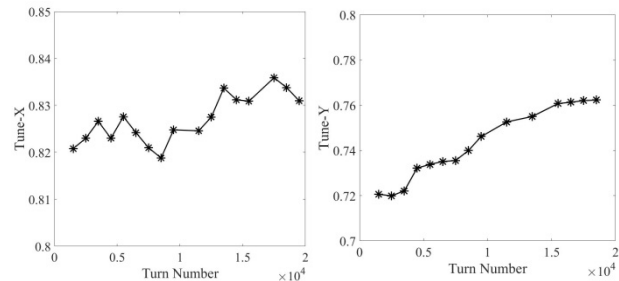


Figure 10: The tune variation during acceleration process over one cycling period.

CONCLUSION

Careful preparation work was performed before the beam commissioning of CSNS/RCS. Systematic magnet measurements were undertaken to study the magnetic field characteristics of magnets at CSNS/RCS. To reduce the magnetic field tracking errors at CSNS/RCS, a method of wave form compensation for RCS magnets, was investigated. The systematic study of the effects of fringe field and interference of quadrupoles at CSNS/RCS was done before the beam commissioning. Because of the careful preparation for beam commissioning, the beam commissioning of CSNS/RCS went very smoothly.

REFERENCES

- [1] S. N. Fu *et al.*, “Status of CSNS Project”, in *Proc. IPAC’13*, Shanghai, China, May 2013, pp. 3995-3999.
- [2] S. Wang *et al.*, “An Overview of Design for CSNS/RCS and Beam Transport”, *Science China Physics, Mechanics & Astronomy*, vol. 54, pp. 239-244, 2011.
- [3] S. Y. Xu *et al.*, “Study of wave form compensation at CSNS/RCS magnets”, *Nucl. Instrum. Methods Phys. Res. A*, vol. 897, pp. 81-84, 2018.
- [4] Mei. Yang *et al.*, “Magnetic fringe field interference between the quadrupole and corrector magnets in the CSNS/RCS”, *Nucl. Instrum. Methods Phys. Res. A*, vol. 84, pp. 29-33, 2017.
- [5] L. Li. *et al.*, “Fringe field interference of neighbour magnets in China spallation neutron source”, *Nucl. Instrum. Methods Phys. Res. A*, vol. 840, pp. 97-101, 2016.

HIGH INTENSITY PROTON STACKING AT FERMILAB: 700 kW RUNNING*

R. Ainsworth[†], P. Adamson, B. Brown, D. Capista, K. Hazelwood, I. Kourbanis,
 D. Morris, M. Xiao, M-J. Yang, Fermilab, Batavia, USA

Abstract

As part of the Nova upgrades in 2012, the Recycler was repurposed as proton stacker for the Main Injector with the aim to deliver 700 kW. Since January 2017, this design power has been run routinely. The steps taken to commission the Recycler and run at 700 kW operationally will be discussed as well as plans for future running.

INTRODUCTION

During the long shutdown from May 2012 until September 2013, the Recycler was repurposed from an antiproton storage ring to a proton stacker as part for the NOvA [1] project. The Recycler is a permanent magnet ring consisting of strontium ferrite gradient magnets and strontium ferrite quadrupoles in the straight sections.

Table 1: Typical Recycler Properties for Beam Sent to NuMI

Parameter	RR	unit
Q_h	25.42	
Q_v	24.42	
ξ_h	-6	
ξ_v	-7	
$\epsilon_{n,95\%}$	15	π mm mrad
$\epsilon_{L,95\%}$	0.08	eV s
Intensity	51×10^{12}	ppp
V_{RF}	80	kV
Max Beam Power	730	kW (1 hr average)

NuMI in 2018 are shown in Table 1. This paper will discuss the steps required to reach that goal and will focus on the changes since summer 2016. An outline of the commissioning period from 2013 until 2016 can be found in [3].

PERFORMANCE

Figure 2 shows the the evolution of the NuMI beam power since end of the long shutdown in 2013 until April 1st 2018. The power is initially limited to 240 kW in which only the Main Injector is used. Slip-stacking in the Recycler was commissioned in multiple phases as "2+6", "4+6" and "6+6" in which the first number represents that the number of batches that are slipped. "6+6" slip stacking was established just prior to the 2016 Summer shutdown in which twelve batches from the booster are injected into the recycler which are slip-stacked to make six double intensity batches.

Slip-stacking works by injecting 6 batches at the design momentum of the Recycler ring. These 6 batches are then decelerated by $\Delta f = 1260$ Hz which is given by the product of the booster harmonic number (84) with the booster cycle rate (15 Hz). Six more batches are then injected on-momentum. The decelerated batches will then slip with respect to these on-momentum batches and when the two sets of six batches are overlapped, they are extracted to the Main Injector. A full Recycler ring contains seven batches, however a gap is needed for injection. The slip-stacking procedure results in beam lost from the bucket due to deceleration and the beating of the two RF systems running at different frequencies. Gap clearing kickers [4] are fired just before each injection in order to abort any out of bucket beam in the gap. In order to damp the resistive wall instability, a bunch by bunch damper system is used which damps the two sets of six batches individually. However, when the batches begin to overlap, this system no longer works as it is unable to resolve the individual bunches position. Therefore with no damper during this time (around the seventh injection),

Fermilab Accelerator Complex

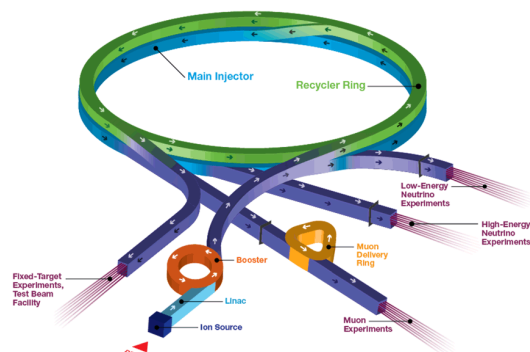


Figure 1: The Fermilab Accelerator complex.

The Recycler performs slip-stacking at 8 GeV which doubles the bunch intensity and then delivers beam to the Main Injector where it is accelerated to 120 GeV and sent to NuMI. The design goal for the NOvA project is for a 700 kW proton beam (48.6×10^{12} protons per pulse (ppp) every 1.333 s.) The recycler also stacks lower intensity beam which is sent to the MI for resonant extraction as well as rebunch protons from 53 MHz buckets to 2.5MHz buckets to be sent to the Muon campus [2].

Since January 2017, the Fermilab accelerator complex (Fig. 1) has been running at the design goal of 700 kW consistently. Some typical Recycler properties for beam sent to

* Operated by Fermi Research Alliance, LLC under Contract No. De-AC02-07CH11359 with the United States Department of Energy.

[†] rainswor@fnal.gov

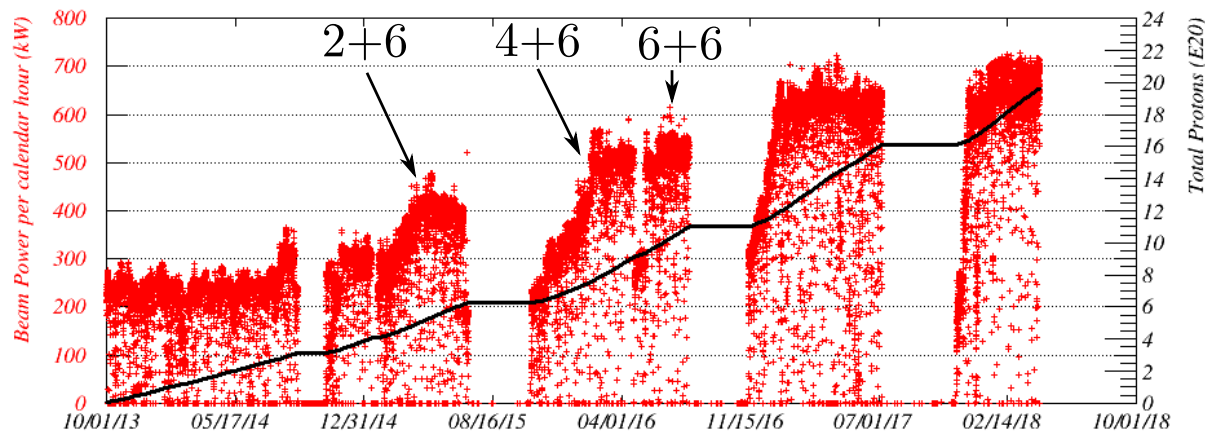


Figure 2: The hourly beam power to NuMI and the total protons delivered since the end of the long shutdown in 2013. The beam power is initially limited to 240 kW when only the Main Injector is used. As Slip-stacking in the Recycler is commissioned, the beam power is steadily increased until January 2017 when the beam power meets the design goal. If SY120 is in the timeline, NuMI will see a 10% decreases in beam power (630 kW).

the chromaticity is increased to stabilise the beam against the instability. At high intensities, large chromaticity is required at the end of the cycle which results in a new set of issues.

The first issue is running high chromaticity resulted in lifetime losses around this ring that were not controlled which were particularly high at lambertson locations. The second issue is a much more constrained tune space. The decelerated bunches during slip stacking have a tune offset compared to the set machine tune caused by chromaticity which to first order is $\sim \frac{\delta p}{p} \xi$. The larger the chromaticity, the larger the tune offset. At -7 chromaticity, this offset is 0.018 compared to 0.054 for -20 chromaticity. This meant that as the chromaticity was increased, the set tune of the machine was lowered to prevent the off-momentum beam being pushed towards the half-integer resonance [5]. Figure 3 show how the losses increased exponentially as the chromaticity was increased during a "4+6" cycle. The black line shows the average of 100 pulses along a blue band showing one standard deviation from this mean. In order to reduce this problem, the tune was lowered as the chromaticity was increased

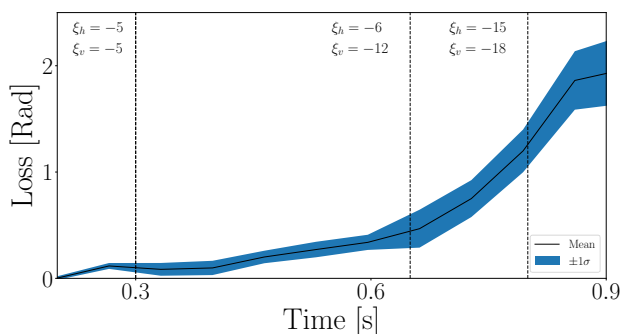


Figure 3: An example of how losses increase with chromaticity. The black line shows the average of 100 pulses along a blue band showing one standard deviation from this mean.

It was found that by introducing an injection phase offset on the first six injected batches, the final chromaticity could be reduced by 2 or 3 units. The injection offset resulted in more beam in the gap however this could be controlled cleanly with the gap clearing kickers rather than losing beam around the ring. Figure 4 shows the beam injected into the Recycler and how much survives. Around 1.2E12 is sent to the abort and $\sim 2E11$ is lost around the ring. The beam lost to the ring shows a non-linear increase towards the end of cycle caused by the high chromaticity running.

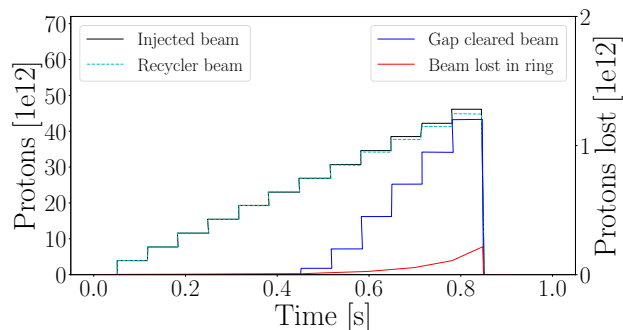


Figure 4: The beam injected into the Recycler during a "6+6" cycle along with the beam sent to the abort and beam lost in the ring in 2016.

Figure 5 shows a typical loss pattern in Rad around the Recycler before the 2016 summer shutdown. The different colours of the losses determine where the loss happened during the cycle. Blue is during the first 6 injections, yellow is the second six and green is during extraction. The worst losses occur at the lambertson locations used to extract beam to the Main Injector located at 232 and the abort lambertson located at 402. The majority of the loss at 402 is caused by the tails of the gap clearing kickers which are fired 13 times

Content from this work may be used under the terms of the CC BY 3.0 licence (© 2018). Any distribution of this work must maintain attribution to the author(s), title of the work, publisher, and DOI.

a cycle. In order to run 700 kW consistently, the transverse losses needed to be controlled better.



Figure 5: Typical loss pattern around the Recycler before the 2016 summer shutdown. Intensity is 42E12 ppp.

COLLIMATION

During the 2016 summer shutdown, a two-stage collimation system [6] was installed in the Recycler to take care of uncontrolled transverse losses. Longitudinal losses from slip-stacking are already controlled using gap clearing kickers. The system consists of a primary scraping foil edge, and two large, 20 ton secondary collimators made from steel and marble. After each injection, a vertical bump is used to move the beam edge towards the collimators in order to let the damper system remove any injection errors.



Figure 6: Typical loss pattern after installing the two stage collimation system. Intensity is around 45E12 ppp.

Figure 6 shows a typical loss pattern around the Recycler ring after the collimators were installed. It can be seen that

the large losses at the MI transfer lambertson were reduced as well as many small losses around the ring caused by limited aperture. Note the intensity is higher compared to Fig. 5 hence why the loss sum is larger. While commissioning the collimators, tests were performed with just the secondary collimators and increased losses were observed at Lambertson locations confirming that a 2 stage system was the most efficient way to operate the collimators.

DIODE DAMPER

While the collimators were able to control a large amount of the transverse losses, there was still a loss associated with running very high chromaticity (-20) at the end of the cycle. During the slipping process the bunch by bunch damper system is turned off as it is unable to resolve the bunches position while they are overlapping. High Chromaticity is therefore needed to suppress the resistive wall instability.

It was proposed by [7] that the slipping motion can be ignored i.e. bunches in both beams doing the same motion. Thus a damper system with a 5 MHz bandwidth looking at the envelope of all bunches motion rather than a bunch by bunch damper would be sufficient.

The damper system follows a similar idea to that of Direct Diode Detection [8]. The output of pickups are sent through a diode followed by a resistor and capacitor in parallel to form peak detectors which provide an envelope of the bunches motion. This is then given to a 3 turn filter with correct coefficients to provide a kick to damp the beam.

The system was successfully implemented in January 2017 and allowed the chromaticity during slipping to be reduced from -20 down to -7. Figure 7 shows the effect of the damper on the loss pattern for the same intensity as in Figure 6. The total loss sum has reduced by almost a factor of two with losses at the Abort and Muon Extraction Lambertsons reduced significantly. The ability to run with much lower chromaticity also provided much more freedom in choosing the working point and to remove the injection phase offsets.

APERTURE IMPROVEMENTS

Following this improvements, the next limiting loss location were at the abort and muon extraction lambertsons. In the 2017 summer shutdown, the permanent magnet lambertson in the abort region was replaced with a powered lambertson with improved aperture to help reduce losses in this area. Figure 8 shows aperture for the old permanent magnet Lambertson (left) and the new Main Injector style lambertson (right) along with solid lines for $\pm 3\sigma$ and dashed lines show $\pm 5\sigma$ for 25 π mm mrad beam. The $\pm 5\sigma$ beam fits comfortably with the lambertson aperture for the new MLAW. The beam pipe leading into the Muon extraction lambertson was also replaced with the larger style elliptical pipe used in the Main Injector. The beta wave in the machine was also modified slightly using quad trims in the 30 section phase trombone to help reduce the beta in the region on the Muon extraction lambertson. Figure 9 shows the loss pat-



Figure 7: Typical loss pattern after the implementation of the the slip stack damper which allowed chromaticity to dropped at the end of the cycle. Intensity is around 45E12 ppp.

terns after these changes for 700 kW operations. The losses seen at the abort lambertson are much reduced and now, almost no loss is seen at the Muon Extraction lambertson.

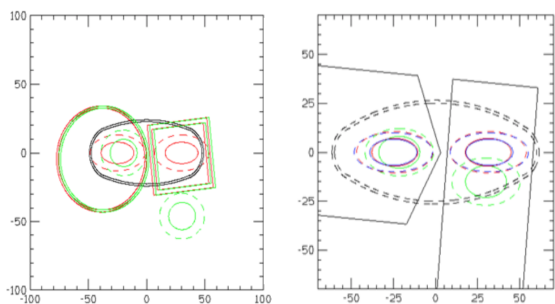


Figure 8: The aperture sizes for the old recycler permanent magnet lambertson (left) and the Main Injector MLAW lambertson (right). The solid line shows $\pm 3\sigma$ and the dashed line $\pm 5\sigma$ for 25 π mm mrad beam.

CURRENT RUNNING

In 2018, both the Recycler and Main Injector have an efficiency of around 98.5%. Figure 10 shows a similar plot to Figure 4. It can be seen that the aborted beam is now a factor of 3 smaller than what it was in 2016. This is partly due to the removal of the injection phase offsets and beam injected from the booster with smaller longitudinal emittance. The losses in the ring is a similar size to before except now more than 2/3 of this is going to the collimators.

INSTABILITIES

During commissioning of the Recycler, a fast instability [9] was previously observed in which attributed to electron cloud in which a small fraction of electrons were trapped



Figure 9: A typical loss pattern after the aperture improvements. Intensity is around 50E12 ppp.

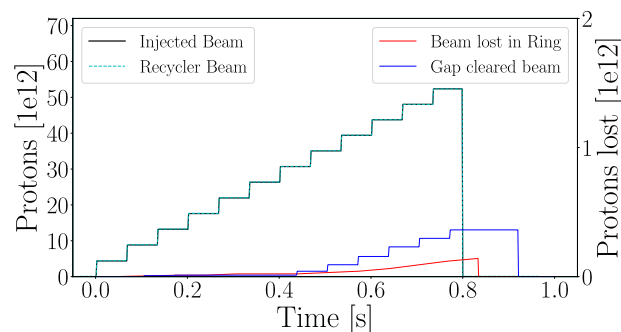


Figure 10: The beam injected into the Recycler during a "6+6" cycle along with the beam sent to the abort and beam lost in the ring in 2018.

in the magnetic field lines of the gradient magnets. This instability has not been observed for some time, most likely due to vacuum scrubbing from the high intensity beam or possibly from a change made to the vacuum system. Efforts to induce this instability for study purposes were also unsuccessful.

Other instabilities that occur such as the resistive wall instability are controlled with dampers and do not affect operations.

RADIATION SURVEYS

While running 700 kW consistently, it is important to keep losses controlled and avoid irradiating the tunnel unnecessarily. Ring wide radiation surveys are performed whenever there is an opportunity to access the tunnel using DALE (Data Acquisition Logging Engine). DALE consists of a Geiger counter which has its position recorded by a wheel and attached to the back of cart. The radiation surveys are important to make sure that our beam loss system is not missing any locations. An example survey made on March 20th 2018 shows radiation hot spots around the tunnel mea-

Content from this work may be used under the terms of the CC BY 3.0 licence (© 2018). Any distribution of this work must maintain attribution to the author(s), title of the work, publisher, and DOI.

sured on the aisle side (Fig. 11). The tunnel houses both the Main Injector and the Recycler so the resulting measurement shows the radiation dose in mRem/hr from both machines. DALE surveys underestimate loss locations where the reading is above 150 mRem/hr. Additional surveys are performed at these points with more accurate equipment.

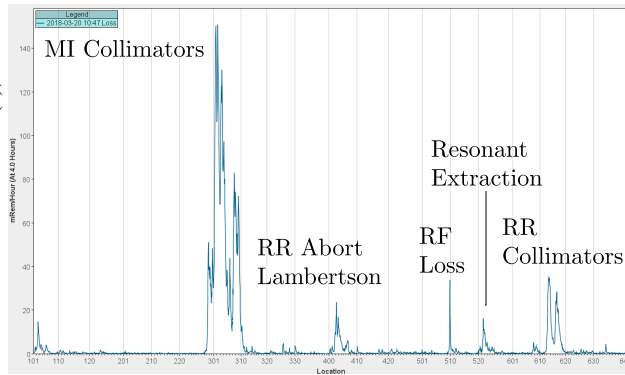


Figure 11: A DALE survey showing loss locations around the tunnel.

The largest spikes are between 301 and 310 which is the location of the Main Injector collimators. The other locations all match with locations shown in the Recycler loss plots with the exception of a large spike seen at 510. This is a Main Injector loss related to transition crossing when the RF voltage is limited due to tripped stations.

SUMMARY AND FUTURE RUNNING

Following a series of improvements with the most significant being the installation of collimators and a damper system for when beams are slipping, the Fermilab accelerator complex delivers 700 kW consistently to NuMI.

The current beam power that can be sent to NuMI is not limited by beam physics but by administrative limits. A new shielding assessment is required for the Main Injector to deliver more protons per hour. Also, there is currently a limit of 54E12 ppp on the NuMI target. Once these limits are removed, we will continue to push the intensity.

Studies are already under way looking at potential issues at higher intensity. In-depth simulations are already underway looking a potential problems from space charge. In the 2018 summer shutdown, there is a plan to install extra sextupoles to allow compensation of the third order resonance to open

up the tune space. Lattice optimisation is underway to move the lattice functions as measured much closer to the design values.

There are plans to perform upgrades to the accelerator complex in the lead up to PIP-II to allow 900 kW beam power for NOvA. For the Main Injector, it is planned to install a first order matched γ_t jump system in the future [10]. This will be important for the planned PIP-II upgrades in which the frequency separation needed for slip stacking will be increased resulting in a larger $\delta p/p$ when crossing transition.

REFERENCES

- [1] D. S. Ayres *et al.*, “The NOvA Technical Design Report”, FERMILAB-DESIGN-2007-01.
- [2] D. Stratakis *et al.*, “Accelerator performance analysis of the Fermilab Muon Campus”, *Phys. Rev. Accel. Beams*, vol. 20, no. 11, p. 111003, 2017, doi:10.1103/PhysRevAccelBeams.20.111003
- [3] P. Adamson, “Reuse Recycler: High Intensity Proton Stacking at Fermilab”, in *Proc. HB’16*, Malmo, Sweden, 2016, doi:10.18429/JACoW-HB2016-THAM1X01
- [4] I. Kourbanis *et al.*, “A Gap Clearing Kicker for Main Injector”, in *Proc. NAPAC’11*, New York, 2011, paper WEP205.
- [5] R. Ainsworth *et al.*, “Simulations and Measurements of Stopbands in the Fermilab Recycler”, in *Proc. IPAC’16*, Busan, Korea, 2016, doi:10.18429/JACoW-IPAC2016-MOP0Y010
- [6] B. C. Brown *et al.*, “Fermilab Recycler Collimation System Design”, in *Proc. NAPAC’16*, Chicago, IL, USA, 2016, doi:10.18429/JACoW-NAPAC2016-WEP0A16
- [7] A. Burov, “Coupled-Beam and Coupled-Bunch Instabilities”, arXiv:1606.07430, 2016.
- [8] M. Gasior and R. Jones, “High sensitivity tune measurement by direct diode detection”, in *Proc. DIPAC’05*, Lyon, France, 2005, CERN-AB-2005-060.
- [9] S. Antipov *et al.*, “Fast Instability Caused by Electron Cloud in Combined Function Magnets”, *Phys. Rev. Accel. Beams*, vol 20, p.044401, 2017, doi:10.1103/PhysRevAccelBeams.20.044401
- [10] R. Ainsworth, S. Chaurize, I. Kourbanis, and E. Stern, “Transition Crossing in the Main Injector for PIP-II”, in *Proc. IPAC’17*, Copenhagen, Denmark, 2017, doi:10.18429/JACoW-IPAC2017-WEPBA039

FAIR COMMISSIONING – CONCEPTS AND STRATEGIES IN VIEW OF HIGH-INTENSITY OPERATION

Ralph J. Steinhagen on behalf of the FC^2WG^* , GSI, Darmstadt, Germany

Abstract

The Facility for Anti-Proton and Ion Research (FAIR) presently under construction, extends and supersedes GSI's existing infrastructure. Its core challenges include the precise control of highest proton and uranium ion beam intensities, the required extreme high vacuum conditions, machine protection and activation issues while providing a high degree of multi-user mode of operation with facility reconfiguration on time-scales of a few times per week. Being based on best-practices at other laboratories, this contribution outlines the applicable hardware and beam commissioning strategies, as well as concepts, beam-based and other accelerator systems that are being tested at the existing facility in view of the prospective FAIR operation.

INTRODUCTION

Civil construction of the initial modularised start version of FAIR has started. Accelerator-related hardware commissioning (HWC) is targeted to commence in 2022, followed by commissioning with beam (BC), and physics user operation by 2025. A schematic overview of the existing and new facility is shown in Figure 1.

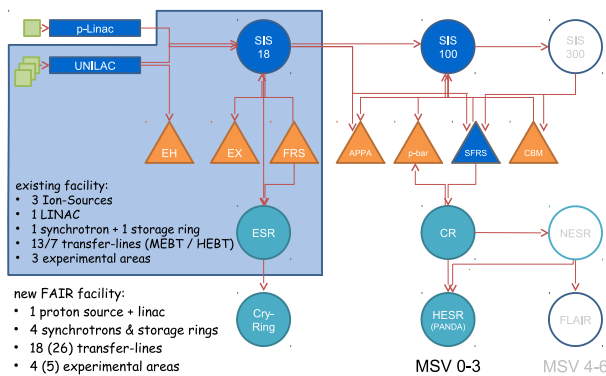


Figure 1: Schematic overview of the existing and new FAIR accelerator facility. The operational complexity increases from presently $O(n^2)$ (GSI) to $O(n^2)$ (FAIR) due to the longer accelerator chains.

In addition to the existing UNILAC [2], SIS18 [3], and ESR [4], the FAIR accelerator complex will extend the existing GSI infrastructure by a dedicated anti-proton production target, the Super Fragment Separator (Super-FRS) for the production of rare isotope beams (RIBs) and five new accelerators [5, 6]: a dedicated high-intensity proton linac [7], the SIS100 synchrotron [8], as well as the experimental CRYRING, CR and HESR storage rings [9, 10].

* FAIR Commissioning & Control Working Group [1], R.Steinhagen@GSI.de

Some of the noteworthy features of FAIR include:

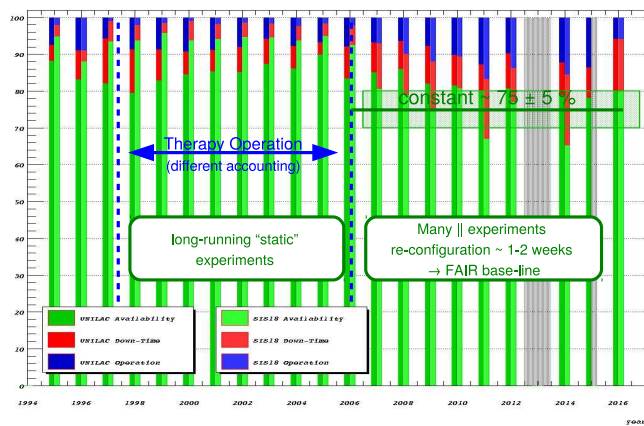
- the control of a wide range of proton, anti-proton, primary and RIBs, with targeted design intensities ranging from $3 \cdot 10^{13}$ ppp (particles-per-pulse) for protons at 29 GeV/u up to $5 \cdot 10^{11}$ ppp for $^{238}\text{U}^{28+}$ at 2.7 GeV/u – a factor 100 higher than similar existing facilities at those energies,
- the flexibility to reconfigure the facility for up to 7 experiments in parallel, with many of these experiments lasting only 5 to 6 days, as well as
- the resulting complexity increase (presently: $O(n^2)$, FAIR: $O(n^5)$) due to the larger facility, longer accelerator chains, and especially more precise beam and machine parameter control that is required at the targeted intensities and energies:
 - excellent XHV vacuum conditions (e.g. SIS100: vacuum $< 10^{-12}$ mbar) and the precise control of dynamic-vacuum or other beam loss mechanism,
 - emittance preservation, control of space-charge, transverse and longitudinal beam dynamics starting in the primary beam pre-injectors, as well as
 - acceptable machine protection and minimisation of machine activation (ALARA-principle: 'As Low As Reasonably Achievable').

OPERATIONAL AVAILABILITY, EFFICIENCY & CHALLENGES

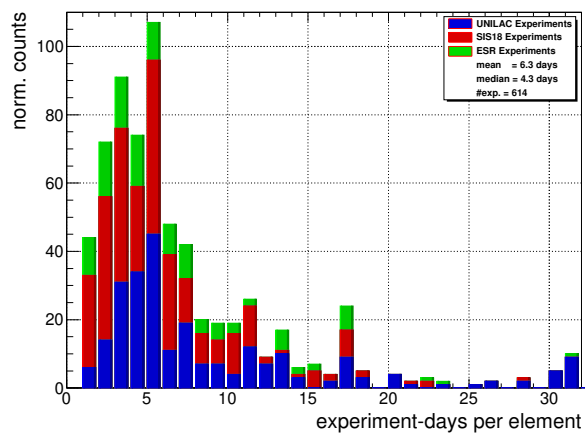
While FAIR will provide highest primary beam intensities and highest selectivity for the rarest of RIBs, an implicit assumption and requirement is that the facilities' flexibility of serving a similar number of parallel-running experiments and similar beam-on-target efficiency (machine availability) will be maintained. Figures 2(a) and 2(b) provide a historic overview of the achieved beam-on-target (BoT) merit figure and typical experiment duration per ion species. Over the past ten years – which is more representative for the targeted FAIR physics programme – GSI could achieve a BoT efficiency figure of about 75 % with respect to the scheduled beam-time while the vast majority of experiments lasted typically less than 5 days, with with the exception of a few long running experiments integrating their data over up to a month for a given species.

With the expected number of parallel experiments, it is expected that the facility and associated beam-production-chains (BPCs, [11]) need to be reconfigured or re-setup about once per day. In addition, the operational complexity increases significantly due to the inherently longer BPCs

Content from this work may be used under the terms of the CC BY 3.0 licence (© 2018). Any distribution of this work must maintain attribution to the author(s), title of the work, publisher, and DOI.



(a) beam-on-target efficiency between 1992 and 2016



(b) average experiment duration per ion species

Figure 2: Beam-on-Target efficiency and average experiment duration per ion-species. Ion source exchanges are factored out from UNILAC and SIS18 data (constant overhead). The availability includes time used for experiments, detector tests, machine development, as well as beam to down-stream accelerators Down-time: unscheduled down-time and standby; Operation: accelerator setup and re-tuning [12].

(linked to the larger number of sequential accelerators), the ALARA principle of minimising activation especially at high energies, as well as accelerator-physics challenges related to high-intensity operation (ie. space-charge, collective effects, etc.). For example, while operating with highest beam intensities, changes to the beam intensities for experiments in or directly after SIS100 need to back propagated through the accelerator chain to either the ion sources, the linac’s RF chopper, or the SIS18 where these intensity changes and losses can be safely accommodated while minimising the activation or other collateral effects (e.g. dynamic vacuum). Since many of the experiments last only two to three days, any of these type of changes or BPC setup need to be executed in a most efficient, safe, and therefore often semi-automated fashion in order to maintain an overall high BoT figure of merit of the specific experiment and facility.

FUNDAMENTAL STRATEGY & PRINCIPLES

The ‘FAIR Commissioning & Control (Sub-) Project’ has been launched in 2015 in order to coordinate the various activities related to:

- the above mentioned operational challenges,
- the development of concepts and efficient strategies for the pending Hardware- (HWC) and Beam Commissioning (BC) of FAIR, as well as
- the integration of the related accelerator equipment into the controls system and machine operation paradigms.

These activities have been sub-divided into two working groups (WGs): the ‘FAIR Commissioning & Control WG’ (FC2WG [1]) which focuses on the accelerator-related system integration, commissioning and operation aspects, and

the ‘FAIR Control Centre WG’ (FCC-WG [13]) which focuses on the control room ergonomics (acoustics, console layout, lighting, etc.), functional relationships between the main control room (MCR) and secondary infrastructure, and civil construction interfaces related to the FAIR Control Centre (FCC [13]).

Both working groups are open to all who can participate and are willing to contribute to these subjects. They follow a long-term strategy and ‘lean principles’ that apply (where applicable) best engineering practices common in the manufacturing industry to the ‘manufacturing of particle beams’ inside the FAIR accelerator facility. These processes are being complemented by best-practices at GSI, CERN and other similar existing large hadron accelerator facilities as well as operational experiences within the high-intensity and high-brightness accelerator community at large. Thus, many of the FC2WG concept and strategies may – by design – appear familiar with those found at other facilities, either because they were assimilated where possible or adapted to the specific needs of FAIR where applicable in order to minimise potential regression with respect to established best-practices operation standards and to avoid ‘reinventing the wheel’¹.

Continuous Improvement

One of the important underlying FC2WG concepts is the ‘continuous improvement’² paradigm that aims at exploiting opportunities for streamlining the setup of new BPCs and to minimise ‘wastes’, sources of errors, or unnecessary intermediate steps. This improvement is driven by a continuous process of identifying opportunities or minimising short-comings, evaluation and planning of possible remedies. Their execution and review of the achieved results are

¹ “Imitation is the sincerest form of flattery”, Charles Caleb Colton

² also: jap. ‘Kaizen’

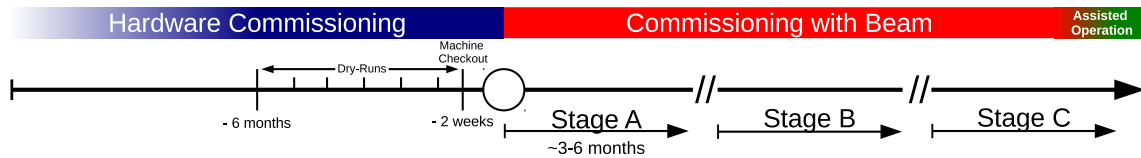


Figure 3: Schematic structure of the targeted hardware- (HWC) and beam commissioning (BC) sequence. SIS100 is expected the first accelerator to start its HWC in 2022, followed by Super-FRS and then the rest of the FAIR facility once Stage-A has been completed for each sub-accelerator along the BPC.

done according to the set optimisation criteria. Two of the common examples are the development of commissioning procedures and 'poka yoke' inspired and design-based minimisation of error sources.

Commissioning Procedures The FAIR HWC as well as BC will be driven by *commissioning procedures* as an evolving operation standards (or 'recipe') that formalise and document the best-practice of how to boot-strap and operate an accelerator efficiently [14, 15]. These procedures are developed, updated and maintained jointly by the various stake-holders (beam physics/machine/system experts etc.) and are kept initially on a light-weight Wiki-based system to facilitate easy editing and once they are more established are being transferred to an approval-based specification document. These procedures define when, where and how the individual accelerator sub-systems and interfaces fit in the overall commissioning and operation concept. These procedures are also the basis for further controls integration steps into semi-automated sequences that shall assist the operator on a day-to-day basis. A schematic view on planned commissioning structure is shown in Figure 3.

The commissioning of FAIR is subdivided into two parts which are executed in overlapping sequence for the given sub-accelerator in the chain once it becomes available:

HWC: focusing on site-acceptance-tests that verify the individual equipment's conformity with contractual design targets. These are typically performed during the initial commissioning, after major upgrades or modifications, or in case the systems' as-good-as-new performance need to be re-validated. Most of these individual systems and commissioning tasks are done in parallel for efficiency reasons and are supported by semi-automated testing tools such as the sequencer [16, 17]. The HWC is coordinated by the machine's sub-project leaders and executed by the equipment group experts responsible for the specific equipment.

Dry-Runs: are rehearsals starting typically three to six month before the actual BC, and tests the conformity of system's controls integration and readiness in view of BC. For this purposes the accelerator is put into a state assuming that beam could be injected into the accelerator sub-sector. Systems that are unavailable at this stage are initially ignored, noted down, and followed-up at a defined later stage until all system become available.

The last dry-run referred to also as 'machine checkout' is an intense accelerator performance tests (e.g. machine patrols, magnet/PC heat runs, etc.) that starts typically two weeks before the targeted BC.

BC: focusing on the commissioning of beam-dependent equipment and on tracking of the beam progress through the BPC. It is further divided and grouped into the following three stages:

Stage-A: using 'pilot beams' or "easily available" ions (e.g. Ar) to perform the most basic checks such as threading, injection, capture, beam cooling, RIB conversion, acceleration (or deceleration in case of storage rings), stripping and extraction. These tests are always done with 'safe' ie. low-intensity and low-brightness beam. Initially low-intensity ions are preferred due to the simpler optics and beam dynamics, and then protons in order to assess high-intensity effects and transition crossing. Prior to moving to the subsequent BC stages, the target is to complete this stage for each FAIR accelerator by 2025.

Stage B: performing the intensity ramp-up and commissioning of special systems. The main aim of this stage is to achieve and maintain the required nominal beam parameters, nominal transmission and beam loss targets, as well as the commissioning and validation of the machine protection and interlock systems. Possibly unsafe operations during this and following stages are always preceded by checks with safe (ie. low-intensity) beams.

Stage C: which focuses on the establishing of routine operation with nominal intensities and the transition to faster semi-automated setup and switching procedures between different BPC or beam parameter sets. N.B. the first time this stage is considered as 'commissioning' or 'assisted operation', but subsequently passes over to 'regular operation', done rather by operators on a 24h/7 shift rota than by system or accelerator experts.

Error Minimisation & Poka-Yoke As schematically illustrated in Figure 4, 'poka yoke'³ is the prevention of

³ A *poka-yoke* is any mechanism in a process that helps an equipment operator to avoid (*yokeru*) inadvertent mistakes (*poka*).

inefficiencies, inconsistencies and wastes by design or 'error proofing' principle – a culture of stopping and fixing problems early, when and where they occur. Its main aim

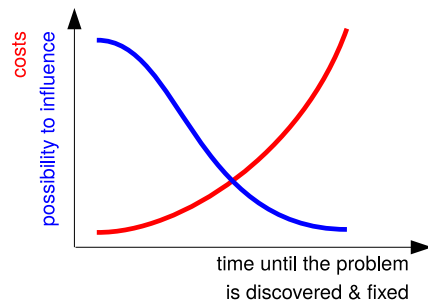


Figure 4: Schematic cost vs. time since a failure has been detected and fixed.

is to minimise error-propagation and to avoid the proliferation of costs of mitigating problems at a late project stage where the possibility of influencing the mitigation is very limited. A common example is, for example, fixing potential sources of problems with high-intensity beams already at the source or while operating with low-intensity rather than with high-intensity beams, or addressing first basic parameters and single-particle effects before moving towards more complex higher-order effects: e.g. first fix injection processes, trajectory, orbit, Q/Q' before addressing space-charge or slow-extraction-related problems. This lead to the introduction and enforcing of a 'pilot-beam' and 'intensity ramp-up' concept, that prescribes to always verify the basic machine function and machine safety with low-intensities prior to increasing and moving on with high-intensity beams.

Respect for People

Another important FC2WG aspect is the development, training, and sufficient support of the personnel. The operators have to perform complex tasks over prolonged periods requiring concentration and their undivided attention. Thus it is important to provide an environment that positively impacts personnel performance and in turn the FAIR performance by minimising disturbing elements (ie. acoustics, lighting, lines of communication, etc.) and activities/tasks that put unnecessary strain on employees. This influenced the design, ergonomics and functional requirements on the FAIR Control Centre [13, 18], as well as the development of smart tools and procedures, such as beam-based feedback and monitoring systems (e.g. [19–21]) or sequencer framework for the semi-automated execution of commissioning procedures [16, 17] in order to automate routine task in order that operator talents are utilised and focused on more important tasks that cannot be automated (e.g. performance improvement, handling of errors and exceptions etc.).

These requirements are particularly important in view of increase of number of accelerators that roughly increase by a factor 4 for FAIR compared to the existing GSI facility and the fact that operators and system experts are expected to

likely remain a scarce resource. Various possible operation paradigms are under evaluation. The extremities are covered by:

- One operator per machine: this scheme focuses on optimising the accelerator individually and is similar to present operation at GSI. The advantages are better skilled operators, causing less operational errors and faster beam set-up for a specific accelerator (only). The disadvantages cover [but are not limited to] reduced interface efficiencies of transferring beams across accelerators domains, limited possibility of setting up multiple experiments in parallel, and limited flexibility of shift planning (an operator can only be replaced by another with the same expertise). This scheme requires a much larger pool of operators (59 compared to presently 23 persons, excluding cryo-operators), increasing the annual operation costs of FAIR, and cannot avoid potentially idle resources when not all accelerators or experiments are being operated.
- One operator per BPC/experiment: this scheme focuses on the optimisation of the beam production chain across accelerators to the experiments and is the proposed control and operation strategy for FAIR. The advantages of this scheme are a more efficient set-up and interface across accelerators and to the experiments, reduced number of required personnel (30–37 compared to presently 23 persons, excluding cryo-operators), the operator being an expert and more highly motivated to deliver the required beam parameter ("my experiment"), and more redundancy thus flexibility with respect to shift planning. Some of the disadvantages to be addressed are better and continuing training requirements for operators, requirement of more common tools and automation of standard processes across accelerators, and adapted console scheme.

Hybrid options between these two extremities are possible and are being evaluated: e.g. that the more experienced shift-leaders/operators that can cover a broader range of accelerator domains are paired with operators that are machine-type specialists (e.g. linacs, ring accelerators).

SEMI-AUTOMATION & BEAM-BASED CONTROL STRATEGY

To optimise turn-around times, to establish a safe and reliable machine operation, and to improve the beam parameter qualities, a shift from a presently predominantly manual 'analog' to an automated 'fully digital' control and operation paradigm is in progress. The aim is to automate routine tasks to minimise inadvertent errors (i.e. 'poka yoke' principle), to aid the frequent machine (re-) set up, to control beam-parameters to a higher precision, and to minimise unnecessary strain on operating crews in order that their talents are optimally utilised and focused on more important tasks that cannot be automated.

Thus a comprehensive suite of semi-automated measurement applications, as well as fully-automated beam-based feedbacks (FBs) is being prepared, and will be deployed as generic tools across all FAIR accelerators. These cover a wide range of beam parameters ranging from beam transmission [21], trajectory, orbit [19], tune and chromaticity [22, 23], machine optics, emittance preservation and manipulations, fast turn-by-turn feedbacks, as well as specialised machine-specific feedbacks, for example, for the optimisation of multi-turn-injection process, slow resonant extraction [20], as well as diagnostics to aid the set up of injection energy, stochastic and electron cooling methods.

As a proof-of-concept, a selected limited set of automated beam parameter measurement and feedback systems have been tested as early prototypes at the SIS18 during the machine development studies in 2016. These are now being deployed operationally during the recommissioning in 2018: a new beam transmission monitoring system, an automated beam parameter scanning application, and a cycle-to-cycle orbit- as well as a macro-spill feedback.

In addition to beam-based FBs, a multitude of additional technical controls services and tools are being developed in view of semi-automation of repetitive tasks that are common during commissioning and operation, e.g.:

- Sequencer [16, 17]: automatising routine tasks, commissioning procedures, as well as automatic 'as-good-as-new' system validation tests that drive preventative maintenance and provide an early warning of potentially compromised machine function,
- Digitizer [24]: which provide comprehensive, generic monitoring of all analog signals to track and quickly isolate faults, to monitor equipment performance, and which is a crucial prerequisite for migrating to the new all-digital FAIR Control Centre,
- Accelerator & Beam Modes [25]: the concept has formalised the existing communication of intended accelerator operation to the experiments, FAIR and wider community of what to expect and when, in order to condition the control sub-system responses accordingly. These modes follow the actual different operation mode of the machine ie. 'NO BEAM', 'PILOT BEAM', 'INTENSITY RAMP-UP', 'ADJUST', and 'STABLE BEAMS'.
- Archiving System [26]: which collects and stores all accelerator data centrally that are pertinent for the analysis of the accelerator performance as well as its proper function.
- Beam Transmission Monitoring System [21]: implementing a beam-based interlock that prevents poor transmission performance across the BPCs, to minimise machine activation, and to avoid scenarios that might cause/or otherwise complicate machine protection incidents.

FAIR CONTROL CENTRE (FCC)

The present GSI main control room is too small for an efficient operation of the substantially larger FAIR accelerator facility, and cannot be easily upgraded to suit the requirements of FAIR, without compromising beam operation of the existing GSI accelerator facility. Thus a new control centre will be constructed on site to be completed by 2023, in time for the HWC of SIS100 [13, 18] with the primary goals being:

- provide sufficient room for the operation of the existing and enlarged accelerator facility,
- provide a public representation that is adapted and that relates to the high-quality level of the research that is performed at FAIR (management of visitors),
- provide an environment that positively impacts personnel performance and in turn the FAIR performance by minimising disturbing elements (ie. strong focus on ergonomics), and
- provide a credible 'vision statement' that facilitates solving issues and facility optimisations by offering an efficient communication platform for operation, accelerator or equipment experts, and experiments.

CONCLUSION

FAIR roughly quadruples in size and has an significantly increased operational complexity in comparison to the existing accelerator facility at GSI. Hardware commission is expected to start with SIS100 in 2022, followed by the (re-)commissioning of 4 accelerator and Super-FRS in quick succession to be ready to provide beam for physics by 2025. Planning and testing of possible commissioning and operation strategies, controls system integration, and semi-automated tools has been started already now with the existing GSI facility as a test-bed.

The underlying core design principles for these activities are coordinated by two WGs open to all who can participate and are willing to contribute to these subjects, and follow lean management principles of *continuous improvement*, *respect for people*, and *poka yoke* (ie. stop-and-fixing errors at the source and when they occur leading to the 'pilot-beam' and 'intensity ramp-up' concepts).

ACKNOWLEDGEMENTS

The presented concepts and strategies are based on existing experience and best-practises at GSI, CERN and other large hadron accelerator facilities. The valuable contributions, advice and recommendations in particular regarding the ergonomics, control room design, and operation from our CERN colleagues R. Giachino, M. Lamont, D. Manglunki, R. Steerenberg, J. Wenninger and others are greatly acknowledged.

REFERENCES

- [1] FAIR Commissioning & Control Project, <http://fair-wiki.gsi.de/FC2WG/>
- [2] L. Groening *et al.*, “Upgrade of the Universal Linear Accelerator UNILAC for FAIR”, in *Proc. IPAC’16*, Busan, Korea, 2016.
- [3] B. Franczak, “SIS18 Parameterliste”, GSI, Darmstadt, Germany, September 10, 1987.
- [4] B. Franzke, “The Heavy Ion Storage and Cooler Ring Project ESR at GSI”, *NIMA*, vol. 287, p. 18, 1987.
- [5] H. H. Gutbrod (ed.) *et al.*, “FAIR Baseline Technical Report”, GSI, Darmstadt, Germany, 2006.
- [6] O. Kester *et al.*, “Status of the FAIR Accelerator Facility”, in *Proc. IPAC’14*, Dresden, Germany, 2014.
- [7] R. Brodhage *et al.*, “Status of the FAIR Proton Linac”, in *Proc. IPAC’15*, Richmond, VA, USA, 2015.
- [8] P. Spiller, “Status of the FAIR Synchrotron Projects SIS18 and SIS100”, in *Proc. IPAC’14*, Dresden, Germany, 2014.
- [9] Michael Lestinsky *et al.*, “CRYRING@ESR: A study group report”, GSI, Darmstadt, Germany, July 26, 2012.
- [10] H. Danared *et al.* “LSR Low-Energy Storage Ring Technical Design Report”, Stockholm University, Sweden, 2011.
- [11] H. Hüther *et al.*, “Realization of a Concept for Scheduling Parallel Beams in the Settings Management System for FAIR”, in *Proc. ICALEPCS’15*, Melbourne, Australia, 2015.
- [12] U. Scheeler, S. Reimann, D. Severin, P. Schütt *et al.*, “Accelerator Operation Report”, GSI Annual Scientific Reports 1992 – 2016, GSI, Darmstadt, Germany, https://www.gsi.de/en/work/research/library_documentation/gsi_scientific_reports.htm
- [13] FAIR Common Specification, “FAIR Control Centre (FCC)”, <https://edms.cern.ch/document/1821654/>
- [14] FAIR Hardware Commissioning <https://fair-wiki.gsi.de/FC2WG/HardwareCommissioning/>
- [15] FAIR Beam Commissioning <https://fair-wiki.gsi.de/FC2WG/BeamCommissioning>
- [16] R. J. Steinhagen, H. Hüther, R. Müller, “The FAIR Sequencer Semi-automation in view of accelerator commissioning and operation”, GSI Scientific Report 2017, GSI, Darmstadt, Germany, 2017.
- [17] V. Baggiolini *et al.*, “A Sequencer for the LHC era”, in *Proc. ICALEPCS’09*, Kobe, Japan, 2009.
- [18] Markus Vossberg *et al.*, “FAIR Control Centre (FCC) - Concepts and Interim Options for the Existing GSI Main Control Room”, in *Proc. IPAC’17*, Copenhagen, Denmark, 2017.
- [19] B. R. Schlei *et al.*, “Closed Orbit Feedback for FAIR”, in *Proc. IPAC’17*, Copenhagen, Denmark, 2017.
- [20] R. J. Steinhagen *et al.*, “Beam-Based Feedbacks for FAIR”, in *Proc. IPAC’17*, Copenhagen, Denmark, 2017.
- [21] FAIR Common Specification, “Beam Transmission Monitoring System”, <https://edms.cern.ch/document/1823362/>
- [22] R. J. Steinhagen, “Tune and Chromaticity diagnostics”, in *Proc. of CAS*, Dourdan, CERN-2009-005, 2008.
- [23] R. J. Steinhagen, “Real-Time Beam Control at the LHC”, in *Proc. PAC’11*, New York, NY, USA, 2011.
- [24] FAIR Common Specification, “Digitization of Analog Signals at FAIR”, <https://edms.cern.ch/document/1823376/>
- [25] FAIR Common Specification, “Accelerator and Beam Modes”, <https://edms.cern.ch/document/1823352/>
- [26] FAIR Common Specification, “FAIR Archiving System”, <https://edms.cern.ch/document/1176039/>

HIGH-POWER BEAM OPERATION AT J-PARC

S. Igarashi[†] for the J-PARC Accelerator Group, KEK/J-PARC Center,
319-1195 Tokai, Naka, Ibaraki, Japan

Abstract

The Japan Proton Accelerator Research Complex (J-PARC) is a multipurpose high-power proton accelerator facility, comprising a 400 MeV linac, a 3 GeV rapid cycling synchrotron (RCS) and a 30 GeV main ring synchrotron (MR). RCS is now providing 500 kW beams to the materials and life science experimental facility (MLF) and its beam power will be increased step by step toward the design value of 1 MW. MR has been operated with the beam power of 500 kW at maximum for the long-baseline neutrino oscillation experiment (T2K). An upgrade plan of MR for the beam power of 1.3 MW for the T2K experiment is promoted with a faster cycling scheme.

INTRODUCTION

The Japan Proton Accelerator Research Complex (J-PARC) is a multipurpose high-power proton accelerator facility, comprising a 400 MeV linac, a 3 GeV rapid cycling synchrotron (RCS) and a 30 GeV main ring synchrotron (MR). RCS is now providing 500 kW beams to the materials and life science experimental facility (MLF) and its beam power will be increased step by step toward the design value of 1 MW [1, 2].

MR has two operation modes: slow extraction (SX) mode and fast extraction (FX) mode. For the SX operation the beam is extracted in about 2 s spill with the cycle time of 5.2 s. The beam spill is then delivered to the hadron hall to produce various secondary particles for the elementary particle and nuclear physics experiments. Proton beams with the power of 51 kW have been delivered for the SX operation [3].

For the FX operation the beam is extracted in one turn after the acceleration with the cycle time of 2.48 s. Proton beams with the power of 500 kW at maximum have been delivered to the long-baseline neutrino oscillation experiment (T2K). Figure 1 shows the beam power since 2010.

Significant experimental achievements have been reported including the first result on CP (charge-parity) violation search obtained from the T2K experiment [4]. The result indicates a potential discovery in the near future and further motivates MR to provide higher intensity beams.

The original design beam power of MR is 750 kW. The plan is to make the cycle time faster from 2.48 s to 1.32 s. New hardware is being made for the faster cycling, such as magnet power supplies, rf system, injection and extraction devices. Further upgrade plan is promoted for the beam power of 1.3 MW with the faster cycling of 1.16 s and intensity upgrade.

This paper describes the recent improvements and the future plan of the beam power upgrade.

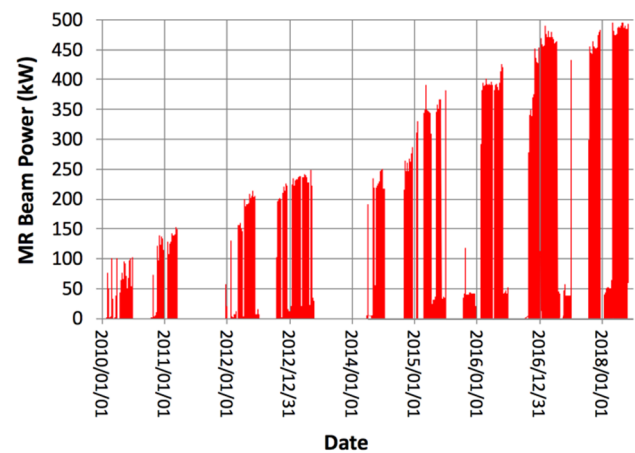


Figure 1: History of MR beam power.

OPERATION STATUS FOR THE FAST EXTRACTION

Eight bunches of beams are injected to MR in 4 times during the injection period of 0.13 s. The acceleration takes 1.4 s and the accelerated protons are then extracted. The recovery for the magnet currents takes 0.94 s and the total cycle is 2.48 s. The operation beam power was about 470 kW to 500 kW in the recent run of April and May of 2018. Figure 2 shows the beam intensity measured with DCCT as a function of the cycle time for a shot of beam power of 504 kW. The number of protons per bunch (ppb) was 3.3×10^{13} at the injection and the number of accelerated protons was 2.61×10^{14} ppp.

The beam loss was estimated to be 273 W during the injection period and 385 W during 0.12 s in the beginning of acceleration. The total beam loss was within the MR collimator capacity of 2 kW. The beam loss at 3-50BT was estimated to be 50 W. It was also within the 3-50BT collimator capacity of 2 kW.

The beam loss distribution in the circumference is shown in Fig. 3. The beam loss is measured with beam loss monitors [5] located at all 216 main quadrupole magnets. The gains of the 24 loss monitors (#1 ~ #20 and #213 ~ #216) including the collimator area are set to low, and the others (#21 ~ #212) have higher gain about 8 times. The beam loss is reasonably localized in the collimator area of (#6 ~ #11). Details of the collimator operation are described in Ref. [6].

[†] susumu.igarashi@kek.jp

Content from this work may be used under the terms of the CC BY 3.0 licence (© 2018). Any distribution of this work must maintain attribution to the author(s), title of the work, publisher, and DOI.

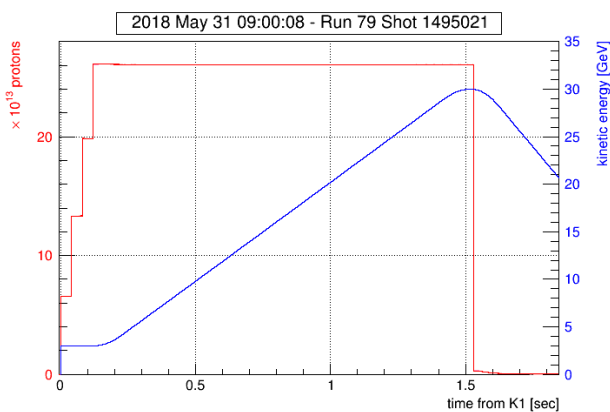


Figure 2: Beam intensity (shown in red) for a user-operation shot of the beam power of 504 kW as a function of the cycle time.

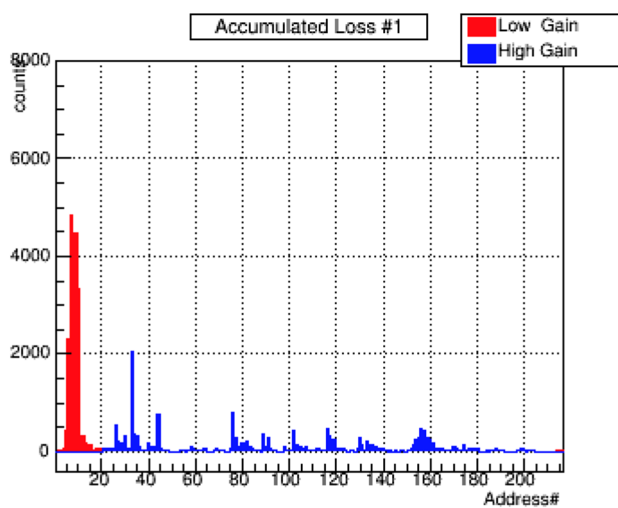


Figure 3: Beam loss distribution measured with beam loss monitors in the circumference as a function of MR address for a shot of the beam power of 504 kW.

RECENT IMPROVEMENTS

Optimization of the RCS Parameters

The large-emittance beam is preferred for the MLF target and for the minimization of the beam loss in RCS. For the transverse painting of the MLF beam, 200π mmmrad is chosen. Because the aperture of MR is relatively smaller with respect to RCS, the parameters, such as the transverse paint, betatron tunes and chromaticity, should be optimized to make small-emittance beams. The RCS parameters for the MR beam are then different those from for MLF beam. The power supplies for the painting magnets and sextupole magnets for the chromaticity correction have been capable of switching patterns for MLF and MR beams. For the painting of the MR beam, we are able to set 50π mmmrad.

The power supplies for the main dipole and quadrupole magnets, however, are not capable of switching patterns. We, therefore, were not able to switch the tune for MLF and MR beams. The correction quadrupole magnets (QDT) have been installed and used for the optics correc-

tion. The QDT magnets has recently been applied for switching tunes [7]. The tunes were then optimized to minimize the beam losses in both MR and RCS with QDT magnets.

RF Pattern

For the recent user operation, the fundamental rf of 155 kV and 2nd harmonic rf of 110 kV have been applied during injection period to improve the bunching factor and to reduce the space charge effects. The bunching factor was measured to be about 0.3 during injection period. In the beginning of acceleration, the fundamental rf voltage turned up to 310 kV in 60 ms and turned down to 256 kV at 0.4 s after the acceleration start until the acceleration end. The 2nd harmonic rf lasts 0.1 s in the beginning of acceleration and turned to 0 kV for the rest of acceleration.

Operation with the Working Point of (21.35, 21.43) and the Space Charge Tune Spread

The working point of MR used to be (22.40, 20.75) for the operation of less than 420 kW until 2016. For higher beam power operation, we started to apply the working point of (21.35, 21.43), because larger space charge tune spread may be afforded there from the structure resonances.

The tune spread was estimated for the beam power of 500 kW using the particle tracking simulation program SCTR [8], which takes the space charge effects into account. The number of ppb was set to 3.2×10^{13} for the cycle time of 2.48 s. The particle distributions for the input of the simulation were reproduced based on the measurements. The transverse 2σ emittance was 15π mmmrad and 19π mmmrad for horizontal and vertical respectively. The bunching factor was set to 0.3. Figure 4 shows the distribution of the tunes of macro particles with the simulation. The operation tune was set to (21.35, 21.43). The tune spread was estimated to be 0.4. There are some resonances of concern, such as a half integer resonance $2\nu_y = 43$ and third order resonances.

The tune shifts depending on the number of injection bunches were observed to be about 0.02 during the injection period [9]. The tunes were then shifted from the working point of the best operation. We have corrected the tune shift and reduced the beam loss accordingly.

Instability Suppression

The chromaticity pattern in the cycle time was optimized to minimize the beam loss. To suppress instabilities, the chromaticity is kept to be negative, typically -7 during injection. If the chromaticity is too small in negative value, instabilities may be observed causing beam losses. If the chromaticity is too large in negative value, we may observe beam losses those are probably due to chromatic tune spread. The optimization is iterated after the change of the beam intensity and parameters of following feedback systems.

To suppress transverse oscillations, the intra-bunch feedback system is applied during injection and in the

beginning of acceleration [10]. The system consists of stripline BPM's which have wide frequency response, a signal processing circuit and stripline kickers with the bandwidth of 100 kHz ~ 100 MHz. BPM signals are sampled at the rate of 64th harmonic of the RF frequency. The signal processing circuit extracts the betatron oscillation signals on each slice and feedbacks kick signals for each slice. The system has been applied effectively during injection and up to 0.12 s after the acceleration start.

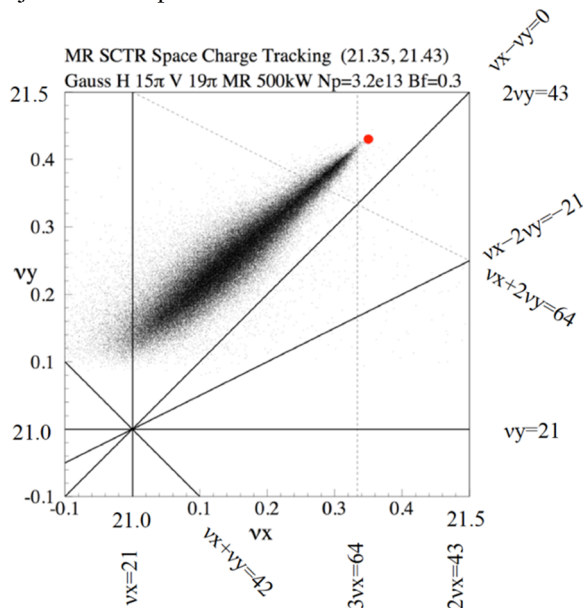


Figure 4: Space charge tune spread and resonances of concern.

Optics Measurement and Correction

We have recovered the effective physical aperture by corrections of the optics and closed orbit distortion (COD). The stripline kickers and the power amplifiers of the intra-bunch feedback system are used for beta measurement during injection and up to 0.37 s after the acceleration start. The kickers are to excite the betatron oscillation. The amplitudes of the oscillation are then measured with all the BPM's. The square root of beta should be scaled to the oscillation amplitude. The dispersion function is derived from the COD for the momentum deviation of $|\delta| < 1.3\%$. The betatron tune during injection and acceleration is measured from the frequency of the betatron oscillation that is induced by the kickers. The results of beta, dispersion and tune are corrected to what we intend to set by adjusting the currents of 11 quadrupole magnet families.

Half Integer Resonance Correction

The FX septum magnets make undesirable quadrupole fields for circulating beams with the leak fields. They were measured for all 8 FX septum magnets. The sum of the strength K1 corresponded to 3% of a main quadrupole magnet. Correction currents for the trim coils of three quadrupole magnets near the FX septum magnets were calculated. The correction has been applied and optics were measured at (21.35, 21.45) near the half integer

resonance of $2\nu_y = 43$. Improvement of the beta modulation was then observed with the correction.

Third Order Resonance Corrections with Trim Coils of Sextupole Magnets

Third order resonances of $\nu_x + 2\nu_y = 64$ and $3\nu_x = 64$ have been corrected with trim coils of four sextupole magnets. The current setting of trim coils of two sextupole magnets was optimized to recover the beam survival for low intensity beams when the tune was set (21.24, 21.38) on the 3rd order resonance of $\nu_x + 2\nu_y = 64$. The amplitude of the resonance strength $G_{1,2,64}$ expressed by Eq. (1) was then measured to be 0.076.

$$G_{1,2,64} = \frac{\sqrt{2}}{8\pi} \beta_x^{1/2} \beta_y k_2 \exp[i(\phi_x + 2\phi_y)] \quad (1)$$

The same procedure was repeated when the tune was set (21.33, 21.41) on the 3rd order resonance of $3\nu_x = 64$. The amplitude of the resonance strength $G_{3,0,64}$ expressed by Eq. (2) was also measured to be 0.055.

$$G_{3,0,64} = \frac{\sqrt{2}}{24\pi} \beta_x^{3/2} k_2 \exp[i(3\phi_x)] \quad (2)$$

Trim coils of four sextupole magnets were used to correct both of $\nu_x + 2\nu_y = 64$ and $3\nu_x = 64$. A solution was solved for a simultaneous equation to reproduce the two resonance strengths of $G_{1,2,64}$ and $G_{3,0,64}$ in the complex planes. It was applied for the high intensity operation and the beam loss was improved. Further optimization was performed with high intensity beams to reduce the beam losses.

Longitudinal Coupled Bunch Instability

Longitudinal dipole oscillations have been observed during acceleration for the beam power of 480 kW or more (Fig. 5). The node analysis indicated that the beam loading of rf cavities was a possible cause [11]. A feedback system to damp the oscillation is being made and tested with low-power beams. The application to high-power beams are in preparation.

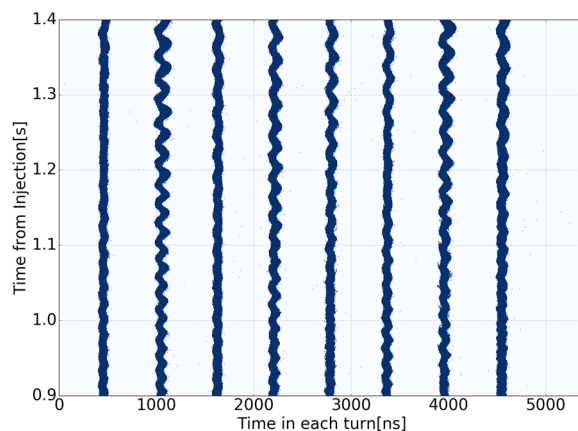


Figure 5: Wave form with the wall current monitor for the beam of 480 kW.

UPGRADE PLAN

Concepts

We plan to make the cycle time faster from 2.48 s to 1.32 s to achieve the original design beam power of 750 kW. The required number of accelerated protons is 2.1×10^{14} ppp which we have already achieved. Further upgrade has been promoted to the beam power of 1.3 MW for the CP violation search in the neutrino oscillation processes. The plan is to make the cycle time faster to 1.16 s and the number of the accelerated protons is to be increased to 3.3×10^{14} ppp. Because the accelerated protons of 2.6×10^{14} ppp has been achieved, about 30% of the intensity upgrade is required.

Hardware Upgrade Plan

For the faster cycling of 1.32 s, the magnet power supplies, rf system, injection and extraction devices are being upgraded. The upgrade will be done by JFY 2021.

The electric power supplier does not allow a large power variation of more than 100 MVA that is estimated with the present scheme of main magnet power supplies. Therefore, the energy recovery scheme has been chosen with bank capacitors [12]. Three new buildings were constructed for the power supplies. A new bending magnet power supply was installed in one of the building and being tested.

The rf cavities are also being upgraded for the faster cycling [13]. For the new target of 1.3 MW, the rf anode current power supplies should be upgraded for the beam loading compensation.

Additional collimators are being considered to upgrade for the total power capability of 3.5 kW [6]. The kicker magnets for injection and extraction are being improved and the septum magnets for injection [14] and extraction [15] are upgraded for the faster cycling.

Simulation Studies for the Upgrade Plan

Transverse profiles of beams from RCS have been measured with multi-ribbon profile monitors (MRPM) at 3-50BT for the intensity of up to 3.5×10^{13} ppb. Based on the measurement, both horizontal and vertical profiles for the simulations were set to be Gaussian distributions with 2σ emittances of 16π mmmrad for beams of 3×10^{13} ppb which was 470 kW equivalent with the cycle of 2.48 s. Emittances of 2σ for both horizontal and vertical distributions were set to be 24π mmmrad for beams of 4×10^{13} ppb which is 1.3 MW equivalent with the cycle of 1.16 s.

The beam survivals for both intensities were estimated with the space charge simulation program SCTR. The simulation result was compared with the measurement for the beam intensity of 470 kW equivalent as in Fig. 6. The simulation result of 470 kW equivalent beam with magnet errors are in good agreement with the measurement. The simulation indicated that the beam of 1.3 MW equivalent would be lost more than 5%, which would not be acceptable for the operation.

The simulation study indicated that the present working point of (21.35, 20.45) was affected by the structure reso-

nances of $\nu_x - 2\nu_y = -21$ and $2\nu_x - 2\nu_y = 0$. Figure 7 shows footprints of 1000 turns of ten test particles for the horizontal and vertical actions of the betatron motions with SCTR. Values of $2J_x + J_y$ of some test particles were approximately invariants, which indicated the coupling resonance of $\nu_x - 2\nu_y = -21$. Values of $J_x + J_y$ of some other test particles were approximately invariants, which indicated the coupling resonance of $2\nu_x - 2\nu_y = 0$. Because the aperture of MR is limited with the collimator of typically 60π mmmrad, any coupling of horizontal and vertical motions would result in beam losses. We would then search for a working point which not affected by the structure resonances.

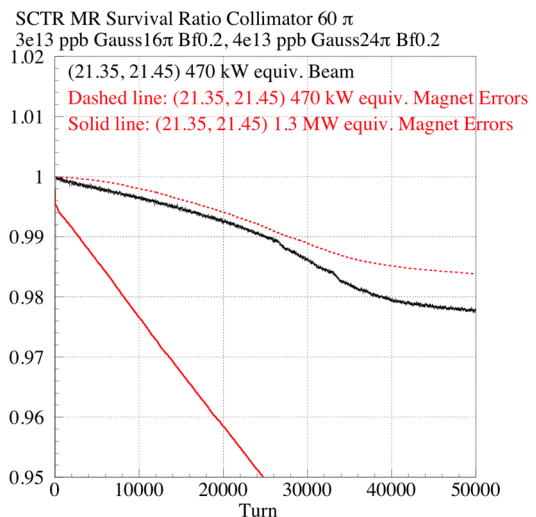


Figure 6: The measured beam survival for 1-batch beam of 470 kW equivalent (black line), simulation results of 470 kW equivalent beam (red dashed line) and simulation results of 1.3 MW equivalent beam (red solid line) for the working point of (21.35, 20.45). Simulation results with magnetic field errors and magnet alignment errors are shown.

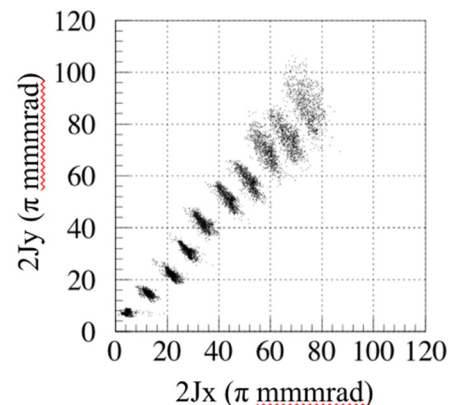


Figure 7: Simulation results of footprints of 1000 turns of ten test particles for the horizontal and vertical actions with SCTR.

Possibilities are being explored with the operation at the working point of (21.40, 20.45), because no low order structure resonances are close to the point (Fig. 8). There is a 4th order structure resonance of $4\nu_y = 81$. It, however,

should be corrected with the octupole magnets. There is also a 6th order structure resonance $2\nu_x - 4\nu_y = -39$. The effect to the beam survival, however, seemed to be small from the simulation. The simulation results are shown in Fig. 9. The simulation without magnet errors indicated that the beam of 1.3 MW equivalent would be lost about 2%, which would be acceptable for the operation. Because the simulation result with the magnet errors indicated worse survival, corrections of non-structure resonances, such as $\nu_x - \nu_y = 1$, should be necessary for the reduction of beam losses.

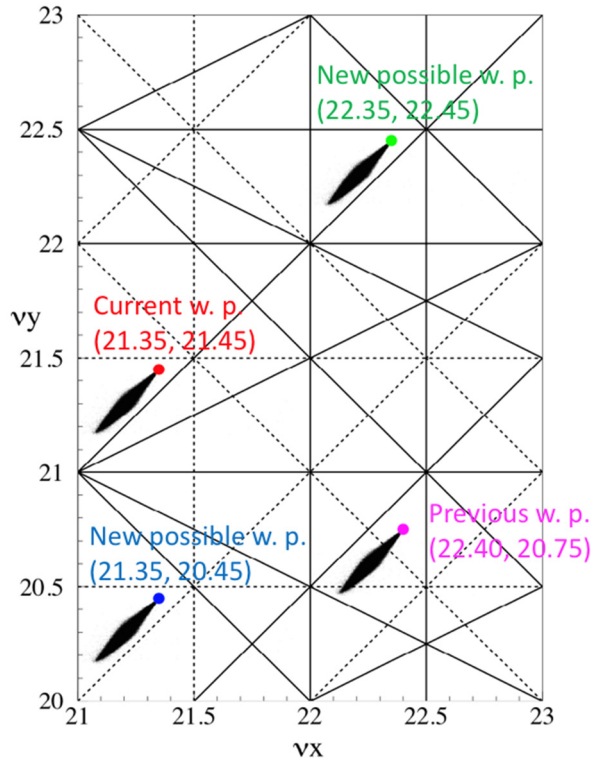


Figure 8: Structure resonances of up to third order (solid lines) and non-structure resonances of half integer and linear coupling resonances (dashed lines). Space charge tune spread shown for the working points of (22.40, 20.75), (21.35, 21.45), (21.35, 20.45) and (22.35, 22.45) for the beam power of 380 kW.

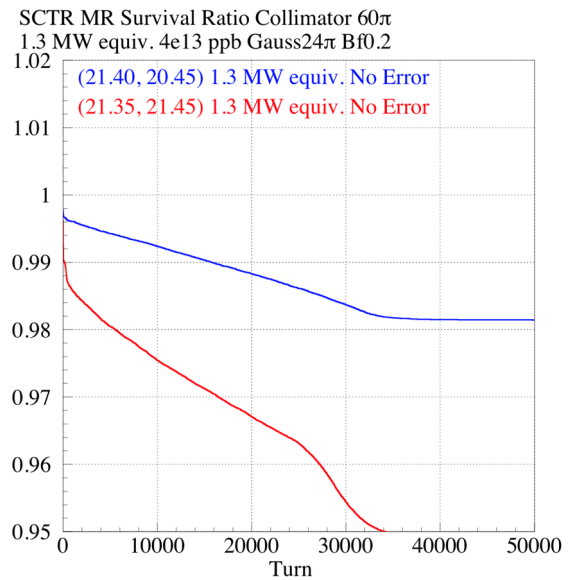


Figure 9: Simulation results of the beam survivals of 1.3 MW equivalent beam for the working point of (21.35, 21.45) (red line) and simulation results for the working point of (21.40, 20.45) (blue line). Simulation results without magnetic field errors and magnet alignment errors are shown.

SUMMARY

J-PARC is a high-power proton accelerator facility increasing the beam power step by step toward the design values. MR has recently delivered beams of the power of up to 500 kW with 2.6×10^{14} ppp and the cycle time of 2.48 s for the neutrino oscillation experiment. The beam loss was observed to be 700 W mostly localized at the collimator section. Recent improvements include the 2nd harmonic rf operation to reduce the space charge effect with a larger bunching factor and corrections of resonances near the operation setting of the betatron tune. We plan to achieve the target beam power of 750 kW by making the cycle time faster to 1.32 s with new power supplies of main magnets, rf upgrade and improvement of injection and extraction devices. Further upgrade plan is promoted for the beam power of 1.3 MW with the faster cycling of 1.16 s and intensity upgrade.

REFERENCES

- [1] H. Hotchi, “J-PARC RCS: Effects of Emittance Exchange on Injection Painting”, presented at the 61st ICFA Advanced Beam Dynamics Workshop on High-Intensity and High-Brightness Hadron Beams (HB’18), Daejeon, Korea, Jun. 2018, paper MOPIWA01, this conference.
- [2] H. Hotchi *et al.*, “Achievement of a Low-Loss 1-MW Beam Operation in the 3-GeV Rapid Cycling Synchrotron of the Japan Proton Accelerator Research Complex”, *Phys. Rev. Accel. Beams*, vol. 20, p. 060402, Jun. 2017.
- [3] M. Tomizawa, “Status and Beam Power Ramp-up Plans of the Slow Extraction Operation at J-Parc Main Ring”, presented at the 61st ICFA Advanced Beam Dynamics Workshop on High-Intensity and High-Brightness Hadron

- Beams (HB'18), Daejeon, Korea, Jun. 2018, paper THA1WD03, this conference.
- [4] K. Abe *et al.*, (T2K collaboration), "Combined Analysis of Neutrino and Antineutrino Oscillations at T2K", *Phys. Rev. Lett.*, 118, 151801, Apr. 2017.
- [5] T. Toyama *et al.*, "Beam diagnostics at the first beam commissioning of the J-PARC MR", in *Proc. 23rd Particle Accelerator Conf. (PAC'09)*, Vancouver, Canada, May. 2009, paper WE4GRC01, pp. 1964-1966.
- [6] M. Shirakata *et al.*, "New Arrangement of Collimators of J-PARC Main Ring", in *Proc. 57th ICFA Advanced Beam Dynamics Workshop on High-Intensity and High-Brightness Hadron Beams (HB'16)*, Malmö, Sweden, Jul. 2016, doi:10.18429/JACoW-HB2016-THAM4Y01
- [7] H. Hotchi *et al.*, "Pulse-by-pulse Switching of Operational Parameters in J-PARC 3-GeV RCS", in *Proc. 9th Int. Particle Accelerator Conf. (IPAC'18)*, Vancouver, Canada, Apr.-May, 2018, doi:10.18429/JACoW-IPAC2018-TUPAL018
- [8] K. Ohmi, *et al.*, "Study of Halo Formation in J-PARC MR", in *Proc. 22nd Particle Accelerator Conf. (PAC'07)*, Albuquerque, NM, USA, Jun. 2007, paper THPAN040, pp. 3318-3320.
- [9] A. Kobayashi, *et al.*, "Tune Shift Measurements with High Intensity Beam", US-Japan Meeting on Accelerators and Beam Equipment for High-Intensity Neutrino Beams, Batavia, IL, U.S.A., May 2018.
- [10] K. Nakamura *et al.*, "Intra-bunch Feedback System for the J-PARC Main Ring", in *Proc. 5th Int. Particle Accelerator Conf. (IPAC'14)*, Dresden, Germany, Jun. 2014, paper THOAA03, pp. 2786-2788.
- [11] Y. Sugiyama *et al.*, "Analysis of Longitudinal Beam Oscillation in J-PARC MR", in *Proc. PASJ'17*, Sapporo, Japan, Aug. 2017, paper WEP081.
- [12] Y. Morita *et al.*, "Development of the J-PARC Main Magnets Power Supplies for High Repetition Operation", *JPS Conf. Proc.*, vol. 8, 012006, Sep. 2015.
- [13] C. Ohmori *et al.*, "The Second Harmonic RF System for J-PARC MR Upgrade", in *Proc. 7th Int. Particle Accelerator Conf. (IPAC'16)*, Busan, Korea, May 2016, pp. 420-422, doi:10.18429/JACoW-IPAC2016-PAPERID-MOPMW011
- [14] T. Shibata *et al.*, "The New High Field Injection Septum Magnet System for Main Ring of J-PARC", in *Proc. 8th Int. Particle Accelerator Conf. (IPAC'17)*, Copenhagen, Denmark, May 2017, pp. 576-578, doi:10.18429/JACoW-IPAC2017-MOPIK034
- [15] T. Shibata *et al.*, "The Development of a New High Field Septum Magnet System for Fast Extraction in Main Ring of J-PARC", in *Proc. 8th Int. Particle Accelerator Conf. (IPAC'17)*, Copenhagen, Denmark, May 2017, pp. 573-575, doi:10.18429/JACoW-IPAC2017-MOPIK033

Content from this work may be used under the terms of the CC BY 3.0 licence (© 2018). Any distribution of this work must maintain attribution to the author(s), title of the work, publisher, and DOI.

AUTOMATED OPERATION OF EBIS INJECTOR AT BNL*

T. Kanesue[†], E. Beebe, S. Binello, B. Coe, M. Costanzo, L. DeSanto, S. Ikeda, J. Jamilkowski, N. Kling, D. Lehn, C.J. Liaw, V. Lo Destro, D. McCafferty, J. Morris, M. Okamura, R. Olsen, D. Raparia, R. Schoepfer, F. Severino, L. Smart, K. Zeno
Brookhaven National Laboratory, Upton, NY 11973, USA

Abstract

The RHIC-EBIS pre-injector is a heavy ion pre-injector to deliver multiple heavy ion species at 2 MeV/u to the AGS-Booster at the RHIC accelerator complex. In addition to collider experiments at RHIC, multiple heavy ion species are used for the NASA Space Radiation Laboratory (NSRL) to evaluate the risk of radiation in space in radiobiology, physics, and engineering. A GCR simulator is one of the operation modes of NSRL to simulate a galactic cosmic ray event, which requires switching multiple ion species within a short period of time. The RHIC-EBIS pre-injector delivers various heavy ion species independently for simultaneous operation of RHIC and NSRL. We developed an automated scheme of the rapid species change and it is routinely used by NSRL or Main Control Room for daily operation without assistance of RHIC-EBIS experts. The number of species change exceeds one hundred. This paper describes the automated operation of the RHIC-EBIS pre-injector and the operational performance.

INTRODUCTION

At BNL, the RHIC-EBIS pre-injector has been operating to provide various heavy ion species for collider experiment at RHIC and NASA Space Radiation Laboratory (NSRL) at the same time since 2010. In addition to high intensity heavy ion beams for collider experiments at RHIC, the RHIC-EBIS pre-injector is required to switch heavy ion species rapidly for NSRL. NSRL is an accelerator-based research laboratory for space radiation research [1]. One of the main sources of radiation in space is Galactic cosmic Ray (GCR), which is composed of high-energy protons and various heavy ion species coming from outside of solar system [2]. The energies of the ions are ranging from a few MeV/u to well above 1 TeV/u, with the peak of the distributions tend to be around 1 GeV/u, which is the energy that the AGS-Booster can supply. Evaluation of the risk of GCR is very important for interplanetary missions beyond Earth in the future. Heavy ions and proton beams from the AGS Booster synchrotron is transported to a target room at NSRL and used for this purpose. Available beam energy range is up to 1.5 GeV/u for heavy ions and 2.5 GeV for protons. The radiation environment of GCR is simulated by rapid change of beam energy and ion species. All heavy ion beams are provided

from RHIC-EBIS and proton beam is supplied from either the 200 MeV Linac or Tandem Van de Graaff. A schematic of the RHIC accelerator complex is shown in Fig. 1 for better understanding the facility.

The RHIC-EBIS pre-injector has been developed to switch ion species for NSRL reliably and automatically using the sequencer without assistance of ion source experts. The sequencer also switches parameters of entire beam line for NSRL including the AGS Booster. The switch is done from either Main Control Room (MCR) or NSRL at their will and it is independent from operation for RHIC. This makes NSRL highly useful and distinguished for space radiation study. Typical available heavy ion species at a time is 10 for solid-state materials and 2 for gaseous species. Since the RHIC-EBIS pre-injector is very reliable, an EBIS operator does not generally need to be involved in routine GCR operation once operational parameters for each species are set up.

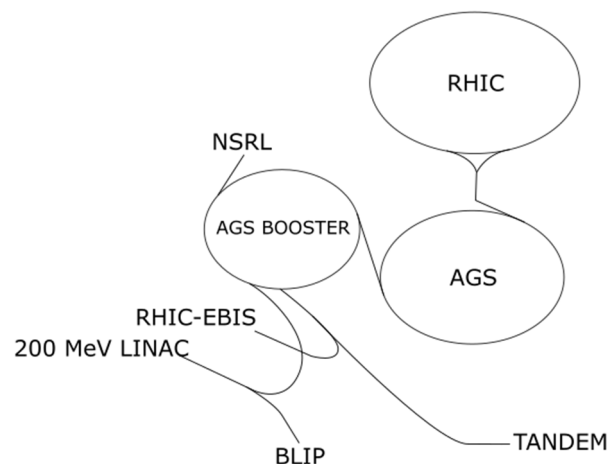


Figure 1: A schematic of RHIC accelerator complex. Heavy ion beams are provided from the RHIC-EBIS. NSRL uses ion beams of up to 1.5 GeV/u of heavy ions and 2.5 GeV of protons accelerated by the AGS Booster. Proton beam for NSRL is delivered from the 200 MeV LINAC or Tandem Van de Graaff. Tandem also serves as a backup for EBIS. For the isobaric collision program in Run-18, Tandem provided ⁹⁶Ru beam for RHIC and the RHIC-EBIS produced ⁹⁶Zr.

* This work has been supported by Brookhaven Science Associates, LLC under Contract No. DE-SC0012704 with the U.S. Department of Energy, and by the National Aeronautics and Space Administration.

[†] tkanesue@bnl.gov

Content from this work may be used under the terms of the CC BY 3.0 licence (© 2018). Any distribution of this work must maintain attribution to the author(s), title of the work, publisher, and DOI.

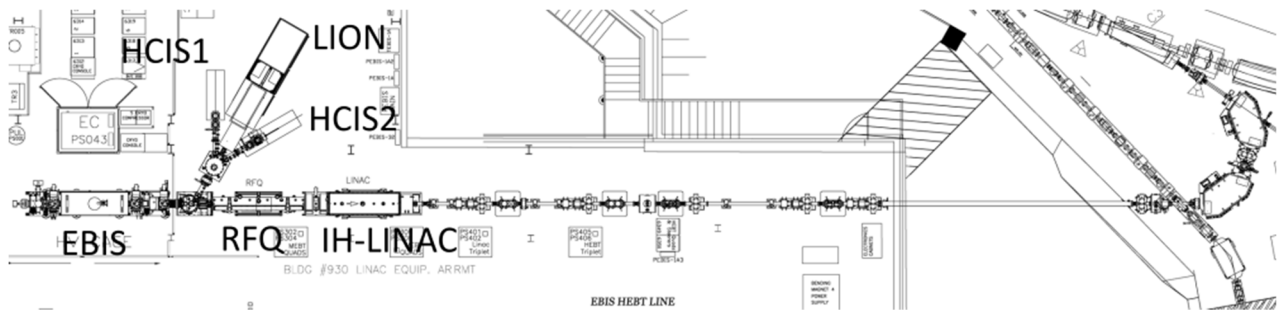


Figure 2: Layout of the RHIC-EBIS pre-injector.

RHIC-EBIS PRE-INJECTOR

Figure 2 shows a layout of the RHIC-EBIS pre-injector. For the rapid species change, an Electron Beam Ion Source (EBIS) is usually operated as charge multiplier and primary ions are injected from external ion sources to keep the ion trap clean. The primary singly charged heavy ions are produced from a laser ion source (LION) for all solid-state materials and two hollow cathode ion sources (HCIS) for gaseous targets. Highly charged ions such as Au³²⁺ or Fe²⁰⁺ from EBIS are accelerated to 2 MeV/u by a RFQ linac and a IH-Linac, both operating at 100.625 MHz. The 2 MeV/u heavy ion beams are injected into the AGS-Booster. The beam line after EBIS is designed to accelerate and transport heavy ions with charge-to-mass ratio more than 1/6 to switch ion species within 1 second.

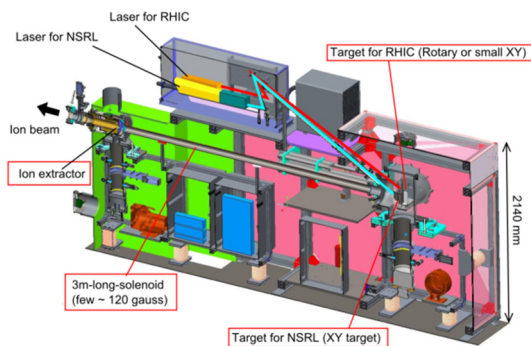


Figure 3: Layout of LION.

The Laser ion source is a key to realization of automated operation and rapid species changes. It can generate ions by laser ablation from any solid-state targets using a high-power laser irradiated on the target surface in vacuum. After a laser is stabilized which takes ~15 min, no warming up is required to switch species and the full performance can be achieved from the first shot. The vacuum pressure at the target chamber is kept below 10⁴ Pa. Species switch is achieved by mechanically changing a target position or by changing a laser spot to shoot a different target. Figure 3 shows a layout of the LION. There are two target systems and corresponding lasers to provide heavy ions for RHIC and NSRL at the same time. For RHIC, one or two ion species are required for the entire run in general. We use rotating disk targets or planer targets on a small two-

dimensional translation stage depending on the conditions of the run. For NSRL, a two-dimensional linear stage, called the XY target, holds multiple targets with the movable range of 250 mm by 50 mm. Typical dimension of one target is 25 mm by 25 mm or 25 mm by 50 mm. About 10 different target species are mounted at a time. The switching time between species depends on the motion of the XY stage. With the current velocity of 1 mm/s, it takes at most 25 s to use the target located at the each end of the holder. In case faster switching is required, a laser spot on the XY target can be shifted by controlling a final mirror located in air, in addition to moving the XY stage, although the current target switching time is satisfactory. The XY target can be used for RHIC simply by switching triggers of laser and so the XY stage serves as a backup for the RHIC operation. These two target systems for RHIC and NSRL are mounted in the same target chamber in vacuum. The laser power density on the target is adjusted between a few 10⁸ W/cm² and 10⁹ W/cm² to optimize the charge stage in induced ablation plasma for singly charged ions. Typical laser energy on a target is between 200 and 500 mJ. The strength of a 3m-long solenoid magnet to transport the laser-produced plasma is adjusted between a few Gauss and 120 Gauss depending on ion species to provide optimum beam for EBIS injection for each species. Ions are extracted by a high voltage at about 19 kV at the end of the solenoid. Typical peak current of the extracted beam is a few hundred μA ~ 1 mA with a pulse width of ~200 μs.

Two HCISs are used to produce ions from gaseous species such as He, Ne, Kr, Ar, or Xe, and can also produce a metal such as Fe or Au simultaneously. Typical ion beam current from HCIS is 5~50 μA and long beam pulse of 10~40 ms in the operation scheme. The available number of gaseous species at a time is limited to one per source so EBIS experts need to replace gas in case more species are needed which takes about 30 min. The ions from LION and HCIS are transported through a common beam line toward an EBIS.

The EBIS utilizes 7~10 A of electron beam with 5 T of the maximum magnetic field at the center of a superconducting solenoid. The EBIS is operated as a charge multiplier, which means ions from external ion sources are trapped and the charge state is increased to the desired value by varying confinement time. Typical charge state of ions is listed in Table 1. The ion injection from

LION uses fast injection scheme and that from HCIS uses slow injection scheme [3]. The different EBIS platform potential is provided for different ion species to match the injection energy of 17 keV/u of a RFQ linac. The EBIS can switch species faster than the basic control cycle of 200 ms.

Table 1: Example of Charge State from EBIS

	Charge State	Q/M	Confinement Time (ms)
He	2	0.500	17
Li	3	0.429	27
B	4	0.364	106
C	5	0.417	51
C	6	0.500	111
O	7	0.438	81
Si	11	0.393	118
Si	13	0.464	418
Ar	11	0.275	36
Ca	14	0.350	106
Ti	18	0.375	242
Fe	20	0.357	242
Fe	24	0.429	822
Kr	18	0.214	45
Xe	27	0.205	81
Ta	38	0.210	217
Au	32	0.162	85
Th	39	0.168	130

The highly charged heavy ions from the EBIS are accelerated by a 3.2 m long RFQ linac, followed by a 2.46 m long IH-Linac [4]. The parameters of the RFQ linac and IH-Linac are summarized in Table 2. The accelerated ions are transported and then guided by two 72.5 degrees dipole magnets for injection into the AGS-Booster. These magnets have 13.5 cm gap height, 1.3 m bend radius, and 1 T maximum field. There is a spiral resonator rebuncher cavity between the RFQ linac and the IH-Linac, and two spiral type debuncher cavities between the IH-Linac and the dipole magnet to reduce the energy spread of the beam for booster injection. The switching time between species is ~1 s, which is mainly caused by the bending magnet.

Table 2: Parameters of the RFQ Linac and the IH-Linac

	RFQ	IH-linac
Frequency (MHz)	100.625	100.625
Input energy (keV/u)	17	300
Output energy (MeV/u)	0.3	2
Charge-to-mass ratio	>0.167	>0.167
Cavity length (m)	3.2	2.46
Power (with beam loading) (kW)	~200	~300

BEAM OPERATION FOR RHIC

RHIC continuously runs from around January to the end of June in general. However, RHIC does not require ion beams from the RHIC-EBIS all time. RHIC is refilled by the injectors at about every 0.5~20 hours depending on the store condition. The store length could be shorter than 30 min for RHIC low energy run. For RHIC injection, the RHIC-EBIS pre-injector provides 12 pulses at 5 Hz within a supercycle, the overall repetitive sequence of the accelerator facility (about 6 s for AGS to use the bunch merge scheme of 12-6-2). Typically, it takes 30 min or more to complete RHIC fill including machine set up. The 12 pulses are also used during store for injector tuning. At times when EBIS is not used for booster, the number of pulses is reduced to one as standby mode to keep the system up and running. The chance of machine failure is increased during the transition between standby mode and operational mode when duty is increased by a factor of 12. The switch between operational and standby mode is automated by the sequencer, and the number of cycles is gradually increased over several minutes. MCR switches the mode at any time.

BEAM OPERATION FOR NSRL

There are three NSRL runs per years in general, and the run starts before RHIC run and end at the similar time as RHIC. High-energy beam from booster is supplied at about every 4 s when RHIC is in shut down. When AGS is running, beam cycles for NSRL are interleaved in the 6 second supercycle period for AGS/RHIC using the Pulse to Pulse Modulation (ppm) feature of EBIS and RHIC injectors. Variety of heavy ion beams is provided from the RHIC-EBIS pre-injector. The number of available species is typically 12 at a time, 10 from LION and 2 from 2 HCISs. For automated operation, EBIS experts tune the RHIC-EBIS pre-injector for different species. The optimized parameters are archived with a standardized name for each ion species and charge state. For NSRL, active and background ppm users are used for the automated species change. Each ppm user contains different machine parameters of different beam characteristics. The archived parameters of next species are restored on a background ppm, and the actual species change occurs by switching the ppm user. During the switch, important devices such as lasers, XY target, vacuum valves are controlled in proper orders by the sequencer. MCR or NSRL can switch species at any time without notifying EBIS experts, without causing any failure of EBIS or resulting in delay of RHIC operation. The species change sequencer checks important parameters of EBIS and external sources to avoid breakdown and missed ion injection into EBIS. The possibility of electron beam fault is higher without ion beam neutralization of electron beam though EBIS is very stable and reliable under the normal operating condition. In addition, the EBIS electron beam used for NSRL beam is suppressed at the moment of the switch to tolerate any possible glitch of timing. This scheme contributed a lot for reliability of the RHIC-EBIS pre-injector. Since 2016, the

Content from this work may be used under the terms of the CC BY 3.0 licence (© 2018). Any distribution of this work must maintain attribution to the author(s), title of the work, publisher, and DOI.

new mode of NSRL operation, GCR simulator, has been developed. This mode is used to simulate the mixed radiation of heavy ions and protons in space by sequences of exposures. A dosimetry system at NSRL precisely controls dose on samples and cut off ion beam about 1 ms and triggers the species change and energy change according to a pre-defined setup file. The number of beam pulse for each species is as low as one.

OPERATIONAL PERFORMANCE

The above-mentioned beam operations for RHIC and NSRL run independently. The number of pulses per supercycle varies from 1 to 13, and the condition of the machine changes frequently on the order of minutes especially during GCR simulator mode. Figure 4 shows an example of a supercycle with both RHIC and NSRL running. EBIS is triggered at 12 times with ET0 trigger at the beginning of the supercycle for RHIC injection, and later EBIS is triggered once for NSRL. The number of pulses for RHIC is reduced to 1 when EBIS is in standby mode and there is no pulse for NSRL when NSRL is in shut down. Despite the large variation of duty and rf power required for different species, Low Level RF systems (LLRF), which is very similar to that developed for the BNL 200 MeV Linac [5], regulate cavity voltage and phase and keep cavity matching by controlling tuner position very well for all rf cavities.

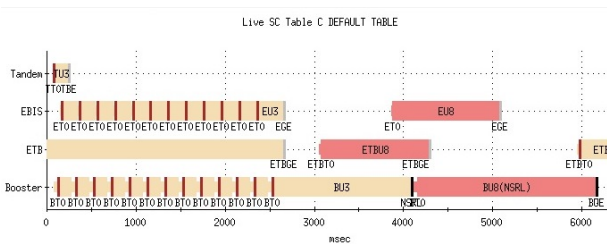


Figure 4: Supercycle when both RHIC and NSRL are running.

Figure 5 shows an example of daily beam operation with both RHIC and NSRL running. The top plot shows Au beam intensity at Booster injection for RHIC, and the bottom plot shows beam intensity at NSRL target room. The GCR simulator mode with proton from the 200 MeV Linac, He from EBIS/HCIS, O, Si, and Fe from EBIS/LION was used. As seen in the figure, beam operation for NSRL and RHIC did not affect each other. NSRL species was changed more than 130 times on that day without troubles on the RHIC-EBIS pre-injector, and stable heavy ion beam are delivered throughout the day without EBIS experts.

Figure 6 shows the details of the automated species change, where species was changed in the order of Si, He, O, Fe, then Si. The number of Au cycles was changed from 12 to 6 during that time (Fig. 6 (a)), but it didn't affect

beam for NSRL. The Au target was mounted on a small 2D stage in LION dedicated for RHIC operation.

This sequence of species change involves the switch from LION-to-HCIS, HCIS-to-LION, LION-to-LION, LION-to-proton, and proton-to-LION. These all worked well. The switching time from the end of a species to the next species for the RHIC-EBIS pre-injector is about 40 sec (Fig. 6 (b)). The dosimetry system controls the exposure time, species and energy changes as shown in Fig. 6 (c).

Total days when EBIS provided beam for NSRL including setup and testing in Run-17 (NSRL 16C, 17A, 17B) and Run-18 so far (NSRL 17C, 18A, 18B) is summarized in Table 3. After the automated rapid species change became available, more species are used in a day. In addition to the listed species, B and Ca produced by EBIS/LION were delivered to NSRL earlier. Also, Cu, Pb, and U were delivered to RHIC with EBIS/HCIS.

For RHIC Run-17, the RHIC-EBIS pre-injector started to provide Au beam from EBIS/LION for injector tuning from April 14, 2017, then RHIC started Au-Au setup from May 30, 2017 after polarized proton program was finished. The Au-Au run ended on June 21, 2017. RHIC Run-18 was for isobaric collision program of ⁹⁶Zr-⁹⁶Ru from March 8 to and low energy Au-Au program after that which will continue until June 18, 2018. ⁹⁶Zr beam was provided from EBIS/LION and ⁹⁶Ru beam was delivered from Tandem Van de Graaf. The RHIC-EBIS pre-injector provided ⁹⁶Zr and Au throughout the isobaric collision experiment, and Au beam after that.

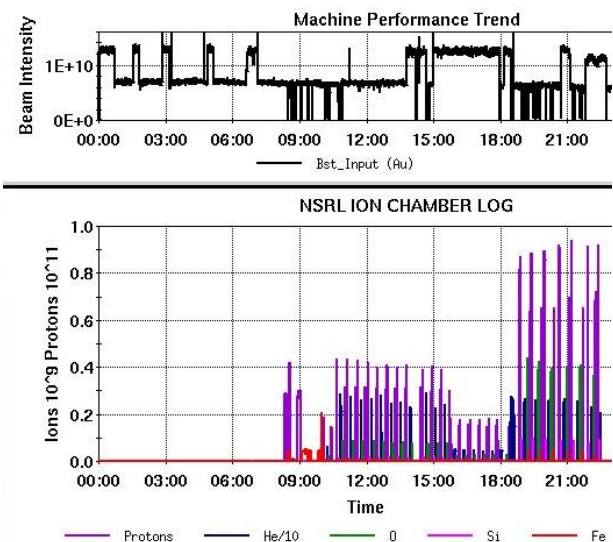


Figure 5: Example of beam usage with both RHIC and NSRL running for a day. Top plot shows Au beam for RHIC at Booster injection. Bottom plot shows ion species at NSRL target room with GCR simulator mode. Proton, He, O, Si, Fe were used on the day.

Table 3: Heavy Ion Species and Number of Days used for NSRL during Run-17 and Run-18

	Species from LION										Species from HCIS					
	Li	C	O	Si	Ti	Fe	Zr	Nb	Ta	Au	Th	He	Ne	Ar	Kr	Xe
Run 17	5	14	20	38	12	51	1	1	5	7	2	35	0	1	4	11
Run 18 (as of 6/6/2018)	0	22	28	49	21	56	0	0	31	5	5	35	8	0	11	16

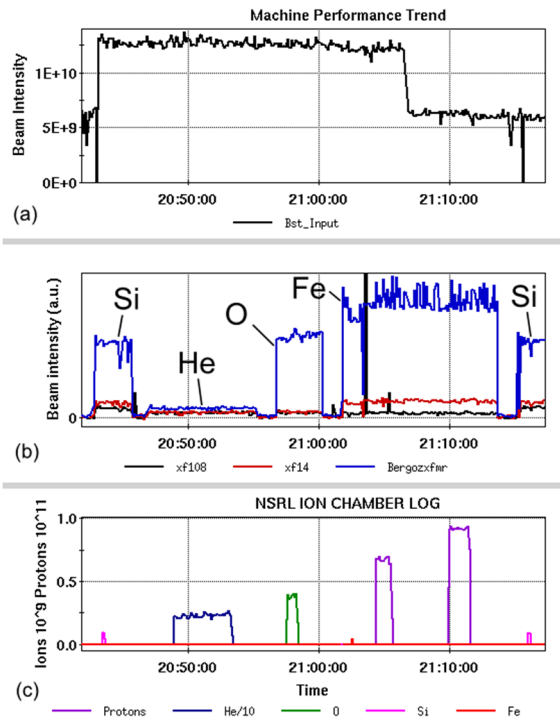


Figure 6: Au beam for RHIC and rapid species change for NSRL with GCR simulator mode. (a): Au Beam for RHIC. (b): beam at Booster injection (black), after IH-Linac (red), and EBIS output (blue). (c): Beam at NSRL target room.

CONCLUSION

At Brookhaven National Laboratory, the RHIC-EBIS pre-injector is providing heavy ion beams for both RHIC collider experiments and NSRL. Since 2016, automated rapid species change and the GCR simulator mode have

been developed and now they are routinely used for NSRL. Available heavy ion species for NSRL at a time is typically 12 and NSRL can switch to any of them at any time without assistance of EBIS experts. The number of species changes per day is more than 100. The reliability of the RHIC-EBIS pre-injector is very high and for normal operation, no EBIS experts are needed. The key component of the fast species change is LION combined with EBIS.

At the RHIC-EBIS the switching time between ion species for RHIC and that for NSRL in a supercycle is about 1 s. The switching time to introduce a new species for NSRL is about 40 s with the automated species switching, and the full beam performance is available from the first shot without warm-up.

REFERENCES

- [1] C. La Tessa *et al.*, “Overview of the NASA space radiation laboratory”, *Life Sciences in Space Research*, vol. 11, pp. 18–23, 2016.
- [2] J. A. Simpson, “Elemental and Isotopic Composition of the Galactic Cosmic Rays”, *Annual Reviews of Nuclear and Particle Sciences*, vol. 33, p. 706, 1983.
- [3] E. Beebe *et al.*, “Reliable operation of the Brookhaven EBIS for highly charged ion production for RHIC and NSRL”, *AIP Conference Proceedings*, vol. 1640, p. 5, 2015.
- [4] J. Alessi *et al.*, “Commissioning of the EBIS-based heavy ion preinjector at Brookhaven”, in *Proc. 25th Linear Accelerator Conf. (LINAC’10)*, Tsukuba, Japan, Sep. 2010, paper FR103, pp. 1033-1037.
- [5] D. Raparia *et al.*, “200 MeV H- linac upgrade at Brookhaven”, in *Proc. 7th Int. Particle Accelerator Conf. (IPAC’16)*, Busan, Korea, May 2016, pp. 968-970, doi:10.18429/JACoW-IPAC2016-MOPOY052

FIXED FIELD ACCELERATORS AND SPACE CHARGE MODELING

A. Adelman^{*}, Paul Scherrer Institut, CH-5232 Villigen, Switzerland
 Ch. Rogers, STFC Rutherford Appleton Laboratory, Didcot, UK
 S. L. Sheehy, University of Oxford, UK

Abstract

The efforts of the Fixed Field Accelerators FFA (formerly known as FFAG accelerators) community to address the high intensity challenge are reviewed. Starting from analytic estimates and linear models for space charge computation, the current possibilities of precise 3D models for start to end modeling are discussed.

HISTORY AND TAXONOMY OF FIXED FIELD ALTERNATING GRADIENT MACHINES

Historical Account

The concept of an FFA is not new. This type of accelerator was invented in the 1950s and 1960s at the same time as the synchrotron was being developed. Much of the early work in developing FFAs was carried out at the Midwestern Universities Research Association (MURA), but only electron FFAs were constructed at the time [1]. More about the history can be found in [2] and the references therein.

Working Principle and Taxonomy

A particular area of recent interest in the field of FFAs is their potential for high-intensity operation, because of their high repetition rate, large acceptance, simpler and cheaper power supplies, and flexibility of the RF acceleration system.

The FFA is a class of circular accelerator that combines properties of both the cyclotron and the synchrotron. It uses a magnetic field which is constant in time, hence the ‘fixed-field’, together with an increased focusing strength achieved using the ‘alternating-gradient’ principle [3]. The RF acceleration scheme is usually variable-frequency, but in some specific instances a fixed-frequency system is possible.

Starting with the idea that FFAs are just accelerators which have both a fixed field and alternating-gradient focusing produces a large spectrum of designs. Most FFAs have a very large dynamic aperture. This flexibility of FFA design has only emerged in roughly the last 15 years and the field continues to be a rich source of novel developments.

The Original or ‘Scaling’ FFA

In 1943 Marcus Oliphant described the idea of the synchrotron as follows:

Particles should be constrained to move in a circle of constant radius thus enabling the use of an annular ring of magnetic field ... which would

be varied in such a way that the radius of curvature remains constant as the particles gain energy through successive accelerations.

He intended that the magnetic field should be varied temporally and the beam should always follow the same annulus. However, in principle there is no reason why the annulus may not change radius and the field vary spatially rather than temporally. This is the fundamental idea behind the FFA. A large variation of the field with radius will constrain the change in radius of the orbits; this can lead to a larger field increase with radius and more compact orbits than in a cyclotron. This is the original type of FFA, which we now call ‘scaling’.

The FFA accelerators, were proposed independently in the early 1950s by Ohkawa in Japan [4], Symon *et al.* in the United States [5], and Kolomensky in Russia [6].

Symon *et al.* proposed:

A type of circular accelerator with magnetic guide fields which are constant in time, and which can accommodate stable orbits at all energies from injection to output energy.

This relies on introducing sectors with a reversed magnetic field into a cyclotron-like machine, producing strong focusing throughout the energy range. The field may rise rapidly with radius such that the orbits are relatively compact over a large energy range.

The field is arranged in such a way that the increase in gradient with momentum results in the beam experiencing the same focusing independent of radius. This means that the betatron tunes are constant for all orbits. This constant focusing (or constant betatron tune) is ensured if two conditions are met. First, the field index k must be constant, where we can define k in terms of the bending radius ρ , the vertical magnetic field B_y , and its derivative in the horizontal direction x :

$$k = -\frac{\rho}{B_y} \frac{\partial B_y}{\partial x}. \quad (1)$$

Therefore we require

$$\left. \frac{\partial k}{\partial \rho} \right|_{\theta=\text{const.}} = 0. \quad (2)$$

The second requirement is that the shape of the particle orbits remains constant as the size of the orbits ‘scales’ with energy, such that each higher-energy orbit is a geometrically similar enlargement of the lower-energy orbits as described by the following equation, derived by Kolomensky [7]:

$$\left. \frac{\partial}{\partial \rho} \left(\frac{\rho_0}{\rho} \right) \right|_{\theta=\text{const.}} = 0. \quad (3)$$

^{*} andreas.adelmann@psi.ch

If the field meets these two conditions, the FFA is referred to as being of the ‘scaling’ variety.

To satisfy these requirements, we use a magnetic field that increases with radius. The particular shape of the field is given by the r^k law with a reference radius r_0 , where the field increase is characterised by the field index, k :

$$B_y = B_0 \left(\frac{r}{r_0} \right)^k. \quad (4)$$

For details, illustrations and other types such as the spiral FFA we refer to [8].

In terms of beam dynamics, it is useful to compare the scaling FFA with a synchrotron. Modern synchrotrons employ the principle of alternating-gradient or ‘strong’ focusing [9,10], in which alternating focusing and defocusing magnets lead to much stronger focusing forces in the transverse plane than in constant-gradient weak-focusing synchrotrons. This alternating-gradient focusing is also employed in the FFA. The transverse beam dynamics in the FFA is therefore much the same as in the synchrotron, at least for a single orbit or energy, in the sense that we may discuss beta functions, dispersion, and so forth. The difference is that in this case the field is highly nonlinear and these transverse optics functions may vary with radius.

The Non-scaling FFA

The non-scaling FFA allows the strict scaling laws applied in the original scaling FFA to be relaxed. The idea of violating the strict scaling law of the FFA occurred to Kent Terwilliger and Lawrence W. Jones in the 1950s [11], but such a machine was never pursued. Two of the main disadvantages of the original FFA are the highly nonlinear magnetic field required and the large aperture of the magnets and RF arising from the shift of the orbit with energy, which can be up to the order of 0.5–1.0 m. The non-scaling FFA arose from the question “what if we violate the scaling law?” Or, more specifically, “What if we take a line tangent to the scaling law, such that the field is linear with radius?” This radical idea led to the linear non-scaling FFA and was proposed in the 1990s [12].

Linear non-scaling FFA The linear non-scaling FFA is so called because it uses only up to linear focusing elements, that is, quadrupole and dipole fields. When only quadrupoles and no higher-order multipoles are used for focusing, the beam shifts outward with acceleration because of dispersion and is subject to a reduced level of focusing. This is really like considering a synchrotron where we do not ramp the magnets with time. In the scaling FFA, this is avoided by varying the gradient with the momentum and by making the beam pipe wider to allow for the orbits moving. But in the linear non-scaling FFA the scaling law is ignored, which allows the gradient to be increased and the the dispersion function to be reduced reduce even further to reduce the shift of the orbit with momentum. To achieve this, a linear non-scaling FFA lattice may use normal bending with a defocusing ‘D’ quadrupole and reverse bending

with a focusing ‘F’ quadrupole, and may (or may not, depending on the design) change at high momentum to use the ‘D’ quadrupole for reverse bending and the ‘F’ for normal bending, as described in Ref. [13].

One must then ask what happens to the beam dynamics in such an accelerator. One consequence is that the orbits no longer ‘scale’, so they are no longer geometrically similar at different energies. The orbits can be made much more compact than in the scaling FFA. However, the most dramatic difference is that the betatron tunes are no longer constant with energy. Betatron tunes are usually designed to be kept constant in order to avoid the effects of resonances. In the linear non-scaling FFA, they vary dramatically throughout the acceleration cycle, crossing not just high-order betatron resonances but also integer resonances.

In theory, if the acceleration is fast enough, the beam may be able to cross betatron resonances before they have time to build up, and therefore any amplitude growth effects may be mitigated. How fast this crossing needs to be depends on imperfections and alignment errors in the machine, and clearly necessitates a fast acceleration rate. In fact, the linear non-scaling FFA was proposed in the context of muon acceleration, where very fast acceleration before the muons decay is an absolute requirement. The many questions surrounding the dynamics of such a machine led to the construction of the first non-scaling FFA accelerator, known as EMMA [14].

FORWARD LOOKING PROJECTS IN THE HIGH INTENSITY FRONTIER

At the high intensity frontier, the KURRI collaboration is pursuing an attempt to understand high intensity effects, with dedicated experiments and modelling efforts. The accelerator complex has been operated for ADSR experiments connecting the 100 MeV proton beam line with the research reactor facility. Upgrade plans to higher energies (300 - 500 MeV) includes a new FFA ring which adopts continuous acceleration with fixed frequency (serpentine acceleration). These higher energy beams can also be used for neutron or muon production experiments as well as ADSR studies. On the modelling front, extensive single particle studies, with a variety of codes, have being conducted [15], in order to validate the models. This code comparison, for example, includes tune computation as shown in Figure 1.

Other ambitious projects have been proposed beyond 1 MW of beam power, for example the MERIT proposal of Mori et al. [16] and the innovative design of S. Machida of an *Scaling Fixed-Field Alternating-Gradient Accelerators with Reverse Bend and Spiral Edge Angle* [17]. The latter is actively pursued as a possible replacement of the ISIS facility in the United Kingdom.

SPACE CHARGE MODELS

In circular accelerators, candidates for emittance growth are the half-integer stop-band that can perturb the beam envelope function, the Montague resonance, and the sum resonance induced by the random skew-quadrupole field.

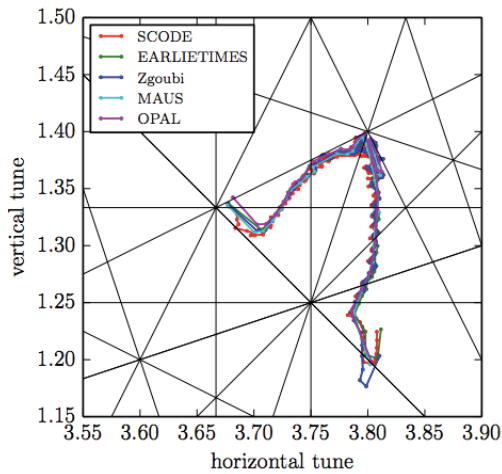


Figure 1: Betatron tune from 11 to 139 MeV of the 150 MeV FFA at KURRI, [15]

In particular, the betatron tunes of non-scaling FFA accelerators may cross many resonances during the beam acceleration. There are a few studies on the effects of resonance crossing in the FFA, which examine only non-systematic resonances, that are in principle correctable [18].

As shown in [19, 20] systematic nonlinear space-charge resonances may cause substantial emittance growth in non-scaling FFA accelerators. To avoid systematic nonlinear space-charge resonances, the phase advance of each non-scaling FFA cell must avoid $\pi/2$ and $\pi/3$.

Lee [19] used 24 FODO cells separated by dipoles. The 4D particle tracking algorithm uses linear maps $M_{1/2}$ for half of the FODO cell, followed by a space-charge kick M_{sc} . The same action is applied at the end of the cell. The M_{sc} is calculated from a Gaussian charge distribution.

Using multi-particle numerical simulations, Lee et al. empirically obtain a minimum tune ramp rate vs the systematic 4th order space-charge resonance strength.

The emittance growth factor, EGF, is defined as the ratio of final emittance to the initial emittance and, can be expressed as

$$EGF = \exp \frac{\lambda 2\pi g^2}{dv/dn}, \quad (5)$$

where g is the stop-band width, dv/dn is the tune-ramp rate, and λ is a constant.

The emittance growth obeys a simple scaling property when the betatron tunes cross the linear half-integer and sum resonances. This limits the betatron tune range and the momentum acceptance for non-scaling FFA accelerators. The EGF is found to obey scaling properties in the linear space-charge tune shift parameter, the tune ramping rate, and stop-band widths of random quadrupole and skew-quadrupole errors.

Basically all theory and single particle models, developed for synchrotrons or cyclotrons and coasting beam analysis

including reduced order space charge models can be applied for FFAs as well.

SPACE CHARGE CODES

COSY INFINITY

The Fast Multipole Method (FMM) is used in COSY INFINITY, that allows the computation of space charge effects of arbitrary and large distributions of particles in an efficient and accurate way. The method relies on an automatic multigrid-based decomposition of charges in near and far regions and the use of high-order differential algebra methods to obtain decompositions of far fields that lead to an error that scales with a high power of the order. Given an ensemble of N particles, the method allows the computation of the self-fields of all particles on each other with a computational expense that scales as $O(N)$. Rigorous estimates are obtained using remainder-enhanced DA methods. All high-order multipoles of the space charge fields are also available, necessarily for the computation of high-order transfer maps and all resulting aberrations. Some FFA modelling is ongoing but not yet published.

ZGOUBI

ZGOUBI is a single particle tracking code that solves the non-linear equation of motion using truncated Taylor expansions of the field and its derivatives up to the 5th order. Recent FFA space-charge works including algorithmic improvements to ZGOUBI is covered in [21], in greater detail.

A frozen space charge model is employed on top of the ZGOUBI model. The assumption is, that the analytic expression of the particle distribution remains the same, so that the analytical solution of the self-induced electric fields does not change. For instance, if we employ a KV beam model, then the problem reduces to calculating the edge radii r_x and r_y of the beam elliptical cross section. Besides, if we cut the magnet into m thin slices, one may assume that the beam radii do not change much within each slice and the error scales as $1/m$.

In Figure 2 the influence of space charge is studied on a coasting beam at 2 different energies.

OPAL

The Lorentz-Force equation is integrated in time using various integration schemes, as described in [22]. Space charge effects are included in the simulation by specifying an appropriate field solver. By default OPAL does not assume any symmetry i.e. is full 3D. The space charge forces are calculated by solving the 3D Poisson equation with various boundary conditions using a standard or integrated Green's function method, or grid based methods, such as a semi-structured finite difference scheme [23] or (in the near future) a full adaptive mesh refinement scheme. The image charge effects of the conducting cathode are also included using a shifted Green's function method, or Robin boundary conditions can be applied in the case of the finite difference

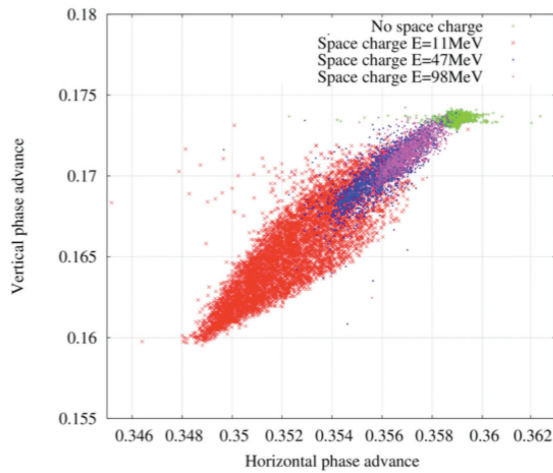


Figure 2: KURRI scaling FFA: $kF = kD = 7.6$, assuming a Gaussian beam distribution equivalent to the KV beam. Space charge tune shift, calculated with a 2D frozen space charge mode, at 11, 47 and 98 MeV [15].

schemes. If more than one Lorentz frame is defined, the total space charge forces are then the summation of contributions from all Lorentz frames, i.e. beams with large energy spread can be modelled.

In order to adequately model FFAs and synchrotrons, a flexible rf-program can be defined by means of a time dependent polynomial, given to each rf-element if necessary.

In order to be able to track through general rings, a *RingDefinition* element was introduced. This new element contains the main characteristics of a generalised ring, such as harmonic number together with the position of initial (ideal) elements and the position of the reference trajectory. This element can be used in combination with *SBEND3D*, misalignments and variable rf-cavity elements to make up a complete and realistic ring covering FFAs and synchrotrons.

First results for the very novel type of FFA [17] is available, as shown in Figure 3.

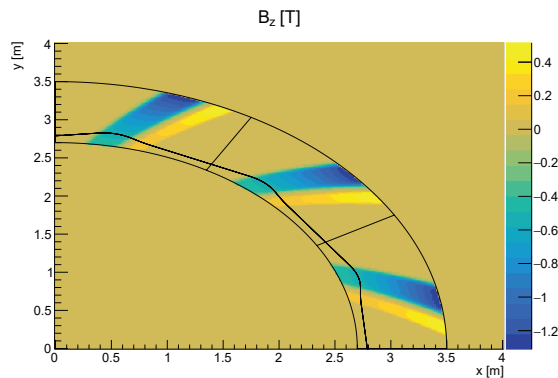


Figure 3: Example of a 12 cell DF spiral type FFA based on [17]. Only 1/4 of the machine is shown.

A last but very interesting feature of OPAL is the ability to search for matched distributions including linear space

charge. This feature allows to search for very well defined initial conditions, such that the second order moments Σ of the distribution obey the condition: $\Sigma^f = \Sigma^i$, where i denotes initial and f final. The condition is found exactly one turn [24].

HIGH INTENSITY CHALLENGES

While scaling laws and reduced order models are of utmost importance in the design of every accelerator, when it comes to high intensity this is not enough. High intensity machines such as SNS or the PSI Cyclotrons are limited by losses mainly caused by halo i.e. particles outside of 4 (5) standard deviations of the particle distribution. Estimation and minimisation of halo is the domain of large scale particle tracking with full 3D space charge. On top of these precise models, the full acceleration cycle has to be covered.

ACKNOWLEDGEMENTS

The authors would like to thank members of the FFA community who have contributed valuable references, images, and discussions. In particular, we would like to thank Dr M. Haj Tahar for comments and material.

REFERENCES

- [1] L. Jones, F. Mills, A. Sessler, K. Symon, and D. Young, *Innovation Was Not Enough*. Singapore: World Scientific, 2009.
- [2] S. L. Sheehy, arXiv:1604.05221v1, 2016
- [3] E. Courant and H. Snyder, *Ann. Phys. (N. Y.)*, vol. 3, no. 1, p. 1, 1958, [http://dx.doi.org/10.1016/0003-4916\(58\)90012-5](http://dx.doi.org/10.1016/0003-4916(58)90012-5)
- [4] T. Ohkawa, *Proc. Annual Meeting of JPS*, 1953.
- [5] K. R. Symon, D. W. Kerst, L. W. Jones, L. J. Laslett, and K. M. Terwilliger, *Phys. Rev.*, vol. 103, no. 6, p. 1837, 1956, <http://dx.doi.org/10.1103/PhysRev.103.1837>
- [6] A. A. Kolomensky, *Journal of Experimental and Theoretical Physics (ZhETF)*, vol. 33, p. 298, 1957.
- [7] A. A. Kolomensky and A. N. Lebedev, *Theory of Cyclic Accelerators Vol. 1*, Amsterdam, Netherlands: North-Holland, 1966.
- [8] S. L. Sheehy *et al.*, arxiv.org/abs/1310.3588
- [9] E. D. Courant, M. S. Livingston, and H. S. Snyder, *Phys. Rev.*, vol. 88, no. 5, p. 1190, 1952, <http://dx.doi.org/10.1103/PhysRev.88.1190>
- [10] E.D. Courant and H.S. Snyder, *Ann. Phys.*, vol. 3, no. 1, pp. 1-48, 1958, [http://dx.doi.org/10.1016/0003-4916\(58\)90012-5](http://dx.doi.org/10.1016/0003-4916(58)90012-5)
- [11] L.W. Jones, “Kent M. Terwilliger, Graduate school at Berkeley and early years at Michigan, 1949–1959”, 1989, *Kent M. Terwilliger Memorial Symposium, Conf. Proc.*, vol. 237, 1991, p. 1.
- [12] C. Johnstone, W. Wan, and A. Garren, “Fixed field circular accelerator designs”, in *Proc. Particle Accelerator Conference*, New York, NY, USA, 1999, p. 3069, <http://dx.doi.org/10.1109/pac.1999.792155>

- Content from this work may be used under the terms of the CC BY 3.0 licence (© 2018). Any distribution of this work must maintain attribution to the author(s), title of the work, publisher, and DOI.
- [13] S. Machida, “Fixed field alternating gradient accelerators”, in *Proc. CERN Accelerator School*, Granada, Spain, 2012, <https://cas.web.cern.ch/cas/Granada-2012/Lectures/GranadaLectures/Machida.pdf>
- [14] S. Machida *et al.*, “Acceleration in the linear non-scaling fixed field alternating gradient accelerator EMMA”, *Nature Physics*, vol. 8, pp. 243–247, Jan. 2012.
- [15] S. L. Sheehy *et al.*, “Progress on simulation of fixed field alternating gradient accelerators”, in *Proc. IPAC’15*, Richmond, VA, USA, May 2015, paper MOPJE077, pp. 495–498.
- [16] Y. Mori *et al.*, in *Proc. 14th Int. Conf. on Muon Spin Rotation, Relaxation and Resonance (SR’17)*, *JPS Conf. Proc.*, vol. 21, p. 011063, 2018, <https://doi.org/10.7566/JPSCP.21.011063>
- [17] S. Machida, *Phys. Rev. Lett.*, vol. 119, p. 064802, 2017. <https://doi.org/10.1103/PhysRevLett.119.064802>
- [18] M. Aiba M and S. Machida, in *Proc. EPAC’04*, p. 2119, 2004, <http://accelconf.web.cern.ch/AccelConf/e04/PAPERS/WEPLT115.PDF>
- [19] S. Y. Lee, *Phys. Rev. Lett.*, vol. 97, no. 10, p. 104801, 2006. 10.1103/PhysRevLett.97.104801
- [20] S. Y. Lee *et al.*, *New Journal of Physics*, vol. 8, p. 11, 2006.
- [21] Malek Haj Tahar, “High power ring methods and accelerator driven subcritical reactor application”, Université Grenoble Alpes, 2017, <https://tel.archives-ouvertes.fr/tel-01611525>
- [22] A. Adelman *et al.*, “The OPAL (Object Oriented Parallel Accelerator Library) Framework”, Paul Scherrer Institut, Villigen, Switzerland, Technical Rep. PSI-PR-08-02, 2008-2018, <https://gitlab.psi.ch/OPAL/src/wikis/home>
- [23] A. Adelman *et al.*, *J. Comp. Phys.*, vol. 229, no. 12, p. 4554, 2010.
- [24] M. Frey, A. Adelman, “Matched Distributions with Linear and Non-Linear Space Charge”, presented at the 21st Int. Conf. on Cyclotrons and their Applications (Cyclotrons’16), Zurich, Switzerland, 2016, paper THC02.

BEAM INSTABILITIES AFTER INJECTION TO THE LHC

H. Timko*, T. Argyropoulos, I. Karpov, E. Shaposhnikova, CERN, Geneva, Switzerland

Abstract

Long-lasting phase oscillations have been observed at injection into the LHC since its first start-up with beam. These oscillations, however, were not leading to noticeable losses or blow-up in operation, and were therefore not studied in detail. In 2017, dedicated measurements with high-intensity bunches revealed that oscillations can lead to losses even slightly below the baseline intensity for the high-luminosity upgrade of the LHC. For the first time, high-resolution bunch profile acquisitions were triggered directly at injection and the formation of large-amplitude non-rigid dipole oscillations was observed on a turn-by-turn basis. First simulations can reproduce this instability via bunch filamentation that takes place after injection, depending on the mismatch between the bunch and bucket size in momentum at injection.

INTRODUCTION

Long-lasting injection oscillations have been observed in the LHC since its very first start-up with beam [1]. At the beam intensities used so far, however, these oscillations did not have any harmful effect on beam quality or luminosity, and were thus not studied in more detail in the past.

In measurements last year [2], oscillations continuing after injection were observed to lead to beam losses on flat bottom, for single bunches with intensities below the HL-LHC target of 2.3×10^{11} ppb [3] at LHC injection.

In Run 1 (2010-2012), and the present Run 2 (2015-2018), the 400 MHz RF injection voltage used in the LHC was 6 MV, with the 200 MHz RF extraction voltage in the SPS being 7 MV plus 1 MV at 800 MHz. In order to minimise injection losses, taking into account injection errors in phase and energy, the injection voltage was chosen to be much larger than the ‘matched’ voltage that is around 2 MV. Throughout Run 3 (2021-2023), a gradual increase of the beam intensity towards the HL-LHC target value is to be expected both in the injectors and the LHC. After the upgrade of the SPS RF system, an extraction voltage of 10 MV can be used, at least for increased intensities, which calls for an LHC injection voltage of 8.6 MV in order to keep the same bucket-height-to-momentum-spread ratio. The increased voltage, together with the doubled intensity from 1.15×10^{11} ppb to 2.3×10^{11} ppb by the time of the HL-LHC era (starting in 2026), results in a power consumption of the LHC RF system which will be close to its limit of 300 kW/klystron [4], should the present baseline of the half-detuning beam-loading compensation scheme be used [3, 5].

A reduced injection voltage is therefore desirable to reduce the power consumption; this would also reduce the mismatch of the bucket height and the momentum spread of the bunch, and thus improve beam stability. On the other hand, an

increased voltage is preferable to limit the injection losses that have to be on a per mil level in the LHC to be below the dump threshold [6, 7].

Another concern for the future is the impact of flat-bottom oscillations on the controlled emittance blow-up during the ramp, where RF phase noise is injected through a feedback loop monitoring the bunch length. The blow-up itself is expected to be more difficult to control with increased intensity [8], and the flat-bottom oscillations have been observed to survive the ramp in some cases [9]. The LHC cannot be operated without the controlled emittance blow-up [10], as otherwise the bunches would cross the threshold of loss of Landau damping during the ramp and blow up violently, in an uncontrolled way.

The losses due to injection oscillations, the RF power consumption, and the stability of the controlled emittance blow-up in the ramp have thus to be treated as connected problems for future high intensities. In this paper, we will focus on the main considerations and observations related to long-lasting injection oscillations.

EXPERIMENTAL OBSERVATIONS

During measurements with a full machine at the nominal intensity of about 1.1×10^{11} ppb in 2016 [9], it was observed that the batches injected later into the machine had stronger dipole oscillations at the end of the flat bottom, and that the amplitude of oscillations had the same pattern along the ring at arrival to flat top as it had before the start of the ramp, see Fig. 1. In other words, the flat bottom oscillations astonishingly survived the 13-million-turn ramp, where RF phase noise is injected all along, in order to blow up the bunch emittance by a factor six.

Dedicated measurements of flat-bottom oscillations were then performed in 2017 [2] with many single bunches in the machine, probing the intensity range of $(0.8-2.2) \times 10^{11}$ ppb. One of the main observations was that a bunch with an initial intensity of 1.9×10^{11} ppb, which is below the HL-LHC target, became unstable after injection and has lost more than 4 % of its intensity over 20 minutes at flat bottom, see Fig. 2. At the same time, the bunch length was increasing by about 10 % over this period, while the natural bunch lengthening due to IBS is only around 3 %.

The emittance growth and particle losses are a result of non-rigid dipole oscillations, as can be seen on the bunch profiles in Fig. 3. Due to the non-rigid nature of these oscillations, many frequently used signals, such as the RF stable phase measurement, which gives the 400 MHz component of the bunch phase w.r.t. the RF phase, show a misleadingly small oscillation; in the case of Fig. 3, roughly 10° peak to peak. In reality, the peak of the bunch profile is oscillating much more violently, 50° peak to peak in our example.

* helga.timko@cern.ch

Content from this work may be used under the terms of the CC BY 3.0 licence (© 2018). Any distribution of this work must maintain attribution to the author(s), title of the work, publisher, and DOI.

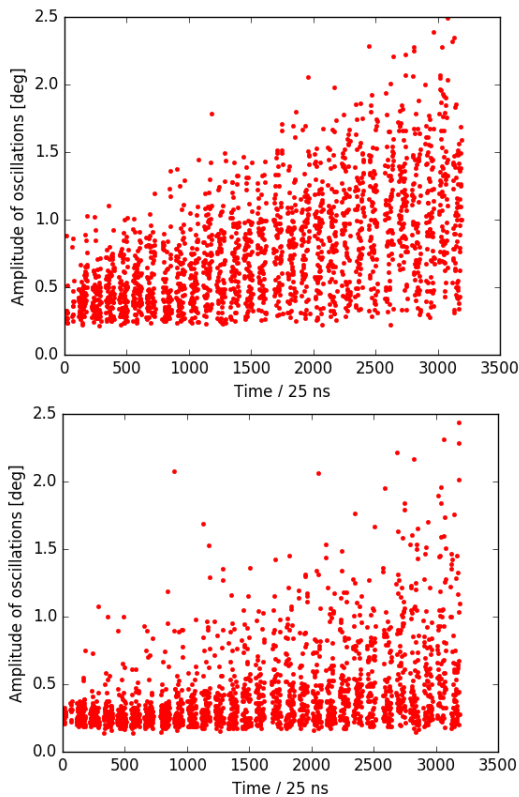


Figure 1: Amplitude of dipole oscillations at the end of flat bottom (top) and at arrival to flat top (bottom).

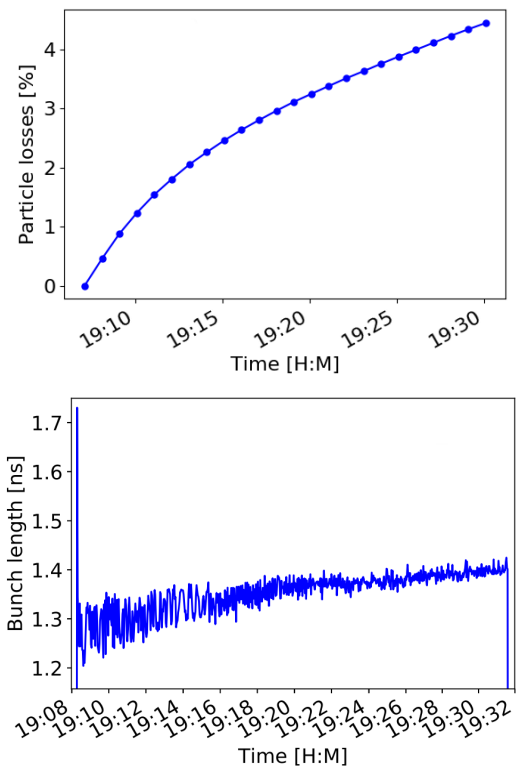


Figure 2: Evolution of particle losses (top) and bunch length (bottom) of an oscillating, unstable bunch.

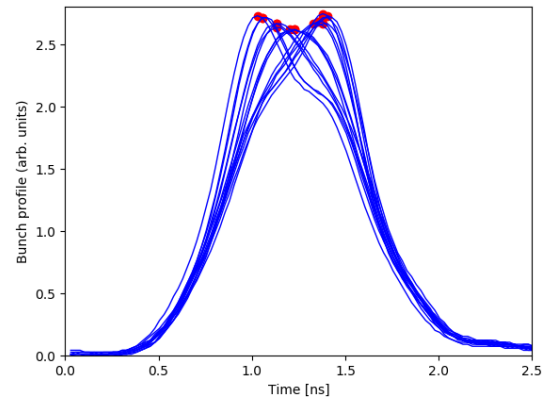


Figure 3: Non-rigid dipole oscillations seen on the bunch profile about one minute after injection.

INSTABILITY FORMATION

In simulations with the CERN BLoND code [11], the formation of the instability could be reproduced whenever the mismatch between the bucket height and the momentum spread of the injected bunch was large enough, i.e. the bunches have to be relatively short at injection or the RF voltage relatively high. In addition, intensity effects due to the LHC inductive impedance impact as well the threshold of these instabilities, which is why in measurements the losses were seen for high-intensity bunches with nominal bunch length and at nominal injection voltage, whereas during operation with nominal intensities no losses are observed.

A realistic injection phase error of 25° was assumed in the simulations, which represents the typical phase and energy errors translated into a pure phase error. Under the present operational conditions, that is, a bunch intensity of about 1.15×10^{11} ppb, an injection voltage of 6 MV, and a first-turn bunch length of about 1.6 ns, the bunch would simply filament and the oscillations would eventually be damped. This is reproduced also in simulations; the oscillations are damped to the noise level after about 350,000 turns, which is about 1,750 synchrotron periods.

In simulations with 1.2×10^{11} ppb using the present impedance model of the LHC at 450 GeV, and the nominal voltage of 6 MV, it is sufficient to decrease the injected bunch length to 1.5 ns to observe significantly less damping. When decreasing further to 1.4 ns, a growth in the oscillation amplitude of the mean bunch position can be observed. For the nominal bunch length of 1.6 ns, undamped oscillations can be observed over 500,000 turns when increasing the injection voltage to 8 MV or, with an even more pronounced oscillation amplitude, to 10 MV.

In an unstable case, see Fig. 4, the bunch is first filamenting in phase space, after which slowly the formation of islands close to the core can be observed. The rotation of these islands in phase space projects to the non-rigid dipole oscillations observed on the bunch profiles. Different regions of the bunch get disconnected, and local loss of Landau damping occurs. As a consequence, the oscillations

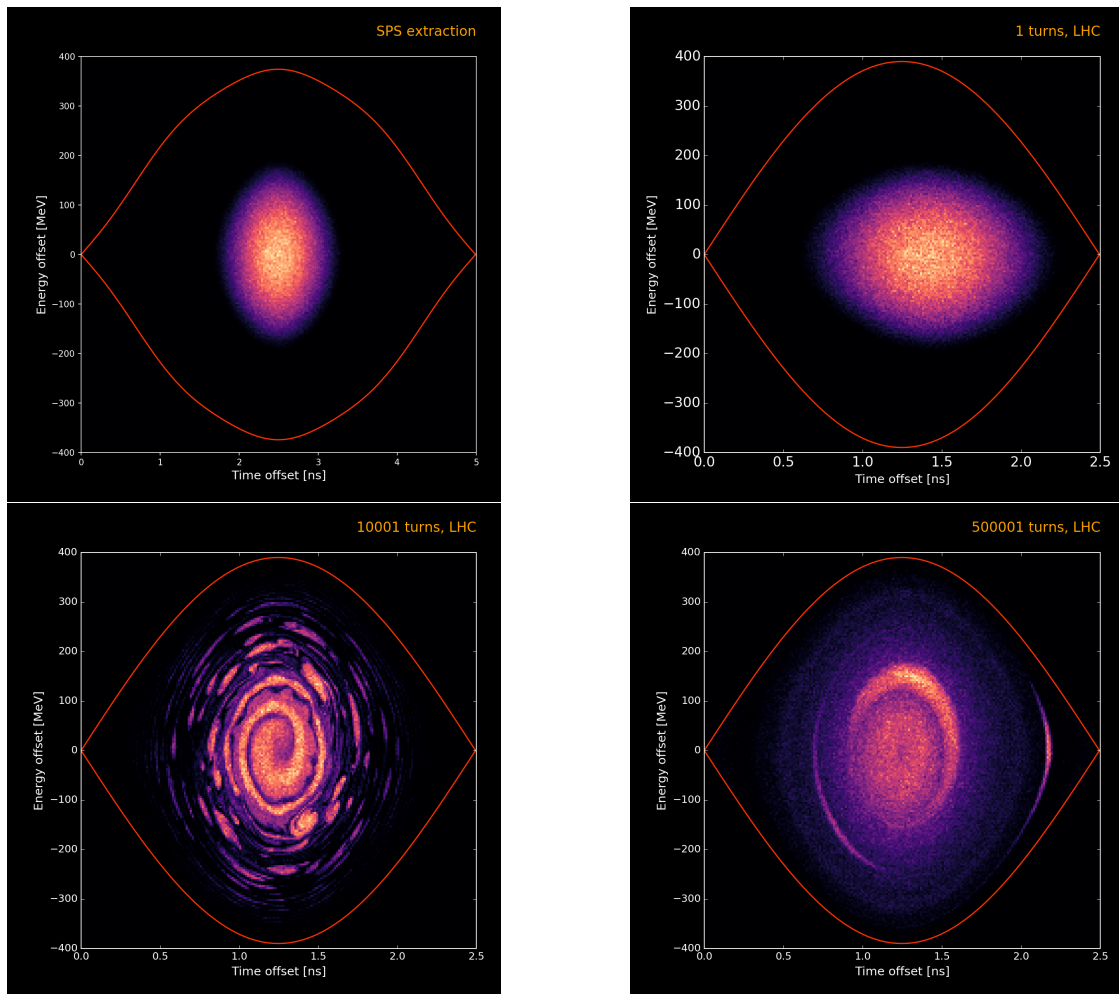


Figure 4: Formation of instability after injection at an intensity of 1.2×10^{11} ppb. The bunch is matched in the SPS double RF bucket (top left). At injection to the LHC with a 25° phase error (top right), the bunch length is 1.4 ns and the RF voltage is 6 MV. First islands form already during the filamentation process (bottom left), resulting in a more pronounced island (bottom right) eventually. A binomial distribution with exponent 1.5 was used.

grow, the bunch length increases, and losses can occur as well.

It should be noted that the beam phase loop is closed during beam operation all the time. However, the feedback loop is acting on the average oscillation amplitude of all the bunches. Injection errors are therefore efficiently damped for the first few injections, but for later injections, the role of the beam phase loop is negligible. This is why in our measurements with single bunches we made sure that the loop is virtually not acting on the bunches and in simulations the loop has not been included at all. In the future, should the external damping of injection oscillations become indispensable, one could use the phase loop with gated phase kicks acting only on the freshly injected bunches.

FIRST SIMULATION SCANS

To avoid the formation of instabilities, a lower injection voltage is thus preferable. On the other hand, as the bunches are arriving from the 200 MHz SPS buckets with phase

and energy injection errors, a higher voltage is desirable to reduce injection losses. First simulation scans have been performed to study the stability and losses as a function of RF voltage and bunch length at injection.

The nominal bunch length for bunches arriving in bunch trains is 1.6 ns at injection; it is difficult for the injectors to produce multi-bunch trains with a shorter bunch length. For a bunch length of 1.6 ns produced with 7 MV at 200 MHz and 1 MV at 800 MHz in the SPS, a more or less matched voltage in the LHC would be around 2 MV. The operationally used injection voltage of 6 MV is, as mentioned earlier, highly unmatched in order to minimise capture losses.

The absolute numbers of the losses heavily depend on the bunch distribution assumed. In particular, losses depend a lot on the tail population, which is difficult to measure experimentally. An accurate way to model the bunch distribution in simulation would be to track the bunches from the controlled emittance blow-up in the SPS, which occurs towards the end of the SPS acceleration ramp, till extraction.

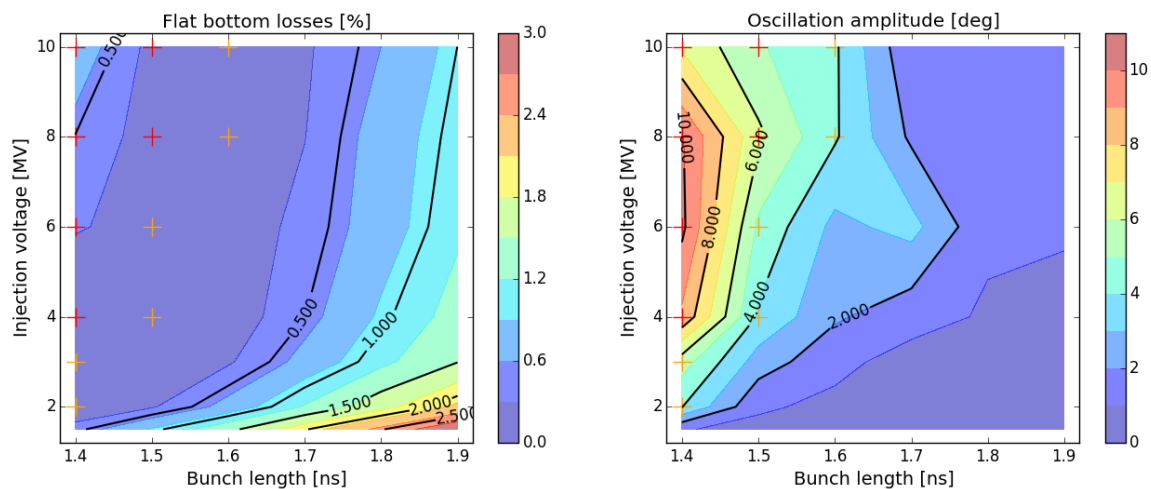


Figure 5: Flat bottom losses (left) and peak-to-peak oscillation amplitude (right) as a function of bunch length and RF voltage at injection. Binomial bunch distribution with exponent 1.5. Undamped and unstable cases are marked with orange and red crosses, respectively.

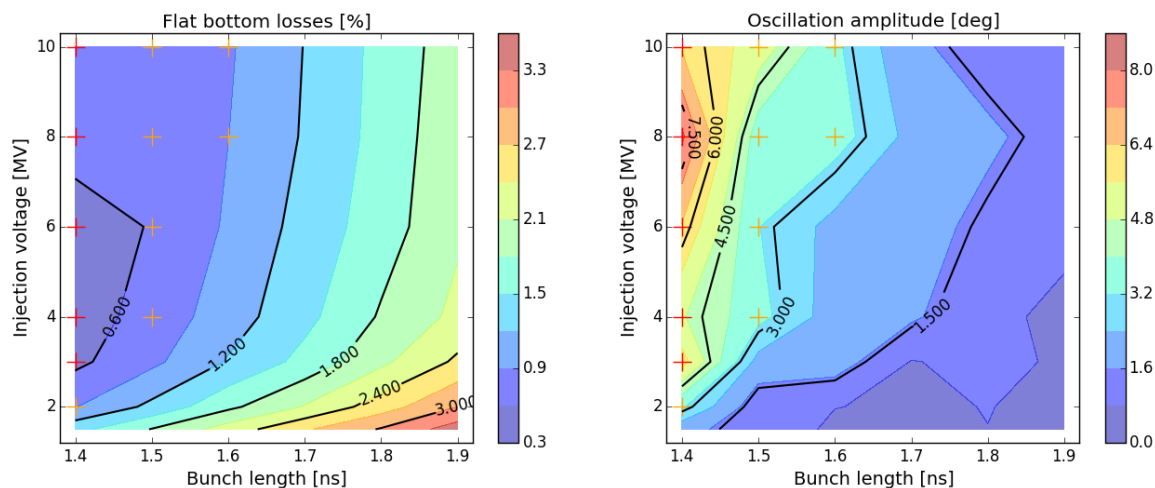


Figure 6: Flat bottom losses (left) and peak-to-peak oscillation amplitude (right) as a function of bunch length and RF voltage at injection. Binomial bunch distribution with exponent 5. Undamped and unstable cases are marked with orange and red crosses, respectively.

During the emittance blow-up, halo particles are driven up to the separatrix, while at extraction the bucket is expected not to be entirely full.

For the preliminary simulation scans presented here, two different bunch distributions have been assumed. First, a binomial distribution function of the action with the exponent 1.5, which is the best fit to (the core of) measured bunch profiles in the LHC [12]. The results are shown in Fig. 5. In a second scan, the exponent 5 was used in order to enhance the tails on purpose; see Fig. 6.

For each combination of injection voltage and bunch length, a single bunch was matched in the SPS double-harmonic RF bucket with intensity effects with the chosen bunch distribution to obtain the desired bunch length. After injection into the LHC with 25° phase error, the bunch

was tracked for 500,000 turns corresponding to about 2500 synchrotron periods.

To determine the overall losses due to long-lasting oscillations (left-hand sides of Figs. 5 and 6), the particles outside the separatrix were counted every 10 turns. First-turn capture losses were ignored. The flat-bottom losses start to take off typically after the oscillations become strong enough; for the case presented in Fig. 4, this happens after roughly 220,000 turns, see Fig. 7. The evolution strongly depends also on the blow-up that occurs in parallel; if violent losses and blow-up occur initially, the slope of the losses becomes less steep afterwards.

The peak-to-peak oscillation amplitude of the mean position of the bunch is shown on the right-hand sides of Figs. 5 and 6. In order to disentangle from the initial oscillations due

Content from this work may be used under the terms of the CC BY 3.0 licence (© 2018). Any distribution of this work must maintain attribution to the author(s), title of the work, publisher, and DOI.

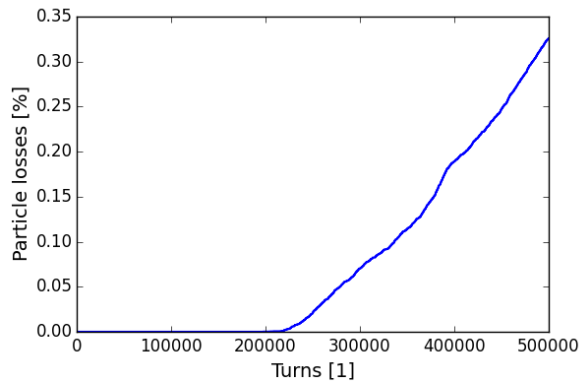


Figure 7: Flat-bottom losses corresponding to the case presented in Fig. 4.

to the phase error at injection, the maximum peak-to-peak amplitude was observed after 250,000 turns. Cases where the oscillation amplitude was undamped after injection till the end of the simulation are marked with orange crosses. Unstable cases where the oscillation amplitude was growing after 250,000 turns are marked with red crosses.

Comparing the two different bunch distributions used, it can be seen that the large tails provide somewhat more damping in this case and reduce the oscillations by about 25 %. On the other hand, the loss levels increase. Globally, however, the overall tendencies of losses and oscillation amplitudes are very similar in both cases.

If we look for a compromise between not-too-high losses and a reasonable stability margin, the regions around 0.5 % losses in Fig. 5 and 1.2 % losses in Fig. 6 are promising. For the nominal beam with 1.6 ns initial bunch length, there seems to be enough margin in terms of losses in order to reduce the injection voltage to 4 MV. This would reduce also the RF power consumption and be beneficial for beam stability. Measurements are scheduled for the near future to verify the optimum injection voltage experimentally.

CONCLUSIONS

Bunch oscillations after injection to the LHC can persist and develop into an instability, depending on the bunch intensity, the injection errors, and the mismatch between the bucket height at injection and the momentum spread of the arriving bunch. In phase space, the formation of islands close to the bunch core during the filamentation process is characteristic for the instability. These islands lead to non-rigid dipole oscillations, as seen on the bunch profiles. The measured peak-to-peak oscillation amplitudes of the profile can be as high as 50° . Under certain circumstances, the oscillations can even survive the controlled emittance blow-up during the ramp and persist till flat top.

The presently used 6 MV injection voltage, although unmatched, was used to reduce capture losses from large bunches arriving with injection errors. The formation of instabilities can be avoided by somewhat decreasing the RF voltage at injection. This will reduce the mismatch at injection and stabilise the beam. A decreased voltage is also

advantageous for reducing the power consumption of the RF system, which will be pushed close or beyond its limits with future high intensities otherwise. First simulations show regions of a good compromise between acceptable losses and oscillations; measurements will be performed soon to confirm the optimum injection voltage.

The injection oscillations can furthermore be damped by the beam phase loop. Presently, the phase loop feedback is acting on the average of all circulating bunches, and as a consequence, is less and less efficient with every new batch injected. In addition, already circulating bunches get kicked with the injection of new bunches. To avoid this, a batch-by-batch operation mode could be implemented, where the phase loop could be ‘masked’ to only act on the freshly injected beam for a while.

REFERENCES

- [1] P. Baudrengnien *et al.*, “Longitudinal Oscillations with Batch Injection in the LHC”, CERN, Geneva, Switzerland, Rep. AT5-Note-2011-031-MD, 2011.
- [2] I. Karpov *et al.*, “LHC MD 2042: Persistent Injection Oscillations”, CERN, Geneva, Switzerland, Rep. CERN-ACC-NOTE-2018-0018, 2018.
- [3] G. Apollinari *et al.*, “High-Luminosity Large Hadron Collider (HL-LHC): Preliminary Design Report”, CERN, Geneva, Switzerland, Rep. CERN-2015-005, 2015.
- [4] H. Timko, P. Baudrengnien, R. Calaga, and E. Shaposhnikova, “The Main RF System and its Implications for HL-LHC”, presented at 7th HL-LHC Collaboration meeting, Madrid, Spain, Nov. 2017, <https://indico.cern.ch/event/647714/contributions/2646158/>
- [5] T. Mastoridis, P. Baudrengnien, and J. Molendijk, “Cavity voltage phase modulation to reduce the high-luminosity Large Hadron Collider rf power requirements”, *Phys. Rev. Accel. Beams*, vol. 20, p. 101003, 2017.
- [6] P. Baudrengnien, “The LHC RF: Operation 2010 and Plans for 2011”, *Proc. 2nd Evian Workshop on LHC Beam Operation*, Evian-les-bains, France, 2010, pp. 41-48.
- [7] G. Guaglio, “Reliability of the Beam Loss Monitors System for the Large Hadron Collider at CERN”, PhD Thesis, No. PCCF-T-0509, Université Clermont Ferrand II – Blaise Pascal, France, 2005.
- [8] H. Timko *et al.*, “LHC MD 1087: Controlled Longitudinal Emittance Blow-up with Short Bunches”, CERN, Geneva, Switzerland, Rep. CERN-ACC-NOTE-2017-0018, 2017.
- [9] J. E. Müller, E. Shaposhnikova, and H. Timko, “LHC MD 652: Coupled-Bunch Instability with Smaller Emittance (all HOMs)”, CERN, Geneva, Switzerland, Rep. CERN-ACC-NOTE-2017-0017, 2017.
- [10] O. Brüning *et al.*, “LHC Design Report”, CERN, Geneva, Switzerland, Rep. CERN-2004-003-V-1, 2004.
- [11] The Beam Longitudinal Dynamics simulation suite BLonD, <http://blond.web.cern.ch>
- [12] J. Estaban Müller, “Longitudinal intensity effects in the CERN Large Hadron Collider”, PhD Thesis, No. 7077, École polytechnique fédérale de Lausanne, Switzerland, 2016.

OPTICAL STOCHASTIC COOLING EXPERIMENT AT THE FERMILAB IOTA RING*

J. D. Jarvis[†], V. Lebedev, H. Piekarz, A. L. Romanov, J. Ruan,
 Fermi National Accelerator Laboratory, Batavia, IL 60510-5011, USA
 M. B. Andorf, P. Piot¹, Northern Illinois University, Dekalb, IL 60115, USA
¹also at Fermi National Accelerator Laboratory, Batavia, IL 60510-5011, USA

Abstract

Beam cooling enables an increase of peak and average luminosities and significantly expands the discovery potential of colliders; therefore, it is an indispensable component of any modern design. Optical Stochastic Cooling (OSC) is a high-bandwidth, beam-cooling technique that will advance the present state-of-the-art, stochastic cooling rate by more than three orders of magnitude. It is an enabling technology for next-generation, discovery-science machines at the energy and intensity frontiers including hadron and electron-ion colliders. This paper presents the status of our experimental effort to demonstrate OSC at the Integrable Optics Test Accelerator (IOTA) ring, a testbed for advanced beam-physics concepts and technologies that is currently being commissioned at Fermilab. Our recent efforts are centered on the development of an integrated design that is prepared for final engineering and fabrication. The paper also presents a comparison of theoretical calculations and numerical simulations of the pickup-undulator radiation and its interaction with electrons in the kicker-undulator.

INTRODUCTION

Beam cooling compresses a beam's phase space by damping incoherent particle motions. It is a principal means of increasing achievable luminosity, preventing emittance growth due to intra-beam scattering (IBS) and other effects, reducing beam losses and improving energy resolution; therefore, it is an indispensable component of any modern collider design. Beam cooling is an expansive area of research with many notable subfields, e.g. radiation, ionization, electron and stochastic cooling.

Van der Meer's Nobel-winning Stochastic Cooling (SC) was vital in the accumulation of antiprotons and in the delivery of the beam quality required for the discovery of the W and Z bosons [1,2]. In SC and its variants, signals from electromagnetic pickups, operating in the microwave regime with a bandwidth on the order of several GHz, are used in negative feedback systems to reduce the phase-space volume of a circulating beam in all degrees of freedom [1-6].

If every beam particle's deviation from the reference particle could be sensed and corrected individually, then the total error in the beam could be removed in a single

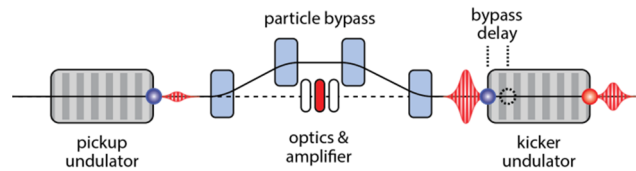


Figure 1: Simplified conceptual schematic of an optical stochastic cooling section. A wavepacket produced in the pickup subsequently passes through transport optics and an optical amplifier. In the kicker undulator, each particle receives an energy kick proportional to its momentum deviation.

pass through a SC system. In practice, the spectral bandwidth, W , of the feedback system (pickup, amplifier, kicker) sets a Fourier-limited temporal response $T \sim 1/2W$, which is very large compared to the intra-particle spacing and limits the achievable cooling rate. With a limited bandwidth on the order of several GHz, conventional SC systems become ineffective for the high-density beams of modern colliders. The realization of high-bandwidth/fast cooling techniques, and their translation into operational systems, is a technological imperative for many future colliders.

OPTICAL STOCHASTIC COOLING

One possible solution is the extension of the SC principle to optical frequencies ($\sim 10^{14}$ Hz). This would increase cooling rates by three to four orders of magnitude, and would be an extraordinary advance in beam-cooling technology. OSC was first suggested in the early 1990s by Zolotarev, Zholents and Mikhailichenko, and replaced the microwave hardware of SC with optical analogs, such as wigglers and optical amplifiers [7,8]. A number of variations on the original OSC concept have been proposed, and its use has been suggested for hadron, heavy-ion, electron-ion and muon colliders and also controlling emittance growth in electron storage rings [9-15]. At present, a proof-of-principle demonstration with protons or heavy ions involves prohibitive costs, risks and technological challenges [16]; however, demonstration of OSC with medium-energy electrons is a cost-effective alternative that enables detailed study of the beam-cooling physics, optical systems and diagnostics [17-20].

In the transit-time method of OSC, shown schematically in Fig. 1 and upon which this program is based, a particle's deviations from the reference particle are encoded in its arrival time at the kicker system by a magnetic bypass [8]. The particle (an electron for purposes of discussion) first emits a radiation packet while traversing a pickup

* Fermi National Accelerator Laboratory is operated by Fermi Research Alliance, LLC under Contract No. DE-AC02-07CH11359 with the United States Department of Energy.

[†] jjjarvis@fnal.gov

undulator (PU), the wavelength of which is given by the usual (planar) undulator relation

$$\lambda_r = \frac{\lambda_u}{2n\gamma^2} \left(1 + \frac{K^2}{2} + \gamma^2 \theta^2 \right), \quad (1)$$

where λ_u is the undulator period, n is the harmonic number, K is the undulator-strength parameter and θ is the observation angle relative to the beam axis.

The radiation packet is transported with (active) or without (passive) amplification to a kicker undulator where it interacts with the same electron. Between the pickup and kicker, the electron traverses a bypass (chicane), which is designed such that a reference particle at the design energy will arrive at the kicker undulator simultaneously with the head of its radiation packet. The energy of the reference particle is unchanged by its interaction with the radiation field in the kicker; however, in the linear approximation, all other particles will have a delay that is proportional to their momentum deviation, $\Delta p/p$, and will receive corresponding corrective kicks towards the design energy.

In this arrangement, the magnitude of the momentum kick received by the particle in a single pass through the cooling system is approximately

$$\frac{\delta p}{p} = -\kappa \sin(k_0 s) \quad (2)$$

where $k_0 = 2\pi/\lambda_r$ and s is the longitudinal displacement of the particle relative to the reference particle after traversing the bypass [16]. The gain parameter κ is given by $\kappa = \sqrt{G} \Delta E / cp$, where G is the power gain of the optical amplifier and ΔE is the maximum energy exchange for a particle in the kicker. The form of ΔE can be estimated analytically by expressing the electric field via the Liénerd-Wiechert relation, and a modified Kirchhoff formula, and subsequently integrating against the motion of a particle phased for maximum kick. This procedure yields

$$\Delta E \approx \frac{\pi q e^2 N_u}{3\epsilon_0 \lambda_r} K^2 \left(1 + \frac{K^2}{2} \right) f_T(K, \gamma \theta_m) \quad (3)$$

as the maximum energy exchange in the kicker without optical amplification. In equation (6), N_u is the number of periods per undulator, and $0 < f_T < 1$ is a correction factor that accounts for longitudinal motions due to large values of K (>1) in the kicker and the finite collection angle of the light optics, θ_m . It is interesting to note that for small K and $f_T = 1$, Equation (6) is identical to twice the energy radiated, in the fundamental band, in a single undulator [21]. This is the amount of radiation detected downstream if the optical delay is detuned by more than the duration of the wavepacket; sweeping the delay through the wavepacket will produce coherent oscillations in the detected radiation of amplitude $\sim \sqrt{G} \Delta E$ [22,23]. This is

an important diagnostic for temporal synchronization of the light and particle optics.

Cooling Rates and Ranges

The most critical parameters in OSC physics are the cooling rates and ranges for the longitudinal and transverse phase planes. In the following analysis we use the usual generalized curvilinear definitions for coordinates and derivatives, and we closely follow the analysis of reference [16]. In the interest of brevity, we enumerate only the salient steps and results. In the linear approximation, a given electron is displaced longitudinally from the reference particle by

$$s = M_{51}x + M_{52}x' + \left(M_{56} - \frac{L_{pk}}{\gamma^2} \right) \frac{\Delta p}{p}, \quad (4)$$

where (x, x') is the transverse position and angle of the particle, L_{pk} is the pickup to kicker distance and M_{51} , M_{52} , M_{56} are the elements of the linear transfer matrix from the exit of the pickup to the entrance of the kicker. The transverse coordinates can be decomposed as betatron and dispersive components as $x = x_\beta + D \Delta p/p$ and $x' = x'_\beta + D' \Delta p/p$, where D and D' are the dispersion and its derivative along the design orbit at the exit of the pickup. Neglecting betatron oscillations, we have

$$s = \left(M_{51}D + M_{52}D' + M_{56} - \frac{L_{pk}}{\gamma^2} \right) \frac{\Delta p}{p} = S_{pk} \frac{\Delta p}{p}, \quad (5)$$

and so for small s , the approximate cooling rate for the longitudinal emittance is then

$$\lambda_s = f_0 \kappa k_0 S_{pk}, \quad (6)$$

where f_0 is the revolution frequency in the ring. Redistribution of the cooling between phase planes does not change the sum of cooling rates [16,24]; it can be shown that the horizontal cooling rate is then

$$\lambda_x = f_0 \kappa k_0 \left(M_{56} - S_{pk} - \frac{L_{pk}}{\gamma^2} \right). \quad (7)$$

Neglecting L_{pk}/γ^2 , which will be small in our case ($<10^{-4}$), we see that the ratio of horizontal and longitudinal cooling rates for a given delay in the chicane is determined entirely by the dispersion and its derivative at the exit of the pickup undulator as

$$\frac{\lambda_x}{\lambda_s} = \frac{M_{56}}{S_{pk}} - 1. \quad (8)$$

Coupling between the x and y dimensions can be provided in the ring, outside of the cooling section, thus providing cooling in all degrees of freedom.

In the case of a particle undergoing betatron oscillations, we can parameterize the argument of equation (5) in terms of normalized betatron and synchrotron amplitudes and phases, (a_x, ψ_x) and (a_p, ψ_p) respectively, as

$$\frac{\delta p}{p} = -\kappa \sin(a_x \sin \psi_x + a_p \sin \psi_p). \quad (9)$$

From equations (5) and (8), we find that the normalized synchrotron amplitude is

$$a_p = -k_0(M_{51}D + M_{52}D' + M_{56}) \left(\frac{\Delta p}{p}\right)_m, \quad (10)$$

where $(\Delta p/p)_m$ is the amplitude of the synchrotron oscillations. Writing the particle coordinates in the action-angle form and invoking the Courant-Snyder invariant, $\tilde{\epsilon}$, and the other Twiss parameters (β, γ, α) we arrive at

$$a_x = -k_0 \sqrt{\tilde{\epsilon}(\beta M_{51}^2 - 2\alpha M_{51}M_{52} + (1 + \alpha^2)M_{52}^2/\beta)}, \quad (11)$$

By averaging the kick over betatron and synchrotron oscillations (over ψ_x and ψ_p), we can determine an average reduction in cooling force. It is given by

$$\begin{bmatrix} F_x \\ F_s \end{bmatrix} = \begin{bmatrix} \lambda_x(a_x, a_p)/\lambda_x \\ \lambda_s(a_x, a_p)/\lambda_s \end{bmatrix} = 2 \cos(k_0 s_0) \begin{bmatrix} J_0(a_p)J_1(a_x)/a_x \\ J_0(a_x)J_1(a_p)/a_p \end{bmatrix}, \quad (12)$$

where J_0 and J_1 are Bessel functions of the first kind, and the $\cos(k_0 s_0)$ term provides for a timing offset between the reference particle ($a_x, a_p = 0$) and its radiation [16,23]. For the reference particle, the bypass will be tuned such that $k_0 s_0 = 0$; however, changes of this delay will produce coherent oscillations in the observed undulator-radiation power, allowing us to determine the optimum setting for cooling. Fig. 2 illustrates the implications of equation (15) for the phase-space dynamics of the particles. The zeros of the Bessel functions comprise various fixed points that establish the cooling ranges of the OSC process. In effect, this normalized (a_x, a_p) space has many cooling zones and stable points to which the particles will be driven. In the ideal case, all beam particles should lie within the cooling zone established by the first zero of J_0 , $\mu_I = 2.405$, and will be cooled in both planes until reaching equilibrium with quantum excitation by SR. In this case, the longitudinal and transverse cooling ranges, n_{σ_p} and n_{σ_x} , are determined by simply solving equations (13) and (14) for $(\Delta p/p)_m$ and $\sqrt{\tilde{\epsilon}}$, with $(a_x, a_p) = \mu_I$, and then normalizing to the beam's rms values, σ_p and $\sqrt{\epsilon_x}$.

We note that when nonlinear path lengthening is included in Equation (7), this cooling surface will be modified for large betatron and synchrotron amplitudes. Note also that the strength and polarity of the heating and cooling zones in Fig. 3 can be modified by changing $k_0 s_0$ [23], and tomographic methods may, in principle, be used to observe the interesting phase space structure that results from equation (15) [25,26].

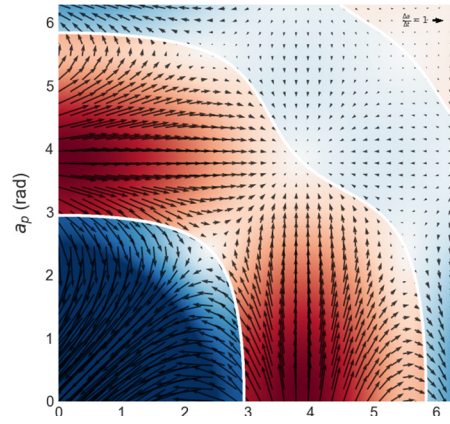


Figure 2: Dependence of the net cooling force on normalized betatron and synchrotron amplitudes in the linear approximation for $k_0 s_0 = 0$. Vector field shows direction of the net cooling/heating.

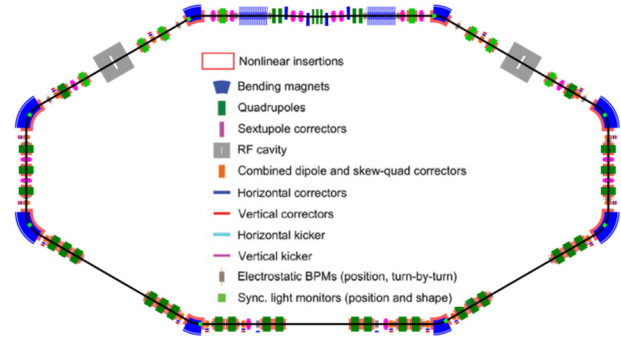


Figure 3: Schematic diagram of the Integrable Optics Test Accelerator ring at FNAL. The base configuration shown here is for the demonstration of nonlinear integrable optics; in OSC configuration, the lower straight is replaced with the insertion shown in Fig. 4.

OSC AT THE IOTA RING

The Integrable Optics Test Accelerator (IOTA) ring, currently being commissioned at the Fermi National Accelerator Laboratory (FNAL), is a unique test facility for advanced beam-physics concepts and technologies [27]. IOTA's scientific program targets fundamental advancements in beam optics, beam cooling and space-charge compensation, and a robust capability to demonstrate OSC physics was used as a key requirement in the ring's design. The ring is shown schematically in its OSC configuration in Fig. 3.

The IOTA OSC demonstration is unique in that the OSC-damping rate will dominate the ring's synchrotron-radiation damping by a factor of ~ 60 in the absence of any optical amplification. This means that fundamental OSC physics can be thoroughly explored, early in the experimental program and decoupled from any amplifier development and integration. This is a major advantage relative to other machines where a demonstration of OSC with electrons has been proposed [17-20].

Electron Optics

The IOTA OSC experiment, shown schematically in Fig. 4, will occupy the straight section at the top of Fig. 3. The four dipoles in the electron bypass (B1-B4) have parallel edges to eliminate geometric focusing; in this case $M_{56} = S_{pk}$, and by equation (11), the coupling of the longitudinal and transverse OSC rates vanishes [16]. To introduce p - x coupling we place a defocusing quadrupole (QX) of strength $\Phi = 1/F$ in the center of the bypass. In this configuration, the cooling ratio is approximately $\lambda_x/\lambda_s \approx \Phi D^* h / (2\Delta s - \Phi D^* h)$, and for $\lambda_x/\lambda_s = 1$ the cooling ranges (corresponding to $(a_x, a_p) = \mu_l$) are approximately

$$n_{os} \approx \frac{\mu_l}{k_0 \sigma_p \Delta s} \quad n_{ox} \approx \frac{\mu_l}{2k_0 \Delta s} \sqrt{\frac{\mathcal{H}^*}{\epsilon_x}}, \quad (13)$$

where Δs is the optical delay for the focusing and amplification systems, h is the horizontal trajectory offset in the chicane, D^* and $\mathcal{H}^* = D^{*2}/\beta^*$ are the dispersion and dispersion invariant (assuming vanishing derivatives for the dispersion and beta-functions in the chicane center), and an asterisk denotes that the value is taken in the center of the chicane. Note that for equal cooling rates, $\Phi D^* h = \Delta s$. While operating with shorter wavelength and longer delay increases the cooling rate, it will result in a corresponding reduction in the effective cooling range.

As discussed in [16], the equations in (16) suggest that for a fixed wavelength and delay, we should optimize the optical lattice to maximize the dispersion invariant in the cooling section and minimize the emittance. The equilibrium emittance grows with the average dispersion invariant in the ring due to quantum excitation, so we should increase the invariant in the cooling section and then reduce it as quickly as possible. Note that our low design energy, 100 MeV, also reduces the equilibrium emittance due to quantum excitation and provides correspondingly larger cooling range. For reasonable levels of dispersion, we should then minimize β^* using ‘‘collider-style’’ optics [16]; the quadrupoles (Q1-Q4) on either side of the bypass provide a small waist in the chicane center and a negative-identity mapping between the pickup (U1) and kicker (U2) in the x -plane. Finally, sextupole pairs in the bypass provide chromaticity correction to minimize second-order path lengthening, which would otherwise reduce the achievable cooling ranges [28].

Light Optics

As shown in Fig. 3, there are two configurations for the passive optical system: three-lens and single lens telescopes. Initial designs considered the use of telescopic optics to suppress depth-of-field effects arising from the finite length of the undulators; however, it was discovered that due to slight overfocusing and reduced chromaticity, the maximum achievable kick for a single-lens telescope was nearly identical to that of the three-lens telescope. The single-lens configuration greatly reduces the complexity of the optical system’s design, engineering and operation, and provides for an accelerated timeline with

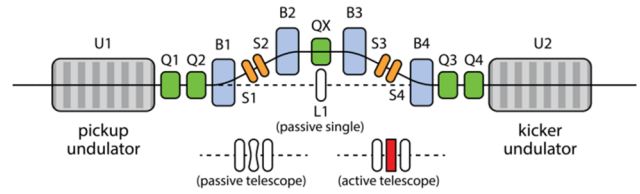


Figure 4: Conceptual schematic of the IOTA OSC insertion with various configurations for the light optics.

Table 1: Design Parameters and Performance Estimates for 0.95- μm and 2.20- μm OSC Configurations in IOTA

Design wavelength, λ_r	0.95 μm	2.20 μm
Number of particles	10^3 - 10^6	
Beam kinetic energy	100 MeV	
Delay in the chicane, Δs	0.648 mm	2.00 mm
Offset in the chicane, h	20.0 mm	35.1 mm
Momentum spread (rms), σ_p	1.00×10^{-4}	1.06×10^{-4}
uncoupled x-emittance (rms); no OSC, e	1.02 nm	2.62 nm
Beta function in chicane center, β^*	0.25 m	0.12 m
Disp. in chicane center, D^*	0.27 m	0.48 m
Disp. invariant in chicane center, \mathcal{A}^*	0.29 m	1.92 m
Undulator period, λ_u	47.77 cm	110.6 cm
Number of und. periods, N_u	7	16
On-axis undulator field, B_0	2.327 kG	1.005 kG
Maximum energy kick, ΔE	91.1 meV	19.6 meV
Cooling rates (λ_x, λ_s)	(66, 64) s^{-1}	(22, 19) s^{-1}
Cooling ranges (λ_x, λ_s)	(5.61, 4.73)	(3.97, 5.7)
Sync. rad. Damping rates (x, s)	(0.5, 1.02) s^{-1}	(0.53, 0.91) s^{-1}

significantly reduced risk. For the active configuration, the radiation must be tightly focused in the center of the telescope for efficient amplification, and the simplest two-lens telescope results in a transfer matrix close to positive identity. Experiments at IOTA will use the single-lens and two-lens telescopes for passive and active cooling, respectively.

Configurations

We have designed OSC systems for two distinct operating wavelengths at IOTA: 0.95 μm and 2.2 μm . The general parameters for passive cooling in these configurations are given in Table 1. The estimated energy kicks include the effects of dispersion and depth of field. Operation at 0.95 μm requires a reduction in delay to preserve the cooling range. The reduced delay does not support the use of a multi-lens telescope; therefore, only the passive, single-lens configuration is possible in this case. While the achievable cooling rate is significantly lower in the 2.2- μm case, there is sufficient delay available to implement a simplified single-stage optical amplifier; however, the performance of amplifiers in the mid IR is significantly lower than those in the visible. We estimate that a single pass amplifier based on amplified spontaneous emission in Cr:ZnSe will only increase the cooling force by a factor of 1.65 [29].

Our initial experimental efforts will focus on the 0.95 μm passive configuration due to its higher cooling rate (~ 2 times greater than the amplified configuration at 2.2 μm), the superiority of optical detectors at this wavelength and enhanced compatibility with other planned studies in IOTA, which involve the storage and characterization of a single electron. Additionally, Due to the

larger beta function in the bypass, the transverse angles of the particles are smaller and non-linear path lengthening is correspondingly reduced. This makes sextupole correction less critical than in the 2.2- μm case and enables the use of shorted versions of the existing IOTA sextupoles. Fig. 5 presents an example Synchrotron Radiation Workshop (SRW) simulation of the electric field experienced in the kicker by an electron phased for maximum energy exchange; the corresponding electron trajectory is shown as well. The estimated energy kicks compare well between our SRW simulations and analytic theory. For example, in our 2.2- μm passive configuration the maximum achievable energy exchange, in the absence of dispersion, is 22.0 meV and 20.1 meV in the theory and simulations respectively. A detailed comparison of our SRW simulations with analytic theory is given elsewhere [29].

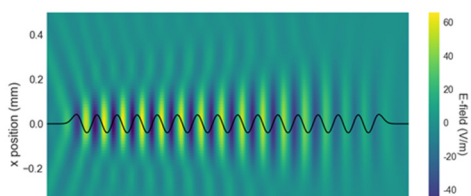


Figure 5: 2D map of the electric field experienced by an electron phased for maximum energy exchange.

Hardware

The OSC experiment requires the design, engineering and construction of a variety of new hardware, including magnets (dipoles, quadrupoles, sextupoles and correctors) and undulators, light optics and support systems and specialized vacuum chambers and beam pipes. We briefly describe some aspects of each and their current status.

Magnets: The dipole magnets require high integrated field quality ($\sim 10^{-4}$) over an aperture of ~ 5 -mm in radius. This can be achieved by use of a monolithic core that is electro-discharge machined to 10- μm precision. An engineering design of the dipole has already been produced and is shown in Fig. 6. The sextupoles for the 0.95- μm experiment are modified versions of the IOTA sextupoles, also shown in Fig. 6, and minimal additional design work will be required. The coupling quad in the center of the chicane will be a Panofsky type and will double as a vertical corrector. Screens are required on most magnetic elements due to their close packing in the bypass. Preliminary magnetic designs for the undulators have been developed and are being optimized to account for saturation effects and thermal considerations.

Light Optics: The tolerances on the light optics are relatively relaxed compared to what is available from manufacturers (central thickness, radius of curvature, etc...). For example, in the 2.2- μm case using a three-lens telescope and BaF₂ optics, our simulations show that typical manufacturing tolerances on central thickness and radius of curvature only produce a few-percent variation in the maximum kick strength. The situation is expected to further improve in the 0.95- μm configuration due to the use of quartz, which is harder than BaF₂ and can be

shaped with higher precision. Positioning of the light optics and will be carried out with a commercial hexapod-like motion solution. The chosen system is non-magnetic and meets the vacuum, range and load requirements for all experimental configurations.

Vacuum chambers: The vacuum-chamber designs are now being discussed with various manufacturers. In order to reduce magnetic errors in the bypass, we are considering two types of chambers: seam-welded chambers of 316LN steel and extruded or seam-welded aluminium chambers. In the former, the welds may have a slight increase in magnetic permeability [30]. We are performing simulations to examine the magnitude of magnetic errors that can be expected. If the errors are unacceptable, then aluminium chambers with bimetallic flanges can be used instead.

Other remarks: We note also that the undulator-radiation measurements will be contaminated to a degree by the synchrotron radiation from the main-ring dipoles. We have simulated this contamination and, at the fundamental frequency, the probability that a detected photon originated from the undulator is $\sim 85\%$. If an appropriate aperture is applied to the dipole vacuum window then this can be improved to $\sim 95\%$.

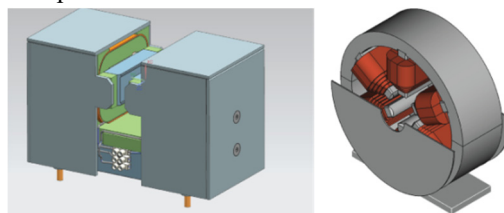


Figure 6: Designs of the OSC chicane dipoles and the IOTA main-ring sextupoles.

CONCLUSION

We have detailed the conceptual design for the planned demonstration of OSC in Fermilab's IOTA ring, which will constitute the first experimental demonstration of OSC. This program will serve as a pathfinder that explores OSC physics, experimental methods and diagnostics, and it will act as a bridge towards development of the OSC systems required by colliders. At the design wavelength, 0.95 μm , the OSC cooling rate will exceed that from synchrotron radiation damping by a factor of ~ 60 in the absence of any amplification. The required hardware system, including magnets, light optics and vacuum chambers and beam pipes are maturing in their design and many elements are ready for fabrication or procurement. The installation of the OSC insert in the IOTA ring is planned for spring of 2019 with an expectation of first cooling in summer of the same year.

ACKNOWLEDGMENTS

Fermilab is managed by the Fermi Research Alliance, LLC for the U.S. Department of Energy Office of Science Contract number DE-AC02-07CH11359.

REFERENCES

- [1] S. van der Meer, “Stochastic damping of betatron oscillations in the ISR”, CERN-ISR-PO-72-31, 1972.
- [2] S. van der Meer, “Stochastic cooling and the accumulation of antiprotons”, Nobel lecture, 1984.
- [3] D. Möhl, G. Petrucci, L. Thorndahl and S. van der Meer, “Physics and Technique of Stochastic Cooling,” *Physics Reports* vol. 58, no. 2, pp. 73-119, 1980.
- [4] S. Chattopadhyay, “Stochastic Cooling of Bunched Beams From Fluctuation and Kinetic Theory,” Ph.D. thesis, Lawrence Berkeley Laboratory, University of California, Berkeley, CA, 1982.
- [5] F. Caspers and D. Möhl, “Stochastic Cooling in Hadron Colliders,” in *Proc. 17th Int. Conf. on High Energy Accelerators (HEACC'98)*, Dubna, Russia, 1998, pp. 398-401.
- [6] J. Marriner, “Stochastic cooling overview”, *Nuclear Instruments and Methods in Physics Research A*, vol. 532, pp. 11-18, 2004.
- [7] A.A.Mikhailichenko, M.S. Zolotorev, “Optical stochastic cooling,” *Phys. Rev. Lett.*, vol. 71, no. 25, p. 4146, 1993.
- [8] M. S. Zolotorev, A. A. Zholents, “Transit-time method of optical stochastic cooling,” *Phys. Rev. E* vol. 50, no. 4, p. 3087, 1994.
- [9] V. A. Lebedev, “Optical Stochastic Cooling in Tevatron,” in *Proc. 46th ICFA Advanced Beam Dynamics Workshop on High-Intensity and High-Brightness Hadron Beams (HB'10)*, Morschach, Switzerland, 2010.
- [10] M. Babzien, I. Ben-Zvi, I. Pavlishin, I. V. Pogorelsky, V. E. Yakimenko, A. A. Zholents, and M. S. Zolotorev, “Optical Stochastic Cooling for RHIC,” *Nuclear Instruments and Methods in Physics Research A*, vol. 532 pp. 345–347, 2004,
- [11] A. Zholents, W.Barletta, S. Chattopadhyay, M. Zolotorev, “Halo Particle Confinement in the VLHC using Optical Stochastic Cooling,” In *Proc. European Particle Accelerator Conf. (EPAC'00)*, Vienna, Austria, 2000, pp. 262-264.
- [12] A. Zholents, M. Zolotorev, and W. Wan, “Optical stochastic cooling of muons,” *Phys. Rev. ST Accel. Beams*, vol. 4, p. 031001, 2001.
- [13] E. G. Bessonov and A. A. Mikhailichenko, “Enhanced Optical Cooling of Particle Beams in Storage Rings,” in *Proc. Particle Accelerator Conf. (PAC'05)*, Knoxville, USA, 2005, pp. 4179-4181.
- [14] E. G. Bessonov, M. V. Gorbunkov, and A. A. Mikhailichenko, “Enhanced optical cooling system test in an electron storage ring,” *Phys. Rev. ST Accel. Beams*, vol. 11, p. 011302, 2008.
- [15] E G Bessonov, M. V. Gorbunkov and A. A. Mikhailichenko, “Enhanced optical cooling of muon beams,” *JINST*, vol. 5, P01011, 2010.
- [16] V. Lebedev, “Optical Stochastic Cooling”, ICFA Beam Dynamics Newsletter, no. 65, pp. 100-116, 2014.
- [17] W. Franklin, *et al.*, “Optical Stochastic Cooling Experiment at the MIT-Bates South Hall Ring,” in *Proc. Int. Workshop on Beam Cooling and Related Topics (COOL'07)*, Bad Kreuznach, Germany, 2007, pp. 117-120.
- [18] E. Bessonov, M. Gorbunkov and A. Mikhailichenko, “To the Optical Stochastic Cooling Test at CESR,” CBN 10-4, 2010.
- [19] W. A. Franklin, “Optical stochastic cooling proof-of-principle experiment,” in *Proc. 22nd Particle Accelerator Conf. (PAC'07)*, Albuquerque, NM, 2007, pp. 1904-1906.
- [20] X. Shen, P. Yu, W. Huang and C. Tang, “Optical Stochastic Cooling in a Low Energy Electron Storage Ring for a Compact X-Ray Source,” in *Proc. 23rd Particle Accelerator Conf. (PAC'09)*, Vancouver, B.C., Canada, 2009, pp. 4378-4380.
- [21] E. G. Bessonov, M. V. Gorbunkov, A. A. Mikhailichenko and A. L. Osipov, “Self-stimulated emission of undulator radiation,” *JINST*, vol. 5, P07004, 2010.
- [22] R. Redwine, “Introduction to Optical Stochastic Cooling and the Bates Linear Accelerator Center at MIT,” Muon Collider Design Workshop, Brookhaven National Laboratory, 2009.
- [23] M. B. Andorf, V. A. Lebedev, P. Piot and J. Ruan, “Optically Based Diagnostics for Optical Stochastic Cooling,” in *Proc. North American Particle Accelerator Conf. (NAPAC'16)*, Chicago, IL, 2016, pp. 779-781.
- [24] Y. S. Derbenev, *Theory of electron cooling*, arXiv:1703.09735 [physics.acc-ph]
- [25] A. Romanov, I. Koop, E. Perevedentsev, D. Shwartz, “Luminosity Estimation and Beam Phase Space Analysis at VEPP-2000,” in *Proc. North American Particle Accelerator Conf. (NAPAC'13)*, Pasadena, CA, 2013, pp. 889-891.
- [26] A. Romanov, I. Koop, E. Perevedentsev, D. Shwartz, “Beam Phase Space Reconstruction For Monitoring the Luminosity in the VEPP-2000 Collider,” in *Proc. 5th Int. Particle Accelerator Conf. (IPAC'14)*, Dresden, Germany, 2014, pp. 3623-3625.
- [27] S. Antipov *et al.*, “IOTA (Integrable Optics Test Accelerator): facility and experimental beam physics program,” *JINST*, vol. 12, T03002, 2017.
- [28] G. Kafka, “Lattice Design of the Integrable Optics Test Accelerator and Optical Stochastic Cooling Experiment at Fermilab,” Illinois Institute of Technology, Chicago, IL, 2015.
- [29] M. B. Andorf, V. A. Lebedev, J. Jarvis and P. Piot, “Computation and Numerical Simulation of Focused Undulator Radiation for Optical Stochastic Cooling,” submitted for publication.
- [30] S-H. Lee, I. Vasserman, S. Sasaki, D. Walters, D-E. Kim, “Magnetic Properties of Undulator Vacuum Chamber Materials for the Linac Coherent Light Source,” in *Proc. 27th Int. Free Electron Laser Conf. (FEL'05)*, Stanford, Ca, USA, Aug. 2005, pp. 383-386.

MOMENTUM SLIP-STACKING SIMULATIONS FOR CERN SPS ION BEAMS WITH COLLECTIVE EFFECTS

D. Quartullo*, T. Argyropoulos, A. Lasheen, CERN, Geneva, Switzerland

Abstract

The LHC Injectors Upgrade (LIU) Project at CERN aims at doubling the total intensity of the Pb-ion beam for the High-Luminosity LHC (HL-LHC) Project. This goal can be achieved by using momentum slip-stacking (MSS) in the SPS, the LHC injector. This RF gymnastics, originally proposed to increase bunch intensity, will be used on the intermediate energy plateau to interleave two batches, reducing the bunch spacing from 100 ns to 50 ns. The MSS feasibility can be tested only in 2021, after the beam controls upgrade of the SPS 200 MHz RF system, so beam dynamics simulations are used to design this complicated beam manipulation. Simulations of the MSS were performed using the CERN BLOnD code with a full SPS impedance model. Attention has been paid to the choice of the RF and machine parameters (beam energy, time duration, RF frequency and voltage programs) to reduce losses and the final bunch length which is crucial for the injection into the LHC 400 MHz buckets. The initial beam parameters used in simulations were obtained from beam measurements in the first part of the SPS cycle taking into account bunch-by-bunch losses on flat bottom and development of bunch instabilities.

INTRODUCTION

The HL-LHC Project at CERN aims at doubling the peak luminosity of the Pb-ion beam after upgrade (2019-2021) [1]. To fulfil this requirement, the baseline of the LIU Project includes the decrease of the bunch spacing in SPS from 100 ns to 50 ns through momentum slip-stacking (MSS) [1]. This technique, already used in operation in Fermilab [2], allows two batches with slightly different momenta to slip relative to each other before being stacked one on top of the other. An RF voltage high enough to recapture the stacked bunches allows to double the bunch intensity at the end of the process. A variant of MSS is considered in the SPS: the two batches are not stacked on top of each other, but interleaved (see Fig. 1). This provides the desired bunch spacing reduction while the bunch intensity remains unchanged.

MSS in SPS is potentially feasible thanks to the large bandwidth of the 200 MHz travelling-wave cavities (TWC) [3]. These will be divided into two groups and the RF frequency of each group will be tuned to one batch. Since independent LLRF controls for the two groups will be available only after upgrade, macro-particle simulations in the longitudinal plane are the only means to verify the MSS feasibility (alternative scenarios are being also considered [4]).

Preliminary simulations performed in 2014 showed promising results [5], however collective effects were not included and beam parameter variations along the batches

* danilo.quartullo@cern.ch

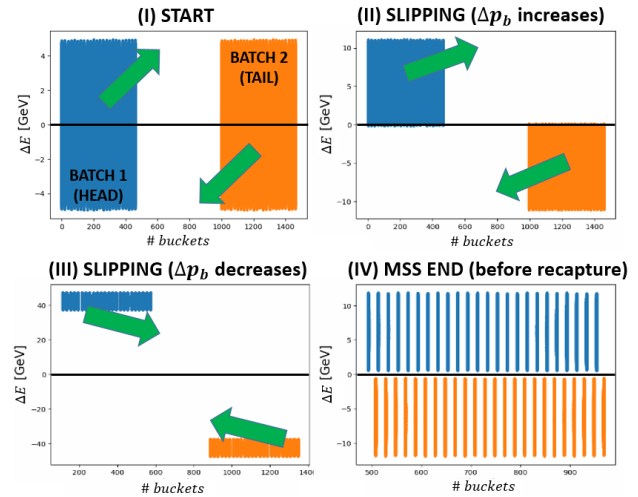


Figure 1: Example of planned MSS procedure in SPS. The two batches, starting from Phase I, move in longitudinal phase space relative to each other. The black line marks $\Delta E = E - E_0 = 0$, where E_0 is the design energy. In Phase II the distance in momentum Δp_b between the batches increases, while the opposite happens in Phase III. Recapture is done in Phase IV.

were not taken into account. In the present work a more elaborated study is presented. Beam measurements provided realistic beam parameters which were used as initial conditions in simulations. Collective effects were included, using an accurate longitudinal impedance model. Machine and RF programs were designed to be used during and after MSS. Effort was spent to develop algorithms able to speed up the settings of the large number of parameters involved during MSS optimisation. The CERN BLOnD macro-particle simulation code [6] has been used for the studies.

SLIP-STACKING PRINCIPLE

MSS is usually performed at constant magnetic field B_0 . The design momentum p_0 is then defined by [7]

$$B_0 R_0 = p_0 / q, \quad (1)$$

where q is the particle charge and the bending radius ρ of the dipole magnets has been approximated with the average machine radius R_0 . Keeping the magnetic field constant and in linear approximation, the following relations hold [7]

$$\frac{\Delta \omega_{rf}}{\omega_{rf,0}} = -\eta_0 \frac{\Delta p}{p_0} = -\eta_0 \gamma_{tr}^2 \frac{\Delta R}{R_0}, \quad (2)$$

where $\omega_{rf} = 2\pi f_{rf}$ is the angular RF frequency, γ_{tr} is the relativistic gamma at transition energy and $\eta_0 = \gamma_{tr}^{-2} - \gamma_0^{-2}$ is the slippage factor. The design $\omega_{rf,0} = h\omega_0$ (with h the

harmonic number) can be derived from p_0 , as well as the design γ_0 . All the variables in Eq. (2) represent changes with respect to the corresponding design quantities. In a reference frame synchronised with the design revolution period T_0 (see Fig. 1), a variation $\Delta\omega_{rf}$ implies a change in the RF phase according to

$$\Delta\phi_{rf} = \frac{2\pi h \Delta\omega_{rf}}{\omega_{rf,0}}. \quad (3)$$

Taking as an example the case in Fig. 1 ($\eta_0 > 0$), the head batch will gain momentum when the RF frequency of the corresponding RF system is decreased. According to Eqs. (2) and (3) the batch will be displaced radially outwards while slipping to the right in phase. An analogous but opposite reasoning applies to the second batch.

The group of RF cavities not synchronized with the batch perturbs its motion. The severity of the perturbation is linked to the distance between batches in phase and momentum. The latter is described by the slip-stacking parameter [8]:

$$\alpha \doteq \frac{\Delta f_{rf,b}}{f_{s0}} = 2 \frac{\Delta E_b}{H_b}, \quad (4)$$

where $\Delta f_{rf,b}$ and ΔE_b are the differences in RF frequency and total energy between the two batches, f_{s0} is the zero amplitude synchrotron frequency of the unperturbed bucket and H_b is half of the bucket height. When $\alpha = 4$, the separatrices of the two batches are tangent to each other. This value has been proven to be a lower limit for dynamic stability [8]. If $\alpha \gg 4$, the perturbation averages within a synchrotron period and its effect is less damaging. However a large α implies a higher RF voltage needed for recapture which leads to a larger emittance blow-up after filamentation. Phase IV in Fig. 1 shows a beam configuration where $\alpha = 4$.

MOMENTUM SLIP-STACKING IN SPS

LHC Pb-ion beam in SPS is currently accelerated from 17 GeV/qc ($\gamma = 7$) to 450 GeV/qc ($\gamma = 191$), where $q = 82$ is the number of protons per ion. Three different optics, called Q20, Q22 and Q26, are available in the SPS, depending on the working point adopted. In all cases, the beam energy crosses the transition energy during the first part of the ramp ($\gamma_{tr}^{Q20} = 18$, $\gamma_{tr}^{Q22} = 20$, $\gamma_{tr}^{Q26} = 23$). The Q20 optics is currently used in operation. The accelerating RF system is the 200 MHz TWC ($h = 4620$). For proton beams, a fourth harmonic RF system (800 MHz) is used in addition to the main one to enhance Landau damping. However, this system is not used presently in operation with ion beams.

MSS Energy and SPS Momentum Program

The first choice to be made is the energy at which slip-stacking should be performed. At injection energy, the presence of relatively strong space charge, intra-beam scattering (IBS) and RF noise prevent us from applying MSS there. On the other hand at flat top all particles lost during the RF manipulations would be transferred to the LHC. For these reasons an intermediate energy plateau has been chosen

(300 GeV/qc) which is quite far from the transition energy with a higher stability threshold compared to the top energy. Since only integer multiples of the CERN PSB cycle (1.2 s) can be added to the currently used SPS momentum program, the length of the plateau was chosen to be 1.2 s. Figure 2 shows the momentum program used in simulations. Out of 1.2 s, 0.8 s were used for MSS, while 0.4 s were utilized to let the bunches filament after recapture.

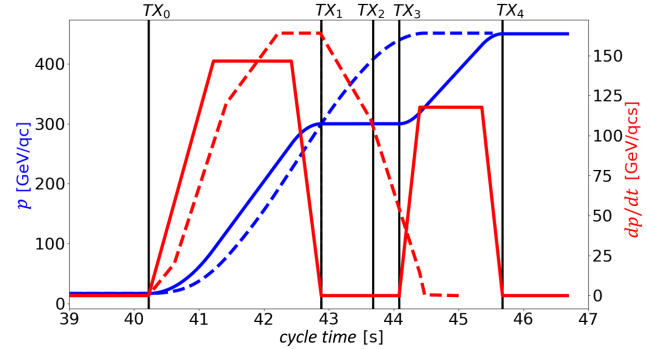


Figure 2: Operational (dashed) and used in simulations (continuous) momentum programs (blue) and their derivatives (red). The label TX_0 marks the ramp start, TX_1 the start of MSS, TX_2 the end of MSS, TX_3 and TX_4 the start and the end of the second ramp.

RF Perturbation and Initial Conditions

Every batch will contain 24 bunches spaced by 100 ns (assuming a 100 ns spacing between the mini-batches coming from the CERN PS). To limit the perturbation of the second RF system on each batch, the two independent 200 MHz groups are switched on only when the corresponding batch passes by. Figure 3 shows cavity voltage measurements for the currently available TWC [9]. The rising and decaying times are similar and ranging from 1 μ s to 1.2 μ s, depending on the cavity length. We expect that this time T_b^{th} , which currently relates to the 4 and 5-section cavities, will be lower during MSS, since the relatively low required voltage for this manipulation can be provided only by the new 3-section cavities. In simulations $T_b^{th} = 1 \mu$ s was assumed.

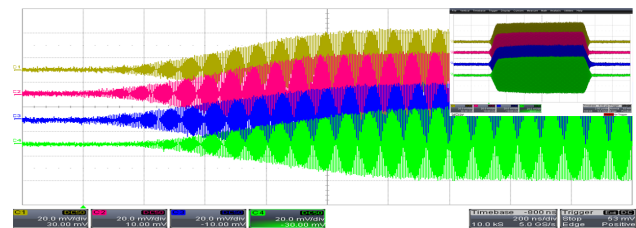


Figure 3: Measurements of cavity voltages for the currently used two 4-section (top) and two 5-section (bottom) TWC (the time division length is 2 μ s) [9]. The top right image shows the RF voltage rise and decay during batch passage.

It is essential that $\alpha \gg 4$ when the distance between the batches T_b is equal to T_b^{th} (to minimize the perturbation effects). We assumed a relatively large $T_b = 2.7 \mu$ s at TX_1 ,

Content from this work may be used under the terms of the CC BY 3.0 licence (© 2018). Any distribution of this work must maintain attribution to the author(s), title of the work, publisher, and DOI.

giving priority to the adiabaticity of the MSS manipulation. Figure 4 shows an example of α evolution during MSS.

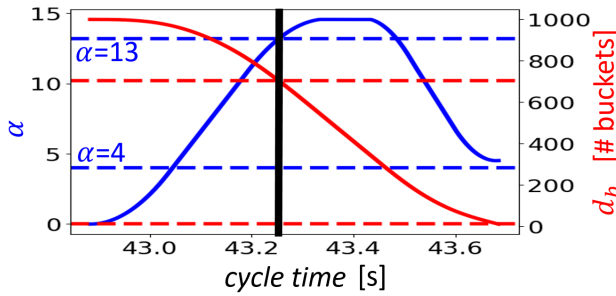


Figure 4: Example of α evolution during MSS ($\alpha_{TX_2} = 4.5$). The black line marks the time when $T_b = T_b^{th}$. The quantity d_b refers to the head-head distance between the batches. At TX_1 $d_b = 1000$ buckets (or $T_b = 2.7 \mu s$), while at TX_2 $d_b = 10$ buckets (bunch spacing at the end of MSS).

Beam measurements of the operational SPS ion cycle [10] were used to set the initial bunch distributions in simulations. Figure 5 shows that the emittance increases by a factor of 2 along 24 bunches in the SPS, whereas the intensity grows by a factor of 1.5 (this variability is due to continuous losses at flat bottom). An extrapolation was done to obtain the beam parameters for the 48 bunches needed for MSS. The emittance ϵ_l was calculated using the full-width-half-maximum bunch length rescaled to $4\sigma_{rms}$ of a Gaussian profile (convention used in SPS). However, as we will see, the bunch profiles obtained after MSS are not Gaussian but they have two peaks. For this reason the bunch length and emittance in the present paper will be determined by the portion of the line density containing 95% of the particles. The fact that in measurements losses happen gradually along the flat bottom indicates that there are strong tails in the bunches. For that reason a binomial distribution with $\mu=5$ was used in the studies.

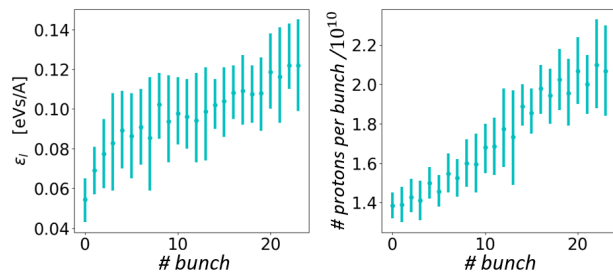


Figure 5: Measured longitudinal emittances and intensities along 24 bunches at 300 GeV/qc.

RF Programs During MSS

During MSS, we suppose that the RF frequency programs of the two 200 MHz RF subsystems are opposite relative to $\omega_{rf,0}$ ($\omega_{rf}^{(1)} + \omega_{rf}^{(2)} = 2\omega_{rf,0}$) and that the two RF voltage programs are equal ($V_{rf}^{(1)} = V_{rf}^{(2)}$). At recapture time TX_2 we have $\omega_{rf}^{(1)} = \omega_{rf}^{(2)} = \omega_{rf,0}$ and a common recapture voltage

V_{rf}^{rc} is used. According to Eq. (2) the RF frequency programs determine the momentum programs applied to the two batches. The voltage program during MSS is computed for constant filling factor of bucket in energy q_e^{MSS} relative to the highest emittance bunch (see Fig. 6).

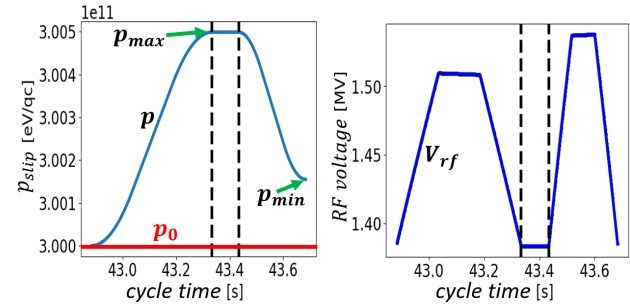


Figure 6: Example of momentum and RF programs for one batch during MSS (same case as in Fig. 4).

The calculation of the momentum program during MSS can be tedious when parameter scans have to be performed for optimization (see next Section) and accurate calibration has to be done case by case to avoid misalignments between the two batches before recapture. Automatic tuning to obtain alignment with arbitrary precision is necessary. Iterative algorithms have been conceived for this purpose, assuming constant emittance and filling factor during MSS.

RF Programs After MSS

The recapture voltage V_{rf}^{rc} is used during the filamentation process in $[TX_2, TX_3]$. Then, the filling factor in energy relative to the highest emittance bunch is computed in TX_3 . The RF voltage program for the second ramp is calculated assuming this filling factor constant. At flat top, with a duration of 1 s, two options for beam transfer to LHC were examined (assuming a maximum available voltage of 15 MV [11]). Bunch compression, where the RF voltage in TX_4 is increased linearly and adiabatically for 0.5 s (or about 180 synchrotron periods) up to 15 MV and then is kept constant until extraction. Bunch rotation, where the RF voltage in TX_4 is used for 0.8 s, then it is increased non-adiabatically (few turns) to 15 MV and after a quarter of synchrotron period the beam is extracted.

ANALYSIS OF SIMULATION RESULTS

In this section, unless otherwise specified, simulation results with the currently used Q20 optics are presented. Given the considerable number of parameters in play and knowing the required constraints at LHC injection, parameter scans were made to find the best combinations. The following fundamental quantities were considered: filling factor q_e^{MSS} (from 0.45 to 0.9, step 0.05), α_{TX_2} (from 3.5 to 8, step 0.5), V_{rf}^{rc} (from 1 MV to 9 MV, step 0.5) and the type of RF manipulation at flat top (compression or rotation).

Two constraints were considered. The first refers to the maximum bunch length at the SPS extraction. This number τ_{max} has to be less than 1.65 ns, since larger bunch lengths

lead to considerable losses when injected to the 400 MHz LHC RF buckets. The second constraint results from the total losses due to the MSS process. This value as defined by the LIU project should be less than 5% [4]. In the following simulations the total losses L_{tot} are defined by the sum of the particles lost in the SPS hitting the beam pipe (L_{SPS}) and the satellite particles which are formed in SPS during MSS and will be transferred to the LHC (S_{LHC}).

Bunch Compression

A combination A is optimal if there exists no other combination B for which $L_{tot}^A > L_{tot}^B$ and $\tau_{max}^A > \tau_{max}^B$. The simulation results with collective effects are shown in Fig. 7 for bunch compression, together with the optimal solutions. Essentially no combination is acceptable, so bunch compression at flat top cannot be adopted. The maximum emittance ϵ_{max} after filamentation should be lower than 0.32 eVs/A to have $\tau_{max} < 1.65$ ns. From Fig. 7 one can see that the real limitation is on τ_{max} (or ϵ_{max}) rather than on L_{tot} . In other words the losses can be almost arbitrarily reduced increasing for example α_{TX_2} and V_{rf}^{rc} while decreasing q_e^{MSS} (and on average we would obtain $\tau_{max} \approx 2$ ns). On the other hand, mostly because of the lower stability limit for α_{TX_2} , it is difficult to have arbitrarily low emittances after filamentation, unless considerable losses are allowed.

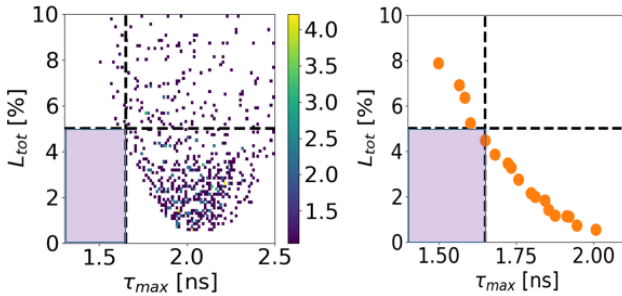


Figure 7: Simulation results (bunch compression) in the L_{tot} - τ_{max} plane (left). The optimal solutions are on the right. The purple area indicates where the constraints are satisfied.

Bunch Rotation

Results for the bunch rotation case are shown in Fig. 8. The average τ_{max} shifts from 2 ns to 1.6 ns, allowing numerous combinations to satisfy the constraints. Considering the optimal solutions and giving priority to losses reduction while keeping some safety margin for τ_{max} , the green dot marks the proposed solution, with $\alpha_{TX_2} = 4.5$, $q_e^{MSS} = 0.65$ and $V_{rf}^{rc} = 8$ MV. The relatively low q_e^{MSS} and α_{TX_2} slightly higher than 4 allow to have low $L_{tot} = 0.43\%$, $S_{LHC} = 0.13\%$ and $L_{SPS} = 0.30\%$.

The feasibility of this solution was verified. The maximum radial displacement for one batch during MSS was 5.67 mm and 7.8 mm if the spread in energy is included (the current one-sided aperture limitation is around 20 mm). The maximum RF frequency spread during MSS was 1 kHz,

three orders of magnitude lower than the RF cavity bandwidth. As for the peak RF voltage, the maximum value during MSS was only 1.54 MV (for one subsystem) and during acceleration to flat top it reached 14.6 MV, still inside the limitations (see also Figs. 4 and 6 which refer to this optimal solution).

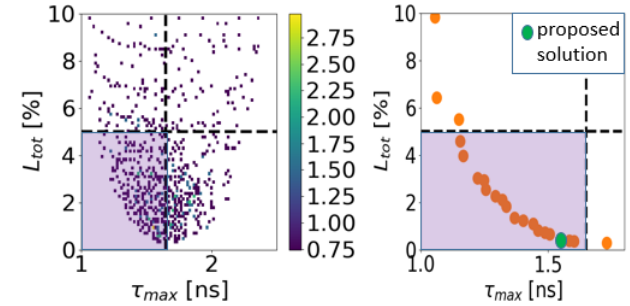


Figure 8: Simulation results (bunch rotation) in the L_{tot} - τ_{max} plane (left). The optimal solutions are on the right. The purple area indicates where the constraints are satisfied.

Figures 9 and 10 show all the significant parameters involved. The green lines mark the chosen combination. Qualitatively, as τ_{max} increases, we can see that L_{tot} , S_{LHC} and L_{SPS} decrease while ϵ_{max} increases. In addition, α_{TX_2} remains constant, q_e^{MSS} decreases and V_{rf}^{rc} increases.

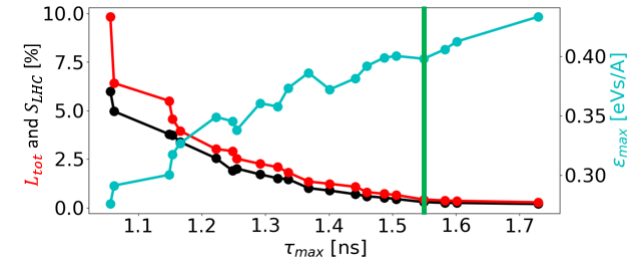


Figure 9: Total losses, satellites (L_{tot} , S_{LHC}) and emittance (ϵ_{max}) as a function of τ_{max} for the optimal solutions in Fig. 8. The green line marks the proposed combination.

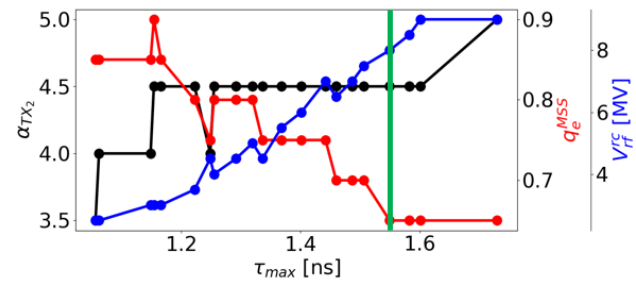


Figure 10: Parameters α_{TX_2} , q_e^{MSS} and V_{rf}^{rc} as a function of τ_{max} for the optimal combinations shown in Fig. 8. The green line marks the proposed combination.

It is expected that all the optimal solutions have $\alpha_{TX_2} \approx 4$, since 4 is the lower limit for stability and larger values would make the solutions not optimal. However $\alpha_{TX_2} \approx 4.5$ gives some safety margin to soften the impact of the chaotic motion

Content from this work may be used under the terms of the CC BY 3.0 licence (© 2018). Any distribution of this work must maintain attribution to the author(s), title of the work, publisher, and DOI.

close to $\Delta E = 0$ since the highest emittance bunches fill almost the full bucket even for low q_e^{MSS} .

Qualitatively, Figs. 9 and 10 are explained below. Going from an optimal combination A to another optimal combination B with $\tau_{max}^B < \tau_{max}^A$ ($\epsilon_{max}^B < \epsilon_{max}^A$) it follows that $V_{rf}^{rc,B} < V_{rf}^{rc,A}$, since the bucket area after recapture has to decrease. To avoid losses in SPS due to particles outside the separatrix of the recapture bucket, one needs $\Delta E_b^B < \Delta E_b^A$. Since α_{TX_2} is roughly constant, the RF voltage $V_{rf,u}$ of the unperturbed bucket of one of the two batches has to decrease ($H_b \propto V_{rf,u}^{1/2}$). The peak energy spread of the bunch inside the unperturbed RF bucket $\Delta \bar{E}$ decreases as well ($\Delta \bar{E} \propto V_{rf,u}^{1/4}$) and thus $q_e^{MSS,B} > q_e^{MSS,A}$. A higher q_e^{MSS} implies larger L_{SPS} . Since the bunch is now closer to the axis $\Delta E = 0$, where the chaotic motion is more significant, $S_{LHC}^B > S_{LHC}^A$. Finally $L_{tot}^B > L_{tot}^A$.

Figure 11 shows the optimal combinations neglecting intensity effects. No significant differences can be noticed, implying that intensity effects do not enhance instabilities which would increase the total losses or blow up the beam.

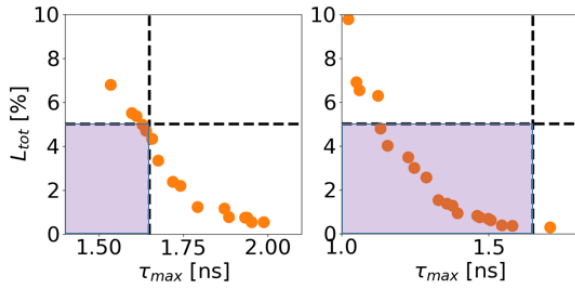


Figure 11: Optimal combinations for the bunch compression (left) and rotation (right) cases without intensity effects.

The two other optics, Q22 and Q26, were also analysed (Fig. 12). Because of the lower slip factor, a slightly higher p_{max} during MSS was needed (keeping constant the time duration). The radial displacement was still inside the aperture limitations and the process was adiabatic. Fixing all the other parameters, a lower slip factor implies a lower q_e^{MSS} which helps in reducing L_{SPS} . The bucket area after recapture decreases as well and this implies a lower τ_{max} . Bunch compression could be adopted if the Q22 (or even better the Q26) optics is chosen, however these optics are more sensitive to IBS and transverse space charge effects.

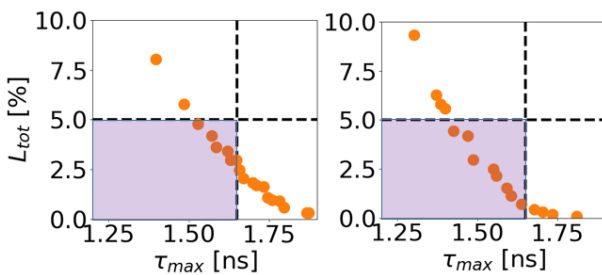


Figure 12: Optimal combinations (compression case) for the Q22 (left) and Q26 (right) optics with intensity effects.

Loss of Landau Damping During MSS

Even if intensity effects do not influence the losses and bunch length, loss of Landau damping was observed: the dipole oscillations due to the RF perturbation during MSS remain up to flat top, being stronger for shorter bunches.

Taking as an example the proposed solution found previously, Fig. 13 shows that dipole oscillations at flat top are higher by two order of magnitudes with intensity effects. The hollow bunch which is formed after recapture filaments perfectly without intensity effects, while a very dense island appears with intensity effects. From Fig. 13 it can be seen that the shortest bunches are the most affected.

Rise of dipole oscillations could be damped by phase loop. In addition, the 800 MHz system could be used to increase the non-linearities of the bunch and make the island in phase space filament. However, simulations using the 800 MHz RF system did not show significant improvement. This can be attributed to the special hollow distribution of the bunches after MSS. Further studies are ongoing.

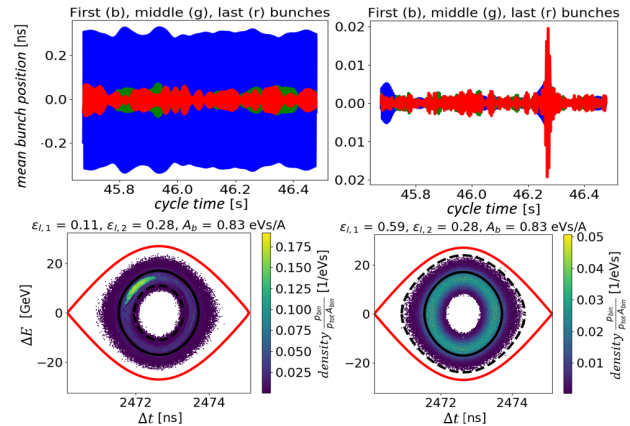


Figure 13: Beam quality with (left) and without (right) intensity effects. Top: bunch positions at flat top for the first (blue), middle (green) and last (red) bunches. Bottom: phase space of the first (smallest) bunch at beginning of flat top.

CONCLUSION

Momentum slip-stacking for LHC ion beams in SPS after LIU upgrades is fundamental to fulfil the requirements imposed by the High Luminosity LHC Project. In this paper the optimum parameters involved in this complicated beam manipulation were suggested. Simulations using the SPS impedance model showed that MSS can be applied under certain conditions, providing at extraction the beam parameters (τ_{max} , intensity) required by the LIU project. However, loss of Landau damping was observed and further studies are needed to find possible cures.

ACKNOWLEDGEMENTS

We would like to thank E. Shaposhnikova for her precious support. Important help was given by our colleagues H. Bartosik, P. Baudrenghien, T. Bohl, K. Iliakis, J. Repond and G. Rumolo.

REFERENCES

- [1] J. Coupard, H. Damerau, A. Funken, R. Garoby, S. Gilardoni, B. Goddard, K. Hanke, D. Manglunki, M. Meddahi, G. Rumolo, R. Scrivens, and E. Shaposhnikova, “LHC Injectors Upgrade, Technical Design Report, Vol. II: Ions,” Tech. Rep. CERN-ACC-2016-0041, CERN, Geneva, Apr 2016.
- [2] J. Eldred, “Slip-Stacking Dynamics for High-Power Proton Beams at Fermilab.” PhD thesis, 2015.
- [3] G. Dome, “The SPS Acceleration System Travelling Wave Drift-tube Structure for the CERN SPS,” tech. rep., 1977. CERN-SPS-ARF-77-11.
- [4] A. Saa Hernandez, “Results from ion studies in PS and SPS from 2016/2017 and planning for 2018.” presentation at the CERN Injector MD day, 2018.
- [5] T. Argyropoulos, T. Bohl, and E. Shaposhnikova, “Slip stacking in the SPS.” presentation at the CERN LIU day, 2014.
- [6] “CERN BLonD code.” <http://blond.web.cern.ch>.
- [7] C. Bovet *et al.*, “A Selection of Formulae and Data Useful for the Design of A.G. Synchrotrons,” CERN-MPS-SI-INT-DL-70-4, 1970.
- [8] F. E. Mills, “Stability of Phase Oscillations Under Two Applied Frequencies,” 1971.
- [9] T. Bohl. CERN, personal communication, 2018.
- [10] A. Lasheen, “Beam Measurements of the Longitudinal impedance of the CERN Super Proton Synchrotron.” PhD thesis, 2017.
- [11] E. Shaposhnikova *et al.*, “Upgrade of the 200 MHz RF System in the CERN SPS,” in Proc. 2nd Int. Particle Accelerator Conf. (IPAC11), San Sebastian, Spain, Sep. 2011, paper MOPC058, pp. 214-216.

STUDIES OF CAPTURE AND FLAT-BOTTOM LOSSES IN THE SPS

M. Schwarz*, H. Bartosik, A. Lasheen, J. Repond, E. Shaposhnikova, H. Timko,
 CERN, Geneva, Switzerland

Abstract

One of the strong limitations for reaching higher beam intensities in the SPS, the injector of the LHC at CERN, are particle losses at flat bottom that increase with beam intensity. In this paper, different sources of these losses are investigated for two available SPS optics, using both measurements and simulations. Part of the losses originate from the PS-to-SPS bunch-to-bucket transfer, because the PS bunches are rotated in longitudinal phase space before injection and do not completely fit into the SPS RF bucket. The injection losses due to different injected bunch distributions were analyzed. Furthermore, at high intensities the transient beam loading in the SPS has a strong impact, which is (partially) compensated by the LLRF system. The effect of the present and future upgraded one-turn delay feedback system and phase loop on flat-bottom losses was studied using the longitudinal tracking code BLonD. Finally, the total particle losses are also affected by limitations in the SPS momentum aperture, visible for higher RF capture voltages in optics with lower transition energy and higher dispersion.

INTRODUCTION

To achieve the luminosity planned by the High Luminosity LHC (HL-LHC) project at CERN, the injected beam intensity in the LHC needs to be 2.3×10^{11} protons per bunch (ppb) and requires an upgrade of the LHC and its injector chain. For the SPS, injector of the LHC, this requires an injected intensity of 2.6×10^{11} ppb, to account for the loss budget of 10% from injection to extraction [1]. These numbers require a doubling of the present nominal SPS beam intensity and are one of the targets of the LHC injectors upgrade (LIU) project. Extrapolating from measurements in 2015 with 2×10^{11} ppb and four batches to HL-LHC intensities, the expected losses could be as high as 20% [2]. Reaching the required 2.3×10^{11} ppb at extraction while staying within the loss budget is challenging and requires a better understanding of the origin of particle losses in the SPS. In this paper, we focus on the analysis of losses during capture and along the flat-bottom.

Capture losses are mainly caused by halos of the bunch distribution delivered by the PS, the injector of the SPS. Several techniques have been studied recently to measure and reduce the longitudinal bunch halo [3]. We studied these losses experimentally by varying the beam intensity and RF bucket area. Measurements are compared to simulations with different initial beam distributions. The simulations were done using the full SPS longitudinal impedance model [4] and several settings of the low-level RF (LLRF) system. But even after the halo particles are lost, the bunches contin-

uously lose particles along the flat bottom. We also present measurements of these flat-bottom losses for different momentum apertures.

MEASUREMENT SETUP

All measurements were done with a single batch of either 48 or 72 bunches, spaced by 25 ns. The RF bucket area was changed by varying the voltage V_{200} of the main 200 MHz Traveling Wave Cavities (TWC). We employed two methods to measure the beam intensity. The first uses a DC Beam Current Transformer (BCT), which yields an absolute number of particles. But it measures the beam current in the ring, and thus does not distinguish between particles captured in the RF buckets and uncaptured particles that still travel in the ring. Moreover, it is not fast enough to resolve the intensity during the first few milliseconds and, therefore, cannot resolve the injected intensity, which is crucial to measure the capture losses. As a second method, we observe the longitudinal bunch profiles with a wall current monitor and an oscilloscope. This allows for a measurement of the bunch-by-bunch intensity on a turn-by-turn basis by integrating the bunch profiles. The intensity was calibrated by the BCT intensity after uncaptured particles were removed either by a tune kicker or acceleration. Unless noted otherwise, all measured intensities and derived quantities were obtained from the integrated bunch profiles. Figure 1 shows beam intensities measured by the BCT (blue) and computed from the integrated bunch profiles (orange). Here, capture losses were enhanced by reducing the main RF voltage and result in a sharp decrease of the beam intensity during the first few

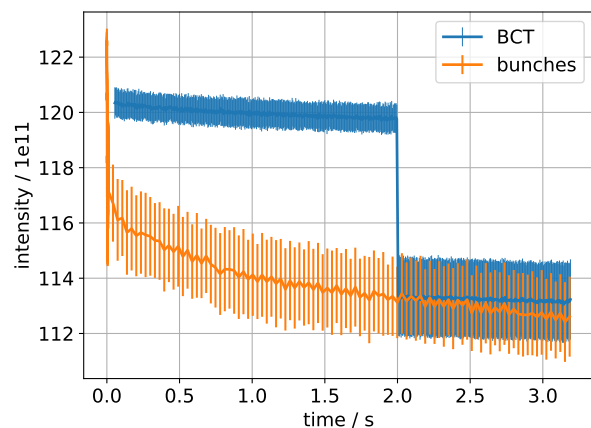


Figure 1: Beam intensity (number of protons), measured by the BCT (blue) and from the integrated bunch profiles (orange). A kick is applied at 2 s to remove the uncaptured particles.

* markus.schwarz@cern.ch

milliseconds. Because the particles lost out of the RF bucket are still circulating in the machine, the BCT intensity is above the bunch intensity until the lost particles are removed by a tune-kick at 2 s. Notice that the bunches continue to lose particles. It is important to keep in mind that the bunch profile is only a projection of the longitudinal phase space distribution and, hence, uncaptured particles below or above the RF bucket are counted as well.

SIMULATION SETUP

Correct simulations of the losses in the SPS require both an accurate initial beam distribution as well as a model of the LLRF system. For our simulations we used the longitudinal tracking code BLoND [5]. Besides being able to compute the effects of the beam induced voltage, BLoND can model beam-based feedbacks.

Initial Beam Distribution

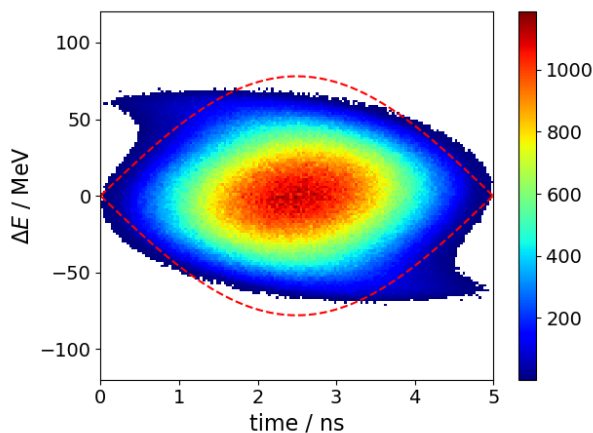


Figure 2: Simulated PS particle distribution with 1.1% of particles in a halo outside the SPS RF bucket (red dashed curve).

Before the bunches are injected into the SPS, they are subject to several RF manipulations in the PS. First, the initial six bunches are split several times to the final number of 72 bunches. With a 4σ bunch length of 14 ns, these bunches do not fit into the 5 ns long SPS RF bucket. As a last step, a bunch rotation is performed in the PS to decrease the bunch length down to 4 ns. However, due to the nonlinearity of the RF voltage, a bunch halo is created that is outside the SPS RF bucket [6].

To vary the initial particle distribution, we simulated the bunch rotation in the PS for different cases, to produce bunches with different halos. In this paper, we characterize the halo by the percentage of macro-particles that are outside the SPS RF bucket. For an RF voltage of 2.0 MV, the three different initial distributions have 0%, 0.3% and 1.1% of the particles outside the RF bucket, see Fig. 2 for an example. Without any beam loading, this would also be the amount of particles lost. In reality losses are higher due to intensity effects in the SPS. The single simulated PS bunch has

four million macro-particles. To create an SPS beam of 72 bunches, we randomly selected 1.5 million macro-particles 72 times and placed them at the center of the SPS bucket, 25 ns apart. The simulations were repeated with different seeds of the random number generator, but yielded nearly identical results.

Modeling of the SPS LLRF System

Due to intensity effects, the SPS RF bucket area is reduced. To take these effects into account, we use the present SPS impedance model in our simulations. It covers frequencies up to 6 GHz [4, 7] and is dominated at low frequencies by the impedance of the main harmonic of the 200 MHz TWC. Presently, the SPS has two ‘short’ and two ‘long’ TWCs with an effective length of 16.082 m and 20.196 m, respectively. Their impedance $Z_{TWC}(\omega)$ can be calculated analytically [8]. To reduce the effective impedance experienced by the beam, each of the four TWCs is equipped with a feed-forward and a one-turn delay feedback system (OTFB) [9]. In this paper, we only model the effect of the OTFB and the feed-forward system was turned off during measurements. A BLoND model for the OTFB is presently under development [10]. Here, we model the effect of the OTFB by its effective impedance reduction factor $\Gamma(\omega)$. In the SPS, the OTFB includes a comb filter to mainly act at multiples of the revolution frequency [9], while in our model we consider only the envelope. The full impedance reduction $\Gamma(\omega)$ is reached only after a transient time τ_{FB} . We model this transient by a time dependent attenuation $a(t)$, i.e. at turn n the impedance of the TWC is given by

$$Z_{TWC,n}(\omega) = Z_{TWC}(\omega) \Gamma(\omega)^{a(n t_{rev})}. \quad (1)$$

The attenuation is modeled as $a(t) = F_{FB} [1 - \exp(-(t - t_0)/\tau_{FB})]$ and starts at time t_0 . At t_0 the attenuation is zero and the impedance in Eq. (1) is not reduced. The attenuation then increases exponentially with time constant τ_{FB} to the final value of F_{FB} .

We adjust the free parameters F_{FB} , τ_{FB} and t_0 by comparing the simulated induced voltage V_{ind} with the measured one. The cavity induced voltage is measured at the RF frequency and the simulated voltage is, therefore, filtered at this frequency. At each turn, the maxima of V_{ind} from measurement and simulation are then compared. The result for 48 bunches and V_{200} of 4.5 MV is shown in Fig. 3. The first turn is without beam and thus no induced voltage. Once the beam is present, the induced voltage reaches its maximum value and is then reduced. Notice that the induced voltage is larger in the ‘long’ cavity, since it depends on the square of the cavity length [8]. The parameter F_{FB} controls the asymptotic value of the impedance reduction, which is reproduced well by the model.

With just the OTFB included in the simulations, the time dependence of the beam intensity is well reproduced, but simulated losses are two- to three times higher compared to measurements. Besides the OTFB, a beam phase loop is also active in the SPS. The phase loop corrects phase

Content from this work may be used under the terms of the CC BY 3.0 licence (© 2018). Any distribution of this work must maintain attribution to the author(s), title of the work, publisher, and DOI.

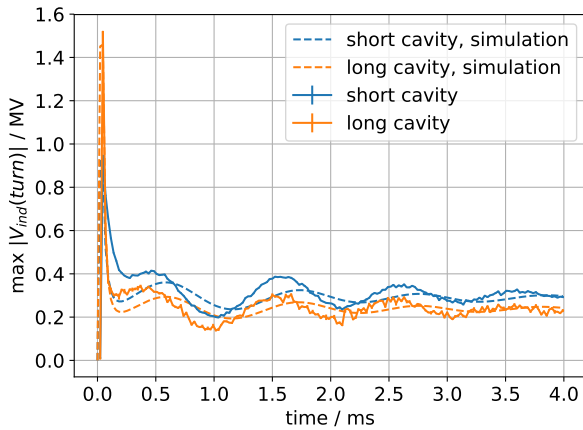


Figure 3: Comparison between measured (continuous lines) and simulated (dashed) maximum induced voltage after injection in the short and long 200 MHz TWCs.

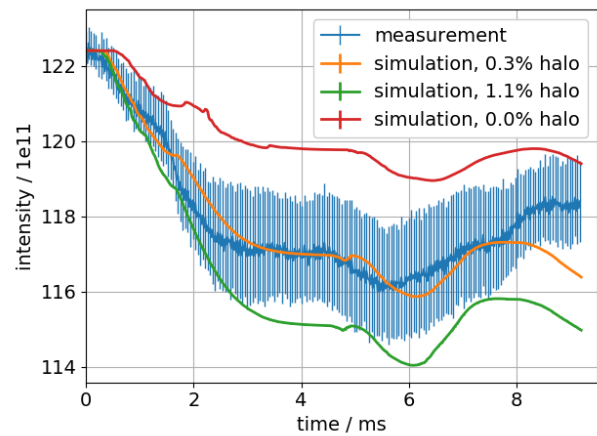


Figure 4: Measured beam intensity (blue) for a beam of 72 bunches with 1.7×10^{11} protons per bunch and V_{200} of 2.0 MV. Simulations were performed for three particle distributions with different halos.

or energy errors of the injected beam by changing the RF frequency. It compares the measured stable beam phase to its reference value. In the SPS, the beam phase is obtained by averaging over the first twelve bunches and the reference phase derived from the momentum program (without beam loading). Since the induced voltage changes the stable phase, the result is that the beam is not centered in the RF bucket. A synchronization (frequency) loop is used in the SPS to center the beam in energy. It is modeled as a frequency loop in BLoND that locks the RF frequency onto the design value.

To compare the losses in simulation to measurements, we computed the losses from the simulated bunch profiles.

LOSSES AT CAPTURE

Figure 4 shows the measured beam intensity during the first 9 ms (corresponding to about 400 turns in the SPS) for a beam of 72 bunches with 1.7×10^{11} ppb and an RF voltage V_{200} of 2.0 MV. This voltage is less than the nominal 3.5 MV and was chosen to enhance the losses at injection. The intensity quickly drops as the halo of particles, which are outside the RF bucket, drift away. After about 350 turns (8 ms) these uncaptured particles drift above or below the RF bucket of a neighboring bunch and the intensity increases again. The simulations differ in the initial macro-particle distribution used. Due to beam loading, even a distribution that would fit entirely into the ‘bare’ SPS RF bucket (0% halos) has losses of about 3%. The amount of losses increases with increasing halo, but the overall shape of the curve remains similar. As can be seen from the simulations, however, the total amount of particles lost depends strongly on the halos.

The distribution of the losses along the batch can be seen in Fig. 5, where we compute the amount of particles lost for each bunch. Already after 1 ms (43 turns) the bunches at the end of the batch have lost twice as much as those at the head, since the beam loading increases along the batch. The beam loading builds up over a distance related to the filling time of the TWCs, which is about 700 ns, covering 28

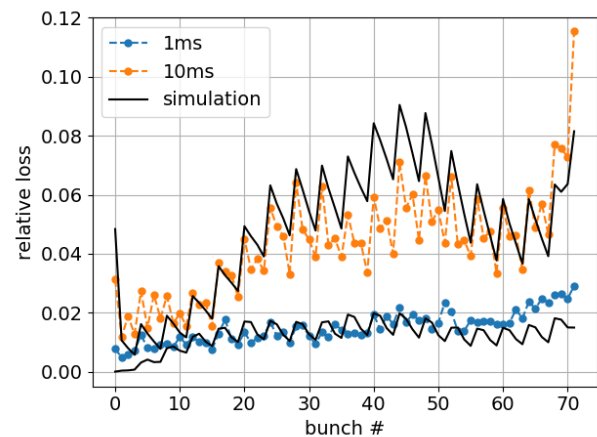


Figure 5: Measured relative particle losses along the batch at 1 ms and 10 ms after injection for the case of Fig. 4. Simulation results are shown by black lines.

bunches. Indeed, Fig. 5 shows a general increase in losses for the first 30 bunches after 10 ms. The fact that the losses are roughly constant for the first twelve bunches is due to the phase loop, which adjusts the RF frequency using the phases of the first twelve bunches.

The measured loss pattern also displays a strong modulation, with a period of four bunches. It results from an imperfect bunch splitting process in the PS, which leads to a modulation of both the bunch length and the intensity along the injected batch. In simulations with 72 identical bunches, the resulting loss pattern follows the measured pattern, but does not display the modulation. When we use a beam where the intensity of the bunches is modulated along the batch (keeping the bunch length constant), the simulated loss pattern does display the same modulation, but the variation from bunch to bunch is not as large as observed. The measured loss pattern can be reproduced in simulations only

when four bunches with different bunch lengths are used and repeated along the batch, see black curves in Fig. 5. This also shows that for losses a control of the injected bunch-by-bunch bunch length is more important than a control of the intensity variation.

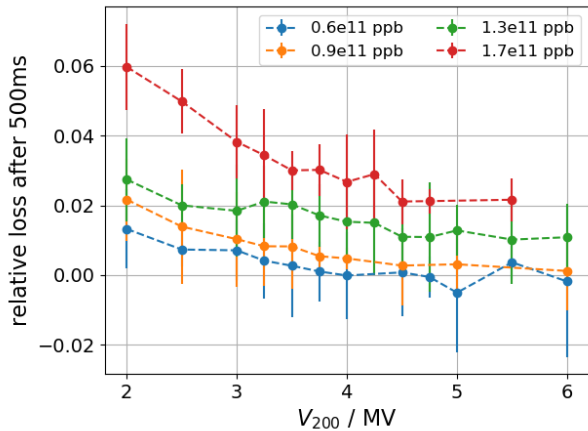


Figure 6: Measured relative particles losses for different V_{200} and different protons per bunch (ppb) for a beam of 72 bunches at 500 ms after injection. Data points joined to guide the eye.

The uncaptured beam has drifted away from the batch after 500 ms [3]. To measure the capture losses, we, therefore, compare the beam intensity at injection to the beam intensity after 500 ms. By changing the voltage V_{200} of the 200 MHz TWC at injection, the available RF bucket area is changed as well. Figure 6 shows the capture losses as a function of V_{200} for bunch intensities between $(0.6 - 1.7) \times 10^{11}$ ppb. Losses decrease for increasing V_{200} but reach a plateau value above ~ 4.5 MV. Above this voltage, the main bunch and most of its halo are captured inside the RF bucket and increasing the RF voltage V_{200} further does not reduce the capture losses (but does affect the losses on the flat-bottom, see next section). If the bunch distributions injected from the PS were not depending on intensity, the loss curves for different intensities were shifted horizontally towards higher V_{200} , since more RF voltage is needed to compensate the increased beam loading. However, Fig. 6 shows a *vertical* offset with increasing bunch intensity. With higher intensity, a larger halo is created in the PS, that cannot be captured inside the SPS RF bucket. The effect of beam loading becomes more evident for smaller V_{200} and higher intensities, because its relative effect, as compared to the main RF voltage, increases for lower V_{200} . Hence, the RF bucket area is reduced and the losses increase.

LOSSES ALONG FLAT BOTTOM

If the losses along the entire flat bottom were solely due to the particles lost at injection, Fig. 6 would suggest to use the maximum capture voltage to reduce the particle losses. If this was done right at injection, it would lead to

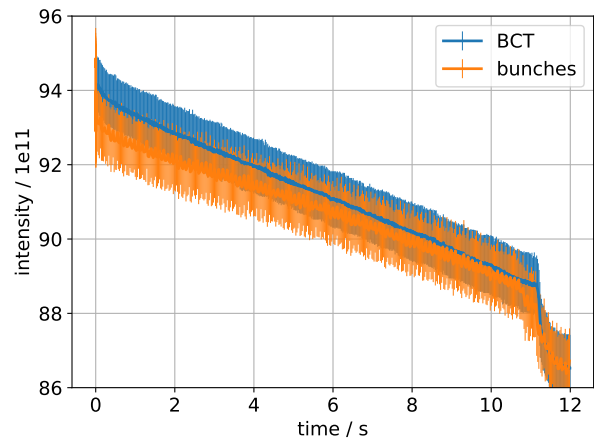
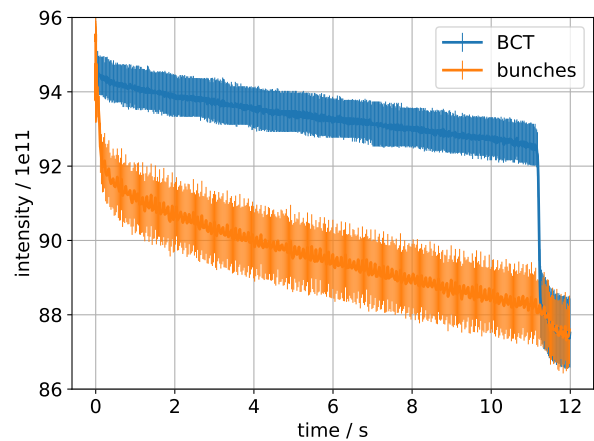


Figure 7: Measured beam intensity during 12 s. The voltage was changed from its nominal value of 4.5 MV to either 3.0 MV (top) or 7.0 MV (bottom) at 50 ms after injection.

a large emittance due to beam filamentation, which would be difficult to accelerate. Instead, we injected the beam with nominal voltage of 4.5 MV and changed the voltage 50 ms after injection during a 100 ms short ramp. At the end of the flat-bottom, another ramp was used to bring the voltage back to the nominal value. Figure 7 (top) shows the measured intensity when the voltage was decreased to 3.0 MV. Since the RF bucket area is reduced, the bunches lose particles and their intensity decreases. But they are still present in the SPS, since the intensity measured by the BCT does not decrease. Notice that the bunches continue to lose particles along the flat-bottom. When the RF bucket area is increased by increasing the voltage to 7.0 MV, see Fig. 7 (bottom), the bunches initially lose significantly less particles. However, the particle loss rate along the flat bottom is increased by about 50% and the final intensity after acceleration is 1% less compared to the case when the voltage was reduced.

These findings can be explained by the limited momentum aperture of the SPS. By increasing V_{200} , the momentum acceptance of the RF bucket is increased. Particles with large momentum-offsets now touch the momentum aperture and get lost. To further study the effect of the momentum

Content from this work may be used under the terms of the CC BY 3.0 licence (© 2018). Any distribution of this work must maintain attribution to the author(s), title of the work, publisher, and DOI.

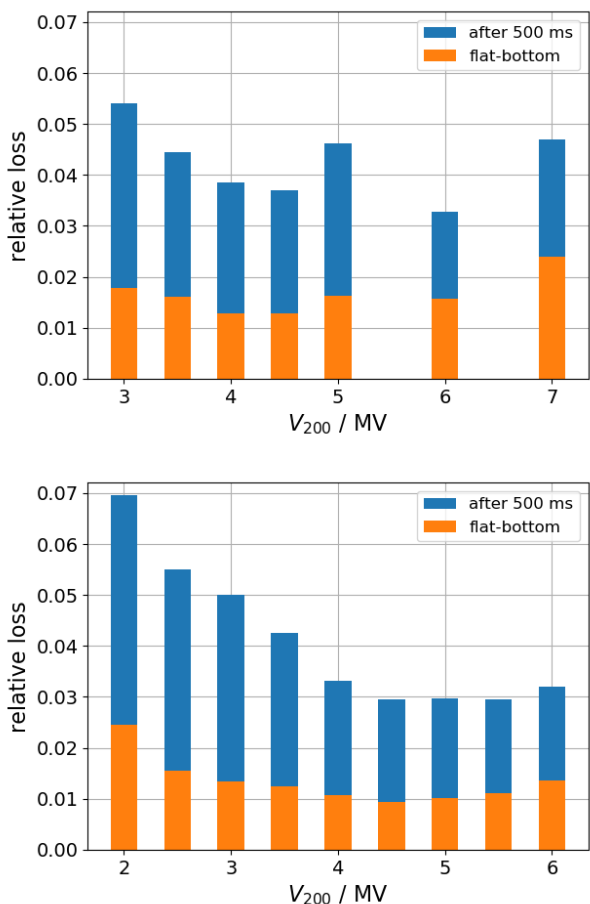


Figure 8: Measured relative particle losses at 500 ms after capture (blue) and during the following 9.5 s of flat bottom (orange) for a beam of 48 bunches in nominal optics ‘Q20’ (top) and an optics with larger momentum aperture ‘Q22’ (bottom).

aperture on the flat-bottom losses, we compared the losses along an 11.1 s long flat-bottom with nominal optics ‘Q20’ to losses in the optics with larger momentum aperture ‘Q22’. This optics has an increased transition energy and, hence, a larger RF bucket area for a given RF voltage. Equivalent voltages that yield the same RF bucket area are related by $V_{Q22} \approx 0.81V_{Q20}$. For equivalent voltages, we observed a reduction in losses by about 1% for intensities below and up to nominal intensities. For higher intensities, and increased beam loading, the losses were comparable.

Figure 8 shows the losses for a beam of 48 bunches with 1.3×10^{11} ppb and a reduced transverse emittance in both optics for different voltages. The losses at 500 ms after injection decrease for higher RF voltage, which is consistent with the increased RF bucket area capturing more halo particles. A minimum in total losses occurs for the nominal 4.5 MV. For higher voltages, the total losses increase again due to the increased loss along the flat bottom. In addition, the flat-bottom losses in the nominal ‘Q20’ optics at 7.0 MV are

about twice as high for the equivalent voltage of 5.7 MV in the ‘Q22’ optics with increased momentum aperture.

CONCLUSION

Particle losses in the SPS are a bottleneck to reach the beam intensities required for the HL-LHC era. Here, we studied two sources of losses that occur at the SPS flat bottom. The first loss occurs at the PS-to-SPS bunch-to-bucket transfer. Halo particles outside the SPS RF bucket are lost. This effect increases with intensity both due to the increased SPS beam loading and bunch distributions from the PS with larger halos. Reproducing these losses in simulations requires modeling the LLRF system. We modeled the effect of the one-turn feedback by its effective impedance reduction. Quantitative agreement with measurements was obtained by including the phase loop as well as the frequency loop. The simulations show a strong sensitivity of the capture losses on the initial bunch distribution.

With an accurate simulation model of the capture losses, we simulated the future high-luminosity beam of 72 bunches with 2.6×10^{11} ppb. With the present, not upgraded, SPS this intensity would lead to capture losses of 6%. Several improvements to the SPS are foreseen within the LIU project. They include the longitudinal impedance reduction of vacuum flanges, an upgrade of the OTFB to obtain an impedance reduction of -26 dB (compared to the present -15 dB), a beam phase loop taking into account all 72 bunches (instead of just twelve), and shorter lengths of the main RF cavities to reduce beam loading. When these future parameters are used in simulations, the capture losses are below 2%.

While the capture losses can be reduced by increasing the RF voltage, the losses along the entire flat bottom are not reduced. One reason for this was found to be the limited momentum aperture. We measured the flat-bottom losses for beams in nominal optics and an optics with increased momentum aperture. For high voltages the flat-bottom losses are reduced by 50% in the optics with larger momentum aperture (‘Q22’). A physical aperture limitation for the ‘Q20’ optics was recently discovered [11], and will be fixed during the upcoming long shutdown to help to improve the flat-bottom losses. RF noise as another source of flat-bottom losses is presently under investigation.

The effect of the momentum aperture limitation is currently not implemented in the simulation code. While this is sufficient for the simulation of the capture losses, it needs to be included to simulate the beam behavior at longer time scales.

ACKNOWLEDGMENT

It is a pleasure to acknowledge the help of our colleagues P. Baudrenghien, B. Goddard, T. Bohl, V. Kain, G. Papotti as well as the PS and SPS operators, the SPS injection losses working group, and the BLonD development team. The help of I. Karpov and P. Kramer during the measurement of the induced voltage is also appreciated.

REFERENCES

- [1] H. Damerau *et al.*, “LHC Injectors Upgrade, Technical Design Report, Vol. I: Protons,” Tech. Rep. CERN-ACC-2014-0337, Dec. 2014. <https://cds.cern.ch/record/1976692>
- [2] H. Bartosik *et al.*, “Beam Dynamics Observations of the 2015 High Intensity Scrubbing Runs at the Cern SPS,” in *Proc. of International Particle Accelerator Conference (IPAC'16)*, (Busan, Korea), Busan, Korea, Jun. 2016, pp. 648–651. doi: 10.18429/JACoW-IPAC2016-MOPOR022.
- [3] A. Lasheen, H. Damerau, J. Repond, M. Schwarz, and E. Shaposhnikova, “Improvement of the longitudinal beam transfer from PS to SPS at CERN,” presented at the IPAC 2018, TH-PAF042, unpublished, Vancouver, BC, Canada, 2018.
- [4] J. E. Campelo *et al.*, “An Extended SPS Longitudinal Impedance Model,” in *Proceedings, 6th International Particle Accelerator Conference (IPAC 2015)*, Richmond, Virginia, USA, May 2015, pp. 360–362. <http://accelconf.web.cern.ch/AccelConf/IPAC2015/papers/mopje035.pdf>
- [5] *CERN Beam Longitudinal Dynamics code BLonD*. <https://blond.web.cern.ch/>
- [6] H. Timko *et al.*, “Longitudinal transfer of rotated bunches in the CERN injectors,” *Phys. Rev. ST Accel. Beams*, vol. 16, no. 5, p. 051004, 2013. doi: 10.1103/PhysRevSTAB.16.051004.
- [7] *SPS longitudinal impedance model*. <https://gitlab.cern.ch/longitudinal-impedance/SPS>
- [8] G. Dôme, “The SPS acceleration system travelling wave drift-tube structure for the CERN SPS,” no. CERN-SPS-ARF-77-11, 26 p, May 1977. <https://cds.cern.ch/record/319440>
- [9] P. Baudreghien and G. A. Lambert, “Reducing the impedance of the travelling wave cavities: feed-forward and one turn delay feed-back,” in *10th Workshop on LEP-SPS performance*, Charmonix, France, 2000, pp. 94–101. <https://cds.cern.ch/record/485863>
- [10] H. Timko, “Simulation of longitudinal intensity effects with LLRF system (BLonD),” presented at the ICFA mini-Workshop on Impedances and Beam Instabilities in Particle Accelerators, Benevento, Italy, 2017.
- [11] V. Kain *et al.*, “Momentum aperture and flat bottom losses,” presented at the SPS injection losses review, CERN, Nov. 2017.

DYNAMIC VACUUM SIMULATION FOR THE BRing

Peng Li¹, Lars Bozyk², Z.Q Dong¹, J.C. Yang¹, Min Li¹, C. Luo¹

¹Institute of Modern Physics, Chinese Academy of Sciences, Lanzhou 730000, China

²GSI Helmholtzzentrum für Schwerionenforschung GmbH, Planckstraße 1, 64291 Darmstadt, Germany

Abstract

A new large scale accelerator facility is being designed by Institute of Modern Physics (IMP) in Lanzhou, which is named as the High Intensity heavy-ion Accelerator Facility (HIAF). This project consists of ion sources, Linac accelerator, synchrotrons (BRing) and several experimental terminals. During the operation of BRing, the heavy ion beams will be easily lost at the vacuum chamber along the BRing and in turn leads to an increase in beam loss rate. In order to control the dynamic vacuum effects induced by the lost beams and design the collimation system for the BRing in the HIAF project, a newly developed simulation program (ColBeam) and GSI's simulation code StrahlSim are both conducted and the dynamic vacuum simulation result is calculated by the StrahlSim. According to the simulation result, 3×10^{11} ppp particles is the maximum beam intensity can be extracted for the current designed BRing vacuum system and collimation system. Higher beam intensity can reach to 5×10^{11} ppp when the Non Evaporable Getter (NEG) coating technology must be implemented for the dipole and quadrupole chamber.

INTRODUCTION

The HIAF project consists of ion sources, Linac accelerator, synchrotrons and several experimental terminals. The Superconducting Electron-Cyclotron-Resonance ion source (SECR) is used to provide highly charged ion beams, and the Lanzhou Intense Proton Source (LIPS) is used to provide H_2^+ beam. The superconducting ion Linac accelerator (iLinac) is designed to accelerate ions with the charge-mass ratio $Z/A=1/7$ to the energy of 17 MeV/u. Ions provided by iLinac will be cooled, accumulated and accelerated to the required intensity and energy in the Booster Ring (BRing), then fast extracted and transferred either to the external targets or the Spectrometer Ring (SRing) [1]. The layout of the HIAF project is shown in Fig. 1.

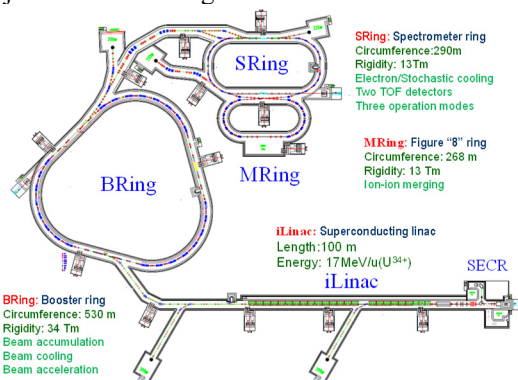


Figure 1: Layout of HIAF project.

BRing AND ITS VACUUM SYSTEM

BRing Lattice and Basic Parameters

The circumference of the BRing is 569.1 meters with three arc sections acts as a charge separator providing a peaked distribution of ionization beam loss and with three long straight sections to provide adequate space for the injection, extraction system and the RF system. A number of different lattice structures have been investigated with respect to the fraction of ions controlled by the collimators and the collimator distance from the beam edge. The final chosen doublet structure assured an almost hundred percent control of single ionized beam ions without affecting the machine acceptance. The beta function and dispersion function of one super cell are shown in Fig. 2.

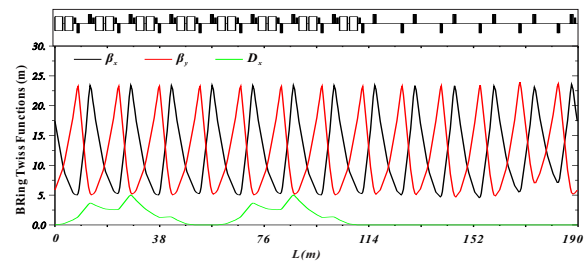


Figure 2: The beta and dispersion function of BRing.

The dipole magnets of BRing adopt traditional technology room temperature yoke magnet and the maximum magnetic field can reach up to 1.6 T. Eight bumpers are divided into two groups, which one group in horizontal and the other group in vertical plane, together with a tilted electrostatic septum are used for the two-plane painting injection. Two kickers located in one straight section are used for the fast extraction. Moreover, the stored ions can be exacted slowly and homogeneously by the slow extraction system consisted of sextupoles, RF excitation and electrostatic septum. An RF cavity with a range of frequency from 0.2MHz to 1.4MHz installed in another dispersion-free straight section is used to capture and accelerate ions.

The BRing dipole magnetic field data cycle of the reference beam uranium $^{238}U^{35+}$ for the fast extraction is shown in Fig. 3.

Content from this work may be used under the terms of the CC BY 3.0 licence (© 2018). Any distribution of this work must maintain attribution to the author(s), title of the work, publisher, and DOI.

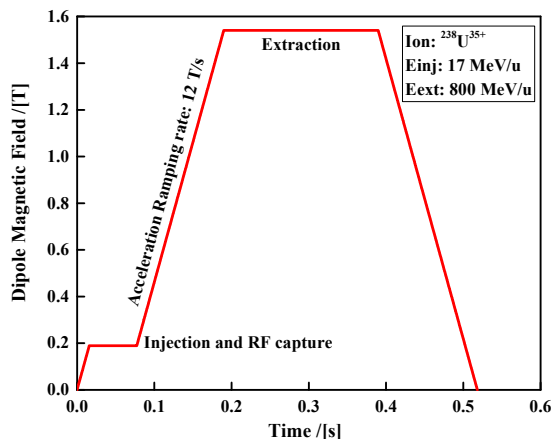


Figure 3: dipole magnetic field data cycle of the $^{238}\text{U}^{35+}$ for the fast extraction mode.

BRing Vacuum System Design

The total inner surface of the BRing vacuum system is about 450 m² and total volume is 11000 L. The all-metal gate valves divide into six sections for separate equipment installment and replacement. All ring components of these sections have to be manufactured of UHV-compatible materials to allow bake-out at the temperature of 300°C [2]. A baking system with the temperature at 300°C for at least 24h will be necessary to obtain a stainless steel outgassing rate of low 10⁻¹³ to 10⁻¹⁴ Torr.l.s⁻¹.cm⁻² as required for BRing.

The evacuation of the BRing vacuum system from atmospheric pressure is done with oil-free roughing and turbo-molecular pumps down to about 10⁻⁸ mbar. Sputter ion pumps (SIP), titanium sublimation pumps (TSP) and NEG pumps are distributed around the synchrotron ring to reach the designed vacuum pressure goal. Sputter ion pumps with pumping speeds of 200~400 l/s remove non-getterable gases such as methane and argon. Titanium sublimation pumps have a high capacity for hydrogen at very low pressure, where the residual gas is mainly H₂ (90%). The NEXTorr is an extremely compact pump which integrates sputter ion pump and NEG pump technologies with larger pumping speed and capacity to sorb gases very effectively down to the XHV level [3]. A schematic drawing of the vacuum layout of one super period of BRing is shown in Fig. 4.

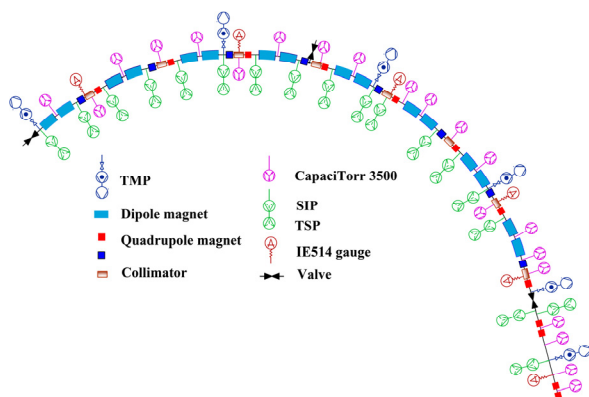


Figure 4: Schematic vacuum layout of one super period of BRing.

BEAM LOSS DISTRIBUTION

Beam Loss Distribution

In order to simulate the charge exchange driven by the beam loss and dynamic vacuum effects in heavy ion synchrotrons, GSI firstly developed a program package named StrahlSim during the past few years [4]. With the scientific collaboration between GSI and IMP, a new program package (ColBeam) designed for optimizing the collimation efficiency is developed by taking different types of errors into account in the accelerator.

With a constant static vacuum pressure around the ring, the beam trajectory for one electron-loss $^{238}\text{U}^{36+}$ is illustrated in Fig. 5(a) with the parameters shown in Table 1. The loss position and intensity of the charge exchanged particle at each point is counted and shown in Fig. 5(b). Semi logarithmic coordinate system is employed to illustrate the beam loss intensity at each position along the BRing. In Fig. 5 (a), the X-axis is the longitudinal positions of the BRing and Y-axis is the logarithmic value of the lost beam intensity at each position.

Table 1: Basic Parameters for Simulation

Reference ion	$^{238}\text{U}^{35+}$
Energy (MeV)	17
Transverse Tune (Qx/Qy)	9.47/9.43
Horizontal emittance (pi mm.mrad) 5-sigma	100
Vertical emittance (pi mm.mrad) 5-sigma	60
Momentum deviation for $^{238}\text{U}^{32+}$	$\sim 10^{-4}$
Charge exchanged ion (Coasting beam)	$^{238}\text{U}^{34+}$ and $^{238}\text{U}^{36+}$

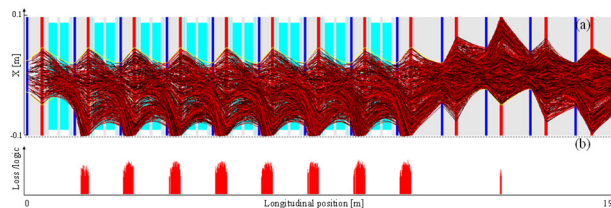


Figure 5: Simulation results for one capture-loss $^{238}\text{U}^{36+}$: (a) Beam loss trajectory. (b) Beam losses distribution. Loss/logic means: the logarithmic value of the lost beam intensity at each position.

DYNAMIC VACUUM SIMULATION

Static Vacuum Pressure Profile

Before the dynamic simulation starts, the static vacuum pressure profile along the BRing is calculated by the StrahlSim. The pressure in the vacuum system of the BRing is initialised with a uniform start value along the ring. For the calculation, a total outgassing rate for stainless steel of 7×10^{-12} Torr.l.s⁻¹.cm⁻².

The static pressure profile of the BRing calculated by the StrahlSim is shown in Fig. 6 with and without NEG coating.

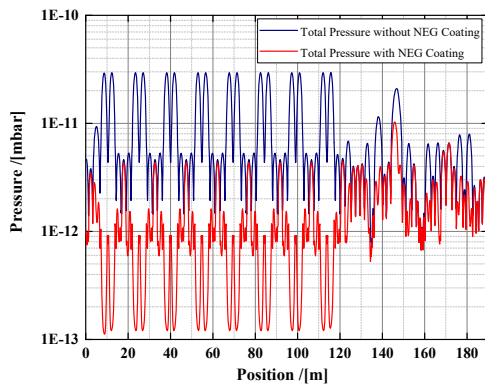


Figure 6: Static pressure profile along the BRing with and without NEG coating.

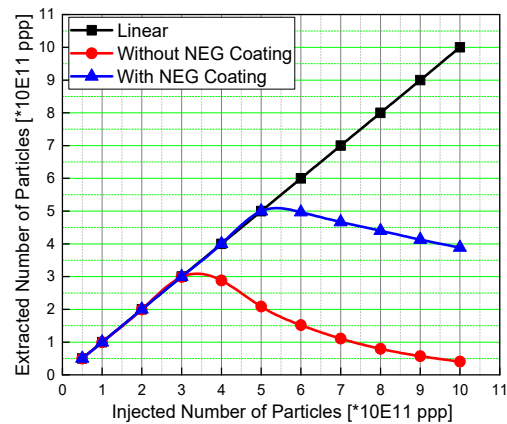


Figure 8: Extracted particle number evolution with injected number of particles.

DYNAMIC VACUUM SIMULATION RESULT

Without ionization loss, the amount of extracted particles linearly depends on the number of injected particles [5]. Due to the dynamic vacuum effects, the transmission decreases with increasing beam intensity. Above a specific number of injected particles, the number of extracted particles decreases.

Without any systemic loss and NEG coating, 3×10^{11} ppp particles are injected into the BRing each time and the pressure is increased to 1×10^{-11} mbar to reach the equilibrium state. The number of particles evolution and the pressure in the BRing with beam intensity 3×10^{11} ppp is shown in Fig. 7.

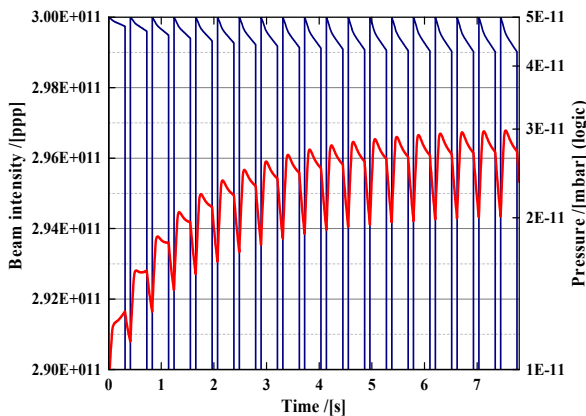


Figure 7: Extraction particle number and the pressure evolution with the synchrotron cycles for the injection beam intensity is 3×10^{11} ppp.

When the injection particles below 3×10^{11} ppp, the dependence of extraction particle number is linear because the desorption molecules can be pumped out. However, with the increasing of the injection particles numbers, the desorption molecules induced by the lost beam number is increasing and can't be pumped out as quickly as possible. Then the vacuum pressure in the synchrotron will not be stable and the ionization rate is increasing. The maximum extraction particle number in the BRing with the injection particle number can be seen in Fig. 8.

CONCLUSION

Beam loss distribution induced by the charge exchanged in the BRing is calculated and present in this paper by using the HIAF simulation code ColBeam which have been verified by the GSI's simulation code StrahlSim. Dynamic vacuum evolution has been simulated by implemented of the StrahlSim based on the current vacuum system design to check the extraction particle number 3×10^{11} ppp whether it can be achieved or not. It is concluded that the design particle number goal can be achieved based on the current vacuum system and collimator system design. More extraction particle number in the BRing can be achieved by implemented the NEG coating technology on the dipole and quadrupole vacuum chamber.

ACKNOWLEDGEMENT

We thank Dr. Peter Spiller (GSI) for providing P. L. an opportunity to work at GSI to learn the collimation. Special thanks to Dr. Lars Bozyk for his directions on collimator design and provide the StrahlSim simulation code. This work is supported by the National Natural Science Foundation of China (Project No. 11675235) and the Youth Innovation Promotion Association of Chinese Academy of Sciences 2016364.

REFERENCES

- [1] "HIAF Conceptual Design Report", unpublished.
- [2] "HIAF BRing vacuum system design report", IMP internal report, 2017.
- [3] NEXTORR_datasheets_2017, https://www.saesgetters.com/sites/default/files/NEXTORR_datasheets_2017_web.pdf
- [4] C Omet, P. Spiller, J. Stadlmann, and D.H.H. Hoffman, *New J. Phys.*, vol. 8, p. 284, 2006.
- [5] L. Bozyk, P. Spiller, "Ionization loss and dynamic vacuum in heavy ion synchrotrons", in *Proc. 8th International Particle Accelerator Conference (IPAC'17)*, Copenhagen, Denmark, 2017, pp. 2201-2204, doi:10.18429/JACoW-IPAC2017-TUPVA056

EFFECT OF THE EXTRACTION KICKERS ON THE BEAM STABILITY IN THE CERN SPS

A. Farricker*, M. Beck, J. Repond, C. Vollinger
CERN, Geneva, Switzerland

Abstract

Longitudinal beam instability in the CERN SPS is a major limitation in the ability to achieve the bunch intensities required for the goals of the High-Luminosity LHC project (HL-LHC). One of the major drivers in limiting the intensity of the machine is the broadband contribution to the beam-coupling impedance due to the kicker magnets.

The extraction kickers (MKE) discussed in this paper are known to give a significant contribution to the overall longitudinal beam-coupling impedance.

We present the results of bench measurements of the MKE's impedance to determine the accuracy of electromagnetic simulation models from which the impedance model—used for beam dynamics simulations—is constructed. In addition, we discuss the feasibility and implementation of beam measurements that can indicate the contribution of the MKE magnets to the longitudinal beam-coupling impedance of the SPS.

INTRODUCTION

Instabilities during the acceleration cycle in the Super Proton Synchrotron (SPS) are a major limitation in achieving the goal of providing nominal bunch intensities of 2.3×10^{11} protons per bunch (ppb) to the High-Luminosity LHC (HL-LHC). In order to achieve this level of beam intensity a major upgrade of the injector chain in the form of the LHC Injectors Upgrade (LIU) project has been undertaken [1].

In terms of the upgrades to the SPS this includes; upgrading of the existing RF systems, upgrading of the existing slow extraction system, and impedance reduction through the shielding of vacuum flanges, all of which is designed to enable the production of stable HL-LHC type beams in the SPS. In addition to this, the identification of existing impedance and minimisation of the impedance of newly installed equipment play a key roll in developing a detailed understanding of what limits the performance of the SPS in terms of beam instability.

Many sources of impedance in the SPS have been identified and characterised. These sources of impedance have then been used to identify in particle tracking simulations which particular sources are limiting. These simulations have been extensively compared with beam measurements and indicate that the impedance model is on the whole a fair representation of the machine—or at least of the components which currently dominate the behaviour of the SPS beam. This paper focuses on the longitudinal plane.

In the year 2016, a detailed study of the properties of the reactive (imaginary) components of the SPS impedance

was carried out through the measurement of the quadrupole frequency shift [2]. Comparisons to the impedance model using the beam tracking code BLOD [3] showed a significant difference which could be attributed to a low frequency (350 MHz) resonance with an R/Q of order $3 \text{ k}\Omega$. The ultimate aim of this measurement is to identify the source of this missing impedance.

One possibility could be an underestimated contribution attributed to the kicker magnets. The most significant contributors to those are the injection kickers (MKP) and the extraction kickers (MKE) which are discussed in detail here.

IMPEDANCE OF THE EXTRACTION KICKERS

In the SPS the extraction systems utilise a combination of septa and kicker magnets. In the current layout, there are seven MKE kickers; four in sextant four and three in sextant six. Prior to the introduction of impedance reducing measures, the MKE was the dominant contribution to the machine impedance (neglecting the 200 MHz RF cavities) and was a cause of single bunch instability through the loss of Landau damping. In 2007, the MKE magnets were modified to reduce the beam coupling impedance through the use of serigraphy (conducting strips that allow a reduced impedance path for the image currents) to help reduce the impedance as well as the beam induced heating [4]. Details of this can be found in Ref. [5] and images of the ferrite core of the magnets are shown in Fig. 1 where the painted serigraphy pattern is clearly visible.

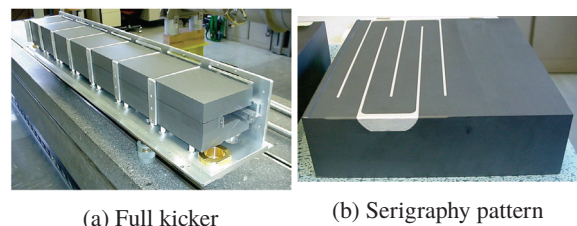


Figure 1: Pictures of the MKE ferrite core showing the core assembly and serigraphy pattern [5].

Simulations

The MKE kicker was remodelled in CST [6] making several changes to the original model developed in 2013 [7]. These changes include:

- The addition of the ground bar.
- Correction to the layout of the serigraphy.

* aaron.farricker@cern.ch

- Serigraphy modelling using the thin panel material in CST MWS.

These relatively small changes have a significant impact on the impedance found when performing wakefield simulations using the wakefield solver in CST MWS. The large difference between the two models is shown in Fig. 2.

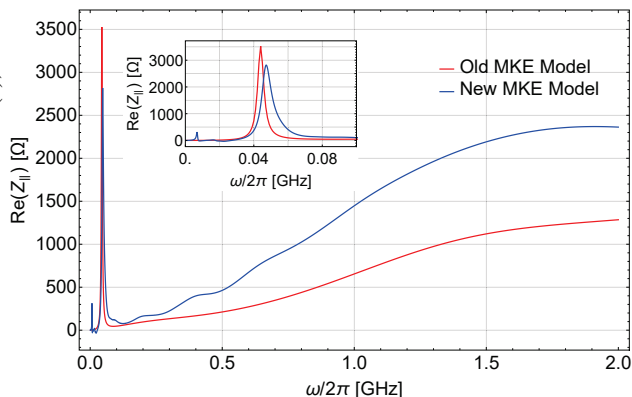


Figure 2: Simulated real part of longitudinal impedance of the MKE kicker as a function of frequency.

The key differences in the impedance are the frequency and width of the serigraphy peak (at around 50 MHz) and the general increase of the broadband impedance by a factor of approximately two. Considering that the MKE is one of the most dominant sources of resistive impedance in the SPS (behind only the 200 MHz cavities and the MKP kickers), this difference becomes concerning. One issue with the new model is that it is unable to reproduce the heating of the kicker ferrites, which has been observed during operation in the SPS.

The heating is highly dependent on the frequency of the serigraphy's resonant peak as an overlap of the resistive impedance with beam spectrum peaks produces heating. The resonant frequency is highly dependent on the ferrite properties, especially on the relative permittivity ϵ_r . The value for high frequencies is constant and around 12. For lower frequencies however, it is probably growing as found in Ref. [5]. Investigations of the correct values are ongoing and simulations here use a constant ϵ_r of 12. In order to determine the contribution of the MKE kicker to the broadband impedance measurements with the coaxial wire method described in Ref. [8] were undertaken.

In Figs. 3 and 4 the good general agreement between the new MKE model and the measured results up to a frequency of 1.5 GHz can be seen. This frequency range is the main area of interest for beam dynamics and heating as this is the region which overlaps with the beam spectrum during normal operation of the SPS. The disagreement at higher frequencies—in particular the clear resonance—is an artifact of the measurement setup introduced by flanging the structure off to enable it to be measured. In addition, the new model accurately reproduces the frequency and peak impedance of the serigraphy peak which is expected to be the dominant contributor to heating of the serigraphed MKE.

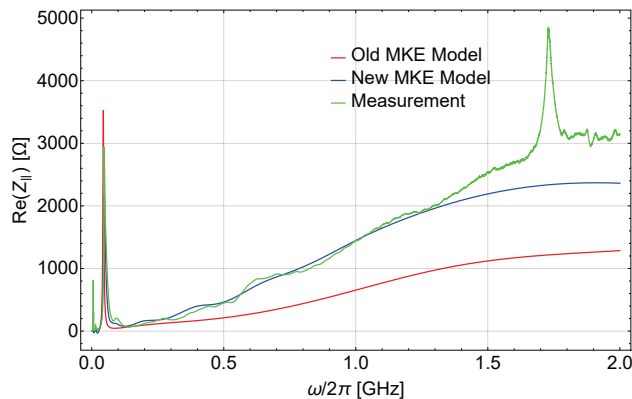


Figure 3: Comparing the simulated longitudinal impedance to the measured impedance. (The measured impedance is calculated using the log formula [8]).

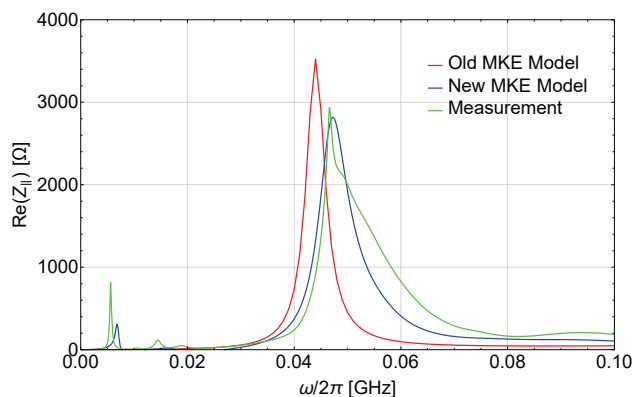


Figure 4: Detailed look at the serigraphy resonance peak shown in Fig. 3.

But as wakefield simulations are compared to wire measurements, the simulated resonance is expected to be lower because the wire introduced for the measurement influences the resonance frequency.

The effect of the significant increase in the contribution of the kickers to the broadband component of the impedance model has to be investigated with respect to the impact on the expected performance in the post-LIU era and the ability to reach the required 2.3×10^{11} ppb with the currently planned improvements.

IMPACT ON THE INSTABILITY THRESHOLD

To predict future intensity threshold and to study devices suspected of lowering the stability in the SPS, the knowledge of the machine longitudinal impedance is crucial. The full post-LIU impedance model [1,9–12] contains various broad- and narrow-band resonances with frequencies up to 4 GHz, including the resistive wall impedance.

Due to its many individual contributors, the model is complex. However, three main categories can be drawn. First, the biggest contribution to the impedance are the travelling-wave RF cavities at 200 MHz with the accelerating and

HOM bands. The beam-coupling impedance in the accelerating band will be reduced by 26 dB after the upgrade of the one-turn delay feedback. A factor three reduction of the impedance of the HOM band at 630 MHz is assumed to be obtained. The second contributor are the vacuum flanges and more generally all vacuum elements which contribute mainly to higher frequencies (>1 GHz). The LIU impedance model assumes shielded QF type vacuum flanges between beam position monitors and magnets and also in the short straight sections. The model contains 29 sector valves of type A (VVSA) and 38 sector valves of type B (VVSB). In addition 25 unshielded pumping ports remain in the model as well. The third and last main contributor are the kicker magnets with seven MKE, 16 MKP and seven other kickers used for tune measurements and dumping of the beam present in the SPS. Their impedance is broad-band and can have a major impact on the single-bunch behaviour and necessarily on the stability of the beam. With the SPS being pushed already to its limits [13], every contribution to the impedance can have a significant impact on the stability. Single resonances contributing to an instability are sometimes difficult to extract.

As stated before, the impedance of the MKE has been re-evaluated and found with a larger broadband impedance. The impact of this additional impedance is studied by means of particle tracking simulations using the code BLoND, developed in the RF group at CERN. Simulations are done for trains of 48 bunches spaced by 25 ns matched with the RF bucket including intensity effects. The LHC proton beams in operation contain 72 bunches but similar stability limits were obtained in simulation with a batch of 48 bunches, which allows the simulation time to be reduced. The beam distribution is chosen in agreement with measurements. Beam-loading with HL-LHC intensity limits the maximum voltage in the 200 MHz RF cavities, V_{200} , to 10 MV; this value is used as a voltage limit in the simulations for all intensities. The 800 MHz RF voltage is fixed to $V_{800} = 0.1 \times V_{200}$ in bunch-shortening mode since it provides increased stability at SPS flat top [1, 14, 15]. The oscillations of the bunch length averaged over the entire batch are used to separate a stable beam from an unstable one.

Figure 5 shows the intensity threshold for the updated and previous model of the MKE impedance. A significant reduction of the threshold is observed for the newly found impedance decreasing the beam stability margin gained by the impedance reduction campaign. This reduction is significant enough that the already proposed impedance reductions may require expanding to encompass more machine elements. To regain margin, it could become necessary to enlarge the scope of the impedance reduction campaign to known contributors to the instability threshold which include the MKP kickers, the VVSA/B sector valves and unshielded/nonconforming pumping ports.

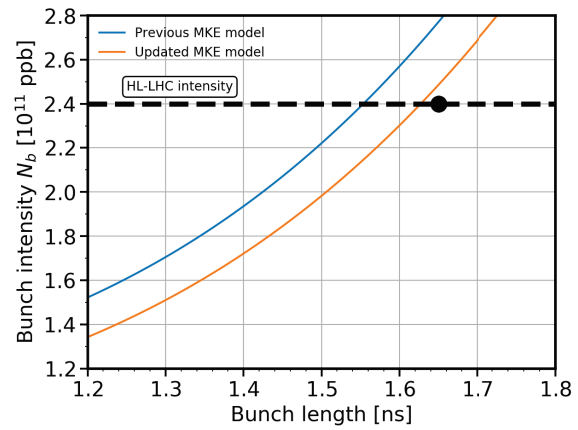


Figure 5: Stability threshold at SPS flat top for a batch of 48 bunches spaced by 25 ns with the previous and updated impedance models of MKE. A significant reduction on intensity threshold is witnessed using the latest MKE impedance model.

BEAM MEASUREMENTS

It is currently not possible to directly measure the intensity threshold in the SPS with beams meeting the HL-LHC requirements and hence infer the impact of the kickers by comparison to predictions. A method that theoretically can determine the kicker impedance with beam is proposed as an alternative.

We propose to measure the resistive component of the impedance through the measurement of the synchronous phase shift similar to what was done in 2004 [16]. In these measurements the RF system was used to define the phase shift. In the proposed measurement two bunches; one of low intensity (reference bunch) and one of high intensity (test bunch) would be used and the relative phase difference between the two will be used to define the synchronous phase shift.

In a single RF system without acceleration, feedback or feedforward, the synchronous phase, ϕ_s is defined by

$$\sin \phi_s = \frac{U}{eV}, \quad (1)$$

where U is the energy lost per turn per particle and V is the amplitude of the RF voltage. By measuring the synchronous phase it is possible to obtain the total energy lost per turn by a bunch. The energy lost by a bunch per turn is directly related to the bunch properties and the impedance of the machine. It can be calculated analytically by

$$U_b = -e^2 N k = -e^2 N \sum_n k_n(\sigma). \quad (2)$$

k_n is the loss factor [17] which for a Gaussian bunch and longitudinal impedance $Z_n(\omega)$ is

$$k_n(\sigma) = \frac{\omega_0}{\pi} \sum_{p=0}^{\infty} \Re[Z_n(p\omega_0)] \exp[-(p\omega_0\sigma)^2]. \quad (3)$$

Content from this work may be used under the terms of the CC BY 3.0 licence (© 2018). Any distribution of this work must maintain attribution to the author(s), title of the work, publisher, and DOI.

N is the number of particles per bunch, σ is the RMS bunch length and ω_0 the revolution frequency of the beam. Equations (1) and (2) link the resistive component of the impedance to the synchronous phase shift, theoretically allowing the contribution of the MKE kicker to be determined. These measurements are complementary to those probing the reactive component of the impedance [2].

BLoND Simulations

To test the feasibility of this measurement, the BLoND code was used. In these simulations the bunches are modelled with a binomial bunch distribution with an exponent of 1.5 and the full SPS impedance model is used. The bunch length σ and number of protons per bunch have been varied from 3–4.5 ns (4σ) and 0.8×10^{11} to 2.8×10^{11} respectively. The final parameter is the voltage in the 200 MHz RF cavities. Lower voltages allow for larger synchronous phase shifts, see Eq. (1), but reducing the bucket area ultimately limits the achievable intensities. In the case of using lower voltages the optics chosen also play a role in defining the bucket area as it depends on the transition energy.

By computing the expected synchronous phase shift and only varying the contribution from the MKE kickers, the dependence on the broadband impedance is obvious. Figure 6 shows the difference in the expected synchronous phase shift from the two MKE models for a bunch length of 3 ns. At high intensity with short bunch lengths and low RF voltage there is a significant difference in the expected phase shifts. Also, this shift is relatively small and in measurement with beam it may not be possible to distinguish the difference.

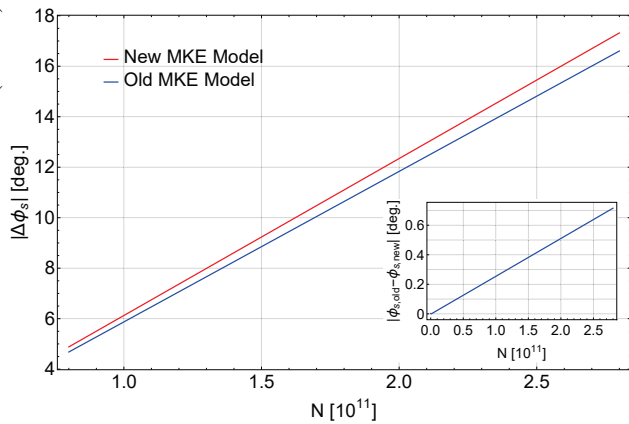


Figure 6: Synchronous phase shift as a function of intensity at $4\sigma = 3.0$ ns with $V_{200} = 2$ MV from BLoND with Q20 optics. The full SPS impedance model is included, only changing the MKE model used.

Preliminary Beam Measurements

To perform the beam measurement, a method of referencing the synchronous phase shift is required. Here two bunches of equal bunch length—one at low intensity (reference bunch) and one at high intensity (test bunch) are used. By doing so, a linear dependency of the relative phase shift

between the two bunches is ensured and the absolute phase shift can be extrapolated.

In order to perform this measurement, it must be ensured that the bunches are far enough apart not to be influenced by the longitudinal long range wakefields. To achieve this, the bunches are maximally spaced in the sub-cycle of the Proton Synchrotron (PS), about one tenth of the SPS length which is more than adequate for the purposes of the measurement.

The profiles of the two bunches are then recorded simultaneously on a single frame of a 25 ps sampling oscilloscope. At each acquisition 250 frames are taken at intervals of every 360 SPS turns and for each frame the bunch length and position is calculated and the relative phase (at 200.22 MHz) is then determined.

The measurements have been performed with a reference bunch intensity of $0.5\text{--}0.6 \times 10^{11}$ ppb and test bunch intensities in the range of $0.8\text{--}2.5 \times 10^{11}$ ppb. Two bunch lengths have been investigated; 3.2 ns and 3.6 ns with a 200 MHz cavity voltage of 2.5 MV.

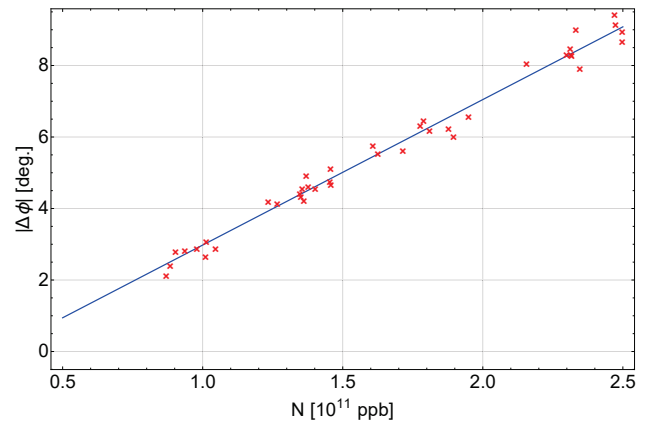


Figure 7: Relative phase shift between the reference and test bunches in the SPS using $V_{200} = 2.5$ MV and $4\sigma = 3.6$ ns.

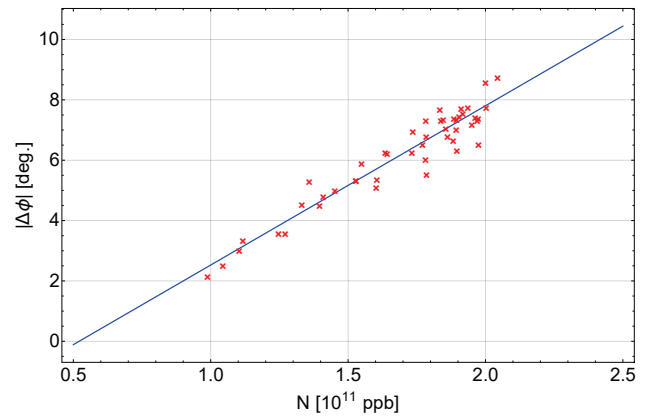


Figure 8: Relative phase shift between the reference and test bunches in the SPS using $V_{200} = 2.5$ MV and $4\sigma = 3.2$ ns.

The data shown in Figs. 7 and 8 clearly indicate the linear dependence of the synchronous phase shift on bunch intensity. The phase shift gradients found are 0.41 and

0.52 deg./10¹⁰ corresponding to an energy loss per turn of 17.9 and 22.7 keV/10¹⁰, respectively. The data for the longer bunch length have less variation due to a more consistent bunch length produced earlier in the accelerator chain. The relatively high intensities used in the 3.2 ns measurements result in a large bunch-by-bunch variation in bunch length. In addition it was not possible to exceed 2.0×10^{11} ppb due to limitations in the injectors. The measured data are compared with BLoND simulations in Fig. 9.

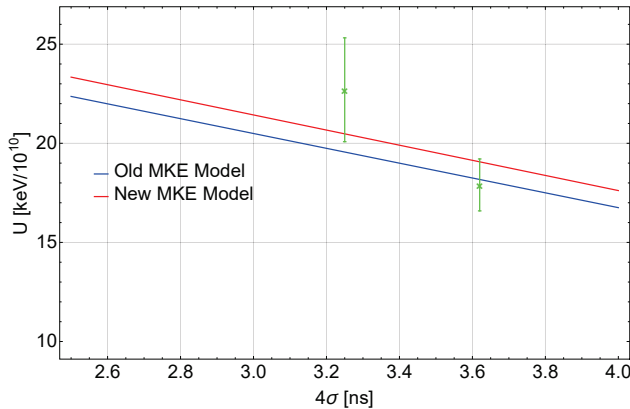


Figure 9: A comparison of the energy loss measured with beam and the results from the BLoND code. The error bars on the measurements represent the 95% confidence level on the fit without weighting factors applied to the data. The full SPS impedance model is included only changing the MKE model used.

In order to obtain a complete picture, further studies with a wider range of bunch intensities, bunch lengths and RF accelerating voltages are required. Due to the significant variation in the bunch length produced earlier in the accelerator chain bunch length corrections have to be applied. The region in which the measurements are most sensitivity to the impedance of the MKE kicker are found at low cavity voltage with short bunch lengths and high intensity. These conditions are difficult to reach and therefore probing the kicker impedance through beam measurements may prove challenging.

SUMMARY

The model of the longitudinal impedance of the extraction kickers in the SPS at CERN has been updated, leading to an increase in the broadband impedance, with values per MKE being roughly double that of the previous model. The larger impedance has been confirmed by coaxial-wire measurements of the kicker. The impact of this significantly higher impedance on the intensity threshold of the post-LIU SPS has been investigated in simulations. The threshold expected is potentially 10% lower than originally anticipated leading to the probable requirement of further impedance reduction in the SPS. Furthermore, a way of measuring the impedance contribution of the kicker has been introduced. Preliminary measurements delivered promising results for benchmarking of the SPS impedance model.

ACKNOWLEDGEMENTS

We would like to thank the BLoND developing team for discussions and optimisations of the code, M. Barnes and V. Vlachodimitropoulos for their support measuring the MKE kicker, A. Lasheen for his help with the beam measurements, and E. Shaposhnikova for her advice and guidance.

REFERENCES

- [1] J. Coupard *et al.*, "LHC Injectors Upgrade TDR", CERN-ACC-2014-0337.
- [2] A. Lasheen and E. Shaposhnikova, "Evaluation of the CERN Super Proton Synchrotron Longitudinal Impedance From Measurements of the Quadrupole Frequency Shift", *Phys. Rev. ST Accel. Beams*, vol. 20, p. 064401, June. 2017.
- [3] CERN BLoND code, <https://blond.web.cern.ch/>
- [4] M. Barnes *et al.*, "Measurement and Analysis of SPS Kicker Magnet Heating and Outgassing with Different Bunch Spacing", in *Proc. PAC'09*, Vancouver, BC, Canada, May 2009, paper FR2RAC02.
- [5] T. Kroyer, F. Caspers and E. Gaxiola, "Longitudinal and Transverse Wire Measurements for the Evaluation of Impedance Reduction Measures on the MKE Extraction Kickers", CERN Note, AB-Note-2007-028, 2007.
- [6] CST Studio Suite 2018, CST AG, Darmstadt, Germany, <http://www.cst.com>
- [7] C. Zannini and G. Rumalo, "EM Simulations in Beam Coupling Impedance Studies: Some Examples of Application", in *Proc. ICAP'12*, Rostock-Warnemünde, Germany, paper WESC11.
- [8] F. Casper, "Impedance Determination", in "Handbook of Accelerator Physics and Engineering", 2nd Edition, A. Chao, K. Mess, M. Tigner and F. Zimmermann, World Scientific, 2013, pp.742–756.
- [9] J.E. Varela *et al.*, "An Extended SPS Longitudinal Impedance Model", in *Proc. IPAC'15*, Richmond, VA, USA, May 2015, paper MOPJE035.
- [10] P. Kramer, C. Vollinger, "Studies for the SPS Travelling Wave Cavities Upgrade", in *Proc. ICFA Mini-Workshop Workshop "Impedances and Beam Instabilities in Particle Accelerators"*, Benevento, Italy, September 2017, to be published.
- [11] N. N. Esfahani, P. Kramer and C. Vollinger, "Equivalent Circuit Modelling of Travelling Wave Accelerating Structures and Its Applications", in *Proc. 47th EuMC*, Nuremberg, Germany, 2017, pp. 572–575.
- [12] E. Shaposhnikova, E. Ciapala, E. Montesinos, "Upgrade of the 200 MHz RF system in the CERN SPS", in *Proc IPAC'11*, San Sebastian, Spain, September 2011, paper MOPC058.
- [13] E. Shaposhnikova *et al.*, "Removing Known SPS Intensity Limitations for High Luminosity LHC Goals", in *Proc. IPAC'16*, Busan, Korea, May 2016, paper MOPOY058.
- [14] T. Argyropoulos, A. Lasheen, J. Repond, E. Shaposhnikova, "Effect of the Various Impedances on Longitudinal Beam Stability in the CERN SPS", in *Proc. IPAC'16*, Busan, Korea, May 2016, paper TUPOR008.

Content from this work may be used under the terms of the CC BY 3.0 licence (© 2018). Any distribution of this work must maintain attribution to the author(s), title of the work, publisher, and DOI.

- [15] T. Bohl, T. Linnekar, E. Shaposhnikova and J. Tuckmantel, "Study of Different Operating Modes of the 4th RF Harmonic Landau Damping System in the CERN SPS", in *Proc. EPAC'98*, Stockholm, Sweden, June 1998, Vol. 1-3, p. 978–980.
- [16] E. Shaposhnikova *et al.*, "Energy Loss of a Single Bunch in the CERN SPS", in *Proc. EPAC'04*, Lucerne, Switzerland, pp. 1909–1911.
- [17] B.W. Zotter and S.A. Kheifets, "Impedances and Wakes in High-Energy Particle Accelerators", 2nd Edition, World Scientific, 2000.

WHAT IS MISSING FOR THE DESIGN AND OPERATION OF HIGH-POWER LINACS?

A. Shishlo[†], Oak Ridge National Laboratory, Oak Ridge, TN 37831, USA

Abstract

The design process, tuning, and operation of high-power linacs are discussed. The inconsistencies between the basic beam physics principles used in the design and the operation practices are considered. The missing components of the beam physics tools for the design and operations are examined, especially for negative hydrogen ion linacs. The diagnostics and online models necessary for tuning and characterization of existing states of the linac are discussed.

INTRODUCTION

The design process of a new high power linac is always a combination of two simultaneous and interacting processes [1]. The first is an engineering design where the available technologies (normal temperature or superconducting) are chosen for each section of the linac; the feasibility, availability, and cost of cavities and magnets are analysed; the limitations of the real estate are considered; and so forth. This part of the design process is mostly related to hardware choice, and it should minimize the overall cost of the new linac construction. The second part is related to the beam physics. The new linac should deliver a beam with necessary properties, and, at the same time, beam loss should be low enough to allow “hands on” maintenance of the linac equipment. Also, this low beam loss requirement will define the necessary tolerance limits for hardware and electronics influencing the final cost of the project. These two parts of the whole design process interact, and usually several iterations between them are necessary to get a good design.

The linac operation cycle can be broken onto three parts: maintenance/upgrade, commissioning/tuning, and production. In this paper I will only consider the tuning component of this cycle, and its dependency on the design and simulation model.

In my opinion, there are several deficiencies in the design and operation processes

- During the physical and engineering design, not enough attention is given to the procedures and hardware for tuning/commissioning of the linac in the operation cycle. With the increasing number of components in future projects this could be a bottleneck for the availability of future linacs.
- The model-based beam loss simulations for tolerance limits in the engineering design should use more realistic models and tuning algorithms.
- The beam loss reduction during operation should be model-based not only for the initial stage of tuning. The final empirical beam loss tuning should also be

replaced with a model-based one. For this, we need benchmarked models.

It is possible that some of these problems cannot be solved for a long time, but we have keep them in mind as our goals. In this paper the examples describing these deficiencies are discussed mainly for the Oak Ridge Spallation Neutron Source (SNS) linac [2].

SNS LINAC

The SNS linac structure is shown in Fig. 1. It has both a normal temperature and a superconducting cold linac. The normal conducting part includes front end, RFQ, medium energy beam transport part (MEBT), drift tube linac (DTL), and coupled cavities linac (CCL). It accelerates beam to 186 MeV. The superconducting linac (SCL) includes 81 cavities and accelerates beam to 1 GeV.

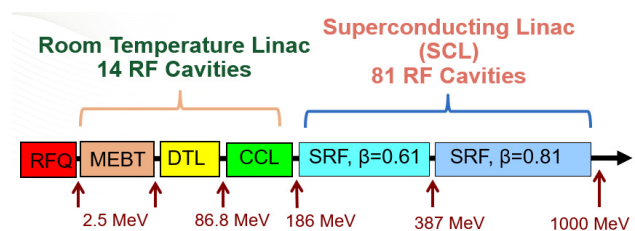


Figure 1: The SNS linac.

SNS LINAC TUNING/COMMISSIONING

In this section the three examples related to the SNS linac tuning are discussed: two examples about RF set up procedures, and one about the orbit correction in CCL. The SNS linac diagnostics includes Beam Position Monitors (BPMs) which are also capable to measure the bunch phase proportional to the bunch arrival time. These BPMs are used for “time-of-flight” measurements.

SCL RF Tuning

The initial design of SCL suggested 100 μ s beam for superconducting cavities tuning [3]. The process was based on the RF cavity response to a beam loading with occasional “time-of-flight” measurements to avoid accumulating errors. The procedure should be repeated for all cavities one by one. At the beginning all cavities are detuned, and, as the process moves on, they will be brought to the resonant frequency. The whole tuning procedure was expected to give an uncertainty of ± 20 MeV in the final beam energy which was a static error.

During the commissioning of the SNS SCL this approach was modified to avoid uncontrollable spraying of superconducting structures with 100 μ s beam. In addition to that, the process of bringing the detuned cavity to the

[†] email address: shishlo@ornl.gov

Content from this work may be used under the terms of the CC BY 3.0 licence (© 2018). Any distribution of this work must maintain attribution to the author(s), title of the work, publisher, and DOI.

resonant frequency takes 10-15 minutes including the bureaucratic overhead, and the total tuning time would be about two 8-hour shifts. Eventually the following modification to the SCL tuning procedure and linac hardware were implemented:

- All SCL cavities are on the resonance frequency all time. To avoid beam acceleration, initially all cavities are at 59 Hz repetition rate of RF pulses. The beam repetition rate for tuning is 1 Hz. The cavities are tuned one by one by switching to 60 Hz and performing “time-of-flight” energy measurements with all available BPMs.
- To avoid the beam loading of the cavities an attenuation system has been installed in MEBT to reduce the beam peak current by 80% or more.
- To reduce the beam loading even further, the Low Energy Beam Transport (LEBT) chopper at the RFQ entrance is used to provide only 1-5 us of beam.
- The SNS ring is used to calibrate the beam final energy with accuracy about 100 keV.
- The tuning process is automated. Now it takes about 45 minutes to tune all RF cavities in SCL.
- In the case of a cavity failure, the SCL can be retuned based on the model without any additional measurements. The cavities’ phases will be changed to return the final beam energy to the initial value.

The fast tuning/retuning technique for new superconducting linacs becomes more important for high availability, because they have hundreds of cavities. The model-based retuning is especially significant for user facilities that need a fast reconfiguration for different experiments.

Warm Linac RF Setup

The SNS normal temperature linac includes 10 long RF structures: 6 DTL and 4 CCL cavities. To setup design values of amplitudes and phases for such type of cavities, the Delta-T procedure was developed at Los Alamos National Lab [4]. This procedure uses only a narrow phase range around the design value ($\sim 10^\circ$), because it is based on a linear model. A more general approach called “Phase scan signature matching” was developed at Fermilab [5]. At SNS both these algorithms were implemented in the high level tuning applications. The scheme describing these methods is shown in Fig. 2. To tune the cavity’s amplitude and phase they use a phase scan of this cavity and data from two BPMs in the next cavity. The downstream cavity should be in the “off resonance” state.

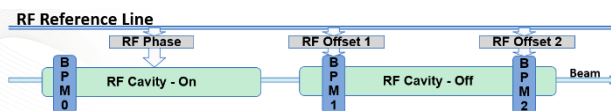


Figure 2: Warm linac RF tuning: DTL and CCL cavities.

During the SNS normal conducting linac commissioning and operations, it was found that tuning applications always needed an expert presence and “try and miss” iterations, because the working region around the design RF amplitude and phase is very narrow. The BPM 1 and 2 (see

Fig. 2) should be calibrated for the “time-of-flight” bunch phase measurements. Later another tuning method was developed which uses only one BPM inside the tuning cavity (BPM0 in Fig. 2). We were lucky to have these inner BPMs at the right positions in the cavities with just a few accelerating RF gaps after the cavity entrance. This configuration allows to perform the cavity phase scan from -180° to $+180^\circ$ without BPM’s signal interruptions for all cavity amplitudes. An example of a resultant BPM’s phase as a function of the cavity’s phase is shown in Fig. 3.

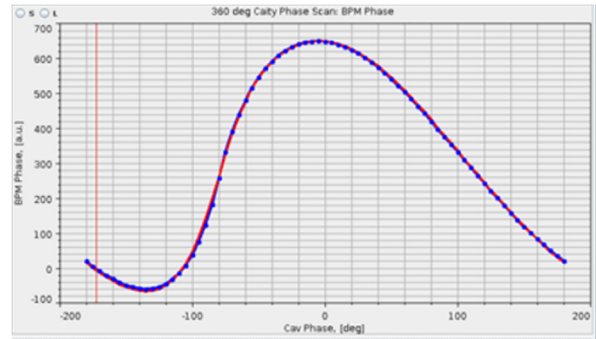


Figure 3: DTL3 phase scan. Blue points are BPM phases. Red line is the model calculation. The vertical red line is a cavity phase working point.

Comparing this data with the model calculation we know how far we are from the cavity design parameters. This method uses only one BPM, so there is no need for the timing calibration. It is also faster than initial methods, and it was easily automated allowing to tune RF in the whole warm linac in 22 minutes. Unfortunately, the initial design did not provide us with the inner BPM in the first DTL cavity, so for this case we still use the phase scan matching method. This example shows the importance to have the right diagnostics at the right places during the design stage.

CCL Orbit Correction

The SNS coupled cavity linac has 48 quadrupole magnets and only 10 BPMs to measure the beam transverse positions. The initial design included more BPMs, but during the cost optimization some BPMs were removed from the CCL lattice. During the commissioning it was found that a standard orbit correction application can easily make BPMs readings close to zero, but beam loss was still too high. To see the real orbit quadrupole gradient scans were performed, and they showed that the orbit between BPMs has ± 3 mm deviation from the quad centres. The quad gradient scans procedure cannot be a part of the routine orbit correction, because it is disruptive and too slow.

The situation was resolved by the development of a more comprehensive model for the beam center motion in the CCL. The new model includes possible transverse offsets of quadrupoles and BPMs from the beam pipe center. The unknown offset parameters were found after several quadrupole gradient scans, and then they were narrowed down by analysis of several hundreds of trajectories in CCL for different quadrupole and dipole corrector fields combinations. The values of the vertical offsets of the quadrupoles

are shown in Fig. 4. The maximal offsets shown in Fig. 4 (± 1 mm) are too big to be real, but they work very well for the new orbit correction algorithm. The new algorithm includes three steps. First, we use beam positions measured by BPMs to figure out the beam position and angles at the CCL entrance. Next we use the inverted transport matrices generated from the magnet fields and offsets to calculate the beam trajectory in the whole CCL. In the third step, we apply the standard orbit correction algorithm for all significant points in the CCL lattice using the simulated trajectory. After correction, the orbit deviation from the center usually is less than 1 mm. This case demonstrates that deficiencies during the design will result in some additional studies and developments needed to provide a reliable and fast beam loss tuning.

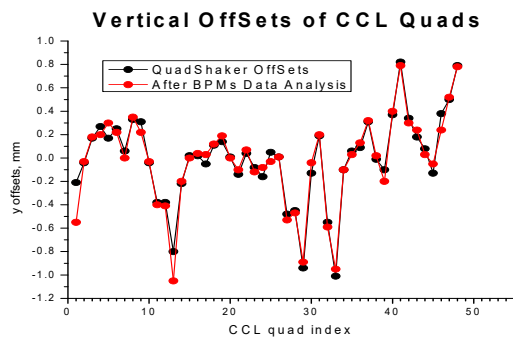


Figure 4: The vertical offsets of the CCL quads used in the model for the specialized orbit correction application.

OPTIMAL TOLERANCE DESIGN PROBLEM

Tolerance limits in the engineering design have a significant impact on the final price tag of the project. The usual procedure to check the acceptable tolerance on beam related parameters includes multiple “end-to-end” simulations with randomly distributed parameters errors. The main goal of the simulations is to estimate if beam losses are on the acceptable level. To get beam loss estimation, the linac model for simulations should be a Particle-In-Cell (PIC) code. In this section of the paper we discuss mainly the RF system errors. The usual numbers for cavities tolerances are 1% in the amplitude and 1° for the phase.

The parameter errors are divided into two different parts: static and dynamic. The distinction between them is very clear for the mechanical alignment errors in lattice components like magnets, RF cavities, apertures etc. If we apply the significant alignment errors to the model, beam loss will show up in the simulations due to the orbit distortion. Then these losses will be eliminated or significantly reduced by the orbit correction with the dipole correctors included in the engineering design. The dynamic errors usually are not compensated in hadron linacs. The source of the static errors is the positioning of the lattice elements during the construction, and for the dynamic errors that could be, for instance, mechanical vibrations. Tolerance limits will be different for static and dynamic errors in the

case of the alignment errors. For the RF parameters tolerances, the situation is not so clear.

This section discusses the following topics related to the tolerance of RF parameters

- The SNS experience with the RF parameters vs. the design values.
- The recent development in the TraceWin code [6] related to the RF tolerances and the tuning procedure simulations.
- The deficiencies in the PIC codes related to beam loss calculations.

SNS RF Settings vs. Design. Static Errors.

Using SNS as an example we consider three types of situations. The first is a MEBT buncher phase setting procedure where we do not have the capability to distinguish between two possible setpoints. The second is the SCL cavities’ field gradients where we do not have a choice, because they are defined by the maximal achievable value. And the third case is for synchronous phases of the SCL cavities that are set to get the local minimum of beam loss.

To setup non-accelerating phases of RF bunchers in the SNS MEBT (see Fig. 1) we use the RF phase scans for different RF amplitudes and the phase signals from downstream BPMs. If the RF phase is the non-accelerating one, the phases from the BPMs will be the same for all RF buncher amplitudes. The result of such scans for one of the BPMs is shown in Fig. 5. The MEBT attenuation system was used for these measurements, so there were no space charge effects. This figure clearly demonstrates the stationary RF phase point with accuracy around 1° . The problem is that different BPMs give different set-points in the range of $\pm 4^\circ$. The possible reason for that is a non-symmetrical longitudinal shape of the bunch, and its transformation along the MEBT. At this moment, we have no means to verify which value is the correct one, and settings found for different BPMs can be used as a starting point for final beam loss tuning. So, this $\pm 4^\circ$ spread could be considered as a legitimate static error of the MEBT RF.

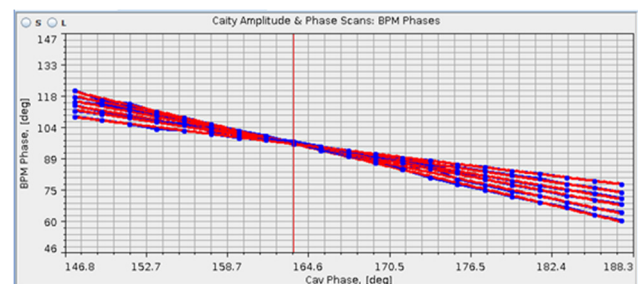


Figure 5: The MEBT buncher #2 phase scans for different amplitudes. Blue points are BPM phases, and red lines are linear fits for different RF amplitudes.

Another example of unexpected deviations from the design parameters is the field gradients of the SCL cavities. Figure 6 shows the measured SNS SCL cavity field gradients and the design values for the medium and high beta sections of the superconducting linac. As we can see, for most cavities in the medium beta region the gradients are

Content from this work may be used under the terms of the CC BY 3.0 licence (© 2018). Any distribution of this work must maintain attribution to the author(s), title of the work, publisher, and DOI.

above the design by 20-40%, and for the high beta they are lower than the design by approximately the same amount. To get the final linac energy near the design we had to keep gradients as high as possible. Figure 6 describes the SNS situation several years ago, but even at that time the linac delivered 1 MW beam with acceptable losses.

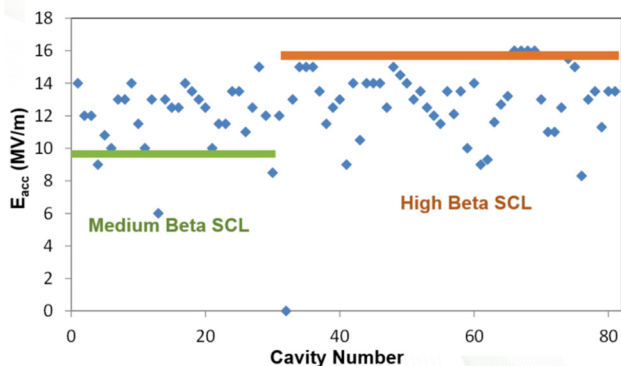


Figure 6: The real field gradients of the SNS SCL cavities. The lines are the design values.

The next example shows the synchronous phases of the SCL cavities during the SNS production run in 2014 (see Fig. 7). These synchronous phases provide a low beam loss tune in SCL despite their significant deviation from the design value of -18° . They were a result of the empirical beam loss tuning after initially setting all of them to the design values. At this moment, we do not understand the reason why the low loss tune needs this behaviour of the synchronous phases along SCL.

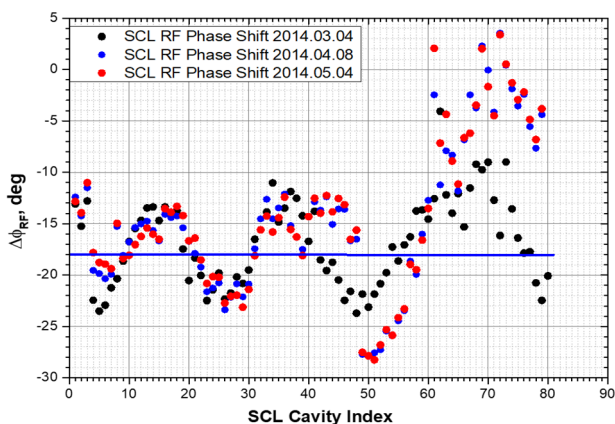


Figure 7: The measured synchronous phases of the SCL cavities for the low beam loss tune. The blue line is the design value.

All the discussed examples show that the realistic static tolerances for RF amplitudes and phases could be much higher than the 1%, 1° standard limits. For dynamics errors, the SNS experience gives 1.5% and 2° values for the SCL RF system which are close to the standard.

RF Static Errors Treatment in Simulations

The big deviations of the RF parameters from the design values in the operational high power linac with acceptable

beam loss shows that our usual treatment of the static errors in the RF system must be reconsidered. As an example of this approach we have a recent modification of the TraceWin code related to this topic [6]. In [6] the longitudinal beam dynamics simulation method has been improved by including more “close-to-real” models for cavities tuning procedure. A specific command has been implemented in TraceWin code to simulate this tuning process. The new method was tested with the MYRRHA linac [7] model. The application of this new method to the simulations reduced the estimation of total beam loss by factor 60.

Despite some logical inconsistencies and unrealistic expectation of the BPM positions accuracy (± 1 mm) in [6], this more realistic approach to the static errors treatment should be welcomed by the community and should encourage more studies in this direction.

Code Deficiencies in Beam Loss Simulations for H⁻ Linacs

We can look at the paper [6] results from another angle. If the change of the static error interpretation method in the model significantly reduced expected beam loss, can we trust these simulations with respect to the beam halo description? We are going to consider this issue in the next section. Here the simulation of the recently discovered Intra-Beam-Stripping (IBSt) mechanism of beam loss in H⁻ linacs [8, 9] is discussed.

The IBSt induced beam losses are important for all high-power H⁻ linacs, and they were not considered in any design of existing H⁻ linacs. At this moment, there is only one code that includes the model for such type of beam loss calculations – TRACK [10]. TRACK is a PIC code, so it is more computationally expensive to use than envelope codes. IBSt induced beam losses are defined by the bunch core, so it should be easily implemented into envelope codes. For now, these losses are usually calculated by using postprocessing scripts analysing the RMS beam sizes along the linac. Incorporating this mechanism into the modern envelope and PIC codes would benefit the community.

OPERATIONS : MODEL BASED BEAM LOSS TUNING

As we mentioned before, the operation cycle includes tuning the accelerator parameters to provide necessary beam properties and the acceptable level of beam loss. Usually the initial tuning is performed by using the online model right in the control room or with precalculated data. The final tuning of high power linacs is always an empirical beam loss reduction by slightly tweaking parameters known to be effective from previous experience. Unfortunately, at this moment we do not have reliable and benchmarked PIC codes capable of beam loss prediction on necessary level of 10^{-4} or less. Also, this type of simulation should include not only the code itself, but also a realistic initial distribution of the bunch particles. At SNS there are plans for studies related to these topics.

Bunch 6D Initial Distribution Studies

To test a new RFQ for the SNS accelerator, a functional copy of the SNS Front End with the H⁻ Ion Source, LEBT, RFQ, and MEFT has been built at SNS. From the beginning this installation was dedicated for beam physics studies, and it is called the Beam Test Facility (BTF). The first accomplished study on BTF was the measurements of the 6D phase space distribution of the particles in the H⁻ bunches from the RFQ [11]. The data analysis is still in progress. The knowledge of the 6D distribution is a necessary step in the experimental benchmark of any PIC code. The next step is a study of halo development for different optics.

Plans for FODO Lattice at SNS BTF

In addition to the existing beam line of BTF, there is a plan to install a FODO lattice with the necessary diagnostics for beam halo formation studies [11]. The combination of known 6D distribution at the entrance of this FODO line, and halo measurements at the exit, will give us a useful instrument for a full benchmark of PIC models.

Backtracking Feature of Codes

The 6D phase space measurement is an ultimate solution for the initial distribution problem, but even right now many linacs have an emittance measuring station somewhere in the lattice. The data from these measurements could be used for the bunch generation in PIC codes assuming zero correlation between planes. Beam diagnostics also can include Bunch Shape Monitors (BSM), but usually they are at different locations. If BSMs are upstream of the transverse emittance stations (the case at SNS), and we want to combine the data, then we need the ability of the code to track the bunch backwards in the lattice. This feature of the code can serve many purposes, but not many codes have it. From the theoretical point of view there is no obstacle for the backward tracking, because all our equations of motion are time reversible.

CONCLUSION

Briefly summarizing the arguments about the missing components in design and operations of the high power linacs, I want to highlight the following

- In the design process, more attention should be paid to the tuning procedures of the linacs including hardware and algorithms.
- To estimate tolerance in engineering design the realistic models and algorithms for beam loss calculations are needed.
- The same realistic models are needed for beam loss tuning during the operations.

ACKNOWLEDGMENTS

This manuscript has been authored by UT-Battelle, LLC, under Contract No. DE-AC0500OR22725 with the U.S. Department of Energy. This research was supported by the

DOE Office of Science, Basic Energy Science, and Scientific User Facilities. The United States Government retains and the publisher, by accepting the article for publication, acknowledges that the United States Government retains a non-exclusive, paid-up, irrevocable, world-wide license to publish or reproduce the published form of this manuscript, or allow others to do so, for the United States Government purposes. The Department of Energy will provide public access to these results of federally sponsored research in accordance with the DOE Public Access Plan (<http://energy.gov/downloads/oe-public-access-plan>).

APPENDIX

Author deeply appreciate very useful advices from A. Aleksandrov (ORNL), P. Ostroumov (FRIB), and B. Mustafa (ANL) during the preparation of this paper.

REFERENCES

- [1] P. Ostroumov, F. Gerigk, "Superconducting Hadron Linacs," *Rev. Accel. Sci. Tech.*, vol. 6, pp. 171-196, 2013.
- [2] S. Henderson *et al.*, "The Spallation Neutron Source accelerator system design", *Nucl Instrum Meth A*, vol. 763, pp. 610-673, 2014.
- [3] J. Stovall *et al.*, "Superconducting linac for the SNS", in *Proc. LINAC'00*, Monterey, CA, USA, Aug. 2000, p. 605.
- [4] K.R.Crandall, "The Delta-T Tuneup Procedure for the LAMPF 805-MHz Linac", LANL Report LA-6374-MS, June 1976.
- [5] T.L. Owens, M.B. Popovic, E.S. McCrory, C.W. Schmidt, and L.J. Allen, "Phase Scan Signature Matching for Linac Tuning", *Particle Accelerators*, vol. 48, pp. 169-179, 1994.
- [6] D. Uriot, "Improvement of the RF field phase & amplitude errors simulation in TraceWin code," in *Proc. IPAC'18*, Vancouver, Canada, April 2018, paper THPAF017.
- [7] D. Vandeplasche *et al.*, "The MYRRHA Linear Accelerator", in *Proc. IPAC'11*, San Sebastian, Spain, Sep. 2011, pp. 2718-2720.
- [8] V. Lebedev *et al.*, "Intrabeam Stripping in H-Linacs", in *Proc. LINAC'10*, Tsukuba, Japan, September, 2012, pp. 929-931.
- [9] A. Shishlo *et al.*, *Phys. Rev. Lett.*, vol 108, p. 114801, 2012.
- [10] V. Aseev *et al.*, "TRACK : The new beam dynamics code", in *Proc. PAC'05*, Knoxville, Tennessee, USA, 2005, pp. 2053-2055.
- [11] A. Aleksandrov *et al.*, "6D Beam Measurement, Challenges and Possibilities", in *Proc. IPAC'18*, Vancouver, Canada, April 2018, paper THXGBE1.

RECENT STUDIES OF BEAM PHYSICS FOR ION LINACS

L. Groening¹, S. Appel¹, M. Chung⁴, X. Du¹, P. Gerhard¹, M. Maier¹, S. Mickat¹,
 A. Rubin¹, P. Scharrer^{1,2,3}, H. Vormann¹, and C. Xiao¹

¹Gesellschaft für Schwerionenforschung, Darmstadt, Germany

²Helmholtz Institute Mainz, Mainz, Germany

³Johannes Gutenberg-University, Mainz, Germany

⁴Ulsan National Institute of Science and Technology, Ulsan 44919, Republic of Korea

Abstract

The UNiversal Linear ACcelerator (UNILAC) at GSI aims at provision of high brilliant heavy ion beams, as its main purpose will be to serve as injector for the upcoming FAIR accelerator complex. To keep acceleration efficient, heavy ions need to be charge state stripped and progress in improving this process is reported. Recent advance in modeling time-transition-factors and its impact on simulation of longitudinal dynamics is presented. The UNILAC injects into the subsequent synchrotron SIS18 applying horizontal multi-turn injection (MTI). Optimization of this process triggered intense theoretical and experimental studies of the dynamics of transversely coupled beams. These activities comprise full 4d transverse beam diagnostics, round-to-flat beam transformation, extension of Busch's theorem to accelerated particle beams, and optimization of the MTI parameters through generic algorithms.

INTRODUCTION

After being upgraded the UNILAC (Fig. 1) together with the subsequent synchrotron SIS18 will serve as injector for FAIR [1]. Three ion source terminals can be operated in pulse-to-pulse switching mode at 50 Hz. One terminal is equipped with an ECR source providing highly charged ions. Followed by an RFQ and an IH-cavity operated at 108 MHz it forms the High Charge Injector (HLI) providing beams at 1.4 MeV/u. Another terminal houses a Penning source (PIG) providing low intensity beams at intermediate charge states at 2.2 keV/u.

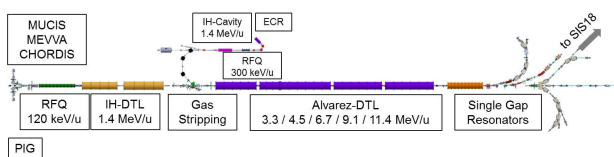


Figure 1: The upgraded UNiversal Linear ACcelerator (UNILAC) at GSI.

The third terminal is dedicated to provision of intense beams of low-charged ions at 2.2 keV/u as well. Intense heavy ion beams are produced in a MEVVA or VARIS. Beams are bunched and pre-accelerated to 120 keV/u along a 9 m long RFQ operated at 36 MHz. Afterwards two IH-cavities provide for acceleration to 1.4 MeV/u, being the exit energy of the High Current Injector (HSI). For uranium the highest particle numbers are obtained by using the charge

state $^{238}\text{U}^{4+}$. After the IH-DTL the acceleration efficiency is increased by passing the beam through a gaseous stripper which delivers the mean charge state of $^{238}\text{U}^{28+}$ at its exit. This increase of charge state is at the expense of intrinsic particle loss. Prior to 2014 about 87% of the uranium ions were stripped to charge states different from $^{238}\text{U}^{28+}$. After dispersive selection of the desired charge state the beam is matched to the subsequent post-stripper Alvarez-type DTL. The latter is operated at 108 MHz and comprises five tanks. Its exit beam energy is 11.4 MeV/u being the injection energy for the synchrotron SIS18. The post-stripper DTL can be fed with beams from the HLI as well. The design parameters to be achieved after the upgrade are listed in Table 1.

Table 1: Beam Design Parameters for the Upgraded UNILAC

Ion A/q	≤ 8.5	
Beam Current	$1.76 \cdot A/q$	mA
Input Beam Energy	1.4	MeV/u
Output Beam Energy	3.0 - 11.7	MeV/u
Emit. (norm., tot.) hor/ver	0.8/2.5	μm
Beam Pulse Length	≤ 1.0	ms
Beam Repetition Rate	10	Hz
Rf Frequency	108.408	MHz

This upgrade program is based on dedicated R&D w.r.t. the provision of high brilliant ion beams. It comprises the optimization of charge state stripping by passing the ion beam through a media as well as the improved modeling of longitudinal beam dynamics along DTL cavities. Diagnostics of the full 4-dimensional transverse phase space including inter-plane correlations was developed and successfully tested. A novel technique allows to transfer emittance from one transverse degree of freedom into the other one, thus increasing the efficiency of multi-turn injection. The modeling of this emittance shaping was simplified significantly by showing that the underlying dynamics are described by extending the Busch theorem from single particles to accelerated beams. Finally, generic algorithms were developed to optimize multi-turn injection into a synchrotron.

INCREASE OF STRIPPING EFFICIENCY

So far, a continuous N_2 jet has been used as stripping medium. The achieved stripping efficiency from $^{238}\text{U}^{4+}$ to $^{238}\text{U}^{28+}$ was 14%. Since 2014 a pulsed gas stripper cell has

been tested [2, 3]. It injects short gas pulses, the length of which matches the beam pulse length into the stripping chamber, producing a high density target without overloading the differential pumping system toward adjacent accelerator systems. Using H₂ the efficiency of stripping into the most populated charge state has been increased from 14% to 21%. Figure 2 compares measured charge state spectra of a uranium beam at 1.4 MeV/u applying a continuous N₂ jet with a spectrum resulting from a pulsed H₂ cell. The rms-width δq of the spectrum from the jet is about 3.6. The width from the pulsed cell is $\delta q \approx 2.3$, i.e. it is reduced by 36%. Another appealing feature of the pulsed stripper is its flexibility w.r.t. the applied back pressures of the single gas pulses as well as to the lengths of the individual pulses. Both can be changed in pulse-to-pulse switching mode of the UNILAC thus eliminating restrictions from the constant back pressure provided by the N₂ jet. Additionally, the set-up can be equipped with a second valve, thus allowing for pulse-to-pulse operation with a second stripper gas.

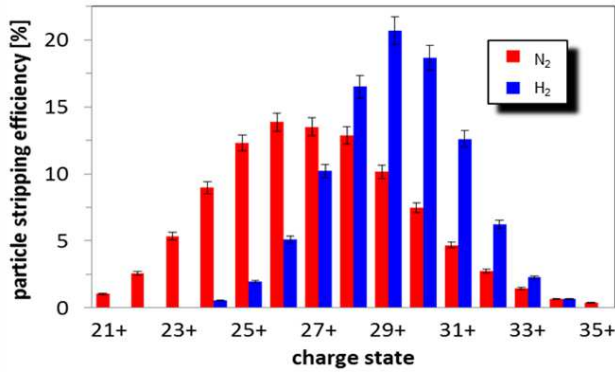


Figure 2: Comparison of measured uranium charge state spectra applying a continuous N₂ jet (red) with a spectrum resulting from a pulsed H₂ cell (blue).

Final optimization and implementation into routine operation of this new stripping set-up have started. A detailed description of the development and testing of the high pressure H₂ gas cell as well as the latest results obtained with the device are reported in [2, 3].

LONGITUDINAL MODELING OF DTLs

Any DTL cavity is a sequence of drifts and finite gaps. The dynamics inside gaps is quite demanding as the effective local forces on the beam particle are explicit functions of time and position. Usually, the equations are solved by doing the approximation that the particle velocity is constant during the gap transit. Although this approximation obviously contradicts to the purpose of gaps, namely increasing the velocity, it delivers reasonable results and generations of DTLs were designed in this way. To a huge fraction this is thanks to the focusing nature of the effective longitudinal lattice. Errors in velocities and rf-phases from that approximations cause oscillation around the design orbit even for the perfect particle. However, the errors are small and machine performance is not seriously harmed. This figure changes, if the

regular longitudinal focusing is weakened or partially abandoned as for the KONUS [4] beam dynamics that slightly moves attention from focusing towards efficiency of acceleration. The UNILAC pre-stripper DTL uses this dynamics for very efficient acceleration of ²³⁸U⁴⁺ and operation revealed that the longitudinal dynamics is very sensitive to small changes of cavity voltages and phases compared to the post-stripper DTL which uses Alvarez-type cavities.

In order to better understand these sensitivities the longitudinal modeling was refined as described in detail in [5]. The static electric field inside gaps is calculated by Fourier-Bessel series as implemented into the BEAMPATH code [6] using

$$E_z = -\cos(\omega t + \psi_0) \sum_{m=1}^M E_m I_0(\mu_m r) \sin\left(\frac{2\pi m z}{\Gamma}\right),$$

$$E_r = \cos(\omega t + \psi_0) \sum_{m=1}^M \frac{2\pi m E_m}{\mu_m \Gamma} I_1(\mu_m r) \cos\left(\frac{2\pi m z}{\Gamma}\right), \quad (1)$$

$$B_\theta = \sin(\omega t + \psi_0) \sum_{m=1}^M \frac{2\pi E_m}{\mu_m \lambda c} I_1(\mu_m r) \sin\left(\frac{2\pi m z}{\Gamma}\right),$$

and

$$\mu_m = \frac{2\pi}{\lambda} \sqrt{\left(\frac{m\lambda}{\Gamma}\right)^2 - 1}, \quad \Gamma = l + 2g + d,$$

$$E_m = \frac{4U}{I_0(\mu_m a)\Gamma} \frac{\pi m(l+g)}{\Gamma} \frac{\sin\left[\frac{\pi m(l+g)}{\Gamma}\right]}{\frac{\pi m(l+g)}{\Gamma}} \frac{\sin\left(\frac{\pi m g}{\Gamma}\right)}{\frac{\pi m g}{\Gamma}}, \quad (2)$$

where I_0 and I_1 are the Bessel functions of zero and first order, ω is the angular frequency of the field, r is the radial coordinate, U is the gap voltage, ψ_0 is the phase at the gap at $t=0$, and a, l, g, d define the gap geometry [5]. The single particle starts moving at $z=0$. Typically the number of Fourier harmonics is $M=30$. The reference particle vector function and its derivative w.r.t. z is defined as

$$Z(t, z) := \begin{bmatrix} z \\ \frac{dz}{dt} \end{bmatrix} = \begin{bmatrix} z \\ \beta c \end{bmatrix} \quad (3)$$

and

$$DZ(t, z) := \frac{dZ(t, z)}{dt} = \begin{bmatrix} \beta c \\ \frac{q}{m_0} E_z(z) \cos(\omega t + \psi_0) \end{bmatrix}. \quad (4)$$

This non-linear differential equation is solved by applying the Bulirsch-Stoer method. Using the refined modeling of a KONUS DTL the sensitivities mentioned above could be reproduced in simulations as reported in [5].

Additionally, the "intermediate" energy phenomenon of UNILAC's last two Alvarez-type cavities was finally modeled 35 years after it has been observed in operation. By chance it was found during commissioning of the fourth (fifth) DTL cavity, that it provides high quality beams with small energy spread, if it is operated just at 80% (70%) of its

Content from this work may be used under the terms of the CC BY 3.0 licence (© 2018). Any distribution of this work must maintain attribution to the author(s), title of the work, publisher, and DOI.

nominal voltage. The output energies are reduced by 34% (32%) compared to the nominal values. Although this was not understood, these beams are supplied to users since many decades to their full satisfaction. Using the advanced modeling these "intermediate" energies were exactly reproduced in simulations. Figure 3 shows the electric field strength along the DTL together with the respective reference particle energy. It reveals that the beam is even temporarily decelerated inside the cavity. The according longitudinal phase space distribution at the cavity exit is displayed in Fig. 4.

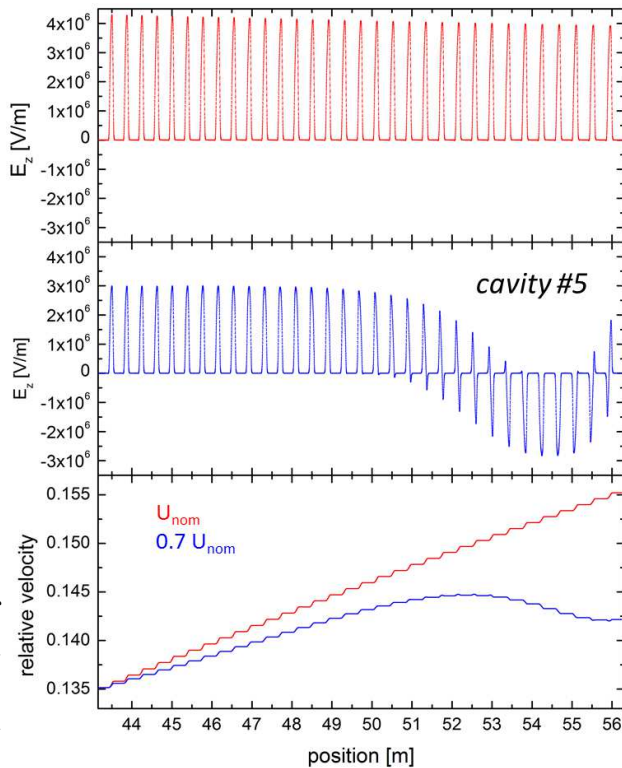


Figure 3: Longitudinal electric field strength as felt by the design particle at nominal cavity voltage (upper), at 70% of the nominal voltage (center), and the respective particle energies along the fifth DTL cavity (bottom).

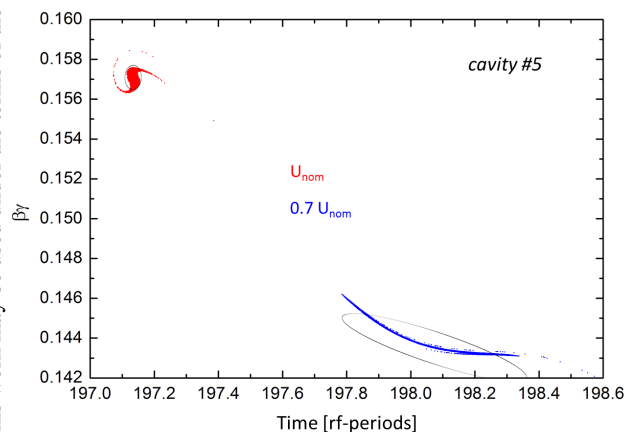


Figure 4: Longitudinal phase space distributions at the exit of the DTL. Red: last DTL cavity operated at nominal voltage. Blue: last cavity operated at 70% of the nominal voltage.

COMPLETE TRANSVERSE 4D BEAM DIAGNOSTICS

For any accelerator or transport lattice which includes elements coupling the transverse planes as solenoids for instance, complete 4d transverse beam diagnostics is required for adequate beam-based modeling of the lattice. The four 2nd order inter-plane correlations must be measured. To our knowledge such measurements never were conducted successfully before at ion energies beyond about 150 keV/u. Applying a slit/grid emittance meter preceded by a skewed quadrupole triplet such measurements were done with an uranium beam at 11.4 MeV/u. Details on this method can be found in [7].

Additionally, the ROTating System for Emittance measurements (ROSE) was developed and commissioned [8] with ⁸³Kr¹³⁺ beam at 1.4 MeV/u and with ²³⁸U²⁸⁺ beam at 5.9 MeV/u. It is a single-plane slit/grid emittance measurement device housed in a chamber which can be rotated around the beam axis (Fig. 5) by any angle θ . For one beam transport setting (a) emittance measurements were performed at rotation angles of 0°, 90°, and at an intermediate angle θ_0 . One additional measurement at θ_0 using a different setting (b) was done. The accuracy of the measured 2nd moments is sufficiently high to define transport sections that can completely decouple the beam with skewed quadrupoles for instance [8].

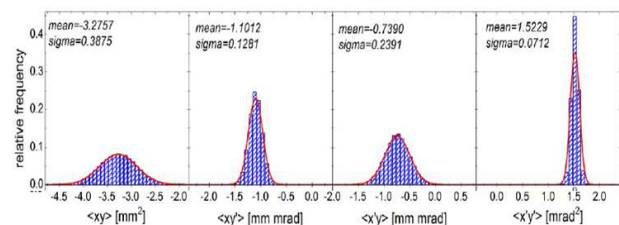
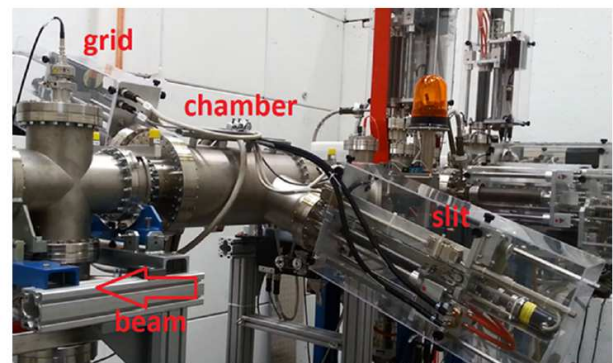


Figure 5: ROTating System for Emittance measurements ROSE (top). Measured 2nd order beam moments that quantify the amount of coupling between the horizontal and vertical plane (bottom).

EXTENSION OF THE BUSCH THEOREM TO BEAMS

In 1926 H. Busch formulated the preservation of the conjugated angular momentum of a single charge particle moving

along a region with longitudinal magnet field [9]. The generalization of the theorem [10] is expressed as

$$\oint_C \vec{v} \cdot d\vec{C} + \frac{eq}{m\gamma} \psi = const. \quad (5)$$

and visualized in Fig. 6. The path integral of the stream of possible particle velocities \vec{v} along a closed contour C confining a fixed set of possible particle trajectories, plus the magnetic flux through the area enclosed by C is an invariant of the motion.

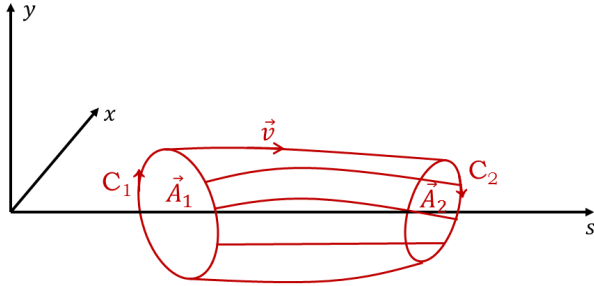


Figure 6: The contour C encloses possible streams of particle trajectories and encloses the area \vec{A} .

In 1992 A.J. Dragt introduced the eigen-emittances [11] as the rms-emittances $\varepsilon_{1/2}$ which the beam acquires after all of its inter-plane correlations have been removed. Accordingly, they are preserved by all linear elements even if they introduce correlations and change the rms-emittances. This section briefly summarizes the results and applications of extending Busch's theorem to accelerated particle beams [12]. The preservation of the sum of the squares of the two transverse eigen-emittances is expressed using conjugated variables. Finally, this preservation delivers a term that is quite similar to Eq. (5)

$$(\varepsilon_{n1} - \varepsilon_{n2})^2 + \frac{4eq\psi\beta\gamma}{m\pi} \oint_C \vec{r}' \cdot d\vec{C} + \left[\frac{eq\psi}{m\pi} \right]^2 = const., \quad (6)$$

where the integral is to be taken of the averaged beam divergence around the curve enclosing the beam rms-area divided by π . This expression connects the normalized eigen-emittances, the beam vorticity, and magnetic flux through the beam rms-area A . It turns out that this conservation law allows for very fast modeling of beam emittance shaping experiments done with electrons and with ions. In many cases application of conservation laws is more efficient w.r.t. solving the underlying equations of motion.

The first application is on Fermilab's flat beam experiment [13], where an electron beam was extracted from a cathode immersed into the magnetic flux B_0 (Fig. 7).

After acceleration to 16 MeV correlations were removed with skew quadrupoles. The final transverse emittance ratio is quickly derived using the extended Busch theorem by applying Eq. (6) at the cathode and at the exit of the beam

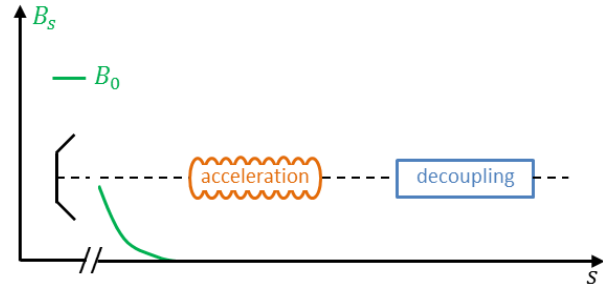


Figure 7: (from [12]) Schematic sketch of the beam line of the experiment performed at NICCAD at FERMILAB [13].

line

$$0 + 0 + \left[\frac{eB_0A_0}{mc} \right]^2 = (\varepsilon_{nf1} - \varepsilon_{nf2})^2 + 0 + 0, \quad (7)$$

which with few steps delivers the formula derived in [13]

$$\varepsilon_{nf1/2} = \pm \mathcal{L}\beta\gamma + \sqrt{(\mathcal{L}\beta\gamma)^2 + (\varepsilon_n'')^2}. \quad (8)$$

The second application is on the EMTEX experiment done at GSI [14,15] being sketched in Fig. 8. A beam of $^{14}\text{N}^{3+}$ was

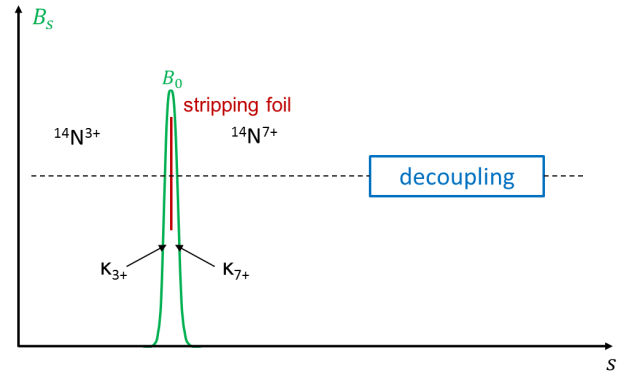


Figure 8: (from [12]) Schematic beam line of EMTEX at GSI for transverse emittance transfer [15].

passed through a solenoid with field B_0 into which charge state stripping to $^{14}\text{N}^{7+}$ was done. Accordingly, the fringe fields act differently on the beam at the solenoid entrance and exit, respectively. The imposed correlations were removed by a quadrupole triplet. The effective repartitioning of the emittances through EMTEX can be derived quickly from the extended Busch theorem. First it is applied to the entrance of the beam line and to the centre of the solenoid right before stripping as

$$\begin{aligned} & (\varepsilon_{x,3+} - \varepsilon_{y,3+})^2 + 0 + 0 \\ &= (\varepsilon_{1f} - \varepsilon_{2f})^2 + \frac{2B_0}{(B\rho)_{3+}} \mathcal{W}_{Af} + \left[\frac{A_f B_0}{(B\rho)_{3+}} \right]^2, \end{aligned} \quad (9)$$

where

$$\begin{aligned} \mathcal{W}_A &= 2A \oint_C \vec{r}'(x, y, s) \cdot d\vec{C} \\ &= \langle y^2 \rangle \langle xy' \rangle - \langle x^2 \rangle \langle yx' \rangle + \langle xy \rangle (\langle xx' \rangle - \langle yy' \rangle) \end{aligned} \quad (10)$$

is twice the beam vorticity multiplied with the beam rms-area. Charge state stripping just changes the beam rigidity but does not change any other beam property (straggling and scattering can be neglected). Afterwards the invariance is re-formulated for the new charge state, i.e., at the centre of the solenoid right after stripping and at the exit of the beam line

$$(\varepsilon_{1f} - \varepsilon_{2f})^2 + \frac{2B_0}{(B\rho)_{7+}} \mathcal{W}_{Af} + \left[\frac{A_f B_0}{(B\rho)_{7+}} \right]^2, \quad (11)$$

$$= (\varepsilon_{x,7+} - \varepsilon_{y,7+})^2 + 0 + 0.$$

Combining these relationships leads to the final repartitioning of the projected beam rms-emittances

$$(\varepsilon_{x,7+} - \varepsilon_{y,7+})^2 = (\varepsilon_{x,3+} - \varepsilon_{y,3+})^2 + (A_f B_0)^2 \left[\frac{1}{(B\rho)_{7+}} - \frac{1}{(B\rho)_{3+}} \right]^2. \quad (12)$$

The equivalent deviation based on solving the equations of motion exceeds several pages [14].

OPTIMIZATION OF RING INJECTION WITH GENERIC ALGORITHM

The efficiency of injection from a linac into a circular accelerator depends on many parameters as position and angle of injected beam (x, x'), initial orbit bump x_b and its reduction rate T , number n of turns during injection, and the horizontal tune Q_x and emittance ε_x from the linac. Optimization of this parameter set was successfully done by applying a generic algorithm as reported in detail in [16]. A number of initial parameter sets is defined and labelled as initial generation. Their fitness w.r.t. efficiency is evaluated and the fittest are mixed pairwise to exchange single parameters combined with small mutations, i.e., arbitrary changes of single parameters. The new generation formed in that way is re-evaluated and the fittest are re-mixed partially with the previous generation to create the subsequent generation. Doing so, very fast convergence is achieved as depicted in Fig. 9 and the final result is much better compared to optimizations without generic algorithms.

The simulations of efficiency were benchmarked [17] with according measurements [18]. Using EMTEX the transverse emittance ratio was varied leaving all other beam parameters unchanged. Figure 10 plots the simulated and measured accumulation rates revealing excellent agreement.

REFERENCES

- [1] FAIR Baseline Technical Report, vol. 2, GSI Darmstadt, Germany, 2006, pp. 335.
- [2] P. Scharrer *et al.*, "Electron stripping of Bi ions using a modified 1.4 MeV/u gas stripper with pulsed gas injection", *J. Radioanal. Nucl. Chem.*, vol. 305, pp. 837-842 (2015), doi:10.1007/s10967-015-4036-2

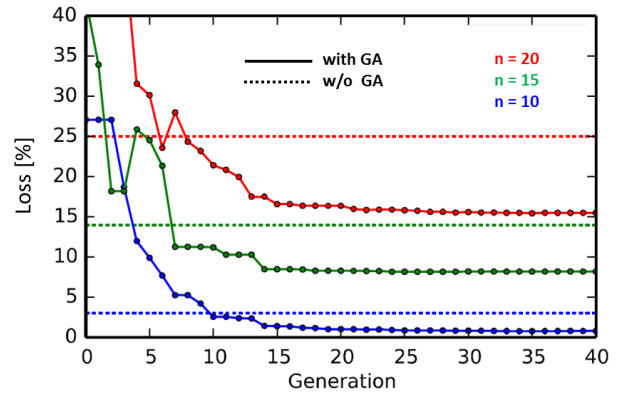
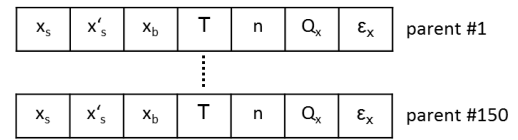


Figure 9: Solid lines: relative beam loss during multi-turn injection as a function of the generation comprising the parameter set used for the injection. Losses are plotted for different numbers of turns during injection. Dotted lines: Losses corresponding to injection parameter sets being obtained without applying generic algorithms.

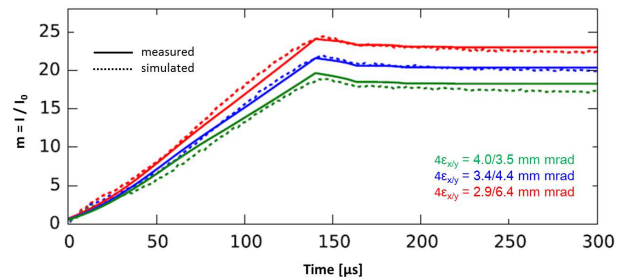


Figure 10: Measured (solid) and simulated (dotted) accumulated current during multi-turn injection as a function of time. Currents are plotted for different transverse emittance ratios provided by the linac through EMTEX.

- [3] P. Scharrer *et al.*, "Measurements of charge state distributions of 0.74 and 1.4 MeV/u heavy ions passing through dilute gases", *Phys. Rev. ST Accel. Beams*, vol. 20, pp. 043503 (2017), doi:10.1103/PhysRevAccelBeams.20.043503
- [4] U. Ratzinger, "The IH-Structure and its Capability to Accelerate High Current Beams", in *Proc. PAC 1991*, San Francisco, CA, USA, pp. 567.
- [5] C. Xiao *et al.*, "Investigations on KONUS beam dynamics using the pre-stripper drift tube linac at GSI", *Nucl. Instrum. Methods Phys. Res. A*, vol. 887, pp. 40 (2018), doi:10.1016/j.nima.2018.01.024
- [6] Y. K. Batygin *et al.*, "Particle-in-cell code BEAMPATH for beam dynamics simulations in linear accelerators and beam-lines", *Nucl. Instrum. Methods Phys. Res. A*, vol. 539, pp. 455 (2005), doi:10.1016/j.nima.2004.10.029
- [7] C. Xiao *et al.*, "Measurement of the transverse four-dimensional beam rms-emittance of an intense uranium beam

- at 11.4 MeV/u”, *Nucl. Instrum. Methods Phys. Res. A*, vol. 820, pp. 14 (2016), doi:10.1016/j.nima.2016.02.090
- [8] C. Xiao *et al.*, “Rotating system for four-dimensional transverse rms-emittance measurements”, *Phys. Rev. ST Accel. Beams*, vol. 19, pp. 072801 (2016), doi:10.1103/PhysRevAccelBeams.19.072802
- [9] H. Busch, “Berechnung der Bahn von Kathodenstrahlen im axialsymmetrischen elektromagnetischen Felde”, *Annalen der Physik*, vol. 81, pp. 974, (1926).
- [10] P. T. Kirstein *et al.*, *Space Charge Flow*. New York, USA: McGraw-Hill Inc., 1967, pp. 14.
- [11] A. J. Dragt, “General moment invariants for linear Hamiltonian systems”, *Phys. Rev. A*, vol. 45, no. 4, pp. 2572 (1992), doi:10.1103/PhysRevA.45.2572
- [12] L. Groening *et al.*, “Extension of Busch’s theorem to particle beams”, *Phys. Rev. ST Accel. Beams*, vol. 21, pp. 014201 (2018), doi:10.1103/PhysRevAccelBeams.21.014201
- [13] P. Piot *et al.*, “Photoinjector generation of a flat electron beam with transverse emittance ratio of 100”, *Phys. Rev. ST Accel. Beams*, vol. 9, pp. 031001 (2006), doi:10.1103/PhysRevSTAB.9.031001
- [14] C. Xiao *et al.*, “Single-knob beam line for transverse emittance partitioning”, *Phys. Rev. ST Accel. Beams*, vol. 16, pp. 044201 (2013), doi:10.1103/PhysRevSTAB.16.044201
- [15] L. Groening *et al.*, “Experimental Proof of Adjustable Single-Knob Ion Beam Emittance Partitioning”, *Phys. Rev. Lett.*, vol. 113, pp. 264802 (2014), doi:10.1103/PhysRevLett.113.264802
- [16] S. Appel *et al.*, “Injection optimization in a heavy-ion synchrotron using genetic algorithms”, *Nucl. Instrum. Methods Phys. Res. A*, vol. 852, pp. 73 (2017), doi:10.1016/j.nima.2016.11.069
- [17] S. Appel *et al.*, “Injection optimization through generation of flat ion beams”, *Nucl. Instrum. Methods Phys. Res. A*, vol. 866, pp. 6 (2017), doi:10.1016/j.nima.2017.05.041
- [18] L. Groening *et al.*, in *Proc. of IPAC 2015*, Richmond, VA, USA, 2015, pp. 153–155, doi:10.18429/JACoW-IPAC2015-MOPWA026

BEAM DYNAMICS OF THE ESS LINAC

Y. Levinsen*, R. De Prisco, M. Eshraqi, N. Milas, R. Miyamoto, C. Plostinar, A. Ponton
ESS, Lund, Sweden

Abstract

The ESS linac will deliver an unprecedented 5 MW of average beam power when completed. Beyond the 90 MeV normal conducting front-end, the acceleration is performed using superconducting structures up to the design energy of 2 GeV. As the ESS will send the beam to a fixed tungsten target, the emittance is not as important a factor as in injectors. However, the losses have to be studied in detail, including not only the average operational loss required to be of less than 1 W/m, but also the accidental losses, losses due to failure and other potentially damaging losses. The commissioning of the ion source and LEBT starts this year and will continue with the RFQ next year. In this contribution we will discuss the beam dynamics aspects and challenges of the ESS linac.

INTRODUCTION

The ESS accelerator is optimised to produce a maximum neutron flux from the target to the experiments, and so by extent most of the accelerator high level parameters becomes secondary. As an example, the cost optimisation exercise finalised in 2013 resulted in a reduced beam energy on target compensated by an increased beam current to keep the same proton beam power on target (i.e. not affecting the neutron flux) [1].

The nominal design parameters of the ESS are 2 GeV beam on target energy with 62.5 mA proton beam current. The pulse length is 2.86 ms and the machine is pulsed at 14 Hz which equates in a 4 % duty factor. These parameters are realised from acceleration through a normal conducting front end that brings the beam energy to about 90 MeV before a super-conducting main accelerator brings the beam energy to 2 GeV. A contingency space and dogleg brings the beam towards the target where it is painted onto the target using a set of horizontal and vertical rastering dipole magnets, as the target would not be able to take the peak current density for extended period of time without a significant transversal defocusing of the beam.

After the first complete baseline design of the accelerator was ready in 2012 [2], the design has undergone several optimisations to improve performance and/or reliability of the machine, and to cost optimize [1, 3, 4]. In the first major cost optimization, the number of cryomodules was reduced to keep cost down while the beam intensity was increased. In other words, the cost was reduced without decreasing performance, but at an increased risk as higher current is generally harder to obtain reliably. The difficulty of tuning the machine increases due to enhanced space-charge forces, and the margin for the couplers reduces since the

more power is consumed by the beam. The contingency space was increased, in order to be able to upgrade to 2.5 GeV beam energy in the future.

An extensive value engineering exercise has been performed across the ESS project, to meet the budget requirements and recover some of the needed contingency funds. That included proposals reducing administrative costs of running the organisation as much as considering descopeing options of the machine that will be easy to recover with minimal cost increase once sufficient funds becomes available. Currently the main implication for the accelerator complex is that the number of RF sources for the superconducting linac will be reduced, meaning that the initial beam power on target is reduced from 5 MW to 3 MW [5].

NORMAL CONDUCTING FRONT END

The beam is generated in a 75 keV microwave discharge ion source [6], which produces a 6 ms beam pulse at 14 Hz with around 90 mA of total current of which around 80 mA are protons. The source is required to deliver the beam pulse with a maximum current fluctuation of 3.5 % at flat top. This type of source is proven to have a very high reliability close to 100 %, and long mean time between failures. It takes around 2 ms for the beam extracted out of the source to plateau, so to get a flat beam pulse we chop off approximately 3 ms of the pulse in the low energy beam transport (LEBT). The beam is focused through two solenoids in the LEBT which also match the beam to the RFQ that then bunches the beam at 352.21 MHz and accelerates it to 3.62 MeV. The last modification of the beam pulse is done by the chopper in the medium energy beam transport (MEBT), that clean the 20 μ s of the head of the pulse. This corresponds approximately to the expected transient of the space-charge compensation in the LEBT [7]. The MEBT chopper has a faster rise/fall time of around 10 ns. The overall layout of the ESS linac is shown in Fig. 1. Figure 2 shows a schematic overview of the pulse modifications.

The RFQ is a four-vane type, consisting of 5 sections and a total length of 4.5 m and a minimum aperture of 3 mm radius. The RFQ runs with a Kilpatrick of 1.9 at 352.21 MHz. A relatively long bunching section allows for a high capture and transmission of the matched beam from the LEBT, which is expected to be above 97% [8]. 60 tuners, 2 couplers with two ports each, and 22 pick-ups should provide the needed flexibility to realise an accurate resonant RF through the section.

Both the LEBT and the MEBT contains an extensive set of beam diagnostics to characterise the beam as well as magnetic elements to match the beam transversally to the downstream sections. The MEBT also contains three buncher cavities to focus the beam longitudinally. The main

* yngve.levinsen@esss.se

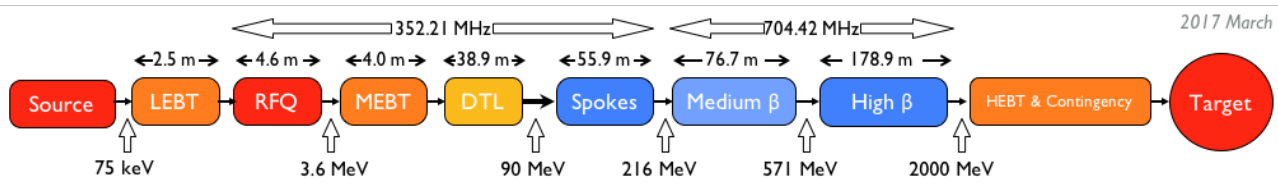


Figure 1: The overall layout of the ESS linac.

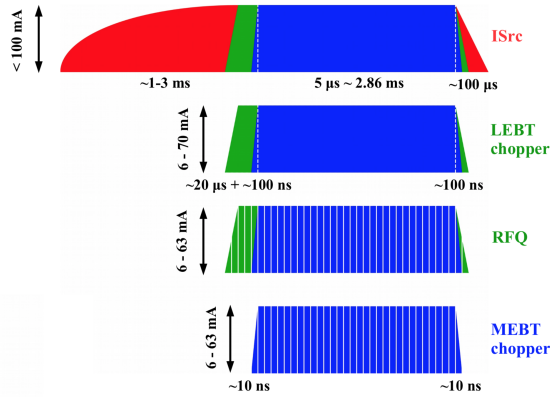


Figure 2: A schematic overview of how the beam pulse changes from 6 ms DC out of the source, to 2.86 ms bunched beam in the ESS front-end. The red part is cleaned by the LEBT chopper, the green cleaned by the MEBT chopper. After the MEBT chopper up to 63 mA beam current remains, with sharp 10 ns pulse edges and a bunching frequency of 352.21 MHz.

chopper is in the LEBT, but has a slower rise time than the fast chopper in the MEBT which purpose is to scrape off the last part of the head and tail of the beam pulse. Details of the LEBT design can be found in [6] and MEBT in [9, 10].

The last section of the normal conducting front end is the DTL, which contains 5 tanks that make up a total length of the section of 38.9 m. The DTL brings the beam energy to 90 MeV [11]. An increase of the beam energy at the entrance of the DTL from 3 MeV in the earlier designs to 3.62 MeV means that the first drift tubes can be longer, which makes them easier to be manufactured and allows for easier installation of quadrupoles. In every second drift tube there is a permanent magnet quadrupole (PMQ), which have a length of 50 mm in tank 1 and 80 mm in tank 2-5.

SUPERCONDUCTING LINAC

There are three superconducting sections in the ESS linac. There is a low energy differential pumping section (LEDP) that separates the two vacuum levels of the warm front-end from the superconducting linac. First there are spoke cavities running at 352.21 MHz, before a frequency jump to 704.42 MHz where two families of elliptical RF cavities accelerate the beam from around 216 MeV to the final beam on target energy. Between each cryomodule in the superconducting linac there is what is called a linac warm unit (LWU). This unit always consist of a quadrupole pair for focusing the beam transversally, resulting in a FODO lattice.

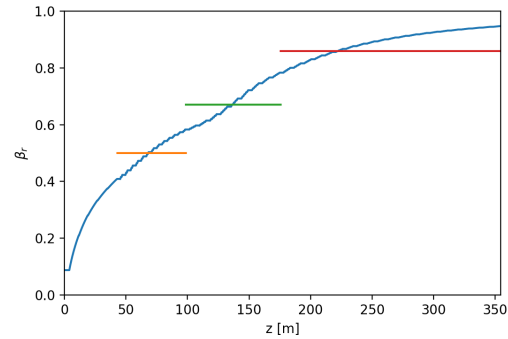


Figure 3: The relativistic β in the ESS linac, with the geometrical β of the three superconducting sections shown as horizontal lines. Spokes in yellow, M β in green and H β in red.

There is a dual plane trajectory corrector in each LWU, and one BPM. There is also space in the LWU for diagnostics

The spoke cavities bring the beam from 90 MeV to 216 MeV through 13 cryomodules containing a spoke cavity pair each. Spoke cavities were chosen due to their retuning capabilities, and due to their large transversal aperture. The spoke cavities are designed for an optimal relativistic β of 0.5. Details about the Spoke cavity design are described in [12].

Two families of elliptical cavities running at 704.42 MHz follows the spoke cavities. The frequency jump means a sudden drop in the size of the RF bucket, something that will easily be a source of beam losses if not handled carefully. This has been shown in our error studies [13].

The first family is denoted as the medium- β cavities, designed for an optimal relativistic β of 0.67. The second family is denoted the high- β cavities with an optimal relativistic β of 0.86. The relativistic β of the ESS linac is shown in Fig. 3. There are 9 medium- β cryomodules and 21 high- β cryomodules. The elliptical section is designed so that the length of one elliptical period (cryomodule+LWU) is exactly equal at 8.52 m. Each cryomodule holds 4 cavities of 6 cells in the medium- β section and 5 cells in the high- β section. The equal length of LWU's and cryomodules makes everything easily interchangeable should that become useful at some point. The LWU's in the elliptical section of the linac are functionally the same as the spoke LWU's, but offer stronger quadrupole and corrector strength, and larger apertures.

Pulsed quadrupole magnets were considered for the LWU's [14], but they are now abandoned. Using pulsed quadrupoles would greatly reduce the heat load and one

would be able to operate without water cooling. However the problem with the pulsed magnets is that the eddy currents generated in the conductive beam chamber becomes too large, so the vacuum pipe becomes too hot [15]. Hence the design is now assuming DC magnets again.

CONTINGENCY AND BEAM TRANSPORT

At the end of the high- β section, the beam has reached the nominal 2 GeV energy. The accelerator has 15 empty slots of same length as medium- and high- β , with the LWU's installed to keep the transversal focusing. This is a contingency space which, if filled with elliptical cavities, will increase the beam on target energy to around 2.5 GeV. After the contingency we have one more LWU before the first dipole of the dogleg. This dipole kicks the beam up at a 4° angle towards the target that is 4.5 m above the beamline of the main accelerator. If this first dipole is turned off, the beam continues straight forward into a defocusing triplet and then the beam hits the tuning beam dump. The dogleg has 12 quadrupoles which maintains a phase advance vertically such that it is an achromatic dogleg allowing longitudinally off-centre particles to follow the same beam trajectory again after the dogleg towards the target.

After the dogleg the beam enters the final section of the accelerator, the accelerator to target (A2T) area. This area consist of 6 quadrupoles that defocuses the beam somewhat and also keep relevant phase advance between critical locations. A rastering system consisting of 4 horizontal and 4 vertical AC dipoles operating at around 30-40 kV paints the beam onto the target in an even Lissajou-pattern [16] and brings down the peak deposited energy density on the target surface. To have this working optimally, one needs control over the phase advance between the second dipole, the action point (centre of rastering system), the cross-over point (location of minimal beam size after last quadrupole) and target surface. Phase advances between these locations should be either 90° or 180° depending on which pair you consider. The most important of those is the action point to cross-over phase advance, which needs to be exactly $90^\circ (+N \times 180^\circ)$.

STUDIES

One of the main concerns when designing such a high power and perhaps more importantly high intensity linac is the beam losses. In particular when we have a superconducting section it is essential that we keep the operational losses to a minimum and that we have good quantitative and qualitative knowledge of where the losses may occur. Additionally, a rigorous protection system must be in place to detect all possible failures early enough to protect the machine. Which in turn means an extensive evaluation of the possible failures needs to be done beforehand.

There have been several large error studies done on the ESS nominal linac design to verify that the machine is expected to be correctable and that the operational losses are expected to respect the general 1 W/m rule of thumb along the linac [13, 17, 18]. These studies are also used to define

the high level requirements of the RF system (amplitude and phase tolerances as seen by the beam), and the larger error studies also provide input to Monte Carlo shower simulations used for example to evaluate locations of beam loss monitors and shielding efficiency.

A perhaps more complex task is to foresee all possible failure modes of a linac. A first step is to look at the effect of blinding out single components (ie single complete failures). This was done for the ESS linac and reported in [19]. For some systems such as the superconducting RF cavities we also looked at the losses arising when the amplitude was decreasing gradually, which allows one to better understand temporal evolution of the losses when knowledge of how quickly the field decays for a given failure scenario is included.

The field flatness in a drift tube linac is strongly dependent on the manufacturing errors, and in turn this affects the stabilization system. The sensitivity of the ESS drift tubes field to the manufacturing errors has been studied and tolerances were defined [20].

The MEBT needs to match the beam to the DTL both transversally through the 11 quadrupoles, and longitudinally through three RF bunchers. Additionally it holds diagnostics and room for the fast chopper and corresponding beam dump. Imperfect matching in the MEBT results in losses downstream, primarily in the DTL but can also cause slow halo growth that results in losses further downstream. The chopper can also be a source of losses if the chopping leaks beam downstream of the chopper dump, and some losses from the partially chopped beam during the chopper rise time is expected [21].

Errors during assembling, brazing and machining of the different parts of the RFQ can result in deviations from the theoretical inter-vane voltage. This alters the quadrupolar components and adds dioplar terms. The errors can be compensated to some extent by tuners. The effect of these errors on the beam dynamics was reported in [8, 22]. The effects of the simplified DTL model typically used in simulations were evaluated in [23] by simulating with detailed 3D field maps of the DTL.

The transmission of the beam through the front-end is an important consideration. Not so much because the losses are necessarily problematic - the beam energy is low so a certain fraction of beam losses can occur without damage to the beam pipe. However one needs to be able to capture enough beam to fulfil the nominal beam parameters. The emittance needs to be small enough so that it fits within the acceptance of the downstream linac, but also not so small that the space-charge forces blows up the beam while the beam energy is still low. Further, a lossy beam in the front end typically drags with it a more dominant halo, which in turn causes losses further downstream where they are more problematic. The transmission studies of the LEBT and RFQ was reported in [24, 25], and it is expected that the ESS front-end will be capable of providing a high capture rate in the RFQ and a very good transmission.

STATUS AND OUTLOOK

A primary concern of the ESS linac is to maintain the very low beam losses even at nominal 5 MW beam power, and many detailed studies have been undertaken to evaluate this, either directly or indirectly. Sections of the linac have been studied independently and larger integrated studies have been done to understand the sum of the effects at play. The ESS lattice design has reached mature stage, and should be capable of delivering the most powerful neutron beam in the world as promised. Today we are closing in on the very first commissioning stages of the accelerator complex [26], and exciting times lie ahead.

REFERENCES

- [1] M. Eshraqi, H. Danared, and D. McGinnis, "Design options of the ESS LINAC," in *Proc. IPAC'13*, Shanghai, China, 2013, paper THPWO072.
- [2] "ESS technical design report," Tech. Rep. ESS-doc-274-v15, 2013.
- [3] M. Eshraqi *et al.*, "The ESS linac," in *Proc. IPAC'14*, Dresden, Germany, 2014, paper THPME043. doi: 10.18429/JACoW-IPAC2014-THPME043.
- [4] E. Bargallo *et al.*, "Value engineering of an accelerator design during construction," in *Proc. IPAC'17*, Copenhagen, Denmark, 2017. doi: 10.18429/JACoW-IPAC2017-MOPIK040.
- [5] C. Plostinar, M. Eshraqi, R. Miyamoto, and M. Munoz, "Beam Commissioning Planning Updates for the ESS Linac," in *Proc. IPAC'17*, Copenhagen, Denmark, 2017. doi: 10.18429/JACoW-IPAC2017-TUPVA131.
- [6] L. Neri *et al.*, "Improved design of proton source and low energy beam transport line for European Spallation Source," *Review of Scientific Instruments*, vol. 85, no. 2, 02A723, Feb. 2014, issn: 0034-6748, 1089-7623. doi: 10.1063/1.4832135.
- [7] N. Chauvin, O. Delferrière, R. Duperrier, D. Uriot, R. Gobin, and P. A. P. Nghiem, "Source and injector design for intense light ion beams including space charge neutralisation," in *Proc. LINAC'10*, Japan, 2010, paper TH302.
- [8] A. Ponton, Y. I. Levinsen, E. Sargsyan, A. C. France, O. Piquet, and B. Pottin, "Voltage Error Studies in the ESS RFQ," in *Proc. IPAC'16*, Busan, South Korea, Jun. 2016, paper TH-PMB039. doi: 10.18429/JACoW-IPAC2016-THPMB039.
- [9] R. Miyamoto, B. Cheymol, M. Eshraqi, and I. Bustinduy, "Beam Physics Design of the ESS Medium Energy Beam Transport," in *Proc. IPAC'14*, Dresden, Germany, 2014, paper THPME045. doi: 10.18429/JACoW-IPAC2014-THPME045.
- [10] I. Bustinduy, R. Miyamoto, M. Magan, and F. Sordo, "Current Status on ESS Medium Energy Beam Transport," in *Proc. HB'14*, USA, 2014, paper TU01AB04.
- [11] R. de Prisco, M. Eshraqi, *et al.*, "ESS DTL Status: Re-design and Optimizations," in *Proc. IPAC'14*, Dresden, Germany, 2014, paper THPME041. doi: 10.18429/JACoW-IPAC2014-THPME041.
- [12] D. Reynet *et al.*, "Design of the ESS Spoke cryomodule," in *Proc. SRF'13*, Paris, France, 2013, paper MOP089.
- [13] Y. I. Levinsen, M. Eshraqi, R. Miyamoto, M. Munoz, A. Ponton, and R. De Prisco, "Beam Dynamics Challenges in the ESS Linac," presented at the HB'16, Malmoe, Sweden, 2016. doi: 10.18429/JACoW-HB2016-TUAM3Y01.
- [14] M. Eshraqi *et al.*, "ESS Linac Beam Physics Design Update," in *Proc. IPAC'16*, Busan, South Korea, 2016, paper MOPOY045. doi: 10.18429/JACoW-IPAC2016-MOPOY045.
- [15] R. De Prisco, E. Sargsyan, and M. Ferreira, "Heating of the Q6 vacuum chamber," Jun. 10, 2016.
- [16] H. D. Thomsen and S. P. Møller, "A linear beam raster system for the european spallation source?" In *Proc. IPAC'13*, Shanghai, China, 2013, paper MOPEA005.
- [17] M. Eshraqi, R. De Prisco, R. Miyamoto, E. Sargsyan, and H. Thomsen, "Statistical Error Studies in the ESS Linac," in *Proc. JACoW*, Geneva, Switzerland, Jul. 2014, pp. 3323–3325, ISBN: 978-3-95450-132-8. doi: 10.18429/JACoW-IPAC2014-THPME044.
- [18] Y. I. Levinsen, "ESS 2015 baseline lattice error study," Tech. Rep. ESS-0049433, Feb. 2016.
- [19] M. Eshraqi, R. de Prisco, R. Miyamoto, and Y. I. Levinsen, "Preliminary Study of the Possible Failure Modes of the Components of the ESS Linac," European Spallation Source ERIC, Tech. Rep. ESS/AD/0057, 2015.
- [20] R. De Prisco, M. Eshraqi, A. Karlsson, Y. Levinsen, and R. Miyamoto, "Implication of manufacturing errors on the layout of stabilization system and on the field quality in a drift tube linac - rf dtl error study," in *Proc. LINAC'16*, East Lansing, MI, USA, Sep. 2016, pp. 290–293, ISBN: 978-3-95450-169-4. doi: 10.18429/JACoW-LINAC2016-MOPLR069.
- [21] R. Miyamoto *et al.*, "Dynamics of bunches partially chopped with the MEBT chopper in the ESS linac," in *Proc. LINAC'14*, Geneva, Switzerland, 2014, paper MOPP039.
- [22] A. Ponton and A. C. France, "Predictability of the beam quality during RFQ voltage tuning," in *Proc. IPAC'17*, Copenhagen, Denmark, 2017. doi: 10.18429/JACoW-IPAC2017-MOPIK096.
- [23] R. De Prisco, M. Eshraqi, A. Karlsson, Y. Levinsen, R. Miyamoto, and E. Sargsyan, "Effect of the Field Maps on the Beam Dynamics of the ESS Drift Tube Linac," in *Proc. IPAC'15*, Richmond, VA, USA, 2015, paper THPF078. doi: 10.18429/JACoW-IPAC2015-THPF078.
- [24] Y. I. Levinsen, M. Eshraqi, L. Celona, and L. Neri, "In-depth analysis and optimization of the european spallation source front end lattice," in *Proc. IPAC'16*, Busan, South Korea, Jun. 2016, paper TUPMR020. doi: 10.18429/JACoW-IPAC2016-TUPMR020.
- [25] O. Midttun, Y. I. Levinsen, R. Miyamoto, and C. Plostinar, "Benchmarking of the ESS LEBT in TraceWin and IBSimu," in *Proc. IPAC'17*, Copenhagen, Denmark, 2017. doi: 10.18429/JACoW-IPAC2017-THPVA013.
- [26] N. Milas *et al.*, "ESS commissioning plans," presented at the HB'18, Daejeon, Korea, Jun. 2018, paper TUA1WD01.

BEAM DYNAMICS SIMULATION AND MEASUREMENTS FOR THE IFMIF/EVEDA PROJECT

M. Comunian, L. Bellan, M. Cavenago, E. Fagotti, F. Grespan, A. Pisent, A. Palmieri, C. Baltador, F. Scantamburlo, L. Antoniazzi, A. Baldo, D. Bortolato, M. Giacchini, M. Montis,
INFN-LNL, 35020 Legnaro, Italy
N. Chauvin, CEA, 91190 Gif-sur-Yvette, France
H. Dzitko, F4E, 85748 Garching, Germany

Abstract

In the framework of IFMIF/EVEDA project the source and RFQ are ready to be tested with beam. In this article the beam dynamics simulation and the measurement performed in preparation of the first beam injection are presented. The installed line is composed by the proton and deuteron Source with the LEBT composed of two sole-noids that inject in the 10 meters long RFQ, the MEBT, diagnostic plate and the beam dump. The line is prepared to be tested with protons of 8 mA in pulsed mode (up to 0.1%).

INTRODUCTION

The Linear IFMIF Prototype Accelerator (LIPAc) is a high intensity deuteron linear accelerator [1]; it is the demonstrator of the International Fusion Material Irradiation Facility (IFMIF) machine within the Engineering Validation Engineering Design Activities (EVEDA) scope. It is presently in an advanced installation phase at Rokkasho under the Fusion Energy Research and Development Directorate National Institutes for Quantum and Radiological Science and Technology (QST), in the prefecture of Aomori, Japan. LIPAc has been designed and constructed mainly in European labs. It is composed of an injector delivered by CEA-Saclay [2,3], a RFQ [4] designed, manufactured and delivered by INFN on April 2016, a superconducting Linac designed by CEA-Saclay [5], RF power, Medium and High Energy Beam Transfer line (MEBT) and a high power Beam Dump supplied by CIEMAT [6]. The coordination of the European activities is managed by F4E and, on Rokkasho site; the Project Team supported by QST is responsible for integration. The beam that will be produced will be a 125 mA CW D⁺ beam at 9 MeV after the SRF cavities, delivered onto the high-power beam dump. Because of the large power deposition, several commissioning stages were foreseen, each one involving a specific part of the machine.

The nominal D⁺ input current to the RFQ is 135 mA.

This paper is divided into two parts: the first part concerns the effect of the residual beam potential after the neutralization process onto the input distribution of the RFQ and the response of it; the second part is dedicated to a different scenario, which is to foresee the behaviour of the RFQ and MEBT with lower current beam. The voltage characterization for different Courant-Snyder parameters of the beam were studied to identify the main characteristics of the beam.

SPACE CHARGE NEUTRALIZATION

In the low energy high intensity transfer line from the source to the RFQ, the beam transport is affected also by other species: the space charge compensation phenomena, s.c.c. (or space charge neutralization) can occur with the generation and superposition to the primary beam by opposite charge particles with a net reduction of the space charge effects.

Therefore, an important part of the beam dynamics characterization of this kind of transfer line concerns the estimation of the so-called secondary plasma effect.

Two s.c.c. models are considered in the simulation: the constant/static and dynamic model. In a constant model of neutralization, the perveance is simply reduced by a factor that is called the space charge compensation ratio, this Beam dynamics model is implemented on the TraceWin code.

In dynamic model of neutralization, the s.c.c. is calculated directly from the electron charge distribution that is superimposed to the ion distribution. Therefore, for the model both the ions and electrons dynamics need to be calculated, this Beam dynamics model is implemented on the Warp code.

BEAM DYNAMICS SIMULATION AT HIGH CURRENT WITH DYNAMIC MODEL OF SSC.

The method applied is using the following assumptions:

- The space charge compensation is a result of a Monte-Carlo process where each secondary particle is generated via a defined cross section, which depends on the energy of the incident particle.
- The secondary particle, electron, is governed by the self and applied field.
- The WARP code can transport all the multiple species.

This model of the dynamic space charge compensation requires extremely time demanding simulations with serial core processing. To reduce the time needed for a run, the parallelized version of the software was used: the 2 m length simulation was subdivided in 20 longitudinal domains, limited by the max core number at disposal of the machine. Anyhow, the simulations required times is the order of weeks to be performed to arrive at an almost steady stationary regime, see Fig. 1.

This framework does not foresee any arbitrary change of neutralization level. The process itself will determine it.

The steps used for the BD simulation are:

1. First set of $\epsilon_{rms,n}$, α , β was calculated via the AXCEL software. The rms quantities were assigned to a parabolic beam distribution placed at the extraction column repeller position.
2. All the line optical elements such as the solenoids and the repeller were set as in reality, with the same applied field.
3. The distribution is transported up to the emittance meter. If the parameter triad agrees within 30% and the simulation current within 20% the mean value of the error bar, the method proceeds with the next measured point. If not, only the Twiss parameters and the emittance are changed.
4. When a rough agreement is obtained, the process is concluded.

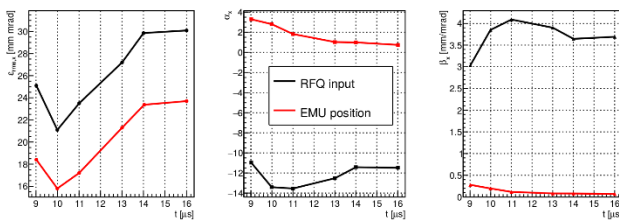


Figure 1: Twiss parameters evolution along the simulation time.

COMPARISON OF SIMULATION AND MEASUREMENT

The simulation consists of 2.397 m long LEBT, starting from the repeller electrode up to the emittance meter (EMU). The repeller electrode is critical for the simulation, because it contributes to the longitudinal boundary of the electrons and cannot be neglected. The initial guess for the beam Twiss were obtained via AXCEL simulation which stops at the repeller position. The WARP software simulates the beam propagation through the LEBT. It was decided to use the multigrid Poisson solver routine to manage the space charge beam dynamics. All the simulations were performed with full 3d geometry to check if the formation of circular structures in the spatial domain. The BD envelope is shown on Fig. 2.

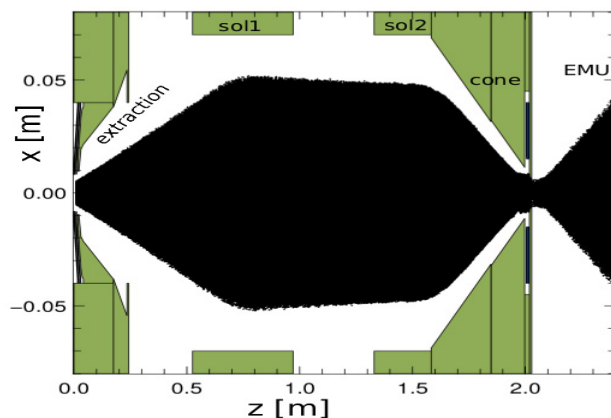


Figure 2: BD simulation from the injector to the EMU.

Respect to the measurement done very interesting results were obtained. Figure 3 shows the comparison between the experimental and simulated phase space.

The simulated point is quite near to the matched point for the RFQ injection Sol2=305 A, Sol1=262 A.

This dynamics model allows to follow the beam profile modifications due to the solenoid strength change with enough precision (less than 5 % difference in the rms quantities between the simulation and the experiment). The central peak position however is not in agreement.

The comparison involves the measured and simulated values with complete model with electron secondaries from wall collisions and with electrons belonging to ionization of the residual gas.

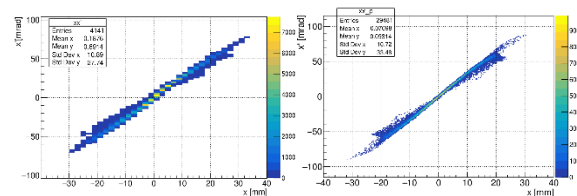


Figure 3 Measured and Simulated Phase Space at EMU position.

RFQ BEAM DYNAMIC SIMULATION

The simulated point was transported through the RFQ to study the transient phenomena by using the same emittance of 0.25 mm mrad and the same Twiss parameters.

The main approximation is the different residual potential (thus s.c.c.) at the RFQ injection: as it was explained before, the simulations were performed with phase A2 layout (i.e. with a diagnostic box after the LEBT cone); therefore, the electrons presence in the region of RFQ injection may not be representative of the real RFQ boundary conditions. However, this problem affects just few mm length of simulation.

Up to three meters, there is the generation of longitudinal emittance and, at the same time, fast oscillations of the transverse emittances caused by the mismatch.

After the gentle buncher, the beam gets to an equilibrium state, with few oscillations on the transverse emittance.

The main losses are concentrated before the 3 m, which corresponds to the end of the gentle buncher section. The integrated power deposited in case of CW beam is 2.9 kW.

Normally the RFQ-designer uses "standard" distributions to predict the RFQ under study, such as the quasistatic waterbag and gaussian. It is worth to compare the predicted losses of these type of distributions with the same Twiss parameters of the WARP simulation, and the relative estimated real distribution. Table 1 shows the transmission, the total kW lost into the RFQ and the Halo parameter relative to each distribution: truncated gaussian at 3σ , quasistatic waterbag and simulated one with WARP. It is possible to see that the approximation holds quite good for the W lost into the RFQ and the losses. However, the estimates with the standard distributions result optimistic as far as the losses are concerned of 2.3%. Therefore, for a fine estimate

Content from this work may be used under the terms of the CC BY 3.0 licence (© 2018). Any distribution of this work must maintain attribution to the author(s), title of the work, publisher, and DOI.

of the transmission it is necessary to study the RFQ acceleration and transport with the realistic distribution. The last but not the least aspect refers to the transient transmission and parameters change due to the build-up of space charge compensation. The RFQ model includes the measured geometry of the cavity [7] and the voltage profile from bead-pull measurements were also implemented in the code TOUTATIS by using a perturbed Vanes file [8]. In Fig. 4 is reported the emittance along the RFQ with Warp result as input distribution.

Table 1: Beam Distribution Effects at End of RFQ

Dist. Type	Tr. Out Emit.	Long. Emitt.	Halo	Losses	Losses Power
Unit	mmrad	MeVdeg		%	W
Warp	0.20	0.17	3.3	16.0	2.9
Gaussian	0.26	0.20	0.8	16.6	3.0
Waterbag	0.27	0.21	0.4	15.7	2.9

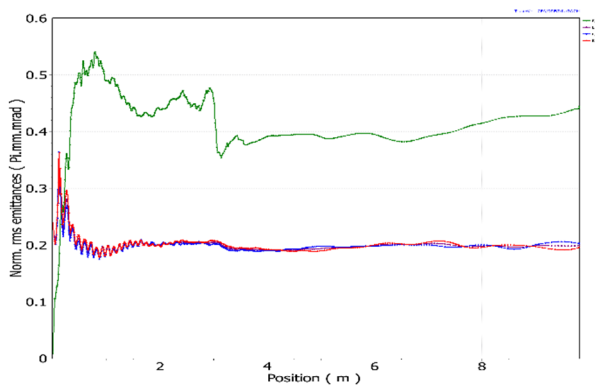


Figure 4: Emittance inside RFQ with real vanes and warp result as input distribution. Green Curve is longitudinal Emittance. The other curve the transverse Emittances.

BD CHARACTERIZATION AT LOW CURRENT

First Beam Operation

The first commissioning stage will involve the injector source, the RFQ and the MEBT with a low power beam dump in pulsed mode, up to 0.1% DC. Due to the potential damage even at low DC that may come from the deuteron beam, and the debug of the Low-Level RF system, it was decided to inject a low current proton beam of 7-9 mA at 50 keV, to avoid large power deposition and to maximize the RFQ acceptance with respect the input mismatch.

Injector Input

The source extraction was designed for a maximum 155 mA deuteron total current beam at 100 keV (D^+ , D_2^+), extracted from an extraction hole of the plasma electrode of 6 mm radius. In January 2018, we tested several configurations at different proton currents at 50 keV, to test the best extraction conditions, reducing the extraction hole down to 3 mm radius.

The results, in agreement with simulations and calculation, consisted of a beam of 13 mA total extracted current

(proton and molecular hydrogen ions) with approximately 7-8 mA proton current. Figure 5 shows the simulated phase space at 20 cm from the extraction hole of the plasma electrode, performed with AXCEL, of the beam above considered.

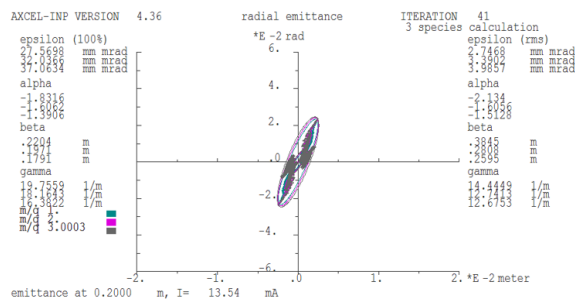


Figure 5: Output at 20 cm from the plasma electrode aperture for 13 mA proton beams.

The divergence of the whole beam is constrained between ± 30 mrad, while the dimension is in between ± 5 mm. The extraction is behaving like an electrostatic lens decreasing the divergence also of the molecular ions of the hydrogen.

Since the beam generalized perveance is one order of magnitude smaller with respect the deuteron beam (10^{-3} for D beam and 10^{-4} for low proton current beam), the space-charge effects in the low energy beam transfer line are depressed with respect to the deuteron case.

In such condition, the trace-forward method, applied in previous studies [9], Fig. 6 shows the results for a certain couple of solenoid field, was chosen to retrieve the beam evolution along the LEBT up to the RFQ. This step is preliminary with respect the study of the voltage characterization.

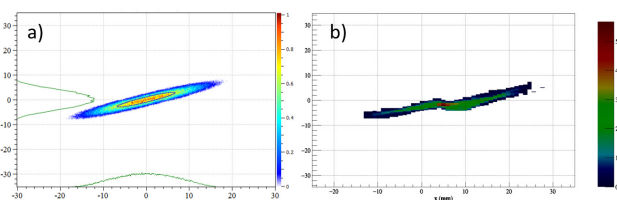


Figure 6: 7 mA proton beam distribution in phase space at the low energy beam transfer line emittance meter position (between the two LEBT solenoids). a) simulated distribution in phase-space, with the same set of solenoid strength b) Measured distribution in phase-space with the same set of solenoid couples. The simulated normalized rms emittance is 0.075 mm mrad, while the measured one is 0.08 mm mrad.

RFQ and MEBT Behaviour

The software used for the transfer lines simulation is TraceWin: the LEBT was implemented in the code with solenoid field-maps; the space-charge compensation trend along z was inserted from a WARP simulation. The RFQ was modelled with TOUTATIS code. The RFQ model includes the measured geometry of the cavity [7] and the

voltage profile from bead-pull measurements were also implemented in the code [8]. Figure 7 shows the reconstructed macro particles density along the accelerator with respect the beam axis for the matched beam. Once the nominal solution is retrieved, it is possible to study the voltage characterization of the RFQ.

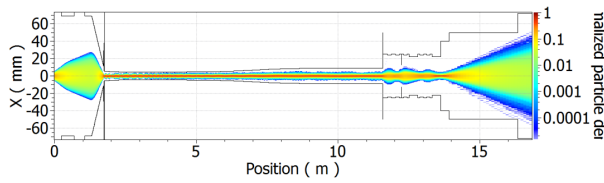


Figure 7: Macro particles densities with respect the beam axis, starting outside the extraction column and up to the LPBD.

Figure 8 shows the voltage calibration of the RFQ with respect to different input mismatches. The transmission is calculated looking at the RFQ input current, measured by an ACCT, at the RFQ output current, measured by another ACCT at the RFQ exit and at the end of the line, at the low power beam dump, equipped like a Faraday Cup. The MEBT quadrupoles (one triplet and one doublet) were set as for the matched beam. The first results is that the 7 mA proton beam will be 100% transmitted even with a mismatch of 220%, confirming the RFQ low sensitivity to solenoid fields setting with respect to the 135 mA D⁺ case, where a mismatch of 20% can cause more losses than 20%. Different curves with respect to different input matching. α indicates a converging or diverging beam at the RFQ input. The different matching was obtained changing the solenoid values in the LEBT model. The difference between the ACCT and the LPBD currents are due to the not accelerated particles, which are not transmitted along the MEBT section due to a sort of energy selection done by the quadrupoles and appropriate placed scrapers.

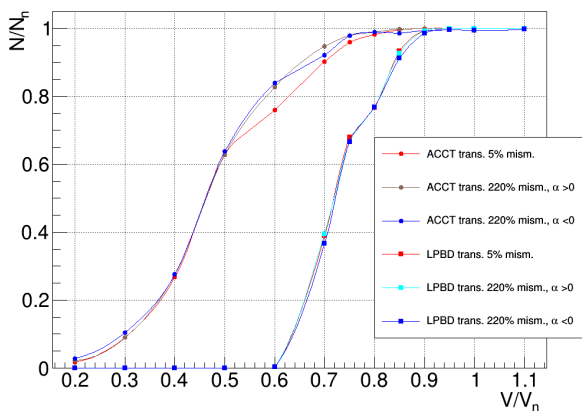


Figure 8: Normalized transmission (N/N_n) with respect to the matched value transmission (N_n) from the RFQ input current (LEBT ACCT) to the output of the RFQ (ACCT) and to the end of the line (LPBD) with respect to different RFQ voltage ratios (V), normalized to the nominal voltage value (V_n).

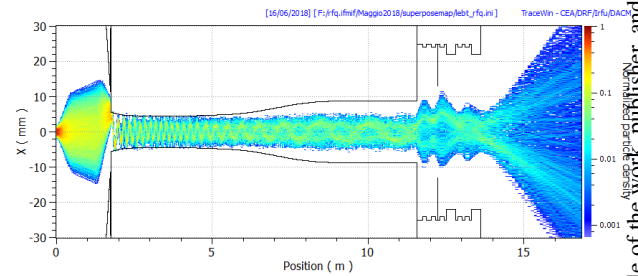


Figure 9: Macro particles density when the second solenoids is off-axis on X of 6 mm.

With the nominal voltage if is present a misalignment of the RFQ respect to the LEBT of 6 mm only on X, without any correction by using the steerers, the 86% of the beam is lost, as reported in Fig. 9.

In Table 2 is reported the effects of the two LEBT solenoids misalignment, without the use of the steerers, at the RFQ exit. The performed statistics is with 100 cases, considering only the maximum displacement on X and Y. Almost all the beam is lost if there is a misalignment of more than 4 mm.

The first days of beam operations have confirmed the results of these simulations, for what the optimum values of the lenses (solenoids) is concerned. An important misalignment between the LEBT and RFQ requires a high value of steerers and requires further tuning work to recuperate the nominal beam transmission (present value is 85%).as well as an upgrade of the model with the extraction region included.

Table 2: Solenoids Misalignment Effects at End of RFQ

Misalignment [mm]	Losses [%]
+/- 1	15.5
+/- 2	45.1
+/- 3	79.1
+/- 4	93.6

CONCLUSION

The space charge neutralization is key phenomena that dominates the beam dynamics of the high intensity LEBT. In this paper, a method was applied to achieve an enough robust model to describe the input of the RFQ: the preliminary study shows that despite the very similar power deposition and losses, the second order moments may vary with respect to the standard design distributions (with the same Courant-Snyder parameters in case of mismatched beam. Further studies are foreseen as well as an upgrade of the model with the extraction region included.

The first beam input of IFMIF-EVEDA RFQ has been chosen and deeply studied. Thanks to its robust beam dynamics, it will allow to debug any possible issue of the RFQ in a safety environment. The current of the beam will be then ramp up to 30 mA, to study the effect of the growing space-charge term in the accelerator.

ACKNOWLEDGEMENTS

The present work has performed in framework of the Broader Approach Agreement. The authors gratefully acknowledge the support of their home institutions and research funders in this work.

DISCLAIMER

Views and opinions expressed herein do not necessarily reflect those of QST, Fusion for Energy, or of the authors' home institutions or research funders.

REFERENCES

- [1] P. Cara *et al.*, “The Linear IFMIF Prototype Accelerator (LI-PAC) Design Development under the European-Japanese Collaboration”, in *Proc. IPAC'16*, Busan, Korea, May 2016, paper MOPOY057, p. 985.
- [2] R. Gobin *et al.*, “Final Design of the IFMIF Injector at CEA/Saclay”, in *Proc. IPAC'13*, Shanghai, China, May 2013, paper THPWO003, p. 3758.
- [3] N. Chauvin *et al.*, “Final Design of the IFMIF-EVEDA Low Energy Beam Transport Line”, in *Proc. PAC'09*, Vancouver, Canada, May 2009, paper TH5PFP004, p.3190.
- [4] M. Comunian and A. Pisent, “Beam Dynamics Redesign of IFMIF-EVEDA RFQ for a Larger Input Beam Acceptance”, in *Proc. IPAC'11*, San Sebastian, Spain, Sep. 2011, paper MOPS031, p. 670.
- [5] H. Dzitko *et al.*, “Technical and Logistical Challenges for IFMIF-LIPAC Cryomodule Construction”, in *Proc. SRF'15*, FRBA01, Whistler, Canada, Sep. 2015, p. 1453.
- [6] I. Podadera *et al.*, “The Medium Energy Beam Transport Line (MEBT) of IFMIF/EVEDA LIPAc”, in *Proc. IPAC'11*, San Sebastian, Spain, Sep. 2011, paper WEPS058, p. 2628.
- [7] A. Palmieri *et al.*, “Tuning the IFMIF 5MeV RFQ Accelerator”, in *Proc. LINAC'16*, East Lansing, MI, USA, Sep. 2016, paper THPLR049, p. 969.
- [8] L. Bellan *et al.*, “Source and LEBT Beam Preparation for IFMIF-EVEDA RFQ”, in *Proc. LINAC'16*, East Lansing, MI, USA, Sep. 2016, paper TUPRC005, p. 420.
- [9] L. Ferrari *et al.*, “Production quality controls and geometric characterization of the IFMIF-RFQ modules via the usage of a Coordinate Measuring Machine”, *Fusion Engineering and Design*, vol. 115, pp. 23-32, 2017.

FIRST HEAVY ION BEAM ACCELERATION WITH A SUPERCONDUCTING MULTI GAP CH-CAVITY

W. Barth^{†,1,2}, K. Aulenbacher^{1,3}, M. Basten⁴, M. Busch⁴, F. Dziuba¹, V. Gettmann¹, M. Heilmann²,
 T. Kürzeder¹, M. Miski-Oglu¹, H. Podlech⁴, A. Rubin², A. Schnase², M. Schwarz⁴, S. Yaramyshev²
¹Helmholtz Institute Mainz, Germany

²GSI Helmholtzzentrum für Schwerionenforschung, Darmstadt, Germany

³Johannes Gutenberg-Universität Mainz, Mainz, Germany

⁴IAP Goethe-Universität Frankfurt, Frankfurt, Germany

Abstract

A newly developed superconducting 15-gap RF-cavity has been successfully tested at GSI Helmholtzzentrum für Schwerionenforschung. After a short commissioning and ramp up time of some days, a Crossbar H-cavity accelerated first time heavy ion beams with full transmission up to the design beam energy of 1.85 MeV/u. The design acceleration gain of 3.5 MV inside a length of less than 70 cm has been verified with heavy ion beam of up to 1.5 particle m_e/m_p . The measured beam parameters showed excellent beam quality, while a dedicated beam dynamics layout provides beam energy variation between 1.2 and 2.2 MeV/u. The beam commissioning is a milestone of the R&D work of Helmholtz Institute Mainz (HIM) and GSI in collaboration with Goethe University Frankfurt (GUF) towards a superconducting heavy ion continuous wave linear accelerator cw-Linac with variable beam energy. Further linac beam dynamics layout issues will be presented as well.

collaboration of GSI, HIM and GUF. The demonstrator setup, embedded in a new radiation protection cave, is located in straightforward direction of the GSI-High Charge State Injector (HLI).

Table 1: Design Parameters of the cw-Linac

Mass/charge		6
Frequency	MHz	216.816
Max. beam current	mA	1
Injection energy	MeV/u	1.4
Output energy	MeV/u	3.5 – 7.3
Output energy spread	keV/u	± 3
Length of acceleration	m	12.7
Sc CH-cavities	#	9
Sc solenoids	#	7

INTRODUCTION

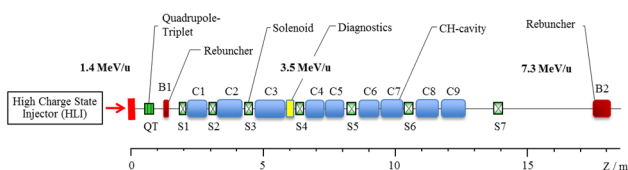


Figure 1: General cw-Linac layout [1].

Nine superconducting CH cavities operated at 217 MHz provide for ion acceleration to beam energies between 3.5 MeV/u and 7.3 MeV/u, while the energy spread should be kept smaller than ± 3 keV/u. A conceptual layout (see Fig. 1) of this sc cw-Linac was worked out eight years ago [1]. It allows the acceleration of highly charged ions with a mass to charge ratio of up to 6. For proper beam focusing superconducting solenoids have to be mounted between the CH cavities. The general parameters are listed in Table 1 [2]. R&D and prototyping (demonstrator project) [3] in preparation of the proposed HElmholtz Linear ACcelerator (HELIAC) is assigned to a

The demonstrator comprises a 15 gap sc CH-cavity (CH0) embedded by two superconducting solenoids; all three components are mounted on a common support frame [4]. The beam focusing solenoids provide maximum fields of 9.3 T, the free beam aperture is 30 mm. A configuration of one main Nb₃Sn-coil and two compensation coils made from NbTi shields the maximum magnetic field of 9.3 T within a longitudinal distance of 10 cm down to 30 mT. The solenoids are connected to LHe ports inside the cryostat by copper tapes allowing dry cooling. The sc CH structure CH0 (Fig. 2) is the key component and offers a variety of research and development [5].

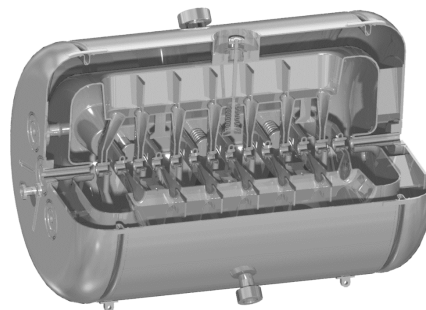


Figure 2: Sectional drawing of the 15-gap demonstrator CH-cavity (CH0).

*Work supported by the BMBF, project number 05P15RFBA, MYRTE which is funded by the European Commission under Project-ID 662186 and Helmholtz International Center for FAIR.

†w.barth@gsi.de

MATCHING SECTION AND EQUUS BEAM DYNAMICS

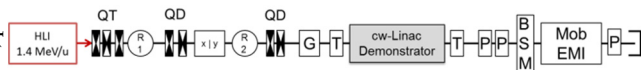


Figure 3: Layout of matching line to the Demonstrator and beam diagnostics test bench; QT = quadrupole triplet, QD = quadrupole duplet, R = rebuncher, X/Y = beam steerer, G = SEM-grid, T = beam current transformer, P = phase probe, BSM = bunch shape monitor, EMI = emittance meter.

The beam dynamics layout behind the HLI at 1.4 MeV/u has been simulated in advance. In a preparing beam test run, it could be confirmed, that the room temperature focusing quadrupoles (triplet and 2 duplets) and 2 rebuncher cavities are sufficient to provide for full 6D-matching to the demonstrator [6]. At the same time, the input beam is axially symmetric for further solenoid focusing due to especially chosen gradients, while bunch length and momentum spread are matched as well. The transport line (see Fig. 3) provides also for necessary beam diagnostics devices. Moreover, beam transformers, Faraday cups, SEM-profile grids, a dedicated emittance meter, a bunch structure monitor and phase probe pickups (beam energy measurements applying time of flight) provide for proper beam characterization behind the demonstrator.

The beam dynamics layout of the sc cw-Linac is based on the EQUUS (EQUidistant mUltigap Structure) concept, as proposed in [7]. It features high acceleration efficiency with longitudinal and transversal stability, as well as a straightforward energy variation. Energy variation can easily be achieved by varying the applied RF-voltage or the RF-phase of the amplifier. Highly charged ions with a mass-to-charge ratio of maximum 6 will be accelerated from 1.4 MeV/u up to 3.5 - 7.3 MeV/u. Energy variation while maintaining a high beam quality is the core issue with respect to beam dynamics, simulated using advanced software [8-9] and previously developed algorithms [10-13]. The cell length inside an EQUUS designed cavity is kept constant and is fixed with a higher (geometrical) β compared to the injection beam energy (constant- β structure). As a consequence the constant- β structure leads to a sliding movement in longitudinal phase space. Trajectory and energy gain depend strongly on the initial phase at the first gap centre and the difference between particle energy and design energy. The corresponding transversal emittance evolution has been measured in a broad range with small emittance growth.

COMMISSIONING OF THE DEMONSTRATOR

The sc 15 gap CH-cavity is directly cooled with liquid helium, supported by a helium jacket made by titanium. The vendor Research Instruments GmbH (RI) provided for sufficient cavity preparation. After high pressure rinsing (HPR) a performance test in a vertical cryostat at low

RF power was performed at IAP, reaching gradients up to 7 MV/m. After the final assembly of the helium vessel and further HPR preparation at RI, the cavity was tested again, but in a horizontal cryostat. The cavity showed improved performance due to an additional HPR treatment, the initial design quality factor Q_0 has been exceeded by a factor of four, a maximum accelerating gradient of $E_{acc} = 9.6$ MV/m at $Q_0 = 8.14 \times 10^8$ has been achieved [14, 15]. Prior beam commissioning of the demonstrator cavity, the RF power couplers [16] were tested and conditioned with a dedicated test resonator. During the operation, the "cold" coupler window has been anchored to the liquid nitrogen supply tube by copper ribbons. In a clean room of class ISO4 the power couplers were integrated in the RF-cavity, as well as three frequency tuners, developed at IAP and manufactured at GSI for the control of resonance frequency. Furthermore, the CH-cavity and both solenoids were assembled on a string. After leak testing of the accelerating string the complete cold mass was integrated [17] into the cryostat outside of the clean room.

FIRST BEAM ACCELERATION

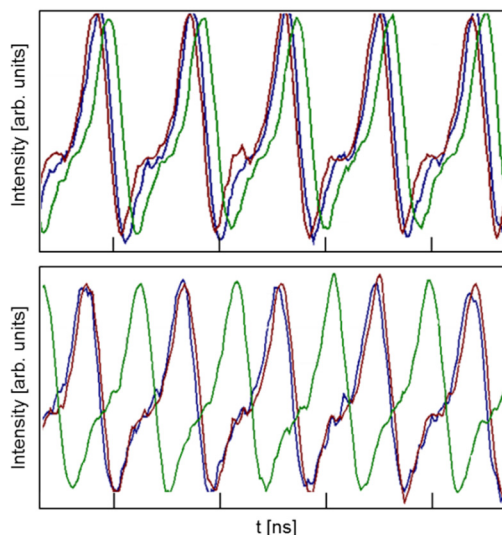


Figure 4: First RF-acceleration with CH-cavity; measured Ar^{11+} -phase probe signals from HLI beam at 1.366 MeV/u (top), RF-frequency is 108.408 MHz ($T = 9.224$ ns). By acceleration up to the nominal beam energy (down), the coarse time of flight between blue and red signal is slightly reduced. The time of flight for the fine measurement between red and green signal is significantly shifted, according to the beam energy of 1.866 MeV/u.

At June 2017, after successful RF-testing of the sc RF-cavity in 2016, set up of the matching line to the demonstrator and a short commissioning and ramp up time of some days, the CH0-cavity first time accelerated heavy ion beams (Ar^{11+}) with full transmission up to the design beam energy of 1.866 MeV/u ($\Delta W_{kin} = 0.5$ MeV/u) [18], as shown in Fig. 4. For the first beam test the sc cavity was powered with 10 Watt of net RF power, providing an

Content from this work may be used under the terms of the CC BY 3.0 licence (© 2018). Any distribution of this work must maintain attribution to the author(s), title of the work, publisher, and DOI.

accelerating voltage of more than 1.6 MV inside a length of 69 cm. Further on the design acceleration gain of 3.5 MV has been verified and even exceeded by acceleration of beam with high rigidity ($A/q = 6.7$). As summarized in Table 2, argon and helium ion beams with different charge state from an ECR ion source (${}^4\text{He}^{2+}$, ${}^{40}\text{Ar}^{11+}$, ${}^{40}\text{Ar}^{9+}$, ${}^{40}\text{Ar}^{6+}$) were accelerated at HLI for further beam tests with the demonstrator. For longitudinal beam matching the rebuncher settings were adapted according to the mass of charge ratio A/q , as well as the acceleration voltage U .

Table 2: RF Parameters for Matched Case

	He^{2+}	Ar^{11+}	Ar^{9+}	Ar^{6+}
A/q	2.0	3.6	4.4	6.7
$U_{\text{Reb1,eff}}$ [kV]	8.3	15.0	18.3	27.9
$U_{\text{Reb2,eff}}$ [kV]	22.7	40.8	49.9	75.9
$E_{\text{acc,CH}}$ [MV/m]	1.8	3.2	3.9	5.9
U_0 [MV]	1.2	2.2	2.7	4.0

$$* E_{\text{acc}} = \text{transit time factor} \times \text{total accelerating voltage} / (n \times 0.5 \times \beta \lambda)$$

A maximum average beam intensity of $1.5 \mu\text{A}$ has been achieved, limited only by the beam intensity of the ion source and maximum duty factor (25%) of the HLI, while the CH-cavity was operated in cw-mode. All presented measurements were accomplished with high duty factor beam and maximum beam intensity from the HLI.

SYSTEMATIC BEAM MEASUREMENTS

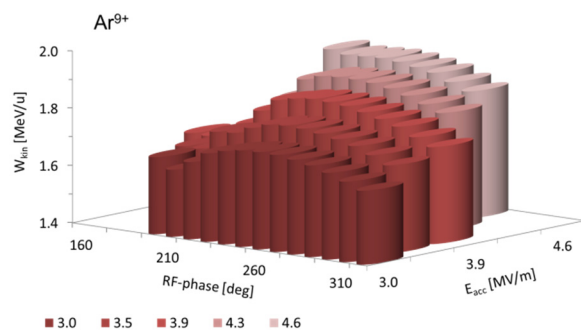


Figure 5: 2D-scan of Ar^{9+} -beam energy versus accelerating gradient and RF-phase [18].

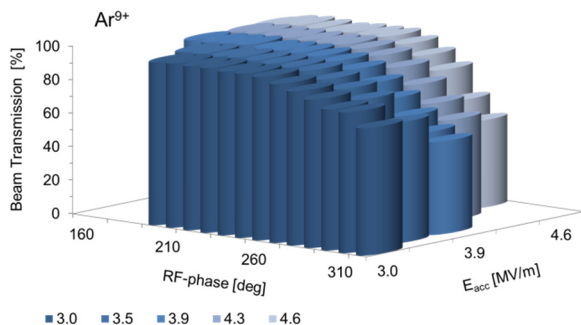


Figure 6: 2D-scan of Ar^{9+} -beam transmission versus accelerating gradient and RF-phase [18].

In Figs. 5 and 6 a full measured 2D-scan of beam energy and beam transmission for a wide area of different accelerating fields and RF-phases is depicted. The linear increase of beam energy with ramped accelerating gradient could be observed for different RF-phase settings, while the beam transmission is kept above 90 %. To aim for the maximum beam energy at a given accelerating gradient the RF-phase has to be adapted slightly. In general these measurements confirm impressively the EQUUS beam dynamics, featuring effectively beam acceleration up to different beam energies without particle loss and significant beam quality degradation. As measured with helium beam, for lighter ions a maximum beam energy of up to 2.2 MeV/u could be reached with the demonstrator cavity, but with reduced beam quality.

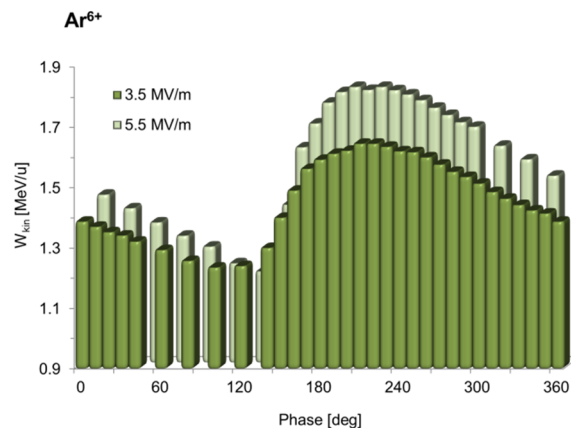


Figure 7: Phase-scan of Ar^{6+} -beam energy for 3.5 MV/m and 5.5 MV/m.

With Ar^{6+} -beam ($A/q = 6.7$), an energy gain above 0.5 MeV/u could be reached with an accelerating gradient of 6 MV/m. As an example Fig. 7 shows a fully measured 360° phase scan for two different accelerating gradients (3.5 MV/m and 5.5 MV/m). All individual data as well as the characteristic shapes of the phase scans are in good agreement according to the accelerating gradient. For an increased gradient the maximum beam energy at an RF-phase of 210° boosts as well, while the minimum beam energy at 130° could be decreased down to 1.2 MeV/u.

The bunch length detected with a bunch shape monitor (BSM) [19, 20] was measured as very sensitive to RF-phase changes. A change of RF-phase by 30° only, leads to a significant change of bunch length (by more than a factor of 4), while the beam transmission is not affected. For further matching to another CH-cavity, the adjustment of the beam energy setting by changing the RF-amplitude is more favourable - compared to changing the RF-phase - as no significant bunch shape change could be observed.

The beam quality has been characterized by measuring the phase space distribution. The measured emittance of the argon beam, delivered by the ECR and HLI, shows an adequate beam quality: the total 90% horizontal beam emittance is measured for $0.74 \mu\text{m}$, while in the vertical plane the total 90% emittance is $0.47 \mu\text{m}$ only. All measurements have been performed without solenoidal field,

Content from this work may be used under the terms of the CC BY 3.0 licence (© 2018). Any distribution of this work must maintain attribution to the author(s), title of the work, publisher, and DOI.

therewith any additional emittance degradation effects by different beam focusing could be avoided. The measured (normalized) beam emittance growth at full beam transmission is sufficiently low: 15 % (horizontal plane) and 10% (vertical plane). Selective measurements at other RF-amplitudes and -phases, as well as for other rigidities confirmed the high (transversal) beam performance in a wide range of different parameters. Besides beam energy measurements the bunch shape was measured after successful matching (see Fig. 8) with the Feshchenko monitor [20]. As shown, an impressive small minimum bunch length of about 300 ps (FWHM) and 500 ps (base width) could be detected, sufficient for further matching to and acceleration in future RF-cavities

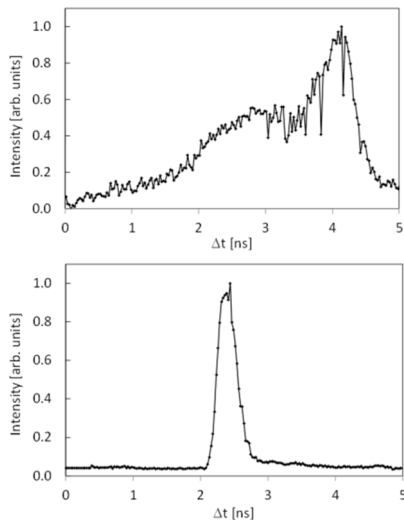


Figure 8: Bunch shape of Ar⁹⁺-beam at 1.366 MeV/u (top) and fully matched at 1.85 MeV/u (down) [18].

ADVANCED LINAC LAYOUT

Up to now, the reference design for the cw-Linac dates back to [1]. Meanwhile many experiences have been gained in design, fabrication and operation of sc CH-cavities and the associated components. In this context, a revision of the Linac layout was recommended. Optimized cavity layouts [21] resulted in modified voltage distributions. Furthermore, the layout - now with three CH-cavities and a rebuncher [22] per cryo module - has been specified with more details. It features high acceleration efficiency with longitudinal and transversal stability, as well as a straightforward energy variation. Energy variation can easily be achieved by varying the applied RF-voltage or the RF-phase of the amplifier. Highly charged ions with a mass-to-charge ratio of max. 6 will be accelerated from 1.4 MeV/u up to 3.5- 7.3 MeV/u. Energy variation while maintaining a high beam quality is the core issue with respect to beam dynamics, simulated using advanced software [8, 9] and previously developed algorithms [10, 13, 23-25].

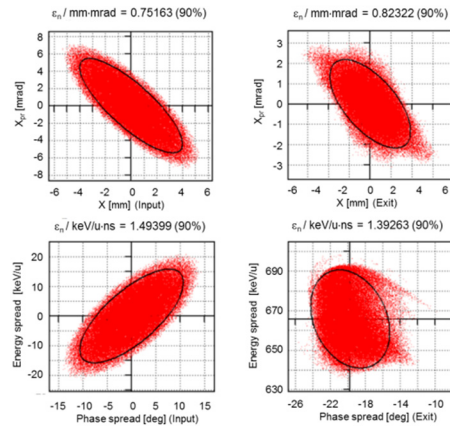


Figure 9: Phase space portraits applying an advanced Linac layout; top: $x - x'$, bottom: $\Delta\phi - \Delta W$, left: CM1-Input (emittance size as at HLI), right: Output of CM4 [26].

Promising power and beam tests with the 15-gap CH0 showed successfully, that higher accelerating gradients can be achieved, thus leading to a more efficient design with four cryo modules (CM1-CM4). Consequently an advanced beam dynamics layout [26] is carried out with respect to the ambitious beam-, RF- and mechanical requirements. Figure 9 shows phase space portraits based on the recent advanced layout applying a max. accelerating gradient of 7.1 MeV/u. Applying the advanced beam dynamics layout for lower mass to charge ratios, significant higher beam energies could be achieved (e.g. up to 14.6 MeV for a p⁺-beam).

SUMMARY

The design acceleration gain of the first sc CH-cavity was achieved with heavy ion beams even above the design mass to charge ratio at full transmission and maximum available beam intensity [27]. The beam quality was measured as excellent in a wide range of different beam energies, confirming the capabilities of the applied EQUUS beam dynamics design. An advanced cw-Linac approach, based on a standard cryomodule equipped with three CH-cavities and a sc-rebuncher [28, 29], demonstrates the high capabilities due to energy variation preserving the beam quality, as shown in the first beam test. This new design could provide beam acceleration for a wide range of different ions (protons to uranium) above the design beam energy, featuring the ambitious GSI-user program [30], while the GSI-UNILAC is upgraded for short pulse high current FAIR-operation [31-33]. The achieved demonstrator beam commissioning is a major milestone paving the way to the cw-Linac HELIAC.

ACKNOWLEDGEMENTS

Successful beam testing could not be accomplished without strong support of highly committed people from different GSI-departments. The beam test is a milestone of the R&D work of HIM and GSI in collaboration with GUF in preparation of a superconducting heavy ion continuous wave linear accelerator.

REFERENCES

- [1] S. Minaev *et al.*, “Superconducting, energy variable heavy ion linac with constant β , multicell cavities of CH-type”, *Phys. Rev. ST Accel. Beams*, vol. 12, pp. 120101, (2009), doi:10.1103/PhysRevSTAB.12.120101
- [2] W. Barth *et al.*, “A superconducting CW-LINAC for heavy ion acceleration at GSI”, EPJ Web of Conferences, vol. 138, article number 01026, (2017), doi:10.1051/epjconf/201713801026
- [3] M. Amberg *et al.*, “Status of the superconducting cw Linac at GSI”, in *Proc. 6th. Int. Symposium on Exotic Nuclei (EXON 2012)*, Vladivostok, Russia, Oct. 2012, pp. 337-346, doi:10.1142/9789814508865_0044
- [4] F. Dziuba *et al.*, “First Cold Tests of the Superconducting cw Demonstrator at GSI”, in *Proc. of RuPAC'16*, St. Petersburg, Russia, Oct. 2016, doi:10.18429/JACoW-RuPAC2016-WECBMH01
- [5] T. Kürzeder *et al.*, “Infrastructure for Superconducting CH-Cavity Preparation at HIM”, in *Proc. IPAC'18*, Vancouver, Canada, 2018, doi:10.18429/JACoW-IPAC2018-WEPML045
- [6] M. Schwarz *et al.*, “Beam Dynamics for the sc cw heavy ion Linac at GSI”, in *Proc of IPAC'15*, Richmond, VA, USA, 2015, doi:10.18429/JACoW-IPAC2015-THPF025
- [7] M. Miski-Oglu *et al.*, “Steps towards superconducting cw-Linac for heavy ions at GSI”, in *Proc of SRF'17*, Lanzhou, China, 2017, doi:10.18429/JACoW-SRF2017-MOPB024
- [8] R. Tiede *et al.*, “LORASR Code Development”, in *Proc of EPAC'06*, Edinburgh, Scotland, 2006, pp. 2194-2196.
- [9] S. Yaramyshev *et al.*, “Development of the versatile multi-particle code DYNAMION”, *Nucl. Instr. Meth. Phys. Res., Sect. A*, vol. 558/1 2006, pp. 90-94, doi:10.1016/j.nima.2005.11.018
- [10] S. Yaramyshev *et al.*, “An advanced procedure for longitudinal beam matching for sc cw heavy ion linacs”, in *Proc of HB'16*, Malmö, Sweden, 2016, doi:10.18429/JACoW-HB2016-THPM9Y01
- [11] M. Schwarz *et al.*, “Beam Dynamics Simulations for the New Superconducting CW Heavy Ion Linac at GSI”, in *Proc of SRF'17*, Lanzhou, China, 2017, doi:10.18429/JACoW-SRF2017-MOPB005
- [12] S.M. Polozov *et al.*, “Beam Dynamics Simulations and Code Comparison for a New CW RFQ Design”, in *Proc of HB'16*, Malmö, Sweden, 2016, doi:10.18429/JACoW-HB2016-MOPL004
- [13] S. Yaramyshev *et al.*, “Virtual charge state separator as an advanced tool coupling measurements and simulations”, *Phys. Rev. ST Accel. Beams* 18, 050103, 2015, doi:10.1103/PhysRevSTAB.18.050103
- [14] F. Dziuba *et al.*, “First Performance Test on the Superconducting 217 MHz CH Cavity at 4.2 K”, in *Proc of LINAC'16*, East Lansing, USA, 2016, doi:10.18429/JACoW-LINAC2016-THPLR044
- [15] F. Dziuba *et al.*, “Performance tests of the superconducting 217 MHz CH cavity”, in *Proc of SRF'17*, Lanzhou, China, 2017, doi:10.18429/JACoW-SRF2017-TUPB024
- [16] M. Heilmann *et al.*, “High power RF coupler for the cw-linac demonstrator at GSI”, in *Proc of IPAC'17*, Copenhagen, Denmark, 2017, doi:10.18429/JACoW-IPAC2017-MOPVA054
- [17] V. Gettmann *et al.*, “Commissioning of a superconducting cw heavy ion Linac@GSI”, in *Proc of SRF'17*, Lanzhou, China, 2017, doi:10.18429/JACoW-SRF2017-MOPB094
- [18] W. Barth *et al.*, “First heavy Ion Beam Test with a superconducting multi gap CH-cavity”, *Phys. Rev. ST Accel. Beams*, vol. 21, pp. 020102, 2018, doi:10.1103/PhysRevAccelBeams.21.020102
- [19] T. Sieber *et al.*, “Bunch Shape Measurements at the GSI cw-Linac Prototype”, *Proc. J. Phys.: Conf. Ser. (Preprint IPAC'18)*, doi:10.18429/JACoW-IPAC2018-WEPAK006
- [20] A. V. Feschenko, “Technique and instrumentation for bunch shape measurements”, in *Proc of RuPAC'12*, St. Petersburg, Russia, Oct. 2016, pp. 181-185, paper FRXOR01.
- [21] M. Basten *et al.*, “First high power measurements of the next sc CH-cavities for the cw heavy ion Linac at GSI”, *Proc. J. Phys.: Conf. Ser. (Preprint IPAC'18)*, doi:10.18429/JACoW-IPAC2018-TUPAF008
- [22] M. Gusarova *et al.*, “Multipactor discharge in superconducting accelerating CH cavities”, *Proc. J. Phys.: Conf. Ser. (Preprint IPAC'18)*, doi:10.18429/JACoW-IPAC2018-TUPAK002
- [23] S. Yaramyshev *et al.*, “Advanced approach for beam matching along the multi-cavity sc cw Linac at GSI”, *Proc. J. Phys.: Conf. Ser. (Preprint IPAC'18)*, doi:10.18429/JACoW-IPAC2018-TUPAK002
- [24] M. Schwarz *et al.*, “Further steps towards the superconducting CW-linac for heavy ions at GSI”, in *Proc. of IPAC'16*, Busan, South Korea, May 2016, doi:10.18429/JACoW-IPAC2016-MOP0Y023
- [25] S. M. Polozov *et al.*, “Beam dynamics study and electro-dynamics simulations for the cw RFQ”, in *Proc. of IPAC'17*, Copenhagen, Denmark, May 2017, doi:10.18429/JACoW-IPAC2017-TUPAB013
- [26] M. Schwarz *et al.*, “Beam dynamics simulations for the new superconducting cw heavy ion Linac at GSI”, *Proc. J. Phys.: Conf. Ser. (Preprint IPAC'18)*, doi:10.18429/JACoW-IPAC2018-TUPAK003
- [27] W. Barth *et al.*, “Superconducting CH-Cavity heavy ion beam testing at GSI”, *Proc. J. Phys.: Conf. Ser. (Preprint IPAC'18)*, doi:10.18429/JACoW-IPAC2018-TUPAK004
- [28] M. Gusarova *et al.*, “Design of the two-gap superconducting re-buncher”, *Proc. J. Phys.: Conf. Ser. (Preprint IPAC'18)*, doi:10.18429/JACoW-IPAC2018-WEPML039
- [29] K. Taletsky *et al.*, “Study of low beta multi-gap superconducting bunchers”, *Proc. J. Phys.: Conf. Ser. (Preprint IPAC'18)*, doi:10.18429/JACoW-IPAC2018-WEPML041
- [30] M. Block *et al.*, “Direct mass measurements above uranium bridge the gap to the island of stability”, *Nature*, vol. 463, (2010), pp. 785, doi:10.1038/nature08774
- [31] W. Barth *et al.*, “ $^{28}\text{U}^{28+}$ -intensity record applying a H_2 -gas stripper cell”, *Phys. Rev. ST Accel. Beams*, vol. 18, pp. 040101, (2015), doi:10.1103/PhysRevSTAB.18.040101
- [32] L. Groening *et al.*, “Benchmarking of measurement and simulation of transverse rms-emittance growth”, *Phys. Rev. ST Accel. Beams*, vol. 11, pp. 094201, (2008), doi:10.1103/PhysRevSTAB.11.094201
- [33] W. Barth *et al.*, “High brilliance uranium beams for the GSI FAIR”, *Phys. Rev. ST Accel. Beams* 20, 050101, (2017), doi:10.1103/PhysRevAccelBeams.20.050101

DESIGN OF LINAC-100 AND LINAC-30 FOR NEW RARE ISOTOPE FACILITY PROJECT DERICA AT JINR

L. V. Grigorenko, A. S. Fomichev, Joint Institute for Nuclear Research, Dubna, Russia
V. S. Duybkov, T. V. Kulevoy¹, Yu. Yu. Lozeev, T. A. Lozeeva, S. M. Polozov, A. V. Samoshin,
National Research Nuclear University-Moscow Engineering Physics Institute, Moscow, Russia
also at NRC Kurchatov Institute-Institute of Theoretical and Experimental Physics, Moscow, Russia

Abstract

DERICA (Dubna Electron-Radioactive Ion Collider Facility) is the new ambitious project under development at JINR [1]. DERICA is proposed as the next step in RIB facilities development. It is planned that in the DERICA project the RIBs produced by the DERICA Fragment Separator (DFS), will be stopped in a gas cell, accumulated in the ion trap and then be transferred to the ion source/charge breeder, creating the highest possible charge state for the further effective acceleration (system {gas cell - ion trap - ion source/charge breeder}). From the accelerator point of view DERICA will include the driver LINAC-100 (energy up to 100 MeV/u) with the operating mode close to CW, the fragment separator, the re-accelerator LINAC-30 (energy up to 30 MeV/u), the fast ramping ring (energy < 300 AMeV), the collector ring and the electron storage ring with an injector. DERICA general concept and first results of LINAC-100 and LINAC-30 general layout are presented in this paper.

INTRODUCTION

Dubna Electron-Radioactive Ion Collider Facility (DERICA) is the new ambitious RIB facility project which was started in 2017. Scientists from a number of research institutes and universities from Russia and other countries took part in DERICA concept [1] preparation: JINR, NRC Kurchatov Institute, Budker INP, NRNU MEPhI, Lomonosov MSU, GSI, HIM and other.

The main aim of the DERICA project is the development and construction of RIB “factory” based on the ion trap for secondary ions. Finally it is planned to have a facility provided the direct radioactive isotopes (RI) studies in ion-electron collisions.

The DERICA complex will include a number of accelerators and other components. The first high-intensity quasi-CW driver linac called LINAC-100 will be used for generation of 50-100 MeV/u heavy ion beams which will be used for secondary RI production. Generated radioactive isotopes will be accumulated in an ion trap and after ionization they will be injected to a re-accelerator LINAC-30. This linac will produce pulses of ion beams in two energy bands (5-10 and 20-30 MeV/u) with smoothly varying energy. First time re-accelerated in LINAC-30 beams are planning to use in experiments with the stationary target. The possibility of LINAC-30 construction before LINAC-100 and its commissioning and operation with ACCULINNA -2 RIB facility are also under discussion (ACCULINNA -2 is the new fragment separator at U-400M cyclotron). The third stage of

DERICA project will include the construction of a fast ramping synchrotron for further secondary radioactive ion beam acceleration up to 300 AMeV/u. A collector ring and an electron storage ring will be constructed during the last stage of DERICA project. After that the main aim of the project will be achieved - direct study of radioactive ions in ion-electron collision will be possible.

DERICA RESEARCH AIMS AND GENERAL CONCEPT

Structure, properties and transformations of atomic nuclei are the main subjects of fundamental researches in low-energy nuclear physics. The comprehensive understanding of structure of atomic nuclei is necessary for description of astrophysical processes, including nucleosynthesis, and for investigations of various cross-disciplinary problems where the nuclear structure plays a key role. Significant progress in this direction has already been achieved, but the aim is still far away. More than three thousand radioactive isotopes (RI) were synthesized before now. According to theoretical estimates from 2000 to 3000 more isotopes are still waiting for its discovery (Fig. 1). Furthermore it is no answer yet even the most fundamental question of nuclear physics: where is the location of borderline of nuclear stability in the major part of the nuclear chart. The dripline is only known for the lightest nuclei (with number of protons $Z < 32$ or number of neutrons $N < 20$), but even here our knowledge almost does not extend beyond it and, thus, the limits of existence of nuclear structure is an open question.

The radioactive isotopes are characterized by an excess of neutrons or protons compared to the nuclear stable nuclides and often have unusual properties. Essential modification of structure of nuclei far from the “stability valley” has already been observed experimentally: discovery of new type of nuclear structure - neutron or proton halo, changes in the shell structure of nuclei caused by disappearance of old and emergence of new magic numbers. Though many of radioactive isotopes are very short-lived, they play a crucial role in the nuclear reactions taking place during the explosive nucleosynthesis. During the supernovae explosions and collisions of neutron stars these processes saturate the interstellar space with elements heavier than lithium. Finally, such processes define the chemical composition of planetary systems and, respectively, the world surrounding us. Another question, important for understanding of the star evolution processes, concerns the properties of neutron matter, which defines the life cycle of the neutron stars. Usual nuclear

matter is almost symmetric and consists of almost equal number of protons and neutrons (the typical ratio N/Z is in the range $1 < N/Z < 1.6$), therefore studies of stable nuclei do not answer this question. Studies of heavy exotic nuclear systems with considerable excess of neutrons ($N/Z > 1.6$) can be a basis for experimental investigation of extremely asymmetric neutron nuclear matter.

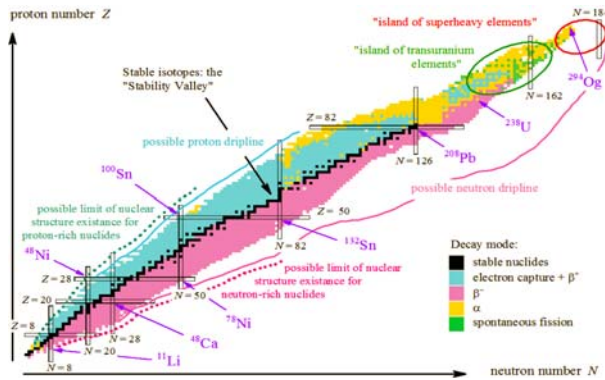


Figure 1: Global structures in the nuclear chart [2]. Vertical and horizontal bands indicate the “magic” numbers corresponding to number of protons Z and number of neutrons N .

Search for solution of these fundamental problems requires studies of unstable isotopes synthesized in laboratory conditions. For this reason, construction of radioactive ion beam (RIB) “factories” nowadays is the highway to the low-energy nuclear physics development. The world-largest such project FAIR (Darmstadt, Germany) is being developed at present [3]. FLNR JINR is one of places where the RIB studies are currently carried out. ACCULINNA and ACCULINNA-2 facilities driven by the U-400M cyclotron are under operation now [4]. The idea of RI-electron collider experiments appeared quite long time ago, reached a stage of well-developed projects and for more than two decades it repeatedly attracts attention of researchers. K4-K10 [5] was the project of FLNR JINR upgrade and transformation into the advanced RI factory. It has been completely accepted in 1990, but has not been implemented for the known non-scientific reasons. The complex included two rings, K4 (storage ring/accelerator with $B_{\max} \rho = 4$ Tm) and the experimental ring K10 (with $B_{\max} \rho = 10$ Tm).

Some ideas of the K4-K10 project were realized or proposed before present in a number of facilities. MUSES project [6] (two rings - storage/cooler and the experimental ring) was an important part of the RI factory development in RIKEN (Japan). It was also cancelled for non-scientific reasons in favor of more easily implementable projects. Now attempts to attack this problem in RIKEN continue within the SCRIT project (Self-Confining Radio-Isotope Ion Target - electron scattering on RI “fixed target” consisting of ions stored in the electromagnetic Penning trap) [7]. The project ELISE [8] is a part of the program of FAIR facility but it is “frozen” at least until 2030. Several ideas of the K4-K10 were realized in the storage complex IMP (Lanzhou, China). How-

ever, because of the low-intensity driver accelerator, the luminosity achieved there is far from sufficient value for the collider studies of electron-ion collisions. The project of a storage ring TSR@ISOLDE [9] at CERN was indefinitely postponed in order to better concentrate efforts on the researches in the fields of physics of ultrahigh energy (LHC, etc.) and antimatter (AD, ELENA, and etc.).

Thus the development and construction of new facility DERICA aimed at studies of the radioactive nuclei properties in the electron-RI collisions in the storage rings looks very actual.

The DERICA project purpose is to construct a unique accelerator and storage ring facility for the pioneering low-energy nuclear physics studies. These include production of still unknown RI, their mass measurements, studies of RI decay modes, fission barriers of heavy nuclei, studies of the nuclear reaction dynamics, and also determination of structure details of exotic nuclei, i.e. measurements of charge and matter radii with a high accuracy. There are some basic qualitative features of the DERICA project to be emphasized. In the K4-K10, MUSES, and ELISE projects the “hot” beam of RI, produced by fragment-separator, is injected into the storage ring and cooled there until it reaches the required quality for the experiments or for the injection into the next experimental ring. In DERICA project, the RIBs is planned to produce by the fragment separator DFS (DERICA Fragment Separator) also but following ions will be stopped in a gas cell, accumulated in an ion trap and then will be transferred to the ion source/charge breeder, creating the highest possible charge state for the further effective acceleration (system {gas cell - ion trap - ion source/charge breeder}). This scheme differs from conventional ISOL technology which is used in SPIRAL-2, ISAC-II and in a number of other operating RIB facilities. It is planning in DERICA project that RI will be re-accelerated by the LINAC-30 accelerator up to the energy of ~ 30 AMeV. For some tasks the higher energies are required. In particular, the effective operation of the electron-RI collider requires energies of the ions about 100 - 300 AMeV. For these purpose, further acceleration from ~ 30 to ~ 300 AMeV will be performed by the booster synchrotron FRR (Fast Ramping Ring) with high ramping rate of the magnetic field. The cycle duration {gas cell - ion trap - ion source/charge breeder} should be 0.1 - 0.3 sec. Depending on the scheme of the post-acceleration (only LINAC-30 or LINAC-30 + FRR) the time before injection into the experimental ring of CR is 0.1 - 1.0 sec. Compared to the earlier suggested approaches, the DERICA concept allows significant improvement of the time preceding the measurements start. This can be crucial for studies of short-lived RI (with $T_{1/2} < 1 - 5$ sec).

DERICA GENERAL LAYOUT, STAGES AND POSSIBLE SITE

The general layout of the DERICA complex is shown in Fig. 2. As one can see, finally DERICA will consist of a number of heavy-ion sources, quasi-CW driver LINAC-

Content from this work may be used under the terms of the CC BY 3.0 licence (© 2018). Any distribution of this work must maintain attribution to the author(s), title of the work, publisher, and DOI.

100, fragment separator DFS, gas cell (ion trap), re-accelerator LINAC-30 with a number of experimental channels, fast ramping ring FRR, collector ion ring CR and electron storage ring ER with injector. Last two rings will be used for direct study of radioactive ion structure in collisions with electrons.

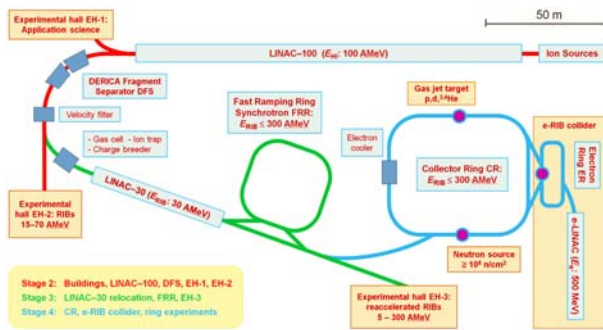


Figure 2: Concept of the DERICA project, stages 2 - 4. Different stages of the project are indicated by colours of beamlines. In the first stage the experiments can be conducted in experimental halls 1 (applied research using stable beams 25 - 100 AMeV) and 2 (direct reaction studies with RIBs at intermediate energies 20 - 70 AMeV). In the second stage high-quality post-accelerated RIBs in a broad energy range (5 - 300 AMeV) become available in experimental hall 2. In the third stage three experimental halls at the CR are added.

A staged implementation of the DERICA project was proposed to have the new experimental and applied researches in each stage (Fig. 2). For the total duration of the project construction 12 - 17 years, the first new experiments would appear already over 5 - 7 years. The stages can be divided like follows:

Stage 0: the scientific agenda is fully formulated, the technical concept is formed, required R&Ds are carried out.

Stage 1: equipment of the {gas cell - ion trap - ion source/charge breeder} system; experiments with stopped RI in the electromagnetic traps; construction and commissioning of the system of RI re-acceleration based on the LINAC-30; high-quality post-accelerated RIBs with energies 5 - 10 and 20 - 30 AMeV become available.

Stage 2: LINAC-100 construction and commissioning; applied studies with high-intensity stable-ion beams; DFS construction and commissioning, reaction studies with RIBs at intermediate energies 20 - 70 AMeV.

Stage 3: gas cell will be constructed; the equipment of the system {gas cell - ion trap - ion source/charge breeder} is relocated from the ACCULINNA-2 to DFS; after its commissioning experiments with RI in electromagnetic traps will become available; LINAC-30 is relocated from the ACCULINNA-2 to the DFS; high-quality post-accelerated RIBs with variably energy of 5 - 30 AMeV become available; intensities of the RIBs at this stage would exceed those available at the Stage 1 by orders; FRR construction and commissioning; high-quality post-accelerated RI beams with energy in the range of 5 - 300 AMeV become available.

Stage 4: CR and ER construction and commissioning; experiments can be performed at three independent experimental locations of the CR ring: (1) a collider experiment on the electron scattering, (2) reactions on the gas jet target [10] and (3) reactions on neutrons from the D+T reaction in the “merged beams” kinematics.

The possible site for the DERICA construction is shown in Fig. 3. It can be placed at JINR FLNR at the place close to the cyclotron U-400 building. The available area near FLNR is more than sufficient for the current DERICA project and for possible future upgrades.

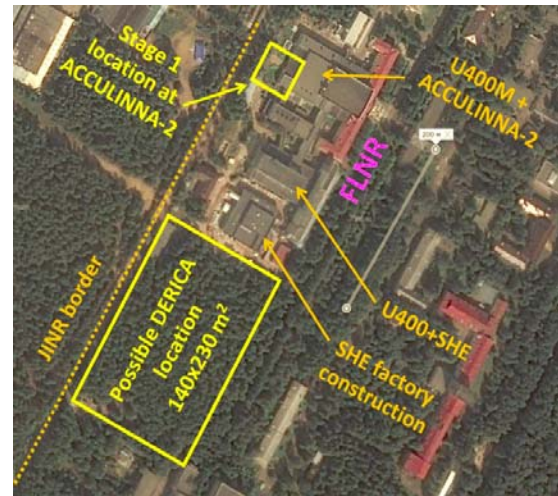


Figure 3: Possible location of the new laboratory at the JINR territory close to FLNR buildings.

LINAC-100 GENERAL LAYOUT AND FIRST BEAM DYNAMICS SIMULATION RESULTS

The general layout of the heavy-ion driver LINAC-100 is shown in Fig. 4. Such layout is similar to conventional driver linacs of many RIB complexes as SPIRAL-2 [11], FRIB [12] etc. Linac will include RFQ section, a number of normal conducting cavities for energies up to ~2-2.5 MeV/u and long medium-energy and high-energy sections which consist of SC cavities. This part of LINAC-100 will include short SC cavities with independent phase control for the high energy gain and SC solenoids or quadrupoles for focusing.

Necessary primary ions for DERICA driver are presented in Table 1. It is clear that for all ions the mass-to-charge ratio is $5.5 < A/Z < 6.0$. Note, that the beam current for a number of ions is non-zero and current will effect to the beam dynamics and accelerating cavities operation sufficiently.

The SC part of the linac is economically allowable in the case of identical cavities; otherwise the total accelerator cost dramatically increases. It means that the wave for all cavities will have the same phase velocity value. Wave and particle synchronous motion will be not observed here due to of particles reference phase slipping. The slipping value should not exceed some allowable limits. Otherwise the rate of the energy gain decreases, both

transverse and longitudinal beam stability disturbs and current transmission decreases. In this case there are a lot of cavities can be used in the accelerator. It is practical to divide them in several groups consisting of identical cavities. It should be noted that phase motion analysis problem is accentuated by the absence of synchronous particle. Analytical and numerical methods of beam dynamics study with accelerator layout optimization were developed at NRNU MEPhI [13-17]. Let us consider first results of the LINAC-100 parts general development and beam dynamics simulations.

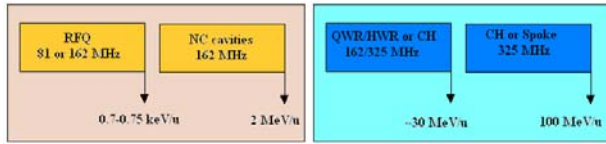


Figure 4: First version of DERICA's driver LINAC-100 general layout.

Table 1: Supposed Primary Beams in the LINAC-100 Accelerator. Most Available Charges of Bi and U Correspond to Modern Capacities of the Intensive Cryogenic ECR Sources

Ion	A/Z	I, μA
$^{11}\text{B}^{2+}$	5.5	> 10
$^{18}\text{O}^{3+}$	6.0	> 10
$^{20,22}\text{Ne}^{4+}$	5.5	> 8
$^{32,36}\text{S}^{6+}$	6.0	> 5
$^{36}\text{Ar}^{6+}$	6.0	> 5
$^{40,48}\text{Ca}^{7+}$	6.0	> 5
$^{56,64}\text{Ni}^{11+}$	5.8	> 5
$^{86}\text{Kr}^{15+}$	5.7	5
$^{132}\text{Xe}^{22+}$	6.0	5
$^{160}\text{Gd}^{27+}$	5.9	5
$^{209}\text{Bi}^{37+}$	5.65	4
$^{238}\text{U}^{40+}$	5.95	$\sim 0.8^*$

*Performance of the modern ECR sources with 28 GHz operating frequency can be as large as $\sim 1 \mu\text{A}$ for $^{238}\text{U}^{40+}$ [18-21].

RFQ for LINAC-100

The operating frequency of RFQ will be defined from the maximal transverse acceptance availability. As it is known, modern ECR ion sources can provide heavy ion beams with high charge state (40+ for U ions, as an example [18-21]). Such beam will have very high transverse emittance. It can achieve 100-200 mm·mrad for the heaviest ion as uranium.

Firstly we compare the acceptance of RFQ linac with operating frequencies of 81 and 162 MHz. Analytical result shows that 81 MHz RFQ is much more preferable for LINAC-100 and the lower frequencies as 54 or 40 MHz can be also discussed. Base parameters of linac both for 81 and 162 MHz are summarized in Table 2, results of the beam dynamics simulation in RFQ linac are presented in Fig. 5. It is clear that the current value of 81 MHz-RFQ acceptance is not enough for LINAC-100 and

it will be further enlarged. The 162 MHz RFQ will not discuss in future therefore.

The design of RFQ cavity will be based on the CW segmented-vane RFQ [22] developed by the joint team of MEPhI, ITEP, GSI and HIM [23-25]. The intervane voltage was limited by 1.3 of the Kilpatrick criterion value for this design.

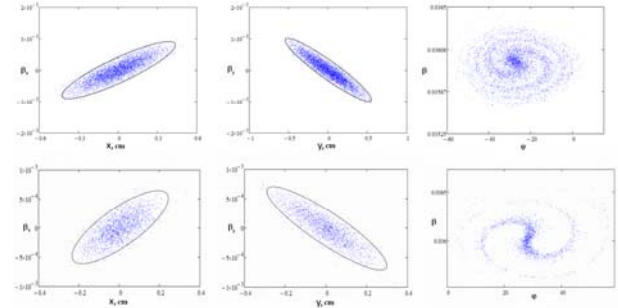


Figure 5: Beam dynamics simulation in RFQ of LINAC-100 (162.5 MHz on top, 81.25 MHz - bottom).

Table 2: Base Parameters of LINAC-100 RFQ both for 81 and 162 MHz

Parameter	Value	
Operating freq., MHz	162.5	81.25
Input energy, keV/u	16.9	16.3
Output energy, keV/u	611.9	614
Max modulation	1.4	1.9
Aperture, mm	3.2	4.4
Particle transmission, %	> 98	99.8
Synchr. phase, grad.	-90 ... -30	-90 ... -30
Voltage, kV	100	100
Initial emittance, mm·mrad	200	200
Length, cm	600	600

Normal Conducting Cavities for Intermediate Energies

The intermediate energy band (after RFQ and up to 2.0-2.5 MeV/u) has some difficulties both from the beam dynamics and the RF efficiency of the accelerating cavities. RFQ is not very effective here because of the low energy gain. But such energies is too low for short (2-gap) SC cavities: the energy gain per cavity should be decreased to 0.25-0.3 MeV per one gap. The longitudinal beam stability cannot be achieved here for higher RF potentials and the acceleration efficiency fall down here.

Let us discuss the possible types of the intermediate energy cavities for LINAC-100: RF Crossed Lenses (a method of ion focusing in linac by RF decelerating fields of crossed lenses, RFCL [26]); modified electrode form RFQ [27]; short 3-cell or 5-cell CH/IH cavities with focusing lenses between resonators.

High-Energy Superconducting Part

The beam dynamics in the superconducting part of LINAC-100 was studied by means of BEAMDULAC-SCL code developed at MEPhI especially for linacs con-

Content from this work may be used under the terms of the CC BY 3.0 licence (© 2018). Any distribution of this work must maintain attribution to the author(s), title of the work, publisher, and DOI.

sisting of short independently phased cavities [14-16, 28-29]. The ion beam motion stability analysis shows that with the slipping factor about 20 % (see Fig. 6) the SC part of the linac will consist of six groups of cavities which have geometrical velocities close to $\beta_g=0.07, 0.10, 0.14, 0.21, 0.30$ and 0.43 . All groups of cavities should be two- or four-gap (two QWR's or HWR's or four-gap CH/IH/Spoke). Using both transfer matrix calculation method [29] and smooth approximation [28] the preliminary SC linac parameters were defined for minimal linac length and lowest cost (Table 3). It is clear that ion injection energy of 1.5 MeV/u is too low for SC part because it will need to reduce the energy gain per cavity to 0.5 MeV. The transverse defocusing will too high in the opposite case and we should to enlarge the number of cavities in the first group that will lead to growth of the linac length and cost. The injection energy should be increased to 2.0-2.5 MeV due to. As one can see, LINAC-100 will consist of 156 four-gap cavities and it's total length will about 140 m. The number of cavity can be reduced in case of higher injection energy but the main problem is observed with high-energy part which consists of 80 cavities. The using of a charge stripper (or two of them) after 3rd group of cavities (or in the other place) can leads to the number of cavities and LINAC-100 length reduction.

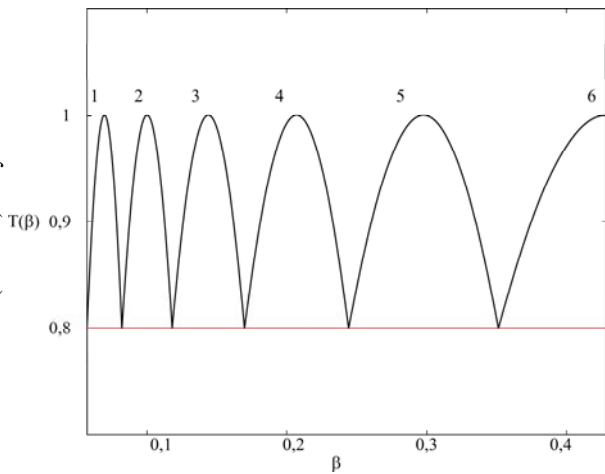


Figure 6: The slipping factor T for each cavities group.

Conventional QWR and HWR cavities can be used in the 1-3 groups. Such cavities are under design and manufacturing by the joint team of JINR, MPhI, ITEP and PTI NANB [30-33]. CH- or Spoke cavities can be used for high-energy groups 4-6.

New effective low-energy CH-cavities were proposed, manufactured (by Research Instruments) and tested at GSI and HIM [34-38]. These cavities will be used in new GSI-CW-Linac which is under construction now. It was shown that multi-gap CH-cavities can be used for comparatively low energies (from $\beta_g \approx 0.06$) and the energy gain per cavity can be very high here - up to 7 MV/m.

LINAC-30 GENERAL LAYOUT AND BEAM DYNAMICS

Some examples of radioactive isotopes which are planning to generate are presented in Table 4. It is clear that all of them have A/Z from 1.6 to 4.0.

There are observed two ways for LINAC-30 development and construction. By the first way we can be used the same technologies and the same cavities (segmented-vane RFQ, a number of normal conducting cavities for intermediate energies and SC part) as for LINAC-100. But LINAC-30 will operate in the pulse mode contrary of LINAC-100. Normal conducting cavities can be used instead of SC one for high energies and the detail comparison of normal conducting and superconducting solutions can be performed to reduce the LINAC-30 length and cost.

Table 3: General Parameters of SC Part of LINAC-100

Group	1	2	3	4	5	6
W_{in} , MeV/u	1.5	3.16	6.59	13.78	29.24	63.8
β_{in}	0.056	0.08	0.12	0.170	0.244	0.351
β_g	0.069	0.01	0.144	0.207	0.298	0.428
W_{out} , MeV/u	3.16	6.59	13.78	29.24	63.8	100.0
β_{out}	0.082	0.12	0.170	0.244	0.351	0.428
T , %	20	20	20	20	20	20
f , MHz	162	162	162	324	324	324
φ_{inj} , deg	-30	-30	-30	-30	-27	-20
U , MV	0.52	1.5	2.7	3.0	6.0	9.5
E , kV/cm	2	4	5.1	7.83	10.9	11.93
N_{gap}	4	4	4	4	4	4
L_{cav} , m	0.257	0.37	0.532	0.383	0.551	0.796
B_{sol} , T	3.1	4.5	5.5	6	7	7.5
L_{sol} , m	0.2	0.2	0.2	0.2	0.2	0.2
L_{per} , m	0.657	0.77	0.932	0.783	0.951	1.196
N_{per}	22	16	18	36	40	24
K_T , %	100	100	100	100	100	100

Table 4: Representative secondary radioactive isotopes for LINAC-30. Mass band is defined from known location of borderline of nuclear stability, the charge state is typical for contemporary ECR ion sources.

Ion	Possible A	Charge	A/Z band
B	8 - 19	5+	1.6 - 3.8
O	13 - 24	8+	1.63 - 3.0
Ar	31 - 46	16+	1.94 - 2.88
Sn	100 - 132	38+	2.63 - 3.47

CONCLUSION

The general layout of new research complex DERICA is presented. This complex is under discussion now and it's construction can be provided at JINR. Possible research aims for DERICA are briefly presented. Start version of LINAC-100 driver is presented and first beam dynamics simulation results are briefly discussed.

ACKNOWLEDGEMENTS

Authors would like to thank Dr. W. Barth and Dr. S. Yaramyshev (GSI/HIM/MEPhI) for fruitful discussions and support. This work was partly supported by the RSF grant No. 17-12-01367.

REFERENCES

- [1] A.S. Fomichev, L.V. Grigorenko, B.Yu. Sharkov *et al.*, Scientific program of DERICA - prospective accelerator and storage ring facility for radioactive ion beam research, <http://aculina.jinr.ru/pdf/DERICA/DERICA-for-ufn-9-en.pdf>
- [2] <http://www.nndc.bnl.gov>
- [3] V.E. Fortov, B.Yu. Sharkov, H. Stöcker, *Phys. Usp.*, vol. 55, pp. 582-602, 2012.
- [4] L.V. Grigorenko, M. S. Golovkov, S.A. Krupko *et al.*, *Phys. Usp.*, vol. 59, p. 321, 2016.
- [5] Yu.Ts. Oganessian, O.N. Malyshev, I.N. Meshkov *et al.*, *Z. Phys.*, vol. 341, p. 217, 1992.
- [6] T. Katayama, T. Suda, I. Tanihata, *Physica Scripta*, issue T104, pp. 129-143, 2003.
- [7] K. Tsukada *et al.*, *PRL*, vol. 118, issue 26, p. 262501, 2017.
- [8] A.N. Antonov *et al.*, *NIM A*, vol. 637, pp. 60-76, 2011.
- [9] M. Grieser *et al.*, *Eur. Phys. J. Special Topics*, vol. 207, pp. 1-117, 2012.
- [10] K. Grigoryev., *Phys. Scripta*, vol. 166, p. 014050, 2015.
- [11] R. Ferdinand, in *Proc. PAC'09*, Vancouver, Canada, May 2009, pp. 4281-4285.
- [12] J. Wei *et al.*, in *Proc. LINAC'16*, East Lansing, MI, USA, Sep. 2016, pp. 1-6.
- [13] G.V. Trubnikov, T.V. Kulevoy, S.M. Polozov *et al.*, *PEPAN Letters*, vol. 13, no 7, pp. 911-914, 2016.
- [14] E. S. Masunov, A. V. Samoshin, *Technical Physics*, vol. 55, issue 7, pp. 1028-1035, 2010.
- [15] E. S. Masunov, A. V. Samoshin, *Atomic Energy*, vol. 108, issue 2, pp. 141-153, 2010.
- [16] E.S. Masunov, A.S. Plastun, A.V. Samoshin, "Problems of Atomic Science and Technology", *Series Nuclear Physics Investigations*, vol. 2, no. 53, pp. 114-117, 2010.
- [17] A.V. Samoshin, S.M. Polozov, in *Proc. LINAC'12*, Tel Aviv, Israel, Sep. 2012, pp. 633-635.
- [18] D. Winklehner *et al.*, in *Proc. BIW'10*, Santa Fe, New Mexico, 2010, pp. 287-291.
- [19] G. Rodrigues *et al.*, *Review of Scientific Instruments*, vol. 85, p. 02A740, 2014.
- [20] C.M. Lyneis *et al.*, 10th Int. Conf. on Ion Sources, Dubna, Russia, September 2003.
- [21] H. W. Zhao *et al.*, *Phys. Rev. AB*, vol. 20, p. 094801, 2017.
- [22] V.A. Andreev, G. Parisi., in *Proc. PAC'93*, Washington, DC, USA, May 1993, pp. 3124-3126.
- [23] S. Polozov *et al.*, in *Proc. HB'16*, Malmö, Sweden, Jul. 2016, pp. 188-190.
- [24] S. Polozov *et al.*, in *Proc. RuPAC'16*, Saint-Petersburg, Russia, Nov. 2016, pp. 267-269.
- [25] S. Polozov *et al.*, in *Proc. IPAC'17*, Copenhagen, Denmark, May 2017, pp. 1333-1336.
- [26] A.I. Balabin, G.N. Kropachev, *NIM A*, vol. 459, pp. 87-92, 2001.
- [27] A.S. Plastun, A.A. Kolomiets, in *Proc. LINAC'12*, Tel Aviv, Israel, Sep. 2012, pp. 41-43.
- [28] A.V. Samoshin, *Problems of atomic science and technology*, vol. 4, no. 80, pp. 78-82, 2012.
- [29] E.S. Masunov, A.V. Samoshin, in *Proc. RuPAC'06*, Novosibirsk, Russia, Sep. 2006, pp. 162-164.
- [30] G.V. Trubnikov, T.V. Kulevoy, S.M. Polozov *et al.*, in *Proc. IPAC'16*, Busan, Korea, May 2016, pp. 941-943.
- [31] M. Gusarova, T. Kulevoy, M.V. Lalayan *et al.*, in *Proc. RuPAC'16*, Saint-Petersburg, Russia, Nov. 2016, pp. 273-275.
- [32] G.V. Trubnikov, A.V. Butenko, N. Emelianov, *et al.*, in *Proc. IPAC'17*, Copenhagen, Denmark, May 2017, pp. 3282-3285.
- [33] G.V. Trubnikov, T.V. Kulevoy, S.M. Polozov *et al.*, in *Proc. RuPAC'16*, 2016, pp. 626-628.
- [34] W. Barth, K. Aulenbacher, M. Basten *et al.*, *Phys. Rev. Accel. Beams*, vol. 21, p. 020102, 2018.
- [35] S. Minaev *et al.*, *Phys. Rev. ST Accel. Beams*, vol. 12, p. 120101, 2009.
- [36] M. Busch, H. Podlech, M. Amberg *et al.*, in *Proc. IPAC'10*, Kyoto, Japan, May 2010, pp. 753-755.
- [37] S. Mickat, M. Amberg, K. Aulenbacher *et al.*, in *Proc. HIAT'12*, Chicago, IL, USA, June 2012, pp. 182-184.
- [38] F. Dziuba, M. Amberg, K. Aulenbacher *et al.*, in *Proc. SRF'17*, Lanzhou, China, Jul. 2017, pp. 440-443.

SUM RESONANCES WITH SPACE CHARGE*

G. Franchetti, GSI, Darmstadt, Germany

Abstract

In the past years several studies, numerical and experimental, have been carried out for enlightening the effect of space charge on stored bunches. The last effort in this quest has regarded the space charge effects on the third order coupled resonance. Experimental studies have been performed at the CERN-PS and a vast simulation effort has followed to interpret the experimental findings. The interpretative base of the analysis relied on: 1) the knowledge of the mechanism of the periodic resonance crossing induced by space charge, which has been identified and confirmed in previous decade 2000-2010; 2) the new revival of the nonlinear dynamics of coupled resonances, alias the fixed-lines. The analysis of the experiment combined together both the mechanisms. However, the discussion made use of an intuitive ansatz based mainly on physics arguments. We shortly present here the re-derivation of the theory of nonlinear dynamics including space charge, and show that we retrieve the concepts used to discuss the analysis of the experiment of the 3rd order coupled resonance.

INTRODUCTION

It is here presented the effect of the space charge in the theory of resonances. The effect of space charge on the beam dynamics in coasting beams is introduced with the following two assumptions:

- 1) The beam is assumed in a stationary state, i.e. the beam distribution does not change during storage;
- 2) The effect of a resonant dynamics is assumed small so to not alter significantly the beam distribution or beam intensity so that the assumption 1) remains valid.

We next briefly discuss these two ansatzes in order to clarify the implications and limits they introduce.

The ansatz 1) means the beam is matched and not subjected to coherent effects that destabilize it. On the other hand, any coherent effect which is stationary and makes the beam envelope oscillate with regular periodic motion can be regarded as included in point 1) as far as it concerns the direct space charge. The ansatz 1) allows to discuss the effect of space charge as created by an “external force” so that in this condition is viewed as an “incoherent” force. Usually the presence of coherent effects is discussed with reference to plasma “coherent effects” such as the Debye length $\lambda_D = \sqrt{\epsilon_0 \gamma^3 m \tilde{v}_x^2 / (q^2 n)}$, where q is the particle charge, m the particle mass, and n the particle density, and \tilde{v}_x is the rms “thermal” velocity component. The Debye length is a characteristic length of a collective motion of charged particles which create a shielding of local perturbations in a plasma.

* This work was supported in part by the European Commission under the HORIZON2020 Integrating Activity project ARIES, grant agreement 730871.

If λ_D is much larger than the inter-particle average distance l_p the space charge force can be treated as a smooth applied force. If in addition λ_D is much bigger than the rms beam radius a_0 the single particle behavior dominates the dynamics (see in Ref. [1]). For a matched beam the thermal velocity is $\tilde{v}_{th}^2 = v_0^2 \tilde{\epsilon}_x / \beta_x$, and for an axi-symmetric Gaussian beam we find

$$\lambda_D^2(r) = \frac{Q_{x0}}{4|\Delta Q_x|} a_0^2 e^{\frac{1}{2} \frac{r^2}{a_0^2}}, \quad (1)$$

where Q_{x0} is the machine tune, ΔQ_x is the incoherent space charge tune-shift, and $r = \sqrt{x^2 + y^2}$. As at each r one finds a specific $\lambda_D(r)$, the most relevant for the Debye collective shielding is the smallest, which is found at $r = 0$. We attempt to capture the incoherent nature of space charge defining a “parameter of incoherence” as $\mathcal{I} = \lambda_D(0)/a_0$: the larger \mathcal{I} the more “incoherent” the direct space charge is. From Eq. (1) we find

$$\mathcal{I} = \sqrt{\frac{1}{4} \frac{Q_{x0}}{|\Delta Q_x|}},$$

so if $|\Delta Q_x|/Q_{x0} = 0.25$ the collective nature of space charge may invalidate ansatzes 1), 2) as $\mathcal{I} = 1$. We instead may “safely” use the ansatzes for a space charge yielding the more conservative $\mathcal{I} = 3$, corresponding to $|\Delta Q_x|/Q_{x0} = 0.027$, a typical value for standard operational regimes in circular accelerators. This is confirmed by numerical studies for Gaussian beams [2], which have shown that space charge collective resonances are not observed. A further argument to develop the theory of resonances with space charge using a model with ansatz 1) and 2) is that long term PIC simulations still suffer of intrinsic noise heating [3–6] although the recent significant progress in creating symplectic PIC algorithms [7].

In ansatz 2) the resonant dynamics is here discussed for a generic sum resonance, which can be generated by magnet errors, or by the incoherent space charge itself as the beam undergoes envelope oscillations driven by the machine optics. The requirement that a resonance does not change the beam distribution is satisfied when the number of beam particles affected by the resonance is small with respect to the total number of beam particles. This means it is assumed only a small fraction of the beam is transported around in the phase space by a resonance. In this treatment we do not consider dynamical effects such as the change of the space charge tune-spread, which would feed back on the dynamics of resonant particles. This approach has a validity when global effects induced by incoherent effects are small on the time scaled considered. A similar assumption is adopted in case of beam loss: we assume the losses to be small on the time scale considered.

RESONANCES

The theory of resonances in accelerators has got a long history. It started in the 50s with [8], and the work of Schoch [9]. The theory was based on a perturbative approach to the Hamiltonian theory. In more recent years the normal form approach has followed the advent of computers and numerical physics [10, 11]. The more popular application of the theory led to the development of driving term methods to measure and correct resonances [12].

The original theory was developed with perturbative methods, and originates a complex structure of patterns in the phase space. Without space charge, coupled resonances in phase space have a particular pattern also called fixed lines [13]. These mathematical objects created by nonlinear coupled resonances were not extensively used for controlling accelerators beams. In literature the reference to fixed lines trace back to the 80's [14, 15]. However, the recent study in Ref. [16] have shown that fixed lines play a fundamental role in determining the dynamics of halo formation in high intensity beams. A recent study of the resonant coupled dynamics is discussed in [17, 18], and is here modified to include space charge.

The approach starts from the single particle Hamiltonian, which is composed by the quadratic potential H_0 and the perturbation part H_1 which has higher order and is originated by the presence of nonlinear errors in magnets. The solution of the equations of motion for the Hamiltonian H_0 is expressed in the Courant-Snyder form $x = \sqrt{\beta_x} a_x \sin(\psi_x + \varphi_x)$, similarly for the y coordinate. For convenience the single particle invariants are re-scaled as $\hat{a}_x = a_x/\epsilon_x, \hat{a}_y = a_y/\epsilon_x$ to the ϵ_x rms beam emittance. The dynamics of particles under the full Hamiltonian $H_0 + H_1$ is derived by keeping the Courant-Snyder form, but allowing the quantities \hat{a}_x, φ_x to vary. The treatment leads to a new set of canonical equations in the quantities $\hat{a}_x, \varphi_x, \hat{a}_y, \varphi_y$ controlled by the Hamiltonian H_1 . These equations are exact, and usually are not easily solvable. However, the mathematical formulation of the canonical equations allows a representation of the problem in terms of a harmonics series. Each term of the series is an oscillating function which frequency is a combination of the machine tunes and the harmonics number m of the distribution of the machine nonlinear errors.

By setting the machine tunes Q_{x0}, Q_{y0} such that the frequency of some harmonics becomes "slow", which happens when Q_{x0}, Q_{y0} are set close $N_x Q_x + N_y Q_y = m$ for the excited resonance, the system of differential equations acquires a dynamics in which the average motion is controlled mainly by the "slow harmonics". It is then used a simplifying ansatz of neglecting all the "fast" oscillating harmonics so to obtain an "easier" set of canonical equations. This is clearly a substantial approximation as all harmonics are neglected but the slowly varying one; for weak errors this approach yields acceptable approximation for modeling the main resonance. After using a canonical transformation to remove the time

dependence from the slowly varying Hamiltonian, we find

$$\tilde{H}_1 = \frac{4}{\epsilon_x} \rho \tilde{a}_x^{n_x/2} \tilde{a}_y^{n_y/2} \cos[N_x \tilde{\varphi}_x + N_y \tilde{\varphi}_y + \alpha] + (\tilde{a}_x t_x + \tilde{a}_y t_y) \frac{2\pi \Delta_{r0}}{L} + \tilde{V} \quad (2)$$

where the $\tilde{\cdot}$ means that the canonical variables are the new one. A nice feature of this transformation is that $\tilde{a}_x = \hat{a}_x, \tilde{a}_y = \hat{a}_y$. The parameters t_x, t_y are defining the canonical transformation and are subject to the condition $N_x t_x + N_y t_y = 1$. This means there are infinite canonical transformations to remove the time dependence in the slowly varying Hamiltonian. The coefficients $\rho \geq 0, \alpha$ are the amplitude and phase of the driving term, which is obtained by the Fourier transform of the resonant term of the perturbing Hamiltonian H_1 . The factor $4/\epsilon_x$ arises from the particular choice of normalization used to define \hat{a}_x, \hat{a}_y . The slowly varying potential \tilde{V} is here only function of the quantities \tilde{a}_x, \tilde{a}_y , which have contributions from all nonlinear components in magnets. Essential in the dynamics is the distance from the resonance $\Delta_{r0} = N_x Q_{x0} + N_y Q_{y0} - m$. This expression is not an arbitrary definition, but arises directly solving the dynamics of slowly varying harmonics.

The stationary solution of the canonical equations for the variables $\tilde{a}_x, \tilde{\varphi}_x, \tilde{a}_y, \tilde{\varphi}_y$ is a fixed point alias a "fixed line", which requires a specific condition on the values of the slowly varying coordinates. For example, for the third order normal resonance in absence of space charge it has already been shown that \tilde{a}_x, \tilde{a}_y of any fixed line is given by

$$\tilde{a}_x = \frac{1}{16} \left[\frac{|\Delta_{r0}| \epsilon_x}{R2\rho} \right]^2 (1 - t_x)^2 \quad (3)$$

$$\tilde{a}_y = \frac{1}{4} \left[\frac{|\Delta_{r0}| \epsilon_x}{R2\rho} \right]^2 t_x (1 - t_x) \quad (4)$$

with $0 \leq t_x \leq 1$, and R the accelerator average radius. The projection in the physical coordinates x, x', y, y' of a fixed line leads to the shapes shown in Fig. 1. The important aspect, somewhat expected by the intuition, is that the amplitude of the fixed lines is related to the distance from the resonance. The stability of resonances, alias the fixed lines, is given by the secondary frequencies, namely the frequency of oscillations of \tilde{a}_x, \tilde{a}_y around the stationary solution. For imaginary frequencies the fixed line becomes unstable.

A graphic representation of the set of fixed lines is given in Fig. 2. The curve shows the collection of stable and unstable fixed lines. Note that in this computation there is no additional source of amplitude dependent detuning.

RESONANCES AND SPACE CHARGE

Under the ansatz 1) and 2), the transverse space charge potential can be written in the analytic form

$$V_{sc} = \frac{K}{2} \int_0^\infty \frac{\exp[-0.5T(t)] - 1}{(a_0 + t)^{1/2} (b_0 + t)^{1/2}} dt \quad (5)$$

with $T(t) = x^2/(a_0^2 + t) + y^2/(b_0^2 + t)$. The quantities a_0, b_0 are the rms sizes matched with the optics structure of the circular

Content from this work may be used under the terms of the CC BY 3.0 licence (© 2018). Any distribution of this work must maintain attribution to the author(s), title of the work, publisher, and DOI.

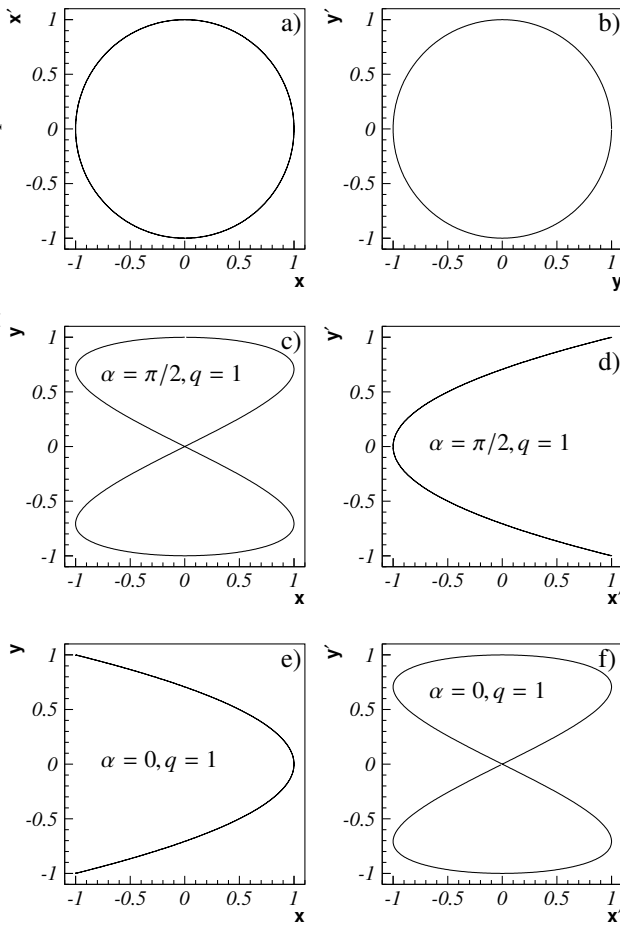


Figure 1: Fixed-line projections in normalized coordinates. The parameter q can be 0, 1 and its value is taken to allow the existence of the fixed line.

machine, namely $a_0^2 = \beta_x(s)\epsilon_x$, $b_0^2 = \beta_y(s)\epsilon_y$. The rms sizes a_0, b_0 exhibit the s dependence deriving from the accelerator structure and so does V_{sc} . This potential generates a Gaussian transverse distribution $\propto \exp[-0.5(x^2/a_0^2 + y^2/b_0^2)]$. It can be proven that the “slowly varying potential” generated by space charge can be retrieved from Eq. (5) and has a form $\tilde{V}_{sc}(\tilde{a}_x, \tilde{a}_y)$ function of the normalized action \tilde{a}_x, \tilde{a}_y only.

This potential enters in Eq. (2) and affects the solution of the stationary values of the canonical variables $\tilde{a}_x, \tilde{\varphi}_x, \tilde{a}_y, \tilde{\varphi}_y$.

The Fourier transform of V_{sc} allows to retrieve the driving terms excited by space charge ρ_{sc}, α_{sc} . So one can find the situation that space charge excites a resonance and also creates the amplitude dependent detuning fixing the position of the fixed lines. We do not discuss here this particular case.

The resonances are characterized by the condition $N_x \tilde{\varphi}_x + N_y \tilde{\varphi}_y + \alpha = \pi q$, with q and integer and by the conditions

$$t_x \frac{\Delta_{r0}}{R} + \frac{\partial \tilde{V}}{\partial \tilde{a}_x} \simeq 0 \quad (6)$$

$$t_y \frac{\Delta_{r0}}{R} + \frac{\partial \tilde{V}}{\partial \tilde{a}_y} \simeq 0 \quad (7)$$

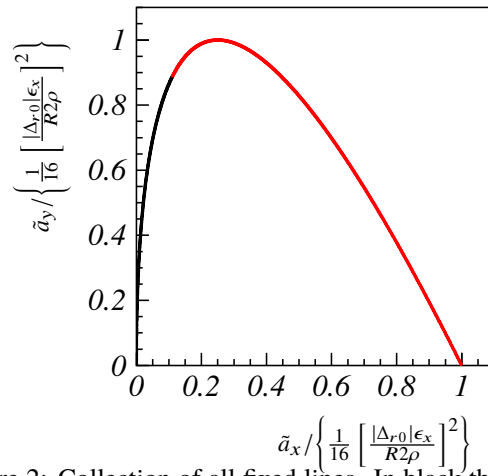


Figure 2: Collection of all fixed lines. In black the stable fixed lines, in red the unstable fixed lines.

It can be proven that these two conditions are necessary and sufficient to the condition

$$\frac{\Delta_{r0}}{R} + N_x \frac{\partial \tilde{V}}{\partial \tilde{a}_x} + N_y \frac{\partial \tilde{V}}{\partial \tilde{a}_y} \simeq 0. \quad (8)$$

In addition it can be proven that $R \frac{\partial \tilde{V}}{\partial \tilde{a}_x} = \Delta Q_x(\tilde{a}_x, \tilde{a}_y)$ is the space charge induced amplitude dependent incoherent detuning. (similarly for the other plane). We therefore find that the condition for reaching a resonance, namely a stationary solution of the canonical equations in the time-independent set of coordinates, is given by

$$\Delta_{r0} + N_x \Delta Q_x(\tilde{a}_x, \tilde{a}_y) + N_y \Delta Q_y(\tilde{a}_x, \tilde{a}_y) \simeq 0. \quad (9)$$

This result is not an ansatz but a direct consequence of the canonical equations of the slow variables. We can use this result to define an extension of the concept of amplitude dependent detuning with the expression

$$\Delta_r(\tilde{a}_x, \tilde{a}_y) = \Delta_{r0} + N_x \Delta Q_x(\tilde{a}_x, \tilde{a}_y) + N_y \Delta Q_y(\tilde{a}_x, \tilde{a}_y) \quad (10)$$

which is an “*amplitude dependent resonance detuning*”, now defined for resonances of any order: the resonance condition is met for \tilde{a}_x, \tilde{a}_y such that $\Delta_r \simeq 0$. This result confirms and gives a theoretical ground to the discussion carried out in Ref. [16]. From Eq. (10) it is evident that there is a maximum *resonance detuning* $\mathcal{D}_{r,sc} = N_x \Delta Q_x(0,0) + N_y \Delta Q_y(0,0)$ due to space charge. The quantities $\Delta_r(\tilde{a}_x, \tilde{a}_y)$, $\mathcal{D}_{r,sc}$ determine the location of the resonance in presence of space charge. The symbol \simeq in Eqs. (6), (7) and (8) is used because we have neglected the contribution of the resonant term in the Hamiltonian. This is equivalent to assume that the driving term ρ is small.

Note that Eq. (10) depends on the two normalized actions \tilde{a}_x, \tilde{a}_y , and it may seem strange. However this is not the case, in fact, there are infinite fixed lines, each identified by a parameter: for example for the case of the 3rd order

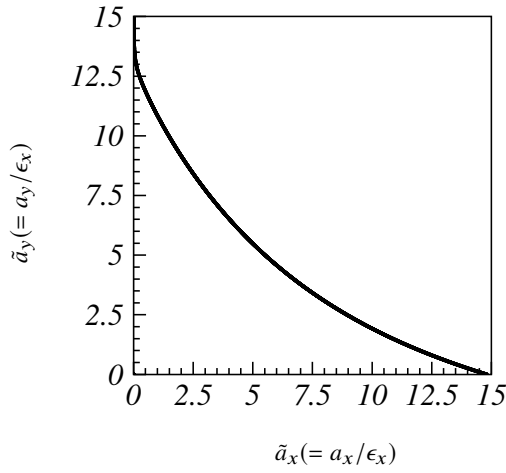


Figure 3: Collection of all fixed lines for a high intensity beam with parameters $\Delta_{r0} = 0.056$, $\mathcal{D}_{r,sc} = -0.174$.

resonance with no space charge the parameter is t_x in the parameterization given by Eqs. (3) and (4). A more general parameterization makes use of the invariant $N_y \tilde{a}_x = N_x \tilde{a}_y + C$ characterizing the dynamics of the slowly varying Hamiltonian. For the third order resonance, fixing t_x is equivalent to fix C . When space charge is included, the parametrization of the fixed lines is more complex and not expressible in a simple analytic formula as in Eqs. (3) and (4). Nevertheless, once C is fixed, it means a specific correlation is chosen in the space of the actions a_x, a_y and the resonance detuning Δ_r defined in Eq. (10) allows to determine the fixed line associated to C .

Therefore for any C the condition $\Delta_r = 0$ allows to estimate the location of the associated fixed line. As an example we show the effect introduced by the space charge on the collection of all the fixed lines shown in Fig. 2 for the case of the third order resonance. The result is shown in Fig. 3 for $\Delta_{r0} = 0.056$, $\mathcal{D}_{r,sc} = -0.174$ corresponding to the settings, beam sizes, and space charge tune-shifts of the CERN-PS measurements in Ref. [16].

A comparison of Fig. 3 with Fig. 2 shows that space charge stabilized all unstable fixed lines, and changed dramatically the shape of the curve in the neighborhood of $\tilde{a}_x = 0$. A direct comparison of the values of \tilde{a}_x, \tilde{a}_y is not possible as the sizes of Fig. 2 scale with Δ_{r0} and go to zero for $\Delta_{r0} \rightarrow 0$. Instead in presence of space charge, if $\Delta_{r0} \rightarrow 0$ the collection of fixed lines in Fig. 3 becomes larger and larger. However, qualitatively, from the pattern in Fig. 3 we learn that space charge changes the direction of the black curve in Fig. 2 and brings it to the point $\tilde{a}_x = 0, \tilde{a}_y \sim [|\Delta_{r0}| \epsilon_x / (R2\rho)]^2 / 16$.

HIGH ORDER RESONANCES WITH SPACE CHARGE

The theoretical approach here discussed allows the computation of the fixed lines in presence of space charge for resonances of any order and arbitrary strength of space charge (in the range of circular machines). We consider for convenience of demonstration the scenario of Ref. [16]. We

keep the space charge tune-shift so $\mathcal{D}_{r,sc} = -0.174$, and $\Delta_{r0} = 0.056$. This is reached by changing the machine tunes Q_{x0}, Q_{y0} and setting it above the resonance of choice, that is we require $0 \leq -\Delta_{r0} / \mathcal{D}_{r,sc} \leq 1$.

In Fig. 4 we show two examples of high order resonances as Poincaré surface of section for fixed lines defined by the parameter $C = 0$. In Fig. 4 top we show $x - y$ projection of the fixed line for the 4th order skew resonance $Q_x + 3Q_y = N$, the strength of the octupole has been artificially enhanced so to enable to the nonlinear tracking the resolution of the resonance. Black dots are the result from the analytic theory; red the dots are the particle positions obtained from tracking turn after turn. The bottom picture shows the 7th order normal resonance $5Q_x + 2Q_y = N$. For sake of comparison we also show in Fig. 5 the fixed line for $Q_x + 3Q_y = N$, but $C = 20$. Comparing Fig. 4 top with Fig. 5 it is visible the change in aspect ratio of the fixed-line according to the value of C . However note: the topology of the two curves remain the same.

SUMMARY

In this proceeding we have shortly presented the theory of resonances with space charge. We have shown that the

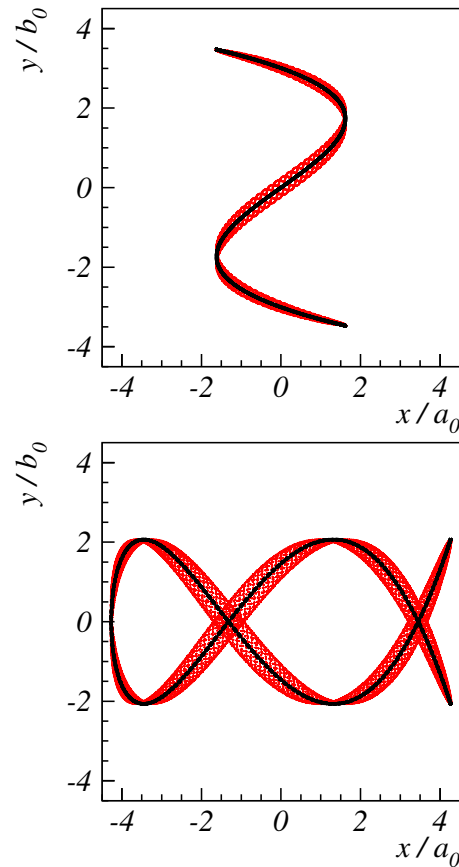


Figure 4: Fixed lines type $C = 0$ in a high intensity beam with $\Delta_{r0} = 0.056$, $\mathcal{D}_{r,sc} = -0.174$. On the top picture the resonance is $Q_x + 3Q_y = N$, bottom picture for $5Q_x + 2Q_y = N$.

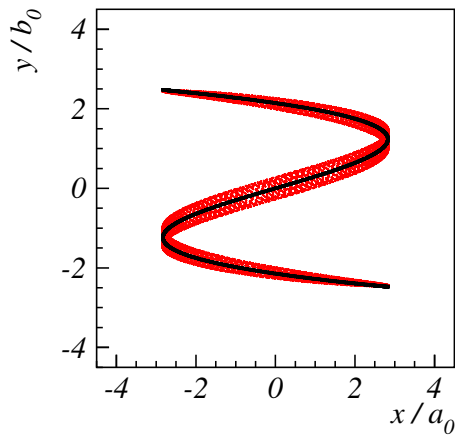


Figure 5: Fixed line for $C = 20$ for a high intensity beam with parameters $\Delta_{r0} = 0.056$, $\mathcal{D}_{r,sc} = -0.174$.

prediction of resonant structures in phase space is possible under a general ansatz. We confirm from a more solid theoretical ground the intuitive approach used in previous work making use of the “*resonance detuning*”. The complexity of the dynamics remains considerable, but in spite of this an analogy with the one dimensional treatment of resonances and space charge is possible. The amplitude dependent detuning can be generalized with the *amplitude dependent “resonance detuning”* $\Delta_r(\tilde{a}_x, \tilde{a}_y)$ and used as a tool for predicting the location of fixed lines

The comparison of particle tracking with the predictions of the theory shows good agreement (Fig. 4, Fig. 5), and this encourages to consider this approach useful to reach quick results to the problem of the periodic resonance crossing induced by high intensity bunched beams stored for long term. The material here presented does not allow a complete discussion of the consequences of the theory and its limits. This subject will be part of a future publication.

ACKNOWLEDGMENT

The author thanks M. Steck, H. Bartosik, and V. Schaa for the corrections and comments.

REFERENCES

- [1] M. Reiser, “Theory and Design of Charged Particle Beams”, WILEY-VCH, 2004.
- [2] I. Hofmann, G. Franchetti, J. Qiang, and R. Ryne, “Self-consistency and coherent effects in nonlinear resonances”, in *Proc. 29th ICFA Advanced Beam Dynamics Workshop on Beam Halo Dynamics, Diagnostics, and Collimation HALO 03*, AIP, New York, 2003, vol. 693, pp. 65. doi:10.1063/1.1638323
- [3] F. Kesting and G. Franchetti, “Propagation of numerical noise in particle-in-cell tracking”, *Phys. Rev. ST Accel. Beams* vol. 18, pp. 114201 (2015). doi:10.1103/PhysRevSTAB.18.114201
- [4] J. Struckmeier, “Stochastic effects in real and simulated charged particle beams”, *Phys. Rev. ST Accel. Beams* vol. 3, pp. 034202 (2000). doi:10.1103/PhysRevSTAB.3.034202
- [5] O. Boine-Frankenheim, I. Hofmann, J. Struckmeier, and S. Appel, “Artificial collisions, entropy and emittance growth in computer simulations of intense beams”, *Nucl. Instrum. Methods Phys. Res., Sect. A*, vol. 770, pp. 164 (2015). doi:10.1016/j.nima.2014.10.004
- [6] I. Hofmann and O. Boine-Frankenheim, “Grid dependent noise and entropy growth in anisotropic 3d particle-in-cell simulation of high intensity beams”, *Phys. Rev. ST Accel. Beams*, vol. 17, pp. 124201 (2014). doi:10.1103/PhysRevSTAB.17.124201
- [7] Ji Qiang, “Symplectic particle-in-cell model for space-charge beam dynamics simulation”, *Phys. Rev. Accel. Beams*, vol. 21, pp. 054201 (2018). doi:10.1103/PhysRevAccelBeams.21.054201
- [8] R. Hagedorn, CERN 57-1, (Proton Synchrotron Division) (1957).
- [9] A. Schoch, “Theory of Linear and Non-Linear Perturbations of Betatron Oscillations in Alternating Gradient Synchrotrons”, CERN 57-21 (Proton Synchrotron Division), Section 14 (1958).
- [10] A. Bazzani *et al.*, “A normal form approach to the nonlinear betatronic motion”, CERN 94-02, SPS+LEP Division, 1994.
- [11] E. Forest, “From Tracking Code to Analysis”, Springer 2016.
- [12] R. Tomás *et al.*, “Measurement of global and local resonance terms”, *Phys. Rev. ST Accel. Beams* vol. 8, pp. 024001 (2005). doi:10.1103/PhysRevSTAB.8.024001
- [13] F. Schmidt, “Untersuchungen zur dynamischen Akzeptanz von Protonenbeschleunigern und ihre Begrenzung durch chaotische Bewegung”, PhD thesis, DESY HERA 88-02 (1988).
- [14] C. J. A. Corsten and H. L. Hagedoorn, “Stopband widths in non-linear sum resonances”, *Nucl. Instrum. Methods*, vol. 216, pp. 25 (1983). doi:10.1016/0167-5087(83)90326-5
- [15] S. Ohnuma, “Comments on Stable Motions in Nonlinear Coupled Resonances”, *IEEE Transaction on Nuclear Science*, vol. NS-28, no. 3, June 1981. doi:10.1109/TNS.1981.4331733
- [16] G. Franchetti, S. Gilardoni, A. Huschauer, F. Schmidt, and R. Wasef, “Space charge effects on the third order coupled resonance”, *Phys. Rev. Accel. Beams*, vol. 20, pp. 081006 (2017). doi:10.1103/PhysRevAccelBeams.20.081006
- [17] G. Franchetti and F. Schmidt, “Extending the Nonlinear-Beam-Dynamics Concept of 1D Fixed Points to 2D Fixed Lines”, *Phys. Rev. Lett.*, vol. 114, pp. 234801 (2015). doi:10.1103/PhysRevLett.114.234801
- [18] G. Franchetti and F. Schmidt, “Fix-lines and stability domain in the vicinity of the coupled third order resonance”, arxiv.org/abs/1504.04389

APPROACHING THE HIGH-INTENSITY FRONTIER USING THE MULTI-TURN EXTRACTION AT THE CERN PROTON SYNCHROTRON

A. Huschauer, H. Bartosik, S. Cettour Cave, M. Coly, D. Cotte, H. Damerau, G. P. Di Giovanni, S. Gilardoni, M. Giovannozzi, V. Kain, E. Koukovini-Platia, B. Mikulec, G. Sterbini, F. Tecker, CERN, CH 1211 Geneva 23, Switzerland

Abstract

Complementary to the physics research at the LHC, several fixed target facilities receive beams from the LHC injector complex. To serve the fixed target physics program at the Super Proton Synchrotron, high-intensity proton beams from the Proton Synchrotron are extracted using the Multi-Turn Extraction technique based on trapping parts of the beam in stable resonance islands. Considering the number of protons requested by future experimental fixed target facilities, such as the Search for Hidden Particles experiment, the currently operationally delivered beam intensities are insufficient. Therefore, experimental studies have been conducted to optimize the Multi-Turn Extraction technique and to exploit the possible intensity reach. The results of these studies along with the operational performance of high-intensity beams during the 2017 run are presented in this paper. Furthermore, the impact of the hardware changes pursued in the framework of the LHC Injectors Upgrade project on the high-intensity beam properties is briefly mentioned.

INTRODUCTION

Since September 2015, the special beam extracted from the CERN Proton Synchrotron (PS) for the Super Proton Synchrotron (SPS) fixed-target physics programme has been generated using the so-called Multi-Turn Extraction (MTE) technique (see [1–4] for more detail). This peculiar extraction technique has superseded the Continuous Transfer (CT) process, proposed in 1973 [5], which occurs over five turns at 14 GeV/c to optimize the duty cycle by filling the SPS with only two subsequent extractions from the PS. The downside of the CT extraction is a significant amount of beam loss occurring at multiple locations around the ring [6], leading to high radiation dose to personnel during accelerator maintenance and repair, as well as to long cool down times.

MTE is a resonant extraction mechanism, which exploits advanced concepts of non-linear beam dynamics and is based on adiabatically crossing a stable fourth-order resonance to perform beam splitting in the horizontal phase space. The resulting beamlets - four islands and one core - are then extracted over five subsequent turns (see [7] for the detail of the implementation and [8] for the theoretical study on the trapping and splitting mechanisms).

The efficiency of the transverse splitting is defined as

$$\eta_{\text{MTE}} = \frac{\langle I_{\text{Island}} \rangle}{I_{\text{Total}}}, \quad (1)$$

where $\langle I_{\text{Island}} \rangle$ and I_{Total} stand for the average intensity in each island and the total beam intensity, respectively. The

nominal efficiency is 0.20, corresponding to an equal beam sharing between islands and core. This figure of merit is derived from the signal of the beam intensity measured in the transfer line joining the PS and the SPS.

An essential challenge encountered during the beam commissioning phase of this unique extraction technique had been the presence of significant fluctuations in η_{MTE} , caused by time-varying high-frequency ripples coming from power converters crucial for the operation of the PS [9].

To satisfy the requests of the SPS fixed-target experiments, the typical proton intensity per PS extraction has been in the range of $N_p = 1.5 - 2 \times 10^{13}$ in the years 2015-17. Note that during the CERN Neutrinos to Gran Sasso [10] run, the typical proton intensity extracted from the PS was $N_p \sim 2.6 \times 10^{13}$ with extraction losses at an average level of $\sim 7\%$ [6].

The summary of the overall MTE performance in terms of beam losses at the PS and SPS is shown in Fig. 1 where, for the sake of comparison, the typical CT performance is also reported. The overall reduction of losses along the accelerator complex over the years is clearly visible. Moreover, the main feature of MTE and the main reason for replacing CT is clearly visible, namely the drastic reduction of losses in the PS ring. In the transfer lines joining the two machines a mild improvement (over the years and with respect to CT) is also visible. The SPS performance is still slightly worse for MTE with respect to CT, although an improvement over the years is visible. Note that the main SPS performance limitation originates from the value of the delivered vertical emittance being at the limit of the machine acceptance, hence explaining the higher losses at injection.

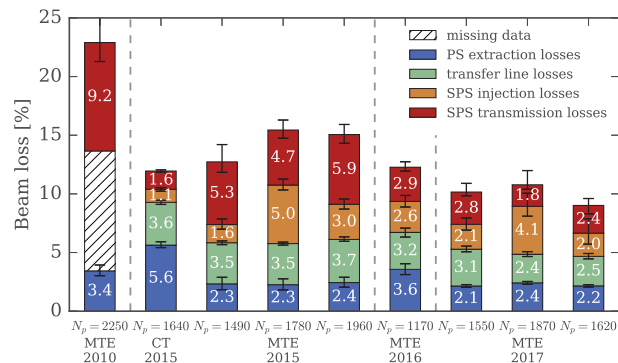


Figure 1: Summary of the beam losses for CT and MTE over the years. For each case the total beam losses are split into the various loss contributions occurring from the PS to the SPS.

Content from this work may be used under the terms of the CC BY 3.0 licence (© 2018). Any distribution of this work must maintain attribution to the author(s), title of the work, publisher, and DOI.

According to future proposals, like the Search for Hidden Particles (SHiP) experiment [11], much higher intensity, reaching up to $2.4 - 2.5 \times 10^{13}$ protons per PS extraction, might be required. In light of these potential needs, an intense experimental campaign has been carried out in 2017 to assess the actual MTE performance for these high-intensity beams. This has been considered an essential step in the formal process of declaring MTE a suitable and definite operational replacement of CT. Note that intensity-dependent effects had been observed with MTE already during its infancy [12] and the theoretical explanation, based on the analysis of indirect space charge effects, has been provided only recently [13].

This paper focuses on the results of the experimental campaign carried out during the whole 2017 PS and SPS proton run. A number of detailed parameter scans will be presented, which were crucial to start with a highly-optimised MTE beam of intermediate intensity. The discussion of the high-intensity tests follows later, including the various steps undertaken in the whole accelerator chain starting from the PS Booster (PSB) to the PS and the SPS.

PREPARATORY STUDIES

Overview of MTE

Figure 2 shows a sketch of the PS ring with the main non-linear magnets required for MTE, namely sextupoles and octupoles. While the sextupoles and the close-by octupoles are located in areas with maximum horizontal and minimum vertical β -functions to enhance their effect, the other distributed octupoles are located in areas with maximum vertical and minimum horizontal β -functions and are used to minimise the non-linear coupling between the two transverse planes [2–4].

The PS cycle for SPS fixed target beam production is shown in Fig. 3 (upper) together with the evolution of the strength of the non-linear magnets used to perform beam trapping and splitting (lower). It is worthwhile mentioning that a non-negligible boost to η_{MTE} is provided by the use of

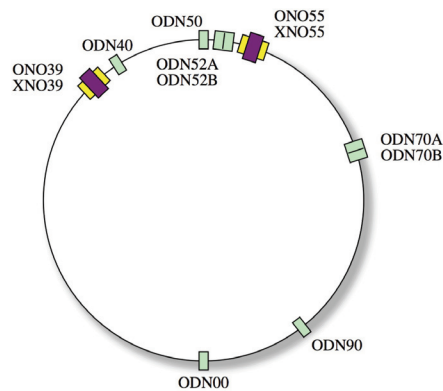


Figure 2: Sketch of the PS ring with the key elements of MTE, i.e. sextupole (called ‘X’) and octupole (called ‘O’) magnets.

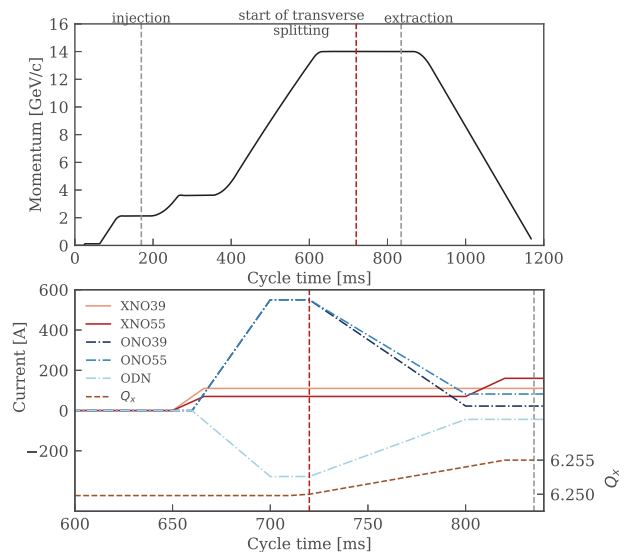


Figure 3: Upper: Sketch of the PS magnetic cycle with the main events. Lower: evolution of the strengths of the main MTE elements. The vertical dashed line indicates the moment of resonance crossing.

a horizontal dipolar excitation during the resonance-crossing process. Such an excitation is imparted by the transverse feedback (TFB) used in open loop and its impact has been analysed in detail in the past [4]. The important dependency of η_{MTE} on the excitation amplitude is shown in Fig. 4.

Transverse Excitation and Core Emittance

Extensive measurements of the transverse emittance of the beam injected in the SPS revealed a large emittance growth in the horizontal plane for the core. This observation triggered a number of investigations. In fact, the use of the transverse dipolar excitation is essential to achieve the nominal value of η_{MTE} . Nevertheless, the emittance growth could be a negative side effect of the excitation of core particles. This possibility has been verified by a detailed measurement campaign, where η_{MTE} and the horizontal emittance growth of the core have been measured as a function of the excitation frequency (see Fig. 5).

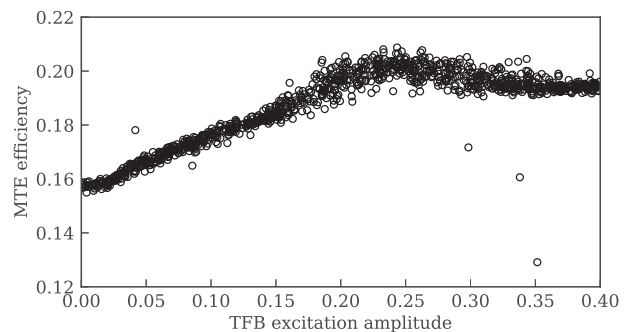


Figure 4: η_{MTE} as a function of the TFB excitation amplitude. Its beneficial impact on η_{MTE} is clearly visible together with a saturation effect.

In the upper part, η_{MTE} shows a dip close to the resonant tune and then stabilises for higher values of the transverse feedback frequency. In the lower part, the emittance growth reveals a rather broad plateau where the emittance increase is smaller than 5%. The nice feature is that a relatively wide range of frequency values exists, for which η_{MTE} is large and constant, while the emittance growth is small. From an operational point of view this means that the transverse feedback can indeed be tuned to maximise its beneficial impact, while keeping the undesired impact on the core emittance under control. However, special care has to be taken when setting the parameters of the transverse feedback. Furthermore, the excitation frequency allows to optimize η_{MTE} to account for unavoidable drifts of the machine tune over time.

Optimisation of the Non-linear Magnets

The operational settings of the non-linear magnets shown in Fig. 3 (lower) have been defined to maximise η_{MTE} (by means of ONO39 and ONO55), to minimise the non-linear coupling between the two transverse planes (by means of the ODN family), and to reduce emittance dilution and extraction losses during the change of the islands' phase prior to extraction (by means of the XNO55 circuit) [4].

Nonetheless, some of the features of the time variation of the sextupoles and octupoles have been revised in view of the high-intensity tests. At first, the octupole circuits have been probed, in particular to assess whether their maximum strength or the slope from the maximum value at resonance crossing to the final one before extraction were optimal. The results of these scans in terms of distribution of measured

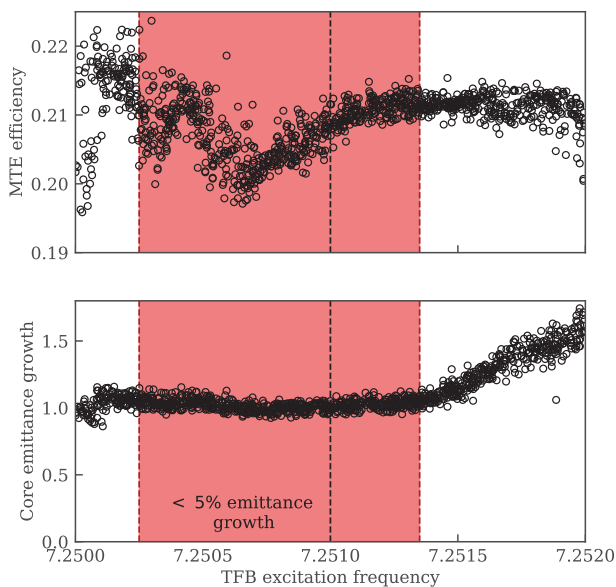


Figure 5: MTE efficiency (upper) and core emittance growth (lower) as a function of the excitation frequency of the TFB. The shaded area corresponds to an emittance growth of less than 5%. A tuning range compatible with high η_{MTE} and low core emittance growth is clearly visible.

η_{MTE} are shown in Fig. 6. A strong dependence on the value of the maximum strength is clearly observed, while a mild increase of the MTE efficiency is measured when the slope is reduced, i.e. the time variation and therefore the adiabaticity of the process is increased.

The impact of the maximum strength of the ODN magnets, which are meant to control the non-linear coupling between the two transverse planes has been probed too and the measurements show that η_{MTE} is essentially independent on the settings of the plateau of the current function of the ODN magnets.

As a final test, the strength of the sextupole XNO55 has been varied and its impact on the extraction losses measured by means of beam loss monitors (BLMs) and the results are reported in Fig. 7. The strength varied corresponds to the final stage of the resonance crossing process, i.e. when the islands are transported towards higher amplitude and their phase is changed in order to prepare for the extraction. This process had already been studied in detail during the first stages of the MTE commissioning and once more, careful setting of the sextupole XNO55 is shown to importantly impact the losses at extraction.

HIGH-INTENSITY TESTS

General Considerations

The constraints on the transverse emittances for the MTE fixed target beams beam parameters are three-fold: firstly, the horizontal emittance received by the PS should be large to increase η_{MTE} ; secondly, the vertical emittance should be as small as possible to overcome the acceptance issues in the SPS; thirdly, extraction losses at PSB should be kept low.

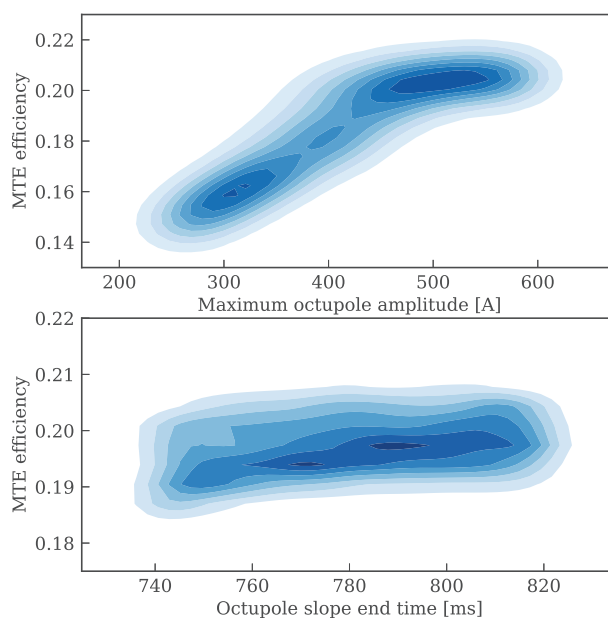


Figure 6: Distribution of efficiency as a function of the maximum strength of octupoles ONO39 and ONO55 (upper) and of their (lower). A strong dependence of η_{MTE} on the strength is visible, while the slope is affecting it only mildly.

Content from this work may be used under the terms of the CC BY 3.0 licence (© 2018). Any distribution of this work must maintain attribution to the author(s), title of the work, publisher, and DOI.

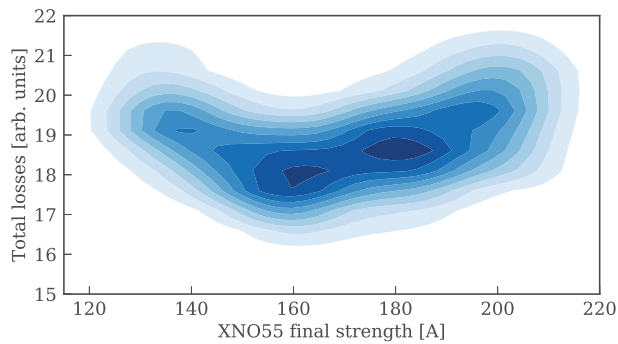


Figure 7: Distribution of extraction losses as a function of the final strength of the sextupole XNO55 during the separation of the islands and the rotation of their phase. A clear dependence is visible.

The high-intensity tests started with a careful preparation of the beam in the PSB. This machine is essential for defining the transverse emittances of the beam that will be transported through the chain to the SPS. Note that the horizontal emittance will be reduced by the splitting process at the PS, while the vertical one is essentially preserved due to the careful adjustment of the PS machine settings to linearly and non-linearly decouple the horizontal and vertical planes.

Satisfying simultaneously the emittance constraints has been a challenge for the PSB specialists, even more as high-intensity beams require to accumulate the injected beam from the Linac 2 over several PSB turns, which naturally increases the emittances. While this is certainly beneficial for the horizontal plane, it is a potential issue for the vertical one. In the end, however, this could be improved by optimizing the PSB working point at injection, which allowed to carry on with the optimization in the downstream accelerators.

PS Results

During the high-intensity tests, three main aspects have been scrutinised at the PS ring: firstly, the dependence of η_{MTE} on intensity; secondly the dependence of extraction losses on intensity; thirdly the beam behaviour in the longitudinal plane during the de-bunching applied after splitting and prior to beam extraction. The last point will not be dealt with in detail in this paper. It is only worth mentioning that no particular issue was observed and that the beam could be kept stable during the de-bunching even at high-intensity.

A comparison of the distribution of η_{MTE} for the operational beam in 2017 (typical intensity around $1.5-1.6 \times 10^{13}$ protons) and for that prepared for the high-intensity tests (typical intensity around 2.4×10^{13} proton) is shown in Fig. 8 (upper). The two distributions are very similar, featuring a rather similar median. The only difference is a larger tail skewed towards low values of η_{MTE} for the case of the high-intensity beam. This is not considered to be a fundamental issue as it could be fixed by working on the reproducibility of the intensity delivered by the Linac 2 and the PSB.

In fact, as it can be seen in Fig. 8 (lower), while η_{MTE} is practically constant for a wide range of beam intensi-

ties (essentially from the operational one and up to about 2.2×10^{13} protons), a small reduction is observed for the case of 2.4×10^{13} protons. Hence, a fluctuating beam intensity could explain the tail.

The second aspect considered during the tests has been the evolution of the beam losses at extraction, which is also a means to evaluate whether the transverse beam properties are changing with intensity. Figure 9 reports the losses at extraction as measured by fast BLMs, which are devices capable of providing the turn-by-turn losses with sub-turn sampling rate. Thus, they allow distinguishing between the losses for the islands (upper) and the core (lower).

The losses are shown as a function of intensity and are given for two key locations in the PS ring, namely the location of the so-called dummy septum [2–4] in straight section (SS) 15 and that of the magnetic extraction septum in SS16. It is worth mentioning that the lower losses for the core extraction are due to the faster rise time of the kickers, with respect to those used for the four islands. The important feature visible in the plots is that the increase of beam losses is to a large extent linear with intensity, thus indicating that no new phenomenon is appearing when intensity is increased.

SPS Results

The final step of the high-intensity studies has been the delivery of the optimised beam from the PS to the SPS. Due to a number of external constraints it has been decided to focus on the setting up of the first injection batch from the PS as a sort of proof of principle, leaving the complete setting up of both batches for later.

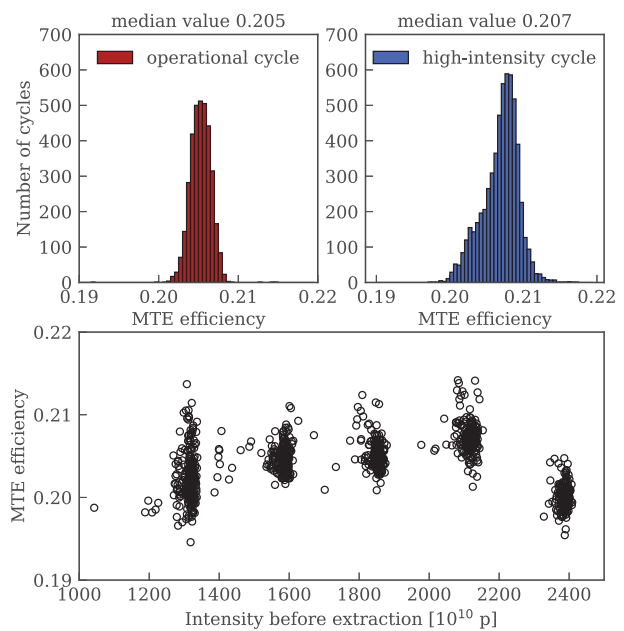


Figure 8: Upper: Distribution of MTE efficiency for the operational (left) and the high-intensity variant (right). The median of the distribution is essentially the same, while a low-efficiency tail is present for the high-intensity beam. Lower: MTE efficiency for various beam intensities.

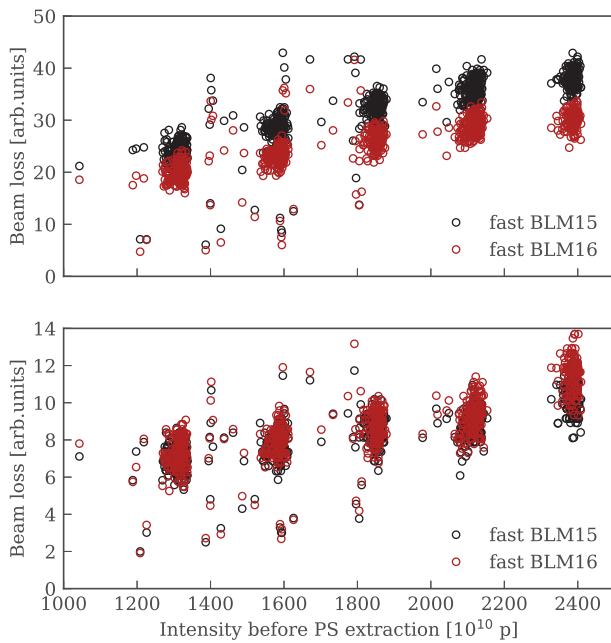


Figure 9: Measured extraction beam losses for the islands (upper) and core (lower) as a function of the total beam intensity. The losses are given in the extraction region, i.e. at the location of the dummy septum in SS15 and of the magnetic septum in SS16.

The main outcome of these tests is reported in Fig. 10 where the transmission through the various stages of the SPS cycle is shown. For the sake of precision, the performance of both injected batches from the PS is reported, but only the first one is meaningful in terms of possible performance-reach estimate. The transmission of the operational MTE beam is also reported for comparison. A reduction of transmission at injection is clearly visible for the high-intensity beam. This is mainly due to the increased value of the vertical emittance, which goes beyond the vertical SPS acceptance, and therefore dominates the performance at injection. In all further stages of the SPS cycle the high-intensity

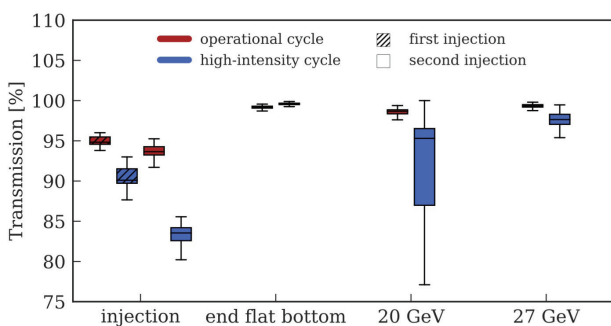


Figure 10: Beam transmission in the SPS between the various stages of its cycle. The data are split up for first and second injection into the SPS. It is worth stressing that a careful tuning could be performed only for the first PS injection.

beam performs similarly to the operational beam, at least the high-end part of the distribution of transmission values is comparable with that of the operational beam. It is worth mentioning that the transmission up to 20 GeV/c includes the start of acceleration as well as transition crossing, which requires careful adjustment of the machine parameters.

These results have been considered as a sign that the SPS can perform equally well with both beams (operational and high-intensity) as long as sufficient commissioning time is allocated and a smaller vertical beam emittance is provided by the PS. Reduced emittances will become available as the planned improvements of the LHC Injectors Upgrade (LIU) project at CERN [14] will be implemented during the Long Shutdown 2 (LS2) starting at the end of 2018.

CONCLUSIONS

MTE started operation in the second half of 2015, thus replacing the CT extraction mode. Since then, the MTE performance has been constantly improved, in particular in the SPS, hence approaching that of CT. It is worth stressing that the latter had gone through a series of optimisations and improvements based on decades of operational experience.

A high-intensity version of MTE has been produced in 2017 and tests were carried out in the PSB, the PS, and the SPS. At the PSB the main challenge has been the generation of the high-intensity beams with low extraction losses while fulfilling the constraints imposed on the transverse emittances by either the PS, i.e. a large horizontal emittance to optimise the MTE efficiency, or the SPS, i.e. a small vertical emittance to minimise the injection losses due to the vertical acceptance. This was successfully achieved, thus allowing to move to the downstream machines.

In the PS, the performance of high-intensity MTE beams is comparable with that of the operational beam. The SPS performance is dominated by the value of the vertical emittance delivered by the PS, where the emittance delivered by the PSB is preserved. The larger vertical emittance with respect to the nominal beam explains the larger losses observed. Considering this aspect, it is clear that the novel LIU beams will mitigate this limitation. All in all, in spite of the very limited set up time, no sign of hard obstacle to further improve the overall performance was found.

Based on the successful outcome of the tests carried out in 2017, it was formally decided to discontinue CT operation and to dismantle the corresponding hardware during LS2.

ACKNOWLEDGEMENTS

We would like to express our warm thanks to the operation crews of the PSB, the PS, and the SPS synchrotrons, who provided invaluable support during the experimental studies discussed in this paper.

REFERENCES

- [1] R. Cappi and M. Giovannozzi, “Novel method for multiturn extraction: trapping charged particles in islands of phase space”, *Phys. Rev. Lett.* vol. 88, p. 104801, 2002.

- [2] J. Borburgh, S. Damjanovic, S. Gilardoni, M. Giovannozzi, C. Hernalsteens, M. Hourican, A. Huschauer, K. Kahle, G. Le Godec, O. Michels, and G. Sterbini, “First implementation of transversely split proton beams in the CERN Proton Synchrotron for the fixed-target physics programme”, *EPL*, vol. 113, p. 34001, 2016.
- [3] S. Abernethy, A. Akroh, H. Bartosik, A. Blas, T. Bohl, S. Cettour-Cave, K. Cornelis, H. Damerau, S. Gilardoni, M. Giovannozzi, C. Hernalsteens, A. Huschauer, V. Kain, D. Manglunki, G. Métral, B. Mikulec, B. Salvant, J.-L. Sanchez Alvarez, R. Steerenberg, G. Sterbini, and Y. Wu, “Operational performance of the CERN injector complex with transversely split beams”, *Phys. Rev. Accel. Beams*, vol. 20, p. 014001, 2017.
- [4] A. Huschauer, A. Blas, J. Borburgh, S. Damjanovic, S. Gilardoni, M. Giovannozzi, M. Hourican, K. Kahle, G. Le Godec, O. Michels, G. Sterbini, and C. Hernalsteens, “Transverse beam splitting made operational: key features of the multi-turn extraction at the CERN Proton Synchrotron”, *Phys. Rev. Accel. Beams*, vol. 20, p. 061001, 2017.
- [5] C. Bovet, D. Fiander, L. Henny, A. Krusche, and G. Plass, “The fast shaving ejection for beam transfer from the CPS to the CERN 300 GeV machine”, *IEEE Trans. Nucl. Sci.*, vol. 20, p. 438, 1973.
- [6] J. Barranco García and S. Gilardoni, “Simulation and optimization of beam losses during continuous transfer extraction at the CERN Proton Synchrotron”, *Phys. Rev. ST Accel. Beams*, vol. 14, p. 030101, 2011.
- [7] M. J. Barnes, O. E. Berrig, A. Beuret, J. Borburgh, P. Bourquin, R. Brown, J.-P. Burnet, F. Caspers, J.-M. Cravero, T. Dobers, T. Fowler, S. Gilardoni, M. Giovannozzi (ed.), M. Hourican, W. Kalbreier, T. Kroyer, F. Di Maio, M. Martini, V. Mertens, E. Métral, K.-D. Metzmacher, C. Rossi, J.-P. Royer, L. Sermeus, R. Steerenberg, G. Villiger, T. Zickler, “The CERN PS multi-turn extraction based on beam splitting in stable islands of transverse phase space: Design Report”, CERN-2006-011, 2006.
- [8] A. Bazzani, C. Frye, M. Giovannozzi, and C. Hernalsteens, “Analysis of adiabatic trapping for quasi-integrable area-preserving maps”, *Phys. Rev. E*, vol. 89, p. 042915, 2014.
- [9] A. Huschauer, M. Giovannozzi, O. Michels, A. Nicoletti, G. Sterbini, “Analysis of performance fluctuations for the CERN Proton Synchrotron multi-turn extraction”, *J. Phys.: Conf. Ser.*, vol. 874, p. 012072, 2017.
- [10] K. Elsener, G. Acquistapace, J.-L. Baldy, A.E. Ball, P. Bonnal, M. Buhler-Broglin, F. Carminati, E. Cennini, A. Ereditato, V.P. Falaleev, P.E. Faugeras, A. Ferrari, G. Fortuna, L. Foà, R. Genand, A.L. Grant, L. Henny, A. Hilaire, K. Hübner, J. Inigo-Golfin, K.-H. Kissler, L.A. López-Hernandez, J.-M. Maugain, M. Mayoud, P. Migliozi, D. Missiaen, V. Palladino, I.M. Papadopoulos, F. Pietropaolo, S. Péraire, S. Ranguod, J.-P. Revol, J. Roche, P.R. Sala, C. Sanelli, G.R. Stevenson, B. Tomat, E. Tsesmelis, R. Valbuena, H.H. Vincke, E. Weisse, M. Wilhelmsson, “The CERN neutrino beam to Gran Sasso (NGS): conceptual technical design”, CERN-98-02, INFN-AE-98-05, 1998.
- [11] G. De Lellis, “Search for Hidden Particles (SHiP): A New Experiment Proposal”, *Nucl. Part. Phys. Proceedings*, vol. 263-264, p. 71, 2015.
- [12] S. Gilardoni, M. Giovannozzi, and C. Hernalsteens, “First observations of intensity-dependent effects for transversely split beams during multiturn extraction studies at the CERN Proton Synchrotron”, *Phys. Rev. ST Accel. Beams*, vol. 16, p. 051001, 2013.
- [13] S. Machida, C. Prior, S. Gilardoni, M. Giovannozzi, A. Huschauer, and S. Hirlander, “Numerical investigation of space charge effects on the positions of beamlets for transversely split beams”, *Phys. Rev. Accel. Beams*, vol. 20, p. 121001, 2017.
- [14] H. Damerau, A. Funken, R. Garoby, S. Gilardoni, B. Goddard, K. Hanke, A. Lombardi, D. Manglunki, M. Meddahi, B. Mikulec, G. Rumolo, E. Shaposhnikova, M. Vretenar, J. Coupard (eds.), “LHC Injectors Upgrade, Technical Design Report, Vol. I: Protons”, CERN-ACC-2014-0337, 2014.

HIGH INTENSITY EFFECTS OF FIXED TARGET BEAMS IN THE CERN INJECTOR COMPLEX

E. Koukovini-Platia*, H. Bartosik, M. Migliorati¹, G. Rumolo, CERN, Geneva, Switzerland
¹ also at University of Rome 'La Sapienza' and INFN, Rome, Italy

Abstract

The current fixed target (FT) experiments at CERN are a complementary approach to the Large Hadron Collider (LHC) and play a crucial role in the investigation of fundamental questions in particle physics. Within the scope of the LHC Injectors Upgrade (LIU), aiming to improve the LHC beam production, the injector complex will be significantly upgraded during the second Long Shutdown (LS2). All non-LHC beams are expected to benefit from these upgrades. In this paper, we focus on the studies of the transverse instability in the Proton Synchrotron (PS), currently limiting the intensity of Time-Of-Flight (ToF) type beams, as well as the prediction of the impact of envisaged hardware modifications. A first discussion on the effect of space charge on the observed instability is also being presented.

INTRODUCTION

The LIU aims to increase the intensity and brightness of the LHC beams in the injector complex by about a factor of two in order to match the High Luminosity LHC (HL-LHC) requirements [1]. It will also maximize the injector reliability and lifetime to cover the HL-LHC era until around 2035. A new H⁻ Linear Accelerator (Linac4) [2] will be employed and major upgrades [3] in the PS Booster (PSB), the PS, and the Super Proton Synchrotron (SPS) are scheduled during the LS2.

Complementary to the high-energy colliders, a new exploratory study group, namely the Physics Beyond Colliders (PBC) [4] group, was officially formed in 2016 to explore the rich scientific potential of the CERN accelerator complex. This involves projects with a different approach to the LHC, HL-LHC and future colliders. The CERN injectors routinely provide non-LHC beams to facilities such as the ISOLDE Radioactive Ion Beam facility, the East Area (EA), the Antiproton Decelerator (AD) and Extra Low ENergy Antiproton (ELENA), the neutron Time-of-Flight facility (n-ToF), the High-Radiation to Materials (HiRadMat), the North Area (NA) and AWAKE.

The policy of the LIU for the non-LHC beams is at the minimum to preserve the present performance in terms of beam intensity and quality. In addition, a positive impact is expected thanks to the upgrades also for this kind of beams. Some of the facilities are in fact requiring or wishing a certain increase in the delivered proton beam intensity. In this paper, we will focus on the ongoing studies for the n-ToF, one of the FT experiments receiving protons from the PS.

* eirini.koukovini.platia@cern.ch

Main Upgrades

The whole injector complex will undergo major upgrades during the LS2 to be able to fulfill the HL-LHC requirements. The upgrades in the PSB include the H⁻ charge exchange injection at 160 MeV instead of the 50 MeV proton injection of today, which will double the beam brightness out of the PSB. Due to a new radiofrequency (RF) system and an upgrade in the main power supply, the beam energy will also be increased from 1.4 GeV to 2 GeV. The 2 GeV extraction septum is already installed and used at 1.4 GeV until the LS2.

In the PS, the protons will be injected at 2 GeV allowing for brighter beams for the same tune shift. Moreover, a dedicated longitudinal feedback system will be used to mitigate the coupled-bunch instabilities and the longitudinal impedance of all the RF cavities in the PS will be reduced by about a factor of two [5] in order to be able to achieve the LIU baseline parameters.

In the SPS, reaching the LIU beam intensity requires a major upgrade of the main 200 MHz RF system in combination with an impedance reduction campaign. A new beam dump system will be placed in the long straight section LSS5 in order to cope with the higher beam intensities.

Regardless of these upgrades, it is necessary to study the future non-LHC beams by means of simulations and, whenever possible, measurements in order to ensure that the desired intensities are reached after the LS2.

ONGOING STUDIES

Future Beam Production in the PSB

The ISOLDE facility, receiving beam from the PSB, considers two operating scenarios after the LIU. The first is to maintain today's beam intensity of 0.8×10^{13} p per pulse per ring. The second is to double the intensity to 1.6×10^{13} p per pulse per ring while the number of cycles is reduced to avoid exceeding the limit of 2 μ A of beam current, imposed by radiation protection (air activation). Space charge studies are ongoing to investigate the production of future high-intensity beams in the PSB.

A possible intensity limitation is a horizontal instability observed in the PSB above a certain intensity [6, 7]. Currently it is suppressed by the transverse damper, however, the origin of the instability remains unknown. The study of this horizontal instability is very important since after the LIU the injection energy will be 160 MeV, i.e. at exactly the energy that the instability appears for certain tune working points. Moreover, higher intensity beams are foreseen after the LS2 and the beams will be accelerated to a higher

Content from this work may be used under the terms of the CC BY 3.0 licence (© 2018). Any distribution of this work must maintain attribution to the author(s), title of the work, publisher, and DOI.

energy of 2 GeV, raising the question whether another critical energy exists for the beam stability. Simulations are ongoing [8].

High Intensity Beam for the NA

The NA receives today a proton beam from the SPS of about 3.5×10^{13} p/spill to fulfill the needs of the experiments. After LS2, an increased intensity of 4×10^{13} p/spill is assumed for future operation. Studies were realized to optimize the efficiency of the Multi-Turn Extraction (MTE) scheme in the PS. Following these efforts, a successful Machine Development showed that the desired intensity of 4×10^{13} p/spill could already be delivered [9], giving confidence that the post-LIU baseline intensity is within reach.

INSTABILITY AT TRANSITION IN THE PS

One of the facilities requiring higher beam intensity after the LIU is the n-ToF. Presently a pulse of around 7×10^{12} p is delivered from the PS to the n-ToF, while 1×10^{13} p per pulse would be the desired intensity in the future.

The PS regularly crosses transition energy and in order to maximize the delivered beam intensity, a second order γ jump scheme is used [10] to artificially increase the transition crossing speed by means of fast pulsed quadrupoles. Despite the fact that the intensity reach is considerably higher with the γ jump scheme active, i.e. it increases from $\sim 180 \times 10^{10}$ protons per bunch (ppb) to $\sim 800 \times 10^{10}$ ppb, one of the main intensity limitations is a fast vertical instability occurring near the transition energy above a certain intensity. Various experimental and simulation studies have been done in the past [11, 12]. The single-bunch instability has been characterized to be of Beam Break-Up (BBU) type due to the frozen synchrotron motion near transition crossing.

For the post-LIU operation, where higher beam intensities and brightnesses are required, it is crucial to identify the main sources of the instability and to propose mitigation techniques.

PS IMPEDANCE MODEL

The transverse PS impedance model has been already computed in earlier studies [13–16]. The main impedance sources such as the resistive-wall assuming a round chamber of 35 mm radius, the indirect space charge, the RF cavities, the kickers, the septum, the transition steps and the vacuum ports are included.

The total vertical PS impedance is plotted in Fig. 1. In dashed lines, the real and imaginary parts of the kickers' impedance are plotted. It can be seen that the real part of the total vertical impedance is dominated by the kickers' contribution up to ~ 0.9 GHz. The maximum in the real part of the kickers' impedance is found at ~ 0.7 GHz, the same frequency as the observed instability at transition, identifying the kickers as the main source of the instability [16]. However, reducing the kickers' vertical impedance is not foreseen within the LIU, making the mitigation studies crucial.

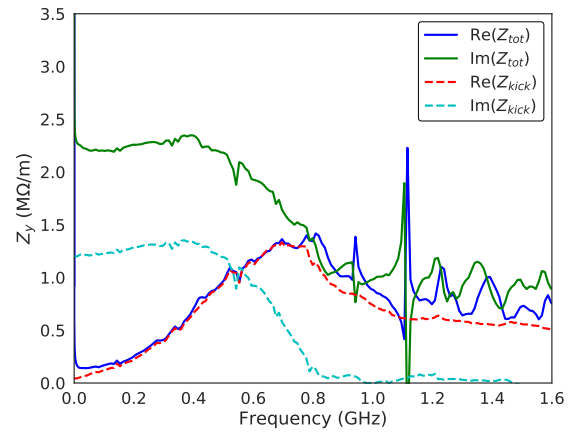


Figure 1: Vertical impedance model of the PS at 7 GeV.

SIMULATIONS WITH PYHEADTAIL

In order to study the fast single-bunch instability and investigate if its main characteristics can be reproduced with numerical simulations, the PyHEADTAIL 6D macroparticle tracking code [17] is used. The wake function is required as input to the code to simulate the effects of wakefields. An example of the transverse wake components, dipolar (dip) and quadrupolar (quad), at 7 GeV are shown in Fig. 2.

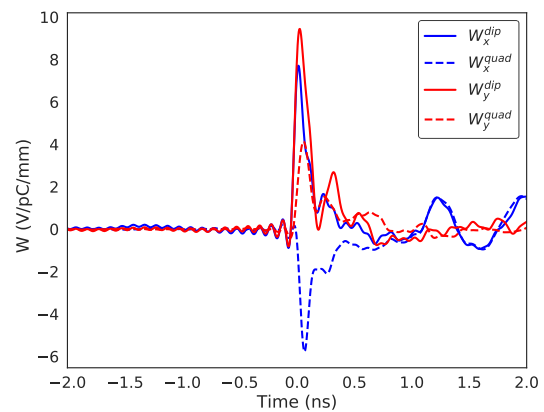


Figure 2: PS wake functions at 7 GeV.

Tune Shifts with Intensity

In the interest of benchmarking the developed PS impedance model, a set of PyHEADTAIL simulations was launched to compare the vertical tune shifts with intensity with the measured ones at different energies. The measured tune shifts at 2.0 GeV, 7.3 GeV, 13.1 GeV and 25.1 GeV were already taken during 2015 and presented in [16], with a chromaticity corrected as close to zero as possible. The comparison of the measured and simulated tune shifts is illustrated in Fig. 3 for the four energies.

At 2.0 GeV, 13.1 GeV and 25.1 GeV, an agreement of 85% to 90% is found between measurements and simulations. At the energy of 7.3 GeV, only 50% agreement is

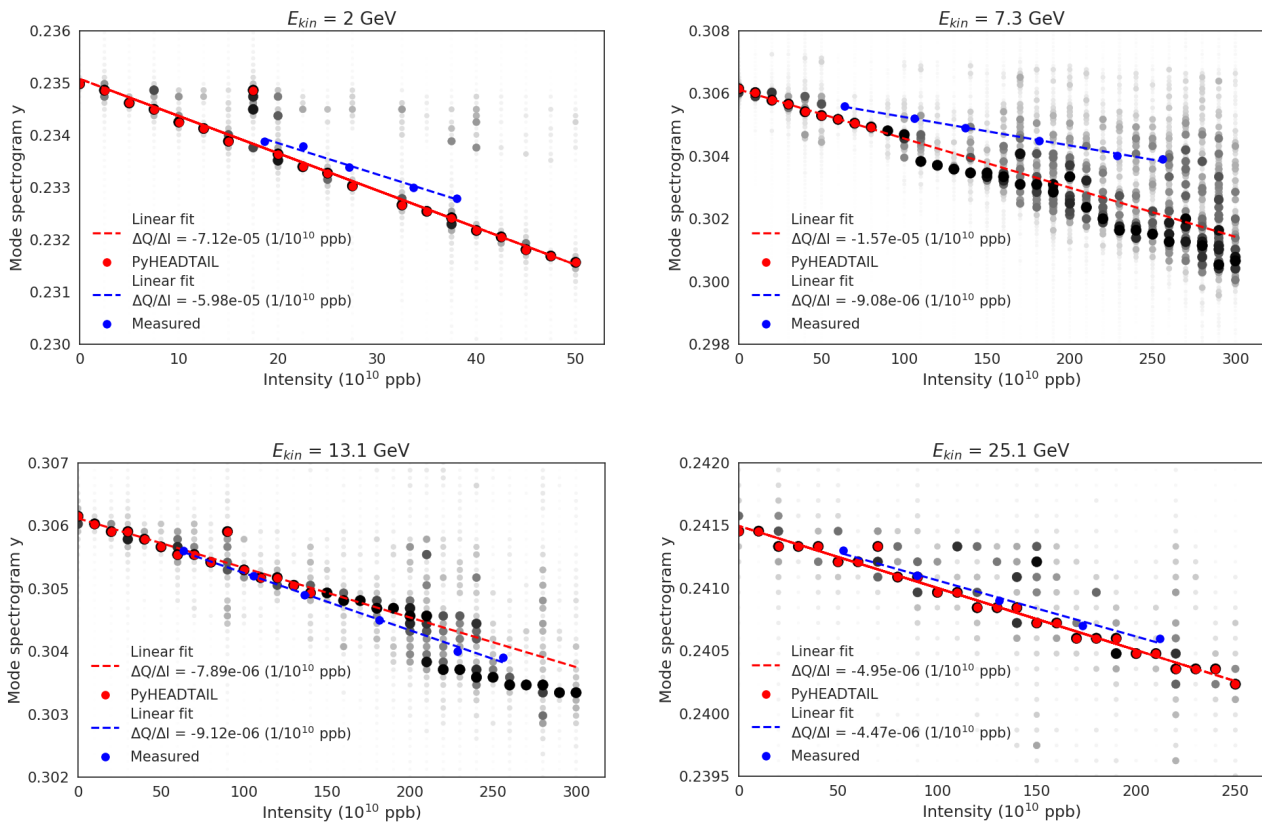


Figure 3: Comparison of measured and simulated tune shifts as a function of beam intensity for energies of 2.0 GeV, 7.3 GeV, 13.1 GeV and 25.1 GeV. Measured data are plotted in blue, simulated data in black and in red are the points used for the linear fit in PyHEADTAIL. An agreement of $\sim 90\%$ is found for all the energies apart from 7.3 GeV.

found. This is a very critical energy indeed, as it is near the transition crossing energy of 6.1 GeV. In the top right plot of Fig. 3, corresponding to the 7.3 GeV case, only the first simulated points marked with red color were used for the linear fit. The reason is that for intensities higher than 65×10^{10} ppb, the vertical centroid exhibits an exponential growth and becomes unstable. The measurements at this very critical energy are planned to be repeated this year before the LS2. Overall, a satisfactory agreement is found for most cases giving confidence that the imaginary part of the PS impedance is well modeled.

Frequency and Threshold of the Instability

In order to identify the critical frequency of the instability, 35000 turns were tracked starting from a relativistic $\gamma = 4.0$ and accelerating the beam up to $\gamma = 7.4$, with a longitudinal emittance of $\varepsilon_z^{rms} = 0.44$ eVs, with zero chromaticity and assuming a Gaussian distribution. Transition occurs at $\gamma = 6.1$, thus allowing sufficient time for the instability to develop in PyHEADTAIL. The acceleration is included in the code by providing the measured change of the particle momenta as a function of γ . Figure 4 shows the comparison of the measured spectrogram with the simulated one. An FFT is performed on the centroid data to obtain the spectrogram. Measurements show the strongest part of the instability to be centered around 0.6 GHz to 0.7 GHz, in agreement with

PyHEADTAIL. In addition, PyHEADTAIL also reproduces very well the onset of the instability in terms of cycle time in the PS with an error smaller than 0.5%.

An intensity scan is performed to identify the instability threshold predicted with PyHEADTAIL. With an emittance of $\varepsilon_z^{rms} = 0.44$ eVs and a transverse physical aperture of 35 mm radius included in the tracking code, the intensity threshold of $\sim 64 \times 10^{10}$ ppb is found. For this intensity, losses of the macroparticles on the vertical aperture are observed in Fig. 5. The predicted threshold is in fact a factor 2.5-3.0 lower than the measured value of $\sim 180 \times 10^{10}$ ppb, indicating that a stabilizing mechanism could be missing in the PyHEADTAIL simulations.

INCLUDING SPACE CHARGE IN PYHEADTAIL

A first hypothesis was that space charge could have an impact on the instability threshold. Up to now, any space charge induced tune spread was completely ignored.

A particle-in-cell (PIC) solver has been implemented in PyHEADTAIL and the simulations were also made available for graphics processing units (GPU) [19]. A 2.5D (i.e. slice-by-slice 2D transverse solving) Poisson solver was used with a 64×64 transverse mesh and 64 longitudinal slices. A smooth approximation was considered and 60 space charge

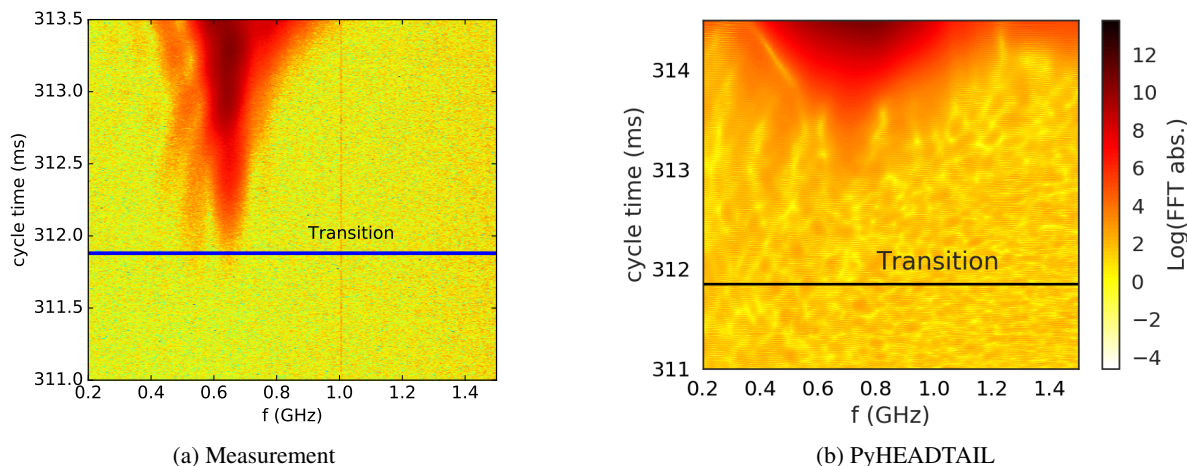


Figure 4: (a) Measured spectrogram with the instability being stronger around 0.6 GHz and 0.7 GHz [18]. (b) Simulated spectrogram with PyHEADTAIL, also indicating that the instability is centered around 0.7 GHz. The tracking code can also accurately reproduce the time in the PS cycle when the instability appears with an error less than 0.5%.

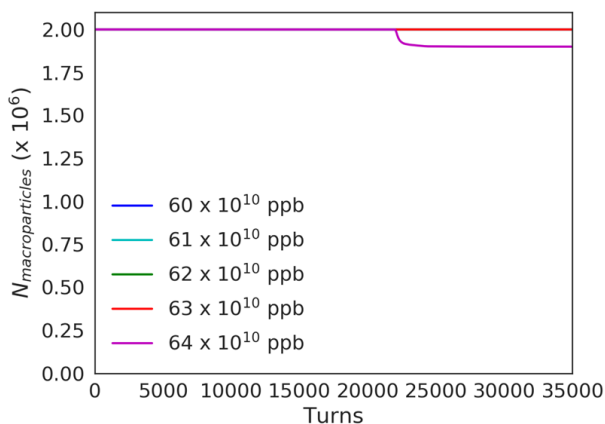


Figure 5: Number of macroparticles as a function of turns in PyHEADTAIL. Initial number of macroparticles is 2×10^6 . Losses are observed near transition crossing for intensities higher than 64×10^{10} ppb.

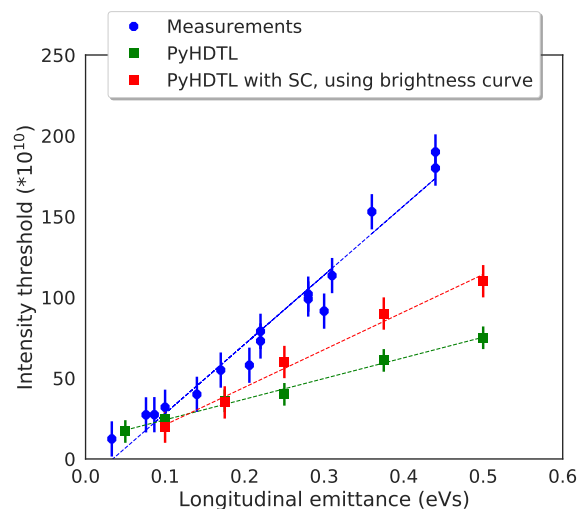


Figure 6: Single bunch intensity thresholds as a function of the longitudinal rms emittance for a ToF-like beam without the γ jump.

kicks were applied along the machine circumference. A convergence study was done prior to the choice of these simulation settings.

Figure 6 shows in blue the measurements in the PS of the single bunch intensity threshold for different longitudinal emittances of a ToF-like beam without the γ jump scheme. A linear dependence is observed. In the same figure, PyHEADTAIL results are plotted in green (PyHDTL) accounting only for the effect of wakefields and neglecting any space charge effects. Although a linear dependence is also found in the simulation results, a significant discrepancy with the measurements can be noted, up to almost a factor 3. In the same figure and in red color, the PyHEADTAIL results including the 2.5D PIC space charge module are shown. The simulations indicate that including space charge effects in the macroparticle tracking model is important and helps

approach the measured values. However, there is still some discrepancy and further studies are ongoing.

An important input for the space charge simulations are the values of the transverse emittances for each longitudinal emittance. At present, the simulated emittance values are assumed to follow the PSB measured brightness curve [20], thus they are intensity dependent. The brightness of the LHC-type beams is determined by the efficiency of the multi-turn injection in the PSB as well as the space charge effects during the injection process. The n-ToF beam follows the same brightness curve, as it was found from measurements, which gave a slope value of ~ 0.011 ($\mu\text{m}/10^{10}\text{p}$). As a first approximation, the horizontal and vertical emittances were assumed to be equal and the values in Table 1 were used in the PyHEADTAIL simulations.

Content from this work may be used under the terms of the CC BY 3.0 licence (© 2018). Any distribution of this work must maintain attribution to the author(s), title of the work, publisher, and DOI.

Table 1: Transverse emittances for each longitudinal emittance, following the measured brightness curve.

ϵ_z^{rms} (eVs)	$\epsilon_{x,y}$ (μm)
0.10	0.3
0.18	0.6
0.25	1.0
0.38	1.5
0.50	2.1

As a next step, more realistic values of the transverse emittances will be used, given the fact that the horizontal emittance is usually larger than the vertical one for the n-ToF beam. For this purpose, the measurements will be repeated and the values of the transverse emittances will be closely monitored.

REMOVAL OF OBSOLETE EQUIPMENT

Obsolete equipment that used to be part of the Continuous Transfer (CT) extraction scheme [21] in the PS was decided to be removed during the LS2. This includes, among other components, the electrostatic septum and kickers used for the generation of the five-turn extraction bump. The aforementioned components were removed from the PS impedance model and a new wake function that does not include the CT equipment was introduced in PyHEADTAIL. The difference in the vertical wake function before and after removing the CT equipment can be seen in Fig. 7.

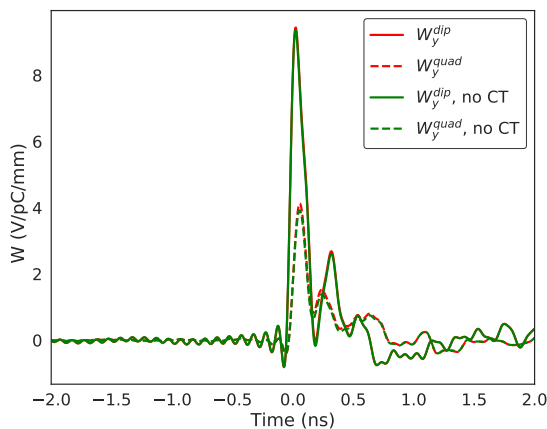


Figure 7: Wake functions with and without the CT equipment. The difference between the two is very small.

Although as a general rule, removing equipment can decrease the impedance of an accelerator, simulations showed that the particular components of the CT extraction do not largely contribute to the total machine impedance. The negligible effect of the envisaged hardware modification was further verified by obtaining the same threshold of 64×10^{10} ppb with PyHEADTAIL, as in the case where the total PS wake field is used. The prediction will be cross-checked

with beam-based measurements after the LS2, however, no significant benefit is expected for the instability threshold.

CONCLUSION

Apart from the LHC-type beams, some FT experiments would certainly benefit from higher intensity and brightness beams that will be available thanks to the LIU.

In particular, the ISOLDE facility could accept a double intensity of 1.6×10^{13} p per pulse per ring after LS2. Ongoing studies will address the question of the full extent of the intensity reach depending on the Linac4 parameters.

Other non-LHC users, such as the n-ToF would desire higher beam intensity after LS2 but current intensity limitations need to be addressed. Progress has been made in the understanding of the fast vertical instability mechanism as well as the influence of space charge on the predicted thresholds. Simulations with PyHEADTAIL indicate that the envisaged removal of the CT equipment will not alter significantly the machine impedance and thus the instability threshold. Other mitigation techniques, such as the optimization of the γ jump scheme, the chromaticity along the cycle and the use of octupoles, are under investigation.

Concerning the NA beam intensity request after the LS2, a successful machine test in 2017 proved that the desired intensity of 4×10^{13} p/spill can already be reached.

ACKNOWLEDGEMENTS

The authors would like to thank A. Oeftiger for the very useful discussions on space charge, M. Schenk for his support with the PyHEADTAIL code, and also A. Huschauer, S. Aumon, N. Wang, E. Métral, N. Biancacci, S. Persichelli and G. Sterbini for their valuable input concerning previous studies in the PS.

REFERENCES

- [1] S. S. Gilardoni *et al.*, “The High Intensity/High Brightness Upgrade Program at CERN: Status and Challenges”, in *Proc. HB’12*, Beijing, China, Sept. 2012, paper TU01A01.
- [2] A. M. Lombardi, “The Linac4 Project”, in *Proc. HB’16*, Malmö, Sweden, July 2016, paper MOAM2P20.
- [3] H. Damerau *et al.*, “Upgrade Plans for the LHC Injector Complex”, CERN, Geneva, Switzerland, Rep. CERN-ATS-2012-111, May 2012.
- [4] Physics Beyond Colliders, <http://pbc.web.cern.ch/>
- [5] K. Hanke *et al.*, “The LHC Injectors Upgrade (LIU) Project at CERN: Proton Injector Chain”, in *Proc. IPAC’17*, Copenhagen, Denmark, May 2017, paper WEPVA036.
- [6] M. McAteer *et al.*, “Observation of Coherent Instability in the CERN PS Booster”, CERN, Geneva, Switzerland, Rep. CERN-ACC-2014-0127, June 2014.
- [7] V. Kornilov *et al.*, “MD on Head-Tail Instability in the PS Booster”, CERN, Geneva, Switzerland, Rep. CERN-ACC-NOTE-2014-0025, Jan. 2013.

- Content from this work may be used under the terms of the CC BY 3.0 licence (© 2018). Any distribution of this work must maintain attribution to the author(s), title of the work, publisher, and DOI.
- [8] M. Migliorati, E. Koukovini-Platia, E. Métral, T. Rijoff, “PSB Instabilities: MD Results, Plans for 2018, and First Simulations”, presented at the LIU-PSB Beam Dynamics Working Group meeting, Geneva, CERN, Apr. 2018.
- [9] A. Huschauer *et al.*, “Approaching the High-Intensity Frontier Using the Multi-Turn Extraction at the CERN Proton Synchrotron”, presented at HB’18, Daejeon, Korea, June 2018, paper WEA1WA02, this conference.
- [10] E. Métral and D. Möhl, “Transition Crossing”, CERN, Geneva, Switzerland, Rep. CERN-2011-004, pp. 59-68, June 2011.
- [11] S. Aumon *et al.*, “Transverse Mode Coupling Instability Measurements at Transition Crossing in the CERN PS”, in *Proc. IPAC’10*, Kyoto, Japan, May 2010, paper TUPD049.
- [12] S. Aumon, “High Intensity Beam Issues in the CERN PS”, Ph.D. thesis, CERN, Geneva, Switzerland, CERN-THESIS-2012-261, 2012.
- [13] CST AG, Darmstadt, Germany, <http://www.cst.com>
- [14] H. Chin, “User’s Guide for ABCI Version 8.7”, CERN, Geneva, Switzerland, Rep. CERN-SL-94-02-AP, Feb. 1994.
- [15] T. Weiland, “Transverse beam cavity interaction, Part I: Short range forces”, *Nucl. Instrum. Methods Phys. Res.*, vol. 212, issues 1-3, p. 13, July 1983.
- [16] S. Persichelli *et al.*, “Transverse beam coupling impedance of the CERN Proton Synchrotron”, *Phys. Rev. Accel. Beams*, vol. 19, p. 041001, Apr. 2016.
- [17] E. Métral *et al.*, “Beam Instabilities in Hadron Synchrotrons”, *IEEE Trans. Nucl. Sci.*, vol. 63, p. 1001, Apr. 2016.
- [18] N. Wang, “Simulation of Instability at Transition Energy With a New Impedance model for CERN PS”, presented at the HSC meeting, Geneva, CERN, Nov. 2015.
- [19] A. Oeftiger, S. Hegglin, “Space Charge Modules for PyHEADTAIL”, CERN, Geneva, Switzerland, Rep. CERN-ACC-NOTE-2016-342, July 2016.
- [20] G. Rumolo *et al.*, “Expected Performance in the Injectors at 25 ns Without and With Linac4”, in *Proc. of Review of LHC and Injector Upgrade Plans Workshop*, Archamps, France, Oct. 2013, CERN-2014-006, pp. 17-24.
- [21] M. Giovannozzi, E. Métral, R. Steerenberg, “PS 4-turn Continuous Transfer Extraction Test”, CERN, Geneva, Switzerland, Rep. AB-Note-2005-006 (MD), Feb. 2005.

MICROBUNCHED ELECTRON COOLING (MBEC) FOR FUTURE ELECTRON-ION COLLIDERS*

Gennady Stupakov[†], SLAC National Accelerator Laboratory, Menlo Park, CA, USA

Abstract

The Microbunched Electron Cooling (MBEC) is a promising cooling technique that can find applications in future hadron and electron-ion colliders. In this paper we give a qualitative derivation of the cooling rate for MBEC and estimate the cooling time for the eRHIC electron-ion collider. We then argue that MBEC with two plasma amplification stages should be sufficient to overcome the emittance growth due to the intra-beam scattering in eRHIC.

INTRODUCTION

The idea of coherent electron cooling has been originally proposed by Ya. Derbenev [1] as a way to achieve cooling rates higher than those provided by the traditional electron cooling technique [2, 3]. The mechanism of the coherent cooling can be understood in a simple setup shown in Fig. 1. An electron beam with the same relativistic γ -

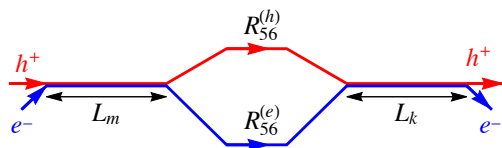


Figure 1: Schematic of the microbunched electron cooling system. Blue lines show the path of the electron beam, and the red lines indicate the trajectory of the hadron beam.

factor as the hadron beam co-propagates with the hadrons in a section of length L_m called the “modulator”. In this section, the hadrons imprint microscopic energy perturbations onto the electrons via the Coulomb force. After the modulation, the electron beam passes through a dispersive chicane section, $R_{56}^{(e)}$, where the energy modulation of the electrons is transformed into a density fluctuation referred to as “microbunching”¹. Meanwhile, the hadron beam passes through its dispersive section, $R_{56}^{(h)}$, in which more energetic particles move in the forward direction with respect to their original positions in the beam, while the less energetic particles trail behind. When the beams are combined again in a section of length L_k called the “kicker”, the electric field of the induced density fluctuations in the electron beam acts back on the hadrons. With a proper choice of the chicane strengths, the energy change of the hadrons in the kicker leads, over many passages through the cooling section, to a gradual decrease of the energy spread of the hadron beam.

* Work supported by the Department of Energy, contract DE-AC03-76SF00515

[†] stupakov@slac.stanford.edu

¹ In a long modulator section the microbunching can be generated directly in the modulator when the energy modulation is converted into a density fluctuation through plasma oscillations [4].

The transverse cooling is achieved in the same scheme by introducing dispersion in the kicker for the hadron beam.

In most cases, the cooling rate in the simple setup shown in Fig. 1 is not fast enough for practical applications. It can be considerably increased if the fluctuations in the electron beam are amplified on the way from the modulator to the kicker. Litvinenko and Derbenev proposed to use for this purpose the gain mechanism of the free electron laser (FEL) [5]. While this may be sufficient for some applications, one of the drawbacks of this approach is a narrow-band nature of the FEL amplifier that may not provide enough gain before the amplified signal saturates [6]. Following an earlier study by Schneidmiller and Yurkov [7] of microbunching dynamics for generation of coherent radiation, Ratner proposed a broadband amplification mechanism [8] in which the amplification is achieved through a sequence of drifts and chicanes such that the density perturbations in the drifts execute a quarter-wavelength plasma oscillation. In a recent paper [9], Litvinenko and co-authors put forward an idea to use a parametric instability in the electron beam caused by a periodic variation of the transverse size of the beam when it propagates through the cooling system.

In this paper, using order of magnitude estimates, we first derive a formula for the cooling rate in the system shown in Fig. 1. We then estimate the cooling rate for the parameters of eRHIC and show that the simple setup of Fig. 1 does not provide a sufficient cooling rate for the electron-ion collider without amplification in the electron channel. Finally, we estimate the amplification through a quarter-period plasma oscillation and argue that two plasma amplification stages should be enough to make the cooling time in eRHIC below one hour.

We use the Gaussian system of units throughout this paper.

QUALITATIVE DERIVATION OF MBEC COOLING RATE

For the hadron-electron interaction we adopt a model in which the interaction is treated as if a hadron were a disk of charge Ze with an axisymmetric Gaussian radial distribution of the rms transverse size Σ . The electron is also modeled by a Gaussian disk of charge $-e$ with the same transverse profile. A similar Gaussian-to-Gaussian interaction model was used in 1D simulations of a longitudinal space charge amplifier in Ref. [10].

The interaction between two charged slices of transverse size $\sim \Sigma$ is efficient only if they are close to each other. If the distance between them is smaller than $\Delta z \lesssim \Sigma/\gamma$, where γ is the Lorentz factor, the electric field of a hadron of charge Ze can be estimated as Ze/Σ^2 , and the interaction force between an electron and a hadron is $\sim Ze^2/\Sigma^2$. For

$\Delta z \gtrsim \Sigma/\gamma$, the interaction force decays as $\sim Ze^2/\Delta z^2\gamma^2$. So for estimates we will assume that, for a given hadron, the dominant contribution to the cooling comes from electrons located within the distance

$$\Delta z \sim \frac{\Sigma}{\gamma}. \quad (1)$$

We use the notation η for the relative energy deviation $\Delta E/E_0$ where E_0 is the nominal energy of the beam. Using the interaction force Ze^2/Σ^2 , a relative energy modulation η_e induced by a hadron in the modulator of length L_m can be estimated as

$$\eta_e \sim \frac{Ze^2}{\Sigma^2} L_m \frac{1}{\gamma m_e c^2} \sim \frac{cZeL_m}{\gamma \Sigma^2 I_A}, \quad (2)$$

where $I_A = m_e c^3/e = 17$ kA is the Alfvén current. Here we assume that a hadron and an electron do not shift longitudinally during the interaction on the length L_m .

The energy perturbation (2) is converted into a density perturbation when the electron beam passes through the chicane $R_{56}^{(e)}$. The optimal value of $R_{56}^{(e)}$ is found from the requirement that the electrons are longitudinally shifted in the chicane by the interaction distance $\sim \Delta z$:

$$R_{56}^{(e)} \sim \frac{\Delta z}{\sigma_\eta^{(e)}} \sim \frac{\Sigma}{\sigma_\eta^{(e)} \gamma}, \quad (3)$$

where $\sigma_\eta^{(e)}$ is the rms relative energy spread in the electron beam. Electrons whose energy is perturbed by η_e due to the interaction with a hadron will have an additional shift $\delta z \sim R_{56}^{(e)} \eta_e$, and this will cause a density perturbation of the order of

$$\delta n_e \sim \frac{\delta z}{\Delta z} n_e \sim \frac{\eta_e}{\sigma_\eta^{(e)} \gamma} n_e. \quad (4)$$

Here δn_e and n_e refer to the number of electrons in the beam per unit length. This density perturbation creates an electric field in the kicker,

$$E \sim e \delta n_e \Delta z \sim e \frac{\eta_e}{\sigma_\eta^{(e)} \gamma} \Sigma n_0. \quad (5)$$

With the optimal choice of the value of the hadron chicane, $R_{56}^{(h)} \sim \Delta z/\sigma_\eta^{(h)} \sim \Sigma/\sigma_\eta^{(h)} \gamma$, where $\sigma_\eta^{(h)}$ is the rms relative energy spread in the hadron beam, the hadron energy change in the kicker, $\sim ZeEL_k$, works against the hadron beam energy spread. This gives the following estimate for the inverse cooling time expressed in the revolution periods,

$$\begin{aligned} N_{\text{cool}}^{-1} &\sim \frac{ZeEL_k}{\gamma m_h c^2 \sigma_\eta^{(h)}} \sim \frac{ZeL_k}{\gamma m_h c^2 \sigma_\eta^{(h)}} e \frac{\eta_e}{\sigma_\eta^{(e)} \gamma} n_e \\ &\sim \frac{(Ze)^2 L_k L_m}{\gamma^3 m_h c^2 \Sigma^3 I_A \sigma_\eta^{(e)} \sigma_\eta^{(h)}} ecn_e \Sigma^2. \end{aligned} \quad (6)$$

Replacing $ecn_e \Sigma^2$ in this formula by the electron beam current I_e and using the notation $r_h = (Ze)^2/m_h c^2$ for the classical hadron radius, we arrive at the following result:

$$N_{\text{cool}}^{-1} \sim \frac{L_k L_m I_e r_h}{\gamma^3 \Sigma^3 I_A \sigma_\eta^{(e)} \sigma_\eta^{(h)}}. \quad (7)$$

As we will see below, this estimate, within a numerical factor, agrees with the result of an accurate theoretical analysis.

RESULTS OF RIGOROUS THEORETICAL ANALYSIS OF THE PROBLEM

A rigorous theoretical analysis of the cooling rate in the model of MBEC outlined in the Introduction was carried out in Ref. [11]. Here we present the main results of that analysis.

As was already mentioned, for the Coulomb interaction of beam particles we used a model of Gaussian slices assuming the transverse charge distribution with the rms size Σ . The longitudinal Coulomb force between two such slices located at distance z is given by the following formula:

$$F_z(z) = -\frac{Ze^2}{\Sigma^2} \Phi\left(\frac{z\gamma}{\Sigma}\right). \quad (8)$$

The plot of function Φ is shown in Fig. 2. This function

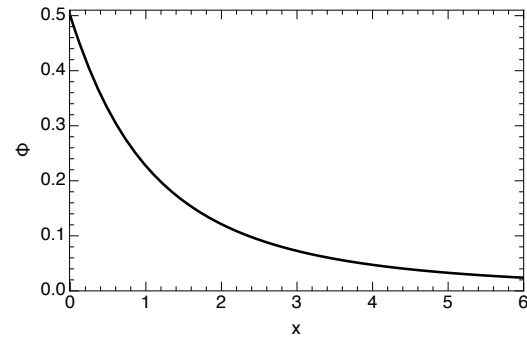


Figure 2: Function $\Phi(x)$ for positive values of the argument.

is odd, and for a negative argument $x < 0$ it is defined by $\Phi(-x) = -\Phi(x)$. The value of this function at the origin is $\Phi(0^+) = \frac{1}{2}$; for $x \gg 1$, we have $\Phi(x) \approx 1/x^2$. For a quick numerical evaluation of this function we found the following interpolation formula,

$$\Phi(x) \approx b \frac{e^{-ax} + 1}{2 + dx + bx^2}, \quad (9)$$

with $a = 1.60081$, $b = 0.499606$ and $d = 0.14579$.

Using this model for the particle interaction, in Ref. [11], we derived the following expression for cooling time N_{cool} evaluated in terms of the revolution periods:

$$N_{\text{cool}}^{-1} = \frac{4}{\pi} F \frac{I_e r_h L_m L_k}{\Sigma^3 \gamma^3 I_A \sigma_\eta^{(h)} \sigma_\eta^{(e)}}, \quad (10)$$

where the form-factor F depends on the strength of the chicanes $R_{56}^{(h)}$ and $R_{56}^{(e)}$. Analysis shows that for the optimal cooling the ratios $q_e = R_{56}^{(e)} \sigma_{\eta}^{(e)} \gamma / \Sigma$ and $q_h = R_{56}^{(h)} \sigma_{\eta}^{(h)} \gamma / \Sigma$ should be made equal, $q_e = q_h = q$; in this case the form-factor F depends only on the parameter q . The plot of the function $F(q)$ is shown in Fig. 3.

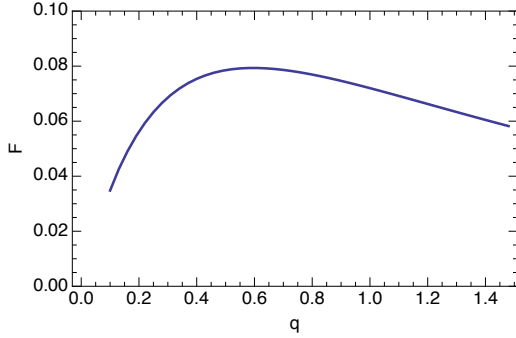


Figure 3: Plot of function $F(q)$ versus q .

We see that the maximum value of function F is reached at $q = 0.6$ and is equal to 0.079. Substituting this value into Eq. (10) we find for the optimized cooling rate:

$$N_{\text{cool}}^{-1} = \frac{0.10}{\sigma_{\eta}^{(h)} \sigma_{\eta}^{(e)}} \frac{1}{\gamma^3} \frac{I_e r_h L_m L_k}{I_A \Sigma^3}. \quad (11)$$

This formula has the same structure as Eq. (7), with an additional numerical factor 0.1. At the optimal cooling rate the chicane strengths are

$$R_{56}^{(e)} = 0.6 \frac{\Sigma}{\sigma_{\eta}^{(e)} \gamma}, \quad R_{56}^{(h)} = 0.6 \frac{\Sigma}{\sigma_{\eta}^{(h)} \gamma}. \quad (12)$$

Because the cooling rate (11) depends on the local electron beam current I_e that varies within the electron bunch, one has to average Eq. (11) taking into account the finite electron bunch length which we denote by $\sigma_z^{(e)}$. Assuming a Gaussian current distribution in the electron beam, $I_e = [Q_e c / \sqrt{2\pi} \sigma_z^{(e)}] \exp[-z^2 / 2(\sigma_z^{(e)})^2]$, where Q_e is the electron beam charge, it is straightforward to calculate that the average electron current a hadron feels over many passages through the electron beam is equal to

$$\bar{I}_e = \frac{Q_e c}{\sqrt{2\pi} [(\sigma_z^{(e)})^2 + (\sigma_z^{(h)})^2]^{1/2}}. \quad (13)$$

For an electron beam several times shorter than the hadron one, we can neglect $\sigma_z^{(e)}$ in this formula in comparison with $\sigma_z^{(h)}$. In this limit, replacing I_e in Eq. (11) by \bar{I}_e , we obtain for the cooling rate

$$N_{\text{cool}}^{-1} = 0.10 \frac{1}{\gamma^3 \sigma_{\eta}^{(h)} \sigma_{\eta}^{(e)}} \frac{Q_e c}{\sqrt{2\pi} \sigma_z^{(h)} I_A} \frac{r_h L_m L_k}{\Sigma^3}. \quad (14)$$

ESTIMATES FOR ERHIC COLLIDER

As a numerical illustration of the general theory presented in the previous sections we will estimate the optimized cooling rate for the nominal parameters of the electron-hadron collider eRHIC [12]. The parameters of the proton beam in eRHIC and of the electron beam in a possible MBEC cooling system are given in Table 1. Substituting these parameters into Eq. (14) gives for the cooling time

$$N_c = 1.5 \times 10^{10}, \quad (15)$$

which, with the revolution period in the RHIC ring of 13 μs , corresponds to 51.5 hours. The optimal parameters of the electron and proton chicanes are $R_{56}^{(h)} = 0.41$ cm and $R_{56}^{(e)} = 2.4$ cm. Of course, such a long cooling time is not sufficient for the eRHIC collider, where the intra-beam scattering (IBS) time scale for the emittance doubling is estimated in the range of 2 hours. We conclude that a simple setup shown in Fig. 1 needs to be augmented by some kind of amplification in the electron channel, as mentioned in the Introduction.

Table 1: Parameters of the eRHIC Collider with a Hypothetical MBEC Cooling Section

Parameter	Value
Proton beam energy	275 GeV
RMS length of the proton beam, $\sigma_z^{(h)}$	5 cm
RMS relative energy spread of the proton beam, $\sigma_{\eta}^{(h)}$	6×10^{-4}
Peak proton beam current, I_h	23 A
RMS transverse size of the beam in the cooling section, Σ	0.7 mm
Electron beam charge, Q_e	1 nC
RMS relative energy spread of the electron beam, $\sigma_{\eta}^{(e)}$	1×10^{-4}
Modulator and kicker length, L_m and L_k	40 m

Our assumption that the hadron-electron interaction results only in the energy perturbation of electrons in the modulator, and not their density, is justified if plasma oscillations in the electron beam can be ignored. Plasma oscillations convert energy perturbations in the beam into density modulations and vice versa in a quarter of the plasma wavelength λ_p , so these effects can be ignored if $\frac{1}{4}\lambda_p$ is much larger than the modulator and kicker lengths. To estimate $\frac{1}{4}\lambda_p$ in the electron beam we can use the following formula, (see, e.g., Ref. [7]),

$$\frac{1}{4}\lambda_{pl} \sim \gamma^{3/2} \Sigma \sqrt{\frac{I_A}{I_e}}. \quad (16)$$

Substituting parameters from Table 1 in this formula, we find that $\frac{1}{4}\lambda_p \lesssim L_m, L_k$ if the electron beam current is limited by $I_e \lesssim 30$ A, which for the given electron beam charge of 1 nC imposes a constrain on the electron bunch length, $\sigma_z^{(e)} \gtrsim 4$ mm.

AMPLIFICATION BY PLASMA OSCILLATIONS IN THE BEAM

To increase the cooling rate, one can add amplification stages in the electron channel [8] as shown in Fig. 4. One

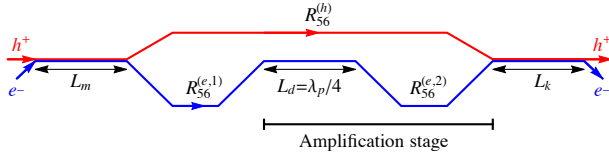


Figure 4: MBEC cooler with one plasma amplification stage.

stage consists of a drift of $\frac{1}{4}$ of the period of the plasma oscillations in the beam followed by another chicane with the dispersion strength $R_{56}^{(e,2)}$.

The mechanism of the plasma amplification can be understood as follows. A perturbation of the electron beam density generated after the chicane $R_{56}^{(e,1)}$ (see Fig. 4), through the Fourier transformation, can be decomposed into sinusoidal density perturbations in the electron beam. Each such perturbation propagating through the drift executes a quarter-wavelength plasma oscillation, which converts the initial density perturbation into a sinusoidal energy modulation. When the beam passes through the chicane $R_{56}^{(e,2)}$ the energy modulation is converted back into a density perturbation with an amplitude that can be larger than the initial one [7, 10]. We can easily estimate the gain factor G of one plasma cascade.

In a cold beam with a sinusoidal plasma oscillation with the wavenumber k the energy perturbation η is related to the density perturbation δn_e by the following relation,

$$\eta \sim \frac{k_b \sqrt{\gamma_e} \delta n_e}{k n_e}, \quad (17)$$

where $k_b = \sqrt{4\pi r_e n_e / \Sigma^2}$. An initial density perturbation δn_e after a quarter of plasma period is converted to an energy perturbation given by this equation. The chicane $R_{56}^{(e,2)}$ at the end of the amplification stage then converts this energy modulation into a density one with the amplitude

$$\delta n'_e \sim \frac{\eta}{\sigma_\eta^{(e)}} n_0 \sim \frac{1}{\sigma_\eta^{(e)}} \frac{k_b \sqrt{\gamma_e}}{k} \delta n_e. \quad (18)$$

We will use for the wavenumber k the characteristic value $1/\Delta z$ of the interaction distance, $k \sim 1/\Delta z \sim \gamma/\Sigma$. We then find for the amplification factor $G = \delta n'_e / \delta n_e$,

$$G \sim \frac{1}{\sigma_\eta^{(e)}} \frac{k_b \sqrt{\gamma_e}}{k} \sim \frac{1}{\sigma_\eta^{(e)}} \sqrt{\frac{I_e}{\gamma I_A}}. \quad (19)$$

The last equation agrees with the result of Ref. [7]. For the parameters from Table 1 and $I_e = 10$ A we find the amplification factor $G \approx 14$ and hence two amplification stages (that is a chicane-drift-chicane-drift-chicane configuration in the electron channel) should be enough to lower the cooling time below 1 hour limit.

ACKNOWLEDGEMENTS

I would like to thank M. Blaskiewicz, F. Willeke and M. Zolotarev for numerous stimulating discussions of the subject of this paper. I am also grateful to E. Shneidmiller and M. Dohlus for clarifying the connection of MBEC with microbunching instability in FELs, and to P. Baxevanis for help with computer simulations.

REFERENCES

- [1] Ya. S. Derbenev, "On possibilities of fast cooling of heavy particle beams," *AIP Conf. Proc.*, vol. 253, pp. 103–110, 1992. doi: 10.1063/1.42152.
- [2] I. Meshkov, "Electron cooling — recent developments and trends," *Nuclear Physics A*, vol. 626, no. 1, pp. 459–471, 1997, Proceedings of the Third International Conference on Nuclear Physics at Storage Rings, ISSN: 0375-9474. <http://www.sciencedirect.com/science/article/pii/S0375947497005708>
- [3] S. Nagaitsev *et al.*, "Experimental demonstration of relativistic electron cooling," *Phys. Rev. Lett.*, vol. 96, p. 044 801, 4 Jan. 2006. doi: 10.1103/PhysRevLett.96.044801.
- [4] G. Wang and M. Blaskiewicz, "Dynamics of ion shielding in an anisotropic electron plasma," *Phys. Rev. E*, vol. 78, p. 026413, 2 Aug. 2008. doi: 10.1103/PhysRevE.78.026413.
- [5] V. N. Litvinenko and Y. S. Derbenev, "Coherent electron cooling," *Phys. Rev. Lett.*, vol. 102, p. 114 801, 11 2009.
- [6] G. Stupakov and M. S. Zolotarev, "Comment on "coherent electron cooling"," *Phys. Rev. Lett.*, vol. 110, p. 269 503, 26 Jun. 2013. doi: 10.1103/PhysRevLett.110.269503.
- [7] E. A. Schneidmiller and M. V. Yurkov, "Using the longitudinal space charge instability for generation of vacuum ultraviolet and x-ray radiation," *Phys. Rev. ST Accel. Beams*, vol. 13, p. 110 701, 11 Nov. 2010. doi: 10.1103/PhysRevSTAB.13.110701.
- [8] D. Ratner, "Microbunched electron cooling for high-energy hadron beams," *Phys. Rev. Lett.*, vol. 111, p. 084 802, 8 Aug. 2013. <https://link.aps.org/doi/10.1103/PhysRevLett.111.084802>
- [9] V. N. Litvinenko, G. Wang, D. Kayran, Y. Jing, J. Ma, and I. Pinayev, "Plasma-Cascade micro-bunching Amplifier and Coherent electron Cooling of a Hadron Beams," *ArXiv e-prints*, Feb. 2018. arXiv: 1802.08677 [physics.acc-ph].
- [10] M. Dohlus, E. A. Schneidmiller, and M. V. Yurkov, "Generation of attosecond soft x-ray pulses in a longitudinal space charge amplifier," *Phys. Rev. ST Accel. Beams*, vol. 14, p. 090 702, 9 Sep. 2011. doi: 10.1103/PhysRevSTAB.14.090702.
- [11] G. Stupakov, "Derivation of the cooling rate for microbunched electron cooling (mbec)," SLAC, Preprint SLAC-PUB-17208, 2018.
- [12] C. Montag *et al.*, "Overview of the eRHIC Ring-Ring Design," in *Proc. of International Particle Accelerator Conference (IPAC'17)*, (Copenhagen, Denmark), ser. International Particle Accelerator Conference, Geneva, Switzerland: JACoW, May 2017, pp. 3035–3037. doi: <https://doi.org/10.18429/JACoW-IPAC2017-WEPIK049>.

SPACE-CHARGE COMPENSATION USING ELECTRON COLUMNS AT IOTA*

B. Freemire[†], S. Chattopadhyay¹, Northern Illinois University, DeKalb, USA
V. Shiltsev, G. Stancari, Fermi National Accelerator Laboratory, Batavia, USA
C.S. Park, Korea University Sejong Campus, Sejong City, South Korea
G. Penn, Lawrence Berkeley National Laboratory, Berkeley, USA
M. Chung, Ulsan National Institute of Science and Technology, Ulsan, South Korea
¹also at Fermi National Accelerator Laboratory

Abstract

Beam loss due to space-charge is a major problem at current and future high intensity particle accelerators. The space-charge force can be compensated for proton or ion beams by creating a column of electrons with a charge distribution matched to that of the beam, while maintaining electron-proton stability. The column is created by the beam ionizing short sections of high pressure gas. The ionization electrons are then shaped appropriately using external electric and magnetic fields. The Integrable Optics Test Accelerator (IOTA) ring at Fermilab is a test bed for mitigation techniques for beam loss and instabilities. A 2.5 MeV proton beamline is under construction in IOTA, to be used to study space-charge compensation using an Electron Column and Electron Lens for a space-charge dominated beam. Simulations using the particle-in-cell code, Warp, have been made to track the evolution of both the electron column and the beam over multiple passes.

INTRODUCTION

Coulomb repulsion, known as the space-charge force within a beam of particles, results in beam loss and component radioactivation in high intensity accelerators. Future proton or ion accelerators and upgrades to existing machines will require better control of beam loss in order to prevent damage to components, minimize cost, and achieve the desired beam power. Compensation of the effects of space-charge by accumulating and trapping electrons through ionization of gas along the beam trajectory has been tested experimentally with limited results, and plans exist for a detailed study of a so-called Electron Column in the Integrable Optics Test Accelerator, currently under construction at Fermilab.

An Electron Column (EC) is similar to an Electron Lens (EL) in that the space-charge force is negated by matching the transverse (and preferably longitudinal) distribution of electrons to that of the beam. In the case of the Electron Column, electrons are obtained by maintaining a short section of beam pipe at a relatively high gas pressure, and capturing and shaping the electrons created by ionization of the gas by

the beam using electrodes at the ends of the Column, and a solenoidal magnetic field. This eliminates the need for the electron gun and collector required by the Electron Lens. The total charge of electrons needed to achieve complete space-charge compensation (SCC) of the beam in the EC is reduced by a factor of (the relativistic) γ^2 .

The plasma ions generated in the Electron Column negatively impact space-charge compensation, and so the magnetic field used to confine the electrons transversely must be weak enough to allow the ions to escape over time. However, the magnetic field must be strong enough to suppress electron-proton instabilities observed in EC experiments in the past [1, 2].

PRIOR SPACE-CHARGE COMPENSATION EXPERIMENTS

Space-charge compensation has successfully been implemented in high current, low energy beams in linacs. Experiments of SCC in circular machines have been performed in the past with limited results.

Institute of Nuclear Physics

Space-charge compensation in a ring was first attempted in 1983 at the Institute of Nuclear Physics in Novosibirsk using a 1 MeV, 8 mA proton beam with a few mTorr of hydrogen gas. There was no stabilizing magnetic field, and so while an increase of nearly an order of magnitude was observed in the beam current, there beam lifetime was reduced and e-p instabilities were significant [1].

Fermilab Tevatron

Two Electron Lenses, the concept on which the Electron Column is based, were operated successfully in the Tevatron at Fermilab [3, 4]. A Lens was modified to operate as a Column by turning off the electron gun and collector and using electrodes and a 3 T longitudinal magnetic field to trap electrons created by ionization of residual gas [5]. Using the 150 GeV proton beam and allowing the vacuum to degrade to about 50 nTorr, accumulation of charge within the Column and a positive tune shift was observed [2]. However, significant vacuum instability was observed, which resulted in beam instability and emittance growth or beam loss.

* Work supported by the US Department of Energy, Office of High Energy Physics, under Contract Nos. DE-AC02-07CH11359 and DE-AC02-05CH1123 and the General Accelerator Research and Development (GARD) Program.

[†] bfreemire@niu.edu

SPACE-CHARGE COMPENSATION EXPERIMENT AT IOTA

The Integrable Optics Test Accelerator (IOTA) is under construction at Fermilab and will host experiments for research and development for technology to be used in the next generation of particle accelerator [6]. Electron Lens and Column experiments are planned, which will allow for testing space-charge compensation schemes using a 2.5 MeV proton beam and a range of parameters in gas density and electrode and magnet field strengths. Construction of the IOTA ring is expected to be complete in August of 2018, with commissioning and the first electron experiments to take place through 2018 and 2019. Installation of the proton RFQ and commissioning of IOTA with protons is expected to take place in late 2019 and early 2020. A schematic of what the Electron Column will look like when installed in IOTA is shown in Figure 1.

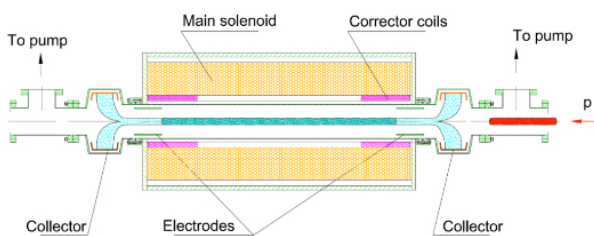


Figure 1: Schematic of the Electron Column in IOTA.

A simulation effort is underway with the goal of studying the evolution of the plasma in the Electron Column and the degree of space-charge compensation expected for varying conditions.

ELECTRON COLUMN SIMULATION PARAMETERS

Simulations of the Electron Column in IOTA have been done using Warp [7]. The results reported here will cover the proton beam in IOTA making two passes through the EC, and the resulting degree of space-charge compensation. Table 1 lists the relevant simulation parameters. Other simulation specifications have been reported elsewhere [8].

A KV beam with the expected proton beam emittance coming from the RFQ was injected at the beginning of the column and the distribution recorded after exiting the column. The plasma distribution after one revolution period (1.83 μ s, compared the the 1.77 μ s beam pulse length) was also recorded. The plasma was then loaded at the beginning of the second pass, and the saved beam particles loaded with the appropriate position and temporal coordinates. Finally, the beam and plasma distributions after the second revolution period were recorded. In this way, two passes of the beam through the EC were simulated, although the rest of the IOTA lattice was not taken into account.

Table 1: Simulation Parameters for the Electron Column in IOTA

Parameter	Value	Unit
Beam species	Proton	
Beam energy	2.5	MeV
Beam current	8	mA
Beam pulse length	1.77	μ s
Gas species	Hydrogen	
Gas density	1.65×10^{13}	cm^{-3}
Ionization cross section	1.82×10^{-17}	cm^2
Plasma energy (spread)	45 (19)	eV (eV)
Column length	1	m
Beampipe radius	2.54	cm
Electrode positions (z)	0, 100	cm
Electrode strength	-5	V
Solenoid field	0.1	T
Macroparticle/timestep	500	
Grid spacing (x,y,z)	(0.5, 0.5, 1.0)	cm
Timestep	70	ps
Simulation length	1.83	μ s

SIMULATION RESULTS

The results showing the degree of space-charge compensation at the center of the Electron Column after the first beam pass are shown in Figure 2. The top plot shows the radial electric field along the x transverse dimension for two cases: the beam only, and the beam with SCC (i.e. ionization of the gas). The bottom plot shows the ratio of the electric field with SCC to that without SCC (beam only). It can be seen that the radial electric field within the beam diameter (vertical lines on the plots) is reduced by a factor of ≈ 2 when SCC is turned on.

Figure 3 shows the distributions of the beam, electrons, and ions at the end of the first pass. The top plot shows the transverse distribution at the center of the Column in the longitudinal dimension, and the bottom plot shows the longitudinal distribution at the center of the Column in the transverse dimension. The distribution of electrons is well matched to the beam (protons) transversely, however the density is not yet matched. The ions, which are not as strongly confined by the magnetic field, have diffused radially and are not as dense in the center of the Column. Longitudinally, electrons are being lost out the ends of the Column as can be seen by their existence outside of the 0-100 cm boundary of the EC, while the ions are less mobile and therefore more well-confined.

Figure 4 shows the radial electric fields and ratio of electric fields for SCC and no SCC at the end of the second pass. Within the beam diameter there is a slight reduction in electric field compared to the first pass, however the build up of ions at the center of the column results in a degradation of SCC for small radii (x values). This can be seen in Figure 5, which shows the transverse and longitudinal distribution of particles at the end of the second pass.

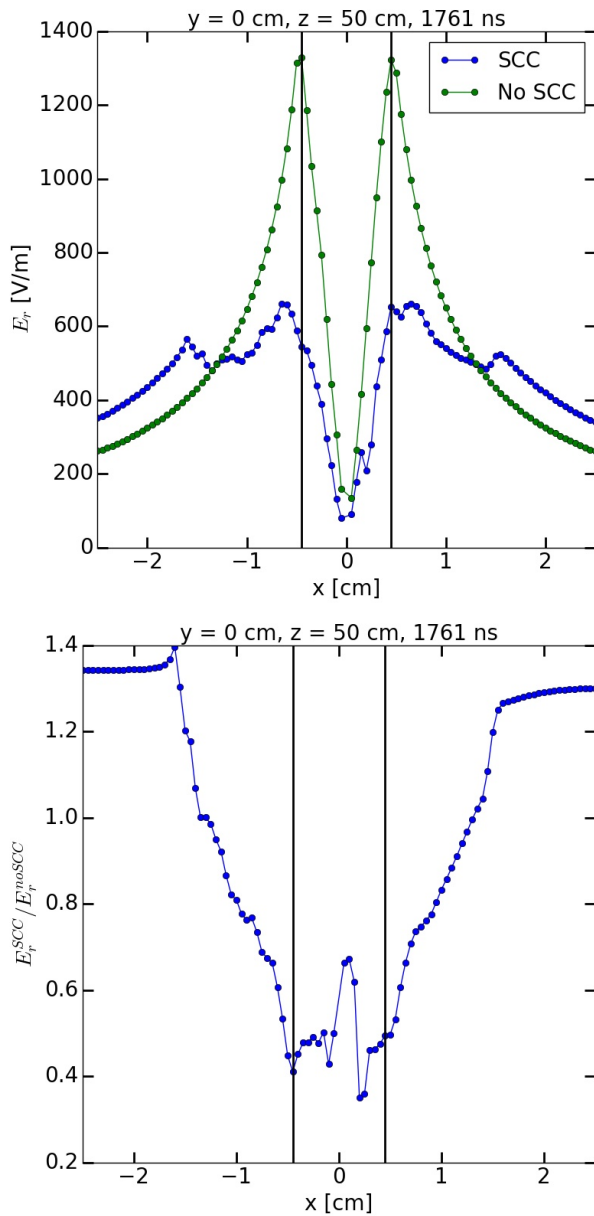


Figure 2: Radial electric field along x in the center of the column in y and z for beam alone (green) and with space-charge compensation (blue) at the end of the first pass of the beam through the Electron Column - top. Ratio of the two electric fields from the top plot - bottom. The vertical lines in both plots denote the boundary of the beam.

At the end of the second pass, the distribution of electrons is still well matched to that of the beam, however the density is now greater. The density of ions is also greater, resulting in the reduction in SCC at the center of the beam seen in Figure 4. This over compensation of electrons, and corresponding increased density of ions can be countered by decreasing the gas density and/or magnetic field strength. Decreasing the gas density is preferable, as this will not affect suppression of e-p instability, however this will increase the length of time it takes the EC to reach full compensation.

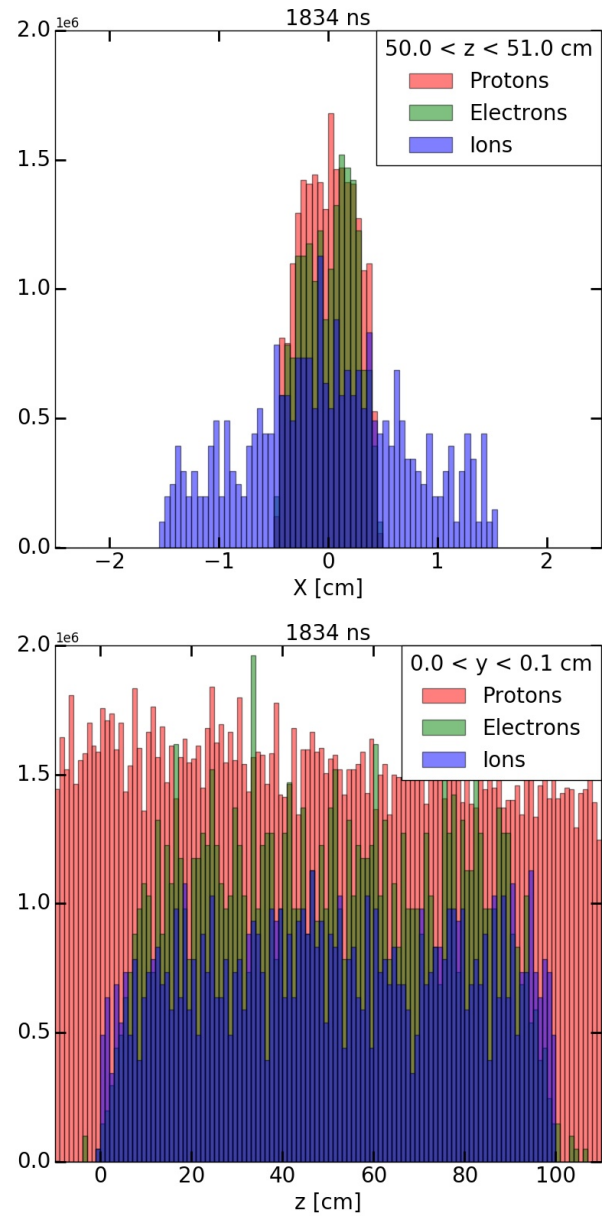


Figure 3: Distribution along x for the beam (red), electrons (green), and ions (blue) at the center of the Electron Column in z just before the beam would reenter the Column for a second pass - top. Note the beam distribution plotted is for the last time step that the beam is in the Column, for reference. Bottom - same as the top, but plotted along z at the center of the Column in y . The bin widths correspond to the simulation grid spacing.

Content from this work may be used under the terms of the CC BY 3.0 licence (© 2018). Any distribution of this work must maintain attribution to the author(s), title of the work, publisher, and DOI.

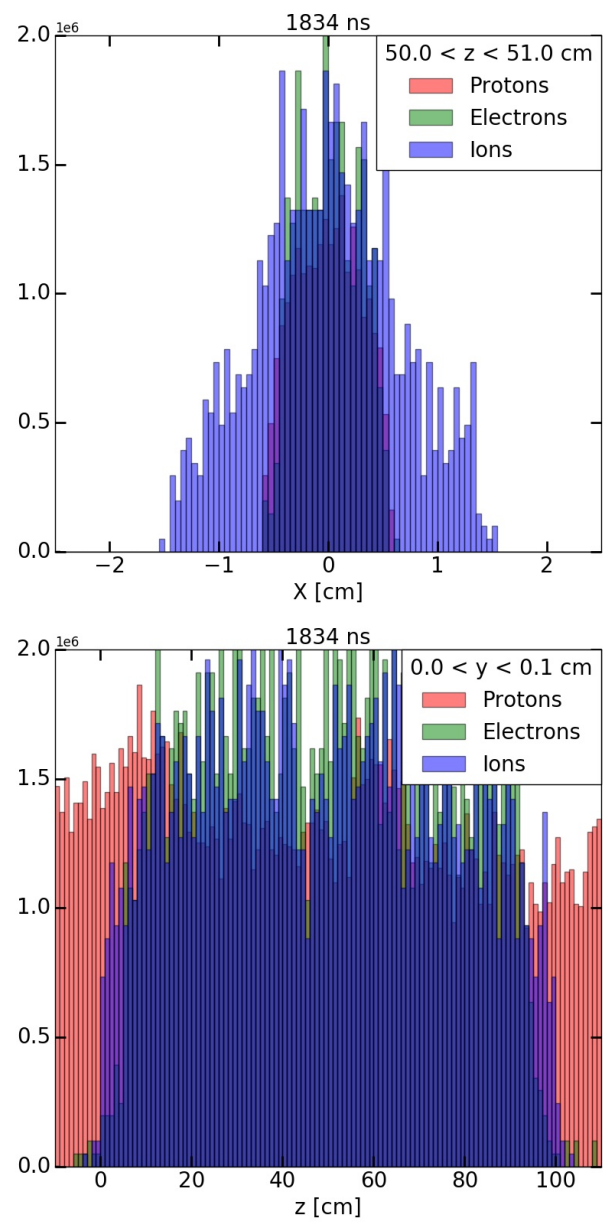
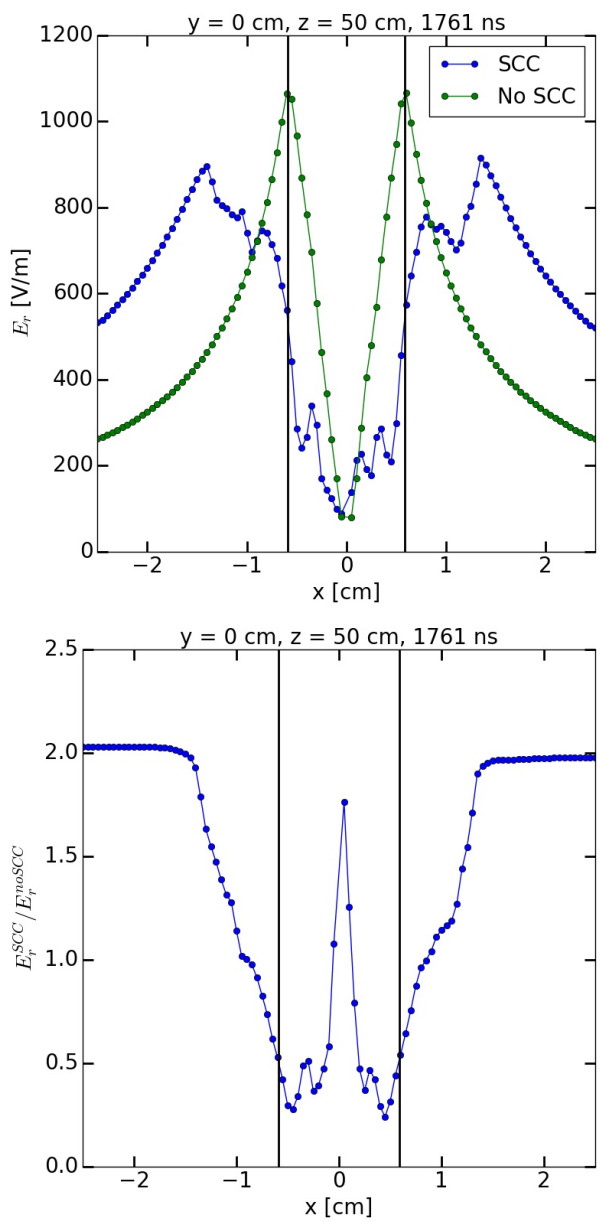


Figure 4: Same as Fig. 2, but at the end of the second pass of the beam through the Column.

Figure 5: Same as Fig. 3, but just before the beam would reenter the Column for a third pass.

It should be noted that a number of important plasma processes are not implemented in these simulations. The first is collisions and therefore energy loss of plasma particles with the surrounding gas. The second is recombination of electrons with ions in the plasma. Both of these effects will contribute to the evolution of the number (and therefore density) of plasma particles.

Nonetheless, these initial simulations indicate that final level of space-charge compensation (whether it be complete compensation or some partial compensation) can be reached within a small number of turns of the beam in IOTA. Additionally, it appears that the gas density can be decreased, which will have a positive impact on the lifetime of the 2.5 MeV proton beam.

CONCLUSION

Space-charge compensation using an Electron Column is planned for the proton experimental program in IOTA. Simulations of two passes of the beam through the Electron Column indicate a significant degree of space-charge compensation can be achieved within a small number of passes. Future plans include incorporating the rest of the IOTA lattice into simulations, and studying the affect on space-charge compensation of varying the parameters, such as gas density and electrode strength, of the Electron Column.

ACKNOWLEDGEMENTS

The authors would like to thank the entire FAST/IOTA team, members of RadiaSoft, and Chad Mitchell for fruitful discussions.

REFERENCES

- [1] G.I. Dimov and V.E. Chupriyanov, “Compensated Proton-Beam Production in an Accelerating Ring at a Current Above the Space-Charge Limit”, *Part. Accel.*, vol. 14, pp. 155-184, 1984.
- [2] V. Shiltsev *et al.*, “Beam Studies with Electron Columns”, in *Proc. PAC’09*, Vancouver, Canada, May 2009, paper TH5PFP020, pp. 3233-3235.
- [3] V. Shiltsev *et al.*, “Experimental demonstration of colliding-beam-lifetime improvement by electron lenses”, *Phys. Rev. Lett.*, vol. 99, no. 24, p. 244801, Dec. 2007.
- [4] V. Shiltsev *et al.*, “Tevatron Electron Lenses: Design and Operation”, *Phys. Rev. ST Accel. and Beams*, vol. 11, p. 103501, Oct. 2008.
- [5] V. Shiltsev, “New Possibilities for Beam-beam and Space-charge Compensation: MCP Gun and Electron Columns,” in *Proc. PAC’07*, Albuquerque, USA, Jun. 2007, paper TUPMN106, pp. 1159-1160.
- [6] S. Antipov *et al.*, “IOTA (Integrable Optics Test Accelerator): facility and experimental beam physics program”, *J. Inst.*, vol. 12, T03002, Mar. 2017.
- [7] A. Friedman *et al.*, “Computational Methods in the Warp Code Framework for Kinetic Simulations of Particle Beams and Plasmas”, *IEEE Trans. Plasma Sci.*, vol. 42, no. 5, p. 1321, May 2014.
- [8] B. Freemire *et al.*, “Simulations of the Electron Column in IOTA”, in *Proc. IPAC’18*, Vancouver, Canada, May 2018, paper TUPAL043.

IBS NEAR TRANSITION CROSSING IN NICA COLLIDER

S. Kostromin, I. Gorelyshev, A. Sidorin, JINR, Dubna, Russia
 V. Lebedev, FNAL, Batavia, Illinois, USA

Abstract

Intrabeam scattering (IBS) of charged particles in a particle beam results in an exchange of energy between different degrees of freedom. That results in an increase of average energy of particles in the beam frame and an increase of the 3D-emittance. The paper considers calculations of beam emittance growth rates for different options of NICA collider and IBS effects in close vicinity of the transition.

INTRODUCTION

Intrabeam scattering (IBS) is a Coulomb scattering of charged particles in a beam. It causes an exchange of energy between various degrees of freedom resulting in an increase of average energy of particles in the beam frame and an increase of the total beam emittance in the 6D phase space.

Anton Piwinski was first who derived equations describing IBS [1]. These equations neglect derivatives of the beta-functions and therefore, strictly speaking, are accurate for rings with “smooth focusing” only. They also represent a good approximation for weak focusing rings. Later, Bjorken and Mtingwa derived equations applicable to the general case [2] where the motion in the transverse planes is still considered being uncoupled. These equations were rederived in Ref. [3] which derivation is based on the Landau kinetic equation [4] and the IBS rates were expressed through symmetric elliptic integrals [5]. This work also showed how the equations can be extended to the case of motion coupled in all three degrees of freedom [5]. These results were used in the calculations of the IBS growth rates for different lattice options of the NICA collider [6] during work on its conceptual design [7]. The maximum energy of the stored ions in the collider is close to the transition energy ($\gamma \approx 5.8$, $\gamma_{tr} \approx 7.1$). That required a detailed study of the IBS phenomena near transition. The obtained results had essential influence on the final lattice design and major parameters of the collider.

IBS GROWTH RATES

We introduce two coordinate systems. The first one is the standard local coordinate frame (LF) for a ring ($x, \theta_x, y, \theta_y, s, \theta_s$); and the second one is the beam frame (BF) moving with the beam where additionally the axes are rotated to coincide with the axes of 6D beam ellipsoid in the 6D phase space (x, v_x, y, v_y, z, v_z). For both systems we assume that the center of the system coincides with the beam center of “gravity”.

Sequence of major steps used for an estimation of the IBS heating rates is shortly summarized as following:

- using known Twiss parameters and the emittances find 6D particle ellipsoid in the BF and its rotation relative to the LF;
- calculate along the ring the growth rates for rms velocities in the BF;
- convert the velocity growth rates to the emittance growth rates in the LF;
- average the obtained data over entire machine circumference to obtain the overall IBS rates.

IBS FOR SMOOTH FOCUSING BELOW AND ABOVE TRANSITION

To understand the how the IBS works let us consider first the IBS in vicinity of the transition energy in the smooth optics for unbunched beam. In this approximation we assume that:

- Twiss parameters are constant along the ring
- vertical dispersion $D_y=0$
- L is the ring circumference, which in the case of bunched beam is related with the rms bunch length by following equation: $\sigma_z \rightarrow L / (2\sqrt{\pi})$.

Using formalism of Ref. [3] we obtain the matrix of velocity second moments’ in the BF:

$$\Sigma_v = \gamma \cdot \beta \cdot c \cdot \begin{pmatrix} \theta_x^2 & 0 & 0 \\ 0 & \theta_y^2 & 0 \\ 0 & 0 & \theta_p^2 \end{pmatrix},$$

where

$$\sigma_x = \sqrt{\varepsilon_x \beta_x + \sigma_p^2 D^2} \quad \sigma_y = \sqrt{\varepsilon_y \beta_y} \quad \theta_{x,y}^2 = \frac{\varepsilon_{x,y}}{\beta_{x,y}} \quad \theta_p^2 = \sigma_p^2 \frac{\beta_x}{\gamma \sigma_x^2}$$

Accounting that there is no rotation of the BF relative to the LF and performing transition from the BF to the LF we obtain the emittance growth rates:

$$\frac{d}{dt} \begin{pmatrix} \varepsilon_x \\ \varepsilon_y \\ \sigma_p^2 \end{pmatrix} = \frac{\sqrt{\pi}}{2\sqrt{2}} \cdot \frac{e^3 N L_c}{M^2 c^3 \sigma_x \sigma_y L \beta^3 \gamma^3 \sqrt{\theta_x^2 + \theta_y^2 + \theta_p^2}} \begin{pmatrix} \beta_x \Psi_{IBS}(\theta_x, \theta_y, \theta_p) + \gamma^2 \frac{D^2}{\beta_x} \Psi_{IBS}(\theta_p, \theta_x, \theta_y) \\ \beta_y \Psi_{IBS}(\theta_y, \theta_p, \theta_x) \\ 2\gamma^2 \Psi_{IBS}(\theta_p, \theta_x, \theta_y) \end{pmatrix}$$

where e is the ion electrical charge, N is the number of ions in the beam, L_c is the Coulomb logarithm, M is the ion mass, c is the speed of light, β and γ are the relativistic factors, D is the horizontal dispersion, and the functions $\Psi_{IBS}(\dots)$ are expressed through the symmetric elliptic integral of the second kind [5].

In the equilibrium all “local temperatures” are equal ($\theta_x = \theta_y = \theta_p$) and do not change with time. That yields:

$$\Psi_{IBS}(\theta_x, \theta_y, \theta_p) = \Psi_{IBS}(\theta_y, \theta_p, \theta_x) = \Psi_{IBS}(\theta_p, \theta_x, \theta_y) = 0.$$

Consequently, this requires:

$$\frac{\varepsilon_x}{\beta_x} = \frac{\varepsilon_y}{\beta_y} = \frac{\sigma_p^2}{\gamma^2} \cdot \frac{\varepsilon_x \beta_x}{\varepsilon_x \beta_x + \sigma_p^2 D^2}.$$

That yields:

$$\frac{\sigma_p^2}{\gamma^2} = \frac{\varepsilon_x}{\beta_x} \frac{1}{1 - \frac{\gamma^2}{\gamma_{tr}^2}}$$

where we took into account that for smooth optics $D=R/Q_x^2$, $\beta=R/Q_x$, and R is the ring radius. The last equation can be fulfilled only below the transition energy when

$$1 - \frac{\gamma^2}{\gamma_{tr}^2} > 0 .$$

This means that above the transition the beam cannot be at the thermal-equilibrium and its 6D-emittance will grow for any combination of beam emittances. However below the transition there is a state where a thermal equilibrium exists and the beam emittances are conserved.

In a real machine optics, where the Twiss parameters change along the ring and the equilibrium does not exist, the beam still may be in a quasi-equilibrium below transition where a temperature exchange between degrees of freedom is absent and the overall emittance growth is suppressed: closer the beam optics is to the smooth optics smaller the emittance growth rates are.

IBS STUDY FOR NICA COLLIDER

The Nuclotron-based Ion Collider Facility (NICA) [6] is under construction at the JINR. It is aimed to the collider experiments with ions and protons and has to provide the ion-ion (Au^{+79}) collisions in the energy range of 1÷4.5 GeV/nucl as well as the proton-ion and polarized proton-proton and collisions. Two collider rings of 503 m circumference are designed to achieve the required luminosities at two interaction points. Each ring has a racetrack shape with two bending arcs and two long straight sections.

A collider lattice development overcame several iterations which took into account an interdependency of major machine parameters. The IBS is one of the major phenomena limiting the luminosity lifetime. It determines the requirements to the beam cooling systems, and thus has a direct influence on the machine operation scenario. An IBS study was performed [7] in the course of optimization of the NICA collider lattice structure.

In transition from the smooth to strong focusing optics one has to average the local IBS rates over the ring:

$$Rate = \sum_i \frac{rate_i ds}{C_{ring}}$$

where $rate_i$ is the local rate of the emittance (ε_x , ε_y or σ_p^2) growth in a sufficiently short length element i where the Twiss parameters may be considered constant. The quasi-equilibrium point for an optics structure is defined by the equality of these averaged IBS rates $\tau_{IBSx} = \tau_{IBSy} = \tau_{IBSp}$.

Initially, the IBS rates were calculated for pure FODO- and ODFDO- (triplet) lattices for the beam energy of 4.5 GeV/nucl. The following conditions were assumed:

- a storage ring consists of from FODO- or ODFDO- cells only (see Figure 1)
- the ring circumference is fixed

- the bunch length and the number of the particles in the beam is fixed
- for a fixed horizontal emittance ε_y and σ_p are adjusted to obtain equal growth rates in all degrees of freedom.

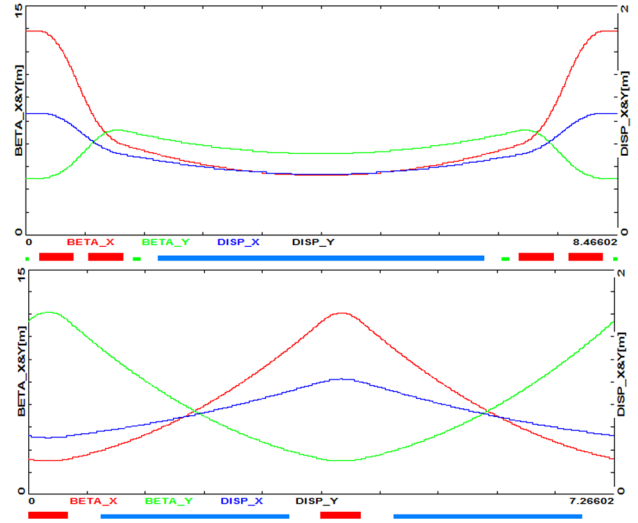


Figure 1: Structures of regular ODFDO- (top) and FODO- (bottom) cells used in the IBS rates calculations.

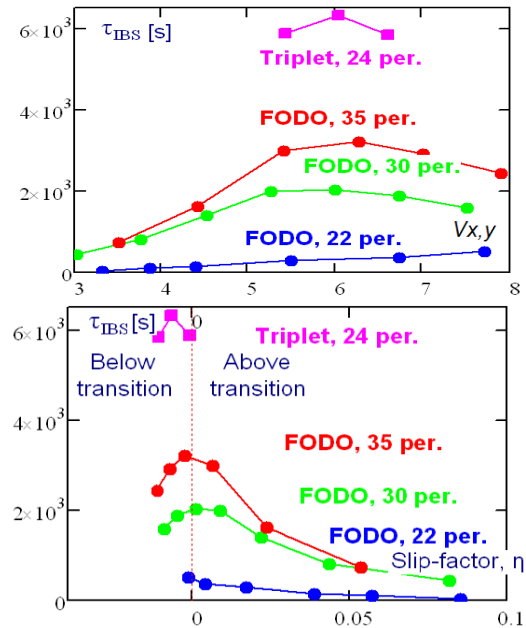


Figure 2: The beam size growth times due to IBS versus ring betatron tune (top), the same data presented as a function of the slip-factor landscape (bottom). The transition ($\eta=0$) is marked by vertical dashed line, where η - is the ring slip-factor.

One can see in Figure 2 that:

- the triplet optics yields about 2 times larger IBS-time than the best of considered FODO optics;
- the minimal beam heating is achieved near transition.

Thus, for “ideal” storage ring without interaction points (IPs) the triplet optics looks preferable from the IBS point of view.

Then, the entire ring optics including IPs (Figure 3) was investigated.

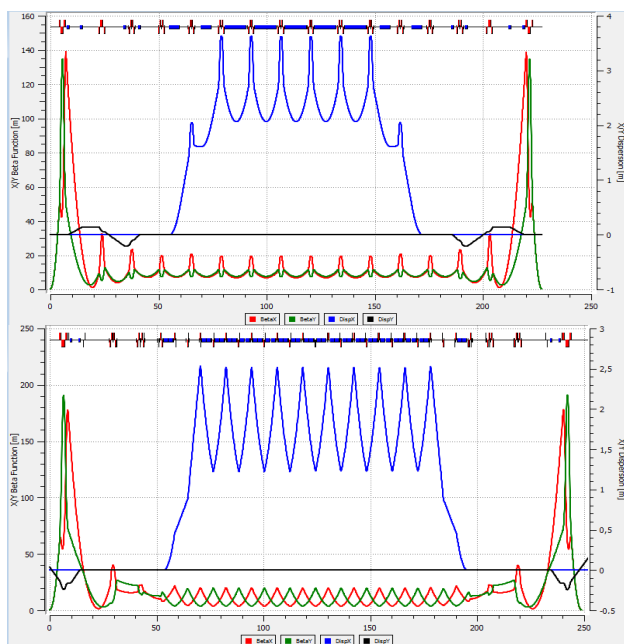


Figure: 3 Collider ring optics (with IPs): ODFDO- (above) and FODO- (below) used for IBS calculations.

A transition from the ideal ring to the collider optics with low- β straight sections increases β -functions in the IP vicinity. That yields an increase of IBS rates.

Finally, the collider ring lattice based on FODO-cells has only ~ 1.5 times larger rates: the growth time of ~ 890 s versus ~ 1350 s for the luminosity of $6 \cdot 10^{27} \text{ cm}^{-2}\text{s}^{-1}$.

The contribution to 6D IBS heating for ODFDO structure (Figure 4) is dominated by straight sections of the ring. The local contribution has the maximum value in the collision point.

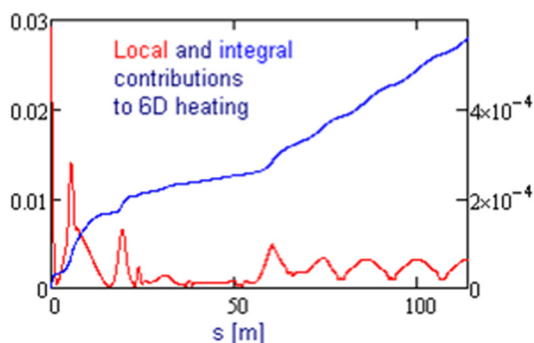


Figure 4: Local (red) and integral (blue) contributions to 6D IBS heating for a quarter of ODFDO structure.

Change of β^* leads to an additional shift out from the quasi-equilibrium point. The IBS times dependence on β -function value at the IPs for triplet and FODO optics are presented in Figure 5.

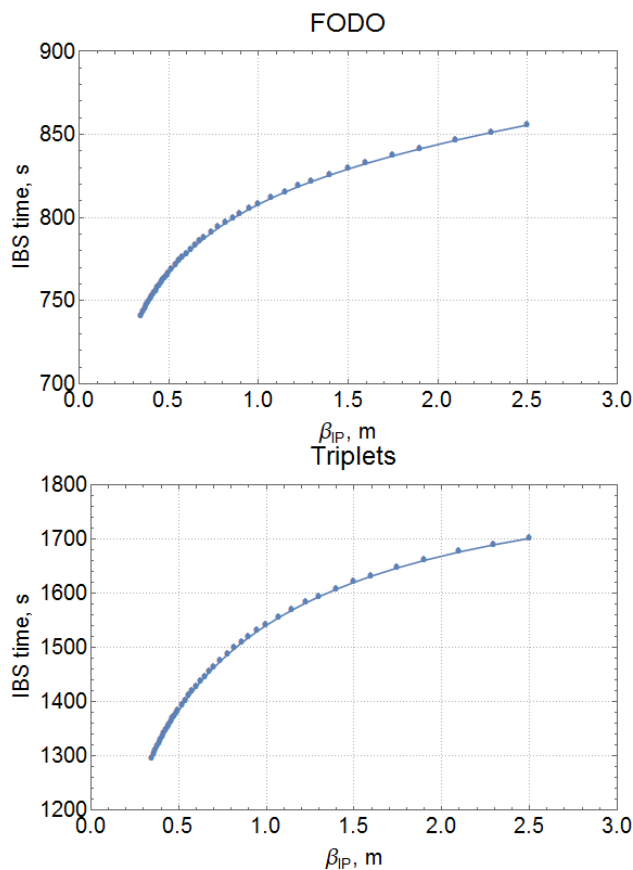


Figure 5: Dependence of IBS times versus β^* for FODO- (upper) and ODFDO- (lower) ring lattice options.

Basing on the results of the IBS studies the FODO structure with 24 cells was chosen as the basis for NICA collider optics. The vertical emittance and the longitudinal momentum spread for $^{197}\text{Au}^{79+}$ beam at quasi-equilibrium are shown in Figure 6 for different energies. The horizontal emittance was chosen to be $1.1 \text{ mm}\cdot\text{mrad}$. The requirements to get at least 6σ aperture determines the ring geometrical acceptance of $40 \text{ mm}\cdot\text{mrad}$.

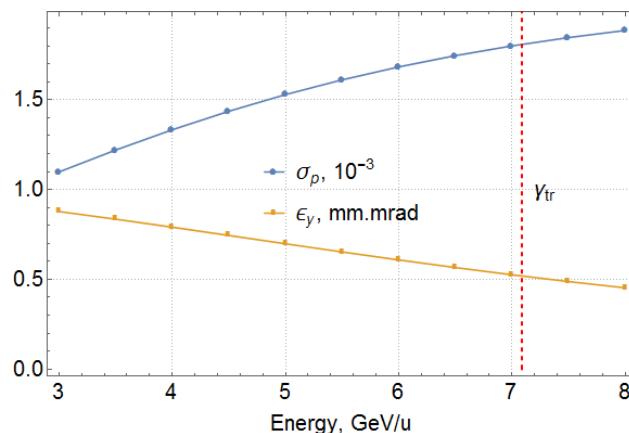


Figure 6: The energy dependence of emittances at equal IBS rates: blue dots for momentum spread, yellow – for vertical emittance.

Content from this work may be used under the terms of the CC BY 3.0 licence (© 2018). Any distribution of this work must maintain attribution to the author(s), title of the work, publisher, and DOI.

The IBS growth rates for the beam intensity of $N = 2 \cdot 10^9$ particles per bunch are shown in Figure 7.

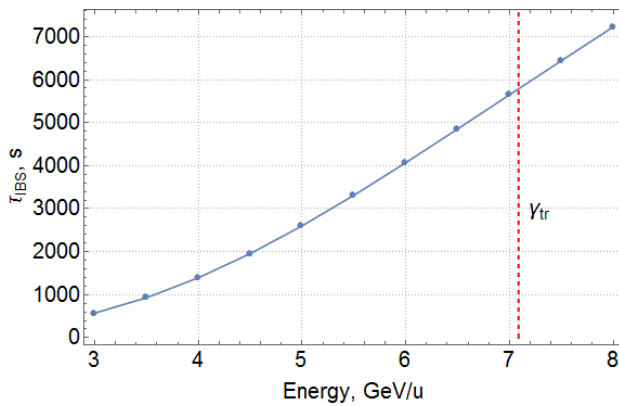


Figure 7: IBS time versus energy for NICA collider lattice at quasi-equilibrium.

CONCLUSIONS

An IBS numerical study was carried out at the development of the NICA collider conceptual proposal. The following conclusions were drawn out:

1. Beam thermal equilibrium for the smooth focusing structures exists only below transition energy.
2. For strong focusing storage rings with regular lattices (no IP insertions) the ODFDO-option gives twice larger IBS times than the FODO- one.
3. IPs' insertions into the lattice structure moves the beam far from the quasi-equilibrium and decreases growth times. That reduces the difference between the triplet and FODO focusing resulting in the difference in the growth rates of only 30%.
4. The FODO-structure was chosen as the base for the NICA collider optics.
5. In the case of real optics the IBS times have no irregular behavior in vicinity of transition energy.

REFERENCES

- [1] A. Piwinski, in *Proc. 9th Int. Conf. on High Energy Accelerators*, Stanford, USA, 1974, p. 405.
- [2] J. D. Bjorken, S. K. Mtingwa, *Part. Accel.*, vol. 13, p. 115, 1983.
- [3] V. Lebedev, V. Shiltsev, *Accelerator Physics at the Tevatron Collider*, Springer, 2014, Chap. 6, p. 191.
- [4] L.D. Landau, *JETP*, vol. 7, p. 203, 1937; *Phys. Zs. Sowjet*, vol. 10, p. 154, 1936.
- [5] S. Nagaitsev, *Phys. Rev. ST Accel. Beams*, vol. 8, p. 064403, 2005.
- [6] G. Trubnikov *et al.*, "Project of the Nuclotron-based Ion Collider fAcility (NICA) at JINR", in *Proc. RuPAC'08*, Zvenigorod, Russia, 2008.
- [7] V. Lebedev, "NICA: Conceptual proposal for collider", MAC, January 2010.

UPGRADED TRANSVERSE FEEDBACK FOR THE CERN PS BOOSTER

A. Blas , G. Kozian, CERN, Geneva, Switzerland

Abstract

A new transverse feedback (TFB) system is being used for the 4 rings of the CERN Proton Synchrotron Booster (PSB). In addition to transverse instabilities mitigation - within the range of 100 kHz to 100 MHz - the system allows for controlled beam emittance blow-up, machine tune measurement and other optic studies. The system was upgraded in order to multiply by 8 its power (800W instead of 100W on each of the 4 kicker electrodes) and in order for its electronic core to employ a digital processing. The transverse feedback adapts automatically to a factor 3 change in the beam revolution period and to any change of the machine tune. It includes an excitation source that combines up to 9 selectable harmonics of the revolution frequency with a selectable amplitude for each. The excitation may be dipolar or quadrupolar. Future possible upgrades will be presented including a setup to tackle half-integer tune values and a digital processing using a fixed clock frequency instead of the revolution frequency clock.

MOTIVATION FOR AN UPGRADE

Table 1: Benefits of the New Hardware

Changes	Benefits
Increased power (1600 W vs 400 W)	Improves S/N in beam transfer function measurement
Extended -3dB bandwidth towards the low frequencies. (10 kHz vs 50 kHz)	Improves the loop phase error at the 1 st betatron line and thus the loop damping time
Digital hardware	<ul style="list-style-type: none"> - Precise loop adjustments along the cycle (phase, gain, delay) - Perfect suppression of the parasitic effect of the beam position offset - Allows for bunch tracking. - Provides an excitation signal tracking automatically the betatron lines. - Provides a quadrupolar excitation on demand - Doesn't required an external adjustable delay using 250 m of cable for each plane. - All the processing on a single VME board instead of 4 different modules - New electronic components available on the market in case of a failure.

The CERN PSB TFB has been successfully used in operation in its original form since 1980 [1]. This initial hardware will remain available, on demand, until 2021 when the PSB will reach its new nominal intensity (1.6 E13 ppp instead of 1E13 as presently). The new hardware installed in 2018 offers some benefits listed above, but comes with a limitation in terms of -3dB upper bandwidth (25 MHz instead of 100 MHz). With the present peak beam intensity a bandwidth of 10 MHz proved to be sufficient, but no reliable prediction can be made with a 60% beam intensity increase and the present coarse impedance model for the PSB ring.

Table 2: Downsides of the New Hardware

Change	Downside
Digital Hardware	Max sampling frequency = 100 MHz which leads to a practical BW of 25 MHz
Digital Betatron phase adjustment	Imposes 2 extra turns delay in the loop-processing path which increases the requirements for a precise estimation of the machine tune (0.01 error on tune corresponds to 10 deg error on the betatron phase).
New PU head amplifier	<ul style="list-style-type: none"> - Does not saturate with the increased beam intensity. - Extended bandwidth in both high and low frequencies. Allows for less phase error on the first betatron line.

DESCRIPTION

Beam Position Monitoring

The beam transverse (H and V) position is sensed using a single "shoe-box" type PU (see Fig. 1) in each of the 4 PSB rings.

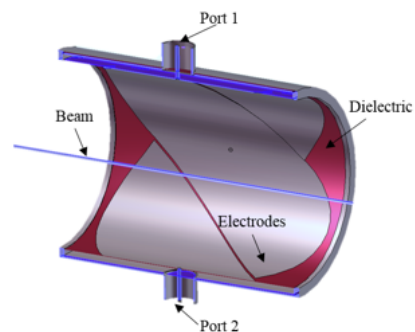




Figure 1: Beam pick-up.

Each PU plate voltage is amplified using a high impedance electronic setup (see Fig. 2) to extend the low frequency cut-off well below the first betatron spectral line. This electronic setup is inspired by what is used with high impedance probes on commercial oscilloscopes.

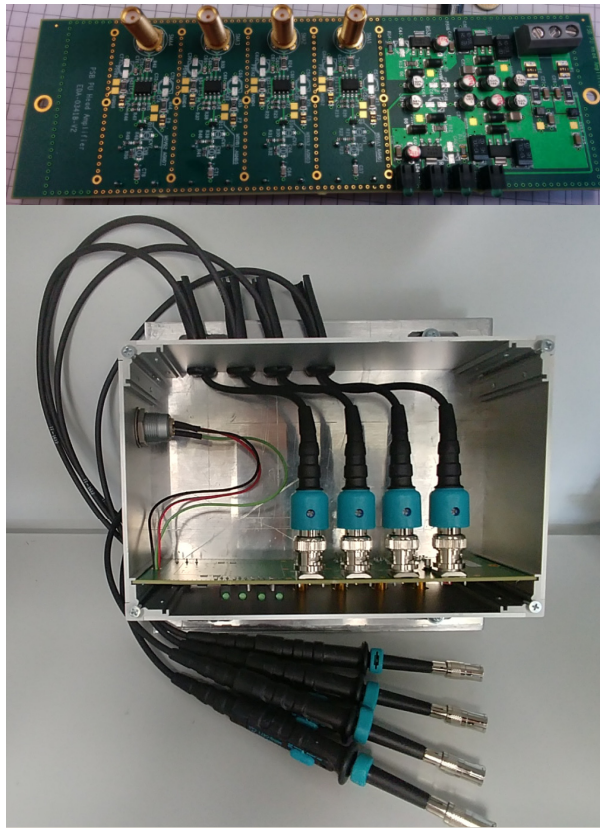


Figure 2: New PU head amplifier.

Beam Offset Suppression

The two amplified signals of a given plane are sent to a so-called Beam-Offset-Suppression System (BOSS) that will first subtract the two voltage values (delta signal) so that a zero is output when the beam travels on the electrical centre of the PU. If a transverse beam position offset is detected, the latter will automatically be cancelled by applying an appropriate gain difference on each of the two PU channels. This analogue BOSS is not strictly required upstream the digital processing, where it could be replaced by a 180 degree combiner, but in case of a beam position offset like during the slow extraction bump, the BOSS should allow for an improved loop gain before saturating the digital input stage and thus improve the system dynamic range.

Digital Processing Unit [2]

The delta signal from the Beam Position Monitor as output by the BOSS is digitized on a Digital Signal Processing Unit (DSPU) using 14 bits converters sampled up to 100 MHz. The transverse feedback loop processing includes four major blocks: gain control, revolution lines mitigation, betatron phase adjustment and automatic delay. Apart from its main features as an instability damper, the DSPU carries also a beam excitation source. The hardware presents itself as VME board (see Fig. 3) with 4 ADCs and 4 DACs connected to a Stratix II FPGA from Altera. One particularity of this board is to have a main sampling clock (at the 64th harmonic of the beam revolution frequency) and its delayed sibling feeding the output DACs. The analogue delay between the two sampling clocks is obtained by a variable delay circuit using selectable sequences of analogue ECL stages.

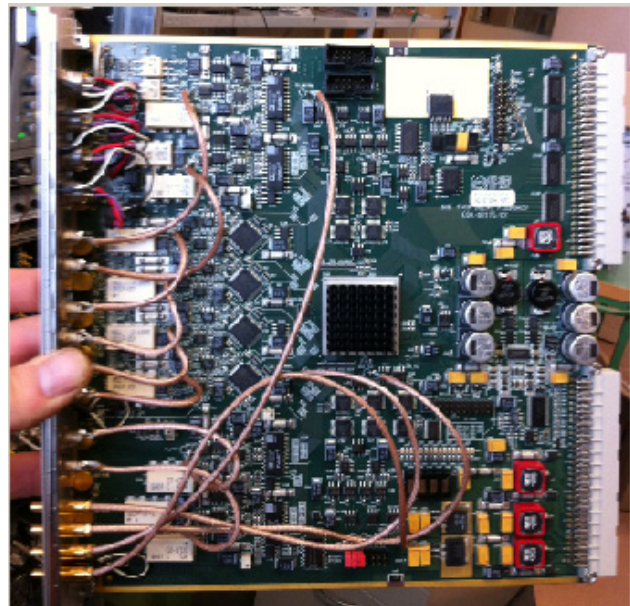


Figure 3: DSPU VME board.

Content from this work may be used under the terms of the CC BY 3.0 licence (© 2018). Any distribution of this work must maintain attribution to the author(s), title of the work, publisher, and DOI.

Revolution Frequency Lines Mitigation

The beam frequency spectrum may show some activity at the harmonics of the revolution frequency. These lines' amplitudes are proportional to the beam position offset that the transverse feedback system is not designed to tackle. These revolution lines are thus parasitic signals that need to be cancelled in order not to saturate uselessly the power stage. When amplified these harmonics of the revolution frequency translate in a local bending dipolar kick with no effect on the beam stability or instability, except when the process leads to a saturation of the system where no superimposed betatron instabilities can manifest themselves anymore.

The analogue BOSS, upstream the digital processing stage, plays the role of suppressing the revolution lines but the actual circuit suffers from some imperfection, and a digital backup was found to be beneficial.

The implementation of the revolution lines' mitigation circuit uses a Notch filter topology (see Fig. 4) subtracting the incoming signal to its sibling delayed by one revolution period (64-samples pipeline-delay clocked at the 64th harmonic of the revolution frequency)

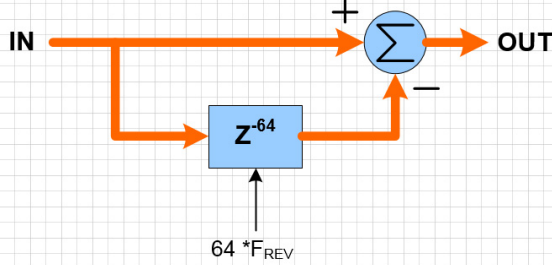


Figure 4: Notch filter.

Betatron Phase Adjustment

The Betatron phase adjustment uses a first order Hilbert filter topology (see Fig. 5). The Hilbert filter frequency response would ideally impose a phase in the form of a square wave, with transitions of the square wave at the multiples of the revolution half-frequency. One side of the revolution line should experience the opposite phase compared to the other side, as expected by signal theory when confronted with a betatron amplitude modulation sampled at the revolution frequency.

The amplitude of the square wave in terms of additional phase within the loop would ideally be set to reach the required value. With a first order implementation, the supposedly square phase-wave looks more like a sinewave for most set values, which means practically that only the peak of the sinewave is at the expected phase-value. This behaviour is nevertheless not harmful as we are dealing with well-defined unique beam betatron lines along the sinewave function. Knowing the betatron tune value and the required phase lag, one needs to select the set-point value of the Hilbert Filter that will provide the appropriate phase lag for the actual betatron line.

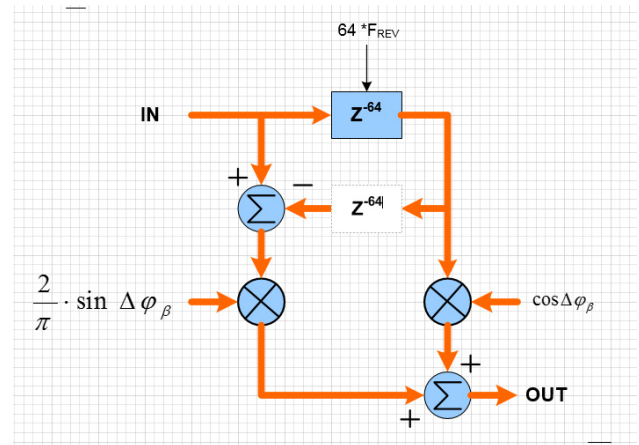


Figure 5: First order Hilbert filter.

Automatic Delay Adjustment

The beam revolution period within the PSB ring evolves from 1666 ns to 546 ns, so by about a factor three. The PU to Kicker distance represents 83% of the circumference and the beam time of flight between these two entities needs to be respected in order to address the appropriate kick to the very particle having been measured. The variable loop delay is obtained by a FIFO (see Fig. 6), using pipelined registers. The number of FIFO registers clocked at $64 \cdot F_{REV}$ represents one part of the delay with a granularity of T_{clk} . A 10 ps resolution “analogue” delay is then added to enhance the available precision.

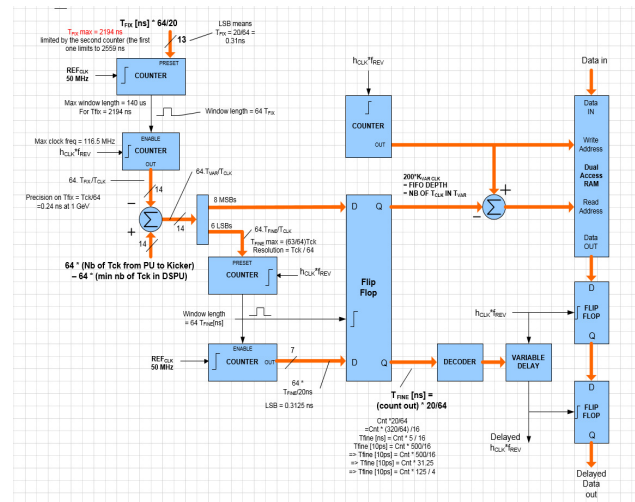


Figure 6: Automatic delay.

The delay is computed first by measuring the revolution time. For this purpose, the $64 \cdot F_{REV}$ ticks are counted within a fixed duration time-window. When the revolution time is known, the real time process need to receive as inputs both the PU-to-kicker distance and the fixed cable delays within the loop. The circuit can then infer the additional delay to add in the feedback loop. The reference window's length for the measurement of the $64 \cdot F_{REV}$ clock sets the precision of the required delay in a context where the revolution frequency would be fixed. During acceleration, a compromise needs to be found, as a too long measurement would induce errors due the varying revolution frequency during the time

of measurement. The fine “analogue delay” for the loop-processed signal is obtained by inserting the analogue delay between the write and read clock of the variable length FIFO streaming the loop data. The challenge here is to avoid indeterminations when sampling data during their transition phase.

Beam Excitation Signal Generation

The excitation signal can be summed to the main loop signal when required. The excitation signal may have three different sources. One external input from the tune measurement system that requires a transverse excitation of the beam to measure the betatron lines’ position, another external input for beam studies and finally an internal source with 9 independent sinewave sources with independent amplitudes, frequencies and relative phases. The 9 sources are designed using Direct Digital Synthesizers (DDS) clocked with an harmonic (64) of the revolution frequency. This allows to set the excitation frequencies as harmonics of the revolution without the hassle of following its progression. Only the progression of the machine tune will need to be accounted for. As an option, up to 3 different programmable windows can be defined within each revolutions in order to excite the beam only partly. Finally, the excitation can be programmed to be either dipolar or quadrupolar. In the latter mode, both kicker plates within the same H or V plans will exhibit the same signal, meaning that the kick force sensed by the particle will be a function of its distance to the centre of the vacuum pipe.

Power Amplifiers [3]

The power stage provides 800 W_{RMS} CW on each 50 Ohms kicker strip-line electrode, instead of 100 W initially. This increase allows for more gain in the loop, thus more headroom for potential high growth rate instabilities. Primarily this increase of power was required to avoid saturation in case of a misbehaviour of the BOSS during the extraction bump (leading to an absence of damping). Then a demand came also from the machine physicists who needed a transverse excitation source, powerful enough during a short time-period, to allow for a beam response with spectral lines popping-out enough from the noise floor. The amplifiers are designed using two stages: one 4 W unit driving a 800 W unit.

Kicker

The kicker in each ring of the PS Booster hosts four 50 Ohms stripline electrodes diametrically opposed in each H and V planes. Each electrode is fed via a 50 Ohm coaxial line that in turn feeds a 50 Ohm cable to a power attenuator.

MEASUREMENTS

The new digital setup with its new amplifiers has been successfully tested in the horizontal plane of the PSB Booster ring 3. This test is not yet backed-up with precise measurements proving the expected benefit on the damping time of beam instabilities but proof has been made that he expected power is sensed by the beam, in excitation mode, as reported by machine physicists during machine

optics measurements [4]. As the present highest intensities (1E13 ppp) were accelerated without losses, it proves that all the signal-processing blocks behave as expected. Without a well-set transverse feedback, losses occur repeatedly with all intensities above 0.35E13 ppp (see Fig. 7). The internal excitation source has not yet been tested with beam, but no surprise is expected as the lab results are totally under specifications.

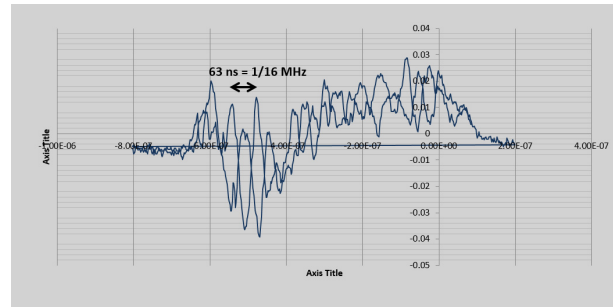


Figure 7: Instabilities cured by the new TFB.

CONCLUSION

A new transverse feedback system has been successfully installed and tested in the CERN PS BOOSTER synchrotron. It offers more power, a sophisticated and previously non-existent transverse beam excitation source, and a new digital processing allowing for an improved damping time, together with more refined control features and tuning capabilities. The new system will also cope with the increased beam intensity expected in 2021 (60% increase). The availability of the transverse feedback with a half integer tune value came lately as a new potential requirement and the latter should be assessed in 2018. A first estimation shows that a second PU and a second kicker would be required for this purpose. The sampling clock of the DSPU is also being scrutinized, as its present varying frequency is not perfectly handled by the FPGA programming applications and its imbedded PLL frequency sources. This inadequacy is even worse when both a clock and its delayed sibling are both used within the same FPGA.

ACKNOWLEDGEMENTS

The authors would like to thank S. Energico and M. Paoluzzi for the design and production of the power amplifiers, M. Haase for the design and production of the 4W drivers, A. Dridi for the water cooling system, A. Meoli for the design of the new PU head-amplifiers, V. Rossi, M. Schokker, and D. Perrelet for the design of the DSPU, L. Arnaudon and D. Landre for the Control equipment of the power units, W. Hofle and R. Louwerse for their general support.

REFERENCES

- [1] The Transverse Feedback System for the CERN PS Booster, C. Christiansen and *et al.*, CERN/PS/BR/81-5, March 1981.
- [2] PS Transverse Damping System for the LHC Beams, CERN, A. Blas *et al.*, 2005, AB/RF Note 2005-027.
- [3] M. Paoluzzi, S. Energico, M. Haase, private communications
- [4] B. Mikulec, private communication

SCALING LAWS FOR THE TIME DEPENDENCE OF LUMINOSITY IN HADRON CIRCULAR ACCELERATORS BASED ON SIMPLE MODELS OF DYNAMIC APERTURE EVOLUTION*

F.F. Van der Veken, M. Giovannozzi, Beams Department, CERN, CH 1211 Geneva 23, Switzerland

Abstract

In recent years, models for the time-evolution of the dynamic aperture have been proposed and applied to the analysis of non-linear betatronic motion in circular accelerators. In this paper, these models are used to derive scaling laws for the luminosity evolution and are applied to the analysis of the data collected during the LHC physics runs. An extended set of fills from the LHC proton physics has been analysed and the results presented and discussed in detail. The long-term goal of these studies is to improve the estimate of the performance reach of the HL-LHC.

INTRODUCTION

Since the advent of the generation of superconducting colliders, the unavoidable non-linear magnetic field errors have plagued the dynamics of charged particles inducing new and potential harmful effects. This required the development of new approaches to perform more powerful analyses and to gain insight in the beam dynamics. It is worth mentioning the work done on the scaling law of the DA as a function of time [1, 2] for the case of single-particle beam dynamics. Indeed, such a scaling law was later successfully extended to the case in which weak-strong beam-beam effects are added to the beam dynamics [3]. More importantly, such a scaling law was proposed to describe the time evolution of beam losses in a circular particle accelerator under the influence of non-linear effects [4], and the proposed model was verified experimentally, using data from CERN accelerators and the Tevatron. Note that such a scaling law for beam intensity as a function of time is at the heart of a novel method to measure experimentally the DA in a circular ring [5].

The model developed represents a bridge between the concept of DA, which is rather abstract, and the beam losses observed in a particle accelerator. Clearly, the next step was to extend the model to describe the luminosity evolution in a circular collider. The first attempts are reported in [6, 7]. However, in those papers the DA scaling law was used without disentangling the contribution of burn off. Although the results were rather encouraging, to recover the correct physical meaning of the model parameters it was necessary to include as many known effects as possible.

This limitation is removed in the model discussed in this paper. In fact, the proposed scaling law is combined with the well-known intensity decay from particle burn off so that a coherent description of the physical process is provided. Moreover, it is worth stressing that the proposed model can be generalised so to consider a time-dependence for some

of the beam parameters describing the luminosity evolution, such as emittance. All detail can be found in Refs. [8, 9]. It is worth mentioning that the scaling law [4] has also been used in the analysis of beam-beam experiments performed at the LHC [10, 11].

LUMINOSITY EVOLUTION WITH PROTON BURN OFF LOSSES

The starting point is the expression of luminosity, which is a key figure-of-merit for colliders and, neglecting the hourglass effect, reads

$$L = \frac{\gamma_r f_{\text{rev}} k_b n_1 n_2}{4\pi\epsilon^* \beta^*} F(\theta_c, \sigma_z, \sigma^*), \quad (1)$$

where γ_r is the relativistic γ -factor, f_{rev} the revolution frequency, k_b the number of colliding bunches, n_i the number of particles per bunch in each colliding beam, ϵ^* is the RMS normalised transverse emittance, and β^* is the value of the beta-function at the collision point. The total beam population is defined as $N_j = k_b n_j$ and the fact that not all bunches are colliding in the high-luminosity experimental points is taken into account by introducing a scale factor.

The factor F accounts for the reduction in volume overlap between the colliding bunches due to the presence of a crossing angle and is a function of the half crossing angle θ_c and the transverse and longitudinal RMS dimensions σ^* , σ_z , respectively according to:

$$F(\theta_c, \sigma_z, \sigma^*) = \frac{1}{\sqrt{1 + \left(\frac{\theta_c}{2} \frac{\sigma_z}{\sigma^*}\right)^2}}. \quad (2)$$

Note that $\sigma^* = \sqrt{\beta^* \epsilon^* / (\beta_r \gamma_r)}$, where β_r is the relativistic β -factor. Equation (1) is valid in the case of round beams and round optics. For our scope, Eq. (1) will be recast in the following form:

$$L = \Xi N_1 N_2, \quad \Xi = \frac{\gamma_r f_{\text{rev}}}{4\pi\epsilon^* \beta^* k_b} F(\theta_c, \sigma_z, \sigma^*) \quad (3)$$

in which the dependence on the total intensity of the colliding beams is highlighted and the other quantities are included in the term Ξ .

Under normal conditions, i.e. excluding any levelling gymnastics or dynamic-beta effects, only the emittances and the bunch intensities can change over time. Therefore, Eq. (1) is more correctly interpreted as peak luminosity at the beginning of the fill, as in general L is a function of time. When the burn off is the only relevant mechanism for

* Research supported by the HL-LHC project

a time-variation of the beam parameters, it is possible to estimate the time evolution of the luminosity, which turns out to be derived from the following equation

$$N'(t) = -\sigma_{\text{int}} n_c L(t) = -\sigma_{\text{int}} n_c \Xi N^2(t) \quad (4)$$

where σ_{int} represents the cross section for the interaction of charged particles and the two colliding beams have been assumed to be of equal intensity. The value used is 73.5 mb for 3.5 TeV and 76 mb for 4 TeV [12, 13] for protons, representing the total inelastic cross-section. Here, n_c stands for the number of collision points.

In the most general case, where both beams can have different intensities, the intensity evolution is described by the following equations

$$\begin{cases} N_1'(t) = -\sigma_{\text{int}} n_c \Xi N_1(t) N_2(t) \\ N_2'(t) = -\sigma_{\text{int}} n_c \Xi N_1(t) N_2(t). \end{cases} \quad (5)$$

It is useful to change to a different time variable, namely

$$\tau - 1 = f_{\text{rev}} t \quad \text{giving} \quad \frac{d}{dt} = f_{\text{rev}} \frac{d}{d\tau}, \quad (6)$$

τ being an adimensional variable representing the number of turns, where a shift of the origin of τ with respect to t has been introduced.

The solution of Eq. (5), indicated as $N_{1,2}^{\text{bo}}(\tau)$ to highlight that it only includes the burn off contribution, can be obtained by re-writing:

$$\begin{cases} \dot{N}_1^{\text{bo}}(\tau) + \dot{N}_2^{\text{bo}}(\tau) = -2\varepsilon N_1^{\text{bo}}(\tau) N_2^{\text{bo}}(\tau) \\ \dot{N}_1^{\text{bo}}(\tau) - \dot{N}_2^{\text{bo}}(\tau) = 0 \end{cases} \quad (7)$$

with

$$\varepsilon = \frac{\sigma_{\text{int}} n_c \Xi}{f_{\text{rev}}} \quad (8)$$

and from which one finds

$$\begin{cases} N_1^{\text{bo}}(\tau) = N_2^{\text{bo}}(\tau) + \xi \\ \dot{N}_2^{\text{bo}}(\tau) = -\varepsilon N_2^{\text{bo}}(\tau) [N_2^{\text{bo}}(\tau) + \xi]. \end{cases} \quad (9)$$

Equation (9) has two solutions depending on the value of ξ . If $\xi = 0$ then

$$\begin{cases} N_1^{\text{bo}}(\tau) = \frac{N_i}{1 + \varepsilon N_i (\tau - 1)} \\ N_2^{\text{bo}}(\tau) = N_1^{\text{bo}}(\tau), \end{cases} \quad (10)$$

where $N_i = N_{i,1} = N_{i,2}$ stands for the initial beam intensity. Otherwise, if $\xi \neq 0$ then

$$\begin{cases} N_1^{\text{bo}}(\tau) = \xi \frac{1}{1 - N_r e^{-\varepsilon \xi (\tau-1)}} \\ N_2^{\text{bo}}(\tau) = \xi \frac{N_r e^{-\varepsilon \xi (\tau-1)}}{1 - N_r e^{-\varepsilon \xi (\tau-1)}}, \end{cases} \quad (11)$$

where $\xi = N_{i,1} - N_{i,2}$ and $N_r = \frac{N_{i,2}}{N_{i,1}}$.

Whenever additional time dependence in the luminosity evolution needs to be taken into account, the solutions (10) and (11) can be extended to take into account these effects (see Refs. [8]).

LUMINOSITY EVOLUTION INCLUDING PSEUDO-DIFFUSIVE EFFECTS

An efficient modelling of the luminosity evolution in a real collider can be obtained either by means of numerical tracking, see e.g. Ref. [14], or by means of analytical or semi-analytical models, see e.g. Refs. [15–17]. However, none of the models studied included the effect of non-linear motion and this is at the heart of the approach proposed in Ref. [7]. The basis for such a model is the evolution of the dynamic aperture (DA) with time in a hadron collider. The analysis of single-particle tracking results showed that the time evolution of the DA follows a simple law [1, 2], whose justification is not only phenomenological. Recently, this approach has been successfully applied to the analysis of intensity evolution in hadron machines [4]. So far, however, the results were obtained in the case of single-particle simulations or whenever the conditions in a particle accelerator were not under the influence of any collective effect. To extend the proposed scaling law to luminosity evolution, it is necessary to show that it is valid also in the presence of beam-beam effects. This is the case at least for the results of numerical simulations in the weak-strong regime, as discussed in Ref. [3], thus opening the possibility to justify the proposed interpretation.

The proposed approach is a refinement of what is presented in Ref. [7] and assumes that all possible pseudo-diffusive effects can be modelled by a scaling of the intensity with time as

$$N(\tau) = N_i \left[1 - \int_{D(\tau)}^{+\infty} dr \hat{\rho}(r) \right] = N_i \left[1 - e^{-\frac{D^2(\tau)}{2}} \right], \quad (12)$$

where

$$D(\tau) = D_\infty + \frac{b}{[\log \tau]^\kappa}. \quad (13)$$

The parameters D_∞, b, κ are normally fitted to the experimental data and the variable τ represents the turn number and satisfies $\tau \in [1, +\infty[$. It is worthwhile stressing some properties of the parameters as highlighted in Refs. [2, 4], where two regimes were identified depending on the signs of the fit parameters.

The further step in view of using this scaling law for the analysis of the evolution of the luminosity requires a number of additional considerations, namely

- The proton burn off occurs mainly in the core of the beam distribution, corresponding to the region of largest particle density. On the other hand, the diffusive processes are mainly affecting the tails of the beam distribution. This, in turn, implies that proton burn off and diffusive phenomena are acting on different parts of the beam distributions and are, hence, essentially decoupled and independent.
- The characteristic times of the two processes are rather different. The burn off takes place at a sub-turn time

scale (for instance, in the case of the LHC, considering only the high-luminosity experiments, the burn off occurs twice per turn), while the pseudo-diffusive phenomena take place on a much longer time scale, as a continuous process.

- The fit parameters in Eq. (13) might depend on the beam intensity. However, if one assumes that the overall intensity variation over one physics fill is not too large, it is then reasonable to consider that the pseudo-diffusive effects are, to a good extent, almost constant.

Then, under these assumptions, it is justified to describe the intensity evolution as

$$\begin{cases} \dot{N}_1(\tau) = -\varepsilon N_1(\tau) N_2(\tau) - \mathcal{D}_1(\tau) \\ \dot{N}_2(\tau) = -\varepsilon N_1(\tau) N_2(\tau) - \mathcal{D}_2(\tau), \end{cases} \quad (14)$$

where the terms \mathcal{D}_i represent the intensity-independent pseudo-diffusive effects. Typical values of ε are 1.1×10^{-24} assuming the beam parameters during the 2011 physics run for protons. Therefore, about 3.1×10^4 particles are removed from the bunches each turn, corresponding to 0.24 ppb.

The explicit expression for $\mathcal{D}_i(\tau)$ can be found by noting that these functions are the solutions of

$$\begin{cases} \dot{N}_1(\tau) = -\mathcal{D}_1(\tau) \\ \dot{N}_2(\tau) = -\mathcal{D}_2(\tau) \end{cases} \quad (15)$$

and that the explicit solution has been assumed to be of the form (12) [3, 4, 7]. Therefore, one obtains

$$\mathcal{D}_j(\tau) = -N_{i,j} D_j(\tau) \dot{D}_j(\tau) e^{-\frac{D_j^2(\tau)}{2}} \quad j = 1, 2. \quad (16)$$

Under the assumptions that the initial beam intensities are the same as well as the terms \mathcal{D}_j , then an explicit expression at the lowest order in ε (see Eq. (8)) can be given for both intensity and luminosity, namely

$$\frac{N(\tau)}{N_i} = \frac{1}{1 + \varepsilon N_i(\tau - 1)} - \left[e^{-\frac{D^2(\tau)}{2}} - e^{-\frac{D^2(1)}{2}} \right] \quad (17)$$

and

$$\begin{aligned} \frac{L(\tau)}{L_i} &= \frac{1}{[1 + \varepsilon N_i(\tau - 1)]^2} - \left[e^{-\frac{D^2(\tau)}{2}} - e^{-\frac{D^2(1)}{2}} \right] \times \\ &\times \left\{ 2 - \left[e^{-\frac{D^2(\tau)}{2}} - e^{-\frac{D^2(1)}{2}} \right] \right\} \end{aligned} \quad (18)$$

where $L_i = \Xi N_{\text{rm}}^2$ is the initial value of the luminosity.

INTEGRATED LUMINOSITY OVER A PHYSICS FILL

The models analysed in the previous sections can be used to derive some useful scaling laws for the integrated luminosity as a function of the length of the physics fill. Indeed,

assuming the simple case of equal intensities for both beams, it is possible to obtain for the burn off part

$$L_{\text{int}}^{\text{bo}}(\tau) = \int_1^\tau d\bar{\tau} L^{\text{bo}}(\bar{\tau}) = \frac{N_i \Xi}{\varepsilon} \frac{\varepsilon N_i(\tau - 1)}{1 + \varepsilon N_i(\tau - 1)}. \quad (19)$$

Note that because

$$L_{\text{int}}^{\text{bo}}(\tau \rightarrow \infty) = \frac{N_i \Xi}{\varepsilon}, \quad (20)$$

one can normalise the integrated luminosity as

$$L_{\text{norm}}^{\text{bo}}(\tau) = \frac{L_{\text{int}}^{\text{bo}}(\tau)}{L_{\text{int}}^{\text{bo}}(\tau \rightarrow \infty)} = \frac{\varepsilon N_i(\tau - 1)}{1 + \varepsilon N_i(\tau - 1)}. \quad (21)$$

Furthermore, by using the normalised turn variable $\bar{\tau} = \varepsilon N_i(\tau - 1)$, $L_{\text{norm}}^{\text{bo}}$ can be recast in the following form

$$L_{\text{norm}}^{\text{bo}}(\bar{\tau}) = \frac{\bar{\tau}}{1 + \bar{\tau}}. \quad (22)$$

Hence, $L_{\text{norm}}^{\text{bo}}(\bar{\tau})$ has a very simple scaling law in terms of $\bar{\tau}$. This allows comparing experimental data from physics runs with different beam parameters, such as β^* , crossing angle, bunch intensity, and number of bunches (see [9]).

To include pseudo-diffusive effects it is enough to apply the computations made before to the general solution of the intensity-evolution equation, based on the sum of components $N_{1,2}^{\text{bo}}(\tau)$ and $N_{1,2}^{\text{pd}}(\tau)$, hence giving

$$L_{\text{norm}}(\tau) = L_{\text{norm}}^{\text{bo}}(\tau) + L^{\text{pd}}(\tau) \quad (23)$$

where $L_{\text{norm}}^{\text{bo}}$ stands for the burn off component of the luminosity evolution derived above, and L^{pd} is the integral of the pseudo-diffusive contribution in Eq. (18):

$$\begin{aligned} L^{\text{pd}}(\tau) &= -N_i \varepsilon \int_1^\tau d\bar{\tau} \left[e^{-\frac{D^2(\bar{\tau})}{2}} - e^{-\frac{D^2(1)}{2}} \right] \times \\ &\times \left\{ 2 - \left[e^{-\frac{D^2(\bar{\tau})}{2}} - e^{-\frac{D^2(1)}{2}} \right] \right\}. \end{aligned} \quad (24)$$

ANALYSIS OF LHC RUN 1 DATA

The models derived will be applied to the analysis of the LHC performance data collected during Run 1. Detailed information on this topic can be found in Refs. [18–21], while in Ref. [22] a preliminary analysis was made, without focusing on models to describe the luminosity and its time evolution. Here, the focus will be on the proton physics run and the data analysed can be found at [23]. Among the full data set available from [23] a selection has been considered including only the fills that resulted in successful physics runs, the so-called stable beams, of a total duration exceeding 10^3 s and featuring $N_{i,1,2} > 10^{13}$ p. Such a filtering allows removing data corresponding to beam commissioning stages or low-luminosity fills, which would not be representative of the typical LHC performance. Additionally we only select those fills that have a number of bunches $k_b > 1300$.

Equations (1) and (2) show that while σ_z has an impact on F , only, the transverse normalised emittances $\epsilon_{x,y}^*$ affect both F and the peak luminosity. The measured data revealed that the variation of σ_z over a typical physics fill does not exceed $\approx 7\%$. Therefore, the time-dependence of σ_z can be safely neglected in the analyses presented in the following sections.

The time-dependence of ε needs to be assessed to decide the approach to be applied to the data analyses. The data have been fitted using an exponential function and the result is given by

$$\Delta \varepsilon(t) = 34.69 e^{-0.1358t} - 35.39 \quad (25)$$

where t is expressed in hours and $\Delta \varepsilon$ in percent. For the majority of fills $\Delta \varepsilon$ does not exceed $\approx 30\%$ and it has been decided to perform the numerical analyses assuming a time-independent ε .

A close inspection of the Run 1 data [22] reveals that for a typical physics fill the quantity $2|N_{i,1} - N_{i,2}|/(N_{i,1} + N_{i,2})$ does not exceed $\approx 10\%$. Hence, in the analysis reported in the following sections, the two initial beam intensities have always been assumed equal. Given that a similar estimate holds also for the intensities at the end of the physics fills, the pseudo-diffusive effects have been assumed to be the same for both beams.

LUMINOSITY EVOLUTION OVER A FILL

The first step in the analysis of the LHC Run 1 data is the fit of the pseudo-diffusive component of the luminosity evolution based on the expression given in Eq. (18).

For this, 24 fills, 10 from 2011 and 14 from 2012, have been selected and fitted individually, also separating the results for the two high-luminosity experiments, ATLAS and CMS. The results are listed in Table 1. Also shown is R_{adj}^2 , the so-called adjusted coefficient of determination, given by

$$R_{\text{adj}}^2 = 1 - \frac{N-1}{N-\nu-1} \frac{\Sigma^2}{\sigma^2}, \quad (26)$$

where N is the sample size, ν the number of fit parameters, Σ^2 the sum of residues squared. Note that R_{adj}^2 compares the fit under consideration to the most naive fit possible, i.e. a constant line through the mean. When $R_{\text{adj}}^2 \ll 1$ (or possibly even negative), the fit is of poor quality as the mean of the data provides a better fit than the proposed model. A good fit has $R_{\text{adj}}^2 \rightarrow 1$, indicating that the residues are small compared to the data variance.

If we look at the results in Fig. 1, we notice that all fits are of particular good quality, as all except one have $R_{\text{adj}}^2 > 90\%$, while for all fits from 2011 this is even $R_{\text{adj}}^2 > 99\%$. There is a clear distinction between the results for 2011 and those for 2012, both in spread, but also in behaviour, as the yearly average value of D_∞ is negative for 2011 whereas it is positive for 2012. Furthermore, it is worth noting that from the lower plots of Fig. 1 no systematic difference between the fitted models based on the ATLAS or CMS data is found.

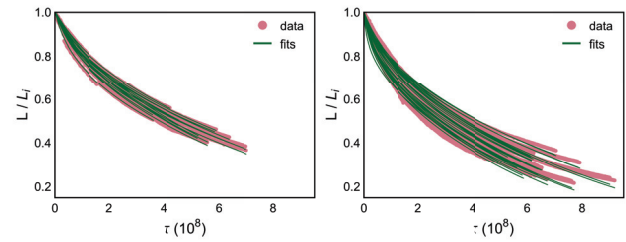


Figure 1: The plots show the measured and fitted curves for L (normalised to the initial fill luminosity L_i) for 2011 (left) and 2012 (right) fills and a very good agreement is clearly visible.

It is useful to fit the data to a slightly adapted model, which has a reduced set of parameters. To this end, we selected three different configurations: one where we fix $\kappa = 2$ (according to the Nekhoroshev estimate [24]) and fit b and D_∞ ; one where we fix $D_\infty = 0$ (as it is approximately the average of Run 1) and fit b and κ ; and one where we fix both $\kappa = 2$ and $D_\infty = 0$ and fit only b , thus leaving only one model parameter.

The resulting weighted average parameter values are listed in Table 1. The difference between the fills from 2011 and from 2012 persists in all fit versions, for this reason we did not calculate the total average parameter values over the two years of Run 1. When one parameter is fixed ($\kappa = 2$ or $D_\infty = 0$) the fit quality is almost unaffected, but when two parameters are fixed (both $\kappa = 2$ and $D_\infty = 0$ at the same time), there is a clear worsening of the fit (even though the overall quality remains rather good). This indicates that fixing one parameter delivers a fit that is as good as using the full parameter set, given the existence of an approximate degeneracy of the parameter space. The case $\kappa = 2$ is preferred over $D_\infty = 0$, because of its justification on the basis of the Nekhoroshev theorem.

ANALYSIS OF INTEGRATED LUMINOSITY

The second step consists of establishing the model for the integrated luminosity delivered in a single fill for physics.

As a first investigation, the pseudo-diffusion model has been fitted to the complete Run 1 dataset. This is shown on the left side of Fig. 2, and the values of the fit parameters including the associated errors are reported in Table 1.

The pseudo-diffusive effect on a yearly basis is shown in the right plot of Fig. 2, and a difference between the two years is seen, which does not exceed 20%. Careful inspection reveals that the same difference exists in the data, thus confirming that the model reproduces closely the features of the dataset. The parameter values for the yearly fits are also given in Table 1. Note that now $D_\infty < 0$ for 2011, exactly like in the non-integrated case.

A comparison of the fit parameters for the unintegrated and integrated cases reported in Table 1 shows that the values are compatible, within the errors, for the case of three-

Table 1: Summary of the fit parameters and associated errors corresponding to the expression of $L^{pd}(\tau)$, for different model parameters and for different data subsets, and both for the unintegrated and integrated luminosity. The error on the fit parameters is estimated using the BCa interval [25], and in the unintegrated case the presented values are the weighted averages over the fills.

	D_∞	b	κ	\bar{R}^2_{adj} [%]
unintegrated: 2011	-0.61 ± 0.71	180 ± 210	1.64 ± 0.40	99.759
$\kappa = 2$	-0.44 ± 0.19	920 ± 73	–	99.736
$D_\infty = 0$	–	1900 ± 940	2.41 ± 0.19	99.726
$\kappa = 2, D_\infty = 0$	–	752 ± 18	–	97.469
2012	0.36 ± 0.41	1200 ± 680	2.19 ± 0.24	96.531
$\kappa = 2$	0.20 ± 0.26	670 ± 110	–	96.232
$D_\infty = 0$	–	200 ± 200	1.84 ± 0.26	96.037
$\kappa = 2, D_\infty = 0$	–	748 ± 23	–	93.492
integrated: Run 1 (2011+2012)	0.44 ± 0.54	460 ± 110	1.92 ± 0.31	96.433
$\kappa = 2$	$0.497^{+0.095}_{-0.054}$	556^{+20}_{-37}	–	96.440
$D_\infty = 0$	–	177^{+30}_{-43}	$1.517^{+0.052}_{-0.094}$	96.434
$\kappa = 2, D_\infty = 0$	–	740.0 ± 1.1	–	96.208
2011	$-0.43^{+0.38}_{-0.14}$	350^{+150}_{-80}	$1.68^{+0.16}_{-0.13}$	97.835
$\kappa = 2$	$-0.03^{+0.10}_{-0.13}$	757^{+49}_{-35}	–	97.847
$D_\infty = 0$	–	830^{+370}_{-200}	$2.04^{+0.13}_{-0.09}$	97.848
$\kappa = 2, D_\infty = 0$	–	$744.0^{+1.6}_{-1.8}$	–	97.857
2012	0.82 ± 0.52	560 ± 114	2.08 ± 0.35	95.746
$\kappa = 2$	$0.77^{+0.13}_{-0.06}$	455^{+21}_{-49}	–	95.754
$D_\infty = 0$	–	81^{+15}_{-26}	$1.25^{+0.06}_{-0.13}$	95.737
$\kappa = 2, D_\infty = 0$	–	738.2 ± 1.4	–	95.166

parameter fit, while the compatibility degrades as the number of fit parameters is reduced, the case with fixed κ being more compatible between the non-integrated and integrated luminosity models, than that with D_∞ . This confirms once more that fixing κ is the best option among those with reduced fit parameters.

CONCLUSIONS

The luminosity models proposed have been benchmarked against the data from the LHC Run 1, with special emphasis on the years 2011 and 2012, showing a remarkable power in reproducing and describing the observed behaviours of luminosity as a function of time and of integrated luminosity.

Given the encouraging results of the analyses reported in this paper, the data from Run 2 will be considered next, as the higher beam energy that characterises the proton physics in Run 2 opens a new domain in terms of beam behaviour, such as strong longitudinal emittance damping due to synchrotron radiation as well as a burn-off dominated regime.

Ultimately, we aim at applying these model to the HL-LHC in order to provide more accurate estimates of its performance reach.

ACKNOWLEDGEMENTS

One of the authors (MG) would like to thank A. Bazzani for interesting discussions and G. Arduini, V. Lebedev, S. Na-

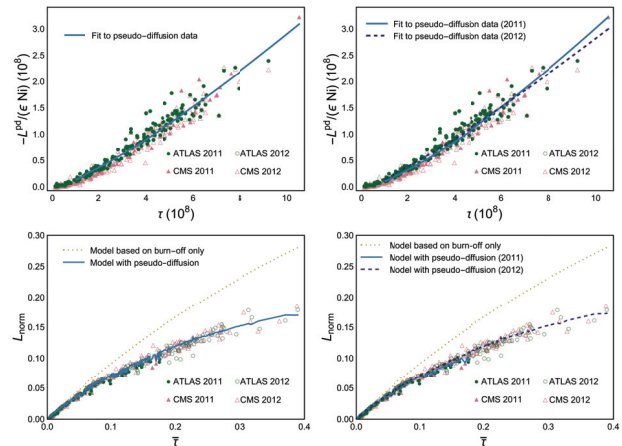


Figure 2: Pseudo-diffusive contribution to the integrated luminosity (upper row) and normalised luminosity (lower row) as a function of turn number resp. normalised time. The model has been fitted using the complete set of 2011 and 2012 data (left), and separately year by year (right).

gaitsev, V. Shiltsev, L. Vorobief, T. Zolkin for interesting and stimulating remarks. We would like to thank R. De Maria and G. Iadarola for help with data extraction.

REFERENCES

- [1] M. Giovannozzi, W. Scandale, E. Todesco, “Prediction of long-term stability in large hadron colliders”, *Part. Accel.*, vol. 56, p. 195, 1996.
- [2] M. Giovannozzi, W. Scandale, E. Todesco, “Dynamic aperture extrapolation in presence of tune modulation”, *Phys. Rev. E*, vol. 57, p. 3432, 1998.
- [3] M. Giovannozzi, E. Laface, “Investigations of Scaling Laws of Dynamic Aperture with Time for Numerical Simulations including Weak-Strong Beam-Beam Effects”, in *Proc. IPAC’12*, New Orleans, LA, USA, May 2012, paper TUPPC086, p. 1359.
- [4] M. Giovannozzi, “Proposed scaling law for intensity evolution in hadron storage rings based on dynamic aperture variation with time”, *Phys. Rev. ST Accel. Beams*, vol. 15, p. 024001, 2012.
- [5] E. Maclean, M. Giovannozzi and R. Appleby, “Novel method to measure the extent of the stable phase space region of proton synchrotrons using Nekoroshev-like scaling law”, in preparation.
- [6] M. Giovannozzi, “Simple models describing the time-evolution of luminosity in hadron colliders”, in *Proc. IPAC’14*, Dresden, Germany, Jun. 2014, paper TUPRO009, p. 1017.
- [7] M. Giovannozzi, C. Yu, “Proposal of an Inverse Logarithm Scaling Law for the Luminosity Evolution”, in *Proc. IPAC’12*, New Orleans, LA, USA, May 2012, paper TUPPC078, p. 1353.
- [8] M. Giovannozzi, F.F. Van der Veken, “Description of the luminosity evolution for the CERN LHC including dynamic aperture effects. Part I: the model”, submitted for publication. arXiv:1806.03058 [physics.acc-ph]
- [9] M. Giovannozzi, F.F. Van der Veken, “Description of the luminosity evolution for the CERN LHC including dynamic aperture effects. Part II: application to Run 1 data”, submitted for publication. arXiv:1806.03059 [physics.acc-ph]
- [10] M. Crouch, “Luminosity performance limitations due to the beam-beam interaction in the LHC”, Thesis, University of Manchester, U.K.
- [11] M. Crouch, T. Pieloni, R.B. Appleby, J. Barranco-García, X. Buffat, M. Giovannozzi, E.H. Maclean, B.D. Muratori, C. Tambasco, “Dynamic aperture studies of long-range beam-beam interactions at the LHC”, in *Proc. IPAC’17*, Copenhagen, Denmark, May 2017, paper THPAB056, p. 3840.
- [12] The ATLAS and CMS Collaborations, “Expected pile-up values at HL-LHC”, ATL-UPGRADE-PUB-2013-014, 2013.
- [13] D. Contardo, private communication, 3 December 2014.
- [14] R. Bruce, J. M. Jowett, M. Blaskiewicz, W. Fischer, “Time evolution of the luminosity of colliding heavy-ion beams in BNL Relativistic Heavy Ion Collider and CERN Large Hadron Collider”, *Phys. Rev. ST Accel. Beams*, vol. 13, p. 091001, 2010.
- [15] E. McCrory, V. Shiltsev, A. J. Slaughter, A. Xiao, “Fitting the luminosity decay in the Tevatron”, in *Proc. PAC’05*, Knoxville, TN, USA, May 2005, paper TPAP036, p. 2434.
- [16] V. Shiltsev, E. McCrory, “Characterizing luminosity evolution in the Tevatron”, in *Proc. PAC’05*, Knoxville, TN, USA, May 2005, paper TPAP038, p. 2536.
- [17] M. Benedikt, D. Schulte, F. Zimmermann, “Optimizing integrated luminosity of future hadron colliders”, *Phys. Rev. ST Accel. Beams*, vol. 18, p. 101002, 2015.
- [18] M. Lamont, “The LHC from Commissioning to Operation”, in *Proc. IPAC’11*, San Sebastian, Spain, Sep. 2011, paper MOYAA01, p. 11.
- [19] S. Myers, “The First Two Years of LHC Operation”, in *Proc. IPAC’12*, New Orleans, LA, USA, May 2012, paper MOXBP01, p. 1.
- [20] J. Wenninger, R. Alemany-Fernandez, G. Arduini, R.W. Assmann, B.J. Holzer, E.B. Holzer, V. Kain, M. Lamont, A. Macpherson, G. Papotti, M. Pojer, L. Ponce, S. Redaelli, M. Solfaroli Camillocci, J.A. Uythoven, W. Venturini Delsolaro, “Operation of the LHC at High Luminosity and High Stored Energy”, in *Proc. IPAC’12*, New Orleans, LA, USA, May 2012, paper THPPP018, p. 3767.
- [21] M. Lamont, “The First Years of LHC Operation for Luminosity Production”, in *Proc. IPAC’13*, Shanghai, China, May 2013, paper MOYAB101, p. 6.
- [22] M. Giovannozzi, “Some considerations on the p-p performance of the LHC during Run I”, CERN-ACC-NOTE-2013-0039.
- [23] <https://lhc-statistics.web.cern.ch/LHC-Statistics/index.php>
- [24] N. Nekhoroshev, “An exponential estimate of the time of stability of nearly-integrable Hamiltonian systems”, *Russ. Math. Surv.*, vol. 32, p. 1, 1977.
- [25] J. Fox, “Applied Regression Analysis and Generalized Linear Models”, SAGE Publications. Mar., 2015.

BEAM LOADING AND LONGITUDINAL STABILITY EVALUATION FOR THE FCC-ee RINGS

I. Karpov*, P. Baudrenghien, CERN, Geneva, Switzerland

Abstract

In high-current accelerators, interaction of the beam with the fundamental impedance of the accelerating cavities can limit machine performance. It can result in a significant variation of bunch-by-bunch parameters (bunch length, synchronous phase, etc.) and lead to longitudinal coupled-bunch instability. In this work, these limitations are analysed together with possible cures for the high-current option (Z machine) of the future circular electron-positron collider (FCC-ee). The time-domain calculations of steady-state beam loading are presented and compared with frequency-domain analysis.

INTRODUCTION

The future circular electron-positron collider (FCC-ee) is considered to be built in four energy stages, defined by physics program [1]. To keep the same power loss budget for the synchrotron radiation in each machine, the beam current will be gradually reduced for each energy stage from 1.4 A to 5.4 mA. The Z machine, with parameters summarized in Table 1, can suffer from beam loading issues, which can result in modulation of the cavity voltage and beam parameters. The coupled-bunch instability due to fundamental cavity impedance can also be a limiting factor.

In general, there are two methods to calculate the beam induced transients: in frequency domain and time domain. The former, developed by Pedersen [2], is usually called a small-signal model. It allows to calculate the modulation of cavity voltage produced by modulation of the beam current. The latter method is the tracking of the beam and a simulation of the RF system evolution in time domain [3,4] which comes to the steady-state regime after many synchrotron periods. Considering a machine with large circumference, high beam current, and large number of bunches, as for the case of the Z machine, applicability of both existing approaches is questionable.

In this work, we present results of beam loading analysis in superconducting rf cavities modeled by a lumped circuit with a generator linked to the cavity via a circulator [5]. It allows us to get steady-state solution for beam and cavity parameters (beam phase, cavity voltage amplitude and phase) for arbitrary beam currents and filling schemes. The longitudinal coupled-bunch instability is estimated using the standard equations from Ref. [6]. Mitigations of both issues using the direct rf feedback around the cavity are also discussed.

Table 1: The parameters of the Z machine of FCC-ee used for calculations in this work [7]. The bunch length is given for the case of non-colliding beams defined by equilibrium of quantum excitation and synchrotron radiation (SR).

Parameter	Unit	Value
Circumference, C	km	97.75
Harmonic number, h		130680
rf frequency, f_{rf}	MHz	400.79
(R/Q)	Ω	42.3
Beam energy, E	GeV	45.6
DC beam current, $I_{\text{b,DC}}$	A	1.39
Number of bunches per beam, M		16640
Bunch population, N_{p}	10^{11}	1.7
rms bunch length, σ	ps	12
Momentum compaction factor, α_p	10^{-6}	14.79
Synchrotron tune, Q_s		0.025
Longitudinal damping time, τ_{SR}	ms	415.1
Total rf voltage, V_{tot}	MV	100
Number of cavities N_{cav}		52

BEAM LOADING BASICS

We consider short electron bunches for which the average of the rf component of the beam current $\langle I_{\text{b,rf}} \rangle$ is twice the DC beam current $I_{\text{b,DC}}$. For the steady-state beam loading, the generator current I_{g} can be derived from the lumped circuit model [5, 8] shown in Fig. 1:

$$I_{\text{g}} e^{i\phi_{\text{L}}} = \left[\frac{V_{\text{cav}}}{2(R/Q)} \left(\frac{1}{Q_{\text{L}}} + \frac{1}{Q_0} \right) + I_{\text{b,DC}} \cos \phi_s \right] \quad (1)$$

$$- i \left[I_{\text{b,DC}} \sin \phi_s + \frac{V_{\text{cav}} \Delta \omega}{\omega_{\text{rf}} (R/Q)} \right], \quad (2)$$

where ϕ_{L} is the loading angle, V_{cav} is the cavity voltage, (R/Q) is the ratio of the shunt impedance to the quality factor of the cavity fundamental mode, $Q_{\text{L}} = Z_{\text{c}}/(R/Q)$ is the loaded quality factor expressed using the coupler impedance Z_{c} , Q_0 is the cavity quality factor, $\omega_{\text{rf}} = 2\pi f_{\text{rf}}$ is the rf angular frequency, $\Delta \omega = \omega_0 - \omega_{\text{rf}}$ is the cavity detuning, ω_0 is the cavity resonant frequency, ϕ_s is the bunch stable phase (electron machine convention). Considering superconducting cavity with $Q_0 \gg Q_{\text{L}}$, the loading angle ϕ_{L} can be expressed from Eq. (2) as

$$\tan \phi_{\text{L}} = - \frac{\tan \phi_s + Y \sin \phi_s}{1 + Y \cos \phi_s}, \quad (3)$$

* ivan.karpov@cern.ch

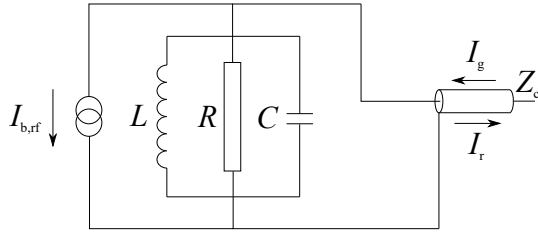


Figure 1: The lumped circuit model: a cavity is modeled by LCR-block, the coupler by a connected transmission line of impedance Z_c , and the beam by a current source. $I_{b,rf}$ is the beam current, I_g is the generator current, I_r is the reflected current, which is absorbed in the matched load (a generator is connected via a circulator).

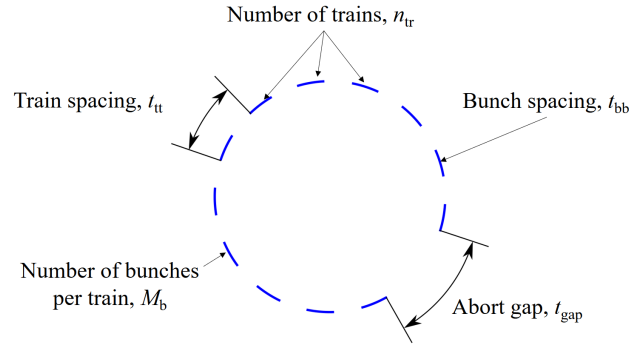


Figure 2: Sketch of the filling schemes used for the present study.

where $Y = 2I_{b,DC}(R/Q)Q_L/V_{cav}$ is the relative beam loading, and the detuning angle is defined as

$$\tan \phi_z = \frac{2Q_L \Delta\omega}{\omega_{rf}}. \quad (4)$$

To minimize the generator power, one can define the optimum values for the cavity detuning

$$\Delta\omega_{opt} = -\omega_{rf} \frac{I_{b,DC}(R/Q) \sin \phi_s}{V_{cav}}, \quad (5)$$

and for the coupler quality factor

$$Q_{L,opt} \approx \frac{V_{cav}}{2(R/Q)I_{b,DC} \cos \phi_s}. \quad (6)$$

For the optimum parameters however, the beam is unstable because the second Robinson limit [9] is reached, which reads as

$$Y < -\frac{2 \sin \phi_s}{\sin(2\phi_z)}, \quad (7)$$

when no loops around the cavity are present.

TRANSIENT BEAM LOADING

In operation of the Z machine different filling schemes can be used. To perform systematic analysis of the transient beam loading, we introduce the filling schemes following [10], which are schematically shown in Fig. 2. We consider a beam containing M bunches, which can be grouped in n_{tr} equal trains with a distance between first bunches of the consecutive trains t_{tt} . This distance should be a multiple of bunch spacings t_{bb} . Each train contains a number of filled buckets $M_b \leq t_{tt}/t_{bb}$. The beam has a regular filling, which can also contain an abort gap of length t_{gap} . Thus, the DC beam current depends on the filling scheme

$$I_{b,DC} = \frac{n_{tr} M_b N_p e}{T_{rev}} = \frac{\langle I_{b,rf} \rangle}{2}, \quad (8)$$

with $T_{rev} = 2\pi/\omega_{rev}$ - the revolution period, ω_{rev} - the angular revolution frequency, and N_p - the number of particles per bunch.

Steady-state Time-domain Approach

To calculate modulation of beam and cavity parameters due to modulation of the rf component of the beam current, the following equation can be used [8]

$$I_g e^{i\phi_L} = \frac{V(t)}{2(R/Q)} \left(\frac{1}{Q_L} - 2i \frac{\Delta\omega}{\omega_{rf}} \right) + \frac{dV(t)}{dt} \frac{1}{\omega_{rf}(R/Q)} + \frac{I_{b,rf}(t) e^{-i(\phi_s + \phi_b(t))}}{2}. \quad (9)$$

Here, the generator current is assumed be to constant, ϕ_b is the beam phase modulation, and the cavity voltage V is modulated in the form

$$V(t) = A(t) e^{i\phi(t)}, \quad (10)$$

where A is the amplitude of the cavity voltage, and ϕ is the phase of the cavity voltage with respect to rf phase $\omega_{rf}t$. Combining these equations and separating the real and imaginary parts, we get the following system of equations

$$\frac{dA(t)}{dt} = -\frac{A(t)}{\tau} + (R/Q)\omega_{rf} \times \left\{ I_g \cos[\phi_L - \phi(t)] - \frac{I_{b,rf} \cos[\phi_s + \phi_b(t) + \phi(t)]}{2} \right\}, \quad (11)$$

$$\frac{d\phi(t)}{dt} = \Delta\omega + \frac{(R/Q)\omega_{rf}}{A} \times \left\{ I_g \sin[\phi_L - \phi(t)] + \frac{I_{b,rf}(t) \sin[\phi_s + \phi_b(t) + \phi(t)]}{2} \right\}, \quad (12)$$

where $\tau = 2Q_L/\omega_{rf}$ is the cavity filling time. The stable phase in this case is not constant due to amplitude modulation of the cavity voltage, which should be taken into account by using the relation

$$N_{cav} A(t) \cos[\phi_s + \phi_b(t) + \phi(t)] = eU_0, \quad (13)$$

where eU_0 is the energy loss per turn due to synchrotron radiation, and N_{cav} is the number of cavities. Modulation of A , ϕ , and ϕ_b results in bunch-by-bunch variation of the bunch length, the synchrotron tune, and can lead to a collision point shift in the detectors. Unfortunately Eqs. (11-13) can not be solved analytically, but below the results of numerical calculations will be presented.

Frequency Domain Calculations

The main equations from the small-signal model [11] are summarized below. The normalized modulations of the beam current a_b and the cavity voltage amplitude a_V are

$$I_{b,rf} = 2I_{b,DC} [1 + a_b(t)], \quad A(t) = V_{cav} [1 + a_V(t)], \quad (14)$$

correspondingly. Assuming small modulation ($|a_V| \ll 1$, $|\phi| \ll 1$, $|a_b| \ll 1$, and $|\phi_b| \ll 1$), the transfer functions from the beam amplitude to the cavity voltage amplitude, cavity voltage phase, and the beam phase are

$$\frac{\tilde{a}_V}{\tilde{a}_b} = -\frac{\Delta\omega_{opt}}{D(s)} \left[\frac{\Delta\omega_{opt}}{\sin^2\phi_s} - \Delta\omega + \left(s + \frac{1}{\tau}\right) \cot\phi_s \right], \quad (15)$$

$$\frac{\tilde{\phi}}{\tilde{a}_b} = -\frac{\Delta\omega_{opt}}{D(s)} \left[\left(\frac{\Delta\omega_{opt}}{\sin^2\phi_s} - \Delta\omega \right) \cot\phi_s + \left(s + \frac{1}{\tau}\right) \right], \quad (16)$$

$$\frac{\tilde{\phi}_b}{\tilde{a}_b} = \frac{\Delta\omega_{opt}}{D(s) \sin^2\phi_s} \left(s + \frac{1}{\tau}\right), \quad (17)$$

$$\text{where } D(s) = \left(s + \frac{1}{\tau}\right)^2 - \Delta\omega \left[\frac{\Delta\omega_{opt}}{\sin^2\phi_s} - \Delta\omega \right], \quad (18)$$

and \tilde{a} is the Laplace image of the variable a . For the optimum detuning ($\Delta\omega = \Delta\omega_{opt}$), there is no solution because these equations have a pole at $s = 0$, which corresponds to the second Robinson limit. For a slightly larger detuning, $\Delta\omega = \Delta\omega_{opt}/\sin^2\phi_s$, simple first order responses can be obtained from Eqs. (15-17)

$$\frac{\tilde{a}_V}{\tilde{a}_b} = \frac{-1}{1 + \tau s}, \quad \frac{\tilde{\phi}}{\tilde{a}_b} = -\frac{\Delta\omega_{opt}\tau}{1 + \tau s}, \quad \frac{\tilde{\phi}_b}{\tilde{a}_b} = \frac{\Delta\omega_{opt}\tau}{(1 + \tau s) \sin^2\phi_s}. \quad (19)$$

This detuning is used in calculations below with expense of slightly larger generator power.

Results and Comparisons

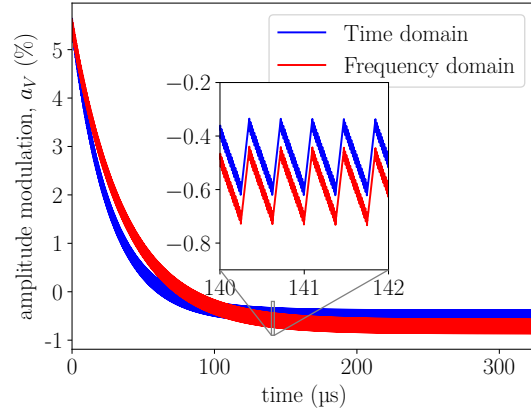
To solve Eqs. (11–13), the Euler method was used with total calculation time of 5 revolution periods, which was sufficient to get the steady-state solution since $\tau < T_{rev}$. An example of a reasonable agreement of time-domain and frequency-domain (Eq. (19)) calculations is shown in Fig 3. There is a strong modulation due to the abort gap and a fine structure due to the gaps between trains.

To study systematically modulation of the beam and the cavity parameters, the scan for different train spacings was performed for a fixed bunch spacing $t_{bb} = 15$ ns (Fig. 4). For each train spacing the peak-to-peak value of the beam phase modulation (the top plot) and the phase modulation of the cavity voltage (the bottom plot) are calculated. The results obtained in frequency domain are slightly larger than in time domain. We argue that the difference is due to a strong beam current modulation, while for the frequency-domain calculations it is assumed that $a_b \ll 1$.

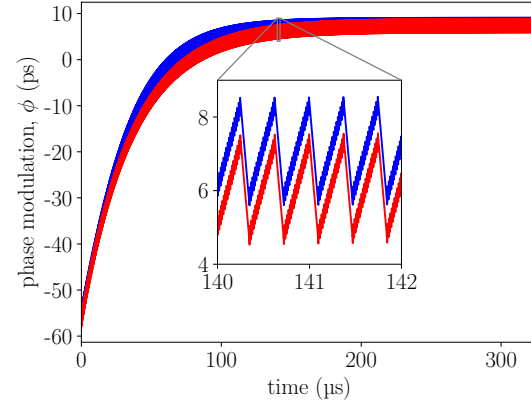
We propose to use the following equations to estimate the peak-to-peak beam phase modulation

$$\max\phi_b - \min\phi_b = \left| \frac{\Delta\omega_{opt}t_{gap}}{\sin^2\phi_s} \right|, \quad (20)$$

$$t_{tt,rf} = 150, t_{bb} = 15.0 \text{ ns}, M_b = 19, n_{tr} = 865, t_{gap} = 2.4 \mu\text{s}$$



$$t_{tt,rf} = 150, t_{bb} = 15.0 \text{ ns}, M_b = 19, n_{tr} = 865, t_{gap} = 2.4 \mu\text{s}$$



$$t_{tt,rf} = 150, t_{bb} = 15.0 \text{ ns}, M_b = 19, n_{tr} = 865, t_{gap} = 2.4 \mu\text{s}$$

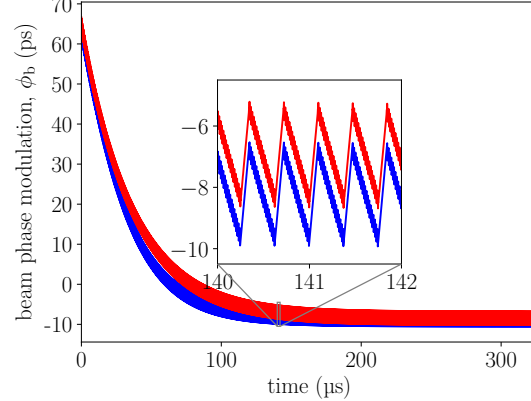


Figure 3: Comparison of the time-domain (Eqs. (11–13)) and the frequency-domain approaches (Eqs. (19)) for the Z machine for the detuning $\Delta\omega = \Delta\omega_{opt}/\sin^2\phi_s = 13.1$ kHz. The amplitude modulation of the cavity voltage (the top plot), the phase modulation of the cavity voltage (the center plot), and the beam phase modulation (the bottom plot) within one turn are shown.

and peak-to-peak phase modulation of the cavity voltage

$$\max\phi - \min\phi = |\Delta\omega_{opt}t_{gap}|. \quad (21)$$

They agree very well with the results of the time-domain calculations (see the dashed black lines and the blue solid lines in Fig. 4, correspondingly). The dependence of the

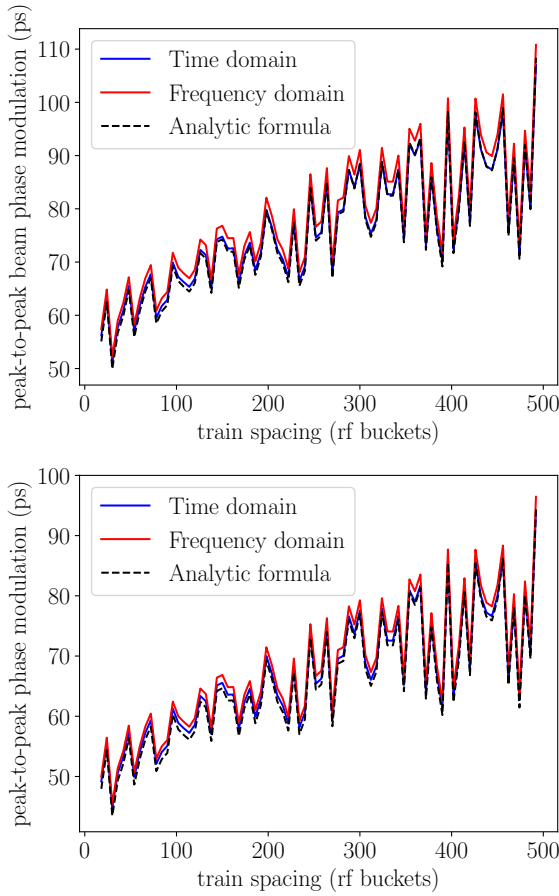


Figure 4: Dependence of the peak-to-peak values for the beam phase modulation (the top plot) and the phase modulation of the cavity voltage (the bottom plot) on the train spacing for the bunch spacing of 15 ns. The results from the analytic formulas are given by Eq. (20) (the top plot) and by Eq. (21) (the bottom plot).

product of the cavity detuning and the abort gap length on the train spacing for different bunch spacings is shown in Fig. 5. In general, larger bunch spacing leads to a smaller value of $|\Delta\omega_{\text{opt}}t_{\text{gap}}|$. For $t_{\text{tr}}f_{\text{rf}} > 100$, this product is larger than 0.15 for all bunch spacings, which corresponds to 60 ps peak-to-peak phase modulation of the cavity voltage and about 70 ps peak-to-peak beam phase modulation. However, in operation the shift of collision point can be eliminated by matching abort gap transients.

LONGITUDINAL COUPLED-BUNCH INSTABILITY

The equation used for calculation of the growth rate of longitudinal coupled-bunch instability can be found in textbooks (for example in [6]). For short Gaussian bunches and a mode m it is

$$\frac{1}{\tau_{\text{inst},m}} = \frac{\eta\omega_{\text{rf}}I_b\text{DC}N_{\text{cav}}}{4\pi EQ_s} \{ \text{Re} [Z(\omega_{\text{rf}} + (m + Q_s)\omega_{\text{rev}})] - \text{Re} [Z(\omega_{\text{rf}} - (m + Q_s)\omega_{\text{rev}})] \}, \quad (22)$$

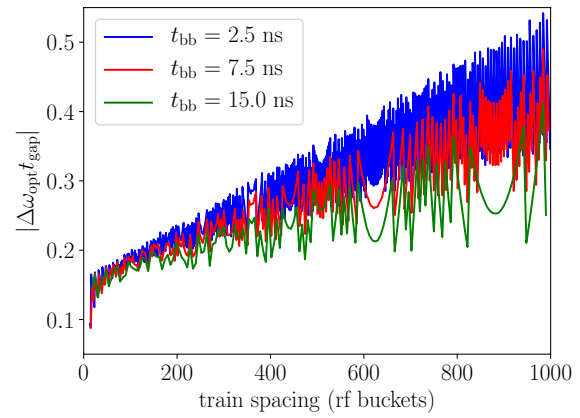


Figure 5: Dependence of the peak-to-peak phase modulation of the cavity voltage from Eq. (21) on the train spacings for different bunch spacings.

where $Z(\omega)$ is the longitudinal cavity impedance. Without detuning ($\Delta\omega = 0$), the growth rates of the modes are negligible in comparison to the synchrotron radiation damping rate $1/\tau_{\text{SR}}$. For the detuning $\Delta\omega = \Delta\omega_{\text{opt}}/\sin^2\phi_s$, the largest growth rate is for the mode $m = -4$ with a rise time of about 10 revolution periods (see Fig. 6).

To avoid longitudinal coupled-bunch instability one can use the direct rf feedback around the cavity [12]. It reduces the impedance seen by the beam in the region relevant for the beam stability. The impedance of the closed loop in this case is

$$Z_{\text{cl}}(\omega) = \frac{Z(\omega)}{1 + GZ(\omega)e^{-i\tau_d\omega + i\phi_{\text{adj}}}}, \quad (23)$$

where G is the feedback gain, τ_d is the overall loop delay, and ϕ_{adj} is the phase adjustment. The flat response is achieved for $1/G = (R/Q)\omega_{\text{rf}}\tau_d$.

For $\tau_d = 700$ ns (the loop delay in the LHC [13]), the direct rf feedback significantly suppresses the growth rates of longitudinal coupled-bunch modes so they are below the synchrotron radiation damping rate (see Fig. 7). Additional

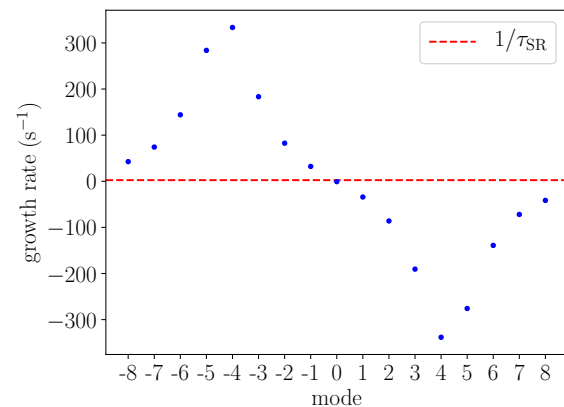


Figure 6: Growth rates of longitudinal coupled-bunch modes from Eq. (22) for the cavity detuning $\Delta\omega = \Delta\omega_{\text{opt}}/\sin^2\phi_s = 13.1$ kHz.

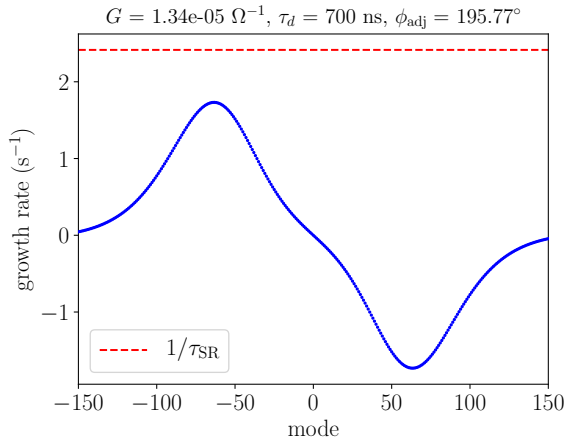


Figure 7: Growth rates of longitudinal coupled-bunch modes in the presence of the direct rf feedback calculated using Eqs. (22, 23) for the cavity detuning $\Delta\omega = \Delta\omega_{\text{opt}}/\sin^2\phi_s = 13.1$ kHz.

reduction of the impedance around multiples of the revolution harmonic using one-turn delay feedback could be evaluated in further studies.

PARTIAL COMPENSATION OF TRANSIENT BEAM LOADING

If the beam induced modulations are not acceptable, one can try to reduce the transients by the direct rf feedback. In this case the system of equations for the phase and the amplitude evolution of the cavity voltage can be obtained from Eq. (9) by substitution

$$I_g e^{i\phi_L} \rightarrow I_g e^{i\phi_L} - G \left[A(t) e^{i\phi(t)} - A_{\text{ref}}(t) e^{i\phi_{\text{ref}}(t)} \right], \quad (24)$$

where the amplitude $A_{\text{ref}}(t)$ and phase $\phi_{\text{ref}}(t)$ of the reference signal are obtained from the amplitude $A_0(t)$ and the phase $\phi_0(t)$ modulations calculated with the constant generator current and no rf feedback

$$A_{\text{ref}}(t) e^{i\phi_{\text{ref}}(t)} = V_{\text{cav}} + (1 - k) \left[A_0(t) e^{i\phi_0(t)} - V_{\text{cav}} \right]. \quad (25)$$

Here, k is the compensation factor. The comparison of beam phase modulation with the direct rf feedback for $k = 0$ and $k = 0.3$ is shown in Fig. 8. For $k = 0.3$, one can see about 20% reduction of the beam phase modulation with about 5% increase of the instantaneous generator power $P = (R/Q)Q_L |I_g|^2 / 2$ (see Fig. 9). Further optimizations with different filling schemes and direct rf feedback parameters are needed to minimize transient beam loading.

CONCLUSIONS

In the present work the beam loading in FCC-ee high-current machine was analyzed. For the assumed regular filling schemes, the main contribution to the phase and amplitude modulation of the cavity voltage comes from the abort gap. The resulted peak-to-peak value of the bunch-by-bunch

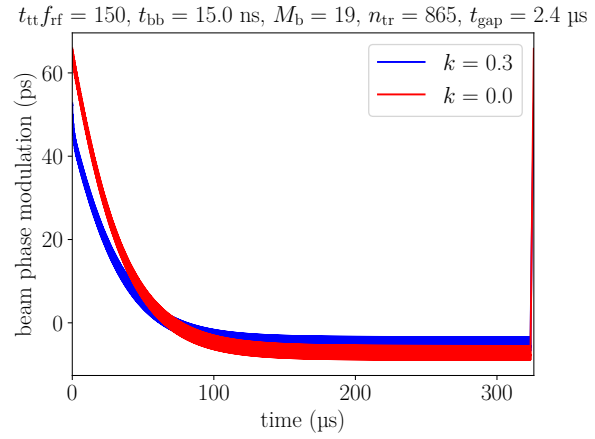


Figure 8: Comparison of beam phase modulation with the direct rf feedback for different compensation factors k .

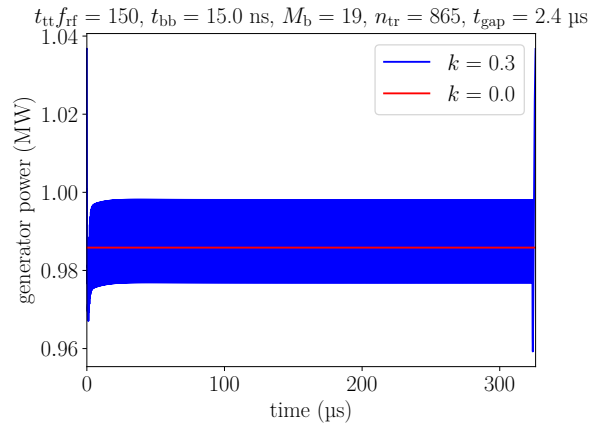


Figure 9: Instantaneous generator power with the direct rf feedback for calculations shown in Fig. 8.

phase modulation is larger than 70 ps for the abort gap longer than 2 μs . The larger train spacings lead to stronger modulation of cavity and beam parameters, which can be reduced by using filling schemes with the larger bunch spacings.

The growth rates of the first several longitudinal coupled-bunch modes are larger than the synchrotron radiation damping rate for the optimum detuning, that is about four times the revolution frequency. The direct rf feedback with the overall loop delay $\tau_d = 700$ ns can stabilize the beam.

The direct feedback can also mitigate the transient beam loading with the cost of an additional generator power. For the discussed example, about 5% increase of the generator power is sufficient to reduce the bunch-by-bunch phase modulation by 20%.

ACKNOWLEDGEMENTS

We thank Elena Shaposhnikova, Rama Calaga, Andrew Butterworth, Olivier Brunner, and Dmitry Teytelman for useful discussions and comments.

REFERENCES

- [1] F. Zimmermann, M. Benedikt, D. Schulte, and J. Wenninger, “Challenges for highest energy circular colliders”, in *Proc. IPAC’14*, Dresden, Germany, Jun. 2014, paper MOXAA01, pp. 1-6.
- [2] F. Pedersen, “Beam loading effects in the CERN PS booster”, *IEEE Trans. Nucl. Sci.*, vol. 22, no. 3, pp. 1906–1909, Jun. 1975, doi:10.1109/TNS.1975.4328024
- [3] J. M. Byrd, S. De Santis, J. Jacob, and V. Serriere, “Transient beam loading effects in harmonic rf systems for light sources” *Phys. Rev. ST Accel. Beams*, vol. 5, no. 9, pp. 1–11, Sep. 2002, doi:10.1103/PhysRevSTAB.5.092001
- [4] C. Rivetta, T. Mastorides, J. D. Fox, D. Teytelman, and D. Van Winkle, “Modeling and simulation of longitudinal dynamics for Low Energy Ring–High Energy Ring at the Positron-Electron Project”, *Phys. Rev. ST Accel. Beams*, vol. 10, p. 022801, Feb. 2007, doi:10.1103/PhysRevSTAB.10.02280
- [5] D. Boussard, “RF power estimates for a hadron collider”, CERN, Geneva, Switzerland, Rep. CERN-SPS-ARF-DB-GW-NOTE-84-9, Feb. 1984.
- [6] K. Y. Ng, Longitudinal coupled-bunch instabilities, in *Physics of intensity dependent beam instabilities*, World Scientific Publishing Co. Re. Ltd., 2006, pp. 311–314.
- [7] K. Oide *et al.*, “FCC-ee optics update”, presented at FCC Week 2018, Amsterdam, the Netherlands, Apr. 2018, unpublished.
- [8] J. Tückmantel, “Cavity-beam-transmitter interaction formula collection with derivation”, CERN, Geneva, Switzerland, Rep. CERN-ATS-Note-2011-002 TECH, Jan. 2011.
- [9] K. W. Robinson, “Stability of beam in radiofrequency system”, Harvard University, Cambridge, USA, Rep. CEAL-1010, Feb. 1964.
- [10] I. Karpov, R. Calaga, and E. Shaposhnikova, “HOM power in FCC-ee cavities”, CERN, Geneva, Switzerland, Rep. CERN-ACC-2018-0005, Jan. 2018.
- [11] F. Pedersen, “RF cavity feedback”, CERN, Geneva, Switzerland, Rep. CERN-PS-92-59-RF, Dec. 1992.
- [12] D. Boussard, “Control of cavities with high beam loading,” *IEEE Trans. Nucl. Sci.*, vol. 32, no. 5, pp. 1852–1856, May 1985, doi:10.1109/TNS.1985.4333745
- [13] P. Baudreghien and T. Mastoridis, “Fundamental cavity impedance and longitudinal coupled-bunch instabilities at the High Luminosity Large Hadron Collider”, *Phys. Rev. Accel. Beams*, vol. 20, no. 1, pp. 1–13, Jan. 2017, doi:10.1103/PhysRevAccelBeams.20.101003

OVERVIEW OF THE CERN PSB-TO-PS TRANSFER LINE OPTICS MATCHING STUDIES IN VIEW OF THE LHC INJECTORS UPGRADE PROJECT

V. Forte*, S. Albright, W. Bartmann, G. P. Di Giovanni, M. A. Fraser, C. Hessler, A. Huschauer, A. Oeftiger, CERN, Geneva, Switzerland

Abstract

At injection into the CERN Proton Synchrotron (PS) a significant horizontal emittance blow-up of the present high brightness beams for the LHC is observed. A partial contribution to this effect is suspected to be an important mismatch between the dispersion function in the transfer line from the PS Booster (PSB) and the ring itself. This mismatch will be unacceptable in view of the beam parameters requested by the LHC Injectors Upgrade (LIU) project with high longitudinal emittance and momentum spread. To deliver the requested beam parameters the PSB-to-PS transfer line will be upgraded and the optics in the line changed to improve the matching from all the four PSB rings. A re-matching campaign from the PSB ring 3 has been carried out to evaluate the impact of the present optics mismatch as a source of emittance growth both in simulations and measurements.

INTRODUCTION

The LIU project [1] at CERN aims at renovating the LHC injector chain in order to produce beams with twice the brightness. The achieved and future LIU beam parameters are reported in Table 1 [2]. The new high brightness LIU beams for the LHC foresee a higher longitudinal emittance ϵ_z and a larger contribution in momentum spread $\delta p/p_{rms}$ in order to keep the Laslett maximum transverse space charge tune shift ($\Delta Q_x, \Delta Q_y$) limited. The single bunch intensities N are doubled and the normalised horizontal (x) and vertical (y) transverse emittances ϵ will be similar to the values of today.

Table 1: LIU LHC Beam Parameters at PS Injection: Achieved and LIU Target [2]

Beam type	Energy [GeV]	N [$\times 10^{10}$ p]	ϵ_z [eVs]	$\epsilon_{x,y,0}$ [μm]	$\delta p/p_{rms}$ [$\times 10^{-3}$]	Tune spread [$\Delta Q_x, \Delta Q_y$]
Achieved						
LHC Standard	1.4	16.84	1.2	2.25	0.9	(0.25, 0.30)
LHC BCMS		8.05	0.9	1.2	0.8	(0.24, 0.31)
LIU						
LHC Standard	2	32.50	3	1.8	1.5	(0.18, 0.30)
LHC BCMS		16.25	1.48	1.43	1.1	(0.20, 0.31)

* vincenzo.forte@cern.ch

PRESENT PERFORMANCE OF LHC BEAMS AT PS INJECTION

An unexpected horizontal emittance growth in the order of $\sim 40\%$ is measured at PS injection during present operation. Figure 1 shows the statistics during LHC fills with BCMS bunches in 2018. The vertical emittance is preserved.

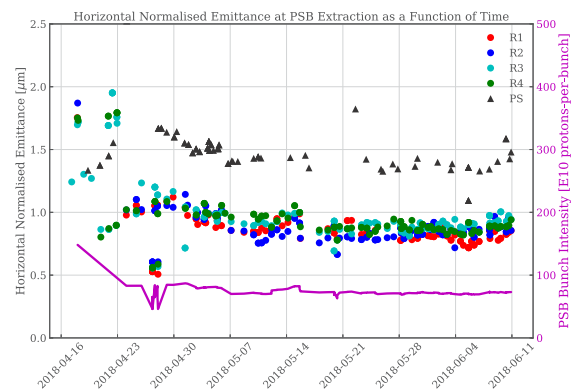


Figure 1: Horizontal emittances and intensity for LHC BCMS [3] beams at PSB extraction and PS injection during 2018 run.

To date, the beam injected into the PS has always been mismatched in dispersion with respect to the PS closed solution, as the simultaneous matching of the optics from the four rings of the PSB is not possible by using only ten available quadrupoles in the transfer line [4]. An eleventh quadrupole, which could improve the matching, would also be available but is placed inside a shielding wall and is not used in operation for safety and maintenance reasons. However, it is available for machine development (MD) purposes [5].

The LIU project imposes a budget of emittance growth of 5% between the PSB (extraction) and PS (extraction), thus the present dispersive mismatch would not be tolerated. In fact, by using the LIU parameters of Table 1 in the present optics, the horizontal dispersive mismatch would reach an unacceptable value of 30% at 1.4 GeV and 24% at 2 GeV (due to the difference in $\delta p/p_{rms}$). For this reason the transfer line between PSB and PS will be renovated after the Long Shutdown 2 (LS2) in 2020. In particular, the focusing structure in the transfer line between PSB and PS will be modified in order to provide dedicated optics settings for LIU [6]. Such optics will grant good matching in the horizontal plane, while some small residual and unavoi-

able mismatch is foreseen in the vertical plane due to edge focussing effects of the vertical recombination dipoles [7].

PSB-TO-PS TRANSFER LINE

The PSB-to-PS transfer line is composed of two parts: the first is the BT line, which is common with the other PSB users: in fact, by the means of a horizontal switching dipole, the bunches can be directed either to the PS (through the BTP line), or to the ISOLDE experiment [8], or to the PSB external beam dump, which is placed at the end of a measurement line (BTM). The BT line has five quadrupoles, which can be pulsed at every cycle with different values. The BTP line has six quadrupoles, including the one in the wall, whose values have to be kept constant for different cycles. Thus, only the five BT quadrupoles can be used in parallel operation for MD. However, they are not sufficient to guarantee a perfect analytical matching of eight parameters, i.e. Twiss ($\alpha_{x,y}$, $\beta_{x,y}$) and dispersion $D_{x,y}$ and $D'_{x,y}$.

Therefore, a re-matched optics which could minimise dispersion mismatch was computed using the MAD-X code [9] and used in MDs in 2017. The strengths of the quadrupoles that were used in 2017 parallel MDs are reported in Table 2.

Table 2: Operational and Re-matched (Dispersion-free) Optics for Parallel MDs: Normalised Quadrupolar Gradients k_1 and Currents I

Quadrupole	k_1 [m ⁻²]	I [A]	k_1 [m ⁻²]	I [A]
	Operational optics		Re-matched optics	
BT.QNO10	-0.66749	186	-0.92797	174.99
BT.QNO20	0.63160	176	0.66356	184.90
BT.QNO30	-0.28709	80	-0.26986	75.2
BT.QNO40	0.92347	256.79	0.99735	277.33
BT.QNO50	-0.73445	174.75	0.77117	183.49
BTP.QNO10	0	0	0	0
BTP.QNO20	0.52130	148.4	0.52130	148.4
BTP.QNO30	-0.48497	138.08	-0.48497	138.08
BTP.QNO40	0.62693	179.49	0.62693	179.49
BTP.QNO50	-0.53563	152.73	-0.53563	152.73
BTP.QNO60	0.6689	190.46	0.6689	190.46

SENSITIVITY ANALYSIS ON SINGLE QUADRUPOLE STRENGTH

A sensitivity analysis was performed by varying the BT.QNO10 strength, in order to optimise the mismatch factor $M_{\text{tot},x,y}$, as shown in simulation in Fig. 2, bottom-right. $M_{\text{tot},x,y}$ is defined as the quadratic sum of the components of emittance growth due to the betatron and dispersive mismatches, $M_{\beta_{x,y}}$ (Eq. (1) [10]) and $M_{D_{x,y}}$ (Eq. (2) [11]).

$$M_{\beta_{x,y}} = \frac{\Delta\epsilon_{x,y}}{\epsilon_{0,x,y}} = \frac{1}{2} \left[\frac{\beta_{x,y,\text{PS,closed}}}{\beta_{x,y,m}} + \frac{\beta_{x,y,m}}{\beta_{x,y,\text{PS,closed}}} + \left(\frac{\alpha_{x,y,m}}{\beta_{x,y,m}} - \frac{\alpha_{x,y,\text{PS,closed}}}{\beta_{x,y,\text{PS,closed}}} \right)^2 \beta_{x,y,\text{PS,closed}} \beta_{x,y,m} \right] - 1 \quad (1)$$

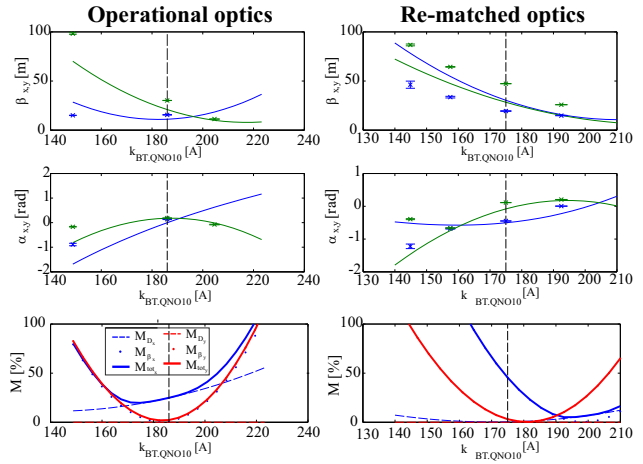


Figure 2: BT.QNO10 sensitivity analysis. Top-centre: simulated (solid lines) and estimated (markers with 1σ errorbar) $\alpha_{T,x,y}$ and $\beta_{T,x,y}$ from three screens measurements for the horizontal (blue) and vertical (green) planes. Bottom: simulated mismatch factors for $\epsilon_{0,x} = 1.1 \mu\text{m}$, $\epsilon_{0,y} = 1.05 \mu\text{m}$ and $\delta p/p_{\text{rms}} = 0.879 \times 10^{-3}$. The vertical dashed lines represent the nominal values.

$$M_{D_{x,y}} = \frac{\Delta\epsilon_{x,y}}{\epsilon_{0,x,y}} = \frac{1}{2} \frac{\Delta D_{x,y}^2 + (\beta_{x,y,T} D'_{x,y} + \alpha_{x,y,T})^2}{\beta_{x,y,T} \epsilon_{x,y,0,g}} \left(\frac{\delta p}{p_{\text{rms}}} \right)^2 = \frac{1}{2} \frac{\Delta \bar{D}_{x,y}^2 + \Delta \bar{D}'_{x,y}^2}{\epsilon_{x,y,0,g}} \left(\frac{\delta p}{p_{\text{rms}}} \right)^2 \quad (2)$$

where $\epsilon_{x,y,0,g}$ are the geometrical transverse emittances and $\beta_{x,y,m}$ and $\alpha_{x,y,m}$ are the Twiss parameters at the PS injection point (located at the end of the exit flange of septum in section 42), $\beta_{x,y,\text{PS,closed}}$ and $\alpha_{x,y,\text{PS,closed}}$ are the PS closed solutions, and $D_{x,y}$ and $D'_{x,y}$ are the components of the normalised dispersion vector, $\bar{D}_{x,y} = \frac{D_{x,y}}{\sqrt{\beta_{x,y}}}$ are the normalised dispersion components.

$\beta_{x,y,m}$ and $\alpha_{x,y,m}$ were estimated from a three-screen analysis [12] performed by measuring the single-pass beam profiles in three secondary emission monitor (SEM) grids placed just after injection in the PS. The analysis is based on the betatron beam sizes at the three grids. The betatron beam sizes are computed by quadratically subtracting the dispersive component from the total beam size measured at each grid, i.e.:

$$\sigma_{\beta_{x,y}} = \beta_{x,y} \epsilon_{x,y,g} = \beta_{x,y} \frac{\epsilon_{x,y}}{\beta_{\text{rel}} \gamma_{\text{rel}}} = \sqrt{\sigma_{\text{tot},x,y}^2 - D_{x,y}^2 \frac{\delta p^2}{p_{\text{rms}}^2}} \quad (3)$$

where β_{rel} and γ_{rel} are the relativistic Lorentz factors.

The results showed that the model and the measurements are in disagreement (see Fig. 2). Investigations are ongoing to understand the possible reasons, such as errors in the quadrupole transfer functions or the full deconvolution of the momentum distribution from the total beam [13].

Content from this work may be used under the terms of the CC BY 3.0 licence (© 2018). Any distribution of this work must maintain attribution to the author(s), title of the work, publisher, and DOI.

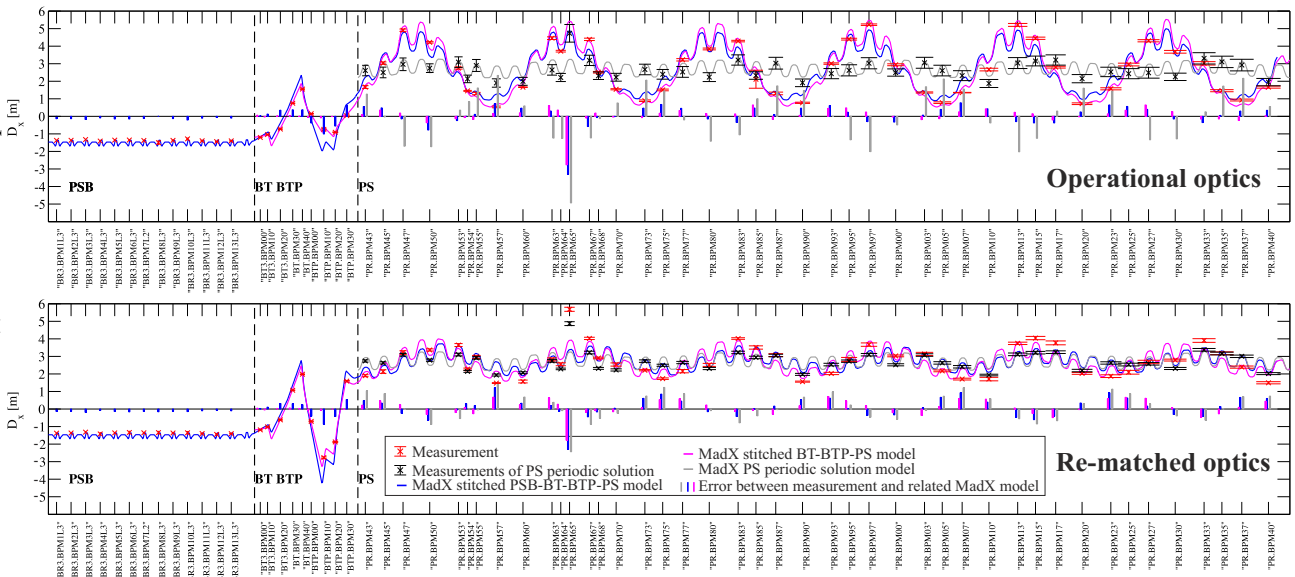


Figure 3: Dispersion measurements and simulations in the PSB-BT-BTP-PS line.

Nevertheless the analysis showed that the empirical $M_{\beta_{x,y}}$ is reduced to $\sim 3\%$ by increasing the current of BT.QNO10 by 10% in the re-matched optics. The three SEM grids are located in even numbered sections in the PS, where the closed solution of the Twiss parameters and dispersion functions are very similar. By correcting the current in BT.QNO10 by 10%, the total beam sizes measured at the location of the grids were very similar, indicating good matching. This optimisation is taken into account in the rest of the paper for the re-matched optics case. In order to confirm such a finding, a turn-by-turn beam profile matching monitor is, in this sense, fundamental; the fast electronics to make the SEM grid in section 52 able to read in multi-turn mode is in preparation and will be ready at the end of June 2018.

Transfer Line Initial Conditions

The initial conditions of the Twiss parameters at the beginning of the transfer line were measured using the three-screen method in the SEM grids of the BTM line with the operational optics, by using different beams. In particular, low intensity single LHC bunches with different of $\delta p/p_{rms}$ values were used in order to have a negligible influence of the dispersive profile contribution. Results showed good agreement with the nominal extraction parameters [14].

DISPERSION MEASUREMENTS

Dispersion measurements from the PSB to the PS were performed for both optics. The dispersion was measured by varying the extraction radio-frequency (RF) frequency, e.g. momentum, of the PSB and linearly correlating the related momentum offset to the positions recorded on beam position monitors (BPM) from the PSB (last turn) to the PS (first turn). The measurements showed a good correlation between model and measurements after re-matching the initial conditions of the dispersion model at the beginning of the BT line, as shown in Fig. 3. Dispersion in a drift behaves

like a ray. Hence the initial conditions of $D_{x,y}$ and $D'_{x,y}$ were calculated by linearly extrapolating to the beginning of the line the value of dispersions measured at the first two BPMs of the line which are placed in a drift region.

The dispersion was measured turn-by-turn in the PS. Measurements in Fig. 4 were performed by switching the RF cavities OFF. In fact, before the beam de-bunches inside the machine, it is possible to record the beam position for several turns from which one can derive the PS dispersion closed solution and the maximum amplitude of the normalised dispersion vector \bar{D} .

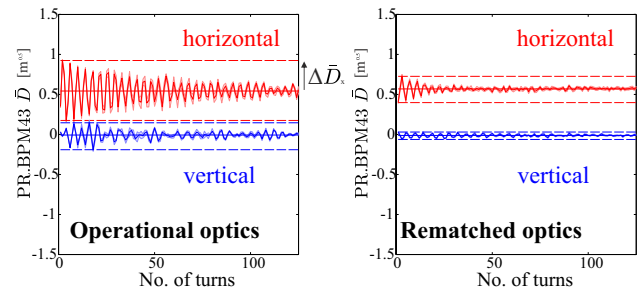


Figure 4: Turn-by-turn dispersion measurements in the PS around the closed solution (solid horizontal lines) keeping the RF cavities OFF at the first PS BPM after injection.

Dispersive Mismatch Factor $\lambda_{x,y}$ from Dispersion Measurements

The amplitude of the turn-by-turn dispersion oscillation around its closed solution was used to approximate the emittance growth due to dispersive mismatch of Eq. (2) to:

$$M_{D_{x,y}} \approx \lambda_{x,y} \frac{1}{\epsilon_{x,y,0,g}} \left(\frac{\delta p}{p}_{rms} \right)^2, \quad \lambda_{x,y} = \frac{1}{2} \max(\Delta \bar{D}_{x,y}^2) \quad (4)$$

The advantage of using this approximation is that the term $\lambda_{x,y}$ is a constant at every PS BPM and can be directly cal-

culated from measurements. In fact, $\max(\Delta\bar{D}_{x,y})$ represents the amplitude of the normalised dispersion mismatch vector when $\Delta\bar{D}'_{x,y} = 0$. Figure 5 shows the result of the calculation of $\lambda_{x,y}$ for the horizontal and vertical plane in the two considered optics. Figure 6 shows a color map of M_{D_x} for the operational optics (calculated $\lambda_{\text{average},x}=0.08$) by using Eq. (4).

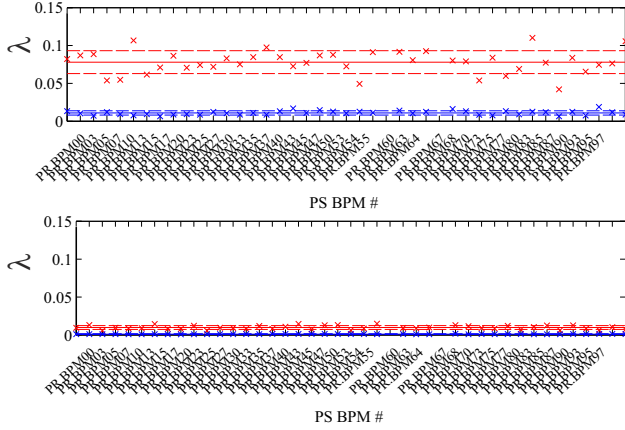


Figure 5: The $\lambda_{x,y}$ factor for the operational (top) and re-matched (bottom) optics in the horizontal (red) and vertical (blue) planes at the PS BPM locations. The horizontal solid lines represent the average value, the horizontal dashed lines are ± 1 standard deviation.

Thus, M_{D_x} for an operational BCMS beam, i.e. $\epsilon_{0,x,y} = 1 \mu\text{m}$ and $\delta p/p_{\text{rms}} = 0.9 \times 10^{-3}$, is $\sim 15\%$, while it is 8 times smaller (2%) in the case of re-matched optics, as $\lambda_{\text{average},x} = 0.01$ in this case. The estimated M_{D_y} is $< 2\%$ for such beams, thus negligible. Table 3 shows the summary for the two optics.

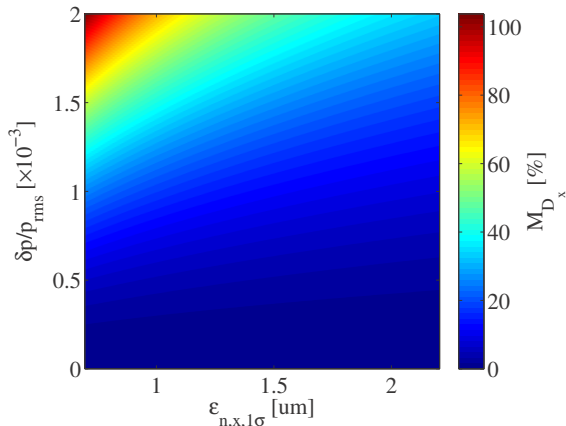


Figure 6: Operational optics: estimated emittance growth related to dispersion mismatch for different emittances and momentum spreads (see Eq. (4)) at 1.4 GeV.

Dispersive Mismatch Factor $\lambda_{x,y}$ from Emittance Measurements

If the dispersive effect is dominant in terms of emittance growth, it should be possible to derive the dispersive mis-

Table 3: Summary of expected emittance growth for operational and re-matched optics, derived from three-screen and dispersion measurements using Eqs. (1) and (4).

	$M_{\beta x}$ [%]	$M_{\beta y}$ [%]	M_{Dx} [%]	M_{Dy} [%]	$M_{\text{tot},x}$ [%]	$M_{\text{tot},y}$ [%]
Operational optics	6	6	15	2	16	6
Rematched optics	3	3	2	0	4	3

match factor $\lambda_{x,y}$ from transverse emittance blow-up $\Delta\epsilon_{x,y}$ measurements. In fact, starting from Eq. (4), one can derive

$$\lambda_{x,y} = \frac{\Delta\epsilon_{x,y}}{\beta_{\text{rel}}\gamma_{\text{rel}} \frac{\delta p}{p}_{\text{rms}}^2} \quad (5)$$

Measurements of LHC Standard “long” bunches, i.e. total bunch length of 210 ns, at different longitudinal emittances were performed in 2017 in the operational optics in order to assess the expected dependency of the blow-up with the momentum spread for large longitudinal emittance beams and also assess the threshold in which space charge might dominate. Figure 7 shows a clear linear correlation between emittance growth and $(\delta p/p_{\text{rms}})^2$ for longitudinal emittance larger than 1.6 eVs. For lower longitudinal emittances, other effects are dominant. Suspected cause could be the interaction with the horizontal PS integer resonance $Q_x = 6$ due to transverse space charge. For larger longitudinal emittances, the slope of the linear fit in the plot (divided by $\beta_{\text{rel}}\gamma_{\text{rel}}$) corresponds to the value of λ_x . However the calculated $\lambda_x \approx 0.3$ is much higher than the one derived from the previous dispersive measurements, suggesting again that other phenomena are involved in the emittance growth on top of the dispersive mismatch.

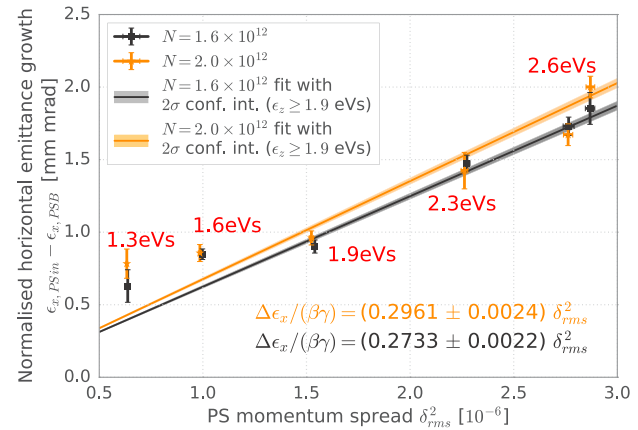


Figure 7: Correlation between normalised transverse emittance growth and energy spread squared for LHC Standard “long” bunches. Transverse emittances are calculated by deconvolving the non-Gaussian momentum spread distribution [13]. The slope remains the same for the usual Gaussian least-squares fit to determine the transverse emittance.

TRANSVERSE EMITTANCE MEASUREMENTS

The transverse emittance was measured during the sensitivity scan analysis for PSB R3 single BCMS bunches of $\sim 83 \times 10^{10}$ ppb. The cycle was set in order to have reduced coupling, low chromaticity and transfer feedback ON. The measurements are shown in Fig. 8. The emittance at extraction from the PSB was evaluated through the PSB wirescanner and three SEM grids in the BTM line. The two different techniques used to measure emittance give different results [15].

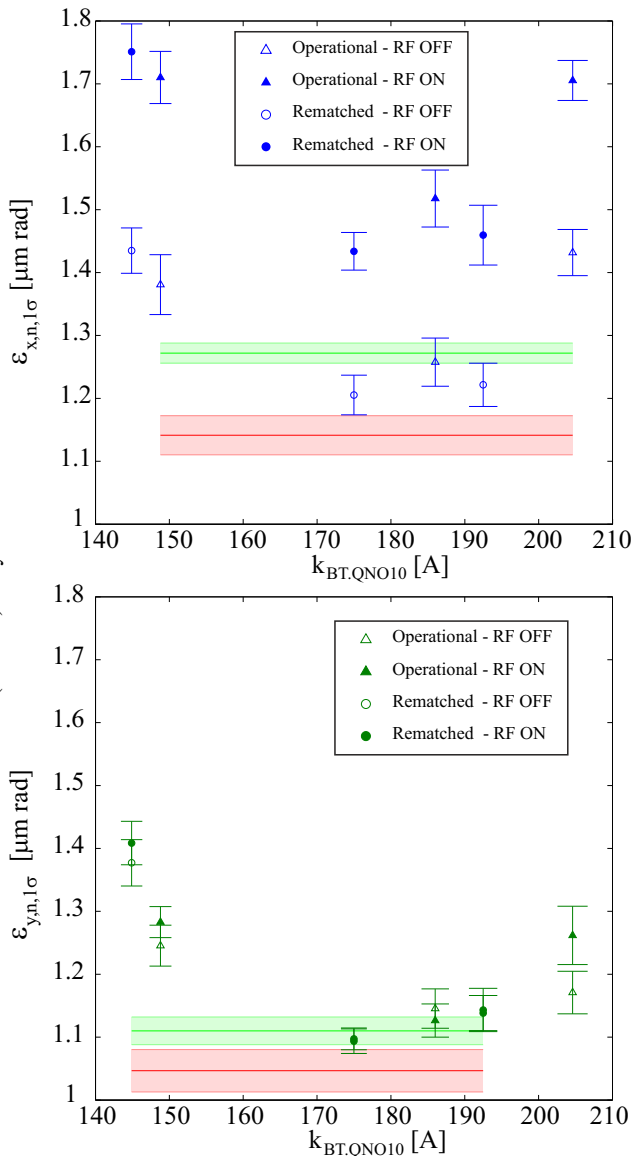


Figure 8: Normalised rms horizontal (top) and vertical (bottom) transverse emittances during the sensitivity scan of BT.QNO10. The horizontal errorbars are measurements performed with the PSB wirescanner (red) and the three SEM grids in the BTM line (green).

In the PS, the emittances are measured 15 ms after injection and are calculated from the Gaussian fit of the total

profile by using momentum spread subtraction in quadrature, as in Eq. (3). Only a slight reduction was achieved for the horizontal emittance. However, a big jump in the horizontal plane ($\sim 0.2\text{-}0.3 \mu\text{m}$) is present between the measurements done with the RF cavities ON or OFF. Investigations on the sources of such discrepancy are on-going.

CONCLUSIONS AND OUTLOOK

An unexpected horizontal emittance growth in the order of 40-50% is measured after injection in the machine for LHC beams. The PS operates with a large horizontal dispersion mismatch, which will be compensated for the future LIU optics. In order to assess whether such blow-up is related to optics mismatch between the PSB-to-PS transfer line and the PS, a thorough analysis of the transfer line optics from PSB to PS was performed in 2017. The measured horizontal mismatch for the operational optics is in the order of 16% for LHC BCMS beams and justifies only partially the measured emittance growth. The large dispersive mismatch was compensated by the means of a new optics, which can be used in parallel operation. A sensitivity scan of the gradient of a single quadrupole in the line allowed to optimise the matching, leading to an expected empirical total emittance growth induced by betatron and dispersive mismatches $<5\%$.

However, emittance measurements performed with the wirescanner showed only a slight improvement, but underlined a clear difference when the RF cavities in the PS are ON or OFF.

Further investigations are continuing in 2018, focussing on a new dedicated optics with full analytical matching to the PS, on the effect of the RF on the bunches at injection and on an improved knowledge of the present transfer line parameters, e.g. quadrupole gradients error through kick response analysis.

ACKNOWLEDGEMENTS

The authors would like to thank the PSB and PS operation teams for the constant support during the measurements.

REFERENCES

- [1] The LIU project: <https://espace.cern.ch/liu-project/default.aspx>
- [2] G. Rumolo, "LIU Target Beam Parameters", CERN EDMS: 1296306
- [3] H. Damerau *et al.*, "LHC Injectors Upgrade Technical Design Report", CERN-ACC-2014-0337
- [4] A. Jansson, M. Lindroos, M. Martini, and K. Schindl, "Study of emittance blowup sources between the PS booster and the 26-GeV PS", CERN-PS-98-058-OP
- [5] M. Benedikt *et al.*, "Study of a new PSB-to-PS transfer line optics with improved dispersion matching by means of turn-by-turn beam profile acquisitions", PS/AE/Note 2001-003 (MD)
- [6] W. Bartmann *et al.*, "New PSB H⁻ Injection and 2 GeV Transfer to the CERN PS", in *Proc. HB'14*, East-Lansing, MI, USA, paper WEO4AB02, pp.320.

- [7] W. Bartmann, V. Forte, and M. Fraser, “Emittance growth at PS injection according to model”, Presentation at CERN Machine Studies Working Group Meeting (MSWG), <https://indico.cern.ch/event/578789>
- [8] The ISOLDE experiment: <http://isolde.web.cern.ch/active-experiments>
- [9] MAD - Methodical Accelerator Design: <http://mad.web.cern.ch/mad/>
- [10] M. Giovannozzi, “Sources of emittance growth”, CERN Accelerator School (CAS) 2009.
- [11] B. Goddard *et al.*, “Expected emittance growth and beam tail repopulation from errors at injection into the LHC”, in *Proc. PAC’05*, Knoxville, TN, USA, 2005, paper MPPE011, pp. 1266.
- [12] G. Arduini *et al.*, “Measurement of the optical parameters of a transfer line using multi-profile analysis”, CERN-PS-98-032-CA
- [13] A. Oeftiger, H. Bartosik, A. Findlay, S. Hancock, and G. Rumolo, “Flat bunches with a hollow distribution for space charge mitigation”, in *Proc. IPAC’16*, Busan, Korea, pp. 652–655, doi:10.18429/JACoW-IPAC2016-MOPOR023
- [14] V. Forte, M. A. Fraser, and W. Bartmann, “Status of injection and transfer studies”, Presentation at LIU PS beam dynamics meeting, <https://indico.cern.ch/event/671971/>
- [15] G. P. Di Giovanni *et al.*, “Comparison of Different Transverse Emittance Measurement Techniques in the Proton Synchrotron Booster”, presented at IPAC2018, Vancouver, BC, Canada, paper MOPMF054.

MULTI-PARTICLE SIMULATIONS OF THE FUTURE CERN PSB INJECTION PROCESS WITH UPDATED LINAC4 BEAM PERFORMANCE

V. Forte*, C. Bracco, G.P. Di Giovanni, M. A. Fraser, A. M. Lombardi, B. Mikulec
 CERN, Geneva, Switzerland

Abstract

In the framework of the LHC Injectors Upgrade (LIU) project, the injection process in the CERN Proton Synchrotron Booster (PSB) will be renovated after the connection with the Linac4. A new H^- charge exchange injection system using a stripping foil is foreseen to increase the brightness of the stored beams and to provide high flexibility in terms of emittance tailoring at 160 MeV. Realistic multi-particle simulations of the future injection processes for high brightness beams (i.e. for the LHC) and high intensity beams (i.e. for the ISOLDE experiment) are presented in this paper. The simulations are based on the present performance of Linac4 and include scattering induced by the foil, space charge effects and compensation of the lattice perturbation introduced by the bumpers of the injection chicane.

INTRODUCTION

The LHC injectors upgrade (LIU) project [1] at CERN aims at renovating the LHC injector chain in order to produce beams with twice the present brightness for the LHC. The PSB is the first synchrotron of the injector chain, it is constituted by four superimposed rings and has the important role of defining the beam brightness B for the LHC beams:

$$B = \frac{N}{0.5(\epsilon_{x,n} + \epsilon_{y,n})} \quad (1)$$

where N is the bunch intensity and $\epsilon_{x,y}$ is the normalised transverse emittance. The PSB will start operating in connection with the new Linac4 [2] in 2020 after the long shutdown 2 (LS2). Major upgrades will be the introduction of a conventional H^- charge exchange multi-turn injection system with injection chicane and stripping foil and the injection energy will be increased to 160 MeV, which will increment the relativistic $\beta_{rel}\gamma_{rel}^2$ by a factor 2, thus allowing to double the brightness for the LHC beams. The LIU proton beam parameters are summarised in [3].

Linac4 started its commissioning phase in 2016 [4]. Between 2016 and 2017 about three months of operation was carried out to test the new injection system. Half of the injection chicane was mocked up and operated during the so-called “half-sector tests” [5]. During this time, different foils, which will be used to strip the injected H^- ions to the circulating H^+ , were tested. The quality of these foils in terms of stripping efficiency, emittance blow-up and losses [6] induced by scattering is fundamental for the production of high brightness beams.

* vincenzo.forte@cern.ch

MAIN LINAC4 AND PSB BEAM PARAMETERS

The reliability run of Linac4 is on-going [7]. The quality of the Linac4 beams is a prerequisite to achieve the target intensities and brightness for all the PSB users. The range of intensities per bunch stored in the PSB spans between 10^9 and 10^{13} protons per bunch (ppb). The maximum number of injection turns in each PSB ring is defined by the maximum pulse length of the new beam injection (BI) distributor (DIS), which is located in the PSB beam injection line. This device allows injections over 150 PSB turns per ring and distributes the beam to the four superimposed rings of the PSB. The revolution period of the PSB ($T_{rev,PSB}$) at 160 MeV is $\sim 1 \mu s$. The Linac4 beam parameters requested by the PSB are summarised in [8].

Current

The Linac4 current is fundamental to determine the maximum number of protons that can be collected in any of the four PSB rings. An interesting feature of Linac4 is the possibility to chop parts of the pulse with the chopper [9]. The chopper is used to fit the Linac4 bunchlet trains (1 every 2.8 ns) in the longitudinal phase space of the radio-frequency (RF) bucket of the PSB. The “chopping factor” (CF) is defined as the portion of beam average current in output from the chopping stage with respect to the average current at the entrance of the chopper, as shown in Fig. 1. Typical values of CF are around 0.6, but, in principle, any value between 0 and 1 is permitted.

Two beam transformers, L4L.BCT3113 and L4L.BCT4013, located at the entrance and the exit of the chopper respectively, can be used to measure the input and output currents. In the ideal case of a perfectly flat Linac4 pulse, the peak current at the entrance I_{peak} of the chopper corresponds also to the average current $I_{avg} = I_{peak}$, calculated along one $T_{rev,PSB}$. After the chopping stage, the average current is reduced by CF to $I_{avg} = CF \times I_{peak}$.

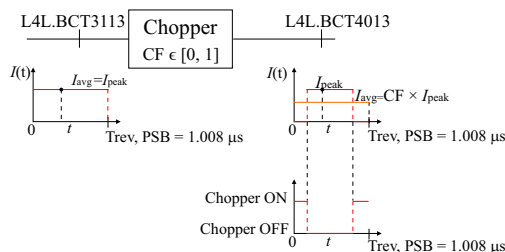


Figure 1: A sketch of the Linac4 current before and after the chopping.

The intensity N per PSB turn can be expressed as:

$$\frac{N}{\text{PSB turn}} = \int_0^{T_{\text{rev, PSB}}} I(t) dt \times \frac{1}{\text{proton charge}} = \quad (2)$$

$$= (\text{CF} \times I_{\text{peak}} \times T_{\text{rev, PSB}}) \times \frac{1}{1.6 \cdot 10^{-19}} \text{ [ppb/turn]}$$

As an example, parameters for the production of a single bunch for the LIU Standard LHC beams production ($N_{\text{target}} = 3.42 \times 10^{12}$ ppb), assuming the desired $I_{\text{peak}} = 40 \cdot 10^{-3}$ A and $\text{CF}=0.61$ [8, 10], are shown:

$$\frac{N}{\text{PSB turn}} = (0.61 \times 40 \cdot 10^{-3} \times 1.008 \cdot 10^{-6}) \times \frac{1}{1.6 \cdot 10^{-19}} = 1.512 \cdot 10^{11} \text{ ppb/turn} \quad (3)$$

This leads to the number of turns needed to reach the target intensity:

$$\text{Nr. of PSB turns} = \frac{N_{\text{target}}}{\frac{N}{\text{PSB turn}}} = \frac{3.42 \cdot 10^{12}}{1.512 \cdot 10^{11}} \approx 23 \quad (4)$$

Presently, a peak current of $I_{\text{peak}} = 20$ mA could be achieved at the entrance of the chopper, thus the same bunch intensity would be produced in 45 turns (neglecting losses in the PSB). It is clear that, given the allowed 150 injection turns per ring, the Linac4 current becomes a limiting parameter for the maximum intensity of high intensity users (e.g. ISOLDE).

Moreover, in the case of non-flat pulses, as presented in Fig. 2, the jitter around the average value would affect the actual intensity reach for a given N_{target} . For this reason it is important to have a stable average current at the chopper entrance. The stability requirements [8] are of maximum jitter $\pm 5\%$ for high intensity beams (600 μs pulse length) and $\pm 2\%$ for LHC beams (160 μs pulse length) in the assumption that the transmission from the chopper to the PSB is unaltered. Present realistic pulse shapes at the exit of the ion source fulfil the specifications in the assumption that the pulse arrives unaltered to the entrance of the chopper.

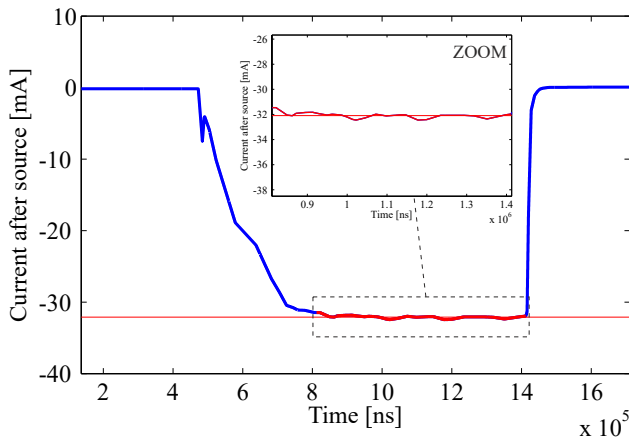


Figure 2: A measured H^- Linac4 current profile at the exit of the ion source. The red line lasts 600 μs (~ 600 PSB turns, i.e. 4×150 turns per PSB ring). The measured jitter around the average current is $\sim 2\%$.

Transverse Emittance

The impact of a different starting emittance for the high brightness beams was analysed to evaluate the influence on the final emittance of the accumulated beams in the PSB. Due to the lower current, the updated transverse emittances of the Linac4 microbunches are also reduced to $\epsilon_{x,y,1\sigma} \approx 0.3 \mu\text{m}$ [7], with respect to the values that were used in 2016 [10], i.e. $\epsilon_{x,y,1\sigma} \approx 0.4 \mu\text{m}$.

TRACKING SIMULATIONS

Results of tracking simulations are shown in this paper for the LHC, where high brightness is desired, and for the high intensity ISOLDE beams [11], where many turns of injection and reduced losses ($< 2\%$ after injection) are needed. The simulations include the multi-turn injection process, transverse and longitudinal space charge, minimisation of the beta-beating induced by the injection chicane fall, injection in accelerating bucket in double RF with $8 \text{ kV}_{h=1} + 6 \text{ kV}_{h=2}$ in antiphase and $\dot{B}\rho = 10 \frac{Tm}{s}$, where h is the harmonic number. The transverse tune is the optimised one for LHC [10], i.e. $(Q_x, Q_y) = (4.43, 4.60)$.

LIU LHC Standard Simulations

The brightness curves (intensity vs. average normalised transverse emittances) for the LIU LHC Standard ($N = 3.42 \times 10^{12}$ ppb) beams have been simulated for the previous beam parameters [8, 10]. The injection process consists of threading a pencil beam from Linac4 with a given offset with respect to the closed orbit, determined by the “slow” (BSW) and the “fast” (KSW) bump magnets at -80.9 mm at the stripping foil location. A sketch of the new injection system is shown in Fig. 3

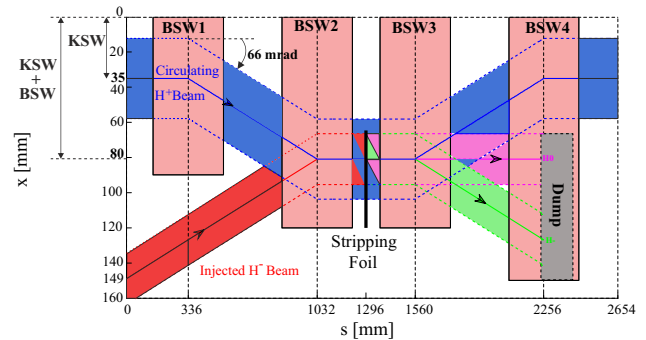


Figure 3: View from top of the future injection “chicane” for the H^- injection scheme, defined by the BSW magnets. The beginning of the process with the foil hits by the injected H^- beam (red), which is stripped into the circulating H^+ proton beam (blue). The unstripped H^- (light green) and the H^0 (magenta) hit a beam dump inside the BSW4 and are lost [12].

The emittance after tracking for 10 ms was in both planes $\sim 1.2 \mu\text{m}$, i.e. 30% less than the LIU LHC limit $\epsilon_{x,y,n} = 1.7 \mu\text{m}$, for horizontal and vertical injection offsets up to 3 mm [10]. Figure 4 shows the final emittances for different injection offsets.

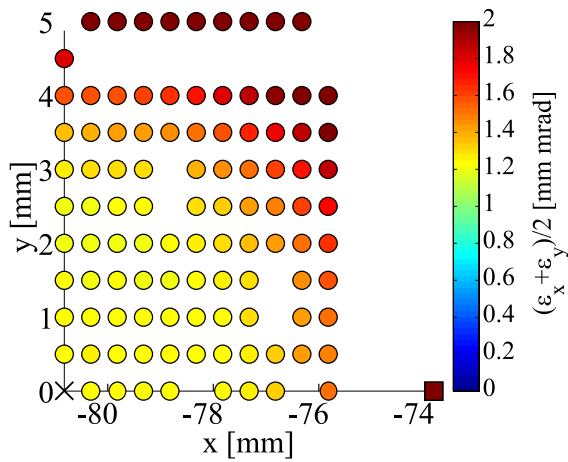


Figure 4: The final emittances 10 ms after injection for $I_{\text{peak}} = 40$ mA and $\epsilon_{x,y,n,0} = 0.4 \mu\text{m}$ and different transverse offsets [10].

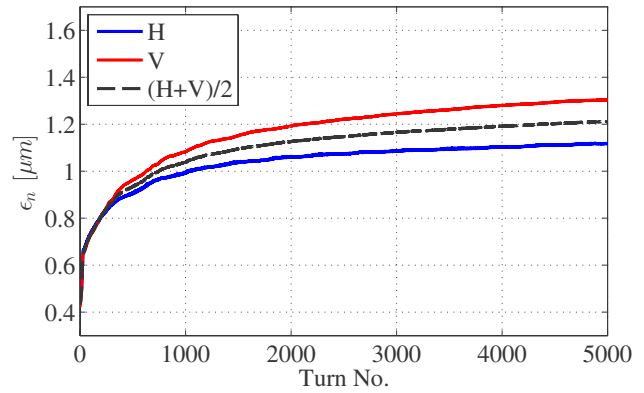


Figure 6: “On-axis” injection: horizontal (H), vertical (V) and $(H+V)/2$ emittance evolutions for the case with mismatched initial distributions and updated parameters, i.e. $I_{\text{peak}}=20$ mA and $\epsilon_{x,y,1\sigma} \approx 0.3 \mu\text{m}$.

No space charge - emittance growth due to foil scattering Tracking without space charge was carried out to assess the impact of the new starting emittances on the final blow-up due to the scattering of the foil. The foil has $200 \mu\text{g}/\text{cm}^3$ thickness. Injections up to 90 turns, which would theoretically correspond to $I_{\text{peak}}=10$ mA, were performed by injecting “on-axis”, i.e. on the closed orbit $(x,y)=(-80.9,0)$ and starting from different transverse emittances (see Fig. 5). The maximum emittance growth after 45 turns was around 66%, which is lower than the LHC Standard emittance limit.

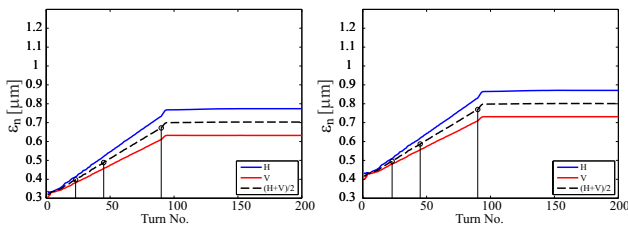


Figure 5: Emittance growth due only to foil scattering and starting from different transverse emittances.

A comparison with the matched optics with updated and past parameters is shown in Fig. 7. The final emittance is in all cases $\epsilon_{x,y,n} \sim 1.2 \mu\text{m}$ after 5000 turns, very similar to the one that one would obtain by injecting for 23 turns, i.e. considering $I_{\text{peak}} = 40$ mA, and starting from $\epsilon_{x,y,n,0} = 0.4 \mu\text{m}$. This confirms that, for the “on-axis” injection, the emittance blow-up is dominated by space charge and that the new initial emittance and number of injected turns have a small impact.

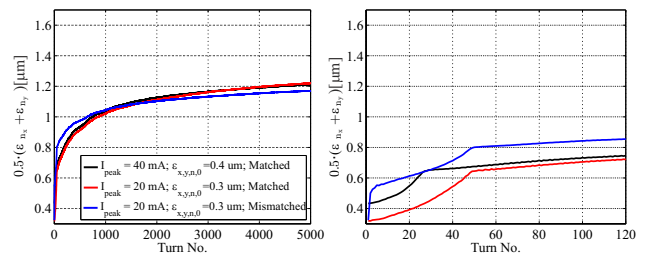


Figure 7: Average Emittance growth for “on-axis” injection during first 5000 (left) and 120 turns (right) for matched and mismatched optics.

“On-axis” injection - with space charge “On-axis” simulations were carried out considering 45 turns injection and $\epsilon_{x,y,n,0} = 0.3 \mu\text{m}$. Tracking with mismatched optics between Linac4 and PSB was also performed. In particular, at the foil, $\beta_{x,y}$ were increased by 20%, $\alpha_{x,y}$ were increased from 0 to 0.4 rad, D_x was increased by 20%, the angular offsets x' and y' from 0 to 0.4 mrad [8]. The emittance evolution for the mismatched case is shown in Fig. 6.

“Off-axis” injection - with space charge An injection offset of $(\Delta x, \Delta y)=(2, 2)$ mm was considered for the “off-axis” injection. Such an offset was chosen in order to stay inside the $\epsilon_{x,y,n} \sim 1.2 \mu\text{m}$ region of Fig. 4 and still have 1 mm margin for the transverse intra-bunch deflection of the beam incoming from Linac4 [8]. Simulations in Fig. 8 show that, by exceeding the proposed offset, the average emittance quickly exceeds the LIU LHC limit.

Content from this work may be used under the terms of the CC BY 3.0 licence (© 2018). Any distribution of this work must maintain attribution to the author(s), title of the work, publisher, and DOI.

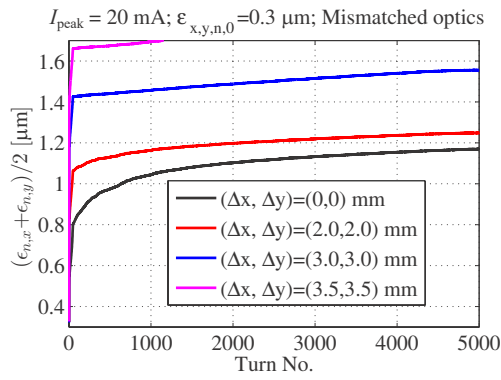


Figure 8: Average transverse emittances for different injection offsets.

Simulations with the same Linac4 current, emittance and optics match/mismatch conditions as for the “on-axis” case are shown in Fig. 9. Figure 10 shows that a 6% increase is visible in the average final emittance for the case with the optics mismatch.

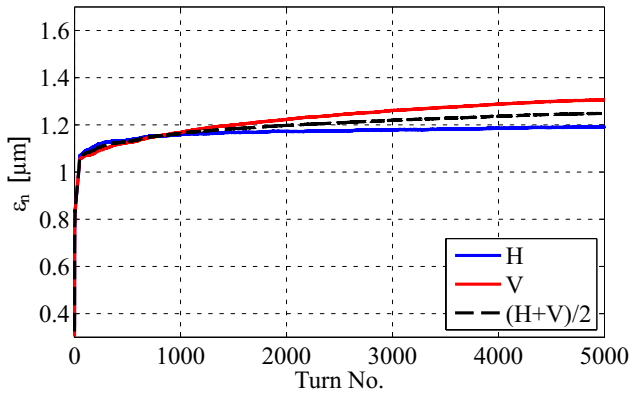


Figure 9: “Off-axis” injection: horizontal (H), vertical (V) and (H+V)/2 emittance evolutions for the case with mismatched initial distributions and updated parameters.

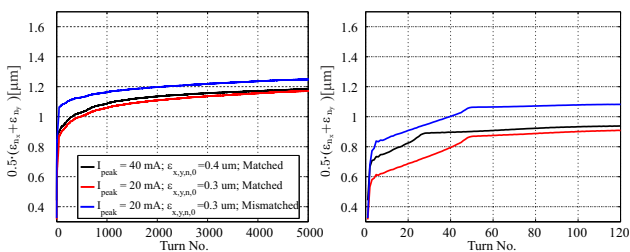


Figure 10: Average Emittance growth for “off-axis” injection during first 5000 (left) and 120 turns (right) for matched and mismatched optics.

The initial emittance has a small impact on the final emittance also in this case (<2% difference), as shown in Fig. 11.

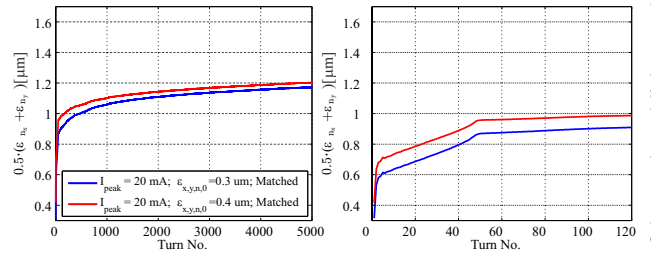


Figure 11: Average emittance growth for “off-axis” injection during first 5000 (left) and 120 turns (right) for different initial emittance and matched optics.

ISOLDE Beams Simulations

Simulations for the present ISOLDE bunches were performed by considering $N_{\text{target}} = 1 \times 10^{13}$ ppb. The longitudinal painting technique will be adopted in this case. Following the optimisation in [13], in order to paint a longitudinal matched area of 1.5 eVs, 124 turns are needed with an energy spread of 120 keV from the Linac4 de-buncher and an energy swing amplitude of ± 0.8 MeV from the Linac4 PIMS cavities [14] as shown in Fig. 12.

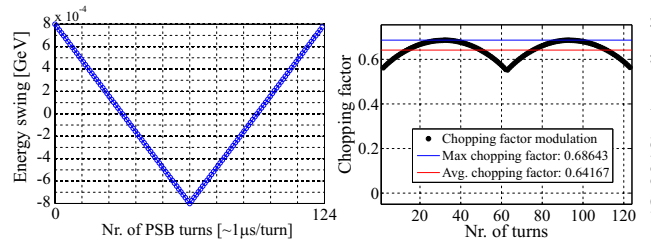


Figure 12: Energy swing (left) and chopping factor (right) patterns for $N_{\text{target}} = 1 \times 10^{13}$ ppb in 124 turns.

As one can see, for this particular longitudinal painting choice with $CF_{\text{avg}}=0.64$, $I_{\text{peak}}=20$ mA leaves only 20% of margin to reach the target intensity in 150 turns. For this reason the reduction of the current pulse jitter and the losses in the PSB during injection become critical.

In the transverse plane, the ISOLDE beams require horizontal painting at injection through the modulation in time of the current of the KSW magnets, which contribute to the initial offset with -35 mm to be added to the -46 mm of the slower BSW magnets. The vertical emittance is determined by a fixed injection offset of 6 mm in this case. Once determined the longitudinal painting pattern, the KSW modulation function [15] has to be adapted to the number of injection turns needed to reach N_{target} and the target horizontal emittance. A possible KSW offset modulation function is shown in Fig. 13.

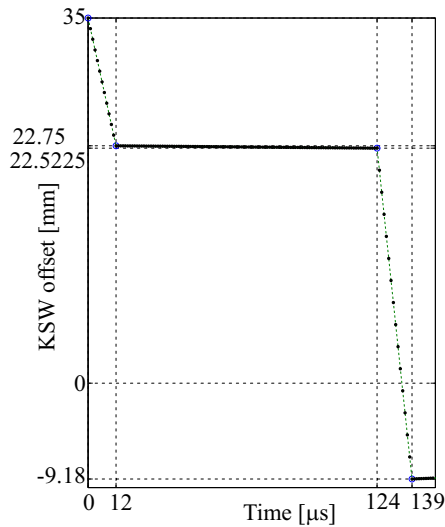


Figure 13: KSW offset modulation for 124 turns injection.

Two new beam absorbers, a fixed and a moving mask, will be added during the Long Shutdown 2 (LS2) [16]. Tracking simulations were performed taking into account the most restrictive aperture bottleneck introduced by the new beam absorbers. The emittance and intensity evolutions are shown in Fig. 14.

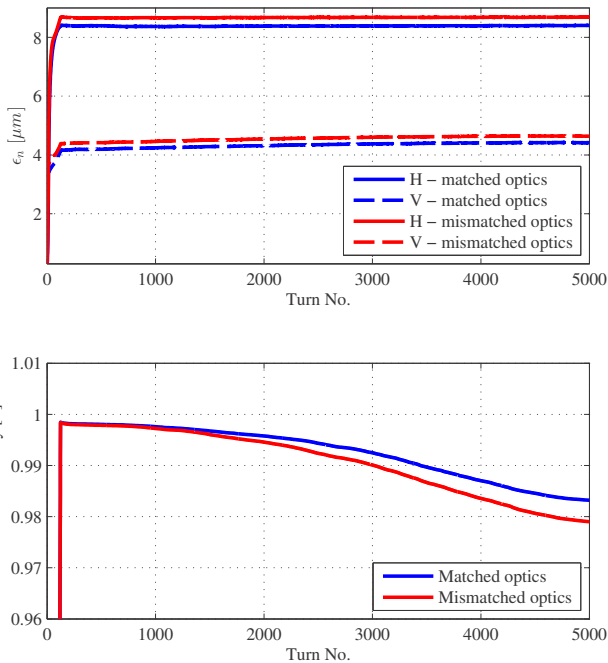


Figure 14: Results of tracking studies for an ISOLDE beam at $N_{\text{target}} = 1 \times 10^{13}$ ppb.

The integrated losses are in the order of 2%, mainly localised at the location of the movable absorbers, as shown in Fig. 15. Only a small amount of losses (few permille) are concentrated close to the injection region, probably induced by the scattering process with the foil. The horizontal losses ($\sim 3\%$) are mainly constituted by similar amount of particles, which are not captured in the RF bucket during

the longitudinal painting process. Such losses are localised mainly at the location of the masks and partially around the machine, where the horizontal aperture is +57 mm.

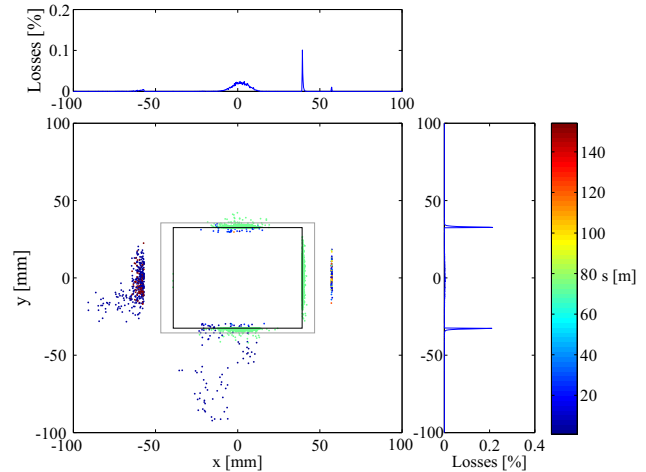


Figure 15: Loss distribution during the full tracking with PSB longitudinal position (s) in color-code. The rectangles represent the minimum aperture of the two new masks (movable - black, fixed - grey). The masks are located at around $s=75$ m (green markers).

CONCLUSIONS

The recent performance of the Linac4 corresponds to $I_{\text{peak}}=20$ mA before chopping and a transverse normalised emittance $\epsilon_{x,y,n} = 0.3 \mu\text{m}$. New simulations for the PSB injection process of the LIU LHC Standard beams were performed with these latest parameters. Space charge, optics mismatch, scattering foil and beta-beating compensation due to the lattice perturbation introduced by the injection bump were included in the tracking studies. The results showed a negligible impact with respect to the target performance with Linac4 $I_{\text{peak}}=40$ mA and emittance $\epsilon_{x,y,n} = 0.4 \mu\text{m}$, if other requested Linac4 parameters are inside the defined range [8].

Simulations for high intensity beams (ISOLDE) showed that, with the present current, the PSB should be able to produce bunches of 1×10^{13} ppb in 124 turns, which might vary depending on the choice of longitudinal painting parameters. If one considers a maximum of 150 turns injection per ring, this leaves only 20% to other sources of errors, like pulse flatness and losses inside the ring.

Future studies will include the study of LIU LHC BCMS beams and the modelisation and tracking of realistic fringe fields for the chicane magnets.

ACKNOWLEDGEMENTS

The authors would like to warmly thank the Linac4, the PSB-OP and LIU-PSB teams and for the continuous support.

REFERENCES

- [1] The LIU project:
<https://espace.cern.ch/liu-project/default.aspx>
- [2] The Linac4 project: <http://linac4-project.web.cern.ch/linac4-project/>
- [3] G. Rumolo, “LIU Target Beam Parameters”, CERN EDMS: 1296306
- [4] A. M. Lombardi *et al.*, “Linac4: from initial design to final commissioning”, in *Proc. IPAC'17*, Copenhagen, Denmark, doi:10.18429/JACoW-IPAC2017-TUYA1
- [5] B. Mikulec *et al.*, “Commissioning and result of the half sector test installation with 160 MeV H⁻ beam from Linac4”, in *Proc. IPAC'17*, Copenhagen, Denmark, doi:10.18429/JACoW-IPAC2017-MOPIK047
- [6] M. Aiba, C. Carli, B. Goddard, and W. Weterings, “Stripping foils for the PSB H⁻ injection system”, sLHC Project Note 0005.
- [7] G. Bellodi, “Linac4 Commissioning Status and Challenges to Nominal Operation”, presented at HB2018, Daejeon, Korea, paper MOA1PL03, this conference.
- [8] B. Mikulec, C. Bracco, G. P. Di Giovanni, and V. Forte, “Beam requirements for Linac4 Connection to the PS Booster”, CERN EDMS: 1898179
- [9] J. Arnaudon, “Linac4 technical design report”, CERN-AB-2006-084
- [10] V. Forte, “Performance of the CERN PSB at 160 MeV with H⁻ charge exchange injection”, Ph.D. thesis, U. Blaise Pascal, Clermont-Ferrand, CERN-THESIS-2016-063
- [11] The ISOLDE experiment:
<http://isolde.web.cern.ch/active-experiments>
- [12] H. Damerau *et al.*, “LHC Injectors Upgrade Technical Design Report”, CERN-ACC-2014-0337
- [13] V. Forte *et al.*, “The PSB operational scenario with longitudinal painting injection in the post-LIU era”, in *Proc. IPAC'17*, Copenhagen, Denmark, 2017, doi:10.18429/JACoW-IPAC2017-WEPVA035
- [14] F. Gerigk and R. Wegner, “Design of the PI-Mode Structure (PIMS) for Linac4”, in *Proc. PAC'09*, Vancouver, BC, Canada, paper FR5REP051.
- [15] J. Abelleira, “KSW waveforms for PSB users with H⁻ injection”, CERN EDMS: 1527891
- [16] H. Bartosik, G. P. Di Giovanni, B. Mikulec, and F. Schmidt, “PS Booster beam absorber/scrapper after LS2”, CERN EDMS: 1578463

SPS LONG TERM STABILITY STUDIES IN THE PRESENCE OF CRAB CAVITIES AND HIGH ORDER MULTIPOLES*

A. Alekou^{†1, 2}, R. B. Appleby², H. Bartosik¹, R. Calaga¹, M. 'Carla¹, Y. Papaphilippou¹
¹CERN, Geneva, Switzerland

²University of Manchester and Cockcroft Institute, UK

Abstract

A local Crab Cavity (CC) scheme will recover the head-on collisions at the IP of the High Luminosity LHC (HL-LHC), which aims to increase the LHC luminosity by a factor of 3-10. The tight space constraints at the CC location result in axially non-symmetric cavity designs that introduce high order multipole CC components. The impact of these high order components on the long term stability of the beam in the SPS machine, where two prototype crab cavities are presently installed in the CERN SPS to perform tests with beam, is presented. Furthermore, the Dynamic Aperture is studied in the presence of the SPS errors. Future plans are discussed.

INTRODUCTION

The High Luminosity LHC (HL-LHC) aims to increase the LHC luminosity to $L \sim 5 \cdot 10^{34} \text{ cm}^{-2} \cdot \text{s}^{-1}$. Among others upgrades, a Crab Cavity (CC) scheme will be implemented that will recover the head on collisions at the Interaction Point (IP). Since the CCs have never been used in proton machines, it is of paramount importance to test the validity of the scheme before its installation in the LHC. With this in mind, the SPS machine will serve as a test-bed of two vertical HL-LHC prototype CCs, installed one right next to each other, from April to November 2018.

The tight space constraints in the HL-LHC call for asymmetric cavity designs that include high order multipole components which could affect the long term Dynamic Aperture (DA). The DA in a perfect (no errors) SPS machine are presented in this paper for different CC configurations. Simulations in the presence of SPS multipoles are also presented.

CRAB CAVITY MULTIPOLES IN A PERFECT SPS LATTICE

The DA of a perfect (no errors, chromatic sextupoles for chromaticity correction are ON) SPS machine was simulated for different CC configurations:

- SPS, no CCs
- SPS, with CCs
- SPS, with CCs + Q
- SPS, with CCs + S
- SPS, with CCs + O
- SPS, with CCs + QSO,

where SPS is the bare SPS lattice without aperture. In the cases where multipoles were used only one crab cavity RF

multipole error was applied (Q: Quadrupolar, S: Sextupolar, O: Octupolar) at the location of the first CC; QSO stands for the case where all multipole errors were applied at the same time. Since the SPS experiments will be performed with different CC phase configurations, at a first stage the CCs were simulated in a phase-cancelling mode, where the first and second CC were set to 0° and 180° respectively, whereas at a second stage the two CCs were simulated having their phase set to 0° . In the first case, the effect of the kick of the first CC is cancelled by the effect of the kick of the second; in the latter case the effect of the second kick is added to that of the first one.

The SPS parameters at the location of the CCs are given in Table 1 and the values of crab cavity RF multipoles, taken from [1], in Table 2. Note that the SPS CC experiments

Table 1: Parameter Table

Parameter	Value
nCavities	2
s Location [m]	6312.7213, 6313.3213
Transverse tilt [deg]	90
V_{kick} per cavity [MV]	3.4
f [MHz]	400
β_{x1}, β_{y1} [m]	29.24, 76.07
β_{x2}, β_{y2} [m]	30.31, 73.82
μ_{x1}, μ_{y1}	23.88, 23.90
μ_{x2}, μ_{y2}	23.89, 23.90
D_{x1}, D_{y1} [m]	-0.48, 0.0
D_{x2}, D_{y2} [m]	-0.50, 0.0
D'_{x1}, D'_{y1} [m]	-0.02, 0.0
D'_{x2}, D'_{y2} [m]	-0.02, 0.0
Q_x, Q_y	26.13, 26.28
α_c	0.0019
E_{inj} [GeV]	26.00
γ_{rel}	27.71
$\epsilon_{n,x}, \epsilon_{n,y}$ [$\mu\text{m} \cdot \text{rad}$]	2.50, 2.50
V_{RF} [MV]	2
$\Delta p/p$	1.00E-3
Bunch length [m]	0.23
ϵ_s [eV · s]	0.5

will be performed at four different energies: 26, 55, 120 and 270 GeV, for various CC voltage values. The simulations were performed for the injection energy, $E = 26$ GeV, as this exhibits the largest CC kick, with $V_{\text{CC}} = 2$ MV, $\Delta p/p = 10^{-3}$ and $Q'_{x,y} = 0.0$. The indices 1,2 indicate the first and second CC respectively.

* Work supported by ...
 † androula.alekou@cern.ch

Table 2: Values of CC Multipoles in Units of mTm/mⁿ⁻¹

Multipole	Value
b ₂ (Q)	-0.06
α ₃ (S)	1159
b ₄ (O)	-4

The simulations were performed using MAD-X [2] and SixDesk [3], for 1E6 turns. Since the CCs are vertical, quadrupolar and octupolar errors are normal multipoles (b₂, b₄), whereas the sextupolar errors are skewed (α₃).

The DA with respect to angle for the studies described in the previous section are shown in Fig. 1 for the cases where the CCs are in a phase-cancelling (top) or same-phase (bottom) mode respectively.

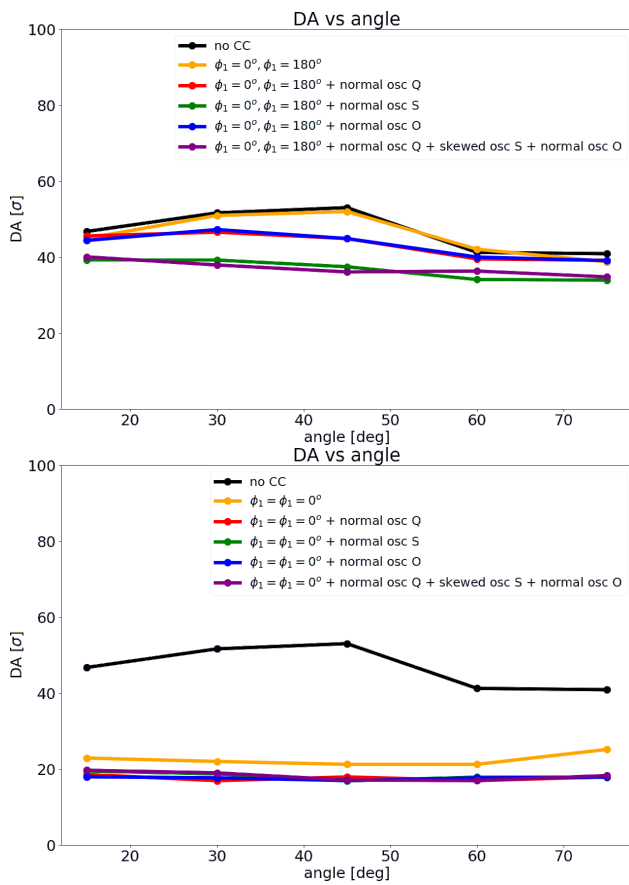


Figure 1: DA in σ with respect to angle in transverse phase space for the cases where the CCs are in a phase-cancelling mode (top), i.e. $\phi_1 = 0^\circ$ and $\phi_2 = 180^\circ$, and a same phase mode (bottom), i.e. $\phi_{1,2} = 0^\circ$.

From Fig. 1 (top) it can be seen that, as expected, the DA when the CCs are in the phase-cancelling mode (orange line) is very similar to the case where no CCs are present (black line). Note that all multipoles have an insignificant impact on the DA. The skewed sextupole (green line) has a slightly larger effect which can be expected as it is the strongest. The DA when all multipoles are used simultaneously (purple

line) is very similar to that of the skewed sextupole case and is as high as 40-45 σ .

On the other hand, when the CCs have the same phase the DA is reduced by a factor of almost 3, as shown in Fig. 1 (bottom). Note that in this case the sextupolar multipole (green line), and the case where all multipoles are used simultaneously (purple line) have a very similar effect to that of the other multipoles.

NON-LINEAR OPTICS FROM CHROMATICITY MEASUREMENTS

The results above use the nominal SPS optics model, which accounts only for non-linear fields produced by the chromatic sextupoles. On the other hand other sources of non-linearities are known to be present in the SPS, among which the most important ones are the odd multipoles produced by the error harmonics of the main dipole magnets and remanent fields in sextupoles and octupoles due to magnetic hysteresis, the latter relevant only at low energies. Some effort has been made in order to establish the SPS non-linear optics model with beam-based measurements at injection energy (26 GeV), the latest results being summarized in Ref. [4].

By repeating chromaticity measurements (see Figure 2) with 3 different optics (Q20, Q22, Q26, where the integer part of tune is 20, 22 and 26 and the non-integer part is 0.13 and 0.18 in the H and V plane respectively), exhibiting different betatron and dispersion functions, it was possible to disentangle the contribution of the different non-linear errors. Thus an effective optics model has been built by fitting the

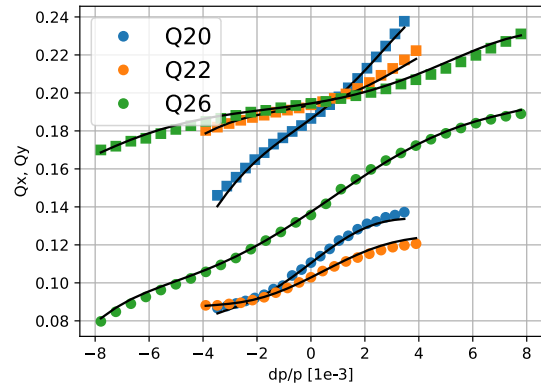


Figure 2: Horizontal (dots) and vertical (square) fractional tune measured during a typical momentum scan for Q20, Q22 and Q26. Because of the different dispersion values in the 3 optics, the dp/p range has been adjusted in order to cover the same radial excursion. The chromaticity computed from the effective model obtained from the fit of the 3 measurements is also shown (black curves).

strength of the multipolar errors in order to reproduce the experimental observations with the 3 different optics. The procedure has been repeated 5 times for different machine configurations, allowing to establish an average model and to evaluate the statistical uncertainties.

To confirm the validity of the effective non-linear model at higher energy, a single chromaticity measurement of the Q26 optics at 270 GeV was acquired and used to fit a model containing the odd multipoles produced by dipoles only. Independent parameters for each multipolar error have been allowed for each of the two different kinds of SPS dipoles, MBA and MBB.

Table 3 shows a comparison of the simplified model measured at 270 GeV against what was measured at injection energy [4]. The two models are found to be compatible, except for the sextupolar component of the MBA dipoles (b_{3a}). However such a discrepancy is likely to be attributed to a calibration error of the sextupoles used to correct chromaticity. The overall good agreement extends the validity of the effective model measured at injection energy to the conditions used for the CC simulations.

Table 3: Multipole Errors from SPS Nonlinear Model

Multipole	26 GeV	270 GeV
$b_{3a}[\text{m}^{-2}]$	$(-2.8 \pm 0.6) \cdot 10^{-3}$	$8.1 \cdot 10^{-4}$
$b_{3b}[\text{m}^{-2}]$	$(1.6 \pm 0.3) \cdot 10^{-3}$	$1.1 \cdot 10^{-3}$
$b_{5a}[\text{m}^{-4}]$	-7.9 ± 0.5	9.2
$b_{5b}[\text{m}^{-4}]$	-6.8 ± 1.5	-10
$b_{7a}[\text{m}^{-6}]$	$(8.8 \pm 2.6) \cdot 10^4$	$1.3 \cdot 10^5$
$b_{7b}[\text{m}^{-6}]$	$(1.7 \pm 0.8) \cdot 10^5$	$1.4 \cdot 10^5$

The effect the CCs have on the DA depends strongly on the CC voltage and the initial $\Delta p/p$ or longitudinal action, z ; particles with large initial $\Delta p/p$ or z will perform large synchrotron oscillations and will therefore experience a larger CC kick variation. Figure 3 illustrates the minimum DA for 1E6 turns in the SPS, in the presence of errors up to b_5 when both CCs are operated with their phase set to 0° ; the CC multipoles were not included since it was demonstrated they have only minor effect on DA (Fig. 1, bottom).

The results depict the effect of a varying voltage per CC, from 0.0 MV to 2.5 MV, and for different longitudinal actions, z_{init} , and $(\Delta p/p)_{\text{init}} = 0$. The lines represent the physical aperture. Note that at $z_{\text{init}} = 200$ mm, i.e. $1 \sigma_z$ at E_{inj} , the physical aperture reduces from 7.63σ in the absence of CC kicks to 3.16σ for 2.5 MV per CC. For $V_{\text{CC}} = 2$ MV the DA is reduced to half for particles with $z_{\text{init}} = 200$ mm. Note that for large z_{init} and CC voltage values the limitation comes from the DA rather than the physical aperture. It should be highlighted that this study is optimistic as the b_7 multipoles were not included.

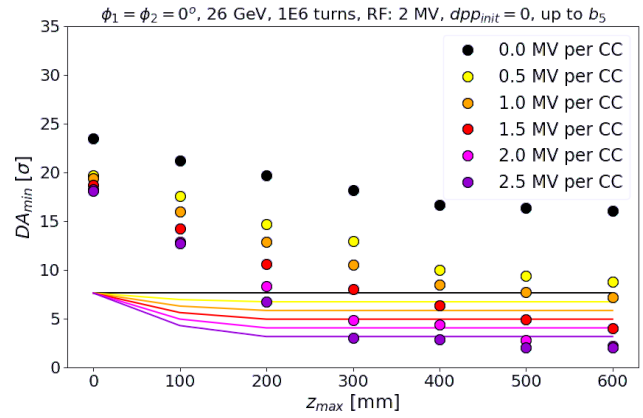


Figure 3: Minimum DA for values of voltage per CC from 0.0 MV to 2.5 MV, for different longitudinal actions, z_{init} and $(\Delta p/p)_{\text{init}} = 0$.

CONCLUSIONS AND FUTURE PLANS

The HL-LHC aims to increase the LHC luminosity by incorporating, amongst others, a CC scheme. The first time that CCs will be used with a proton beam will be in 2018 during the CC SPS experiments, for which two vertical prototype HL-LHC CCs have been installed in the SPS one right next to the other. Simulations were performed to study the DA in the SPS for different beam, CC and machine configurations. In the ideal SPS lattice with chromatic sextupoles, but without including any machine errors, the DA is reduced by a factor of two when the CCs are operated with $\phi_1 = \phi_2 = 0^\circ$ and their maximum voltage of 3.4 MV, whereas it is practically not affected by the CC multipoles.

When including the SPS errors up to b_5 , the DA is reduced significantly to values as low as 5σ . For $V_{\text{CC}} = 2$ MV the DA is reduced to half for particles with an initial longitudinal position of $z_{\text{init}} = 200$ mm (1σ at E_{inj}). The reason for the strong reduction of the DA is under investigation.

REFERENCES

- [1] J. Barranco Garcia *et al.*, “Long term dynamics of the high luminosity Large Hadron Collider with crab cavities”, *Phys. Rev. Accel. Beams*, vol. 19, no. 10, p. 101003, 2016, doi: 10.1103/PhysRevAccelBeams.19.101003
- [2] <http://mad.web.cern.ch/mad/>
- [3] http://sixtrack-ng.web.cern.ch/SixTrack/doc/sixdesk/sixdesk_env.html
- [4] M. Carla, H. Bartosik, M. Beck, K. Li, and M. Schenk, “Studies of a new optics with intermediate transition energy as alternative for high intensity LHC beams in the CERN SPS”, in *Proc. IPAC’18*, Vancouver, British Columbia, Canada, paper TUPAF022, doi:10.18429/JACoW-IAC2018-TUPAF022

FERMILAB – THE PROTON IMPROVEMENT PLAN (PIP)*

F.G. Garcia[†], S. Chaurize, C. Drennan, K. Gollwitzer, V. Lebedev, W. Pellico, J. Reid, C.Y. Tan, R.M. Zwaska, Fermi National Accelerator Laboratory, Batavia, IL 60510, USA

Abstract

The Fermi National Accelerator Laboratory (FNAL) Proton Source is composed of three machines: an injector line, a normal conducting LINAC and a Booster synchrotron. The Proton Improvement Plan (PIP) [1] was proposed in 2011 to address the necessary accelerator upgrades and hardware modification to allow an increase in proton throughput, while maintaining acceptable activation levels, ensuring viable operation of the proton source to sustain the laboratory HEP program. The strategy for increasing the proton flux is achieved by doubling the Booster beam cycle while maintaining the same intensity per cycle. For the Linac, the focus within PIP is to address reliability. A summary of work performed, and respective results will be presented.

INTRODUCTION

Over the past decade, Fermilab has focused effort to increase the average beam power delivered to the neutrino and muon program. PIP was a campaign to perform numerous upgrades to the existing proton source machines. Prior PIP, Booster could provide $1.1E17$ protons per hour, with protons per batch at $4.5E12$ at 7.5Hz with 90% efficiency and 85% uptime. By the end of PIP, Booster can reliably provide $2.4 E17$ protons per hour, with intensity per cycle at $4.5E12$ protons per pulse and beam cycle rate at 15 Hz with 92% efficiency and 90% uptime.

The primary users of a high-intensity proton beam are the 8 GeV Booster Neutrino beamline (BNB), the 120 GeV Neutrino at Main Injector (NuMI) and the muon campus.

HIGH PROTON FLUX OPERATION

Achieving greater than 80 kW beam power from Booster required increasing the repetition rate from 7.5 Hz to 15 Hz while maintaining the same beam intensity per cycle. To accomplish the increase in repetition rate, the Booster RF power system underwent a significant upgrade. Figure 1 shows the proton delivered per day and the integrated protons delivered since 1994 up to 2018.

As can be seen, proton flux has seen a rapid increase with yearly output exceeding the previous.

RF Power System

Of the various contributors to limited repetition rates for the Booster Accelerator, the Booster RF system has often been cited as a primary factor. The reason for that is that the system has never been designed to accelerate beam at the sustained rates now being expected. The fundamental

limitations have been due to RF hardware limitations. To improve the Booster RF reliability, the upgrade of the power amplifier is one of the main efforts inside PIP.

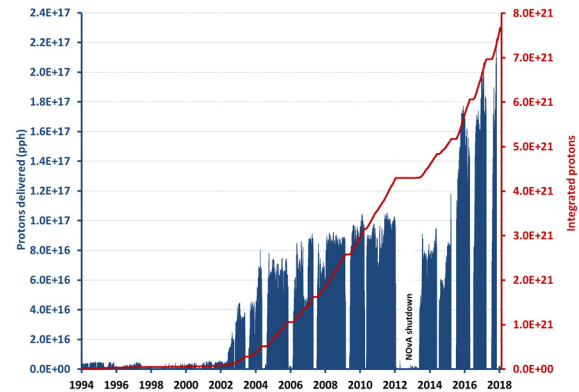


Figure 1: Booster integrated and per day protons delivery.

Cavity and tuner refurbishment The cavity and associated tuners, 3 per cavity, **require** cooling improvements to support higher repetition rates. Each cavity was removed from operation to be inspected, cleaned, tuners re-work, vacuum certified and tested at 15 Hz to certify operations prior to being installed in the tunnel again.

The ferrite tuner cone cooling path had been disconnected many years ago because of water leak history. As part of the refurbishment each tuner needed to be completely disassembled and the cooling channels reworked.

Solid State upgrade The Booster RF system, among its kindred Main **Injector** RF systems, has the oldest equipment and exhibits, not surprisingly, the least reliability. The driver amplifier tubes and the Cascode sections of the cavity mounted Power Amplifier (PA) was especially vulnerable to more frequent failures. The repair of the RF system was also compromised by the increased activation of components.

The greatest RF system reliability came with the complete installation of a solid-state RF driver and new Modulator in the equipment galleries and a new final stage amplifier at the enclosure cavity.

Notch and Cogging Upgrades

The Booster notch system is used to create a gap (aka “notch”) in the beam for the extraction kickers. The phase I for this upgrade was to move the notch kickers and install a beam absorber for the notched beam. At 15 Hz the total beam power lost predicted in the tunnel is 270 W.

As a phase II of this upgrade, a new complement of 6 short kickers with respective new power supplies replaced the existing system. This allowed the relocation of the operational losses created by the notch into the absorber. Further efforts were pursued and successfully implemented

* Work supported by Fermi Research Alliance, LLC under Contract No. DE-AC02-07CH11359 with the U.S. Department of Energy, Office of Science, Office of High Energy Physics.

[†] fgarcia@fnal.gov

Content from this work may be used under the CC BY 3.0 licence (© 2018). Any distribution of this work must maintain attribution to the author(s), title of the work, publisher, and DOI.

which allowed the complete elimination of the notch creation in the Booster tunnel. This system is the Linac Laser Notch system, which will be described below. Nevertheless, this system is used as a secondary resource to clean the abort gap even further.

The cogging system was improved to reduce the manipulation of the radial orbit. The new scheme utilizes all of the 48 horizontal dipole correctors locations to change the magnetic field during the acceleration cycle. The gap creation was used to be at 700 MeV with the RF cogging system and it was moved to 400 MeV as shown in Fig. 2. Reducing the beam losses at the notch creation by 40% and the total cycle loss by 15%.

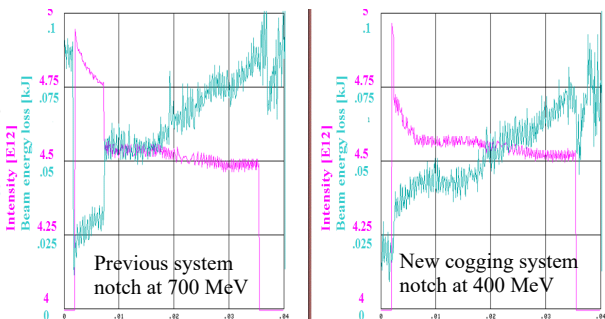


Figure 2: Magnetic Cogging system before (left) and after (right) update.

Laser Notch

A laser notch system [2] was built to create the notch within linac beam pulse at 750 keV, where activation issues are negligible. The laser system design has three stages of fiber and two stages of solid state amplification. This creates a burst of spatially a temporally uniform 200 MHz pulses, each with 2 mJ of energy to match ion bunch structure out of the RFQ to create a set of notches in the linac pulse at the Booster revolution period. Figure 3 shows the effect on the Booster beam losses when the linac laser notch system is OFF and ON.

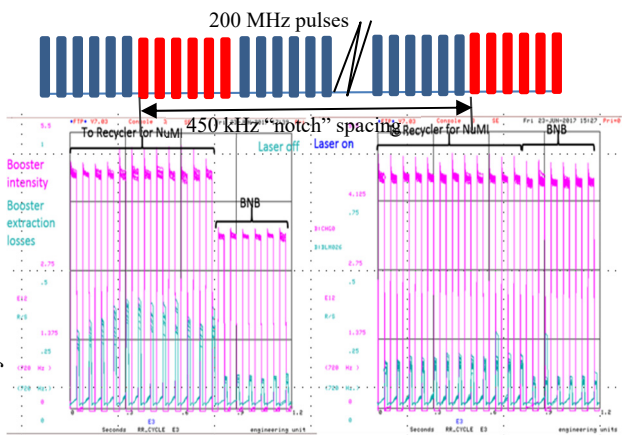


Figure 3: Linac Laser Notch system pulse pattern and impact on beam losses in Booster when the system is (OFF) and (ON).

Perpendicular Bias Second Harmonic Cavity

A perpendicular bias second harmonic RF cavity [3] (Fig. 4) is currently being constructed for use in the Fermilab Booster. The cavity will operate at $\sim 76 - 106$ MHz, twice the fundamental RF frequency, but will be turned on only during injection, and transition or extraction. Its main purpose is to reduce beam loss in Booster. After three years of optimization and study, the cavity design has been finalized and most of the parts are being manufactured and will be installed during the lab-wide summer 2018 shutdown.

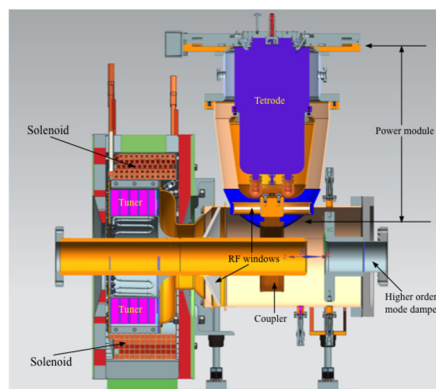


Figure 4: Cross sectional view of the 2nd harmonic cavity.

VIABILITY AND RELIABILITY

PIP strategy to address viability and reliability is to replace systems with obsolete parts and significant contributions to machine downtime. This front has been the focus for the pre-accelerator and the linac machines.

Injector Line

Since 1978, The Fermilab injector line consisted of two 750 keV Cockcroft-Walton accelerators and two magnetron H- sources. Based on the successful design at BNL (Brookhaven National Laboratory), under PIP, the injector was upgraded with a 200 MHz RFQ [4] (Radio Frequency Quadrupole) in 2012. The new design is divided into three parts: the ion source, the low energy beam transport (LEBT) and the medium energy beam transport (MEBT).

The ion source contains two H- magnetron at 35 keV and beam current around 60 mA with a power efficiency of about 60 mA/kV.

The LEBT optics is a standard one where two solenoids are separated by a short distance so that the beam at the source and at the entrance of the RFQ are at the focal points of each solenoid. In this region, an Einzel lens is installed near the entrance of the RFQ and will be used as a chopper system.

The MEBT lattice is composed of two quadrupole doublets and a buncher cavity.

With the new injector line, beam capture in the linac improved by nearly 30%.

Linac

The FNAL Linac accelerator accelerates H⁻ ions from 750 keV to 400 MeV. The low energy Linac section, built

in 1969, uses 201.25 MHz Alvarez drift tube cavities powered by a 5 MW triode power tube (therein referred as 7835) accelerating beam up to 116 MeV, while the high energy section uses 805 MHz side coupled cavities powered by a klystron to boost the beam energy from to 400 MeV.

Solid State upgrade The Linac RF drive system consisted of variety of solid **state** amplifier, pentode, tetrode and triode vacuum tubes. The DTL system used over 75 tubes from 10 different vendors to operate. Under PIP, the tube consumption was reduced by 70% with upgrade to solid state technology.

200 MHz RF system The 201.25 MHz RF power system was a major concern for many years in regards long term operational reliability and viability. The issue is specialized maintenance required and extensive downtime generated by this system, specially the hard tube modulator. The risk is that power tubes could become unobtainable to support operations and additional vacuum tube could become obsolete. PIP strategy was to build-up a 4-year in-house inventory of the 7835, develop a workable plan to replace the final amplifier in case the tube line is discontinued and replaced the high voltage modulator with present day technology. For the former, a 200 MHz, 5 MW, 15 Hz klystron tube was developed as a viable solution for the replacement of the 7835 triode while a for the later, an in-house design of a 35 kV, Marx-topology modulator to drive the triode was developed. This will be discussed further below.

Marx Modulator The original high voltage modulator for the 7835 power amplifier (PA) was the major source of downtime, accounting for over 50% of the downtime in the last 15 years. The Linac modulator was built in the late 1960's, used vacuum switch **tubes**, discontinued in the early 2000s, to provide pulsed voltage to the anode of the 7835 PA. Furthermore, most of the relays, power supplies, diagnostics, and interlocks circuits, were obsolete and increasingly difficult to maintain. Within PIP, the strategy to mitigate the reliability issue was to replace the hard-tube modulator with a modern solid-state modulator which improves reliability, lower operational costs while maintaining the same waveform accuracy required to accelerate the beam.

The new modulator design topology was developed by the Fermilab Accelerator Division Electrical Engineering Department (AD/EE) [5]. A sub-set of the most critical Marx-Modulator parameters are shown in Table 1.

Table 1: Marx Modulator Main Parameters

Parameter	Value	Units
Maximum voltage	35	kV
Maximum current	375	A
Voltage regulation	±25	V
Pulse Repetition Rate	15	Hz
Maximum pulse width	460	µs
Minimum slew rate	15	kV/µs
Rise/Fall time	50-150	µs

Marx-modulator works by charging individual cells in parallel and discharging in series. The power is delivered to each cell via charging diodes and filter network. There is a total of 54 cells and they are divided into two categories: i) 42 switching cells which are used to create the basic waveform and produce the fast beam pulse rise/fall time and ii) 12 regulating cells which are sued to compensate for capacitor droop and provide the necessary beam top tilt. In Fig. 5, an illustration of the waveform is shown.

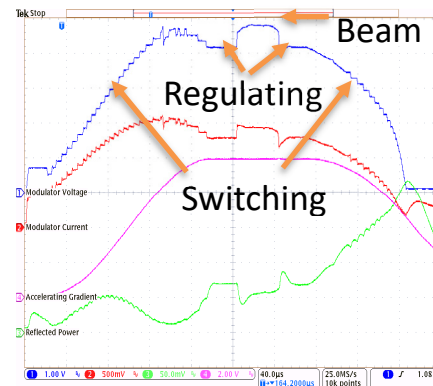


Figure 5: Linac Marx-Modulator typical waveform.

As of the date of this paper, 3 of the 5 DTL RF stations have been upgraded to Marx-Modulator. Figure 6 shows a comparison before and after of the beam pulse-by-pulse variation.

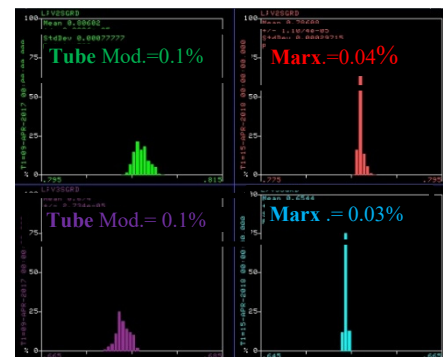


Figure 6: Gradient stability before (left) and after (right) Marx-Modulator upgrade.

CONCLUSION

The Proton Source has been the workforce of the Fermilab experimental physics program. Injector and Linac is expected to continue be operational at least until middle 2020's when a new higher energy linac is supposed to be operational, but Booster is expected to continue be operational for at least 2 more decades. PIP successful reached all its original goals and is on track to be complete by the end of calendar year 2018.

ACKNOWLEDGEMENTS

This work would not have been possible without the dedication and tireless efforts of many members of the Proton Source Department, Accelerator Division Support Department, Accelerator Physics Center (APC), Technical Division and Particle Physics Division (PPD). The author is grateful for helpful discussion with Salah Chaurize, William Pellico, David Johnson, Trevor Butler.

REFERENCES

- [1] W. Pellico, *et al.*, "The Proton Improvement Plan", in *Proc. IPAC'14*, Dresden, Germany, Jun. 2014, p. 3409, paper THPME075.
- [2] D. Johnson, "MEBT Laser 11Notcher (Chopper) for Booster Loss Reduction", presented at HB2018, Daejeon, Korea, paper THP1WC01, this conference.
- [3] R. Madrak, "The FNAL Booster Second Harmonic RF Cavity", presented at HB2018, Daejeon, Korea, paper THP2WC01, this conference.
- [4] C.Y. Tan, D.S. Bollinger, K.L. Duel, J.R. Lackey, W.A. Pellico, "The FNAL Injector Upgrade", FERMILAB-CONF-11-072-AD.
- [5] T.A. Butler, F.G. Garcia, M.R. Kufer, H. Pfeffer, D. Wolff, "Design of a Marx-Topology Modulator for FNAL Linac", FERMILAB-CONF-15-094-AD, arXiv:1504.07589.

STUDIES OF TRANSVERSE INSTABILITIES IN THE CERN SPS

M. Beck^{*1}, H. Bartosik, M. Carlà, K. Li, G. Rumolo, M. Schenk², CERN, Geneva, Switzerland
 Ursula van Rienen, University of Rostock, Rostock, Germany
¹also at University of Rostock, Rostock, Germany
²also at EPFL, Lausanne, Switzerland

Abstract

In the framework of the LHC Injectors Upgrade (LIU), beams with about twice the intensity compared to the present values will have to be accelerated by the CERN SPS and extracted towards the LHC. Machine studies with intensity higher than the nominal LHC beam have shown that coherent instabilities in both transverse planes may develop at injection energy, potentially becoming a limitation for the future high intensity operation. In particular, a transverse mode coupling instability is encountered in the vertical plane, the threshold of which can be sufficiently increased by changing the machine optics. In addition, a headtail instability of individual bunches is observed in the horizontal plane in multi-bunch operation, which requires stabilization by high chromaticity. The PyHEADTAIL code has been used to check if the present SPS impedance model reproduces the experimental observations. The instability growth rates have been studied for different machine optics configurations and different chromaticity settings. In addition, other stabilizing mechanisms like tune spread from octupoles or the transverse damper have also been investigated.

INTRODUCTION

To achieve higher luminosity in the experiments of the Large Hadron Collider (LHC), CERN has launched the High Luminosity LHC (HL-LHC) project [1]. To satisfy the increased demands of the collider, the LHC injectors have to be adapted. These modifications are warped up in the LHC Injector Upgrade (LIU). For the Super Proton Synchrotron (SPS), the last injector in the LHC injector chain, the intensity accelerated after the upgrade is supposed to nearly double with respect to currently operated intensities.

The Transverse Mode Coupling Instability (TMCI) represents one of the most important intensity limitations in the SPS at injection. Before the LHC era the SPS was operated with the so called Q26 optics with an integer tune of 26 and characterized by its low TMCI threshold would have limited the maximum intensity delivered to the LHC. To improve the intensity threshold, enabling operation with LHC intensities and even leaving margins for future intensity goals, the low gamma transition optics, the Q20 optics with an integer tune of 20, were introduced. However, the low gamma transition in combination with LIU intensities leads to an increased beam loading that probably cannot be compensated by the RF power amplifiers, not even after the upgrade of the RF system foreseen by LIU [2]. Therefore, a Q22 optics with an integer tune of 22 and intermediate transition energy has

been proposed, relaxing the demands on the RF power amplifiers but also leading to a intermediate stability threshold. The intensity threshold the TMCI imposes has already been studied for the Q26 and the Q20 optics [3]. Here, for the first time, it has been investigated in depth for the newly proposed Q22 optics.

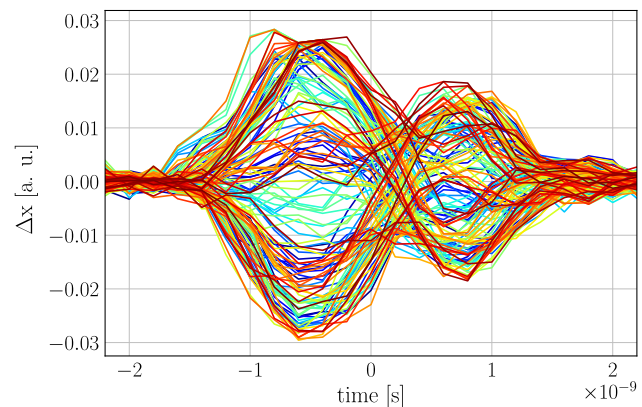


Figure 1: Measured horizontal mode 1 instability. The amplitude of the instability is plotted over time with respect to the center of the bucket over 140 consecutive turns.

In the present injector chain configuration the LIU intensity cannot be reached therefore the only way to predict the behavior of the machine after the upgrade is simulations. In the case of the SPS mainly beam dynamics simulations in PyHEADTAIL [4] are used. These simulations rely on models of the machine. Due to its small vertical aperture, transverse instability studies in the SPS historically concentrated on the vertical plane. To verify the models of the horizontal plane a measurement campaign has been launched. In recent high intensity multi-bunch runs in the SPS a horizontal single-bunch instabilities (see Fig. 1) were observed and are currently being studied and characterized. As the horizontal plane could become a potentially limiting factor, the campaign to verify the horizontal models has been extended to also investigate high intensity instabilities and possible damping mechanisms. Its current status is presented here. The horizontal studies concentrate on the Q20 optics as that is the baseline for LIU [2].

TMCI MEASUREMENTS

The TMCI intensity threshold can be estimated by Eq. 1 [5]. It is dependent on the machine radius R and revolution frequency ω_0 , the slippage factor η , the longitudinal emittance ϵ_z , the transverse betatron function β_y , vertical chromaticity Q'_y and on Z_y^{BB} the broadband impedance res-

* mario.beck@cern.ch

Content from this work may be used under the terms of the CC BY 3.0 licence (© 2018). Any distribution of this work must maintain attribution to the author(s), title of the work, publisher, and DOI.

onator model of the machine and its resonance frequency ω_r .

$$N_{thr}^{TMC} = \frac{16\sqrt{2}}{3\pi} \frac{R|\eta|\epsilon_z}{\beta_y e \beta^2 c} \frac{\omega_r}{|Z_y^{BB}|} \left(1 + \frac{Q'_y \omega_0}{\eta \omega_r} \right) \quad (1)$$

The influence of the changeable machine parameters on the threshold is investigated here.

For the measurements, the optics are set up with a slightly positive vertical chromaticity ($Q'_y = 0.7$) to ensure the suppression of the mode zero head-tail instability excited at negative chromaticity. The nominal value of 2.7 MV for the RF voltage was found scaling the voltage used in the Q20 optics with the ratio of the gamma transitions. The nominal longitudinal emittance for the measurements is $\epsilon_z = 0.32$ eVs.

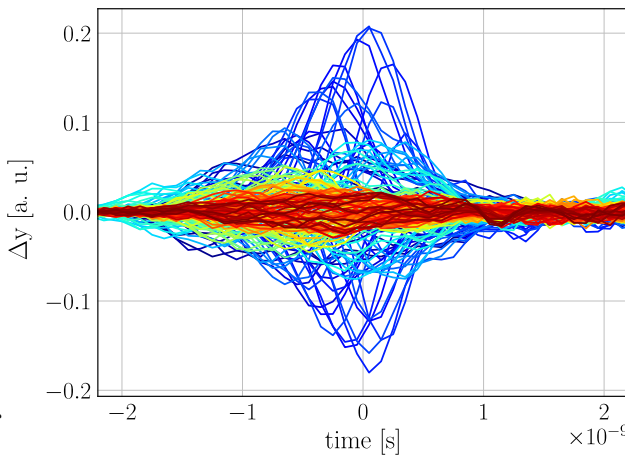


Figure 2: Measured TMCI in the vertical plane. The amplitude of the instability is plotted over time with respect to the center of the bucket over 200 consecutive turns.

The TMCI threshold is measured by injecting a single bunch into the SPS and ramping up its intensity over consecutive shots. The intensity measured in the SPS after 200 ms by the beam current transformer, is then compared to the intensity extracted from the Proton Synchrotron (PS), its injector. Whenever the intensity in the SPS is significantly lower, a very fast TMCI is observed. The head-tail monitor then shows the typical traveling wave pattern as displayed in Fig. 2.

Influence of Emittance

First the machine is run with nominal longitudinal emittance ($\epsilon_z = 0.32$ eVs). The TMCI threshold for this case is found at 2.5×10^{11} protons per bunch (ppb) as shown in Fig. 3.

For the next measurement the emittance is changed by reducing the RF-bucket size in the PS-Booster, the second accelerator in the CERN proton accelerator chain. Figure 4 shows a TMCI threshold of about 1.7×10^{11} ppb for a longitudinal emittance of 0.22 eVs. The linear dependency predicted by Eq. 1 is confirmed as the ratio of emittance to intensity threshold is constant for both emittance measurements.

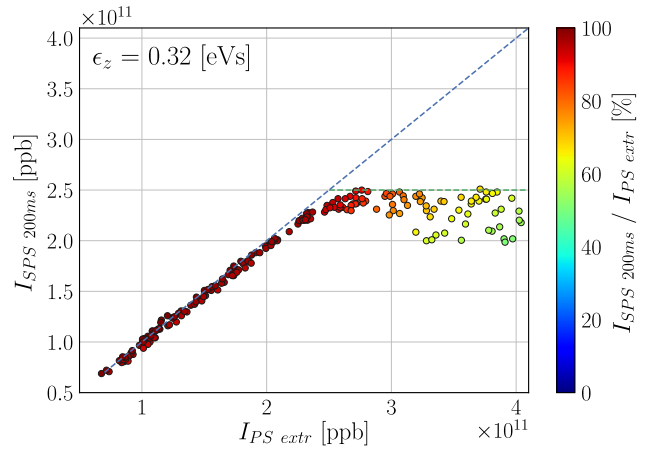


Figure 3: Intensity in the SPS left 200 ms after injection over the intensity extracted from the PS. Color-coded is the percentage of particles left in the SPS after 200 ms with respect to the number of particles extracted from the PS. The green dashed line represents the TMCI threshold obtained from the measured data.

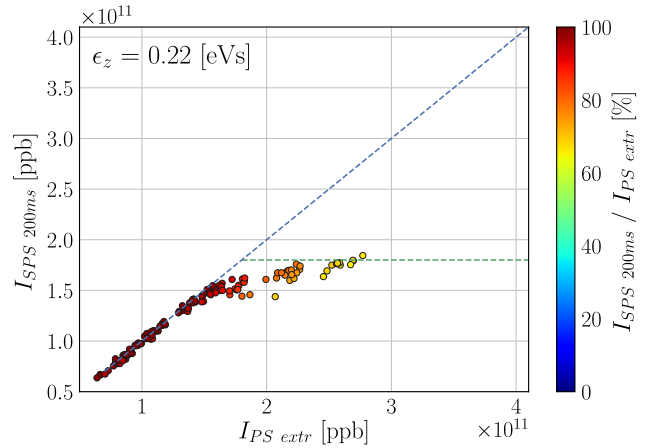


Figure 4: Intensity in the SPS left 200 ms after injection over the intensity extracted from the PS. Color-coded is the percentage of particles left in the SPS after 200 ms with respect to the number of particles extracted from the PS. The green dashed line represents the TMCI threshold obtained from the measured data.

Influence of RF Voltage

A change of the cavity RF voltage influences the synchrotron motion of the particles, which affects the TMCI threshold. A particle with faster synchrotron motion is affected by the coupling modes for a shorter time, leading to a slower instability development.

$$\epsilon_z = 4\pi \frac{Q_s}{\eta R} p_0 \sigma_z^2 \quad (2)$$

The longitudinal emittance is linearly dependent on the synchrotron tune Q_s (Eq. (2) [6]) which scales with the square

root of the RF voltage V (Eq. (3) [6]).

$$Q_s = \sqrt{\frac{eV\eta h}{2\pi E_0\beta^2}} \quad (3)$$

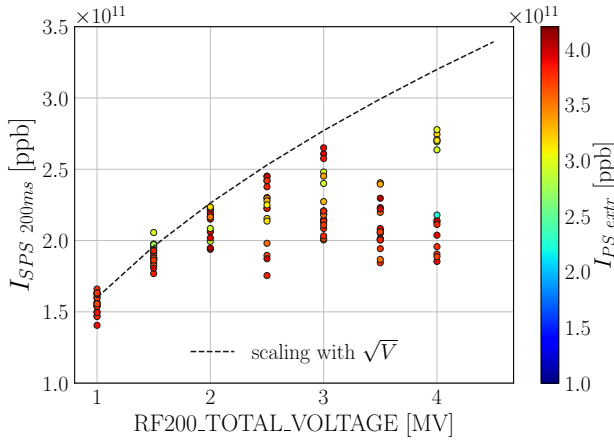


Figure 5: Intensity in the SPS left 200 ms after injection over the RF voltage of the SPS main cavities (RF200). Color-coded is the number of particles extracted from the PS. The dashed black line scales with the square root of the voltage.

As expected, the measurements show a square root dependency of the threshold on the RF voltage (see Fig. 5). This scaling does not hold for voltages over 3 MV as injection losses already dominate in this case.

Influence of Chromaticity

The TMCI threshold is dependent on the chromaticity (Eq. (1)). To confirm this dependency different values of Q'_y have been probed for their threshold.

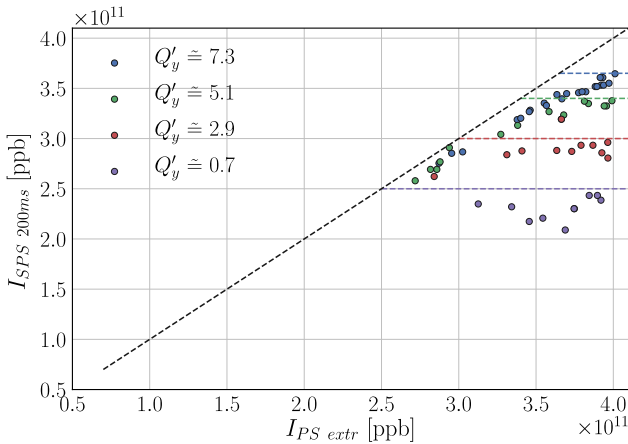


Figure 6: Chromaticity scan. Again the intensity in the SPS left 200 ms after injection is plotted over the intensity extracted from the PS. Shots with different chromaticity are represented with different colors.

The results of this scan shown in Fig. 6 confirm the prediction. The threshold is clearly increased for higher chromaticity values.

Compare Measurements with Simulations

To compare the measurements with PyHEADTAIL a scan over intensity and emittance has been executed. The results are shown in Fig. 7. A general behavior where lower emittance results in a lower TMCI threshold is observed. The lower the emittance the lower the TMCI threshold. As TMCI is an extremely fast instability it was not possible to fit its growth-rate. Here the ratio of intensity measured in the SPS after 200 ms and the intensity extracted from the PS is used as a substitute.

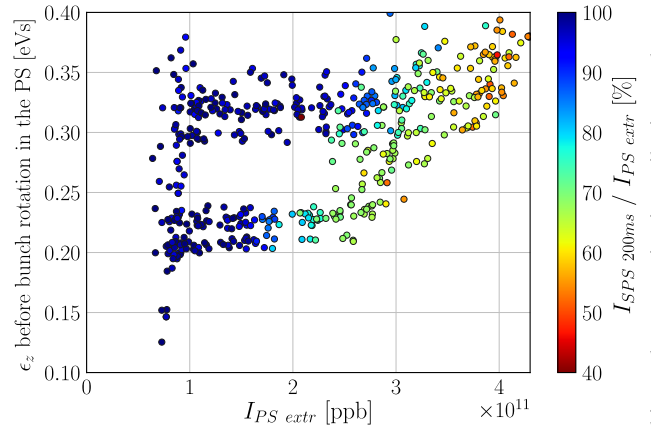


Figure 7: Measured longitudinal emittance against intensity extracted from the PS. Color-coded is the percentage of particles left in the SPS after 200 ms with respect to the number of particles extracted from the PS.

The simulations of the TMCI threshold in PyHEADTAIL are done employing the same parameter values as used for the measurement in the machine. Simulations (Fig. 8) and measurements show a good agreement. Even if the growth-rate is compared to the ratio between particles after 200 ms in the SPS and particles extracted from the PS, the general behavior of the TMCI threshold is well reproduced. On the other hand, the island of slow growth-rate seen in Fig. 8 could not be observed in measurements.

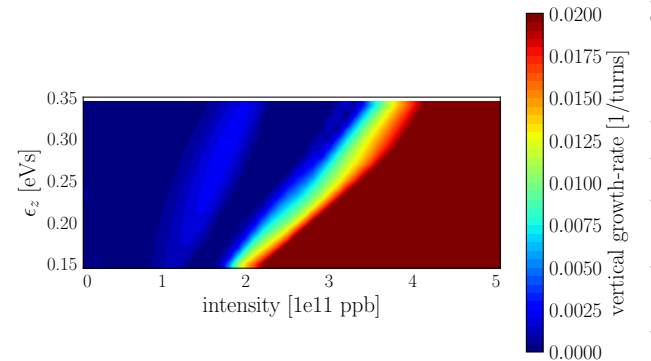


Figure 8: Simulated scan of the longitudinal emittance against intensity. Color-coded is the vertical growth-rate of occurring instabilities.

Beam Condition After TMCI

To investigate the beam condition after the occurrence of TMCI, emittance studies have been done. For this purpose, horizontal and vertical rotational wire scanners are used in the SPS to measure the emittance of a beam developing TMCI. A rotational wire scanner measures the emittance two times, once swinging into the beam and once going back to its parking position. Unfortunately, as the TMCI is very fast, it was not possible to measure the emittances before and after the instability. Therefore the emittance of shots with intensities below the TMCI threshold are compared to the shots with intensities above it.

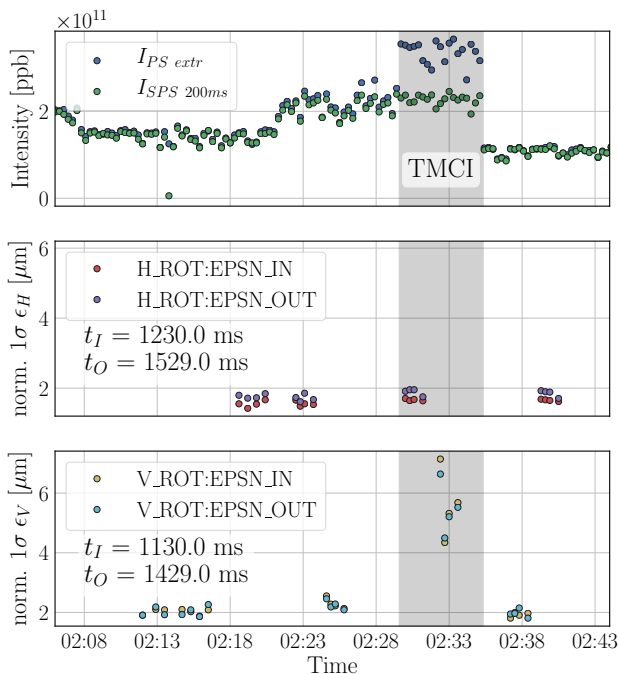


Figure 9: Intensity history and rotational wire-scans in horizontal and vertical plane over time. t_I and t_O denote the time in the SPS cycle when the in- and outgoing scan took place (injection at 1015 ms).

In Fig. 9 the results of the measurements are plotted. The blow-up in the vertical plane due to the instability is clearly observed. The emittance in the horizontal plane is not changed by the instability.

STUDIES OF THE HORIZONTAL PLANE

The influence of the damper and the linear chromaticity on instabilities in the horizontal plane has already been published in [7]. For the future operation of the SPS with LIU intensities the octupole could become an important tool to keep the beam stable. The stabilization mechanism is based on the amplitude detuning introduced by the octupoles. That crates a tune spread leading to Landau damping. The focus here lies on the effect the octupoles have on instabilities in the SPS.

Octupole Studies

The possibility to stabilize the beam using octupoles has been investigated in measurements. In this case single bunches with intensities of $2e10$ ppb are used. While the vertical chromaticity was kept at a positive value, the horizontal chromaticity was set to -2 to provoke a mode zero head-tail instability in the horizontal plane. The aim is to cure this instability using the octupoles.

Three groups of Landau octupoles in the SPS are used for the measurements; the group next to the focusing quadrupoles (LOF) the one next to the defocusing quadrupoles (LOD) as well the Landau octupoles for extraction (LOE). As the LOE are not used during operation anymore, not all of them are connected to a power supply. For these studies only the octupoles LOE1202 and LOE3302 were used. They are situated in regions with a small horizontal dispersion so that they mainly create amplitude detuning and hardly any second order chromaticity. The LOF act mainly on the horizontal plane, the LOD mainly on the vertical plane.

First a scan over the magnetic strength value K of the LOFs is done (blue curve in Fig. 10). For absolute K_{LOF} values of 6 m^{-4} the instability is damped. However, the LOFs do not only produce amplitude detuning (a_{xx}) but also second order chromaticity (Q''_x) in the horizontal plane. To investigate the damping mechanism, only a_{xx} respectively only Q''_x shall be introduced. The optics simulation software MADX [8] and the optics model of the SPS are used to calculate K values for the LODs, LOFs and LOEs to compensate a_{xx} respectively Q''_x in the machine.

To measure the effect of Q''_x on the mode 0, the general idea is to set up the LOEs to compensate the a_{xx} introduced by the LOFs and the LODs to compensate the introduced amplitude detuning cross term a_{xy} . For a scan over second order horizontal chromaticity a set of values for all three octupole groups is calculated with MADX. For every measurement point Q''_x is set to the value needed as well as a_{xx} and a_{xy} to zero. To crosscheck a_{xx} has been verified to be compensated well at different settings of Q''_x . The results of this Q''_x scan results in the green curve in Fig. 10. The curve follows remarkably well the blue curve of the K_{LOF} scan in the same figure. This leads to the impression that the damping of the LOFs is mainly due to the second order chromaticity.

For the scan over a_{xx} the compensation strategy is different; the LOEs are used to create the a_{xx} as they produce only little Q''_x . a_{xy} is then compensated mainly by the LODs (supported by the LOFs). MADX is used again to determine K values producing the desired amount a_{xx} with zero Q''_x and a_{xy} . To compare the results to the K_{LOF} scan MADX is also used to calculate the K values that would be needed for the LOFs to produce the same a_{xx} values (the effects of Q''_x and a_{xy} these values introduce, too are ignored). The horizontal chromaticity during the last measurement was -1.3 , which produces a mode zero with a lower growth-rate. That is the reason for the lower value of the a_{xx} scan curve

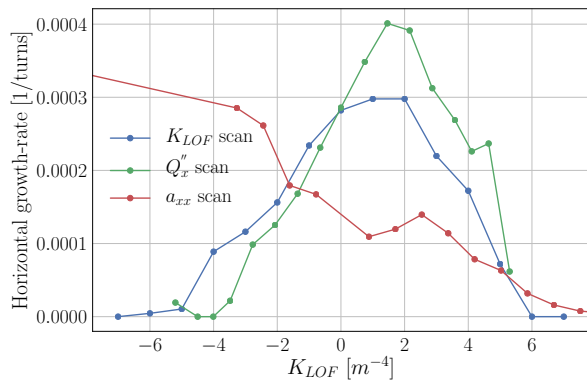


Figure 10: Octupole scan for different settings. The measured growth-rate is plotted over the the K_{LOF} value set. For the Q_x'' / a_{xx} scan the LOE and LOD octupoles have been used to compensate the a_{xx} / Q_x'' produced by the LOF. The growth-rate for every measured point is averaged over multiple shots.

in Fig. 10 for deactivated octupoles ($K_{LOF} = 0 \text{ m}^{-4}$). For the two other scans (with $Q_x' = -2$) the values obtained without octupoles are nearly identical, speaking for a good quality of the measurement.

For positive values of K_{LOF} up to 6 m^{-4} the second order chromaticity seems to drive the beam unstable, working against a_{xx} . Negative amplitude detuning values do not seem to be able to stabilize the beam meaning that for negative values Q_x'' is the stabilizing mechanism. A possible explanation for the inability of negative a_{xx} to stabilize the beam that is the tune spread introduced by the amplitude detuning enlarges an existing tune spread driving the beam into a resonance. This would also explain the losses observed during the measurements. For that reason simulations are very complicated and still ongoing.

CHECKING THE IMPEDANCE MODEL

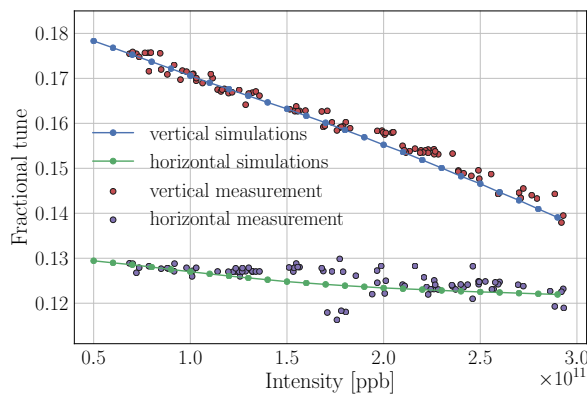


Figure 11: Scan of the fractional tune over the intensity for the Q20 optics. Simulations are compared to the measured fractional tune of shots with different intensities.

To be sure that the impedance model of the simulations is correct and to keep track of the changes in the machine, verification measurements were executed. In [7] the effect of first order chromaticity on a provoked instability has been

investigated and the results were compared to the model finding a good agreement and confirming the impedance model. Here the fractional tune in both planes has been measured for different intensities and compared to simulations. The settings of the machine were reproduced in simulations and compared to the measurements.

Figure 11 shows the results. The simulations reproduce the measurements in both planes. The fluctuation of the measured values around the simulation is due to measurement error and the fact that the limited number of turns used to determine the fractional tune.

CONCLUSION

To crosscheck the SPS impedance model, tune shift versus intensity scans have been compared to measurements. The good agreement speaks for a highly realistic machine model. The effect of the SPS octupoles on a deliberately created beam instability has been investigated in measurements. The different damping mechanisms introduced by the octupoles have been also looked at separately by compensating the others. The TMCI threshold of the newly proposed Q22 optics has been studied in depth for the first time and was found at 2.5×10^{11} ppb. Furthermore the dependency of the threshold on multiple parameters has been investigated.

REFERENCES

- [1] G. Apollinari, I. Béjar Alonso, O. Brüning, M. Lamont, and L. Rossi, “High-Luminosity Large Hadron Collider (HL-LHC): Preliminary Design Report”, CERN Yellow Reports: Monographs. Geneva: CERN, 2015, <http://cds.cern.ch/record/2116337>
- [2] H. Damerou, A. Funken, R. Garoby, S. Gilardoni, B. Goddard, K. Hanke, A. Lombardi, D. Manglunki, M. Meddahi, B. Mikulec, G. Rumolo, E. Shaposhnikova, M. Vretenar, and J. Coupard, “LHC Injectors Upgrade, Technical Design Report, Vol. I: Protons,” Tech. Rep. CERN-ACC-2014-0337, Dec 2014, <http://cds.cern.ch/record/1976692>
- [3] H. Bartosik, G. Iadarola, Y. Papaphilippou, G. Rumolo, B. Salvant, and C. Zannini, “TMCI thresholds for LHC single bunches in the CERN SPS and comparison with simulations,” no. CERN-ACC-2014-0119, p. 4 p, Jun 2016, <http://cds.cern.ch/record/1742183>
- [4] PyHEADTAIL, <https://github.com/PyCOMPLETE/PyHEADTAIL>
- [5] H. Bartosik, Y. Papaphilippou, and M. Benedikt, “Beam dynamics and optics studies for the LHC injectors upgrade,” Oct 2013, presented 13 Nov 2013, <http://cds.cern.ch/record/1644761>
- [6] A. W. Chao and M. Tigner, *Handbook of Accelerator Physics and Engineering*. Singapore: World Scientific, 1999, <https://cds.cern.ch/record/384825>
- [7] M. Beck, H. Bartosik, M. Carla, K. Li, G. Rumolo, M. Schenk, and U. van Rienen, “Studies of Horizontal Instabilities in the CERN SPS,” in *Proc. IPAC'18*, Vancouver, BC, Canada, 2018, doi:10.18429/JACoW-IPAC2018-THPAF034
- [8] MADX, <http://mad.web.cern.ch/mad>

Content from this work may be used under the terms of the CC BY 3.0 licence (© 2018). Any distribution of this work must maintain attribution to the author(s), title of the work, publisher, and DOI.

PROGRESS AND PLAN OF THE FAST PROTECTION SYSTEM IN THE RAON ACCELERATOR

Hyunchang Jin*, Yongjun Choi, Sangil Lee

Rare Isotope Science Project, Institute for Basic Science, 34047 Daejeon, Korea

Abstract

In the RAON accelerator, beams generated by ion sources like ECR-IS or ISOL are accelerated to an energy of up to 200 MeV/u before reaching the laboratory target, and the beam power reaches up to about 400 kW at that moment. During transportation of such a beam, if beam loss occurs due to a device malfunction or a sudden change in beam condition, the accelerator can be severely damaged. Therefore, we have developed a machine protection system to protect the devices by minimizing the damage and to operate the accelerator in safe. As part of the RAON machine protection system, a FPGA-based fast protection system (FPS) that can protect devices within a few tens of microseconds after detecting the moment of beam loss has been developed since 2016. The development and test of the FPS prototype was successfully completed last year, and we are now preparing for mass production of the FPS. Here we will present the progress of the FPS development and the future plan for the FPS in the RAON accelerator.

INTRODUCTION

RAON accelerator produces beams with high energy and high power for a variety of scientific experiments [1]. However, unexpected factors can cause beam loss during delivery of these beams to the laboratories, which can lead to severe damage to the accelerator equipment. To minimize the damage, we have been developing a machine protection system (MPS). As shown in Fig. 1, the RAON MPS protects the accelerator by stopping the beam after collecting interlock signals from each device. This MPS consists of a fast protection system (FPS) and a slow interlock system (SIS) depending on the response time of the interlock signal. The field-programmable gate array (FPGA) based FPS responds to interlock signals within a few tens of microseconds and the programmable logic controller (PLC) based SIS within a few tens of milliseconds. There are also the run permit system (RPS) and the post-mortem system (PMS) for more stable and efficient operation of the MPS. The RPS is operated based on EPICS, and it is a system to determine the beam operation by checking information corresponding to machine mode and beam mode before starting the accelerator operation. The PMS is a system which identifies and analyzes the reason of the beam loss.

In the next chapters, we are going to explain the development status and the plan of the FPS, which plays the most important role in the MPS. To achieve faster processing speed, the FPS requires the FPGA based fabrication, and thus the prototype development was started from 2016 and

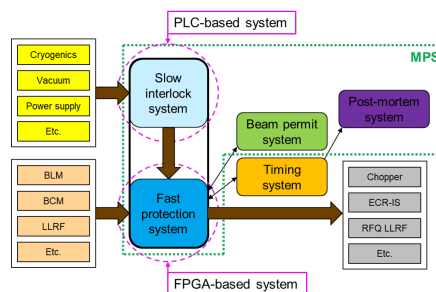


Figure 1: Layout of the RAON machine protection system, which consists of the fast protection system, the slow interlock system, the run permit system, and the post-mortem system.

completed by early 2017. After testing with individual devices, the beam test was successfully finished in fall of 2017, and the FPS product is currently being developed based on the prototype. The FPS product, which will be completed at the end of 2018, will be installed in the accelerator gallery after 2019, and the commissioning will be continued.

FAST PROTECTION SYSTEM PROTOTYPE

The FPS prototype was made by using five ZC706 evaluation boards and consists of one mitigation node, three acquisition nodes, and one event generator as shown in Fig. 2. The acquisition node acts as a slave that collects interlock signals from each accelerator equipment and sends an interlock information to the mitigation node. The mitigation node acts as a master to send signals to the devices that stop the beam when it detects an interlock signal. In the prototype, the EPICS IOC is run on an external PC and the collected information from the mitigation node can be monitored and controlled with the CS-Studio (CSS).

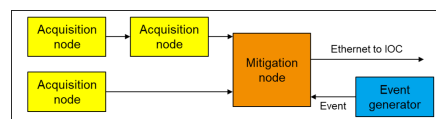


Figure 2: Block diagram of the fast protection system prototype. It consists of one mitigation node, three acquisition nodes, and one event generator.

The prototype was individually tested with the the SIS prototype, the AC current transformer, and so on. After that, the beam test was successfully carried out at the RISP SCL demo [2] by generating an interlock signal during actual beam operation and stopping the beam with the LEPT chop-

* hcjin@ibs.re.kr

per. Figure 3 shows the beam current before and after the FPS activation at the SCL demo. With several tests, the FPS prototype performance was verified. The details of the FPS prototype was presented at the ICABU 2017 workshop [3]. Based on the prototype results, we have been developing the FPS product using Xilinx zynq chip.

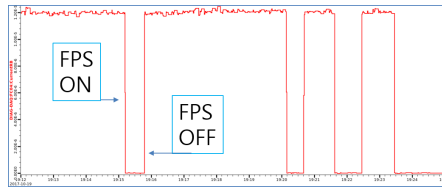


Figure 3: Beam test result of the fast protection system prototype at the RISP SCL demo.

DEVELOPMENT OF FAST PROTECTION SYSTEM

Prior to the mass production of the FPS, one chain consisting of one mitigation node and seven acquisition nodes as shown in Fig 4 are under developing. Each acquisition node can collect 64 interlock signals, and the collected information is finally transmitted to the mitigation node. The FPS based on the zynq chip can expect the fast signal processing by using a programmable logic (PL), and a processing system (PS) can drive an EPICS IOC with the petalinux system.

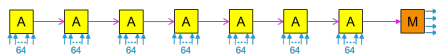


Figure 4: Layout of one chain in the FPS. It is composed of one mitigation node and seven acquisition nodes.

The configuration of the mitigation node is shown in Fig 5. The mitigation node is designed to transmit information from the acquisition nodes through the optical cable of 5 Gbps speed and send the signal to the chopper, RFQ LLRF etc. to stop the beam when an interlock signal is generated. Eight SFP+ transceivers are installed for the optical communication with acquisition nodes and an event generator, and a zynq XCZU9EG chip is used to implement the FPS function. Also Ethernet, USB, UART, and JTAG ports are supported for external interfaces. Twenty four SMA connectors are installed to transmit signals to the beam stopping devices.

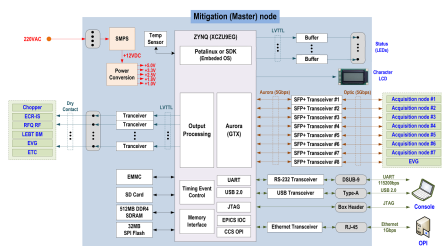


Figure 5: Configuration of the FPS mitigation node.

Unlike the mitigation node, the acquisition node does not require high specification, so the ZYNQ XC7Z100 chip is used. Four SFP+ transceivers are installed for the optical communications, and an interface terminal block is installed for collecting 64 signals from the accelerator equipment. It also supports Ethernet, USB, JTAG, and UART ports for external connections. The configuration of the acquisition node is shown in Fig 6.

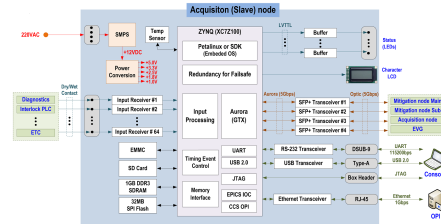


Figure 6: Configuration of the FPS acquisition node.

Along with the printed circuit board (PCB) fabrication of the FPS, the external hardware shapes are also being produced. Figure 7 and 8 show the geometries of the mitigation node and acquisition node up to the present. On the front panel, devices for external interfaces such as SFP+ transceivers, Ethernet port, JTAG port, etc. are inserted in all nodes. On the rear side, the mitigation node has 24 SMA ports for sending signals to the beam stopping devices, and the acquisition node has 64 input connectors for collecting external interlock signals.



Figure 7: Hardware shape of the FPS mitigation node.



Figure 8: Hardware shape of the FPS acquisition node.

Information for monitoring and managing the FPS can be found at the CSS operator interface (OPI) through the EPICS IOC running in the PL area. To this, we are currently working on the production of the CSS OPIs. Figure 9 shows one of the FPS CSS OPIs. In addition to OPI for operating FPS, OPIs for operating RPS and PMS are also under development.

Content from this work may be used under the terms of the CC BY 3.0 licence (© 2018). Any distribution of this work must maintain attribution to the author(s), title of the work, publisher, and DOI.



Figure 9: CSS OPI screen of the fast protection system.

PLAN OF FAST PROTECTION SYSTEM

The mitigation node and acquisition nodes under development will be installed in the control rack located in the accelerator gallery and will be operated together with other control devices such as a timing system and a SIS. As shown in Fig. 10, the mitigation node will be located in the injector section where the beam stopping devices are located, and the acquisition nodes will be installed along the long acceleration sections to collect interlock signals from peripheral devices. To support the beam operations of two low energy superconducting linac sections the mitigation nodes can be separately located and operated in each injector section.

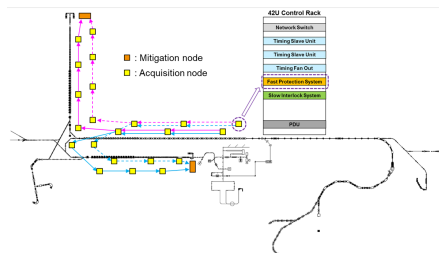


Figure 10: Layout of the RAON fast protection system.

For the beam operation from the low energy superconducting section (SCL3) to the high energy superconducting section (SCL2) in the RAON accelerator, the mitigation node consists of two units considering the backup. Also, the total of 49 acquisition nodes are installed, which are divided into 7 chains for efficient FPS operation, and more than 3,000 signals can be collected. Figure 11 shows the configuration of the FPS. The development of the one chain will be finished at

the end of 2018, and then the remaining nodes will be made. The installation of the FPS in the accelerator gallery will be continued according to the beam commissioning schedule.

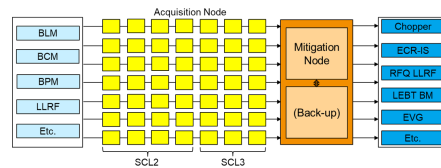


Figure 11: Architecture of the fast protection system from SCL3 to SCL2.

SUMMARY

We have described the development status of the FPS and its future plan. The FPS prototype had been developed, and the beam test was successfully carried out until the end of 2017. Based on this result, the Xilinx zynq based FPS products are under development. The hardware and software for the mitigation node and the acquisition node are under development, and this development is scheduled to be completed by the end of 2018. After the development, we are planning the commissioning of the FPS product after installing at the RAON accelerator based on the beam commissioning schedule.

ACKNOWLEDGEMENTS

This work was supported by the Rare Isotope Science Project of Institute for Basic Science funded by Ministry of Science, ICT and Future Planning and National Research Foundation of Korea (2013M7A1A1075764).

REFERENCES

- [1] D. Jeon *et al.*, "Design of the RAON accelerator systems", *Journal of the Korean Physical Society*, vol. 65, pp. 1010-1019, 2014.
- [2] H. Jin *et al.*, "Start-to-end simulation for the RISP test facility", *Nuclear Instruments and Methods in Physics Research A*, vol. 799, pp 37-43, 2015.
- [3] ICABU2017, <https://indico.cern.ch/event/647155/>

TEMPERATURE MEASUREMENT OF CLYOMODULES*

Heetae Kim[†], Yoochul Jung, Jong Wan Choi, Yong Woo Jo, Min Ki Lee, Moo Sang Kim,
Juwan Kim, Youngkwon Kim and Hoechun Jung,
Rare Isotope Science Project, Institute for Basic Science, Daejeon 34047, Republic of Korea

Abstract

A quarter-wave resonator (QWR) and a half-wave resonator (HWR) cryomodules and the control systems such as programmable logic controller (PLC) are developed. Temperature sensors such as Cernox-1050 are calibrated and applied to the cryomodules. Preparation of vertical test is introduced. QWR and HWR cryomodules are fabricated and tested by using the developed PLC control system. The PLC rack and temperature monitors are shown and the human machine interfaces (HMI) screen is shown when the HWR cryomodules is tested at 2 K.

INTRODUCTION

Liquid helium and liquid nitrogen are commonly used as coolants for cryogenic systems and the effect of thermal radiation is important in design of cryogenic systems. Properties of superfluid helium fog were investigated [1-3] and n-dimensional blackbody radiation was studied [4]. The size effect of thermal radiation [5, 6] and the effective temperature of non-uniform temperature distribution were investigated [7, 8]. RAON accelerator system was designed [9] and superconducting radio frequency (SRF) test facility was constructed [10, 11]. The SRF test facility consists of cleanroom, cryogenic system, vertical test and horizontal test. Cavity processes and cavity assemblies are performed in the cleanroom.

In this research we calibrate temperature sensors and apply them to cryomodules. Preparation of liquid helium and liquid nitrogen transfer lines, vertical test and horizontal test are introduced. PLC rack and HMI screen are shown to control and monitor the cryomodules.

TRANSFER LINES

Both liquid helium and liquid nitrogen transfer lines are needed to test QWR and HWR cryomodules in horizontal test facility. Figure 1 shows the fabrication process of liquid helium and liquid nitrogen transfer lines for cryomodules test from (a) through (f). The fabrication process consists of cutting, welding and leak test. About 20 turns of multi-layer foil insulation are used to cover the each of the transfer lines which includes the inlet and outlet of liquid nitrogen and liquid helium. Figure 1 (i) and (j) show the baking process by using heating wires for two days while pumping the vacuum area. Liquid nitrogen is used to cool down the thermal shield of cryomodules and liquid helium is used to cool down the helium reservoirs and cavities of cryomodules.

* This work was supported by the Rare Isotope Science Project of Institute for Basic Science funded by the Ministry of Science, ICT and Future Planning (MSIP) and by the National Research Foundation (NRF) of the Republic of Korea under Contract 2013M7A1A1075764.

[†] kimht7@ibs.re.kr

TEMPERATURE SENSOR

Temperature sensors such as Cernox-1050 are calibrated with physical property measurement system (PPMS) [12]. Figure 2 shows the resistance measurement as a function of temperature for five Cernox-1050 temperature sensors. The resistance of temperature sensors decreases as temperature increases because the sensors are semiconductor. The dependence of resistance on temperature can be explained well by Drude model [12].

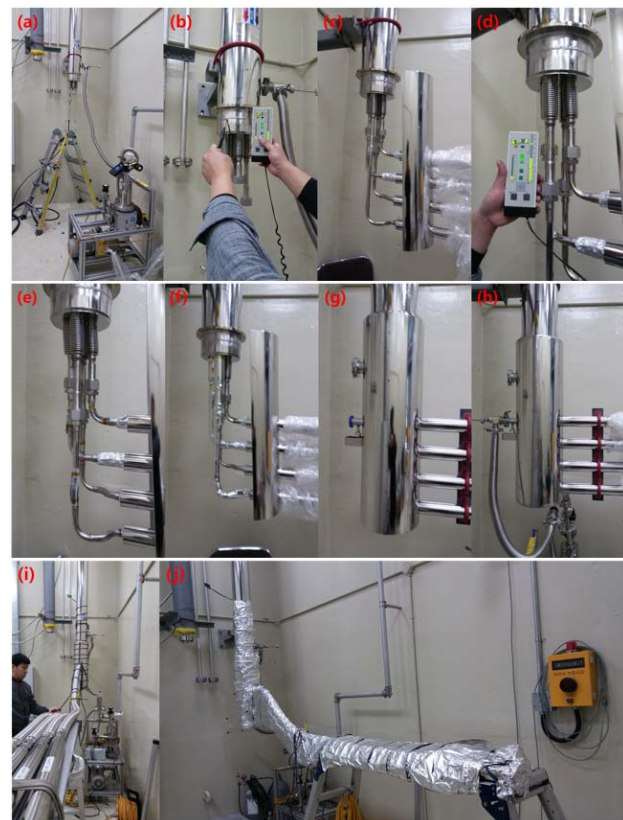


Figure 1: Fabrication process of liquid helium and liquid nitrogen transfer lines for cryomodules test from (a) through (f).

The temperature sensors are calibrated from 1.9 K to 325 K. After calibration, the calibration data is saved as 340 files for each temperature sensors. The calibrated data of 340 files are uploaded to temperature monitors using Lake Shore Curve Handler. Figure 3 represents the locations of temperature sensors in the QWR cryomodule. The calibrated sensors are attached on cryomodules to monitor temperature.

Content from this work may be used under the terms of the CC BY 3.0 licence (© 2018). Any distribution of this work must maintain attribution to the author(s), title of the work, publisher, and DOI.

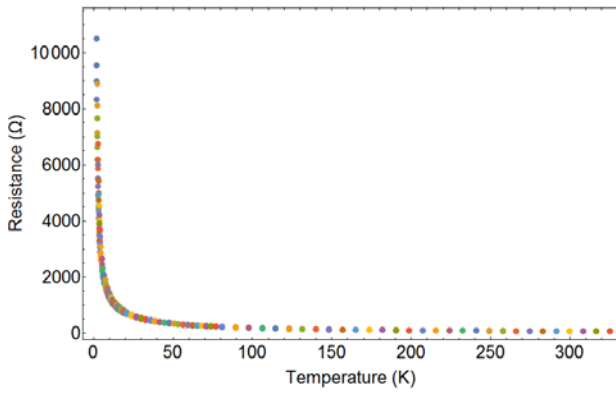


Figure 2: Resistance measurement as a function of temperature for temperature sensors.

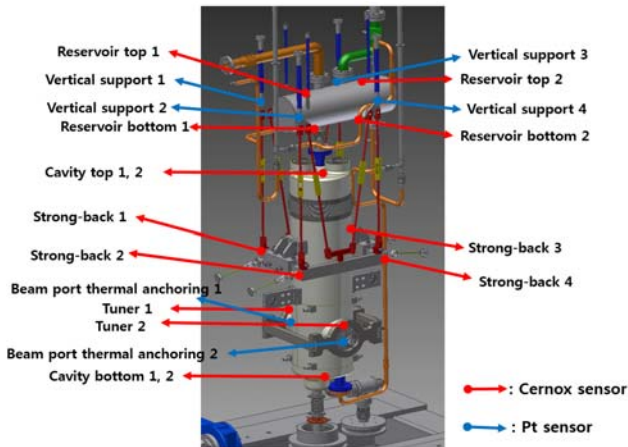


Figure 3: Locations of temperature sensors in a QWR cryomodule.

PREPARATION FOR VERTICAL TEST

The superconducting cavity made of Nb was performed with Buffered Chemical Polishing (BCP), High Pressure Rinsing (HPR), and High Temperature Heat Treatment, and then the cavity is assembled inside the cleanroom of class 10 of SRF test facility. Figure 4 shows the resistivity measurement of Nb as a function of temperature. The resistivity of Nb is measured with PPMS. The resistivity of Nb decreases as temperature decreases, which is a characteristic of conductors. The Nb also shows first-order phase transition at 9.3 K in Fig. 4. The Nb is also known as type-II superconductor.

The vertical test, the performance test of the superconducting cavity, is performed at vertical test site in SRF test facility. The superconducting cavities passed the performance test are assembled to cryomodules. Figure 5 represents the preparation of the vertical test for a cavity in cleanroom, two cavities prepared for cryostat installation and the top view of the cryostat. The superconducting cavities which are assembled in cleanroom and are passed leak test, are installed in the cryostat's top flange and then are moved to the vertical test site. After that, it is ready to do the vertical test. An ion pump is turned on to maintain the vacuum of cavities and the supply and recovery pipes of liquid helium and liquid nitrogen are connected to the

cryostat. Connect the purging pipe for the helium zone of the cryostat, high frequency signal cables, temperature sensor cables and pressure sensor cables, and then check the operation of all the sensors. Finally, the cooling preparation for the vertical test is ready once the cryostat is purged with helium gas.

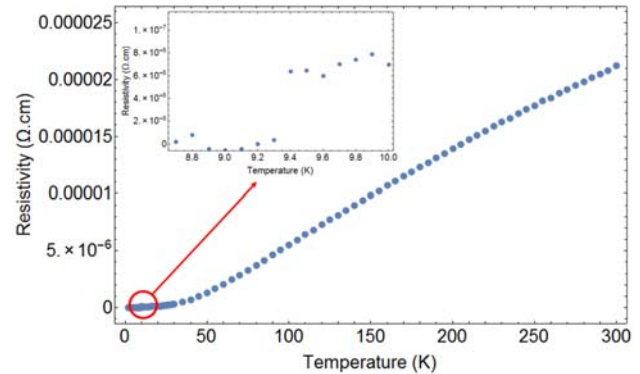


Figure 4: Resistivity of Nb as a function of temperature.

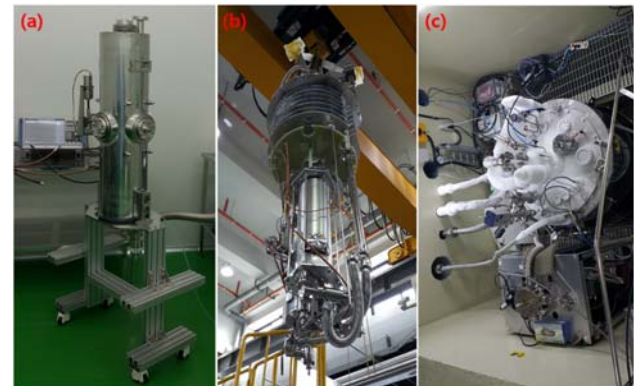


Figure 5: Preparation of vertical test for (a) a cavity in cleanroom, (b) two cavities prepared for cryostat installation and (c) the top view of a cryostat.

The performance test of superconducting cavities begins once the temperature of cavities becomes 4.3 K by circulating the cryostat with liquid nitrogen and liquid helium. Conditioning is performed in order to make the maximum electric field by changing the frequency and power in which a variable coupler is used for the superconducting cavity. After finishing conditioning, the figure of merit of cavity which includes Q factor, frequency change with respect to pressure (df/dp), etc., are measured through Voltage Controlled Oscillator Phase Locked Loop (VCO PLL). The Q factor is measured by using the input and output power of the cavity. The efficiency of the cavity increases as the value of the Q factor increases because stored energy in cavity is high compared with energy loss in cavity. The cavity becomes more stable as the value of df/dp representing the frequency change with respect to external pressure becomes lower.

CONTROL SYSTEM FOR HORIZONTAL TEST

After finishing vertical test, the cavities are assemble to cryomodule in cleanroom. Figure 6 represents the QWR and HWR cryomodules. The QWR cryomodule is installed for a linear accelerator demonstration after horizontal test and the HWR cryomodule is under horizontal test by connecting the HWR cryomodule with transfer lines and by using PLC.



Figure 6: Cryomodules for (a) HWR and (b) QWR.



Figure 7: Control system of cryomodules for (a) PLC rack and (b) temperature monitors.

Compact Logix PLC and Studio 5000 software of Rockwell Automation is used to develop the PLC program for HWR cryomodules. Allen bradley PLC controls pumps, heaters and valves. The PLC communicates with temperature monitors through ethernet cable. PLC and EPICS control and monitor pumps, heaters, valves and temperature sensors through switching hub. Figure 7 shows the PLC rack and temperature monitors for

cryomodules. The PLC are designed to control QWR and HWR cryomodules.

PLC human machine interface (HMI) screen for HWR cryomodules is shown in Fig. 8. It consists of 4 K helium reservoir, 2 K helium reservoir, two cavities, etc. Temperatures in many locations are monitored in the HMI screen. Vacuum pressures of cavity and vessel and vapor pressures of helium reservoirs are also monitored in the HMI screen. The drive frequency for the HWR cryomodule is 162.5 MHz and the cavities are operated at 2 K.

Temperature of cavity can be measured well by using the vapor pressure of liquid helium when the temperature is especially below 4.3 K. The temperature measurement of Cernox sensor depends on the contact between cavity jacket and sensor.

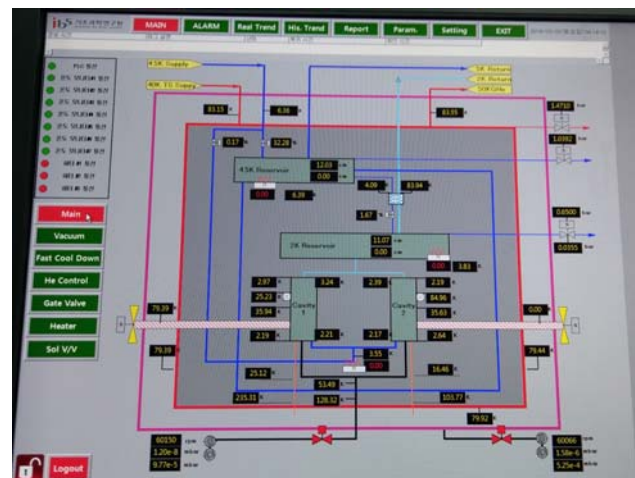


Figure 8: HMI screen for HWR cryomodules.

SUMMARY

We have developed QWR and HWR cryomodules and tested the cryomodules with PLC. Temperature sensors are calibrated by using PPMS and applied to the cryomodules. QWR and HWR cryomodules are fabricated and tested by using developed control systems such as PLC. The PLC rack and temperature monitors are shown and the HMI screen is shown when the HWR cryomodule is tested at 2 K.

REFERENCES

- [1] Heetae Kim, Kazuya Seo, Bernd Tabbert and Gary A. Williams, "Properties of Superfluid Fog produced by Ultrasonic Transducer", *J. of Low Temperature Physics*, vol. 121, p. 621, 2000.
- [2] Heetae Kim, Kazuya Seo, Bernd Tabbert and Gary Williams, "Properties of Superfluid Fog", *Europhysics Letters*, vol. 58, p. 395, 2002.
- [3] Heetae Kim, Pierre-Anthony Lemieux, Douglas Durian, and Gary A. Williams, "Dynamics of normal and superfluid fogs using diffusing-wave Spectroscopy", *Physical Review E*, vol. 69, p. 0614081, 2004.
- [4] P.T. Landsberg and A. De Vos, "The Stefan-Boltzmann constant in n-dimensional space", *J. Phys.A Math.Gen.* vol. 22, p.1073, 1989.

- Content from this work may be used under the terms of the CC BY 3.0 licence (© 2018). Any distribution of this work must maintain attribution to the author(s), title of the work, publisher, and DOI.
- [5] Soon-Jae Yu, Suk Joo Youn, and Heetae Kim, “Size effect of thermal radiation”, *Physica B*, vol. 405, p.638, 2010.
- [6] Heetae Kim, Seong Chu Lim, and Young Hee, “Size effect of two-dimensional thermal radiation” *Phys. Lett. A*, vol. 375, p. 2661, 2011.
- [7] Heetae Kim, Myung-Soo Han, David Perello, and Minhee Yun, “Effective temperature of thermal radiation from non-uniform temperature distributions and nanoparticles”, *Infrared Physics & Technology*, vol. 60, p. 7, 2013.
- [8] Heetae Kim, Chang-Soo Park, and Myung-Soo Han, “Effective temperature of two dimensional material for non-uniform temperature distribution”, *Optics Communications*, vol. 325, p. 68, 2014.
- [9] D. Jeon *et al.*, “Design of the RAON accelerator systems”, *Journal of the Korean Physical Society*, vol. 65, p. 1010, 2014.
- [10] Heetae Kim, Yoochul Jung, Jaehye Shin, Seon A Kim, Woo Kang Kim, Gunn-Tae Park, Sangjin Lee, Young Woo Jo, Shinwoo Nam, and Dong-O Jeon, “Raon Superconducting Radio Frequency Test Facility Construction”, in *Proc. LINAC’14*, Geneva, Switzerland, 2014, paper TUPP086, pp. 625-627.
- [11] Wookang Kim, Mijoung Joung, Yoochul Jung, Heetae Kim, Jongwon Kim, Youngkwon Kim, Ilkyoung Shin, “Fabrication and Low Temperature Test Plan for Rare Isotope Science Project”, in *Proc. LINAC’16*, East Lansing, MI, USA, Sep. 2016, paper TUPLR072, pp. 585-587.
- [12] Heetae Kim, Yoochul Jung, Yong Woo Jo, Min Ki Lee, Jong Wan Choi, Youngkwon Kim, Juwan Kim, Won-Gi Paeng, Moo Sang Kim, Hoechun Jung and Young Kwan Kwon, “Temperature Measurement Techniques for RAON Cryomodule”, *Applied Science Convergence Technology*, vol. 27, p. 30, 2018.

STUDY ON THE LEAKAGE FIELDS OF THE SEPTUM AND LAMBERTSON MAGNETS DURING THE BEAM COMMISSIONING*

M.Y. Huang^{1,2#}, S. Wang^{1,2}, S.Y. Xu^{1,2}

¹Institute of High Energy Physics, Chinese Academy of Sciences, Beijing, China

²Dongguan Neutron Science Center, Dongguan, China

Abstract

For China Spallation Neutron Source (CSNS), the septum magnets are the key parts of the injection system and the lambertson magnet is the key part of the extraction system. If the leakage fields of the septum and lambertson magnets are large enough, the circular beam orbit of rapid cycling synchrotron (RCS) would be affected. In this paper, during the beam commissioning, the leakage fields of the septum and lambertson magnets will be studied and their effects on the circular beam orbit will be given and discussed.

INTRODUCTION

China Spallation Neutron Source (CSNS) is a high power proton accelerator-based facility [1] whose technical acceptance had been completed in March 2018. Its accelerator consists of an 80 MeV H-Linac and a 1.6 GeV rapid cycling synchrotron (RCS) with a repetition rate of 25 Hz which accumulates an 80 MeV injection beam, accelerates the beam to the designed energy of 1.6 GeV and extracts the high energy beam to the target. The design goal of beam power for CSNS is 100 kW and can be upgraded to 500 kW [2].

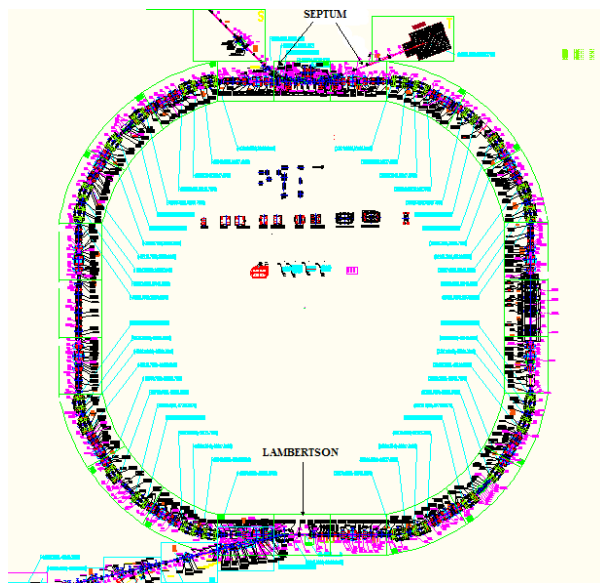


Figure 1: Layout of the CSNS/RCS system.

For CSNS, the septum magnets are the key parts of the injection system and the lambertson magnet is the key

part of the extraction system [3, 4]. Figure 1 shows the layout of the CSNS/RCS system. The magnetic test results show that the leakage fields of the septum and lambertson magnets are very small and meet the physical design requirements [5]. During the beam commissioning, in order to obtain the accurate circular beam orbit, the leakage fields of the septum and lambertson magnets should be studied and their effects on the circular beam orbit should be discussed and removed.

LEAKAGE FIELDS OF THE SEPTUM MAGNETS

There are two septum magnets (septum-1 and septum-2) in the injection system. The magnetic test results show that the maximum leakage field value of the septum magnets is 12 Gs and the leakage field value at the position where the circular beam passes is smaller than 1 Gs. Therefore, the leakage fields of the two septum magnets meet the physical design requirements.



Figure 2: Horizontal circular beam orbits while the power of the septum-2 magnet is on (above) or off (below).

During the beam commissioning, in order to confirm that the leakage fields of the septum magnets have no effects on the circular beam, the leakage fields of the septum magnets need to be studied and measured. By comparing different circular beam orbits while the powers of the septum magnets are on and off, the effects of the leakage fields of the septum magnets on the circular beam can be estimated. Figure 2 shows different horizontal circular beam orbits while the power of the septum-2 magnet is on or off. Figure 3 shows different vertical circular beam orbits while the power of the septum-2

* Work supported by National Natural Science Foundation of China (Project Nos. 11205185)

huangmy@ihep.ac.cn

Content from this work may be used under the terms of the CC BY 3.0 licence (© 2018). Any distribution of this work must maintain attribution to the author(s), title of the work, publisher, and DOI.

magnet is on or off. It can be found that, no matter the power of the septum-2 magnet is on or off, the horizontal and vertical circular beam orbits are nearly unchanged. Therefore, it can be confirmed that the leakage fields of the septum magnets have no effects on the horizontal and vertical circular beam orbits.



Figure 3: Vertical circular beam orbits while the power of the septum-2 magnet is on (above) or off (below).

LEAKAGE FIELD OF THE LAMBERTSON MAGNET

There is only one lambertson magnet in the extraction system. The magnetic test results show that the maximum leakage field value of the lambertson magnet is 4 Gs and the leakage field value at the position where the circular beam passes is smaller than 2 Gs. Therefore, the leakage field of the lambertson magnet meets the physical design requirements.

Similar to the septum magnets, during the beam commissioning, whether the leakage field of the lambertson magnet has effects on the circular beam should be confirmed. Or else the accurate circular beam orbit cannot be obtained. By comparing different circular beam orbits while the power of the lambertson magnet is on and off, the effects of the leakage field of the lambertson magnet on the circular beam can be estimated. Figure 4 shows different horizontal circular beam orbits while the power of the lambertson magnet is on or off. Figure 5 shows different vertical circular beam orbits while the power of the lambertson magnet is on or off. It can be found that, no matter the power of the lambertson magnet is on or off, the horizontal and vertical circular beam orbits are nearly unchanged. Therefore, it can be confirmed that the leakage field of the lambertson magnet has no effects on the horizontal and vertical circular beam orbits.



Figure 4: Horizontal circular beam orbits while the power of the lambertson magnet is on (above) or off (below).



Figure 5: Vertical circular beam orbits while the power of the lambertson magnet is on (above) or off (below).

CONCLUSIONS

There are two septum magnets in the injection system and one lambertson magnet in the extraction system. The magnetic test results show that the leakage fields of the septum and lambertson magnets are very small and meet the physical design requirements. However, during the beam commissioning, in order to obtain the accurate circular beam orbit, the leakage fields of the septum and lambertson magnets need to be studied and their effects on the circular beam orbit should be discussed and removed. In this paper, by comparing different circular beam orbits while the powers of the septum and lambertson magnets are on and off, the effects of the leakage fields of the septum and lambertson magnets on the circular beam were estimated. It can be confirmed that the leakage fields of the septum and lambertson magnets have no effects on the horizontal and vertical circular beam orbits.

ACKNOWLEDGMENTS

The authors want to thank other CSNS colleagues for the discussions and consultations.

REFERENCES

- [1] S. Wang *et al.*, “Introduction to the overall physics design of CSNS accelerators”, *Chin Phys C*, vol. 33, no. S2, pp. 1-3, Jun. 2009.
- [2] CSNS Project Team, “China Spallation Neutron Source Feasibility Research Report”, unpublished.
- [3] J. Wei *et al.*, “China Spallation Neutron Source-an overview of application prospects”, *Chin Phys C*, vol. 33, no. 11, pp. 1033-1042, Nov. 2009.
- [4] M.Y. Huang *et al.*, “Effects of injection beam parameters and foil scattering for CSNS/RCS”, *Chin Phys C*, vol. 37, no. 6, p. 067001, Jun. 2013, doi: 10.1088/1674-1137/37/6/067001
- [5] M.Y. Huang *et al.*, “Study on the magnetic measurement results of the injection system for CSNS/RCS”, in *Proc. HB’16*, Malmo, Sweden, Jul. 2016, pp. 46-48, doi: 10.18429/JACoW-HB2016-MOPR002

MAGNETIC FIELD TRACKING AT CSNS/RCS

S. Y. Xu*, S. N. Fu, S. Wang, W. Kang, X. Qi
 CSNS/IHEP, CAS, Dongguan, 523803, P.R. China

Abstract

Because of the differences of magnetic saturation and eddy current effects between different magnets, magnetic field tracking errors between different magnets is larger than 2.5% at the Rapid Cycling Synchrotron (RCS) of Chinese Spallation Neutron Source (CSNS), and the induced tune shift is larger than 0.1. So large tune shift may lead the beam to pass through the resonance lines. To reduce the magnetic field tracking errors, a method of wave form compensation for RCS magnets, which is based on transfer function between magnetic field and exciting current, was investigated on the magnets of CSNS/RCS. By performing wave form compensation, the magnetic field ramping function for RCS magnets can be accurately controlled to the given wave form, which is not limited to sine function. The method of wave form compensation introduced in this paper can be used to reduce the magnetic field tracking errors, and can also be used to accurately control the betatron tune for RCS. By performing wave form compensation, the maximum magnetic field tracking error was reduced from 2.5 % to 0.08 % at CSNS/RCS. The wave form compensation was applied to CSNS/RCS commissioning.

INTRODUCTION

The Chinese Spallation Neutron Source (CSNS) is an accelerator-based science facility. CSNS is designed to accelerate proton beam pulses to 1.6 GeV kinetic energy, striking a solid metal target to produce spallation neutrons. CSNS has two major accelerator systems, a linear accelerator (80 MeV Linac) and a rapid cycling synchrotron (RCS). The function of the RCS accelerator is to accumulate and accelerate protons from the energy of 80 MeV to the design energy of 1.6 GeV at a repetition rate of 25 Hz [1, 2]. The magnetic field tracking is an important issue for CSNS/RCS. The magnetic field tracking errors between the quadrupoles and dipoles can induce tune shift. If the tune shift induced by magnetic field tracking errors is large enough to pass through the resonance line, emittance growth as well as beam losses will occur [3-5].

Because of the magnetic saturation and the eddy current effects, there may be magnetic field tracking errors between different magnets of CSNS/RCS. For the magnets of RCS, which are powered by resonant circuits [6, 7], the exciting current and magnetic field is unable to be controlled step by step during ramping. For this type of magnets, the feed-back system is unable to be used to accurately control the magnetic field ramping wave form. The accurate magnetic field tracking was achieved by performing harmonic filed correction at J-PARC/RCS [8]. To

reduce the magnetic field tracking errors for CSNS/RCS, a method of wave form compensation for RCS magnets was investigated. By performing wave form compensation, the magnetic field ramping function for RCS magnets can be accurately controlled to the given wave form, which is not limited to sine function.

INTRODUCTION OF THE NEW METHOD OF WAVEFORM COMPENSATION

The new method of waveform compensation is based on transfer function between magnetic field and exciting current of the magnets of RCS. Higher order time harmonics of exciting current, which are computed based on transfer function, are injected into the magnets to compensate higher order time harmonics of magnetic field, and the magnetic field during the exciting current ramping can be accurately controlled.

The flow process for the harmonic compensation is shown in Fig. 1. For a start, the magnetic field and exciting current at different time during the exciting current ramping are measured by using the harmonic coil measurement system [9, 10], and then the fit of the transfer function $I=F_{Down}(B)$ and $I=F_{Upward}(B)$ are made to reduce the effect of measurement noise. $I=F_{Upward}(B)$ and $I=F_{Down}(B)$ are the transfer functions for that the exciting current ramping upward and downward respectively. By using the transfer function, the exciting current as a function of time $I(t)$ corresponding to the given magnetic field pattern $B(t)$ is derived. Then the DC offset and time harmonics of the derived current are obtained through FFT to $I(t)$. The magnetic field as a function of time can be accurately compensated to the given pattern $B(t)$ by inputting the obtained DC offset and time harmonics of the current into the resonant power supply.

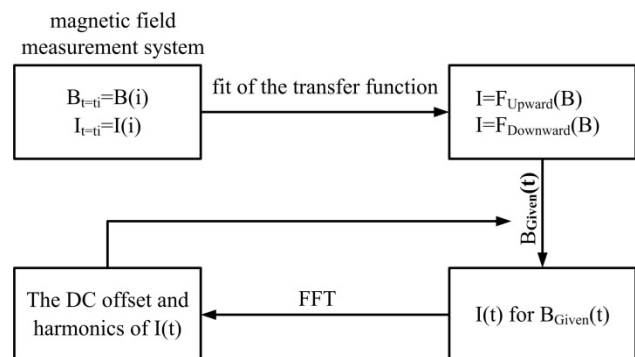


Figure 1: The flow process diagram for the harmonic compensation.

For the magnet of RCS with serious magnetic saturation and eddy current effects, the magnet field control accuracy is not high enough with only once waveform compensation, such as 206Q of CSNS/RCS. The method

Content from this work may be used under the terms of the CC BY 3.0 licence (© 2018). Any distribution of this work must maintain attribution to the author(s), title of the work, publisher, and DOI.

* xusy@ihep.ac.cn

of waveform compensation introduced in this paper can be performed repeatedly.

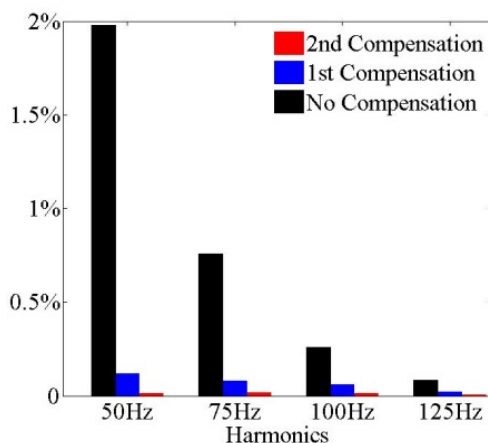


Figure 2: Comparison of the ratio of higher order harmonics and fundamental harmonics with and without waveform compensation.

The magnetic field of 206Q was compensated to sine pattern by using twice waveform compensation, and the test results are shown in Fig. 2. The higher order harmonics were effectively reduced by using once waveform compensation, but the ratio of some higher order harmonics and fundamental harmonic is still high, such as 50Hz harmonic, which is larger than 0.1% of fundamental harmonic. By using the second time waveform compensation, which is based on the transfer function between magnetic field and exciting current after the first time harmonic compensation, all the higher order harmonics were reduced to lower than 0.02% of fundamental harmonic. In other words, the magnetic field of 206Q was compensated to almost sine pattern by using twice waveform compensation. On the same principles, the method of waveform compensation can be performed even more times to achieve higher magnetic field control accuracy for the magnets of RCS with serious magnetic saturation and eddy current effects.

APPLICATION OF THE METHOD OF WAVE FORM COMPENSATION TO CSNS/RCS

The method of wave form compensation for magnets of RCS was applied to CSNS/RCS to reduce the magnetic field tracking errors between different magnets. There are one type of dipole named 160B and four types of quadrupoles, named 272Q, 253Q, 222Q and 206Q respectively at CSNS/RCS. Because of the differences of magnetic saturation and eddy current effects between these five types of magnets, there are magnetic field tracking errors between different magnets before wave form compensation, as shown in Fig. 3. The maximum magnetic field tracking error between the dipole and quadrupoles is larger than 2.5% over the ramping process, and the induced tune shift is larger than 0.1. So large tune shift may lead the beam to pass through the resonance lines.

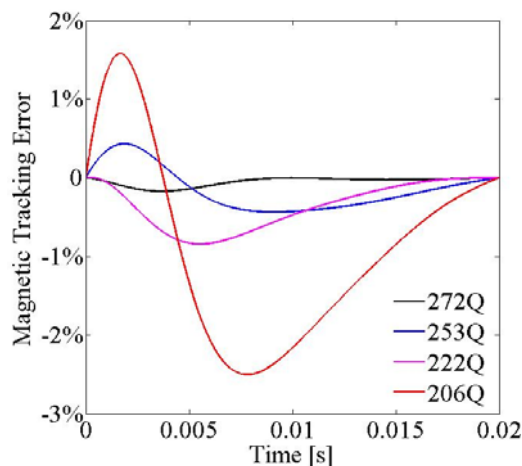


Figure 3: Magnetic field tracking errors between the dipole and four types of quadrupoles over the ramping process with no wave form compensation.

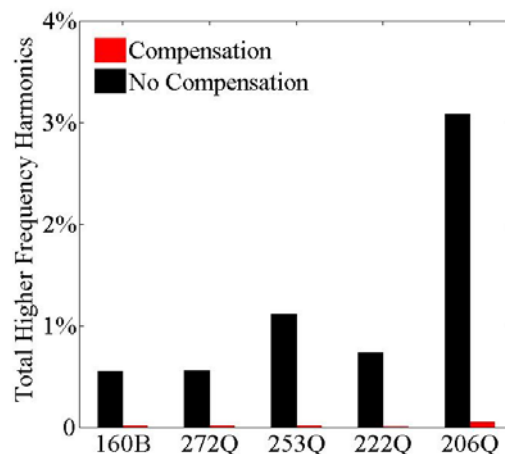


Figure 4: Comparison of the ratio of total higher order harmonics and fundamental harmonic with and with no wave form compensation for different types of magnets of CSNS/RCS.

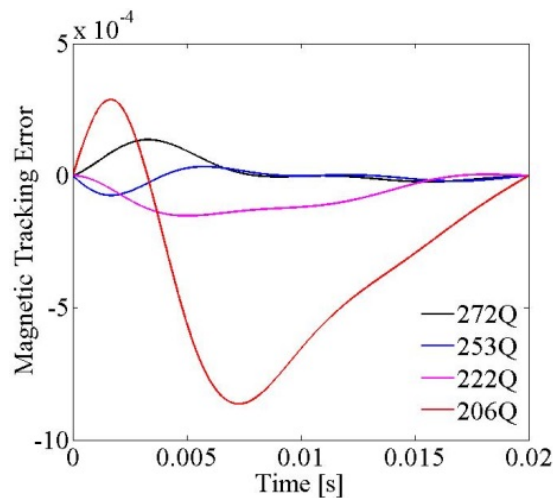


Figure 5: Magnetic field tracking errors between the dipole and four types of quadrupoles over the ramping process after wave form compensation.

Content from this work may be used under the terms of the CC BY 3.0 licence (© 2018). Any distribution of this work must maintain attribution to the author(s), title of the work, publisher, and DOI.

To reduce the magnetic field tracking errors between different magnets, wave form compensation was performed on all the magnets of CSNS/RCS. The magnetic field ramping functions for all the magnets were compensated to sine pattern. As shown in Fig. 4, higher order time harmonics of magnetic field for all the types of magnets were reduced to almost zero by performing wave form compensation, with only fundamental harmonic remained. The maximum magnetic field tracking error between the dipole and quadrupoles was reduced from 2.5% to 0.08%, as shown in Fig. 5, and the maximum tune shift over the ramping process was reduced from 0.1 to 0.004.

APPLICATION OF THE METHOD OF WAVE FORM COMPENSATION TO CSNS/RCS COMMISSIONING

The method of wave form compensation for magnets of RCS was applied to CSNS/RCS commissioning. The AC mode beam commissioning of CSNS/RCS with the injection energy of 80 MeV was started on January 18, 2018, and 1.6 GeV acceleration was successfully accomplished for the first beam shot. The beam transmission rate got 100% after performing the match of dipole magnetic field and RF frequency on the same day, as shown in Fig. 6.

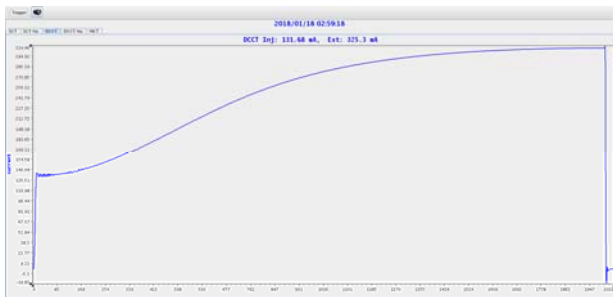


Figure 6: The beam current over one cycling period. Beam current increase with the increase of revolution frequency.

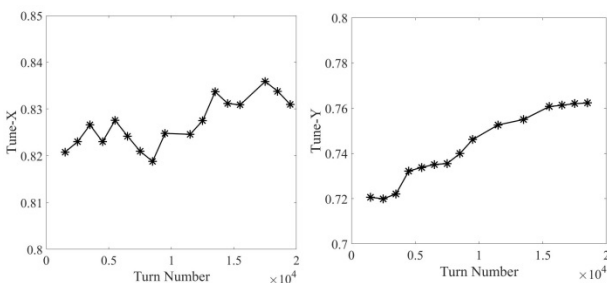


Figure 7: The tune variation during the acceleration process over one cycling period.

The tunes are measured during the acceleration process over one cycling period. The measurement results are shown in Fig. 7. The variation of horizontal tune is less than 0.02, and the variation of vertical tune is about 0.04. The tune variation during the acceleration process is significantly smaller than the tune shift induced by the magnetic field tracking errors without wave form compensa-

tion, which is 0.1. However, the tune variation during the acceleration process is bigger than the tune shift induced by the magnetic field tracking errors with wave form compensation, which is 0.004. The tune variation during the acceleration process can be induced by space charge effects, the mismatch between magnetic field and RF frequency, and timing errors between different magnet power supplies, except for the magnetic field tracking errors induce by the differences of higher order harmonics between different magnets.

CONCLUSION

A method of wave form compensation for the magnets of RCS is introduced in this paper. The method of wave form compensation can be used to accurately control the magnetic field ramping. The method of wave form compensation was applied to CSNS/RCS commissioning. The magnetic field tracking errors between different magnets are effectively reduced, and the beam commissioning of CSNS/RCS went smoothly.

REFERENCES

- [1] S. N. Fu *et al.*, “Status of CSNS Project”, in *Proc. IPAC’13*, Shanghai, China, May 2013, pp. 3995-3999.
- [2] S. Wang, *et al.*, “An Overview of Design for CSNS/RCS and Beam Transport”, *Science China Physics, Mechanics & Astronomy*, vol. 54, pp. 239-244, 2011.
- [3] H. Hotchi *et al.*, “Effects of Magnetic Field Tracking Errors on Beam Dynamics at J-PARC RCS”, in *Proc. PAC’07*, Albuquerque, NM, USA, Jun. 2007, pp. 4078-4080.
- [4] S. Y. Xu *et al.*, “Effects of Magnetic Field Tracking Errors and Space Charge on Beam Dynamics at CSNS/RCS”, in *Proc. HB’12*, Beijing, China, Sep. 2012, pp. 484-486.
- [5] S. Y. Xu *et al.*, “Study on the Effects of Chromaticity and Magnetic Field Tracking Errors at CSNS/RCS”, *Chinese Physics C*, vol. 38, pp. 68-71, 2014.
- [6] N. Tani *et al.*, “Design of RCS Magnets for J-PARC 3-GeV Synchrotron”, *IEEE Tran. Appl. Supercond.*, vol. 14, pp. 409-412, 2004.
- [7] S. N. Fu *et al.*, “Proton Accelerator Development in China”, *AC13*, pp. 57-61, 2013.
- [8] N. Tani, *et al.*, “Magnet System of the J-PARC RCS”, 3th ACFA-HPPA Mini-Workshop, 2008.
- [9] J. X. Zhou *et al.*, “A Harmonic Coil Measurement System Based on a Dynamics Signal Acquisition Device”, *Nucl. Instrum. Methods Phys. Res. A*, vol. 624, pp. 549-553, 2010.
- [10] J. X. Zhou, *et al.*, “AC Magnetic Field Measurement of CSNS/RCS Quadrupole Prototype”, *Nucl. Instrum. Methods Phys. Res. A*, vol. 654, pp. 72-75, 2011.

STUDY ON THE PHASE SPACE PAINTING INJECTION DURING THE BEAM COMMISSIONING FOR CSNS*

M.Y. Huang^{1,2#}, S. Wang^{1,2}, S.Y. Xu^{1,2}

¹Institute of High Energy Physics, Chinese Academy of Sciences, Beijing, China

²Dongguan Neutron Science Center, Dongguan, China

Abstract

During the beam commissioning of China Spallation Neutron Source (CSNS), different injection methods were used in different periods. In the early stage, since the precise position of the injection point was unknown and the beam power was relatively small, the fixed point injection was selected. In the later period, in order to increase the beam power and reduce the beam loss, the phase space painting method was used. In this paper, the phase space painting in the horizontal and vertical planes is studied in detail and the beam commissioning results of different painting injection are given and discussed. In addition, different injection effects of the fixed point injection and painting injection are compared and studied.

INTRODUCTION

China Spallation Neutron Source (CSNS) is a high power proton accelerator-based facility [1] and its technical acceptance had been completed in March 2018. The accelerator consists of an 80 MeV H⁻ Linac and a 1.6 GeV rapid cycling synchrotron (RCS) with a repetition rate of 25 Hz which accumulates an 80 MeV injection beam, accelerates the beam to the designed energy of 1.6 GeV and extracts the high energy beam to the target. The design goal of beam power for CSNS is 100 kW and capable of upgrading to 500 kW [2].

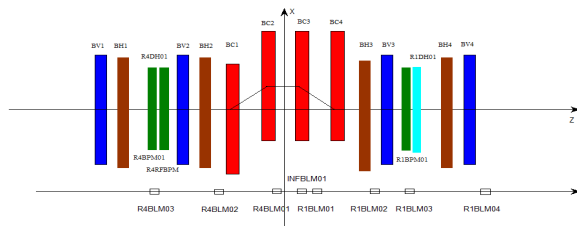


Figure 1: Layout of the CSNS injection system.

For the high intensity proton accelerators, in order to reduce the beam loss caused by the space charge effects, the phase space painting method is used for injecting the beam of small emittance from the Linac into the large ring acceptance [3]. For CSNS, the position painting was used in both horizontal and vertical planes. Figure 1 shows the layout of the CSNS injection system. It can be found that, there are four dipole magnets (BH1-BH4) used for painting in the horizontal plane and other four

dipole magnets (BV1-BV4) used for painting in the vertical plane [4].

In the early stage of CSNS beam commissioning, since the precise position of the injection point was unknown and the injection beam power was relatively small, in order to inject the beam into the RCS as soon as possible, the fixed point injection method was selected. Latter, in order to increase the beam power and reduce beam loss, the phase space painting in the horizontal plane was used. Finally, the phase space painting in both horizontal and vertical planes was used, and the painting ranges and painting curves were studied and optimized.

In our early paper, we had studied and discussed the fixed point injection during the beam commissioning for CSNS [5]. In the following sections, the phase space painting in the horizontal and vertical planes during the beam commissioning will be studied and discussed.

HORIZONTAL PAINTING INJECTION

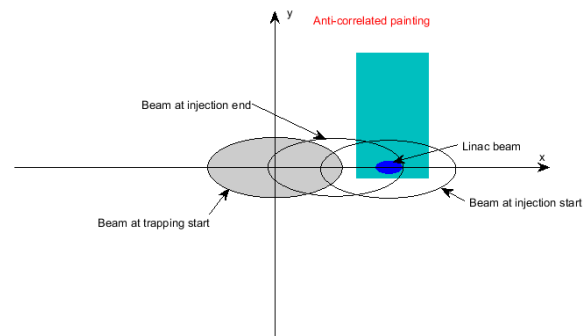


Figure 2: Positions of the ring acceptance ellipse during the horizontal painting injection.

In the middle of beam commissioning, in order to increase the beam power and reduce the beam loss, the phase space painting in the horizontal plane was used. Figure 2 shows the positions of the ring acceptance ellipse during the horizontal painting injection process. For CSNS, the fixed point injection was changed to the horizontal painting injection on Nov. 9, 2017. During the beam commissioning, by comparing the results of the fixed point injection and horizontal painting injection, it can be found that there are many advantages to applying the horizontal painting injection. Figure 3 shows the beam loss of the Linac and RCS while the fixed point injection and horizontal painting injection were used. It can be seen that the beam loss in the injection region while the horizontal painting was used is much smaller than that while the fixed point injection was used.

*Work supported by National Natural Science Foundation of China (Project Nos. 11205185)

#huangmy@ihep.ac.cn

Content from this work may be used under the terms of the CC BY 3.0 licence (© 2018). Any distribution of this work must maintain attribution to the author(s), title of the work, publisher, and DOI.

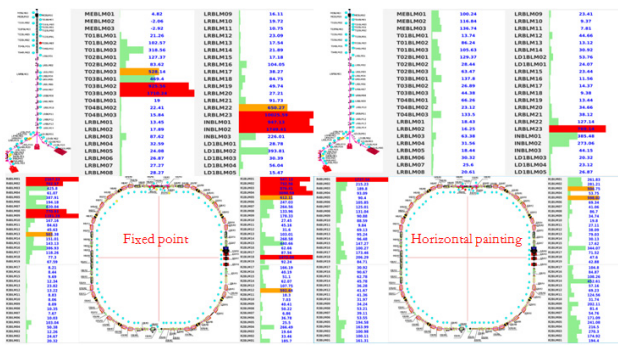


Figure 3: Beam loss of the Linac and RCS while the fixed point injection (left) and horizontal painting injection (right) were used.

While the fixed point injection was used, there was a suddenly beam loss during the injection process no matter the matching of the injection beam and circular beam [5]. However, while the horizontal painting injection was used, the suddenly beam loss during the injection process was gone. Figure 4 shows the RCS DCCT displays while the fixed point injection and horizontal painting injection were used. It can be found that, for the horizontal painting injection, the suddenly beam loss was gone and the injection efficiency had increased very much. Therefore, the beam power can be further improved.

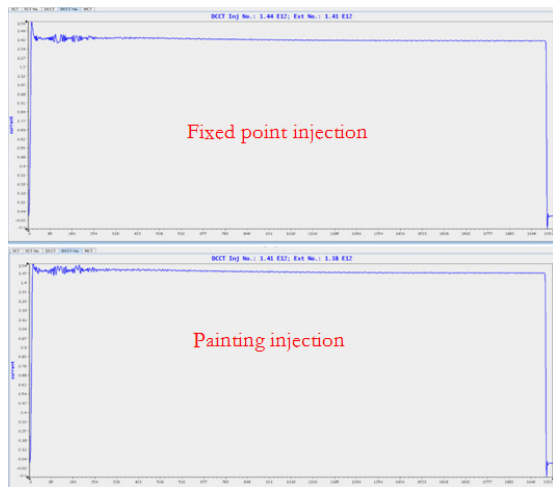


Figure 4: RCS DCCT displays while the fixed point injection and horizontal painting injection were used.

HORIZONTAL AND VERTICAL PAINTING INJECTION

In the process of further increasing the beam power, the space charge effects of cumulative beam would be increased so as to cause larger beam loss. Under the circumstances, the painting in both horizontal and vertical planes needs to be considered. Figure 5 shows the positions of the ring acceptance ellipse during the horizontal and vertical painting injection process. For CSNS, the horizontal and vertical painting injection were both used and optimized on Feb. 13, 2018.

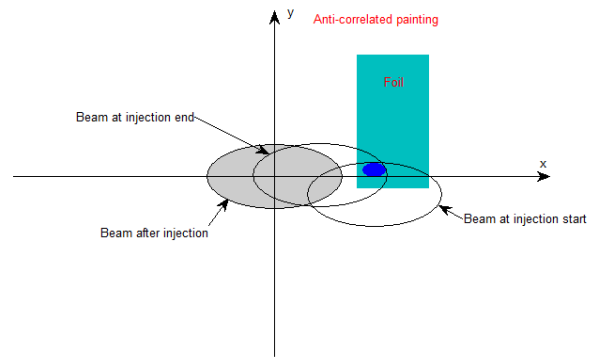


Figure 5: Positions of the ring acceptance ellipse during the horizontal and vertical painting injection.

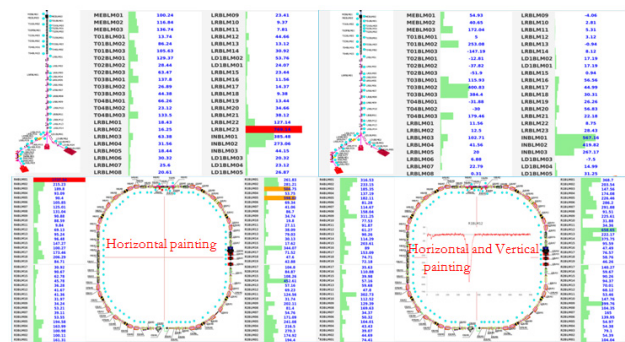


Figure 6: Beam loss of the Linac and RCS while the horizontal painting injection (left) and horizontal & vertical painting injection (right) were used.

During the beam commissioning, by comparing the results of the horizontal painting injection and horizontal & vertical painting injection, it can be found that there are some advantages to applying the phase space painting in both horizontal and vertical planes. Figure 6 shows the beam loss of the Linac and RCS while the horizontal painting injection and horizontal & vertical painting injection were used. It can be seen that the beam loss in the injection region while the phase space painting in both horizontal and vertical planes was used is smaller than that while only horizontal painting injection was used. In addition, the beam power had increased from 13 kW to 23 kW. In the future, in order to further improve the beam power, the painting curves and painting ranges in the horizontal and vertical planes need to be further optimized.

CONCLUSIONS

In the middle of CSNS beam commissioning, the fixed point injection was changed to the horizontal painting injection. The beam commissioning results showed that the beam loss in the injection region while the horizontal painting was used was much smaller than that while the fixed point injection was used. In addition, for the horizontal painting injection, the suddenly beam loss that appeared in the fixed point injection process was gone and the injection efficiency had increased very much.

In the latter period of beam commissioning, the

painting in both horizontal and vertical planes was used for the beam injection. The beam commissioning results showed that the beam loss was much reduced and the beam power had increased from 13 kW to 23 kW. In the future, in order to further improve the beam power, the painting curves and painting ranges in the horizontal and vertical planes need to be further optimized.

ACKNOWLEDGMENTS

The authors want to thank other CSNS colleagues for the discussions and consultations.

REFERENCES

[1] S. Wang *et al.*, “Introduction to the overall physics design of CSNS accelerators”, *Chin Phys C*, vol. 33, no. S2, pp. 1-3, Jun. 2009.

- [2] CSNS Project Team, “China Spallation Neutron Source Feasibility Research Report”, unpublished.
- [3] J. Wei *et al.*, “China Spallation Neutron Source-an overview of application prospects”, *Chin. Phys. C*, vol. 33, no. 11, pp. 1033-1042, Nov. 2009.
- [4] M.Y. Huang *et al.*, “Effects of injection beam parameters and foil scattering for CSNS/RCS”, *Chin. Phys. C*, vol. 37, no. 6, p. 067001, Jun. 2013, doi:10.1088/1674-1137/37/6/067001.
- [5] M.Y. Huang *et al.*, “Study on the fixed point injection during the beam commissioning for CSNS”, presented at the *9th Int. Particle Accelerator Conf. (IPAC'18)*, Vancouver, BC, Canada, May, 2018, paper TUPAL005, unpublished.

Content from this work may be used under the terms of the CC BY 3.0 licence (© 2018). Any distribution of this work must maintain attribution to the author(s), title of the work, publisher, and DOI.

possible, simple timing adjustment of eight kickers was made and the beam loss of the extraction system was controlled at a relatively small level. Firstly, the relative timing of different kickers was adjusted and the relative timing errors were controlled at a small level. Figure 4 shows the current curves of eight kickers after the relative timing adjustment of eight kickers. It can be seen that the relative timing errors of different kickers were small and reasonable. Secondly, the overall timing adjustment of eight kickers was made and the beam loss of the extraction system was relatively small. Figure 5 shows the two extracted bunches which set at different positions of the current curves of eight kickers. It can be found that, by the overall translation of the current curves of eight kickers, the two extracted bunches can be placed on the flat tops of the eight current curves, as shown in the sub graph (c) of Fig. 4. After that, the two bunches can be extracted from the RCS smoothly.

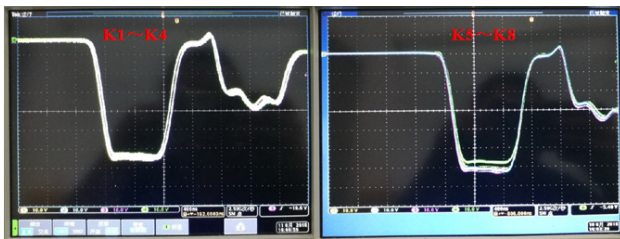


Figure 4: Current curves of eight kickers after the relative timing adjustment of eight kickers.

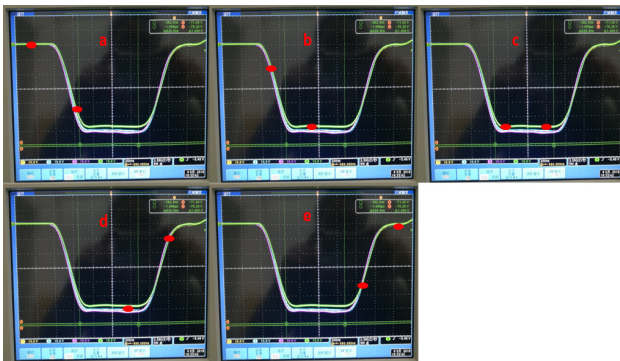


Figure 5: Two extracted bunches which set at different positions of the current curves of eight kickers.

During the beam commissioning, if one extracted bunch or two extracted bunches are not placed on the flat tops of the current curves of some kickers, the two extracted bunches would have different extraction coordinates which can be measured by the BPMs on the beam transport line from the RCS to the target (RTBT). In addition, there may be large beam loss on the RTBT which can be detected by the BLMs. In order to reduce the beam loss and make the two extracted bunches have the same extraction coordinates, the independent timing adjustment of different kickers was studied and made. Figure 6 shows the two extracted bunches which set at different positions of the kicker current curve. It can be found that, by the translation of the kicker current curve, the two extracted bunches can be placed on the flat tops

of the kicker current curve, as shown in the sub graph (c) of Fig. 6. If the two extracted bunches can be placed on the flat tops of the current curves of eight kickers, they would have the same extraction coordinates and can be extracted from the RCS smoothly. Figure 7 shows the beam loss display of the RCS and RTBT. It can be known that the beam loss of the extraction system is very small.

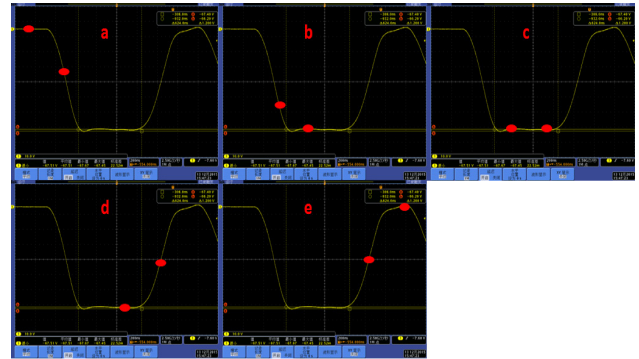


Figure 6: Two extracted bunches which set at different positions of the kicker current curve.

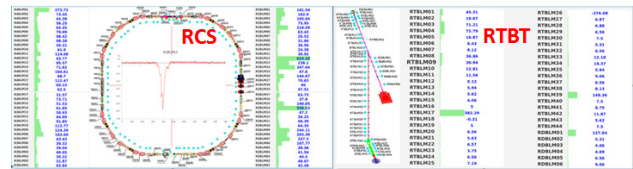


Figure 7: Beam loss display of the RCS and RTBT.

A METHOD TO CALIBRATE THE KICKER CURRENT CURVES

By adjusting the timing of the kicker, the current curve of the kicker would be translation. Then, the extracted bunch can be placed on different positions of the current curve and the BPM (such as RTBPM01) on the RTBT can measure different position information of the bunch. Therefore, after adjusting the timing of the kicker, by using the position information measured by the BPM on the RTBT, the kicker current curve can be calibrated.

During the calibration experiment of the kicker current curves, the timing of eight kickers should be adjusted well firstly. In addition, to make the experiment simple, single bunch mode would be selected, as shown in Fig. 8. By measuring the position information of the bunch, the position of the kicker current curve where the bunch placed on can be calculated. Figure 9 shows the single extracted bunch which sets at different places of the kicker current curve. It can be found that, if all the positions of the kicker current curve are calculated, the kicker current curve can be calibrated. This calibration method can be applied for all the eight kickers and will be confirmed in the future beam commissioning.

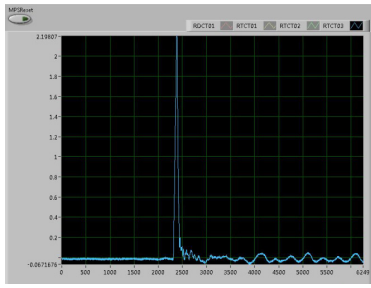


Figure 8: Display of the single extracted bunch measured on the RTBT.

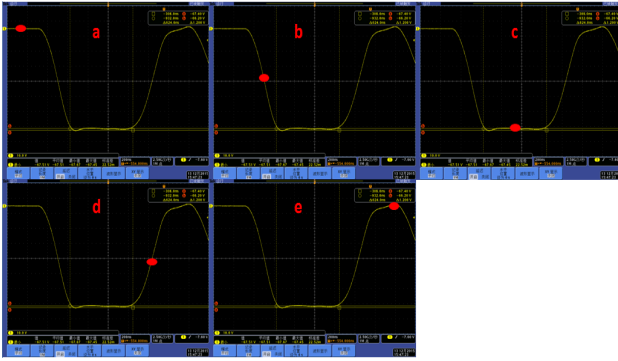


Figure 9: Single extracted bunch which sets at different positions of the kicker current curve.

CONCLUSIONS

During the beam commissioning, the timing adjustment of eight kickers is a very important problem. It consists of two parts: the overall timing adjustment of eight kickers and the independent timing adjustment of different kickers.

In the early stage of beam commissioning, the beam power and extraction beam size are relatively small. In order to extract the beam from the RCS as soon as possible, simple timing adjustment of eight kickers, including the relative timing of different kickers and the

overall timing adjustment of eight kickers, should be made which can also make the beam loss of the extraction system at a relatively small level. Latter, in order to reduce the beam loss and make the two extracted bunches have the same extraction coordinates, the independent timing adjustment of different kickers was studied and made.

During the timing adjustment of the kickers, by using the position information measured by the BPM on the RTBT, a possible method to calibrate the kicker current curves was developed. This calibration method would be confirmed in the future beam commissioning.

ACKNOWLEDGMENTS

The authors want to thank other CSNS colleagues for the discussions and consultations.

REFERENCES

- [1] S. Wang *et al.*, “Introduction to the overall physics design of CSNS accelerators”, *Chin Phys C*, vol. 33, no. S2, pp. 1-3, Jun. 2009.
- [2] CSNS Project Team, “China Spallation Neutron Source Feasibility Research Report”, unpublished.
- [3] M.Y. Huang *et al.*, “Effects of injection beam parameters and foil scattering for CSNS/RCS”, *Chin Phys C*, vol. 37, no. 6, p. 067001, Jun. 2013, doi: 10.1088/1674-1137/37/6/067001
- [4] M.Y. Huang *et al.*, “Study on the magnetizing relationship of the kickers for CSNS”, in *Proc. IPAC’17*, Copenhagen, Denmark, May 2017, pp. 582-584, doi: 10.18429/JACoW-IPAC2017-MOPIK036
- [5] G.H. Rees, “Extraction”, unpublished.
- [6] M.Y. Huang *et al.*, “Study on the fixed point injection during the beam commissioning for CSNS”, in *Proc. IPAC’18*, Vancouver, BC, Canada, May 2018, paper TUPAL005.

RESONANCE STOP-BANDS COMPENSATION AT BOOSTER RING OF HIAF*

J. Li[†], J. C. Yang, HIAF design group, Institute of Modern Physics, CAS, 730000 Lanzhou, China

Abstract

Booster Ring (BRing) of the new approved High Intensity heavy-ion Accelerator Facility (HIAF) in China is designed to stack $0.3\text{-}1.0\cdot 10^{11}$ number of $^{238}\text{U}^{35+}$ ions by painting injection and deliver over such intensity beam in extraction. However, depressed tune spread caused by space charge effect crosses the low-order resonance stop-bands after bunching the storage beam. To keep a low beam loss during crossing, stop-band compensation scheme is proposed covering the whole process of RF capture and early acceleration.

INTRODUCTION

Facility Layout

The High Intensity heavy-ion Accelerator Facility (HIAF) is a new heavy ion accelerator complex under detailed design by Institute of Modern Physics of Chinese Academy of Sciences [1]. Two typical particles of $^{238}\text{U}^{35+}$ and proton are considered in its design. The 34 Tm booster ring (BRing) is planned to stack beam intensity up to space charge limit at the injection energy 17 MeV/u and deliver over such intensity beam through HIAF FRagment Separator (HFRS) and further to Spectrometer Ring (SRing) at 800 MeV/u.

The particles derive from a Superconducting Electron Cyclotron Resonance (SECR) ion source or an intense H_2^+ source, and are accelerated by an ion linear accelerator (iLinac) and an booster ring (BRing). The iLinac can accelerate $^{238}\text{U}^{35+}$ to 17 MeV/u and H_2^+ to 48 MeV at entrance of the BRing. The beam will be injected with multi-turn two-plane painting scheme together with stacking in the BRing and extracted with fast kicker or resonant sextuples after being accelerated to 0.8 GeV/u. Following the extraction, $^{238}\text{U}^{35+}$ is stripped to bare ion at HFRS or bombing targets to generate secondary beams that will also be separated by HFRS. Finally, the selected ions is guided to external target or injected into the SRing for high-precision experimental measurement. In addition, five external target stations of T1 - T5 is arranged at HIAF for nuclear and atomic experimental researches with energy range 5.8-800 MeV/u for uranium beam.

The BRing has a three-folding symmetry lattice around its circumference of 569.1 m. Each super-period consists of an eight-FODO-like arc and an over 70 m long dispersion-free straight section reserved for two-plane painting injection, Extraction and RF cavities respectively. Figure 1 shows layout of the BRing lattice of one super-period.

The BRing operates at three modes of normal, slow extraction, and proton. Ions like $^{238}\text{U}^{35+}$ beam will operate

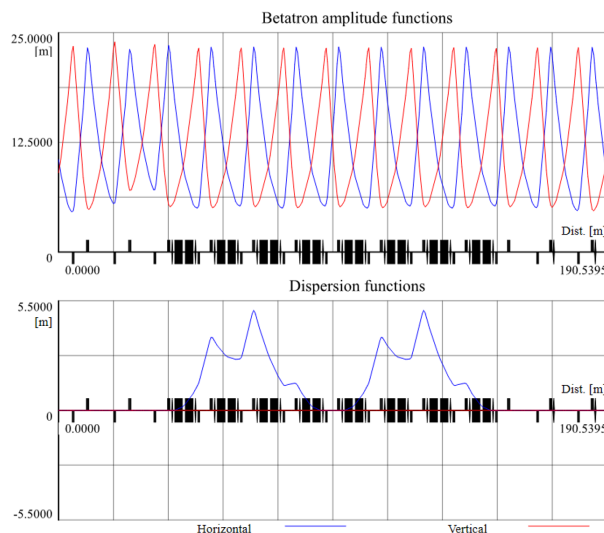


Figure 1: BRing lattice for one super-period.

at the first mode and finish painting injection within 150 revolution turns. Main parameters of the BRing are listed in Table 1.

Table 1: Main Parameters of $^{238}\text{U}^{35+}$ at the BRing

Circumference	569.1 m
Max. magnetic rigidity	34 Tm
Periodicity	3
Injection energy	17 MeV/u
Betatron tune	(9.47,9.43)
Acceptance ($H/V, \delta p/p$)	$200/100\pi\text{mmrad}, \pm 5.0\%$

RESONANCE AND STOP-BANDS

Space Charge Effects and Betatron Resonances

The space charge effect of intensive highly charged particle beam creates depressed spread in tune space. This spread width grows several times when the beam gets bunched during RF cavity capture.

Figure 2 shows the space charge effect deduced tune spread by bunched $^{238}\text{U}^{35+}$ beam at intensity of $1.0\cdot 10^{11}$ ion number. The BRing nominal working point (9.47, 9.43) seats next to the linear coupling difference resonance of $\nu_x - \nu_y = 0$. The only low-order systematic or structure resonance appeared in the figure is $2\nu_x - \nu_y = 9$ shown as blue solid line while the betatron ones as dot lines. The 4th-order resonances are ignored due to weak effect.

The $1.0\cdot 10^{11}$ ions produces a vertical spread about 0.15 after injection by two-plane painting methods. In the calculation [2], the uranium beam has a uniform distribution in transverse phase space and longitudinal Gaussian one,

* Work supported by NSFC (Grant No. 11475235)

[†] lijie@impcas.ac.cn

Content from this work may be used under the terms of the CC BY 3.0 licence (© 2018). Any distribution of this work must maintain attribution to the author(s), title of the work, publisher, and DOI.

the emittances $200/100\pi\text{mmrad}$ that equals to the synchrotron acceptance, a momentum spread $\pm 2.5\%$, and a bunching factor 0.4 after dual RF capture. The figure also shows an overlap of tune spread with two 3^{rd} -order betatron resonances.

As a conventional experience in synchrotron operation, the maximum transverse emittance is usually smaller than the acceptance. This will result in a larger spread and consequently more low-order resonance crossing at the same intensity of storage beam. Resonance will cause emittance growth or beam loss when the tune of particle sits just upon low-order resonance stop-bands.

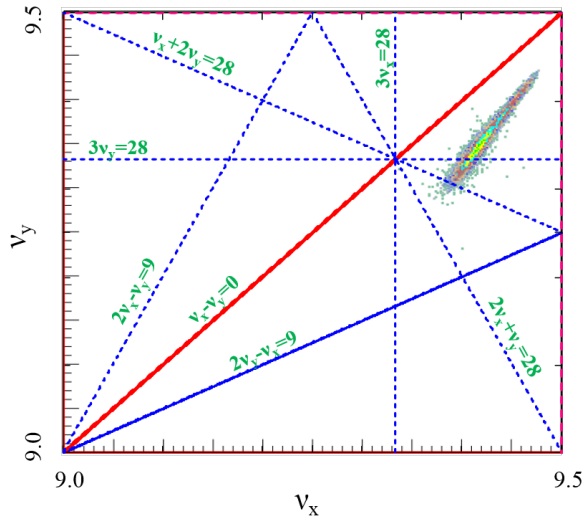


Figure 2: Tune spread of $^{238}\text{U}^{35+}$ beam and low-order resonances in tune diagram i.e., linear difference coupling (red dotted line), 3^{rd} -order betatron (blue dotted line) and structure or systematic (blue solid line), and two half-integer resonances; The nominal working point at injection plateau is (9.47, 9.43).

To enlarge valid space for expanded tune at high intensity, multipole magnetic fields compensation or correction are proposed to decrease stop-bands that are mainly derived from magnets misalignment or magnetic field imperfections. Compensation of the following low-order betatron resonances are considered at the injection plateau and early stage of $^{238}\text{U}^{35+}$ beam acceleration at the BRing.

Stop-bands and Sources

Resonances stop-bands concerned with the BRing and their main sources are listed as:

- (a) Stop-bands from half-integer resonances of $2\nu_x = 19$ and $2\nu_y = 19$
 derived from quadrupole fields imperfection and high-order field component of magnets and to be compensated with normal quadrupole fields
- (b) Linear coupling difference resonance $\nu_x - \nu_y = 0$

derives from longitudinal magnetic fields like solenoid, rotation of quadrupoles, magnets offset, and high order field component; to be compensated with skew quadrupole fields

- (c) The 3^{rd} -order betatron resonances $3\nu_x = 28$ and $\nu_x + 2\nu_y = 28$, and systematic resonance $2\nu_y - \nu_x = 9$
 derives from high-order components of magnets and sextuple alignment; to be compensated with normal sextuple field
- (d) The 3^{rd} -order resonances $3\nu_y = 28$ and $2\nu_x + \nu_y = 28$
 derives from high-order components of magnets and sextuple alignment; to be compensated with skew sextuple fields

Table 2 lists the mainly concerned magnet misalignment details at the BRing. We included all misalignment into the BRing lattice for tacking [3]. Figure 3 gives the tracking result where κ represents the normalized resonance strength or beam loss rate. The figure indicates a obvious resonances ridge of linear coupling $\nu_x - \nu_y = 0$ and 3^{rd} -order systematic $2\nu_y - \nu_x = 9$. Among all the magnet misalignment effect on stop-bands strength, transverse tilt at horizontal x and vertical y planes contribute the most, transverse offset the second, and rotation around the longitudinal axis s do the least.

Table 2: Magnet Misalignments

Type	Dipole	Quadrupole	Sextuple
Offset x,y (mm)	0.2	0.15	0.15
Tilt x,y (mrad)	0.2	0.2	0.5
Rotation (mrad)	0.2	0.2	0.5
Offset s (mm)	0.2	0.2	0.2

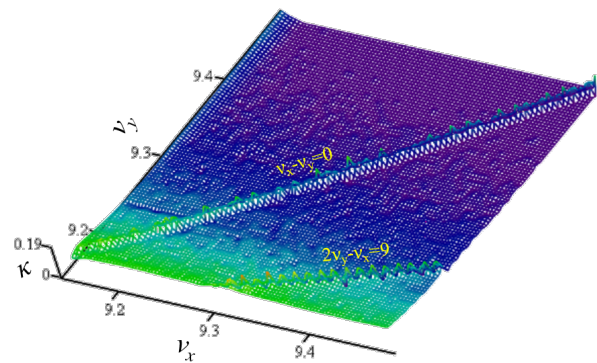


Figure 3: Resonances stop-bands from all the contributed misalignment of main magnets.

Another stop-bands contribution source is the non-zero betatron amplitude of stored particles. Because of large transverse emittance at the BRing, the two stop-bands ridges shown in Fig. 3 is also appeared in Fig. 4 even without all the concerned misalignment in tracking. But this contribution

has a weaker effect on the stop-band strength than that by misalignment. In addition, the ridges grow when the tune get close to the integer-resonances.

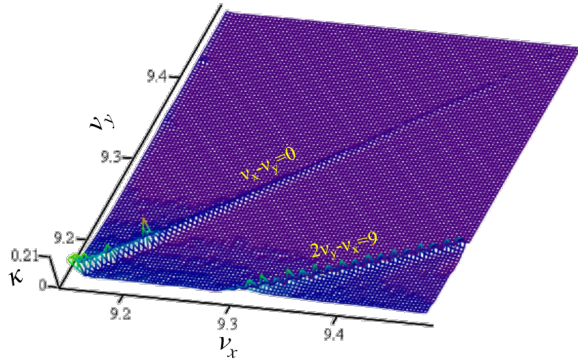


Figure 4: Resonances stop-bands contributed from particle betatron amplitude at the BRing.

Tune Spread Dependence on Energy

The BRing repetition rate is about 2 Hz. One cycle consists of 20 ms for ramping up to the injection plateau, 2 ms for painting injection, 50 ms for RF capture, and over 110 ms of acceleration, and 100 ms on the top plateau, and ramping down in 200 ms. If we take 0.4 as the maximum valid vertical tune spread for storage beam, then it will shrink to 0.1 when the synchrotron ramps up to 200 MeV/u according to spread calculation. Then, the effect of low-order resonance can be eliminated after acceleration due to not overlapping with the stop-bands any more. Thus, the compensation is needed only below 200 MeV/u at the BRing.

COMPENSATION SCHEME

According to misalignment parameters listed in Table 2 and magnetic field disturbance imperfections, we compensated the concerned stop-bands with special multipole magnetic fields. The phase advance $\Delta\phi$ between compensating elements obeys the following relationship:

$$\frac{\Delta\phi}{Q_{x,y}} \cdot M \rightarrow (n + \frac{1}{2})\pi \quad (1)$$

where $Q_{x,y}$ is the horizontal or vertical working point, M is the resonance number of $j\nu_x + k\nu_y = M$, and j, k, n , are any integers. Meanwhile, a large ratio between the two transverse betatron functions at the position of compensation elements is helpful to release the field strength requirement.

Half-integer Resonance

The compensation of half-integer resonance is reserved for shifting working points above half-integer $2\nu_y = 19$. The imperfections bring a stop-band width of 0.002. We use two trim coils combined with the existed quadruples at straight section to make compensation. The designed strength is 0.004 m^{-2} and 1.5% strength of the standard quadruple at injection plateau.

Linear Difference Coupling

Four skew quadruple field elements by adding cores and additional windings upon orbit correctors are proposed to make compensation. This type corrector has four magnet cores with two opposite ones providing steering field and all the four ones produce skew quadruple field. They have the same length of 0.3 m and design strength of 0.025 m^{-2} .

To check the linear coupling stop-band compensation effect under the misalignment listed in Table 2, we scan the tune space and give the tracking result in Fig. 5. It shows that most part of the linear coupling stop-band is compensated by the skew quadruple fields. However, the compensation also excites two betatron third-order resonances $3\nu_y = 28$ and $2\nu_x + \nu_y = 9$, among them $2\nu_x + \nu_y = 9$ shows the strongest ridge in tune space of Fig. 5.

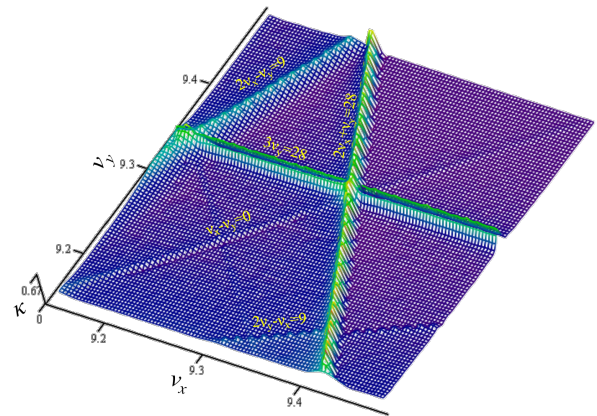


Figure 5: Compensation effect of linear coupling stop-bands with magnets misalignment.

We also adjust the BRing working point to (4.7, 4.7) just upon the linear coupling difference resonance stopbands. The misalignment is also amplified by double the maximum tilt of the main magnets for contrast. This produces 0.01 width stop-bands. The tracking shows that the remained intensity is decreased to 78% after 350 turns, while the loss rate is only 2% for the case of compensation with skew quadruple fields. The details are shown by Fig. 6.

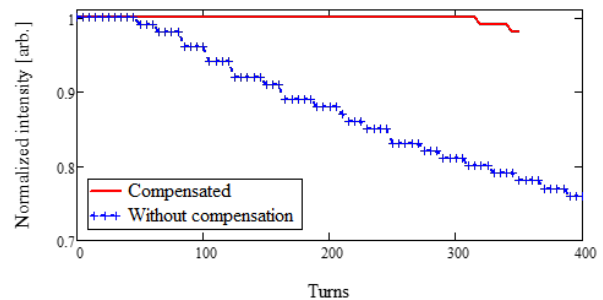


Figure 6: Compensation checking through intensity evolution under enhanced tilt misalignment

3rd-order Resonance

The imperfections around the synchrotron create a stop-band width 0.001 for $\nu_x + 2\nu_y = 28$ and 0.0007 for $3\nu_x = 28$ at injection energy. Following the principle in formula (1), four trim sextuples used for chromaticity correction at the arc section are considered to produce normal sextuple field for compensation with a strength of 0.05 m^{-3} . The misalignment and error also induced a stop-band of 0.006 for $2\nu_y - \nu_x = 9$, that will be corrected by four trim sextuple for chromaticity correction at the arc section with a strength of 0.2 m^{-3} and length of 0.3 m.

The stop-band width is 0.002 for $2\nu_x + \nu_y = 28$ and $3\nu_y = 28$ at injection energy. We introduce four new skew sextuples to make compensation with strength of 0.2 m^{-3} . They locate at the straight sections but separated by the arc section.

CONCLUSION

Space charge effect of high intensity uranium ions stacking at the BRing induces depressed tune spread and low-order

stop-bands crossing. Their compensation details are discussed. The compensation results are checked by tracking as well.

REFERENCES

- [1] J.C. Yang *et al.*, "High Intensity heavy ion Accelerator Facility (HIAF) in China", *Nucl. Instr. and Meth. B*, vol. 317, pp. 263–265, 2013.
- [2] A. Shishlo *et al.*, "The Particle Accelerator Simulation Code PyORBIT", *Procedia Computer Science*, vol. 51, pp. 1272–1281, 2015.
- [3] M. Berz, "The code COSY INFINITY", *Conference Record of the 1991 IEEE Particle Accelerator Conference*, pp. 354–356, 1992.

SIMULATION OF THE AXIAL INJECTION BEAM LINE OF THE RECONSTRUCTED U200 CYCLOTRON OF FLNR JINR

N. Kazarinov[†], G. Gulbekian, I. Ivanenko, I. Kalagin, J. Franko
 Joint Institute for Nuclear Research, 141980, Dubna, Russia

Abstract

Flerov Laboratory of Nuclear Reaction of Joint Institute for Nuclear Research begin the works under reconstruction of the cyclotron U200. The reconstructed cyclotron is intended for acceleration of heavy ions with mass-to-charge ratio A/Z within interval from 5 to 8 up to energies 2 and 4.5 MeV per unit mass. The intensity of the accelerated ions will be about 1 μA for lighter ions ($A \leq 86$) and about 0.1 μA for heavier ions ($A \geq 132$). The cyclotron will be used in the microchip SEE testing. The injection into cyclotron will be realized from the external superconducting ECR ion source. The simulation of the axial injection system of the cyclotron is presented in this report.

INTRODUCTION

Flerov Laboratory of Nuclear Reaction of Joint Institute for Nuclear Research begins the works under the conceptual design of Radiation Facility based on the DC130 cyclotron [1], that will be created as a deep reconstruction of the old cyclotron U200 [2]. Main parameters of DC130 cyclotron presents Table 1.

Table 1: DC130 Cyclotron Main Parameters

Pole (extraction) radius, m	1(0.88)	
Magnetic field, T	1.729÷1.902	
Number of sectors	4	
RF frequency, MHz	10.622	
Harmonic number	2	3
Energy, MeV/u	4.5	1.993
A/Z range	5.0÷5.5	7.577÷8.0
RF voltage, kV	50	
Number of Dees	2	
Ion extraction method	electrostatic deflector	
Deflector voltage, kV	60	

The irradiation facility will be used for Single Event Effect (SEE) testing of microchips by means of ion beams (^{16}O , ^{20}Ne , ^{40}Ar , ^{56}Fe , $^{84,86}\text{Kr}$, ^{132}Xe , ^{197}Au and ^{209}Bi) with energy of 4.5 MeV per unit mass and having mass-to-charge ratio A/Z in the range from 5.0 to 5.5.

Besides the research works on radiation physics, radiation resistance of materials and the production of track membranes will be carrying out by using the ion beams with energy of about 2 MeV per unit mass and A/Z ratio in the range from 7.58 to 8.0.

The acceleration of ion beam in the cyclotron will be performed at constant frequency $f = 10.622$ MHz of the RF-accelerating system for two different harmonic numbers h . The harmonic number $h = 2$ corresponds to the ion

beam energy $W = 4.5$ MeV/u and value $h = 3$ corresponds to $W = 1.993$ MeV/u. The intensity of the accelerated ions will be about 1 μA for lighter ions ($A \leq 86$) and about 0.1 μA for heavier ions ($A \geq 132$).

The axial injection system of DC130 cyclotron will be adapted from the existing IC100 cyclotron one [3].

This report presents the simulation of the beam dynamic in the axial injection beam line of DC130 cyclotron. The simulation was carried out by means of MCIB04 program code [4].

ECR ION SOURCE

The ion beams are produced in superconducting ECR ion source DECRIS-SC designed in Flerov Lab of JINR [5]. The working frequency DECRIS-SC is equal to 18 GHz. It is able to produce the beams of ion from ^{22}Ne to ^{209}Bi . The ion beam currents at the source exit sufficient for the facility operation is contained in Table 2.

Table 2: Ion Beam Current Extracted from DECRIS-SC

Ion	Current, pmcA	Ion	Current, pmcA
$^{22}\text{Ne}^{4+}$	~ 50	$^{132}\text{Xe}^{23+}$	~ 4
$^{40}\text{Ar}^{7+}$	~ 30	$^{132}\text{Xe}^{24+}$	~ 4
$^{56}\text{Fe}^{10+}$	~ 4	$^{197}\text{Au}^{34+}$	~ 0.3
$^{84}\text{Kr}^{15+}$	~ 8	$^{209}\text{Bi}^{37+}$	~ 0.2

In adaptation, the distance between extraction hole of the ion source and first focusing solenoid of transport beam line will be reduced significantly to avoid the losses of the ion beam.

The charge state distribution of argon beam current used in simulation is shown in Fig. 1.

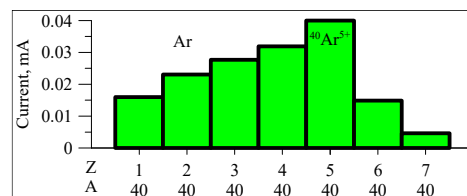


Figure 1: Ar beam current distribution.

The parameters of the ion beams at the extraction hole of ECR ion source are contained in Table 3.

Table 3: Parameters of Ion Beam Used in Simulation

Injected ions	$^{209}\text{Bi}^{38+}$	$^{40}\text{Ar}^{5+}$
A/Z	5.5	8.0
Extraction voltage U_{inj} , kV	16.8	10.9 (17.3)
Beam current [μA]	10	40
Beam diameter, [MM]	8	
Emittance, π mm×mrad	217	225 (180)

[†] nyk@jinr.ru

BEAM LINE SCHEME

The scheme of the beam line is shown in Fig. 2.

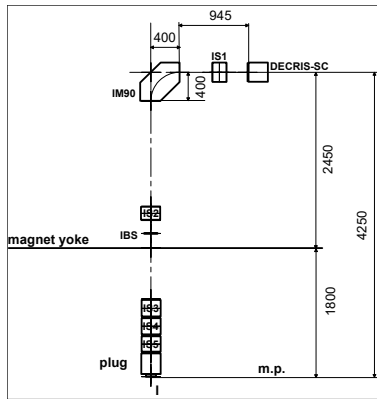


Figure 2: Scheme of the axial injection beam line.

The length of the beam line is equal to 5.423 m. The 90-degree analysing magnet IM90 separates the injected beam. The solenoidal lenses IS1-5 focus and match beam with the acceptance of the spiral inflector I for all level of the magnetic field. The sinusoidal buncher IBS increases the beam capture into acceleration.

ANALYZING MAGNET IM90

The analysing magnet IM90 has a bending radius R_M equal to 0.4 m and maximum magnetic field 0.16 T. The existence magnet of IC100 cyclotron axial injection beam line [3] will be used.

SOLENOIDS IS1,2

The solenoids IS1,2 are the part of existing IC100 cyclotron axial injection beam line [3]. Its maximum magnetic field induction is equal to 0.5 T.

SOLENOIDS IS3-5

The distribution of the magnetic field in the channel depends significantly on its magnitude at the center of the cyclotron B_0 (see Fig. 3).

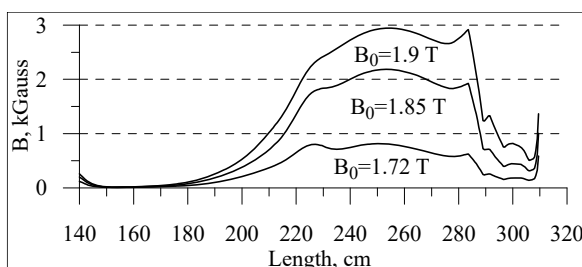


Figure 3: Cyclotron field distribution in beam line.

At low levels of the magnetic field it is necessary to use a focusing solenoid placed at the minimum distance from the median plane of the cyclotron magnet (IS5 in Fig. 2) [6]. At high levels, the cyclotron magnetic field strongly focuses the beam and it needs to be compensated by

means of additional solenoids (IS3, 4 in Fig. 2) as in the axial injection channel of the U-400M cyclotron [6].

The diameter of the hole in the yoke of the U200 magnet is equal to 136 mm. This does not allows placing solenoids with the maximum magnetic field induction greater than 1.5 kGauss. The diameter of the hole should be increased up to 262 mm that will give opportunity to achieve the necessary field magnitude for internal diameter of the vacuum tube 100 mm.

The scheme of solenoids IS3-5 is presented in Fig. 4. The Table 4 contains the parameters of solenoids. The computer model of the solenoids for the POISSON program code [7] is shown in Fig. 5. Figure 6 gives the on-axis distribution of the magnetic field of solenoids IS3-5.

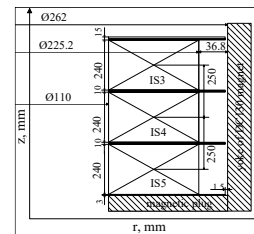


Figure 4: Scheme of solenoids IS3, 4, 5.

Table 4: Solenoids IS3,4,5 Parameters

Maximum induction, kG	3.38
Vacuum tube inner diameter, mm	100
Winding inner diameter, mm	110
Winding outer diameter, mm	225.2
Turn number	150
Winding resistance, Ohm	0.03122
Current, A	450
Voltage, V	14.0
Power supply, kW	6.3

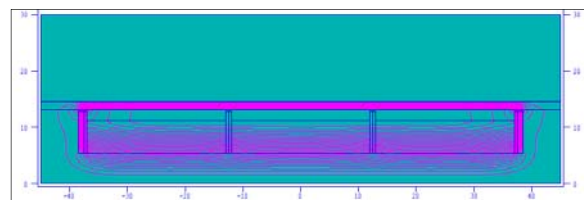


Figure 5: Computer model of solenoids. Dimensions are given in cm.

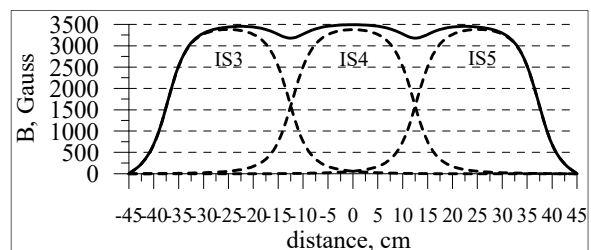


Figure 6: On-axis magnetic field of solenoids.

MAGNETIC PLUG

To ensure 100% efficiency of ion beam transfer, it is necessary to change the aperture of the magnetic plug. The scheme of proposed magnetic plug is shown in Fig. 7.

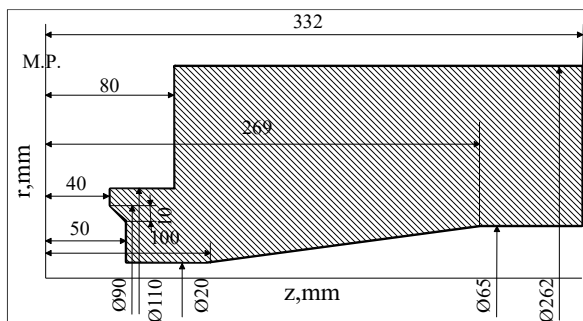


Figure 7: Magnetic plug scheme.

SINUSOIDAL BUNCHER IBS

To improve the efficiency of beam capture into the acceleration mode a sinusoidal (one harmonic) buncher IBS, located outside the yoke of the magnet at a distance of 2.0 m from the median plane of the cyclotron, is used. The maximum applied voltage at the grids of buncher is 480 V for the injecting ions having $A/Z = 5.5$. The efficiency of bunching is approximately equal to 2 (see Fig. 8).

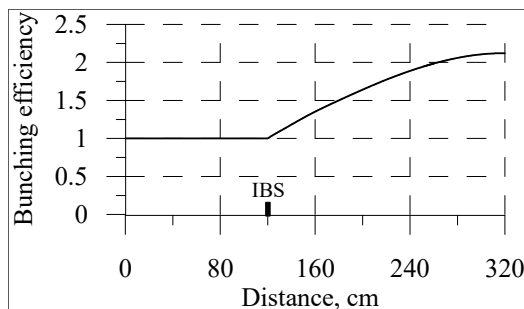


Figure 8: Bunching efficiency.

SPIRAL INFLECTOR I

The magnetic radius of the spiral inflector ρ_M is chosen equal to 2.3 cm. In the case of harmonic number $h = 2$, for this value of ρ_M , the ECR extraction voltage U_{inj} varies from 15.26 kV to 16.79 kV for ions having A/Z in the range $5.0 \div 5.5$.

While, in the case of $h=3$ extraction voltage will not exceed 10.9 kV for injecting ions having A/Z in the range $7.57 \div 8.0$. This leads to an increase of the emittance of the injected beam and a decrease of the beam bunching efficiency, because of the increasing of the beam self field.

Therefore, in the case $h = 3$ it is desirable to work with a second magnetic inflector having an magnetic radius increased up to 2.9 cm. The extraction voltage will then be in the range $U_{inj} = 16.3 \text{ kV} \div 17.3 \text{ kV}$.

SIMULATION RESULTS

Simulation of ion beam injection in the cases $A/Z = 5.5, 8.0$ are carried out. For the maximum value of $A/Z = 8$ two variants of the spiral inflector were considered. In all cases, the transfer efficiency is equal to 100%.

$$A/Z=5.5, B_0=1.902 \text{ T}, \rho_M=2.3 \text{ cm}$$

Transport of $^{209}\text{Bi}^{38+}$ ion beam was considered. In this case the magnetic field at the center of the cyclotron $B_0 = 1.9021 \text{ T}$ is maximal. The focusing solenoid IS5 is turned off ($B_{IS5} = 0$) and the matching with acceptance of the inflector is performed by focusing solenoid IS2 and compensating ones IS3,4 ($B_{IS2} = 1.906 \text{ kG}$, $B_{IS3} = B_{IS4} = -1.930 \text{ kGs}$). Figure 9 shows the cyclotron field (red line) and the total field of the cyclotron and focusing solenoids (black line).

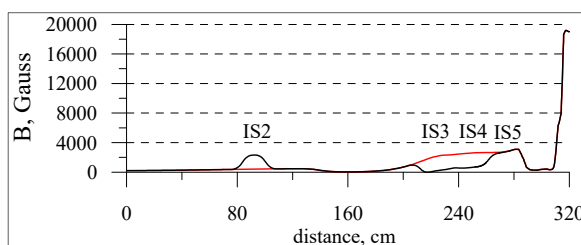


Figure 9: Cyclotron (red line) and total (black line) longitudinal magnetic field in vertical part of beam line. $^{209}\text{Bi}^{38+}$ ion beam transport.

The horizontal (H) and vertical (V) envelopes of $^{209}\text{Bi}^{38+}$ ions in the beam line is shown in Fig. 10.

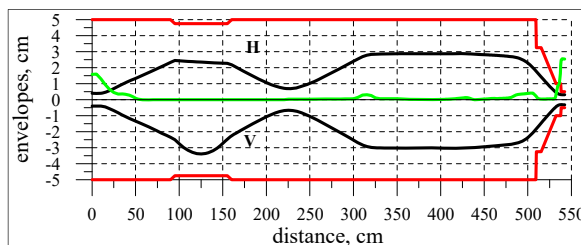


Figure 10: Horizontal (H) and vertical (V) $^{209}\text{Bi}^{38+}$ beam envelopes, aperture (red line) and longitudinal magnetic field (green line).

The beam envelopes in vicinity of magnetic plug and inflector are presents in Fig. 11.

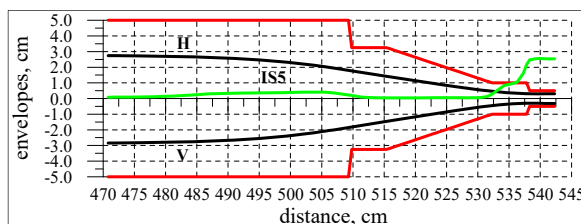


Figure 11: Horizontal (H) and vertical (V) $^{209}\text{Bi}^{38+}$ beam envelopes near magnetic plug and inflector.

Content from this work may be used under the terms of the CC BY 3.0 licence (© 2018). Any distribution of this work must maintain attribution to the author(s), title of the work, publisher, and DOI.

The dependence on distance along the beam line of the beam emittance is shown in Fig. 12.

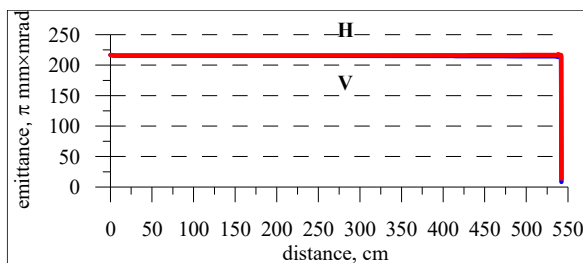


Figure 12: $^{209}\text{Bi}^{38+}$ beam emittance.

The bunching efficiency in this case is equal to 2.1 (see Fig. 8)

$$A/Z=8.0, B_0=1.8445 \text{ T}, \rho_M=2.3 \text{ cm}$$

Transport of $^{40}\text{Ar}^{5+}$ ion beam was considered. In this case the magnetic field at the center of the cyclotron $B_0 = 1.8445 \text{ T}$. In the regime with an intermediate magnitude of magnetic field in the center of the cyclotron, the compensating solenoids IS3,4 are switched on ($B_{\text{IS3}} = B_{\text{IS4}} = -2.0 \text{ kGs}$) and matching with the inflector acceptance is provided by solenoids IS2,5 ($B_{\text{IS2}} = 2.519 \text{ kG}$, $B_{\text{IS5}} = 1.209 \text{ kG}$). Figure 13 shows the cyclotron field (red line) and the total field of the cyclotron and focusing solenoids (black line).

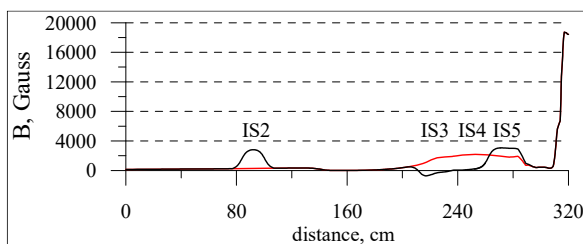


Figure 13: Cyclotron (red line) and total (black line) longitudinal magnetic field in vertical part of beam line. $^{40}\text{Ar}^{8+}$ ion beam transport.

The horizontal (H) and vertical (V) envelopes of $^{40}\text{Ar}^{5+}$ ions in the beam line is shown in Fig. 14.

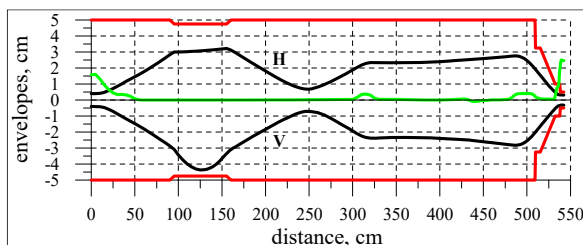


Figure 14: Horizontal (H) and vertical (V) $^{40}\text{Ar}^{5+}$ beam envelopes, aperture (red line) and longitudinal magnetic field (green line).

The beam envelopes in vicinity of magnetic plug and inflector are presents in Fig. 15.

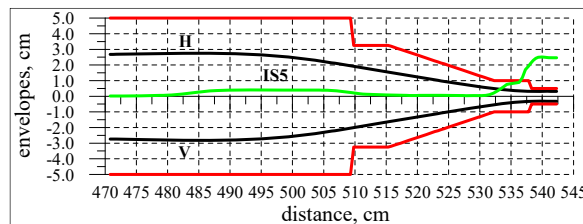


Figure 15: Horizontal (H) and vertical (V) $^{40}\text{Ar}^{5+}$ beam envelopes near magnetic plug and inflector.

The dependence on distance along the beam line of the beam emittance is shown in Fig. 16.

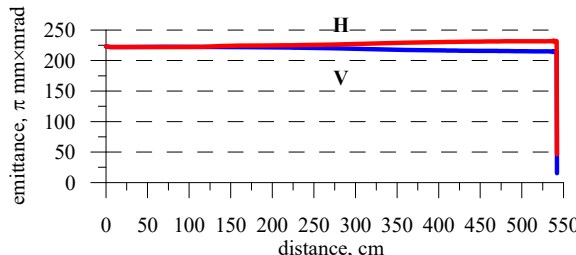


Figure 16: $^{40}\text{Ar}^{5+}$ beam emittance.

The bunching efficiency in this case is equal to 1.6 (see Fig. 17). The voltage at the grids is equal to 160 V.

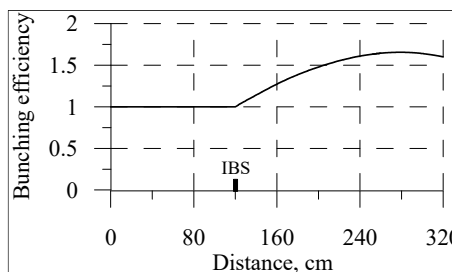


Figure 17: Bunching efficiency. $^{40}\text{Ar}^{5+}$ beam transport.

$$A/Z=8.0, B_0=1.8445 \text{ T}, \rho_M=2.9 \text{ cm}$$

Transport of the same ion beam $^{40}\text{Ar}^{5+}$ was considered. In this case, the magnetic field at the center of the cyclotron does not change. The magnetic field induction of the compensating solenoids IS3,4 does not change also. The field of solenoids IS2,5 will be greater than in the previous case due to increasing of the extraction voltage U_{inj} up to 17.26 kV ($B_{\text{IS2}} = 3.211 \text{ kG}$, $B_{\text{IS5}} = 1.953 \text{ kG}$).

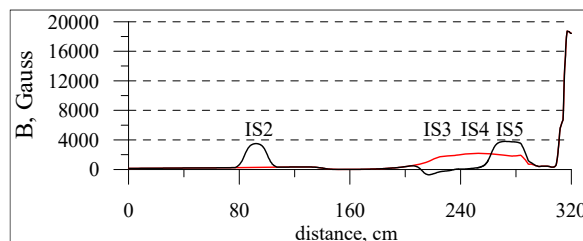


Figure 18: Cyclotron (red line) and total (black line) longitudinal magnetic field in vertical part of beam line. $^{40}\text{Ar}^{8+}$ ion beam transport, $U_{\text{inj}} = 17.26 \text{ kV}$.

Figure 18 shows the cyclotron field (red line) and the total field of the cyclotron and focusing solenoids (black line).

The horizontal (H) and vertical (V) envelopes of $^{40}\text{Ar}^{5+}$ ions in the beam line is shown in Fig. 19.

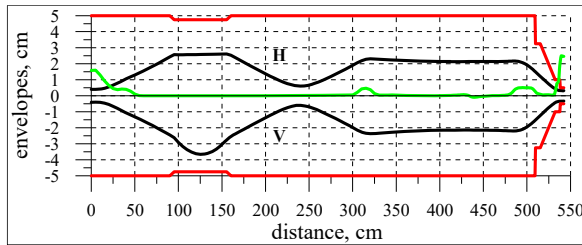


Figure 19: Horizontal (H) and vertical (V) $^{40}\text{Ar}^{5+}$ beam envelopes, aperture (red line) and longitudinal magnetic field (green line), $U_{inj} = 17.26$ kV.

The beam envelopes in vicinity of magnetic plug and inflector are presents in Fig. 20.

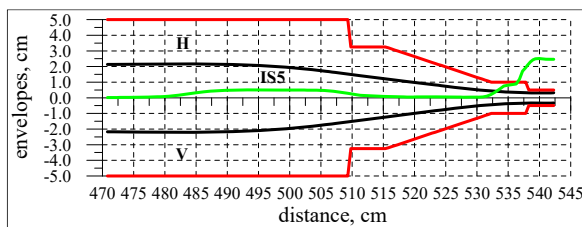


Figure 20: Horizontal (H) and vertical (V) $^{40}\text{Ar}^{5+}$ beam envelopes near magnetic plug and inflector, $U_{inj} = 17.26$ kV.

The dependence on distance along the beam line of the beam emittance is shown in Fig. 21.

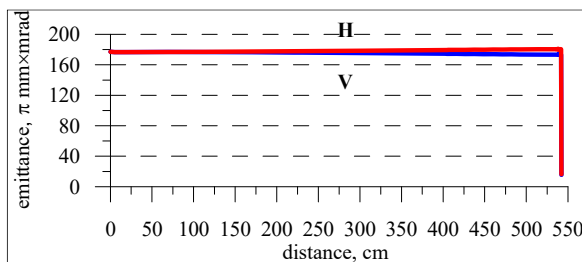


Figure 21: $^{40}\text{Ar}^{5+}$ beam emittance, $U_{inj} = 17.26$ kV.

The bunching efficiency in this case is equal to 1.81 (see Fig. 22). The voltage at the grids is equal to 300 V.

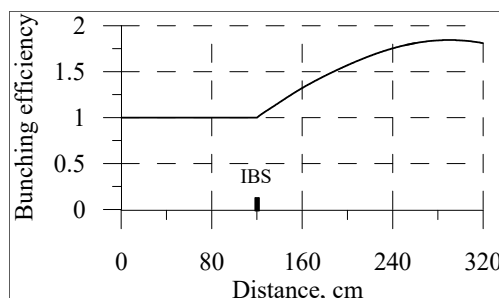


Figure 22: Bunching efficiency. $^{40}\text{Ar}^{5+}$ beam transport, $U_{inj} = 17.26$ kV.

SUMMARY

The axial injection system of DC130 cyclotron allows transporting with of 100% efficiency all ion beams declared in the project of Radiation Facility [1].

The comparison of simulation results shows the advantage of using the spiral deflector with increased up to 2.9 cm magnetic radius under work of RF with ion beams of low energy ($W = 1.993$ MeV/u).

The maximum magnetic field induction of solenoids IS3-5 is not greater than 2.0 kGauss. This gives opportunity to decrease the diameter of the hole in the yoke of the magnet by decreasing the number of layers and outer diameter of solenoidal winding.

REFERENCES

- [1] N. Kazarinov *et al.*, “Conceptual Design of FLNR JINR Radiation Facility Based on DC130 Cyclotron”, presented at HB2018, Daejeon, Korea, June, 2018, paper THA2WD03, this conference.
- [2] G. Gulbekyan, B. Gikal, I. Kalagin, N. Kazarinov, “Status Report and Future Development FLNR JINR Heavy Ions Accelerators Complex”, in *Proc. of 11-th Int. Conf. on Heavy Ion Acc. Tech., HIAT'09*, Venezia, Italy, June 2009, pp. 59-63.
- [3] B. Gikal, S. Dmitriev, G. Gulbekian, N. Kazarinov *et al.*, “Cyclotron Based Complex IC-100 for Scientific and Applied Research”, in *Proc. 18-th Int. Conf. on Cyc. and their App., CYC07*, Giardini Naxos, Italy, October 2007.
- [4] V. Aleksandrov, N. Kazarinov, V. Shevtsov, “Multi component ion beam code-MCIB04”, in *Proc. RuPACXIX*, Dubna, 2004.
- [5] A.A. Efremov, V.V. Bekhterev, S.L. Bogomolov *et al.*, “Status of the ion source DECRIS-SC”, *Review of Scientific Instruments*, vol. 77, no. 03A320, pp. 235-239, 2006.
- [6] N. Kazarinov, “Axial Injection Beam Lines of the Cyclotrons”, *Physics of Particles and Nuclei Letters*, vol. 7, no. 7, pp. 494-497, 2010.
- [7] Reference Manual for the POISSON/SUPERFISH Group of Codes, Los Alamos National Laboratory Report LA-UR-87-126, 1987.

Content from this work may be used under the terms of the CC BY 3.0 licence (© 2018). Any distribution of this work must maintain attribution to the author(s), title of the work, publisher, and DOI.

CONCEPTUAL DESIGN OF FLNR JINR RADIATION FACILITY BASED ON DC130 CYCLOTRON

N. Kazarinov[†], P. Apel, V. Bekhterev, S. Bogomolov, V. Bashevoy, O. Borisov, G. Gulbekian, J. Franko, I. Ivanenko, I. Kalagin, V. Mironov, S. Mitrofanov, A. Tikhomirov, V. Semin, V. Skuratov, Joint Institute for Nuclear Research, 141980, Dubna, Russia

Abstract

Flerov Laboratory of Nuclear Reaction of Joint Institute for Nuclear Research begins the works under the conceptual design of radiation facility based on the DC130 cyclotron. The facility is intended for SEE testing of microchip, for production of track membranes and for solving of applied physics problems. The DC130 cyclotron will accelerate the heavy ions with mass-to-charge ratio A/Z of the range from 5 to 8 up to fixed energies 2 and 4.5 MeV per unit mass. The intensity of the accelerated ions will be about 1 μA for lighter ions (A from 20 to 86) and about 0.1 μA for heavier ions (A from 132 to 209). The injection into cyclotron will be realized from DECRIS-SC the external superconducting ECR ion source. The main magnet and acceleration system of DC130 is based on the U200 cyclotron ones that now is under reconstruction. The conceptual design parameters of the various systems of the cyclotron and the set of experimental beam lines are presented in this report.

INTRODUCTION

The irradiation facility will be used for Single Event Effect testing of microchips by means of ion beams (^{16}O , ^{20}Ne , ^{40}Ar , ^{56}Fe , $^{84,86}\text{Kr}$, ^{132}Xe , ^{197}Au and ^{209}Bi) with energy of 4.5 MeV per unit mass and having mass-to-charge ratio A/Z in the range from 5.0 to 5.5. Besides the research works on radiation physics, radiation resistance of materials and the production of track membranes will be carrying out by using the ion beams with energy of about 2 MeV per unit mass and A/Z ratio in the range from 7.58 to 8.0. The facility is based on DC130 isochronous cyclotron.

The working diagram of DC130 cyclotron is shown in Fig. 1. The acceleration of ion beam in the cyclotron will be performed at constant frequency $f = 10.622$ MHz of the RF-accelerating system for two different harmonic numbers h . The harmonic number $h = 2$ corresponds to the ion beam energy $W = 4.5$ MeV/u and value $h = 3$ corresponds to $W = 1.993$ MeV/u. The intensity of the accelerated ions will be about 1 μA for lighter ions ($A \leq 86$) and about 0.1 μA for heavier ions ($A \geq 132$).

The design is based on existing systems of IC100 (Fig. 2) and U200 (Fig. 3) cyclotrons [1].

The axial injection system and beam line for track membranes production will be adapted from the existing IC100 cyclotron systems.

In the frame of reconstruction of U200 to DC130 it is planned to upgrade the cyclotron magnetic structure,

replace the magnet main coil and renovate RF system. Other systems: beam extraction, vacuum, cooling, control electronics will be new.

The experience of working at U400, U400M cyclotrons [2] will be used during developing the experimental channels for SEE testing of microchips.

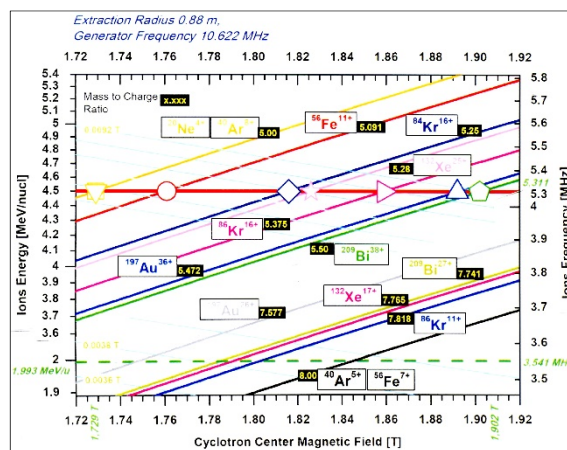


Figure 1: Working diagram of DC130 cyclotron.



Figure 2: Layout of IC100 cyclotron.



Figure 3: Layout of U200 cyclotron.

[†] nyk@jinr.ru

The main parameters of DC130 cyclotron are contained in Table.1.

Table 1: DC130 Cyclotron Main Parameters

Pole (extraction) radius, m	1(0.88)	
Magnetic field, T	1.729÷1.902	
Number of sectors	4	
RF frequency, MHz	10.622	
Harmonic number	2	3
Energy, MeV/u	4.5	1.993
A/Z range	5.0÷5.5	7.577÷8.0
RF voltage, kV	50	
Number of Dees	2	
Ion extraction method	electrostatic deflector	
Deflector voltage, kV	60	

AXIAL INJECTION SYSTEM

The axial injection system of DC130 cyclotron will be adapted from the existing IC100 cyclotron one consisted of superconducting ECR ion source – DECRIS-SC [3] and transport beam line [4].

DECRIS-SC Ion Source

DECRIS-SC is 18 GHz superconducting ion source designed in Flerov Lab of JINR. It is able to produce the beams of ion from ²²Ne to ²⁰⁹Bi. The ion beam currents at the source exit sufficient for the facility operation is contained in Table 2.

Table 2: Ion Beam Current Extracted from DECRIS-SC

Ion	Current, pmcA	Ion	Current, pmcA
²² Ne ⁴⁺	~ 50	¹³² Xe ²³⁺	~ 4
⁴⁰ Ar ⁷⁺	~ 30	¹³² Xe ²⁴⁺	~ 4
⁵⁶ Fe ¹⁰⁺	~ 4	¹⁹⁷ Au ³⁴⁺	~ 0.3
⁸⁴ Kr ¹⁵⁺	~ 8	²⁰⁹ Bi ³⁷⁺	~ 0.2

In adaptation, the distance between extraction hole of the ion source and first focusing solenoid of transport beam line will be significantly reduced to avoid the losses of the ion beam.

Axial Injection Beam Line

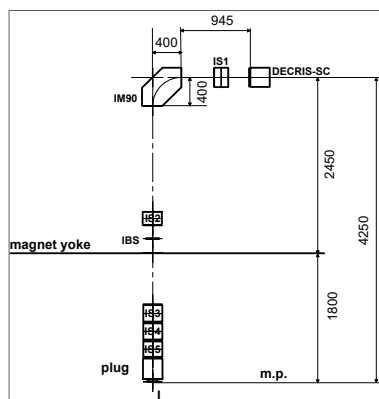


Figure 4: Scheme of the axial injection beam line.

The scheme of the beam line is shown in Fig. 4. The length of the beam line is equal to 5.423 m. The 90-degree analysing magnet IM90 separates the injected beam. The solenoidal lenses IS1-5 focus and match beam with the acceptance of the spiral inflector I for all level of the magnetic field. The sinusoidal buncher IBS increases the beam capture into acceleration. The design transport efficiency is equal to 100% for all type of the ion beam accelerated in the cyclotron. The envelopes of ²⁰⁹Bi³⁸⁺ ion beam are shown in Fig. 5. More detail information about axial injection beam line contains in report WEP2P0027 [5] at this conference.

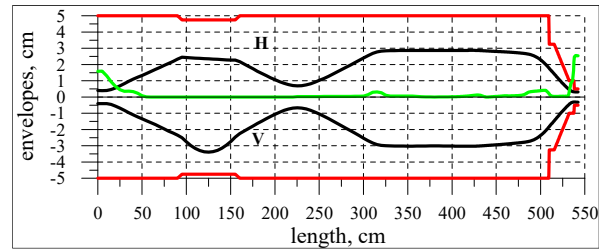


Figure 5: Horizontal (H) and vertical (V) envelopes of ²⁰⁹Bi³⁸⁺ ion beam; aperture (red line); longitudinal magnetic field (green line).

DC130 MAGNETIC SYSTEM

The magnetic system of DC130 cyclotron will be based on the existing U200 cyclotron one. The magnetic field distribution in the median plane of the DC130 cyclotron magnet has been found by means of computer simulation with 3D OPERA program code [6]. The computer model of the magnet is shown in Fig. 6. The main parameters of the magnet are contained in Table 3.

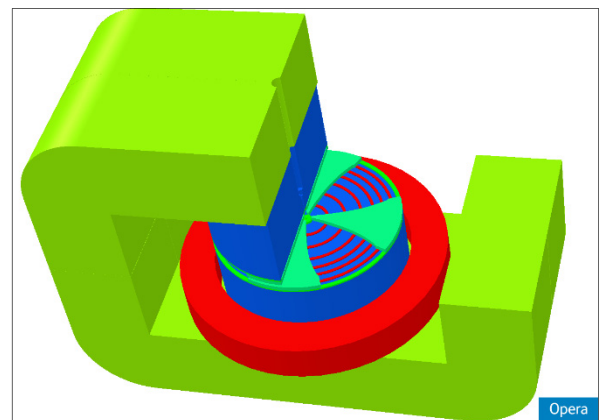


Figure 6: Computational model of cyclotron magnet.

Table 3: DC130 Cyclotron Magnet Main Parameters

Size of the magnet, mm	5000×2100×3600
Diameter of the pole, mm	2000
Distance between the poles, mm	160
Number of the sectors pairs	4
Sector angular extent (spirality)	43° (0°)
Sector height, mm	45

Content from this work may be used under the terms of the CC BY 3.0 licence (© 2018). Any distribution of this work must maintain attribution to the author(s), title of the work, publisher, and DOI.

Distance between the sectors (magnet aperture), mm	30
Distance between the sector and pole (for correcting coils), mm	20
Number of radial coils	6
Maximal power, kW	≈ 300

The operation mode change will be implemented only by variation the level of the magnetic field in the range from 1.729T to 1.902T and its isochronous distribution will be formed operationally by means of six radial correcting coils. The real magnetic field and isochronous ones radial distributions for three operation modes are shown in Fig. 7. At the middle level (red lines) the formation of the magnetic field has been made by shaping of the sector height from the pole side. In accordance with magnetic field distribution, each radial coils should be capable to produce ± 600Gs of correction magnetic field. The estimated current of the coil is equal to 15000 At. We consider the possibility of reducing the range of the magnetic field of the cyclotron and, as a consequence, the magnitude of the coil current.

The detail information about magnetic system of DC130 cyclotron contains in report THPWWC03 [7] at this conference.

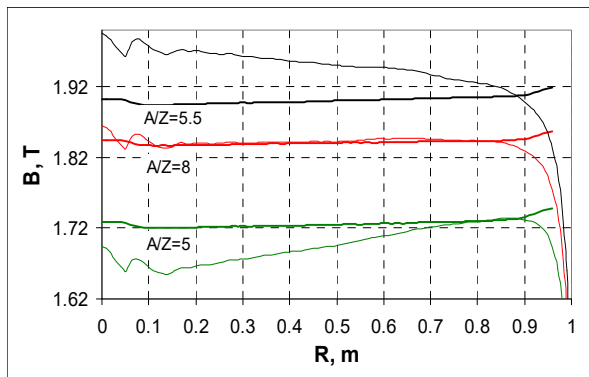


Figure 7: Magnetic field radial distributions.

RF SYSTEM

The working frequency of RF system is constant and equal to 10.622 MHz. The scheme of RF-resonator is shown in Fig. 8. The dashed line designates the placement of the ground plate. Two generators are used for independent feed of two RF resonators.

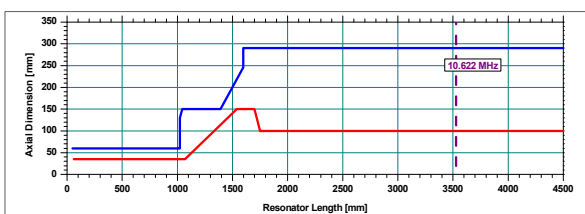


Figure 8: Scheme of RF-resonator.

The feedback system ensures precise tuning of RF phase and amplitude at both dees independently. The evaluated power of each RF generator is equal to 11.5 kW.

BEAM EXTRACTION SYSTEM

The scheme of beam extraction system of DC130 cyclotron is shown in Fig. 9. The dashed line is the cyclotron orbit corresponding to average radius of 88 cm. The red line is extraction orbit ending in the object point of the experimental beam lines. The beam extraction system includes the electrostatic deflector ESD and two magneto static channel MC1,2. In accordance with results of simulation, the maximum voltage at the deflector ESD is equal to 60 kV. The magnetic field gradients in MC1,2 channels are equals to 25 T/m and 8 T/m correspondingly.

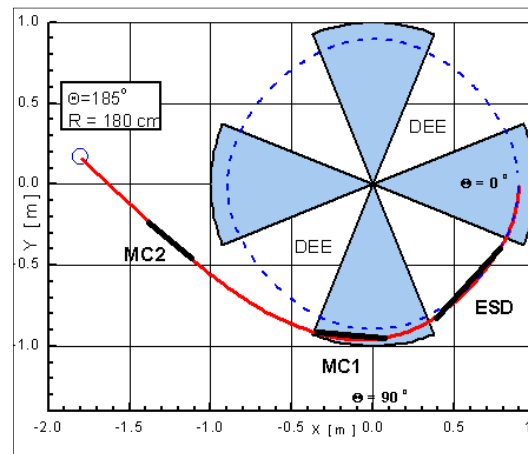


Figure 9: Scheme of DC130 extraction system.

VACUUM SYSTEM

In the axial injection beam line, the allowable average pressure of the residual gas is $1.5 \cdot 10^{-7}$ Torr. Such pressure can be provided using two turbomolecular and two cryopumps with a total pumping speed of 1600 l/s. The ion losses due to charge exchange process in the beam line is less than 15%.

The vacuum system of the DC130 cyclotron should provide the average residual gas pressure in the vacuum chamber at the level $7 \cdot 10^{-8}$ Torr. This level of pressure will be achieved with the help of turbomolecular and cryopumps with a total pumping speed of 15000 l/s.

OTHER SYSTEMS

The water-cooling and control systems will be upgraded.

EXPERIMENTAL BEAM LINES

The set of the experimental beam lines includes Track Membrane line, SEE testing line and Radiation Physics line. The scheme of the experimental beam lines is shown in Fig. 10. The common part of the channel consists of extraction bending magnet, the quadrupole lens triplet and

commutating magnet. The center of the extraction bending magnet is an object point for all beam line.

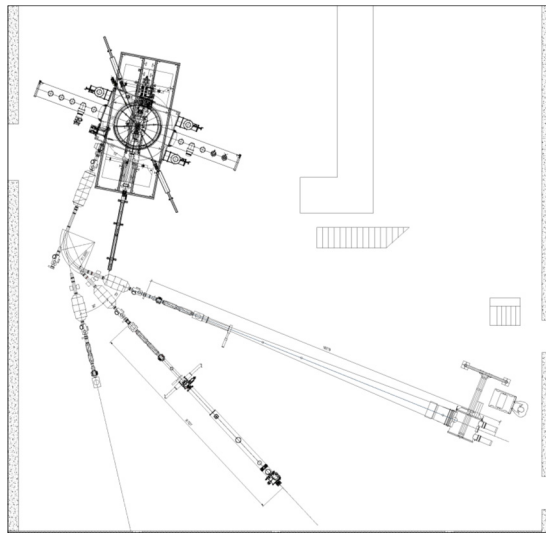


Figure 10: Scheme of experimental beam lines. From left to right: RP line; SEE testing line; TM line.

Radiation Physics Beam Line

RP line has a focusing quadrupole triplet and electromagnetic two-coordinate beam scanning system provides the homogeneous ion distribution at the irradiated surface.

SEE Testing Beam Line

During developing the experimental channels for SEE testing of microchips, we will use the experience of working at U400, U400M cyclotrons [2]. The lower energy SEE testing beam line of U400M cyclotron will be adapted to ion beam parameters of irradiation facility. This beam line contains: ion beam transportation system, beam monitoring system, energy measurement system and user vacuum test chamber with a mounting and positioning assembly to hold the sample in the irradiation field. The layout of the experimental set up is given in Fig. 11.

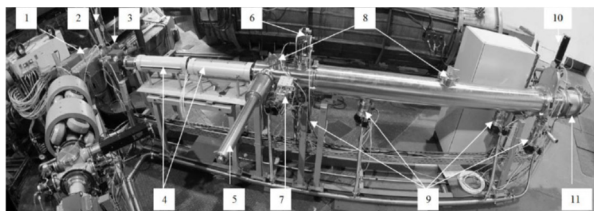


Figure 11: Layout of U400M SEE testing set up [2].

The beam leading line is separated from a bending magnet (1) by vacuum gate valve (2). The two-coordinate steering magnet (3) guides the beam through variable size diaphragm placed in entrance of the 50 Hz two-plane magnetic scanning system (4). This system provides exposure over the target area 200x200 mm² with inhomoge-

neity less than 30% in the flux range of $1 \div 10^5$ particles/(cm²s).

The degrader (5) with tantalum foils of various thickness gives possibility to choose appropriate ion energy and the Linear Energy Transfer function (LET) value.

Diagnostic elements such as Faraday cup (6) and luminophor screen (7) are used during beam tuning at high intensity.

Energy of particles passed through the foils as well as initial ion energy is measured by Time-Of-Flight (TOF) method with the help of two pick up electrodes (8).

The vacuum system of the beam line consist of three turbo molecular pumps (9). The vacuum gate valve (10) separates from the ion transport line the user target chamber (11) that is equipped with own vacuum system. This system is fast enough to pump down the chamber in less than 10 minutes.

The outer and inner view of user target chamber are given in Fig. 12.

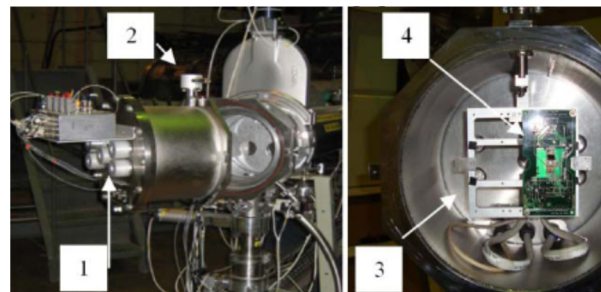


Figure 12: Outer (left) and inner (right) view of user target chamber.

The chamber has inner diameter of 28 cm and depth of 30 cm. The beam diagnostic elements (1) and user connectors are placing on the end flange of the chamber. Testing targets (4) are mounting on the frame (3) that can be tilted to the ion beam direction within $0 \div 75$ degrees by using turning gear (2).

Track Membrane Beam Line

The beam line for track membranes production will be adapted from the existing IC100 cyclotron one [4]. The experience of creating TM beam line for DC110 cyclotron [8] will be used also. The TM beam line of IC100 and DC110 cyclotrons are shown in Fig. 13 and 14.



Figure 13: TM beam line of IC100 cyclotron [4].

TM beam line consists of an initial constant aperture section with diameter of 100 mm and the special channel, made in the form of a rectangle expanding to an area of 300 x 700 mm².

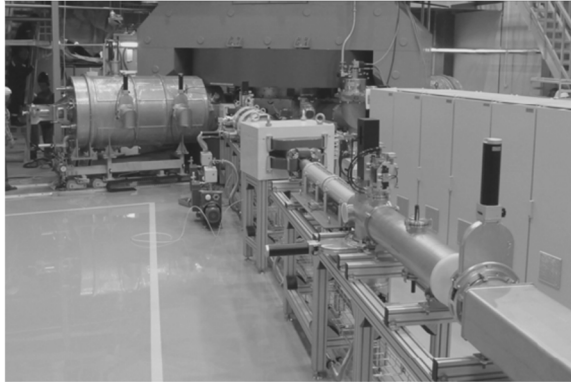


Figure 14: TM beam line of DC110 cyclotron [8].

The optical system of the channel consists of a triplet of quadrupole lenses, correcting magnets, and a scanning system for the ion beam. A horizontal scanner is based on a bending magnet supplied by a saw tooth current. Vertical scanner may be performed as electrostatic deflector [8] or alternatively as the horizontal one [2]. The working frequency of horizontal scanner is equal to 100 Hz. The electrical vertical scanner has frequency 2 kHz.

Control, blocking of the scanning system and monitoring of its parameters are the part of accelerator control system. Faraday Cups and profiler are installed in the diagnostic boxes for monitoring the beam parameters.

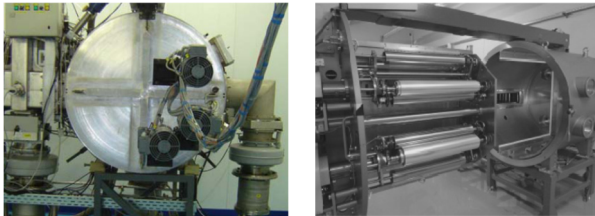


Figure 15: Film irradiation device of IC100 [4] (left) and DC110 [8] (right) cyclotrons.

TM beam line is equipped with a specialized device (see Fig. 15) intended for heavy ion irradiation of polymer film moving in the irradiated zone.

The vacuum system of TM beam line should provide the average residual gas pressure at the level $5 \cdot 10^{-6}$ Torr.

REFERENCES

- [1] G. Gulbekyan, B. Gikal, I. Kalagin, N. Kazarinov, "Status Report and Future Development FLNR JINR Heavy Ions Accelerators Complex", in *Proc. of 11-th Int. Conf. on Heavy Ion Acc. Tech., (HIAT09)*, June 2009, Venezia, Italy, June 2009, pp.59-63.
- [2] S. Mitrofanov, B. Gikal, G.G. Gulbekyan, I.V. Kalagin, N.F. Osipov, S.V. Paschenko, V.A. Skuratov, Yu.G. Teterev, V.S. Anashin, "Testing of Electronic Components at FLNR JINR Accelerator Complex: Current Status and the 7-Year Roadmap", in *Proc. XXV Russian Part. Acc. Conf. (RUPAC'16)*, St. Petersburg, Russia, November 2016.
- [3] A.A. Efremov, V.V. Bekhterev, S.L. Bogomolov et al., "Status of the ion source DECRIS-SC", *Review of Scientific Instruments*, vol. 77, pp. 235-239, no.03A320, 2006.
- [4] B. Gikal, S. Dmitriev, G. Gulbekian, N. Kazarinov, et al., "Cyclotron Based Complex IC-100 for Scientific and Applied Research", in *Proc. 18-th Int. Conf. on Cyc. and their App., CYC07*, Giardini Naxos, Italy, 1-5 October 2007.
- [5] N. Kazarinov, J. Franko, G. Gulbekian, I. Ivanenko, I. Kalagin, "Simulation of the Axial Injection Beam Line of the Reconstructed U200 Cyclotron of FLNR JINR", presented at HB2018, Daejeon, Korea, June 2018, paper WEP2PO027, this conference.
- [6] "OPERA-3D Reference Manual", Oxford OX5 1JE, England, October 2012.
- [7] G. Gulbekian, I. Kalgin, N. Kazarinov, I. Ivanenko, J. Franko, "The Choosing of Magnetic Structure of Isochronous Cyclotron DC-130 for Applied Application", presented at HB2018, Daejeon, Korea, June 2018, paper THPW003, this conference.
- [8] B.N. Gikal et al. "Development, Creation, and Startup of the DC110 Heavy Ion Cyclotron Complex for Industrial Production of Track Membranes", *Physics of Particles and Nuclei Letters*, vol. 11, no. 2, pp. 137-150, 2014.

A 4D EMITTANCE MEASUREMENT DEVICE FOR THE 870 keV HIPA INJECTION LINE

R. Dölling[†], M. Rohrer, Paul Scherrer Institut, 5232 Villigen PSI, Switzerland

Abstract

A 4D emittance measurement device has recently been installed in PSI's high intensity proton accelerator (HIPA) after the acceleration tube of the Cockcroft-Walton pre-accelerator. A pinhole collimator is moved 2D transversally and at each collimator position, the resulting beamlet is downstream scanned 2D by vertically moving over it a horizontal linear array of small electrodes. The properties of this setup and the intended use are discussed.

INTRODUCTION

In HIPA [1-3] a 10 mA DC proton beam is extracted [4] from a microwave driven volume source [5]. It is matched by a nearly fully space-charge compensated two-solenoid LEBT [4] to a 810 keV electrostatic acceleration tube driven by a Cockcroft-Walton [6]. In a 870 keV transport line of magnetic quadrupoles [3, 7] the beam is bunched [8, 3] and matched to the Injector 2 cyclotron [9], where it is collimated at the first five turns to the production current of 2.2 mA [10, 11, 3]. The space charge dominated bunches are rolled up [12-17] during acceleration and the CW 50 MHz bunched beam of 72 MeV and 2.2 mA is matched by another transport line of magnetic quadrupoles to the Ring cyclotron, where the beam is accelerated to 590 MeV [18, 3, 19]. After extraction [20], it is sent via the targets M and E, producing muons and pions, to the spallation neutron source SINQ [21, 22], or alternatively switched to the ultra-cold neutron source UCN for a few seconds every few minutes [23].

Limitation of beam losses above a few MeV and of the resulting activation of machine components is important. Guided by Joho's N^{-3} scaling law [24-26] the RF cavities in the Ring cyclotron were replaced, almost doubling their accelerating voltages [1, 25], and the beam current could be raised over the years at a constant level of beam losses. The sensitivity of the losses in the Ring cyclotron to the settings of ion source and collimation at the first turns of Injector 2 [3] as well as the positive effect of scraping the beam at certain collimators in the 870 keV injection line [27] indicate that a further reduction of beam losses at higher energies can be expected for a refined collimation in the 870 keV line and the centre region of Injector 2.

In a production machine such substantial hardware changes must be well-directed. A detailed understanding of the transport of beam core and halo based on "advanced beam dynamics simulations" including detailed 6D beam distributions and space charge is required [28, 29]. Simulations of this type were performed for segments of the accelerator chain [14, 18, 30-33], but only idealized starting distributions were used. A start-to-end simulation and a more detailed machine model are still under development.

The need for these simulations was also demonstrated by the failed commissioning of the superbuncher [29, 30, 34] which caused too large beam losses. (In contrary to the bunchers in the 870 keV line, badly affected beam particles cannot be collimated downstream at low activation cost.) Further analytical studies, such as [35], are needed to support the development of simulation tools.

Simulations as presented in [36] would also allow to determine the degree and effect of space-charge compensation (SCC) in the 870 keV transport line from a comparison with measured beam profiles. However, the use of oversimplified simulations of only a part of the line [37] is not conclusive. A measurement of the local compensation in a drift section of the line [38] indicated a compensation degree of 44% at $1e-4$ mbar, and only 11% at $1.2e-5$ mbar, N_2 gas pressure, which is still about a factor of 3 above the N_2 gas pressure at standard operation. This result cannot, however, simply be extrapolated into the magnets and to the full line since the distribution of the compensation electrons is affected by the magnetic fields, the bunching and other parameters [36, 39].

Most changes in collimation and beam optics were realized in the early years of operation. This was guided by beam dynamics considerations, educated guesses, simulations using Transport, Turtle [40] and other codes. Extensive empirical tuning by the operators played a significant part in the optimization. However, there is still potential for optimisations which do not require hardware changes; e.g. the tests of a "smooth" beam optic in the 870 keV beam line [41], which should result in a lower emittance growth, could be pursued. Only minor optics modifications have been implemented since 2006, such as an even lower numbers of turns in the cyclotrons and a dispersion free section in the 72 MeV beam line [29]. In spite of having not contributed to the optics of the production beam up to now, "advanced" simulations are the most promising approach to significant improvements.

The 4D emittance measurement (^{4D}EM) should provide simulations of downstream and upstream beam transport with a detailed truly 4D start distribution of the 870 keV 10 mA H^+ beam leaving the acceleration tube (Fig. 1). However, we also expect evidence on the reproducibility of ion source and SCC in the 60 keV LEBT. Similar to the bunch-shape measurements at higher energies [42], the ^{4D}EM is not intended as a tool for daily operation, but for beam dynamics development purposes.

SETUP

The ^{4D}EM has been squeezed into the beginning of the 870 keV transport line, without changing the quadrupole positions (Figs. 1 and 2) by removing an unused slit and integrating existing collimators for machine protection into its two vacuum chambers.

[†] rudolf.doelling@psi.ch

Content from this work may be used under the terms of the CC BY 3.0 licence (© 2018). Any distribution of this work must maintain attribution to the author(s), title of the work, publisher, and DOI.

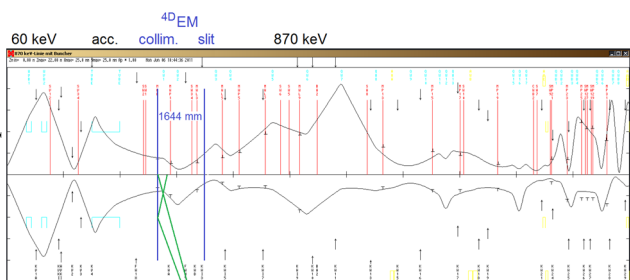


Figure 1: Beam transport from ion source to Injector 2 cyclotron. Vertical (above) and horizontal (below) 2σ envelopes from Transport [40] fit to measured profile width. SCC is included only as correction factors to space charge. Green lines indicate the beam divergence which is accepted by the 4^{D}EM at axis and 10 mm away from it.

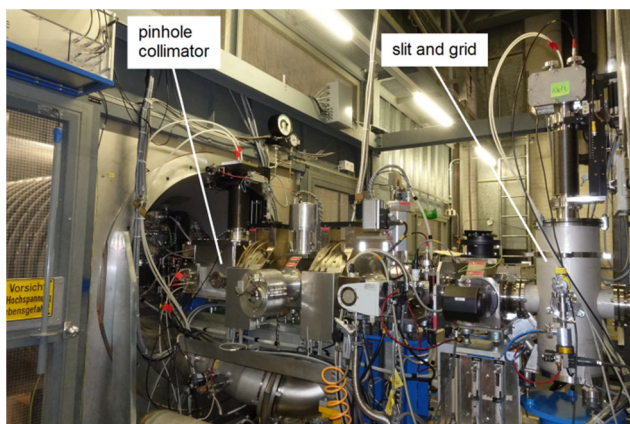


Figure 2: 4^{D}EM in 870-keV beam line.

Pinhole Collimator

The upstream vacuum chamber houses a cooled collimator which, if inserted, stops the full beam with the exception of a 0.3 mm diameter beamlet (Fig. 3). The collimator can be moved vertically and horizontally for ± 20 mm by a 2-axis feedthrough driven by stepper motors. This allows to scan the slightly convergent circular beam of ~ 10 mm core diameter.

A fixed pre-collimator of 40 mm x 40 mm aperture cuts the beam tails. In between, a suppressor electrode biased to -600 V prevents secondary electrons from the collimator to change SCC in the preceding 1.2 m drift space. The bias is maintained when the 4^{D}EM is not used.

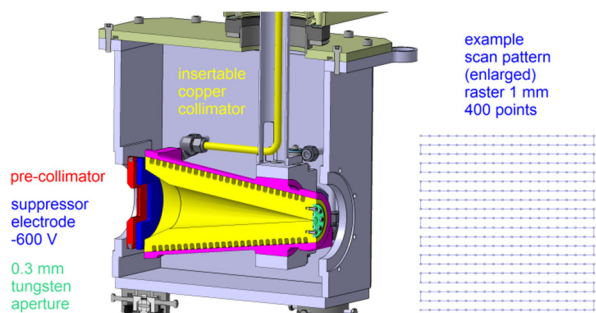


Figure 3: Upstream chamber with pinhole collimator.

Cooling grooves are milled into the collimators OFHC copper body and covered by a brazed 1.4435 stainless steel jacket. The pinhole aperture is eroded into a tungsten insert screwed to the copper block. If the device is not used, the water speed is reduced from 5 to 1 m/s to prevent corrosion.

Thermal Load

Thermal demands to the collimator are high, especially with the beam off-centre. (A pepperpot was not considered for this reason.) Due to the short length and the large transverse measurement range, it cannot handle the full beam power. The critical parameter in the chosen design is the yield stress. The yield stress index (YSI), the ratio of von-Mises stress to yield stress, should stay below 1.0 to prevent thermomechanical failure of the copper [43]. Simulations were performed with Comsol [44] assuming a Gaussian beam with $\sigma_x = \sigma_y = 2.5$ mm which couples into the cone surface, the temperature dependent copper yield stress used in [43] and a thermal resistance of 28 K/(W/mm²) of the copper-water boundary at the cooling channel surface. Accordingly a reduction of beam power to 2.5 kW is needed to satisfy the YSI criterion. At the same time copper temperatures and power densities at the cooling channel are moderate (Fig. 4).

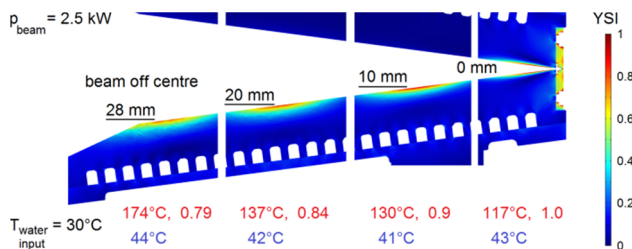


Figure 4: YSI for four different beam offsets. The plot is combined from four simulations, showing only the regions with large YSI values. Red: Maxima of copper temperature and YSI. Blue: Maxima of copper temperature at water boundary.

This will constrain operation to pulsed beam with a duty cycle of up to 25 %. Pulsing with an adjustable duty cycle is provided by deflecting the beam at the end of the LEBT with a fast kicker magnet at a rate of 500 Hz. The effect of pulsing to the SCC along the drift space from acceleration tube to collimator has to be determined.

Slit and Grid

In the downstream chamber, a slit is scanned vertically over the beamlet for up to 80 mm (Fig. 5). Behind the slit a co-moving grid of readout electrodes is formed by a stack of 160 0.4 mm thick copper sheets, isolated by 100 μm Kapton foils. The foils are retracted at the face and the stack is tilted by 4° in order to hide the foils from the beam. The slit base plate is water cooled. During measurement, the water speed is reduced from 7 to 1.3 m/s to decrease microphonic noise.

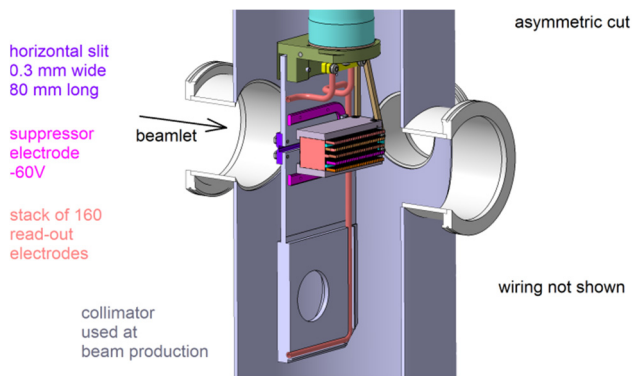


Figure 5: Downstream chamber with slit and grid.

Electronics

The three stepper motors are controlled by a 4-channel Meson-VME module [45], which also measures the signal currents at pre-collimator, collimator and slit plate. This module also sends a trigger impulse to the five 32-channel LogIV [46], which then read the 160 grid signals as a waveform in coincidence with the trajectory of the slit.

MEASUREMENT PROCEDURE

Envisaged Measurement Procedure

Before inserting collimator and slit, the beam is switched off and the in-between quadrupoles QWA1/2 are de-gaussed. With water flows adjusted and collimator and slit moved to start positions, the beam is switched on and the measurement sequence begins: The slit moves downward by, e.g., 80 mm at a constant speed of 25 mm/s and the grid currents are measured in parallel at a rate of 50 samples/s, each averaged over 20 ms. (Short ramps are added for acceleration and deceleration.) Then the collimator moves to the next point, followed by an upward scan of the slit. The collimator trajectory, e.g., as in Fig. 3, will be executed within ~26 minutes.

Estimated Performance

This demonstrates that the resolution (in this case, 1 mm spatial and 0.31 mrad angular) is in practice restricted by available measurement time and beam stability. Accuracy and reproducibility will also depend on the quality of de-gaussing of the in-between quadrupoles.

The full angular range allows to display fractions of H_2^+ and H_3^+ (within the spatial range), which survived magnetic filtering in the LEBT and are separated by a steerer magnet located 0.52 m upstream of the collimator aperture. Measurement time may be halved by reducing the ± 24 mrad angular range vertically to the perimeter of the H^+ emittance distribution.

At a 10 mA pulsed beam at 10% duty cycle, the largest signal current (averaged over the pulsing) at a single grid electrode is estimated to 10 nA. With a lower current limit of the LogIV of a few pA, a dynamic range of phase space density of 1000 results. Other than in a pepperpot measurement, no information is lost by an overlap of angular distributions of beamlets.

PROTECTION

End switches control the position of the drives to prevent thermal overload. The beam is switched off if the pinhole collimator is in transit from its parking to working position or if the slit is moved in when the collimator is not at the working position. Furthermore, all water circuits are supervised for sufficient flow and upper limits for the signal currents from collimators and slit are enforced.

It is difficult to safely protect the pinhole collimator against overly focused beam which may lead to severe damage. Limits will be set to the solenoid currents in the LEBT to keep beam size within a certain range. Beam size can also be checked with the upstream beam-induced fluorescence monitor [47]. However, supervision will still be less stringent and redundant than e.g. at the 72-MeV beam dump BX2 after the Injector 2 [48].

OUTLOOK

The project is presently on hold due to a lack of resources. The measurement software has still to be written, including suitable depictions of the 4D distribution which is not directly displayed as in the case of the pepperpot with screen. In addition to commissioning we will attempt to improve the thermal capability towards full current operation. We will also seek a better understanding of the fatigue limit of the present collimator configuration.

ACKNOWLEDGEMENTS

We thank Mischa Tahedl for creating the 3D model and the drawings and contributing to supervision of manufacturing and acquisition of components, Roger Senn for mounting, testing and inserting the mechanics, Urban Frei and Gregor Gamma for installing the electronics and testing, and Hubert Lutz and Patric Bucher for integration into the machine control system and run permit system.

AUTHOR CONTRIBUTIONS

RD conceived the device, specified its physics layout and wrote the paper. MR provided the detailed mechanical layout and contributed to the figures.

REFERENCES

- [1] M. Seidel *et al.*, “Production of a 1.3 MW proton beam at PSI”, in *Proc. IPAC'10*, Kyoto, Japan, May 2010, paper TUYRA03, pp. 1309-1313.
- [2] M. Seidel *et al.*, “High intensity operation and control of beam losses in a cyclotron based accelerator”, in *Proc. HB'12*, Beijing, China, Sept. 2012, paper THO1C01, pp. 555-559.
- [3] T. Stammach *et al.*, “The PSI 2 mA beam and future applications”, in *Proc. Cyclotrons'01*, East Lansing, MI, USA, May 2001, pp. 423-427.
- [4] M. Olivo, “Operational experience with the SIN 870 keV Cockcroft-Walton pre-injector”, in *Proc. Cyclotrons'86*, Tokyo, Japan, Oct. 1986, pp. 519-522.
- [5] C. Baumgarten *et al.*, “A compact electron cyclotron resonance proton source for the Paul Scherrer Institute’s proton

- accelerator facility”, *Rev. Sci. Instrum.*, vol. 82, p. 053304, May 2011, doi :10.1063/1.3590777
- [6] M. Olivo, “Initial operation of the SIN 860 keV Cockcroft-Walton pre-injector”, in *Proc. Linac'84*, Seeheim, Germany, May 1984, pp. 380-382.
- [7] C. Markovits *et al.*, “The 870 keV high intensity proton beam transfer line for the Injector 2 cyclotron at SIN”, in *Proc. PAC'87*, Washington, D:C., USA, Mar. 1987, pp. 1954-1956.
- [8] G. Grillenberger *et al.*, “Commissioning and tuning of the new buncher system in the 870 keV injection beamline”, in *Proc. Cyclotrons'07*, Giardini Naxos, Italy, Oct. 2007, pp. 464-466.
- [9] W. Joho *et al.*, “Commissioning of the new high intensity 72 MeV Injector II for the SIN Ring cyclotron”, in *Proc. PAC'85*, Vancouver, BC, Canada, May 1985, pp. 2666-2668.
- [10] J. Stetson *et al.*, “The commissioning of PSI Injector 2 for high intensity, high quality beams”, in *Proc. Cyclotrons'92*, Vancouver, BC, Canada, July 1992, pp. 36-39.
- [11] A. Kolano, “A precise 3D beam dynamics model of the PSI Injector II”, Ph.D. thesis, University of Huddersfield, Huddersfield, UK, 2017, <http://eprints.hud.ac.uk/id/eprint/31753/>
- [12] S. Adam, “Calculation of space-charge effects in isochronous cyclotrons”, in *Proc. PAC'85*, Vancouver, BC, Canada, May 1985, pp. 2507-2509.
- [13] S. R. Koscielniak *et al.*, “Simulation of space-charge dominated beam dynamics in an isochronous AVF cyclotron”, in *Proc. PAC1993*, Washington, D.C., USA, May 1993, pp. 3639-3641.
- [14] J. J. Yang *et al.*, “Beam dynamics in high intensity cyclotrons including neighboring bunch effects: Model, implementation, and application”, *Phys. Rev. ST Accel. Beams*, vol. 13, p. 064201, Jun. 2010, doi :10.1103/PhysRevSTAB.13.064201
- [15] A. Goto, “Mechanism of formation of a round beam by space-charge forces in cyclotrons”, *RIKEN Accel. Prog. Rep.* Vol 44, 2011, pp. 107-108.
- [16] R. Baartman, “Space charge limit in separated turn cyclotrons”, in *Proc. Cyclotrons'13*, Vancouver, BC, Canada, Sep. 2013, paper WE2PB01, pp. 305-309.
- [17] C. Baumgarten, “Transverse-longitudinal coupling by space charge in cyclotrons”, in *Proc. Cyclotrons'13*, Vancouver, BC, Canada, Sep. 2013, paper WE2PB03, pp. 315-319.
- [18] Y. J. Bi *et al.*, “Towards quantitative simulations of high power proton cyclotrons”, *Phys. Rev. ST Accel. Beams*, vol. 14, p. 054402, May 2011, doi :10.1103/PhysRevSTAB.14.054402
- [19] W. Joho, “High intensity beam acceleration with the SIN cyclotron facility”, in *Proc. Cyclotrons'86*, Tokyo, Japan, Oct. 1986, pp. 31-37.
- [20] M. Olivo, “The electrostatic extractor channel for the SIN 590 MeV Ring cyclotron”, in *Proc. Cyclotrons'75*, Zurich, Switzerland, Aug. 1975, pp. 292-296.
- [21] U. Rohrer, “590 MeV proton beam lines”, aea.web.psi.ch/Urs_Rohrer/MyWeb/pkana1.htm
- [22] D. Reggiani, “Extraction, transport and collimation of the PSI 1.3 MW proton beam”, in *Proc. HB'12*, Beijing, China, Sep. 2012, paper WEO3A03, pp. 373-377.
- [23] D. Reggiani *et al.*, “A macro-pulsed 1.2 MW proton beam for the PSI ultra cold neutron source”, in *Proc. PAC'09*, Vancouver, BC, Canada, May 2009, paper TU6RFP086, pp. 1748-1750.
- [24] W. Joho, “High intensity problems in cyclotrons”, in *Proc. Cyclotrons'81*, Caen, France, Sept. 1981, pp. 337-347.
- [25] T. Stambach *et al.*, “Potential of cyclotron based accelerators for energy production and transmutation”, in *Int. Conf. on Accelerator-Driven Transmutation Technologies and Applications*, Las Vegas, NM, USA, July 1994, AIP Conf. Proc. 346, 1995, pp. 229-235, doi :10.1063/1.49093
- [26] U. Schryber *et al.*, “High power operation of the PSI accelerators”, in *Proc. Cyclotrons'95*, Cape Town, South Africa, Oct. 1995, pp. 32-38.
- [27] G. Fabian, PSI, private communication, 2001.
- [28] A. Adelman *et al.*, “Precise simulations of high-intensity cyclotrons”, PSI Scientific Report 2010, Villigen, Switzerland, pp. 54-55.
- [29] M. Humbel *et al.*, “Tuning of the PSI 590 MeV Ring cyclotron for accepting and accelerating a rebunched 72 MeV proton beam”, in *Proc. Cyclotrons'13*, Vancouver, BC, Canada, Sep. 2013, paper TH1PB02, pp. 437-439.
- [30] A. Adelman *et al.*, “Beam dynamics studies of the 72 MeV beamline with a super buncher”, in *Proc. EPAC'04*, Lucerne, Switzerland, July 2004, paper WEPLT048, pp. 1945-1947.
- [31] A. Adelman *et al.*, “Recent results on simulations of high intensity beams in cyclotrons”, in *Proc. Cyclotrons'04*, Tokyo, Japan, Oct. 2004, pp. 425-429.
- [32] S. Wei *et al.*, “Update on the IW2 transfer line simulations”, presented at PSI, Villigen, Switzerland, March 6, 2012, unpublished.
- [33] N. J. Pogue *et al.*, “OPAL simulations of the PSI Ring cyclotron and a design for a higher order mode flat top cavity”, in *Proc. IPAC'17*, Copenhagen, Denmark, May 2017, pp. 3891-3894, doi :10.18429/JACoW-IPAC2017-THPAB077.
- [34] M. Humbel *et al.*, “Experience with and theoretical limits of high intensity high brightness hadron beams accelerated by cyclotrons”, in *Proc. HB'04*, Bensheim, Germany, Oct. 2004, *AIP Conf. Proc.* 773, 2005, pp. 313-317, doi :10.1063/1.1949553
- [35] C. Baumgarten, “Cyclotron closed orbits on a radial grid”, *Nucl. Instr. Meth. A*, vol. 647, pp. 31-33, 2014, doi :10.1016/j.nima.2014.11.022
- [36] D. Noll *et al.*, “The particle-in-cell code bender and its application to non-relativistic beam transport”, in *Proc. HB2014*, East Lansing, MI, USA, Oct. 2014, paper WEO4LR02, pp. 304-308.
- [37] S. Adam *et al.*, “Steps to enhance the knowledge on space charge effects”, in *Proc. Cyclotrons'01*, East Lansing, MI, USA, May 2001, pp. 428-430.
- [38] J. Sherman *et al.*, “H⁺ beam neutralization measurements at 870 keV beam energy”, *Rev. Sci. Instrum.*, vol. 63, pp. 2776-2778, Apr. 1992.
- [39] R. Dölling *et al.*, “Radial distribution of space-charge force in compensated positive-ion beams”, in *Proc. ICIS'97*, Taormina, Italy, Sep. 1997, *Rev. Sci. Instrum.*, vol. 69, pp. 1094-1099, doi :10.1063/1.1148650

- [40] U. Rohrer, PSI Graphic Transport Framework based on a CERN-SLAC-FERMILAB version by K. L. Brown *et al.*, http://aea.web.psi.ch/Urs_Rohrer/MyWeb
- [41] R. Dölling, “Sanfte Optik in der 870-keV-Linie”, PSI, Villigen, Switzerland, Internal Rep. HIPA-BEAMDY-DR84-008.00-080310, Mar. 2010.
- [42] R. Dölling, “Progress with bunch-shape measurements at PSI’s high-power cyclotrons and beam lines”, in *Proc. HB’12*, Beijing, China, Sep. 2012, paper MOP253, pp. 187-191.
- [43] Y. Lee *et al.*, “Simulation based optimization of a collimator system at the PSI proton accelerator facilities”, in *Proc. IPAC’10*, Kyoto, Japan, May 2010, paper THPEC088, pp. 4260-4262.
- [44] COMSOL Multiphysics, release 5.3a, <http://www.comsol.com>
- [45] E. Johansen, “VME Meson design specification”, PSI, Villigen, Switzerland, Jun. 2010, unpublished.
- [46] P. A. Duperrex *et al.*, “Latest diagnostic electronics development for the Proscan proton accelerator”, in *Proc. BIW’04*, Knoxville, TN, USA, May 2004, *AIP Conf. Proc.*, vol. 732, pp. 268-275, 2004.
- [47] L. Rezzonico *et al.*, “A profile monitor using residual gas”, in *Proc. Cyclotrons’89*, Berlin, Germany, May 1989, pp. 313-316.
- [48] L. Rezzonico *et al.*, “Surveillance protection of a 150 kW proton beam dump”, in *Proc. BIW’00*, Cambridge, MA, USA, May 2000, *AIP Conf. Proc.*, vol. 546, pp. 555-562, 2000.

A SECONDARY EMISSION MONITOR IN THE SINQ BEAM LINE FOR IMPROVED TARGET PROTECTION

R. Dölling[†], M. Rohrer, Paul Scherrer Institut, 5232 Villigen PSI, Switzerland

Abstract

A 4-strip secondary-emission monitor (SEM) has been installed in the beam line to the SINQ neutron source to detect irregular fractions of the megawatt proton beam which might damage the spallation target. We discuss the estimated performance of the monitor as well as its design and implementation.

INTRODUCTION

A key issue to ensure safe operation of the SINQ spallation target is to prevent a too large current density of the proton beam at the target. Recently, a campaign has been launched in order to improve the fast detection of such improper beam delivery [1]. Already small beam fractions accidentally bypassing the upstream muon production target TE result in a significant increase of current density at the SINQ target. This 'irregular' beam fraction has not been decelerated and hence is shifted vertically in the dispersive section at wire monitor MHP55X/56Y.

The SEM MHB28 has been placed in the aperture of the wire monitor (Fig. 1) to provide a permanent monitoring of irregular beam in the upcoming beam period. It consists of four parallel foil strips, two above the beam and two below. The basic approach is to fix the position of the main part of the beam by limiting the allowed beam fraction on the inner strips to a few percent. Irregular beam is then prevented by limiting the allowed beam fraction on the outer strips to much less than one percent.

A similar approach, based on the vertical collimator KHNY30 located inside quadrupole QHJ30 1.8 m downstream of MHB28, is already in use [2]. However, its accounted beam fraction is very limited by the heat load and activation tolerated by its uncooled copper blocks. This enforces a wider gap which results in a less strict supervision.

SETUP

The 20 μm Molybdenum foil strips are pre-tensioned by 1.4310 stainless steel springs with 0.42 and 1.3 N to keep them flat even at strong heating (Fig. 2). The clamps are coated at the outside with Diconite[®] DL-5 to allow many thermal cycles without sticking in the guide blocks. The guide blocks are isolated with hidden ceramic spacers from the grounded parts of the ring. All parts made from stainless steel. All 8 foil ends are contacted via clamp/spring/guide block and Kapton isolated wire to a 9-pin D-Sub feedthrough at the wire monitor flange. The clamps protrude up to 20 mm into the 200 mm aperture of the adjacent vacuum chamber, which is not critical at the monitor location. Since the electrodes are largely free standing, we don't use an additional biased electrode for pulling the secondary electrons.

The four foil signals are transported via a shielded cable to the LogIV4x4 read-out electronics outside the vault (similar to [3]). The signals from the other foil ends are transported to the electronics rack in the same way. This allows us to check the presence of the foil strips by injecting a test current from a current source (into the normally open ended cable).

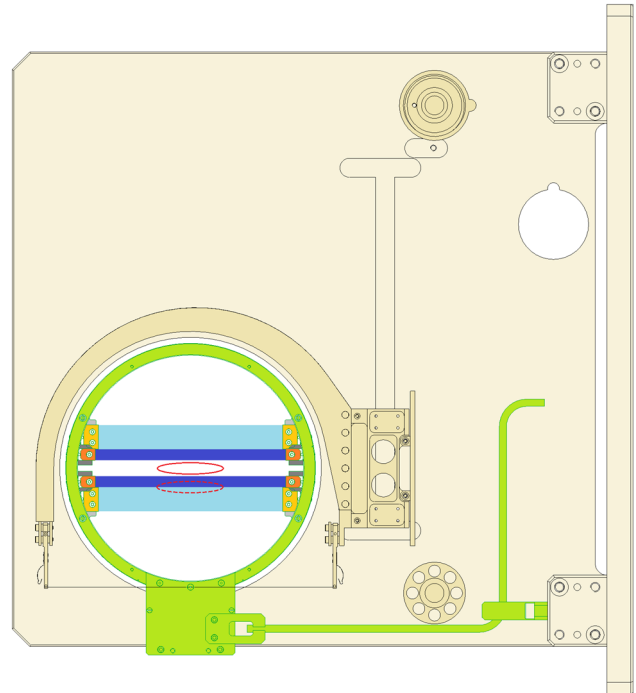


Figure 1: Wire Monitor MHP56Y (front, not all parts shown) and MHP55X (rear side, not visible) with 4-strip SEM MHB28 (green, foil strips blue) inserted and clamped to the base plate. 2σ beam contours are indicated for regular (full red) and irregular (dotted red) beam. Beam comes out of drawing plane.

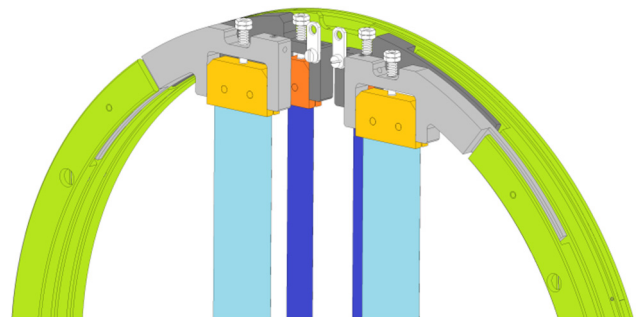


Figure 2: Foil tensioning with springs. Clamps (orange), guide blocks (grey), grounded parts (green), wires not shown. Each spring compressed by 3 mm.

[†] rudolf.doelling@psi.ch

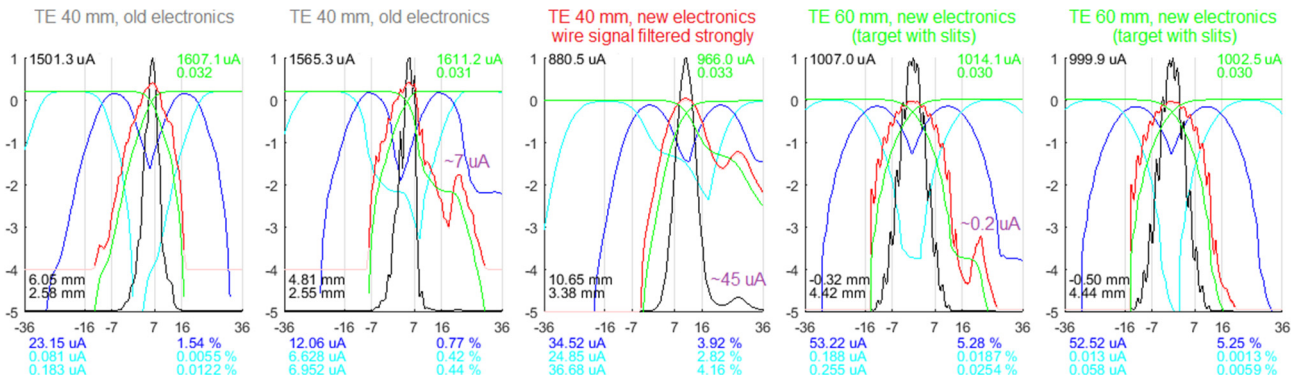


Figure 3: Examples of vertical beam profiles MHP56 with 0/~7/~45/~0.2/0 μA irregular beam current. Horizontal axis: Vertical position in beam pipe [mm]. **Black line**: Wire signal normalized (linear). **Black**: Beam current measured with current monitor MHC6, beam centre position and 1σ width. **Red line**: Beam current line density [$\log(100 \mu\text{A}/\text{mm})$]. **Green lines**: Beam current integrated from left and right [$\log(\text{mA})$]. **Green**: Beam current for $n_{\text{SE}} = 0.030$ and actual secondary emission yield of wire surface $n_{\text{SE,act}}$. **Blue line**: Maximum of both beam currents on inner strips when profile position is assumed to be shifted [$\log(\text{mA})$]. **Blue**: close-to-centre minimum of blue line. **Cyan line**: Maximum of both beam currents on outer strips [$\log(\text{mA})$] at same assumed profile shift. **Upper cyan**: Maximum of both beam currents on outer strips at inner-strips-minimum. **Lower cyan**: Same, but in a range of ± 2 mm around inner-strips-minimum.

BEAM PROPERTIES, STRIP SIZE AND PERFORMANCE OF SUPERVISION

Beam properties at MHP55X/56Y have been determined from 330 sets of beam profiles taken in the years 2008 - 2017 during beam production and beam development. With the 40 mm thick TE, the 1σ beam width is typically 2.9 ± 0.9 mm vertically (and 14-15 mm horizontally). The irregular beam is shifted by 17 mm. Strip sizes and positions are adapted to this situation. They are chosen in a way that the centred regular beam passes both inner strips to a sufficient degree, but practically not the outer strips, while a significant part of the irregular beam passes the lower outer strip. We use a width of 9 mm for the inner strips, of 20 mm for the contiguous outer strips and 14 mm for the central gap.

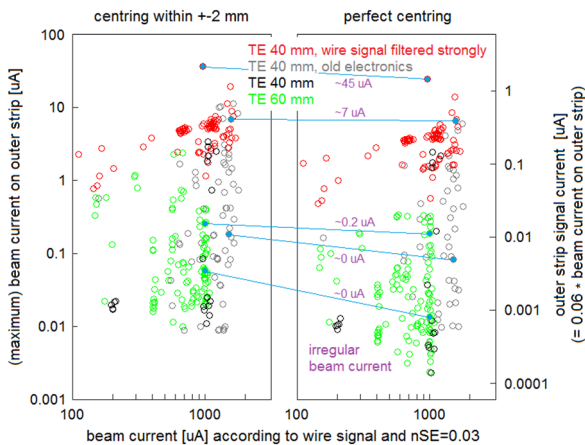


Figure 4: Maximum beam current passing one of the outer strips. The corresponding strip signal currents are estimated on the basis of the average secondary emission yield of $n_{\text{SE}} = 0.030$ deduced for the surface of the two $48 \mu\text{m}$ Molybdenum wires of the wire monitor. The five examples from Fig. 3 are marked in blue.

The sensitivity of this setup to irregular beam can be estimated from previously measured profiles using the evaluation depicted in Fig. 3: It is assumed that the beam can be centred vertically (to minimize the maximum of the signal currents of the inner strips) either perfectly or with an accuracy of ± 2 mm. Under this condition, the beam currents to be expected at the outer strips (the lower cyan numbers in Fig. 3) are given by Fig. 4. Comparison with profile shapes indicate that irregular beam correlates with beam current on the lower outer strip above $0.1 \mu\text{A}$ for profiles taken with the present wire monitor electronics (black and green points in Fig. 4) and above $1 \mu\text{A}$ for the former slower and less sensitive electronics (grey points). The irregular beam current is then of the order of the beam current passing the lower outer strip.

Practically, the performance of supervision of irregular beam by the basic approach of just limiting the outer strip signal currents is limited by the quality of vertical beam 'centredness' which can be reached in everyday operation and during beam current ramping. An active beam centring, e.g., on the basis of the position information from the relative difference of the signal currents from the inner strips, could be helpful. To prevent frequent interlocks due to a centring margin of, e.g., ± 6 mm, we have to set a correspondingly higher switch off (interlock) limit of $0.6 \mu\text{A}$, set in the read-out electronics for the outer strip signal currents, corresponding to an irregular beam fraction of the order of $10 \mu\text{A}$ (estimated from Fig. 3). Inclusion of position information from the inner strips into the evaluation would improve this. Hereto an algorithm can be derived from a simulation of strip currents assuming a Gaussian vertical beam profile of nominal width.

In the case of sole irregular beam, this supervision will fail, if the associated unusual steering cannot be detected or prevented. At an unexpectedly small vertical width of the regular beam, irregular beam can be limited only by limiting the beam currents to the inner strips. The margin cannot, however, be set as low as needed.

Content from this work may be used under the terms of the CC BY 3.0 licence (© 2018). Any distribution of this work must maintain attribution to the author(s), title of the work, publisher, and DOI.

The irregular beam fraction can also be observed in the horizontal beam profile at the next downstream wire monitor as evident in Fig. 5. Due to the overly strong low pass filtering of the signal at that time, the local current density was likely to have been greater increased than it appears.

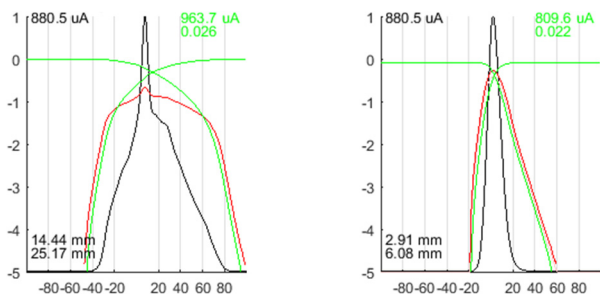


Figure 5: Horizontal (left) and vertical (right) profile at wire monitors MHP57/58, located 6.27 m downstream of MHP55/56, corresponding to the third profile in Fig. 3.

FOIL PROTECTION

If the 20 μm Molybdenum foil is accidentally hit by the full nominal beam of 1.7 mA, it would not melt even at the lower observed beam width. However, the strips would survive only a few days due to vapour pressure and evaporation at an estimated temperature of $\sim 1920^\circ\text{C}$ (at assumed emissivity $\epsilon = 0.24$, material data from [4]). Also, foil tension would be lost due to creep within hours. To prevent such damage in the long term, the maximum temperature has to be kept to below $\sim 1470^\circ\text{C}$ (at $\epsilon = 0.19$). This can be reached either by reducing the foil thickness to 6 μm , or by reducing the core beam current density. Assuming a Gaussian profile, the latter can be provided by limiting the beam current passing an inner strip to $\leq 200 \mu\text{A}$, which is somewhat above the observed values for a centred beam (Fig. 6). However, this requires centring within a margin of $\pm 4 \text{ mm}$ (estimated from Fig. 3).

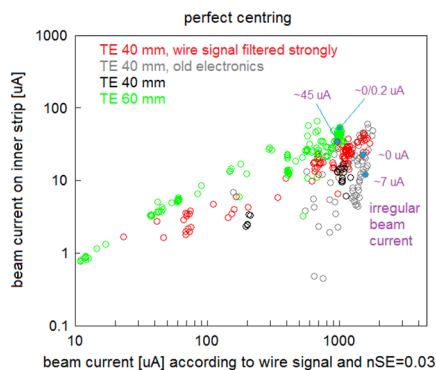


Figure 6: Maximum beam current passing one of the inner strips at centred beam. It is mainly given by current and vertical size of the regular beam.

SCATTERING AND ACTIVATION

Scattering of the beam by the 20 μm Molybdenum foil strips should be negligible for the further transport according to TURTLE simulations [5].

In the long term, the integrated beam current hitting the strips of MHB28 will be substantial. Activation will be concentrated to the centre part of the strips. At an eventual exchange of the monitors, the strips may be cut away and removed first with a dedicated tool. Since beam losses are comparatively low in this part of the beam line, the surrounding monitor components are much less activated and well accessible [6].

OUTLOOK

The SEM was installed at the end of the 2018 shut-down (Fig. 7) and will soon be exposed to the production beam. We will learn if vertical position stability and centring will suffice to uphold the mentioned or lower interlock levels, if the downstream beam loss stays unaffected and if radiation damage will occur to the foil. With this we may conclude on the need and feasibility of a harp, covering the full vertical beam profile.



Figure 7: Monitor MHB28 after insertion into MHP55/56.

ACKNOWLEDGEMENTS

We thank Roger Senn for evaluating the insertion environment, proposing a shift from before to inside the profile monitor, mounting and inserting the monitor, Gregor Gamma for installing the electronics and testing, and Hubert Lutz and Patric Bucher for integration into the machine control system and run permit system.

AUTHOR CONTRIBUTIONS

RD conceived the device, analysed the data, specified the physics layout and wrote the paper. MR provided the detailed mechanical layout and contributed to the figures.

REFERENCES

- [1] D. Reggiani *et al.*, “Improving machine and target protection in the SINQ beam line at PSI-HIPA”, in *Proc. IPAC’18*, Vancouver, BC, Canada, Apr.-May 2018, paper WEPAL068.
- [2] U. Rohrer, “First beam tests with the new slit collimator in the proton beam line to SINQ”, PSI, Villigen, Switzerland, Annual Report 2004, Vol. VI, pp. 23-26.
- [3] R. Dölling, “Profile, current and halo monitors of the Proscan beam lines”, in *Proc. BIW’04*, Knoxville, TN, USA, May 2004, *AIP Conf. Proc.*, vol. 732, pp. 244-252, 2004.

- [4] Plansee Group, Molybdän,
www.plansee.com/de/werkstoffe/molybdaen.html
[5] D. Reggiani, PSI, private communication, Jan. 2018.

- [6] R. Dölling *et al.*, “Beam diagnostics at the high power proton beam lines and targets at PSI”, in *Proc. DIPAC'05*, Lyon, France, Jun. 2005, paper ITTA02, pp. 228-232.

Content from this work may be used under the terms of the CC BY 3.0 licence (© 2018). Any distribution of this work must maintain attribution to the author(s), title of the work, publisher, and DOI.

A TEST OF STRIPPER FOIL LIFETIME IN PSI'S 72 MeV PROTON BEAM

R. Dölling[†], R. Dressler, Paul Scherrer Institut, 5232 Villigen PSI, Switzerland
 L. Calabretta, INFN-LNS, Catania, Italy

Abstract

A test of the lifetime of an amorphous carbon foil of $\sim 79 \mu\text{g}/\text{cm}^2$ was performed at PSI in the transfer line between Injector 2 and Ring cyclotron during the regularly beam production. The 72 MeV ~ 1.7 mA proton beam had a central current density of $\sim 2.8 \text{ mA}/\text{cm}^2$. Two spots on the foil were irradiated alternatively with in total three fractions of 17, 52 and 119 mAh. Foil thickness was measured before and after irradiation at several positions via the energy loss of α -particles from a ^{241}Am source in the foil. We discuss the observed foil damage as well as the experimental setup, the estimation of the beam parameters and practical boundary conditions.

INTRODUCTION

In the proposed IsoDAR experiment a 60 MeV/amu 5 mA H_2^+ molecular beam is extracted by an electrostatic deflector from a cyclotron and transported to a Be/Li target to produce $\bar{\nu}_e$ and to investigate the existence of sterile neutrinos [1, 2]. It is convenient to strip the H_2^+ ions to produce a proton beam in order to mitigate the beam losses along the transport line and to reduce the magnetic rigidity of the beam and cost of the magnetic quadrupoles and dipoles. To achieve a dissociation efficiency of $1\text{-}10^{-9}$ a foil thickness of $\sim 280 \mu\text{g}/\text{cm}^2$ is required. For this test a thinner foil thickness was selected to minimize the beam losses along the transport line.

FOIL PREPARATION

The amorphous carbon foil of 69 mm x 49 mm was delivered by ACF Metals (Tucson, Arizona) with a nominal surface density of $71 \mu\text{g}/\text{cm}^2 \pm 10\%$ and metallic impurities < 100 ppm. At INFN-LNS the foil was floated in a water bath onto a graphite frame of 4 mm thickness. It was foreseen to mount the foil on the frame on three sides. However, it was not possible to pull the holder out of the bath without disrupting the foil. Hence, a self-adhesive Kapton tape of 20 μm thickness was attached to the holder, giving support at the fourth side. In addition, the dried foil is clamped in a sandwich between two frames. The unsupported foil area of 54 mm x 32 mm is sufficient to largely avoid activation of the frame and to accommodate for two separate beam spots.

IRRADIATION IN PROTON BEAM

Setup

We chose the location of bunch-shape measurement MXZ3/4 [3], because it is well accessible and the beam is approximately circular with Gaussian profile and has limited vertical tails in order to avoid activation of the frame.

From comparison with the losses caused by the 30 μm carbon wire of the monitor, we could also predict the downstream additional beam losses and that no beam interlocks would result. (We were uncertain as to whether this would cause additional activation downstream.)

The frame was mounted onto the MXZ3 wire fork in the vault at a service day (Fig. 1). To prevent disruption of the foil during pumping and venting of the beam line, Poral filters were placed between turbo pump and pre-vacuum reservoir and at the venting valve. After pumping and beam tuning, the foil was moved to the beam axis at switched off beam to prevent damage to the Kapton strip. The beam current was increased over minutes to allow outgassing. After each fraction the foil was retracted from the beam (with beam switched off) and visually inspected through the KF-50 window at the next service day.

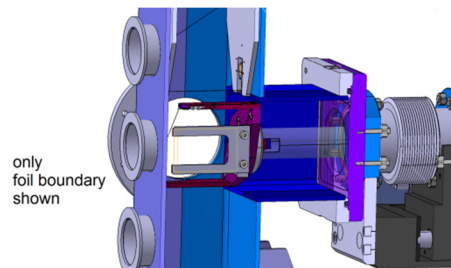


Figure 1: Frame attached to MXZ3 wire fork.

Beam Current, Charge and Density

Unfortunately, with the foil installed, the beam size could not be measured directly. Beam profiles and the dependence of beam size on beam current were, however, measured extensively in 2012/13 in the course of bunch-shape measurements [3] and have appeared to be constant over the years. Since beam optics remained unchanged for the foil measurements in 2016, we conclude from the earlier measurements to a 1σ beam width of 3.1 ± 0.3 mm horizontally and vertically, at a beam current of 1.7 mA. Intensity profiles are close to a Gaussian but vertical tails are less developed.

Table 1: Three Irradiation Fractions at Two Spots

#	Spot	Prevalent current [mA]	Time inserted [h]	Beam charge [mAh]	Central beam charge density [mAh/cm ²]
1	1	1.715	10.2	16.9	28.0
2	2	1.721 (2.037*)	31.5	51.6	85.5
3	1	1.705 (2.015*)	72.9	119	197

* Increased beam current for UCN operation: Every 5 minutes for 5 s (resulting in a central current density of $3.4 \text{ mA}/\text{cm}^2$), followed by a decrease to 0.75 mA and a slow ramping up again within ~ 25 s.

[†] rudolf.doelling@psi.ch

The foil temperature in the beam centre was estimated from the equilibrium of stopping power in the foil and black body radiation to be 608°C (645°C*) using an emissivity of 0.5. No loss of thickness due to the evaporation of carbon is expected. Frame temperature was estimated to stay below 60°C.

Beam Losses

Increased beam losses due to the inserted foil were measured at a few downstream loss monitors but remained far below the beam switch-off levels that protect against thermal damage. The most prominently increased signal is shown in Fig. 2 for the three irradiation fractions. Radiation surveys at service days before and after the fractions did not exhibit an increase of activation in beam lines or Ring cyclotron.

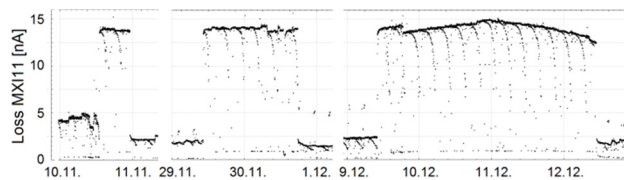


Figure 2: Signal of loss monitor MXI11, located 4.9 m downstream of the foil. (Periodic structures are due to aliasing of sampling and periodic beam current changes.)

Foil Damage

Each fraction resulted in a footprint in the foil, showing radial kinks with increasing charge (Figs. 3, 4). A sizeable rupture was observed at the location of highest charge density (Fig. 4d) after the 3rd fraction, a single retraction movement and a following 22 days waiting period. Later on, an isolated small crack in the periphery was also identified in back-light inspection (Fig. 4g). Presumably, the hole was formed from a crack, with the foil rolling in, away from the beam centre (Fig. 3). In contrary to a non-irradiated foil (Fig. 4h) the rolling in stops at the radial kinks.

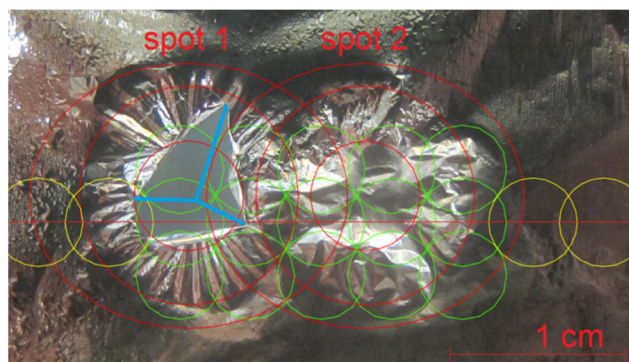


Figure 3: Foil front side after 3rd fraction (seen in beam direction). Red: Beam radius $1\sigma/2\sigma/\max$ predicted from earlier measurements and drive movement. Only the vertical beam position was assumed to be 1.5 mm above axis for better agreement. Blue: Assumed split lines of foil. Green: Regions of thickness measurement before and after irradiation. Yellow: Ditto, only after irradiation.

The total beam loss signal MXI11 varied only by ± 1.3 nA during the third fraction, which is normal. The signal increase due to the foil varied only by +10%/-15%. The variation caused by the rolling in seen in Fig. 3 would result in a larger drop. We therefore suspect, although inconclusively, that the rolling in appeared largely after irradiation. An online measurement, e.g. based on light transmission, would give better information.



Figure 4: a) Foil before irradiation. b-d) After 1st/2nd/3rd fraction, in vacuum. e-g) Afterwards in air. h) Other foil, damaged at mounting. a,e,f,h) front, b-d, g) rear side.

THICKNESS MEASUREMENT

Investigation of the foil thickness was performed utilizing the energy loss of α -particles traveling through matter. This is a non-destructive contact free method well suited for thin samples which are highly activated or very sensitive and frangible. But only averaged values of the energy loss over relative large areas down to a few mm² can be measured.

Before beam exposure an average energy attenuation of 59.8 keV of the ²⁴¹Am main α -peak (5485.6 keV) caused by the tested foil regions was measured. For the average α -energy of 5456 keV during the passage, the corresponding stopping power is 0.7561 keV/($\mu\text{g}/\text{cm}^2$) [4]. It is used throughout in the following. We conclude an average foil thickness of 79.1 $\mu\text{g}/\text{cm}^2$, somewhat larger than specified.

Laboratory Setup

A ²⁴¹Am source of 15.2 kBq with 7 mm diameter of deposited activity was placed at one side of the foil opposite of a Canberra PD50-11-300AM ion implanted PIPS detector in a distance of 31.2 mm. Two apertures each with 6 mm diameter were placed in front of source and detector to collimate the emitted α -particles passing the foil and limit the angle of incidence with the detector surface (Fig. 5). The detector setup was placed at a flange in a vacuum chamber of same type as in the beam line. The feed-through with frame and foil attached could be inserted unchanged. A dry prepump provided 10⁻³ mbar. The chamber was light tight to prevent detector background.

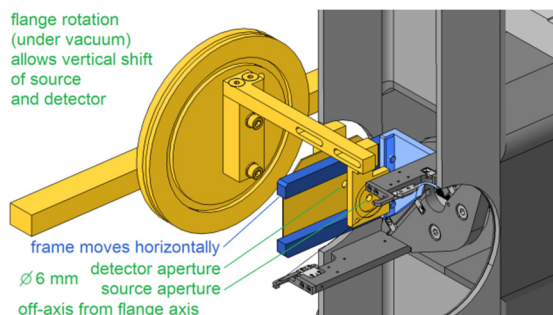


Figure 5: Setup for thickness measurement (exploded view, source, foil, detector, electronics not shown). The detector feed is transferred to the outside via an electrical feed-through. The electronics is attached at the flange handle (in air), to keep the cable capacitance small.

A charge sensitive preamplifier (Canberra 2003BT) was connected to the PIPS detector. Standard NIM counting modules were utilized to amplify and digitize the signals. The pulse height spectra were registered using the Canberra Genie2000 spectroscopy suite. The energy resolution (FWHM) was determined from the width of the main peak to be 12.4 keV. In our set-up, changes of the peak maxima of down to 3 keV can be detected corresponding to thickness variations of 4 $\mu\text{g}/\text{cm}^2$.

Measurement and Evaluation

To check the time stability of the measurement setup, a series of 50 consecutive spectra each of 1 h counting time

were conducted before beam exposure without any sample in-between the source and the detector. It was found that the position of the main ²⁴¹Am α -peak was changing at maximum 0.2 keV with a standard deviation of 0.06 keV. After beam exposure, the same was done placing the centre of spot 2 between the source and the detector resulting in 1.0 keV and 0.41 keV, respectively.

Individual regions of the foil (indicated by green and yellow circles in Fig. 3) were examined by recording pulse height α -spectra of 1000 s before and after the beam exposure. After five to nine consecutive measurements with the foil in-between, the foil was retracted and a “blank measurement” was performed to be sensitive to changes of the detector response. The position of the main ²⁴¹Am α -peak varied in all of these “blank measurements” less than 0.6 keV.

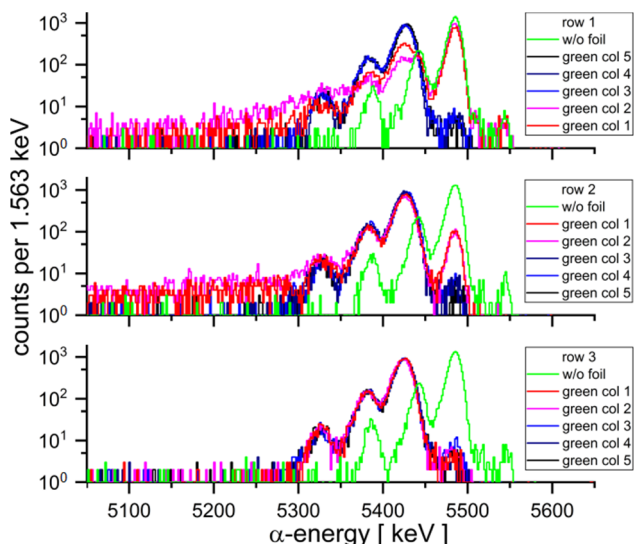


Figure 6: Post-irradiation α -spectra of green regions compared to measurements without the stripper-foil.

Table 2: Peak Shifts and Deduced Thickness Change

Row	Color	1	2	3	4	5
Column numbers are given with respect to positions of the green circles in Fig. 3 from left to right. (Ditto for yellow circles.)						
Peak shift [keV] compared to averaged blank measurements						
before beam exposure (averaged blank meas.: 5485.5 keV)						
1	green	59.8	60.2	59.7	59.6	59.5
2	green	61.2	60.7	60.2	59.7	59.7
3	green	60.4	60.4	59.6	59.4	59.6
after beam exposure (averaged blank meas.: 5485.4 keV)						
1	green	0.3	0.4	59.1	59.6	57.1
2	green	0.3	0.4	60.0	57.4	58.9
3	green	60.3	61.9	60.5	59.7	60.0
2	yellow	60.1	60.0	60.3	58.8	
Max. difference of thicknesses [$\mu\text{g}/\text{cm}^2$] before vs. after irradiation						
1	green	78.9	79.2	0.7	0.1	3.2
2	green	80.5	79.7	0.2	3.0	1.1
3	green	0.1	-2.0	-1.3	-0.4	-0.5

Content from this work may be used under the terms of the CC BY 3.0 licence (© 2018). Any distribution of this work must maintain attribution to the author(s), title of the work, publisher, and DOI.

At the hole location, the α -spectra consist of superposition from α -particles without and with attenuation by passing the foil. Figure 6 (red and cyan lines of rows 1, 2) illustrates this in comparison with unaffected regions and measurements without foil (green lines). This corresponds well to the findings in Fig. 3. The energy loss of the α -particles passing the foil matches almost perfectly the energy gaps between the individual α -peaks of ^{241}Am and hampers a detailed analysis. More sophisticated algorithms must be applied for a rigorous peak deconvolution, as demonstrated in [5]. However, we restrict the data evaluation of each irradiated region given in Table 2, to the determination of the maximum peak shift of the main α -peak (nominal 5485.6 keV) which corresponds to the strongest decrease in thickness in the region.

It turned out that the thicknesses of the investigated areas varied in a band of $2.4 \mu\text{g}/\text{cm}^2$ width before beam exposure. After beam exposure, local thicknesses changed significantly only at the regions corresponding to the hole. The rolling in of the foil, however, cannot be easily deduced due to the overlaid multiplet structure of ^{241}Am .

CONCLUSION

Irradiation of spot 2 with an accumulated central beam charge density of $85 \text{ mAh}/\text{cm}^2$ resulted within the measurement uncertainty of the applied method of $4 \mu\text{g}/\text{cm}^2$ not in a thickness decrease of the carbon foil. During or after the third fraction, which increased the central beam charge density of spot 1 from 28 to $225 \text{ mAh}/\text{cm}^2$, a hole has been formed at the spot centre. Destruction of the foil seems to be promoted by the inner tension, which is present already in the not irradiated foil. A process, somehow providing relaxation of the foil after mounting to the frame, may enhance the foil lifetime. The small thickness of the foil may be the main reason of foil rolling in. A $280 \mu\text{g}/\text{cm}^2$ foil may result in a better performance in spite of the expected higher temperatures.

At TRIUMF, with H^- beams of comparable maximum beam current density ($\sim 1.3 \text{ mA}/\text{cm}^2$), thicker foils ($\leq 2 \text{ mg}/\text{cm}^2$) of highly oriented pyrolytic graphite survived much higher input power surface densities, accumulated beam charges (500 mAh) [6, 7] and maximum beam charge densities ($\sim 6300 \text{ mA}/\text{cm}^2$) [8].

ACKNOWLEDGEMENTS

We thank Jose Alonso from LBL for proposing the foil test together with LC and for useful comments on foil handling and thickness measurement, Carmelo Marchetta for attaching the foil to the holder, Sascha Graf for designing the added mechanical parts, Roger Senn for mounting and installing the mechanical setup and conducting most of the thickness measurements and Daniela Kiselev for predicting foil activation levels.

AUTHOR CONTRIBUTIONS

LC provided foil and holder. RDr provided, set-up and maintained the α -spectroscopy electronics, supervised the thickness measurement and analysed the data. RDö conceived the beam test setup and the thickness measurement environment, coordinated the measurements, analysed the beam test data and wrote the paper with significant contributions of the other authors.

REFERENCES

- [1] J. J. Yang *et al.*, “Beam dynamics simulation for the high intensity DAE δ ALUS cyclotrons”, *Nucl. Instr. Meth.*, vol. 704, pp. 84-91, 2013, doi:10.1016/j.nima.2012.12.050
- [2] M. Abs *et al.*, “IsoDAR@KamLAND: A conceptual design report for the technical facility”, Nov. 2015, arXiv:1511.05130
- [3] R. Dölling, “Progress with bunch-shape measurements at PSI’s high-power cyclotrons and beam lines”, in *Proc. HB’12*, Beijing, China, Sep. 2012, paper MOP253, pp. 187-191.
- [4] J. F. Ziegler, J. P. Biersack, M. D. Ziegler, “SRIM – The Stopping and Range of Ions in Matter”, Maryland, SRIM Co., 2008, <http://srim.org>
- [5] R. Dressler, “Characterisation of sample and target thicknesses using advanced alpha-spectroscopy simulation”, Annual Report 2016, Laboratory of Radiochemistry, University Bern and PSI, pp. 8-9.
- [6] Y. N. Rao *et al.*, “TRIUMF extraction foil developments and contamination reduction”, in *Proc. Cyclotrons’13*, Vancouver, BC, Canada, Sep. 2013, paper TU3PB04, pp. 269-271.
- [7] I. Bylinskii *et al.*, “Recent developments for cyclotron extraction foils at TRIUMF”, in *Proc. IPAC’18*, Vancouver, BC, Canada, May 2018, paper TUPAL062.
- [8] Y. N. Rao, TRIUMF, private communication, Jun. 2018.

EXPERIENCE AND PERSPECTIVE OF FFAG ACCELERATOR*

Y. Mori[†], Institute for Integrated Radiation and Nuclear Science, Kyoto University, Osaka, Japan

Abstract

A number of Fixed Field Gradient(FFAG) Accelerator has been developed and built after the world first proton FFAG was developed at KEK in 1999. In this paper, the experiences of the operational FFAG accelerators mostly constructed in Japan and also, the perspective for high intensity beam with a novel scheme are described.

INTRODUCTION

An idea of fixed field alternating gradient (FFAG) accelerator was proposed by Ohkawa in 1953, After this, several electron models were developed at MURA in 19060's. In 1999, the world first proton FFAG model(pop FFAG) with rf acceleration shown in Fig. 1 was developed at KEK [1, 2]. Since then, various types of FFAG accelerators have been developed and constructed.

The FFAG accelerators, which are fully operational at the moment, are mostly scaling type. The scaling type of FFAG accelerator has an unique feature where the beam focusing is zero-chromatic. This defeats the problems caused by the betatron resonances in the beam motions during acceleration, which could lead fast acceleration or even cw beam acceleration. The first proton model (pop FFAG) almost satisfied the zero chromatic constraint. However, the real machines, sometimes, this situation could not be perfectly satisfied because of the field defects and errors.

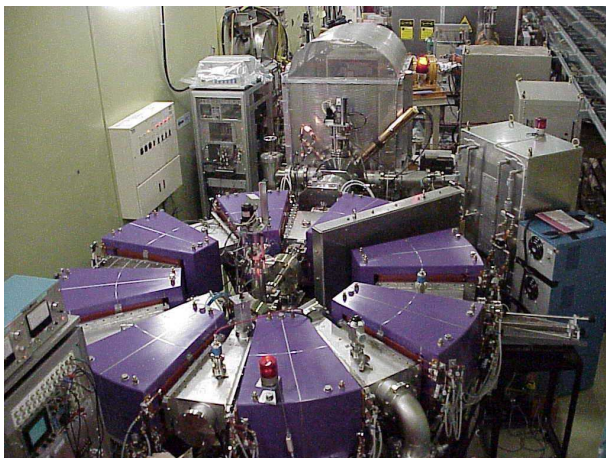


Figure 1: The first proton scaling FFAG model (pop FFAG) developed at KEK.

To overcome these problems practically, techniques of the betatron tune control and/or the fast resonance crossing should be needed.

* Work partially supported by ImPACT Program of Council for Science, Technology and Innovation(Cabinet Office, Government of Japan)

[†] mori@rri.kyoto-u.ac.jp

Recently, we have proposed a new type of strong focusing ring accelerator, named "Harmotron"(Harmonictron) for high intensity beam acceleration [3].

The requirements in beam optics and behaviors of realizing a 100 MW class of beam power in medium energy hadron(proton/deuteron) accelerators should be as follows; (1) continuous wave (cw) beam acceleration, (2) strong beam focusing in 3D space, and (3) ease of beam extraction. There is no such circular hadron accelerator exists to satisfy these requirements so far . Only a linear accelerator can do.

On the other hand, "Hamotron" could satisfy all of these requirements. The Harmotron is based on a vertical scaling FFAG and, for beam acceleration, harmonic jump acceleration (HNJ) [4, 5] is applied with constant rf frequency acceleration. The HNJ acceleration in vertical scaling FFAG, allows a strong phase focusing without having a transition energy because the momentum compaction is zero in the vertical scaling FFAG, and brings also a large turn separation at the highest energy to make beam extraction easier.

This paper presents the issues experienced in the operational FFAG accelerators and also gives the perspective of future high intensity FFAG, "Harmotron".

OPERATION OF SCALING FFAG

In the scaling FFAG accelerator, there are two types:one is a horizontal type and the other a vertical one. Each type has a different shape of the magnetic field configuration to satisfy the zero chromaticity. In the horizontal scaling FFAG,

$$B_y = B_0(R/R_0)^k, \quad (1)$$

where k is a geometrical field index. Most of the present operational scaling FFAG accelerators are horizontal type.

The first proton model (pop FFAG), which is also a horizontal type, almost satisfied the zero chromatic constraint and the variation of betatron tunes during beam acceleration either for horizontal or vertical direction were less than 0.05 as shown in Fig. 2.

Since the field shapes in the real machine should not be perfect because the unexpected construction mistakes and errors happen, the betatron tunes are not always constant during beam acceleration.

In the 150MeV proton FFAG accelerators built at KEK and Kyushu Univ., the betatron tunes vary during beam acceleration as shown in Fig. 3. As can be seen from this figure, the betatron tunes cross two resonance lines of the normal third integer resonances: $3Q_x = 11$ and $Q_x - 2Q_y = 1$. On the other hand, the scaling FFAG with FDF lattice has a good tunability to control the betatron tunes. The vertical tune, in particular, can move largely by changing the magnetic field strength of F and D magnets (F/D ratio) .

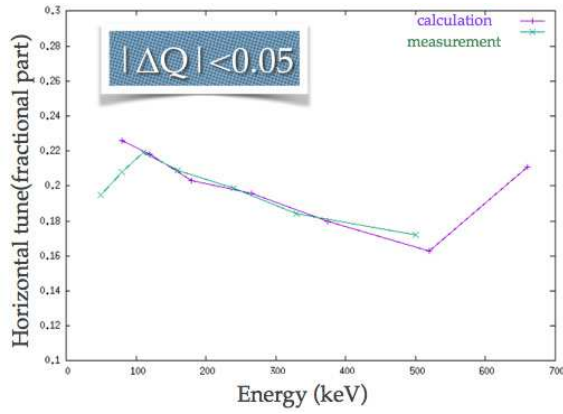


Figure 2: Measured horizontal tune variation of proton scaling FFAG model (pop FFAG) developed at KEK.

The vertical tune depends approximately on the F/D ratio (flutter) as follows.

$$Q_y = (-k^2 + F^2)^{1/2} : F^2 = \frac{1 + \alpha^2}{1 - \alpha^2}. \quad (2)$$

Here, α shows a F/D ratio and F is a flutter.

This scheme was used to avoid the resonance line of $Q_x - 2Q_y = 1$. As shown in Fig. 4, the vertical tune was slightly (+0.02) pushed up by decreasing the F/D ratio, so that the beam loss caused by crossing the resonance could be cured. Although the tune control with this technique is useful, there is a side effect. The closed orbits are changed when the F/D ratio(flutter) varies and displacements of the injection and extraction orbits occur. It requires sometimes harmful works to minimize the injection and extraction optics errors.

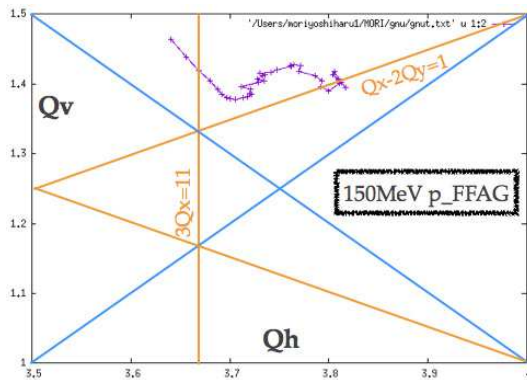


Figure 3: Tune variation of 150MeV proton scaling FFAG developed at KEK.

For the resonance of $3Q_x = 11$, it was difficult to avoid it with controlling the tunes, except increasing the injection energy. Thus, fast resonance crossing was only choice to overcome it. In crossing of the non-linear resonance, the emittance growth during crossing is determined by the crossing speed and the effects from the driving term of the non-linear forces and non-linear detuning, which presents an adiabatic parameter as shown below.

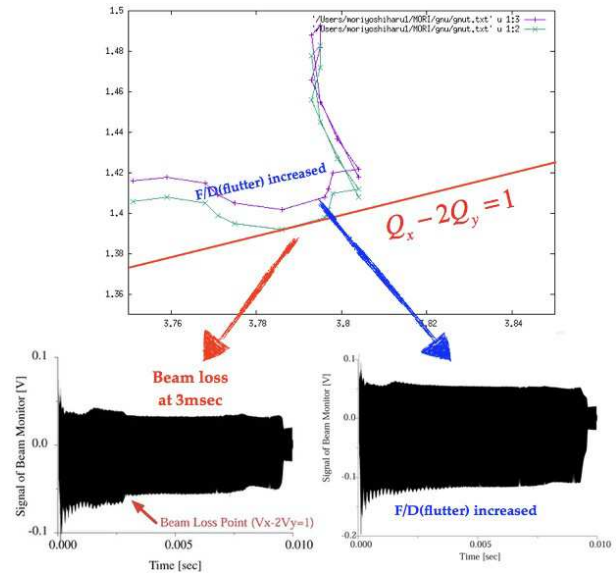


Figure 4: Tune control with F/D ratio(flutter) manipulation and curing the beam loss.

$$\alpha_a = \left(\frac{\epsilon}{4\pi\Delta_N\Delta_e} \right)^{3/2}. \quad (3)$$

Here, Δ_N is a non-linear tune shift(detuning) and Δ_e is an excitation width (driving term), ϵ is a change of tune per revolution (resonance crossing speed). If the parameter, α_a , is greater than 7 or so, the emittance growth caused by the resonance crossing could be eliminated [6]. In case of 150MeV proton FFAG shown in Fig.3, $\alpha_a \gg 10$, thus, there was no significant effect in crossing the resonance line of $3Q_x = 11$.

PERSPECTIVE FOR HIGH INTENSITY

There are some restricted requirements for beam behaviors and technical issues in realizing a future high intensity medium energy hadron accelerators. The requirements are,

- (1) Continuous wave (cw) beam acceleration,
- (2) Strong beam focusing in 3D space, and
- (3) Ease of beam extraction.

In order to realize the cw beam acceleration, the guiding(focusing) magnetic field must be static and the rf frequency of rf acceleration should be constant. As for the beam focusing, alternating gradient(AG) focusing in transverse direction and phase focusing (synchrotron oscillation) in longitudinal direction allow the strong focusing in 3D space. In circular accelerator realizing the cw beam operation, a large turn separation is essential for making the beam extraction easier.

There is no circular accelerator to satisfy all these requirements so far. Cyclotron cannot satisfy the requirement of (2) because of no phase focusing in isochronous acceleration. Synchrotron is a pulse operated accelerator, which is impossible to accelerate the beam continuously. The fixed field alternating gradient (FFAG) accelerator cannot satisfy all

Content from this work may be used under the terms of the CC BY 3.0 licence (© 2018). Any distribution of this work must maintain attribution to the author(s), title of the work, publisher, and DOI.

these requirements, either. Directing the strong focusing in 3D space, constant rf frequency acceleration becomes impossible and a pulsed operation is inevitable like synchrotron. If the cw operation is aimed, then, the strong focusing in longitudinal direction must be given up just like cyclotron.

In order to overcome these difficulties, a new scheme of accelerator, named "Harmotron (Harmonictron)", has been proposed. The details are shown in our recent paper [3].

The Harmotron consists of a vertical scaling FFAG accelerator with harmonic number jump (HNJ) acceleration. The idea of the vertical scaling FFAG accelerator was originally proposed by Ohkawa [7] in 1955 and analyzed in detail by Brooks recently [8]. The feature that orbit radius is always constant means the zero-momentum compaction and no transition energy exists in the vertical scaling FFAG.

In the relativistic energy range, where particle velocity almost equals light velocity, a light mass particle such as the electron can be accelerated with constant frequency rf field in the vertical scaling FFAG accelerator. Thus, Ohkawa named it "electron cyclotron". Even non-relativistic particle such as proton can be accelerated by the rf field which synchronizes a time revolution elapsing around the ring for each turn as in the ordinary proton synchrotron. In the vertical scaling FFAG accelerator, the momentum compaction becomes always zero as mentioned above because the orbit radius is constant during acceleration (Fig. 5). Thus, the transition energy is infinite, in other words, no transition energy exists, and the beam is accelerated always below transition in the vertical scaling FFAG so that many problems caused by the transition energy can be avoided.

The idea of HNJ acceleration has been proposed by Ruggiero in 2006 and developed recently [4, 5]. The scheme of HNJ acceleration, however, has some difficulties to accelerate heavy particles such as protons or deuterons for a wide range of medium (non-relativistic) energy because the transition energy exists where the slippage factor becomes zero. In order to eliminate the transition energy inherently, momentum compaction in beam dynamics must be zero like linear accelerator. A vertical scaling FFAG accelerator makes the momentum compaction zero because of a constant orbit radius whatever the beam energy.

The magnetic field strength changes exponentially in the vertical direction to keep a zero chromatic beam optics with constant orbit radius in the vertical scaling FFAG shown as,

$$B_y = B_0 \exp(my). \quad (4)$$

Here, a characteristic number m is expressed with a field index, n , as,

$$m = n\rho. \quad (5)$$

The linearized particle motion in the transverse direction which is subject to a skew quadrupole magnetic field can be expressed by the betatron equations in skew coordinates under the approximation of no orbit curvature effect ($\rho \rightarrow$ large).

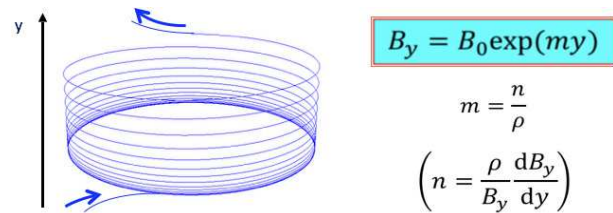


Figure 5: Schematic drawing of vertical FFAG and the magnetic field configuration for vertical direction.

The characteristic number of m specifies the orbit displacement, y_d , between initial momentum (p_i) and final beam momentum (p_e) as $m = (1/y_d) \ln(p_e/p_i)$. If p_e/p_i equals 3 and y_d is less than 1 m, then, m should be more than $1.1 m^{-1}$. The typical machine parameters of a vertical scaling FFAG accelerator which accelerates proton from 50 MeV to 500 MeV has been examined and the details are shown in the paper [3].

Applying HNJ acceleration to the vertical scaling FFAG, heavy particles such as the proton can be accelerated in wide range of the non-relativistic energies with a fixed frequency rf acceleration which allows a cw operation. We name this new type of accelerator based on vertical scaling FFAG with HNJ acceleration as "Harmotron".

From the synchronization condition of HNJ acceleration, the required energy gain to jump an integer harmonic number Δ_i/h of harmonics between the turns i and $i+1$ can be expressed with [5],

$$E_{i+1} - E_i = \frac{\Delta_i h}{f_{rf} (\frac{dT}{dE})_{E=E_i}}. \quad (6)$$

Here, T is a revolution time of piecewise linearized around the particle energy.

The term dT/dE of required energy gain in Eq. (6) can be expressed in the following equation with a slippage factor.

$$\frac{dT}{dE} = \frac{\eta \gamma^2 C}{M_0 c (\gamma^2 - 1)^{3/2}}, \quad (7)$$

where C is the circumference of the ring, c is light velocity and M_0 is rest mass energy. Since the momentum compaction is zero in Harmotron (vertical scaling FFAG), Eq. (6) can be expressed as,

$$E_{i+1} - E_i = - \frac{\Delta_i h M_0 c (\gamma^2 - 1)^{3/2}}{f_{rf}} \frac{c}{C}. \quad (8)$$

As can be seen from this equation, the required energy gain per turn is a function of γ_i since f_{rf} is constant and $\Delta_i h$ should be a negative value for acceleration.

The rf voltage and/or phase have to be changed to satisfy the energy gain per turn shown in Eq. (8) in HNJ acceleration. A couple of schemes have been proposed to change the rf voltage or phase during acceleration by Ruggiero in his original paper [4], however, practical difficulties arise for realizing them.

In HNJ acceleration of medium energy heavy particle, the energy change per each turn is so large that adiabatic condition in longitudinal focusing (synchrotron oscillation) may not be satisfied enough to keep within the large longitudinal beam acceptance. Thus, preserving the adiabatic condition of synchrotron oscillation during acceleration is important to keep a large phase space acceptance.

The criterion of adiabaticity for rf acceleration can be expressed as [9],

$$\Omega_s \gg \frac{1}{\Omega_s} \frac{d\Omega_s}{dt}, \quad (9)$$

where $\Omega_s/2\pi$ is a synchrotron frequency. When this condition is satisfied, the particles are well trapped by a rf bucket and accelerated. The above condition can be evaluated with the adiabatic parameter which is given by the following equation when the rf phase is constant π [10, 11].

$$n_{ad} = \frac{\Omega_s T_r}{1 - [V_i/(V_i + \Delta V)]^{1/2}}. \quad (10)$$

Here, V_i is the total rf voltage of i -th turn and ΔV is the increment of rf voltage derived by the rf cavity after i -th turn, T_r is a transit time of the rf cavity gap. The parameter, n_{ad} , counts the adiabaticity of the system showing how slow is the change of the bucket height with respect to the synchrotron frequency. When $n_{ad} \gg 1$, the system can be adiabatic.

The adiabatic condition in HNJ acceleration could be satisfied by distributing the multi rf cavities in the ring (see Fig. 6) and tuning the frequency of each rf cavity [5, 12]. If the rf system consists of N rf cavities, the adiabatic parameter shown in Eq. (10) becomes approximately $N/2$ times bigger than that for a single rf cavity.

The rf frequency of each rf cavity distributed homogeneously around the ring can be obtained with the following equation [5].

$$f_{i,j} = f_{ref} \left[1 + \frac{2j + N + 1}{2N} \frac{\Delta_i h}{h_i} \right]^{-1}, \quad (11)$$

where i is the turn number, j is the cavity number, h_i is a harmonic number and f_{ref} is a reference rf frequency.

As long as h_i is larger than its variation $\Delta_i h$, the frequency of each cavity is independent of the turn number and is approximately given as,

$$f_i \approx f_{ref} \left[1 - \left(\frac{2j + 1}{2N} + \frac{1}{2} \right) \frac{\Delta_i h}{h_i} \right], \quad (12)$$

Thus, the rf frequency of each cavity is independent of the turn number and increases monotonically when $\Delta_i h$ is negative as a function of the cavity number. Moreover, if $h_i \gg \Delta_i h$, then, f_i becomes f_{ref} .

When the rf voltage is constant, the rf phase in HNJ acceleration can be varied during beam acceleration. If the

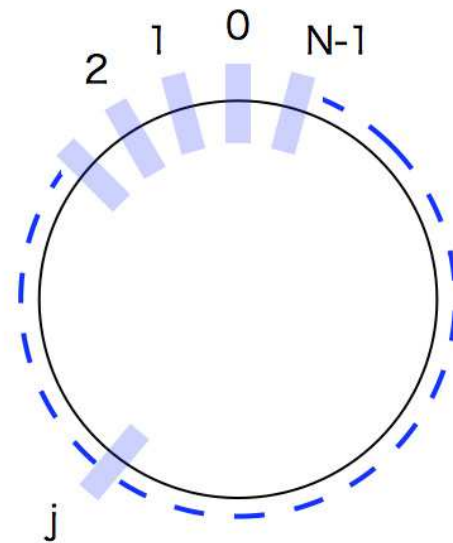


Figure 6: Adiabatic condition in rf acceleration can be introduced with multi rf cavities distributed around the ring, which allows to satisfy the adiabatic condition.

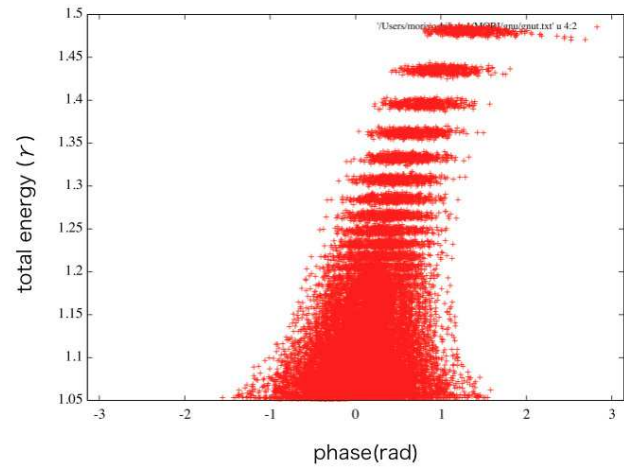


Figure 7: The beam tracking simulation results for the longitudinal beam motions for the phase spread of $\sigma=1$ rad at initial beams.

longitudinal adiabatic condition is satisfied during beam acceleration, the particles could be well captured by the rf bucket and accelerated around the stable phase.

The beam tracking simulation results for the longitudinal beam motions for different phase spread initial beams are presented in Fig. 7. In this case, the number of rf cavities is 32 which are homogeneously distributed around the ring, and the rf voltage of 1.41 MV is constant during the beam acceleration. As can be seen from this figure, the particles are well captured and accelerated up to the maximum energy following the rf stable phase, and the phase acceptance at the beam injection is quite large, which is more than 70% of 2π . This means that an adiabatic beam capture process is fulfilled in the HNJ acceleration using many rf cavities with

a small rf voltage which are distributed around the ring. The particles are captured adiabatically and well accelerated in a bucket with harmonic number jump.

SUMMARY

Since the world first proof of principle proton FFAG model was developed at KEK, various types of FFAG accelerators have been built. The operational FFAG accelerators are mostly scaling type and, in the real machines, practical techniques of manipulating the betatron tunes and/or the fast resonance crossing are needed because sometimes large magnetic field errors exist.

For future high intensity medium-energy hadron accelerator, a new scheme consisting of a vertical FFAG and harmonic number jump(HNJ) acceleration, named "Harmotron", has been proposed.

The Harmotron has a couple of unique features. Since no transition energy exists in Harmotron, a wide range of beam energy becomes possible with a monotonic change of harmonic number in HNJ acceleration. By keeping enough adiabaticity in longitudinal motions to capture and accelerate the particles efficiently by distributing many rf cavities around the ring, HNJ acceleration with a constant rf voltage becomes possible, so that the cw operation with large longitudinal acceptance can be realized.

ACKNOWLEDGEMENT

The authors would thank sincerely to Prof. Sato, Dr. Kin-syo and Prof. Ishi for valuable discussions.

REFERENCES

- [1] Y. Mori *et al.*, in *Proc. EPAC'98*, Stockholm, Sweden, Jun. 1998, paper THOB038.
- [2] M. Aiba, Y. Mori, Y. Sato *et al.*, in *Proc. EPAC'00*, Vienna, Austria, Jun. 2000, paper MOP1B21.
- [3] Y. Mori, Y. Yonemura, and H. Arima, *Memoirs of the Faculty of Engineering*, Kyushu University, vol. 77, no. 2, December 2017.
- [4] A. G. Ruggiero, *Phys. Rev. ST Accel. Beams*, vol. 9, p. 100101, 2006.
- [5] T. Planche *et al.*, *Nucl. Instr. Meth.*, vol. A632, pp. 7-17, 2011.
- [6] M. Aiba, S. Machida, Y. Mori, in *Proc. EPAC'04*, Lucerne, Switzerland, Jul. 2004, pp. 2119-2121.
- [7] T. Ohkawa, *Phys. Rev.*, v. 100, p. 1247, 1955.
- [8] S. Brooks, *Phys. Rev. ST Accel. Beams*, vol.16, p. 084001, 2013.
- [9] B. W. Montague, CERN 77-13, pp.63-81, 1977.
- [10] C.G. Lilliequist and K.R. Symon, MURA-491, 1959.
- [11] K.Y. Ng, FNAL Report, FERMILAB-FN-0943-APC, 2012.
- [12] J.S. Berg, in *Proc. 2006 International Workshop on FFAG Accelerators*, pp. 69-76, 2007.

STATUS AND BEAM POWER RAMP-UP PLANS OF THE SLOW EXTRACTION OPERATION AT J-PARC MAIN RING

M. Tomizawa*, Y. Arakaki, T. Kimura, R. Muto, S. Murasugi,
 K. Okamura, Y. Shirakabe and E. Yanaoka, KEK, 305-0801 Tsukuba, Japan

Abstract

A 30 GeV proton beam accelerated in the J-PARC Main Ring (MR) is slowly extracted by the third integer resonant extraction and delivered to the hadron experimental hall. Slow extraction from the MR has a unique characteristics that can be used to obtain a low beam loss rate. The beam has a large step size and small angular spread at the first electrostatic septum (ESS), enabling a low hit rate of the beam. A dynamic bump scheme has been applied to reduce the beam loss. We have attained 51 kW operation at 5.2s cycle in the latest physics run. A suppression of instability during debunch process is also essential as well as low beam loss tunings. Plans toward a beam power ramp-up will be reported.

INTRODUCTION

A high-intensity proton beam accelerated in the J-PARC main ring (MR) is slowly extracted by the third integer resonant extraction and delivered to the hadron experimental hall to drive various nuclear and particle physics experiments. Most of the proposed experiments are best performed using a coasting beam without an RF structure and a uniform beam intensity during the extraction time. One of the critical issues in slow extraction (SX) of a high intensity proton beam is an inevitable beam loss caused by the extraction process at septum devices. Slow extraction from the J-PARC MR has unique characteristics that can be used to obtain a low beam loss rate as described in next section [1]. In the actual beam tunings, septa positions of the ESSs and the first and second magnetic septa (SMS1 and SMS2) must be finely adjusted to minimize the beam loss as well as the dynamic bump orbit tuning. The beam loss is sensitive to the horizontal chromaticity, which has a strong nonlinearity for momentum and is set to minimize the beam loss rate [1]. We encountered several high intensity issues. The horizontal and vertical chromaticities are set to negative values to suppress a transverse instability during injection, acceleration and debunching period. The horizontal chromaticity is set near zero just before extraction starts. At beam powers above 30 kW, we observed a transverse beam instability during debunching associated with a vacuum pressure rise. This instability increases the beam loss in SX. To suppress this instability, the beam from the RCS is injected into the RF bucket with a phase offset [2]. In this paper, J-PARC slow extraction schemes, a current status and future plans toward a higher beam power for 30 GeV slow extraction are reported. A preliminary result for a 8 GeV slow extraction

test for the muon to electron conversion search experiment (COMET) will be also briefly presented.

J-PARC SLOW EXTRACTION SCHEME

Efficient Slow Extraction

The characteristics of slow extraction in the J-PARC MR can be summarized as follows [1]; (1) We have two ESSs. The first ESS (ESS1) is located in the section between adjacent focusing quadrupole magnets as shown in Fig. 1. This section has the highest β_x (40 m) in the ring. A large step size Δ at ESS1 can be achieved without causing any primary beam loss in other places, where the step size Δ is shown in Fig. 2. The large Δ reduces the hit rate of the beam on the septum of ESS. (2) The long straight section, where the ESSs are located, is dispersion-free. If the horizontal chromaticity is set to a small enough value during the extraction, the momentum dependence of the separatrix can be neglected. (3) When a bump orbit, which shifts the circulating beam toward the septum of the ESS1, is constant during extraction, the outgoing arm of the separatrix has different angles ($x' = dx/ds$) at the septum position at the start and end of extraction, as shown in the upper part of Fig. 2 (fixed bump scheme). On the other hand, this angular difference is sufficiently small if the orbit bump is changed during the extraction, as shown in the lower part of Fig. 2 (dynamic bump scheme). This scheme reduces the hit rate from the sides of the ESS and downstream septa.

Spill Regulations

The time structure of the extracted beam intensity (beam spill) is controlled by the following quadrupole magnets: two extraction-pattern quadrupole magnets (EQs) and one ripple-

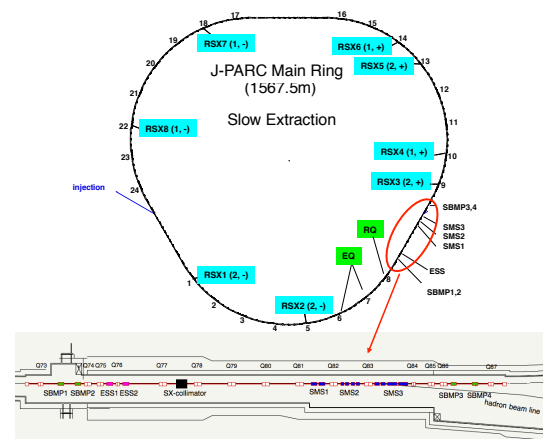


Figure 1: Layout of J-PARC slow extraction devices.

* masahito.tomizawa@kek.jp

Content from this work may be used under the terms of the CC BY 3.0 licence (© 2018). Any distribution of this work must maintain attribution to the author(s), title of the work, publisher, and DOI.

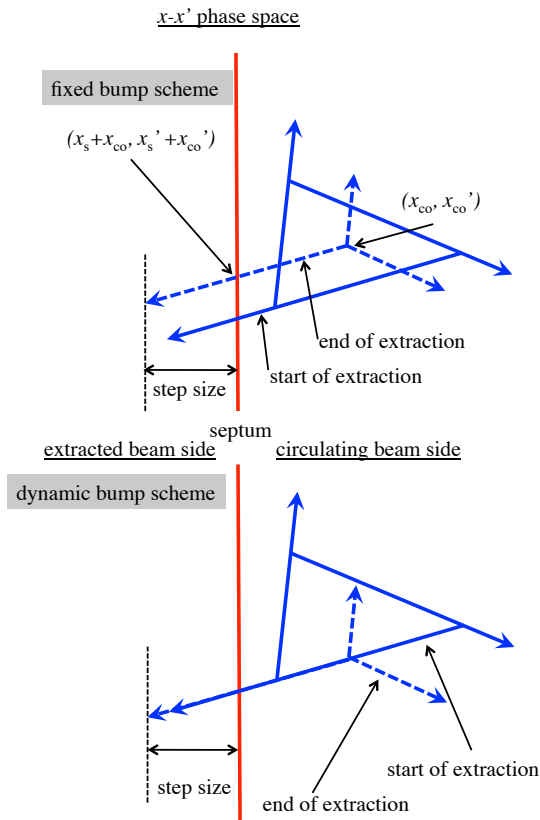


Figure 2: Fixed and dynamic bump scheme.

compensation quadrupole magnet (RQ). These quadrupole magnets are located in the arc section upstream of the LSS for slow extraction, as shown in Fig. 1. The EQs usually produce a beam spill with a flat shape by modulating the tune ramping speed. The RQ compensates for tune ripples originating in the main quadrupole and bending power supplies. A feedback control unit based on a Digital Signal Processor (DSP) has signal input ports for the gate logic, spill intensity and circulating beam intensity. The spill intensity monitor is a photomultiplier tube with a plastic scintillator placed near a 100- μm -thick aluminum foil separating the upstream and downstream vacuums of the hadron beam line. A typical EQ current is 50~100 A. A horizontal tune shift is 0.01 at 100 A. To improve the spill structure further, we have applied two transverse RF fields to the circulating beam during slow extraction [1]. The transverse RF fields are generated by two sets of horizontal strip-line kickers.

HIGH INTENSITY PHENOMENA AND MITIGATIONS

RF Beam Loading Compensation

The beam is debunched by turning off the RF voltage at the beginning of the flat top. The momentum shift (deceleration) during debunch process was observed in an early stage of the beam commissioning. The momentum shift was increased with the beam power up, and achieved to -1% level at 10 kW beam. This large momentum shift drastically increased

the beam loss in the slow extraction. The momentum shift is mainly caused by the beam loading of the RF cavities. The beam loading of the RF cavities has been compensated by a feedforward technique [3]. At 51 kW beam power, the momentum shift is suppressed to -0.3% level.

Tunes, Chromaticity Adjust and Bunch by Bunch Feedback

In the beam commissioning for the beam power-up, a coherent transverse beam oscillation (beam instability) was observed. A week chromaticity correction mitigates the instability. However the chromatic tune spread induces a beam loss by betatron resonance. The chromaticities and tunes have been carefully chosen from the flat bottom to the flat top. The horizontal and vertical chromaticities are set to -3.5 and -2.0 at the before acceleration and then to -5.0 and -7.1 at the top energy, respectively. Before the start of the slow extraction, the horizontal chromaticity is set near zero to make an achromatic condition. Horizontal and vertical bunch by bunch feedback using strip line kickers has been introduced to suppress the instability during the flat bottom.

RF Phase Offset

We encountered the beam loss increase in the slow extraction around 30 kW beam power [2]. This involves a vacuum pressure rise in the whole ring. The electron cloud has been observed during the debunch timing. The wall current monitor or the fast CT during the debunch process shows an indication that longitudinal coupled bunch instability occurred. The high frequency components (30–50 MHz) in the beam was seen by the wall current monitor or the FCT. We guess the beam loss increase is caused by a transverse beam instability accompanied electron cloud triggered by longitudinal beam instability which makes a frequency modulation causing multipacting and vacuum pressure rise [2, 4]. In order to mitigate this phenomena, the beam bunch is injected in the RF bucket with a phase offset of 50 to 55 deg [2]. This phase offset injection spreads longitudinal beam emittance and suppress the instability. This phase offset injection is essential for present high power SX operation. We have confirmed the instability for 7.6×10^{13} protons can be suppressed at 60 deg. phase offset.

PRESENT BEAM PERFORMANCES

In the SX startup in April 2018, the first ESS had a serious trouble that several septum ribbons were broken by an accidental hit of the circulating beam, and one of them touched on the high voltage electrode. The SX operation restarted one month later temporarily by moving the second ESS to the first ESS position. In 2017's summer shutdown, an ESS with a titanium vacuum vessel has been installed at the first ESS position and the second ESS has been returned to the original position. The SX operation (RUN78) after the installation has been conducted from January to February in 2018. The beam intensity gradually increased from 10 kW

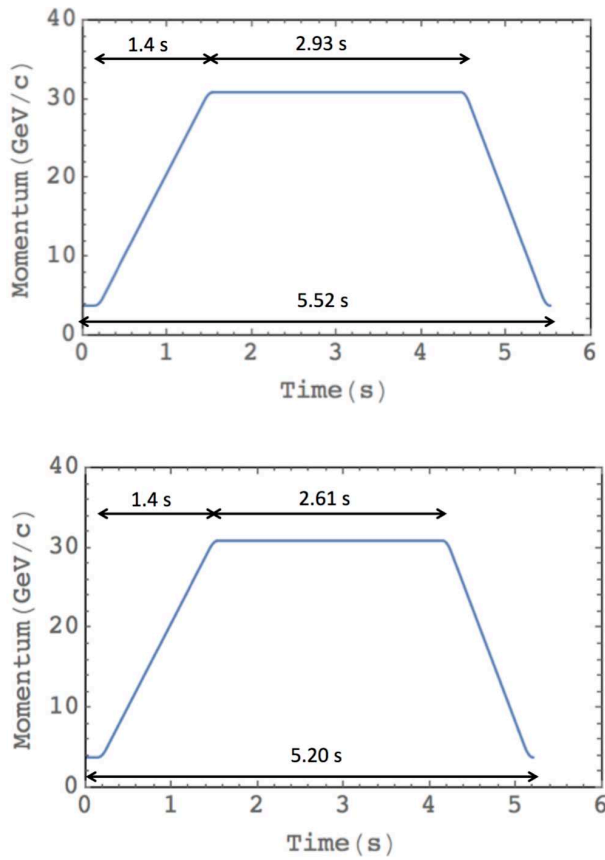


Figure 3: Acceleration patterns.

suppressing a vacuum pressure rise and a spark of the ESSs. In the RUN78, cycle period of the MR has been changed from 5.52 to 5.20 s as shown in Fig. 3 by shortening the flat top by 0.32 s keeping the beam extraction time of 2 s. This increased the beam power by 6%. Finally, the proton number per pulse has been increased to 5.5×10^{13} ppp corresponding to 51 kW, which is a maximum beam power limited by the target capacity. Figure 4 (a) and (b) show distribution and time structure of the beam loss around the SX area at 51 kW operation, (c) and (d) are DCCT signal and the beam loss distribution in the whole ring. A very high slow extraction efficiency of 99.5% was stably kept also at 51 kW operation. The beam power in RUN79 (June, 2018) is 51 kW, which is same as that of RUN78.

Figure 5 shows the extracted beam spill monitored at the beam transport line to the hadron hall. The typical duty factor indicating the time structure of the spill is 50% of ideal case. The time structure of the beam spill was regulated by a feedback due to fast-response quadrupole magnet RQ. Transverse RF fields with frequencies corresponding to the horizontal betatron frequency and with a noise width are applied to the circulating beam by the strip-line kickers to improve the spill duty factor. The RF fields quickly push the beam to the resonance by increasing the betatron amplitude. An RF of 47.47 MHz with a flat noise spectrum of 0.2 kHz was applied in RUN79. A transverse RF of 0.2525 MHz with a 0.0625 MHz noise width is also applied by another

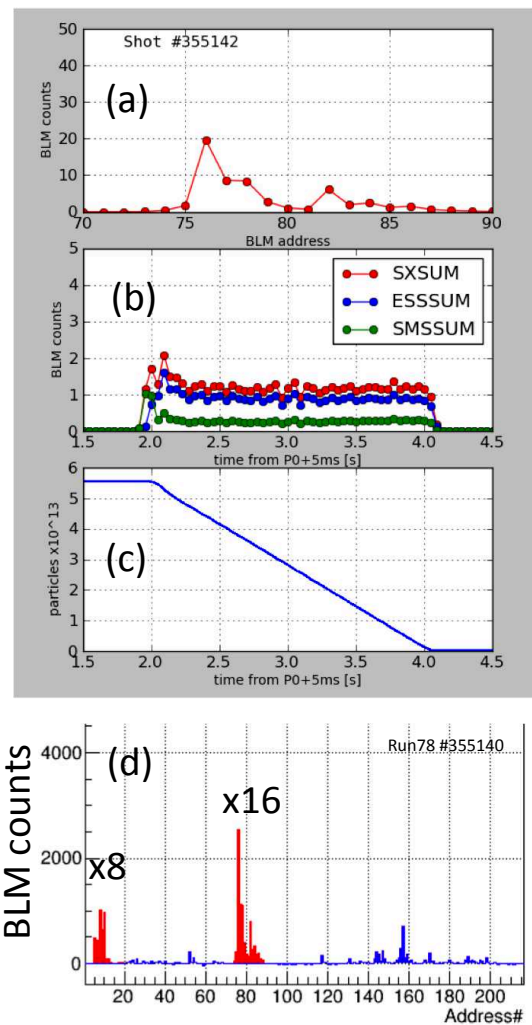


Figure 4: Beam loss distributions, beam loss time structure and DCCT.

set of strip-line kicker. The extraction efficiency has slightly worsened from 99.52% to 99.46% by transverse RF tuning to improve the spill duty in this run. The correction coils of the main quadrupole and bending magnets are shorted during the slow extraction by semiconductor switches. This suppresses large spill spikes sometimes occur. Figure 5 shows the time structure and the FFT spectra of the spill signal. 600, 900, 1200 and 1800 Hz sharp peaks have been seen as well as a broad peak below 200 Hz.

Figure 6 shows residual radioactivity surveyed at 6.5 h after the beam was stopped. 51 kW beam was applied over 1 week by slow extraction operation until the beam was stopped. The maximum dose was just upstream of the ESS1, and was 6.5 mSv/h on the surface. The survey result can be understood in light of the achieved small beam loss rate. At the end of RUN78, a trial at a higher beam power has been conducted. We have succeeded in the slow extraction at 62.8 kW (6.8×10^{13} ppp). The slow extraction efficiency was 99.47%, which was slightly worsened than that of the 51 kW one at RUN78. In this test, the RF phase offset is 50 deg., which is same as the 51 kW one.

Content from this work may be used under the terms of the CC BY 3.0 licence (© 2018). Any distribution of this work must maintain attribution to the author(s), title of the work, publisher, and DOI.

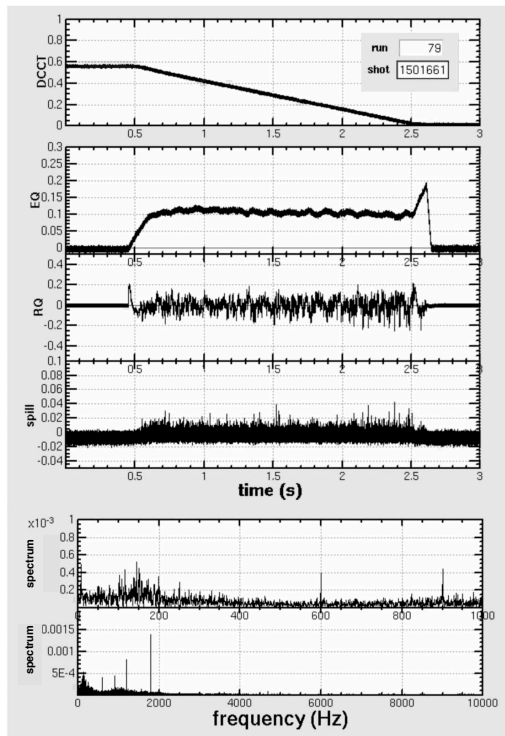


Figure 5: DCCT, EQ, RQ currents, time structure and frequency spectrum of the beam spill.

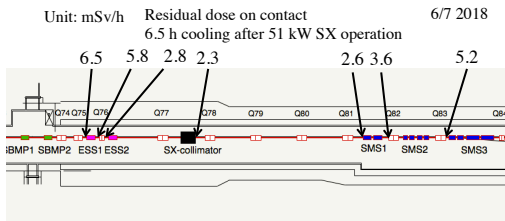


Figure 6: Residual dose measured after 51 kW SX operation.

8 GEV SLOW EXTRACTION

Planned muon to electron conversion search experiment (COMET) needs 8 GeV bunched proton beam with a 1 MHz pulse structure. In this experiment, ratio of residual beam intensity inter-bunch to the main bunch intensity, which is expressed as extinction, should be less than 10^{-9} . In RUN78, we have succeeded in slow extraction of 8 GeV protons with 7.3×10^{12} ppp required for COMET phase I, and the extinction obtained from time structure of secondary pions generated from the target is less than the required value.

BEAM STOP SYSTEM

After the target melting incident inducing a radioactive materials leakage in 2013, a slow extraction stop system (SX abort system) has been introduced. The EQ power supply was modified to turn off the output current within 1 ms from an interlock signal, which keeps away the horizontal tune from the resonance and immediately stops the slow extraction. The currents of the resonant sextupole and the bump magnets are also stopped by the interlock signal. The

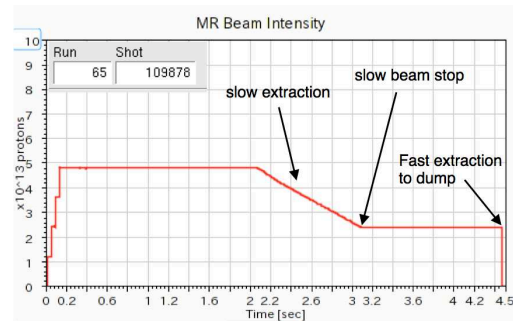


Figure 7: Slow extraction stop by the beam loss at ESS.

four bump currents are proportionally decreased to zero within 150 ms to keep the closed orbit. The beam remained in the ring after the beam stop circulates till the end of the flat top, and kicked out by the kickers and delivered to the abort dump. The SX abort occurs by interlocks of such as extracted beam rate, beam loss in the slow extraction devices or the hadron beam lines, which can protect the septa devices and the target. Figure 7 shows a real example of the SX abort by the beam loss increase at the ESS. The SX abort system is indispensable to protect the septa devices and the target in the present high power operation.

FUTURE PLANS

Main Power Supply Upgrade

The bending and main quadrupole power supplies of the MR will be replaced to rise a repetition rate from 0.40 Hz to 0.77 Hz and the beam power for a neutrino oscillation program within several years [5]. The repetition time for the slow extraction can be reduced to 3.7 s with a flat top of 2.4 s to keep the present beam on time of 2 s. The preparation time before the start of slow extraction will be shortened by 0.23 s saving the bump rise time. 100 kW operation will be achieved at this repetition period, if 7.7×10^{13} ppp can be extracted slowly. This proton number would be achievable without a serious hard work from the high power tests mentioned above.

Instability Suppression During Debunch

The beam instability during the debunch process is one of the key issue toward a higher beam power slow extraction. A mitigation of the longitudinal phase space localization is effective to suppress this instability as described above. A phase jump technique to stay the beam on an unstable fix point (USFP) of the separatrix can be effective since the momentum spreads with duration on the USFP. Optimization of the RF voltage and the duration on the USFP by the simulation is underway. We have a plan to introduce a VHF cavity to spread the longitudinal emittance uniformly, which is also effective to suppress the instability. The design of the cavity is underway by the RF group.

Titanium ESS

A titanium vacuum vessel is superior than a stainless one from the residual radiation point of view. The first ESS has been already replaced from the stainless one to the titanium one and utilized for the slow extraction operation. The yoke straining the septum ribbons is also made of titanium. We have a plan to replace the second ESS from stainless to titanium one. Though a high voltage test for the titanium ESS2 is now in progress, 110 kV higher than nominal voltage at a gap of 25 mm has been already achieved without any trouble.

Carbon Nanotube ESS

1 mm wide and 30 μm thick tungsten ribbons (including 26% rhenium) have been strained on the yoke at every 3 mm pitch as the septum of the present ESS. Septum material with a low density such as carbon nanotubes (CNT) is preferable to reduce the secondary particle generation rate in the same beam hit rate on the septum. Recently 30 ~ 90 μm thick CNT wires and 30 μm thick 1 mm wide CNT ribbons have been developed for the ESS septum. Stainless brackets was clamped to each end of the CNT wires and ribbons. Preliminary tensile test showed the wires and the ribbons were resistant for a stress of 361 MPa and 200 MPa, respectively. We have a plan to strain the CNT wires on a short yoke and supply a high voltage in vacuum, which is financially supported by Grants-in-Aid for Scientific Research in Japan and the U.S.-Japan Science and Technology Cooperation Program.

Scatterer

A scatterer (diffusers) can be put upstream of the ESS. If the scatterer material and its geometry is a good condition, the beam hitting on the scatterer spatially diffuses by multiple scattering and the beam hit rate at the downstream ESS is reduced. Total beam loss in the scatterer and the ESS can be reduced. In the recent simulation, in case a 50 μm thick and 1 mm wide tungsten ribbon is put at 350 mm upstream of the present ESS, total beam loss is reduced by 36% in the MARS simulation [6]. In other case, the present ESS septum length is shortened from 1.5 m to 1.0 m, and in the upstream 0.5 m space, 30 μm thick and 1 mm wide titanium ribbons are strained every 9 mm pitch as the scatterer, which results in a 50% loss reduction by preliminary MARS simulation. We have a plan to introduce a real scatterer after a further simulation study.

Stretcher

The MR provides 30 GeV high-intensity protons to the neutrino experimental facility (NU) by fast extraction as well as to the hadron experimental facility (HD) by slow extraction. A stretcher ring (SR) has been proposed to ensure that the integrated proton number on target from the slow extraction is sufficient [7]. A beam accelerated at 30 GeV in

the MR is transferred to the SR and is slowly extracted over several seconds. While the slow-extraction procedure is performed, a beam can be accelerated in the MR and delivered to the NU. The arc sections of the SR consist of superconducting combined-function magnets and separated-function magnets (a hybrid lattice configuration). A 30 GeV beam transfer line from the MR to the SR uses superconducting combined magnets with dipole and quadrupole functions. The transferred beam is injected into an arc section of the SR. The POT (integrated proton number on target) from the slow extraction using the SR scheme triples while the POT at the NU remains the same as that of the present scheme.

CONCLUSIONS

The J-PARC slow extraction has a unique scheme using a dynamic bump under achromatic condition to derive a high extraction efficiency. The beam instability caused during a debunch process is a critical issue for beam power ramp-up. Phase offset injection for a RF bucket has mitigated the instability well at present operation. We have attained 51 kW operation at 5.2 s keeping a high extraction efficiency of 99.5%. This is a major milestone for the J-PARC accelerator complex. A spiky spill time structure has been improved by implementing the spill feedback using a fast response quadrupole and applying the transverse RF fields. A 8 GeV beam has successfully slow-extracted in the beam test for COMET phase I experiment. Measured extinction shows a promising result. Upgrade plans with the slow extraction have been discussed.

REFERENCES

- [1] M. Tomizawa *et al.*, "Slow extraction from the J-PARC main ring using a dynamic bump", *Nucl. Instr. and Method A*, to be published.
- [2] M. Tomizawa, "Slow Extraction Projects at J-PARC", *FNAL Accelerator Physics and Technology Seminar*, 27 Aug., 2015.
- [3] F. Tamura *et al.*, "Multiharmonic rf feedforward system for compensation of beam loading and periodic transient effects in magnetic-alloy cavities of a proton synchrotron", *Phys. Rev. ST Accel. Beams*, vol. 16, p. 051002, 2013.
- [4] K. Ohmi *et al.*, "E-cloud observations and simulation at J-PARC", presented at E-CLOUD'18, La Biodola, Isola d'Elba, Italy, 3-7 Jun., 2018.
- [5] S. Igarashi, "High power beam operation at J-PARC", presented at HB'18, Daejeon, Jun. 2018, paper TUA2WD02, this workshop.
- [6] R. Muto *et al.*, "Simulation study of beam scatterer for beam loss mitigation in slow extraction at J-PARC MR", *Proc. 2017 Particle Acc. Sci. Japan*, 2017, p. 892.
- [7] M. Tomizawa *et al.*, "Beam Optics Design of Stretcher Ring and Transfer Line for J-PARC Slow Extraction", in *Proc. IPAC'18*, Vancouver, BC, Canada, Apr.-May 2018, doi: 10.18429/JACoW-IPAC2018-TUPML055

Content from this work may be used under the terms of the CC BY 3.0 licence (© 2018). Any distribution of this work must maintain attribution to the author(s), title of the work, publisher, and DOI.

HIGH-BRIGHTNESS CHALLENGES FOR THE OPERATION OF THE CERN INJECTOR COMPLEX

K. Hanke, S. Albright, R. Alemany Fernandez, H. Bartosik, E. Shaposhnikova, H. Damerau, G. P. Di Giovanni, B. Goddard, A. Huschauer, V. Kain, A. Lasheen, M. Meddahi, B. Mikulec, G. Rumolo, R. Scrivens, F. Tecker, CERN, Geneva, Switzerland

Abstract

CERN's LHC injectors are delivering high-brightness proton and ion beams for the Large Hadron Collider LHC. We review the present operation modes and beam performance, and highlight the limitations. We will then give an overview of the upgrade program that has been put in place to meet the demands of the LHC during the High-Luminosity LHC era.

INTRODUCTION

The proton injector chain of CERN's Large Hadron Collider (LHC) consists presently of a 50 MeV proton linac (Linac2), the Proton Synchrotron Booster (PSB), the Proton Synchrotron (PS) and the Super Proton Synchrotron (SPS).

Linac2 is equipped with a duoplasmatron source and a three-tank drift tube linac operating at 202.56 MHz, which accelerates the protons up to 50 MeV. At injection into the PSB a beam current of 140-150 mA protons is operationally achieved.

Before arriving at the PSB, the beam pulse coming from Linac2 is distributed vertically into four parts, which are then sequentially injected into the four PSB rings. The PSB is a stack of four superposed rings, which accelerate the protons up to 1.4 GeV before the beams are vertically recombined and transferred to the PS. The injection process into the PSB is a multi-turn injection using an injection septum and a horizontal injection bump that is reduced in amplitude during the injection process. The incoming beamlets are scraped by the septum at their first passage, but also during their following turns in the PSB rings, which leads to beam loss in the order of 50% during injection. In combination with space charge at low energy, the resulting transverse emittance of the beams produced by the PSB is a linear function of the number of injected turns. Typically, for high-intensity beams as for example delivered to the isotope separator facility ISOLDE, around 10-13 turns are injected. This results in a large transverse emittance, which is however not critical for these types of beams. Beams for the LHC, where the transverse emittance and hence the beam brightness are critical, are produced with about 2-3 injected turns. Figure 1 illustrates the principle of multi-turn injection into the PSB. Figure 2 shows the measured transverse emittance in the PSB as a function of the extracted intensity for today's operation with Linac2 (upper curves) as well as a simulation for the operation with Linac4 (lower curve) [1].

The PS accelerates further the beams coming from the PSB to 26 GeV for the LHC-type beams. Moreover, the PS performs complex RF manipulations during the cycle,

which split, merge or approach the bunches coming from the PSB longitudinally. With these RF manipulations, the longitudinal parameters of the beams going to the LHC are defined.

The last stage of acceleration happens in the SPS, where the protons are accumulated from multiple injections from the PS, and are accelerated from 26 GeV to 450 GeV before being transferred to the LHC. The challenge in the SPS is to minimise beam loss and to preserve the transverse emittances despite the long injection plateau of several seconds.

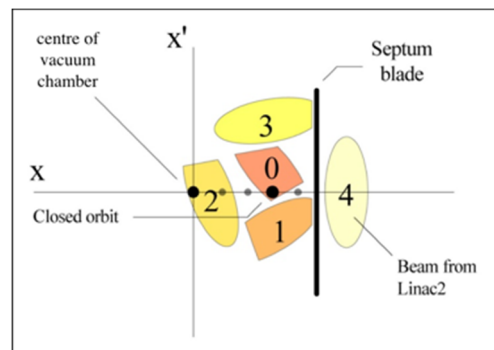


Figure 1: Multi-turn injection of the beam coming from Linac2 into the PSB.

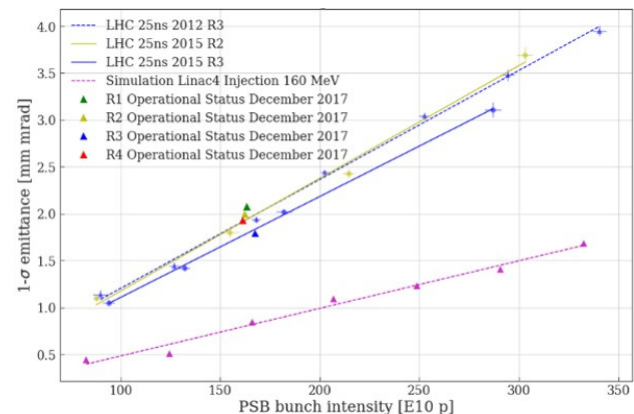


Figure 2: Transverse emittance versus bunch intensity in the PSB. The upper data are measured for different PSB rings and correspond to today's production scheme with Linac2. The lower curve is a simulation for Linac4 injecting into the PSB.

LHC-TYPE BEAMS FROM THE EXISTING CERN INJECTORS

CERN’s injectors are able to produce a whole spectrum of beams for the LHC. This ranges from low-intensity single-bunch beams for LHC commissioning to the production beams for luminosity runs. Apart from that, a whole range of special beams can be produced for machine studies or to adapt to special situations. In the following paragraphs we will focus on the two main production beams for the LHC, the 25 ns bunch spacing beam and the so-called BCMS (Batch Compression, Merging and Splitting) beam.

Standard 25 ns Beam

As outlined in the previous section, the transverse emittance and hence the beam brightness is presently defined through the multi-turn injection process into the PSB. For a standard 25 ns bunch spacing beam for the LHC, about 2-3 turns need to be injected into the PSB rings, which results in 160×10^{10} protons per bunch with a normalised transverse emittance of about 2π mm mrad (note that the original specification for this beam was 2.5π mm mrad).

The PSB executes two cycles to fill the PS, one using all four rings with one bunch each at extraction ($h = 1$) and a second one using only two of the four rings. With this scheme the PSB produces six bunches at 1.4 GeV energy, which are transferred in two extractions (4 + 2 bunches) to the PS. As the time delay between two PSB extractions is 1.2 s, the first injected batch has to wait at the PS flat bottom.

In the PS the beam is accelerated to a top energy of 26 GeV and at the same time the bunches are longitudinally split at an intermediate and final energy. This scheme employs consecutively the RF harmonics 7, 21, 42 and 84, which leads to a 12-fold splitting of each bunch. The resulting number of bunches produced from the six bunches coming from the PSB is hence 72. The longitudinal emittance of these resulting bunches is 0.35 eVs. Figure 3 is a tomographic picture which shows the triple splitting of the six (4 + 2) bunches coming from the PSB.

The 72 bunches coming from the PS are then transferred to the SPS where the challenge is to inject them with a minimum of beam loss and to accelerate them while conserving the beam brightness.

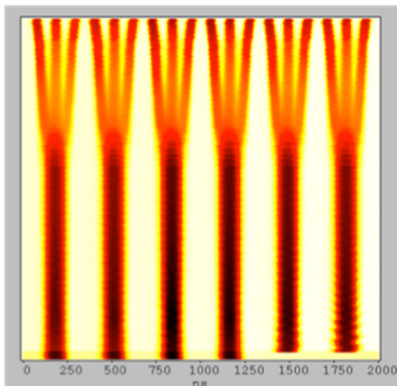


Figure 3: Triple splitting of six PSB bunches in the PS generating the bunch structure for the 25 ns LHC beam.

BCMS Beam

In addition to the standard 25 ns beam, a scheme has been developed to improve the beam brightness. Due to the multi-turn injection into the PSB, the transverse emittance can be reduced by injecting fewer turns into the PSB rings. In the BCMS scheme, instead of taking six PSB bunches into $h = 7$ buckets, the PS takes eight bunches into $h = 9$. The total intensity is then distributed across eight PSB bunches rather than six ones. Accordingly, the injected intensity per PSB ring and thus the transverse emittance can be reduced. A new scheme had to be implemented to obtain the required LHC beam parameters from eight bunches instead of six: the BCMS injection scheme. First, a compression is performed by incrementing the harmonic number from $h = 9$ to 14. Then, a bunch merging puts the harmonic number back to $h = 7$. From this point, the RF gymnastics are similar to the nominal beam, with the bunches split in three, then two and two again. The number of bunches produced is different from the normal scheme: eight bunches are merged into four, multiplied by three, two and two again. The result is 48 bunches spaced by 25 ns, which is less than the nominal 72 bunches. Therefore, the PS and SPS have to perform more cycles to fill the entire LHC, but the gain in transverse emittance leads to higher beam brightness. Figure 4 is a tomographic picture of the BCMS process in the PS. Eight bunches coming in two injections from the PSB are first merged and undergo then a triple splitting.

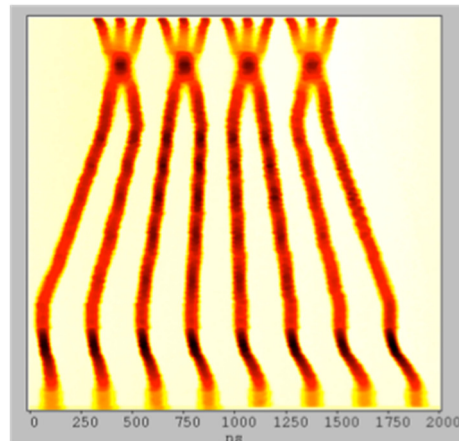


Figure 4: RF gymnastics performed in the PS in order to generate the BCMS beam.

Beam Transfer and Injection

In order to deliver high-brightness beams to the LHC, it is critical to transfer the beam from one injector synchrotron to the next with a minimum of beam loss and emittance blow-up.

Some unexplained blow-up of the transverse emittance during transfer from the PSB to the PS is presently subject of intense studies [2, 3]. One of the possible causes being investigated is betatron and dispersion mismatch at PS injection. It is hoped that more insight can be gained by installing a turn-by-turn profile measurement in the PS, planned in the course of 2018. This monitor would give

Content from this work may be used under the terms of the CC BY 3.0 licence (© 2018). Any distribution of this work must maintain attribution to the author(s), title of the work, publisher, and DOI.

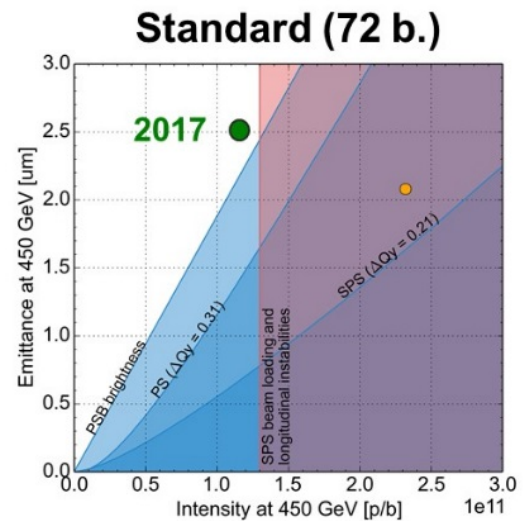
important information about transverse beam size oscillations at injection, which would point to injection mismatch. While the suspected mismatch is mainly present in the horizontal plane, there is also some vertical blow-up observed along the PS cycle [4].

Regarding the transfer of the beam from the PS to the SPS, the critical issues are mostly found in the longitudinal plane. A bunch rotation is performed in the PS, originally using one 40 MHz and two 80 MHz cavities in order to fit the bunches into the 5 ns SPS RF buckets. The development of uncaptured tails due to non-linear forces is an issue, which has been improved by employing two 40 MHz cavities. This scheme has successfully been used during the 2017 run. Nevertheless, there are remaining longitudinal losses at capture, flat bottom, and start of the acceleration in the SPS. The capture losses are mostly due to the longitudinal distribution after bunch rotation in the PS and to RF transients during the first few ms in the SPS. The losses on the flat bottom are due to particles close to the separatrix. Minimizing the capture losses by increasing the RF voltage in the SPS is limited by the requirement to have a matched particle distribution, the momentum acceptance and the available RF voltage needed to maintain the bucket area during the ramp.

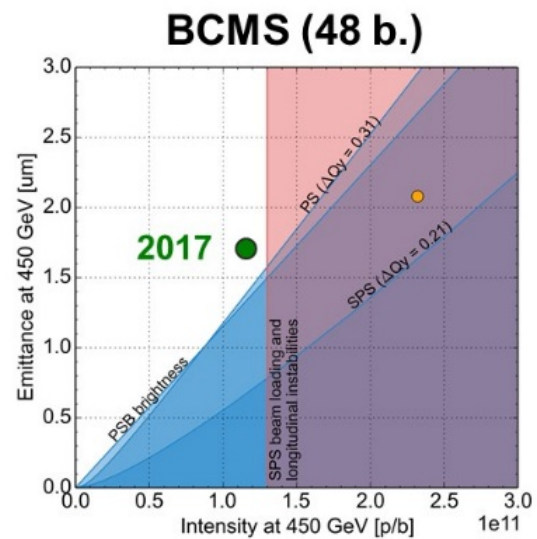
Limitations of the Present Scheme

The various processes described in the previous sections ensure the delivery of high-brightness beams well within the requirements of the LHC. However, the multi-turn injection into the PSB and a number of other effects (e.g. emittance blow up due to space charge, instabilities) lead to a limitation in the brightness that can be achieved. For the SPS, the main limitations come from the beam-loading at very high beam intensity which reduces the available RF voltage, longitudinal instabilities linked to the machine impedance, the electron cloud effect, which at 25 ns spacing can make operation impossible through high vacuum or transverse instabilities, and the high stored beam energy, which requires significant upgrades of all beam intercepting protection devices in the ring and transfer lines.

Figure 5 shows the measured 2017 performance of the injector chain for the LHC 25 ns beam and for the BCMS beam. The various lines indicate processes, which limit the achievable beam brightness, the most stringent one being the brightness curve due to the PSB injection scheme discussed earlier. The green point indicates the beam performance achieved in 2017. It can be seen that the operationally achieved beam brightness is very close to the identified limitations, and that further improvement of the beam brightness as required by the High-Luminosity LHC project (orange point) is not achievable with the present scheme.



1.15e11 / 2.5 um



1.15e11 / 1.7 um

Figure 5: Measured 2017 beam performance for the standard 25 ns beam and BCMS beam. The present beam performance is very close to the theoretical limitations of the present scheme.

LHC INJECTORS UPGRADE

In order to deliver high-brightness beams to the LHC in the High-Luminosity LHC era, CERN has put in place the LHC Injectors Upgrade (LIU) project. This project comprises the replacement of Linac2 by a new H⁺ linac (Linac4) with an increased injection energy in the PSB, the increase of the top energy of the PSB from 1.4 GeV to 2.0 GeV and upgrades of the PS and SPS synchrotrons [5].

Linac4

Linac4 is a 160 GeV H^- linac, which has been constructed over the past decade at CERN and which is presently performing a reliability run. Due to the increased energy, the H^- injection, horizontal phase-space painting and the possibility of energy variability and longitudinal micro-bunch tailoring via a fast chopper located at low energy, Linac4 will allow removing the current space charge detuning bottleneck reached with the high-current Linac2 beam.

PSB Upgrade

The upgrade of the PSB consists of two major parts. With the connection of Linac4 to the PSB, the injection scheme will be upgraded to charge exchange injection of H^- ions. This change will significantly reduce beam loss in the injection area and will allow for tailoring the horizontal emittance by means of phase space painting. At the same time, the injection energy will be increased from 50 MeV to 160 MeV. With this increase in beam energy the relativistic $\beta\gamma^2$ factor increases by a factor of 2. The space charge tune shift decreases hence by a factor 2, thus doubling the intensity that can be accumulated within a given emittance.

The second component of the upgrade program is the increase of the extraction energy from presently 1.4 GeV to 2.0 GeV. The underlying idea is to reduce space charge effects at injection into the PS, thus removing this bottleneck. The expected gain can again be deduced from the ratio of the $\beta\gamma^2$ factor at 1.4 GeV and 2.0 GeV, which is 1.63 and corresponds to an intensity increase of 60% within given emittance values.

PS Upgrade

The upgrade program of the PS focuses on issues both in the transverse and longitudinal plane. In the transverse plane, the direct space-charge tune spread pushes the beam on betatronic resonances causing beam loss and transverse emittance blow up. The upgrade of the injection energy to 2 GeV will help to overcome this limitation. The transverse damper was also upgraded to cope with transverse instabilities and to reduce injection errors.

Concerning the longitudinal plane, coupled bunch instabilities appearing after the transition energy would limit the maximum intensity per bunch well below the 2.6×10^{11} p+ per bunch of the future HL-LHC type beam if no counter-measures were taken. A new dedicated longitudinal damper, based on a Finemet® cavity and a new low-level RF (LLRF) have been installed during LS1 to stabilise the beam. The electronics of the 1-turn delay feedback was also renovated with a new digital system for the main accelerating cavities. The high-frequency cavities are being equipped with additional multi-harmonic feedbacks.

Beyond these main upgrade items, new hardware items are being constructed, as for example beam instrumentation, RF upgrade and beam dumps.

SPS Upgrade

The present baseline for the LIU-SPS upgrade results from the extensive effort invested in the analysis and understanding of the SPS limitations during the past decade. Main upgrade items are the 200 MHz RF system and its low-level RF. The LLRF and power system of the fourth harmonic 800 MHz RF system has also been already upgraded. The existing transverse damper system is also being upgraded with new low-level controls and dedicated pick-ups. The preparation for the upgrade of the 200 MHz RF continues with the prototyping of the power amplifiers now under way, the design of the new power and HOM couplers in progress and the layout change to the RF cavities and associated SPS straight section defined.

In order to fight electron cloud effects, amorphous carbon coating of the vacuum chamber was fully validated as a mitigation measure using a sputtering technique, which does not require the removal of the vacuum chamber from the magnet. This technique will be applied to selected elements of the machine.

To cope with the increased intensity, various machine protection elements will be upgraded and a new internal beam dump will be installed.

Concerning beam instrumentation, performance upgrades of almost every system have been defined and specified, for example the installation of new high-resolution wire scanners.

Ions

The HL-LHC is requested to deliver Pb-Pb collisions with an integrated luminosity of 10 nb^{-1} at top energy to each of the ALICE, ATLAS and CMS experiments in four heavy-ion runs between LS2 and LS4 [6]. From this requirement, the following target parameters, based on extrapolated performance with seven injections in 2016, can be derived: A total of 1256 bunches per ring in the LHC with 1.9×10^8 lead ions per bunch and $1.5 \mu\text{m}$ rad of normalized emittance at injection.

The strategy to reach the required performance is:

- Increase of the beam intensity by modification of the Linac3 source extraction system to remove an aperture limitation. This upgrade took place in 2015 and allowed 40% beam intensity increase.
- An intensive program of machine studies, starting in 2015 for optimization and understanding of the machine limitations in LEIR and SPS. As a result of the LEIR studies an increment of 30% in extracted intensity could be achieved. However, the SPS remains the bottleneck of the Pb-ion injector chain and more studies will be conducted to lift this limitation.
- Batch expansion and bunch splitting in the PS to reach a bunch spacing of 100 ns, which was already demonstrated before the Long Shutdown 1 (LS1).
- Implementation of the momentum slip stacking in the SPS during LS2 with a new low-level RF system reducing the bunch spacing down to 50 ns, the only way to double the number of bunches in LHC.

Content from this work may be used under the terms of the CC BY 3.0 licence (© 2018). Any distribution of this work must maintain attribution to the author(s), title of the work, publisher, and DOI.

Thanks to the Linac3 modifications and LEIR machine studies, these two machines are the first ones in the Pb-ion injector chain that demonstrated the capability of delivering the required HL-LHC beam parameters during operation in 2016.

Expected Performance after LIU Upgrade

With the various upgrades foreseen by the LIU project in place after the second long LHC shutdown (LS2), many of the present intensity limitations will disappear or be mitigated. In particular, the H^- stripping injection in the PSB and the increase of the top energy of the PSB are expected to push the brightness limitations of the injector chain. As can be seen in Fig. 2, the simulated PSB brightness curve with Linac4 lies well below the present measured ones and has a smaller slope. Figure 6 illustrates the extrapolated performance reach of the injector chain with the full LIU upgrade in place. The request of the High-Luminosity LHC can be met.

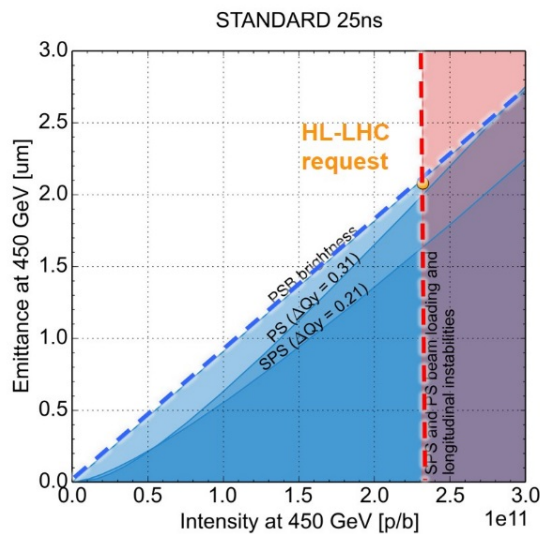


Figure 6: Performance reach of the injector complex after LIU upgrade. The request of the High-Luminosity LHC can be met.

CONCLUSION

CERN’s LHC injectors deliver today a variety of high-brightness beams to the LHC. While the present request of the LHC can be satisfied or exceeded, the future HL-LHC program is requesting beam parameters which are out of reach of the present injector complex. In order to enable the injectors to deliver the requested beam intensity and beam brightness, CERN has put in place a massive upgrade program, the LIU project. The upgrade will be performed during LS2 in 2019/20. Simulations show that the upgraded machines will meet the brightness requirements in the HL-LHC era.

REFERENCES

- [1] E. Benedetto *et al.*, “Machine Development Studies in the CERN PS Booster in 2016, in *Proc. 8th Int. Particle Accelerator Conf. (IPAC’17)*, Copenhagen, Denmark, May 2017, pp. 3339-3342, doi:10.18429/JACoW-IPAC2017-WEPVA037
- [2] F. Tecker, “Emittance Preservation in the Injectors”, *8th LHC Operations Evian Workshop*, Evian, France, Dec. 2017.
- [3] F. Tecker, “Injectors, Performance and Prospects”, *LHC Performance Workshop 2018*, Chamonix, France, Jan. 2018.
- [4] H. Bartosik, “Beam from the Injectors”, *7th LHC Operations Evian Workshop*, Evian, France, Dec. 2016.
- [5] K. Hanke *et al.*, “The LHC Injectors Upgrade (LIU) Project at CERN: Proton Injector Chain”, in *Proc. 8th Int. Particle Accelerator Conf. (IPAC’17)*, Copenhagen, Denmark, May 2017, pp. 3335-3338, doi:10.18429/JACoW-IPAC2017-WEPVA036.
- [6] H. Bartosik *et al.*, “The LHC Injectors Upgrade (LIU) Project at CERN: Ion Injector Chain”, in *Proc. 8th Int. Particle Accelerator Conf. (IPAC’17)*, Copenhagen, Denmark, May 2017, pp. 2089-2092, doi:10.18429/JACoW-IPAC2017-TUPVA020

OPERATIONAL CHALLENGES AND PERFORMANCE OF THE LHC DURING RUN II

R. Steerenberg, J. Wenninger, CERN, Geneva, Switzerland

Abstract

The CERN Large Hadron Collider Run II saw an important increase in beam performance through both, improvements in the LHC and an increased beam brightness from the injectors, leading to a peak luminosity that exceeds the LHC design luminosity by more than a factor two. This contribution will give an overview of run 2, the main challenges encountered and it will address the measures applied to deal with and make use of the increased beam brightness. Finally potential areas where further performance improvement can be realized will be identified.

INTRODUCTION

Following the first Long Shutdown (LS1) in 2013 and 2014 during which the CERN Large Hadron Collider (LHC) and in particular the superconducting magnet interconnections were consolidated, the machine was re-commissioned at an energy of 6.5 TeV per beam in 2015, signalling the start of LHC Run II, covering the years from 2015 until the second Long Shut down (LS2) that will start in December 2018.

MULTI-ANNUAL OVERVIEW OF LHC RUNNING AND PERFORMANCE

Year 2015

The year 2015 was dedicated to establishing operation at 6.5 TeV per beam and with standard 25 ns bunch spacing [1], in order to prepare for substantial luminosity production during the years running up to LS2. The first three months were dedicated to magnet powering tests and the magnet training campaign to establish a reliable and reproducible magnet performance at magnetic fields equivalent to 6.5 TeV beam energy.

The beam commissioning was accomplished, using the 50 ns bunch spacing, considering that much experience was gained during Run I, but also to avoid electron cloud effects during this period. By mid-July, following a scrubbing run, the standard 25 ns bunch spacing was used, initially with a reduced number of bunches to limit the total intensity and stored energy. Consequently, the beam intensity was ramped up until the end of the year by increasing step-wise the number of bunches injected to 2244 bunches per beam. Despite the prolonged periods of e-cloud scrubbing, the intensity ramp up was mostly limited by the heat load induced on the cryogenic system [2].

Year 2016

The year 2016 required only 4 weeks for the beam commissioning and was directly followed by an intensity ramp up and luminosity production, using the standard 25 ns bunch spacing. From Fig. 1, one can perceive that this was

also the first year with substantial luminosity production. On 26 June, after careful optimisation of the machine settings and beam brightness in the injectors, the LHC attained its design luminosity of $1 \times 10^{34} \text{ cm}^{-2}\text{s}^{-1}$. In parallel, the injector chain prepared a high brightness 25 ns beam, based on a Batch Compression Merging and Splitting (BCMS) scheme [3]. The LHC took this beam successfully for the first time for physics on 19 July, resulting in a transverse emittance at the start of stable beams of $\sim 2 \text{ mm mrad}$. This, in combination with a reduction of the half crossing angle from $185 \mu\text{rad}$ to $140 \mu\text{rad}$ on 23 September, gave rise to a further gradual increase of the peak luminosity, as can be observed in Fig. 2, with a record peak luminosity of $1.4 \times 10^{34} \text{ cm}^{-2}\text{s}^{-1}$.

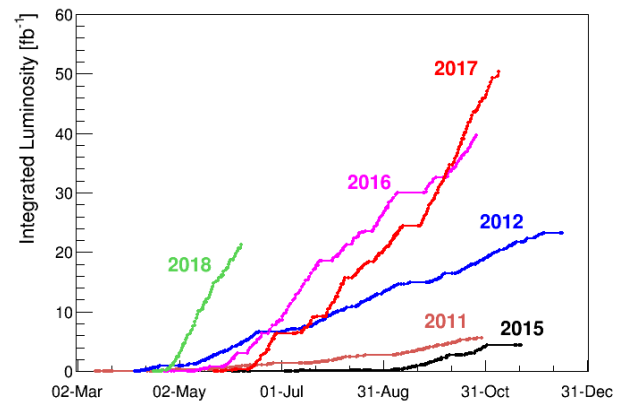


Figure 1: Multi-annual overview of the yearly integrated luminosity.

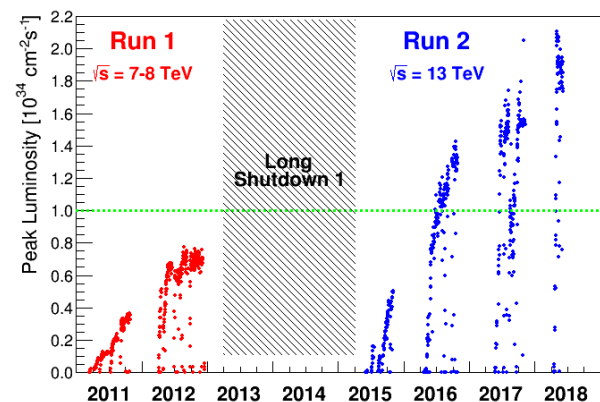


Figure 2: Multi-annual overview of the peak luminosity.

On 10 August an intermittent inter-turn short circuit was observed in one of the dipole magnets in half cell 31 left of IP2 (31L2) that is part of Sector 1-2, one of the eight sectors that constitute the LHC. Despite this, luminosity production continued with extra protection measures in place, but the decision was taken to replace the magnet during the

Content from this work may be used under the terms of the CC BY 3.0 licence (© 2018). Any distribution of this work must maintain attribution to the author(s), title of the work, publisher, and DOI.

upcoming Extended Year End Technical Stop (EYETS) of 2016-2017, which required a prolongation of the EYETS by one additional month.

The proton physics run ended on a very positive note with 40 fb⁻¹ integrated. The LHC continued running successfully for another 4 weeks with proton lead collisions.

Year 2017

Following the magnet replacement in Sector 1-2, requiring warming up and cooling down the 3 km-long sector, the hardware re-commissioning of the nearly 1600 circuits included a long list of additional tests to be performed on the sector that underwent the thermal cycle.

The first beam was injected on 29 April and first stable beams, with only a few bunches, was established on 23 May. Subsequently a period with interleaved commissioning and intensity ramp up followed. Before reaching 2556 bunches in stable beams on 19 July a one-week scrubbing run was performed to reduce the secondary electron emission yield of the beam screen, hence the production of electron clouds.

Earlier, already during the commissioning with beam, abnormal background radiation and sudden beam losses, some leading to beam dumps, were observed in the beam vacuum for both beams at the level of a magnet interconnect of half-cell 16 left of IP2 (16L2). These losses were induced by an accidental inlet of air into the beam vacuum with the beam screen at 20 K, following the magnet replacement [4, 5]. On 10 August a beam screen flushing was attempted where the beam screen is warmed up from its usual 20 K to 80 K with the aim to evaporate frozen gas and condensate it on the surrounding cold bore, out of the sight of the beam. Unfortunately, this flushing even degraded the situation.

Since the loss mechanism was suspected to be influenced by electron cloud, the injector chain produced the 25ns 8b4e beam that was used in the LHC as of 4 September. The 8b4e beam structure consists of eight bunches spaced by 25 ns followed by four empty buckets. This interleaved with SPS and LHC injection kicker gaps is then repeated around the circumference of the LHC, resulting in 1916 bunches per beam, and suppressing the electron cloud production drastically. Once proven successful in mitigating the 16L2 issue, this scheme was further enhanced in the injectors and a high brightness version, based on Batch Compression and Splitting was developed (8b4e-BCS). The main beam parameters for these beams that allowed efficient luminosity production, despite the 16L2 issue, are given in Table 2.

Following further measurements and studies on the available aperture it was decided to reduce the β -function at IP1 and IP5 from 40 cm to 30 cm. This together with the 8b4e-BCS beam resulted on 2 November in a new record of $2.06 \times 10^{34} \text{cm}^{-2}\text{s}^{-1}$ for the peak luminosity as can be seen in Fig. 2. and Table 2. The number of inelastic collisions per bunch crossing (pile-up) in the experiments ATLAS and CMS was beyond the acceptable, consequently the instantaneous luminosity was levelled to $1.5 \times 10^{34} \text{cm}^{-2}\text{s}^{-1}$, using levelling by beam separation.

The 2017 proton physics run that was hampered by the 16L2 issue nevertheless ended with a record integrated luminosity of 50 fb⁻¹.

Year 2018 (Current Year)

Although successful, but after running for a large part of 2017 with the 8b4e-BCS beam, all four experiments requested to revert from the 1868 bunches per beam for the 8b4e-BCS to the 2556 bunches of the BCMS beam. However, this could not be achieved without resolving the 16L2 issue. Therefore, Sector 1-2 was warmed up to 90 K during the YETS of 2017-2018, allowing the evacuation of about 7 litres evaporated gasses like oxygen and nitrogen, but not the water vapour, which was estimated to be 0.1 gram per beam vacuum [6].

The first beam was injected on 30 April and first stable beams, with only a few bunches, was established on 23 April. Subsequently, a period with interleaved commissioning and intensity ramp up followed. Before reaching 2556 bunches in stable beams on 5 May, which was thirteen days ahead of schedule.

During the intensity ramp-up, beam losses induced by 16L2, although much lower than in 2017, were present and closely monitored. These beam losses, see Fig. 3, are of two types: firstly, a steady-state or constant beam loss that depends on the total number of particles per beam. This beam loss is substantially lower than the threshold that could provoke a beam dump, thanks in particular to a special solenoid that was installed during the second half of 2017 [7]. Secondly, erratic beam loss spikes that add to the steady-state losses, potentially surpassing the dump threshold. The steady-state beam losses increase when the number of bunches increases, but the frequency of the beam loss spikes decreased the longer the beam circulates in the machine. These spikes were “conditioned away”, allowing running with the 2556-bunch BCMS beam in 2108.

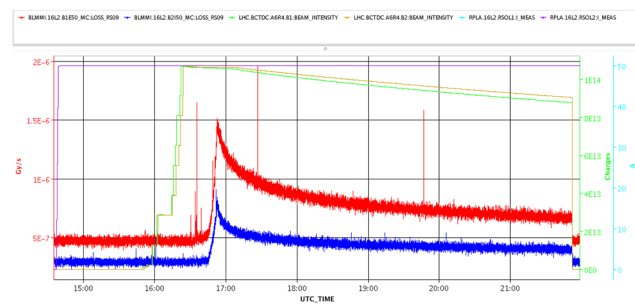


Figure 3: Beam loss monitors measurements in 16L2. The steady-state beam losses with superposed beam loss spikes for beam 1 (red) and beam 2 (blue).

The target for the 2018 proton physics run that ends on 27 October is to accumulate 60 fb⁻¹ of integrated luminosity. The year will end with a 24-day lead-lead ion run before going into a 1-week magnet training test to estimate the time required to increase the collision energy up to 7 TeV after LS2. A detailed breakdown of the days spend in each operational phase is given in Table 1.

Table 1: Time Allocation to the Different Operational Phases in 2018

Phase	Days	Ratio [%]
Comm. & Intensity ramp up	33	13.4
Scrubbing (e-cloud)	1	0.4
25 ns proton physics	131	53.3
Special physics runs	17	6.9
Setting up Pb-Pb ion run	4	1.6
Pb-Pb ion physics run	24	9.8
Machine Development	20	8.1
Technical Stops (3x)	12	4.9
Technical recovery	4	1.6
Total	246	100

Performance Summary

The LHC machine and beam parameters for the years 2015 to 2018 are summarised in Table 2. The LHC machine availability and Stable Beam time for Run II are given in Fig. 4. Figure 2 shows the increase of the peak luminosity over the years, but also the slope with which this peak luminosity is reached is every year steeper, indicating an efficient re-commissioning of the machine and a fast intensity ramp up. The design luminosity of $1 \times 10^{34} \text{ cm}^{-2} \text{ s}^{-1}$ is indicated by the green line and was passed for the first time in 2016 and on 2 November 2017 the peak luminosity reached, was more than twice the design peak luminosity. The yearly integrated luminosity plot for the years 2011 until 2018 is given in Fig. 1. From this one can clearly distinguish the commissioning years 2011 (Run I) and 2015 (Run II) from the production years 2012, 2016, 2017 and 2018. The total integrated luminosity for each run is given in Fig 5. The target for the total integrated luminosity until end of Run II is 150 fb^{-1} , which is well in reach for 2018, the last year before LS2.

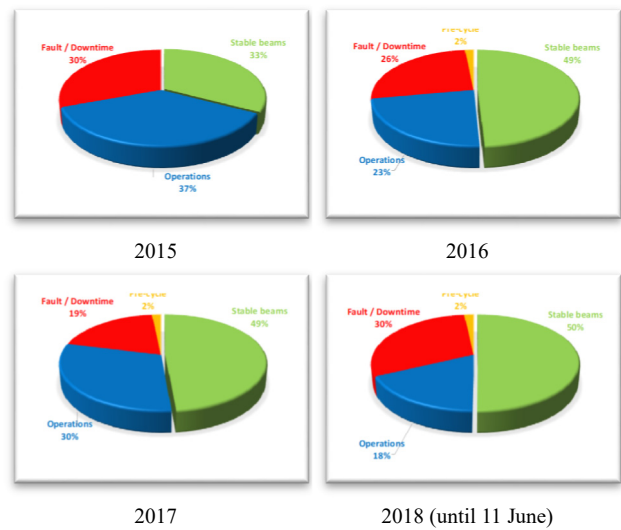


Figure 4: LHC availability for the years of Run II.

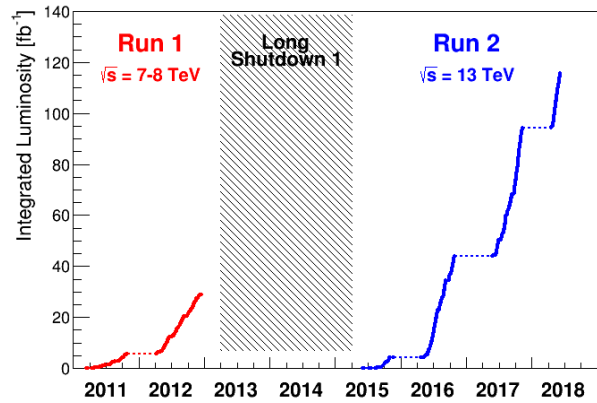


Figure 5: Multi-annual overview of the total integrated luminosity for Run I and Run II.

Table 2: Overview of LHC Machine and Beam Parameters for Run II Compared to the Design Values

Parameter	Design	2015	2016	2017	2018
	Beam type: Std	Std	Std/BCMS	BCMS	8b4e 8b4e-BCS BCMS
Energy [TeV]	7	6.5	6.5	6.5	6.5
Number of bunches per ring	2808	2244	2040/2076	2556	1916 1868 2556
Bunch spacing [ns]	25	25	25	25	25 25 25
Bunch population N_b [10^{11} p/b]	1.15	1.15	1.2	1.2	1.2 1.25 1.2
Transv. norm. emittance SB ϵ_n [mm mrad]	3.75	3.5	3.5/2.1	2.1	2.3 1.8 2
Betatron function at IP1 and IP5 β^* [m]	0.55	0.8	0.4	0.4	0.4/0.3 0.3 0.3/0.25 ⁽³⁾
Half crossing angle [μrad]	142.5	145	185	150	150 150/110 ⁽¹⁾ 160/130 ⁽¹⁾
Peak luminosity [$10^{34} \text{ cm}^{-2} \text{ s}^{-1}$]	1	0.55	0.83/1.4	1.74	1.9 2.06/1.5 ⁽²⁾ 2.1
Maximum pile up μ (per bunch crossing)	~ 20	~ 15	$\sim 20/35$	~ 45	70/60 ⁽²⁾ 80/60 ⁽²⁾ 60
Stored beam energy [MJ]	360	270	345	320	240 245 320
Integrated luminosity per year [fb^{-1}]	n.a.	4.2	39.7	50.2	n.a.

⁽¹⁾ Minimum crossing angle during crossing angle anti-levelling

⁽²⁾ Value after luminosity-levelling by separation

⁽³⁾ Minimum betatron function during betatron anti-levelling

SOME BEAM PERFORMANCE CHALLENGES

Tune & Chromaticity Shifts

On a plateau, like for beam injection where the magnet current is stable, the magnetic field multipoles drift due to current redistribution in superconducting cables, leading to drifts in tune Q and chromaticity Q' [8, 9]. These drifts whose magnitudes depend on the magnet powering history, need to be compensated. For the LHC this is implemented in the form of a feedforward based on a field description model (FiDeL). This accurate feedforward maintains the tune Q and chromaticity Q' constant along the entire plateau, but does not take into account any tune changes induced by the beam itself during the injection process.

The beam injection process in the LHC consists of accumulating a large number of high brightness bunches that itself will provoke a tune shift. This instantaneous Lasselst tune shift is corrected taking into account the beam intensity.

Both mechanisms have been tested and deployed and are successfully used in the day-to-day operation of the LHC.

Electron Cloud and Heat Load

Since the start of LHC operation with bunch trains e-cloud has been observed and represents one of the main performance limitations for the LHC. These e-clouds cause transverse emittance blow up and potentially can run the beam unstable, causing losses. In addition their production puts a large constraint on the cryogenic system as they form a major source of heat load on the beam screen. Continued studies have largely enhanced the understanding of the phenomena and have led to the development of very powerful measurement and simulation tools [10].

The production of e-cloud strongly depends on the secondary electron emission yield of the beam screen. Simulations and experience have shown that the surface of the beam screen can be conditioned by exposing the beam screen for prolonged period to high rates of e-cloud.

In practice, at the start of a yearly run and once the LHC is sufficiently commissioned to house a large number of bunches at low energy, a scrubbing run of which the length varies from one to about five days, depending on the work performed during the YETS (e.g. vacuum chamber opening) is scheduled to re-establish conditions that allow to accelerate safely a full machine to high energy for collisions. The running for physics will then further, although slightly, scrub the machine.

Transverse Emittance Growth

The transverse emittance is together with the beam intensity one of the main parameters for high luminosity production. It is therefore important to preserve the emittance as much as possible and to minimize blow up in any of the processes. Intense measurement campaigns and careful analysis have revealed that the transverse emittance blows up beyond expectations which are deduced from

simulations [11, 12], principally during the injection plateau and acceleration. IBS is the dominating factor for the emittance growth at low energy. However, the growth rate is larger than the IBS contribution and therefore requires further investigation and understanding.

Table 3: Emittance Growth per Process and Beam Type

Process	BCMS		8b4e-BCS	
	H [%]	V [%]	H [%]	V [%]
Injection	15	9	17	15
Acceleration	5	22	43	45

The main contribution to the transverse emittance blow up appears during acceleration and can amount to an emittance growth of up to $\sim 45\%$ in the vertical plane for the highest brightness beam (8b4e-BCS) and $\sim 22\%$ for the BCMS beam (Table 3). A reduction of this growth will directly translate in a higher peak luminosity, but the mechanism behind the blow up is not yet fully understood and a working group, combining all the observations and concentrating efforts to understand and possibly mitigate the issue has been established. Minimizing this emittance growth will be very important, as during Run III the beam brightness from the upgraded injectors will gradually increase.

Beam Life Time

Beam lifetime is normally dominated by luminosity burn-off, but beam loss through other mechanisms can contribute to the reduction of the beam life time. A big effort is made to build a solid luminosity model for the LHC [12], allowing comparison between the theory, the theoretical model and beam observations, hence providing understanding on the amount of non-luminosity burn-off losses.

This model has already identified currently unexplained losses at the start of collisions and shows that the lifetime of beam 2 during the remainder of the fill is not too far away from model-based lifetime. However, there is a significant difference in lifetime for beam 1, which is being studied, but remains not fully understood. The intensity pattern along the bunch trains during collisions hints e-cloud as a potential source, but this remains to be confirmed.

PREPARING THE FUTURE

In view of the HL-LHC operation, some methods and principles foreseen are already being implemented and tested on the LHC to validate them fully and to gain operational experience.

Levelling & Anti-Levelling

Luminosity levelling is generally applied to reduce the number of inelastic collisions per bunch crossing when the instantaneous luminosity, the collider can provide, too high is. This has been done routinely for the two low luminosity experiments (ALICE and LHCb) since the start of the LHC.

However, in 2017 the achieved peak luminosity also exceeded the pile-up limit of ATLAS and CMS, hence levelling by beam separation was applied.

As a result of luminosity burn-off during collisions the dynamic aperture increases, allowing for the reduction of crossing angles and β -functions and therefore increasing the instantaneous luminosity [13]. This anti-levelling scheme has been developed, tested and validated during dedicated machine development (MD) sessions and deployed in steps. In the second half of 2017 the anti-levelling by reducing the half crossing angle from 150 μ rad in three steps to 120 μ rad was deployed and used operationally. In 2018 the steps were removed and since then a more continuous crossing angle anti-levelling, based on the dynamic aperture evolution is used. Also the β^* anti-levelling was added to reduce the β^* from 30 cm to 25 cm in two steps [14].

Both anti-levelling schemes increase the luminosity production with a few percent, but the gain in operational experience is also very important for the HL-LHC era.

Achromatic Telescopic Squeeze Optics

The Achromatic Telescopic Squeeze (ATS) allows for very small β -functions in the IPs, while correcting the chromatic aberrations induced by the inner-triplets on either side of the experiments [15], required for the HL-LHC [16]. This scheme has been developed, tested and validated during dedicated machine development (MD) sessions and came to sufficient maturity in 2016 to be deployed operationally at the start of 2017.

In the year preceding the deployment and with the aim of optimising of the magnetic cycle, part of the squeeze was started during the ramp, using the process called Combined Ramp & Squeeze (CRS) [17]. This allows arriving at the 6.5 TeV flat top with a β^* of 1 m for the two high luminosity experiments (ATLAS and CMS). A further squeeze down to a β^* of 30 cm is applied on the flat top. The last part of this squeeze, from a β^* of 40 cm to 30 cm, is relying on the ATS. In 2018 two further squeeze steps down to 27.5 cm and 25 cm were added towards the end of the fill with the aim to optimise luminosity production after sufficient luminosity burn-off.

ACKNOWLEDGEMENTS

The authors thank all the persons and teams that make a big effort to reach these outstanding machine and beam performances we enjoy today and are in debt to many of them for the material used for this paper.

CONCLUSION

LHC Run II is successfully underway to reach the goal of 150 fb⁻¹ set for Run I and Run II. The machine and beam performance are continuously improved through thorough understanding of the underlying systems and physics processes, but there are still challenges among which beam emittance growth and beam life time optimisation.

Run II saw also important steps towards HL-LHC operation. The ATS optics was successfully deployed and used,

although not yet to its full extend. Luminosity levelling and anti-levelling, based on beam separation, crossing angle and β^* are now used routinely and will be further develop.

REFERENCES

- [1] O. S. Brüning, P. Collier, P. Lebrun, S. Myers, R. Ostojic, J. Poole, and P. Proudlock (Eds), "LHC Design Report", CERN, Geneva, Switzerland, Rep. CERN-2004-003-V-1, 2004.
- [2] G. Ferlin *et al.*, "Cryogenics", *LHC Performance Workshop*, Chamonix, France, TE-CRG-OA, 2016.
- [3] H. Damerou *et al.*, "RF manipulations for higher brightness LHC-type beams", in *Proc. IPAC'13*, Shanghai, China, May 2013, paper WEPEA044.
- [4] J.M. Jiménez *et al.*, "Observations, Analysis and Mitigation of Recurrent LHC Beam Dumps Caused by Fast Losses in Arc Half-Cell 16L2", presented at *Proc. IPAC'18*, Vancouver, Canada, Apr. 2018, paper MOPMF053, unpublished.
- [5] B.Salvant *et al.*, "Experimental Characterisation of a Fast Instability Linked to Losses in the 16L2 Cryogenic Half-Cell in the CERN LHC", presented at IPAC'18, Vancouver, Canada, Apr. 2018, paper THPAF058, unpublished.
- [6] G. Berliozzi *et al.*, "Vacuum Observations in 16L2 and Implications", presented at 332nd CERN LHC Machine Committee (LMC), Dec. 2017, <https://indico.cern.ch/event/689424/>
- [7] G. Arduini *et al.*, "Resistive Solenoid in the 16L2 Interconnect" presentation at the 319th CERN LHC Machine Committee (LMC), Sep. 2017, <https://indico.cern.ch/event/665902/>
- [8] M. Schaumann *et al.*, "Feed-Forward Corrections for Tune-and Chromaticity Injection Decay During 2015 LHC Operation", in *Proc. IPAC'16*, Busan, Korea, May 2016, paper TUPMW026.
- [9] M. Schaumann *et al.*, "Tune and Chromaticity: Decay and Snapback", presented at 6th Evian Workshop on LHC Operation, Evian, France, 2015.
- [10] G. Rumolo *et al.*, "Electron Cloud at the LHC and LHC Injectors", in *Proc. IPAC'17*, Copenhagen, Denmark, May 2017, paper MOZA1.
- [11] M. Hostettler *et al.*, "Emittance Evolution in the LHC: From Injection to Collisions", presented at 8th Evian Workshop on LHC Operation, Evian, France, 2017.
- [12] F. Antoniou *et al.*, "LHC Luminosity Modeling for Run II", in *Proc. IPAC'16*, Busan, Korea, May 2016, paper TUPM0026.
- [13] M. Hostettler *et al.*, " β^* Levelling Using the LHC Lumi Server (MD 2427)", CERN, Geneva, Switzerland, Rep. CERN-ACC-NOTE-2018-0001, 2018.
- [14] M. Hostettler *et al.*, "Online Luminosity Control and Steering at the LHC", in *Proc. ICALEPC'17*, Barcelona, Spain, Oct. 2017, paper TUSH201.
- [15] S. Farthouk *et al.*, "The Achromatic Telescopic Squeezing Scheme: Basic Principles and First Demonstration at the LHC", in *Proc. IPAC'12*, New Orleans, LA, USA, May 2012, paper TUPPR068.
- [16] G. Apollinari, I. Béjar Alonso, O. Brüning, P. Fessia, M. Lamont, L. Rossi, L. Tavia (Eds) "High-Luminosity Large Hadron Collider (HL-LHC) Technical Design Report V. 0.1", CERN, Geneva, Switzerland, Rep. CERN-2017-007-M, 2017.
- [17] M. Solfaroli *et al.*, "Combined Ramp and Squeeze to 6.5 TeV in the LHC", in *Proc. IPAC'16*, Busan, Korea, May 2016, paper TUPMW031.

Content from this work may be used under the terms of the CC BY 3.0 licence (© 2018). Any distribution of this work must maintain attribution to the author(s), title of the work, publisher, and DOI.

REAL-TIME MEASUREMENT OF FLUCTUATIONS OF BUILDING FLOOR AND INSTALLED DEVICES OF LARGE SCIENTIFIC EQUIPMENT*

Hyojin Choi[†], Sangbong Lee, Hong-Gi Lee, Jang Hui Han, Seung Hwan Kim, Heung-Sik Kang
 Pohang Accelerator Laboratory, Pohang, Korea

Abstract

Several parts that comprise the large scientific equipment should be installed and operated at precise three-dimensional location coordinates X, Y, and Z through survey and alignment to ensure their optimal performance. As time goes by, however, the ground goes through uplift and subsidence, which consequently changes the coordinates of installed components and leads to alignment errors ΔX , ΔY , and ΔZ . As a result, the system parameters change, and the performance of the large scientific equipment deteriorates accordingly. Measuring the change in locations of systems comprising the large scientific equipment in real time would make it possible to predict alignment errors, locate any region with greater changes, realign components in the region fast, and shorten the time of survey and realignment. For this purpose, a WPS's (wire position sensor) are installed in undulator section and a HLS's (hydrostatic leveling sensor) are installed in PAL-XFEL building. This paper is designed to introduce installation status of HLS and WPS, operation status.

INTRODUCTION

All components of PAL-XFEL were completely installed in December 2015, and Hard X-ray 0.1nm lasing achieved through its beam commissioning test and machine study on March 16, 2017. The beam line users are use the hard x-ray since March 22, 2017 [1, 2].

The HLS and WPS system has been installed since September 2016 to measure and record changes of the building floor and devices in real time (see Fig. 1) [3, 4].

THE NECESSITY OF THE SURVEY EQUIPMENT

If the position of the parts for the installed optical mechanism is changed or altered due to vibration, all of the properties of the optical mechanism may be debilitated. So, the optical mechanism should be installed in the isolation optical table. Since the surface flatness of the table hardly

changes, the position of the parts for the installed optical mechanism won't change as well. The smart table has the maintenance function of automatically keeping the table surface horizontal when the height of the building floor is altered. The isolation function prevents the vibration of the building floor from being transmitted to the optical mechanism installed on top of the table to prevent errors that arise due to the shaking of the optical mechanism. The optical mechanism installed on the optical table may be tested for a long time while stably maintaining the characteristics of the optical mechanism.

The scale of large scientific equipment is as large as several hundred meters to several kilometers and the degree of precision and stability of the specification is high. Various feedback functions are applied to meet the specifications of large scientific equipment. However, there is a limit to overcoming the degradations of large scientific equipment that caused by devices position moving with only the feedback function. Therefore, a lot of time and money have to be made a payment in order to perform the realignment task after surveying the position of all installed components after periodically stopping the operation of large scientific equipment [5].

While the accelerator operating that generates the radiation that is harmful to the human body, people cannot conduct surveying work in the tunnel. If there were a survey system that can monitor the position of the building floor and the components during the operation of the scientific equipment, it would be much easier to sort out areas that have many changed and that also save time and money for the realignment working. To do so, survey systems such as the HLS and WPS are installed on the PAL-XFEL.

There is workshop that discuss about the techniques and experiences necessary for tasks such as surveys and alignments of large scientific equipment. Also, workshop for improving changes and vibration problems of the building floor through building construction works are being held as well [6, 7].

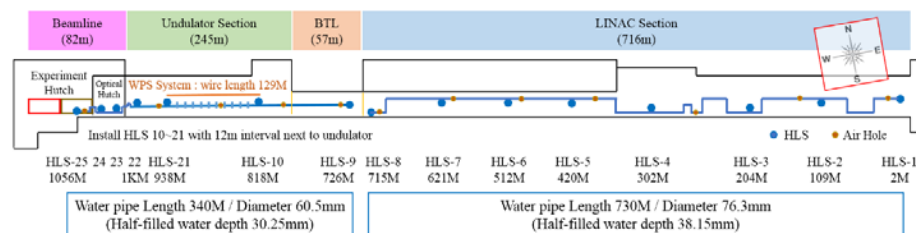


Figure 1: The position of HLS and WPS and specification of HLS water pipe in PAL-XFEL (Top view).

*Work supported by Ministry of the Science, ICT and Future Planning

[†]choihyo@postech.ac.kr

HLS SYSTEM

The construction process and inspection method of the HLS system for PAL-XFEL is as shown in Table 1. In order to design the HLS and the waterpipe, it is necessary to understand various physical phenomena that occur within the waterpipe (see Fig. 2).

Table 1: Construction and Inspection of HLS

- (1) Selection of HLS: self-calibration.
- (2) Calculation of pipe diameter suitable for the length of the waterpipe.
- (3) Installation of air hole: improvement of differences in atmospheric pressure and air flow within the waterpipe.
- (4) Periodic inspection of HLS system.
- (5) Inspection of water height variation that is caused by the tide.

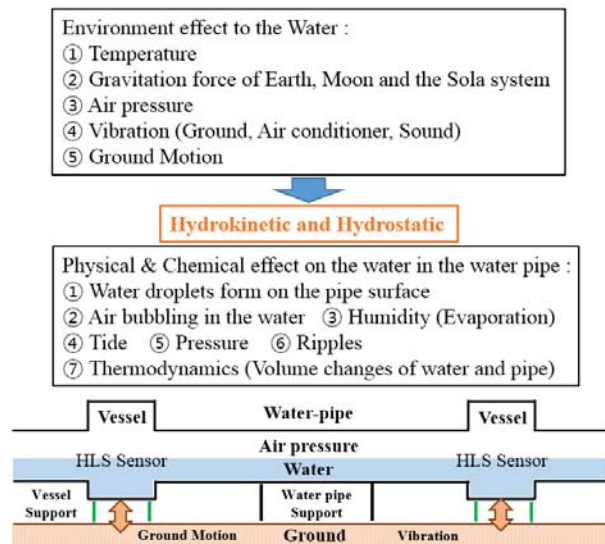


Figure 2: The surrounding environment influencing HLS.

(1) The physical and electrical characteristics of the components constituting the sensor change over time. This produces sensor measurements incorrect. In order to reduce measurement errors, the sensor has to be periodically inspected. Since the HLS that is produced by the budker institute of nuclear physics (BINP) in Russia has the self-calibration function, it can obtain reliable measurements through self-calibration even when the characteristics and the surrounding environments (temperature, atmospheric pressure) of the electronic components have changed over time. Self-calibration is an advanced design technique.

(2) The most important part of the HLS system is the waterpipe that provides measurement reference. One thing that should be taken in to consideration in the process of designing the waterpipe is the water flow. A pipe of an appropriate diameter for the waterpipe has to be selected so that the water will smoothly flow within the waterpipe and maintain the right level. The water inside the waterpipe changes in height twice a day due to the tidal-force. If the

water does not flow smoothly in accordance with the revolution period of the moon, a bottleneck phenomenon will occur within the waterpipe and the water won't be able to maintain the reference level anymore.

(3) As water only maintains equilibrium with the force of gravity, the water flow rate slows down if there is a pressure difference inside the waterpipe or if the airflow is not fast enough. Air holes were installed at intervals of 100 meters in order to eliminate atmospheric pressure differences within the waterpipe and to smooth out the air flow. As a result, the water flow was improved and the time required for the water to maintain balance was reduced.

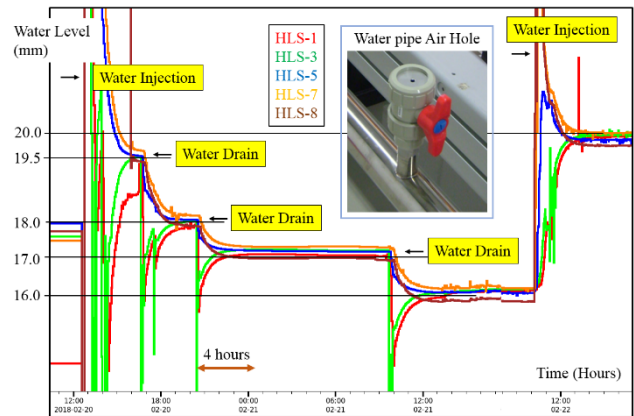


Figure 3: Test for flow of water in the water pipe.

(4) The height of the waterpipe must be constant. If the height of the waterpipe is not constant, changes in the HLS measurement will be inconsistent during the inspection process of the water injection or the water will take a long time to achieve balance. This simple inspection method enables you to check the conditions of the HLS and waterpipe that constitute the HLS system (see Fig. 3).

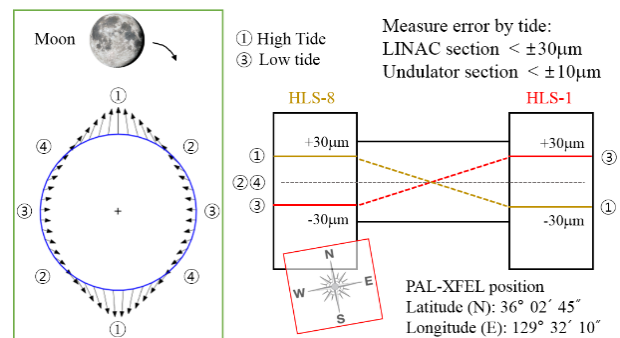


Figure 4: HLS's measurement error by tides.

(5) The height of the water within the waterpipe always changes due to the flowing phenomenon of the water that is caused by the tidal force. This may be the factor that produces error in the HLS measurement, but the HLS measurement can be revised after measuring the water height change caused by the tide. When designing the HLS system, it is important to take into consideration that the longer the waterpipe is, the longer it takes for the water to balance and the variation of the water height caused by the tide gets greater (see Fig. 4).

WPS SYSTEM

The construction process of the WPS system and the correction method of the measurement for PAL-XFEL are shown in Table 2.

Table 2: Construction and Correction of WPS

- (1) Selection of WPS and wire.
- (2) Sag calculation according to the length of the wire and WPS support design.
- (3) Position change correction of the wire stretched post.

(1) The most important thing in selecting the WPS system is the wire material that provides the reference. Carbon wire is a light and conductive material that does not change in length even when the temperature and humidity of the surrounding environment changes or even when tension is applied for a long time.

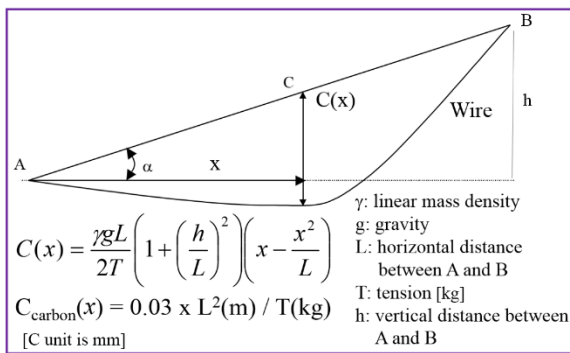


Figure 5: Wire sag calculation.

(2) The wire sag is determined by the length of the wire as well as the pulling tension of the wire. Due to the nature of the carbon, there is no change in the sag of the wire once it has been installed. The height of the WPS support should be adjustable so that WPS can be installed in accordance with the sag condition of the wire. A wire protecting duct should be installed so that the wire does not shake due to the wind that is generated by the air conditioning equipment (see Fig. 5).

(3) The wire stretched post is installed on the building floor. If the wire stretched post is moved due to the deformation of the building floor, the position of the wire which provides the reference also changes. After measuring the change of the wire stretched post by using the HLS (Y axis height) and the tilt meters (roll and pitch), the measurement value of the HLS measurement may be corrected after calculating the position change of the wire (see Fig. 6).

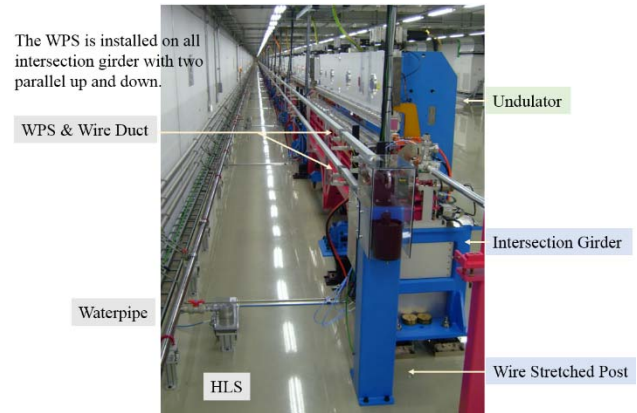
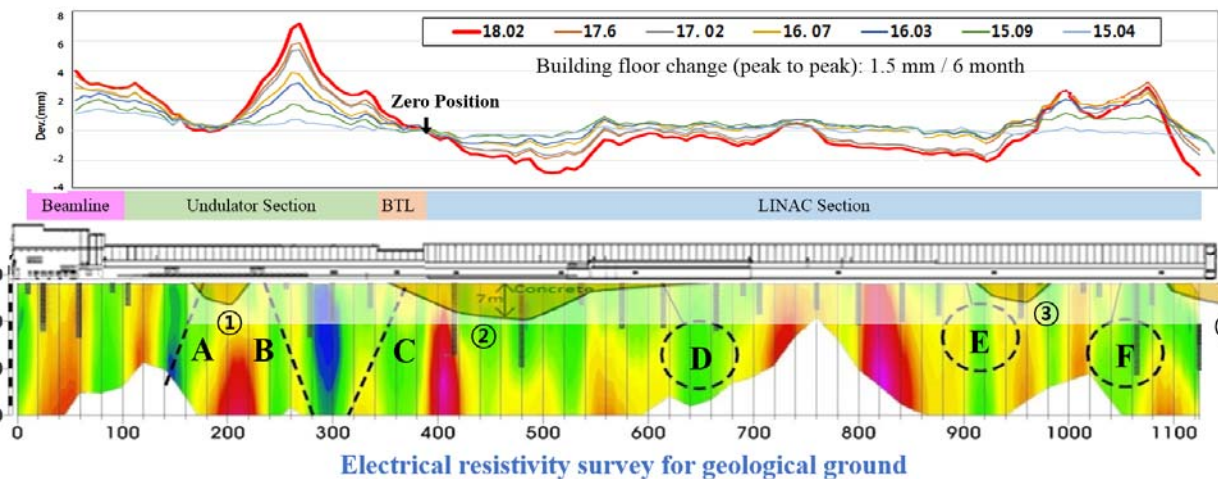


Figure 6: Installed HLS and WPS in Undulator section.

SUMMARY

For an efficient alignment of large scientific equipment, it is required to the survey system to observe and record the position changes of components and building floor. The PAL-XFEL uses the HLS system to survey the deformation of the building floor, and WPS system to survey the 2D (X/Y axis) position change of the devices. By using the survey system, it is possible to easily find out the area where the position change is severe and perform the realignment work (see Fig. 7).

Installing the waterpipe for HLS use in sections of 500 meters is considered to be a method of reducing HLS measurements errors caused by tide rather than installing them at long length of several kilometres.



A, B, C: Estimated fault fracture zone / D, E, F: Estimated local anomaly zone / ①②③④: Concrete replacement area

Figure 7: Ground structure and motion of building floor of PAL-XFEL. (Side view).

Content from this work may be used under the terms of the CC BY 3.0 licence (© 2018). Any distribution of this work must maintain attribution to the author(s), title of the work, publisher, and DOI.

REFERENCES

- [1] I.S. Ko *et al.*, “Construction and Commissioning of PAL-XFEL Facility”, *Applied Science*, vol. 7, no. 5, p. 479, 2017, doi:10.3390/app7050479
- [2] H.-S. Kang *et al.*, “Hard X-ray free-electron laser with femto-second-scale timing jitter”, *Nature Photonics*, vol. 11, p. 708, 2017, doi:10.1038/s41566-017-0029-8
- [3] HJ Choi *et al.*, “Wire position system to consistently measure and record the location change of girders following ground changes”, *Journal of Physics: Conf. Series*, vol. 874, p. 012088, 2017, doi:10.1088/1742-6596/874/1/012088
- [4] Hyojin Choi *et al.*, “HLS System to Measure the Location Changes in Real Time of PAL-XFEL Devices”, in *Proc. IPAC’18*, Vancouver, Canada, May 2018, paper WEPAL070.
- [5] L.S. Nadolski, “Between model and reality, Part II”, *CERN Accelerator School - Beam Diagnostics*, Dourdan, France, May 2008, CERN-2009-005, pp. 237-244.
- [6] International Workshops on Accelerator Alignment (IWAA), <http://www-conf.slac.stanford.edu/iwaa/>
- [7] Workshop on Ambient Ground Motion and Vibration Suppression for Low Emittance Storage Ring, <https://indico.ihep.ac.cn/event/7204/>

COMMISSIONING STATUS OF LINEAR IFMIF PROTOTYPE ACCELERATOR (LIPAc)

A. Kasugai*, T. Akagi, T. Ebisawa, Y. Hirata, R. Ichimiya, K. Kondo, S. Maebara, K. Sakamoto,
T. Shinya, M. Sugimoto, QST Rokkasho Fusion Institute, Rokkasho, Japan
J. Knaster, A. Marqueta, G. Pruneri, F. Scantamburlo
IFMIF/EVEDA Project Team, Rokkasho, Japan
P-Y. Beauvais, P. Cara, A. Jokinen, D. Gex, I. Moya, G. Phillips, H. Dzitko, R. Heidinger
F4E, Garching, Germany
P. Abbon, N. Bazin, B. Bolzon, N. Chauvin, S. Chel, R. Gobin, J. Marroncle, B. Renard
CEA/Saclay, Gif-sur-Yvette, France
L. Antoniazzi, L. Bellan, D. Bortolato, M. Comunian, E. Fagotti, F. Grespan, I. Kirpichev,
C. de la Morena, M. Montis, A. Palmieri, A. Pisent, INFN-LNL, Legnaro, Italy
C. Jimenez-Rey, P. Mendez, J. Molla, I. Podadera, D. Regidor, M. Weber
CIEMAT, Madrid, Spain

Abstract

Significant progress was obtained on the installation and commissioning of the Linear IFMIF Prototype Accelerator (LIPAc). On the injector experiment, the emittance of $0.2 \pi \text{mm}\cdot\text{mrad}$ has been demonstrated, which is well smaller than that of required value ($0.3 \pi \text{mm}\cdot\text{mrad}$). Eight sets of RF modules (175 MHz, 200 kW for each) were connected to the RFQ with 8 coaxial waveguides, and RF conditioning has been started. With a simultaneous power injection from 8 RF modules into the RFQ and careful conditioning, a required RF field for the 5 MeV D+ beam acceleration was obtained at short pulse. The pulse extension is underway toward the CW operation. The first H+ beam acceleration will be started in June 2018. After the H+ beam commissioning, D+ beam acceleration will be implemented aiming at 5 MeV 125 mA, 0.1% duty. In parallel, the preparation of SRF (superconducting Radio-Frequency linac), which accelerates the D+ beam up to 9 MeV, has proceeded.

INTRODUCTION

The International Fusion Materials Irradiation Facility (IFMIF) aims to provide an accelerator-based, D-Li neutron source to produce high energy neutrons at sufficient intensity and irradiation volume for DEMO reactor materials qualification. The IFMIF/EVEDA project, which is part of the Broader Approach (BA) agreement between Japan and EU, has the mission to work on the engineering design of IFMIF and to validate the main technological challenges [1, 2]. The LIPAc being developed in the IFMIF/EVEDA project has the objective to demonstrate 125 mA/CW deuterium ion beam acceleration up to 9 MeV and is composed of 10 major systems as shown in Figure 1. Especially, important main accelerator parts are an injector, a Radio Frequency Quadrupole Linac (RFQ) accelerator, and a first part of superconducting RF (SRF) Linac.

The LIPAc is under validation. The first accelerator component which allows the production of a 140 mA-100 deuteron beam has been already demonstrated the commissioning at Rokkasho showing promising performance. The validation of the second phase (100 keV to 5 MeV), so called RFQ acceleration phase, has been just started after the installation of RF system, RFQ, MEFT (Medium Energy Beam Transport), diagnostic plate (D- Plate) and low-power beam dump (LPBD). The third phase, so called final phase, will be the integrated commissioning of the LIPAc up to 9 MeV with its SRF, HEBT (High Energy Beam Transport) and high-power beam dump. The duration of the project has been recently extended by about 3 years up to March, 2020 what allows the completion of the commissioning and operation of the whole accelerator at the nominal 1 MW beam power.

INSTALLATION FOR THE RFQ EXPERIMENT

The major components installed in the accelerator vault, injector, RFQ, MEFT, DP and LPBD, are shown in Figure 2. Their positions and beam axis were carefully aligned using the laser tracker. The RF power is transmitted with coaxial RF lines connecting the 8-RF modules and the corresponding 8 RF couplers of the RFQ. Such a simultaneous power injection using 8 ports is a first trial for the RFQ and enables the beam acceleration experiment up to 5 MeV/130 mA. The duty cycle is limited to 0.1% because of the heat removal capacity of LPBD and interceptive diagnostic tool. The CW beam operation can be carried out after the high power beam dump is installed.

RFQ

The LIPAc RFQ is the longest one in the world and has 9.8 m length in total. It was manufactured in INFN, Italy and assembled up to tripartition of the whole cavity. After combining them to a single cavity in a temporary position in

* kasugai.atsushi@qst.go.jp

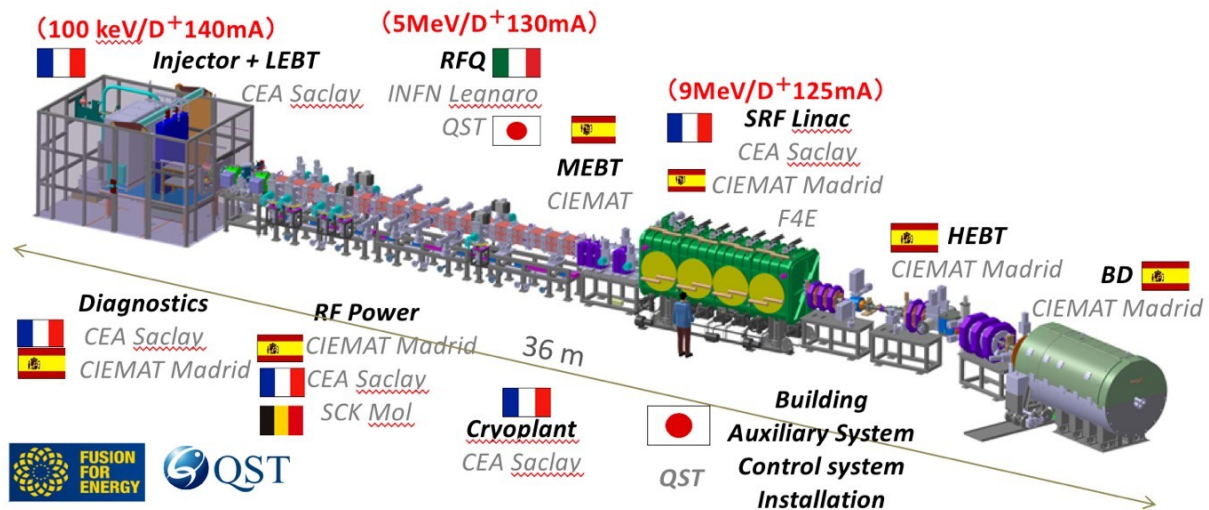


Figure 1: Configuration of LIPAc.

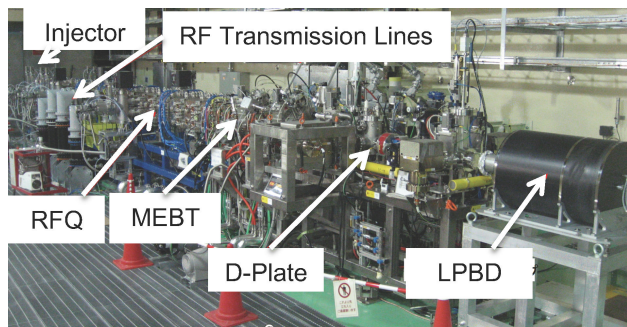


Figure 2: Accelerator components of IFMIF prototype accelerator.

the accelerator vault, the field and frequency tuning (the low power test) was conducted by means of the bead perturbation method as shown in Figure 3(a).

110 adjustable tuners were replaced with final tuners in 3 steps and all the test was completed 2016. After that, the vacuum equipment was assembled, and the baking of the cavity was done. The vacuum system check-out started, and finally the cryopumps were started [3]. The coaxial waveguides were connected and tested with control system [4] to RFQ in 2017 after the completion of the highpower test of the RF modules. All preparation for RFQ commissioning was completed in July 2017 as shown in Figure 3(b).

RF SYSTEM

The RF power system as shown in Figure 4 consists of eight RF chains amplifying RF at 175 MHz up to 200 kW in CW or pulse waveform. The RF output power of individual chain is injected into the RFQ cavity through RF couplers respectively. Each RF chain synchronizes to the master RF chain through 10 MHz distributed from the White Rabbit to LLRF of the eight chains. The input power to the RFQ cavity (forward power) and reflected power from the cavity are detected from the directional coupler. Using a feedback



Figure 3: Progress of RFQ installation from (a) April 2016 to (b) June 2017.

system, the forward power from seven slave RF chains follow the reference RF power from the master RF chain. This function is essential to the RFQ linac since the RF power into the cavity must be balanced and in-phase [5].

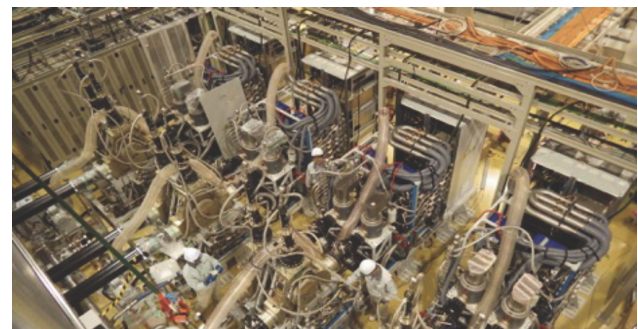


Figure 4: Installation of RF System.

BEAM INJECTOR

The injector is composed of ECR ion source, 100kV beam extraction electrodes system with the secondary electrons repeller at the exit of extractor and Low Energy Beam Transport (LEBT) line. The alignment and the precision of the gap distance of the electrodes are very important to achieve the optimal beam performance. The low emittance beam can be obtained at high current beam through the careful tuning of the injector components. Figure 5 shows an example of the experimental results, extraction voltage dependence on the emittance of the 100 keV pulsed D+ beam at the various extracted beam current, 155 mA, 165 mA and 175 mA. These emittances were measured after the first solenoid of LEBT, however the emittances at the RFQ entrance point were almost same with them, which was confirmed through the series of injector beam commissioning campaigns in 2015 and 2016.

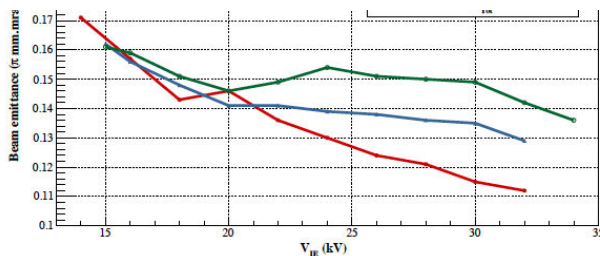


Figure 5: An example of injector beam performance: beam emittance vs. voltage of first extraction gap for D+ beam with energy 100 keV and various extracted beam current, 155, 165 and 175 mA (pulsed beam with 5% duty cycle and 2msec width).

RFQ COMMISSIONING

The commissioning of the individual RF chains was completed using the dummy load up to 200kW/CW in July 2017, and the RF conditioning has been started after the coaxial transmission lines were connected to the RFQ. A precise synchronization of the amplifiers phase and amplitude with an active feedback loop is realized by a fully-digitalized low level RF control unit combined with the “White Rabbit”. The RF injection with 8 chains synchronization succeeded first time and the RF conditioning activity has been started in October 2017. One of the milestones of the RF conditioning was to obtain the maximum vane voltage in the RFQ cavity 132 kV, which corresponds approximately to the required target value to accelerate D+ beam as shown in Figure 6. This was realized relatively smooth RF conditioning by adopt-

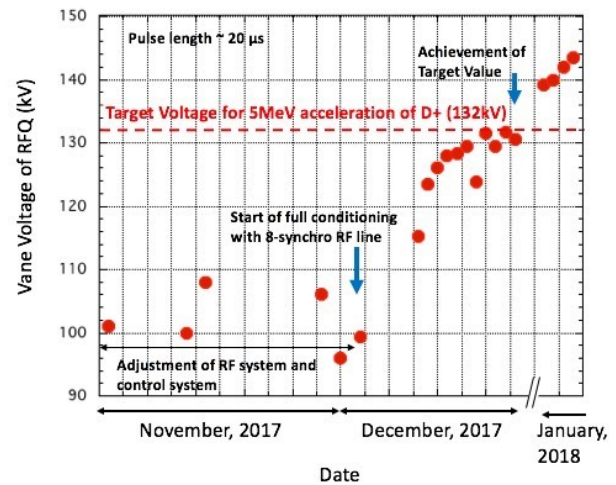


Figure 6: History of RF conditioning id RFQ up to target voltage for D+ acceleration.

ing an automatic rearming system of RF system when RF stops by multipactoring etc. The RFQ beam commissioning will be started firstly from June 2018 using the H+ beam to avoid the unnecessary activation and, after the enough H+ beam testing, the D+ beam acceleration up to 5 MeV will be implemented from the end of 2018.

ACKNOWLEDGMENTS

One of the authors (A. K.) would like to acknowledge Dr. Y. Shimosaki for supporting this presentation.

REFERENCES

- [1] J. Knaster *et al.*, “IFMIF, the European–Japanese efforts under the Broader Approach agreement towards a Li(d,xn) neutron source: Current status and future”, *Nucl. Mater. Energy*, vol. 9, pp. 46–54, (2016), doi:10.1016/j.nme.2016.04.012
- [2] J. Knaster, A. Moeslang, and T. Muroga, *Nature Physics*, vol. 12, pp. 424–434, (2016), doi:10.1038/nphys3735
- [3] K. Kondo *et al.*, “Linear IFMIF Prototype Accelerator (LI-PAC): Installation activities for Phase-B beam commissioning in Rokkasho”, *Nucl. Mater. Energy*, vol. 15, pp. 195–202, (2018), 10.1016/j.nme.2018.04.011
- [4] Y. Hirata *et al.*, *Nucl. Mater. Energy* to be accepted.
- [5] T. Shinya *et al.*, “Status of the RFQ linac installation and conditioning of the Linear IFMIF Prototype Accelerator”, *Nucl. Mater. Energy*, vol. 15, pp. 143–147, (2018), doi:10.1016/j.nme.2018.04.001

REVISITING THE LONGITUDINAL 90 DEGREE LIMIT FOR SUPERCONDUCTING LINEAR ACCELERATORS

Ingo Hofmann*, ^{1, 2}, Technische Universität Darmstadt, Darmstadt, Germany

¹also at GSI Helmholtzzentrum für Schwerionenforschung GmbH, Darmstadt, Germany

²also at Goethe Universität, Frankfurt am Main, Germany

Abstract

In the design of high-intensity linear accelerators one of the generally adopted criteria is not to exceed a zero-current phase advance per focusing period of 90° in order to avoid the space charge driven envelope instability, or a coinciding fourth order space charge structure resonance. Recently it was claimed that in certain structures such a constraint is not always necessary in the longitudinal plane (I. Hofmann and O. Boine-Frankenheim, Phys. Rev. Lett. 118, 2017). In FODO focusing structures with an rf gap per drift, for example, the transverse focusing period only induces a very weak (negligible) space charge force in the longitudinal plane. Hence, the longitudinal 90° stopband is practically irrelevant and values of $k_{0,z}$ - as usual defined per transverse focusing period - significantly above 90° are possible in such structures, which grants additional design freedom. It is also shown that the latter is theoretically limited by a novel type of instability, the coupled envelope “sum mode”, which can be avoided by observing $k_{0,z} + k_{0,x,y} < 180^\circ$. Application of this finding is primarily for superconducting linear accelerators with high accelerating gradients.

INTRODUCTION

The existence of a stopband at 90° phase advance has resulted in the definition of a well-known design limit for high intensity accelerators. After numerous theoretical studies (see, for example, Ref. [1]) and an early transport experiment [2] the first experimental study confirming the existence of such a 90° stopband in the transverse plane for an operational high-current linac was reported in Ref. [3]. This experiment also gave evidence of a fourth order space charge structural resonance in this stopband rather than the traditionally expected envelope instability. For a detailed theoretical discussion of the competing effects of this fourth order structural resonance with the envelope instability in the common 90° stopband see Ref. [4]; further details of the correlation with the upper respectively lower edge of the stopband are discussed in Ref. [5].

The significance of the *transverse* 90° stopband as linac design limitation is unquestioned. However, a corresponding longitudinal stopband - traditionally assumed at $k_{0,z} \approx 90^\circ$ - has been assumed as given. Recently the need for a re-examination of this assumed limit was suggested in Ref. [6] for FODO-type lattices with more than one rf gap per transverse focusing period.

REVIEW OF THE LONGITUDINAL 90° STOPBAND

We first review the 90° longitudinal stopband for a periodic solenoid lattice with an rf gap between solenoids (assuming, for simplicity, no acceleration), where the longitudinal cell definition coincides with the transverse one as shown in Fig. 1.

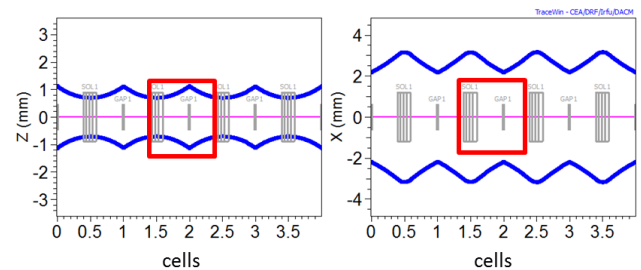


Figure 1: Layout of solenoid lattice example.

We use the TRACEWIN [7] code and assume an ellipsoidal bunch with equal emittances in x, y, z and Gaussian distribution (cut at 3σ) in a lattice with $k_{0,z} = 120^\circ$ ($k_{0,x,y} = 60^\circ$) and a space charge depressed $k_z = 76^\circ$. Results for the rms emittances and self-consistent phase advances are shown in Fig. 2. There is a clear evidence of the 90° longitudinal stopband due to the fact that the longitudinal period is identical to the transverse one.

As expected, there is a significant rms emittance growth, which resembles qualitatively the behaviour in the transverse stopband [4]. The rms emittances show an initial rise of about 40%, followed by a plateau and a second phase with large growth of over 200%. The phase space plots confirm that the initial rise is due to a fourth order space charge structure resonance, and - after a mode switch on the plateau - a following envelope instability. Note that the strong envelope instability also manifests itself in oscillations of the rms phase advance plotted in the centre graph of Fig. 2.

The complete stopband is shown in Fig. 3. For comparison we also show the stopband for $k_{0,z} = 100^\circ$, which is considerably smaller due to the lower current needed for resonance. Both stopbands start - similar to the transverse case - for $k_z < 90^\circ$ and lead to significant rms emittance growth. Inspection of phase space plots allows to distinguish between two emittance growth regimes: the initial one up to the plateau, which is ascribed to the fourth order space charge resonance, followed by the envelope instability regime. It is thus possible to distinguish in Fig. 3 between growth attributed to the fourth order structure resonance and the total growth by the additional envelope instability

* i.hofmann@gsi.de

Content from this work may be used under the terms of the CC BY 3.0 licence (© 2018). Any distribution of this work must maintain attribution to the author(s), title of the work, publisher, and DOI.

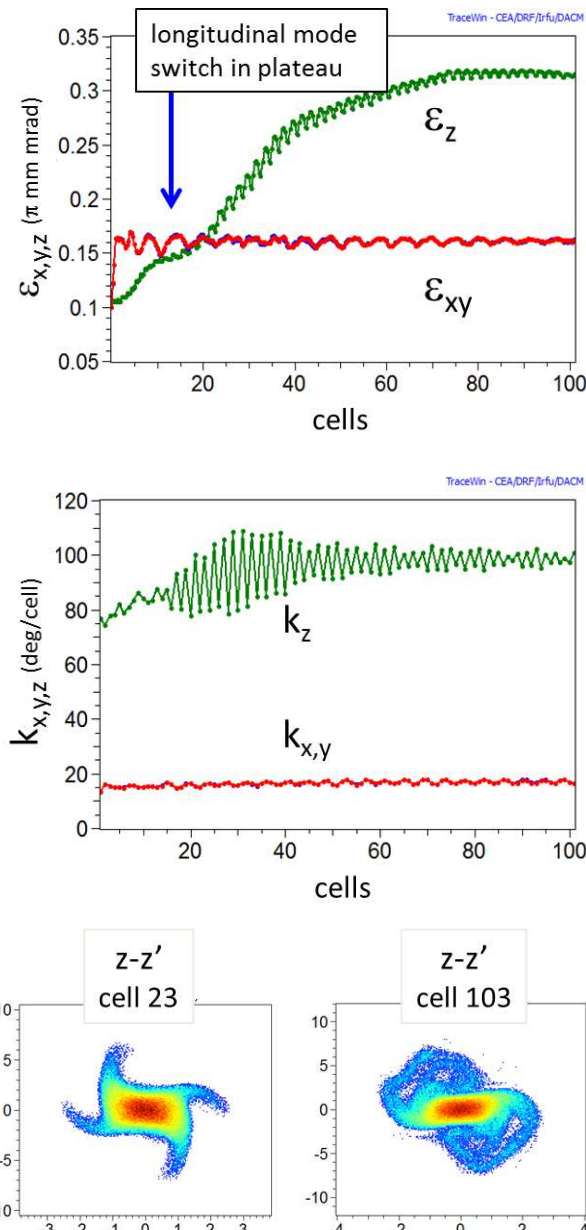


Figure 2: Rms emittances (top graph) and dynamical phase advance (centre graph) for solenoid lattice with $k_{0,z} = 120^\circ$, $k_z = 76^\circ$. Bottom graph: Longitudinal phase space at cells 23 (left) and 103 (right)).

effect. Note that Fig. 2 suggests that the envelope growth is retarded due to the exponential nature of growth from the initial very small mismatch; obviously the envelope growth occurs earlier, if a larger initial mismatch is assumed.

FODO LATTICE WITH RF GAPS

The result differs significantly if the periodic solenoid lattice is replaced by a FODO lattice with rf gaps in each drift as indicated in the example shown in Fig. 4.

The periodicity of the transverse focusing lattice, including the space charge force from the matched envelope with the same periodicity, determines the effective transverse force periodicity. It is traditionally assumed that due to

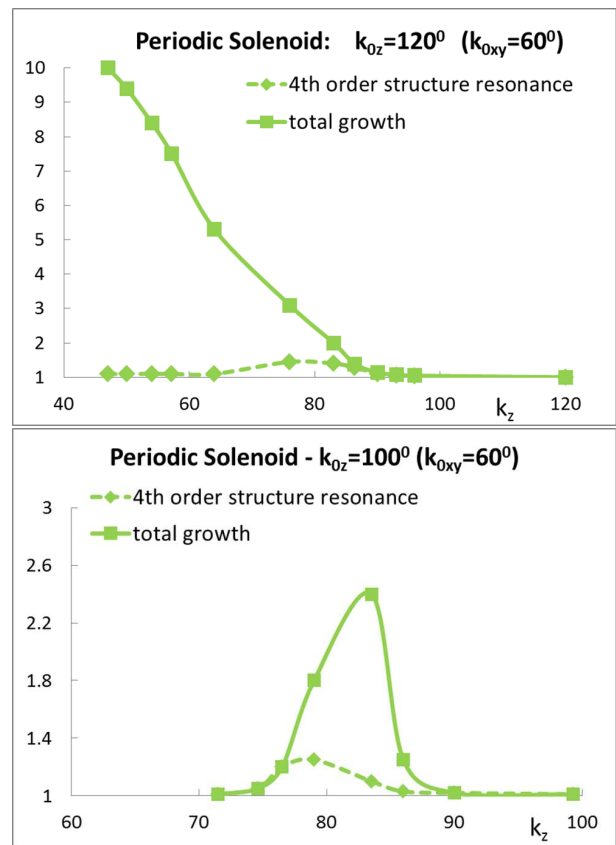


Figure 3: Complete stopband for solenoid lattice with $k_{0,z} = 120^\circ$ (top graph) and $k_{0,z} = 100^\circ$ (bottom graph).

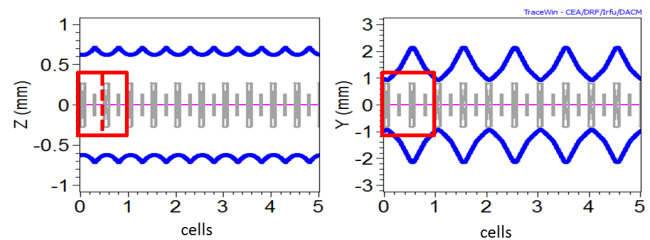


Figure 4: Example of FODO lattice with rf gaps leading to effectively halved longitudinal periods.

space charge coupling the same periodicity also applies to the longitudinal degree of freedom. We argue, however, that in the absence of space charge the relevant longitudinal period is obviously the rf period, which is half the transverse focusing period in a lattice of the kind in Fig. 4. Including space charge of a *well-matched* beam this is still approximately valid: the longitudinal space charge force of a uniform beam depends only on the transverse cross sectional area [8]. Hence, it can be assumed that it is practically identical in half-cells with focusing or with defocusing quadrupoles, and that this is also valid approximately for non-uniform beams. Thus, the effective longitudinal force periodicity even with space charge can be assumed to be given by the rf period, over which length the effective phase advance is only half as large as over the transverse focusing period.

In Fig. 5 we show the simulation results for this lattice and the same parameters as in the solenoid example ($k_{0,z} = 120^\circ$) and confirm absence of any emittance growth effect, hence no 90° stopband. Note that the initial jump of rms emittances is due to “nonlinear field energy” effects [8]. Actually, this

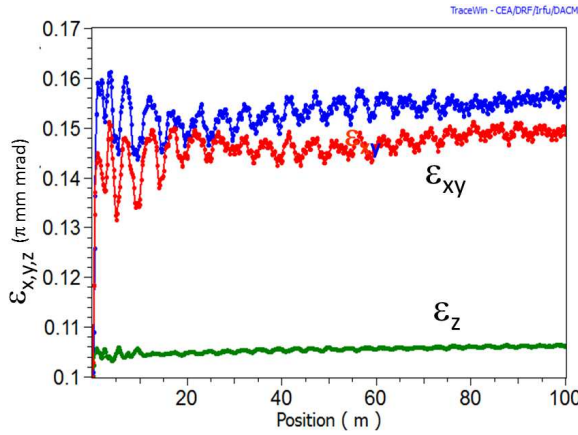


Figure 5: Rms emittances for FODO and rf gap lattice with $k_{0,z} = 120^\circ$, $k_z = 76^\circ$.

stopband has migrated to twice as large values of $k_{0,z}$ and k_z as a consequence of the halved longitudinal period. We note that the same migration also includes the accompanying structural fourth order space charge resonance, which always accompanies the envelope mode [4].

SUM ENVELOPE INSTABILITY LIMIT

The next question is whether the absence of the 90° stopband means complete freedom of choosing $k_{0,z} > 90^\circ$. This is not the case due to the existence of a “sum envelope” criterion as was shown in Ref. [6].

In this context it is first helpful to remind that the conventional 90° envelope instability is a 1:2 parametric resonance, where the envelope eigenmode oscillates at half the frequency of the periodically varying focusing (including space charge). One can thus approximate the parametric envelope instability condition - for example in the xy -planes - by using a smooth approximation formula, which describes approximately the shift of the centre of the stopband [9]:

$$\omega \equiv 2k_{0,xy} - \Delta k_{2,coh} = \frac{1}{2}360^\circ. \quad (1)$$

Here ω stands for the second order envelope mode “frequency” ($= 2k_{0,xy}$ for vanishing space charge) and $\Delta k_{2,coh}$ (> 0) for its shift due to the coherent action of space charge. The factor $\frac{1}{2}$ is characteristic for the parametric nature and absent if lattice driven resonances were considered (all in units of degrees per focusing lattice period).

Analogous to the conventional 90° envelope instability in a single plane the presence of space charge coupling between different degrees of freedom can lead to a “sum envelope” instability between the longitudinal and transverse planes as described in Ref. [6]. The resulting *sum envelope* condition

can be written in the following way

$$\omega \equiv k_{0,z} + k_{0,x} - \Delta k_{sum,coh} = \frac{1}{2}360^\circ, \quad (2)$$

where $\Delta k_{sum,coh}$ is a coherent sum specific tune shift comparable in size with the average value of the longitudinal and transverse incoherent space charge tune shifts.

This is demonstrated in Fig. 6 for a Gaussian beam with $k_{0,z} = 120^\circ$ ($k_z = 92^\circ$) and $k_{0,xy} = 90^\circ$ in the above described FODO lattice with initially equal emittances. Note that the actual emittance growth is relatively steep - after a phase of exponential growth from the small initial noise level. The phase space plots indicate the second order nature of the instability.

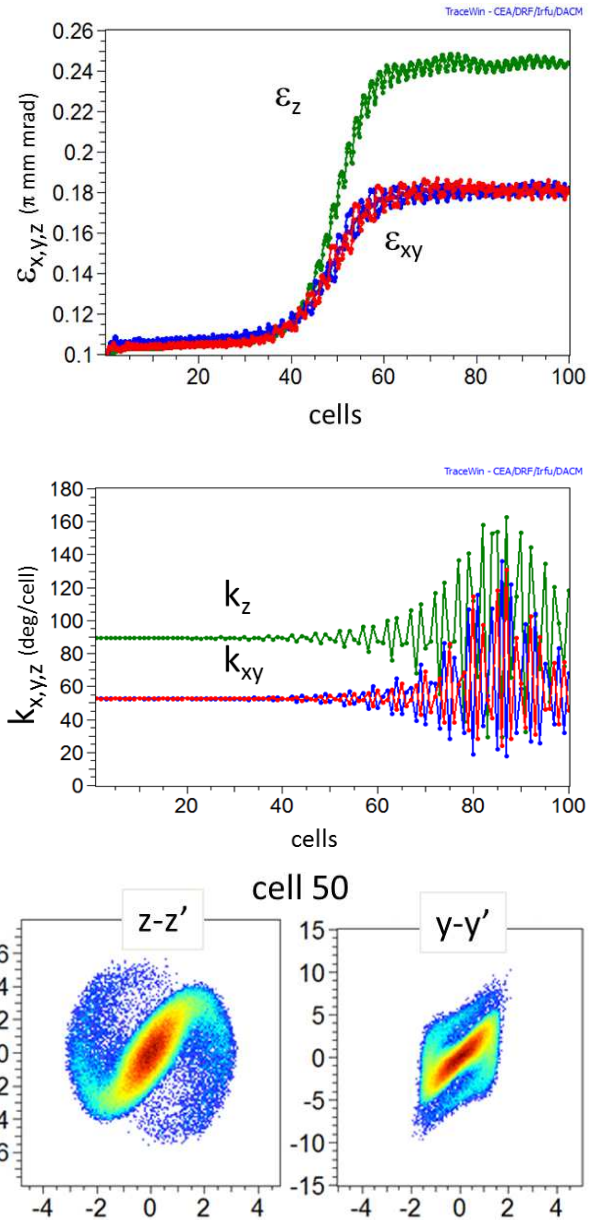


Figure 6: Sum envelope instability in FODO and rf gap lattice with $k_{0,z} = 120^\circ$ and $k_{0,xy} = 90^\circ$ showing rms emittances, phase advances and phase space plots.

Content from this work may be used under the terms of the CC BY 3.0 licence (© 2018). Any distribution of this work must maintain attribution to the author(s), title of the work, publisher, and DOI.

A characteristic feature is the synchronous development of emittances and envelopes in the coupled planes. Note that z couples with both, x and y , if phase advances as well as emittances in x and y are close to each other as is the case here. Thus, the growth of ϵ_z is close to $\epsilon_x + \epsilon_y$.

For completeness we mention that the coherent *sum parametric* mode discussed here is essentially distinct from the well-known *single particle sum resonances* in a coupled lattice with skew quadrupoles. In the latter the coupling is external and not by a collective space charge force, besides the absence of the 1:2 parametric feature expressed by the factor $\frac{1}{2}$ in Eq. (2) [10].

OVERVIEW CHART

Our findings are summarized in the schematic chart of Fig. 7 valid for a lattice with halved longitudinal period as in Fig. 4. Indicated are stopbands of second (envelope) and third order parametric effects – structural resonances (see also Refs. [4, 9]) – as well as the resulting extended design region. The positive diagonal is indicating the “main 2:2 resonance” responsible for emittance exchange.

The $xy - z$ sum envelope instability driven by the transverse lattice periodicity is described by the negative diagonal following the parametric sum rule of Eq. (2). Note that all stopbands are schematically shifted (to larger values of $k_{0,z}$) to take into account the finite space charge effects, and assuming a moderate (fixed) value of space charge tune depression. The transverse envelope instability (combined with the fourth order space charge structure resonance) is associated with 90° following Eq. (1). For the longitudinal plane the usually assumed limit of $k_{0,z} < 90^\circ$ is replaced by the more extended triangular region extending up to $k_{0,z} < 180^\circ$. Likewise, the longitudinal fourth order space charge structure resonance competing with the envelope instability in the same stopband undergoes the same movement.

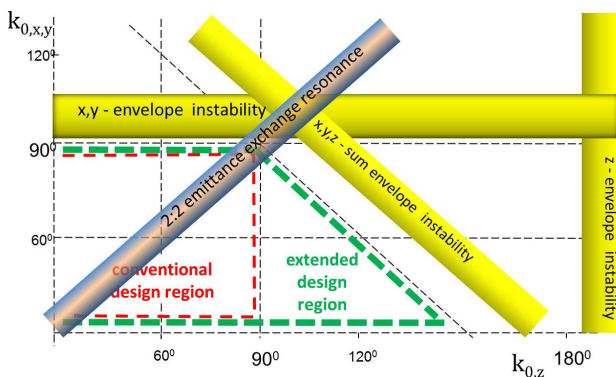


Figure 7: Schematic stability chart in the longitudinal-transverse plane for a lattice with two rf gaps per transverse focusing period, showing the extended design region (dashed green border).

SUMMARY

In summary, the effectively shortened period in the longitudinal direction for FODO-type lattices helps to enlarge

significantly the usable area of longitudinal phase advances beyond 90° . It is shown that a new upper limit exists, which is given by the sum envelope instability stopband. In practical terms the sum envelope limit can be relaxed if the transverse phase advance is lowered. Detailed studies are needed to verify to what extent specific lattices, where the strict longitudinal periodicity is significantly interrupted, can still benefit from the enlargement of the usable area beyond the longitudinal 90° . Such deviations from strict periodicity could be, for example, due to missing cavities between cryomodules. Beam dynamics risks as well as safety of superconducting cavity operation must be balanced against desirable hardware and cost savings. Furthermore, it appears that in many cases replacing quadrupole focussing by solenoids - for the sake of creating shorter longitudinal periods - is no longer necessary.

REFERENCES

- [1] J. Struckmeier and M. Reiser, “Theoretical studies of envelope oscillations and instabilities of mismatched intense charged-particle beams in periodic focusing channels”, *Part. Accel.*, vol. 14, pp. 227–260, 1984.
- [2] M. G. Tiefenback and D. Keefe, “Measurements of Stability Limits for a Space-Charge-Dominated Ion Beam in a Long a. G. Transport Channel”, *IEEE Trans. Nucl. Sci.*, vol. 32, pp. 2483–2485, 1985, doi:10.1109/TNS.1985.4333954
- [3] L. Groening *et al.*, “Experimental Evidence of the 90° Stop Band in the GSI UNILAC”, *Phys. Rev. Lett.*, vol. 102, pp.234801, 2009, doi:10.1103/PhysRevLett.102.234801
- [4] I. Hofmann and O. Boine-Frankenheim, “Space-Charge Structural Instabilities and Resonances in High-Intensity Beams”, *Phys. Rev. Lett.*, vol. 115, pp. 204802, 2015, doi:10.1103/PhysRevLett.115.204802
- [5] I. Hofmann, “Coherent Parametric Instabilities”, in *Space Charge Physics for Particle Accelerators*, Springer, New York, 2017, chapter 7, pp. 81–113.
- [6] I. Hofmann and O. Boine-Frankenheim, “Dispersion-Induced Beam Instability in Circular Accelerators”, *Phys. Rev. Lett.*, vol. 118, pp. 154801, 2017, doi:10.1103/PhysRevLett.118.154801
- [7] D. Uriot and N. Pichoff, “Status of TraceWin Code”, in *Proc. IPAC’15*, Richmond, VA, USA, May 2015, pp. 92–94, doi:10.18429/JACoW-IPAC2015-MOPWA008
- [8] Thomas P. Wangler, *RF Linear Accelerators*, Second Edition, Wiley-VCH, 2008, doi:10.1002/9783527623426
- [9] I. Hofmann and O. Boine-Frankenheim, “Parametric instabilities in 3D periodically focused beams with space charge”, *Phys. Rev. Accel. Beams*, vol. 20, pp. 014202, 2017, doi:10.1103/PhysRevAccelBeams.20.014202
- [10] O. Boine-Frankenheim, I. Hofmann, and J. Struckmeier, “Parametric sum envelope instability of periodically focused intense beams”, *Physics of Plasmas*, vol. 23, no. 9, pp. 090705, 2016, doi:10.1063/1.4963851

HIGH-INTENSITY BEAM DYNAMICS SIMULATION OF THE IFMIF-LIKE ACCELERATORS

Seok Ho Moon and Moses Chung, UNIST, Ulsan 44919, Republic of Korea

Abstract

The IFMIF (International Fusion Material Irradiation Facility) project is being considered to build fusion material test facility. The IFMIF will use two accelerators to generate high energy neutrons. However, the IFMIF accelerators have been designed to have much higher beam power and beam current than the existing accelerators, so space charge effect is very strong. This raises big concerns about beam loss and beam transport stability, thus detailed high-intensity beam dynamics study of the IFMIF-like accelerators is indispensable. This research aims to perform source to target simulation of the IFMIF-like accelerator. The simulation has been carried out by two different kinds of simulation codes because the IFMIF accelerator has distinctive features. One is TRACEWIN simulation code which was used in IFMIF initial design. The other is WARP 3D PIC code which can precisely calculate space charge effects.

INTRODUCTION

The IFMIF accelerator accelerates D^+ with 125 mA beam current. The high beam current makes strong space charge effect and it derives serious concern about beam transport stability. Therefore, beam dynamic study must be handled carefully. We do simulation for LEBT and MEBT of IFMIF-like beam line. Both LEBT and MEBT simulations are done by WARP and TRACEWIN simulation codes.

Simulation Code

Two kinds of simulation codes are used in simulation. One is WARP which was developed by LBNL. Calculation algorithm of the WARP is PIC (Particle in Cell). Therefore, it can precisely simulate space charge effect. The other one is TRACEWIN which was made by CEA – Saclay. It uses second order momentum and macroparticle in simulation.

Low Energy Beam Transport

Basically, LEBT consists of ECR ion source, two solenoids and RFQ injection cone. ECR ion source makes D^+ beam with 0.064π mm.mrad emittance and 100 keV beam energy.

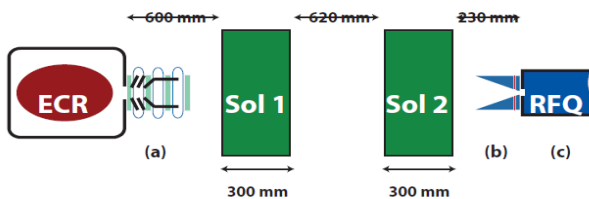


Figure 1: Schematic of IFMIF LEBT [1].

Figure 1 shows the schematic of IFMIF LEBT. In more detail, beam pipe radius is 80 mm and becomes smaller at RFQ injection cone. Radius of RFQ injection cone is 35 mm at entrance and 12 mm at exit. Magnetic field strength of solenoid 1 is 0.37 T and 0.47 T for solenoid 2. LEBT aims to make a beam with 0.233π mm.mrad emittance at the exit of LEBT. To achieve the goal, IFMIF LEBT uses SCC (Space Charge Compensation).

Space Charge Compensation

Space charge compensation which will be written as SCC in this paper is one of methods to reduce space charge of beam. It uses residual gas to reduce space charge effect.

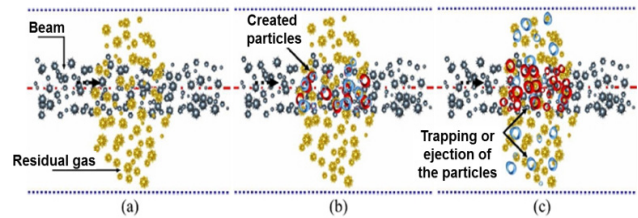


Figure 2: Outline of Space Charge Compensation [2].

Figure 2 shows the outline of space charge compensation. As shown in Fig. 2, beam particles interact with residual gas and they make ions. Ions which have the same charge type as the beam are propelled from beam, whereas ions which have different charge type with the beam are trapped to beam. The trapped ions (or electrons) reduce space charge of the beam. SCC needs time for stabilization which is also called as neutralization time written as Eq. (1):

$$\tau_n = \frac{1}{n_g \sigma_i v_b}, \quad (1)$$

Where n_g is gas density in beam line, σ_i is ionization cross section of beam-residual gas interaction, and v_b is velocity of beam particle. In this study, neutralization time is 6 μ s.

Medium Energy Beam Transport

MEBT aims to manipulate beam before beam goes into SRF (Super Conducting Radio Frequency) beam line.

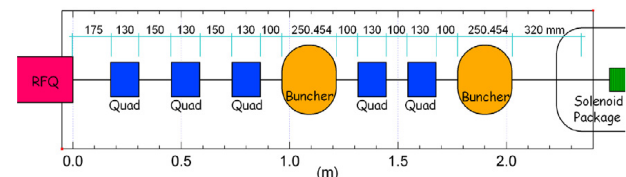


Figure 3: Schematic of IFMIF MEBT [3]

Content from this work may be used under the terms of the CC BY 3.0 licence (© 2018). Any distribution of this work must maintain attribution to the author(s), title of the work, publisher, and DOI.

As shown in Fig. 3, the length of MEBT is about 2 m. It consists of triplet, doublet, and two bunchers. In the simulation, magnetic gradients of quadrupole 1, 2, and 3 are 25 T/m, and 20.5 T/m for quadrupole 4 and 20 T/m for quadrupole 5. Buncher frequency is 175 MHz and maximum E_0LT value for buncher is 350 kV.

LEBT SIMULATION

LEBT simulation has been done for 2 different cases. One is ‘Without SCC case’ and the other is ‘With SCC case’. Those two cases are simulated in both WARP and TRACEWIN.

Table 1: Initial Beam Parameters (LEBT) [1]

Beam Parameter	Initial Value
Beam Current	125 mA
Beam Energy	100 keV
Normalized Emittance	0.064 π .mm.mrad
Twiss Parameter	α :0.8, β : 2.0

Table.1 is about initial beam parameters for LEBT simulation. Beam parameters are those of IFMIF except the Twiss parameters.

Without SCC

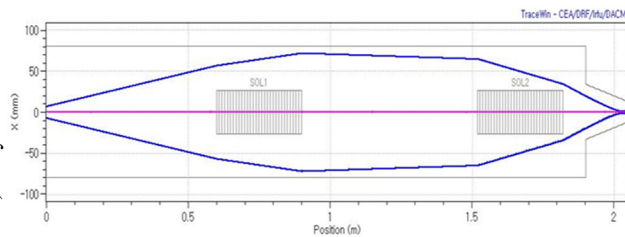


Figure 4: Z-X Plot from TRACEWIN (Without SCC).

As shown in Fig. 4, maximum envelope radius is almost 80 mm and maximum rms radius is around 35 mm. Also normalized emittance is 0.2796 π mm.mrad at the exit of LEBT.

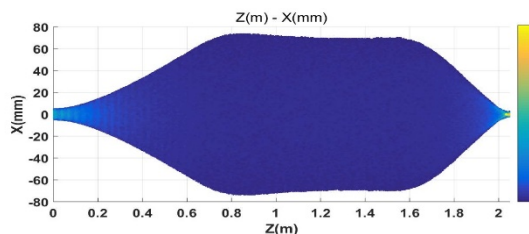


Figure 5: Z-X Plot from WARP (Without SCC).

Figure 5 is plot for WARP simulation. WARP simulation shows similar result with TRACEWIN simulation. Maximum envelope radius is almost 80 mm and maximum rms radius is around 40 mm. Normalized emittance is 0.3697 π mm.mrad. It is a little bit bigger than TRACEWIN result.

In both WARP and TRACEWIN simulations, calculated normalized emittances are much higher than our target

value. Also, maximum beam envelope is around 80mm, so beam loss is concerned in real experiment.

With SCC

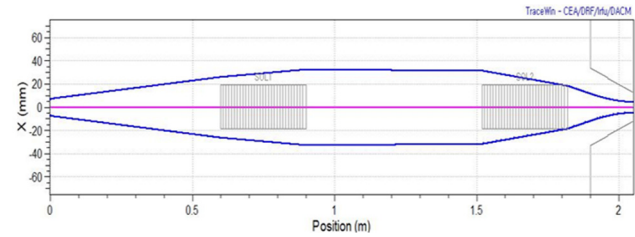


Figure 6: Z-X Plot from TRACEWIN (With SCC).

TRACEWIN simulation is done with compensation factor of 0.75. Maximum beam radius is around 35 mm. Maximum rms radius is around 16 mm and normalized emittance at the exit of LEBT is 0.1228 π mm.mrad which satisfies the target value.

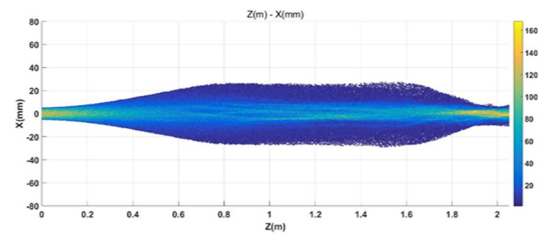


Figure 7: Z-X Plot from WARP (With SCC).

WARP simulation doesn’t use compensation factor, but instead it uses full atomic processes. Therefore, Figures 6 and 7 show a little difference. Maximum beam radius in WARP simulation is around 30 mm which is smaller than TRACEWIN value. From the WARP, maximum rms radius is around 10 mm and normalized emittance is 0.1763 π mm.mrad at the exit of LEBT. However, instability was observed in the WARP simulation

Instability Issue

Only WARP supports full atomic processes and it makes some difference between TRACEWIN and WARP simulation results. One of the difference is instability. Instability was observed only in WARP simulation.

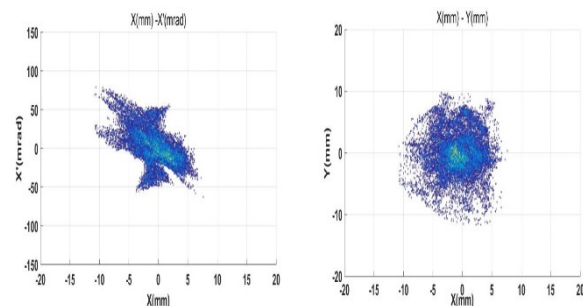


Figure 8: X-X’ (left) and X-Y (right) at LEBT exit.

In Fig. 8, tail shape has appeared, and beam shape collapsed. The cause of instability is not clear yet, but we suspect that it is a kind of two stream instability.

MEBT SIMULATION

Table 2: Initial Beam Parameters (MEBT) [4]

Beam Parameter	Initial Value
Beam Current	125 mA
Beam Energy	4.98 MeV
longitudinal	0.3 π .mm.mrad
Emittance	
Twiss Paramter	αX : -1.95, βX : 0.37 αY : 1.5, βY : 0.355

Table.2 is about initial beam parameters of MEBT simulation. Beam parameters for MEBT simulation are those of IFMIF except the Twiss parameter. Twiss parameters are optimized values obtained from our simulation.

Simulation Results

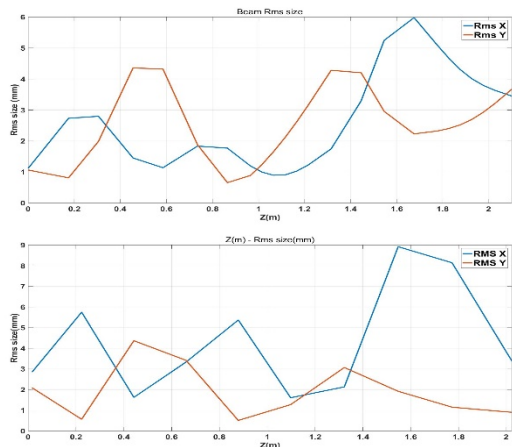


Figure 9: RMS X, Y (top: TRACWIN, bottom: WARP).

Figure 9 shows RMS radius history in TRACEWIN and WARP. Tendency of TRACEWIN and WARP is similar for rms x value. At MEBT exit, rms x value is 8 mm at TRACEWIN and 7.5 mm at WARP. However, rms y value becomes different after second buncher. WARP roughly supports RF lattice so we use time varying electric field in WARP simulation instead, which seems to make such difference. Optimization is one of the future plans.

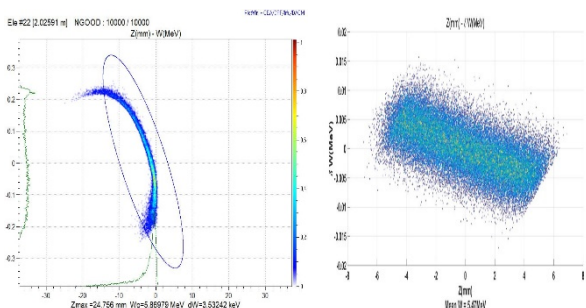


Figure 10: Z-Energy (left: TRACEWIN, right: WARP).

Buncher gives kick to beam, in such way that particles at tail of the bunch become faster so it makes velocity bunching. At MEBT exit rms z value is around 3 mm in both TRACEWIN and WARP. However, as we can see in Fig. 10, phase diagrams are different between two codes, so further optimization and comparison will be done in future.

Peak Current Issue

Average beam current of IFMIF accelerator is 125 mA and operation type is CW. After RFQ, continuous beam becomes bunched and the peak current will be higher than 125mA. Therefore, we do simulation with higher current for MEBT simulation.

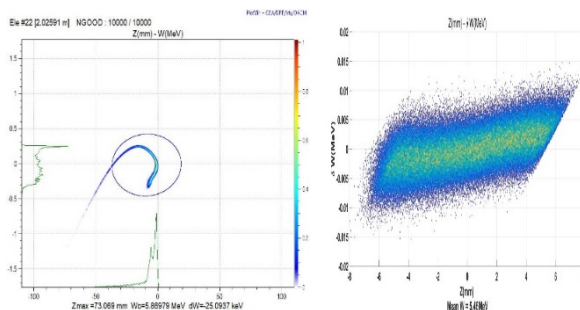


Figure 11: Z- Energy with 375mA peak current (left: TRACEWIN, right: WARP).

The simulation is done with 375 mA peak current case. As shown in Fig. 11, the buncher fails to make velocity bunching because of the stronger longitudinal space charge. Bunch length become larger even we use buncher to suppress bunch length growth.

CONCLUSION & FUTURE PLAN

Space Charge Compensation is an essential tool in IFMIF LEBT beam line. If we don't use SCC in IFMIF LEBT, serious beam loss may occur. Furthermore, without SCC, normalized emittance is higher than target value. We can achieve the normalized emittance goal only when we use SCC.

MEBT works well for the nominal beam conditions but if peak current becomes higher, it doesn't work well. The simulation case presented here is one of the extreme cases; nonetheless we note bunchers of the MEBT need to be designed with margin.

Instability has been observed in the LEBT WARP simulation. Finding the cause of the instability or optimization of the LEBT WARP simulation will be carried out as future works.

In MEBT simulation, different features exist between TRACEWIN and WARP results. It is likely caused by RF lattice setting in the WARP simulation. It should also be optimized in the future.

REFERENCES

- [1] N. Chauvin, O.Delferriere, R.Duperrier, R.Gobin, P.A.P. Nghiem and D. Uriot, “Final Design of the IFMIF – EVEDA Low Energy Beam Transport Line”, in *Proc. PAC’09*, Vancouver, BC, Canada, 2009, paper TH5PFP004, pp. 3190-3192.
- [2] N. Chauvin, “Space-Charge Effect”, Oct. 2014, p.12, DOI:10.5170/CERN-2013-007.63
- [3] I. Podadera, J. Calvo, J.M. Carmona, A.Ibarra, D. Iglesias, A.Lara, C. Oliver and F. Toral, “The Medium Energy Beam Transport Line (MEBT) of IFMIF/EVEDA LIPAC”, in *Proc. IPAC’11*, San Sebastian, Spain, 2011, paper WEPS058, p. 2658.
- [4] M. Comunian, A. Pisent, E. Fagotti and P.A. Posocco, “Beam Dynamics of the IFMIF-EVEDA RFQ”, in *Proc. EPAC’08*, Genoa, Italy, 2008, paper THPP075, pp 3536-3538.

INFLUENCE OF THE CAVITY FIELD FLATNESS AND EFFECT OF THE PHASE REFERENCE LINE ERRORS ON THE BEAM DYNAMICS OF THE ESS LINAC

R. De Prisco*, Lund University, Lund, Sweden

R. Zeng, ESS, Lund, Sweden

K. Czuba, T. Leśniak, R. Papis, D. Sikora and M. Żukociński, ISE, Warsaw University of Technology

Abstract

The particle longitudinal dynamics is affected by errors on the phase and amplitude of the electro-magnetic field in each cavity that cause emittance growth, beam degradation and losses. One of the causes of the phase error is the change of the ambient temperature in the LINAC tunnel, in the stub and in the klystron gallery that induces a phase drift of the signal travelling through the cables and radio frequency components. The field flatness error of each multiple cell cavity is caused by volume perturbation, cell to cell coupling, tuner penetration, etc. In this paper the influences of these two types of errors on the beam dynamics are studied and tolerances for keeping beam quality within acceptable limits are determined.

INTRODUCTION

The European Spallation Source, ESS, is designed to deliver 5 MW proton beam power on the target while keeping the beam induced losses below 1 W/m throughout the LINAC. This implies the need of accurate models of the accelerating cavities and of the focusing structures to correctly describe the beam dynamics: *only an accurate beam dynamics can allow the calculation of a reliable loss map.*

The use of a simplistic multi-cell cavity model can lead to a wrong estimation of the loss pattern along the accelerator: losses in the normal conducting section, due to a simplistic model, can mask dangerous losses in the high energy part of the LINAC. Vice versa losses in the high energy sections, due to a simplistic model, can lead to an unjustified reductions of the tolerances and, so, to a higher cost. In addition we want to underline that an accurate model of the multi-cell cavities becomes extremely important when one wants to define the tolerances for the sub-systems, as the Low Level RF, LLRF, and the Phase Reference Line, PRL, that induce, usually, errors one order of magnitude smaller than the *static* [1] ones.

In this paper:

- we present a *new* model to calculate the amplitude errors of the accelerating field in a multi-cell cavity: errors are applied on the geometrical parameters of the cavity; then the accelerating field is calculated solving the Maxwell equations over all the cavity;
- we underline the differences between the two models repeating the same error study two times, changing

only the way to calculate the accelerating field within the Drift Tube Linac, DTL, and looking at the beam dynamics parameters at the end of the high- β cavities;

- we use the new model to introduce also the flatness errors in the Super Conducting, SC, cavities in order to estimate an acceptable tolerance of their field flatness; these errors were never introduced in all the previous studies;
- we look at the effect of the LLRF phase and amplitude errors and at the Reference Line, RL, phase error errors using the new multi-cell cavity model for all the cavities present in the ESS LINAC.

THE MULTI-CAVITY MODEL

Let consider a generic cavity of 3 cells, shown in Fig. 1.

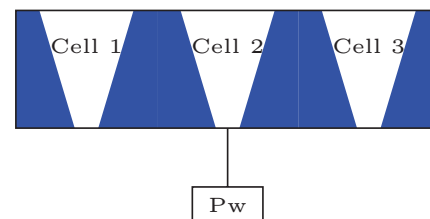


Figure 1: Multi-cell cavity of 3 cells.

It is important to underline that a mechanical error in a cell influences the accelerating field, E_0 , in *all* the cells of the cavity and not only in the cell where the error is located [2].

In the previous error studies [3] [4] the cells of the multi-cell cavities were modeled as a sequence of independent gaps, as shown in Fig. 2, and the errors were applied directly, cell by cell, on the amplitude of the accelerating field, considered a random variable. From now we call this model *old* model.

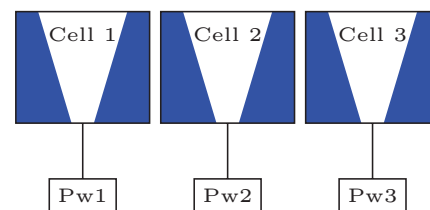


Figure 2: Multi-cell cavity as sequence of independent gaps.

Many particle tracking codes describe all the cells in the same cavity as a sequence of independent one-cell cavities

* renato.deprisco@ess.se

Content from this work may be used under the terms of the CC BY 3.0 licence (© 2018). Any distribution of this work must maintain attribution to the author(s), title of the work, publisher, and DOI.

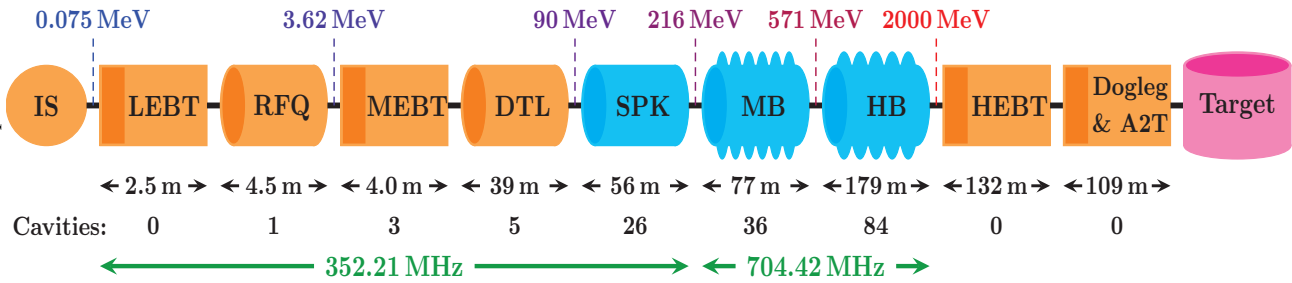


Figure 3: ESS LINAC layout. The beam energy, in MeV, at some locations, is set out above the layout. The length of each section, in m, is set out in the first line below the layout. The number of cavities of each section is set out in the second line below the layout. The operating frequency (green color) of each section is set out in the third line below the layout.

(or gaps). It is up to the user to make sure that the accelerating field of a sequence of independent gaps, that represents a cavity, is a solution of the Maxwell equations within the same cavity.

In this paper, instead, an iterative procedure is defined to calculate E_0 for each cavity: a set of tolerances is specified for all the geometrical parameters of each multi-cell cavity; then the electromagnetic field is calculated solving the Maxwell equations within the same cavity. The algorithm is shown in Fig. 4 where E_d is the maximum desired accelerating field. From now we call this model *new* model.

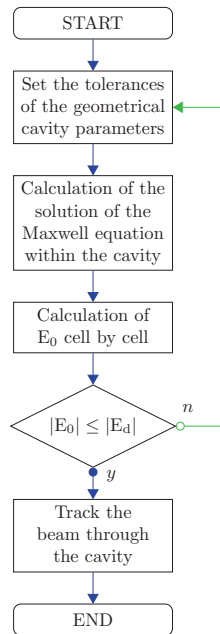


Figure 4: Algorithm to calculate the accelerating field E_0 .

Let consider a SC cavity for example. The geometrical details of a right half cell are shown in Fig. 5: the dome semi-axes are A_D and B_D ; the iris semi-axes are A_I and B_I ; the full cell length is L ; the bore radius is R_b ; the full cavity diameter is D .

At first the errors are applied individually for each geometrical parameter in order to calculate the *flatness sensitivity*

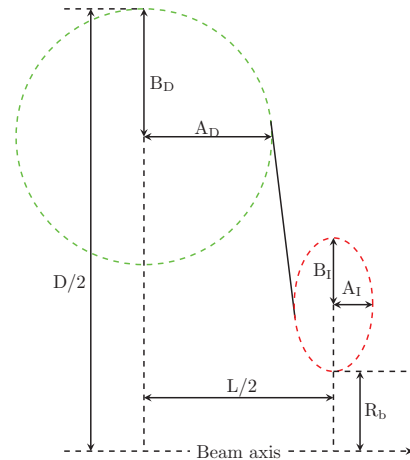


Figure 5: Details of right half cell of SC cavities.

to each parameter. In a second step all the errors are applied simultaneously in order to set the *final* geometrical tolerances that keep the flatness of the accelerating field within the desired limit.

MULTI-CELL CAVITIES IN THE ESS

The layout of the ESS LINAC [5] [6] is shown in the Fig. 3. The Ion Source, IS, is followed by the Low Energy Beam Transport, LEBT. Then there is the Radio frequency Quadrupole, RFQ, of 4.5 m. Within the Medium Energy Beam Transport, MEBT [7], there are 3 buncher cavities. *These are the only cavities that can be properly simulated using the old model since they are single-cell cavities.* The DTL is composed by 5 multi-cell cavities of 61, 34, 29, 26 and 23 cells [8] [9] and it is followed by 26 Spoke, SPK, cavities. Then there are 36 Medium- β , MB [10], cavities of 6 cells each and 84 High- β , HB [11], cavities of 5 cells each.

COMPARISON OF THE TWO MODELS

For the beam dynamics studies reported in this paper the beam is generated at the RFQ input with a gaussian distribution truncated at 4σ . The nominal RFQ output distribution is saved and used as input distribution for the rest of the ESS LINAC. The beam parameters at the RFQ output and their

tolerances are reported in the Table 1. The number of particles used is 1 M and the statistic of each study is based on 1000 linacs. The space charge routine used is PICNIC [1].

Table 1: Tolerances of the Beam at the MEBT Input

dx, dy [mm]	dx', dy' [mrad]	dE [keV]	$\Delta\epsilon_{x,y,z}$ [%]	$M_{x,y,z}$ -	dI [mA]
0.3	1	36.2	5	5	0.625

The following *static* [1] errors are included, modeled as random variables uniformly distributed within their tolerances: the quadrupole transverse position, dx, dy, rotation, $d\phi_x$, $d\phi_y$, $d\phi_z$, gradient, dG, and multipoles, dG_n (n=3,4,5), errors; cell field phase, $d\phi_s$, error; cavity field, dE_k , and phase, $d\phi_k$, error. The tolerances of the static errors are reported in the Table 2. The subscript B refers to the MEBT, S to the Super Conducting, SC, cavities: spoke, medium- β and high- β cavities. In red the tolerances related to the flatness of the multi-cell cavities.

Table 2: Static Error Tolerances from the MEBT to HB

Parameter	CAV _B	DTL	QUAD _{B,S}	CAV _S
dx, dy [mm]	0.5	0.1	0.2	1.5
$d\phi_x, d\phi_y$ [deg]	0.115	0.5	-	0.129
$d\phi_z$ [deg]	-	0.2	0.06	-
ΔG [%]	-	0.5	0.5	-
$\Delta E_0, \Delta E_k$ [%]	-1	1,1	-, -	5,1
$\Delta\phi_s, \Delta\phi_k$ [deg]	-1	0.5,1	-, -	-,1

The tolerances for the flatness of the accelerating field E_0 in the multi-cell cavities are red-highlighted in the Table 2. The flatness in the DTL is defined as:

$$\Delta E_0 = 100 \cdot \frac{|E_0 - E_d|}{E_d},$$

while for the SC cavities as:

$$\Delta E_0 = 100 \cdot \frac{|E_{p,MAX}| - |E_{p,min}|}{\frac{1}{N} \sum_{c=1}^N |E_{p,c}|},$$

where $E_{p,c}$ is the peak axial accelerating field in the cell c in a multi-cell cavity of N cells and $E_{p,MAX}$ and $E_{p,min}$ the maximum and the minimum peak respectively.

To compare the two models we perform two error studies (up to the high- β cavities) where the errors are changed in the same way linac by linac. The only difference is the method used to calculate the accelerating field into the DTL [8] [12] [13]: in the first study we use the new model, in the second one the error of the accelerating field E_0 , cell by cell, is modeled as a random variable uniformly distributed within its tolerance. The field flatness is kept within 1% in the DTL [14] on top of the *nominal* E_0 [15] and within 5% in the SC cavities. It is important to underline that, from this moment, we suppose that the interfaces of the DTL and the DTL stabilization system are *fully integrated* [16] in the

design to avoid the *self perturbation phenomena* [15] of these components. We remember, again, that to compare the two models only the *static* [1] errors are considered.

The RMS emittance growths in the horizontal, $\Delta\epsilon_x$, vertical, $\Delta\epsilon_y$, and longitudinal, $\Delta\epsilon_z$, plane at the end of the high- β cavities are shown in Fig. 6. It is evident that the old model underestimates hugely the emittance growths in all the planes.

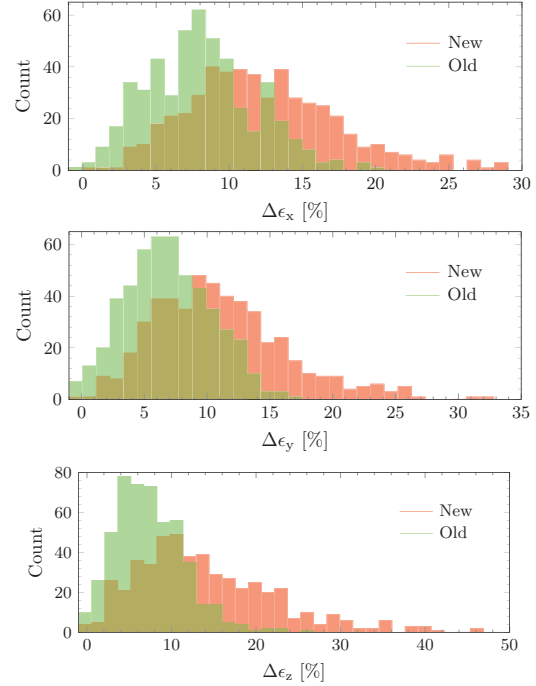


Figure 6: From top to bottom: Additional RMS emittance growth in the horizontal, $\Delta\epsilon_x$, vertical, $\Delta\epsilon_y$, and longitudinal, $\Delta\epsilon_z$, plane at the end of the high- β cavities. The red color indicates that the accelerating field into the DTL is calculated solving the Maxwell equations (new method) while the green color indicates that E_0 , within the DTL, is modeled as a random variable uniformly distributed within its tolerance (1%).

To emphasize the difference of the two models in the Fig. 7 is shown the longitudinal halo parameter h_z .

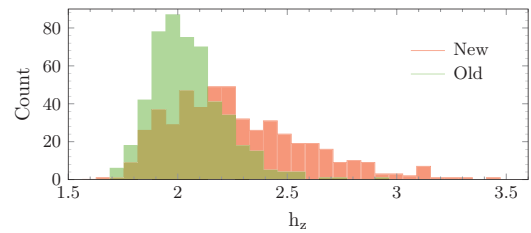


Figure 7: Halo Parameter, h_z , at the end of the high- β cavities when the flatness of E_0 , within the DTL, is 1%. The difference in the histograms is due *only* to the modelization of the accelerating field into the DTL since all the other errors are the same linac by linac.

Content from this work may be used under the terms of the CC BY 3.0 licence (© 2018). Any distribution of this work must maintain attribution to the author(s), title of the work, publisher, and DOI.

The comparison clearly shows that the new cavity model is very important to model the long multi-cell cavities as the DTL: the tolerance of the flatness in the long multi-cell cavities has a huge impact on the beam parameters of the downstream sections. The emittance growth and the halo on the longitudinal plane increase the probability to have particles which are not captured by the RF bucket after the frequency transition (352,21MHz/704,42MHz) at the interface SPOKE/MEDIUM- β cavities.

PHASE REFERENCE LINE

The Phase Reference Distribution System, PRDS, shown in Fig. 8, consists of two sub-systems: the main PRDS, called PRL, and the local PRDS (from the PRL outputs, in the tunnel, to the devices in the klystron gallery). The main PRDS is an in-kind contribution from ISE, Warsaw University of Technology [17] [18]. The main PRDS can be divided in the PRL, the PRL temperature control system, the PRL pressure and humidity control system and the PRL data acquisition and monitoring system. The PRDS design is based on 3 fundamental assumptions:

1. the first assumption is to use a passive synchronization scheme where the pick-up cables from RF cavities and BPMs/LBMs are paired and length-matched to the corresponding reference cables from the PRDS. This minimizes the phase drift errors between these 2 cables and enables precise synchronization since both cables are exposed to the same environment conditions and experience the same drift. This allows to make the main PRDS totally passive and to place it in the accelerator tunnel where other synchronization systems with active drift compensation techniques cannot be used;
2. the second assumption is to distribute two phase reference sinusoidal signals: 352.21 MHz and 704.42 MHz since there are accelerating cavities operating at both frequencies;
3. the third fundamental assumption is to use the same physical structure to distribute both frequencies because of the limited space in the accelerator tunnel.

The two phase reference sine waves, at 352 MHz and at 704 MHz, are synthesized in the Master Oscillator, MO, source and, then, amplified to the level of $\sim +50$ dBm each in the high power amplifier stage. This is done in MO racks located in the klystron gallery. The two-tone high-power signal is, then, transmitted with a single 7/8" flexible cable from the gallery down to the tunnel through a stub. Here the signal is split by a high power divider and is sent to the two branches of the main line.

The PRL is the backbone of the ESS accelerator synchronization system. It provides the phase reference signals for LLRF systems, BPM, Beam Position Monitor, systems and LBM, Longitudinal Beam Monitor, systems with low phase noise and low phase drifts all along the ~ 600 m long machine. There are 155 LLRF systems, 101 BPM systems and

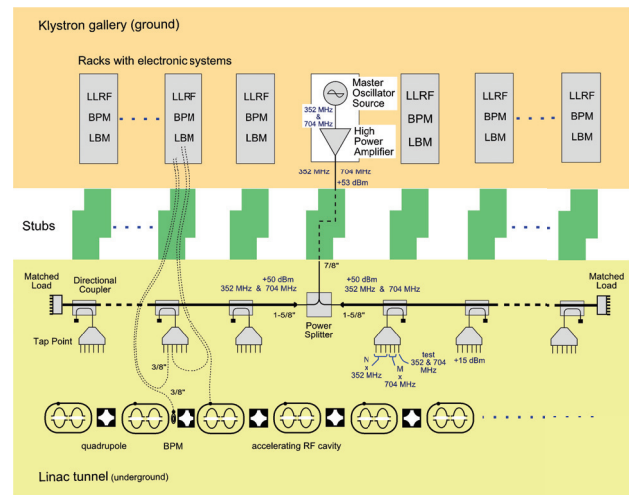


Figure 8: Conceptual schematic of the PRDS.

4 LBM. The PRL itself is ~ 581 m long according to the current design. It starts at ~ 7 m from the IS and ends ~ 15 m before the target. It means that the PRL is located along the entire length of the tunnel (~ 540 m) and enters in the target building.

The line is suspended from the ceiling and it is above the accelerator components. The input of the main line is located in the \sim middle of the line itself. There are two branches: one toward the ion source and another one toward the target. This solution minimizes the power drop due to the attenuation in the transmission line. The two branches are terminated with matched loads to minimize the reflections. The line is an air-filled coaxial transmission type. It is realized in 1-5/8" rigid coax standard due to relatively low attenuation and temperature drifts.

The main line provides the reference signal to 58 Tap Points, TPs, located in different positions along the tunnel: custom designed directional couplers transmit a portion of the reference signal from the main line to the TPs. The couplers are located in the TP positions. The TPs are custom designed modules which split the input reference signal into multiple outputs. In this way just one TP, associated to a coupler, provides multiple signals to many instruments which are in close proximity in the tunnel. This solution allow to save space and to reduce costs: dedicated couplers for each reference output without multi-channel TPs would be significantly more expensive and impractical for the ESS.

Each TP becomes crucial for the temperature stabilization because of the significant heat transfer related to the cables connected to the PRL in the TP positions. This is why each TP has a dedicated temperature control loop which has to ensure temperature stable boarder conditions to the temperature control system.

A cavity pick-up signal cable is bundled together with the corresponding reference cable from the TP and this length-matched cable pair goes to LLRF rack. Similarly, a probe signal cable from each BPM/LBM is bundled together with the corresponding reference cable from the tap point and this

length-matched cable pair goes to BPM/LBM rack. This solution minimizes the phase drift errors between the two cables in the pair and enables precise synchronization since both cables are exposed to the same environment conditions and experience the same drifts.

The point where the phase stabilization begins is the input to the high power amplifiers shown in Fig. 8. This point represents the phase reference fiducial in the signal distribution system from where the phase errors are controlled and minimized. In the tunnel the signal phase is stabilized, indirectly, controlling the environment conditions (temperature, pressure, humidity) while in the the MO racks and *from the MO to the tunnel the signal phase is stabilized, directly, using active electronic signal phase compensation.*

Since the physical length of a coaxial cable changes as the temperature of the cable changes, inducing a signal phase drift, the temperature around the cable has to be controlled within a small variation to reduce phase drift. Basing on measurements, the phase drift of a 1-5/8" rigid line is $\sim 8.48^\circ/\text{C}$ over 600 meters (the temperature coefficient is $\sim 0.0141^\circ/\text{C}/\text{m}$). Therefore the temperature of the cable should be kept within $\pm 0.1^\circ\text{C}$ to maintain the phase stability within $\pm 1^\circ$ over the whole LINAC. The easiest way to meet this requirement is to heat up the rigid line to few degrees above ambient temperature using a heating cable wrapped around the outer conductor and to stabilize it using a feedback loop. A thermal insulation will be placed on the coaxial rigid line to equalize the temperature along the line and to slow down its cooling. The thickness of the insulation should not exceed 40 mm basing on simulations and measurements made at the Lund University.

The pressure and humidity control system is responsible for control and stabilization of pressure and humidity in the PRL. Humidity stabilization is achieved by filling the PRL with nitrogen gas which is dry thus solves problem of atmospheric air humidity changes. Pressure stabilization is realized with pneumatic automation system that controls pressure of the nitrogen gas in the PRL.

GLOBAL ERROR STUDY

A final end to end error study is performed to analyze the effect of all the errors together including the LLRF errors and the PRL phase errors. The LLRF errors are modeled as gaussian random variables with zero-average and standard deviation set out in the Table 3.

Table 3: Dynamic [1] Errors Tolerances

Parameter	CAV _B	DTL	CAV _S
ΔE_k [%]	0.2	0.2	0.1
$\Delta \phi_k$ [deg]	0.2	0.2	0.1

The PRL phase errors are modeled so that:

- the phase difference between two consecutive cavities does not exceed 0.05° ;

- the phase difference between two generic points in the ESS LINAC does not exceed 2° .

The static errors applied after the high- β cavities are set out in Table 4.

Table 4: Static Error Tolerances After the High- β Cavities

Parameter	QUAD	DIP
dx, dy [mm]	0.2	0.2
$d\phi_x, d\phi_y$ [deg]	0	0
$d\phi_z$ [deg]	0.06	0.06
ΔG [%]	0.5	0.05

The power losses, shown in Fig. 9, are due, mainly, to the particles which were in the tail of the beam at the RFQ output or which have not been captured inside the RF bucket after the frequency transition (352,21MHz/704,42MHz) at the interface SPOKE/MEDIUM- β cavities.

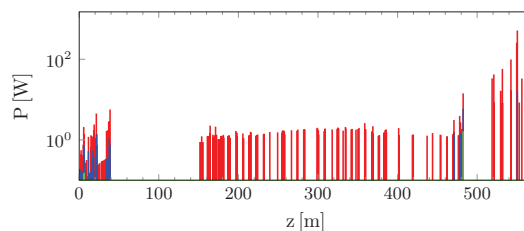


Figure 9: Power loss (per element) at 100% (red), 99% (blue) and 95% (green) confidence levels along the ESS LINAC.

CONCLUSION

The cavity model is important for the reliability of the beam dynamics parameters and of the power loss map: losses in the normal conducting section, due to a simplistic model, can mask dangerous losses in the high energy part of the LINAC. Vice versa losses in the SC section, due to a simplistic model, can lead to an unjustified reductions of the tolerances and, so, to a higher cost.

The studies show that modeling the error of the accelerating field, cell by cell in a multi-cell cavity, as a random variable, uniformly distributed within its tolerance, causes an underestimation of the emittance growth and of the halo parameters. The larger the number of cells is in a multi-cell cavity, the higher the underestimation of the beam dynamics parameters is. This means that the new cavity model is very important for the long multi-cell cavities as the DTL.

In the case of the ESS LINAC the global error study with the new model of the multi-cell cavities shows that the considered tolerances, including the SC flatness errors and RL phase errors, give a loss map more dense than the maps of the previous studies in the worst cases, but the loss peaks are compatible with the power level considered acceptable in the previous studies.

The beam in this study is generated at the RFQ entrance: a realist beam out of the IS may cause more losses.

REFERENCES

- [1] R. De Prisco *et al.*, “ERROR study on normal conducting ESS LINAC,” in *Proc. 27th Linear Accelerator Conf. (LINAC’14)*, Geneva, Switzerland, September 2014, paper THPP042, pp. 942–944.
- [2] R. De Prisco *et al.*, “ESS DTL RF modelization: field tuning and stabilization,” in *Proc. 4th Int. Particle Accelerator Conf. (IPAC’13)*, Shanghai, China, May 2013, paper THPWO070, pp. 3918–3920.
- [3] M. Eshraqi *et al.*, “Statistical error studies in the ESS LINAC,” in *Proc. 5th Int. Particle Accelerator Conf. (IPAC’14)*, Dresden, Germany, June 2014, paper THPME044, pp. 3323–3325.
- [4] Y. Levinsen *et al.*, “Beam dynamics challenges in the ESS LINAC,” in *Proc. 57th ICFA Advanced Beam Dynamics Workshop on High-Intensity and High-Brightness Hadron Beams (HB’16)*, Malmö, Sweden, July 2016, paper THPME044, pp. 315–318.
- [5] M. Lindroos *et al.*, “ESS Progressing into Construction,” in *Proc. 7th Int. Particle Accelerator Conf. (IPAC’16)*, Busan, Korea, May 2016, paper FRYAA02, pp. 4266–4270.
- [6] A. Ponton *et al.*, “ESS Normal Conducting Linac Status and Plans,” in *Proc. 27th Linear Accelerator Conf. (LINAC’14)*, Geneva, Switzerland, September 2014, paper THPP044, pp. 948–950.
- [7] R. Miyamoto *et al.*, “Beam Physics Design of the ESS Medium Energy Beam Transport,” in *Proc. 5th Int. Particle Accelerator Conf. (IPAC’14)*, Dresden, Germany, June 2014, paper THPME045, pp. 3326–3328.
- [8] R. De Prisco *et al.*, “ESS DTL status: redesign and optimizations,” in *Proc. 5th Int. Particle Accelerator Conf. (IPAC’14)*, Dresden, Germany, June 2014, paper TUAM3Y01, pp. 3314–3316.
- [9] M. Comunian, F. Grespan, and A. Pisent, “ERROR study on normal conducting ESS LINAC,” in *Proc. 27th Linear Accelerator Conf. (LINAC’14)*, Geneva, Switzerland, September 2014, paper THPP086, pp. 1047–1049.
- [10] P. Michelato *et al.*, “INFN Milano - LASA activities for ESS,” in *Proc. 17th Int. Conf. on RF Superconductivity (SRF’15)*, Whistler, Canada, September 2015, paper FRIOC02, pp. 1081–1084.
- [11] G. Devanz *et al.*, “ESS elliptical cavities and cryomodules,” in *Proc. 16th Int. Conf. on RF Superconductivity (SRF’13)*, Paris, France, September 2013, paper FRIOC02, pp. 1218–1222.
- [12] F. Grespan *et al.*, “ESS DTL Design and Drift Tube Prototypes,” in *Proc. 27th Linear Accelerator Conf. (LINAC’14)*, Geneva, Switzerland, September 2014, paper THPP044, pp. 1050–1052.
- [13] F. Grespan, “RF properties of the tank 5, pickup, RF coupler, RF windows, post coupler, thermo-mechanical simulations, field tuning, tuning in operation,” <http://indico.esss.lu.se/event/348/session/3/material/2/0.pptx>
- [14] R. De Prisco *et al.*, “Implication of manufacturing errors on the layout of the stabilization system and on the field quality in a drift tube linac - RF DTL error study,” in *Proc. 28th Linear Accelerator Conf. (LINAC’16)*, East Lansing, Michigan, September 2016, paper MOPLR68, pp. 290–293.
- [15] R. De Prisco *et al.*, “Effect of the field maps on the beam dynamics of the ESS drift tube LINAC,” in *Proc. 6th Int. Particle Accelerator Conf. (IPAC’15)*, Richmond, Virginia, May 2015, paper THPF078, pp. 3864–3866.
- [16] R. De Prisco *et al.*, “Integration of interfaces and stabilization system in the design of a drift tube linac,” in *Proc. 28th Linear Accelerator Conf. (LINAC’16)*, East Lansing, Michigan, September 2016, paper MOPLR70, pp. 294–297.
- [17] M. Żukocinski *et al.*, “Phase reference distribution system for European Spallation Source,” <http://www.l1rf2017.org/pdf/Posters/P-95.pdf>
- [18] K. Czuba *et al.*, “Concept of the phase reference line for the European Spallation Source,” in *Proc. 22th Int. Microwave and Radar Conf. (MIKON’18)*, Poznań, Poland, May 2018.

LONGITUDINAL DYNAMICS OF LOW ENERGY SUPERCONDUCTING LINAC*

Zhihui Li[†], The Key Laboratory of Radiation Physics and Technology of Education Ministry, Institute of Nuclear Science and Technology, Sichuan University, 610065, Chengdu, China

Abstract

The superconducting linac is composed of short independent cavities, and the cavity occupies only a small portion (1/4 to 1/6) of the machine compared with the normal conducting one. When phase advance per period is greater than 60 degrees, the smooth approximation is no longer valid and the longitudinal motion has to be described by time dependent system. With the help of Poincare map, the single particle nonlinear time dependent longitudinal motion is investigated. The study shows that when phase advance per period is less than 60 degrees, the system can be well described by smooth approximation, that means there is a clear boundary (separatrix) between stable and unstable area; when phase advance is greater than 60 degrees, the system shows a quite different dynamic structures and the phase acceptance is decreased significantly compared with the smooth approximation theory predicated, especially when phase advance per period is greater than 90 degrees. The results show that even for low current machine, the zero current phase advance should be kept less than 90 degrees to make sure there is no particle loss because of the shrink of the longitudinal acceptance.

INTRODUCTION

Keeping the zero current phase advance per period less than 90 degrees to avoid the envelope instability driven by space charge force has been widely accepted as one of the fundamental design principles of the high current linear accelerators [1], but for low current machine, should we still keep the zero current phase advance per period less than 90 degree? As the advance of the superconducting technology, more and more long pulse or continues wave ion accelerators adopt the superconducting acceleration structures just behind the RFQ because of their excellent properties, such as low AC power consumption, large beam tubes, great potential in terms of reliability and flexibility thanks to its independently-powered structures. The superconducting cavity can provide much higher acceleration field compared with the normal conducting one and can get higher acceleration efficiency, but at the same time the beam also suffers much stronger transverse defocusing from the higher electromagnetic field in the superconducting cavities, so there must be enough transverse focusing elements to confine the beam within the aperture, especially at low energy part, where it usually needs one focusing elements per cavity. However, the existence of the static magnetic field will increase the surface resistance of the superconducting cavity and may cause it to quench, so the cavity needs to be well screened from any static magnetic field, which makes it impossible to integrate the transverse focusing lens with the cavity just as the normal conducting

Alvarez DTL cavity does. As a consequence, the focusing period length will be much larger than the normal conducting one. The long period length, high acceleration gradient to fully utilize the potential of the superconducting cavities and large synchronous phase for large acceptance, all these makes the zero current phase advance per period greater than 90 degrees. In this paper, we proposed a model that can describe the longitudinal motion of low energy superconducting linac properly, and the longitudinal motion of low energy superconducting linac is explored.

MODEL DESCRIPTION

The longitudinal motion in linac is usually described by the following equations [2],

$$w' = \frac{dw}{ds} = B(\cos\phi - \cos\phi_s) \quad (1)$$

$$\phi' = \frac{d\phi}{ds} = -Aw \quad (2)$$

where $w \equiv \delta\gamma = \frac{W-W_s}{mc^2}$, $A \equiv \frac{2\pi}{\beta_s^3 \gamma_s^3 \lambda}$, $B \equiv \frac{qE_0 T}{mc^2}$.

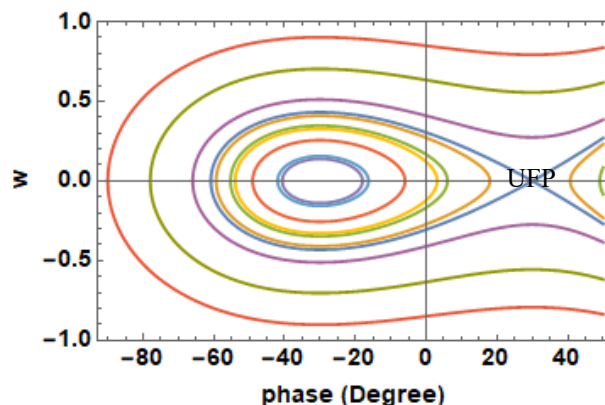


Figure 1: Phase portrait of smooth approximation longitudinal motion, the blue line is the separatrix.

The longitudinal motion equations are derived based on thin gap approximation and average in one period, they can also be directly derived from traveling wave approximation. When acceleration rate is small and the parameters A and B can be looked as constant, then the dynamics system described by equations (1) and (2) is time independent and integrable. The first motion constant is the energy or Hamiltonian of the system

$$\frac{A}{2}w^2 + B(\sin\phi - \phi\cos\phi_s) = H_\phi, \quad (3)$$

and they are a good approximation of the longitudinal motion of the normal conducting linac, such as DTL structures. The most significant characteristic property of the system is that the trajectory of the particle in phase space is confined on the curve of (3), and the stable area is defined by the curve which pass the unstable fixed point, the boundary of the stable and unstable area is called separatrix. The stable and unstable area has a clear boundary and the phase portrait is shown in Fig. 1.

For the low superconducting accelerators, the lattice is shown in Fig. 2, the cavity filling factor which is defined as

$$\eta = L_c/L, \quad (4)$$

where L_c is the effective length of the cavity and L is the period length. Because of the existence of the long drifts between cavities, the cavity filling factor for low energy superconducting linac is very small, usually between 0.2 to 0.25 and the validation of the smooth approximation is questionable. We propose that the longitudinal motion in low energy superconducting linac can still be described by equation (1) and (2), while the parameter B is time dependent defined as,

$$B = \begin{cases} \frac{qE_0T}{mc^2}, & 0 < s < \eta L \\ 0, & \eta L < s < L \end{cases}, \quad (5)$$

Then the system is time dependent nonlinear system.

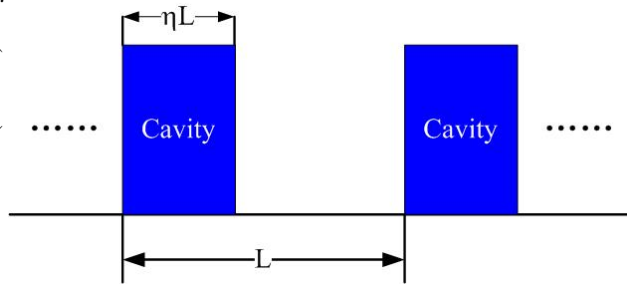


Figure 2: Longitudinal lattice structure.

LINEAR DYNAMICS

In order to investigate the time dependent nonlinear system, we first linearize the equation (2) at the stable fixed point $(\phi_s, 0)$ and the linear motion equation is

$$x'' + k^2x = 0, \quad (6-1)$$

and

$$k^2 = \begin{cases} -AB\sin\phi_s, & 0 < s < \eta L \\ 0, & \eta L < s < L \end{cases}. \quad (6-2)$$

where $x = \phi - \phi_s$. The lattice is equivalent to a periodic focusing channel composed by two elements, a solenoid and a drift space. By transform matrix, we can get the linear property of the system. The period transform matrix of the lattice is,

$$T = T_c T_d$$

where T_c and T_d is the transform matrix of cavity and drift space, respectively and they are

$$T_d = \begin{pmatrix} 1 & (1-\eta)L \\ 0 & 1 \end{pmatrix}, \quad (7)$$

$$T_c = \begin{pmatrix} \cos\theta & \frac{L_c}{\theta} \sin\theta \\ -\frac{\theta}{L_c} \sin\theta & \cos\theta \end{pmatrix}. \quad (8)$$

and

$$\theta = \sqrt{k}L_c \quad (9)$$

is the focusing angle of the cavity. From the transform matrix of the system we can deduce the relation between phase advance per period σ and the main parameters of the focusing lattice,

$$\cos\sigma = \cos\theta - \frac{1-\eta}{2} \frac{\theta \sin\theta}{\eta} \quad (10)$$

we see if the cavity filling factor is 1, that means the linac is composed by cavities just like DTL structure, then $\sigma = \theta$ and is obviously true. If filling factor is less than 1, then $\sigma > \theta$.

When $\sigma \ll 1$ and $\theta \ll 1$, we can get

$$\sigma = \theta/\sqrt{\eta} \quad (11)$$

which is equivalent to the lattice that is composed by cavity with filling factor 1 and the acceleration gradient ηE_0 , that is the smooth approximation. In conclusion, when smooth approximation is valid, the phase advance per period is proportional to focusing angle of the cavity, and the proportional parameters is $1/\sqrt{\eta}$. The phase advance per period as function of cavity focusing angle is shown in Fig.3, where the dotted line is the relation of equation (11), i.e. the smooth approximation results and the solid line is the relation of equation (10). We can see when phase advance is greater than 60 degrees, the relation (10) and (11) shows obvious difference in case of filling factor is less 1. From the discussion above, we can conclude that the smooth approximation is only valid when phase advance is less than 60 degrees.

When acceleration gradient and length of the cavity is fixed, as the filling factor is decreased, the phase advance is increased quickly and which will impose an important limitation of the applicable cavity voltage for high current machine, where the phase advance should be less than 90 degrees. And with the filling factor decrease, the focusing strength is decreasing with sqrt of filling factor:

$$k_l = \frac{\sigma}{L} \approx \frac{\theta}{L_c} \sqrt{\eta}.$$

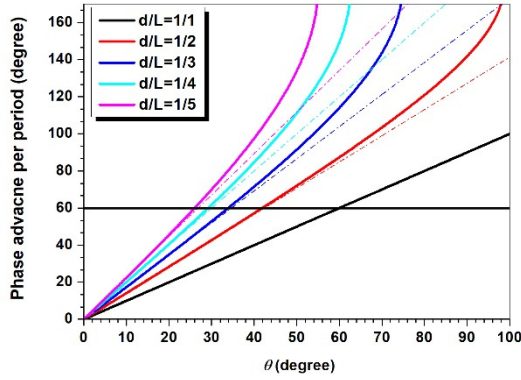


Figure 3: Phase advance per period as function of filling factor and focusing angle of cavity.

NONLINEAR DYNAMICS

If we define a vector as

$$\vec{x} = (\phi, w),$$

then equation (1) can be write as a vector differential equation

$$\frac{d\vec{x}}{ds} = f(\vec{x}, s). \quad (12)$$

The function f is periodic function of s with period of L . introducing the new variable $t=s/L$, system (12) transforms into the autonomous system

$$\begin{cases} \frac{d\vec{x}}{ds} = f(\vec{x}, tL) \\ \frac{dt}{ds} = 1/L \end{cases} \quad (13)$$

in dimensional 3. The flow in phase space intersect with the plane

$$t = n, n \in Integer,$$

and we project the intersection point onto the plane $t=0$, the trajectory of the intersect point will reveal the dynamics structure of the system, just as Fig. 4 shows.

By applying the method mentioned above, we can get some information of the dynamics structures of the system (13). The results are summarized as following:

- 1) The dynamics structure is directly depended on the phase advance per period. When phase advance is less than 60 degrees, the dynamics structures is identical with that of smooth approximation time independent one, i.e., there is a clear boundary between stable and unstable area, and the size of the stable area is exactly same as the time independent system, just as Fig. 5 shows. It also proves that smooth approximation is valid when phase advance is less than 60 degrees;

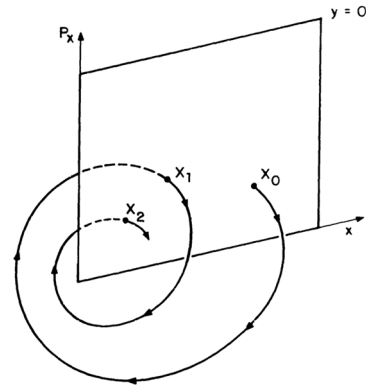


Figure 4: Poincare map in extended phase space.

2) As phase advance per period increasing, the stable area is shrinking, especially when $\frac{\sigma}{2\pi} = q/p$, where p and q are integers, the islands around the stable area appear and the strongly reducing the limit of stability around the origin. This can be explained as the existing of the high order fixed points [3]. The phase portrait with phase advance of 90 degrees, 110 degrees and 120 degrees are shown in Figs. 6-9;

3) When phase advance is 120 degrees, there are six third order fixed points, 3 of them are centre type, and 3 of them are saddle type. When phase advance is 120 degrees, the saddle type fixed points collides with the origin and the stable area shrinks to zero, i.e., there is no stable area in phase space.

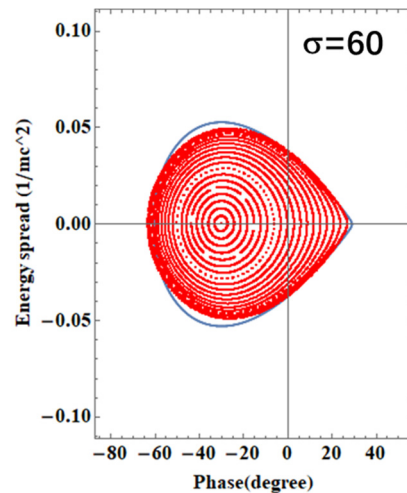


Figure 5: Phase portrait with phase advance 60 degrees.

PHASE ACCEPTANCE

We have calculated numerically the limit of stability of the time dependent system of longitudinal motion along phase axis by checking that the orbit remain bounded after 1000 iterates. The results are depicted in Fig. 9. We can the sudden shrink of the stable area at the rational tune. The phase acceptance remained constant for phase advance less than 60 degrees, then at around 70 degrees, the stable phase

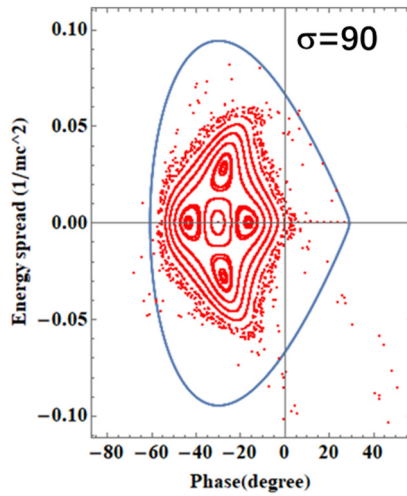


Figure 6: Phase portrait with phase advance 90 degrees.

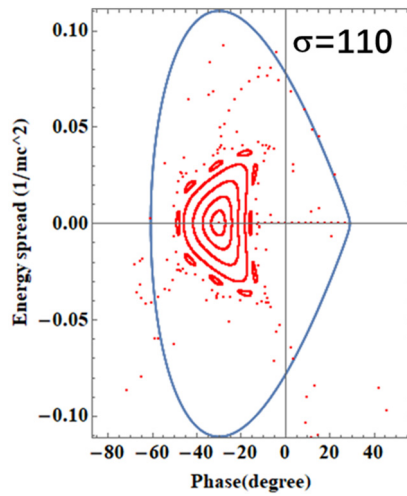


Figure 7: Phase portrait with phase advance 110 degrees.

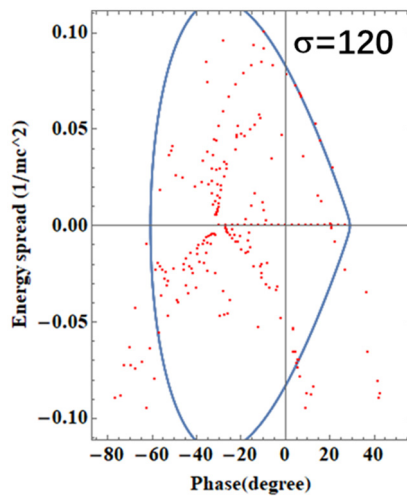


Figure 8: Phase portrait with phase advance 120 degrees.

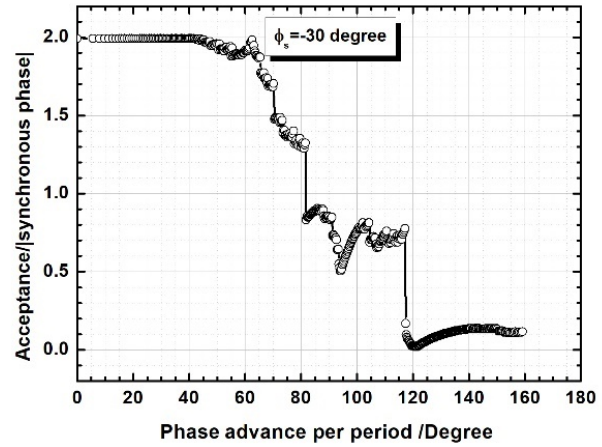


Figure 9: Phase acceptance as function of phase advance per period.

boundary decreases to about 1.5 times the synchronous phase, and at about 80 degrees, the boundary is decreased to about 0.8 times the synchronous phase, and when phase advance is greater than 120 degrees, the stable area is almost zero, and the motion becomes unstable universally. Further study shows, the aperture is only the function of phase advance, the trend is almost same for different synchronous phase

CONCLUSION

The longitudinal motion of linac composed with short independent cavities separated by long drifts should be described by the time dependent motion equation of (5), the smooth approximation is only valid when phase advance is less than 60 degrees. As phase advance increase, the stable area is shrinking and when phase advance is greater than 120 degrees, there is almost no stable area and the motion becomes unstable. This is very important in linac design especially at low energy and phase jump point, where phase acceptance is very critical and special attention should be paid to avoid the particle loss because of the small phase acceptance at these points.

REFERENCES

- [1] F. Gerigk, "Space and Beam Halos in Proton Linacs", in *Physics and Technology of Linear Accelerator Systems*, H. Wiedmann *et al.*, New Jersey, USA: World Scientific.
- [2] T. P. Wangle, *Principles of RF Linear Accelerators*, New York, NY, USA: John Wiley & Sons.
- [3] R. Dilao and R. Alves-Pires, *Nonlinear Dynamics in Particle Accelerators*, Singapore: World Scientific.

HALO FORMATION OF THE HIGH INTENSITY BEAMS IN A PERIODIC SOLENOID FOCUSING FIELDS*

Y. L. Cheon[†], M. Chung

Ulsan National Institute of Science and Technology, Ulsan, Korea

Abstract

Transport of high-intensity beams over long distances can be restricted by space-charge fields which can lead to the beam emittance growth and particle losses in accelerators. The lost particles cause serious radioactivation of the accelerator structure and disturb the proper propagation of the beam. The space-charge fields can be calculated by using Poisson's equation from the charge density profile. There are several ways to focus the charged particles in accelerators, but we are going to consider a periodic solenoidal magnetic focusing field. For the Kapchinskij-Vladimirskij (K-V) beams, the space charge field is linear but the envelope can be mismatched and have parametric resonances of the envelope instabilities particularly in periodic solenoid fields. The perturbed oscillations of the core and test particles can generate resonances following by the halo formations. Also, charge non-uniformity can make halos because of the non-linear space charge force.

INTRODUCTION

High-intensity charged particle beams can be used in various kinds of research like astrophysical nuclear reaction experiments, finding new particles in a standard model, application for cancer treatment and fusion material test such as International Fusion Materials Irradiation Facility (IFMIF). During the transport of the high-intensity beams which are space charge dominated, halo particles can be generated by the envelope mismatch [1] or the non-uniformities of charged particle distributions [2, 3]. We are going to describe the halo formations of uniform density beams whose core is not matched, and Gaussian density beams on the matched condition. To do that, in this paper, we just deal with the periodic solenoidal focusing field which has advantages over other focusing methods that it's much simpler and cheaper in the experimental aspect, rotationally symmetric, and more efficient in terms of beam emittance control [4]. Also it is more suitable for the numerical analysis using the smooth approximation [5, 6].

TRANSVERSE BEAM DYNAMICS UNDER A PERIODIC SOLENOID FOCUSING

A longitudinal solenoid focusing function can be expressed by $\kappa_z(s) = \kappa_z(s + S) = q^2 B_z^2(s) / 4\gamma_b^2 \beta_b^2 m^2 c^4$, where $B_z(s) = B_z(0, s)$ is the magnetic field on the z axis, S is the period of the focusing field. For a simple model, it's

assumed that $\kappa_z(s) = \kappa_z(0) = \text{const.}$ when $0 \leq s \leq \frac{\eta}{2}S$ & $S(1 - \frac{\eta}{2}) \leq s \leq S$, and $\kappa_z(s) = 0$ when $\frac{\eta}{2} \leq s \leq S(1 - \frac{\eta}{2})$ [5].

Envelope Equation

With the dimensionless parameters and variables defined by $s/S \rightarrow s, r_b/\sqrt{\epsilon S} \rightarrow r_b, S^2 \kappa_z \rightarrow \kappa_z$, and $SK/\epsilon \rightarrow K$, the normalized envelope equation for a symmetric envelope radius r_b becomes [5–8]

$$\frac{d^2 r_b(s)}{ds^2} + \kappa_z(s) r_b(s) - \frac{K}{r_b(s)} - \frac{1}{r_b^3(s)} = 0, \quad (1)$$

where ϵ is the beam emittance and $K = 2q\lambda/\gamma_b^3 \beta_b^2 mc^2$ is the normalized beam perveance in which λ is the line charge density of the beam. The normalized vacuum phase advance over one axial period of such a focusing field is given approximately by $\sigma_0 = \int_0^1 \sqrt{\kappa_z(s)} ds = \sqrt{\eta \kappa_z(0)}$, and normalized depressed phase advance which is considered as the degree of the space charge force is given by $\sigma = \int_0^1 \frac{ds}{r_b^2(s)}$.

Equation of Motion of a Charged Particle

In order to use the particle-core model for the study of halo formations, we will only deal with the transverse particle motions in the transverse phase space (x, y directions) and neglect the longitudinal effects (z or s direction) of space charge force and acceleration of the particles.

The dynamics of charged particles in the simple solenoid focusing model is easily analyzed in the Larmor frame [9] which rotates with the Larmor frequency around the axis of the solenoid. In Larmor frame, the equation of motion of a charged particle, with the space charge force (F_{sc}) is

$$x''(s) + \kappa_z(s)x(s) - KF_{sc}(x, r_b) = 0, \quad (2)$$

where $F_{sc}(x, r_b) = x(s)/r_b^2(s)$ for $x(s) < r_b(s)$ and $1/x(s)$ for $x(s) > r_b(s)$ for the uniform density beams.

However in real frame, with nonzero canonical angular momentum of the particles, the generalized equations of motion of a charged particle under the periodic solenoid field can be expressed by [9]

$$x''(s) - 2\sqrt{\kappa_z(s)}y'(s) - \frac{K}{2}F_{sc,x}(x, y) = 0, \quad (3)$$

$$y''(s) + 2\sqrt{\kappa_z(s)}x'(s) - \frac{K}{2}F_{sc,y}(x, y) = 0, \quad (4)$$

which are coupled between x and y directions and the longitudinal acceleration term (γ') is neglected. For simple case of zero canonical angular momentum, the coupled equations become a simple form in radial direction r, which is

$$r''(s) + \kappa_z(s)r(s) - \frac{K}{2}F_{sc,r}(r) = 0. \quad (5)$$

* Work supported by the National Research Foundation of Korea (Grant No. NRF-2017M1A7A1A02016413)

[†] mchung@unist.ac.kr

ENVELOPE OSCILLATIONS

In this section, we will see the envelope instabilities that explore mismatched, nonlinear resonances and chaotic behaviors in the beam envelope oscillations [5].

With solving Eq.(1), we plotted the envelope oscillations in phase plane $r_b - r'_b$, with different values of space charge perveance and focusing parameters. All points in the figures are plotted in every S lattice period (Poincare surface of section plots) for the trajectories of many different envelope initial conditions for propagation over 300 lattice periods.

Figure 1 shows the envelope motions without the space charge term, i.e, $K = 0$. The values of normalized parameters correspond to $\eta = 1/6, \kappa_z(0) = 3.79(\sigma_0 = 45.5^\circ)$. As you can see in the figure, there's a fixed point on the phase plane which represents the matched beam. It corresponds to a periodic solution to the envelope equation in every lattice period and the corresponding initial condition is $r_b(0) = 1.16, r'_b(0) = 0$. Around the fixed point, there are infinite number of invariant tori, each of which describes a mis-matched beam whose envelope exhibits stable betatron oscillations about the envelope of the matched beam because of the initial mismatch.

On the other hand, with non zero perveance, the space charge effects induce parametric resonances as well as the matched and mismatched oscillations as shown in Fig.2. Here, the values of normalized parameters correspond to $K = 3, \eta = 1/6, \kappa_z(0) = 3.79(\sigma_0 = 45.5^\circ)$ and the initial condition of a fixed point is $r_b(0) = 2.3, r'_b(0) = 0$. There coexist 4-th and 5-th order resonances in this phase space. The 5-th order resonance corresponds to the five elliptical regions in the vicinity of the fixed point. It has betatron wave number of $2\pi/5$, so a trajectory in one of the five islands will hop from one to another island until it comes back to its starting point after five turns [10].

For sufficiently large perveance values, the envelope oscillations become chaotic for some mismatched conditions. The phase space contains chaotic orbits which are very sensitive to initial conditions [5].

HALO FORMATIONS IN A PARTICLE CORE MODEL

From now, we will see the halo formations of charged particles in the particle-core model.

Halo formation of high-intensity beams which are space charge dominated can lead to beam emittance growth and particle losses in accelerators [11–14], and there are many reasons for the halos during the beam transport.

- Envelope instabilities related to the mis-matched and the n-th order parametric resonances (in the previous section).
- Halo formations generated by the resonances between the core oscillation and that of test particles (Particle-Core model) [1, 2, 15–17].
- Charge non-uniformity that induce the non-linear space charge force [3, 18].

We are going to describe the halo formations and chaotic motions both in the uniform charge density beams that are not matched, and non-uniform (Gaussian) charge density beams that are matched in the solenoid focusing field. To do that, we solved the equations of motion in our simulation to understand the motions between the core and test particles.

Particle Core Model of Uniform Density Beams

By solving Eq.(2) for the uniform density beam, the trajectories of many test particles with different initial positions are plotted in the phase plane in every lattice period for propagation over 300 lattice periods (see Fig.3).

Figure 3(a) shows the motion of test particles in the case of matched beam. They have stable circular or elliptical orbits in the phase space. But in the case of the mis-matched beam [see Fig.3(b)], we can see irregular trajectories around the center and chaotic motions that move in and out of the central region. Particularly, for the 5-th order resonant instability [see Fig.3(c)], particles are plotted in every 5 lattice period because such core oscillations have $2\pi/5$ frequency and return to the starting point every 5 lattice period. We can see resonant trajectories symmetrically generated in the space.

Outside the beam boundary, particles experience a nonlinear force proportional to $1/x$ and it is independent of the size of the beam. But when the test particles pass through the beam core, they are decelerated by the space charge force as they approach the core and accelerated as they leave the core. Also the space charge force within the beam boundary is dependent of the size of the envelope radius. Therefore, the unstable core oscillations like mis-matched and n-th order parametric resonances induce non-linear space charge forces to the charged particles and generate resonances accompanied by the chaotic and halo formations.

Particle Core Model of Gaussian Density Beams

$$\rho(\vec{x}) = \frac{\lambda}{2\pi\sigma_x\sigma_y} \exp\left(-\frac{x^2}{2\sigma_x^2} - \frac{y^2}{2\sigma_y^2}\right) \quad (6)$$

If a charge density of the beam has Gaussian distribution [Eq.(6)], the corresponding electric fields calculated by Poisson's equation are [19, 20]

$$E_{sc,x}(x, y) = 2\lambda \frac{1 - e^{-r^2/\sigma_r^2}}{r^2} x, \quad (7)$$

$$E_{sc,y}(x, y) = 2\lambda \frac{1 - e^{-r^2/\sigma_r^2}}{r^2} y, \quad (8)$$

where $r^2 = x^2 + y^2$. In this equation, σ_r is the rms radial size of the Gaussian profile and it corresponds to $\sigma_r = \sigma_r(s) = r_b(s)/\sqrt{2}$, where $r_b(s)$ is the envelope radius coming from the initial condition of the matched beam by solving the Eq.(1). $r_b(s)/\sqrt{2}$ is the rms size of the matched beam with uniform density profile and it's same with $\sigma_r(s)$ based on the concepts of **Equivalent beams** [9]. Therefore, Eqs.(7) and (8) can be substituted into the Eq.(3) and (4) so that the space charge terms become $F_{sc,x} = E_{sc,x}/\lambda$ and $F_{sc,y} = E_{sc,y}/\lambda$.

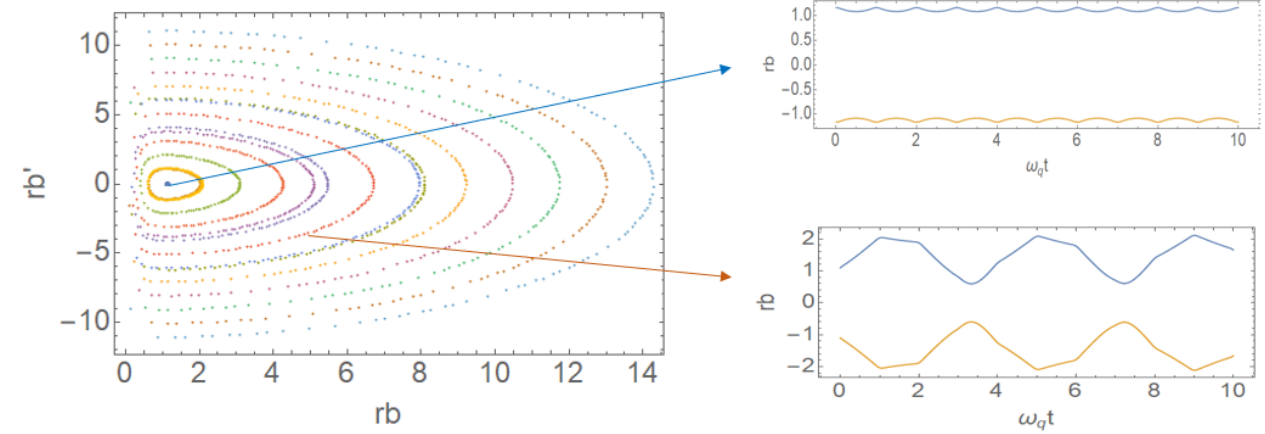


Figure 1: Envelope oscillations on phase plane of $r_b - r'_b$. The values of parameters correspond to $K = 0, \eta = 1/6, \kappa_z(0) = 3.79(\sigma_0 = 45.5^\circ)$. A fixed point on the phase space shows a periodic solution in which initial conditions are $r_b(0) = 1.16, r'_b(0) = 0$. Around the fixed point, there are infinite number of invariant tori having stable betatron oscillations.

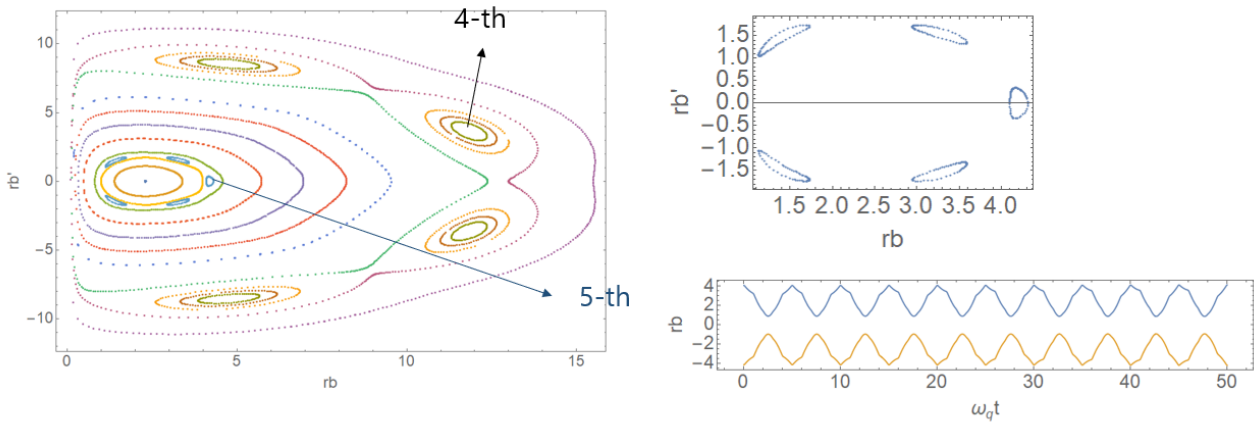


Figure 2: Envelope oscillations on phase plane of $r_b - r'_b$. The values of parameters correspond to $K = 3, \eta = 1/6, \kappa_z(0) = 3.79(\sigma_0 = 45.5^\circ)$. The 5th order resonance corresponds to the five elliptical regions in the vicinity of the fixed point and it has betatron wave number of $2\pi/5$.

For symmetric case with $\sigma_x = \sigma_y = \sigma_r/\sqrt{2}$ in Eq.(6), the space charge term in Eq.(5) becomes $F_{sc,r} = 2 \frac{1-e^{-r/\sigma_r^2}}{r}$.

First, the radial motions of particles in the symmetric Gaussian beams are shown in Fig. 4. For zero perveance, they have uniform and stable oscillations. For $K=3$ and tune depression $\eta \equiv \frac{\sigma}{\sigma_0} = 0.26$, phase space in Fig. 5 shows a region of two concentric curves centered on the fixed points symmetrically located on the x axis. This kind of orbits can be also seen in the resonant motions of mis-matched core and test particles in the uniform density beam under a continuous focusing field [1]. And outside the outer separatrix, particles form quasi-elliptical trajectories. Figure 6 is in different parameters with 60 or 90 degrees of phase advance. There's a similar separatrix symmetrically located on the x axis around a center. But outside region, many other resonant trajectories appear as the distance from the center increases.

For more detailed analysis of the Fig. 6, we expand the exponential part of $F_{sc,r}$ in Eq.(5) by using the Taylor expansion. If we just keep the linear and 2nd order terms, the 4-th order resonance between the matched core (e.g. $\sigma_{env} = 360^\circ$) and test particles can be generated when the phase advance of the particle is about 90° (e.g. $\sigma = 90^\circ$) [21, 22]. The first figure of Fig. 7 shows the 4-th order resonance around the center of the phase plane. If we add the higher order terms more and more (see middle and last figures in Fig. 7), we can see similar trajectories near the center but more resonances are generated as distance increases and become closer to the Fig. 6.

Next, in the case of non-zero canonical momentum under solenoidal focusing field, we have to solve the coupled equations of motion [Eq.(3) and (4)] to see particle motions in real frame. Figure 8 shows the trajectories of many test particles plotted in x-y phase plane with the scale of matched beam radius. A black circle with radius 1 on the x-y plane is

Content from this work may be used under the terms of the CC BY 3.0 licence (© 2018). Any distribution of this work must maintain attribution to the author(s), title of the work, publisher, and DOI.

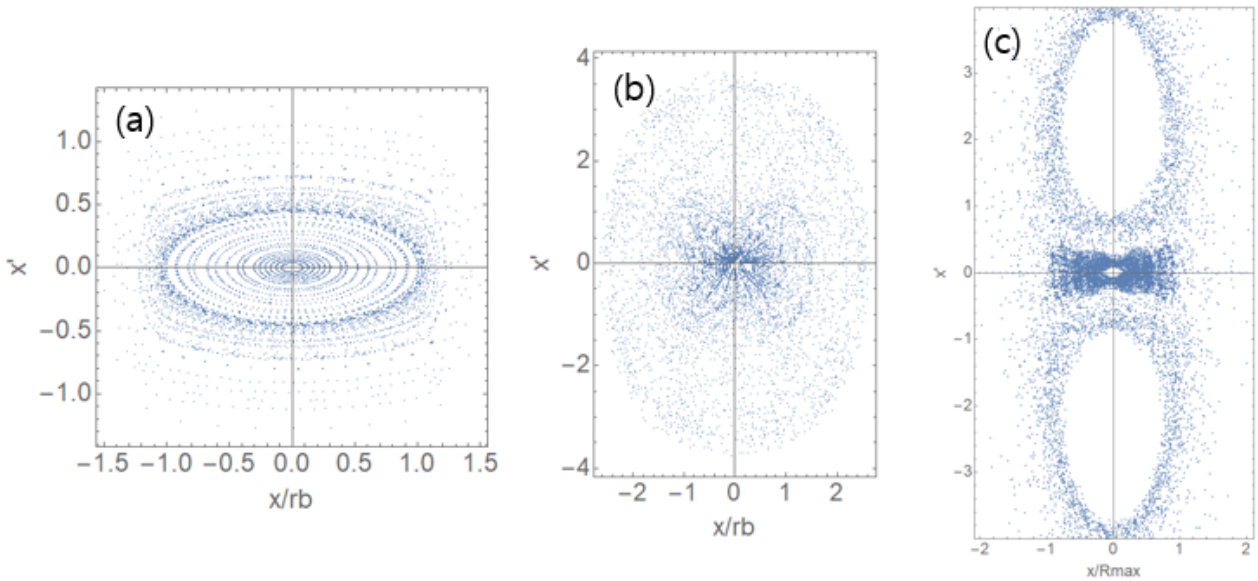


Figure 3: Test particle trajectories of uniform density beams. The corresponding parameters are $K = 3$ and (a) $\sigma_0 = 45.5^\circ$, (b) $\sigma_0 = 45.5^\circ$, (c) $\sigma_0 = 45.5^\circ$. Beam core oscillation is in matched, mis-matched, and the 5th order parametric resonance condition, respectively.

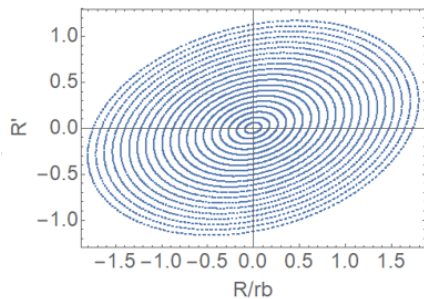


Figure 4: Test particle trajectories of the symmetric Gaussian charge density beam. The corresponding parameters are $K = 0$, $\sigma_0 = 45.5^\circ$, $\sigma = 45.5^\circ$.

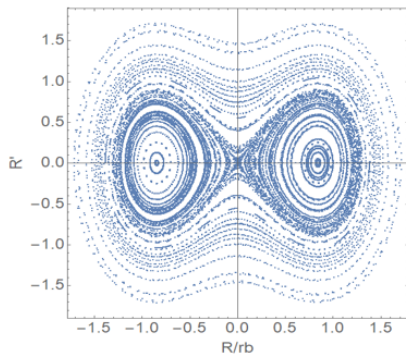


Figure 5: Test particle trajectories of the symmetric Gaussian charge density beam. The corresponding parameters are $K = 3$, $\sigma_0 = 45.5^\circ$, $\sigma = 12^\circ$.

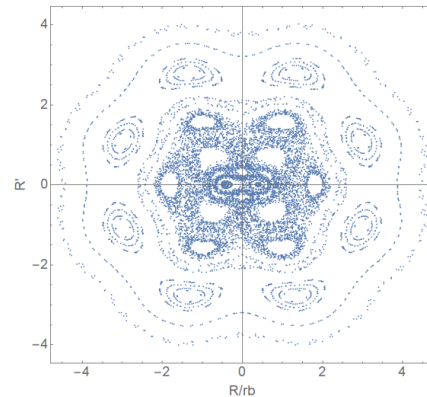


Figure 6: Test particle trajectories of the symmetric Gaussian charge density beam. The corresponding parameters are $K = 2.3$, $\sigma_0 = 115^\circ$, $\sigma = 90^\circ$.

the envelope boundary of the beam. For a detailed study of the test particle motions, let's see a single particle motion. When a single particle is initially loaded within the beam boundary (see Fig. 9), it takes the chaotic orbits that lead to the escape of particle from the beam interior to outside. But as you can see in (c), at very close to the beam boundary, charged particles doesn't go inside the region at which they initially loaded. When a single particle is initially distributed outside the beam boundary (see Fig. 10), it also doesn't go inside the beam interior and doesn't go farther than the particles of Fig. 9. They have chaotic trajectories around the region where they first are.

Test particle orbits can take different kinds of chaotic trajectories depending on the different classes of initial con-

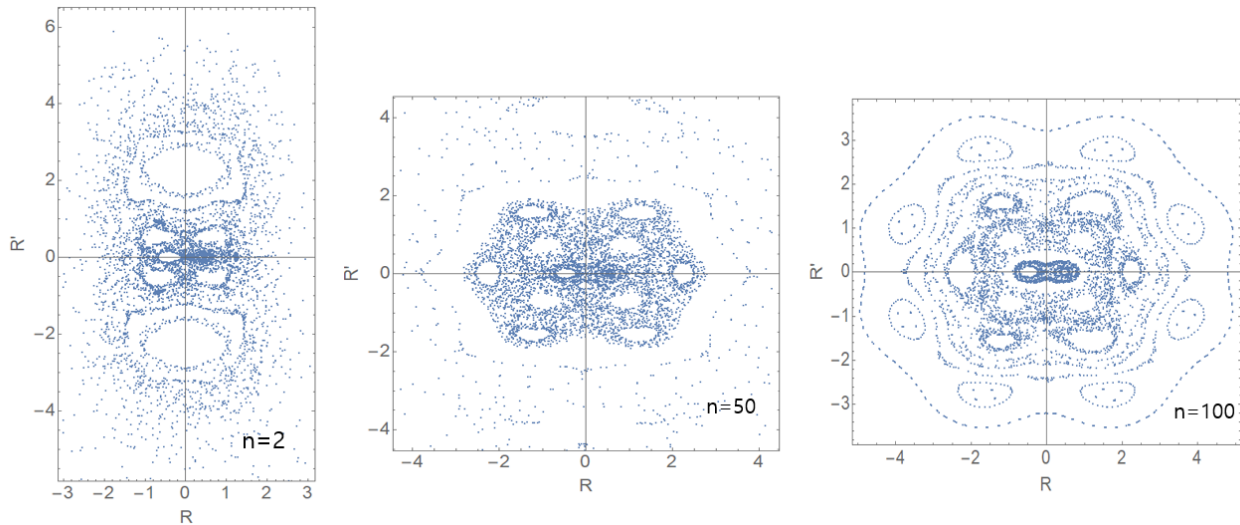


Figure 7: Test particle trajectories of the symmetric Gaussian charge density beam by using Taylor expansion of the exponential part in the space charge force. The corresponding parameters are $K = 2.3$, $\sigma_0 = 115^\circ$, $\sigma = 90^\circ$. (First) $n \leq 2$ terms generate 4-th order resonance around the center. And add the higher order terms (middle) $n \leq 50$, (last) $n \leq 100$.

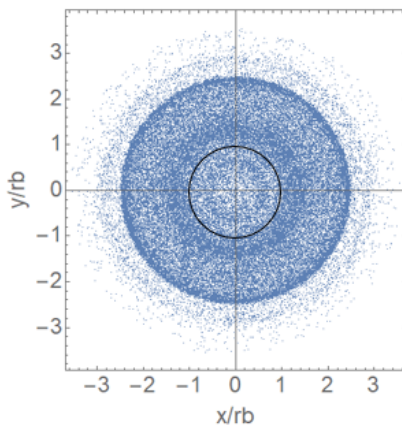


Figure 8: By solving the coupled equations of motion, many test particles are plotted in x - y phase plane with the scale of matched beam radius rb .

ditions in phase space. They can take orbit that is chaotic but stays confined within the outer beam boundary and also leads to the escape of particles from the beam interior to outside, which can become halo particles. When the inside particles go closer to the beam boundary, it tends to be accelerated by the space charge force and resonated with the vibrating beam core so that they can get energy to go farther and make halos.

CONCLUSION

In the high-intensity charged particle beam dynamics, the space charge effects are one of big considerations in terms of the beam emittance growth and halo formations during the beam transportation. Even though the space charge force is linear in the uniform charge density (K-V beam), there can be

a mis-matched core motions because of the initial mismatch. Then the unstable oscillations of the core can generate resonances with the test particles, which can be described by using the particle-core model simulations. Especially under the periodic solenoid magnetic field, the higher order envelope resonances are also generated. For non-uniform charge density beams (Gaussian), the space charge force is non-linear so that it affects the particle motions even though the core is matched. To see the non-linear effects on the halo formations, we solved the radial (in the case of symmetric Gaussian beam) and coupled equations of motion with many test particles and a single particle motion. The particle-core model doesn't consider the self-consistency that can be achieved only from the Particle-In-Cell (PIC) simulations. Moreover, there's no longitudinal effects of the space charge force and acceleration. So we can study further by including those additional effects on the beam dynamics and apply to the design of the halo and beam loss diagnostics.

REFERENCES

- [1] T. P. Wangler, "Particle-core model for transverse dynamics of beam halo", *Phys. Rev. Accelerators and Beams*, vol. 1, no. 9, 1998.
- [2] Q. Qian, R. C. Davidson, C. Chen, "Chaotic particle motion and halo formation induced by charge nonuniformities in an intense ion beam propagating through a periodic quadrupole focusing field", *Physics of Plasmas*, vol.2 no. 7, pp.2674–2686, 1995.
- [3] Q. Qian, R. C. Davidson, C. Chen, "Halo formation induced by density nonuniformities in intense ion beams", *Phys. Rev. E*, vol. 51, no. 6, p. R5216, 1995.
- [4] I. Hofmann, "Performance of solenoids versus quadrupoles in focusing and energy selection of laser accelerated protons",

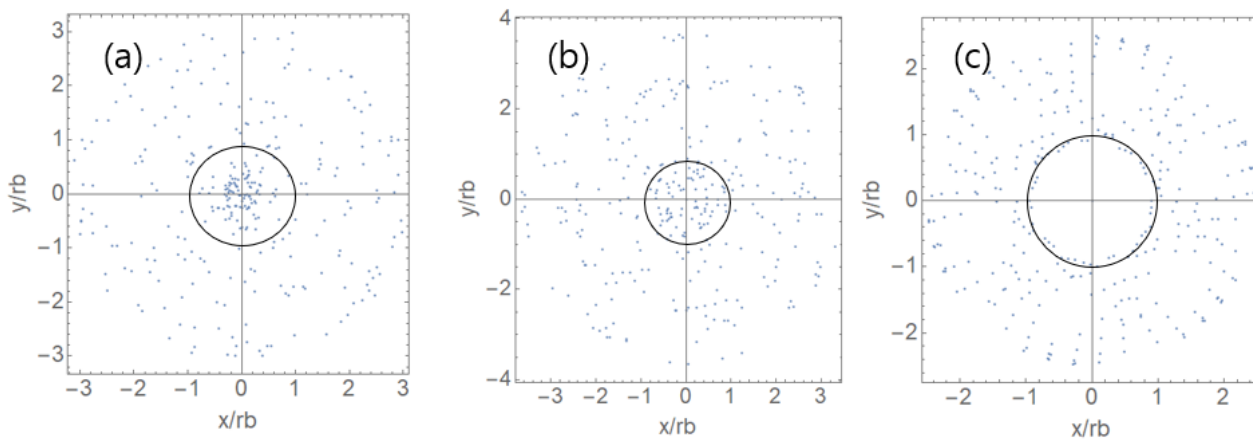


Figure 9: A single particle motion of Fig. 8, with different initial conditions. A particle is initially loaded outside the beam boundary (a black circle) which are (a) $(\frac{x}{r_b})^2 + (\frac{y}{r_b})^2 = (0.1)^2$, (b) $(\frac{x}{r_b})^2 + (\frac{y}{r_b})^2 = (0.7)^2$, (c) $(\frac{x}{r_b})^2 + (\frac{y}{r_b})^2 = (0.9)^2$.

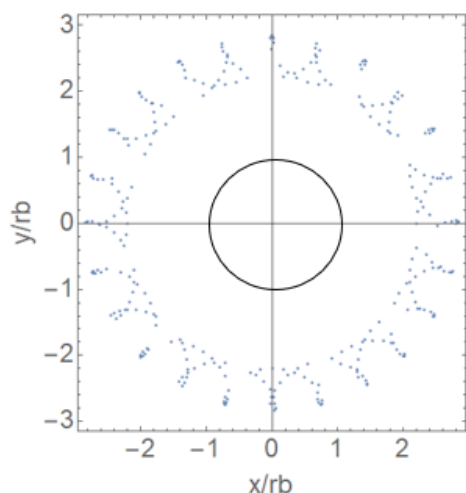


Figure 10: A single particle motion of Fig. 8, with different initial conditions. A particle is initially loaded inside the beam boundary (a black circle) which is $(\frac{x}{r_b})^2 + (\frac{y}{r_b})^2 = (2.2)^2$.

Phys. Rev. Accelerators and Beams, vol. 16, no. 4, p. 041302, 2013.

- [5] C. Chen, R. C. Davidson, “Nonlinear resonances and chaotic behavior in a periodically focused intense charged-particle beam”, *Phys. Rev. Lett.*, vol. 72, p. 14, p. 2195, 1994.
- [6] R. C. Davidson, H. Qin, “An introduction to the physics of intense charged particle beams in high energy accelerators”, World Scientific, 1994.
- [7] I. M. Kapchinskij, V. V. Vladimirkij, “Limitations of proton beam current in a strong focusing linear accelerator associated with the beam space charge”, in *Proc. HEACC 1959*, Geneva, Switzerland, Sep. 1959, pp.274–287.
- [8] R. C. Davidson, “Physics of nonneutral plasmas”, *World Scientific Publishing Company*, 2001.
- [9] M. Reiser, “Theory and design of charged particle beams”, *John Wiley & Sons*, 2008.
- [10] I. Hofmann, “Space Charge Physics for Particle Accelerators”, *Springer*, 2017.
- [11] J. M. Struckmeier, J. Klabunde, “On the stability and emittance growth of different particle phase-space distributions in a long magnetic quadrupole channel”, *Part. Accel.*, vol. 15, pp.47–65, 1984.
- [12] A. Pathak, S. Krishnagopal, “Higher order mode beams mitigate halos in high intensity proton linacs”, *Phys. Rev. Accelerators and Beams*, vol. 20, no. 1, p. 014201, 2017.
- [13] G. Franchetti, I. Hofmann, D. Jeon, “Anisotropic free-energy limit of halos in high-intensity accelerators”, *Phys. Rev. Lett.*, vol. 88, no. 25, p. 254802, 2002.
- [14] F. Gerigk, “Beam halo in high-intensity hadron accelerators caused by statistical gradient errors”, *Phys. Rev. Accelerators and Beams*, vol. 7, no. 6, p. 064202, 2004.
- [15] J. S. O’Connell, “Beam halo formation from space-charge dominated beams in uniform focusing channels”, in *Proc. PAC’93*, pp. 3657-3659, 1993.
- [16] T. F. Wang, “Particle-core study of halo dynamics in periodic-focusing channels”, *Phys. Rev. E*, vol. 61, no. 1, p. 855, 2000.
- [17] J. Qiang, R. D. Ryne, “Beam halo studies using a three-dimensional particle-core model”, *Phys. Rev. Accelerators and Beams*, vol. 3, no. 6, p. 064201, 2000.
- [18] I. Hofmann *et al.*, “Stability of the Kapchinskij-Vladimirkij (KV) distribution in long periodic transport systems”, *Part. Accel.*, vol. 13, pp. 145-178, 1982.
- [19] M. A. Furman, “Compact complex expressions for the electric field of two-dimensional elliptical charge distributions”, *American Journal of Phys.*, vol. 62, no. 12, pp.1134–1140, 1994.
- [20] G. Stupakov, P. Gregory, “Classical Mechanics and Electromagnetism in Accelerator Physics”, *Grad. Texts Math.*, 2018.
- [21] L. Groening *et al.*, “Experimental observation of space charge driven resonances in a linac”, in *Proc. LINAC’10*, Tsukuba, Japan, Sep. 2010, paper TH303.
- [22] D. Jeon, L. Groening, G. Franchetti, “Fourth order resonance of a high intensity linear accelerator”, *Phys. Rev. Accelerators and Beams*, vol. 12, no. 5, p. 054204, 2009.

Content from this work may be used under the terms of the CC BY 3.0 licence © 2018). Any distribution of this work must maintain attribution to the author(s), title of the work, publisher, and DOI.

REQUIREMENTS AND RESULTS FOR QUADRUPOLE MODE MEASUREMENTS

Adrian Oeftiger*, CERN, Geneva, Switzerland

Abstract

Direct space charge may be quantified, and hence the beam brightness observed, by measuring the quadrupolar beam modes in the CERN Proton Synchrotron (PS). The spectrum of the transverse beam size oscillations (i.e. the quadrupolar beam moment) contains valuable information: the betatron envelope modes and the coherent dispersive mode indicate optics mismatch, while their frequency shifts due to space charge allow a direct measurement thereof. To measure the quadrupolar beam moment we use the Base-Band Q-meter system of the PS which is based on a four electrode stripline pick-up. Past experiments with quadrupolar pick-ups often investigated coasting beams, where the coherent betatron and dispersion modes correspond to single peaks in the tune spectrum. In contrast, long bunched beams feature bands of betatron modes: the mode frequencies shift depending on the transverse space charge strength which varies with the local line charge density. By using the new transverse feedback (TFB) in the PS as a quadrupolar RF exciter, we measured the quadrupolar beam transfer function. The beam response reveals the distinct band structure of the envelope modes as well as the coherent dispersive mode.

INTRODUCTION

The transverse second-order moments of a beam distribution can be measured with the aid of sensitive quadrupolar pick-ups (QPU) featuring four electrodes in quadrupolar configuration. In particular under stable beam conditions, the oscillations about the matched beam values can give insight on transverse emittances, optics mismatch, and space charge strength. Our measurements with the QPU at the CERN Proton Synchrotron aim to characterise the new high brightness beams in the context of the LHC Injector Upgrade [1]. The goal is to establish a direct experimental method to assess space charge strength, which can also be used to benchmark advanced numerical simulation set-ups.

In the past, QPU studies have been conducted both in the time domain (fitting the quadrupole moment for emittance measurements, cf. [2, 3]) and more often in the frequency domain. The frequency domain is advantageous in the sense that the oscillatory or differential signal content is much less noise affected than the absolute signal values. Beam frequency response measurements have been used e.g. for emittance measurements [4], while space charge studies cover the majority of QPU studies [5–8].

The CERN PS provides good experimental conditions to establish the method enabling us to study various space charge strengths and tune coupling conditions. The present hardware includes the new transverse feedback system which

we exploit to measure the quadrupolar beam transfer function in order to characterise the quadrupolar eigenmodes. The planned upgrades of the BBQ systems in the PS Booster and the Super Proton Synchrotron will extend the availability of quadrupolar moment measurements to these machines.

This paper first reviews the theoretical basics yielding the expressions for modes of quadrupolar order. We employ the smooth approximation where not explicitly stated otherwise, i.e. the lattice functions remain constant along the ring. A more comprehensive overview of most of the derivations and arguments is given in Ref. [9, chapter 2]. The next section describes the experimental set-up for the quadrupolar beam transfer function measurement in the CERN PS and presents the measured beam frequency response. Eventually, these results are briefly compared to numerical simulations carried out with PyHEADTAIL [10] using a self-consistent 3D space charge model [11].

THEORETICAL CONSIDERATIONS

Let $\zeta \doteq (x, y, z, x', y', \delta)$ denote the vector of the six phase space coordinates of the beam particles. The spatial coordinates x and y measure the horizontal and vertical displacement from the orbit, while z indicates the longitudinal spatial displacement from the RF wave's zero crossing. The canonical momenta p_x, p_y, p_z are embedded in $x' \doteq p_x/p_0$, $y' \doteq p_y/p_0$ and $\delta = (p_z - p_0)/p_0$ while the beam momentum $p_0 = \beta\gamma m_p c$ is considered constant, denoting with β the beam speed in units of speed of light c , with γ the relativistic Lorentz factor of the beam and with m_p the mass per particle.

It is well known that in a coasting beam with a transverse uniform Kapchinskij-Vladimirskij (KV) distribution [12], the particles oscillate at one single incoherent tune. The defocusing nature of transverse space charge translates to the incoherent tune being negatively shifted from the bare machine tune. This KV tune shift is frequently used as a unit to express the strength of space charge in a machine, it amounts to

$$\Delta Q_{x,y}^{KV} = -\frac{K^{SC} R^2}{4\sigma_{x,y}(\sigma_x + \sigma_y)Q_{x,y}}, \quad (1)$$

where R denotes the effective machine radius, $\sigma_{x,y}$ the transverse r.m.s. beam sizes and $Q_{x,y}$ the transverse bare machine tunes. The dimensionless space charge perveance reads

$$K^{SC} \doteq \frac{q\lambda}{2\pi\epsilon_0\beta\gamma^2 p_0 c} \quad (2)$$

with q the charge per particle, λ the line charge density in C/m and ϵ_0 the vacuum permittivity.

If the beam is transversely Gaussian normal distributed, space charge becomes non-linear. The linearised slope of

* adrian.oeftiger@cern.ch

Content from this work may be used under the terms of the CC BY 3.0 licence (© 2018). Any distribution of this work must maintain attribution to the author(s), title of the work, publisher, and DOI.

the self-fields in the core of the Gaussian distribution then amounts to twice the linear slope of the *r.m.s.-equivalent* KV distribution. On the other hand, space charge becomes very weak for the halo particles far outside the core. Therefore, the space charge shifted incoherent tunes $\Delta Q_{x,y}^{SC}$ spread from close to the bare betatron tune $Q_{x,y}$ to twice the KV incoherent tune shift:

$$\max \{ \Delta Q_{x,y}^{SC} \} = 2 \cdot \Delta Q_{x,y}^{KV} \quad (3)$$

In terms of the coherent perspective, the transverse dipolar moments of the beam distribution f ,

$$\langle u \rangle(s) = \int d^6 \zeta u f(\zeta; s) \quad (4)$$

for $u = x, y$ and s the path length along the ring, remain unaffected by space charge: due to Newton's principle of *actio = reactio*, the sum of all binary forces between the particles vanishes. Direct space charge hence plays a role only from the quadrupolar moments on,

$$\sigma_u(s) = \int d^6 \zeta (u - \langle u \rangle)^2 f(\zeta; s) \quad (5)$$

In the transverse plane, the quadrupolar moments are often referred to as envelopes. Assuming beams of elliptic symmetry with a monotonically decreasing distribution within a constant focusing channel with decoupled optics, the *r.m.s.* envelope equations [12, 13] describe the evolution of these quadrupolar moments $\sigma_{x,y}(s)$ along the ring,

$$\begin{aligned} \frac{d^2 \sigma_x}{ds^2} + K_x \sigma_x - \frac{\epsilon_{x,geo}^2}{\sigma_x^3} - \frac{K^{SC}}{2(\sigma_x + \sigma_y)} &= 0 \\ \frac{d^2 \sigma_y}{ds^2} + K_y \sigma_y - \frac{\epsilon_{y,geo}^2}{\sigma_y^3} - \frac{K^{SC}}{2(\sigma_x + \sigma_y)} &= 0 \end{aligned} \quad (6)$$

Here, $K_{x,y} = (\beta_{x,y})^{-2} = (Q_{x,y}/R)^2$ represent the external focusing in each plane with $\beta_{x,y}$ denoting the constant betatron functions. The (possibly slowly changing) geometric transverse emittances $\epsilon_{\{x,y\},geo}$ provide the respective thermal barrier term. Last but not least, the space charge perveance term couples the two envelope equations.

By linearising Eq. (6) around the equilibrium values of the quadrupolar moments, one can solve the corresponding eigenvalue problem. Under stable beam conditions (e.g. neglecting modes that can change the emittance) one finds two quadrupolar eigenmodes of the envelope equations at the two tunes Q_{\pm} . In their expressions (see e.g. Ref. [9, Eq. (2.110)]) one readily finds a term proportional to the expression of the incoherent KV tune shift Eq. (1). After substituting this term and neglecting quadratic orders, one readily derives the general relation

$$\Delta Q_{x,y}^{KV} = \frac{1 + \frac{\sigma_{y,x}}{\sigma_{x,y}}}{2Q_{x,y}} \Lambda \quad (7)$$

where the physical observables (i.e. the quadrupolar modes Q_{\pm} , bare machine tunes $Q_{x,y}$ and the beam size ratio σ_y/σ_x)

are explicitly contained in the quantity

$$\Lambda \doteq \frac{Q_+^2 + Q_-^2 - 4 [Q_x^2 + Q_y^2]}{4 + 3 \frac{\sigma_y}{\sigma_x} + 3 \frac{\sigma_x}{\sigma_y}} \quad (8)$$

Λ is negative (such as $\Delta Q_{x,y}^{KV}$) which reflects the defocusing effect of direct transverse space charge. The general expression Eq. (7) for the quadrupolar modes (first derived in [14]) has two well-known limit cases:

1. the decoupled split tunes case (e.g. [5, first Eq.]) with independent horizontal and vertical mode, and
2. the fully coupled axi-symmetric case (e.g. [15, Eqs. (26) and (28)]) with the anti-symmetric and the breathing mode.

Equation (7) in principle allows to measure the strength of space charge (in units of the KV tune shift) directly through the observation of the quadrupolar frequencies. Reference [16] discusses how approaching the coupling resonance reflects on the KV tune shift when comparing to the decoupled split tunes formula.

The power of the envelope equations lies in the *r.m.s.-equivalence* of beam distributions, whose collective second-order dynamics are uniquely described by Eq. (6) [13, 15, 17]. Suppose two different transverse distributions of the same *r.m.s.* sizes (e.g. the above Gaussian and KV distribution): even though the incoherent tunes may be distributed very differently, the coherent behaviour of these two *r.m.s.-equivalent* beams under space charge will be identical.

Until here we have discussed coasting beam conditions. Under typical synchrotron conditions, longitudinal motion is orders of magnitude slower than the transverse particle oscillations. This variation in bunched beams can hence be considered adiabatic, which leads to longitudinally varying space charge conditions for the transverse beam dynamics. In the incoherent picture, the above space charge tune shift Eq. (1) then effectively scales with $\Delta Q_{x,y}^{KV} = \Delta Q_{x,y}^{KV}(z) \propto \lambda(z)$. Ref. [6] discusses the corresponding implications for the collective motion by investigating the three-dimensional envelope equations including the longitudinal σ_z envelope. For long bunches and low synchrotron frequency, the transverse and longitudinal degrees of freedom indeed decouple resulting in coasting beam like conditions for the transverse plane, cf. e.g. [6, Fig. 2]. Consequently, the transverse quadrupolar modes remain well described by the previous two-dimensional expressions, which now depend on the varying longitudinal line charge density $\lambda(z)$. Considering the quadrupolar frequency spectrum for a typical parabolic bunch shape, one therefore now expects two *bands of envelope modes*, one for the higher $Q_+(z)$ and one for the lower $Q_-(z)$ (which can in principle overlap for strong space charge). Each band ranges from the vanishing space charge conditions at the head and tail of the bunch to the strongest transverse self-fields at the bunch core. The former condition leaves Q_{\pm} close to $2Q_{x,y}$ while the latter translates to maximally reduced Q_{\pm} . This *coherent* tune spread of

the envelopes due to the longitudinal bunch profile should not be confused with the *incoherent* tune spread of a transverse non-uniform distribution (such as the aforementioned Gaussian normal distribution).

In the case of linear coupling (through skew quadrupole components in the external magnetic fields), additional $K_{xy}\sigma_{x,y}$ coupling terms enter the envelope equations Eq. (6). This system of equations has been solved in Ref. [18] and two additional distinct odd modes are found (again restricting ourselves to stable beam conditions). For vanishing space charge, the two even quadrupolar modes Q_{\pm} reduce to $2Q_x$ and $2Q_y$, while the two odd modes essentially reduce to $|Q_x - Q_y|$ and $|Q_x + Q_y|$.

One more important ingredient to understand the eigenmodes within the quadrupolar spectrum of a beam with finite momentum spread is due to the dispersion function D_x generated by the horizontal bending magnets in a planar circular machine. With the dispersive contribution to the horizontal r.m.s. beam size,

$$\sigma_x^2 = \beta_x \epsilon_{x,\text{geo}} + D_x^2 \delta^2 \quad , \quad (9)$$

the set of coasting-beam envelope equations Eq. (6) correspondingly extends to a third equation for the dispersion function modified by space charge [19, 20]. This additional degree of freedom gives rise to yet another second-order eigenmode, the *coherent dispersion mode*. At zero current and no synchrotron motion, its tune Q_d is identical to the horizontal bare tune Q_x , while Q_d decreases with increasing space charge.

MEASUREMENTS

Set-up

In the PS, the stripline pick-up PR.BQL72 in section 72 is part of the base-band Q-measurement (BBQ) system. For our measurements, the four electrodes top (T), bottom (B), left (L) and right (R) are configured in quadrupolar mode yielding the following combined signal of induced voltages,

$$V_q = (V_L + V_R) - (V_T + V_B) \quad . \quad (10)$$

This combination results in the QPU time signal for the k th turn

$$\begin{aligned} S_{\text{QPU}}(k) &\propto \langle x^2 \rangle - \langle y^2 \rangle \\ &= \sigma_x^2(k) - \sigma_y^2(k) + \langle x \rangle^2(k) - \langle y \rangle^2(k) \quad , \quad (11) \end{aligned}$$

where $\langle \cdot \rangle$ refers to the integration over phase space $\int d^6 \zeta f(\zeta; k)$. Analogous to the set-up in [8], we are mainly interested in the frequency content of this signal in order to determine the quadrupolar eigenmodes of the proton beam. To this end, summation and subtraction of the induced electrode potentials are carried out in analog. Only then is the result digitised in order to improve the resolution of the generally very small quadrupolar signal amplitudes.

In order to measure the quadrupolar beam transfer function, we excite the beam via the kicker plates of the new TFB

system of the PSB in section 97. First, the orbit has been corrected to minimise the induced difference signal on the kicker plates. To increase the sensitivity, the 20 dB attenuators between the plate signals and the read-out electronics have been removed. The centred orbit should suppress dipolar feed-down of the quadrupolar excitation.

When pulsing the RF quadrupole at revolution frequency, i.e. $h = 1$, it acts like an additional static quadrupolar field to the beam. We characterised the strength of this RF quadrupole by measuring the tune difference comparing between no voltage and maximum amplitude (i.e. an input signal before the amplifier of 1 V peak-to-peak). The dipolar tunes have been determined by mixing all 43 BPM positions per plane [21] and evaluate the assembled signal via SUSSIX frequency analysis [22]. When scanning the relative phase between the RF quadrupole and the beam, we found a statistically significant maximum tune difference of $\Delta Q_x = 3 \times 10^{-3}$ and $\Delta Q_y = 2 \times 10^{-3}$.

This is a significant static impact on the beam, leading to the conclusion that the TFB in quadrupolar configuration should indeed be strong enough to resonantly excite the quadrupolar beam eigenmodes at the respective frequencies.

For the quadrupolar beam transfer function measurement, we start from a nominal LHC25 beam preparation cycle set-up in the PS. In the upstream injector, the Booster, the beams are prepared with a longitudinal acceptance bottleneck (equivalently to LHCINDIV beams) in order to achieve large transverse emittances and low intensities. The machine and beam parameters have been summarised in Table 1. The KV tune shift of the operational LHC25 beams is about a factor 5 higher (fivefold bunch intensity at roughly the same transverse emittance).

Table 1: PS Machine and Beam Parameters

Lorentz factor PS injection	$\gamma = 2.49$
revolution frequency	$f_{\text{rev}} = 437 \text{ kHz}$
beam intensity	$N = 0.3 \times 10^{12} \text{ ppb}$
number of bunches stored	1
transverse emittance	$\epsilon_{x,y} = 2.3 \text{ mm mrad}$
average betatron function	$\beta_x \approx \beta_y \approx 16 \text{ m}$
average dispersion	$D_x \approx 3 \text{ m}$
r.m.s. momentum deviation	$\sigma_{\delta} = 1 \times 10^{-3}$
bunch length	$B_L = 180 \text{ ns}$
synchrotron tune	$Q_s = 1.67 \times 10^{-3}$
KV space charge tune shift	$\Delta Q_{x,y}^{\text{KV}} = 0.02$

In the PS, usually the skew quadrupole magnets are powered as to provide strong linear coupling in the optics in order to suppress horizontal head-tail instabilities [23]. We removed the linear coupling globally within a small time window of 15 ms during the cycle by adjusting the skew quadrupole components using the closest tune approach [24]. During 12 ms of this window the TFB has been pulsed

Content from this work may be used under the terms of the CC BY 3.0 licence (© 2018). Any distribution of this work must maintain attribution to the author(s), title of the work, publisher, and DOI.

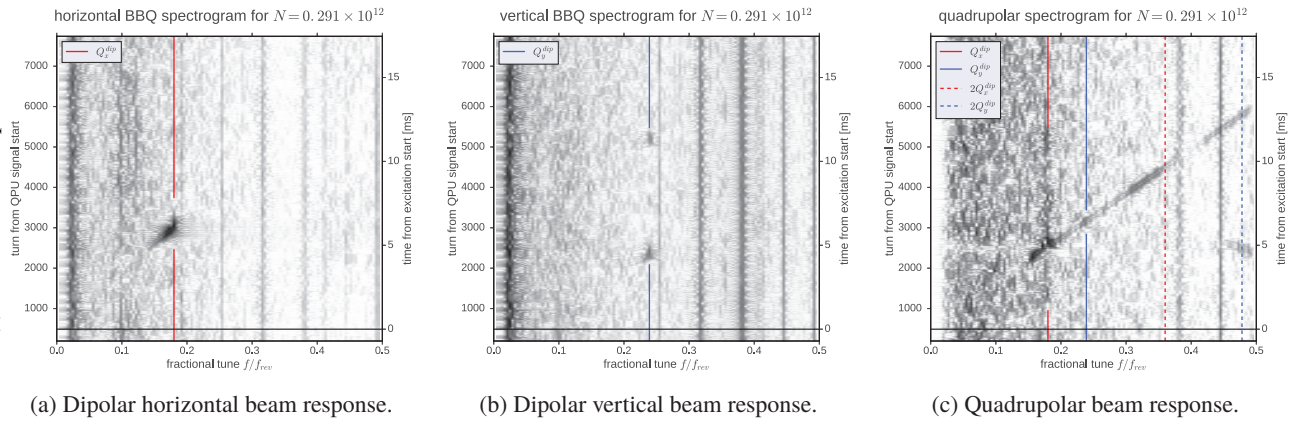


Figure 1: Spectrograms of dipolar BQS69 signals and the quadrupolar BQL72 signal.

in quadrupolar mode by means of an external waveform generator: its excitation signal was split for each transverse plane with one of the two channels inverted, amplified and eventually fed to the kicker plates. As the hybrid splitter and inverter were limited to RF above 2 MHz, we chirped between 2.19 MHz to 2.4 MHz corresponding to harmonic $5.01 \leq h \leq 5.49$. This swept frequency range covers all relevant quadrupolar eigenmodes for bare machine tunes below a fractional tune of $q_{x,y} \leq 0.25$. In principle, quadrupolar excitation at beam eigenfrequencies directly results in emittance growth – thus, the frequency sweep needs to be fast enough to treat this chirp as a mere perturbation to the beam. We ensured the validity of this assumption by comparing flying wire scan profiles before and after the excitation indicating negligible transverse r.m.s. emittance growth, $\Delta\epsilon_{x,y}/\epsilon_{x,y} \leq 5\%$.

Results

Along with the quadrupolar S_{QPU} signal we also recorded the dipolar signals from the shoe-box pick-up BQS69 with an optimised linear response. Figure 1 presents spectrograms of the corresponding dipolar and quadrupolar turn-by-turn data based on a 256 turn sliding FFT window. Figs. 1a and 1b show the tunes Q_x, Q_y as dipolar beam eigenmodes for the horizontal and vertical plane, respectively. Tune shifts from impedances and indirect space charge are of the order $O(10^{-3})$ [25], such that for the present low beam intensities the measured dipolar tunes do not differ significantly from the bare machine tunes. The quadrupolar signal S_{QPU} during the excitation is shown in Fig. 1c: note the two envelope bands below $2Q_x, 2Q_y$ which are absent in the dipolar spectra. The two instrumentation-based frequencies $0.381f_{rev}$ and $0.445f_{rev}$ are beam independent and are ignored here (similar irrelevant constant frequency lines exist in the dipolar spectra).

The turn where $S_{QPU}(k)$ maximally correlates with the reconstructed chirp excitation signal $I_{exc}(k)$ yields the start of excitation. The sinusoidal beam response contained in S_{QPU} can be interpreted like a modulation of the original excitation signal, in analogy to radio signal as a modulation

on top of a baseband frequency. Demodulation of $S_{QPU}(k)$ with the zero-padded $S_{exc}(k)$ and its 90° shifted quadrature signal $C_{exc}(k)$ (which can be obtained e.g. by a Hilbert filter) gives the in-phase I and quadrature Q components of the beam response,

$$I(k) = S_{QPU}(k) \cdot S_{exc}(k) \quad (12)$$

$$Q(k) = S_{QPU}(k) \cdot C_{exc}(k) \quad (13)$$

Filtering I and Q with a triangular Savitzky-Golay low-pass filter of 65 turns width then extracts the pure beam response content around the excitation baseband. Plotting the filtered amplitude $\sqrt{I^2 + Q^2}$ vs. the instantaneous excitation frequency $f_{exc}(k)$ yields the frequency response of the beam, which is depicted in Fig. 2. The two envelope bands are

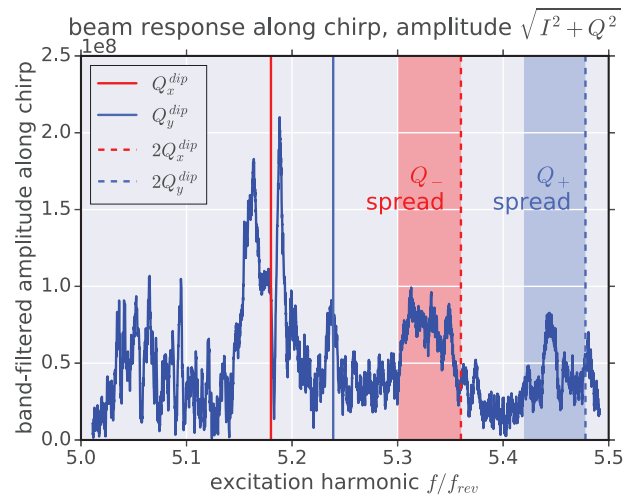


Figure 2: Demodulated frequency response of the beam.

indicated by “ Q_{\pm} spread”. The colour areas mark their estimated extents below the measured dipolar tunes $2Q_{x,y}$ of about

$$\Delta Q_+ \approx 0.058 \quad \text{and} \quad \Delta Q_- \approx 0.06 \quad (14)$$

Under the assumption that only direct space charge contributes to the envelope spread, applying Eq. (6) to these

values and the beam parameters of Table 1 yields KV tune shifts of $\Delta Q_x^{KV} \approx 0.05$ and $\Delta Q_y^{KV} \approx 0.04$ – twice as much as the computed value in Table 1 based on Eq. (1).

The beam response shows the dipolar peaks at Q_y and with small amplitude at Q_x . The latter is neighboured by a large and wide peak on the left and a narrow peak on the right. The left peak is a candidate for the coherent dispersive mode shifted downwards from Q_x by space charge.

NUMERICAL SIMULATIONS

PyHEADTAIL Simulations on the GPU with a 3D particle-in-cell space charge model yield the quadrupolar eigenmodes of the PS bunch. The macro-particle simulations are based on linear betatron motion in a constant focusing channel with non-linear synchrotron motion. Without taking into account dispersion and chromaticity, the simulated quadrupolar spectrum exhibits envelope bands whose width identically reproduces Eq. (7). When including effective dispersion at $D_x = 3$ m, the coherent dispersive mode enters the spectrum as a distinct peak located at Q_x . Increasing the synchrotron tune for vanishing space charge shows that the coherent dispersive mode splits into two peaks at $Q_x \pm Q_s$. This separation almost vanishes for the usual PS conditions at $Q_s = 0.0017$, cf. Table 1. For finite space charge, the coherent dispersive mode indeed shifts below Q_x as explained in the theory section. However, only including the natural linear chromaticity of the PS, $Q'_x = -0.83Q_x$ and $Q'_y = -1.12Q_y$, recovers the measured location of the coherent dispersive mode. Most importantly, chromaticity effectively broadens the width of the envelope bands to almost twice the value as observed without chromaticity. Figure 3 compares these simulation results for the $\sigma_x^2 - \sigma_y^2$ signal (without the dipolar contributions) to the measured beam frequency response. Applying SUSSIX frequency analysis reveals the contained side-band structure proving the influence of the longitudinal plane: the coherent dispersive mode splits into several peaks in distance of Q_s and the same happens to the envelope bands.

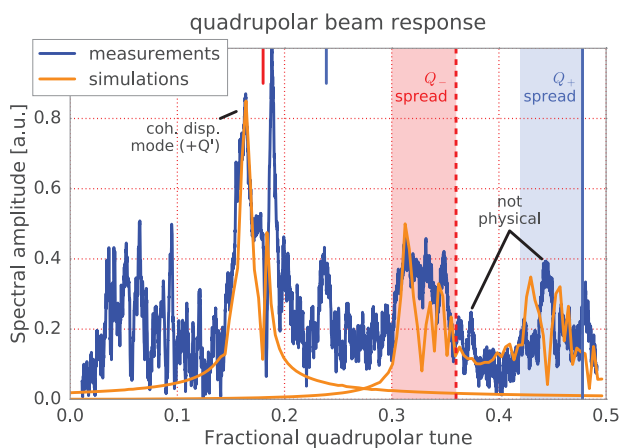


Figure 3: Comparison between measured beam frequency response and simulated eigenmodes.

CONCLUSION

This paper presented the direct measurement technique of space charge in units of the incoherent KV tune shift via the corresponding frequency shift of coherent quadrupolar i.e. second-order modes. The measured quadrupolar frequency response of bunched beam at the CERN PS shows the expected envelope bands. This clearly qualifies the PS hardware equipment: the kicker plates of the PS transverse feedback system in quadrupolar configuration sufficiently excite the beam to observe the typically rather weak envelope eigenmodes by the stripline pick-up, which thus proves to be sensitive enough. Furthermore, the second-order coherent dispersive mode has been identified as a significant spectral component. The comparison of the measurements with numerical simulations points out chromaticity as a major impact: finite chromaticity considerably modifies the quadrupolar eigenmodes by (i.) broadening the envelope bands and (ii.) splitting the coherent dispersive mode into side-bands. The former observation has necessarily to be taken into account when inferring the incoherent KV tune shift from the envelope band width.

Next steps for the on-going CERN studies include (i.) quadrupolar beam transfer function measurements at vanishing chromaticity, (ii.) further investigation of injection oscillations, in particular Chernin's odd envelope modes when injecting from decoupled transfer line optics into tightly coupled PS optics, and (iii.) dedicated space charge experiments such as resonance studies. A theoretical analysis of quadrupolar modes at finite linear chromaticity could vastly improve the present understanding, which to the knowledge of the author has so far not been investigated.

ACKNOWLEDGEMENTS

The author would like to thank Simon Albright, Heiko Damerau, Elias Métral, Guido Sterbini, Malte Titze and Panagiotis Zisopoulos for fruitful discussions as well as Marek Gasior, Tom Levens and Marcel Coly for their kind technical support. Research supported by the HL-LHC project.

REFERENCES

- [1] H. Damerou *et al.*, “LHC Injectors Upgrade, Technical Design Report, Vol. I: Protons,” Tech. Rep. CERN-ACC-2014-0337, Dec. 2014.
- [2] R. H. Miller, J. E. Clendenin, M. B. James, and J. C. Shepard, “Nonintercepting emittance monitor,” Stanford Linear Accelerator Center, Tech. Rep., 1983.
- [3] A. Jansson, “Noninvasive single-bunch matching and emittance monitor,” *Physical Review Special Topics-Accelerators and Beams*, vol. 5, no. 7, p. 072 803, 2002.
- [4] C.-Y. Tan, “Using the quadrupole moment frequency response of bunched beam to measure its transverse emittance,” Fermi National Accelerator Laboratory (FNAL), Batavia, IL, Tech. Rep., 2007.
- [5] M. Chanel, “Study of beam envelope oscillations by measuring the beam transfer function with quadrupolar pick-up and kicker,” in *European Particle Accelerator Conference (EPAC 1996)*, 1996, pp. 1015–1017.
- [6] T. Uesugi *et al.*, “Observation Of Quadrupole Mode Frequency And Its Connection With Beam Loss,” no. KEK-99-98, 1999.
- [7] R. C. Bär, “Untersuchung der quadrupolaren btf-methode zur diagnose intensiver ionenstrahlen,” Universität Frankfurt, Germany, 2000.
- [8] R. Singh *et al.*, “Observations of the quadrupolar oscillations at gsi sis-18,” in *International Beam Instrumentation Conference*, 2014.
- [9] A. Oeftiger, “Space Charge Effects and Advanced Modelling for CERN Low Energy Machines,” PhD thesis at EPFL, Lausanne, Switzerland, 2016.
- [10] K. Li *et al.*, “Code development for collective effects,” no. CERN-ACC-NOTE-2017-0008, WEAM3X01. 7 p, Jul. 2016.
- [11] A. Oeftiger and S. E. Hegglin, “Space charge modules for PyHEADTAIL,” no. CERN-ACC-2016-0342, MOPR025. 6 p, Jul. 2016.
- [12] I. M. Kapchinskij and V. V. Vladimirkij, “Limitations of proton beam current in a strong focusing linear accelerator associated with strong space charge,” in *International Conference on High Energy Accelerators*, 1959, pp. 274–288.
- [13] F. J. Sacherer, “Rms envelope equations with space charge,” *IEEE Transactions on Nuclear Science*, vol. 18, no. 3, pp. 1105–1107, 1971.
- [14] W. Hardt, “On the Incoherent Space Charge Limit for Elliptic Beams,” *CERN ISR-INT-300-GS-66-2*, Jan. 1966.
- [15] R. L. Gluckstern, “Oscillation Modes in Two Dimensional Beams,” in *Proton Linear Accelerator Conference*, vol. C700928, 1970, p. 811.
- [16] E. Métral, “General formula to deduce the space charge tune spread from a quadrupolar pick-up measurement,” no. CERN-ACC-2016-0097, MOPR024. 4 p, Jul. 2016.
- [17] P. M. Lapostolle, “Quelques propriétés essentielles des effets de la charge d’espace dans les faisceaux continus,” CERN, Geneva, Tech. Rep. CERN-ISR-DI-70-36. ISR-DI-70-36, Aug. 1970.
- [18] D. Chernin, “Evolution of RMS beam envelopes in transport systems with linear X-Y coupling,” *Part. Accel.*, vol. 24, pp. 29–44, 1988.
- [19] M. Venturini and M. Reiser, “Self-consistent beam distributions with space charge and dispersion in a circular ring lattice,” *Phys. Rev. E*, vol. 57, pp. 4725–4732, 4 Apr. 1998.
- [20] M. Venturini and M. Reiser, “Rms envelope equations in the presence of space charge and dispersion,” *Phys. Rev. Lett.*, vol. 81, pp. 96–99, 1 Jul. 1998.
- [21] P. Zisopoulos, F. Antoniou, E. Hertle, A.-S. Muller, and Y. Papaphilippou, “Transverse Tunes Determination from Mixed BPM Data,” no. CERN-ACC-2015-289, TUPJE042. 4 p, 2015.
- [22] R. Bartolini and F. Schmidt, “SUSSIX: A computer code for frequency analysis of non-linear betatron motion,” 1998.
- [23] E. Métral, “Theory of coupled Landau damping,” *Part. Accel.*, vol. 62, no. CERN-PS-99-011-CA, 259. 14 p, Feb. 1999.
- [24] P. P. Bagley and D. L. Rubin, “Correction of transverse coupling in a storage ring,” in *Particle Accelerator Conference, 1989. Accelerator Science and Technology., Proceedings of the 1989 IEEE*, Mar. 1989, 874–876 vol.2.
- [25] S. Persichelli *et al.*, “Chromaticity Dependence of the Transverse Effective Impedance in the CERN Proton Synchrotron,” no. CERN-ACC-2015-337, MOPJE047. 4 p, 2015.

BPM TECHNOLOGIES FOR QUADRUPOLEAR MOMENT MEASUREMENTS

A. Souнас*, M. Gasior, T. Lefevre
 CERN, Geneva, Switzerland

Abstract

Quadrupolar pick-ups (PU) have attracted particular interest as candidates for non-intercepting beam size and emittance measurements. However, their application has been proven to be limited. Two fundamental factors make beam size measurements with quadrupolar PUs exceptionally challenging: first, the low quadrupolar sensitivity of PUs and second, the parasitic position signal incorporated into the measured quadrupolar quantity. In this paper, the basic concepts of the quadrupolar measurements are reviewed with a special focus on the challenging nature of the measurements. Additionally, the potential use of existing beam position monitor (BPM) technology is studied. Recent tests performed with BPMs in the Large Hadron Collider (LHC) are discussed. Preliminary measurements demonstrate promising results.

INTRODUCTION

Quadrupolar moment measurement based on electromagnetic pick-ups (PU), like beam position monitors (BPM), have been widely studied as non-intercepting diagnostics to determine the transverse beam size and emittance [1–7]. They are based on the extraction of the second-order moment of the PU signals which contains information about the beam size. In particular, the beam size signal is incorporated into the quantity $\sigma_x^2 - \sigma_y^2$, where σ_x and σ_y are the r.m.s. beam dimensions in the transverse plane. Using at least two PUs at locations with different lattice parameters, the r.m.s. beam size and emittance can be evaluated by solving a linear system of equations [1, 8].

Despite the simplicity of the concept, quadrupolar measurements are very challenging in reality. Two fundamental factors make beam size measurements with quadrupolar PUs a difficult task. The first factor is related to the fact that the quadrupolar moment constitutes only a very small part of the total PU signal which is dominated by the monopole (intensity) signal. As a consequence, the quadrupolar moment can be easily lost due to imperfections in the measurement system such as asymmetries and electronic noise. The second factor concerns the parasitic signal from beam position incorporated into the quadrupolar moment together with the desirable beam size information as $\sigma_x^2 - \sigma_y^2 + x^2 - y^2$, where (x, y) is the beam centroid. As a consequence, the quadrupolar measurement may be dominated by the beam position signal if the beam is significantly displaced.

In this work, we study the potential use of existing BPM technologies for quadrupolar measurements. To this end, a detailed review of the above mentioned limitation factors

is first given in order to understand the challenges of the quadrupolar measurements. Several tests have been performed using some BPMs in the Large Hadron Collider (LHC). In order to efficiently cancel the parasitic effect of the beam position, an alignment technique based on movable PUs has been applied. Both absolute and differential measurements are discussed in terms of their performance and limitations. Preliminary measurements demonstrate the potentiality to use existing BPM technology as a basis for future quadrupolar measurement system.

MEASUREMENT APPROACH

In order to understand the principle of quadrupolar measurements, one can start by studying the 2D case of an electrostatic Pick-Up (PU) in a circular beam pipe, as illustrated in Fig.1. Assuming a relativistic beam, sufficiently longer than the PU buttons, the signal induced on the electrodes can be analytically approximated by the following multipole expansion, [2, 9],

$$U_{h1} = i_b(c_0 + c_1 D_x + c_2 Q + c_3 M_{3,x} + \dots) \quad (1a)$$

$$U_{h2} = i_b(c_0 - c_1 D_x + c_2 Q - c_3 M_{3,x} + \dots) \quad (1b)$$

$$U_{v1} = i_b(c_0 + c_1 D_y - c_2 Q + c_3 M_{3,y} + \dots) \quad (1c)$$

$$U_{v2} = i_b(c_0 - c_1 D_y - c_2 Q - \underbrace{c_3 M_{3,y} + \dots}_{\text{High Order Moments}}), \quad (1d)$$

High Order Moments

where i_b is the beam intensity, c_i are coefficients depending on the PU geometry and $D_{x/y}$, Q , and $M_{i \geq 3, x/y}$ are quantities which contain information about the beam position and size. In particular, the dipole terms, $D_{x/y}$, are directly connected to the beam position, i.e. $D_x = x$ and $D_y = y$. On the other hand, the second-order quadrupolar term, Q , contains information about both beam position and size and it is given by the following equation:

$$Q = \sigma_x^2 - \sigma_y^2 + x^2 - y^2. \quad (2)$$

Higher order terms can be neglected since they contribute much less to the total signal. The coefficients c_i are given as a function of the PU aperture radius, ρ , and the angular size of the buttons, a , according to the following equations [9]:

$$c_0 = \frac{a}{2\pi} \quad (3a)$$

$$c_1 = \frac{1}{\rho} \frac{2 \sin(a/2)}{\pi} \quad (3b)$$

$$c_2 = \frac{1}{\rho^2} \frac{\sin(a)}{\pi} \quad (3c)$$

$$c_3 = \frac{1}{\rho^3} \frac{2 \sin(3a/2)}{3\pi}. \quad (3d)$$

* apostolos.souнас@cern.ch

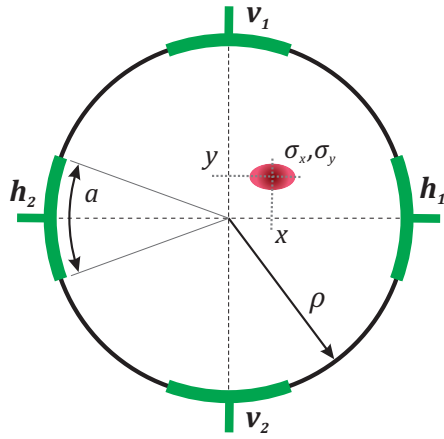


Figure 1: Cross-section of a circular button Pick-Up (PU). The PU aperture is equal to $d = 2\rho$ and each electrode has an angular width a . An infinitely long beam at position (x, y) with respect to the pipe centre is considered.

Looking at Eqs. (1), the monopole and dipole terms can be cancelled by subtracting the sum of the signals on each plane: $\Sigma_{hor} - \Sigma_{ver} = (U_{h1} + U_{h2}) - (U_{v1} + U_{v2})$. Then, using the following normalized quantity,

$$R_q = \frac{U_{h1} + U_{h2} - U_{v1} - U_{v2}}{U_{h1} + U_{h2} + U_{v1} + U_{v2}}, \quad (4)$$

one can get the quadrupole term as

$$Q = q_f R_q, \quad (5)$$

where $q_f = c_0/c_2$.

The previous analysis is not restricted only to the simplistic example of a 2D circular PU but can be extended to any family of capacitive PUs with different aperture shapes [10]. What changes in every case is the form of the coefficients c_i which is a unique property of the PU geometry.

CHALLENGES

Despite the simplicity of the concept, quadrupolar measurements have been shown to be challenging in reality. There are, fundamentally, two limitation factors that make beam size measurements via quadrupolar PUs a difficult task: first, the low quadrupolar sensitivity, c_2/c_0 , and second, the parasitic position signal, $x^2 - y^2$, incorporated into the quadrupolar term Q . Both factors may result in critical errors, as discussed in the following.

Low Quadrupolar Sensitivity

Considering the example of a 2D circular PU one can see from Eqs. (3) that each multipole moment M_i is inversely proportional to the factor ρ^i , i.e. $M_i \propto 1/\rho^i$. As a consequence, the contribution of the multipole terms to the electrode signals drops exponentially as the order i increases with a rate equal to $1/\rho$. In particular, the contribution of the quadrupolar moment to the total signal can be approximated as

$$\frac{M_2}{M_0} = \frac{c_2}{c_0} Q \propto (\sigma/\rho)^2, \quad (6)$$

where σ represents an effective beam size which, for simplicity, can be approach by the dominant beam size component, e.g. σ_x for a horizontally flat beam. Under the assumption of relativistic beams, Eq. (6) is valid for a wide range of different PU designs, [10], and gives a qualitative rule of thumb regarding the quadrupolar sensitivity.

In realistic cases, the factor $(\sigma/\rho)^2$ is significantly small due to the fact that PUs are normally designed with an aperture much larger than the nominal beam size in order to avoid particle losses. Therefore, the quadrupolar moment constitutes only a small part of the total PU electrode signal which is dominated by the monopole moment. As an example, the quadrupolar sensitivity of the LHC BPMs spans within the range $0.02 - 0.04 \text{ dB/mm}^2$ for PUs at locations where the beam size is expected to be in the order of $\sim 1 \text{ mm}$ at injection energy, i.e. at 450 GeV . It becomes, then, clear that the quadrupolar signal may be easily lost due to imperfections in the data acquisition process, like asymmetries or noise. As Fig. 2 demonstrates, even a slight cabling asymmetry between the PU channels in the order of few per milles leads to significant errors $\sim 20\%$.

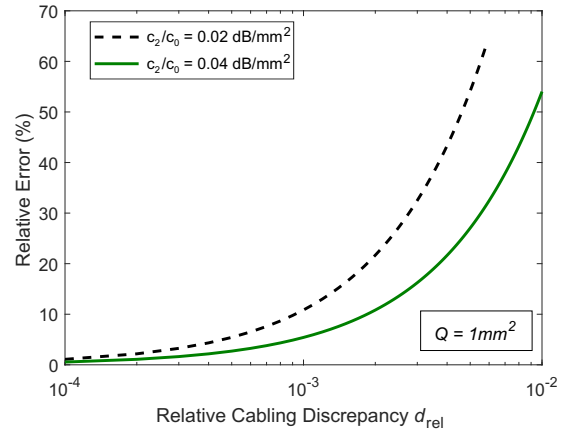


Figure 2: Relative error in quadrupolar measurement assuming a quadrupolar term $Q = 1 \text{ mm}^2$ and a slightly cabling asymmetry between the PU channels. In particular, three channels (e.g. h_1 , v_1 and h_2) are considered to have a nominal cabling response g , i.e. $V_{out} = gV_{in}$, while the 4th (e.g. h_2) has a relative cabling discrepancy d_{rel} , i.e. $V_{out} = (1 + d_{rel})gV_{in}$.

Parasitic Position Signal

Particle beams rarely traverse the center of a PU, adding parasitic position information to the quadrupolar moment. This parasitic signal, $Q_p = x^2 - y^2$, may remarkably deform the desired beam size information $Q_\sigma = \sigma_x^2 - \sigma_y^2$, even for small beam displacements, as shown in Fig. 3. To overcome this effect, the parasitic part, Q_p , can be subtracted from the total quadrupolar quantity Q by manipulating the PU as a normal BPM. In particular, by measuring the beam position, (x_m, y_m) , the beam size part, Q_σ , can be evaluated as $Q_{\sigma,m} = Q - x_m^2 + y_m^2$.

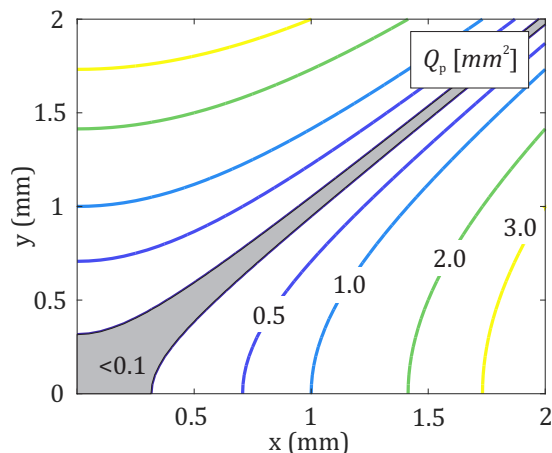


Figure 3: Parasitic position signal, Q_p for different beam displacements.

Although the above correction improves the measurement of Q_σ , a significant part of Q_p may remain under realistic conditions. Figure 4 depicts the expected error in Q_σ when some imperfections on the BPM system are considered. As can be seen, even for small errors in the position measurements, the error in Q_σ may be remarkably large for big beam displacements.

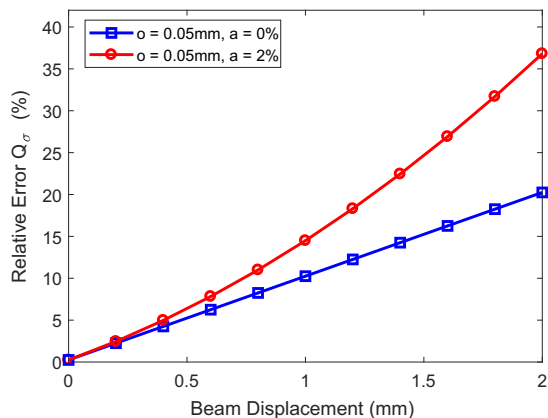


Figure 4: Relative error in Q_σ (beam size part), after the subtraction of Q_p (parasitic part) via position measurements. An offset o and a scaling factor a has been considered, i.e. $x_m = x + o + ax$. Only beam displacement in the horizontal plane has been taken into account.

MEASUREMENTS WITH EXISTING BPM TECHNOLOGY

BPMs constitute one of the most critical instrumentation system in particle accelerators. Their technology has been continuously advancing due to the need for precise position measurements for several kinds of beam configurations. Although BPMs design is optimized for position measurements the existing BPM technology can be potentially used as a basis for quadrupolar measurements.

In the context of LHC beam position measurement system several PUs are equipped with DOROS electronics, a diode-based acquisition system proved to provide stable and high resolution position measurements at some of the most critical LHC locations [11, 12]. Although these PUs are intended to work as BPMs, their signals are processed separately allowing us to perform quadrupolar measurements. Following, we present some tests we have performed using some of the existing LHC BPMs including collimator and circular button PUs.

Beam Centering via Movable PUs

As discussed in the previous Section, off-centered beams may result in crucial errors in quadrupolar measurements. Even if a direct subtraction via position measurements is applied, a significant part of the parasitic signal may remain under realistic conditions. To overcome this problem, the position signal can be efficiently cancelled by centering the beam via movable PUs, as demonstrated in a previous work [13]. In order to form 4-electrodes movable PUs we have used sets of horizontal and vertical collimators, as illustrated in Fig. 5. Profiting from the moving functionalities of collimators in both axes, these PUs can be aligned with the beam in order to remove the parasitic position part Q_p from the quadrupolar signal Q .

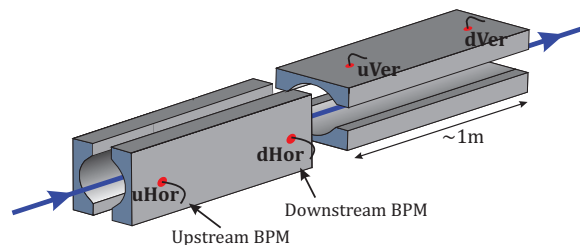


Figure 5: Schematic drawing of a Horizontal - Vertical collimator set in LHC with embedded BPMs. Two sets of BPMs are installed in each collimator forming in total four different combinations of 4-electrode PUs

The beam centering is performed within a two-step procedure. First, the PU is centred along the main axis (e.g. the Hor. axis for a Hor. collimator) using BPM position readings. However, this is not possible for the secondary axis (e.g. the Ver. axis for a Hor. collimator) since there are no electrodes to directly read the beam position. In this case, the center is detected through quadrupolar measurements by performing position scans along the secondary axis. In particular, as the PU moves away from the beam the quadrupolar moment changes quadratically according to Eq. (2). Therefore, the beam displacement is measured by detecting the extrema of the quadrupolar moment measurement, as shown in the example of Fig. 6.

To get a deeper insight on our measurements, Fig. 7 illustrates the absolute change on the quadrupolar term, $\Delta Q = Q - Q_0$, as the PUs move away from the measured beam location y_0 . Very good agreement between the measurements and the expected change due to the beam dis-

Content from this work may be used under the terms of the CC BY 3.0 licence (© 2018). Any distribution of this work must maintain attribution to the author(s), title of the work, publisher, and DOI.

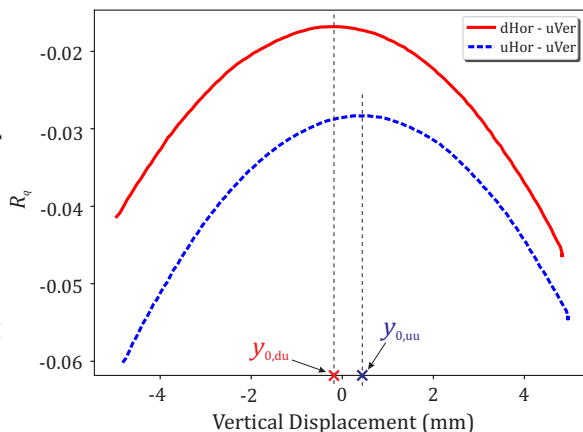


Figure 6: Normalized quantity R_q (see Eq. (4)) as measured during a vertical scan of a horizontal collimator. The collimator aperture is 33.2mm . The vertical displacement is measured by using a Linear Variable Differential Transformer (LVDT) system [11]

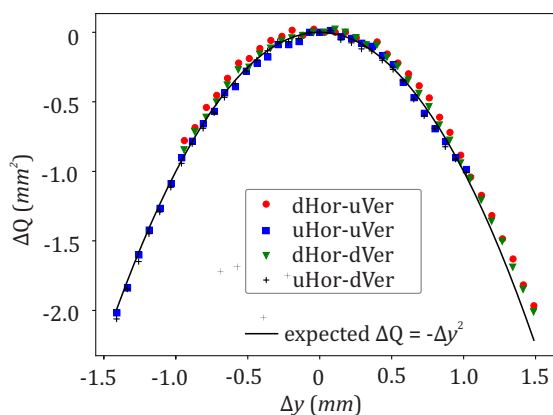


Figure 7: Change of the quadrupolar term, ΔQ , as measured during the vertical scan of the example of Fig. 6. The aperture of both horizontal and vertical PUs is 33.2mm . Coefficient q_f (see Eq. (5)) has been numerically derived via 3D electromagnetic simulations.

placement is shown for all the different PU combinations demonstrating a first validation of our quadrupolar measurements.

Absolute and Differential Measurements

Looking carefully at the results obtained through the beam alignment process, we can extract some important information about the quality of the quadrupolar measurements. As observed in Fig. 6, the locations of the extrema during the vertical scan differ not only in the horizontal axis (information about the beam center) but also in the vertical one. In fact, the difference on the normalized quantity R_q can be directly translated into a difference in the absolute quadrupolar measurement since $Q = q_f R_q$. For the particular example of Fig. 6, this difference is $Q_{du} - Q_{uu} \sim 2.5\text{mm}^2$ which is significantly large contrary to the fact that the two BPM sets are placed one close to each other. On the other hand,

differential measurements present a very good trend since all the BPM sets follow the expected behaviour as shown in Fig. 7.

To better understand the behaviour of the quadrupolar measurements we have performed some emittance scans, forced by the LHC transverse damper (ADT) system [14]. To ensure that the influence of the parasitic position signal is negligible we had first applied the beam centering procedure as previously described. Figure 8 illustrates results as obtained using a full set of four Hor.-Ver. collimator BPMs during a horizontal emittance blow-up. Looking at the absolute quadrupolar measurements (left side) we can clearly observe discrepancies between the four BPM sets. However, despite the large offsets, the measurements demonstrate a stable behaviour of the system. Taking out the offsets (right side) a nice agreement between all the different BPM sets is observed during the blow-up. As expected, the quadrupolar quantity increases in consistency with the emittance blow-up in the horizontal plane (a decrease would be expected in the case of a vertical blow-up).

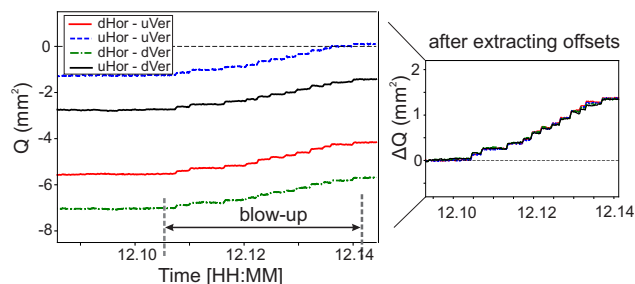


Figure 8: Quadrupolar measurements during an emittance blow-up forced by the LHC Transverse Damper system (ADT). A Hor.-Ver collimator BPM setup has been used. Left: Absolute measurements. Right: Differential measurements (extracting all the offsets at the beginning of the blow-up).

Taking profit of the good differential measurements, we have also performed quadrupolar measurements during the LHC energy ramp. For these measurements, collimator BPMs are not suitable since the beam presents significant displacements during the ramp. Instead, we have preferred some circular button BPMs, fixed to the beam pipe, at locations with small beam position change during the ramp. Figure 9 illustrates the quadrupolar evolution as measured by the selected BPMs. The evolution is in consistency with the behaviour expected by the optics model and according to the lattice parameters given in Table 1. In particular, the quadrupolar signal increase when $\beta_x < \beta_y$ since $Q \approx \sigma_x^2 - \sigma_y^2 < 0$ and because the beam size shrinks during the ramp. In contrast, the opposite behaviour is expected when $\beta_x > \beta_y$. To validate even more the BPM measurements comparative values as obtained using Wire Scanners measurements are depicted. As can be seen, the BPM measurements are in very good agreement with the Wire Scanners ones during most of the ramp evolution time.

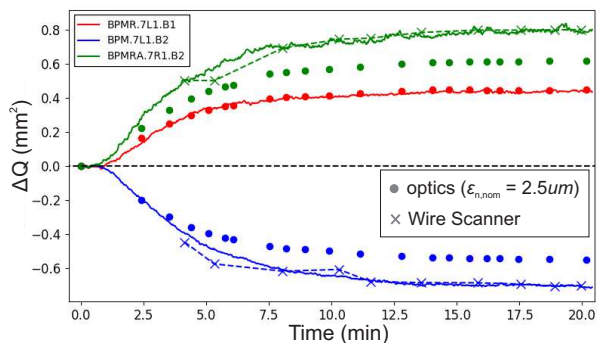


Figure 9: Differential quadrupolar measurement during an LHC energy ramp from 450 GeV to 6.5 TeV. Three circular button BPMs have been used. Results corresponding to the optics model (assuming nominal emittance) and to measurements from Wire Scanners are depicted as well.

Table 1: Lattice Parameters (β_x, β_y) [m] at Start and End of LHC Ramp

	450 GeV	6.5 TeV
BPMR.7L1.B1	(48, 141)	(41, 143)
BPM.7L1.B2	(168, 56)	(140, 36)
BPMRA.7R1.B2	(62, 187)	(53, 138)

CONCLUSION

This paper reviewed the challenges of beam size measurements via quadrupolar PUs in connection with some recent beam measurements using existing BPM technology. Two limitation factors make beam size measurements with quadrupolar PUs a difficult task: first, the low quadrupolar sensitivity and second, the parasitic effect of beam position. To examine the possible use of existing BPM technology for quadrupolar measurements several tests have been performed in LHC. The parasitic position signal has been efficiently removed by using collimators with embedded BPMs which allow beam centering at the PU locations. Through several tests, it was demonstrated that differential measurements provide promising results and can be potentially used to measure the emittance evolution during the energy ramp. On the other hand, absolute measurements are dominated by large and systematic offsets. These can potentially come from small asymmetries between the four PU electrodes. To this end, new calibration schemes, able to take into the challenging nature of the quadrupolar measurements, are currently being ventured.

ACKNOWLEDGEMENTS

The authors would like to thank the LHC collimation team and especially G. Valentino, A. Mereghetti and S. Redaelli for their kind support during the beam measurements with collimator BPMs. We would like also to thank J. Olexa for his invaluable help in the commissioning of DOROS electronics.

REFERENCES

- [1] R.H. Miller, J.E. Clendenin, M.B. James, and J.C. Sheppard, “New methods of measuring emittance using beam position monitors”, in *Proc. 12th Int. Conf. on High Energy Accelerators (HEAC’83)*, Fermilab, IL, USA, 1983, pp. 603–605.
- [2] S.J. Russell and B.E. Caristen, “Measuring Emittance Using Beam Position Monitors”, in *Proc. 1993 Particle Accelerator Conf. (PAC’93)*, Washington, DC, USA, 1993, pp. 2537–2539.
- [3] T. Suwada, “Multipole Analysis of Electromagnetic Field Generated by Single-Bunch Electron Beams”, *Jpn. J. Appl. Phys.*, vol. 40, pp. 890–897, Jan. 2001.
- [4] A. Jansson, “Noninvasive single-bunch matching and emittance monitor”, *Phys. Rev. ST Accel. Beams*, vol. 5, no. 7, p. 072803, 2002.
- [5] P. Li, B.G. Sun, Q. Luo, X.H. Wang, H.L. Xu and P. Lu, “New methods of measuring emittance using beam position monitors.”, in *2007 IEEE Nuclear Science Symposium (NSS’07) Conf. Record*, Honolulu, Hawaii, USA, 2007, pp. 1675–1678.
- [6] K. Yanagida, S. Suzuki, and H. Hanaki, “Design study of beam position monitors for measuring second-order moments of charged particle beams”, *Phys. Rev. ST Accel. Beams*, vol. 15, no. 1, p. 012801, Jan. 2012.
- [7] Z-J. Wang *et al.*, “Noninterceptive transverse emittance measurements using BPM for Chinese ADS R&D project”, *Nucl. Inst. Meth. Phys. Res., Sect. A*, vol. 816, pp. 171–175, 2016.
- [8] A. Jansson, “Non-Invasive Measurement of Emittance and Optical Parameters for High-Brightness Hadron Beams in a Synchrotron”, Ph.D. thesis, Phys. Dept., Stockholm University, Sweden, and CERN, Geneva, Switzerland, Rep. CERN-PS-2001-014-OP, CERN-THESIS-2001-03, 2001.
- [9] J.A.T. Kamga, W.F.O Müller, and T. Weiland, “Analytical and numerical calculation of the second-order moment of the beam using a capacitive pickup”, *Phys. Rev. Accel. Beams*, vol. 19, no. 4, p. 042801, Apr. 2016.
- [10] S.S. Kurennoy, “Nonlinearities and effects of transverse beam size in beam position monitors”, *Phys. Rev. ST Accel. Beams*, vol. 4, no. 9, p. 092801, 2001.
- [11] G. Valentino *et al.*, “Final implementation, commissioning, and performance of embedded collimator beam position monitors in the Large Hadron Collider”, *Phys. Rev. Accel. Beams*, vol. 20, no. 8, p. 081002, Aug. 2017.
- [12] M. Gaşior, G. Baud, J. Olexa, G. Valentino, “First Operational Experience with the LHC Diode Orbit and Oscillation (DOROS) System.”, in *Proc. 5th Int. Beam Instrumentation Conf. (IBIC’16)*, Barcelona, Spain, 2016, paper MOPG07.
- [13] A. Sounas *et al.*, “Beam Size Measurements Based on Movable Quadrupolar Pick-ups.”, in *Proc. 9th Int. Particle Accelerator Conf. (IPAC’18)*, Vancouver, BC, Canada, 2018, paper WEPAF080.
- [14] E. Gorbachev *et al.*, “Transverse damping systems for the future CERN LHC”, in *Proc. 2001 Particle Accelerator Conf. (PAC’01)*, Chicago, IL, USA, 2001, vol. 2, pp. 1237–1239.

ESS nBLM: BEAM LOSS MONITORS BASED ON FAST NEUTRON DETECTION

T. Papaevangelou[†], H. Alves, S. Aune, J. Beltrami, Q. Bertrand, B. Bolzon, M. Combet, T. Bey, N. Chauvin, D. Desforge, M. Desmons, Y. Gauthier, E. Giner-Demange, A. Gomes, F. Gougnaud, F. Harrault, F. J. Iguaz, T. Joannem, M. Kebbiri, C. Lahonde-Hamdoun, P. Le Boulout, P. Legou, O. Maillard, Y. Mariette, A. Marcel, J. Marroncle, C. Marchand, M. Oublaïd, V. Nadot, G. Perreu, O. Piquet, B. Pottin, Y. Sauce, L. Segui, F. Senée, J. Schwindling, G. Tsiledakis, R. Touzery, O. Tuske, D. Uriot, IRFU, CEA, Université Paris-Saclay, F-91191 Gif-sur-Yvette, France
M. Pomorski, CEA-LIST, Diamond Sensors Laboratory, F-91191, Gif sur Yvette, France
I. Dolenc-Kittelmann, R. Hall-Wilton¹, C. Höglund², L. Robinson, P. Svensson, T. J. Shea, European Spallation Source ERIC, SE-221 00, Lund, Sweden

¹also Mid-Sweden University, SE-851 70, Sundsvall, Sweden

²also Thin Film Physics Division, Department of Physics, Chemistry and Biology (IFM), Linköping University, SE-581 83 Linköping, Sweden

V. Gressier., IRSN, BP3, 13115 Saint-Paul-Lez-Durance, France

K. Nikolopoulos, School of Physics and Astronomy, University of Birmingham, B15 2TT, UK

Abstract

A new type of Beam Loss Monitor (BLM) system is being developed for use in the European Spallation Source (ESS) linac, primarily aiming to cover the low energy part (proton energies between 3-100 MeV). In this region of the linac, typical BLM detectors based on charged particle detection (i.e. Ionization Chambers) are not appropriate because the expected particle fields will be dominated by neutrons and photons. Another issue is the photon background due to the RF cavities, which is mainly due to field emission from the electrons from the cavity walls, resulting in bremsstrahlung photons. The idea for the ESS neutron sensitive BLM system (ESS nBLM) is to use Micromegas detectors specially designed to be sensitive to fast neutrons and insensitive to low energy photons (X and gammas). In addition, the detectors must be insensitive to thermal neutrons, because those neutrons may not be directly correlated to beam losses. The appropriate configuration of the Micromegas operating conditions will allow excellent timing, intrinsic photon background suppression and individual neutron counting, extending thus the dynamic range to very low particle fluxes.

INTRODUCTION

The high intensity of the ESS beam implies that even a loss of a small fraction of the beam could result in significant irradiation and destruction of accelerator equipment. The Beam Loss Monitor systems must be capable of detecting the smallest possible fraction of beam loss, approaching 0.01 W/m loss, preventing activation of machine components and allowing hands-on maintenance. Two types of BLM systems will be deployed, each providing unique capabilities [1-3]. The first type is based on an ionization chamber (ICBLM) [4], a simple and proven detector, but with reduced ability to discriminate beam losses in

the low energy part of the linac against background from the accelerating structures [5]. The second type (nBLM) is based on a neutron sensitive detector with a Micromegas readout [6]. This is a system of higher complexity, but with the ability to discriminate between neutrons produced by loss of low energy protons, and photons produced by field emission in the cavities.

The two systems will cover the linac complementarily, with the nBLM aiming primarily to cover the low energy part of the accelerator (up to 90MeV) and the ICBLM the high energy part. Monte Carlo simulations are used to optimize the locations of the detectors, such that coverage and redundancy are provided for machine protection and spatial resolution is provided for diagnostic purposes [7].

THE ESS NBLM SYSTEM

Micromegas [8, 9] is a Parallel Plate Detector (PPD) with three electrodes, cathode, micromesh and anode. The micromesh separates the two regions of the detector: the conversion or drift region between the cathode and the micromesh where the primary ionization occurs and the amplification region between the micromesh and the anode, which is narrow, typically 50-100 microns wide. Since its invention in 1996 by I. Giomataris and G. Charpak, Micromegas has been used in many different applications and particle physics experiments. As all Micro Pattern Gaseous Detectors (MPGD), Micromegas offers robustness, high gain, fast signals, high rate capabilities, better aging properties, low cost and simplified manufacturing processes compared to traditional gaseous detectors.

The flexibility in the choice of the gas, the operating conditions and the construction materials allows us to tune the sensitivity of the detector to the different particles and adapt its response to specific experimental requirements. Using appropriate neutron-to-charge converters and neutron absorbing materials, it is possible to adapt the detector to a wide range of neutron measurements [10].

[†] email address : thomas.papaevangelou@cea.fr

Micromegas for Neutron Detection

The Micromegas detectors for the ESS nBLM system are specifically designed to be sensitive to fast neutrons and intrinsically insensitive to photons (X- and γ -rays), while signals from thermal neutrons are suppressed.

The detection of the fast neutrons is performed with two different approaches (Figure 1). In one approach we use a hydrogen rich convertor in order to detect the proton recoils that are created by the elastic scattering of the incoming neutrons. In this setup, the detector is intrinsically blind to low energy neutrons because only the fast ones ($E_n > \sim 0.5$ MeV) can create recoils with significant range to enter the detector drift region. The suppression of gammas is based on the much smaller ionization of the gas by the photo-electrons compared to proton recoils. This kind of detector has a preferred direction for neutron detection, while the efficiency ranges between $10^{-5} - 10^{-3}$ for neutron energies 0.5 - 10 MeV. The timing response of such detector is very fast (at the level of ns) and the duration of a neutron induced signal is of the order of 50 - 100 ns.

In the second approach we use as convertor a material with high (n, α) cross-section, such as ^{10}B and we surround the detector with a neutron moderator (i.e. polyethylene). In order to reject incoming slow neutrons, we use an external neutron absorber like boron-rich rubber, with the cut-off energy determined by the absorber thickness. The gamma rejection is based again on the difference in the ionization between electrons and alphas or heavier ions. Such a detector has 4π acceptance for neutrons. The detection efficiency is practically constant over a large energy range (from eV up to tens of MeV) and as high as few %. However, the neutron moderation process will delay a big part of the events for times from some 10 ns to 200 μs .

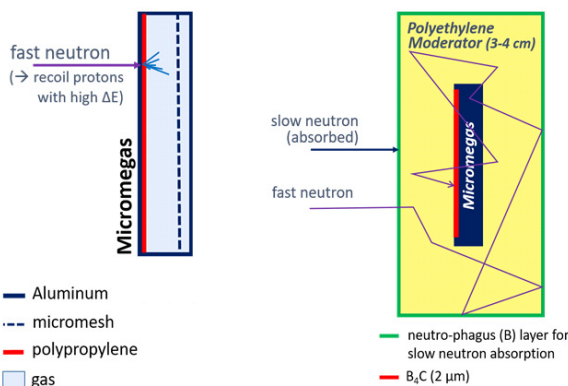


Figure 1: Neutron detection principle of the “fast” (left) and of the slow detector (right).

Both detectors will be operated in counting mode, being thus sensitive to individual neutrons, but in case of very high fluxes they will pass automatically to current mode.

Detector of the ESS nBLM System

A common design has been adopted for both fast and slow detector chambers, the only difference being the cathode (drift) electrode. In the case of the fast detector it is a 125 μm Mylar foil with an aluminum deposit of 50 nm in

order to apply the polarization voltage. This was preferred to aluminized polypropylene (1 mm thick) due to the long term stability of the aluminum layer, though it is less efficient for neutron detection by a factor ~ 2 . The foil is glued to an aluminum plate for robustness.

In the case of the slow detector, the drift electrode consists of an Al plate that is coated with $^{10}\text{B}_4\text{C}$. Various thicknesses between 0.2 and 1.5 μm were chosen, allowing to tune the detector by up to a factor of 7.5. The samples were prepared using direct current magnetron sputtering from $^{10}\text{B}_4\text{C}$ sputtering targets (with a ^{10}B enrichment of $> 96\%$) in an industrial coating unit (CC800/9, CemeCon AG, Germany) in the ESS Detector Coatings Workshop in Linköping, Sweden. The coating parameters were similar to the ones used in [11-13] and fulfill the requirements for film purity, homogeneity, and long-term stability.

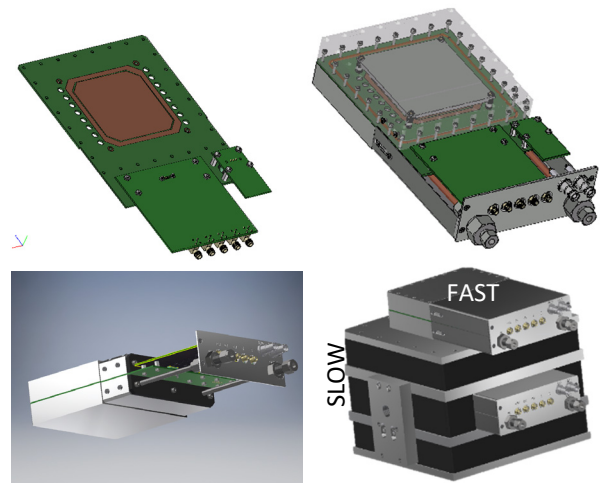


Figure 2: Schematic view of the Micromegas readout and chamber. Assembly of one fast and one slow detector including polyethylene moderator and borated rubber absorber.

The active area of the detector is $8 \times 8 \text{ cm}^2$, segmented in 4 strips that can be read independently or as one. The Micromegas is built with the standard bulk technique [14] and is filled with a mixture of He + iC_4H_{10} (10%). The aluminium plate with the neutron convertor is placed at a distance of 1-5 mm from the mesh, defining the conversion (or drift) region of the detector. The chamber dimension is $15 \times 25 \times 5 \text{ cm}^3$, while for the slow detector with the polyethylene moderator it is $25 \times 25 \times 15 \text{ cm}^3$. The detectors can be deployed independently or as an assembly of one fast and one slow module (Figure 2). A total of 42 fast and 42 slow detectors will be deployed along the ESS accelerator mostly at the region of the MEBT, DTLs and Spokes [1, 2].

Each detector will be equipped with a front-end electronics card (FEE), which includes 2 FAMMAS current amplifiers (Fast Amplifier Module for Micromegas ApplicationS) [15], low voltage filters and two output driver buffers. The consumption of the card is less than 200 mW and allows the operation in both counting and current mode.

Content from this work may be used under the terms of the CC BY 3.0 licence (© 2018). Any distribution of this work must maintain attribution to the author(s), title of the work, publisher, and DOI.

System Architecture

The architecture of the ESS nBLM system is shown in Fig. 3. Besides the Micromegas detectors, it includes: the back-end electronics (BEE) and data acquisition system (DAQ), high and low voltage power supplies, the gas recirculation system and the user interface and data archiving system. As with most other ESS diagnostic systems, the nBLM BEE is based on the MicroTCA.4 platform, while EPICS servers are used for the controls and monitoring.

The acquisition of the analogue signal of each detector is done by an IOxOS IFC_1410 AMC which is planned to be equipped with one IOxOS ADC_3111 FMC boards. Each FMC board has 8 channels and is acquiring data at

250 MS/s. The IFC carrier is equipped with FPGA devices which perform the real time signal processing without dead time. The Micromegas detector is a proportional avalanche chamber, where individual neutrons can create a pulse. The acquisition can be performed both in counting or current mode, passing automatically to each mode depending on the actual particle rate. A value of the number of counts and the current per μs , correlated to the beam loss can be used for the machine protection and monitoring purposes. The counting mode allows the monitoring of very low losses in long terms, while simulations performed with GEANT4 show that the detectors can give multiple counts within $1 \mu\text{s}$ when low energy protons are lost at level of 0.01 W/m .

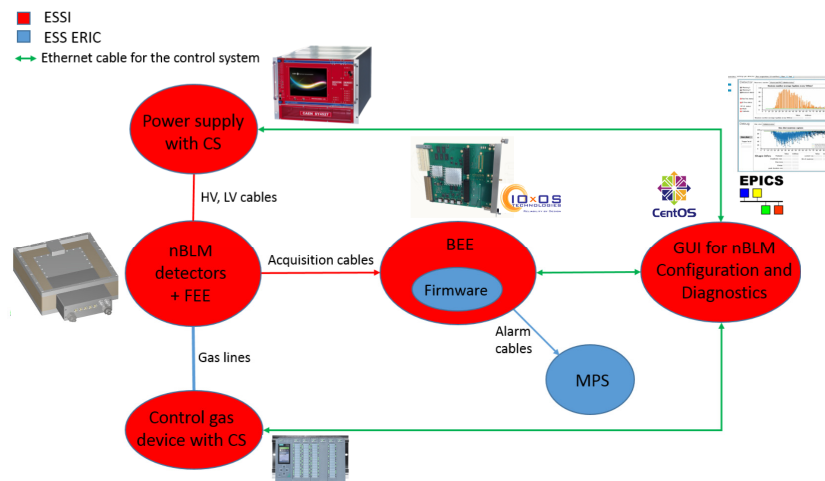


Figure 3: Architecture of the EPICS based Control System of ESS nBLM. The fast acquisition and the communication to ESS Machine Protection System is done by FPGAs running on a MicroTCA.4 platform.

In order to guarantee a stable operation on a time scale of years, the nBLM chambers will need a continuous flow of gas at the level of 0.1 l/h . The detectors will be grouped in series in six gas lines running along the linac. A PLC with Siemens S7-1500 CPU will be in charge of controlling and monitoring the gas flow. The detectors are designed to be able to perform stably for several hours in case the flow is interrupted, while the system will be able to detect a leak or the presence of impurities in the line and provide the health status to the EPICS GUI. The GUI will also control several CAEN SY4527 crates, which will be used to control the high and low voltage power supplies. The 48 channel CAEN A7030 cards will provide the HV on the mesh (-500V) and the drift (-700V) of each Micromegas detector in independent lines. The 8 channel CAEN A-2519 modules will be used to power the FEE cards, using 1 channel per group of 2-6 detectors.

DETECTOR PERFORMANCE

The ESS nBLM is an innovative system that has not been used before in accelerator diagnostics. Thus, the response of the system to the ESS linac conditions can only be estimated based on Monte Carlo simulations and detector tests in other facilities.

The simulations that were performed during the design and optimization phase of the project have shown that, under different scenarios [2, 7], a full beam loss in the DTL region would imply a significant number of counts in the nearest detectors in the first μs after the loss (few tens when the loss is at the first DTL, $>10^4$ when at the last one) [16]. This response would allow the early signalization in case of accidental loss, while the relative response of the detectors deployed along the linac will provide information for the location of the loss. In the case of normal operation, the system will be sensitive to very low neutron fluxes, providing valuable data for material activation and beam tuning.

The actual calibration of beam losses as a function of the count rate will be done during the commissioning phase of the linac. Meanwhile, we have performed detector tests in several facilities in order to validate the simulations, optimize the design and provide a proof of principle. More tests are planned, including one in Linac4 by September 2018.

Efficiency for Neutrons - Gamma Suppression

The AMANDE facility at IRSN [17], situated at Cadarache center, provides monoenergetic neutron fields, appropriate to measure the detection efficiency as a function of the neutron energy. The measurements (Figure 4) were performed in March 2018. The first results from the analysis allowed us to fix some parameters of the detectors, such

as the material of the neutron converter of the fast detector and the B₄C layer thickness and the size of the polyethylene moderator of the slow one.



Figure 4: The setup at the AMANDE facility. The actual detector under testing is the slow one (white), while the fast one (black) was moved on the side.

The measured detection efficiency of the fast detector is shown in Fig. 5, and for the slow for different moderator thickness in Fig. 6. The efficiency of the slow detector is calculated taking into account the surface of the moderator (25×25 cm²) and not only the active area (8×8 cm²). This implies that the detector would give a count rate of few s⁻¹ for a neutron fluence rate of 1 s⁻¹cm⁻².

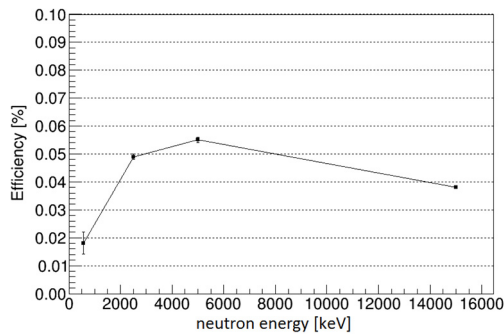


Figure 5: Neutron detection efficiency of the fast detector as a function of the neutron energy.

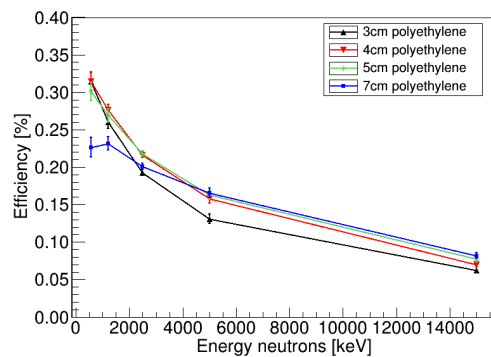


Figure 6: Neutron detection efficiency of the slow detector for different thicknesses of the polyethylene moderator.

In the case of 565 keV neutron field, a LiF target is used. There is therefore a contamination by 6-7 MeV gammas

coming from the ¹⁹F(p, αγ)¹⁶O reaction. By using an AlF₃ target with the same thickness of fluorine, it is possible to isolate the response of the detector to gammas compared to the mixed field. The results are shown in Fig. 7 for the fast and in Fig. 8 for the slow detector.

Even though that 565 keV is very close to the lower limit of the sensitivity of the fast detector, it is clear that applying a threshold in the pulse amplitude it is possible to completely suppress the gammas while maintaining a good efficiency for the neutrons. As mentioned before, this suppression is an intrinsic characteristic of the detector and is due to the much higher ionization power of the proton recoils compared to the electrons that are produced by the gammas. It can be optimised with the choice of the operating voltages, the gas and the drift gap.

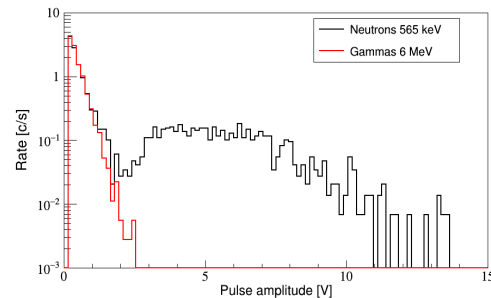


Figure 7: Response of the fast detector to the gammas from the ¹⁹F(p, αγ)¹⁶O reaction and to the mixed field of gammas and 565 keV neutrons.

In the case of the slow detector the suppression is even stronger, because the ionization is caused by the α or ⁷Li particles emitted by the ¹⁰B(n,α)⁷Li reaction. This allows us to reduce the drift gap (it was 0.4 mm compared to 2 mm for the fast) and the detector gain, suppressing thus the gammas even further. In parallel, since most of the reactions are caused by thermalized neutrons, the same suppression factor is possible independently of the initial energy of the incoming neutron.

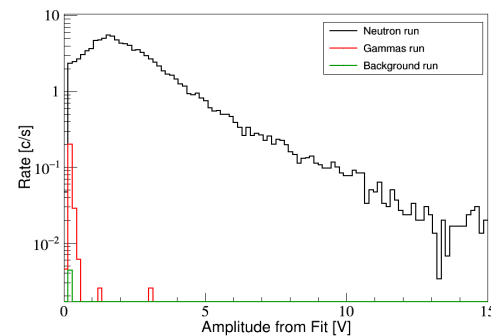


Figure 8: Response of the slow detector to the gammas from the ¹⁹F(p, αγ)¹⁶O reaction and to the mixed field of gammas and 565 keV neutrons.

Time Response – Proof of Principle

During the 1st quarter of 2018 a series of tests were performed at the IPHI proton beam at CEA Saclay [18]. In part of those tests, a Be target was used in order to produce a

Content from this work may be used under the terms of the CC BY 3.0 licence (© 2018). Any distribution of this work must maintain attribution to the author(s), title of the work, publisher, and DOI.

neutron field. Both nBLM prototypes were used in order to measure the neutron flux distribution, but also to study the response of the detectors in a pulsed beam.

The energy of the proton beam was 3 MeV and the duration of a pulse about 90 μs , at a repetition frequency of 1 Hz. The data were taken using the FAMMAS amplifiers, which allowed us to study the pulse characteristics, (risetime, duration and amplitude distributions, noise) and develop the algorithms to be used in the FPGA of the ESS nBLM acquisition system.

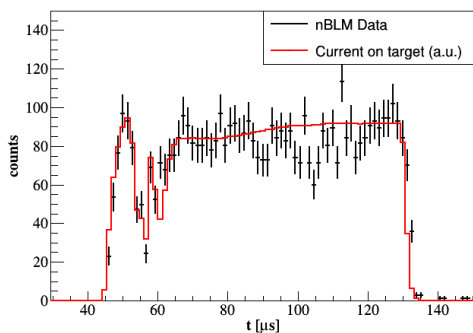


Figure 9: Time response of the fast detector in comparison with the intensity of current in the target.

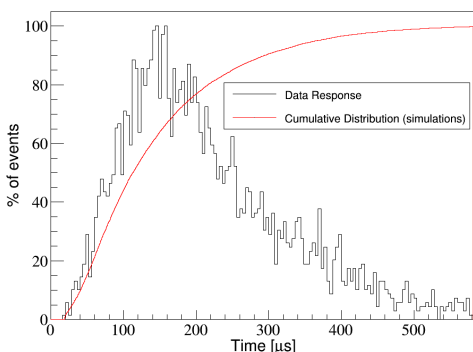


Figure 10: Time structure of the events in the slow detector following the 100 μs proton beam pulse. The response is slow due to the moderation time of the neutrons in the polyethylene, represented here by the red curve that shows the cumulative distribution of the events from a simulated instantaneous pulse.

The results verified the behavior predicted by the simulations [16]. The fast detector has an immediate response and the count rate is in direct correlation with the intensity of the beam current, as it was measured in the target (Fig. 9). In the case of the slow detector, due the moderation time most of the events are recorded with a delay of 100-200 ns. In Fig. 10 the simulated cumulative distribution of the recording time is represented in red, while the measured response to the IPHI pulse is shown in black. However, due to the much higher efficiency of the slow detector compared to fast, a significant number of the events (~5% of the total) will be register within the first μs , so also the slow detector can be used for an early warning in case of accidental beam loss.

We kept taking data with the nBLM prototypes at IPHI even when the Be target was replaced by an Al endcap, and the detectors were still able to register neutron counts. This is an important observation, showing that the detectors have the potential to see beam losses already at the region of the ESS MEBT ($E_p = 3.5$ MeV).

A more systematic proof of principle came from the tests performed at the MC40 Cyclotron of Birmingham University [19], where we irradiated an Al plate with a 28 MeV proton beam. The correlation of the measured count rate and the beam intensity was linear and is shown in Fig. 11. Further tests are planned in order to quantify the neutron yield for materials that are used in the ESS linac.

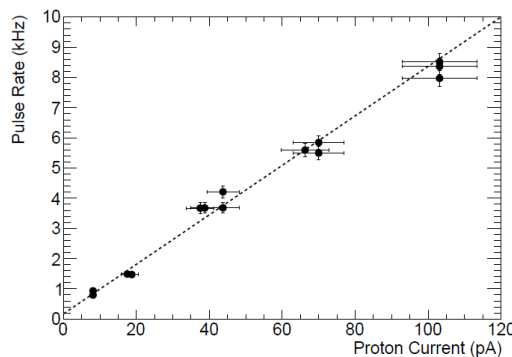


Figure 11: Correlation of the measured count rate with the intensity of the proton beam hitting an aluminium target.

The behaviour of the Micromegas under very high particle fluxes was studied in the facilities of the Orphée nuclear reactor at CEA Saclay. The slow detector, without the moderator, was exposed to 0.01 eV neutrons at a flux of $2 \times 10^6 \text{ s}^{-1} \text{ cm}^{-2}$ operating stably, without discharges. The analysis of the results is ongoing, aiming to the optimization of the detector operation parameters.

CONCLUSIONS

A new type of beam loss monitors is being developed for ESS, based on fast neutron detection with Micromegas detectors. The system is designed to operate both in event counting and current mode. Two types of detectors are used, one called “fast” and one “slow” in order to achieve fast reaction time to accidental beam losses, and enough sensitivity for long term activation protection and beam tuning. Both detectors have shown strong intrinsic gamma to neutron suppression capability.

ACKNOWLEDGMENTS

The authors would like to thank Alain Menelle for his valuable help during the nBLM tests at the Orphée reactor the IRSN team at AMANDE facility.

L. Segui would like to acknowledge the financial support of Enhanced Eurotalents program (an FP7 Marie Skłodowska-Curie COFUND program).

R. Hall-Wilton, C. Höglund and L. Robinson would like to acknowledge financial support of the EU Horizon 2020 BrightnESS project, grant number 676548.

The project was supported by the French in-kind contribution to ESS and the H2020 project AIDA-2020, GA no. 654168.

REFERENCES

- [1] T. Shea *et al.*, “Overview and Status of Diagnostics for the ESS Project”, in *Proc. IBIC'17*, Grand Rapids, MI, USA, Aug. 2017, paper MO2AB2, doi:10.18429/JACoW-IBIC2017-MO2AB2
- [2] I. Dolenc Kittelmann, “nBLM general overview”, *ESS nBLM system CDR-1*, Lund, Sweden, Dec. 2017, <https://indico.esss.lu.se/event/948/contribution/1/material/slides/0.pdf>
- [3] I. Dolenc Kittelmann, “Report on the MC simulations for the ESS BLM”, ESS, Lund, Sweden, Rep. 0066428, Dec. 2016.
- [4] V. Grishin, B. Dehning, A. Koshelev, A. Larionov, V. Seleznev and M. Sleptsov, “Ionization chambers as beam loss monitors for ESS linear accelerator,” in *Proc. IBIC'17*, Grand Rapids, MI, USA, Aug. 2017, paper WEPWC03, p 54.
- [5] A. Zhukov, Experience with the SNS loss monitoring and machine protection, in *Proc. PAC'13*, Pasadena, CA USA, paper WEYA2, p 714.
- [6] J. Marroncle *et al.*, “A New Beam Loss Monitor Concept Based on Fast Neutron Detection and Very Low Photon Sensitivity”, in *Proc. IBIC'17*, Grand Rapids, MI, USA, Aug. 2017, doi: 10.18429/JACoW-IBIC2016-TUAL02
- [7] I. Dolenc-Kittelmann and T. Shea, “Simulations and detector technologies for the beam loss monitoring system at the ESSlinac,” in *Proc. HB'16*, Malmö, Sweden, July 2016, pp. 553–558.
- [8] I. Giomataris, P. Rebourgeard, J.P. Robert, G. Charpak, “MICROMEGAS: a high-granularity position-sensitive gaseous detector for high particle-flux environments”, *Nucl. Instrum. Meth. A*, vol. 376, p. 29, 1996.
- [9] I. Giomataris, “Development and prospects of the new gaseous detector Micromegas”, *Nucl. Instrum. Meth. A*, vol. 419 p. 239, 1998.
- [10] F. Belloni, F. Gunsing, and T. Papapevangelou, “Micromegas for neutron detection and images”, *Mod. Phys. Lett. A*, vol. 28, p. 1340023, 2013, <https://doi.org/10.1142/S0217732313400233>.
- [11] C. Höglund, *et al.*, “B4C thin films for neutron detection”, *J. Appl. Phys.*, vol. 111, p. 104908, 2012.
- [12] C. Höglund *et al.*, “Stability of 10B4C thin films under neutron radiation”, *Radiat. Phys. Chem.*, vol. 113, p. 14, 2015.
- [13] S. Schmidt, C. Höglund, J. Jensen, L. Hultman, J. Birch, and R. Hall-Wilton, “Low Temperature Growth of Boron Carbide Coatings by Direct Current Magnetron Sputtering and High Power Impulse Magnetron Sputtering”, *Journal of Materials Science*, vol. 51, issue 23, 2016.
- [14] I. Giomataris *et al.*, “Micromegas in a bulk”, *Nucl. Instrum. Meth. A*, vol. 560, pp. 405–408, 2006.
- [15] P. Legou, “Beam Spectrometers using Micromegas in Time Projection Chamber mode”, in *Proc. HB'06*, Tsukuba, Japan 2006, paper WEBZ03, p. 256.
- [16] L. Segui, “Monte Carlo results: nBLM response to EES beam loss scenarios”, Rep. CEA-ESS-DIA-RP-0023, July 2017.
- [17] V. Gressier *et al.*, “AMANDE: a new facility for monoenergetic neutron fields production between 2 keV and 20 MeV”, *Rad. Prot. Dos.*, vol. 110, issue 1-4, Aug. 2004, <https://doi.org/10.1093/rpd/nch185>
- [18] F. Senée *et al.*, “Increase of IPHI beam power at CEA Saclay”, presented at *IPAC'18*, Vancouver, Canada, Apr. 2018, paper TUPAF016, unpublished.
- [19] P. Allport *et al.* Al., “Recent results and experience with the Birmingham MC40 irradiation facility”, *JINST*, vol. 12, no. 03, p. C03075, 2017, doi: 10.1088/1748-0221/12/03/C03075

APPLICATION OF MACHINE LEARNING FOR THE IPM-BASED PROFILE RECONSTRUCTION

M. Sapinski*, R. Singh, D. Vilsmeier,
 GSI Helmholtzzentrum für Schwerionenforschung, 64291 Darmstadt, Germany
 J. Storey, CERN, 1211 Geneva 23, Switzerland

Abstract

One of the most reliable devices to measure the transverse beam profile in hadron machines is Ionization Profile Monitor (IPM). This type of monitor can work in two main modes: collecting electrons or ions. Typically, for lower intensity beams, the ions produced by ionization of the residual gas are extracted towards a position-sensitive detector. Ion trajectories follow the external electric field lines, however the field of the beam itself also affects their movement leading to a deformation of the observed beam profile. Correction methods for this case are known. For high brightness beams, IPM configuration in which electrons are measured, is typically used. In such mode, an external magnetic field is usually applied in order to confine the transverse movement of electrons. However, for extreme beams, the distortion of the measured beam profile can occur. The dynamics of electron movement is more complex than in case of ions, therefore the correction of the profile distortion is more challenging. Investigation of this problem using a dedicated simulation tool and machine learning algorithms lead to a beam profile correction methods for electron-collecting IPMs.

INTRODUCTION

Ionization Profile Monitors (IPM) are devices designed to measure beam profile by extracting and detecting the position of the products of the rest gas ionization by the beam. In the most common configuration ions are extracted by external, uniform electric field. In another configuration, more adapted to high brightness beams, electrons are extracted and additional magnetic field is applied to confine their transverse displacement. There is a rich literature related to Ionization Profile Monitors, and one of the best collection of references can be found in [1].

The deformation of the beam profile registered in ion-based IPMs due to beam space charge was investigated in a series of publications [2–5]. The first three publications focus on derivation of a formula, which links the measured and the real sigma of the transverse beam distribution. The most recent formula [4], based on analytical considerations and simulations, is shown in Eq. 1. The coefficients C_1, p_1 are found by fitting the data and N is bunch population.

$$\sigma_{meas} = \sigma_{real} + C_1 N \sigma_{real}^{p_1} \quad (1)$$

The most recent work [5] proposes a method to not only correct beam sigma, but to reconstruct the original distribution of the beam, based on an iterative correction procedure.

* m.sapinski@gsi.de

It is demonstrated, on simulations, that this method is convergent for generalized gaussian distribution.

The electron-collecting IPMs with magnetic field in the range 0.05 T to 0.2 T are successfully used in many machines in Fermilab, BNL, CERN and J-PARC. A significant distortion of the observed beam profile were reported for LHC beams [6]. This beam is smaller and the maximum bunch field higher than in other hadron machines. A comparison of various beam with respect to the space-charge conditions is shown in Fig. 1. Next frontier are electron machines, especially XFELs, where beam size can be as small as 5 μm and the bunch electric field can reach 10^8 V/m.

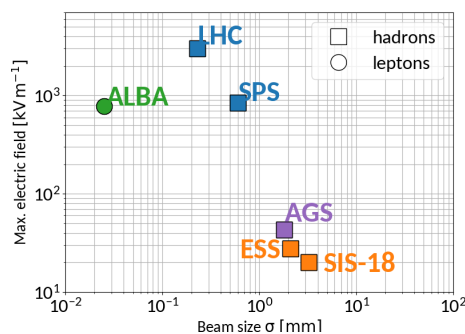


Figure 1: Comparison of typical maximum bunch electric field and beam size for various machines.

SIMULATION TOOLS

Over the years many researchers prepared their own simulation codes to track electron or ion movement in the presence of constant extraction fields and transient bunch fields [7]. These codes are often private, applicable to specific devices, lack maintenance and modern coding. Therefore, we have decided to write a new code, attempting to make it as universal as possible, modern and modular. The program, called Virtual-IPM, is written in python and is available publicly at gitlab.com and in Python Package Index [8].

In the following we will show results of simulation performed using Virtual-IPM. Because of its high space-charge effect we focus on LHC beam, with parameters given in Table 1. The assumed IPM parameters correspond to the devices used in LHC and SPS, except the position resolution, which was adopted from a new device currently being tested on CERN PS [9]. The original LHC IPM position resolution is about 150 μm , and this is not enough to observe the details of the distorted profile. We preferred to apply our analysis to the best currently available technology than to use purely

Content from this work may be used under the terms of the CC BY 3.0 licence (© 2018). Any distribution of this work must maintain attribution to the author(s), title of the work, publisher, and DOI.

theoretical profiles. The values of adequate IPM parameters are listed in Table 2.

Table 1: LHC Beam Parameters Used as Benchmark Example

Parameter	Range
particle type	protons
σ_x	0.23 mm
σ_y	0.27 mm
$4 \cdot \sigma_z$	1.1 ns
N_{bunch}	1.4×10^{11}
bunch spacing	25 ns
E_{beam}	6.5 TeV

Table 2: Assumed IPM Parameters

Parameter	Range
distance between electrodes (d)	85 mm
extraction field E	48 kV/m
magnetic field B	0.2 T
position resolution	55 μm

In the next section we will examine various IPM configurations, as in decision process for a new device design. We use the following coordinate system: x - axis of the beam profile, y - direction of the extraction fields, z - beam direction.

ION DYNAMICS IN PRESENCE OF BEAM FIELDS

Figure 2 shows the time it takes for ions from the ionization event until they reach the detector. Without the space charge the travel time is around 180 ns, but when the space charge is included in the simulation, ions get additional kick which either accelerates them towards the detector or in the opposite direction. The final ion distribution on the detector is very spread and cannot be used for profile measurement, even when using much higher extraction fields.

Examples of ion trajectories, presented as their transverse position as a function of time, are shown in Fig. 3. After closer examination one can see that not only the kick from the bunch where they were produced plays role, but they are also affected by subsequent bunches. However, in this case, the effect of subsequent bunches on ion trajectories is rather small.

PROFILE DISTORTION IN ELECTRON-COLLECTING IPM

Because of their small mass, the electrons are extracted within a few nanoseconds. They spend less time in the high-field region, however the effect of this field on their dynamics is stronger.

One of the first ideas to counteract the profile distortion in IPM was to use magnetic field such, that electrons

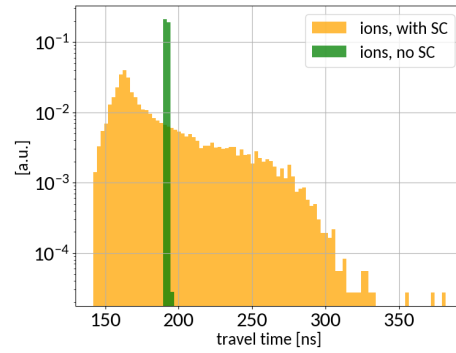


Figure 2: Travel time for ions, with and without space charge.

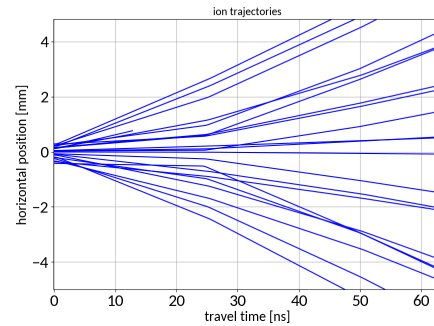


Figure 3: Examples of ion trajectories. The coordinate along the profile of positions are shown as a function of travel time.

would make exactly one revolution before reaching the detector. This idea was originally proposed in [10] to counteract the effect of initial electron velocities due to ionization. After single revolution electrons arrive, in the detector plane (x-z), to the location where they were created, independently of the component of momentum parallel to the detector (x-z). The magnetic field required in this approach is expressed in Eq. 2, where d_{beam} is the distance between the beam center and the detector.

$$B = \pi \sqrt{\frac{2 \cdot m_e \cdot E}{q_e \cdot d_{\text{beam}}}} \quad (2)$$

The main downside of this approach is a component of electron velocity perpendicular to the detector surface (y). This component affects the time of flight of the electron to the detector and for those electrons the Eq. 2 no longer holds. Figure 4 shows the original beam profile and the profiles observed in IPM with and without the space charge. Even without the space charge, small LHC beams cannot be measured using this approach.

Figure 5 shows the quality of the measured profile as a function of applied magnetic field. The "integer number of revolutions" - effect is visible as a series of local minima of the curves. Use of higher values of magnetic field show clear advantage, especially when the space charge is taken into account. Therefore, in most electron-based IPMs, the

Content from this work may be used under the terms of the CC BY 3.0 licence (© 2018). Any distribution of this work must maintain attribution to the author(s), title of the work, publisher, and DOI.

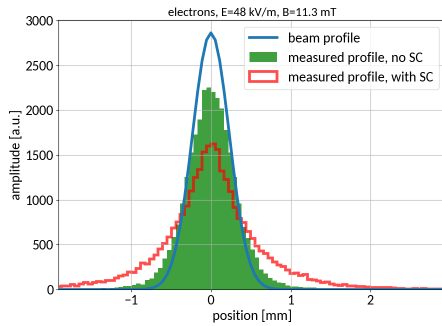


Figure 4: Simulated distortion of beam profile measured in LHC IPM.

magnetic fields of about 100 mT is used. Figure 6 shows the distortion of the registered beam profile for LHC IPM. In order to compensate this distortion a magnetic field of at least 0.6 T would be needed.

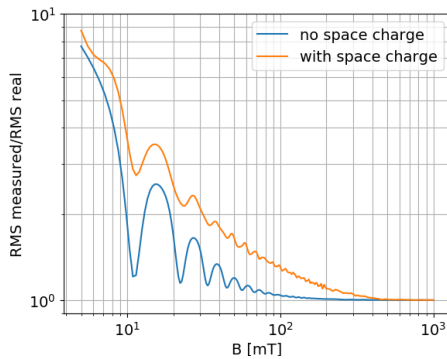


Figure 5: Dependency of the profile distortion on the IPM magnetic field.

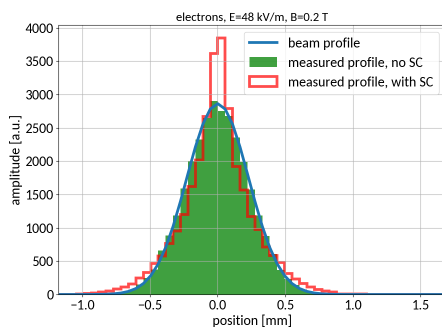


Figure 6: Simulated distortion of beam profile measured in LHC IPM.

The intuitive explanation of the profile deformation is that the electrons are pushed out of the area of the profile with large electric field towards the peak and towards the tails. Figure 7 shows vertical position of the electrons (y) as a function of the travel time. The electrons are trapped inside the bunch potential well until the bunch passes, therefore

the deformation depends not only on the electric field in the position of ionization, but also on the time they spend trapped.

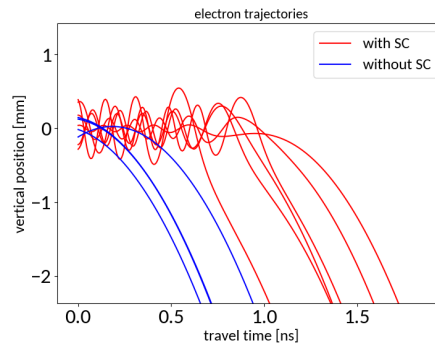


Figure 7: Simulated trajectories of the electrons. The vertical position as a function of time, zoomed to the first 1.5 ns after ionization.

PROFILE CORRECTION IN ELECTRON-COLLECTING, MAGNETIC IPM

Strong, large aperture magnets are big and expensive, therefore other ways to resolve profile deformation problem are discussed.

Electron Sieve

The idea of applying various deconvolution functions to components of the profile characterized by various gyroradius was investigated in [11, 12]. Theoretical results are promising, however practical realization of an "electron sieve" is difficult and has not been realized yet.

Obtaining Beam Width Using Machine Learning

Universal approximation theorem [13, 14] states that a feed-forward network, with a single hidden layer, containing a finite number of neurons, can approximate any continuous functions. The problem of profile distortion in IPM can be solved by a function which maps the distorted profile to real beam profile or beam width. Therefore, the artificial neural network (ANN) is a good tool to deal with the distortion.

In our first approach [15], a simple 2-layer ANN was used to find the original beam sigma. The network input was the distorted profile, bunch length and bunch population. The network was trained on a "grid" of 375 models and tested on models with beam size different than the one used for training models. Optical point spread function was applied to the input profile and robustness of the network to noise was investigated.

The second approach [16] was focused on testing and comparison of various Machine Learning algorithms. Linear Regression, Ridge Regression, Kernel Ridge regression, Support Vector Machine Regression and ANN were compared. The algorithms were trained on 13500 random models and tested on a different sample of 2000 random beam

parameter sets. All models, also Linear Regression, performed well.

Linear Regression Linear regression model is the simplest of investigated algorithms. It can be expressed by Eq. 3.

$$\sigma_x = W^T \cdot x + b \quad (3)$$

where x is a vector containing input profile together with bunch length and charge, W is vector of weights and b is bias vector. W and b are found using fitting procedure, typically based on minimizing Mean Square Error.

Figure 8 shows a typical distribution of residuals obtained on validation sample after fitting procedure. The accuracy obtained on this sample is better than micrometer with sub-micrometer precision. This is already a very good result and it could be concluded that, in absence of significant noise, linear regression could be used for profile width reconstruction in IPM.

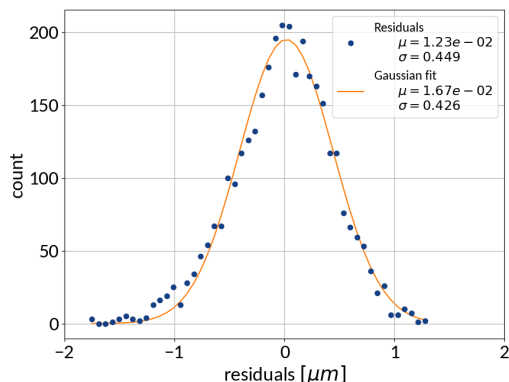


Figure 8: Residuals obtained with linear regression.

Profile Correction Using Neural Network

In order to reconstruct original beam profile, the neural network has been modified. The output of the network contains now not the beam sigma but the whole profile made of 98 fixed bins. The network has two hidden layers with arbitrary 88 neurons each.

The input and output profiles were normalized and centred. The network was trained and validated on the same samples of randomly chosen models as described before. The training converged after about 30 epochs.

In order to assess the quality of the profile reconstruction, a mean squared deviation (MSD) between the original profile and the distorted or corrected profile were calculated. Figure 9 presents the distribution of MSD for deformed and corrected profile for the validation sample. Improvement is clearly visible.

In the next step, the same ANN, trained on gaussian profiles only, was applied to beams with transverse profiles characterized by generalized gaussian and q-gaussian distributions. An example of MSD distribution for generalized

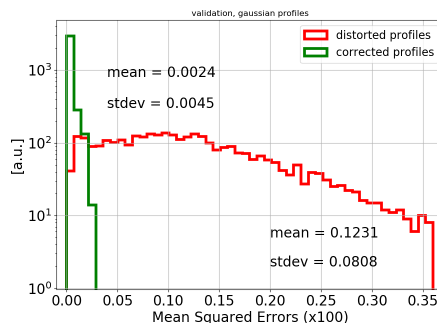


Figure 9: Mean Squared Deviation for gaussian profiles before and after correction.

gaussian profiles with $\beta = 3$ is shown in Fig. 10. A improvement is visible, even if the network was trained on gaussian profiles only, what might suggest that ANN learned about the way the space charge distorts the profiles and not about a particular transformation of gaussian profiles.

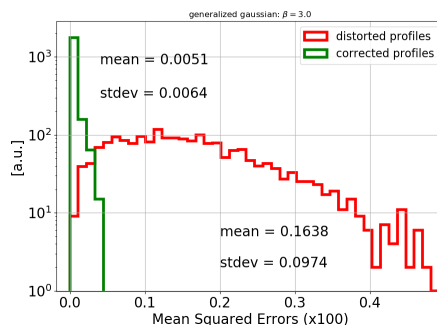


Figure 10: MSD for profiles with generalized gaussian distribution with $\beta = 3$: before and after correction.

An example of particularly distorted profile reconstruction for the generalized gaussian case is shown in Fig. 11. Similar procedure was tested successfully on other distributions.

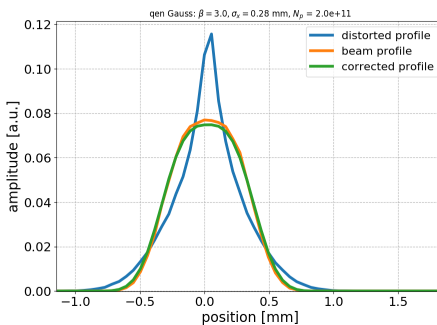


Figure 11: A case with particularly distorted profile. Original beam distribution is generalized gaussian with $\beta = 3$. ANN corrects the profile very accurately.

IPM FOR ULTRA LOW EMITTANCE BEAMS

Measurement of micrometer-scale beam size, like the one in Free Electron Lasers (XFEL), is a challenge for modern diagnostic methods. Here we want to draw attention to an approach which uses space-charge driven deformation of the profile to assess the maximum electric field of a bunch and therefore, when the bunch length and population can be independently measured, the bunch width. In some sense this idea is an alternative to the one presented in [17], which uses the measurement of ion energy.

Table 3: SwissXFEL Beam Parameters

Parameter	Range
particle type	electrons
σ_x	5-7 μm
σ_y	5 μm
σ_z	21 fs
N_{bunch}	230 pC
E_{beam}	5.8 GeV

In this example we use SwissXFEL beam parameters listed in Table 3. Figure 12 shows profiles obtained for various values of original beam size. The shape of the measured profile not only extends to measurable scales (mm instead of μm) but also strongly depends on the original beam size. This indicates that the measurement of the original beam width is viable.

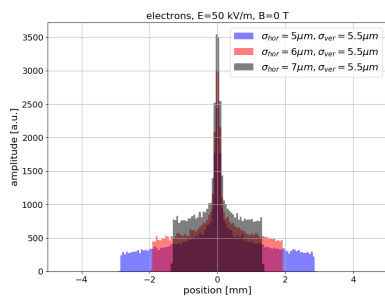


Figure 12: Beam profiles simulated for various SwissXFEL beam sizes.

CONCLUSIONS

Machine learning algorithms have proven to be very efficient in various applications. Here we successfully used them for finding a correction to a complex dynamical process which affects beam profile measurement in Ionization Profile Monitors. Interestingly, an Artificial Neural Network trained on one type of beam profiles perform efficient correction on other types of profiles, suggesting that what network has really learned is the dynamics of the bunch field interaction with electrons and not a particular transformation of gaussian profile. Another interesting conclusion from the

investigation is that even a much simpler, especially in interpretation, Linear Regression algorithm, performs as good as neural network in reconstructing the original beam width, suggesting that the deformation has a linear nature. At the end we propose to make use of profile distortion to measure size of micrometer-scale beams.

REFERENCES

- [1] D. Bartkoski, "Analysis, Prototyping, and Design of an Ionization Profile Monitor for the Spallation Neutron Source Accumulator Ring", PhD diss., University of Tennessee, 2013.
- [2] E. Thern, "Space-Charge Distortion in the Brookhaven Ionization Profile Monitor", in *Proc. PAC'87*, Washington DC, USA, Mar. 1987, p. 646.
- [3] W. Graves, "Measurement of Transverse Emittance in the Fermilab Booster", PhD diss., University of Wisconsin, 1994.
- [4] J. Amundson, J. Lackey, P. Spentzouris, G. Jungman, L. Spentzouris, "Calibration of the Fermilab Booster ionization profile monitor", *Phys. Rev. ST Accel. Beams* vol. 6, p. 102801, 2003.
- [5] J. Egberts, "IFMIF-LIPAc Beam Diagnostics: Profiling and Loss Monitoring Systems", PhD diss., Universite Paris Sud, 2012.
- [6] M. Sapinski *et al.*, "The First Experience with LHC Beam Gas Ionization Monitor", in *Proc. IBIC'12*, Tsukuba, Japan, Oct. 2012, paper TUPB61.
- [7] M. Sapinski *et al.*, "Ionization Profile Monitor Simulations - Status and Future Plans", in *Proc. IBIC'16*, Barcelona, Spain, Sep. 2016, paper TUPG71.
- [8] D. Vilsmeier, P. Forck, M. Sapinski, "A Modular Application for IPM Simulations", in *Proc. IBIC'17*, Grand Rapid, Michigan, USA, Aug. 2017, paper WEPCC07.
- [9] S. Levasseur *et al.*, "Time-resolved Transverse Beam Profile Measurements with a Rest Gas Ionisation Profile Monitor Based on Hybrid Pixel Detectors", in *Proc. IPAC'18*, Vancouver, Canada, May 2018, paper WEPAL075.
- [10] F. Hornsta, M. Trump, "A High Resolution Highly Sensitive Nonintercepting Beam Profile Monitor For The Los Alamos Meson Facility (LAMPF)", in *Proc. of Proton Linear Accelerator Conference*, Batavia, Illinois, USA, 1970.
- [11] D. Vilsmeier, B. Dehning, M. Sapinski, "Investigation of the effect of beam space-charge on electrons in ionization profile monitors", in *Proc. HB'14*, East Lansing, MI, USA, November 2014, paper MOPAB42.
- [12] D. Vilsmeier, "Profile distortion by beam space charge in Ionization Profile Monitors", CERN-THESIS-2015-035.
- [13] G. Cybenko, "Approximations by superpositions of sigmoidal functions", *Mathematics of Control, Signals, and Systems*, vol. 2, no. 4, pp. 303-314, 1989, doi:10.1007/BF02551274
- [14] K. Hornik, "Approximation Capabilities of Multilayer Feedforward Networks", *Neural Networks*, vol. 4, no. 2, pp. 251-257, 1991.
- [15] R. Singh, M. Sapinski, D. Vilsmeier, "Simulation supported profile reconstruction with machine learning", in *Proc. IBIC'17*, Grand Rapid, Michigan, USA, Aug 2017, paper WEPCC06.

- [16] D. Vilsmeier *et al.*, "Reconstructing Space-Charge Distorted IPM Profiles with Machine Learning Algorithms", in *Proc. IPAC'18*, Vancouver, Canada, May 2018, paper WEPAK008.
- [17] R. Tarkeshian, J. L. Vay, R. Lehe, C. B. Schroeder, E. H. Esarey, T. Feurer, W. P. Leemans *Phys. Rev. X* 8, 021039.

MEBT LASER NOTCHER (CHOPPER) FOR BOOSTER LOSS REDUCTION*

D.E. Johnson[#], T.R. Johnson, C. Bhat, S. Chaurize, K. Duel, P. Karns, W. Pellico, B.A. Schupbach,
K. Seiya, D. Slimmer, Fermilab, Batavia, Illinois, USA

Abstract

In synchrotrons, beam extraction is accomplished by a combination of kicker magnets and septa which deflect the beam from one accelerator into another. Ideally the extraction kicker field must rise in a beam-free region in the synchrotron (aka "notch"), to avoid beam loss at high field during the extraction kicker rise time. In the case of the Fermilab Booster, which utilizes multi-turn injection and adiabatic capture, the notch is created in the ring at the injection energy using fast kickers which deposit the beam in a shielded absorber within the accelerator tunnel. This process, while effective at creating the extraction notch, was responsible for a significant fraction of the total beam-loss power in the Booster tunnel and created significant residual activation within the Booster tunnel in the absorber region and beyond. With increasing beam demand from the Experimental Program, the Fermilab Proton Improvement Plan (PIP) initiated an R&D project to build a laser system to create the notch within a Linac beam pulse at 750 keV, where activation is not an issue. This paper will discuss the loss reduction in the Booster, increased efficiency, and increased proton throughput, and its integration into the accelerator complex. We will also touch on other potential applications for this bunch-by-bunch neutralization approach.

INTRODUCTION

With the transition from the Collider Era to the Intensity Frontier in 2011, it became clear that, to meet the demands of the existing Neutrino and future Muon and Neutrino Experimental Programs as well as the Fixed target area programs, the Accelerator and its infrastructure needed upgrades. A series of task-forces and workshops were held [1-3] to define the necessary improvements and upgrades such that the Proton Source will 1) remain viable and provide reliable operation of the Linac and Booster through 2025, 2) assure beam operation of the Linac and Booster at 15 Hz and 3) double the proton flux (to 2.25E17 protons/hour) while maintaining the 2010 residual activation levels. These goals make up the essence of the multi-year Proton Improvement Plan (PIP) starting in 2012. At the start of PIP another project, "The 750 keV RFQ Injector Upgrade", [4] was well underway as a project to replace the 40+ year-old Cockcroft-Walton pre-accelerator with a more modern and reliable radio-frequency quadrupole (RFQ) and associated source and transport line(s) for injection into Tank 1 of the Linac.

*Operated by Fermi Research Alliance, LLC under contract No. DE-AC02-07CH11359 with the United States Department of Energy.
[#]DEJ@fnal.gov

FERMILAB PROTON SOURCE

The Fermilab Proton Source is comprised of a dual ion source providing a continuous current of H⁻ ions, a low energy beam transport (LEBT) line, a 750 keV RFQ operating at 201.25 MHz, a medium energy beam transport (MEBT) line, to match between the RFQ and Tank 1 of the 15 Hz 400 MeV Linac which injects into the Booster.

The Fermilab Booster is a combined function synchrotron with magnet systems resonantly powered at 15 Hz. The synchrotron has an injection energy of 400 MeV and extraction energy of 8 GeV, with an acceleration cycle of ~33 ms. Injection into the Booster is multi-turn injection with adiabatic capture into stationary 38 MHz buckets. The RF harmonic number of the Booster is 84. The Linac pulse length is equal to the number of turns to be injected times the revolution period of the Booster (2.21 μsec) at injection.

To cleanly extract the beam at the top energy of 8 GeV, an 80 ns no-beam gap (notch) must be created in the Booster ring after adiabatic capture into the 38 MHz buckets, while at the injection energy. The 80 ns gap is required for the Booster extraction kicker rise time and is equivalent to sixteen 201.25 MHz Linac bunches. This has historically been performed by a series of fast kickers [5] which will remove three of the 84 bunches into an absorber inside the Booster tunnel.

Although this is only a small fraction of the beam in Booster, it represents about 30% of the total lost beam power. Fermilab's administrative loss limit assures that the average loss around the ring does not violate the 1 W/m level. Obviously, the losses are not uniform around the ring, they are typically concentrated in the injection and extraction regions as well as the internal absorbers for collimation and notch production.

To be able to increase the throughput of the Booster the loss associated with the production of the extraction notch in the Booster tunnel must be significantly reduced or eliminated. Moving this process out of the Booster tunnel to the 750 MeV MEBT, is expected to significantly reduce Booster total lost power allowing a proportional increase in accelerated beam intensity (throughput), a positive step in addressing the third goal in the PIP.

The PIP initiated an R&D project to build a laser system to create the required series of notches within a Linac beam pulse at 750 keV. The concept is that 80 ns sections of the Linac pulse at the Booster injection revolution period will be removed. As the Linac pulse is injected into the Booster these no-beam sections (or notches) will line up on top of one another thus creating a "ready-made" notch at injection. Assuming a 90% efficiency in the creation of the notch in the Linac pulse, the Booster kicker needs to only remove the remaining 10% of the beam into the absorber.

Figure 1 shows the 15 Hz Linac pulses in the top pane and a single Linac pulse segmented into sections at the Booster revolution period in the lower pane.

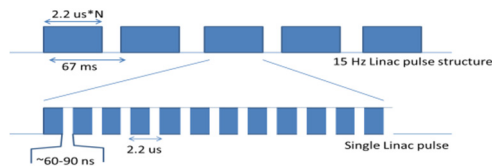


Figure 1: Schematic of Linac pulses at 15 Hz (top) and a single pulse showing multiple notch structure (bottom). The 201.25 MHz linac bunch structure is not shown.

LINAC NOTCHER CONCEPT

The technique employed to produce the notches in the Linac pulse is to remove the outer electron of selected H⁻ ions using photoionization [6]. There have been discussions on using lasers to create a notch in the Linac beam in the past [7-9]. The laser system developed under PIP was designed to minimize the peak laser pulse energy required for neutralizing H⁻ ion bunches exiting the RFQ, utilizing two techniques. First the laser pulses match the temporal structure (spacing and bunch length) of the ions exiting the RFQ. In addition, laser system operates in a burst mode at the Booster injection revolution frequency. Each burst contains a group of 201.25 MHz laser pulses, which in the current scenario is 16 pulses to create an 80 ns notch

At the early stages of design, the expected notch width was ~ 60 ns and the number of injected turns was 10-12. In the current operational scenario, with 18 turn injection, the laser system creates 19 bursts (one to sharpen the head of the Linac pulse and the rest of the 18 to create the required notches within the Linac pulse), each Linac cycle.

The second technique employed to minimize the required peak laser pulse energy is the utilization of a non-resonant interaction cavity with parallel mirrors. [10] The geometry of this cavity (mirror separation, separation between interactions, and laser injection angle) is adjusted such that the velocity of the laser advancing downstream on the axis between the parallel mirrors matches the ion velocity traveling through the cavity. This allows the laser to interact many times with the ion bunch as it progresses down the cavity [11]. The number of interactions depends on the beam line space available, the length of the optical cavity (in the present implementation the mirrors are only 27mm long) and the distance between successive interactions (currently ~1.1mm). We typically strive for 21 up to 27 interactions as the ions pass thru the cavity.

Estimation of Required Laser Energy

When the probability of interaction between the photons and electrons is high and the mechanism does not depend on the electron intensity [6], the fraction of electrons that are detached from the moving H⁻ ions is given by [12]

$$F_{neut} = N/N_0 = (1 - e^{-f_{CM}\sigma(E)\tau}), \quad (1)$$

where f_{CM} is the flux of photons at the interaction point in the rest frame of the H⁻ [photons/cm²/sec], $\sigma(E)$ is the photoionization cross section for photon energy E, and τ is the interaction time of the photons and electrons. The center of mass flux can be expressed in lab frame parameters as

$$f_{CM} = \gamma \left(\frac{E_{laser} \lambda_{LAB}}{hc \tau_{laser}} \right) \left(\frac{1}{A_{laser}} \right) (1 - \beta \cos \theta), \quad (2)$$

where E_{laser} is the laser pulse energy, λ_{LAB} is the lab frame wavelength of the laser, τ_{laser} is the laser pulse length, A_{laser} is the laser cross sectional area, γ and β are relativistic parameters, and θ is the interaction angle between the photons and H⁻

Given the vertical beam size of the ion bunch and the cavity geometry, we use Eq. 1 and 2 to calculate the neutralization as a function of laser pulse energy. We show three different calculations in Figure 2 to reflect the energy savings from the two energy-saving techniques. The three curves are: 1) a single 80 ns laser pulse is used to create a complete notch (red, solid line), 2) a single interaction with the 2 ns laser pulse, to match the ion bunch length) without utilizing the interaction cavity (blue, dot-dash), and 3) with a 2 ns laser pulse utilizing the interaction cavity with 27 interactions (black, dashed).

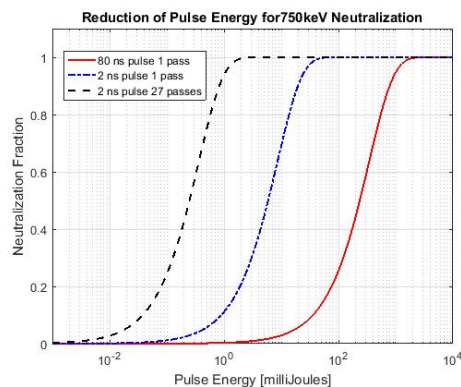


Figure 2: Neutralization of a single bunch with and without the use of a multiple interaction cavity.

To neutralize 99% of an ion bunch, it would require 47 mJ in a single pass interaction while only 2 mJ for a cavity with 23 interactions. For 95%, it would be 25 mJ vs 1 mJ per bunch.

LASER SYSTEM DESIGN

The laser system may be characterized as a flexible hybrid burst-mode laser system with a master-oscillator-power-amplifier (MOPA) architecture. The spatial properties of the final amplifier output are controlled to match the vertical dimension of the ion beam, which in our case we require the spatial cross section of the laser to be 1 mm × 7 mm vertically. Figure 3 shows a block diagram of the laser system. The MOPA architecture indicates starting with a low power diode laser and impressing the desired laser pulse structure on this seed source. This is then amplified through a series of CW pumped fiber amplifiers, a pulsed pumped fiber amplifier, brought into free space with the final amplification from two dual pass diode pulse pumped

Content from this work may be used under the terms of the CC BY 3.0 licence (© 2018). Any distribution of this work must maintain attribution to the author(s), title of the work, publisher, and DOI.

solid state laser amplifiers. After the final amplifier the transverse spatial profile is modified to create a roof-top profile and a cylindrical telescope is used to create a narrow horizontal profile at the entrance of the cavity.

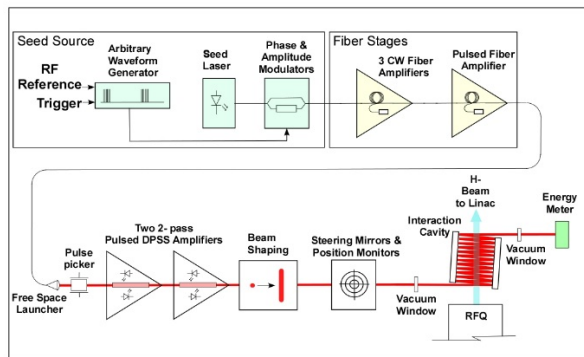


Figure 3: Block diagram of the laser system and optical transport to the interaction cavity.

Instrumentation

To tune and monitor the operation of the laser system and injection into the interaction cavity several commercial instruments and several Fermi designed/built pieces of instrumentation are utilized. The instrumentation falls into a few categories to measure, 1) average power, 2) pulse amplitudes, 3) total laser pulse energy each 15 Hz Linac cycle, 4) laser positions in transport to the interaction cavity, and 5) IR capable video camera to monitor the laser bounce spacing inside the interaction cavity.

Controls

The LabView front-end software that is used to monitor and control all the amplifiers, Data Acquisition system, and associated hardware. The program is a flexible queue driven state machine composed of independent tasks such as the 1) GUI interface, 2) main accelerator controls system interface for operational monitoring and control, 3) hardware monitoring, and 4) a very flexible waveform creation for the laser pulses. All communication with hardware is via USB. Since the laser system is in a very noisy electrical environment, a significant effort was required to minimize interference with hardware communication. In addition, automatic recovery routines for identified hardware communication errors have been implemented. Accelerator Operations interface to the front end is via a Java Graphical Monitoring page, closed circuit video channels, and standard parameter pages, and alarm monitoring. Figure 4 shows the image of the main page LabView front-end GUI interface. Other functions such as piezo-electric mirror control and Optical Beam Position Monitor positions of the laser trajectory into the optical cavity, parameter setting limits, DAQ configuration, and alarm configuration are accessible through tabs at the top of the GUI. Access to the flexible waveform generation is through a "button" at the bottom of the page.



Figure 4: Laser Notcher front-end GUI.

Installation

The complete laser system and the free space optics is contained in a custom 19 inch electronics rack with the free space amplifiers and free-space optics in a light tight optics box sitting on top of the electronics rack. The centerline elevation of the beam line is 41 inches above the floor. The elevation of the free space optical path must match the beam line elevation.

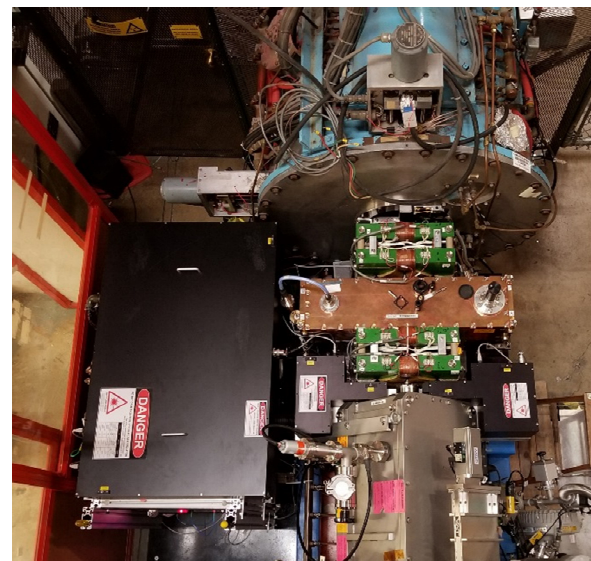


Figure 5: Installation of Laser Notcher in the Linac.

A light tight transport enclosure and a light tight laser dump enclosure are used to transport the laser from the optics box, through the interaction cavity, and finally to a dump energy meter to measure the laser energy after the interaction cavity.

The complete system is portable and can be rolled in and set in place. The optics box is aligned so that the laser output trajectory is perpendicular to the ion beam trajectory and at the correct elevation. The interaction cavity is built into the output flange of the RFQ. Figure 5 shows the laser system installed between the RFQ and tank 1 of the Linac.

Comparison of Neutralization Measurements with Estimates

We utilize a resistive wall current monitor (WCM), located midway down the Linac, to monitor the individual

201.25 MHz bunch intensities for each Linac cycle and a fast photodiode (PD) to monitor the laser pulse amplitude out of the final amplifier. The top pane in Fig. 6 shows the WCM and PD for an entire Linac cycle (magenta) and the laser bursts (green) responsible for each notch. The bottom pane shows an expanded view of the first notch along with the laser pulses that neutralized each bunch within the notch. On either side of the 80 ns notch are the un-affected bunches.

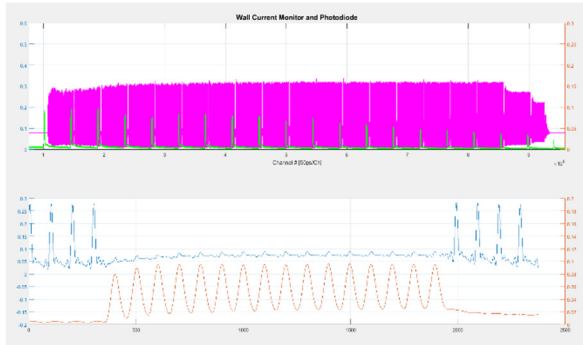


Figure 6: Wall current monitor and photodiode signal showing the burst spacing (top pane) and the detail of the first notch (bottom pane).

We compare the bunch intensity of the bunches ‘in the notch’ that have been neutralized by the laser to the nearest ‘un-affected’ bunches to determine the level of neutralization (see bottom pane in figure 6).

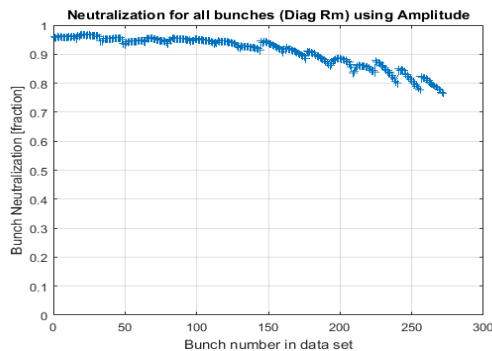


Figure 7: Measured neutralization of every bunch within the 17 notches created in a Linac pulse for 18 turn Booster injection.

Looking at Figure 7, one can clearly see that the first half of the bunches are neutralized to the 90 to 96% level and slowly tails off to the 75% level for the 17th notch as the current configuration lacks the stored energy necessary to maintain this number of uniform pulses. Using the fast photodiode monitoring the output of the last amplifier and an energy meter located in the laser dump, we calculate the pulse energy of each 201.25 MHz laser pulse.

Correlating the level of neutralization for each bunch within all notches with the laser pulse energy allows us to compare the neutralization as a function of energy. Figure 8 shows the results of the latest neutralization measurements and the neutralization estimation as a function of energy for 27 interactions

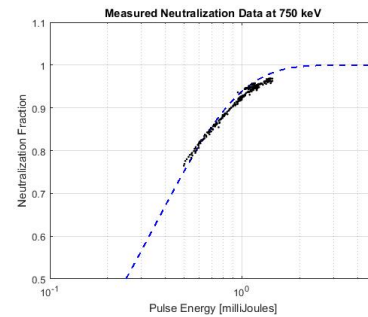


Figure 8: Comparison of measured neutralization with the predicted neutralization for 27 interactions.

BOOSTER INJECTION

The current injection process into Booster is known as Early Injection Scheme (EIS) [13] where the start of injection occurs on the decreasing dipole magnetic field 200 μ s before its minimum is reached. The goal of this scheme is to increase the number of Booster turns (BT) for injected beam and provide more time for adiabatic capture of the beam to preserve longitudinal emittance of the beam at injection. However, the revolution period during the injection process is not constant. It is, therefore, important to adjust the spacing of the notches in the Linac beam so that all the notches line up on top on one another through injection and retain 80 ns gap in the injected beam after the completion of the injection process. During injection a small amount of the Booster 38 MHz RF voltage is present. Once injection is finished, the amplitude of the 38 MHz RF is adiabatically increased to capture the bunches within the 38 MHz bucket. The center of the notch must line up with one of the 38 MHz buckets to keep the notch symmetric.

Longitudinal beam dynamics simulations carried out by including 80 ns notch in each BT beam convincingly show that the particle leakage into the notch during beam capture is less than 1-2% if beam capture commences immediately after the beam injection. However, in the current operation we observe \sim 15% of beam particle leakage by the end of the capture. In any case, we have greatly benefited in reducing the beam loss in the Booster ring due to the Laser notcher.

IMPACT ON OPERATIONS

The motivation for developing the laser notcher system was loss reduction in the Booster tunnel. As mentioned earlier, the process of creating the notch at injection energy was effective, but it contributed about 30% to the total loss power budget of the Booster. When the Booster and its notching process is “well” tuned up, without the laser notcher, the throughput for Booster is about 2.0-2.1 E17/hour with the Booster losses remaining within the 1W/m loss level. With the application of the laser notcher in combination with the current Booster notcher (to provide cleanup of the notch, the throughput rises to the level of 2.4-2.5 E17/hour with the Booster losses remaining within the 1W/m level, about a 20% increase in throughput.

Content from this work may be used under the terms of the CC BY 3.0 licence (© 2018). Any distribution of this work must maintain attribution to the author(s), title of the work, publisher, and DOI.

When running with the laser notcher system on, we observed an increase in the amount of beam that can be accelerated in the Booster. Figure 9 shows the impact on Booster intensity (magenta) and extraction losses (cyan). The plot on the left (laser off) shows the Booster cycle intensity of $4.7E12$ protons per Booster cycle (ppBc) for the NuMI cycles (on the left) and $3.4 E12$ for the BNB cycles (on the right). The right plot (laser on) shows the reduction of the NuMI extraction losses by $\sim 40\%$ for the same intensity and a $\sim 40\%$ increase in the beam on the BNB cycles with the same extraction loss level.

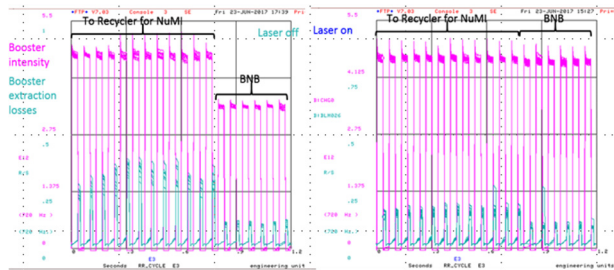


Figure 9: Comparison of Booster cycle intensity and extraction losses with the laser notcher on and off.

HE PATH FORWARD

Since we embarked on the R&D project to create a bunch-by-bunch H^- neutralization system for notch creation in the existing Linac beam pulse, various other applications of this technique have surfaced. This concept of bunch-by-bunch interaction with the laser system coupled to our non-resonant interaction cavity has led to proposals of creating laser systems for other applications such as arbitrary bunch chopping, transverse and longitudinal collimation, extraction of various bunch intensities from H^- transport line, etc. One such proposal is to create a laser transverse collimation system for complete Linac pulses. This was successfully tested last summer for a Linac pulse with a length of about $2.2 \mu s$, a single Booster turn.

To accomplish this, we utilized 1) our flexible waveform generation program to create a waveform of 440 201.25 MHz laser pulses (each 2 ns long) to interact with every bunch in the Linac pulse and 2) our patented beam shaping device to redistribute the total energy of the pulse, i.e. change the spatial profile from a single roof-top profile to a pair of laser spots separated by 4-5 mm,

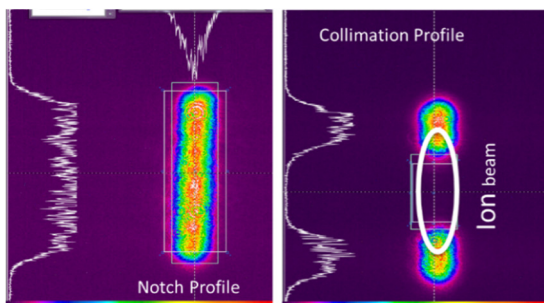


Figure 10: Transverse profile of laser pulse used for notching (left) and the one used for vertical transverse collimation (right).

thus, only neutralizing the tails of the vertical spatial profile as shown in the right hand picture of Figure 10.

Although the impact of the laser on the vertical profile could not be discerned on a multiwire in the injection region, the reduction of bunch intensity for all bunches in the Linac pulse could clearly be seen on the WCM and the losses in the injection region showed a clear reduction when the laser was turned on.

Another potential utilization of this technique is momentum collimation in a Linac. Currently, it has been conceived that reduced momentum spread of the beam from the Linac at injection might improve the beam capture efficiency. It has been proposed that the laser system could be set up to collimate in longitudinal phase. This may be accomplished by creating two laser pulses for each bunch by splitting a single laser pulse and directing one through a variable optical delay line and re-combining. The temporal spacing of the recombined pulse can be adjusted to vary the extent of neutralization of the head and tail of the bunch.

For applications requiring interaction with all bunches in a Linac pulse (high duty factor), the amplifier system must be capable of providing 1) enough stored energy for uniform energy extraction by all seed laser pulses, or 2) a fast gain media pumping to allow uniform amplification of all laser pulses. Because of the advancement in specialty large mode area gain fibers and the large peak and average power handling capability these gain media, these media are becoming more attractive as final amplifier stages. Even though these fiber gain medias do not suffer thermal lensing and wedging issues found in solid state gain media (c.f. Nd :YAG) due to non-uniform temporal pulsing, they have their own limitations due to non-linear instabilities at high peak powers. Currently, fiber amplifiers are available with 300 kW peak and ~ 200 W average power capabilities. Progress continues in the development of even higher peak power capability.

CONCLUSION

We have developed the first of its kind bunch-by-bunch H^- neutralization system for the purpose of loss reduction in the Fermilab Booster. This is being utilized to create the Booster extraction gap or notch in the Linac pulse. The system has successfully led to a significant increase in proton throughput.

We continue to understand and improve the operation of the system in the Linac. We continue to develop and improve the non-resonant interaction cavity. We continue the R&D to develop a quasi CW amplifier system that will be compatible with long pulse operation required for collimation applications and other applications.

ACKNOWLEDGEMENTS

We would like to acknowledge the staff of the Accelerator Division at Fermilab and the staffs at Optical Engines, Northrup Grumman, and PriTel for the support and help with this ambitious project.

REFERENCES

- [1] W. Pellico, “Proton Source Improvement Plan Workshop an Overview”, Fermilab internal Beams Document 3731-v1, December 6, 2010.
- [2] R. Webber, W. Pellico, V. Lebedev, D. McGinnis, “A Plan for Delivery for 8-GeV protons through 2025 at Fermilab”, Fermilab Internal Beams Document 3781-v2, Feb. 22, 2011.
- [3] Fermilab Proton Improvement Plan Design Handbook, Fermilab Internal Beams Document #4053-v3, February 22, 2012.
- [4] C.Y. Tan *et al.*, “The 750 MeV RFQ Injector Upgrade”, “Fermilab Internal Beams Document #3646-v16, December 11, 2013.
- [5] S. Chaurize, K. Seiya, V. Sidorov, C. Jensen, I. Rakhno, I. Tropin, R. Tesarek, W. Pellico, “Optimization of the Notch System in Fermilab Booster”, in *Proc. IPAC'17*, Copenhagen, Denmark, May 2017, paper TUPIK117.
- [6] H.C. Bryant and E.P. MacKerrow, “Accelerator-Based Atomic Physics Techniques and Applications”, ed. S.M. Shafroth, J.C. Austin, (1997) chapter 6, page 183.
- [7] R. Tomlin, “Ion Beam Notcher Using a Laser”, in *Proc. PAC'01*, Chicago, IL, USA, Jun. 2001, p. 3912.
- [8] Xi Yang and C. Ankenbrandt, “Design Report of the Laser System for Notching H⁻ Beams at Booster Injection RF Frequency in the 750 keV Linac”, Fermilab FN-0765-AD, April 2005.
- [9] Xi Yang and C. Ankenbrandt, “Reducing the Extraction Loss via Laser Notching the H⁻ Beam at the Booster Injection Revolution Frequency”, Fermilab FN-0767-AD, May 2005.
- [10] R.E. Shafer, Laser Diagnostics for High Current H⁻ Beams”, in *Proc. 1998 Beam Instrumentation Workshop* (Stanford). A.I.P. Conf. Proceedings, (451), 191.
- [11] D.E. Johnson *et al.*, “The Linac Laser Notcher for the Fermilab Booster”, in *Proc. LINAC'16*, East Lansing, MI, USA, Sep. 2016, paper TH2A01, pp. 710-714.
- [12] R.C. Connolly *et al.*, “A transverse Phase Space Measurement Technique for High Brightness H⁻ Beams”, *Nucl. Inst. Methods A*, vol. 312, pp 415-419, 1992.
- [13] C. M. Bhat, “R&D on Beam Injection and Bunching schemes in the Fermilab Booster,” in *Proc. HB'16*, Malmö, Sweden, Jul. 2016, p 293.

STATUS OF PROOF-OF-PRINCIPLE DEMONSTRATION OF 400 MeV H- STRIPPING TO PROTON BY USING ONLY LASERS AT J-PARC

P.K. Saha*, H. Harada, M. Kinsho, A. Miura, M. Yoshimoto, J-PARC Center, Japan
Y. Irie, I. Yamane, High Energy Accelerator Research Organization, Japan
H. Yoneda, Y. Michine, University of Electro-Communications, Tokyo, Japan

Abstract

In order to demonstrate the Proof-of-Principle (POP) of H⁻ stripping to protons by using only lasers, experimental preparations at the RCS (Rapid Cycling Synchrotron) of J-PARC (Japan Proton Accelerator Research Complex) are in progress. The ultimate goal is to make a breakthrough in the conventional H⁻ charge-exchange injection by overcoming the practical limitations and issues associated with stripper foil used for that purpose so far. Extremely high residual radiation due foil scattering beam losses as well as unreliable and short lifetime of the foil are already serious issues in all existing high intensity proton machines. To establish our new principle, a POP demonstration will be carried out for the 400 MeV H⁻ beam energy. A vacuum chamber for the POP demonstration has been installed at the end section of J-PARC Linac. During previous year we have many progresses on studies of H⁻ beam manipulations, establishment of measurement principle and also R&D of the lasers. The present status and detail strategy of the POP demonstration of 400 MeV H⁻ stripping to protons by using only lasers are presented.

INTRODUCTION

The charge exchange injection (CEI) of H⁻ by using a stripper foil is an effective way to increase the proton beam power in a synchrotron or storage ring [1, 2]. Two electrons from the H⁻ are stripped of by the foil, leaving only protons to inject into the circular accelerators. The fundamental advantage of the CEI is that, it allows stacking many turns without linear growth in emittance because of injecting in a different charge state. The technique thus provides the opportunity of unlimited multi-turn injection until stacking particles exceed aperture of the circular accelerators. By using CEI with foil, high power beam of 1 MW has already been achieved [1, 2], but the next generation innovative physics research as well as industrial applications require multi-MW beam power. Although continuous efforts on durable foil production made remarkable progress on the foil lifetime [3], it is still unclear how to deal with multi-MW beam power. It is hard to maintain reliable and longer lifetime due to overheating of the foil, and may be it is the most serious concern and a practical limitation to realize a multi-MW beam power [4]. In addition, extremely high residual activation near the stripper foil due to foil scattering beam losses during injection is also another serious issue for facility maintenance [5].

The lifetime of the foil does not always mean a complete breaking or failure of the foil. Due to high power beam irradiation, foil degradation such as, foil thinning, pinhole formation and deformations cause a rapid increase of the waste beam, and it results a foil replacement with a new one. A frequent replacement of the foil magazine involves unhealthy exposure to radiation for the workers. To reduce the number of hits on the foil by the circulating beam, large amplitude transverse painting injection scheme by using controlled time dependent offset of the circulating beam during the injection time has been adopted in the RCS [6–8]. On the other hand, a relatively thicker foil of 333 μg/cm² is used to achieve higher stripping efficiency of 99.7% due to limited capacity of the waste beam dump at RCS [9]. The stripping efficiency drops even for a little of foil thinning and results an increase of the waste beam power. Significant foil degradation has already been measured even only at 0.3 MW beam power operation of J-PARC RCS [10, 11]. At the design 1 MW beam power and beyond, the practical limitation of the foil lifetime may come from foil degradation, which results an increase of the waste beam power at the dump.

In order to overcome the limitations and issues associated with the stripper foil, a foil-less H⁻ CEI is thus very essential. The laser-assisted H⁻ stripping was originally proposed two decades ago [12], and it is being extensively studied for 1 GeV H⁻ beam at the SNS (Spallation Neutron Source) in Oak Ridge [13–15]. However, the method has a difficulty, especially at lower H⁻ energies due to extremely high magnetic fields are needed in addition to the laser [16]. To overcome the difficulties with extremely high magnetic fields, we proposed a new method of H⁻ stripping to protons by using only lasers [17]. To establish our method, a proof-of-principle (POP) demonstration of 400 MeV H⁻ stripping to protons by using only lasers will be performed at J-PARC.

PRINCIPLE OF H⁻ STRIPPING TO PROTON BY USING ONLY LASERS

In order to avoid the difficulties of using extremely high magnetic field required in the laser-assisted H⁻ stripping method, especially at lower H⁻ beam energy, we consider a new method by using only lasers [17]. Figure 1 shows a schematic view of our newly proposed method. It is similar to the laser-assisted H⁻ stripping method but magnetic stripping of H⁻ to H⁰ and H^{0*} to proton (p) in the 1st and 3rd steps, respectively are replaced by lasers. The widely available high power Nd:YAG lasers can be used for those purposes in order to utilize large photo-detachment and photoionization cross sections, in the 1st and 3rd steps, re-

* E-mail address: saha.pranab@j-parc.jp

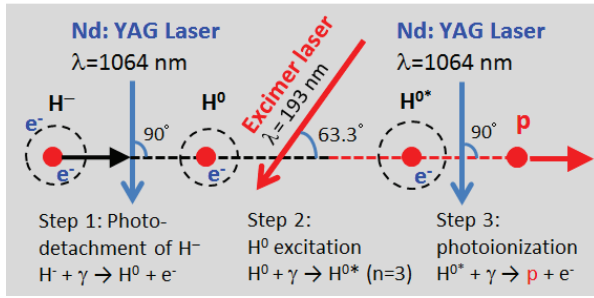


Figure 1: Schematic view of H^- stripping to proton by using only lasers. Noted parameters are typical ones for the 400 MeV H^- beam energy.

Table 1: Typical Laser Parameters for 400 MeV H^- Stripping to Proton

Process	E_{ph} (eV)	λ (nm)	α (deg.)	λ_0 (nm)	Laser
$H^- \rightarrow H^0$	1.67	1064	90	743	Nd:YAG
$H^0 \rightarrow H^{0*}$	12.1	193	63.3	102	ArF Excimer
$H^{0*} \rightarrow p$	1.67	1064	90	743	Nd:YAG

spectively. The 2nd step is the excitation of ground state $n=1$ ($1s$) H^0 atom to higher states up to $n=3$ ($3p$) denoted as H^{0*} . An ArF excimer laser of 193 nm is suitable for that purpose.

Table 1 gives the details of laser parameters for the present purpose. Due to the Doppler effect, laser wavelength, λ in particle laboratory frame (PLF) is shifted to λ_0 of the H^0 atom in the particle rest frame (PRF), given by

$$\lambda = \lambda_0(1 + \beta \cos \alpha) \quad (1)$$

where β (0.713) and γ (1.4263) are relativistic parameters of H^- at 400 MeV, α is the collision angle between laser and the beam in PLF. The advantage of using Nd:YAG lasers for the 1st and 3rd steps is that the direct high power IR (Infrared) laser beams can be used for those purposes. The laser beam angle to both H^- and H^{0*} are set to be 90 degrees in order to utilize the maximum photodetachment and photoionization cross sections given to around 750 nm of the laser wavelength in PRF [18].

EXPERIMENTAL SETUP AND PRESENT STATUS OF POP DEMONSTRATION

Figure 2 shows a schematic view of the end section of J-PARC L-3BT (Linac to 3-GeV beam transport), where the POP demonstration of 400 MeV H^- stripping by lasers has to be carried out. The red rectangular box at the downstream of the beam halo scraper section shows the place to set experimental devices for the laser and H^- interaction point (IP). Downstream of the IP, three charge fractions can be simultaneously measured in the separated beam lines. Namely, fully stripped p , neutral H^0 (by further stripping) and the unstripped H^- can be measured in the 100-degree beam dump, 90-degree beam dump and the RCS injection

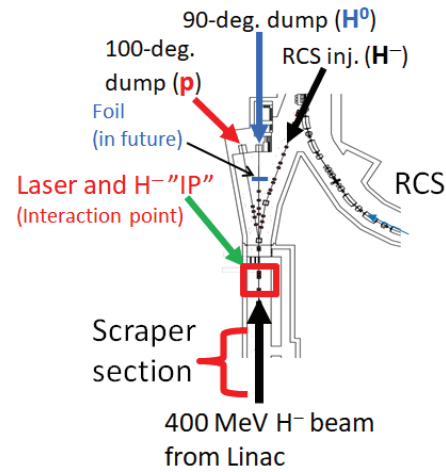


Figure 2: Schematic view of end section of J-PARC L-3BT. The red rectangular box at the downstream of the scraper section shows the place to set experimental devices for the IP of laser and H^- beam. All three charge fractions can be simultaneously measured in the downstream beam lines.

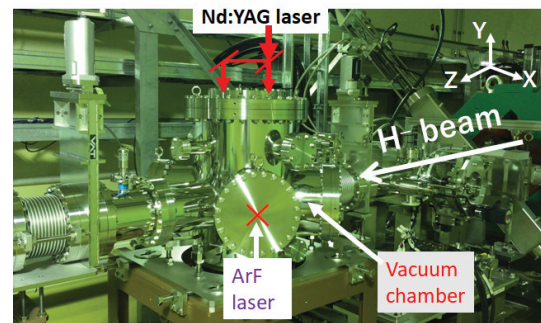


Figure 3: Picture of vacuum chamber installed in the beam line. The laser windows are relatively bigger for multiple purposes including variation of the laser angle for eventually varying the laser wavelength by utilizing the Doppler effect.

line, respectively. The H^0 being neutral charge, we will install a carbon foil at the 90 degree beam dump, to strip them to protons to measure.

Figure 3 shows the picture of the vacuum chamber which has already been installed in the beam line the POP demonstration of 400 MeV H^- stripping by lasers. The Nd:YAG lasers light splitting by the beam splitter will be directed vertically from the top, where the ArF excimer laser will be in the horizontal direction interaction with H^0 at the center of the chamber defined as IP. The window sizes in the chamber for laser lights are comparatively bigger for multiple purposes. By changing the interaction angle we can eventually change λ_0 due to Doppler effect (Eq. 1) to measure the dependence of the production yield on laser wavelength or in other words the cross section. For example, the designed angle of the ArF laser is 63.3° , but it can be varied down to 47° to try for direction ionization of the ground state H^0 (-13.6 eV).

Content from this work may be used under the terms of the CC BY 3.0 licence (© 2018). Any distribution of this work must maintain attribution to the author(s), title of the work, publisher, and DOI.

Optimization of the H^- Beam

In order to achieve sufficient H^- overlapping with the laser pulse, especially for higher excitation of the H^0 , optimizations of the H^- (H^0) beam are very important. For example, to eliminate the transition frequency spread due to the energy spread in the H^- beam, so that all particles satisfy Eq. 1, the dispersion derivative (D') of the H^- is very essential [13, 14]. The D' is expressed as

$$D' = -(\beta + \cos\alpha)/\sin\alpha \quad (2)$$

where, β is the relativistic parameter of the H^- and α is the interaction angle. The D' is -1.3 for the H^0 excitation.

Figure 4, shows the 1st measurement result of the dispersion (D) function along the L-3BT including the laser stripping IP region. The D and its derivative D' are ideally kept zero, but in a trial we obtained D' of about -0.13 by keeping D to be zero at the IP as shown by the black and red lines, respectively. Further studies are planned to obtain the D' as required and also for the transverse beam manipulations at the IP.

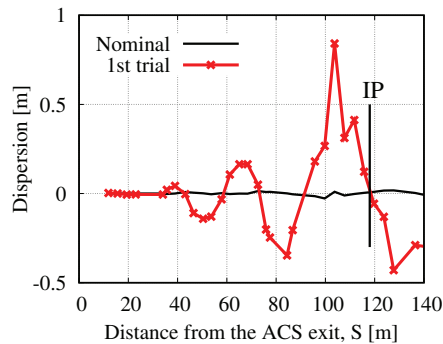


Figure 4: First measurement results of D function manipulation at the IP. The D' is obtained to be -0.13 in a first trial. Further studies will be done to obtain a required value.

Progress of R&D Studies of Lasers

In addition to the H^- manipulation, detail R&D studies of the lasers are also very essential to meet the experimental requirements. The R&D studies of the lasers for the POP demonstration and also for realistic implementation of the H^- CEI system by using lasers have been started recently. At present, detail studies are being done mainly for the 1064 nm Nd:YAG laser. Figure 5 shows the transverse profile at maximum energy of 200 mJ measured at the exit of the laser without any optimization. Further studies are in progress. Realistic setup for the laser beam transportation has been constructed in the laser room to optimize before installing at the accelerator tunnel. The control of the laser beam angle without changing its position at the desired location by using automatic stage controller has also been done successfully. As for the excimer laser, the detail R&D studies are expected to start soon. However, at the first stage, we planned to study the H^- neutralization (step 1) by using Nd:YAG laser in this fiscal year.

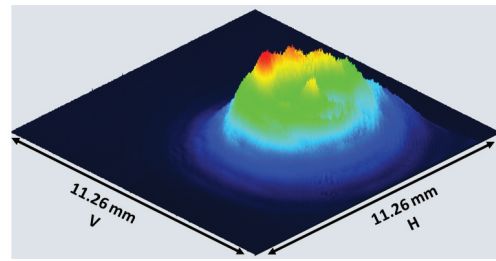


Figure 5: Typical transverse profile of 1064 nm Nd:YAG laser with 200 mJ. The profile can be optimized as required depending on the H^- beam at the IP.

Measurement Technique of Stripping Efficiency

Figure 6 shows the typical pulse structures of the Linac beam at different stages including the injected ones in the RCS. For the POP demonstration, we consider only a single micro pulse of the 400 MeV H^- beam with around 100 ps duration (variable), which has a frequency of 324 MHz as shown at the bottom of the figure. It is very essential to establish a precise technique to measure even a single and tiny micro pulse. For that purpose, we consider using stripline BPM (beam position monitor) pickup signal taken by a fast oscilloscope.

To demonstrate the measurement technique we used one of the horizontal charge-exchange type beam halo scraper (carbon foil) placed upstream of the IP [19]. The scraper are used to remove halo in the H^- beam. The part of the H^- intercepted by scraper are stripped to p and dumped to the 100-degree beam dump (see. Fig. 2). The scraper foil is thick enough ($600 \mu\text{g}/\text{cm}^2$) to strip more than 99.998% of H^- to protons, if intercepted by the scraper [9]. The un-stripped H^- at the RCS injection line and the stripped p at the 100-degree beam dump line separated by bending magnets at the downstream of IP are simultaneously measured by two BPMs.

Figure 7 shows expanded view of few micro pulses for p (left) and H^- (right) measured by BPM pickups for different positioning of the scraper. The p at the 100-degree beam dump is maximum when the H^- beam is fully intercepted by scraper, while it is minimum (nothing) when the scraper is removed from the beam line. The opposite situation is true for the H^- beam measured at the RCS injection line. The p charge fraction for each pulse is obtained from the ratio of integrated yields with scraper partially in (red) to that with scraper fully in (pink). The H^- fraction is also individually obtained in the same way (ratio of data with black and blue). Figure 8 shows p and H^- charge fractions for some typical pulses, when the scraper was partially inserted. The solid lines are averaged values for these 10 pulses and were obtained to be $35.67 \pm 0.26\%$, and $64.15 \pm 0.25\%$, for p and H^- , respectively. The charge fractions of each individual 324 MHz micro pulse is precisely obtained from the measured H^- and p pulses. The present method can be thus utilized for measuring the stripping efficiency of a single micro pulse in the POP demonstration.

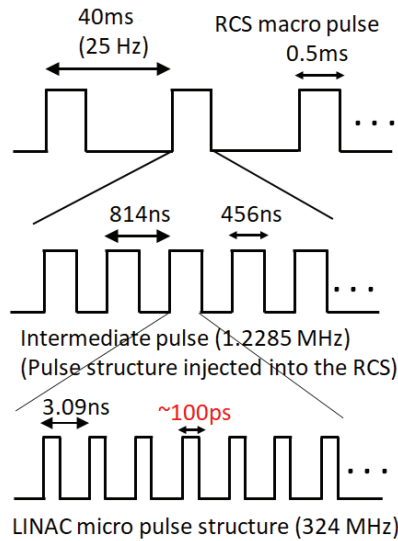


Figure 6: Pulse structures of the Linac beam. A single micro pulse at 324 MHz of around 100 ps is considered for the POP demonstration of 400 MeV H^- stripping by using lasers.

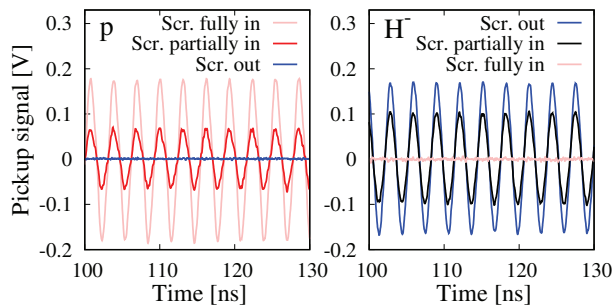


Figure 7: Expanded view of few micro pulses for p (left) and H^- (right) simultaneously measured by BPM pickups at the 100-degree beam dump and the RCS injection lines, respectively for different positioning of the scraper.

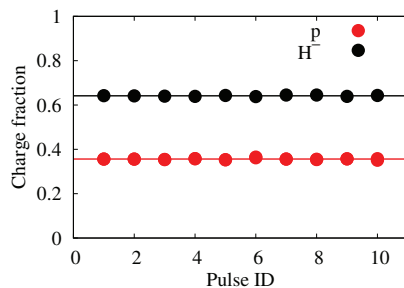


Figure 8: The p and H^- charge fractions for individual micro pulse were obtained from the ratio of integrated yields as shown in Fig. 7.

Expected Stripping Efficiency

The primary motivation of the POP demonstration is to establish the feasibility of the present method of H^- stripping to proton by using only lasers. We consider only a single micro pulse of the 400 MeV H^- beam with a pulse duration of 100 ps (variable), which has a frequency of 324 MHz.

As the laser pulses are long enough (10 ns FWHM), we consider a longer H^- pulse with smaller momentum spread. The Nd:YAG laser energy is sufficiently enough for stripping at the 1st and 3rd steps, while the excitation efficiency of the ArF laser determines the overall result. Figure 9 shows the estimated excitation efficiency (EE) of the H^0 to H^{0*} ($n=3$) as a function of peak power (P_{peak}) of the ArF 193 nm excimer laser. An excimer laser pulse energy of 10 mJ with 10 ns duration gives a P_{peak} of 1 MW to obtain EE of about 90%.

Figure 10 shows a typical H^- signal (black) measured by a BPM pickup. A typical excimer laser pulse is shown by the blue curve. The red curve an expected change of the H^- signal due to its stripping to p by the lasers, where 90% EE is can be achieved for at least a single pulse which overlaps with at the center of the laser pulse.

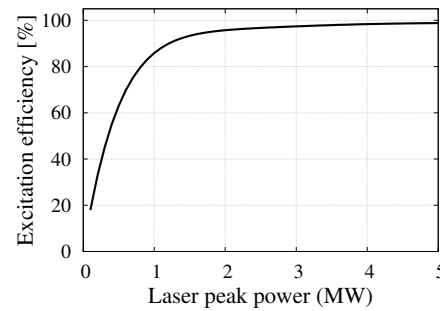


Figure 9: Estimated EE of the H^0 to H^{0*} ($n=3$) as a function of P_{peak} of the excimer laser. The EE can be achieved nearly 90% with P_{peak} of 1 MW (10 mJ).

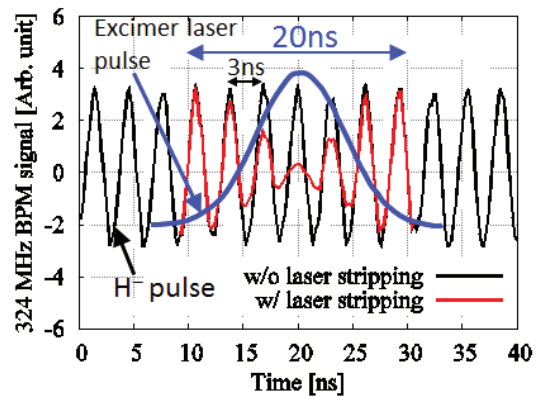


Figure 10: A typical 324 MHz H^- micro pulse structure measured by BPM pickup (black). The blue curve demonstrates an excimer laser pulse. The H^- pulses are expected change like the red curve due to its stripping to p by the lasers. Here we assume 90% EE at the peak of the laser pulse.

The reason why we consider only a single micro pulse for the POP demonstration is that in the practical application we can utilize a laser optical resonator ring [13], which we called laser storage ring or any new applications to cover all micro pulses during 0.5 ms long injection time. The seed lasers would be needed capable of running only at 25 Hz. The laser pulse will be injected into the laser storage ring of 324 MHz, where laser pumping has to be done in order to

Content from this work may be used under the terms of the CC BY 3.0 licence (© 2018). Any distribution of this work must maintain attribution to the author(s), title of the work, publisher, and DOI.

recover the laser energy loss during multiple transmissions through optical devices in the ring. Detail R&D studies of the laser for that purpose have also been started.

APPLICATION OF TWO MIRROR CAVITY FOR REDUCING LASER ENERGY

In addition to the R&D of the laser resonator ring or any other applications for the laser stripping CEI system, it is also important to study for reducing individual pulse energy of the laser. One efficient way is to consider an application of two mirror laser cavity systems at the IP as a next step after the POP demonstration. Such a cavity system called “Linac laser notcher” with Nd:YAG laser for 0.750 MeV H^- beam neutralization to make a gap in the CW beam was developed at Fermi National Accelerator Laboratory (FNAL), and it has already been implemented for the accelerator routine operation [20]. The laser light takes multiple reflections in the cavity so that the H^- pulse has multiple interactions while passing through the cavity. The reduction of the laser energy is almost proportional to the number of interactions take place. In principle, the maximum number of interaction can be reached up to the number of laser reflections.

Figure 11 shows a schematic view of two mirror cavity considered for vertical multiple reflections of the Nd:YAG laser, which can be applied for the 1st and 3rd steps of our laser stripping scheme at J-PARC. The ArF excimer laser is shown for only a single pass, but a similar cavity can be considered in the horizontal direction too.

Figure 12 shows estimated neutralization fraction (NF) of the H^- as a function of laser for multiple interactions by using two mirror laser cavity as shown in Fig. 11 [21]. The energy of the seed laser can be reduced by about one order of magnitude for 10 interactions as compared to that of a single interaction. Similarly, such a reduction of the UV laser energy would be very efficient for the H^0 excitation.

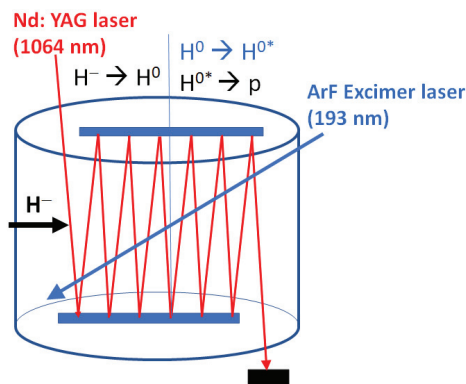


Figure 11: Schematic view of application two mirror laser cavity system for multiple interactions of the H^- and H^{0*} at the 1st and 3rd steps. Similarly, another cavity system can also be applied for the H^0 excitation by excimer laser.

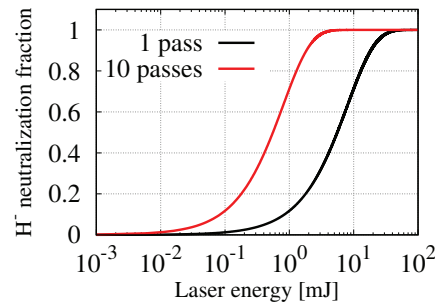


Figure 12: Estimated NF of H^- as a function of laser energy for multiple interactions in a laser cavity. The energy of the seed laser can be reduced by one order of magnitude for 10 interactions as compared to that of a single interaction.

SUMMARY

In order to realize laser stripping H^- charge exchange injection system, a POP demonstration of H^- stripping to protons by using only lasers will be performed at J-PARC. The advantage of the present method over the proceeding research at the SNS is to avoid the difficulties of using extremely high magnetic fields for stripping of H^- to H^0 and H^{0*} to p at the 1st and 3rd steps, respectively. The lower the H^- beam energy, the higher the magnetic fields are required. Instead, we will utilize large photodetachment and photoionization cross sections for the same purposes.

The POP demonstration will be carried out at the L-3BT of J-PARC Linac for the H^- beam energy of 400 MeV. At first, we plan to study the 1st step in this fiscal year, which is the neutralization of 400 MeV H^- by the Nd:YAG laser of 1064 nm. For the POP demonstration, the Nd:YAG laser pulse splitted by beam splitter will be used for both 1st and 3rd steps, while an excimer laser will be used for H^0 excitation up to $n=3$ state. We expect about 90% stripping efficiency for at least a single micro pulse of the H^- beam of about 100 ps. The practical application of H^- laser stripping for the total injection period of 0.5 ms depends on the successful utilization of the laser resonator ring or any other useful applications.

In order to sufficiently reduce the energy of individual laser pulse, we consider an application of the two mirror cavity system at the IP for multiple interaction of individual H^- pulse with the reflected laser pulses, while passing through the laser cavity.

ACKNOWLEDGEMENT

The authors would like to acknowledge many of our J-PARC colleagues for continuous support and cooperation on the present studies as well as concerning our future plan. It is also our opportunity to acknowledge Dr. T. Gorlov, Dr. S. Cousineau, and Dr. Y. Liu of SNS for development of the simulation tool, many helpful discussions. We appreciate extensive cooperation of Mr. David E Johnson of FNAL for the application of two mirror laser cavity system at J-PARC.

REFERENCES

- [1] High-intensity Proton Accelerator Project Team, “Accelerator Technical Design Report for J-PARC”, JAERI-Tech 2003-044 and KEK Report 2002-13.
- [2] J. Wei *et al.*, *Phys. Rev. ST Accel. Beams*, vol. 3, p. 080101, 2000.
- [3] I. Sugai *et al.*, *Nucl. Ins. and Meth. A*, vol. 590, p. 16, 2006.
- [4] M.A. Plum *et al.*, *Phys. Rev. ST Accel. Beams*, vol. 14, p. 030102, 2011.
- [5] “Radio-activation Caused by Secondary Particles Due to Nuclear Reactions at the Stripper Foil in the J-PARC RCS”, in *Proc. of IPAC’17*, Copenhagen, Denmark, 2017, paper TUPVA093, p. 2300.
- [6] P.K. Saha *et al.*, *Phys. Rev. ST Accel. Beams*, vol. 12, p. 040403, 2009.
- [7] H. Harada *et al.*, *Nucl. Ins. and Meth. A*, vol. 602, p. 320, 2009.
- [8] H. Hotchi *et al.*, *Phys. Rev. ST Accel. Beams*, vol. 15, p. 040402, 2012.
- [9] P.K. Saha *et al.*, *Nucl. Ins. and Meth. A*, vol. 776, p. 87, 2015.
- [10] P.K. Saha *et al.*, *Phys. Rev. ST Accel. Beams*, vol. 14, p. 072801, 2011.
- [11] P.K. Saha *et al.*, *J. Radioanal Nucl. Chem.*, vol. 305, p. 851, 2015.
- [12] Isao Yamane, *Phys. Rev. ST Accel. Beams*, vol. 1, p. 053501, 1998.
- [13] V. Danilov *et al.*, *Phys. Rev. ST Accel. Beams*, vol. 6, p. 053501, 2003.
- [14] V. Danilov *et al.*, *Phys. Rev. ST Accel. Beams*, vol. 10, p. 053501, 2007.
- [15] S. Cousineau *et al.*, *Phys. Rev. Lett.*, vol. 118, p. 074801, 2017.
- [16] P.K. Saha *et al.*, “Preliminary Studies of Laser-assisted H⁻ Stripping at 400 MeV”, in *Proc. of IPAC’15*, Richmond, VA, USA, 2015, paper THPF043, p. 3795.
- [17] Isao Yamane, Hiroyuki Harada, Saha Pranab and Shinichi Kato, *J. of Part. Acc. Soc. Japan* vol. 13, p. 1, 2016, (In Japanese).
- [18] L. M. BRANSCOMB, “Physics of the One-And-Two-Electron Atoms”, edited by F. Bopp and H. Kleinpoppen, North-Holland, 1968.
- [19] K. Okabe *et al.*, *Nucl. Ins. and Meth. A*, vol. 811, p. 11, 2016.
- [20] David E. Johnson *et al.*, “The Linac Laser Notcher for the Fermilab Booster”, in *Proc. of LIAC’16*, East-Lansing, MI, USA, 2016, paper TH2A01, p.710.
- [21] David E. Johnson, Private communications, 2018.

DESIGN OF 162-MHz CW BUNCH-BY-BUNCH CHOPPER AND PROTOTYPE TESTING RESULTS*

A. Shemyakin[†], C. Baffes, J.-P. Carneiro, B. Chase, A. Chen, J. Einstein-Curtis, D. Frolov, B. Hanna, V. Lebedev, L. Prost, A. Saini, G. Saewert, D. Sun, Fermilab, Batavia, IL 60510, USA
D. Sharma, Raja Ramanna Center for Advanced Technology (RRCAT), India
C. Richard, Michigan State University, East Lansing, MI, USA

Abstract

The PIP-II program of upgrades proposed for the Fermilab accelerator complex is centered around an 800 MeV, 2 mA CW SRF linac. A unique feature of the PIP-II linac is the capability to form a flexible bunch structure by removing a pre-programmed set of bunches from a long-pulse or CW 162.5 MHz train, coming from the RFQ, within the 2.1-MeV Medium Energy Beam Transport (MEBT) section. The MEBT chopping system consists of two travelling-wave kickers working in sync followed by a beam absorber. The prototype components of the chopping system, two design variants of the kickers and a 1/4-size absorber, have been installed in the PIP-II Injector Test (PIP2IT) accelerator and successfully tested with beam of up to 5 mA. In part, one of the kickers demonstrated a capability to create an aperiodic pulse sequence suitable for synchronous injection into the Booster while operating at 500 V and average switching frequency of 44 MHz during 0.55 ms bursts at 20 Hz. This report presents the design of the PIP-II MEBT chopping system and results of prototypes testing at PIP2IT.

INTRODUCTION

In the coming decade, Fermilab plans to replace the existing linac with a new 800 MeV SRF H⁻ accelerator, a.k.a. PIP-II [1]. Presently, its first application is expected to be the injection into the Booster while later delivering a high-power beam simultaneously to multiple experiments. In the scheme proposed in [2] for the latter, a RF cavity with transverse field operating at a frequency of $(n+1/2) \times 162.5$ MHz (so-called RF splitter) placed downstream of the linac, distributes bunches to three channels according to the phase of their arrival. Since requirements for the beam time structure are likely to be very different for various experiments, the scheme suggested installing in the MEBT a dedicated fast chopping system (chopper) capable of removing individual bunches from initially true CW beam coming out of the 162.5 MHz RFQ. Only bunches fitting to the combined pattern of experiments' requests are passed for acceleration, while others are dumped within the MEBT.

Capability to create an arbitrary bunch pattern is beneficial for the scenario of the Booster injection as well. The fundamental bunch frequency of the PIP-II linac, 162.5 MHz, and the Booster frequency at injection, 44.7 MHz

are not harmonically related. In the bucket-to-bucket injection scenario described in [1], the chopper removes the bunches that would arrive at the boundaries of separatrix, creating an optimum longitudinal distribution and equal population of the Booster bunches. In addition, it creates a gap in the Booster bunches sequence to fire the extraction kicker at the end of the acceleration cycle.

The concept of the chopper as well as its prototype components were tested at the PIP-II Injector Test (PIP2IT, [3]) accelerator.

CHOPPER CONCEPT AND CHOICE OF PARAMETERS

The chopper consists of a set of electrostatic deflectors (kickers) and a beam absorber accepting the unwanted bunches. Bunch-by-bunch selection assumes that the kickers are capable of fully deflecting a "removed" bunch while perturbing minimally the neighbouring "passing" bunches. Full deflection is defined as separation of the passing and removed bunches in the transverse direction (chosen for PIP-II vertical and marked as Y in the text) by $6\sigma_y$, where σ_y is the vertical rms beam size at the absorber.

The deflection voltage pulse needs to travel along the kicker with the speed matching the velocity of the 2.1 MeV H⁻ ions, 20 mm/ns. Therefore, a corresponding travelling-wave structure is required.

The main parameters defining the scheme choices are the vertical emittance ($\sim 0.2 \mu\text{m rms n}$) and the achievable kicker plate voltage amplitude, i.e. difference of the voltage between states of passing and removing the bunches. The latter was chosen to be 500 V. Then, the minimum kicker gap was defined by the expected beam size plus space to accommodate the trajectories of both passing and removed bunches. The gap was further increased by $\sim 20\%$ while limiting the entrance and exit apertures of the kicker with electrodes exclusively dedicated to protection of the kicker structure from irradiation by the beam. The kickers need to fit between the quadrupole triplets (650 mm flange-to-flange), which in turn defined the length of the deflecting plates, 0.5 m. To achieve the required separation, the deflection is provided by two kickers placed at $\sim 180^\circ$ betatron phase advance between them. The absorber follows the last kicker with an additional $\sim 90^\circ$ phase advance.

To decrease the power density of the removed bunches at the absorber surface, it is positioned at a small angle with respect to the beam. To keep the distances between the focusing elements constant through the MEBT, the length of the absorber surface is also 0.5 m. Both absorber

* This manuscript has been authored by Fermi Research Alliance, LLC under Contract No. DE-AC02-07CH11359 with the U.S. Department of Energy, Office of Science, Office of High Energy Physics

[†]shemyakin@fnal.gov

and kickers were originally specified and designed to be CW-capable. Some of the parameters of the chopping system elements are presented in Table 1, and the vertical envelopes of the passing and removed bunches simulated for the PIP-II are shown in Fig. 1.

Table 1: Parameters of the Chopper Elements

Parameter	Value	Units
Kicker deflection angle*	7.4	mrad
Gap between kicker plates	16	mm
Gap in the kicker protection electrode	13	mm
Kicker plate length	500	mm
Maximum power from beam loss, CW	40	W
Maximum accidental beam loss	20	J
Absorber surface length	500	mm
Maximum power at absorber, CW	21	kW

* Deflection angle is defined as the angle between passed and removed trajectories created by one kicker.

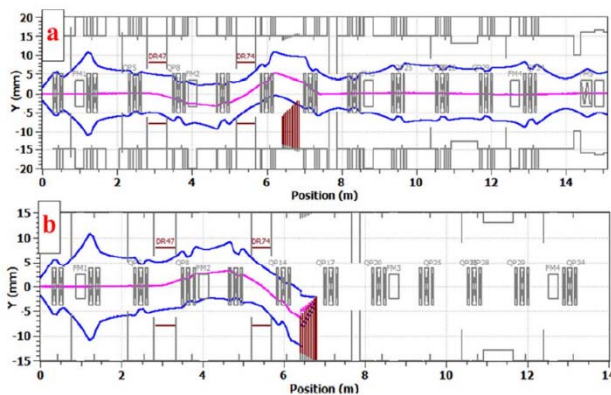


Figure 1: 3σ vertical envelope simulated with Tracewin [4] showing passing (a) and removed (b) trajectories.

KICKERS

Two versions of the kicker and driver, referred below by their impedance, 50 and 200 Ohm, were developed [5] and tested with beam.

50 Ohm Version

The 50-Ohm kicker consists of two identical structures shown in Fig. 2. The beam is deflected by voltage applied to 25 planar electrodes connected in vacuum by coaxial cables with the length determined by necessary delays. Cooling of the Teflon-insulated cables is provided by clamps, which, in turn, are cooled by water flowing through the channels in the structure. The low-power RF measurements showed the excellent agreement with the specified phase velocity (20.08 mm/ns) and low dispersion.

The kicker was expected to be driven by two 0.7 kW CW wideband (0.05 – 1 GHz) linear amplifiers produced by industry. To decrease the low frequency content of the output signal, the 6.15 ns pulse affecting an individual bunch is formed bipolar with zero average voltage. Effects from non-linearities of the amplifier, imperfections of its frequency response and dispersion in cables and the

kicker structure are corrected by pre-distorting the driving signal (see details of proof-of-principle test in [5]).

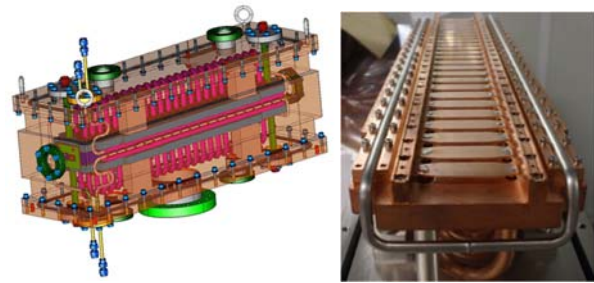


Figure 2: 50-Ohm kicker structure: 3D model and one assembled plate.

Due to budgetary constraints, such amplifiers were not acquired, and the beam tests were performed with the kicker driven by a pair of power amplifiers operating at 81.25 MHz. In this mode, the neighbouring bunches were deflected in opposite directions by ± 250 V on each plate.

The same amplifiers were used to test the thermal characteristics of the kicker. The kickers were subjected to the total power of 2.8 kW CW (374 V per plate) for ~ 100 hours with no changes observed and vacuum at the end $< 10^{-7}$ Torr. The insertion loss during these tests was 0.27 dB.

200 Ohm Version

The travelling wave structure of the 200 Ohm kicker is composed of two helices each with 47 welded plates facing the beam (Fig. 3). Its detailed description can be found in Ref. [6].

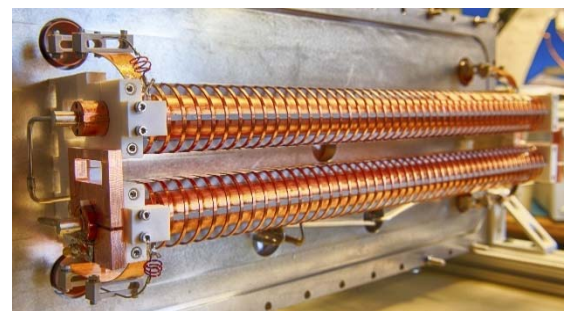


Figure 3: Photo of the fully assembled 200 Ohm kicker's two-helix structure.

The high characteristic impedance enables using a fast switch to generate the voltage waveform at the kicker electrodes. As reported in Ref. [6], two prototype switch drivers used in the beam tests are capable of switching the plate voltage between zero and 500 V in 4 ns at rates up to the maximum interesting rate of 81.25 MHz, corresponding to the deflection of every other bunch. The limit for the combination of the macro-pulse length and switching frequency is determined by the heat removal from the switch transistors. The present version with the transistors mounted on G10 and cooled by forced air is limited to CW average switching rate of 500 kHz.

While the RF loss in the structure is low (~ 8 W per helix), the possibility of uncontrolled beam loss of up to 40

Content from this work may be used under the terms of the CC BY 3.0 licence (© 2018). Any distribution of this work must maintain attribution to the author(s), title of the work, publisher, and DOI.

W was foreseen. To ensure the kicker’s survival in this scenario, it was subjected to a thermal test, in which a DC current was injected, corresponding to 40 W deposited in each helix. No dramatic vacuum degradation or changes in kicker characteristics were observed.

ABSORBER

The absorber concept [7] features a grazing angle of incidence (29mrad) that decreases the peak power density absorbed at the surface to 17 W/mm²; longitudinal segmentation to relieve thermally-induced stresses; and the molybdenum alloy TZM for the absorbing surface.

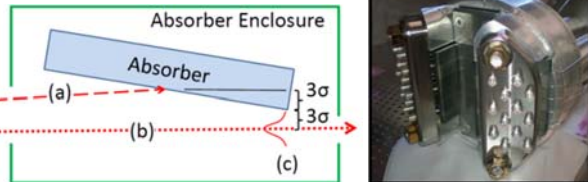


Figure 4: Left: separation scheme with (a) removed beam, (b) passing beam, (c) 6σ shift between two trajectories. Right: photo of the absorber prototype.

Two ¼ length prototypes were manufactured and tested with an electron beam at a dedicated test stand [7]. In part, the second prototype, shown in Fig. 4 (right) photo successfully went through a thermocycle test with more than 10⁴ “30s on- 30s off” cycles at the power density deposited by the electron beam exceeding the level expected for the PIP2IT full – size absorber. This prototype was installed into PIP2IT downstream of the kickers.

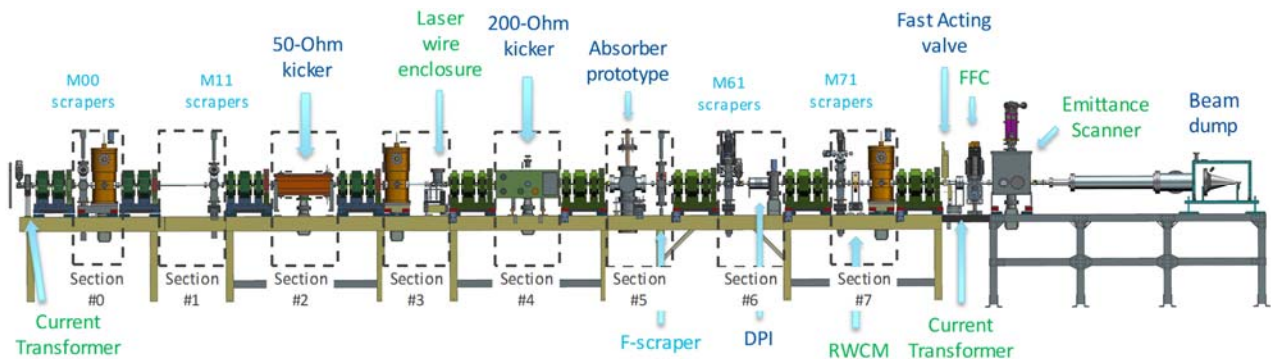


Figure 5: Medium Energy Beam Transport line (side view)

Current transformers are located at the beginning and end of the MEBT; the beam current can be measured from the beam dump as well. An emittance scanner was used to record the vertical beam phase portraits, and a Resistive Wall Current Monitor (RWCM) provided information about the population of the bunches.

TESTS AND RESULTS

Kicker Deflection

Deflection of both kickers was characterized in the MEBT configuration before installation of the DPI, which allowed transporting both “passing” and “removed”

PIP2IT WARM FRONT END

Beam tests of the chopper elements prototypes were performed at the PIP2IT, which presently consists of a 30 kV H⁻ ion source, a LEBT, a 2.1 MeV RFQ capable of accelerating up to 10 mA CW beam, a 10-m long MEBT where the chopper elements are located, and a beam dump [8].

The MEBT (Fig. 5) is a succession of nine “sections” (650-mm long flange-to-flange for sections #1 through #7, and 480 mm for section #0), delimited by transverse focusing assemblies, two quadrupole doublets and 7 triplets. Each group includes a Beam Position Monitor (BPM), whose capacitive pickup is bolted to the poles of one of the quadrupoles. Longitudinal focusing is provided by 3 bunching cavities. The kicker and absorber prototypes are installed in sections 2,4, and 5. In the MEBT configuration shown in Fig. 5, the absorber prototype is followed by a Differential Pumping Insert (DPI). This 200 mm (L) × 10 mm (ID) beam pipe reduces the flux of gas released from the bombardment of the absorber with H⁻ ions into the future cryomodules downstream.

Movable scrapers [9] installed with the main goal to protect the cryomodules against an errant beam or halo were also used to measure the beam size. Shown in Fig. 5 are 4 sets of 4 scrapers (each set consists of a bottom, top, right and left scraper) plus a temporary set of two scrapers (a.k.a. F-scraper, top and right), which was extensively used to characterize the kickers performance.

trajectories to the beam dump with low losses. An Arbitrary Waveform Generator [6] drove the kicker to deflect every other bunch. Then the vertical F-scraper was moved in, and the dump current was recorded as a function of the scraper position. If the two trajectories are well separated, the scan shows two ‘steps’ (Fig. 6).

Quantitatively, the scraper profiles are fitted with a function corresponding to the sum of 2 Gaussian 1D profiles, where the fitting parameters are the mean value of each Gaussian and σ_y , which is assumed to be the same for bunches belonging to either trajectory. The difference between the 2 mean values is the bunch separation. From this, both the optimum phase of the kicker w.r.t. the beam

and the deflection angle at the kicker exit can be inferred. To have good separation and good transmission of both trajectories to the dump, the beam is heavily scraped off in the vertical direction with two scraping stations upstream of the chopper, producing a flat beam.

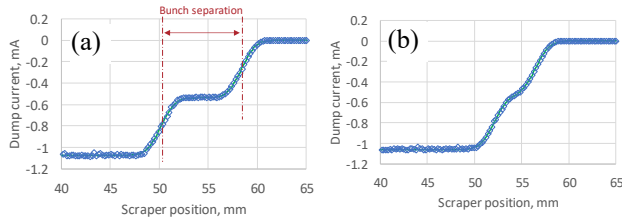


Figure 6: F-scrapers profiles for different delays between the phase of the beam and the 50 Ohm kicker's. (a) Optimum delay; (b) Shifted by 1.73 ns w.r.t. the optimum delay. The beam current after scraping is 1.1 mA (5 mA initially). The fitted rms beam size is 1.15 mm, and the bunch separation is 8.2 mm (a) and 4.4 mm (b).

Routine phasing of the kickers uses the BPM immediately downstream of the F-scrapers. A fast scope records the differential signal from the BPM vertical plates and calculates the difference between peaks of the signals from neighbouring bunches. The kicker delay is varied until this difference is maximized. However, for numerical characterization, the procedure using the F-scrapers (Fig. 6) is employed. The bunch separation plotted as a function of the kicker delay represents the temporal shape of the kicker signal smoothed by the finite length of the beam bunches (Fig. 7).

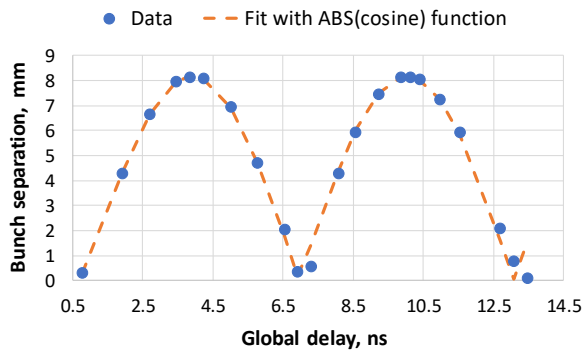


Figure 7: Example of phasing delay of the 50 Ohm kickers with scraper scans.

Using the optical model of the beam line [10], the maximum spatial separation between bunches measured with the F-scrapers is translated into the amplitude of the angular deflection by the kicker. The error of this reconstruction is estimated to do not exceed 5%. In some measurements with the 50 Ohm kicker, there was a significant scatter (~5%) of deflections, likely related to drifts of the kicker's power amplifiers. Within these errors, the measured deflections were in a good agreement with the expected values (7.4 mrad for 500 V plate voltage change).

200 Ohm Version Tests

Several additional tests were performed with the 200 Ohm kicker. One of them is an estimate of the perturbation passing bunches experience. The kicker voltage does not exactly reach the ground potential when the passing bunch arrives, and the bunch centroid undergoes a small deflection. This deflection was measured using the flat beam with the sequence of deflecting every other bunch ("81.25 MHz") and intercepting the removed bunches. The trajectory of the passing bunches was recorded with BPMs and compared to the trajectory with the kicker off. The resulting deflection at nominal parameters was found to be 0.3 mrad, which for the nominal beam creates an emittance dilution of <5%. Note that the average deflection is expected to be lower for other patterns of bunch removal.

Another test is a verification that a difference between the nominal velocity of ions and the phase velocity of the kicker does not affect the deflection amplitude. In these measurements, the phase and amplitude of bunching cavity #2 are changed such as to keep focusing constant but the energy is varied by ± 87 keV. The energy change is then verified from changes of the phases of the downstream BPMs, and the bunch separation is measured at the kicker delay optimum for each energy, E . While one of the points measured is unexplainably shifted, the main effect appears to be a decrease of the deflection with energy as $1/E$, as it would be in the case of a perfect match, and the contribution of a velocity mismatch to the maximum deflection is less than 5% (Fig. 8). Note that if the main goal of the measurement were to compare the kicker phase and ions velocity, a measurement at the rising or falling edges rather than at the maximum would have a better sensitivity to the velocity mismatch.

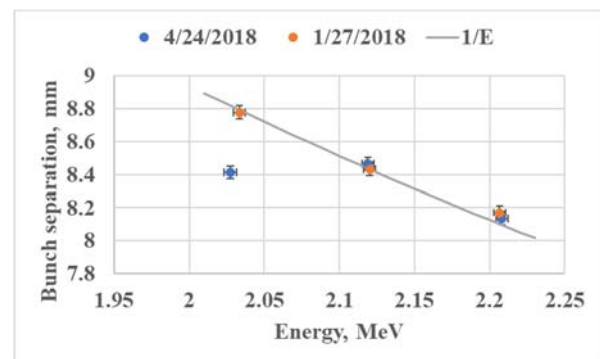


Figure 8: dependence of the bunch separation measured with the F-scrapers on the beam energy. Two sets are measured at different voltage of the kicker plate power supply, with separation scaled to 500 V. The solid curve is $1/E$ dependence drawn through the point measured at the nominal energy.

The 200 Ohm kicker driver in combination with the flat beam and partial insertion of the F-scrapers allows forming arbitrary bunch sequences. Several examples were implemented and recorded with the RWCM: 81.25 MHz

Content from this work may be used under the terms of the CC BY 3.0 licence (© 2018). Any distribution of this work must maintain attribution to the author(s), title of the work, publisher, and DOI.

(already mentioned); a pattern with randomly selected passing and removed bunches; one pattern suitable for the Mu2e experiment (repeatable pattern of 200 ns of passing bunches followed by 1.6 μ s of removed bunches); and aperiodic sequence envisioned for Booster injection. The latter pattern lasted for 0.55 ms macro-pulses, the entire length of the Booster injection (Fig. 9).

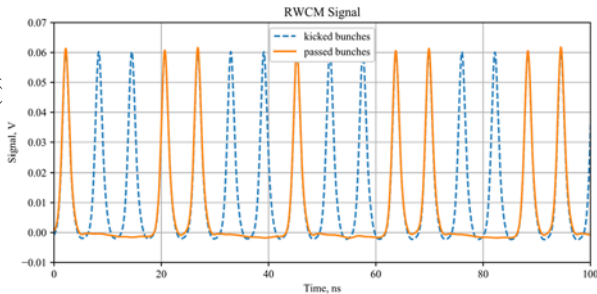


Figure 9: Part of the RWCM signal recording the 0.55 ms Booster injection sequence (orange), superimposed over the signal when the kicker is off (blue). 1.1 mA flat beam.

To test survival of both the driver and the kicker structure for extended operation, the beam was run for 24 hours (with 95% beam availability) at parameters expected for Booster injection [1] 5 mA \times 0.55 ms \times 2.1 MeV \times 20 Hz with the kicker pulsing as depicted in Fig. 9. In addition, a higher-power beam, up to 5 kW, was passed through both (non-pulsing) kickers. No problems were observed even with multiple interruptions induced by the beam touching the kickers. Thus, the Machine Protection System monitoring of the kicker protection electrodes' currents protected the kickers effectively.

Two Kickers Working Together

Preliminary tests were performed with two kickers operating in sync with the 81.25 MHz pattern. The first test was a sanity check, where the kickers, phased individually in advance, were deflecting the flat beam. The total deflection, estimated by the scope signal from the downstream BPM, was equal to the sum of deflections by each kicker. Note that more accurate measurements with F-scraper scans (as in Fig. 6) cannot be performed in this case because the separation is too large to transport both trajectories to the dump with low losses.

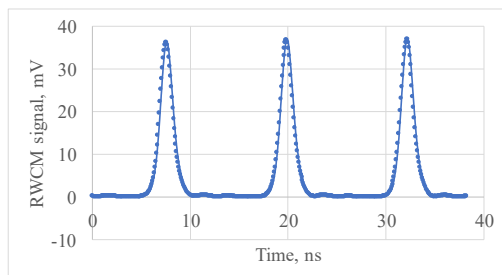


Figure 10: RWCM signal of an initially 5 mA beam with two kickers operating synchronously at 81.25 MHz.

The second test was performed with a full-intensity beam to mimic operation in a high-power mode, though the pulse length was still 10 μ s. The scrapers upstream of the chopping system were moved to the beam boundary as they were during high-power runs, intercepting \sim 1% of the beam current. After careful tuning with dipole correctors through the tight apertures of the pulsing kickers, the beam losses to their protection electrodes were decreased to below 10 μ A each, which, according to previous measurements, ensures that the loss power to the kickers stays well below the specified 40 W.

Then the F-scraper was moved in to the position where the beam current to the dump dropped by a factor of two in comparison with the case of the kickers being turned off. The RWCM signal showed that the intensity of the removed bunches dropped below 2% of the passing ones (Fig. 10).

Absorber Prototype

While time limitations did not allow to test the absorber prototype with the highest power available, it was irradiated for 36 hours with 98% beam up-time with the following parameters: 1.75 ms \times 20 Hz \times 10 mA \times 2.1 MeV = 735 W (with the kickers off). No damage or deterioration was observed.

Tuning of the beam position at the absorber surface was expected and initially made using thermocouples squeezed between the TZM bricks forming the absorbing surface. A surprising help came from imaging of the surface with a camera in the visible spectrum. Even though the surface was not hot enough for thermal radiation, and the OTR light should be too faint to be observed, a bright light clearly indicated the beam position at the absorber surface (Fig. 11). The present speculation is that it is related to poor vacuum in the time of the measurements (up to $6 \cdot 10^{-6}$ Torr) because no pumping had been installed yet.

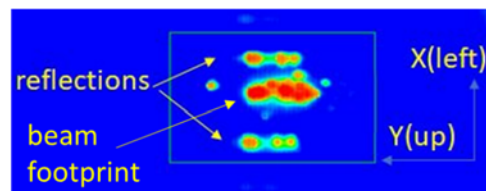


Figure 11: Fi Image, in false colors, of the beam footprint at the absorber surface. Side traces are reflections from the absorber walls. The length of the footprint (along the beam axis) is \sim 40 mm. 3 ms \times 20 Hz \times 10 mA.

SUMMARY AND PLANS

Prototypes of two kicker variants and of the absorber were successfully tested with a 2.1 MeV H⁻ beam at PIP2IT. The 200 Ohm kicker version demonstrated all capabilities required for PIP-II operation with bucket-to-bucket injection to Booster. A full-size absorber is being manufactured, and production of two kickers and their drivers (200 Ohm version) is expected in 2019. When PIP2IT operation resumes after installation of the cryo-modules, the chopping system will demonstrate being

able to deliver a beam with nominal parameters chopped according to the Booster injection requirements.

ACKNOWLEDGMENT

The authors are thankful to the many people who contributed to building the prototype chopping system and helped with the measurements, including B. Fellenz, D. Franck, M. Hassan, S. Khole, D. Lambert, W. Mueller, R. Neswold, D. Nicklaus, A. Saewert, V. Scarpine, J. Simmons, R. Thurman-Keup.

REFERENCES

- [1] PIP-II Conceptual Design Report (2017); <http://pip2-docdb.fnal.gov/cgi-bin/ShowDocument/docid=113>
- [2] Project X Reference Design Report (2013); <http://projectx-docdb.fnal.gov/cgi-bin/ShowDocuent/docid=776>
- [3] P. F. Derwent *et al.*, “PIP-II Injector Test: challenges and status”, in *Proc. LINAC’16*, East Lansing, MI, USA, 2016, paper WE1A01, pp. 641-645.
- [4] TraceWin code, <http://irfu.cea.fr/Sacm/logiciels/>
- [5] V. Lebedev *et al.*, “Progress with PXIE MEBT chopper”, in *Proc. IPAC’12*, New Orleans, LA, USA, 2012, paper WEPD078.
- [6] G. Saewert *et al.*, “First Performance results of the PIP2IT MEBT 200-Ohm kicker prototype”, in *Proc. IPAC’18*, Vancouver, BC, Canada, 2018, paper WEPML021.
- [7] A. Shemyakin and C. Baffes, “High power density test of PXIE MEBT absorber prototype”, in *Proc. LINAC’14*, Geneva, Switzerland, 2014, paper THPP055.
- [8] L.R. Prost, R. Andrews, C.M. Baffes, J.-P. Carneiro, B.E. Chase, A.Z. Chen, E. Cullerton, P. Derwent, J.P. Edelen, J. Einstein-Curtis, D. Frolov, B.M. Hanna, D.W. Peterson, G.W. Saewert, A. Saini, V.E. Scarpine, A.V. Shemyakin, V.L. Sista, J. Steimel, D. Sun, A. Warner, C.J. Richard, V.L. Sista, “PIP-II Injector Test Warm Front End: Commissioning Update”, in *Proc. IPAC’18*, Vancouver, Canada, 2018, paper THYGBF2.
- [9] A. Saini and A. Shemyakin, “Optical design of the PI-Test MEBT beam scraping system”, in *Proc. LINAC’16*, East Lansing, MI, USA, 2016, paper THPRC026.
- [10] A. Shemyakin, J.-P. Carneiro, B. Hanna, V. Lebedev, L. Prost, A. Saini, V. Scarpine, V.L. Sista, C. Richard, “Experimental study of beam dynamics in the PIP-II MEBT prototype”, presented at HB’18, Daejeon, Korea, June 2018, paper MOP1WB03, this conference.

THE FNAL BOOSTER 2ND HARMONIC RF CAVITY*

R. Madrak[†], J. Dey, K. Duel, M. Kufer, J. Kuharik, A. Makarov, R. Padilla, W. Pellico, J. Reid, G. Romanov, M. Slabaugh, D. Sun, C. Y. Tan, I. Terechkin,
Fermilab, Batavia, IL, 60510, USA

Abstract

A second harmonic RF cavity which uses perpendicularly biased garnet for frequency tuning is currently being constructed for use in the Fermilab Booster. The cavity will operate at twice the fundamental RF frequency, from ~76 - 106 MHz, and will be turned on only during injection, and transition or extraction. Its main purpose is to reduce beam loss as required by Fermilab's Proton Improvement Plan (PIP). After three years of optimization and study, the cavity design has been finalized and all constituent parts have been received. We discuss the design aspects of the cavity and its associated systems, component testing, and status of the cavity construction.

INTRODUCTION

The defining feature of this cavity is its on-axis tuner using aluminum doped garnet: National Magnetics AL-800. The tuning is achieved by sweeping the bias magnetic field, which is perpendicular to the RF magnetic field. This is different from many wideband cavities which use materials such as NiZn ferrite, where the ferrite is biased parallel to the RF magnetic field. Using garnet is desirable because the saturation magnetization is typically lower than in ferrite, and with a realistic magnetic system it can be biased to saturation where losses are lower. However, to maintain tunability, the bias must then be perpendicular to the RF magnetic field instead of parallel. If the tunability is sufficient, substantially higher shunt impedances can be attained.

Several cavities with a perpendicular bias [1] have been constructed and used operationally [2], but these have limited tuning range. Both TRIUMF/LANL [3] and the SSC Low Energy Booster [4] developed prototype cavities with large tuning ranges, but none of these cavities were ever used with beam.

PURPOSE

It is well known that by flattening the bucket at injection, it is possible to increase the capture efficiency because of increased bucket area and a reduction in space charge density [5]. Although beam capture in Booster is already quite efficient, greater than 90% for 5.3×10^{12} protons, there is still an activation problem due to beam loss. Therefore, even a gain in efficiency of a few percent can help mitigate this problem. This is the main motivation for the installation of a 2nd harmonic cavity in the Booster. The cavity will be turned on for approximately

3 ms at injection, with 100 kV peak gap voltage.

At transition, the main mechanism for beam loss is bucket mismatch and not from space charge [6]. The 2nd harmonic cavity can be used to shape the bucket so that the beam is better matched to it before and after transition. At extraction, the cavity can be used to linearize the voltage during bunch rotation so that there can be a reduction in the tails of the rotated distribution. For more details and references, see [7].

CAVITY DESIGN

A model of the cavity is shown in Fig. 1. The flange-to-flange length is 844 mm, the aperture is 76 mm, and the shunt impedances are 96 k Ω and 180 k Ω , at 76 MHz and 106 MHz, respectively. The shunt impedance R_{sh} is defined as $V_p^2/2P$, where P is the average dissipated power and V_p is the peak voltage.

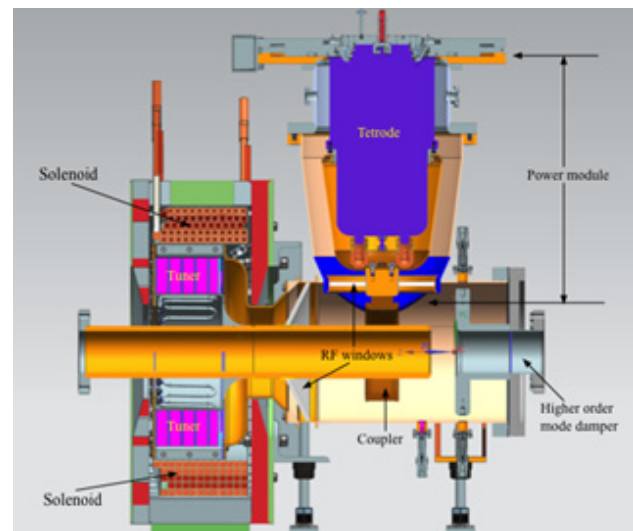


Figure 1: Model of the finalized cavity design [8,9]. The length is 844 mm from flange to flange.

The cavity is a quarter wave type and is shorted at the garnet end. The magnetic field in the garnet rings is generated by a solenoid contained within a flux return and two pole pieces. Two alumina windows are used so that the tuner rings and the power amplifier (PA) are outside of the cavity/beamline vacuum. The power amplifier, which uses a cathode driven Eimac Y567B (4CW150000) tetrode, sits between the garnet and the gap end, and is capacitively coupled by a ring which surrounds the cavity's center conductor. The accelerating gap end has a Smythe [10] type higher order mode damper.

Although perpendicularly biased cavities have the advantage that RF losses are lower, the tuning range for this particular cavity is large and there are many technological

* Operated by Fermi Research Alliance, LLC under Contract No. DE-AC02-07CH11359 with the United States Department of Energy
[†] madrak@fnal.gov

challenges to overcome. Some of the concerns are 1) Achieving the required tuning range using a realistic bias magnetic field, 2) Keeping the magnetic field in the tuner as uniform as possible (including minimizing the effect of eddy currents), 3) Taking into account higher local permeability and heating of the garnet in areas of lower magnetic field, 4) Including the power amplifier/tetrode in the RF model to take into account the impact of the additional volume and tetrode output capacitance on the cavity tuning range, 5) Choosing a design concept for the tuner that would simplify removal of the heat generated by both the RF and eddy currents, and 6) Finding a safe alternative to using BeO as the heat transfer material.

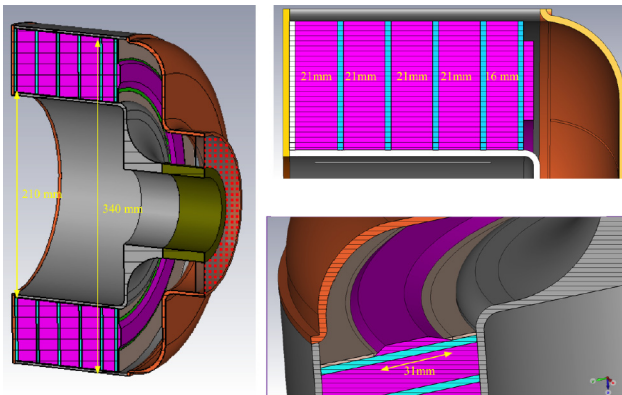


Figure 2: The tuner section of the cavity.



Figure 3: Layout and photographs of the garnet and alumina sides of a tuner ring.



Figure 4: Tuner Shim Ring. The full ring consists of one ring of alumina on the bottom, one garnet ring, a second ring of alumina, and finally the angled shim ring.

TUNER

The tuner section of the cavity is shown in Fig. 2. Each of the five rings uses National Magnetics AL-800 material, which is aluminium doped garnet. The saturation magnetization ($4\pi M_s$) is 800 G and the Curie temperature is 210 °C. The OD and ID of the rings are 340 mm and 210 mm, respectively, and the thickness is 21 mm. The

garnet rings, shown in Fig. 3, are made from eight sectors which are epoxied (Stycast 2850FT, Catalyst 9) together. This allowed the use of an existing oven with a well-known temperature distribution. To remove heat from the garnet material, each ring is epoxied to a 3 mm thick alumina (99.5%) ring. Each garnet sector is cut from a brick along with a small “witness sample”, which is to be used for quality control.

Regions of high RF power loss occur where the bias magnetic field approaches the gyromagnetic resonance value, and the power loss in the material increases sharply. The transition area between the garnet and the beam pipe is especially vulnerable in this respect due to large changes in the permeability of the media. To improve the field quality in this area, a specially shaped shim ring was added to the front of the tuner stack. A photograph of it is shown in Fig. 4. With the addition of the shim, the minimum value of the magnetic field in the garnet increases from 33 Oe to 69.3 Oe. This is comfortably higher than 27 Oe, the field at which the gyromagnetic resonance occurs for the lowest frequency.

The cavity frequency is tuned by changing the bias magnetic field in the garnet, which changes the permeability in the garnet. The entire Booster ramp occurs during a period of ~ 33 ms. It was necessary to take steps to reduce the eddy currents induced in the walls of the cavity during the ramp, which would generate heat and distort the bias field. The center and outer conductors in the tuner part of the cavity are made from stainless steel, which has poor conductivity. Also, they are divided into four azimuthal sections, which interrupts the azimuthal component of the eddy currents. In order that the stainless steel not cause RF losses, the center and outer conductors are copper plated on the sides which encompass the RF volume.

The RF heat generated in the garnet, which has poor thermal conductivity, is transferred by the alumina disks to the center and outer conductors, which are water cooled. The design is such that the temperature in the garnet does not exceed 100 °C. This water cooling also serves to remove heat generated by eddy currents.

Solenoid and Bias Supply

The bias magnetic field is generated between the two poles of a magnet with solenoidal windings. The fast cycling of the Booster at 15 Hz required that the yoke be made from silicone steel laminations to reduce the effects of eddy currents.

The complete winding is made of two coils wound using 0.46” square copper wire with a 0.25” hole for cooling. The total number of turns is 60. A photograph is shown in Fig. 5. The coils can be powered independently, or connected in series. In the present design the series connection is used. The required current ramps for the cavity to operate at injection, transition, and extraction, are shown in Fig. 6.

Due to funding constraints in FY2018, the complete bias supply has not yet been purchased. The bias supply now consists of four Performance Controls, Inc. GA301-

Content from this work may be used under the terms of the CC BY 3.0 licence (© 2018). Any distribution of this work must maintain attribution to the author(s), title of the work, publisher, and DOI.

VP amplifiers in parallel, and will be upgraded in the future with another seven or eight such supplies. So, initially, due to the limited amount of power from the existing supply, the cavity will be operated only for the first 3 ms at the most critical beam loss points, which is during injection/capture.



Figure 5: The bias solenoid with the end plates removed.

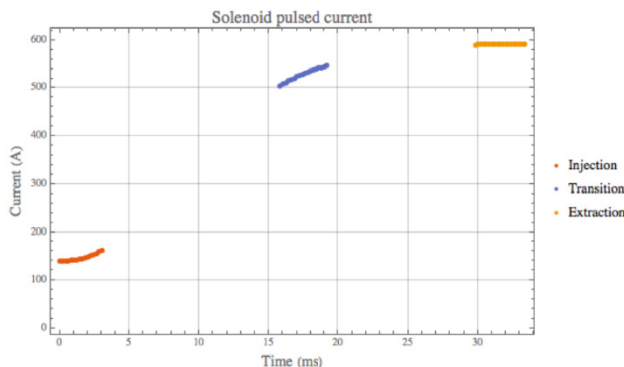


Figure 6: The current pulses required to bias the garnet during the critical periods. The current ramp outside these regions will be determined operationally.

GARNET CHARACTERIZATION

The accurately model the cavity it was necessary to know the garnet permeability as a function of magnetic field. The real (μ') and imaginary (μ'') parts of the permeability determine the tuning range and losses, respectively. The magnetic field in the tuner is never perfectly uniform, and to properly model the device, it must be known at every point in the tuner for all bias settings. Since such data is not published, the static permeability and loss tangent were measured as a function of magnetic field using a set of ten AL-800 garnet rings (3.0" OD, 0.65" ID,

and 0.5" thick), and a solenoid. A more detailed discussion of these measurements may be found in [11].

Static Permeability

Ten stacked rings were placed inside the solenoid, which has a ferrite flux return on the bottom and sides. A steel plug was inserted on top to improve the uniformity of the magnetic field within the samples. Three Hall-type magnetic probes were used to measure the magnetic field at the top, bottom, and middle of the stack as a function of solenoid current.

The static magnetization curve was then extracted by iteratively adjusting the magnetization curve used in the simulation of the setup, until the simulation results matched measurements. The initial $\mu(B)$ curve was a guess based on the vendor's data for the initial permeability (~ 50), and a theoretical value of the permeability well above saturation.

Loss Tangent

To measure the magnetic loss tangent of the garnet, a quarter wave coaxial test resonator was constructed and filled with the same set of garnet rings that were used for the static permeability measurement. The resonator was placed inside of the solenoid, and the resonant frequency and quality factor Q of the cavity was measured as a function of bias current. As Q is an integrated quantity, and the loss tangent depends on the magnitude of the magnetic field and the frequency, an iterative approach was used (as before) since the field in the sample is not uniform.

Magnetic power losses are traditionally characterized by a loss coefficient α . Since $\alpha \ll 1$, the theoretical expression for the loss tangent can be written in a simplified form:

$$\tan \delta_{\mu} = \frac{\mu''}{\mu'} \approx \frac{\alpha \omega \omega_M (\omega_0^2 + \omega^2)}{(\omega_0^2 - \omega^2)(\omega_0^2 - \omega^2 + \omega_M \omega_0)}$$

where $\omega = 2\pi f$ is the RF frequency, H_0 is the magnetic field in the material, $\omega_0 = \mu_0 \gamma H_0$ is the precession frequency, $\gamma = e/m_e$ is the gyromagnetic ratio, $\omega_M = \mu_0 \gamma M_s$, where M_s is the saturation magnetization. For a material with properties parameterized by ω_M at a point with the field given by ω_0 and at RF frequency ω , the loss tangent is proportional to α .

Values of α for the AL-800 were determined for each current setting in the solenoid by adjusting its value in the model until the predicted values of Q and f were the same as seen in the data. It was close to constant, except below ~ 40 A, where a sharp rise was observed. This can be explained by the onset of gyromagnetic resonance in some (initially small) parts of the sample, an effect which was not seen in the modelling. Therefore, it was concluded that α is constant with a value of 0.0033.

Tuner Ring Testing

To verify that the magnetic properties of all garnet rings are identical (or close), a test setup was constructed to measure each fully assembled ring. It consists of a test cavity and a bias magnetic system and was designed to

ensure that the magnetic field in the garnet was as uniform as possible. The setup of the low power RF cavity and bias system are shown in Fig. 7. Two weakly coupled probes are used to measure the frequency and Q . These vary depending on the bias magnetic field in the ring, which is generated by the solenoid. For measurement, the garnet/alumina rings are placed in the large OD section of the cavity at the shorted end.

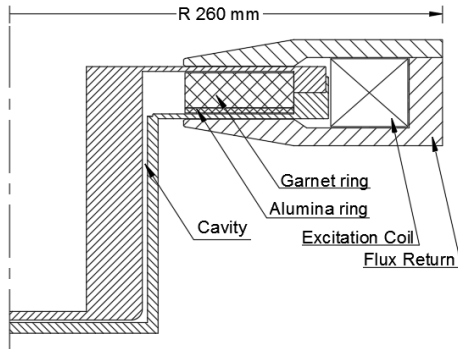


Figure 7: Schematic of the tuner test cavity with magnet.

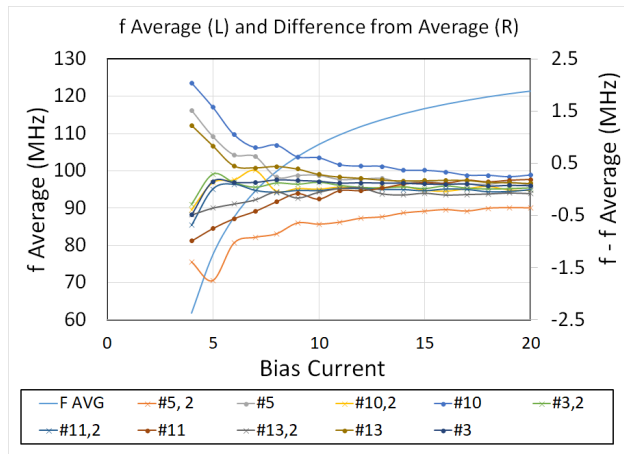


Figure 8: Measured frequency (average and difference from average) for the five tuner rings. The plot shows two measurements for each ring.

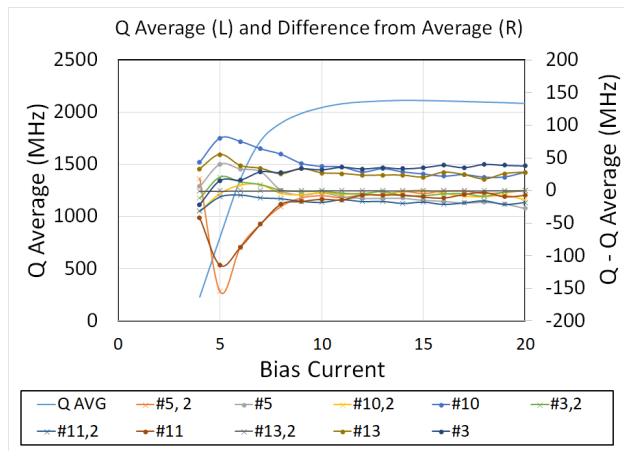


Figure 9: Measured Q (average and difference from average) for the five tuner rings. The plot shows two measurements for each ring.

The biasing coil is made from 224 turns of #10 square copper wire. The flux return is made from 1010 low carbon steel.

Figs. 8 and 9 show the measured resonant frequency and quality factor (Q) of the test cavity with each of the five tuner rings. Two measurements are shown for each ring to quantify the repeatability of the measurements. Between successive measurements of the same ring, the cavity top was removed and then reinstalled. The results for the frequency agree well with predictions from simulation (which used sample measurements discussed earlier in this section) and show acceptable scatter, in that the differences between the measured values for one ring are similar to the differences for two different rings. The Q measurements are also uniform from ring to ring, but in this case, it was not possible to match measurement data with simulation. This may be because the loss coefficient α is not constant, although initial measurements on smaller samples seemed to indicate otherwise. Nevertheless, the rings are very uniform in their material properties indicating good quality control by the vendor.

In addition to measuring the properties of the fully assembled rings, the static permeability was measured for each witness sample, corresponding to each sector from each and every ring. The permeability measurements from all witness samples show that they are satisfactorily uniform. This consistency gives confidence that the sectors of the fully assembled garnet rings do not have significant variation in their magnetic properties. More details regarding the witness sample measurements and ring measurements may be found in [12].

POWER AMPLIFIER TESTS

According to specifications, the Y567B tetrode (Eimac 4CW150000) which will be used in the PA for this cavity can operate up to 108 MHz with 150 kW of power dissipated in the anode. Still, it was desirable to verify this by power testing the tetrode at our operating frequencies. In initial tests at 76 MHz an output power of ~ 140 kW was obtained (the cavity requires 52 kW at injection). Before power testing at 106 MHz (the extraction frequency) it was necessary to modify the drive part of the PA.

A cathode resonator is used to match the 50Ω output impedance of the TOMCO 8 kW solid state driver amplifier (SSD) to the tetrode input capacitance. It is a shorted transmission line with inductive impedance opposite that of the tetrode input capacitance, and is resistively loaded to make the resonance very broad to accommodate the ~ 30 MHz frequency swing. Its dimensions were initially chosen so that the reflected power was minimized at 76 MHz, where the cavity's shunt impedance is lower, but still acceptable at 106 MHz. After constructing the first cathode resonator, it was found that its response at 106 MHz was barely acceptable and not as predicted by the modelling. The trend indicated that the effective input capacitance was frequency dependent. A new model which took this into account was used in the subsequent calculations. The cathode resonator was then redesigned so that the reflected power was minimized at 91 MHz

Content from this work may be used under the terms of the CC BY 3.0 licence (© 2018). Any distribution of this work must maintain attribution to the author(s), title of the work, publisher, and DOI.

instead of 76 MHz, as in the initial design. Though the cavity will never operate at 91 MHz, this configuration produced acceptable amounts of reflected power at both 76 and 106 MHz.

With the redesigned cathode resonator, the PA was tested at both 76 and 106 MHz. At 76 MHz a quarter wave output (anode) resonator was used. At 106 MHz, a quarter wave resonator would have been impractically small, so a 3/4 wavelength resonator was used. A water cooled 50Ω load is loop-coupled to the anode resonator to absorb the output power, which is measured calorimetrically (by change in water temperature). For several values of DC anode voltage, the drive power was increased until the screen current was 300 mA. We obtained 110 kW and 145 kW maximum output power at 76 MHz and 106 MHz, respectively. Fig. 10 shows various quantities for the 106 MHz test. Details of the PA tests are documented in [13].

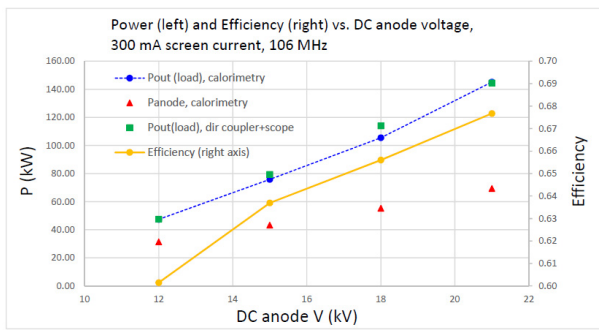


Figure 10: Output power, power dissipated in the anode, and efficiency for Y567B tests at 106 MHz.

CONSTRUCTION STATUS

All the cavity parts have been received. The conical and flat windows are shown in Fig. 11. The former is used to isolate the tuner volume, and the latter, the PA volume, from the rest of the cavity. This is so any outgassing materials used in the tuner construction do not contaminate the vacuum space, and so a PA may be changed without breaking the beam/cavity vacuum.

Other critical parts are shown in Fig. 12. At the time of this writing, the PA window has just been welded into the cavity, and the PA outer conductor has been welded on. This is shown in Fig. 13.

CONCLUSION

We have designed and are in the process of constructing a 2nd harmonic cavity for the Fermilab Booster. We have measured the magnetic properties of the fully assembled tuner rings and their corresponding witness samples. The permeability and losses in the material are very uniform.

The cavity will be tested early this summer and installed into the Booster during a planned shutdown. If successful, this will be the first operational broadband perpendicularly biased cavity and it will be a significant technical achievement for accelerators.

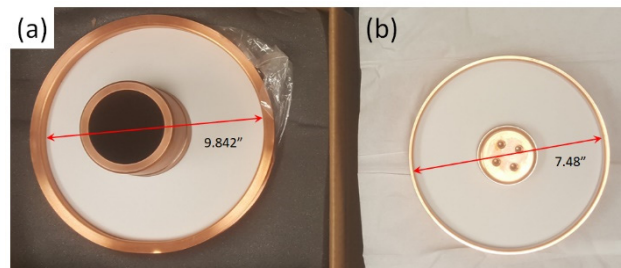


Figure 11: (a) Conical tuner window and (b) flat input window.



Figure 12: Copper and stainless-steel parts of the cavity. (a) and (b): Garnet-free region of the tuner outer conductor. (c): Section of the tuner outer conductor which will contain the garnet. Both parts of the tuner outer conductor are split into four azimuthal sections to reduce eddy currents. (d) and (e): Two outer conductor sections of the PA part of the cavity. They contain ports for airflow, water cooling, monitoring, and the anode DC voltage input. (f): The PA center conductor which supports the tetrode and makes electrical contact with its anode. (g): The ring which capacitively couples the PA to the cavity. (h): The tuner center conductor with cooling lines. (i): The HOM damper cavity. (j): The main cavity outer conductor (vacuum section). The PA section shown in (e) will be attached at the large hole in the OD.



Figure 13 : The partially assembled cavity.

ACKNOWLEDGMENTS

Many thanks to National Magnetics for the manufacture of our garnet and the assembly of the tuner rings with our required consistency and precision.

REFERENCES

- [1] S. Hanna, “Applications of Ferrite and Ferromagnets in Tuning RF Cavities for Accelerators,” *Journal of Applied Physics*, vol. 75, p. 5625, 1994.
- [2] R. Madrak, “A New Slip Stacking RF System for a Two-fold Power Upgrade of Fermilab’s Accelerator Complex,” *NIM in Phys Res A*, vol. 758, pp. 15-25, 2014.
- [3] R. L. Poirier, “Perpendicular Biased Ferrite-Tuned Cavities,” in *Proc. of the 1993 Particle Accelerator Conference*, Washington, DC, USA, May 1993, pp. 753 – 757.
- [4] C. C. Freidrichs *et al.*, “Design of an Accelerating Cavity for the Superconducting Super Collider Low-Energy Booster,” in *Proc. of the 1991 IEEE Particle Accelerator Conference*, San Francisco, CA, USA, May 1991, pp. 1020-1022.
- [5] W. Weng and J. Kats, “Effects of the Second Harmonic Cavity on RF Capture and Transition Crossing,” in *XVth International Conf. on High Energy Accelerators*, Hamburg, Germany, 1992.
- [6] C. Bhat and C. Y. Tan, “Fermilab Booster Transition Crossing Simulations and Beam Studies,” in *Proc 57th ICFA Advanced Beam Dynamics Workshop on High-Intensity and High Brightness Hadron Beams (HB’16)*, Malmö, Sweden, Jul. 2016, pp. 242-246.
- [7] C. Y. Tan, “Technical Report on the Perpendicular Biased 2nd Harmonic Cavity for the Fermilab Booster,” <http://beamdocs.fnal.gov/AD-public/DocDB/ShowDocument?docid=6113>
- [8] C. Y. Tan *et al.*, “A Perpendicular Biased 2nd Harmonic Cavity for the Fermilab Booster,” in *Proc IPAC’15*, Richmond, VA, USA, May 2015, pp. 3358-3360.
- [9] R. Madrak *et al.*, “Progress on the Design of a Perpendicularly Biased 2nd Harmonic Cavity for the Fermilab Booster,” in *Proc. NAPAC’16*, Chicago, IL, USA, Oct. 2016, pp. 130-133.
- [10] W. Smythe, T. Enegren, and R. Poirier, “A Versatile RF Cavity Mode Damper,” in *Proc. EPAC’90*, Nice, France, Jun. 1990, pp. 976-978.
- [11] R. Madrak *et al.*, “Measurements of the Properties of Garnet Material for Tuning a 2nd Harmonic Cavity for the Fermilab Booster,” in *Proc. NAPAC’16*, Chicago, IL, USA, Oct 2016, pp 134-136.
- [12] R. Madrak *et al.*, “Garnet Ring Measurements for the Fermilab Booster 2nd Harmonic Cavity,” in *Proc. IPAC’18*, Vancouver, BC, Canada, May 2018, paper WEPML011.
- [13] R. Madrak *et al.*, “Y567B Power Amplifier Tests at 76 and 106 MHz,” <http://beamdocs.fnal.gov/AD-public/DocDB/ShowDocument?docid=5350>

LLRF STUDIES FOR HL-LHC CRAB CAVITIES

P. Baudrenghien, CERN, 1211 Geneva, Switzerland

T. Mastoridis, California Polytechnic State University, San Luis Obispo, 93407 California, USA

Abstract

The HL-LHC upgrade includes sixteen Crab Cavities (CC) to be installed on both sides of the high luminosity experiments, ATLAS and CMS. Two issues have been highlighted for the Low Level RF: transverse emittance growth (and associated luminosity drop) caused by CC RF noise, and large collimator losses following a CC trip. A prototype cryomodule with two CCs has been installed in the SPS, and tests have started in May 2018 with beam. This paper briefly reports on preliminary results from the SPS tests. It then presents emittance growth calculations from cavity field phase and amplitude noise, deduces the maximum RF noise compatible with the specifications and presents a possible cure consisting of a feedback on CC phase and amplitude. To reduce the losses following a CC trip we propose to implement transverse tail cleaning via the injection of CC noise with an optimized spectrum, which selectively excites the particles of large transverse oscillation amplitudes.

INTRODUCTION: LHC CRAB CAVITIES

The HL-LHC upgrade aims at a tenfold increase in p-p integrated luminosity compared to the present LHC. This will be achieved with a doubling of the bunch intensity ($2.2 \cdot 10^{11}$ p/bunch) and a reduction of the beam transverse size at the Interaction Points (IP) 1 (ATLAS experiment) and 5 (CMS). The bunch spacing (25 ns) and the total number of bunches (~ 2800) will not be changed. An upgrade of the LHC injector chain was launched to achieve the bunch intensity increase, and should be completed by early 2021. Stronger insertion magnets will be installed on each side of the two experiments to reduce the transverse emittance. The β^* will be reduced from the design 55 cm to 15 cm [1].

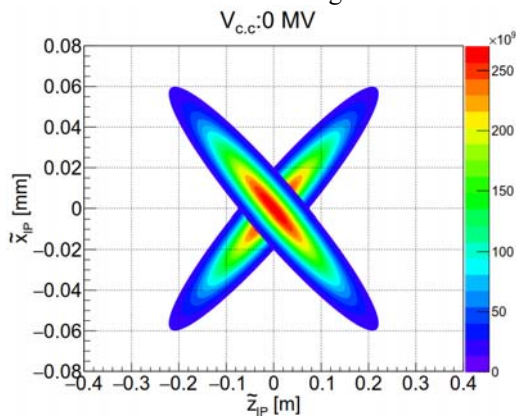


Figure 1: HL-LHC bunch crossing without crabbing.

The LHC beams circulate in a common chamber for ~ 100 m on each side of the IPs. In this zone the beams must be separated transversely to avoid detrimental long-range beam-beam interactions. Separation is accomplished by in-

roducing a crossing angle, which must scale with the inverse of the transverse beam size at the IP to maintain a constant normalized separation. The HL-LHC full crossing angle will be $500 \mu\text{rad}$, to be compared to the present $280 \mu\text{rad}$.

Bunch crossing at an angle with very small transverse beam size leads to a reduction of luminosity, quantified by a factor R . Figure 1 shows the HL-LHC bunches ($\sigma_z = 9$ cm) crossing at a $250 \mu\text{rad}$ half-crossing angle, assuming a Gaussian distribution. The luminosity reduction factor is

$$R(\theta) = \frac{1}{\sqrt{1 + \left(\frac{\sigma_z \theta}{\sigma_r}\right)^2}} \quad (1)$$

where θ is the full crossing angle, σ_z is the rms bunch length and σ_r^* is the rms transverse bunch size at the IP in the crossing plane. The later alternates between vertical and horizontal (ATLAS and CMS). Without crab cavities the peak luminosity is reduced by a factor of 3 compared to head-on collision.

Crab cavities are RF deflectors, phased so that the longitudinal bunch centroid receives no kick, while the head and tail receive transverse kicks in opposite directions, to rotate the bunch and restore almost head-on collisions at the IPs (Fig. 2).

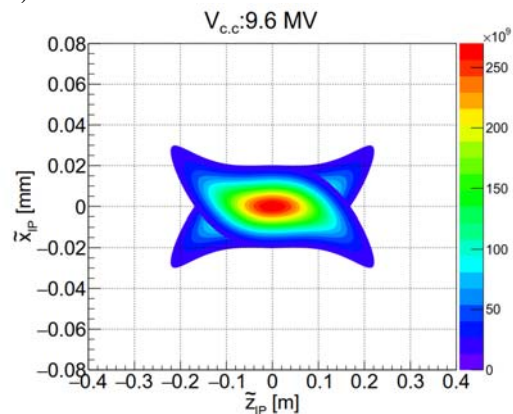


Figure 2: HL-LHC bunch crossing with full crabbing.

The LHC crab cavities operate at the 400.8 MHz fundamental that is also the accelerating frequency. The effect of the RF curvature is clearly visible, caused by the large bunch length. KEK used a Global Crabbing Scheme, with the bunch rotation propagating all around the machine [2]. In the HL-LHC the crabbing will be localized around IP1 and 5: there will be two CCs at -90 degree betatron phase advance ahead of the IP initiating the rotation, and two CCs at 90 degree phase advance after the IP to stop the rotation. Crabbing therefore does not propagate in the rest of the ring. The LHC will not use the full crabbing shown on Fig.

Content from this work may be used under the terms of the CC BY 3.0 licence (© 2018). Any distribution of this work must maintain attribution to the author(s), title of the work, publisher, and DOI.

2 since the experiments would not cope with the peak luminosity due to pileup. Instead, we will use a partial compensation with 6.8 MV only, that can be provided using two crab cavities (Fig. 3). Both β^* and crabbing voltage will actually be programmed during an HL-LHC fill to optimize integrated luminosity while keeping instantaneous luminosity at a level comfortable for the detectors [3], a strategy called lumi-leveling. HL-LHC will include sixteen CCs total, two per beam and per IP side around ATLAS and CMS.

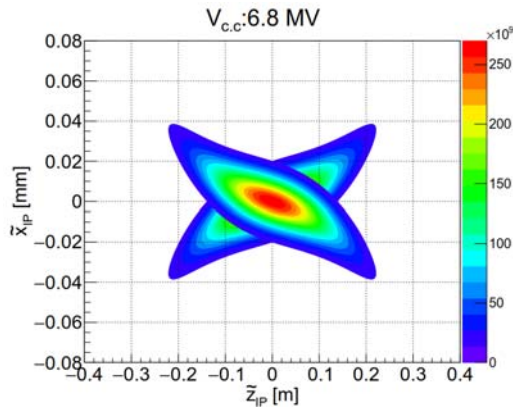


Figure 3: HL-LHC bunch crossing with the planned partial crabbing.

FIRST SPS TESTS

Before installing the sixteen cavities in the LHC during the Long Shutdown 3 (2024-2025?), it was decided to first test two cavities in the SPS, with a high intensity proton beam. Although CCs have been operated successfully in KEK [2], the HL-LHC differs in several points: first we will use local crabbing, and it is important to show that we can regulate individual CC voltage amplitude/phase precisely to null the effect outside the IP1-5 regions. Second, CCs have never been used with hadrons. In lepton machines, synchrotron radiation provides a very fast damping mechanism for the emittance growth caused by RF noise. Bunch shortening is observed in the LHC at 6.5 TeV but the damping time is tens of hours. As a consequence RF noise can be very detrimental in the CCs when used with protons. Third, it is essential to measure the exact HOM frequencies in operation and the extracted power with high intensity beam.

A cryomodule containing two CCs has been installed in the SPS during the 2018 winter break. The two cavities are of the Double Quarter Wave type (DQW), oriented to produce vertical crabbing [1]. With two cavities we can test the precision of field regulation by operating them in counter-phasing mode. Figure 4 shows the cryomodule and cavities [4]. Each cavity is intended to be operated at 3.4 MV. There is zero beam loading in a CC if the beam is centered. In the HL-LHC design we have accepted a ± 2 mm beam offset. The Q_L was then selected to minimize the required power with this offset, for the HL-LHC beam intensity (1.1 A DC), resulting in $Q_L=500000$ [1]. The coupling is identical in the SPS CCs.

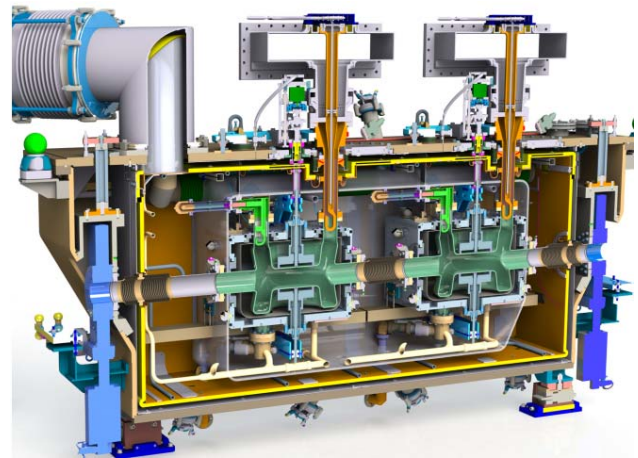


Figure 4: The SPS cryomodule with two CCs.

The CCs are made of plain Niobium, to be operated at 2 deg K. Due to problems with the cryogenics, the May 2018 tests were done at 4.5 deg K. At that temperature, He ebullition leads to a fluctuation of the cavity tune by more than one cavity bandwidth (400 Hz, single sided), observed with a period around one second. The CC tuning system acts by mechanical pressure on the deflecting gap, and is not fast enough to track these fluctuations. Fortunately, the tune is reasonably stable over a timescale of a few minutes. Tests were therefore possible without a tuning loop, at a reduced voltage (1 MV for CC1, 100 kV for CC2 due to poor conditioning). The first SPS test was conducted at a fixed 26 GeV energy corresponding to 400.528 MHz RF frequency that is still in the tuning range. Although the tune was not controlled, field regulation was provided by a strong RF feedback with a small loop delay ($< 2 \mu s$). We used a single $1.1 \cdot 10^{11}$ p bunch. Before injection the CCs were switched ON, the amplifier drive was ramped-up and the RF feedback was closed. Then the bunch was injected, followed by the rephasing of the bunch to the CC RF. A phase scan was performed at 26 GeV and the crabbing was measured with a Head-Tail monitor (Fig. 5). The instrumentation was not calibrated (no correction for cable attenuation). Nevertheless comparison with Fig. 1-3 clearly indicates the expected crabbing. A second test was performed at 270 GeV: the CCs were OFF at injection and during the acceleration ramp. At the beginning of the 270 GeV plateau the single bunch was rephased to the CC reference RF. Then the CCs were ramped up in voltage and crabbing was observed during the 10 s long 270 GeV plateau. We observed no measurable degradation of intensity or emittance during these ten seconds, but the timescale is of course orders of magnitude from the 5-10 hours of an LHC physics fill. In June the CCs will be warmed-up for an intervention on the cryogenics that will enable operation at 2 deg K in July, with batches of up to 288 p bunches.

Content from this work may be used under the terms of the CC BY 3.0 licence (© 2018). Any distribution of this work must maintain attribution to the author(s), title of the work, publisher, and DOI.

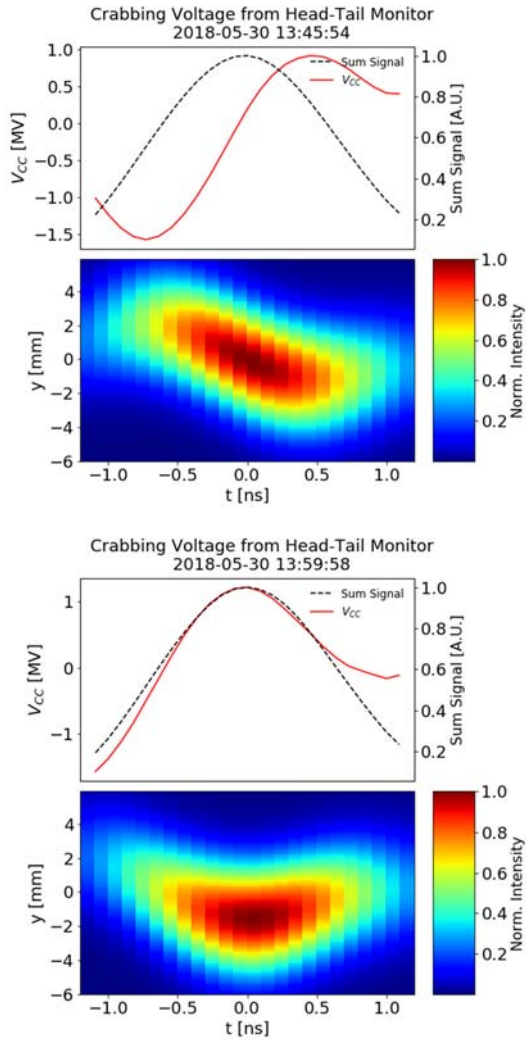


Figure 5: SPS test. Crabbing measured with a Head-Tail monitor. The monitor measures the transverse position (Delta signal) and the longitudinal profile (Sum signal), along the z-direction. The 2-D plots are then reconstructed assuming Gaussian distributions. Top: 0 deg CC phase w.r.t. bunch core, bottom 90 deg.

LOW LEVEL RF

General Architecture

The cavity field is measured and regulated via a strong feedback. The method is similar to the one used for the LHC accelerating cavities. The gain of any feedback system is limited by the loop delay. The delay was therefore minimized in the HL-LHC layout: amplifiers and LLRF will be installed in four caverns located close to the CCs. The resulting loop delay of less than 2 μ s allows a regulation bandwidth up to 100 kHz. Within this band, the noise in the CC field will follow the imprecision of the demodulator (receiver noise) [5].

Detrimental Effects of RF Noise

The CC RF noise reduces luminosity through transverse emittance growth. The RF noise in the CC gives random

transverse kicks to the passing particles, resulting in emittance growth in the crabbing plane. The un-normalized emittance growth rate due to both phase and amplitude noise was derived by the authors [6]. For phase noise we have

$$\frac{d\varepsilon_x}{dt} = \beta_{cc} \left(\frac{eV_0 f_{rev}}{2E_b} \right)^2 C_{\Delta\phi}(\sigma_\phi) \quad (2)$$

$$C_{\Delta\phi}(\sigma_\phi) = e^{-\sigma_\phi^2} \left[I_0[\sigma_\phi^2] + 2 \sum_{l=1}^{\infty} I_{2l}[\sigma_\phi^2] \right] \quad (3)$$

where e is the charge of a proton, V_0 is the voltage of the crab cavity, f_{rev} is the revolution frequency, E_b the beam energy, σ_ϕ the rms bunch length (in radian), I_l is the modified Bessel function of the first kind, $\rho(\nu)$ is the betatron tune distribution, and $S_{\Delta\phi}$ is the phase noise power spectral density (with units of rad^2/Hz). Eq. 2 can be interpreted as follows: the effect of phase noise depends on the overlap between noise spectrum and betatron tune distribution. As the particle samples the noise at each turn, the phase noise spectrum is aliased at f_{rev} . Phase noise gives dipole kicks to the core of the bunch but does not shake the particles at $\pm\pi/2$ phase offsets. This effect is represented by the “geometric factor” $C_{\Delta\phi}$ that decreases with bunch length [6]. The phase noise induced emittance growth is reduced by the transverse damper. As it gives the same kick to all particles, the damper efficiency decreases with bunch length. Its effect can be described by a correction factor R_d , dependent on both bunch length and Beam Transfer Function. Refer to reference [6] for details. Amplitude noise induces head-tail motion of the bunch that the damper cannot correct as the mean bunch signal is zero. Formulas have also been derived for the resulting emittance growth

$$\frac{d\varepsilon_x}{dt} = 2\beta_{cc} \left(\frac{eV_0 f_{rev}}{2E_b} \right)^2 C_{\Delta A}(\sigma_\phi) \quad (4)$$

$$C_{\Delta A}(\sigma_\phi) = e^{-\sigma_\phi^2} \sum_{l=0}^{\infty} I_{2l+1}[\sigma_\phi^2] \quad (5)$$

where ν_s is the synchrotron tune and $S_{\Delta A}$ is the (relative) amplitude noise power spectral density (with units of $1/Hz$). The voltage power spectral density is $S_{\Delta V} = V^2 S_{\Delta A}$. The effect depends on the overlap between amplitude noise spectrum and the aliased synchro-betatron bands. The “geometric factor” now increases with bunch length as amplitude noise kicks the head and tail more than the core. The HiLumi LHC beam parameters at the *end of the fill* are presented in Table 1.

Table 1: Parameters at the End of Fill, with 15 cm β^*

f_{rev} (Hz)	ν	V_o (MV)	β_{cc} (m)	ϵ_n ($\mu\text{m. rad}$)	E_b (TeV)	σ_ϕ (rad)	σ_w
11245	62.31	3.4	4000	2.5	7	0.67	0.003

We quote the normalized transverse emittance. The transverse damper gain will be 0.04 (50 turns damping time) giving a reduction factor of 0.097 for the phase noise effect. We are considering 100 kHz regulation bandwidth. The receiver noise will thus appear in the cavity field in that range and will contribute to the infinite integrals of Equations 2 and 4. The noise from the four cavities per beam and per plane are added in power, assuming that they are uncorrelated. We are allowed a transverse emittance growth rate target of approximately 1.6%/hour to sufficiently reduce the integrated luminosity loss over a physics fill [3]. Using the above equations we can calculate the maximum acceptable phase and amplitude noise: we get -153 dBc/Hz at offsets from 3 kHz (first betatron band) to 100 kHz (regulation bandwidth). Compared to the measured -130 dBc/Hz of the LHC accelerating system, such a low noise spectrum is very challenging. We consider -143 dBc/Hz as a more reasonable target. This in turn would generate an unacceptable 16%/hour reduction in integrated luminosity.

RF Noise Mitigation

We propose to reduce the effect of the CC RF noise using a dedicated feedback system that would use the CCs as transverse kicker [5]. The intra-bunch transverse distortion measured by a wideband acquisition Pick-Up (such as the Head-Tail monitor shown on Fig.5) can be processed to generate two data at each bunch passage: one is the transverse position averaged over the whole bunch (Sum signal), the second one is the difference between averages done over longitudinal head and tail of the bunch (Difference signal). After processing (filtering and phase shift), these two inputs are fed back onto the CC reference voltage: the Sum signal generates a correction to the CC phase and the Difference signal to the amplitude. The amplitude and phase feedback systems were first examined separately, by only using one type of noise kick and feedback at a time. Simulations were done using the Python package Py-HEADTAIL, a software package developed at CERN for simulation of multi-particle beam dynamics [7].

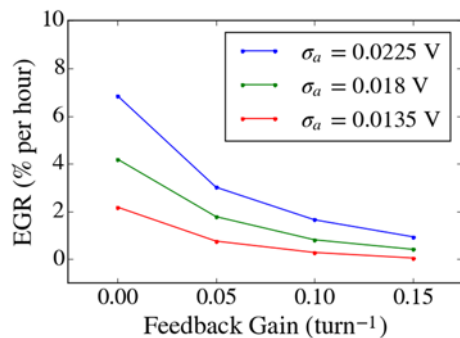


Figure.6: Emittance growth rate from amplitude feedback acting on amplitude noise.

Results are shown on Fig. 6, 7. The vertical axis of these figures represents the percent increase in emittance per hour. A significant reduction in emittance growth rate is achieved as the feedback gains are increased. Then both feedback systems were combined to act on both types of noise simultaneously. As expected, the two feedback systems behave independently, without interference from one another.

Such a feedback system will see its performances degraded by loop delay or betatron tune spread. Sensitivity to these parameters has been studied [5]. An additional limitation is the noise in the Pick-Up measurement chain. The Head-Tail monitor signals of Fig. 5 are averaged over many turns. For the proposed CC feedback system to work, averaging can be done over a time-span that is the inverse of the 100 kHz RF noise bandwidth (400 bunches). The feasibility of the system depends on the maximum acceptable level of measurement noise before it becomes inefficient (excitation vs. damping). Detailed simulations have been performed [5]. The design of a wide-band, high-precision transverse measurement system will be done in synergy with the HL-LHC transverse damper upgrade. We count on this scheme to gain the extra 10 dB noise reduction required.

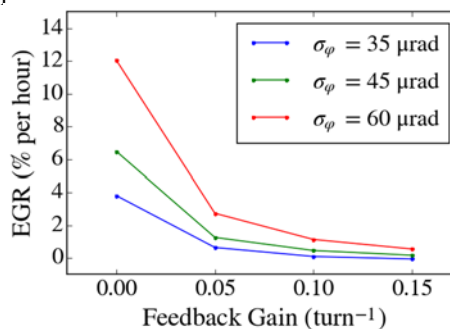


Figure.7: Emittance growth rate from phase feedback acting on phase noise.

Exploiting RF Noise.

Recall that the HL-LHC will use a local crabbing scheme. The companion cavities on the other side of the IP must cancel the rotation initiated by the cavities at the entry side. Outside the IP region there is no crabbing and the transverse collimators can be placed very close to the beam. If a CC fails (RF trip, quench, etc...), the crabbing will propagate outside the IP. A trigger will immediately be sent to the beam dump system and the beam will be extracted to protect the machine. But the beam dump system requires up-to three machine turns to react. During that time, the collimators will scrape the transverse tails of the beam and high tail population could cause damage [8]. We must therefore keep the tail population controlled during the physics fill. One solution is the electron lens collimator [9]. We propose an alternative (or complement) method using the CCs. The particles in the transverse tails have a different betatron frequency than the ones in the core. This dependence is a result of the non linearities caused by beam-beam effects and octopole field. The RF noise action can then be limited to tail particles if shaped correctly.

Content from this work may be used under the terms of the CC BY 3.0 licence (© 2018). Any distribution of this work must maintain attribution to the author(s), title of the work, publisher, and DOI.

Simulations were done with the injection of RF phase noise in a CC [10]. A white RF noise does not change the functional form of the transverse action and tune distributions. The final distribution is a scaled version of the original. Equations 2, 4 indicate that the term in the summation is proportional to the product of the noise power spectral density and the tune distribution. As a result, the noise PSD must be large at the tunes of the particles that we wish to continuously drive to the collimators in order to keep a low population in the tails. Figure 8 shows an example noise distribution used in simulations. Noise amplitude increases at a constant rate from 0 to a maximum over about 154 Hz. Zero noise is injected at and above the third-integer tune, to avoid resonance. This noise distribution was specifically designed to trim particles 2σ from the phase space origin in the x-dimension. 3546 Hz corresponds to the approximate betatron frequency of particles oscillating out to 2σ in the horizontal plane for a non-integer average betatron tune of about 0.3. Figures 9 show the resulting tune distribution. The dashed line presents the initial distribution with all particles removed past the 2σ threshold. It is evident from these figures that this tail cleaning scheme performs very well.

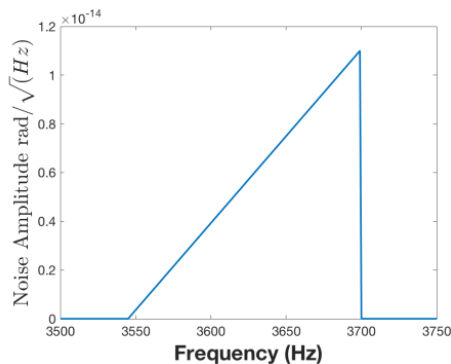


Figure 8: 2σ tail cleaning noise for the x-dimension.

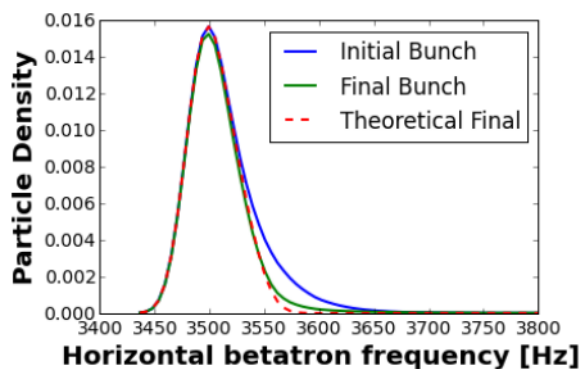


Figure 9: Tune distribution before and after 2σ tail cleaning simulation.

Figure 10 shows the bunch distribution in phase space before and after the simulation. The majority of particles beyond 2σ were pushed out and removed by the collimators.

CONCLUSION

We have reported on the first CC tests with beam in the SPS. Analytical formulas have been presented for the emittance growth rate caused by CC phase and amplitude noise. Given a budget of 1.6 %/hour with the *end of fill* parameters, the noise must be reduced to -153 dBc/Hz at offset larger than 3 kHz. We consider -143 dBc/Hz as a challenging but reasonable target. In order to gain the extra 10 dB we propose a feedback system that measures bunch transverse displacement plus head-tail motion, and feedback on the CC voltage phase and amplitude respectively. Simulations show that the method can provide the required extra 10 dB if we keep the noise in the Pick-Up chain sufficiently low. A possible use of the CC for transverse tail cleaning was presented. We propose to continuously inject phase noise in the CC, with a spectrum such that it excites the particles with large betatron oscillations only. Simulations were presented that confirm the feasibility.

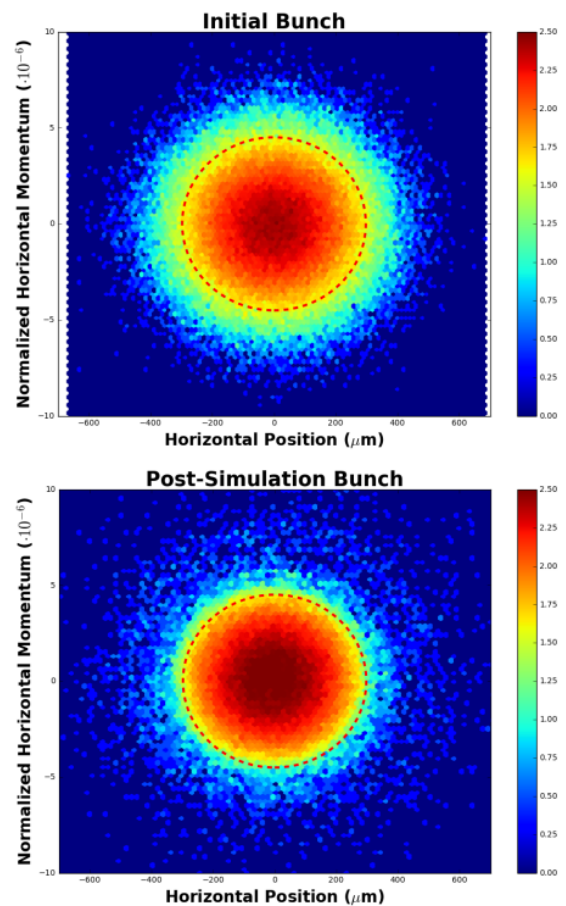


Figure 10: Phase space before a 2σ tail cleaning simulation (top) and after the cleaning (bottom). The red dotted line is 2σ from the origin.

ACKNOWLEDGEMENTS

A large team has been involved in the SPS CC tests reported in the second section of this paper. We can only mention a few: R. Calaga (project leader), O. Capatina

(cryomodule), E. Montesinos (amplifiers), L. Carver (machine development organization), T. Levens (instrumentation), K. Brodzinski (cryogenics). The simulations of the CC feedback were done by A. Daw and P. Nguyen. S. Steeper, D. Tucker and D. Wieker have contributed to the evaluation of the CC for tail cleaning. We also thank E. Yamakawa who provided the plots showing theoretical crabbing.

REFERENCES

- [1] G. Apollinari *et al.*, “High-Luminosity Large Hadron Collider (HL-LHC). Preliminary Design Report”, CERN-2015-005, Dec 17th, 2015, <http://cds.cern.ch/record/2116337>
- [2] Y. Funakoshi, “Operational experience with crab cavities at KEKB”, <http://arxiv.org/pdf/1410.4036>
- [3] E. Metral *et al.*, “Update of the HL-LHC operational scenarios for proton operation”, CERN-ACC-NOTE-2018-0002, <http://cds.cern.ch/record/2301292/files/CERN-ACC-NOTE-2018-0002.pdf>
- [4] C. Zanoni *et al.*, “The Crab Cavity Cryo-module for the SPS test”, 2017 *J. Phys.: Conf. Ser.* vol. 874, p. 012092, <http://iopscience.iop.org/article/10.1088/1742-6596/874/1/012092>
- [5] P. Baudrenghien, T. Mastoridis, A. Daw, P. Nguyen, “Estimates of and a Cure for Transverse Emittance Growth due to RF Noise in the High Luminosity LHC Crab Cavities”, submitted for publication to *Phys. Rev. ST Accel. Beams*.
- [6] P. Baudrenghien and T. Mastoridis, “Transverse emittance growth due to rf noise in the high-luminosity lhc crab cavities,” *Phys. Rev. Accel. Beams* vol. 18, p. 101001, 2015, <https://journals.aps.org/prab/abstract/10.1103/PhysRevSTAB.18.101001>
- [7] G. Rumolo, F. Zimmermann, “Practical User Guide for HEADTAIL”, CERN-SL-NOTE-2002-036, <http://cds.cern.ch/record/702717/files/sl-note-2002-036.pdf>
- [8] A. Garciat *et al.*, “Limits on Failure Scenarios for Crab Cavities in the HL-LHC”, in *Proc. IPAC'15*, Richmond, VA, May 2015, paper THPF095, <http://accelconf.web.cern.ch/AccelConf/IPAC2015/papers/thpf095.pdf>
- [9] M. Fitterer *et al.*, “Hollow Electron Beam Collimation for HL-LHC - Effects on the Beam Core”, in *Proc. IPAC'17*. Copenhagen, Denmark, May 2017, paper WEOBA2, <http://accelconf.web.cern.ch/AccelConf/ipac2017/papers/weoba2.pdf>
- [10] P. Baudrenghien, T. Mastoridis, S. Steeper, D. Tucker, D. Wieker, “Crab Cavity effects on transverse distribution evolution and tail cleaning in the HL-LHC”, CERN-ACC-NOTE-2018-0042, <https://cds.cern.ch/record/2320889/files/CERN-ACC-NOTE-2018-0042.pdf>

THE CHOOSING OF MAGNETIC STRUCTURE OF ISOCHRONOUS CYCLOTRON DC-130 FOR APPLIED RESEARCHES

I.A. Ivanenko[†], G. Gulbekian, I. Kalagin, N. Kazarinov, J. Franko, JINR, Dubna, 141980, Russia

Abstract

At the present time, the activities on creation of the new multipurpose isochronous cyclotron DC130 are carried out at the FLNR, JINR. The cyclotron DC130 is intended for microchip testing, production of track pore membranes and for applied physics. The cyclotron will accelerate the heavy ions with mass-to-charge ratio A/Z from 5 to 8 up to the fixed energies 2 and 4.5 MeV per nucleon. The main magnet and acceleration system of DC130 are based on the U200 cyclotron that now is under reconstruction. At the present paper, the method of choosing of main magnet parameters of cyclotron is described.

INTRODUCTION

The main direction of scientific program of Flerov Laboratory of Nuclear Reactions of Joint Institute for Nuclear Research (FLNR JINR) is the synthesis of heavy and exotic nuclei. Furthermore, the different applied researches and acceleration technology investigation are carried out. Total operating time of FLNR cyclotrons reach more than 16000 hours per year and continue to growth. At the present time the activities on creation of the new dedicated cyclotron DC130 for applied researches are carried out. The main usage of the new cyclotron will be the track pore membrane production and microchip testing [1]. DC130 will be created as a deep reconstruction of the old cyclotron U200.

U200 CYCLOTRON

U200 isochronous cyclotron had been in operation at FLNR, JINR, since 1971 and provided the production of nuclear beams with $A/Z=3\div 5$ at energies up to 9 MeV/nucleon [2]. The cyclotron magnet has H – type yoke and produce magnetic field up to 2T. Two-meter diameter pole and four pairs of straight sectors form the isochronous and focusing conditions for acceleration. Two 45-degree-dees of RF accelerating system are placed in the opposite valleys between the sectors. Main parameters of the magnet are presented in Table 1. At a present time U200 cyclotron is decommissioned and prepared to reconstruction to the new cyclotron DC130.

NEW DC-130 CYCLOTRON

The new multipurpose cyclotron DC130 is intended for different tasks of applied researches. The main activities will be in the microchip testing and production of track pore membranes. For microchip testing, the heavy ions from Ne up to Xe and Bi with the fixed energy 4.5 MeV/nucleon will be available. For that activities it will be possible to accelerate ions with mass to charge ratio from 5 to 5.5, for example $^{20}\text{Ne}^{4+}$, $^{209}\text{Bi}^{38+}$. The beams will be accelerated on the 2 harmonic of RF with the fixed frequency 10.622MHz of RF generator.

[†] ivan@jinr.ru

Table 1: Main Parameters of U200 / DC130 Magnet

Parameter	Value
Main size of the magnet, mm	5000x2100x3600
Diameter of the pole, mm	2000
Distance between the poles, mm	150 / 160
Number of the sectors pairs	4
Sector angular extent (spirality)	43° (0°)
Sector height, mm	46 / 45
Distance between the sectors (magnet aperture), mm	30
Distance between the sector and pole (for correcting coils), mm	14 / 20
Number of radial coils	6
Maximal power, kWt	≈300

The production of track pore membranes will be based on the intensive beams of heavy ions from Ar to Bi with the fixed energy 2 MeV/nucleon. The mass to charge ratio varies from 7.58 to 8, for example $^{197}\text{Au}^{26+}$, $^{40}\text{Ar}^{5+}$. The frequency of RF generator for that operation mode will be the same, 10.622MHz, but the beams will be accelerated on the 3 harmonic of RF.

The operation mode substitution will be implemented only by changing the level of the magnetic field in the wide range from 1.729T to 1.902T and its isochronous distribution will be formed operationally by means of six radial correcting coils.

In the frame of reconstruction of U200 to DC130 it is planned to upgrade the cyclotron magnetic structure, replace the magnet main coil and renovate RF system. Other systems, axial injection, beam extraction, vacuum, cooling, control electronics will be new.

MAGNETIC FIELD FORMATION

The compact type magnet of the old, U200 cyclotron will be upgraded to accelerate in new operation modes. The deep reconstruction of the magnet means that the yoke will stay the same, but dimensions of working area, sectors, shims and central plug must be changed. The diameter of the pole is fixed by the yoke dimension and equal 2 meters. The pole diameter and the beams energy define the levels of the isochronous magnetic field at the cyclotron center from 1.729T to 1.902T. 160mm gap between the upper and lower poles was chosen as a compromise between field level and magnet aperture. Four pairs of straight, 43-degrees sectors form the isochronous and focusing conditions

for the beam acceleration. The sectors height is 45mm. 20mm gap between pole and sector is fixed for placing of the correcting coils. 30mm gap between the sectors will be enough for beam transmission without aperture losses. The chosen parameters form the azimuth variation of the magnetic field and provide the needed focusing properties with betatron oscillations $Q_r=1.01$ and $Q_z=0 - 0.3$.

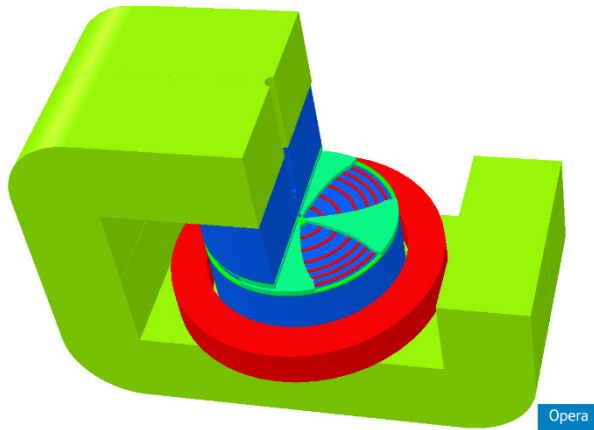


Figure 1: DC130 magnet computer model.

The first step of magnetic field formation, the computer modelling, is held with TOSCA code. The model of the magnet was created on the base of U200 cyclotron drawings (Fig. 1). The second step will be a final formation during the magnetic field mapping. For that, a removable shim as a part of magnetic structure will be used.

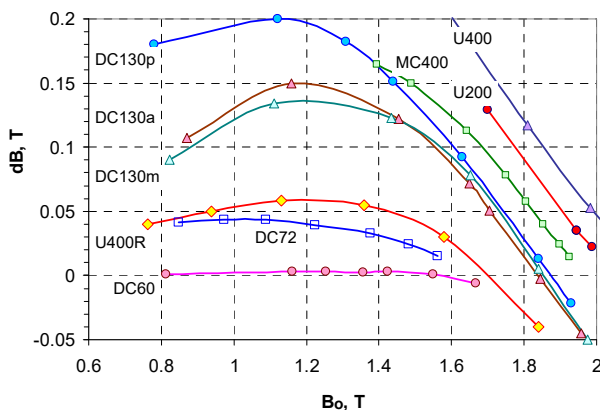


Figure 2: dB(B) functions for operated and projected FLNR cyclotrons.

The important parameter to form of the multi-particle cyclotron magnetic field is a dB(B) function, there dB is a radial growth of the magnetic field in dependence of the field level. dB(B) function has an original behaviour for each cyclotron magnetic structure and depends on dimensions and shape of the elements of magnet, saturation property of the metal. In Fig. 2, dB(B) functions for some FLNR cyclotrons are presented [3].

For multi-particle cyclotron, the dB(B) functions of the magnet may not coincide with the isochronous growth of the magnetic field of some operation modes. Furthermore, at the same level of magnetic field, the operation modes

with different dB could be used. At this case, the isochronous field for each mode is formed operatively by means of correcting coils. The goal of the computer modelling is to find the optimal shape of the magnet structure to minimize the power of correcting coils.

The formation of cyclotron magnetic field can be carried out by shaping of sector profile as axially, and azimuthally. In the frame of optimization of DC130 magnet, the three methods of sector shaping were investigated.

The first and more commonly used method is a changing of sector azimuthal profile. At this case, the machining and placing of the sector is easier technologically. To achieve the isochronous distribution, the azimuthal profile of DC130 sectors must be cut from both sides by curved line with a deep up to 54mm. That complicate the use of removable sector - edge shims. The behaviour of corresponding dB(B) function is presented in Fig. 2 as DC130m line.

The second method is a shaping of the sector height from the cyclotron median plane side. At this case, the sector edges stay straight, that is convenient for placing of removable shims. The disadvantage of this method is a very high sensitivity of magnetic field to the accuracy of machining of sector surface. Sharp edges of the surface profile lead to local field perturbations. For DC130 this sensitivity is about 60Gs/mm and highly depends on the radius. It means that the machining of the surface must be smoothed by curves or many small steps. It is rather complicated and expensive. The corresponding dB(B) function is presented in Fig. 2 as DC130a line.

The third method is a shaping of the sector height from the pole side. Because the shaped surface is closed from cyclotron median plane by sector itself, the sector could be machined more roughly by small number of steps with height of 5 – 10 mm (Fig. 3) and the field distribution will stay a smooth. The corresponding dB(B) function is presented in Fig. 2 as DC130p line.



Figure 3: The shaping of DC130 sector height from the pole side.

The disadvantage of this method is an arising of magnetic force of attraction between upper and lower sectors in the case, when the gap between pole and sector more than gap between the sectors. For DC130 the gap between sectors is 30 mm. The calculations shown that the noses of

Content from this work may be used under the terms of the CC BY 3.0 licence (© 2018). Any distribution of this work must maintain attribution to the author(s), title of the work, publisher, and DOI.

sectors, where gap between sector and pole is 38 mm, are attracted one to another with 13000N. The outer parts of sectors, where gap between sector and pole is 20 mm, are attracted to the poles with the force about 15000N.

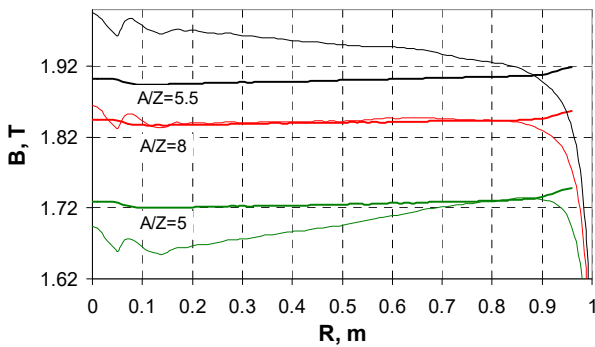


Figure 4: The isochronous and real magnetic field for characteristic operation modes. The sector is shaped by height from the pole side.

In Fig. 5, the lines present dB(B) dependence of real magnetic field for three methods of DC130 sector shaping. Dots present the value of radial growth of isochronous fields for some characteristic operation modes. The difference between the real and isochronous magnetic field will be compensated by radial correcting coils. The degree of correction could be estimated as ± 500 Gs for operation modes with lower 1.729T and higher 1.902T magnetic field levels.

For DC130 the shaping of the sector height from the pole side was chosen as more convenient for sector machining and for placing the removable shims on the straight edges of sectors. Furthermore, from Fig. 4, the operation mode for acceleration of ions with $A/Z=8$ is chosen as nominal, where isochronous magnetic field will be formed only by metal, without use of correcting coils.

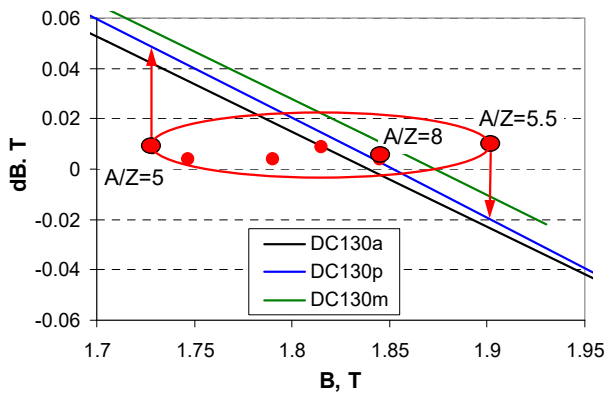


Figure 5: dB(B) functions for three ways of sector shaping and characteristic operation modes.

For DC130 cyclotron magnet the two methods to form the magnetic field at the extraction radius are used. The first one is the chamfer 20x20mm at the outer edge of the sector, see Fig. 3. The chamfer lifts the average field and kick up the flutter at the extraction radiuses, Figs. 6 and 7.

The second one is the ring shim, that is placed between sector and pole at the outer radiuses 960 – 1000 mm. The ring shim lifts the field, especially at the “valley” between the sectors, that leads to decreasing of the flatter. The use of both methods give the increasing of the beam final energy and efficiency of extraction. Furthermore, the use of both methods gives the compensation of the flatter growth and lets to avoid the dangerous resonances at the last orbits.

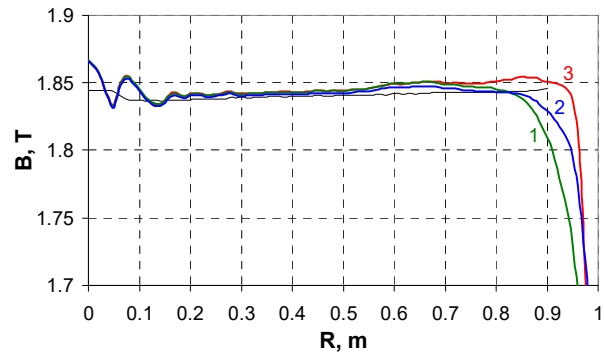


Figure 6: Average magnetic field for cases: 1 – without ring shim and chamfer; 2 – with ring shim; 3 – with ring shim and chamfer.

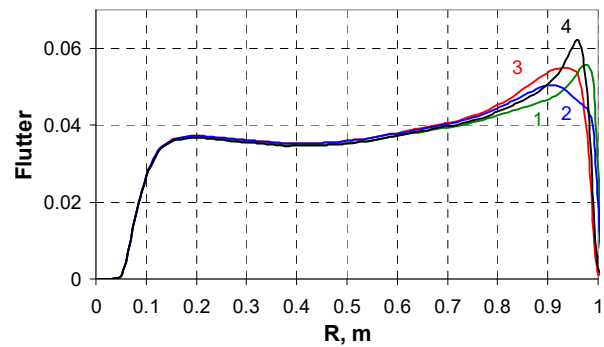


Figure 7: Flutter for cases: 1 – without ring shim and chamfer; 2 – with ring shim; 3 – with ring shim and chamfer; 4 – with chamfer.

RADIAL CORRECTING COILS

To form the isochronous magnetic field for different acceleration modes the radial correcting coils will be used. The coils compensate the difference between isochronous and real magnetic fields. According to Fig. 5, the level of the field compensation must be up to ± 500 Gs for the operation modes with lower 1.729T and upper 1.902T magnetic field levels. For nominal operation mode, acceleration of ions with $A/Z=8$ at $B_0=1.8$ T, the real magnetic field is formed as isochronous by metal only, and the correcting coils are not used. The other goal of radial coils is to correct the beam phase shifting, that arises due to the local magnetic field perturbations. For that purpose, about ± 100 Gs of correction field is enough. The third, additional goal is a correction of possible median shifting of the beam. This shifting could be corrected by means of radial component of magnetic field. To produce Br component, the last coil

has two separate power supplies for upper and lower sub-coils. As a result, DC130 cyclotron magnet must be equipped with radial coils for producing +/-600Gs of correction magnetic field. The coils will be placed in the 20mm gap between pole and sectors.

The number of radial coils is chosen as a compromise between the cost of manufacturing and exploitation and, the accuracy of magnetic field correction. For DC130 cyclotron the 5 radial coils are placed according Eq. (1).

$$R_n = \frac{R_k}{\sqrt{k}} * \sqrt{n} \quad (1)$$

where $n=1 \dots 5$ is a number of coil, $R_k=900\text{mm}$ – radius of the last coil with $k=5$.

The additional coil for field correction at the centre is placed at the radius 220mm. In Fig. 8, the positions and field contributions of DC-130 radial coils with 50A current supply is presented.

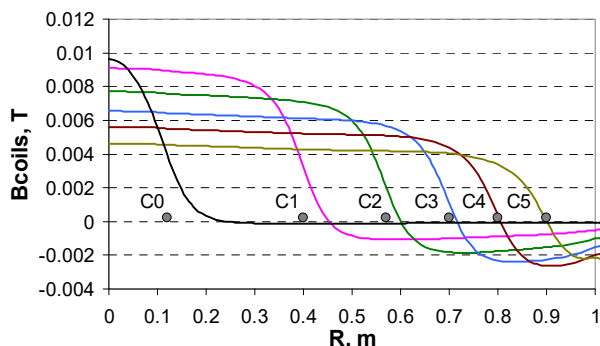


Figure 8: The positions and contributions of the radial coils at the average magnetic field, level 1.729T.

The results of computer formation of test operational modes at the lower, 1.729T, nominal, 1.845T, and higher, 1.902T, levels of magnetic field are presented in Figs. 9, 10 and 11. At figures the “formed field” means the result of correction of the base magnetic field with usage of radial correcting coils. The criteria for the correction is the minimization of the “beam phase” deviation during acceleration. As a result, the phase shifting of accelerated beam at the “formed” magnetic field is no more than $\pm 10^\circ$ for operational modes at lower and higher levels of magnetic field and about $\pm 2^\circ$ for nominal operational mode. The computer formation of the test operational modes, define the needed maximum of the radial coils power consumption as $1500\text{A} \cdot \text{turn}$. For that, the high current coils with 5 turns and 300A of current supply could be used. The wire with $10 \times 10\text{mm}$ cross-section and inner $d5\text{mm}$ hole for cooling is chosen. The alternative is a low current coils with 60 turns and 26A of current supply. At this case, the wire has $2 \times 7\text{mm}$ cross-section and coils are placed in a cooled aluminium box.

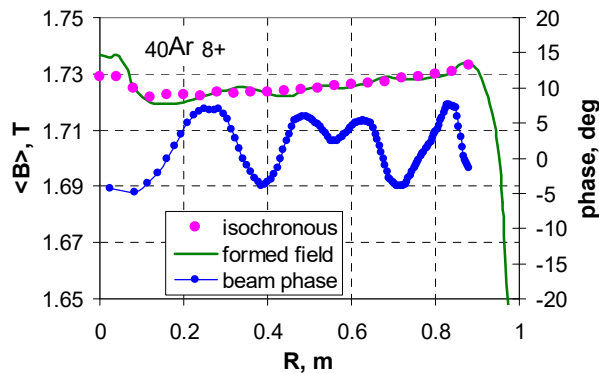


Figure 9: The isochronous and formed magnetic field for $40\text{Ar}8+$ acceleration mode.

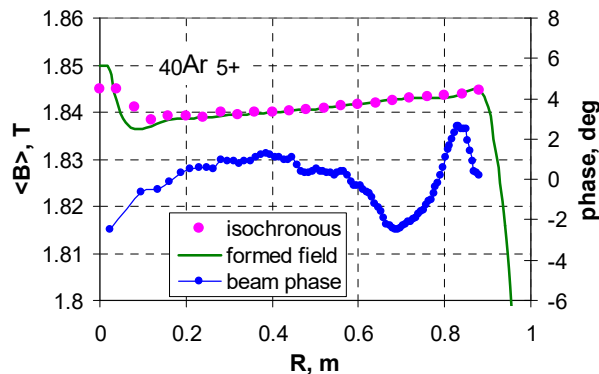


Figure 10: The isochronous and formed magnetic field for $40\text{Ar}5+$ acceleration mode.

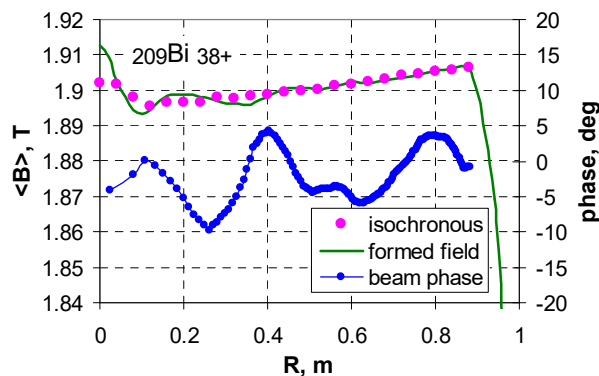


Figure 11: The isochronous and formed magnetic field for $209\text{Bi}38+$ acceleration mode.

CONCLUSION

At the present time, the project of DC130 cyclotron is at the design stage. New cyclotron is intended for applied applications only. The main activity, 6000 hours per year, will be in microchip testing, production of track pore membranes and different applied researches. The criteria of choosing of magnetic structure is a compromise between the costs of manufacturing and exploitation. The cyclotron will provide the fast changing and the optimal parameters for wide range of the given operational modes.

REFERENCES

- [1] S. Mitrofanov *et al.*, “SEE testing facilities at FLNR accelerator complex. State of the art and future plans”, in *Proc. 24th Russian Particle Accelerator Conf. (RuPAC'14)*, 6-10 Oct. 2014, Obninsk, Russia, paper, WECA12, pp. 152-154.
- [2] B. N. Gikal *et al.*, “U200 cyclotron operating experience and upgrade”, JINR preprint, 9-83-311, Dubna, 1983.
- [3] I. A. Ivanenko *et al.*, “The Model of DC72 Cyclotron Magnet. The Research of the Sector Shimming Methods for Obtaining the Working Magnetic Field for Light and Heavy Ions Acceleration”, in *Proc. 8th European Particle Accelerator Conference (EPAC'02)*, Paris, France, 3-7 Jun. 2002, pp. 2349-2351.

List of Authors

Bold papercodes indicate primary authors; ~~crossed-out~~ papercodes indicate 'no submission'

— A —			
Abbon, P.	THP1WB01	Bertrand, Q.	THA1WE04
Adamson, P.	TUA1WD04	Bey, T.	THA1WE04
Adelmann, A.	TUP1WA02	Bhat, C.M.	THP1WC01
Ainsworth, R.	TUA1WD04	Biancacci, N.	MOP2WA05
Akagi, T.	THP1WB01	Binello, S.	TUA2WD03
Albright, S.C.P.	WEP2P0006, THA1WD04	Bjørsvik, E.R.	MOP2WA04
Alekou, A.	WEP2P0008	Blas, A.	WEP2P0001
Aleksandrov, A.V.	MOP1WB02	Blokland, W.	MOP1WB02, TUP2WE01
Aleman-Fernández, R.	THA1WD04	Bogomolov, S.L.	WEP2P0028
Alves, H.	THA1WE04	Bolzon, B.	THP1WB01, THA1WE04
Amorim, D.	MOP2WA05	Borisov, O.N.	WEP2P0028
An, Y.W.	TUA1WD03	Bortolato, D.	WEP1WB02, THP1WB01
Andorf, M.B.	TUP2WA01	Bozyk, L.H.J.	TUP2WA04
Antipov, S. A.	MOP2WA05, THA1WE01	Bracco, C.	WEP2P0007
Antoniuzzi, L.	WEP1WB02, THP1WB01	Brown, B.C.	TUA1WD04
Apel, P.Yu.	WEP2P0028	Buffat, X.	MOP2WA03, MOP2WA05
Appel, S.	WEA2WB02	Busch, M.	WEP1WB03
Appleby, R.B.	WEP2P0008	Butenko, A.V.	TUA2WC02
Arakaki, Y.	THA1WD03		
Argyropoulos, T.	TUP1WA03, TUP2WA02	— C —	
Aulenbacher, K.	WEP1WB03	Calabretta, L.	WEP2P0033
Aune, S.	THA1WE04	Calaga, R.	WEP2P0008
		Capista, D.	TUA1WD04
		Cara, P.	THP1WB01
		Carbajo Perez, D.	TUP2WE04
		Carlà, M.	WEP2P0008, WEP2P0011
		Carneiro, J.-P.	MOP1WB03, THP1WC03
		Carver, L.R.	MOP2WA03, MOP2WA05
		Cavenago, M.	WEP1WB02
		Cettour-Cave, S.	WEA1WA02
		Chancé, A.	THP1WB02
		Chang, W.	TUA1WC03
		Chapochnikova, E.	TUP2WA03, THA1WD04
		Chase, B.E.	THP1WC03
		Chattopadhyay, S.	WEA2WA04
		Chaurize, S.	WEP2P0010, THP1WC01
		Chauvin, N.	THP1WB01, WEA1WB02,
			WEP1WB02, THP1WB02 ,
			THA1WE04
		Chel, S.	THP1WB01
		Chen, A.Z.	THP1WC03
		Chen, J.	TUA1WD03
		Chen, M.	TUA2WC03
		Cheng, A.Q.	TUA2WC03
		Cheon, Y.L.	THP2WB05
		Chin, Y.H.	MOP2WA02
		Chirpaz-Cerbat, D.	TUA2WC01
		Cho, Y.-S.	TUA1WB02
		Choi, C.O.	TUA2WC04
		Choi, H. J.	THA2WD03
		Choi, J.W.	WEP2P0016
		Choi, Y.	WEP2P0015
— B —			
Baffes, C.M.	THP1WC03		
Bakinowskaya, A.A.	TUA2WC02		
Baldo, A.	WEP1WB02		
Baltador, C.	WEP1WB02		
Barth, W.A.	WEP1WB03		
Bartmann, W.	WEP2P0006		
Bartosik, H.	MOA1PL01 , MOP2WA04,		
	TUP2WA03, WEA1WA02,		
	WEA2WA01, WEP2P0008,		
	WEP2P0011, THA1WD04		
Bashevov, V.	WEP2P0028		
Basten, M.	WEP1WB03		
Baturitski, M.A.	TUA2WC02		
Batygin, Y.K.	MOP2WB03		
Baudrenghien, P.	WEP2P0003, THP2WC02		
Bazin, N.	THP1WB01		
Beauvais, P.-Y.	THP1WB01		
Bechtold, A.	TUA1WC01		
Beck, M.S.	MOP2WA04, TUP2WA05,		
	WEP2P0011		
Beebe, E.N.	TUA2WD03		
Bekhterev, V.	WEP2P0028		
Bellan, L.	WEP1WB02, THP1WB01		
Bellodi, G.	MOA1PL03 , MOP2WB02		
Beltramelli, J.	THA1WE04		
Benedetti, S.	MOP2WB02		
Berkovits, D.	TUA1WC01		

Content from this work may be used under the terms of the CC BY 3.0 licence (© 2018). Any distribution of this work must maintain attribution to the author(s), title of the work, publisher, and DOI.

Chung, M. **MOP2WB05**, **WEA2WB02**,
WEA2WA04, **THP2WB02**,
THP2WB05
 Chung, Y.S. **TUP1WE01**
 Coe, B.D. **TUA2WD03**
 Coly, M. R. **WEA1WA02**
 Combet, M. **THA1WE04**
 Compton, C. **TUA1WC03**
 Comunian, M. **WEP1WB02**, **THP1WB01**
 Costanzo, M.R. **TUA2WD03**
 Cotte, D.G. **WEA1WA02**
 Cubizolles, R. **TUA2WC01**
 Curry, D. **MOP1WB02**
 Czuba, K. **THP2WB03**

— D —

Damerau, H. **WEA1WA02**, **THA1WD04**
 de la Morena, C. **THP1WB01**
 De Prisco, R. **TUA1WD01**, **WEP1WB01**,
THP2WB03
 Demyanov, S.E. **TUA2WC02**
 DeSanto, L. **TUA2WD03**
 Desforge, D. **THA1WE04**
 Desmons, M. **THA1WE04**
 Dey, J.E. **THP2WC01**
 Di Giovanni, G.P. **WEA1WA02**, **WEP2P0006**,
WEP2P0007, **THA1WD04**
 Dölling, R. **WEP2P0030**, **WEP2P0032**,
WEP2P0033
 Dolenc Kittelmann, I. **THA1WE04**
 Dong, Z. **TUP2WA04**
 Dou, W.P. **MOP2WB04**
 Drennan, C.C. **WEP2P0010**
 Dressler, R. **WEP2P0033**
 Du, X. **WEA2WB02**
 Ducrot, L. **WEA1WB02**
 Duel, K.L. **THP1WC01**, **THP2WC01**
 Dumas, J. **TUA2WC01**
 Duperrier, R.D. **TUA2WC01**
 Duris, J.P. **THA2WE01**
 Dusatko, J.E. **MOP2WA04**
 Dylan, D. **THA2WE01**
 Dyubkov, V.S. **WEP1WB04**
 Dzitko, H. **WEP1WB02**, **THP1WB01**
 Dziuba, F.D. **WEP1WB03**

— E —

Ebisawa, T. **THP1WB01**
 Edelen, A.L. **TUA1WC04**
 Einstein-Curtis, J. **THP1WC03**
 Emelianov, N. **TUA2WC02**
 Eshraqi, M. **TUA1WC02**, **TUA1WD01**,
WEP1WB01
 Evans, N.J. **TUP2WE01**

— F —

Fagotti, E. **WEP1WB02**, **THP1WB01**
 Farricker, A. **TUP2WA05**
 Fedotov, A.V. **THA2WD02**
 Ferrand, G. **TUA2WC01**
 Fischer, W. **TUP1WE02**
 Fomichev, A.S. **WEP1WB04**
 Forte, V. **WEP2P0006**, **WEP2P0007**
 Fox, J.D. **MOP2WA04**
 Franchetti, G. **WEA1WA01**
 Franko, J. **WEP2P0027**, **WEP2P0028**,
THP2WC03
 Fraser, M.A. **WEP2P0006**, **WEP2P0007**
 Freemire, B.T. **WEA2WA04**
 Frolov, D. **THP1WC03**
 Fu, S. **WEP2P0018**

— G —

Garcia Morales, H. **TUP1WE02**
 Garcia, F.G. **WEP2P0010**
 Garnett, R.W. **MOP2WB03**
 Gąsior, M. **THA1WE03**
 Gastineau, B. **TUA2WC01**
 Gauthier, Y. **THA1WE04**
 Gérardin, F. **THP1WB02**
 Gerhard, P. **WEA2WB02**
 Gettmann, V. **WEP1WB03**
 Gex, D. **THP1WB01**
 Giacchini, M.G. **WEP1WB02**
 Gilardoni, S.S. **WEA1WA02**
 Giner-Demange, E. **THA1WE04**
 Giovannozzi, M. **WEA1WA02**, **WEP2P0002**
 Gobin, R. **THP1WB01**
 Goddard, B. **THA1WD04**
 Gollwitzer, K. E. **WEP2P0010**
 Gomes, A. **THA1WE04**
 Gong, D.J. **WEA1WB01**
 Gorelyshev, I.V. **WEP1WA03**
 Gougnaud, F. **THA1WE04**
 Grespan, F. **WEP1WB02**, **THP1WB01**
 Gressier, V. **THA1WE04**
 Grigorenko, L.V. **WEP1WB04**
 Groening, L. **WEA2WB02**
 Gu, X. **TUP1WE02**
 Gulbekyan, G.G. **WEP2P0027**, **WEP2P0028**,
THP2WC03
 Gusarova, M. **TUA2WC02**

— H —

Hall-Wilton, R.J. **THA1WE04**
 Han, B. **MOP1WB02**
 Han, J.H. **THA2WD03**
 Hanke, K. **THA1WD04**
 Hanna, B.M. **MOP1WB03**, **THP1WC03**
 Hao, J.K. **TUA2WC03**

Harada, H. **THP1WC02**
 Harrault, F. **THA1WE04**
 Hartung, W. **TUA1WC03**
 Hazelwood, K.J. **TUA1WD04**
 He, Y. **MOP1WB01**, **MOP2WB04**,
THP2WB06
WEA2WB01
 He, Z.Q. **WEA2WB01**
 Heidinger, R. **THP1WB01**
 Heilmann, M. **WEP1WB03**
 Heßler, C. **WEP2P0006**
 Hirata, Y. **THP1WB01**
 Höfle, W. **MOP2WA04**
 Höglund, C. **THA1WE04**
 Hofmann, I. **THP2WB01**
 Hong, I.S. **TUA2WC04**
 Hotchi, H. **MOP1WA01**
 Huang, M.Y. **TUA1WD03**, **WEP2P0017**,
WEP2P0022, **WEP2P0023**
 Huschauer, A. **WEA1WA02**, **WEP2P0006**,
THA1WD04

— I —

Iadarola, G. **WEP1WA01**
 Ichimiya, R. **THP1WB01**
 Igarashi, S. **TUA2WD02**
 Iguaz Gutierrez, F. J. **THA1WE04**
 Ikeda, S. **TUA2WD03**
 Ikegami, M. **WEA2WB01**
 Irie, Y. **THP1WC02**
 Ishi, Y. **TUP2WE03**
 Ivanenko, I.A. **WEP2P0027**, **WEP2P0028**,
THP2WC03
TUP2WE03
 Iwamoto, Y. **TUP2WE03**

— J —

Jamilkowski, J.P. **TUA2WD03**
 Jang, H. **TUA2WC04**
 Jang, J.-H. **MOP2PL03**
 Jarvis, J.D. **TUP2WA01**
 Jeon, D. **THP1WB03**
 Ji, H.F. **TUA1WD03**
 Jia, H. **MOP2WB04**
 Jiménez-Rey, D. **THP1WB01**
 Jin, D.P. **WEP2P0023**
 Jin, H. **WEP2P0015**
 Jo, Y.W. **WEP2P0016**
 Joannem, T.J. **THA1WE04**
 Johns, G.D. **MOP1WB02**
 Johnson, D.E. **THP1WC01**
 Johnson, T.R. **THP1WC01**
 Jokinen, A. **THP1WB01**
 Jung, H.C. **WEP2P0016**
 Jung, Y. **WEP2P0016**
 Justice, T.A. **MOP1WB02**

— K —

Kain, V. **WEA1WA02**, **THA1WD04**
 Kaizer, B. **TUA1WC01**
 Kalagin, I.V. **WEP2P0027**, **WEP2P0028**,
THP2WC03
TUA2WD03
 Kanesue, T. **THA2WD03**
 Kang, H.-S. **THP1WC01**
 Karns, P.R. **TUP1WA03**, **WEP2P0003**
 Karpov, I. **TUA2WC02**
 Karpovich, V.A. **THP1WB01**
 Kasugai, A. **WEP2P0027**, **WEP2P0028**,
THP2WC03
 Kazarinov, N.Yu. **THA1WE04**
 Kebbiri, M. **TUP1WE01**
 Kim, G.D. **WEP2P0016**
 Kim, H. **WEP2P0016**
 Kim, J.W. **WEP2P0016**
 Kim, M.S. **WEP2P0016**
 Kim, S.-H. **MOP1WB02**
 Kim, S.H. **THA2WD03**
 Kim, S.H. **TUA1WC03**
 Kim, Y. **WEP2P0016**
 Kimura, T. **THA1WD03**
 Kinsho, M. **THP1WC02**
 Kirpichev, I. **THP1WB01**
 Kling, N.A. **TUA2WD03**
 Knaster, J. **THP1WB01**
 Kondo, K. **THP1WB01**
 Kostromin, S.A. **WEP1WA03**
 Kotzian, G. **MOP2WA04**, **WEP2P0001**
 Koukovini-Platia, E. **WEA1WA02**, **WEA2WA01**
 Kourbanis, I. **TUA1WD04**
 Küchler, D. **MOP2WB02**
 Kürzeder, T. **WEP1WB03**
 Kufer, M.R. **THP2WC01**
 Kuharik, J. **THP2WC01**
 Kulevoy, T. **TUA2WC02**, **WEP1WB04**
 Kuriyama, Y. **TUP2WE03**
 Kwon, J.W. **TUP1WE01**

— L —

Lahonde-Hamdoun, C. **THA1WE04**
 Lalayan, M.V. **TUA2WC02**
 Lamas Garcia, I. **TUP2WE04**
 Lasheen, A. **TUP2WA02**, **TUP2WA03**,
THA1WD04
THA1WE04
 Le Bourlout, P. **THA1WE04**
 Lebedev, V.A. **MOP2WA01**, **MOP1WB03**,
TUP2WA01, **WEP1WA03**,
WEP2P0010, **THA1WE01**,
THP1WC03
 Lee, D.Y. **TUA2WC04**
 Lee, H.-G. **THA2WD03**
 Lee, M. **WEP2P0016**
 Lee, S. **WEP2P0015**
 Lee, S.B. **THA2WD03**

Content from this work may be used under the terms of the CC BY 3.0 licence (© 2018). Any distribution of this work must maintain attribution to the author(s), title of the work, publisher, and DOI.

Lee, Y. **TUP2WE02**
 Lefèvre, T. **THA1WE03**
 Legou, Ph. **THA1WE04**
 Lehn, D. **TUA2WD03**
 Leseigneur, F. **TUA2WC01**
 Leśniak, T.P. **THP2WB03**
 Levens, T.E. **MOP2WA04**
 Levinsen, Y. **TUA1WD01, WEP1WB01**
 Li, H.P. **TUA2WC03**
 Li, J. **WEP2P0024**
 Li, K.S.B. **MOP2WA03, MOP2WA04, WEP2P0011**
 Li, M. **TUP2WA04**
 Li, P. **TUP2WA04**
 Li, Y. **TUA1WD03**
 Li, Z. **THP2WB04**
 Liaw, C.J. **TUA2WD03**
 Liu, S.H. **MOP2WB04, THP2WB06**
 Liu, Y. **MOP2WB01**
 Lo Destro, V. **TUA2WD03**
 Lombardi, A.M. **WEP2P0007**
 Lozeev, Y. **WEP1WB04**
 Lozeeva, T.A. **TUA2WC02, WEP1WB04**
 Lu, X.H. **TUA1WD03**
 Luck, C.F. **TUP2WE01**
 Luner, J. **TUA1WC01**

— M —

Madec, C. **TUA2WC01**
 Madrak, R.L. **THP2WC01**
 Maebara, S. **THP1WB01**
 Maier, M.T. **WEA2WB02**
 Maillard, A. **MOP2WA03**
 Maillard, O. **THA1WE04**
 Makarov, A.V. **THP2WC01**
 Maksimenko, S.A. **TUA2WC02**
 Marcel, A. **THA1WE04**
 Marchand, C. **THA1WE04**
 Mariette, Y. **THA1WE04**
 Marqueta, A. **THP1WB01**
 Marroncle, J. **THP1WB01, THA1WE04**
 Marti, F. **WEA2WB01**
 Maruta, T. **WEA2WB01**
 Mastoridis, T. **THP2WC02**
 Matsievskiy, S.V. **TUA2WC02**
 Matsuda, H. **TUP2WE03**
 McCafferty, D.R. **TUA2WD03**
 McIntire, M.W. **THA2WE01**
 Meddahi, M. **THA1WD04**
 Meigo, S.I. **TUP1WE03, TUP2WE03**
 Méndez, P. **THP1WB01**
 Mereghetti, A. **TUP1WE02**
 Mether, L. **WEP1WA01**
 Métral, E. **MOP2WA03, MOP2WA05**
 Michine, Y. **THP1WC02**
 Migliorati, M. **TUP2WE04, WEA2WA01**

Mikulec, B. **WEA1WA02, WEP2P0007, THA1WD04**
 Milas, N. **TUA1WD01, WEP1WB01**
 Miller, S.J. **TUA1WC03**
 Mirarchi, D. **TUP1WE02**
 Mironov, V.I. **WEP2P0028**
 Miski-Oglu, M. **WEP1WB03**
 Mitrofanov, S.V. **WEP2P0028**
 Miura, A. **MOP2WB01, THP1WC02**
 Miyamoto, R. **TUP2WE02, TUA1WD01, WEP1WB01**
 Miyao, T. **MOP2WB01**
 Mollá, J. **THP1WB01**
 Montis, M. **WEP1WB02, THP1WB01**
 Moon, S.H. **THP2WB02**
 Mori, Y. **THA1WD01**
 Morris, D.K. **TUA1WD04**
 Morris, J. **TUA2WD03**
 Moya, I. **THP1WB01**
 Muñoz, M. **TUA1WD01**
 Murasugi, S. **THA1WD03**
 Muto, R. **THA1WD03**

— N —

Nadot, V. **THA1WE04**
 Nakamoto, T. **TUP2WE03**
 Nemchenko, R.E. **TUA2WC02**
 Nghiem, P.A.P. **WEA1WB02**
 Niita, K. **TUP2WE03**
 Nikolopoulos, K. **THA1WE04**
 Nusbaum, D. **TUA1WC01**

— O —

Oeftiger, A. **WEP2P0006, THA1WE02**
 Okamura, K. **THA1WD03**
 Okamura, M. **TUA2WD03**
 Olsen, R.H. **TUA2WD03**
 Ostroumov, P.N. **WEA2WB01**
 Otani, M. **MOP2WB01**
 Oublaid, M. **THA1WE04**

— P —

Padilla, R.D. **THP2WC01**
 Palmieri, A. **WEP1WB02, THP1WB01**
 Papaevangelou, T. **THA1WE04**
 Papaphilippou, Y. **WEP1WA02, WEP2P0008**
 Papis, R. **THP2WB03**
 Park, B.-S. **TUA2WC04**
 Park, C.S. **WEA2WA04**
 Pellico, W. **WEP2P0010, THP1WC01, THP2WC01**
 Penn, G. **WEA2WA04**
 Perillo, A. **TUP2WE04**
 Perreu, G. **THA1WE04**
 Perry, A. **TUA1WC01**

Peters, C.C. **MOP1WB02**
 Petrakovsky, V.S. **TUA2WC02**
 Phillips, G. **THP1WB01**
 Pichoff, N. **TUA2WC01, THP1WB02**
 Piekarz, H. **TUP2WA01**
 Piot, P. **TUP2WA01**
 Piquet, O. **THA1WE04**
 Pisent, A. **WEP1WB02, THP1WB01**
 Plaisant, Th. **TUA2WC01**
 Plostinar, D.C. **TUA1WD01, WEP1WB01**
 Plouin, J. **TUA2WC01**
 Plum, M.A. **MOP1WB02**
 Pobol, I.L. **TUA2WC02**
 Podadera, I. **THP1WB01**
 Podlech, H. **WEP1WB03**
 Pokrovsky, A.I. **TUA2WC02**
 Polozov, S.M. **TUA2WC02, WEP1WB04**
 Pomorski, M. **THA1WE04**
 Ponton, A. **WEP1WB01**
 Popielarski, J.T. **TUA1WC03**
 Popielarski, L. **TUA1WC03**
 Pottin, B. **THA1WE04**
 Prior, C.R. **TUP1WA01**
 Prost, L.R. **MOP1WB03, THP1WC03**
 Pruneri, G. **THP1WB01**

— Q —

Qin, H. **MOP2WB05**
 Quan, S.W. **TUA2WC03**
 Quartullo, D. **TUP2WA02**

— R —

Rakhman, A. **TUP2WE01**
 Raparia, D. **TUA2WD03**
 Ratner, D.F. **THA2WE01**
 Redaelli, S. **TUP1WE02**
 Regidor, D. **THP1WB01**
 Reid, J. **WEP2P0010, THP2WC01**
 Renard, B. **THP1WB01**
 Repond, J. **TUP2WA03, TUP2WA05**
 Richard, C.J. **MOP1WB03, THP1WC03**
 Rivetta, C.H. **MOP2WA04**
 Robinson, L. **THA1WE04**
 Rodionova, V.N. **TUA2WC02**
 Rodnizki, J. **TUA1WC01**
 Rogers, C.T. **TUP1WA02**
 Rohrer, M. **WEP2P0030, WEP2P0032**
 Romanov, A.L. **TUP2WA01**
 Romanov, G.V. **THP2WC01**
 Ronningen, R.M. **TUP2WE03**
 Ruan, J. **TUP2WA01**
 Rubin, A. **WEA2WB02, WEP1WB03**
 Rumolo, G. **MOA1PL02, WEA2WA01, WEP1WA01, WEP2P0011, THA1WD04**
 Rybarczyk, L. **MOP2WB03**

— S —

Saewert, G.W. **THP1WC03**
 Saha, P.K. **THP1WC02**
 Saini, A. **MOP1WB03, THP1WC03**
 Saito, K. **TUA1WC03**
 Sakamoto, K. **THP1WB01**
 Samoshin, A.V. **TUA2WC02, WEP1WB04**
 Sapinski, M. **THA2WE02**
 Satoh, D. **TUP2WE03**
 Sauce, Y. **THA1WE04**
 Scantamburlo, F. **THP1WB01, WEP1WB02**
 Scarpine, V.E. **MOP1WB03**
 Scharrer, P. **WEA2WB02**
 Schenk, M. **MOP2WA03, MOP2WA04, WEP2P0011**
 Schnase, A. **WEP1WB03**
 Schoepfer, R. **TUA2WD03**
 Schupbach, B.A. **THP1WC01**
 Schwarz, M. **TUP2WA03**
 Schwarz, M. **WEP1WB03**
 Schwindling, J. **THA1WE04**
 Scrivens, R. **THA1WD04**
 Segui, L. **THA1WE04**
 Seiya, K. **THP1WC01**
 Semin, V.A. **WEP2P0028**
 Senée, F. **THA1WE04**
 Seol, K.T. **TUA2WC04**
 Severino, F. **TUA2WD03**
 Shaposhnikova, E.N. **TUP1WA03**
 Sharma, D. **THP1WC03**
 Shatokhin, V.L. **TUA2WC02**
 Shea, T.J. **TUP2WE02, THA1WE04**
 Sheehy, S.L. **TUP1WA02, WEA2WA03**
 Shemyakin, A.V. **MOP1WB03, THP1WC03**
 Shen, L. **WEP2P0023**
 Shibata, T. **MOP2WB01**
 Shiltsev, V.D. **WEA2WA04**
 Shima, T. **TUP2WE03**
 Shinya, T. **THP1WB01**
 Shirakabe, Y. **THA1WD03**
 Shishlo, A.P. **MOP1WB02, WEA1PL01, THA1WB02**
 Shor, A. **TUA1WC01**
 Shparla, D.A. **TUA2WC02**
 Shvedau, A. **TUA2WC02**
 Sidorin, A.O. **TUA2WC02, WEP1WA03**
 Sikora, D. **TUP2WB03**
 Silverman, I. **TUA1WC01**
 Simeoni, W. **WEA1WB02**
 Singh, R. **THA2WE02**
 Sista, V.L. **MOP1WB03**
 Skuratov, V.A. **WEP2P0028**
 Slabaugh, M. **THP2WC01**
 Slimmer, D. **THP1WC01**
 Smart, L. **TUA2WD03**

Content from this work may be used under the terms of the CC BY 3.0 licence (© 2018). Any distribution of this work must maintain attribution to the author(s), title of the work, publisher, and DOI.

Sobenin, N.P. TUA2WC02
 Son, K.T. TUA2WC04
 Sounas, A. THA1WE03
 Southern, T.B. MOP1WB02
 Stancari, G. TUP1WE02, WEA2WA04
 Stark, S. TUA1WC03
 Steck, M. MOP1WA03
 Steerenberg, R. THA2WD01
 Steinhagen, R.J. TUA2WD01
 Sterbini, G. WEA1WA02
 Stockli, M.P. MOP1WB02
 Storey, J.W. THA2WE02
 Stupakov, G. WEA2WA02
 Sugimoto, M. THP1WB01
 Sun, D. THP1WC03, THP2WC01
 Surkov, D.V. TUA2WC02
 Svensson, P. THA1WE04
 Syresin, E. TUA2WC02

— T —

Taletskiy, K.V. TUA2WC02
 Tan, C.-Y. WEP2P0010, THP2WC01
 Tang, J.Y. MOP1WB02
 Tecker, F. WEA1WA02, THA1WD04
 Teofili, L. TUP2WE04
 Terechkine, I. THP2WC01
 Thomsen, H.D. TUP2WE02
 Tikhomirov, A. WEP2P0028
 Timko, H. TUP1WA03, TUP2WA03
 Toivanen, V. MOP2WB02
 Tomizawa, M. THA1WD03
 Touzery, R. THA1WE04
 Trubnikov, G.V. TUA2WC02
 Tsiledakis, G. THA1WE04
 Turgut, O. MOP2WA04
 Tuske, O. THA1WE04

— U —

Uesugi, T. TUP2WE03
 Uriot, D. WEA1WB02, THP1WB02,
 THA1WE04

— V —

Valette, M. WEA1WB02
 Valishev, A. WEA1PL02
 Van der Veken, F.F. WEP2P0002
 van Rienen, U. WEP2P0011
 Vilsmeier, D.M. THA2WE02
 Vollinger, C. TUP2WA05
 Vormann, H. WEA2WB02

— W —

Wagner, J.F. TUP1WE02

Wang, C. MOP2WB04
 Wang, F. TUA2WC03
 Wang, S. MOP2PL01, TUA1WD03,
 WEP2P0017, WEP2P0022,
 WEP2P0023
 Wang, Z.J. MOP2WB04, THP2WB06
 Weber, M. THP1WB01
 Wei, J. WEA2WB01
 Weissman, L. TUA1WC01
 Welton, R.F. MOP1WB02
 Wenander, F.J.C. MOP2WB02
 Wenninger, J. THA2WD01
 Woo, H.J. TUP1WE01

— X —

Xiao, C. WEA2WB02
 Xiao, M. TUA1WD04
 Xu, S.Y. TUA1WD03, WEP2P0017,
 WEP2P0018, WEP2P0022,
 WEP2P0023
 Xu, T. TUA1WC03

— Y —

Yamane, I. THP1WC02
 Yamazaki, Y. WEA2WB01
 Yan, F. WEA1WB01
 Yanaoka, E. THA1WD03
 Yang, J.C. MOP1WA02, TUP2WA04,
 WEP2P0024
 Yang, M.-J. TUA1WD04
 Yang, Y. WEA2WB03
 Yao, W. WEA1WB01
 Yaramyshev, S. WEP1WB03
 Yashima, H. TUP2WE03
 Yin, D.Y. TUP2WA06
 Yoneda, H. THP1WC02
 Yoshiie, T. TUP2WE03
 Yoshimoto, M. THP1WC02
 Yurevich, S.V. TUA2WC02

— Z —

Zaleski, V.G. TUA2WC02
 Zeng, R. THP2WB03
 Zeno, K. TUA2WD03
 Zhao, Q. MOP2PL02, WEA2WB01
 Zhu, F. TUA2WC03
 Zhu, P. WEP2P0023
 Żukociński, M. THP2WB03
 Zvyagintsev, V. TUA2WC02
 Zwaska, R.M. WEP2P0010

Institutes List

BARC

Mumbai, India

- Sista, V.L.

Belarussian State University, Scientific Research Institute of Nuclear Problems

Minsk, Belarus

- Rodionova, V.N.

Birmingham University

Birmingham, United Kingdom

- Nikolopoulos, K.

BNL

Upton, Long Island, New York, USA

- Beebe, E.N.
- Binello, S.
- Coe, B.D.
- Costanzo, M.R.
- DeSanto, L.
- Fedotov, A.V.
- Fischer, W.
- Gu, X.
- Ikeda, S.
- Jamilkowski, J.P.
- Kaneshue, T.
- Kling, N.A.
- Lehn, D.
- Liaw, C.J.
- Lo Destro, V.
- McCafferty, D.R.
- Morris, J.
- Okamura, M.
- Olsen, R.H.
- Raparia, D.
- Schoepfer, R.
- Severino, F.
- Smart, L.
- Zeno, K.

BSU

Minsk, Belarus

- Karpovich, V.A.

CalPoly

San Luis Obispo, California, USA

- Mastoridis, T.

CEA/DRF/IRFU

Gif-sur-Yvette, France

- Chancé, A.

CEA/DRT/LIST

Gif-sur-Yvette Cedex, France

- Pomorski, M.

CEA/DSM/IRFU

France

- Abbon, P.
- Bazin, N.
- Bolzon, B.
- Chauvin, N.
- Chel, S.
- Ducrot, L.
- Gobin, R.
- Marroncle, J.
- Renard, B.

CEA/IRFU

Gif-sur-Yvette, France

- Chauvin, N.
- Gérardin, F.
- Nghiem, P.A.P.
- Papaevangelou, T.
- Pichoff, N.

CERN

Geneva, Switzerland

- Albright, S.C.P.
- Alekou, A.
- Alemany-Fernández, R.
- Amorim, D.
- Antipov, S. A.
- Argyropoulos, T.
- Bartmann, W.
- Bartosik, H.
- Baudreghien, P.
- Beck, M.S.
- Bellodi, G.
- Benedetti, S.
- Biancacci, N.
- Bjørsvik, E.R.
- Blas, A.
- Bracco, C.
- Buffat, X.
- Calaga, R.
- Carbajo Perez, D.
- Carlà, M.
- Carver, L.R.
- Cettour-Cave, S.
- Chapochnikova, E.
- Coly, M. R.
- Cotte, D.G.
- Damerau, H.
- Di Giovanni, G.P.
- Farricker, A.
- Forte, V.
- Fraser, M.A.
- Garcia Morales, H.

- Gąsior, M.
- Gilardoni, S.S.
- Giovannozzi, M.
- Goddard, B.
- Hanke, K.
- Heßler, C.
- Huschauer, A.
- Höfle, W.
- Iadarola, G.
- Kain, V.
- Karpov, I.
- Kotzian, G.
- Koukovini-Platia, E.
- Küchler, D.
- Lamas Garcia, I.
- Lasheen, A.
- Lefèvre, T.
- Levens, T.E.
- Li, K.S.B.
- Lombardi, A.M.
- Meddahi, M.
- Mereghetti, A.
- Migliorati, M.
- Mikulec, B.
- Mirarchi, D.
- Métral, E.
- Oeftiger, A.
- Papaphilippou, Y.
- Perillo, A.
- Quartullo, D.
- Redaelli, S.
- Repond, J.
- Rumolo, G.
- Schenk, M.
- Schwarz, M.
- Scrivens, R.
- Shaposhnikova, E.N.
- Sounas, A.
- Steerenberg, R.
- Sterbini, G.
- Storey, J.W.
- Tecker, F.
- Teofili, L.
- Timko, H.
- Valette, M.
- Van der Veken, F.F.
- Vollinger, C.
- Wagner, J.F.
- Wenander, F.J.C.
- Wenninger, J.

CIEMAT

Madrid, Spain

- de la Morena, C.
- Jiménez-Rey, D.
- Kirpichev, I.
- Mollá, J.
- Méndez, P.
- Podadera, I.
- Regidor, D.
- Weber, M.

Cockcroft Institute

Warrington, Cheshire, United Kingdom

- Appleby, R.B.

CSNS

Guangdong Province, People's Republic of China

- Lu, X.H.

CSU

Fort Collins, Colorado, USA

- Edelen, A.L.

ENS

Paris, France

- Maillard, A.

EPFL

Lausanne, Switzerland

- Mether, L.
- Schenk, M.

ESS

Lund, Sweden

- De Prisco, R.
- Dolenc Kittelmann, I.
- Eshraqi, M.
- Hall-Wilton, R.J.
- Höglund, C.
- Lee, Y.
- Levinsen, Y.
- Milas, N.
- Miyamoto, R.
- Muñoz, M.
- Plostinar, D.C.
- Ponton, A.
- Robinson, L.
- Shea, T.J.
- Svensson, P.
- Zeng, R.

F4E

Germany

- Beauvais, P.-Y.
- Dzitko, H.
- Gex, D.
- Jokinen, A.
- Phillips, G.

Fermilab

Batavia, Illinois, USA

- Adamson, P.
- Ainsworth, R.
- Baffes, C.M.
- Bhat, C.M.
- Brown, B.C.
- Capista, D.

- Carneiro, J.-P.
- Chase, B.E.
- Chaurize, S.
- Chen, A.Z.
- Dey, J.E.
- Drennan, C.C.
- Duel, K.L.
- Einstein-Curtis, J.
- Frolov, D.
- Garcia, F.G.
- Gollwitzer, K. E.
- Hanna, B.M.
- Hazelwood, K.J.
- Jarvis, J.D.
- Johnson, D.E.
- Johnson, T.R.
- Karns, P.R.
- Kourbanis, I.
- Kufer, M.R.
- Kuharik, J.
- Lebedev, V.A.
- Madrak, R.L.
- Makarov, A.V.
- Morris, D.K.
- Padilla, R.D.
- Park, C.S.
- Pellico, W.
- Piekarz, H.
- Piot, P.
- Prost, L.R.
- Reid, J.
- Romanov, A.L.
- Romanov, G.V.
- Ruan, J.
- Saewert, G.W.
- Saini, A.
- Scarpine, V.E.
- Schupbach, B.A.
- Seiya, K.
- Shemyakin, A.V.
- Shiltsev, V.D.
- Slabaugh, M.
- Slimmer, D.
- Stancari, G.
- Sun, D.
- Tan, C.-Y.
- Terechkine, I.
- Valishev, A.
- Xiao, M.
- Yang, M.-J.
- Zwaska, R.M.

FRIB

East Lansing, USA

- Chang, W.
- Compton, C.
- Hartung, W.
- He, Z.Q.
- Ikegami, M.
- Kim, S.H.
- Marti, F.

- Maruta, T.
- Miller, S.J.
- Ostroumov, P.N.
- Popielarski, J.T.
- Popielarski, L.
- Ronningen, R.M.
- Saito, K.
- Stark, S.
- Wei, J.
- Xu, T.
- Yamazaki, Y.
- Zhao, Q.

Fusion for Energy

Garching, Germany

- Cara, P.
- Heidinger, R.
- Moya, I.

GANIL

Caen, France

- Toivanen, V.

GSI

Darmstadt, Germany

- Appel, S.
- Barth, W.A.
- Bozyk, L.H.J.
- Du, X.
- Franchetti, G.
- Gerhard, P.
- Groening, L.
- Heilmann, M.
- Hofmann, I.
- Maier, M.T.
- Rubin, A.
- Sapinski, M.
- Scharrer, P.
- Schnase, A.
- Singh, R.
- Steck, M.
- Steinhagen, R.J.
- Vilsmeier, D.M.
- Vormann, H.
- Xiao, C.
- Yaramyshev, S.

HIM

Mainz, Germany

- Aulenbacher, K.
- Barth, W.A.
- Dziuba, F.D.
- Gettmann, V.
- Kürzeder, T.
- Miski-Oglu, M.
- Scharrer, P.

IAP

Frankfurt am Main, Germany

- Basten, M.
- Busch, M.
- Podlech, H.
- Schwarz, M.
- Wagner, J.F.

- Yao, W.
- Zhu, P.

IKP

Mainz, Germany

- Aulenbacher, K.

IBS

Daejeon, Republic of Korea

- Choi, C.O.
- Choi, J.W.
- Choi, Y.
- Chung, Y.S.
- Hong, I.S.
- Jang, H.
- Jang, J.-H.
- Jeon, D.
- Jin, H.
- Jo, Y.W.
- Jung, H.C.
- Jung, Y.
- Kim, G.D.
- Kim, H.
- Kim, J.W.
- Kim, M.S.
- Kim, Y.
- Lee, D.Y.
- Lee, M.
- Lee, S.
- Park, B.-S.
- Seol, K.T.
- Son, K.T.
- Woo, H.J.

IMP/CAS

Lanzhou, People's Republic of China

- Dong, Z.
- Dou, W.P.
- He, Y.
- Jia, H.
- Li, J.
- Li, M.
- Li, P.
- Liu, S.H.
- Wang, C.
- Wang, Z.J.
- Yang, J.C.
- Yang, Y.
- Yin, D.Y.

INFN-Roma1

Rome, Italy

- Migliorati, M.

INFN/LNL

Legnaro (PD), Italy

- Antoniazzi, L.
- Baldo, A.
- Baltador, C.
- Bellan, L.
- Bortolato, D.
- Cavenago, M.
- Comunian, M.
- Fagotti, E.
- Giacchini, M.G.
- Grespan, F.
- Montis, M.
- Palmieri, A.
- Pisent, A.
- Scantamburlo, F.

IF-UFRGS

Porto Alegre, Brazil

- Simeoni, W.

IFMIF/EVEDA

Rokkasho, Japan

- Knaster, J.
- Marqueta, A.
- Pruneri, G.
- Scantamburlo, F.

INFN/LNS

Catania, Italy

- Calabretta, L.

IHEP

Beijing, People's Republic of China

- An, Y.W.
- Chen, J.
- Fu, S.
- Gong, D.J.
- Huang, M.Y.
- Ji, H.F.
- Jin, D.P.
- Li, Y.
- Shen, L.
- Wang, S.
- Xu, S.Y.
- Yan, F.

INP BSU

Minsk, Belarus

- Baturitski, M.A.
- Maksimenko, S.A.

IRFU, CEA, University Paris-Saclay

Gif-sur-Yvette, France

- Alves, H.
- Aune, S.
- Beltramelli, J.

- Bertrand, Q.
- Bey, T.
- Bolzon, B.
- Chauvin, N.
- Chirpaz-Cerbat, D.
- Combet, M.
- Cubizolles, R.
- Desforge, D.
- Desmons, M.
- Dumas, J.
- Duperrier, R.D.
- Ferrand, G.
- Gastineau, B.
- Gauthier, Y.
- Giner-Demange, E.
- Gomes, A.
- Gougnaud, F.
- Harrault, F.
- Iguaz Gutierrez, F. J.
- Joannem, T.J.
- Kebbiri, M.
- Lahonde-Hamdoun, C.
- Le Boulout, P.
- Legou, Ph.
- Leseigneur, F.
- Madec, C.
- Maillard, O.
- Marcel, A.
- Marchand, C.
- Mariette, Y.
- Marroncle, J.
- Nadot, V.
- Oublaid, M.
- Perreu, G.
- Pichoff, N.
- Piquet, O.
- Plaisant, Th.
- Plouin, J.
- Pottin, B.
- Sauce, Y.
- Schwindling, J.
- Segui, L.
- Senée, F.
- Touzery, R.
- Tsiledakis, G.
- Tuske, O.
- Uriot, D.

IRSN

Saint-Paul-Lez-Durance, France

- Gressier, V.

ISA

Aarhus, Denmark

- Thomsen, H.D.

ITEP

Moscow, Russia

- Kulevoy, T.

J-PARC, KEK & JAEA

Ibaraki-ken, Japan

- Otani, M.
- Shibata, T.

JAEA/J-PARC

Tokai-Mura, Naka-Gun, Ibaraki-Ken, Japan

- Harada, H.
- Hotchi, H.
- Kinsho, M.
- Matsuda, H.
- Meigo, S.I.
- Miura, A.
- Saha, P.K.
- Yoshimoto, M.

JAEA

Ibaraki-ken, Japan

- Iwamoto, Y.
- Satoh, D.

JINR/FLNR

Moscow region, Russia

- Fomichev, A.S.
- Grigorenko, L.V.

JINR/VBLHEP

Dubna, Moscow region, Russia

- Gorelyshev, I.V.

JINR

Dubna, Moscow Region, Russia

- Apel, P.Yu.
- Bashevoy, V.
- Bekhterev, V.
- Bogomolov, S.L.
- Borisov, O.N.
- Butenko, A.V.
- Emelianov, N.
- Franko, J.
- Gulbekyan, G.G.
- Ivanenko, I.A.
- Kalagin, I.V.
- Kazarinov, N.Yu.
- Kostromin, S.A.
- Mironov, V.I.
- Mitrofanov, S.V.
- Semin, V.A.
- Sidorin, A.O.
- Skuratov, V.A.
- Syresin, E.
- Tikhomirov, A.
- Trubnikov, G.V.

KAERI

Daejeon, Republic of Korea

- Cho, Y.-S.

61st ICFA ABDW on High-Intensity and High-Brightness Hadron Beams HB2018, Daejeon, Korea JACoW Publishing
 ISBN: 978-3-95450-202-8

Content from this work may be used under the terms of the CC BY 3.0 licence (© 2018). Any distribution of this work must maintain attribution to the author(s), title of the work, publisher, and DOI.

KEK/JAEA
 Ibaraki-Ken, Japan
 • Liu, Y.

KEK
 Ibaraki, Japan
 • Arakaki, Y.
 • Chin, Y.H.
 • Igarashi, S.
 • Irie, Y.
 • Kimura, T.
 • Miyao, T.
 • Murasugi, S.
 • Muto, R.
 • Nakamoto, T.
 • Okamura, K.
 • Shirakabe, Y.
 • Tomizawa, M.
 • Yamane, I.
 • Yanaoka, E.

Korea University
 Seoul, Republic of Korea
 • Kwon, J.W.

Kyoto University, Research Reactor Institute
 Osaka, Japan
 • Ishi, Y.
 • Kuriyama, Y.
 • Mori, Y.
 • Uesugi, T.
 • Yashima, H.
 • Yoshiie, T.

LANL
 Los Alamos, New Mexico, USA
 • Batygin, Y.K.
 • Garnett, R.W.
 • Rybarcyk, L.

LBNL
 Berkeley, California, USA
 • Penn, G.

Mainz University
 Mainz, Germany
 • Scharrer, P.

MEPhI
 Moscow, Russia
 • Dyubkov, V.S.
 • Gusarova, M.
 • Kulevoy, T.
 • Lalayan, M.V.
 • Lozeev, Y.
 • Lozeeva, T.A.

• Matsievskiy, S.V.
 • Nemchenko, R.E.
 • Polozov, S.M.
 • Samoshin, A.V.
 • Shatokhin, V.L.
 • Sobenin, N.P.
 • Surkov, D.V.
 • Taletskiy, K.V.
 • Zvyagintsev, V.

Northern Illinois University
 DeKalb, Illinois, USA
 • Chattopadhyay, S.

Northern Illinois University
 DeKalb, Illinois, USA
 • Andorf, M.B.
 • Freemire, B.T.
 • Piot, P.

NSCL
 East Lansing, Michigan, USA
 • Richard, C.J.

NTG Neue Technologien GmbH & Co KG
 Gelnhausen, Germany
 • Bechtold, A.

ORNL RAD
 Oak Ridge, Tennessee, USA
 • Curry, D.
 • Evans, N.J.
 • Johns, G.D.
 • Peters, C.C.
 • Southern, T.B.

ORNL
 Oak Ridge, Tennessee, USA
 • Aleksandrov, A.V.
 • Blokland, W.
 • Han, B.
 • Justice, T.A.
 • Kim, S.-H.
 • Luck, C.F.
 • Plum, M.A.
 • Rakhman, A.
 • Shishlo, A.P.
 • Stockli, M.P.
 • Tang, J.Y.
 • Welton, R.F.

PAL
 Pohang, Kyungbuk, Republic of Korea
 • Choi, H. J.
 • Han, J.H.
 • Kang, H.-S.

- Kim, S.H.
- Lee, H.-G.
- Lee, S.B.

Physical-Technical Institute of the National Academy of Sciences of Belarus

Minsk, Belarus

- Bakinowskaya, A.A.
- Petrakovsky, V.S.
- Pobol, I.L.
- Pokrovsky, A.I.
- Shparla, D.A.
- Shvedau, A.
- Yurevich, S.V.
- Zaleski, V.G.

PKU

Beijing, People's Republic of China

- Chen, M.
- Cheng, A.Q.
- Hao, J.K.
- Li, H.P.
- Quan, S.W.
- Wang, F.
- Zhu, F.

PPPL

Princeton, New Jersey, USA

- Qin, H.

PSI

Villigen PSI, Switzerland

- Adelman, A.
- Dressler, R.
- Dölling, R.
- Rohrer, M.

QST

Aomori, Japan

- Akagi, T.
- Ebisawa, T.
- Hirata, Y.
- Ichimiya, R.
- Kasugai, A.
- Kondo, K.
- Maebara, S.
- Sakamoto, K.
- Shinya, T.
- Sugimoto, M.

RCNP

Osaka, Japan

- Shima, T.

Research Organization for Information Science & Technology

Ibaraki, Japan

- Niita, K.

Rostock University, Faculty of Computer Science and Electrical Engineering

Rostock, Germany

- van Rienen, U.

Royal Holloway, University of London

Surrey, United Kingdom

- Garcia Morales, H.

RRCAT

Indore (M.P.), India

- Sharma, D.

Saint Petersburg State University

Saint Petersburg, Russia

- Sidorin, A.O.

Sapienza University of Rome

Rome, Italy

- Migliorati, M.

Scientific-Practical Materials Research Centre of the National Academy of Sciences of Belarus

Minsk, Belarus

- Demyanov, S.E.

SCU

Chengdu, People's Republic of China

- Li, Z.

SLAC

Menlo Park, California, USA

- Duris, J.P.
- Dusatko, J.E.
- Fox, J.D.
- McIntire, M.W.
- Ratner, D.F.
- Rivetta, C.H.
- Stupakov, G.

Soreq NRC

Yavne, Israel

- Berkovits, D.
- Kaizer, B.
- Luner, J.
- Nusbaum, D.
- Perry, A.
- Rodnizki, J.
- Shor, A.
- Silverman, I.
- Weissman, L.

Content from this work may be used under the terms of the CC BY 3.0 licence (© 2018). Any distribution of this work must maintain attribution to the author(s), title of the work, publisher, and DOI.

Stanford University

Stanford, California, USA

- [Turgut, O.](#)

- [Czuba, K.](#)
- [Leśniak, T.P.](#)
- [Papis, R.](#)
- [Sikora, D.](#)
- [Żukociński, M.](#)

STFC/RAL/ASTeC

Chilton, Didcot, Oxon, United Kingdom

- [Sheehy, S.L.](#)

STFC/RAL/ISIS

Chilton, Didcot, Oxon, United Kingdom

- [Prior, C.R.](#)
- [Rogers, C.T.](#)

TEMF, TU Darmstadt

Darmstadt, Germany

- [Hofmann, I.](#)

The University of Manchester, The Photon Science Institute

Manchester, United Kingdom

- [Mirarchi, D.](#)

TRIUMF, Canada's National Laboratory for Particle and Nuclear Physics

Vancouver, Canada

- [Zvyagintsev, V.](#)

UCSC

Santa Cruz, California, USA

- [Dylan, D.](#)

UMAN

Manchester, United Kingdom

- [Appleby, R.B.](#)

UNIST

Ulsan, Republic of Korea

- [Cheon, Y.L.](#)
- [Chung, M.](#)
- [Moon, S.H.](#)

Univ. degli Studi di Padova

Padova, Italy

- [Bellan, L.](#)

University of Electro-communications

Tokyo, Japan

- [Michine, Y.](#)
- [Yoneda, H.](#)

Warsaw University of Technology, Institute of Electronic Systems

Warsaw, Poland

Name	Affiliation
Aaron Farricker	CERN
Adrian Oeftiger	CERN
Alexander Huschauer	CERN
Alexander Valishev	Fermi National Accelerator Laboratory
Alexei V. Fedotov	Brookhaven National Laboratory
Alfred Blas	CERN
Andreas Adelman	Paul Scherrer Institut
Andrei Shishlo	ORNL
Apostolos Sounas	CERN
Auralee Edelen	Fermi National Accelerator Laboratory (Fermilab)
Baudrenghien	CERN
Bum-Sik Park	IBS
Byoung Seob Lee	Korea Basic Science Institute
Byounghwi, Kang	IBS
Chang-Kyu Sung	UNIST
Charles Peters	Spallation Neutron Source
Chong Shik Park	Fermi National Accelerator Laboratory (Fermilab)
Chris Prior	STFC Rutherford Appleton Laboratory
Christine Schwarz	-
Daniele Mirarchi	CERN
David Amorim	CERN
David Bruhwiler	RadiaSoft LLC
David Johnson	Fermi National Accelerator Laboratory
Dayu Yin	Institute of Modern Physics, CAS
Do Gyun Kim	IBS
Donghyun Kwak	UNIST
Dong-O Jeon	IBS
Eirini Koukovini-platia	CERN
Elena Shemyakina	-
Eunje Lee	Korea Atomic Energy Research Institute (KAERI)
F. Zhu	Institute of Heavy Ion Physics, Peking University
Fang Yan	IHEP
Fernanda G. Garcia	Fermi National Accelerator Laboratory
Frederik Van der Veken	CERN
Gennady Stupakov	SLAC
Giovanni Rumolo	CERN
Giulia Bellodi	CERN
Giuliano Franchetti	GSI Helmholtzzentrum für Schwerionenforschung GmbH
Hannes Bartosik	CERN
Hee-Seock Lee	Pohang Accelerator Laboratory
Heetae Kim	IBS/RISP
Helga Timko	CERN
Hideaki Hotchi	JAEA/J-PARC
Hidefumi Okita	Kyoto University
Hoechun Jung	IBS
Hong, In-Seok	IBS
Hyock-Jun Son	IBS
Hyo-jin Choi	Pohang Accelerator Laboratory (PAL)
Hyun Man, Jang	IBS
Hyunchang Jin	IBS
Hyung Jin Kim	IBS
Ingo Hofmann	GSI/Technical University Darmstadt
Inwoo Chun	Korea University

Name

Affiliation

Ivan Ivanenko	FLNR JINR
Ivan Karpov	CERN
Jangyoul Kim	IBS
Jean-Michel Lagniel	GANIL
Jie Li	Institute of Modern Physics
Ji-Ho Jang	IBS
John Popielarski	Michigan State University
Jonathan Jarvis	Fermi National Accelerator Laboratory
Jongdae Joo	IBS
Joseph Patrick Duris	SLAC National Accelerator Laboratory (SLAC)
K. Hanke	CERN
Kevin Li	CERN
Kwon Jangwon	IBS/RISP
Lars Groening	GSI Helmholtzzentrum für Schwerionenforschung GmbH
Lee Jin Ho	IBS
Lee, Min Ki	IBS
Leo Weissman	Soreq NRC
Lorenzo Teofili	Sapienza University of Rome
Lotta Mether	CERN
Mamad Eshraqi	European Spallation Source ERIC
Marco Schippers	Paul Scherrer Institut
Mariusz Sapinski	GSI Helmholtzzentrum für Schwerionenforschung GmbH
Markus Schwarz	CERN
Markus Steck	GSI Helmholtzzentrum für Schwerionenforschung GmbH
Maruta Tomizawa	KEK/J-PARC
Michael Schenk	CERN & EP2I
Michele Comunian	INFN - LNL
Michiko Minty	Brookhaven National Laboratory
Moses Chung	UNIST
Natalia Milas	European Spallation Source ERIC
Nicolas Chauvin	CEA/IRFU
Nicolas Pichoff	CEA/IRFU/DACM
Nikolay Kazarinov	JINR
P. A. Phi NGHIEM	CEA/IRFU
Panagiota Papakonstantinou	IBS/RISP
Papaevangelou	CEA/IRFU/Université Paris-Saclay
Park, Young Ho	IBS
Peng Li	Institute of Modern Physics, CAS
Peter Forck	GSI Helmholtzzentrum für Schwerionenforschung GmbH
Pranab Saha	J-PARC
Prof. Y.Mori	Kyoto University
Qiang Zhao	Michigan State University
Quartullo Danilo	CERN
Raisa Kazarinova	JINR
Ralph J. Steinhagen, GSI	GSI Darmstadt
Rende Steerenberg	CERN
Rihua Zeng	European Spallation Source ERIC
Rob Ainsworth	Fermi National Accelerator Laboratory
Robyn Madrak	Fermi National Accelerator Laboratory
Rudolf Doelling	Paul Scherrer Institut
Sangil, Lee	IBS
Sasha Shemyakin	Fermi National Accelerator Laboratory
Seok Ho Moon	UNIST

Name	Affiliation
Sergei Kostromin	JINR
Sergey M. Polozov	NRNU MEPhI
Seung Hee Nam	Korea University
Seunghyun Lee	Korea Atomic Energy Research Institute (KAERI) Korea Multi-purpose Accelerator Complex (KOMAC)
Sheng Wang	IHEP
Shin, Taeksu	IBS
Shin-ichiro Meigo	JAEA/J-PARC
Shou Yan Xu	Institute of High Energy Physics, Chinese Academy of Sciences(CAS)
Shuang Ruan	Institute of Modern Physics, Chinese Academy Sciences
Shuhui Liu	Institute of Modern Physics, CAS
Sukjin Choi	IBS
Sun Chan Jeong	IBS
Susumu Igarashi	KEK
Taekyung Ki	IBS
Takeshi Kanesue	Brookhaven National Laboratory
Valeri Lebedev	Fermi National Accelerator Laboratory
Vincenzo Forte	CERN
Weiping Dou	Institute of Modern Physics, CAS
Willem Blokland	ORNL
Winfried Barth	GSI Helmholtzzentrum für Schwerionenforschung GmbH
Woo, Hyung Joo	IBS/RISP
Yannis Papaphilippou	CERN
Yao Yang	Institute of Modern Physics, CAS
YeonseI Chung	IBS/RISP
Yong Ho Chin	KEK
Yong Liu	KEK
Yongjoong Lee	European Spallation Source ERIC
Yong-Sub Cho	KAERI
Yoolim Cheon	UNIST
Yoshito Shimosaki	National Institutes for Quantum and Radiological Science and Technology (QST)
Yosuke Iwamoto	JAEA
Youngjin, Kim	IBS
Yuri Batygin	Los Alamos National Laboratory
Zhihui LI	Institute of Nuclear Science and Technology